PROCEEDINGS OF SPIE

SPIE—The International Society for Optical Engineering

First International Symposium on

Laser Precision Microfabrication

Isamu Miyamoto
Koji Sugioka
Thomas W. Sigmon
Chairs/Editors

14–16 June 2000
Omiya, Saitama, Japan

Organized by
JLPS—Japan Laser Processing Society
RIKEN—The Institute of Physical and Chemical Research (Japan)
SPIE—The International Society for Optical Engineering

Sponsored by
USAFOSR AOARD—U.S. Airforce Office of Scientific Research
Asian Office of Aerospace Research and Development
Saitama Foundation for Culture and Industry (Japan)

DISTRIBUTION STATEMENT A
Approved for Public Release
Distribution Unlimited



Volume 4088

DEPARTMENT OF THE AIR FORCE
ASIAN OFFICE OF AEROSPACE RESEARCH AND DEVELOPMENT (AOARD)
UNIT 45002, APO AP 96337-5002

6 Dec 00

MEMORANDUM FOR Defense Technical Information Center (DTIC)
8725 John J. Kingman Road, Suite 0944
Fort Belvoir VA 22060-6218

FROM: AOARD
Unit 45002
APO AP 96337-5002

SUBJECT: Submission of Document

1. Conference Proceedings from the "First International Symposium on Laser Precision Microfabrication" held 14-16 Jun 00, in Omiya, Saitama, Japan, is attached as a DTIC submittal.

2. Please contact our Administrative Officer, Dr. Jacque Hawkins, AOARD, DSN: 315 229-3388, DSN FAX: 315-229-3133; Commercial phone/FAX: 81-3-5410-4409/4407; e-mail: hawkinsj@aoard.af.mil, if you need additional information.

TERENCE J. LYONS, M.D., M.P.H.
Director, AOARD

Attachments:
1. AF Form 298/Documentation Page (CSP-00-07)
2. DTIC Form 50/DTIC Accession Notice
3. Conference Proceedings of "First International Symposium on Laser Precision Microfabrication"

20001213 153

REPORT DOCUMENTATION PAGE

Form Approved

OMB No. 0704-0188

The public reporting burden for this collection of information is estimated to average 1 hour per response, including the time for reviewing instructions, searching existing data sources, gathering and maintaining the data needed, and completing and reviewing the collection of information. Send comments regarding this burden estimate or any other aspect of this collection of information, including suggestions for reducing the burden, to Department of Defense, Washington Headquarters Services, Directorate for Information Operations and Reports (0704-0188), 1215 Jefferson Davis Highway, Suite 1204, Arlington, VA 22202-4302. Respondents should be aware that notwithstanding any other provision of law, no person shall be subject to any penalty for failing to comply with a collection of information if it does not display a currently valid OMB control number.

PLEASE DO NOT RETURN YOUR FORM TO THE ABOVE ADDRESS.

1. REPORT DATE *(DD-MM-YYYY)*	2. REPORT TYPE	3. DATES COVERED *(From - To)*
06-12-2000	Conference Proceedings	14-16 Jun 00

4. TITLE AND SUBTITLE

Laser Precision Microfabrication (LPM 2000), held 14-16 Jun 00, in Omiya, Saitama, Japan

5a. CONTRACT NUMBER

F6256200M9111

5b. GRANT NUMBER

5c. PROGRAM ELEMENT NUMBER

6. AUTHOR(S)

Conference Committee

5d. PROJECT NUMBER

5e. TASK NUMBER

5f. WORK UNIT NUMBER

7. PERFORMING ORGANIZATION NAME(S) AND ADDRESS(ES)

Osaka University, Graduate School of Engineering, Department of Manufacturing Science
2-1 Yamada-oka, Suita
Osaka 565-0871
Japan

8. PERFORMING ORGANIZATION REPORT NUMBER

N/A

9. SPONSORING/MONITORING AGENCY NAME(S) AND ADDRESS(ES)

AOARD
UNIT 45002
APO AP 96337-5002

10. SPONSOR/MONITOR'S ACRONYM(S)

AOARD

11. SPONSOR/MONITOR'S REPORT NUMBER(S)

CSP-00-07

12. DISTRIBUTUION/AVAILABILITY STATEMENT

Approved for public release; distribution is unlimited.

13 SUPPLEMENTARY NOTES

14. ABSTRACT

CONFERENCE PROCEEDINGS INCLUDES:

Overview of Microfabrication; Ultrafast-Pulse Processing; Modification; Fundamental Aspects; Microfabrication; Industrial Applications; Laser Systems and Optical Elements; Surface Microstructuring; Microwelding and Cutting; Pulsed –Laser Deposition; Microsystems; Glass Materials Processing, and Advanced Applications.

15. SUBJECT TERMS

Lasers, Micro Fabrication

16. SECURITY CLASSIFICATION OF:			17. LIMITATION OF ABSTRACT	NUMBER OF PAGES	19a. NAME OF RESPONSIBLE PERSON
a. REPORT	b. ABSTRACT	c. THIS PAGE			Joanne H. Maurice
U	U	U	UU	410	19b. TELEPHONE NUMBER *(Include area code)* +81-3-5410-4409

Standard Form 298 (Rev. 8/98)
Prescribed by ANSI Std. Z39.18

First International Symposium on

Laser Precision Microfabrication

Isamu Miyamoto
Koji Sugioka
Thomas W. Sigmon
Chairs/Editors

14–16 June 2000
Omiya, Saitama, Japan

Organized by
JLPS—Japan Laser Processing Society
RIKEN—The Institute of Physical and Chemical Research (Japan)
SPIE—The International Society for Optical Engineering

Sponsored by
USAFOSR AOARD—U.S. Airforce Office of Scientific Research
Asian Office of Aerospace Research and Development
Saitama Foundation for Culture and Industry (Japan)

Cooperating Organizations
HTS—High Temperature Society of Japan
JSAP—The Japan Society of Applied Physics
JSPE—The Japan Society for Precision Engineering
JWES—The Japan Welding Engineering Society
JWS—The Japan Welding Society
LSJ—The Laser Society of Japan
CRC$_{AST}$—Collaborative Research Center for Advanced Science and Technology, Osaka University (Japan)



Volume 4088

Published by
SPIE—The International Society for Optical Engineering

SPIE is an international technical society dedicated to advancing engineering and scientific applications of optical, photonic, imaging, electronic, and optoelectronic technologies.



The papers appearing in this book compose the proceedings of the technical conference cited on the cover and title page of this volume. They reflect the authors' opinions and are published as presented, in the interests of timely dissemination. Their inclusion in this publication does not necessarily constitute endorsement by the editors or by SPIE. Papers were selected by the conference program committee to be presented in oral or poster format, and were subject to review by volume editors or program committees.

Please use the following format to cite material from this book:

Author(s), "Title of paper," in *First International Symposium on Laser Precision Microfabrication*, Isamu Miyamoto, Koji Sugioka, Thomas W. Sigmon, Editors, Proceedings of SPIE Vol. 4088, page numbers (2000).

ISSN 0277-786X
ISBN 0-8194-3731-X

Published by
SPIE—The International Society for Optical Engineering
P.O. Box 10, Bellingham, Washington 98227-0010 USA
Telephone 1 360/676-3290 (Pacific Time) • Fax 1 360/647-1445
http://www.spie.org/

Copyright©2000, The Society of Photo-Optical Instrumentation Engineers.

Copying of material in this book for internal or personal use, or for the internal or personal use of specific clients, beyond the fair use provisions granted by the U.S. Copyright Law is authorized by SPIE subject to payment of copying fees. The Transactional Reporting Service base fee for this volume is $15.00 per article (or portion thereof), which should be paid directly to the Copyright Clearance Center (CCC), 222 Rosewood Drive, Danvers, MA 01923 USA. Payment may also be made electronically through CCC Online at http://www.directory.net/copyright/. Other copying for republication, resale, advertising or promotion, or any form of systematic or multiple reproduction of any material in this book is prohibited except with permission in writing from the publisher. The CCC fee code is 0277-786X/00/$15.00.

Printed in the United States of America.

Contents

xi *Conference Committee*
xv *Introduction*

OVERVIEW OF MICROFABRICATION

1 **Laser precision microfabrication in Japan** [4088-01]
I. Miyamoto, Osaka Univ. (Japan); T. Ooie, Shikoku National Industrial Research Institute (Japan); S. Takeno, Mitsubishi Electric Corp. (Japan)

9 **Overview of laser microprocessing: fundamentals, practical applications, and future prospects** [4088-02]
V. P. Veiko, St. Petersburg Institute of Fine Mechanics and Optics (Russia)

ULTRAFAST-PULSE PROCESSING

17 **Surface and bulk ultrashort-pulsed laser processing of transparent materials** [4088-03]
I. V. Hertel, R. Stoian, D. Ashkenasi, A. Rosenfeld, Max Born Institute (Germany); E. E. B. Campbell, Univ. of Gothenburg (Sweden) and Chalmers Univ. of Technology (Sweden)

25 **395-nm and 790-nm femtosecond laser ablation of aluminum-doped zinc oxide** [4088-05]
M. Okoshi, K. Higashikawa, M. Hanabusa, Toyohashi Univ. of Technology (Japan)

29 **Formation of photonic crystals by femtosecond laser microfabrication** [4088-06]
H. Misawa, S. Juodkazis, H.-B. Sun, S. Matsuo, Univ. of Tokushima (Japan); J. Nishii, Osaka National Research Institute (Japan)

33 **Internal modification of glass materials with a femtosecond laser** [4088-07]
K. Hirao, ERATO/Japan Science and Technology Corp. and Kyoto Univ. (Japan)

40 **Time-resolved dynamics of plasma self-channeling and bulk modification in silica glasses induced by a high-intensity femtosecond laser** [4088-10]
S.-H. Cho, H. Kumagai, K. Midorikawa, RIKEN—The Institute of Physical and Chemical Research (Japan); M. Obara, Keio Univ. (Japan)

44 **Observation of voids and optical seizing of voids in silica glass with infrared femtosecond laser pulses** [4088-11]
W. Watanabe, T. Toma, K. Yamada, Osaka Univ. (Japan); J. Nishii, Osaka National Research Institute (Japan); K. Hayashi, Sumitomo Heavy Industries, Ltd. (Japan); K. Itoh, Osaka Univ. (Japan)

48 **Micromachining with high-repetition-rate femtosecond laser sources** [4088-12]
E. Baubeau, R. Le Harzic, C. Jonin, E. Audouard, S. Mottin, M. Courbon, P. Laporte, Univ. Jean Monnet St.-Étienne (France)

51 **Transient light-induced refractive index change made by laser microfabrication in nitroaniline-doped PMMA film** [4088-65]
K. Yamasaki, S. Juodkazis, M. Watanabe, S. Matsuo, Univ. of Tokushima (Japan); K. Kamada, K. Ohta, Osaka National Research Institute (Japan); H. Misawa, Univ. of Tokushima (Japan)

MODIFICATION

55 **Laser-induced microstructuring of photonic materials: semiconductors** [4088-13]
J. J. Dubowski, National Research Council of Canada

64 **Micromachining of transparent materials by laser ablation of organic solution** [4088-114]
J. Wang, H. Niino, A. Yabe, National Institute of Materials and Chemical Research (Japan)

70 **F_2 laser ablation of GaN** [4088-16]
T. Akane, K. Sugioka, RIKEN—The Institute of Physical and Chemical Research (Japan); S. Nomura, Univ. of Tsukuba (Japan); K. Hammura, RIKEN—The Institute of Physical and Chemical Research (Japan); K. Obata, N. Aoki, K. Toyoda, Science Univ. of Tokyo (Japan); Y. Aoyagi, K. Midorikawa, RIKEN—The Institute of Physical and Chemical Research (Japan)

73 **Applications of pulsed lasers in low-temperature thin film electronics fabrication** [4088-14]
T. W. Sigmon, D. Toet, P. G. Carey, P. M. Smith, P. Wickboldt, Lawrence Livermore National Lab. (USA)

80 **Pulsed laser nitridation of InP** [4088-67]
N. Aoki, Science Univ. of Tokyo (Japan); T. Akane, K. Sugioka, RIKEN—The Institute of Physical and Chemical Research (Japan); K. Toyoda, Science Univ. of Tokyo (Japan); J. J. Dubowski, National Research Council of Canada; K. Midorikawa, RIKEN—The Institute of Physical and Chemical Research (Japan)

FUNDAMENTAL ASPECTS

84 **Molecular dynamics simulation of ablation process with ultrashort-pulsed laser** [4088-17]
E. Ohmura, Osaka Univ. (Japan); I. Fukumoto, RIKEN—The Institute of Physical and Chemical Research (Japan); I. Miyamoto, Osaka Univ. (Japan)

90 **Optical emission of plasmas in ultraviolet and infrared laser ablation of graphite by time-resolved spectroscopy** [4088-96]
T. Shinozaki, Shikoku National Industrial Research Institute (Japan) and Japan Science and Technology Corp.; T. Ooie, T. Yano, M. Yoneda, Shikoku National Industrial Research Institute (Japan)

94 **Effects of repetitive irradiation in laser ablation of aluminum in gases observed by photoacoustic and imaging techniques** [4088-20]
Y. Ito, I. Oguro, Nagaoka Univ. of Technology (Japan); S. Nakamura, Nagaoka College of Technology (Japan)

98 **Ultrashort-pulsed laser microstructuring of diamond** [4088-18]
M. D. Shirk, P. Molian, C. Wang, K. M. Ho, Iowa State Univ. (USA); A. P. Malshe, Univ. of Arkansas (USA)

102 **Effects of laser pulse shape on jetlike plasma formation in laser ablation of metals under atmosphere at high fluence: observation by nanosecond imaging technique** [4088-69]
S. Kiyoku, Y. Kurosaki, I. Oguro, Nagaoka Univ. of Technology (Japan); S. Nakamura, Nagaoka College of Technology (Japan); Y. Ito, Nagaoka Univ. of Technology (Japan)

106 **Molecular dynamics analysis on physical phenomena of metal with evaporation induced by laser irradiation** [4088-70]
I. Fukumoto, Japan Atomic Energy Research Institute; E. Ohmura, Osaka Univ. (Japan); A. Zhidkov, A. Sasaki, T. Utsumi, Japan Atomic Energy Research Institute; I. Miyamoto, Osaka Univ. (Japan)

MICROFABRICATION

110 **Novel technology for laser precision microfabrication of hard materials** [4088-21]
K. Sugioka, K. Midorikawa, RIKEN—The Institute of Physical and Chemical Research (Japan)

118 **Novel results of laser precision microfabrication with excimer lasers and solid state lasers** [4088-22]
U. Stamm, M. Fiebig, Lambda Physik AG (Germany); S. V. Govorkov, E. E. Mayer, Lambda Physik, Inc. (USA); R. Osmanov, Lambda Physik AG (Germany); M. J. Scaggs, E. V. Slobodchikov, A. O. Wiessner, D. Basting, Lambda Physik, Inc. (USA)

124 **Excimer laser microfabrication and micromachining** [4088-24]
M. C. Gower, Exitech Ltd. (UK)

132 **High-efficiency microdrilling of silicon wafer using excimer laser** [4088-26]
S. Asada, T. Sano, I. Miyamoto, Osaka Univ. (Japan)

136 **Micromachining using femtosecond lasers** [4088-27]
H. K. Tönshoff, A. Ostendorf, S. Nolte, F. Korte, T. Bauer, Laser Zentrum Hannover e.V. (Germany)

140 **Micromachining with ultrafast lasers** [4088-28]
K. Shihoyama, A. Furukawa, Hoya-Continuum (Japan); P. Bado, A. A. Said, Clark-MXR, Inc. (USA)

144 **Technique of microfabrication suitable for machining submillimeter-wave components** [4088-71]
W. Y. Liu, D. P. Steenson, M. B. Steer, Univ. of Leeds (UK)

INDUSTRIAL APPLICATIONS

148 **Laser via-hole drilling of printed wiring board** [4088-29]
T. Okada, Matsushita Electric Industrial Co., Ltd. (Japan)

154 **Present status of excimer laser exposure apparatus** [4088-30]
A. Suzuki, Canon Inc. (Japan)

160 **Local annealing of shape memory alloys using laser scanning and computer vision** [4088-31]
M. Hafez, Y. Bellouard, T. C. Sidler, R. Clavel, R.-P. Salathé, Swiss Federal Institute of Technology/Lausanne

164 **Virtual engineering helps to get laser adjustment industrially accepted** [4088-32]
B. Müller, Univ. of Erlangen-Nuremberg (Germany)

168 **High-resolution contact lithography by excimer lasers** [4088-73]
H. Huang, D. Lu, L. Du, Y. Zhao, C. Yuan, B. Jiang, R. Wang, Shanghai Institute of Optics and Fine Mechanics (China)

171 **Inorganic-organic hybrid material for lithography** [4088-74]
L. Pang, Y. Yan, G. Jin, M. Wu, Tsinghua Univ. (China)

175 **Etching characteristics of the PDP barrier rib pastes by focused Ar^+ laser and Nd:YAG laser** [4088-75]
M. Ahn, K. Lee, H. Lee, C. Lee, Inha Univ. (Korea)

179 **Thermomechanical mechanisms of laser cleaning** [4088-76]
V. P. Veiko, E. A. Shakhno, S. V. Nikolaev, St. Petersburg Institute of Fine Mechanics and Optics (Russia)

183 **N_2 laser stereo-lithography** [4088-77]
S. Satoh, T. Tanaka, N. Hayashi, C. Yamabe, Saga Univ. (Japan)

187 **Hole drilling of glass substrates with a slab waveguide CO_2 laser** [4088-78]
Y. Yoshida, Toyo Univ. (Japan); Y. Kobayashi, T. Zhang, Yamanashi Univ. (Japan); H. Yajima, Y. Hashidate, H. Ogura, Matsushita Research Institute of Tokyo Inc. (Japan)

LASER SYSTEMS AND OPTICAL ELEMENTS

191 **High-repetition-rate ArF excimer laser for microlithography** [4088-80]
O. Wakabayashi, T. Enami, K. Ishii, K. Terashima, Y. Itakura, T. Watanabe, T. Ohta, A. Ohbu, H. Kubo, H. Tanaka, S. Andou, T. Matsunga, H. Umeda, T. Suzuki, A. Sumitani, H. Mizoguchi, Komatsu Ltd. (Japan)

195 **High-power second harmonic generation with free-running Nd:YAG slab laser for micromachining applications** [4088-35]
S. Favre, T. C. Sidler, R.-P. Salathé, Swiss Federal Institute of Technology/Lausanne

199 **Efficient high-pulse-energy green beam generation by intracavity frequency doubling of a quasi-cw laser-diode-pumped Nd:YAG laser** [4088-81]
S. Konno, Y. Inoue, T. Kojima, S. Fujikawa, K. Yasui, Mitsubishi Electric Corp. (Japan)

201 **Ultrafast fiber lasers: alternative light sources for industrial material processing** [4088-37]
G. Sucha, H. Endert, IMRA, America, Inc.

205 **Evaluation of characteristics of VUV optical materials irradiated by F_2 laser** [4088-79]
Y. Itakura, F. Yoshida, Y. Kawasa, A. Sumitani, O. Wakabayashi, H. Mizoguchi, Komatsu Ltd. (Japan)

209 **Laser processing system for microdrilling of printed circuit boards** [4088-104]
J. Nishimae, Y. Satoh, T. Kojima, Mitsubishi Electric Corp. (Japan); T. Fukushima, Nagoya Works, Mitsubishi Electric Corp. (Japan)

212 **Development of the enhanced concurrent in-line inspection system for CO_2 laser drilling machine** [4088-106]
H. Nagatoshi, K. Isaji, T. Sugiyama, H. Karasaki, Matsushita Industrial Equipment Co., Ltd. (Japan); M. Kato, Matsushita Electric Industrial Co., Ltd. (Japan)

216 **Laser microprocessing unit and its application** [4088-111]
K. Fukumitsu, T. Oie, Hamamatsu Photonics K.K. (Japan)

220 **Micro materials processing with high-power diode lasers** [4088-113]
F. G. Bachmann, Rofin-Sinar Laser GmbH (Germany); R. Takahashi, S. Fujishima, Rofin-Marubeni Laser K.K. (Japan)

SURFACE MICROSTRUCTURING

224 **UV laser ablative shaping of optical surface using ArF laser** [4088-38]
T. Jitsuno, Osaka Univ. (Japan); K. Tokumura, Nalux Co., Ltd. (Japan); H. Tamamura, Sony/Tektronix Corp. (Japan)

228 **Nonlithographic coherent array of ultrafine particles on an irradiated material using Nd:YAG laser: influence of the laser fluence on the microstructure** [4088-39]
Y. Kawakami, E. Ozawa, Vacuum Metallurgical Co., Ltd. (Japan)

232 **Kinetic study of nanofabrication on gold films by atomic force microscope tips under laser radiation** [4088-83]
B. Hu, Y. F. Lu, Z. H. Mai, W. D. Song, W. K. Chim, National Univ. of Singapore

236 **Laser surface annealing of Ni-base superalloy for enhancement of material performance in hydrogen environment** [4088-84]
A. Hirose, L. Liu, K. F. Kobayashi, Osaka Univ. (Japan)

240 **Laser texturing process and surface quality control** [4088-41]
J. Jiang, Shanghai Jiao Tong Univ. (China); Y. He, Y. Yan, Shanghai Baosteel Group Corp. (China); W. Zhao, Harbin Institute of Technology (China); Y. Xu, Shanghai Baosteel Group Corp. (China)

244 **Thermohydrodynamics analysis on the mechanism of bump formation in laser texturing** [4088-82]
E. Ohmura, R. Murayama, I. Miyamoto, Osaka Univ. (Japan)

MICROWELDING AND CUTTING

248 **Micromachining with a frequency-converted diode-pumped Nd:YAG laser** [4088-42]
K. Hartke, EWI (USA); K. King, Cutting Edge Optronics, Inc. (USA); D. F. Farson, The Ohio State Univ. (USA); K. Ely, EWI (USA)

252 **High-precision microcutting of ceramics with short-pulsed solid state lasers** [4088-43]
J. Radtke, T. Abeln, M. Weikert, F. Dausinger, Univ. of Stuttgart (Germany)

256 **Laser microcaving of steel with solid state lasers** [4088-44]
T. Abeln, J. Radtke, M. Weikert, F. Dausinger, Univ. of Stuttgart (Germany)

260 **Laser joining of microcomponents with fiber lasers and diode lasers** [4088-45]
A. Gillner, L. Bosse, T. Kramer, A. Olowinsky, M. Wild, Fraunhofer Institute for Laser Technology (Germany)

264 **Pulsed Nd:YAG laser welding of titanium ear implants** [4088-46]
J. Gedopt, E. Delarbre, Vito Corp. (Belgium)

268 **Compact multisensor laser scanning head for processing and monitoring microspot welding** [4088-47]
M. Hafez, K. Julliard, S. Grossmann, L. Olivetta, T. C. Sidler, R.-P. Salathé, Swiss Federal Institute of Technology/Lausanne; H.-P. Schwob, Lasag Industrial Lasers (Switzerland); T. Blom, W. Hoving, Philips Ctr. for Manufacturing Technology (Netherlands)

272 **New interferometric method to measure the complete geometry of the keyhole** [4088-89]
M. M. S. Gualini, Pakistan Institute of Lasers and Optics; H. Steinbichler, Steinbichler Optotechnik GmbH (Germany)

276 **Microsoldering using a YAG laser: on lead-free solder** [4088-91]
S. Nakahara, T. Kamata, N. Yoneda, S. Hisada, T. Fujita, Kansai Univ. (Japan)

280 **Plasma behaviors in laser cutting** [4088-90]
H. Horisawa, Tokai Univ. (Japan); M. Tamura, S. Kimura, Toshiba Corp. (Japan)

284 **Fundamental study about molten metal of laser cutting** [4088-92]
T. Fushimi, H. Nakajima, H. Horisawa, S. Yamaguchi, N. Yasunaga, T. Fujioka, Tokai Univ. (Japan)

287 **Fundamental study about CO_2 laser welding of titanium aluminide intermetallic compound** [4088-93]
G. Kuwahara, S. Yamaguchi, K. Nanri, M. Ootani, M. Tetsuka, S. Seto, Tokai Univ. (Japan); M. Arai, Ishikawajima-Harima Heavy Industries Co., Ltd. (Japan); T. Fujioka, Tokai Univ. (Japan)

291 **Effect of nozzle shape on surface integrity in microcutting with pulsed YAG laser** [4088-94]
Y. Okamoto, Y. Uno, Okayama Univ. (Japan); N. Miyanagi, Hitachi Construction Machinery Co., Ltd. (Japan)

295 **Method to evaluate Nd:YAG laser microscopic spot welding process using reflected laser power** [4088-95]
S. Park, R. Honma, I. Miyamoto, Osaka Univ. (Japan)

299 **Selective laser sintering with heat of formation by using reactive materials** [4088-107]
T. Kamitani, O. Yamada, Y. Marutani, Osaka Sangyo Univ. (Japan)

PULSED-LASER DEPOSITION

303 **Observation of nanoparticle formation process by two-dimensional laser-induced fluorescence, UV Rayleigh scattering, and re-decomposition laser-induced fluorescence methods** [4088-48]
J. Muramoto, T. Inmaru, Y. Nakata, T. Okada, M. Maeda, Kyushu Univ. (Japan)

307 **Influence of laser fluence on the synthesis of carbon nitride thin films by nitrogen-ion-assisted pulsed-laser deposition** [4088-50]
J. P. Zhao, Z. Y. Chen, T. Yano, T. Ooie, M. Yoneda, J. Sakakibara, Shikoku National Industrial Research Institute (Japan)

311 **Preparation of metal oxide thin films using coating photolysis process with ArF excimer laser** [4088-51]
T. Tsuchiya, A. Watanabe, Y. Imai, H. Niino, A. Yabe, I. Yamaguchi, T. Manabe, T. Kumagai, S. Mizuta, National Institute of Materials and Chemical Research (Japan)

315 **Preparation of conducting polymer thin films by UV laser-assisted deposition** [4088-52]
S. Nishio, M. Okumura, Y. Taketani, A. Matsuzaki, H. Sato, Mie Univ. (Japan)

MICROSYSTEMS

319 **Nanosatellites and MEMS fabrication by laser microprocessing** [4088-53]
H. Helvajian, P. D. Fuqua, W. W. Hansen, S. W. Janson, The Aerospace Corp. (USA)

327 **Microgroove fabrication with excimer laser ablation techniques for optical fiber array alignment purposes** [4088-54]
K. Naessens, A. Van Hove, T. Coosemans, S. Verstuyft, L. Vanwassenhove, P. Van Daele, R. G. Baets, Univ. of Ghent (Belgium)

333 **Fabrication of Ce:YIG film for electric and magnetic field sensor by pulsed-laser deposition and laser-induced forward transfer** [4088-55]
Y. Nakata, Y. Tashiro, T. Okada, M. Maeda, Kyushu Univ. (Japan); S. Higuchi, Central Research Institute of Electric Power Industry (Japan); K. Ueda, Kyushu Univ. (Japan)

337 **Electro-osmotic flow control in microchannels produced by scanning excimer laser ablation** [4088-56]
F. Wagner, P. W. Hoffmann, Swiss Federal Institute of Technology/Lausanne

341 **Three-dimensional microassembling technique applying laser trapping** [4088-97]
D. Sawaki, Toyohashi Univ. of Technology (Japan); J. Ikeno, Saitama Univ. (Japan); O. Horiuchi, Toyohashi Univ. of Technology (Japan); T. Kasai, Saitama Univ. (Japan)

GLASS MATERIALS PROCESSING

345 **Advanced laser microfabrication of photonic components** [4088-57]
P. R. Herman, K. P. Chen, Univ. of Toronto (Canada); P. B. Corkum, A. Naumov, Steacie Institute for Molecular Sciences (Canada); S. Ng, J. Zhang, Univ. of Toronto (Canada)

351 **Laser processing of convex structures in chalcogenide glasses** [4088-58]
T. Gotoh, K. Tanaka, Hokkaido Univ. (Japan)

355 **Laser ablation process of quartz material using F_2 laser** [4088-59]
T. Jitsuno, H. Mikata, Osaka Univ. (Japan); K. Tokumura, Nalux Co., Ltd. (Japan); N. Kuzuu, Fukui Univ. (Japan); N. Kitamura, Osaka National Industrial Research Institute (Japan); Y. Kawaguchi, Chugoku National Industrial Research Institute (Japan)

359 **Optical diagnostics in laser-induced plasma-assisted ablation of fused quartz** [4088-98]
M. H. Hong, National Univ. of Singapore; K. Sugioka, RIKEN—The Institute of Physical and Chemical Research (Japan); Y. F. Lu, National Univ. of Singapore; K. Midorikawa, RIKEN— The Institute of Physical and Chemical Research (Japan); T. C. Chong, National Univ. of Singapore

363 **Laser method for marking bar codes on glass substrates** [4088-103]
H. Hayakawa, Yaskawa Electric Corp. (Japan)

367 **Photo-induced refractive-index changes in filaments formed in glass with femtosecond laser pulses** [4088-99]
K. Yamada, T. Toma, W. Watanabe, Osaka Univ. (Japan); J. Nishii, Osaka National Research Institute (Japan); K. Itoh, Osaka Univ. (Japan)

ADVANCED APPLICATIONS

371 **Laser surface cleaning: basic understanding, engineering efforts, and technical barriers** [4088-60]
Y. F. Lu, W. D. Song, M. H. Hong, Z. M. Ren, Y. W. Zheng, National Univ. of Singapore

380 **Laser processes for precise microfabrication of magnetic disk-drive components** [4088-61]
A. C. Tam, IBM Almaden Research Ctr. (USA)

385 **Optical radiation pressure micromachining using a small particle** [4088-62]
H. Shimizu, T. Miyoshi, Osaka Univ. (Japan); S. Kiyono, Tohoku Univ. (Japan)

389 **Micropeak array in the scribe line on a wafer** [4088-63]
T. Chiba, R. Komura, A. Mori, Komatsu Ltd. (Japan)

393 **Matrix-assisted laser transfer of electronic materials for direct-write applications** [4088-64]
R. C. Y. Auyeung, H. D. Wu, SFA Inc. (USA); R. Modi, George Washington Univ. (USA); A. Piqué, J. M. Fitz-Gerald, Naval Research Lab. (USA); H. D. Young, S. Lakeou, SFA Inc. (USA); R. Chung, Geo-Centers, Inc. (USA); D. B. Chrisey, Naval Research Lab. (USA)

397 **In-vivo results of corneal surface measurement with optical methods** [4088-100]
M. M. S. Gualini, Pakistan Institute of Lasers and Optics; H. Steinbichler, Steinbichler Optotechnik GmbH (Germany); W. A. Khan, Al-Shifa Trust Eye Hospital (Pakistan)

401 **Removal process of metal thin films during laser rear patterning** [4088-101]
T. Sano, I. Miyamoto, Osaka Univ. (Japan)

405 *Abstract of paper 4088-109: Microcutting with pulsed fundamental-mode Nd:YAG slab laser, T. Sidler, S. Favre, S. Benjamin, R.-P. Salathé*

408 *Author Index*

Symposium Committees

Symposium Chairs

Isamu Miyamoto, Osaka University (Japan)
Koji Sugioka, RIKEN—The Institute of Physical and Chemical Research (Japan)
Thomas W. Sigmon, Lawrence Livermore National Laboratory (USA)

Program Committee

Paul Christiansen, Potamac Photonics, Inc. (USA)
Friedrich Dausinger, University of Stuttgart (Germany)
Costas P. Grigoropoulos, University of California/Berkeley (USA)
Paul R. Herman, University of Toronto (Canada)
Jürgen Ihlemann, Laser Laboratorium Göttingen (Germany)
Shin-ichi Ishizaka, Japan Steel Works, Ltd.
Yoshiro Ito, Nagoako University of Technology (Japan)
Takahisa Jitsuno, Osaka University (Japan)
Ernst W. Kreutz, Lehrstuhl für Lasertechnik (Germany)
William P. Latham, Air Force Research Laboratory (USA)
Yongfeng Lu, National University of Singapore
Sumio Nakahara, Kansai University (Japan)
Etsuji Ohmura, Osaka University (Japan)
Toshihiko Ooie, Shikoku National Industrial Research Institute (Japan)
Richard M. Osgood, Columbia University (USA)
Andreas Ostendorf, Laser Zentrum Hannover e.V. (Germany)
Alan B. Petersen, Spectra-Physics Lasers (USA)
Tomokazu Sano, Osaka University (Japan)
Andrew C. Tam, IBM Almaden Research Center (USA)
Masaaki Tanaka, Mitsubishi Electric Corporation (Japan)
Jay F. Tu, Purdue University (USA)
Kunihiko Washio, NEC Corporation (Japan)
Akira Yabe, National Institute of Materials and Chemical Research (Japan)

Steering Committee

Toshimitsu Akane, RIKEN—The Institute of Physical and Chemical Research (Japan)
Kenshi Fukumitsu, Hamamatsu Photonics K.K. (Japan)
Seiji Iwama, Shibaura Mechatronics Corporation (Japan)
Takahisa Jitsuno, Osaka University (Japan)
Teruyoshi Kadoya, Trumpf Corporation (Japan)
Kazuo Kamada, Matsushita Electric Works, Ltd. (Japan)
Hidehiko Karasaki, Matsushita Industrial Equipment Company, Ltd. (Japan)
Osamu Miyata, Denso Corporation (Japan)
Sumio Nakahara, Kansai University (Japan)
Hiroyuki Niino, National Institute of Materials and Chemical Research (Japan)
Etsuji Ohmura, Osaka University (Japan)

Toshihiko Ooie, Shikoku National Industrial Research Institute (Japan)
Marek Osiński, University of New Mexico (USA)
Tomokazu Sano, Osaka Unversity (Japan)
Koji Sugioka, RIKEN—The Institute of Physical and Chemical Research (Japan)
Osamu Wakabayashi, Komatsu Ltd. (Japan)

Session Chairs

Overview of Microfabrication
Andrew C. Tam, IBM Almaden Research Center (USA)
Koji Sugioka, RIKEN—The Institute of Physical and Chemical Research (Japan)

Ultrafast-Pulse Processing
Malcolm C. Gower, Exitech Ltd. (UK)
Akira Yabe, National Institute of Materials and Chemical Research (Japan)
Uwe Stamm, Lambda Physik AG (Germany)
Saulius Juodkazis, University of Tokushima (Japan)

Modification
Yongfeng Lu, National University of Singapore
Koichi Toyoda, Science University of Tokyo (Japan)

Fundamental Aspects
Ingolf V. Hertel, Max Born Institute (Germany)
Toshihiko Ooie, Shikoku National Industrial Research Institute (Japan)

Microfabrication
Xianfan Xu, Purdue University (USA)
Shin-ichi Ishizaka, Japan Steel Works Ltd.
Jan J. Dubowski, National Research Council of Canada
Etsuji Ohmura, Osaka University (Japan)

Industrial Applications
Vadim P. Veiko, St. Petersburg Institute of Fine Mechanics and Optics (Russia)
Kunihiko Washio, NEC Corporation (Japan)

Laser Systems and Optical Elements
Alan B. Petersen, Spectra-Physics Lasers (USA)
Takahisa Jitsuno, Osaka University (Japan)

Surface Microstructuring
Heinrich Endert, IMRA (USA)
Yoshiro Ito, Nagaoka University of Technology (Japan)

Microwelding and Cutting
Friedrich Dausinger, University of Stuttgart (Germany)
Takashi Ishide, Mitsubishi Heavy Industries, Ltd. (Japan)

Pulsed-Laser Deposition
Frank Wagner, Swiss Federal Institute of Technology/Lausanne
Fumio Kokai, Institute of Research and Innovation (Japan)

Microsystems
Peter R. Herman, University of Toronto (Canada)
Sumio Nakahara, Kansai University (Japan)

Glass Materials Processing
Andreas Ostendorf, Laser Zentrum Hannover e.V. (Germany)
Junji Nishii, Osaka National Research Institute (Japan)

Advanced Applications
Henry Helvajian, The Aerospace Corporation (USA)
Isamu Miyamoto, Osaka University (Japan)

Introduction

Recent advances in laser technologies with short-pulse and short-wavelength beams have accelerated the growth in laser precision microfabrication (LPM) in electronics, optoelectronics, micromachining, medical devices, etc. In view of the great impact of LPM, JLPS—Japan Laser Processing Society and RIKEN—The Institute of Physical and Chemical Research provided an international forum for exchanging technical information between fundamental researchers and end users in different industrial fields of LPM around the world. The main focus included analyzing the present status of fundamentals and applications, defining critical techniques to be developed, and forecasting future markets of laser precision microfabrication.

The First International Symposium on Laser Precision Microfabrication (LPM2000) is, without any doubt, the first attempt to provide an international forum in which such a varied group can assemble. The symposium was held at Omiya, Saitama Prefecture, Japan, as a three-day event (June 14–16, 2000) consisting of 15 oral sessions along with a poster session. More than 100 oral and poster papers were submitted from 16 countries in Asia, Europe, and North America. This volume presents the proceedings from LPM2000. It is actually meaningful that the first LPM symposium was held in Japan, which is known to fabricate more than half of the microelectronic devices in the world, and where laser technologies play an important role. The LPM symposium will be held every year in the Pacific Rim; the second symposium, LPM2001, will be in Singapore.

Our great thanks must go to the members of the program and organizing committees, to the invited speakers, and to all of the participants for making LPM2000 so successful. We also extend our thanks to RIKEN and SPIE for helping to organize this meeting. Finally, we respectfully acknowledge the U.S. Air Force Office of Scientific Research and Development (USAFORS/AOARD) and Saitama Foundation for Culture and Industry for their financial support provided to this symposium.

Isamu Miyamoto
Koji Sugioka
Thomas W. Sigmon

Laser precision microfabrication in Japan

Isamu Miyamoto*, Toshihiko Ooie**, Shozui Takeno***

*Department of Manufacturing Science, Graduate School of Engineering, Osaka University, 2-1 Yamada-Oka, Suita, Osaka 565-0871, Japan,
E-mail:miyanoto@mapse.eng.osaka-u.ac,jp
**Shikoku National Industrial Research Institute, Agency of Industrial Scoemce and Technology, MITI, 2217-14 Hayashi-cho, Takamatsu, Kagawa 761-0395, Japan
*** Manufacturing Engineering Center, Mitsubishi Electric Corporation, 1-1 Tshukaguchi-Honmachi 8-Chome, Amagasaki, Hyogo 661-8661, Japan

Electronic devices such as handy phones and micro computers have been rapidly expanding their market recent years due to their enhanced performance, down sizing and cost down. This has been realized by the innovation in the precision micro-fabrication technology of semiconductors and printed wiring circuit boards (PWB) where laser technologies such as lithography, drilling, trimming, welding and soldering play an important role. In photo lithography, for instance, KrF excimer lasers having a resolution of 0.18 μm has been used in production instead of mercury lamp. Laser drilling of PWB has been increased up to over 1000 holes per second, and approximately 800 laser drilling systems of PWB are expected to be delivered in the world market this year, and most of these laser processing systems are manufactured in Japan. Trend of laser micro-fabrication in Japanese industry is described along with recent topics of R&D, government supported project and future tasks of industrial laser precision micro-fabrication on the basis of the survey conducted by Japan laser Processing Society.

Keywords: laser, industry, precision micro-fabrication, semiconductor, PWB

1. Introduction

Electronic devices for consumers such as handy phones, PDA, digital camera and microcomputers have been rapidly expanding their market recent years. For instance, the number of handy phone sold in world market in 1999 reached approximately 230 millions sets, as shown in **Fig. 1**. This number is expected to reach 300 million sets this year. According to other survey, much larger number, even 400 million sets are expected in 2000 **[1]**. It should be noted that more than half of electronic parts are manufactured in Japan.

Such rapid expansion of electronic market has been supported by the innovation of precision micro-fabrication technology of electronic devices. Weight and size of electronic devices are rapidly decreasing, although the performance have been enhanced so that the amount of data is increasing from voice communication to internet and then picture/music as shown in **Fig. 2 [2]**. In spite of such technical advances, the cost of PWB is dramatically decreasing due to sever commercial competition in **Fig. 2**.

Such a situation has been realized by the innovation in the precision micro-fabrication technology of semi-conductors and printed wiring circuit boards (PWB) where laser-based technologies such as lithography, drilling, trimming, welding and soldering play an important role.

Japan Laser Processing Society (JLPS), non profit organization containing 140 company members, made a 4-year survey to analyze present atatus and future aspect of Japanese laser industry from 1996. Laser precision micro-fabrication in Japan in terms of technical trend in

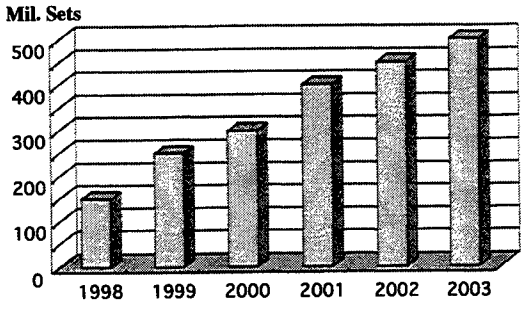


Fig. 1 World market for cellular phone (Motolora)

First International Symposium on Laser Precision Microfabrication, Isamu Miyamoto, Koji Sugioka, Thomas W. Sigmon, Editors, Proceedings of SPIE Vol. 4088 (2000) © 2000 SPIE · 0277-786X/00/$15.00

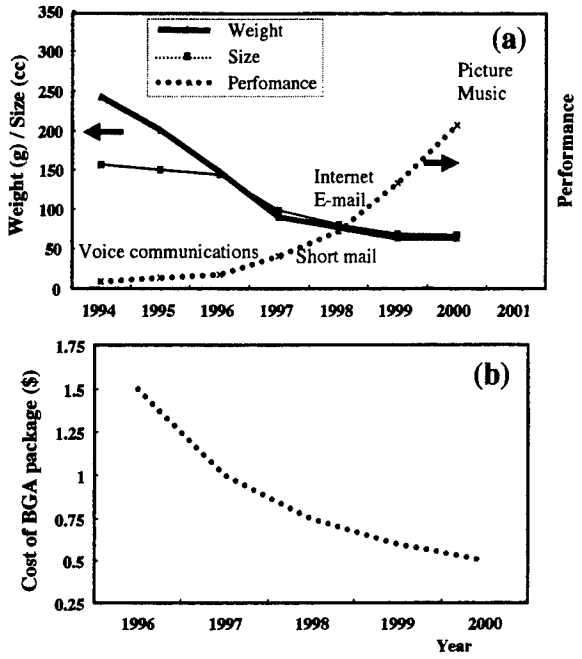


Fig. 2 Trend of down sizing and performandece of cellular phone (a), and PWB cost in BGA package (JPCA:2000) (b).

industry, recent R&D topics and government supported projects is discussed on the basis of the survey conducted by non profit organization, Japan Laser Processing Society **[3]**. Future aspects of laser precision micro-fabrication are also described

2. Recent trend of LPM in Japanese industry

2.1 Lithograpy

KrF excimer lasers began to be used for photo lithography in production from 1996 due to their improved stability as well as high spatial resolution. They have been used in production for 64 – 256 Mbit DRAM, and the number of the laser lithography became much larger than that of the mercury lamp today (**Fig. 3**) **[4]**. KrF excimer lasers with higher power and reduced cost of operation are required to be developed for higher productivity. The resolution of 0.18 μm has been attained in production and 0.12 μm in laboratory level (**Fig. 4**) by enlarging NA, narrowing spectral width and the improvement of the resist material. The resolution is expected to reach down to less than 0.1μm with ArF excimer laser, which is required for 4 Gbit DRAM.

The number of excimer lasers sold in Japan became as large as that of the mercury lamp in 1998, and is increasing rapidly expected to reach 600 units in 2000 where lasers lithography is predominant **[5]**. Most of these laser lithography systems are manufactured in Japan.

2.2 Ablation processing

Most PWB has a build-up structure with blind holes with diameters of less than 150 μm (**Fig.5**), and laser drilling technology of micro-via hole using CO_2 lasers has been developed instead of mechanical drilling in the middle of 1990's.

Figure 6 shows the production amount of the build-up board in main four areas **[6]**. The amount of the production in Japan is seen to be much larger than that in US, Europ and other Asian coutries, and world market is, without any doubt, led by Japanese industry.

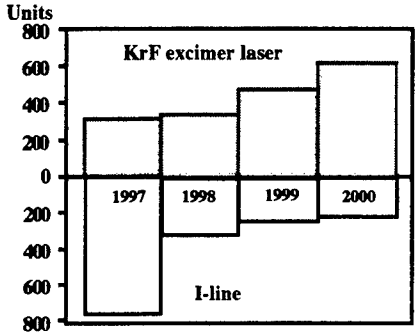


Fig. 3 Excimer laser system for lithography sold a year in Japan.

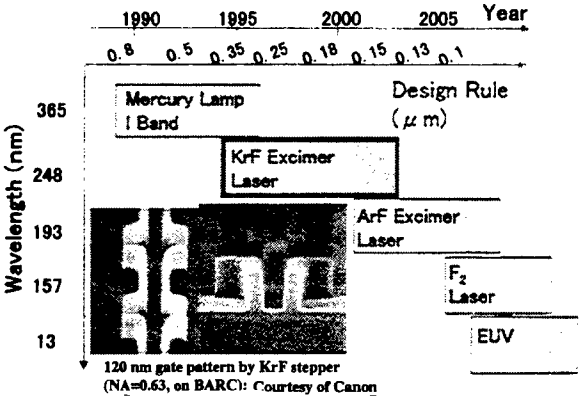


Fig. 4 Trend of photolithography.

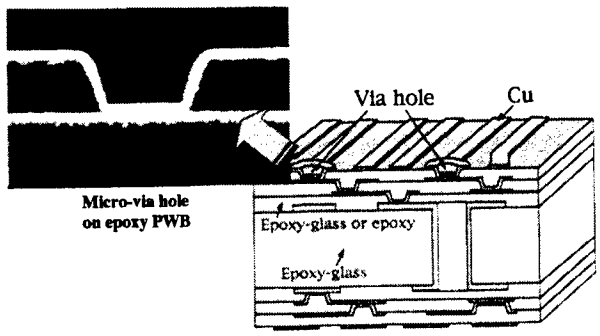


Fig.5 Schematics of PWB using micro-via holes.

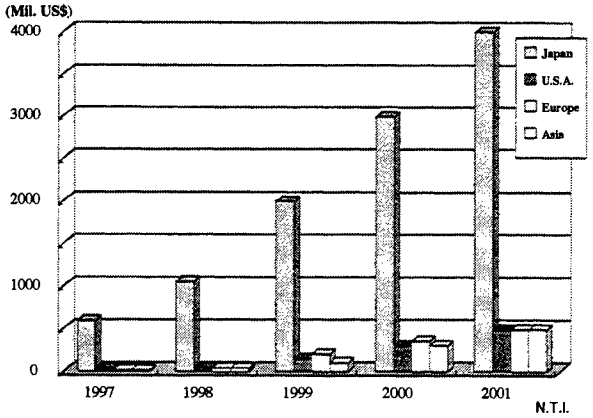


Fig.6 World micro-via hole board production forecasted.

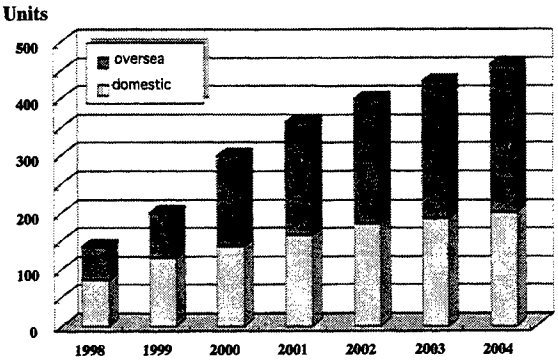


Fig. 7 Market trend of CO_2 laser drilling system.

The number of laser drilling system sold a year is increasing rapidly, and is estimated to reach 300 units in 2000 as shown in **Fig. 7 [7]**. Other survey estimates that much larger number of approximately 800 units is sold this year.

The performance of via hole laser depends on the performance of lasers and peripheral systems. Three types of CO_2 lasers, TEA laser, slab type laser with RF excitation and 3-axis cross flow type laser with SD excitation have been developed for via-hole drilling, by Lumonics, Coherent and Mitsubishi Electric Co, respectively. Laser drilling systems mounting these lasers are used in production mainly in Japan, Taiwan and Korea. CO_2 lasers can be used for via holes of the diameter down to 50-70 μm. For drilling of smaller via holes, SHG YAG lasers expected to be used.

Increasing the productivity is one of the most important tasks for realizing cost down. Drilling rate is actually limited by scanning rate of the laser beam, which is determined by the performance of the galvano-mirrors. The drilling speed of PWB, which was 500 holes per second three years ago, has increased up to 1100 holes per second mainly by the improvement of galvano mirror system. Increasing drilling rate is a big issue of technology development between makers.

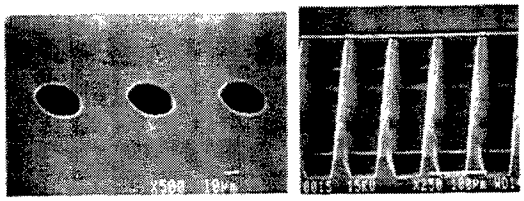


Fig. 8 Drilling of ink jet nozzle for PC printer by using KrF excimer laser (diameter: 30~70 μm).

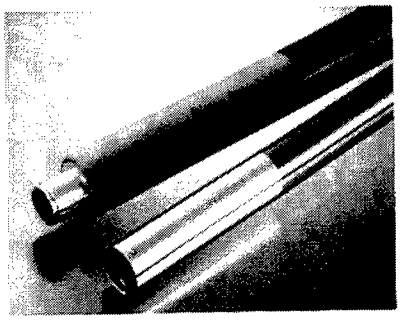


Fig. 9 Recycling of used dram for copy machine by removing damaged surface film.

Interesting laser drilling technique other than via holes is drilling of ink jet nozzle for personal computers. Very precise holes of 30 to 70 μm diameter in polysulphon can be drilled by using KrF excimer (**Fig. 8**) **[8]**. The laser is irradiated with a mask projection optics at a magnification of 1/4 to drill 64 to 160 holes in the area of 5 to 10 mm. Approximately 50 systems using KrF excimer laser are working for this purpose in Canon. Drilling of alumina ceramic for medical filter has been also developed by Omron where holes of 4 microns in diameter are drilled in alumina ceramics of 50 microns thickness byKrF excimer laser **[9]**.

A hybrid cutting technique of KFRP was developed by Mitsubishi Heavy Industry for the parts of helicopter by using KrF excimer and CO_2 lasers **[10]**. This material was manufactured by time consuming manual operations including cutting and then polishing. In the newly developed system, CO_2 laser cuts the material at higher speeds, and then excimer laser removes carbonized layer to provide clear cut face at reasonable speeds.

A technique for recycling of roller film for copy machines has been developed in a Japanese Job shop, Shinozaki Works. Two millions of aluminum roller drams for copy machine are wasted a year, causing environmental pollution. To cope with this problem, they developed a technology to remove the surface film by using TEA CO_2 laser without damaging the alminum roll. It takes approximately 20 seconds to remove the film from the dram with diameter 30 mm and length 250 **(Fig. 9)[11]**.

2.3 Annealing

The number of LCD desktop PC sold in Japanese market is increasing rapidly. Conventional display units have been replaced by LCD panels. Recently, over 60% of LCD panels in world market are produced in Korea, Japan and Taiwan **Fig. 10 [12,13]**. Laser annealing is the most important technique for high-quality LCD with sufficient brightness, response for many electronic devices, and KrF excimer laser is irradiated to change an a-Si into a p-Si. The mobility of electrons is drastically improved by the technique resulting a "bright" LCD with higher response **(Fig. 11) [14]**. Although this technology was proposed in early period, introduction to real production had been so delayed until the development of a line-shaped beam with sufficient uniformity. The maximum size of p-Si TFT panel is increasing rapidly to replace larger display unit. Since the length of the shaped beam limits the size of poly-crystal TFT panels, longer and uniform laser beam with higher power is required for this application.

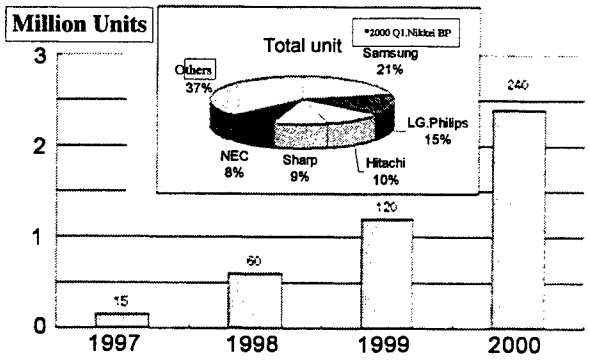


Fig. 10 LCD disk top PC sold in world market.

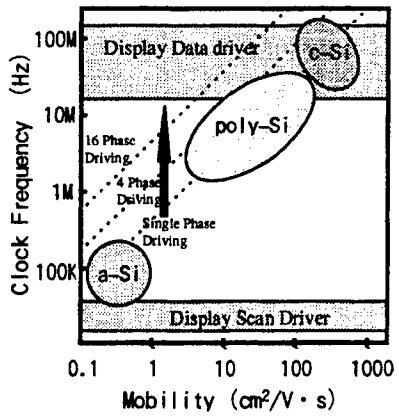


Fig. 11 Mobility of amorphous and crystal silicon.

2.4 Joining:

Laser welding has been finding a variety of applications in automobile, electronic, machinery and steel making industry by using CO_2 and YAG lasers **[15]**. For precision micro-fabrication, pulsed YAG lasers are widely used in a variety of electronic parts, which include optical modules, hard-disk magnetic head suspension, electron gun for TV tube, miniature power relay, coin-type battery, pressure sensor, valve ABS and lithium ion battery as shown in **Fig. 13**. This is because laser can provide precision micro-welding with negligible thermal distortion at high productivity .

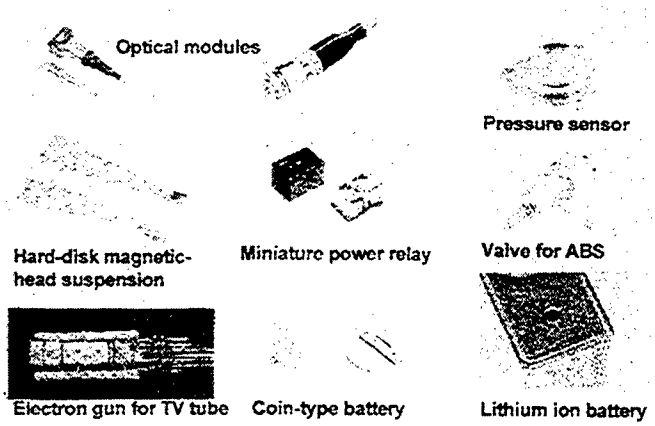


Fig. 12 Examples of micro-welding of electronic parts by pulsed Nd:YAG laser (courtesy of NEC).

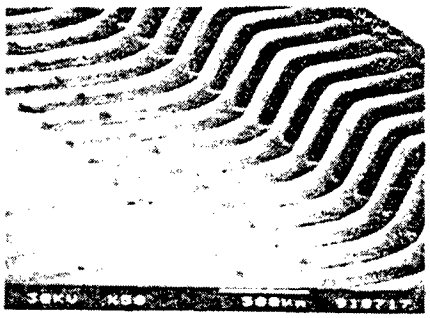


Fig. 13 Fluxless laser micro-soldering of tape carrier package (Mitsubishi Electric Co).

A novel micro soldering technique using YAG laser was developed for TCP (tape carrier package) by Mitsubishi Electric Co. In this technology, a focused YAG laser beam spot is moved along the outer lead by using galvanometric mirrors **(Fig. 13) [16,17]**. Fluxless soldering was realized by removing oxide film on the solder by irradiating focused YAG laser beam with high power density. Joining of approximately 500 joints has been carried out in less than 8 sec with monitoring the beam path. Minimum lead space attained by this technique is as small as a hundred microns.

2.5 Others applications

Laser surface modification has been developed for pretreatment to enhance the characteristics of wire bonding by Matsushita Electric Works **[18]**. The probability of rupture at the bonding interface can be drastically reduced by cleaning effect of the bonding interface and the surface modification of gold plated layer to reduce the stress concentration of the wire bonding region by the irradiation of KrF excimer laser **(Fig. 14)**.

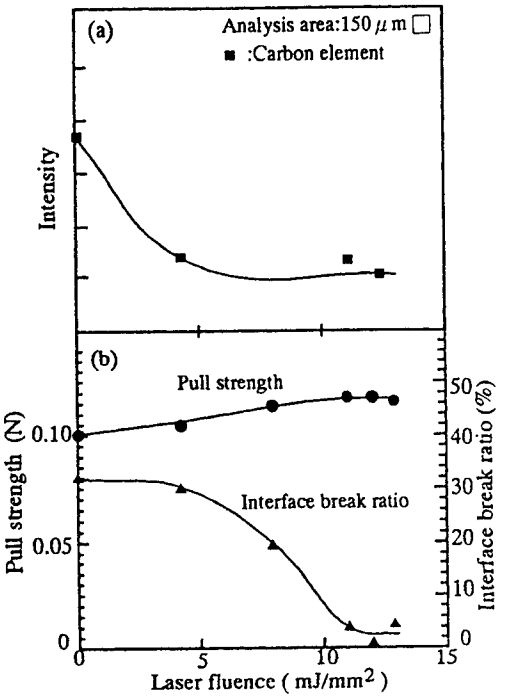


Fig. 14 Laser surface modification in pretreatment for wire bonding surface.

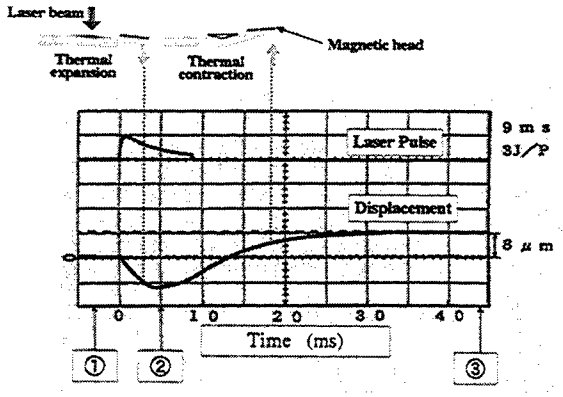


Fig. 15 Displacement by laser micro forming

Table 1 Government supported laser projects in Japan.

Flexible Manufacturing System Complex Provided with Laser Duration:'77~'85 Total Budget:~13.5billion/ 9Yrs.	Cutting, Metal Forming, Laser and Processing CO_2 laser, YAG lsaer), Assembling, Diagnosis, etc.
Advanced Material Processing and Machining Technology Research Project Duration:'86~'94 Total Budget:~16.1billion/ 9Yrs.	High-Power Excimer Laser, High-Density Ion Beam, Ultra-precision Machining and Processing Technology etc.
Advanced Photon Processing and Measurement Technologies Duration:'97~'01 Total Budget(Plan):~7billion/ 5Yrs.	Processing, Measurement, All Solid-State Laser

It is necessary to adjust the height of magnetic head precisely in DVC (digital video for consumer). Precision micro-bending technique has been developed for adjusting the height of by Matsushita Electric Co instead of conventional mechanical technique **[19]**. In the micro-bending, the head goes down during laser pulse due to thermal expansion, and then goes up due to thermal shrinkage during cooling process, providing the accuracy less than 0.5 μm as shown in **Fig 15.**

3. Topics and future aspects

3.1 National projects

Three national projects based on lasers have been carried out since 1977 in Japan as shown in **Table 1.** First, CO_2 and YAG lasers were developed along with a variety of processing techniques in Flexible Manufacturing System Complex Provided by Laser between '77 and '85 with the total budget of 13 billion yen. Second, high power excimer lasers were developed for precision fabrication in AMMTRA (Advanced Material-Processing and Machining Technology Association) between '86 and '94 with the budget of 16 billion yen **[21]**.

Third, all solid state lasers have been developed in Advanced Photon Processing and Measurement Technology started in '97 with 14 members of company and a university as a five year-program with a budget of 7 billion yen **[22]**. The project includes developments of photon beam generation technology, photon-applied micro- and macro-processing technology and photon-applied measurement technology, as shown in **Fig. 16.**

In photon beam generation technology, high-power all solid state lasers and tightly-focusing all solid-state lasers are developed. For high power lasers, compact and portable systems with output power of 10 kW are developed with LD pumping. 3-5 kW YAG lasers have been so far developed by Fanuc and Toshiba. They are applied to macroscopic processing such as welding thick sections of large-scale transports and structures and creation of ecological production system. A tightly-focusing all solid state lasers include disk type fiber laser and harmonic generation. They are required to meet the demands for precision materials processing, and high-speed precision processing. Average power of 320 W with 28% was developed by Mitsubishi Electric Co. with novel pumping technology (**Fig. 17**). They also developed high power green beams of 152 W and high power UV beams of 20 W have been developed so far **[23]**.

Photon-applied microscopic processing includes preparation of ultra-fine particles, synthesizing ultra-fine particles for quantum functional structures, direct printing technology for micro-circuit. In the project conducted by Matsushita **[24]**, the band gap is controlled by decreasing the particle size so that wavelength of optical emission can be controlled, in contrast

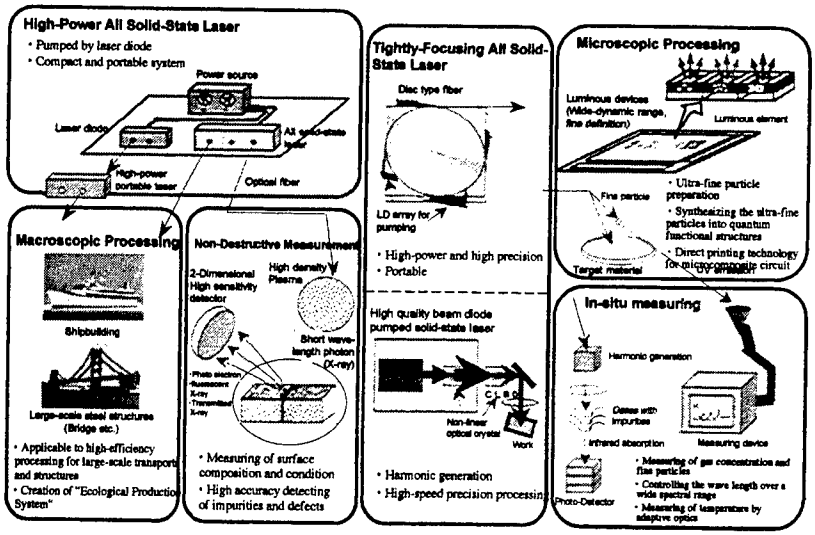


Fig.16 Program of Advanced Photon Processing and Measurement technology (1997-2001).

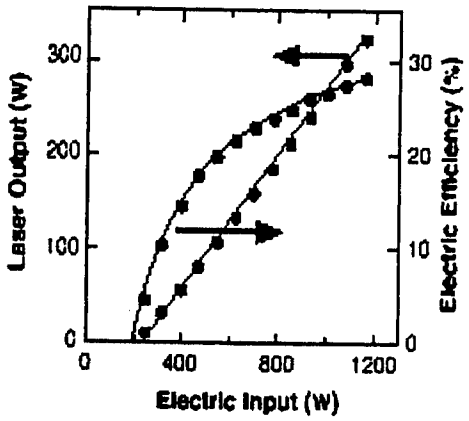


Fig. 17 High efficient laser-diode module using wedge shaped lens (Mitsubishi Electric Co)

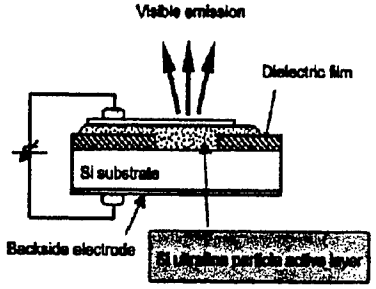


Fig. 18 Laser fabrication of ultrafine Si particles of 1-50 nm for new opto-electronic devices (Matsusita).

to the conventional technology where hazard materials such as Ga and As were doped to control the band gap of semiconductors; red and blue emission has been obtained by controlling the size of ultra-fine Si particle produced by laser ablation (**Fig. 18**). Other interesting application of laser ablated ultra-fine particles is 3 dimensional micro-structuring such as micro-electrode of field emission display [25].

3.2 Topics of R&D

A new method for the fabrication of precise optics using laser ablative figuring (LAF) has been developed at Osaka University [26]. The phase error of transmission wave front is collected by laser ablation with in-situ measurement using a wave front detecting interferometer. Glass-plastic hybrid plates of 5 cm in diameter are used, and a flat surface and spherical lens has been fabricated with the phase error better than $\lambda/6$.

Short wavelength lasers are also attractive for micro machining by restricting the absorption depth. Clean ablation of materials with little thermal influence has been accomplished by simultaneous irradiation of VUV and UV lasers. This is accomplishes by the excited-state absorption mechanism where transient absorption increase of UV beam transmitted by fused silica during VUV beam irradiation is realized [27].

A lot of research work using ultra short pulse lasers has been carried out for ablation, micro-bending, modification and so on. Ablation by ultra-short pulse laser is expected to be a useful tool for precision micro-fabrication with negligible heat affected zone. Almont no ultra short pulse lasers has been used in production, although mask repair system using ps pulse laser has been recently developed for 1G-4GDRAM by NEC [28]. This is because the photon price is so expense, the laser systems are not reliable enough for production use and the processing mechanism is not well understood in ultra-short pulse region. Phenomena occurring during ultra short pulse laser irradiation have been studied by molecular dynamic simulation [29]. In this analysis, the ablation process can be visualized for different materials including Al, Cu and Si, and distributions of size and velocity of the ablated particle are also analyzed along with ablation efficiency as a function of laser fluence. The disarray of atomic configuration caused by laser irradiation can be also analyzed by molecular dynamic simulation where edge dislocations propagate at velocity of longitudinal wave with following the laser-induced shock wave (**Fig.19**).

Much attention has been paid to micro structures induced by ultra-short pulse. Refractive index of the order of 10^{-2} to 10^{-3} has been continuously induced by the irradiation of focused femto second laser in silica glass,

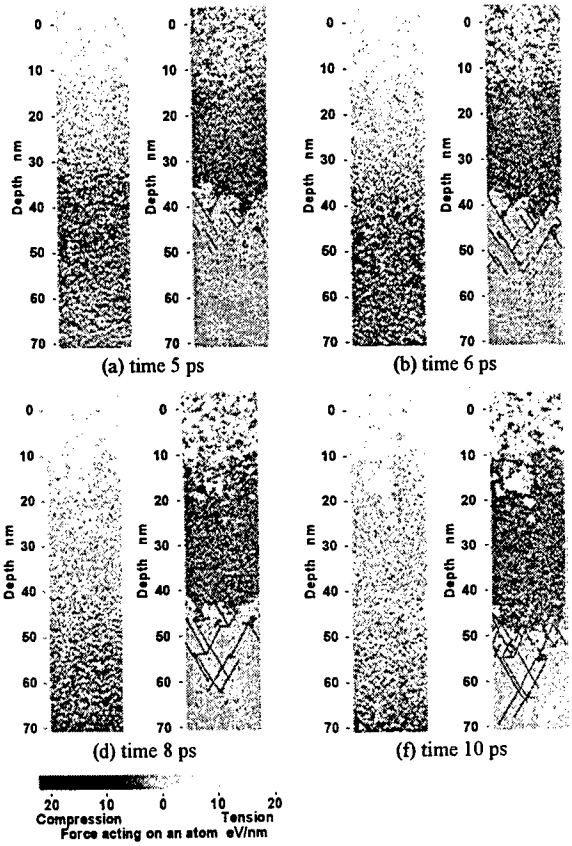


Fig. 19 Stress state (left) and disarray of atomic configuration (right) simulated by Molecular Dynamics (pulse conditions: 30 GW/cm²; 5 ps).

borosilicate glass, chalcogenide glass and so on [31]. This can be applied to drawing 3D optical fiber (**Fig. 20**). Optical wave guide can be also made by using excimer lasers [32]. High laser power of the order of TW enables multi-photon absorption in transparent materials, on which a response of materials confines the spatial resolution of fabrication elements to the size less than optical diffraction limit [33]. This offers a possibility to tailor the 3D memory, photonic band gap structures and so on. Layer-by-layer structure with the lateral lattice constant of 1.4 μm has been realized.

3.2 Future aspects in industrial applications

Preciseness, productivity and reliability are required for production uses of laser precision micro-fabrication. In drilling and cutting applications, productivity can be determined by peripheral equipment to manipulate focused laser beam spot such as galvanometric mirror system and linear transition systems, since the laser performance is sufficiently high. In laser drilling of PWB, for instance, the process speed of 1000 holes/s is limited actually by the beam manipulation system. Different optical systems have been developed to in-

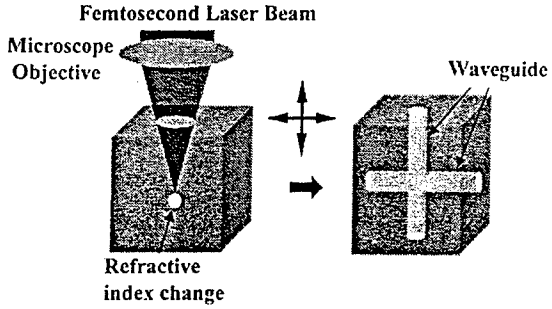


Fig. 20 Scheme of 3D drawing of optical wave guide by ultra short pulse laser.

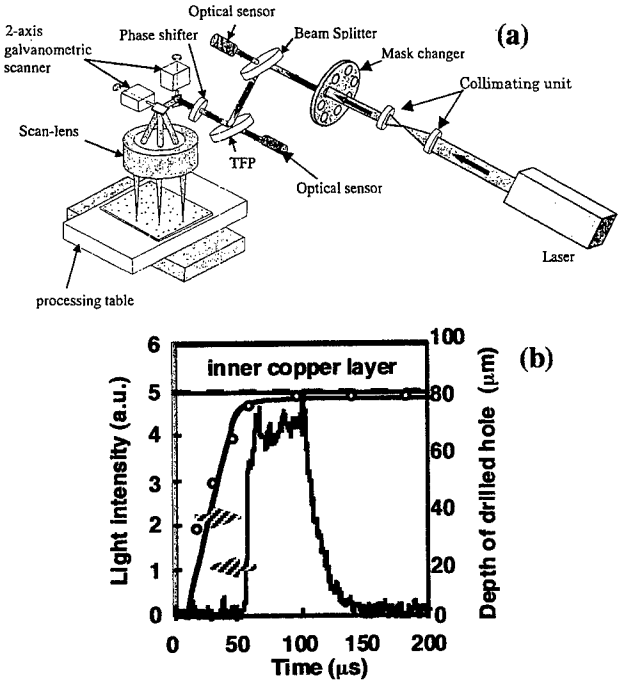


Fig. 21 In-monitoring system for quality assurance of CO_2 laser drilling via hole for PWB detecting: (a) reflected laser beam and (b) light emission.

crease drilling speed further; Sumitomo Heavy Industry has developed the twin head system with the drilling speed of 1400 holes/s, and Mitsubishi ElectricCo. holographic technology with maximum drilling rate of 4000 holes/s [34].

Quality assurance is essential in industrial applications of laser precision micro-fabrication. Although a lot of effort has been made to improve the laser performance in long and short term operations, in-process monitoring for quality assurance is necessary, since the quality of laser fabrication is also seriously affected not only by parameters of laser beam but by material conditions such as geometrical preciseness and surface conditions. It should be noted that the process

speed in laser micro-fabrication is so high that off-line inspection techniques are not realistic. Thus it is necessary to develop sensitive detectors for process diagnostics.

In-process monitoring system, for instance, has been developed by Matsushita Electric in CO_2 laser drilling PWB **[35]** where the bottom area of laser-drilled hole at the inner copper foil in via hole can be monitored by detecting the reflected laser intensity by using a HgCdTe sensor (**Fig.21a**). Simpler in-process monitoring system using a photo diode was also developed in Osaka University to detect light emission from the laser irradiation zone (**Fig.21b**) **[36]**.

Lasers have been increasingly accepted in industry. The largest market of laser precision micro-fabrication is expected to be electronic industry. For realizing wider acceptance of laser micro-fabrication in industry, lasers with shorter pulse and/or shorter wavelength and peripheral equipment with higher performance and low cost are required. It is also important that laser engineers and researchers should understand not only laser processing but also general production.

Aknowledgement

The authors wish to thank the members of working group of Japan Laser Processing Society, "Future Technology of Laser Precision Micro-Fabrication", for their discussion and assistance in publishing this article.

References

[1] Gartner Group Dataquest: *28 February, 2000*

[2] Takahashi et al :*Journal of Japan Institute of Electronics PackagingVol.3 No.3 May 2000 P188*

[3] WG-JLPS: *Future technology of Laser Precision Micro-fabrication (2000)*

[4] Semiconductor Industry Association: *International Technology Roadmap for Semiconductors (1999) 73*

[5] Shinpo: *'99/2000 Japan Laser World & Trend (1999)*

[6] N. T. Information Ltd

[7] Kimera Research: *2000 Electronics Packaging New Material Hand Book (2000)*

[8] A. Gotoh et al: *Proc.35th Symposium of Japan Laser Processing Society (1995) 129*
I. Miyamoto: *J. Precision Engineering, Vol. 65 (1998) 1560*

[9] J. Takeda et al: *Proc.34th Symposium of Japan Laser Processing Society (1995) 203*

[10] T. Ishide et al: *Proc. ECLAT (1996) pp.805*

[11] K. Kokuhuda et al: *Proc. 42th Symposium of Japan Laser Processing Society (1997) pp.61 (in Japanese)*

[12] Quarterly Large-Area TFT LCD Shipment Report, *Display Search, Austin (2000Q1).*

[13]Nikkei MA (on WEB), Press Release, 21 Mar. 1998.

[14] F. Okumura: *Proc.42th Symposium of Japan Laser Processing Society (1997) 121*

[15] I. Miyamoto: *Proc. Laser Materials Processing Conference, LIA Vol. 85 (1998) A-122*

[16] A. Adachi et al: *Proc. Laser Materials Processing Conference, LIA Vol. 80 (1995) 35*

[17] K. Murakami: *Study on Laser Soldering of Micro Lead (Doctor thesis) (1997)*

[18] N. Asahi and J. Tatsuta: *Proc. Mate'98, 4th Symposium on "Microjoining and Assembly Technology in Electronics (1998) 173*

[19] K. Funami and T. Okada: *J. Japan Laser Processing Society, Vol. 4, No.3 (1997) 253*

[20] M. Ikeda: *Proc. Laser Materials Processing Conference, ICALEO84, LIA Vol. 44 (1984)*

[21] K. Haruta: *Proc. Laser Materials Processing Confer-ence, ICALEO93, LIA Vol. 77 (1993) 271*

[22] Pamphlet published by RIPE (R&D Institute for Photonics Engineering) (2000)

[23] S. Fujikawa et al: *3rd Workshop on Advanced Photon Processing and Measurement Technologies, 31 May (2000) 79*

[24] T. Makino et al: *ibid (2000) 11*

[25] E. Ozawa et al: *ibid (2000) 19*

[26] T. Jitsuno et al: *Proc. LPM2000 (2000)*

[27] J. Zhang et al: *Applied Physics, A64 (1997)*

[28] http://mirror.icp.nec.co.jp/japanese/newsrel/9910/2901.html

[29] E. Ohmura, I. Fukumoto and I. Miyamoto: *Proc. Laser Materials Processing Conference, LIA Vol. 85, Orlando, ppA-45*

[30] E. Ohmura, I. Fukumoto and I. Miyamoto: *Int. J. Jpn Soc. Precision Engineering, Vol. 32 (1998) 248*

[31] D.P.Davis, K. Miura, N. Sugimoto and K. Hirao: *Optics Letters, Vol. 21 (1996) pp 1792*

[32] J. Nisii and H. Yamanaka: *Applied Optics, Vol. 36, No. 27 (1997) pp.6852*

[33] M. Watabnabe et al: *Jpn Applied Physics, Vol. 37 (1998) L1527*

[34] y. satoh et al: *Proc.44th Symposium of Japan Laser Processing Society (1998) 105*

[35] H. Karasaki et al: *Proc. Laser Materials Processing Conference, LIA Vol. 85, Orlando, ppG-50*

[36] T. Nakayama, T. Sano and I. Miyamoto: *Proc. Laser Applications in Microelectronic and Optoelectronic Manufacturing, SPIE Vol. 3618 (2000) pp*

Overview of laser microprocessing: fundamentals, practical applications and future prospects

Vadim P. VEIKO

Laser Applications Engineering and Applied Ecology Department,
St.Petersburg Federal Institute of Fine Mechanics (Technical University)
14 Sablinskaya str., 197101, St.Petersburg, Russia
E-mail: veiko@lastech.ifmo.ru
Phone/Fax: +7.812.2333406

Keywords: laser, microtechnology, ablation, quality, liquid, vapors

Today the laser technologies are widely used in the processing of materials, including also the precise microshaping. Deep UV lasers have very good prospects in the lithography, used for fabrication of chips, while the femtosecond pulsed lasers open the new horizons for the micro- and submicroprofilling. But these are the field of the future prospects. As for today state-of-the-art, contribution to the application of lasers for these purposes are the numerous advantages of the laser techniques over the traditional methods, such as: – wide variety of materials to be treated, – possibility of achieving narrow cuts and practically waste-free separation, – small heat-affected zone, – minimal mechanical effect and minimum thermal deformations, – possibility of microshaping along a complex profile in two, or even three, dimensions, – possibility of fast and precise process switch-on and off and to include in the processing feedback on the treated paremeters.

1. Introduction

Laser microtechnology in general develops for the next three most important areas:

microelectronics (ME) — thin films local deposition and removal that means laser trimming and mask saving, laser lithography and micromachining and also laser micropattering in general, as well as annealing, local doping, welding etc etc. [1]

micromechanics (MM) — laser cutting, holes drilling, marking, engraving, scribing, thermal cleaving, welding, hardening etc etc. [2] for many purposes at instrument making, for precision operations in automotive and aerospace technologies and for every kind of microsystem technique.

microoptics (MO) — laser fabrication of microoptical components by surface treatment like microstructuring, microprofiling, polishing and smoothing, and by structure changing like laser densification of porous glasses, amorphization of glass ceramics, extratempering mechanical forces and plasma-assisted microshaping in a softened-phase etc etc. [3].

These areas together provide the progress in many novel directions of engineering like information, communication, medicine, microrobotics and other, which often include micro-opto-electro-mechanical (MOEM) systems as one integrated unit.

We will consider below only microshaping processes which include such fields like laser lithography for ME, precision laser cutting for MM, laser microstructring of MO, including laser polishing of surfaces (and will ignore heating-based processes like annealing, hardening, welding etc) (fig.1).

Basic physical processes of laser microshaping are:

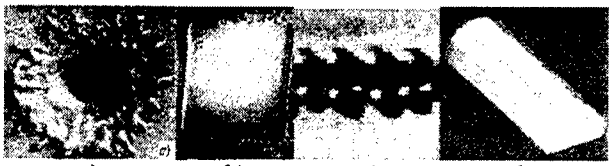
– evaporation, ablation — for any materials [1, 2];
– heating (added by some mechanical actions) — for microshaping of glass components only [3];
– etching and other processes typical for microlectronics for thin films and layers [4];
– 3D laminated increasing — cutting of paper (LOM), polymerisation of photopolymers (SL), synthering of (ceramic) powders (SLS) [4].

But laser ablation-based processes are the most popular. That is why these kinds of microshaping processes we will discuss here.

In spite of external differences in ME, MM and MO applications: different materials (films, metalls, glasses etc) and different lasers (wave-lengths and power) the essence of all of them is the same: due to high absorption materials are finally ablate, and heat processes (melting and evaporation) define the shape changing (fig.1).

The problem for all these areas, which could be pointed: how to improve accuracy and quality of laser microshaping and to increase productivity at the same time?

First International Symposium on Laser Precision Microfabrication, Isamu Miyamoto, Koji Sugioka,
Thomas W. Sigmon, Editors, Proceedings of SPIE Vol. 4088 (2000) © 2000 SPIE · 0277-786X/00/$15.00



a) b) c) d)

Fig.1. General view of laser microshaping results:
a) hole d = 100 μ, steel, Nd:Glass lasers, $\tau = 10^{-3}$ c;
b) square shape (10x10 μ) element, chromium film, N_2–laser, $\tau = 10^{-8}$ c, h = 10^{-1} μ;
c) cut CW CO_2–laser stainless steel; thickness – 3 mm;
d) CW CO_2–laser profilling of quartz–glass.

2. Fundamentals

2.1. The physical model of laser microshaping

Main stages:

– absorption of laser radiation by the law $q(x) = q_0(1-R)e^{-\alpha x}$ at the light penetration depth $\delta = 1/\alpha \sim 10^{-5}$–$10^{-6}$ sm for metals;

– heating of the metarial up to melting point T_m;

– melting after absorption of the latent heat of melting L_m;

– heating up to the vaporization (boiling) point $T_v = T_b|_{P=P_{atm}}$;

– vaporization (usually from liquid phase) after absorption of the latent heat of vaporization L_v;

– vaporization front movement inside the material with the speed V_0.

The one–dimensional vaporization model

Required energy E (neglecting of thermoconductivity)is equal to $E = \Omega[\rho c T_m + L_m + \rho c(T_v - T_m) + L_v]$ (1), where $\Omega = hS$ is the volume of the heated zone.

In terms of power density the equation (1) transforms to $q = h(\rho c T_v + L_m + L_v)/t$ (2), where usually $\rho c T_v \approx 10^3$ J/cm^3, $L_m \le 10^3$ J/cm^3, $L_v \ge 10^4$ J/cm^3.

Vaporization front penetration speed (in assumption that the absorbed energy is spent for the vaporization only (neglecting $\rho c T_v$, $L_m << L_v$) V_0 is equal to $V_0 = q/L_v$ (3).

Qualitative characteristics of the one–dimensional model of microshaping

– The depth of the hole h increases linearly with the duration of action τ, with the speed V_0: $h = V_0\tau = \frac{q}{L_v}\tau$ (4);

– The diameter of the hole does not increases: $d = d_0 = const$;

– No liquid phase — only vapor products;

– The accuracy would be ideal;

– The quality would be ideal.

Two–dimensional model

The one–dimensional model cannot be applied to describe the hole–growth kinetics since as soon as hole depth h becomes comparable with the light–spot size r_0, the effect of the hole walls on to the kinetics of its formation can no longer be neglected.

The increasing of the depth h can be described as before (equation 4) by the vaporization model, but calculation of the hole diameter d change is much more complicated due to the interplay of many factors affecting the heating and destruction of the walls.

This includes at first liquid phase appearance due to melting of material between the isotherms of the surface vaporization T_v and melting T_m (under surface).

Other important factors which affect the process are (fig.2):

– vapor condensation,

– direct light absorption by the walls due to beam defocusing,

– light scattering by the plume,

– radiative and convective heat–exchange between the vapor jet and the walls,

– heat–conduction.

This list of phenomena should be added by:

– surpluss vapors pressure which should remove the melted material from the hole (cut) and

– scrinning effect by the erosion products (vapor plus liquid) to the incident radiation.

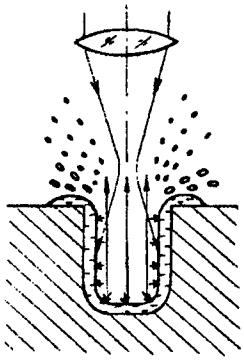


Fig.2. The schematic diagramm of laser microshapinng

The main effects limiting quality of laser microshaping

We can conclude now that in every real laser microshaping process significant fraction of the liquid phase remains at the irradiated zone after the end of the laser pulse.

Formation of a large amount of liquid and its incomplete removal from the surface (hole cut) are, in general, adverse and hard–to–control phenomena which cause a considerable decrease of the efficiency and quality of laser microshaping

The redistribution of the liquid prior to crystallization plays a decisive role in a final shape formation. As a result of the redistribution, the surface shape to the end of solidification can differ substantially from that determined by the beam geometry, the vaporization kinetics, and the hydrodynamic rejection of part of the liquid–phase material at the end of the laser pulse.

Main reasons for liquid phase increase are:

- the decrease of the light flux density due to the gradual beam-defocusing with the hole–depth growth;
- the slow power decrease at the pulse trailing edge contributes to the increase of the volume of liquid–phase residue at the surface after the pulse;
- extra duration of the action time: the longer is the action time, the greater is the melted volume and, therefore, the greater is the hole size and cut width scatter; in addition, a long action time causes the development of a zone of considerable size where oxidation and structural changes occur, as well as the appearance of defects on the hole (cut) surface as a result of the increase of the depth of heat–affected layer.

Another sources of inaccuracy in microshaping are:

- the inhomogeneity of transversal beam intensity distribution due to mode character of laser generation;
- the blurring of the light spot edges at processing in the focal plane.

Results of physical models consideration [6]:

1. The main factor limiting quality of laser microshaping is the liquid phase appearance.

2. The general reason of the liquid phase appearance is melting of material at the size, which approximately estimated as: $x_m \sim \sqrt{a\tau}$ (5) (a — thermodiffusivity coefficient).

3. The most important reason of the liquid phase movement is the recoil vapor pressure action P_p, which approximately proportional to: $P_p \approx \frac{F_p}{S} = \frac{mW}{S\tau} \sim \frac{W}{\tau}$ (6), where F_p is recoil force, S — light spot square, m and W are evaporated mass and the speed of vapor's movement.

4. To provide conditions for minimization of liquid phase it is necessary to optimize of a laser beam as a tool for microshaping and properly:

– energetical and temporal characteristics which depend on laser source parameters;

– spatial characteristics which depend on laser beam and optical system parameters and

– by optimization of the laser–matter interaction process characteristics.

5. The easiest way to satisfy the quality requirements – is to provide the conditions where the one–dimensional model works.

2.2. Requirements to the laser source

Which laser mode is better: continuos-wave(CW) or pulse-repetition (PR)?

From the point–of–view of energy losses, pulse–repetition laser generation mode is much better than continuous–wave one.

To compare necessitive power for microshaping with CW and PR lasers let us calculate it, taking into account that to change a shape means to heat material up to evaporation temperature T_{ev}.

For CW laser corresponding power P_{cw} it is possible to calculate from temperature threshold for stationary conditions $T_v = qr_o/\kappa$ (7) [1] (r_o — light spot radius, k — thermoconductivity coefficient), where from $P_{cw} = \pi r \kappa T_v / A$ [8].

For PR laser corresponding threshold should be calculated from pulse condition [1] $T_p = 2Aq\sqrt{a\tau}/\kappa\sqrt{\pi}$ (9) (A — light absorbance), where pulse power $P_p = \pi\kappa r^2 T_p \sqrt{\pi}/2A\sqrt{a\tau}$ (10) and average power $\overline{P}_p = \pi\kappa r^2 f T_p \sqrt{\pi\tau}/2A\sqrt{a}$ (11) (f is a pulse repetition rate). Now we can define searched ratio:

$$\boxed{\overline{P}_p / P_{cw} = r_0 f\tau / \sqrt{a\tau}} \qquad (12)$$

Let us estimate it for τ = 1ms, f = 1kHz, r_o = 100 μ, a = 0,1cm/s, $\sqrt{a\tau}$ = 100 μ, $r_0/\sqrt{a\tau} \cong 1$, $f\tau \cong 10^{-6}$. So, at any rational r_o, a and τ we have $\overline{P}_p << P_{cw}$.

Pulse duration τ defines the next process characteristics:

– pulse energy threshold q_{cw} (formula 9, 10);

– liquid phase amount x_m (formula 5);

– reactive vapor pressure value P_v (formula 6);

– thermomechanical stresses value $F_{tm} \sim \sqrt{\tau}$ (approximately);

– screen effects of vapors to the incident radiation;

– stability of the irradiated size (instability $\sim\sqrt{\tau}$) [1];

– stability of power density threshold depending on size of irradiated zone.

By the all of these reasons than pulse duration is less than better.

Comments:

- the effective action time for continuous–wave lasers is equal to $\tau = d_0/V_{sc}$ (13), where d_0 is the focal spot diameter, V_{sc} is the scanning speed,
- in any case one should check the condition (9, 10),

one should also take into account that $h_v \sim V_0\tau$, and than τ is less than single–pulse hole depth h is smaller.

Laser power P should provide the power density q_i — the more, the better (decrease of liquid phase part) — between the evaporation threshold q_{thresh} (9, 10) and threshold of absorption in erosion plume; usually $q \approx 2–3\ q_{thresh}$.

Calculations show that usually laser power P = 1 kW is necessary (pulse or continuous) for microshaping.

Wavelength λ should be in the region of the high absorbance of the material (visible for metals and other constructional materials, IR for glass, UV for polymers) depending on the optical parameters of the material (R, A $= 1 - R$, $\delta = 1/\alpha$).

Pulse repetition rate f: the most important roles of f are: the direct fluence on the productivity of microshaping and the choice of typical technological operations.

Cost effectiveness

From all of these parameters Nd–YAG–lasers acousto–optically switched ($\tau \sim 10^{-7}$ s, $f \sim 10^4$ Hz), Cu–vapors lasers ($\tau \sim 10^{-8}$ s, $f \sim 10^4$ Hz), excimer lasers ($\tau \sim 10^{-8}$ s, $f \sim 10^3$ Hz) looks preferable for most applications. Sometimes (for glass–ceramic materials, for example) CO_2–laser has a first priority.

2.3. Requirements to an optical system

Any optical system for laser microshaping should meet three basic groups of requirements: those having to do with the laser energy, those connected with the operation field and those related to the system accuracy.

In terms of energy, the system should provide:

- Light intensity sufficient for performing the operation required on the surface treated;
- Maximum utilization of the laser emission energy, depending on the losses on diaphragms (vignetting) and on the optical components (Fresnel reflection and residual absorption).

Among the requirements to the accuracy, we will emphasize:

- The need to have the minimum spot size;
- The need to form a strictly delineated zone of treatment with a given shape;
- The need to obtain minimum edge roughness of the zone irradiated (treated).

In terms of operation field the most important questions are:

- How to cover the full working field by means of opto–mechanical scanning systems or optical projection systems;
- with the acceptable accuracy, productivity and by simplest way.

There are 2 main ways to organize laser beam in space for laser microshaping: 1) to operate in the focal plane (A, fig.3), or 2) to process surface in the projection plane (B, fig.3). The difference is not only in calculation of spot size, but in energy distribution also. In the focal plane A (fig.3) we have Fraunhofer diffraction distribution (Bessel function) — far–field zone, or Gaussian distribution for single–mode laser. In any case spot–size at the focal plane depends on intensity level — than more intensity than less the spot–size — in this sense melted zone much more than evaporated.

Opposite situation in plane B — projection plane B (fig.3) is a Frehnel diffraction zone (near–field) and energy distribution in this plane repeats the energy distribution of the source (or mask — secondary source) plane and could be performed nearly homogeneous — with the step edges and with any shape of the spot (using the corresponding mask).

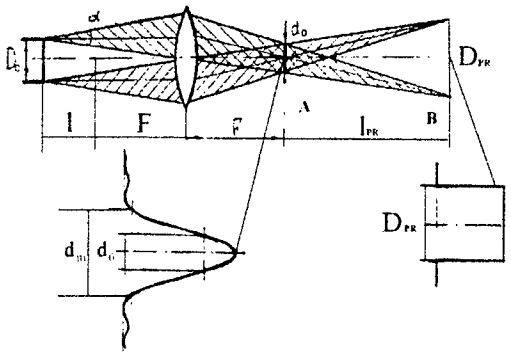


Fig.3. Telecentric model of the laser source (multimode operation) Focal spot $d_0 = \alpha F$, depth of focus $l = 2d_0F/D$ (14) Projection spot $D_{pr} = D\beta$ (15) (β — amplification of optical system, $\beta = F/l_{PR}$)

For the focal spot it is have sense to ask — **what a minimum spot size can be achieved?** There are two possibilities to overcome diffraction limit: 1) in the far–field we have the dependence $d_0(I)$ and d_{min} depends not from optical phenomena but from physical limitations in the area $d_0(I) < \lambda$. For the hole formation in the thin film with the thickness h it was shown [1] that $d_{min} \approx h/2 \div h$ depending on film adhesion to the substrate; 2) near–field lithography where using not conventional optics principals and lenses are used, but nanosized probes placed at nanosize distance from the surface [7].

As for operation field there are two most popular systems — scanning system and projection one. Strong differences in A and B types of scanning systems accuracy, size of field and other parameters partially clear from the fig.4. For details one can be adressed to the papers [5, 8].

Scanning techniques for LM

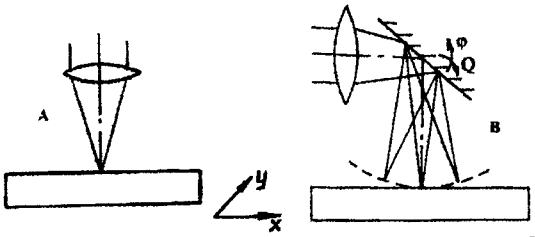


Fig.4. A — A–type–sample surface at the focal plane of a lens
B — B–type–only the central point of the sample surface at the focal plane of lens

Important note: it is evidence, that for stable microshaping conditions (stable quality) one should provide stability of power density q. As it is possible to see from (11) and (13), that required power density q for scanning systems is equal to: $q = hV_{sc}/d_0 L_v$ (16), or in terms of power $\frac{P}{V_{sc}} = hd_0 L_v = \text{const} = B$ (17) that means P, V_{sc} should be constant for stable power. It is especially important for machining of complicated shape patterns with a high speed. In this case it is impossible to hold up the same speed at the direct lines and at the steep turns (short arks). If V_{sc} is not constant but changes along the trajectory in accordance with some law V_{sc} (t), it is impossible to satisfy to the equation (17) $P = BV_{sc}(t)$ with any dynamic control of continuos–wave laser power.

So, only pulse–periodic lasers can provide the condition (17), that means the constant power density of the treated zone and stable quality of laser microshaping.

B–type systems have additional limitations which are just clear from the figure that requirements to increase L and to reduce d are contradictory to requirement to reduce the spot size (look for details [5]).

The principles of projection technique is clear from the fig.3. The advantage of such kind of systems is accuracy at first and complicated (if necessary) shape of image.

The disadvantages connected with energy losses at the mask and contradictions between the size of the operation field and optical resolution at the image [1].

Sometimes the best exit is to use scanning–projection technique by scanning at the A–type system of projected in the square–shape beam (contour–projection method) [1].

We can conclude now from the above given consideration that to improve quality and productivity of laser microshaping it is necessary to use short–pulse lasers with high absorbance in a material with high pulse–repetition frequency and preferably scanning–projection optical system, but of course depending of the operation type. Cost effectiveness limits possible solutions in high degree.

3. Practical applications of laser microshaping

3.1. Microelectronics

Laser technology in microelectronics is widely uses for several kinds of operation [1,2]:

– laser lithography, which includes mask saving, photomask topology correction, mask generation, integrated circuits specification, micromarking etc;

– laser trimming of electronic components like resistors, quartz–resonators and filters, functional trimming of thin–film circuits etc;

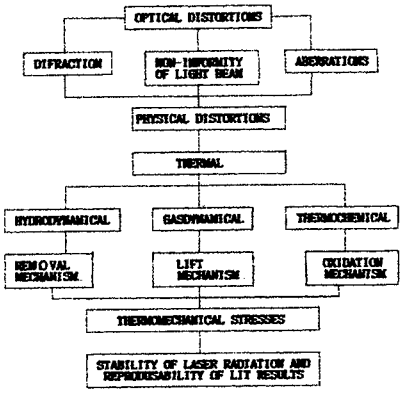
– information recording, as digital data as analog one;

– laser deposition of thin films and structures;

– laser annealing, alloying and doping of semiconductors;

– microwelding, microholes drilling, cutting, scribing etc;

– local laser thermochemical and photochemical operations like CVD, etching, maskless pattering etc.



Scheme 1

Let us point near only the problems and ways to overcome them in laser lithography. It is clear from the scheme 1, where is consequently performed distortions on the way to registrate pattern at the thin film from optical to physical etc. Some of them, hydrodynamical, for example, are illustrated by fig.1, b, where the micropattern, registrated at the Cr–film is shown. To reduce or to eliminate most of them the above given recommendations in the section 2 are quite enough. For more details one can look monograph [1].

3.2. Micromechanics

Let us put in this section most operations with micromechanical components like cutting, holes drilling, thermal cleaving, scribing, marking, engraving, welding, soldering, hardening etc etc.

Most difficult operation is of course precision laser cutting in case when the high quality of the final product required. One of the most famous example is laser figure cutting of medical stents — kind of human vessels prosthetic devices [6, 9]. Stents are originally small steel tube with diameter ~ 1–2 mm with walls thickness about 100 μ. It should be cutted by tricky pattern (fig.5) with minimum amount of any traces of laser treatment like drocces, uneveness, thermal affected zone which is shown at fig. 1c and 6.



Fig.5. Block diagram of the stent before dilatation

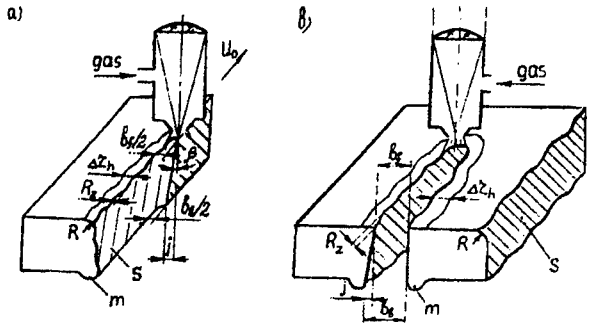


Fig.6. Characteristics of laser cut quality: m — drocces, s — striations, Δr_n — size of thermal affected zone, R — melting radius of the front side, R_z — uneveness of surface, b_f and b_c — width of cut at the front (b_f) and at the back (b_b) side, β — angle of the cut lag and of striations inclination (half cut (a) and full cut (b) view)

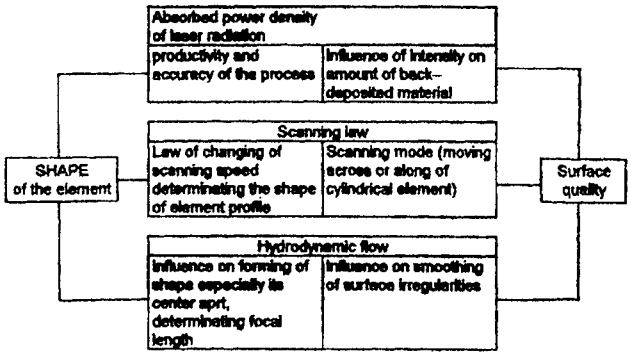
Recommendations given at section 2 can improve the quality stents in high degree.

3.3. Microoptics

It is relatively new area of laser microtechnology, but it looks very promissable [3, 10]. Laser beam being controlled in time and especially in space (on produce many tricky microoptical components). Usually, the thermal action of laser beam uses, that is why most important laser is computer–controlled scanned CO_2–laser [3]. Sometimes it is possible to use excimer laser, preradiate the glass sample by, for example, deep UV to initiate the strong absorbance at the excimer laser wavelength [10].

Different phenomena can be and has been used: densification of porous glasses, amorphisation of glass ceramics, extratempering of optical glasses, microshaping in softened phase etc etc.

The most interesting example in the context of this paper is a direct microprofilling of quartz glass during the process of laser ablation combined with laser "polishing" or smoothening of surface [ ].



Scheme 2. The most significant factors of laser evaporation–ablation technique for shaping and surface quality of optical components

The scheme of laser microprofilling is clear from the fig.7 where laser beam act like a thin diamond tool. The shape of the surface in this case defines by the law of the beam trajectory, and it is no problem to provide the aspheric shape (fig.8). The problem as usual is a liquid (softened) phase appearance which interrupts to realize the high surface quality.

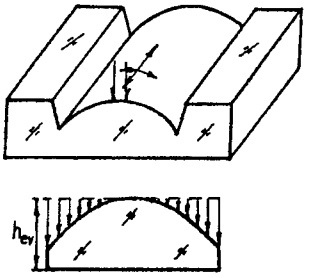


Fig.7. Schemes of laser evaporation of cylindrical surfaces

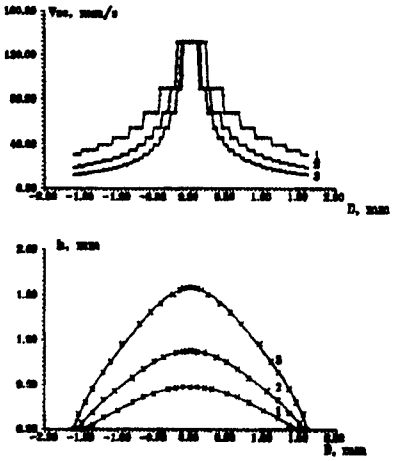


Fig.8. Curves of scanning speed changing at the width of sample V_{sc} (D) for aspherical surface hyperbolic function $y = -\left(0.4 - \sqrt{0.16 + 4.4x^2}/2.2\right)$ with different compression 1, 2, 3 of scanning function y, a), corresponding profiles of fabricated (x) and calculated (–) lenses (b).

The way to solve this problem is not to eliminate or to remove the liquid layer but to use the surface tension for radical improving of the surface quality — like at fire polishing. What is necessary — to carry condition when scanning beam drives the hydrodynamic wave, $V_{sc} \le V_w \frac{h_m}{\mu} \frac{dT}{dz}$ (18) (μ — viscosity). In this case the waves in liquid goes to the edge of the sample like impurities in semiconductors during the cleaning by zone melting (fig.9). This process is easy to realize by combine action of laser beam and H_2–plasma jet [11]. The final result of one of this operations is shown at the fig.9.

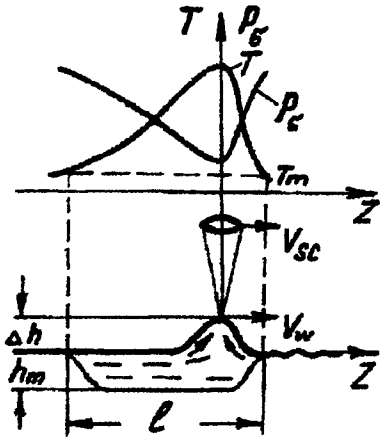


Fig.9. The scheme of the process of glass smoothing by scanning heat source

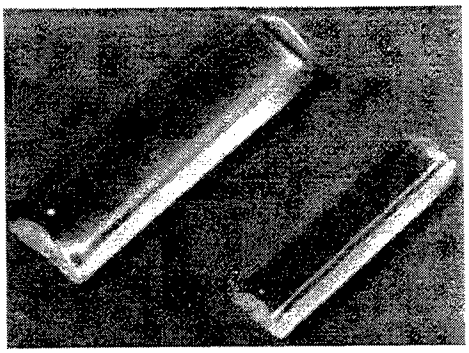


Fig.10. Photo of aspherical cylindrical lenses produced by laser microprofilling simultaneously with H_2–plasma jet surface smoothing

4. Future prospects

It is difficult to forecast future prospects of laser microtechnology by the reason that life sometimes outstrips even the most courageous prognosis.

Nevertheless we shall take the responsibility to suggest some future directions of laser microshaping:

1. 3D microprofilling of complicated–shaped microcomponents and microtools like aspherical optics, master–rigging etc.
2. Nanotechnology (nanometrics–superresoluted components) like submicron lithography, SNOM–tips fabrication etc.
3. Aspherical optics fabrication, especially specified complicated raster optics for semiconductor bars and matrix, as a medical tools at the distal end of fibers.
4. Supersmall mechanical parts from metals, ceramics and plastic for microrobotics, microactuators, medicine, MOEMS.
5. High quality laser microshaping using different medias — in and under water and other solutions using water guiding laser beam etc.
6. Combined laser microshaping assisted by plasma–jet, gas–jet, water–jet, mechanical forces etc etc.

For these purposes the further shortening of time–action will be useful up to femto– and may be attoseconds (Ti–sapphire, excimer lasers), simultaneously with pulse repetition rate increasing.

UV, deep UV and may be X–ray lasers can open new perspective in micro– and nanotechnology may be especially in molecular technologies like biotechnology etc.

New generation of semiconductor lasers with new generation of optics (look p.3.3) could radically change many existed laser-processes.

Cu-vapor lasers due to very good compromise of pulse duration, pulse repetition rate, average power and wavelength probably will move a little Ng–YAG laser from the market especially from the laser systems for simultaneous microshaping and viewing (due to high amplification coeffcient).

Nd–YAG and CO_2–laser based (for different materials) laser system for microshaping due to good compromise of technical parameters and cost efefctiveness will stay at the market as a most popular light sources.

Excimer lasers will be preferrable for treatment of all photosensitive media like polymers (photopolymers) and also for microshaping of biotissues (skin, cornea etc).

5. References

[1] V.P.Veiko, S.M.Metev. Laser–assisted microtechnology. Springer–Verlag, Heidelberg, 1994 (first edition), 1998 (second edition).

[2] I.W.Boyd. Laser Processing of Thin Films and Microastructures Springer Ser. Mat. Sci., Vol.3 (Springer, Berlin, Heidelberg 1987).

[3] V.P.Veiko, E.B.Jakovlev, A.K.Kromin, V.A.Chuiko et al. Laser technologies for miniature optical elements: approachs and solutions.

Proceedings SPIE, v.1992, Miniature and Microoptics, p.114–127, 1993.

[4] D.Bäuerle. Laser Processing and Chemistry, 2nd edn. (Springer, Berlin, Heidelberg 1996).

[5] V.P.Veiko. Principles of optimisation laser–assisted 3D–synthering systems. Proceedings of 5th European Conference on Rapid Prototyping and Manufacturing, Editor Dr. P.M. Dickens, p.141–155, 1996.

[6] V.P.Veiko, V.A.Serebryakov, V.A.Rusov, B.M.Jurkevich. Problem of laser impulse microshaping quality: analysis and synthesis. Proceedings SPIE, v.3822, Computer–Controlled Microshaping, p.68–76, 1999.

[7] V.P.Veiko, Yu.M.Voronin, N.B. Voznessenski, S.A. Rodionov, I.Smirnov, A.Kalachev. Optical nanoprobes for scanning near–field optical microscopy: functions, requirement, fabrication and theoretical reconstruction from far–field investigation. Proceedings SPIE, v.3688, 6th International Conference on Industrial Lasers and Laser Applications '98, p.406–414, 1998.

[8] V.P.Veiko, D.L.Goubanov, A.K.Kromin, S.A.Rodionov, A.T.Shakola, V.A.Chuiko, B.P.Timofeev, E.B.Jakovlev. Comparison of scanner and plotter systems for laser–assisted rapid prototyping technique. Proceedings SPIE, v.3091, Laser Applications Engineering (LAE–96), p.49–57, 1997.

[9] Y.P.Kathuria. Laser Microprocessing of Stent for Medical Therapy. 1998 International Symposium on micromechatronics and human science, p.111–114.

[10] K.Sugioka et al. Multiwavelength irradiation effect in fused quartz ablation using vacuum–ultraviolet Raman laser. Applied Surface Science 96–98 (1996), p.347–351.

[11] V.P.Veiko, A.T.Shakola, V.A.Chuiko, A.K.Kromin, E.B.Jakovlev. Aspherization of cylindrical lenses by laser irradiation. Proceedings SPIE, v.2687, Miniaturized Systems with Microoptics and Micromechanics, p.156–166, 1996.

Surface and bulk ultra-short pulsed laser processing of transparent materials

Ingolf V. HERTEL, Razvan STOIAN, David ASHKENASI*, Arkadi ROSENFELD, and Eleanor E.B. CAMPBELL**

Max Born Institute, Max-Born-Strasse 2a, D-12489 Berlin, Germany
E-mail: hertel@mbi-berlin.de
**now with LMTB, Berlin-Adlershof, Germany, **Department of Experimental Physics, University of Gothenburg and Chalmers University of Technology, S-41296, Gothenburg, Sweden*

Ultrashort pulsed laser ablation of dielectrics has been investigated using ex-situ morphological examinations in combination with in-situ time-of-flight mass spectrometry of the ablated species. Analysis of the energy spectrum of the ablation products provides a wealth of information on the processes occurring during femtosecond laser ablation of materials. The presentation will focus on the case of sapphire (Al_2O_3) and discuss the fundamental processes in ultrashort pulsed laser sputtering. Two different ablation phases have been identified, a „gentle" phase with low ablation rates and a „strong" etch phase with higher ablation rates, but with limitation in structure quality. A comparison of the energy and momentum distributions of ejected ions, neutrals and electrons allows one to distinguish between non-thermal and thermal processes that lead to the macroscopic material removal. Fast positive ions with equal momenta are resulting from Coulomb explosion of the upper layers at low fluence and low number of irradiating laser pulses („gentle" etch phase). Pump-probe studies with fs laser pulses reveal the dynamics of excitation and electron mediated energy transfer to the lattice. At higher laser fluences or after longer incubation, evidence for phase explosion can be derived from both the morphology of the surface and the results of the in-situ experiments.

Keywords: ultra-short pulsed laser processing, dielectrics, ablation, velocity distribution, Coulomb explosion, phase explosion, self-focusing.

1. Introduction

Improved availability and compactness of ultra-short, sub-ps pulsed solid state lasers has stimulated a growing interest in the exploiting of the enhanced flexibility of femtosecond-technology for micro-machining. Disregarding price and user friendliness of present laser systems - which will improve massively in the coming years – ultra-short laser pulses offer a variety of advantages for precision micro fabrication. Presently, the first designated commercial femtosecond machining stations are available for an expanding market. Due to lower energetic thresholds for sub picosecond ablation and the controllability of individual laser pulses (e.g. by laser pulse length) the amount of energy deposited into the processed sample can be minimised and highly localised. This leads to a reduction of unwanted thermal effects, a minimisation of energy diffusion, and little débris (material ejection) so that very clean microstructures can be achieved with pulses optimised for the individual application. Fig. 1 illustrates as an example that the most perfect micropores can be achieved with 800 nm, 200 fs pulses in c-Al_2O_3 (sapphire) – while other materials, e.g. CaF_2 may well require picosecond treatment for optimal results [1]. Also non-linear optical effects may be exploited: efficient multi-photon absorption allows one to modify transparent materials even inside the bulk and to obtain sub wavelength structure sizes. Self-focusing due to the non-linear optical Kerr effect may be used to induce long, narrow 3D-modification traces into the bulk of wide band gap materials. Long, micrometer thin channels can be also drilled taking advantage of the high ablation rates and low heat depositin when employing ultrashort laser pulses [2].

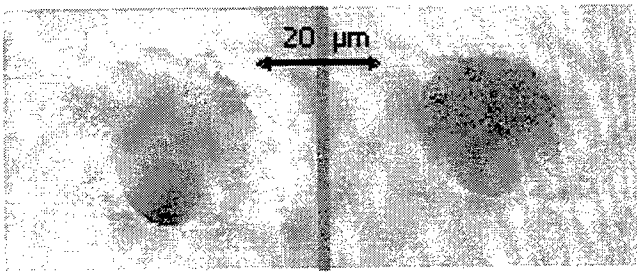


Fig. 1 Micropores in Sapphire created with ultrafast 800 nm laser pulses illustrating the influence of pulse duration (left 4.5 ps, right 200 fs – same laser fluence).

First International Symposium on Laser Precision Microfabrication, Isamu Miyamoto, Koji Sugioka, Thomas W. Sigmon, Editors, Proceedings of SPIE Vol. 4088 (2000) © 2000 SPIE · 0277-786X/00/$15.00

These prospects warrant a detailed understanding of the physical mechanisms involved in material processing with ultrashort laser pulses. From the view point of basic research, sub-picosecond pulses offer additional advantages: In contrast to the more standard investigations of material ablation, or sputtering, with ns laser pulses, they do not interact with the plume of ablated material since the pulse has stopped before the material removal takes place. The avoidance of secondary effects due to plume heating as well as the possibility of pump-probe experiments on a time scale of some tens of femtoseconds to some hundreds of picoseconds makes a detailed investigation and understanding of the laser-matter interactions, energy dissipation and mechanisms of material removal feasible. In addition new avenues are opened to a basic understanding of energy deposition into the sample and to a real time monitoring of the electronic and atomic processes in solids under the ultrashort pulsed laser excitation.

The present study focuses mainly on sapphire (c-Al_2O_3) in view of its many useful mechanical, optical and electrical properties, and also since it shows in a very clear manner two distinctively different ablation phases which are believed to be characteristic for pulsed laser structuring of wide band gap materials [3, 4]. A "gentle" phase is found for low laser fluences (and low numbers of laser shots) which is characterized by the removal of a few nm (20-30 nm) in depth per laser shot, leaving behind a smooth surface. Surface charging and ion Coulomb explosion is found responsible. The "strong" phase is characterized by an order of magnitude higher ablation rate per pulse. It is accompanied by significant plasma light emission and shows a violent expulsion mechanism tentatively assigned to phase explosion. We use

- a quantitative ex situ evaluation of ablation results (AFM, SEM, optical microscope).
- in situ determination of the velocity distribution of ablation products
- and pump-probe techniques

to quantify the appearance of the two phases and glean evidence on the mechanisms and dynamics of the processes involved. The laser pulses as such offer a convenient tool to probe the energy deposition and modification process of the material in very controlled manner. The parameters which we vary are:

- number of pulses/site: N
- pulse duration: τ [ps, fs]
- laser fluence: F [J/cm^2]
- and in the pump probe experiments delay time: Δt.

Our study is guided by the generally accepted picture for the excitation of dielectrics with ultrashort, near infrared or visible laser pulses: The initiating excitation mechanism is believed to be multi-photon absorption, either from already present morphological or structural defect states in the band gap or by interband transitions, which seed free electron heating and additional ionisation due to electron impact. This is followed by photoelectron emission with surface charging and thermalisation of the quasi-free electronic system on a material-dependent time-scale and energy transfer to the lattice by electron-phonon coupling with subsequent heating of the sample. The questions we have tried to answer refer to how and how long does it take for a particle to be emitted and the approach was to identify the paths and temporal characteristics of the energetic channels originating from the laser beam and coupled with the emitted particle itself. What is the energetic spectrum of the emitted particles? What happens to the surface and to the affected bulk after laser irradiation? To what extent can this micron or sub-micron modification be controllable by an optimal choice of laser parameters? What is the role of laser induced defects in surface micro-machining or optical properties of the irradiated solid?

2. Quantitative ex situ identification of gentle and strong ablation phase

It will be shown that a suitable choice of laser parameters can tune the transition between different processes, dominated by either non-thermal or thermal mechanisms, respectively. A first fingerprint of this change in mechanisms is gleaned from determining the material removed by a single,

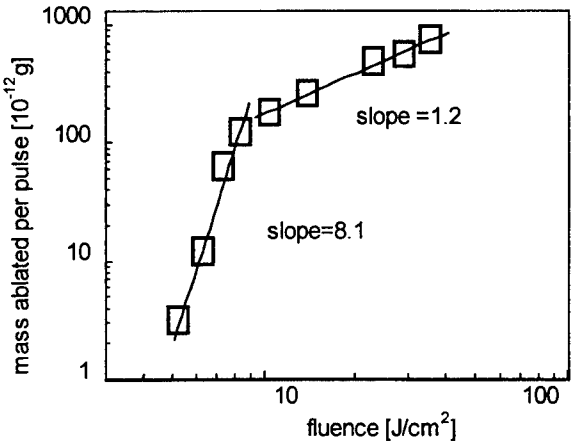
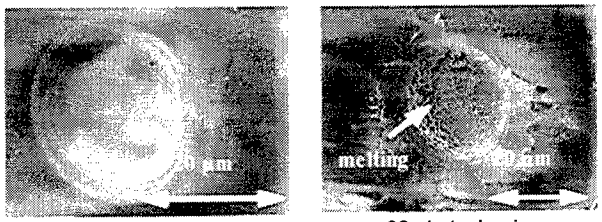


Fig. 2 Log-log plot of the amount of material removed from c-Al_2O_3 after the first laser pulse (800 nm, 100 fs) as function of its fluence.

ultra-short laser pulse a function of fluence. This is shown in Fig. 2 for sapphire at a pulse width of 100 fs as determined by a careful evaluation of the volume of the ablated spot by atomic force microscopy (AFM). At low fluence, it shows in a log-log plot a high slope of ~8, indicative of a high order excitation. At high fluence we observe a nearly linear increase, i.e. the material removal is proportional to incident energy which reflects a thermal process and significant temperature rise of the lattice.



10 shots: *gentle etch phase*

30 shots: beginning of the *strong etch phase*

Fig. 3: Transition from gentle to strong etch phase in c-Al_2O_3.

This change of mechanisms which is attributed to different ablation phases is most evidently identified by the visual appearance of the irradiated area in a scanning electron microscope (SEM). This is illustrated in Fig. 3. The first laser shots above the damage threshold initiate the *gentle etch-phase*. For 200 fs irradiation the gentle etch-phase (N<30) is characterized by an extremely smooth surface (sometimes even smoother than the initial state), both at the sidewall and at the bottom of the dip with almost no pattern developing except ripples [2] and with no debris particles

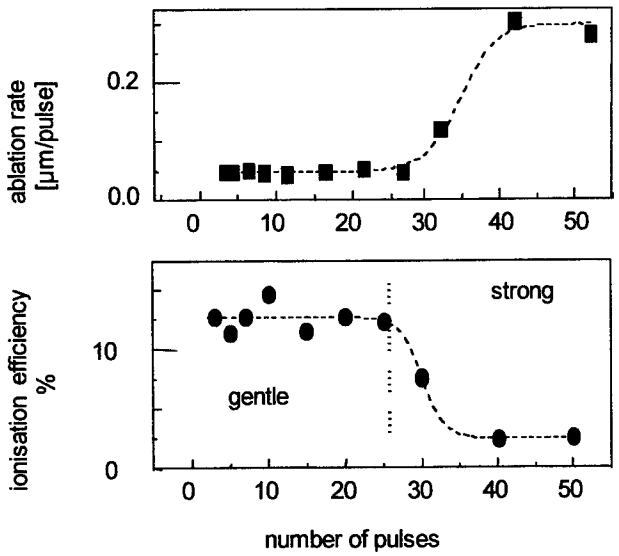


Fig.4: Quantitative determination of the transition from *gentle* to *strong etch phase* by measuring the ablation rate per laser pulse and the degree of ionisation in the plume as a function of the total number of laser pulses N applied to a given site. The pulse duration was τ = 200 fs, the laser fluence F=4.0 J/cm^2.

around the rim. Material is removed with every laser pulse, including the first one. The ablation rate is low, around 20-30 nm/pulse as determined by a volume evaluation using Atomic Force Microscopy (AFM) [4].

At a higher number of laser pulses, the appearance of the spot changes dramatically as illustrated for N=30 in Fig. 3. The surface shows the characteristics of the strong ablation phase: increased roughness and signs of a violent process of thermal nature, among them droplets, melting traces and splintered edges. At a still higher number of shots even crater formation is observed. The mechanisms underlying this *strong etch phase* is basically thermal and may be associated with phase explosion [5, 6].

The change from the gentle to the strong etch-phase occurs between 25 and 30 laser pulses per site at this particular fluence and depends also on fluence and laser pulse width. At the same time the ablation rate increases drastically (~300 nm/pulse). This allows us to determine the crossover between the two phases in a quantitative manner [7] as illustrated in Fig. 4 (upper panel). We can also determine the degree of ionisation in the plume from a quantitative evaluation of the ion current during each shot and comparison with the amount of material ejected. As seen in the lower panel of Fig. 4, the ionisation efficiency also changes dramatically when the mechanism changes from gentle to strong: in this case, the degree of ionisation drops massively. It should be noted that the results of these measurements are not dependent on the repetition rate at which the laser is operated (on sub-Hz and Hz scale).

We attribute these dramatic changes observed as a given site is exposed to a number of laser shots to the build up of defect sites by each laser shot. We clearly observe incubation as discussed in the introduction.

The measurements described above were taken at a fluence of 4 J/cm^2, just above the single shot ablation threshold (3.5 J/cm^2). In addition, the incubation effects manifest

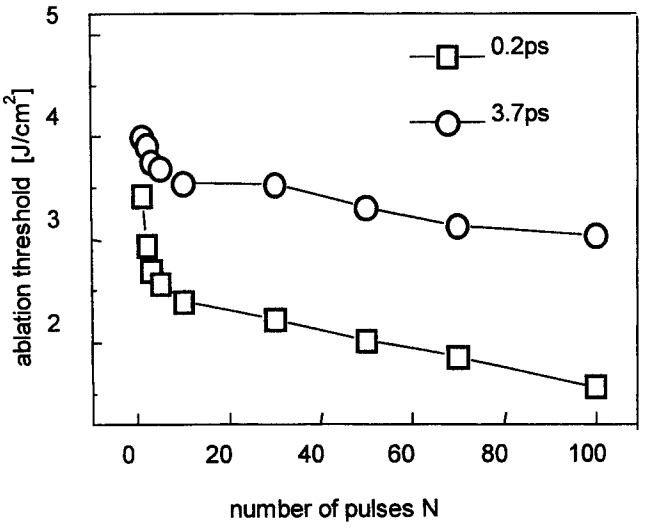


Fig. 5: Reduction of threshold fluence for ablation of sapphire (signalised by a burst in ion emission) as a function of preceding laser shots of the same fluence, documenting incubation. Two different pulse durations are examined, reflecting the well known [4, 8] reduction of threshold fluence as the pulse width is reduced.

themselves also in a visible reduction of the ablation threshold at repetitive irradiation. This is illustrated in Fig. 5 for two different laser pulse widths. The effect of incubation is both modifying the absorbing cross section through defect accumulation and inducing new routes for energy deposition into the lattice besides the electron-phonon coupling. Defects act like trapping centers strongly coupled to the lattice.

3. Velocity distribution of ejected particles (in situ)

In order to gain further insight into the nature of the gentle and strong ablation phases we have also measured the velocity distributions of the emitted particles by a time-of-

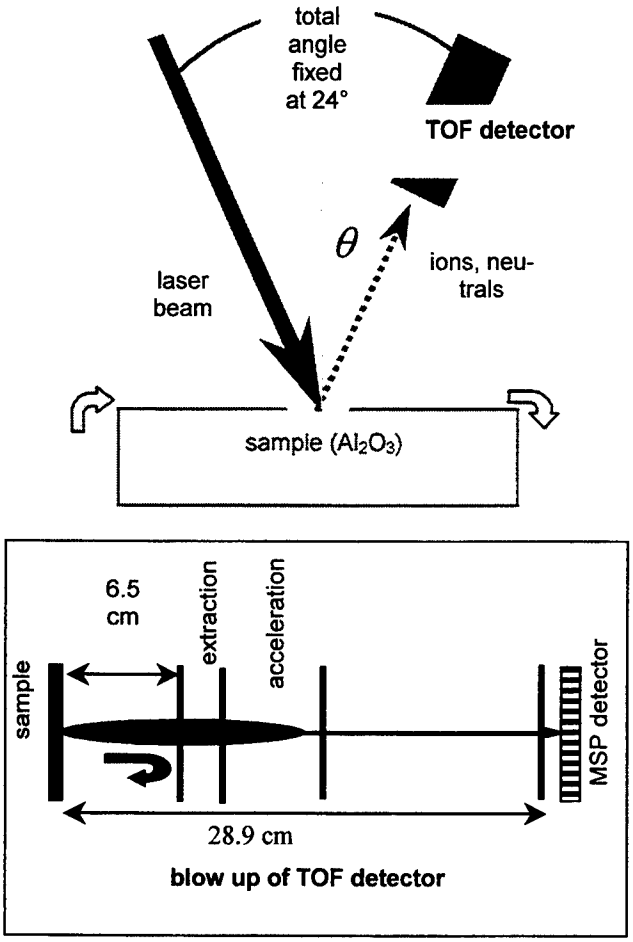


Fig. 6: Schematic of the experimental setup used to determine angular and velocity distributions of ablated particles

flight analysis (TOF) of the particles ejected during each laser shot. A schematic overview of the experimental set-up is shown in Fig. 6.

The target can be rotated around an axis perpendicular to the detection plane so that also angular distributions (θ dependence) of the ablated particles can be determined. The time-of-flight spectrometer (TOF) is a modified Wiley-McLaren setup which can be operated such that both the masses and the velocities of the particles may be determined. This is illustrated in the lower panel of Fig. 6. By letting the ions drift over several cm into a pulsed extraction field the velocity is derived from the time between laser pulse being fired and the extraction field being applied. The measured time of flight spectra are projected onto a velocity scale thereby accounting for the appropriate Jacobian factor.

Two characteristic angular distributions measured with this set-up are shown in Fig. 7. We see that the distributions

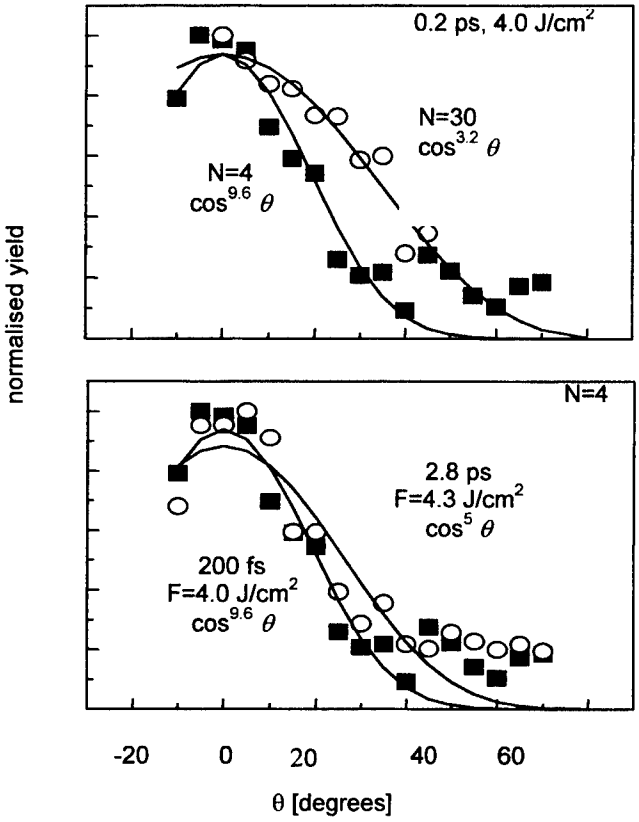


Fig. 7: Angular distribution of ejected ions in the plume for three different sets of laser parameters. Experimental points are given by circles and squares, the $\cos^n\theta$ fits are given by full lines.

are strongly forward peaked, indicating efficient repulsion from the surface while for a purely thermal, statistical emission we would expect a $\cos\theta$ distribution from the laser irradiated spot (although, hydrodynamical effects in the plume will act towards narrowing). We also observe that higher number of shots and longer pulse lengths lead to broader distributions.

More information can be obtained from the velocity distributions, of which two characteristic examples are shown in Fig. 8 (TOF axis normal to the target).

We see distributions with most probable velocities of 20 to 50 km/s, which are far above thermal energies. They are particularly high in the region of gentle etching while the most striking feature observed is a dramatic shift towards lower velocities and also some broadening with increasing

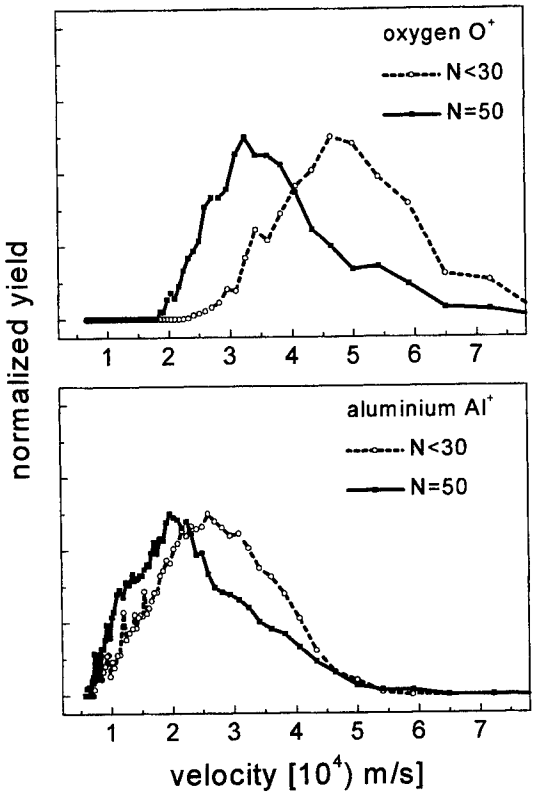


Fig. 8: Some examples of measured velocity distributions of the ions ejected from c-Al_2O_3 irradiated by 200 fs, 4J/cm^2 laser pulses. The most probable velocity stays approximately constant for N≤30 and shifts drastically for larger N towards lower velocities as the strong ablation phase is reached.

number of shots N. The same is observed for larger fluences as well as for increased pulse widths. Generally speaking, the shift occurs at laser parameters for which in the ex situ studies we have observed the transition from the gentle to the strong etch phase.

Fig. 9 summarises some of the data obtained for O^+ an Al^+. We plot the ion kinetic energy E_{kin} as a function of the number of laser shots for one set of laser parameters. We note that the kinetic ion energies observed are far above any reasonable assumption for a purely thermal origin (T/E_{kin} ~10000 K/eV), even in the strong ablation phase. It is, however, interesting to note that the energy of aluminium and oxygen atoms tend to become equal with a high number of shots, i.e. in the strong ablation phase, while they are distinctively different in the gentle ablation phase.

To illustrate this even more clearly, we show these data again in Fig. 10, this time in terms of the ratio between a) most probable momentum and b) most probable energy for the O^+ and Al^+ ions.

It is evident that the momenta of the ions are equal in the gentle etch phase while in the strong etch phase there is a

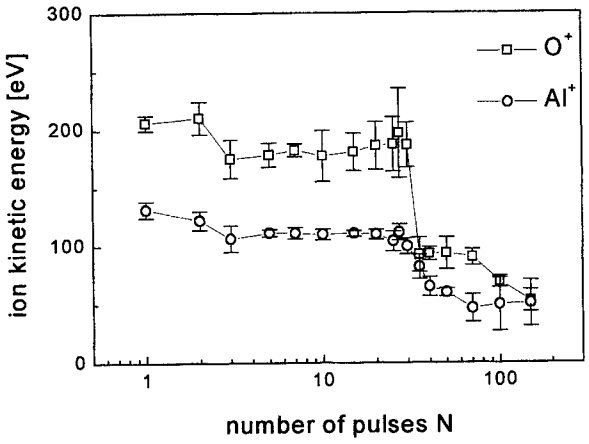


Fig. 9: Most probable kinetic energies of ions ejected normal to the c-Al_2O_3 surface irradiated by 200 fs, 4J/cm^2 laser pulses as a function of the number of laser shots. At a small number of shots Al^+ and O^+ ions have different energies. Note the dramatic drop of energy at around N~30 where the transition from gentle to strong etching occurs.

tendency towards equal energies for both species. This observation give strong evidence that electrostatic forces (Coulomb explosion) dominate the gentle etch phase. If these act for a limited time (the average expulsion time t_{ex}) both ions (having the same charge q) experience the same electric force $F_{El}(t) = eE(t)$ in the space charge field $E(t)$ we expect them to gain the same momentum:

$$p = \int_0^{t_{ex}} F_{El}(t')dt' \approx \overline{F}_{El} t_{ex} \quad (1)$$

As a crucial check we can study doubly charged ions which should have twice the momentum of singly charged ions. This is indeed the case (not shown here [9]). Without going into details here we briefly mention that we have also measured the velocity of the neutral particles expelled from the irradiated area by using a second, post-ionising laser in the extraction zone and repelling the original ions before post-ionisation [10]. We recall that these neutrals constitute 90% of the matter ablated in the gentle and 99% in the strong etch phase. We find that this velocity distribution resembles that of the positive ions in the strong etch phase. This indicates a thermalisation process after the initial ionisation phase from which only the fast Coulomb explosion ions can escape. Additional insight into the processes occurring during the initial phase of the ablation is gained from detecting the emitted electrons and estimating their energy. This can be done by essentially reversing the electric potentials of our TOF spectrometer and negatively biasing the sample. Since the mass spectrometer was not designed for this purpose the energy resolution is rather poor.

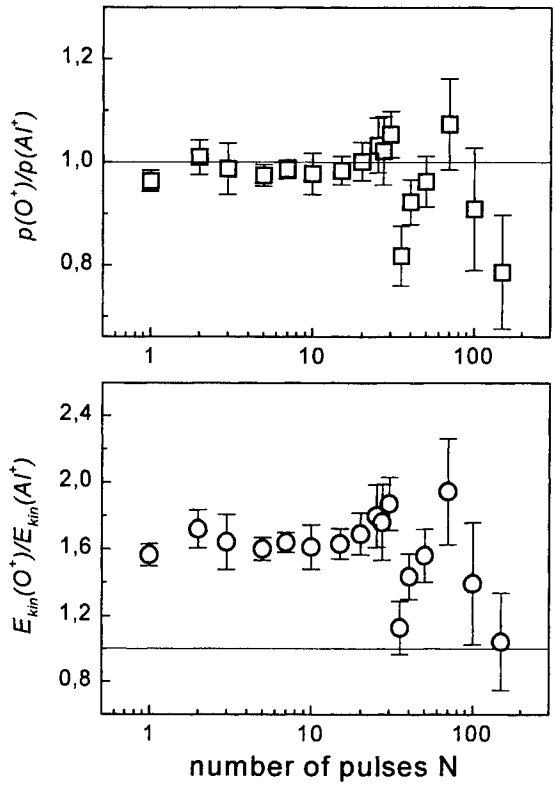


Fig. 10: Ratio of characteristic parameters from measured velocity distributions of O^+ and Al^+ ions. Upper panel: most probable momenta, lower panel: most probable kinetic energies.

Fig. 11 shows the result of this experiment. It still gives us, a very useful overview of what is happening: Clearly, two groups of electrons can be discerned: a very fast distribution arriving at the MSP at times less than a μs, corresponding to several eV of kinetic energy followed by a very slow group of ejected electrons with energies in the range of meV. Obviously, the first group reflects - at least part of - the initially emitted photoelectrons. They originate from direct multiphoton ionisation of the valence band and defect states and from additional laser interaction with the free electrons in the conduction band [11]. They leave the sample at an early time, which leads to the original build-up of the surface charge. The broad distribution of rather slow electrons is characteristic for the electrons simply carried along with the plume and help to partially neutralise the latter as it expands.

Additional evidence for the electrostatic origin of the initial surface break-up in the gentle etch phase comes from a semiquantitative argument. The minimum charge density at the surface necessary to induce Coulomb explosion can simply be estimated from the requirement of electrostatic stress (force per unit area) to overcome the local mechanical (or bonding) stress [12]:

The average electric stress (effective area per particle $S=\pi a_0/4$) is given by

$$\sigma_{El} = \frac{F_{El}}{S} = \frac{f^2 e^2 l}{\pi^2 \varepsilon \varepsilon_0 a_0^4} \qquad (2)$$

when a fraction f of the particles is ionised in the irradiated volume. Here a_0 is the average atomic spacing in the lattice (2 Å), l=3.64 is a factor taking into account the lattice geometry and $\varepsilon \approx 10$ the relative dielectric constant for sapphire. For the bulk material the mechanical stress $\sigma_{Mech} = \Delta x / x\mathsf{E}$ for bond breaking has been estimated by E/10 where E is Young's modulus (335 GPa for sapphire [13]). For atoms in the surface layer this will obviously be smaller and we take a compromise value of E/20. With these values we obtain $f \geq 0.5$ as the critical fraction of ionised species on the surface of the irradiated volume at which surface break-up due to Coulomb explosion is expected to occur [9, 14].

On the other hand, we may also obtain an estimate for f from the experimentally observed (most probable) momenta p of the ions above the threshold. With eq. (1) we derive an average electric force assuming an effective expulsion time of 1 ps (the time scale during which the surface charge remains stable as evidenced by the pump-probe experiments

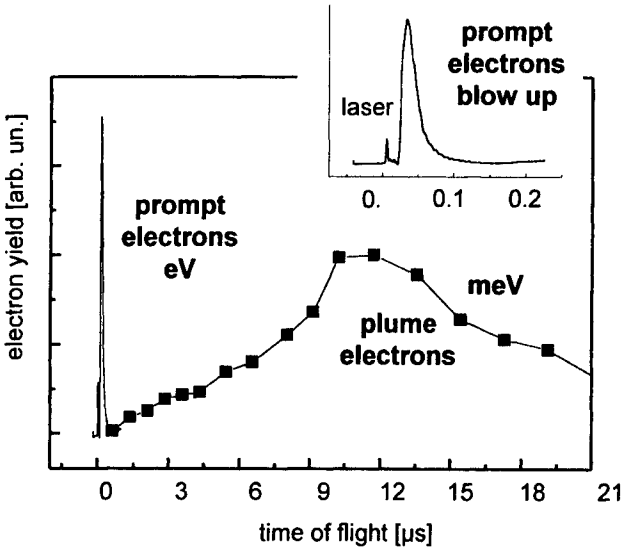


Fig. 11: Time-of-flight measurement for the electrons ejected during the gentle phase for 100 fs irradiation.

described in section 4). From the average electric force we derive finally via eq. (2) f=**0.6-0.8**, in good agreement with the former estimate.

From all these observations we conclude, that Coulomb explosion is indeed a dominant driving mechanism for ion expulsion during the gentle ablation phase. It is most directly seen in the momentum distribution of the ions ejected.

4. Pump-probe measurements

Finally, we report briefly about dynamical studies using femtosecond pump probe techniques which allows us to follow the dynamics of the energy deposition and redistribution process in real time. The experimental set-up is essentially unchanged, except that now we use two laser pulses which are delayed with respect to each other by a variable delay time Δt. Each of these pulses has a fluence below the single shot ablation threshold while both together are sufficient to overcome this value. By exposing the sample subsequently to both of these pulses, we can detect the energy redistribution channels within the sample. The key question here is how long the material remembers that it has been pretreated by the pump pulse.

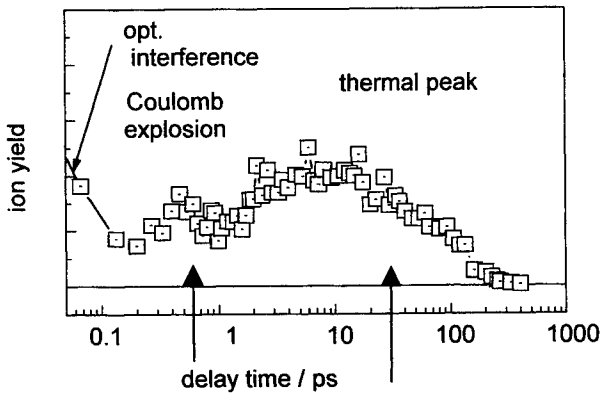


Fig. 12: Fast Al^+ ion signal in a pump-probe ablation measurement on sapphire with 80 fs pulse width.

Fig. 12 shows the fast ion Al^+ yield (20000 m/s) when the sample is irradiated by a first sub-threshold 80 fs pulse and probed with a second, identical pulse, delayed by Δt. Several distinct features have to be distinguished, all of them clearly reproducible.

i.) The maximum observed at zero delay and the corresponding minimum at 0.1 ps between pump and probe pulse simply reflects the optical interference between the two coherent pulses of equal wavelength and is without relevance for the understanding of the ablation process.

ii.) After an initial decrease the signal rises to a first maximum and then decreases again, reaching a minimum at around 1ps. We take this to reflect the initial electron dynamics and electrostatic energy accumulation at the surface: A hot electron bath and a sub-critical charge are initiated by the pump pulse. The second pulse adds to this excitation, the threshold is exceeded and ion ejection occurs. The surface charge build-up is reflected by the maximum around 600 fs followed by decay after 1 ps, which we take as the time period necessary for the surface charge to survive at sufficient magnitude to lead to Coulomb explosion as discussed before. The following decay up to 1ps reflects charge reduction, connected with the emission of charged particles and with neutralization due to carrier diffusion.

iii.) The second rise of the ion signal is attributed to lattice heating due to electron-phonon coupling. In a separate experiment we were able to detect increased optical scattering regarded as the onset of efficient ablation, i.e. the main, neutral component removal on the same time scale.

Support of this interpretation is obtained from measuring the velocity distributions of the ions at the two different delay times marked in Fig. 12. This measurement is presented in Fig. 13. We see very clearly that at short delay time (<1ps) between pump and probe pulse the ion velocity replicates the fast ion distribution which we have observed in the gentle etch phase and which we attributed to Coulomb

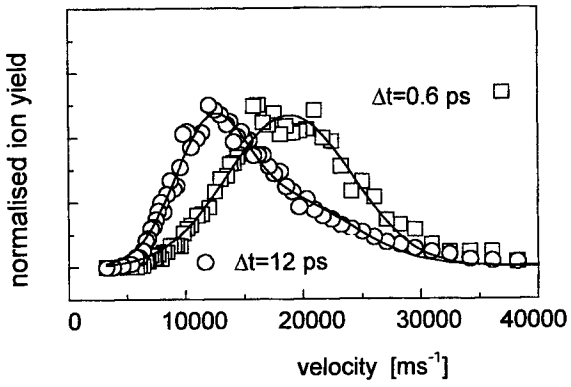


Fig. 13: Measured Al^+ ion velocity distributions at two different delay times Δt between pump and probe pulse marked by arrows in Fig. 12. Squares: Δt = 0.6 ps (Coulomb explosion), circles Δt = 12 ps (thermal origin).

explosion. The dynamics involved in fast ion formation obviously relies on the availability of sufficient electron density in the conduction band to induce efficient photoemission and subsequent charging with IR pulses. In contrast, at long delay times (>10ps) electron energy has been transferred into the lattice so that a strong thermal process becomes effective and absorption of the second laser pulse couples better with the heat bath of the lattice.

In a second pump-probe experiment we have studied the response of the prompt electrons and compared it to the ion yield as illustrated in Fig. 14 (100 fs pulse duration). The electron signal follows the same temporal characteristics as the ion signal we have attributed to Coulomb explosion (the decay at around 1ps in Fig. 12), supporting the idea of electrostatic ion ejection due to efficient photoemission [9]. Also, measuring the slow electron yield (12000 m/s) we record the signature of a pure thermal effect on the time scale of electron-phonon coupling.

5. Conclusion

We have shown that the transition from the gentle to the

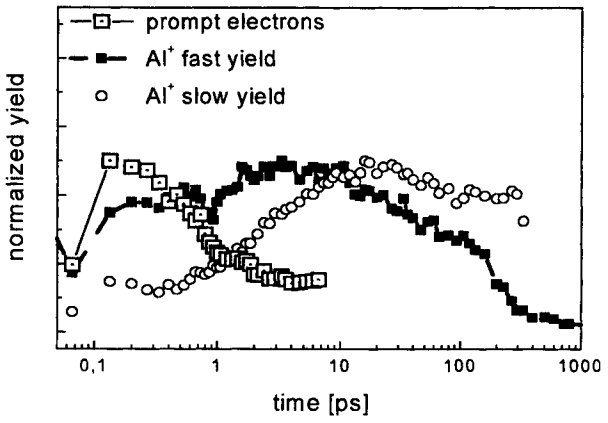


Fig. 14: Prompt electrons (empty squares) and fast (full squares) and slow (open circles) Al^+ ion signal in a pump-probe measurement on sapphire with 100 fs pulse width.

strong etch phase in ultrashort laser ablation of wide band gap materials, here exemplified by c-Al_2O_3, is closely related to the incubation process and can be explored in a quantitative manner. The gentle phase is connected with macroscopic surface break-up due to Coulomb repulsion and efficient emission of fast ions (10% of the total material emitted). At higher fluence and a larger number of laser shots a transition to the strong etch phase is observed, accompanied by a reduction of the degree of ionisation (to about 1%) a drastic increase of the ablation rate and reduction of ion energy which goes along with a quasi thermalisation of the emitted particles, Pump probe experiments allow us to follow the time evolution of the energy deposition and redistribution process and the balance between electrostatic energy accumulation and heat deposition. Surface charging is found to survive beyond the critical value for break-up for about 1 ps. Probe absorption first is maximized at about 600 fs due to better coupling with the hot electron system. Subsequently at about 10 ps, the time scale of electron-phonon thermalisation, the lattice appears to be most susceptible to absorption of probe photons as a consequence of temperature increase. Finally, after several 100 ps the sample has cooled and looses the intermediate ability for very efficient energy absorption. For further details we refer the interested reader to forthcoming publications.

We wish, however, to indicate some potential applications of the present findings which are subject to further studies in our laboratory: Lattice heating by the first pulse and efficient absorption of a second pulse after some ten picoseconds might open new avenues to overcome the well known difficulties with deep hole drilling into transparent materials or surface polishing in precision optics fabrication. Cracks which are observed even with femtosecond lasers could possibly be avoided when ablation in the gentle phase regime is combined with energy deposition into the premolten material by a second pulse.

Acknowledgent

Partial support of this work through BMBF contract 13N7048/7 is gratefully acknowledged.

References

[1] H. Varel, D. Ashkenasi, A. Rosenfeld, R. Herrmann, F. Noack, E.E.B. Campbell, Appl. Phys. A 62, 293, (1996).

[2] E.E.B. Campbell, D. Ashkenasi, A. Rosenfeld, *Lasers in Materials Science* (Trans Tech Publications, Switzerland, 1999).

[3] A.C. Tam, J.L. Brand, D.C. Cheng, W. Zapka, Appl. Phys. Lett. 55, 2045, (1989).

[4] D. Ashkenasi, A. Rosenfeld, H. Varel, M. Wahmer, E.E.B. Campbell, Appl. Surf. Sci. 120, 65, (1997).

[5] R. Kelly, A. Miotello, Appl. Surf. Sci. 96-98, 205, (1996).

[6] L.V. Zhigilei, P.B.S. Kodali, B.J. Garrison, Chem. Phys. Lett. 276, 269, (1997).

[7] R. Stoian, H. Varel, A. Rosenfeld, D. Ashkenasi, E.E.B. Campbell, and R. Kelly, Appl. Surf. Sci. (in press).

[8] B.C. Stuart, M.D. Feit, A.M. Rubenchik, B.W. Shore, M.D. Perry, Phys. Rev. Lett. 74, 2248 (1995), A.-C. Tien, S. Backus, H. Kapteyn, M. Murnane, G. Mourou, Phys. Rev. Lett. 82, 3883, (1999).

[9] R. Stoian, D. Ashkenasi, A. Rosenfeld, E.E.B. Campbell, unpublished.

[10] R. Stoian, D. Ashkenasi, A. Rosenfeld, E.E.B. Campbell, Phys. Rev. B (in press).

[11] Ph. Daguzan, S. Guizard, K. Krastev, P. Martin, G. Petite, Phys. Rev. Lett. 73, 2352, (1994).

[12] R. L. Fleischer, P. B. Price and R. M. Walker, J. Appl. Phys. 36, 3645, (1965).

[13] Handbook of chemistry and physics, ed. D.R. Lide, CRC Press 1993.

[14] R. Stoian, D. Ashkenasi, A. Rosenfeld, M. Wittmann, R. Kelly, E.E.B. Campbell, Nucl. Instr. Meth. Phys. Res. B (in press).

395-nm and 790-nm Femtosecond Laser Ablation of Aluminum-doped Zinc Oxide

Masayuki OKOSHI[a], Kouji HIGASHIKAWA, and Mitsugu HANABUSA

Department of Electrical and Electronic Engineering, Toyohashi University of Technology, Tenpaku, Toyohashi 441-8580, Japan
E-mail: okoshi@eee.tut.ac.jp

We used 395-nm and 790-nm femtosecond laser pulses to deposit aluminum-doped zinc oxide films by pulsed laser deposition. Electrical resistivity of the films was lowered ($5.6 \times 10^{-4}\,\Omega$ cm) at 200℃ for the 395-nm laser pulses, while maintaining the optical transparency. In addition, the deposition rate increased six times. Optical emission was measured to compare the plumes generated by 395-nm and 790-nm laser pulses. We found that the emission from ions was suppressed relative to neutral atoms. Also the kinetic energy of ejected species was nearly doubled for the 395-nm laser pulses.

Keywords: femtosecond laser, pulsed laser deposition, zinc oxide, electrical resistivity, optical transparency, wavelength conversion, optical emission, flight velocity.

1. Introduction

Pulsed laser deposition (PLD), which is based on ablation of target materials by high power density laser pulses, is becoming increasingly popular [1]. So far, nanosecond laser pulses such as excimer laser or Nd:YAG laser are traditionally used in PLD. Recently, reliable femtosecond laser consisted of an oscillator and a regenerative amplifier based on Ti:sapphire have become available, which enables us to excite the targets with extremely high power densities. They have been used for PLD in place of the traditionally used nanosecond laser pulses with promising results [2-5].

A Ti:sapphire femtosecond laser system is generated in the near-infrared region (around 800 nm) , although polymers were ablated by ultraviolet femtosecond laser pulses successfully [6,7]. However, the generation of such short wavelength pulses requires a complicated apparatus, which is not necessarily fit for practical material processing. On the other hand, the laser wavelengths can be halved with a high efficiency simply by passing the femtosecond pulses through a non-linear crystal like β-BaB_2O_4 (BBO). Therefore, by using the wavelength halving technique femtosecond PLD at shorter laser wavelengths can be carried out without adding any complicity.

In the present work, we examined the effect of laser wavelengths on femtosecond PLD of ZnO:Al films using the wavelength conversion technique. ZnO:Al films deposited by PLD are recently used as the electrode for organic light-emitting devices [8]. We were interested to learn how the laser wavelengths influence the film properties, in particular electrical resistivity and optical transparency. Optical emission was measured to compare the plumes generated by 395-nm and 790-nm laser pulses.

a) Present address: Department of Electrical and Electronic Engineering, National Defense Academy, 1-10-20 Hashirimizu, Yokosuka 239-8686, Japan. E-mail: okoshi@nda.ac.jp

First International Symposium on Laser Precision Microfabrication, Isamu Miyamoto, Koji Sugioka, Thomas W. Sigmon, Editors, Proceedings of SPIE Vol. 4088 (2000) © 2000 SPIE · 0277-786X/00/$15.00

In addition, the data for varying doping ratio of ZnO target and new results of optical emission are added to the our previous work [9].

2. Experimental

An arrangement used in the present PLD experiment was described previously [5]. We used 790-nm, 130-fs and 10-Hz laser pulses with pulse energy of 10mJ. And a 0.5-mm thick BBO crystal (Dhow Co.,Ltd.) was used to halve the laser pulses. The pulse energy was reduced from 10 mJ to 3.2 mJ by the wavelength conversion. The laser target was ZnO tablets (Furuuchi Chemicals), 30 mm in diameter and doped with 0.5, 2 and 4 wt.% Al_2O_3. The substrates were 0.3-mm-thick Si (100) and 0.5-mm-thick quartz plate. Hydrogen-terminated Si (100) surface was prepared, as previously described [5].

We measured the room-temperature electrical resistivity of the deposited ZnO:Al films by a four-probe methods. To evaluate the transparency of the films, we used a double-beam monochromator (Hitachi, type100-10) and measured the transmittance in the range of 300 to 900 nm.

3. Results and discussion

3.1 Electrical and optical properties

Figure 1 shows the electrical resistivity of the ZnO:Al films deposited by the 395-nm and 790-nm laser pulses on silicon between room temperature and 250℃. We used a 2 wt.% ZnO:Al target. The electrical resistivity was lower throughout the measured temperature range when deposited by the 395-nm laser pulses. For instance, at a temperature of 200℃, where the films became most conductive, the electrical resistivity was $5.6\times10^{-4}\,\Omega$ cm (for the 395-nm laser pulses) against $3.0\times10^{-3}\,\Omega$ cm (for the 790-nm laser pulses).

The films were grown for 60-min. The deposition rate was 4 nm/min for the 395-nm pulses, and therefore they were 240 nm thick. The films prepared by the 790-nm laser pulses were 40 nm thick.

When we used a 0.5 wt.% ZnO:Al target, the electrical resistivity of the films was slightly lower ($1.8\times10^{-3}\,\Omega$ cm) in only the PLD using 790-nm laser pulses. In the case of 4 wt.% ZnO:Al target, the electrical resistivity was higher, compared to even non-doped ZnO [5].

The transmittance of the ZnO:Al films deposited by the 395-nm and 790-nm laser pulses is compared in Fig. 2. For this measurement, the films were deposited on quartz plates at 200℃. The deposition time was adjusted to make all films 40-nm thick. The transmittance measured above 450 nm was identical for the two films, while below this wavelength the film prepared by the 395-nm laser pulses was more transparent.

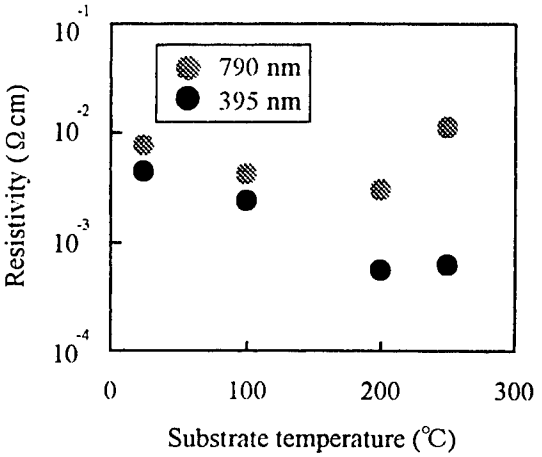


Fig.1 The electrical resistivity of ZnO:Al films deposited by femtosecond PLD at laser wavelengths of 395-nm and 790-nm.

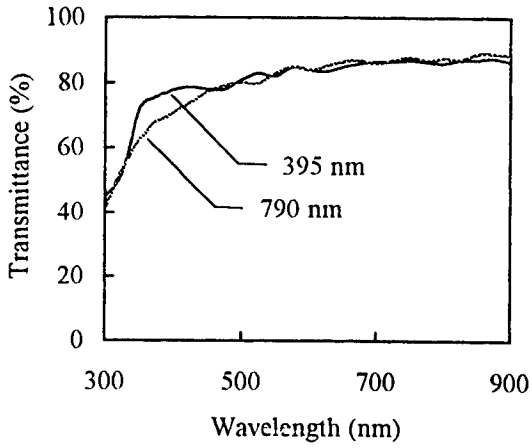


Fig.2 The transmittance of the ZnO:Al films deposited on quartz by 395-nm and 790-nm laser pulses.

3.2 Optical emission studies

Figure 3 shows the optical emission spectra of plumes generated by the 395-nm laser pulses (Fig. 3(a)) and the 790-nm laser pulses (Fig. 3(b)). The light was collected

by a 17-cm lens, which was focused into a space 5 mm apart from the target surface, and analyzed by a 25-cm monochromator. The detector was a photomultiplier (Hamamatsu Photonics R928). Major peaks were identified and marked in the spectra [10]. The emissions from Zn, Zn^+, O and O^+ were observed in the both spectra. Comparing Fig.3 (a) and (b), we found that the Zn^+ emissions became weak relative to the Zn emissions for the 395-nm laser pulses than for the 790-nm laser pulses. A similar tendency was observed for oxygen. In the case of the nanosecond PLD of ZnO, the relative Zn^+ emission intensity also decreased in an order of decreasing laser wavelengths, 248 nm (KrF laser), 532 and 1064 nm (Nd:YAG lasers) [11]. In accordance with this, the film quality was improved at short wavelengths [11-12]. Therefore, the suppression of ions may be linked to the improvement of film quality in both nanosecond and femtosecond PLD of ZnO. A peak observed at 656.2 nm in Fig.3 (a) was induced by H, but we do not understand why hydrogen was generated only by the 395-nm laser pulses.

We also measured the delay of the emission relative to the laser pulses to obtain the flight velocity of O, Zn and Zn^+. The results are shown in Fig.4. We detected the emission at spaces 5 and 10 mm apart from the target surface. Flight velocity, which is obtained by the slope, is summarized in Table 1 together with the kinetic energy calculated from the velocity. It is seen that the 395-nm laser pulses nearly doubled the kinetic energy for the three species. The energetic species may also contribute to the improvement of the film quality.

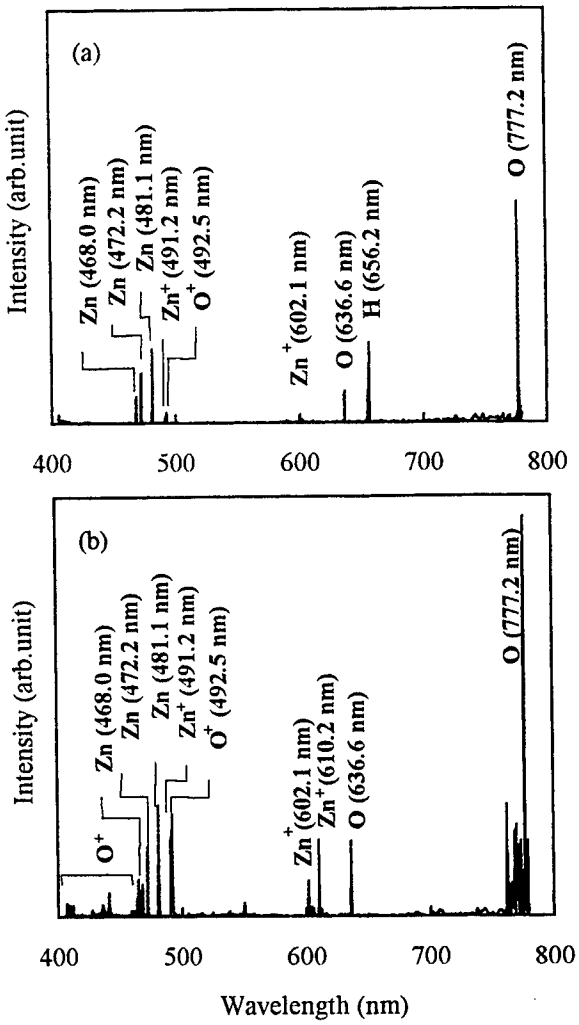


Fig.3 Optical emission spectra of plumes generated by (a) 395-nm and (b) 790-nm laser pulses.

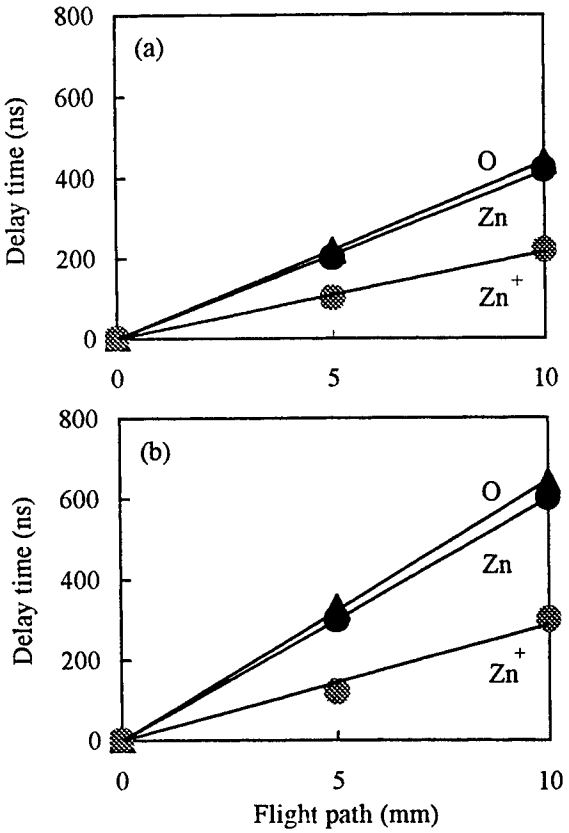


Fig.4 Relation between flight path and delay time of Zn, Zn^+ and O generated by (a) 395-nm and 790-nm laser pulses.

Table 1 Flight velocity and kinetic energy of O, Zn and Zn^+ ejected from a ZnO target by 395-nm and 790-nm femtosecond laser pulses.

	Flight velocity ($\times 10^4$ m/s)		Kinetic energy (eV)	
	395 nm	790 nm	395 nm	790 nm
O	2.3	1.5	44	19
Zn	2.4	1.7	190	100
Zn^+	4.6	3.5	710	410

4. Conclusion

We demonstrated the merit of wavelength conversion from near-infrared (790 nm) to visible light (395 nm) in femtosecond PLD of ZnO:Al films. The electrical resistivity of the films was lowered from $3.0 \times 10^{-3}\,\Omega$ cm to $5.6 \times 10^{-4}\,\Omega$ cm by halving the laser wavelength. The deposition rate increased six times by the conversion in spite of lower pulse energy. The plume generated by the 395-nm laser pulses was characterized by the reduction of the Zn and O ions relative to the neutral atoms. The kinetic energy of O, Zn and Zn^+, which was estimated by measuring the flight velocity, was nearly doubled when the 395-nm pulses were used.

Acknowledgment

This work was supported by Special Coordination Funds from Science and Technology Agency titled "Development of high-density optical pulse generation and advanced material control techniques".

References

[1] D.B.Chrisey, G.K.Hubler: "*Pulsed Laser Deposition of Thin Films*", (Wiley, New York, 1994).
[2] F.Qian, R.K.Singh, S.K.Dutta, and P.P.Pronko: Appl. Phys.Lett. **67**, (1995) 3120.
[3] M.Okoshi, S.Higuchi, and M.Hanabusa: J.Appl.Phys. **86**, (1999) 1768.
[4] M.Okoshi, S.Higuchi, and M.Hanabusa: Appl.Surf.Sci. (in press).
[5] M.Okoshi, K.Higashikawa, and M.Hanabusa: Appl. Surf.Sci. (in press).
[6] R.Srinivasan, E.Sutcliffe, and B.Braren: Appl.Phys.Lett. **51**, (1987) 1285.
[7] S.Küper and M.Stuke: Appl.Phys. B**44**, (1987) 199.
[8] H.Kim, C.M.Gilmore, J.S.Horwitz, A.Pique, H.Murata, G.P.Kushto, R.Schlaf, Z.H.Kafafi, and D.B.Chrisey: Appl. Phys.Lett. **76**, (2000) 259.
[9] M.Okoshi, K.Higashikawa, M.Hanabusa: submitted to Appl.Phys.Lett.
[10] G.R.Harrison: "*M.I.T. Wavelength Tables*", (M.I.T. Press, Cambridge, 1969) pp.13-188.
[11] N.J.Ianno, L.McConville, N.Shaikh, S.Pittal and P.G. Snyder: ThinSolid Films **220**, (1992) 92.
[12] S.Amirhaghi, V.Craciun, F.Beech, M.Vickers, S.Tarling, P.Barnes, and I.W.Boyd: Mater.Res.Soc.Symp.Proc. **285**, (1993) 489.

Formation of Photonic Crystals by Femtosecond Laser Microfabrication

Hiroaki MISAWA*, Saulius JUODKAZIS**, Hong-Bo SUN**, Shigeki MATSUO*, Jyunji NISHII***

*Graduate School of Engineering, The University of Tokushima, 2-1 Minamijyosanjima, Tokushima 770-8506, Japan.
E-mail: misawa@eco.tokushima-u.ac.jp (Corresponding author: H. Misawa)
**SVBL, The University of Tokushima, 2-1 Minamijyosanjima, Tokushima 770-8506, Japan.
***Osaka National Research Institute, 1-8-31 Midorigaoka, Ikeda, Osaka 563-8577, Japan

Keywords: photonic crystals, optical memory, laser microfabrication, photo-polymerisation, two-photon absorption

We report a novel photo-polymerization technique of well-defined three-dimensional (3D) layer-by-layer structures by two-photon absorption (TPA) in resins. By changing the structural parameters such as the rod diameter, pitch (intra-rod distance in plane) and angular orientation between neighbor planes different lattice types can be accomplished. This enables a systematic investigation of optical properties of photonic crystals (PhCs) made by TPA photo-polymerization. The solidified skeleton of PhC can be utilized as a mold to infiltrate solidifiable dye. Selective removal of the solidified resin can yield in a reverse PhC structures. When the defect-layer(s) are introduced into PhC during fabrication the PhC may act as a high-quality microcavity. A defect mode has been observed for the first time in thus-fabricated structures.
Laser-microexplosion fabrication is another promising technique for the PhC and optical memory applications. To achieve an opening of a full-bandgap the media of high dielectric constant is of request (a high dielectric contrast is necessary).

1. Introduction

There is an increasing requirement for the simple proto-typing technologies[1] enabling the fabrication of sub-μm structures. The photo-polymerization as one of the branches of micro-stereolitography[2,3] (μSL) is a promising technique to fabricate fine structures (smaller that the optical diffraction limit) by the use of optical field enhancement in the vicinity of a conducting tip[4] (planar fabrication) or by the scanning a focal point of light inside resin, where photo-induced polymerization is taking place *via* linear[2] or multi(two)-photon absorption,[5] which allows three-dimensional (3-D) fabrication with high resolution.

Another issue, the photonic crystals (PhCs),[6] is closely related to the microfabrication, and only now, more than after a decade the concept was introduced, the PhCs operating in visible emerge.[7,8] This is primarily due to the adaptation of (sub)micro-technology, which made break-through. One particular aspect of photonic bandgap (PBG) effect[9] is of interest, namely, a control over a spontaneous emission (Purcell effect predicted in 1946),[10] which is promising for a number of applications, such as, existence of localized, propagating and diffusion (incoherent propagating) fields,[11] polarization change in emission,[12] selective filters for light detectors,[13] etc. The spontaneous emission rate can be increased by a factor of $3\lambda^3 Q/4\pi^2 V$ in the cavity of the volume V, here Q is the smallest from the two, the cavity quality $Q = \omega/\Delta\omega$ and the material's "quality" $Q = \lambda/\Delta\lambda$ defined by its linewidth $\Delta\lambda$. This number represents the ratio of the density of photonic states in cavity and in material and additionally depends on the refractive index of material. This dependence can be expressed by a factor $1/n$.[3] The introduction of a defect of the volume λ^3 into a PhC lattice can be seen as creation of a micro-cavity in which the spontaneous emission is coupled into the only available photonic mode and the emission is enhanced as long as Q is large. First experimental observation of the Purcell effect was published in 1998.[14] The introduction of the defects in PhCs leads towards light localization, waveguiding,[15] PBG extension in disordered PhCs (the consequence of the effects of PBG and Anderson localization),[16] delay in the light propagation[17] to mention

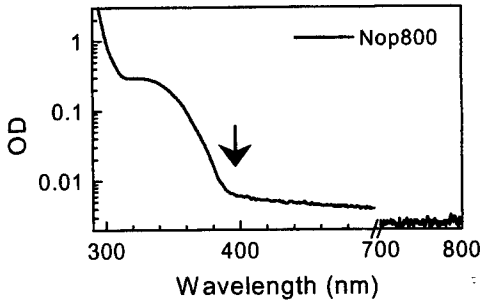


Fig. 1. Absorption spectra of *Nop800* resin diluted in 1-methoxy-2-propanol up to 1 wt%. Thickness of solution was 1 cm. Fabrication wavelength was 398±7 nm (pointed by arrow).

First International Symposium on Laser Precision Microfabrication, Isamu Miyamoto, Koji Sugioka, Thomas W. Sigmon, Editors, Proceedings of SPIE Vol. 4088 (2000) © 2000 SPIE · 0277-786X/00/$15.00

few.

The aim of the present study was to fabricate well-defined 3-D patterns inside resin by two-photon absorption (TPA) using fs-pulses with the eventual task of fabrication the PhC structures employing layer-by-layer technique and introduce the defect layers inside the stack. This shows that μSL can be considered as a tool for PhC fabrication and that after affordable improvement the visible region of operation can be reached.

2. Experimental

Laser setup used for photo-polymerization was fs-Ti:sapphire laser with regenerative amplifier (*Spectra Physics*), which delivered up to 0.6 W at 795 nm and were operating at 1 Hz-1 kHz repetition rate. The second harmonic of these pulses was introduced into microscope with oil-immersion (the refractive index of the oil was n_{oil} = 1.515) objective lens of ×100 magnification and numerical aperture (NA = 1.35) and was used for fabrication inside a resin *Nopcocure 800* (hereinafter *Nop800*) from *San Nopco* (the refractive index of the resin was $n_{Nop800} \approx$ 1.5-1.6), which is based on the acrylic acid ester. The fabrication patterns were pre-programmed and the high resolution (< 5 nm steps in XYZ) piezoelectric stage with the optical shutter were controlled accordingly. U
nsolidified resin was removed by the development in acetone, where structures were soaked for 10-20 min.

3. Results and Discussion

Typical absorption spectra of *Nop800* resin is presented in Fig. 1. The absorption coefficient at 398 nm fabrication wavelength was only 1.4 cm^{-1} for linear absorption and few orders larger for the shorter wavelengths. This shows the suitability of this resin for a curling induced by TPA. An example of the 3-D fabrication is given in Fig. 2. Scanning electron microscopy (SEM, made on *TS-4200, Hitachi*) image of a gear wheel shows that sub-μm features in

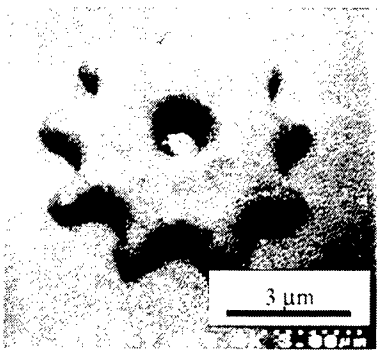


Fig. 2. Scanning electron microscopy (SEM) image of 3-D gear, which was made in *Nop800* using 398 nm irradiation. The height of the gear was ca. 3 μm.

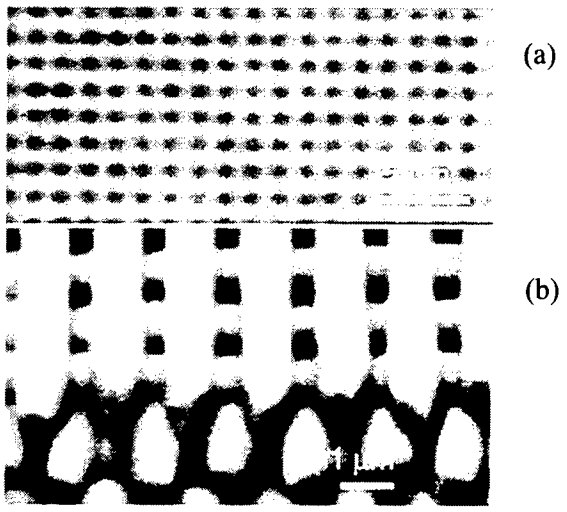


Fig. 3. Optical transmission (a) and SEM (b) images of layer-by – layer PhC fabricated in *Nop800* using 398 nm irradiation (TPA fabrication). The plane (001) is presented in (a). The size of PhC was 40×40 μm^2 and was limited by the working distance of the PZT-stage. Number of layers 20.

fabrication are in principle accessible. The thinning of the wheel cogs' was observed when development procedure was longer. The choice of the resist is due to its high viscosity, which allows to fabricate the structure without a distortion caused by the floating. The novelty of proposed photopolymerization is in free 3-D positioning of focus inside a resin. The drift of the object currently under the fabrication usually is caused by a heat released during a polymerization and was absent in our method. Fs-pulses here has advantage over a continuos wave (cw) laser curling due to less expressed heating induced by light absorption. This is due to a predominantly non-thermal light-material interaction in the case of fs-pulses. It is necessary to point out, that the photo-initiator (or photo-sensitizer with initiator) are usually unknown for customer and the resins are optimized for fabrication made by cw-lasers. Thus, there is room for improvement in the adaptation of resin to fs-fabrication needs taking into accout the complexity of the onset of polymerization.[18] This eventually can yield in the improvement in resolution of fabrication.

Even at the current state the PhC structures can be fabricated as we reported recently.[19] 2-D PhC was made of layer-by-layer structure.[20] It has a symmetry of face centered tetragonal (fct). When $c/a = \sqrt{2}$, the lattice can be derived from face centered cubic (fcc) unit cell with a basis of two rods, here c is the period of stucture along ⟨001⟩ and a is the intra-rod distance in one plane. For the laser fabrication, commonly, we have $c>a>2r$, where r is the diameter of the rod. Fabrication pulse energy was 90 nJ/pulse at irradiation point and was slightly higher than the threshold of photo-polymerization at 70 nJ/pulse. This allowed to fabricate most tiny structures, since the polymerization is taking place only at the apex of the intensity profile of a laser pulse. The

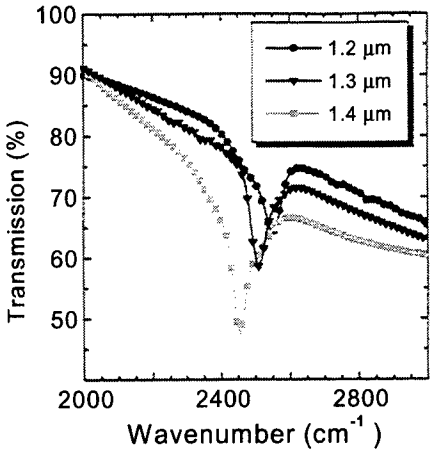


Fig. 4. Transmission spectra of layer-by-layer 2-D PhC along ⟨001⟩ direction. Structures consisted of 20 layers, the inter-rod distance is specified in the inset.

focal spot size can be evaluated as diameter of the Airy disk of diffraction pattern for round aperture (objective lens), where 86% of the light intensity is concentrated (Gaussian beam is considered). This gives $1.22\lambda/NA \approx 374$ nm for aberration-free optics. A mismatch in refractive indexes between immersion-oil/cover-glass and resin is the possible source of the large features in the fabricated structures (an actual rod diameter was less than 1μm). The movement of the sample on a translation stage and the repetition rate of laser were adjusted in such a way that ca. 7-10 nm overlapping was made between adjacent pulses to make PhC

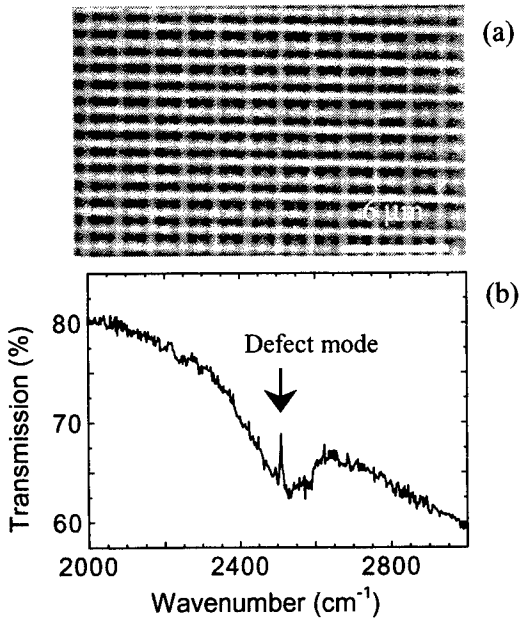


Fig. 5. Optical transmission of (001) plane (a) and SEM image (b) of layer-by-layer PhC fabricated in *Nop800* using 398 nm irradiation (TPA fabrication). The defect-plane, which is the 10th plane (from total 20) with the missing every second in-plane rod is presented in (a).

shown in Fig. 3. Another source of the larger rods in diameter than might be expected from the focusing optics is the partial polymerization by linear absorption, which is not negligible in the vicinity of the focal point, where light intensity reaches $<10^{31}$ photons/cm^{2}s.

The transmission spectra of this 2-D PhC was measured by Fourier transform infrared spectroscopy (FTIR, *ValorIII/Micro20, Jasco*) and showed pronounced PBG effect at around 2500 cm^{-1} (or 0.31 eV on energy scale). It can be seen that the larger the distance between rods the PBG effect is pronounced better (the dip in transmission is larger), probably, due to the better development and removal of the unsolidified resin.. The spectra had been normalized by the transmission of the uniformly solidified bulk resin. The transmittance dips under the normal incidence were at wavenumbers of 2550, 2510, and 2450 cm^{-1} for a = 1.2, 1.3, and 1.4 μm, respectively (N_2 was flowed through the entire light path to suppress the disturbance from the absorption by H_2O and CO_2 during FTIR measurements). The corresponding wavelengths were located inside the transparency window of the resin. An increase in the wavelength of transmission dip versus lattice constant was interpreted by the fact that frequency scales as $1/n$ in a medium of refractive index, n. The mean dielectric constant increased with filling ratio of resin, which accordingly depends on the lattice constant. When the every second rod was missing in the 20-rods stack the defect-related mode was observed inside PBG of PhC (Fig. 5).

PhC can be constructed by packing the microexploded holes, "atoms," into 3D lattice in silica.[21] Intuitively the holes resembled the atoms in Thomson atom model, and therefore we call these structures inlayed-"atom"-like PhCs, which were made by positioning and translating the focal point of the laser irradiation inside silica. Each "atom" was written in a single laser shot. By using a NA = 1.35 objective lens near-spherical voids were obtained and the high reproducibility of their shape was favored by the high stability of the laser pulse output. Since the microexplosion occurs only at the focal point where MPA is taking place, the voids can be spatially arranged freely. Different photonic lattices were realized just by varying computer-aided design program. As an example, one (111) plane of fcc-lattice is shown in (Fig. 6). The entire crystal was created through a layer-by-layer stacking of (111) planes.

To testify photonic bandgap effect, a transmission spectrum was measured (Fig. 6b). The minimum of transmittance occurred at 3490 cm^{-1}. The change of the lattice constant caused an according variation of the wavelength of the transmission dip as predicted by Bragg law, showing that the dip is indeed from the photonic band gap effect. A transmission spectrum was calculated by the full-vector analysis (transfer matrix technique)[22] to reproduce the experimental dip wavelength of 2.87 μm (3490 cm^{-1}), with the void radius r and the difference in the refractive index, Δn, as fitting parameters. As a result, void

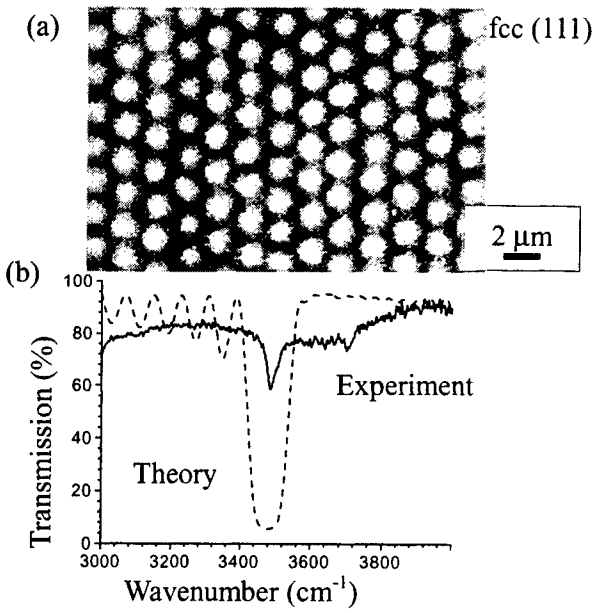


Fig. 6. . 3-D fcc PhC structure. (a) optical microscopic image of a (111) PhC plane, and (b) simulated (dashed line) and measured by FTIR (solid) transmission spectra. Fabrication was made by irradiation with singles pulses of the energy of 2.5 light induced damage thresholds at 800 nm wavelength.

diameter d = 250 nm and Δn = 0.45 gave a good agreement between the measured and calculated dips. The value of d measured by atomic force microscopy (AFM, *Seiko Instruments SPI300*) was larger than 250 nm used in calculations. In order to measure the void diameter, the sample was polished up to the depth of maximum opening of the voxel. The lateral size of the voxel might be altered by polishing and, also, the measurement by AFM must be de-convoluted from the tip's profile, which is not known; that is why we haven't fixed d in the simulation to the value measured by AFM.

1/2/3-D photonic lattices consisting of cylinders can be acquired by stacking microexplosion rods. A direct application to 3D PhC is, layer-by-layer structure, in which adjacent layer is turned by an fixed angle, e.g. 90°, and the nearest layers with the same orientation are made with the half period offset. 2D triangular lattice has the best geometry for achieving a full in-plane band gap for both E-(electric field parallel to the cylinder axis) and H-(magnetic field parallel to the cylinder axis) polarizations as have been shown theoretically[23] and experimentally.[24] Approximately 10% transmission dip for H-polarization occurred at a wavenumber of 4100 cm^{-1}, while that for E-polarization was less pronounced and located at 4000 cm^{-1}.[21] A perfect air rod structure with refractive index difference of 1.45 (air-silica refractive index difference) should permit a full bandgap, i.e., light propagation is forbidden in all direction (in-plane for the 2D periodic lattice) if a sufficient filling ratio was offered. The filling ratio, f, is the percentage of the total volume which is occupied by a dielectric and, in the case of rigid dielectric rods layer-by-layer PhCs, is expressed as $f = \pi r/4a$. However, the diameter of the cylinder was smaller than necessary, while reducing the line spacing or increasing the rod diameter (by increasing the laser power) would lead to a distortion of cylinders.

4. Conclusions

The fs-pulse-induced polymerization is available for 3-D fabrication/prototyping and fabrication of PhCs for infrared spectral region around 4 μm. The optimization of resins and development procedures is expected to shift the operation wavelength towards the optical communication window at 1.3-1.55 μm. This spectral region is also accessible by the fs-microfabrication in solid state materials by micro-explosion technique (allows real 3-D free accsess to the fabrication sites), as it was demonstrated in the case of silica (2.8-2.4 μm). The defect-related mode inside PBG is demonstrated for the first time in photopolymerized PhC.

References

[1] (Recent review) D. T. Pham and R. S. Gault, *Int. J. Machine Tools & Manufacture* **38**, 1257 (1998).
[2] X. Zhang, X. N. Jiang, C. Sun, *Sensors & Actuators* **77**, 149 (1999).
[3] A. Bertch, H. Lorenz, P. Renaud, *Sensors & Actuators* **73**, 14 (1999).
[4] G. Wurtz, R. Bachelot, F. H'Dhili, P. Royer, C. Triger, C. Ecoffet, and D.-J. Lougnot, *Jpn. J. Appl. Phys.* **39**, L98 (2000).
[5] R.A. Borisov et al., *Appl. Phys. B: Lasers & Optics* **67**, 765 (1998).
[6] E. Yablonovitch, *Phys. Rev. Lett.* **58**, 2059 (1987); S. John, *Phys. Rev. B* **58**, 2846 (1987).
[7] D. Normile, *Science* (in news) **286**, 1500 (1999).
[8] M. Campbel, D. N.Sharp, M. T. Harrison, R. G. Denning, A. J. Turberfield, *Nature* **404**, 53 (2000).
[9] (Recent reviews) T. F. Krauss, R. M. De La Rue, *Prog. Quant. Electron.* **23**, 51 (1999); C. Weisbuch, H. Benisty, R. Houdre, *J. Luminesc.* **85**, 271 (2000).
[10] J. D. Joannopoulos, P. R. Villeneuve, S. Fan, *Solid State Communications* **102**, 165 (1997).
[11] Y. Yang, S.-Y. Zhu, H. Chen, H. Zheng, *Physica B* **279**, 155 (2000).
[12] T. Baba, T. Matsuzaki, *Electr. Lett.* **31**, 1776 (2000).
[13] Z. Djuric et al., *Infrared Phys. & Technol.* **40**, 25 (1999).
[14] J. M. Gerard, B. Sermage, B. Gayral, B. Legrand, E. Costard, V. ThierryMieg, *Phys. Rev. Lett.* **81**, 1110 (1998).
[15] S. Kuchinsky, D. C. Allan, N. F. Borrelli, J.-C. Cotteverte, *Opt. Comm.* **175**, 148 (2000).
[16] H. Li, H. Chen, X. Qiu, *Physica B* **279**, 164 (2000).
[17] S. Zhu, N. Liu, H. Zheng, H. Chen, *Opt. Comm.* **174**, 139 (2000).
[18] J. P. Fouassier, D. Ruhlmann, B. Graff, F. Wieder, *Prog. Organic Coatings* **25**, 169 (1995).
[19] H.-B. Sun, S. Matsuo, H. Misawa, *Appl. Phys. Lett.* **74**, 786 (1999).
[20] E. Ozbay, Temelkuran, M. Sigalas, G. Tuttle, C. M. Soukulis, K. M. Ho, *Appl. Phys. Lett.* **96**, 3797 (1996).
[21] H.-B. Sun, Y. Xu, S. Matsuo, H. Misawa, *Opt. Rev.* **6**, 396 (1999).
[22] J. B. Pendry, *J. Mod. Opt.* **41**, 209 (1994).
[23] R. D. Meade, K. D. Brommer, A. M. Rappe, J. D. Joannopoulous, O. L. Alerhand, *Phys. Rev. B* **48**, 8434 (1993).
[24] W. M. Robertson, G. Arjavalingam, R. D. Meade, K. D. Brommer, A. M. Rappe, J. D. Joannopoulous, *J. Opt. Soc. Am B* **10**, 322 (1993).

Internal modification of glass materials with a femtosecond laser

Kazuyuki Hirao[*,**]

[*]*Hirao Active Glass Project, ERATO, Keihanna Plaza,1-7 Hikaridai, Seika-cho, Kyoto 619-0237, Japan*

[**] *Division of Material Chemistry, Graduate School of Engineering, Kyoto University, Sakyo-ku, Kyoto 606-8501, Japan*

E-mail : hirao@bisco1.kuic.kyoto-u.ac.jp

The various microscopic modifications in glasses by ultra-short pulses were examined. It was confirmed that permanent refractive index changes, and creation of microcrystals with second-order nonlinear optical functions could be produced with a femtosecond pulse laser only in selective internal areas in glasses. By using a femtosecond laser with a high repetition rate, permanent optical waveguides can be successfully written in various glasses, where refractive index changes are continuously induced along a path traversed by focal point. We also confirmed that single crystals are created from the core region in the waveguides by the laser irradiation, which is used for various kinds of optical devices.

Introduction

Glass is the most important material in optics, with uses in optical fibers, lenses, mirror substrates, and prisms. In all of these well-known applications, however, glass is almost only used as a passive medium. Since the development of integrated optics, glass is expected to use in active functions as well, such as in amplification, storage, switch, and modulation of light. This is because glass is homogeneous, transparent and can be easily fabricated to various forms in larger size and to fiber.

As a general rule, glass has very low optical nonlinearity, and the application of an electric field does little to the optical wave traveling in the material. It has recently been found that when a high voltage is applied across a SiO_2 plate at a high temperature and after the material is subsequently cooled to room temperature, the poled glass can frequency-double incoming infrared light up to visible light [1]. As early as the beginning of the 1960s, glasses doped with rare-earth ions, such as Nd-doped glass and Er-doped glass, were used as gain media for lasers, which are two examples of the success of the use of doped glass to perform an active optical function [2]. Since then many studies have been carried out on the interaction of intense laser radiation with glass [3, 4]. In particular, we have found that various types of interactions with glass can be produced by using a femtosecond laser operating at the nonresonance wavelength. A short pulse width means that extremely high peak power can be obtained and high intensity light can easily be achieved by focusing the laser beam. The development of high-energy-density femtosecond pulse lasers has prompted us to investigated the unexplored potential for inducing multiphoton photochemical reactions. Now, photoinduced

First International Symposium on Laser Precision Microfabrication, Isamu Miyamoto, Koji Sugioka, Thomas W. Sigmon, Editors, Proceedings of SPIE Vol. 4088 (2000) © 2000 SPIE · 0277-786X/00/$15.00

effects and the creation of induced structures in glasses in the context of photonic devices have been the subject of many publications, including photoinduced refractive-index grating in glass waveguides and fibers, photoinduced second-harmonic generation (SHG), optical storage based on photoinduced refractive-index change, fast modulation and switching of light, photowritten optical waveguides, microcrystallization by femtosecond laser, photoinduced long-lasting fluorescence and valence change of ion species, and photostimulated luminescence in rare-earth-ion-doped glasses.

This study is focused on selected topics which are new and of fundamental importance in the applications of active glasses in photonic devices. For this purpose, we have been researching glasses under the higher electromagnetic fields such as a femtosecond laser from the most basic physics and chemistry to experiments practicable for optical communications.

Here, brief results on some important photoinduced effects of glasses are given in the following.

1) Laser-induced optical waveguides: Permanent optical waveguides can be written in various glasses by using a femtosecond laser, where refractive index changes are continuously induced along a path traversed by the focal point. Producing waveguide-like channels by this technique is much faster, easier and cheaper than constructing a waveguide by standard chemical vapor deposition techniques.

2) Spectral hole-burning for photo-induced optical fiber devices: Spectral hole-burning of Sm^{2+}-doped glass can be achieved at room temperature, which can be used for high-density optical storage. Spectral hole-burning in glass fiber is expected to use for demultiplexers in wavelength mutiplexing optical communication systems.

3) Optical memory based on photoinduced valence state manipulation of rare-earth-ions in glasses: The valence state of rare-earth-ions in glasses, such as Eu, can be modified by exposing to irradiation of femtosecond laser. This effect is inferred to be useful in the fabrication of optical memory devices.

4) Crystal growth by femtosecond laser irradiation: Clear single crystals can be produced by focusing a femtosecond laser beam into a tiny region of a specially designed glass composition containing barium and boron. By moving the focal point, fibrous BaB_2O_4 (BBO) crystals could be grown.

Experimental and Results

1) Laser-induced optical waveguides [5 - 10]

Writing of 3-dimentiomal optical waveguides within glass by a femtosecond laser.

Outline of Research Results : It has been found that focused irradiation of femtosecond laser beam within glass (Fig.1) induces an increase of refractive index (Fig.2). The mechanism is based on the multiphoton absorption due to

the high peak power.

Furthermore, it is confirmed that low-loss optical waveguides with various shapes can be obtained within any place of the glass by scanning the focused spot (Fig.3, 4).

This technique is expected to realize 3-dimentinal optical circuits, photonic crystals, and so on. In addition, 3-dimentional optical memories with ultra-high density are also available using the array of spots with the increased refractive index.

Possible Applications :

1. 3-dimetional optical waveguides
2. Photonic crystals

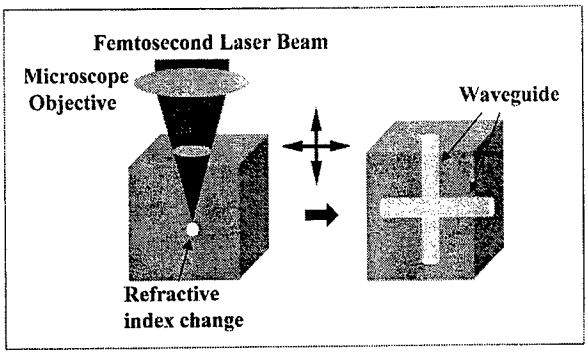


Fig.1 Scheme of waveguide writing

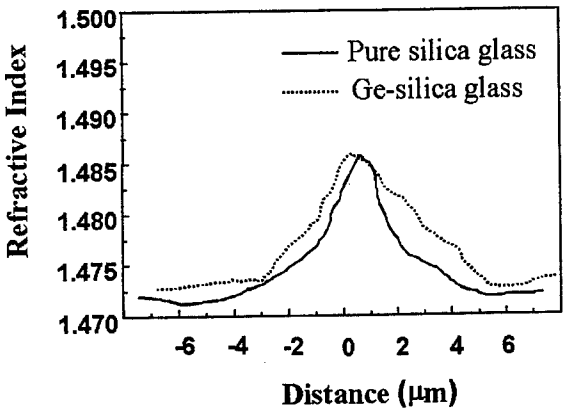


Fig.2 Refractive index profiles across waveguides

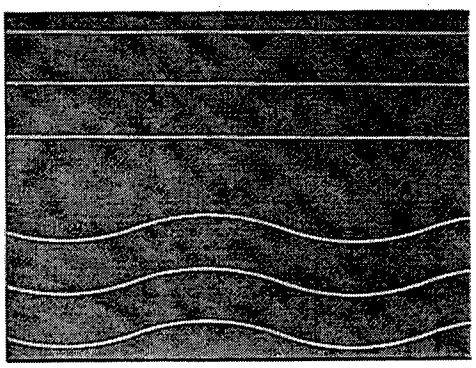


Fig.3 Laser-induced optical waveguides

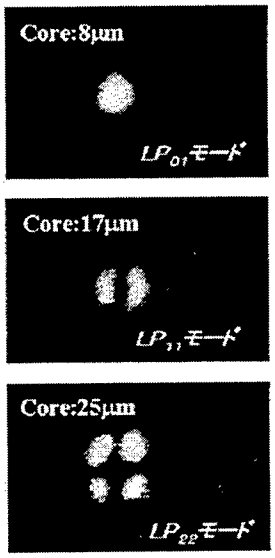


Fig.4 Near-field patterns of guided light from waveguides with different core diameter

2) Spectral hole-burning for photo-induced optical fiber devices [11, 12]

Room temperature hole-burning and femtosecond-laser-induced grating in glass fibers

Outline of Research Results

Persistent hole-burning experiments were performed for Sm^{2+}-doped glass fibers, and the stable hole was confirmed at room temperature (Fig.5). Applications to multi-wavelength memories and wavelength-selective elements in fiber optics are expected.

Long-period fiber gratings were fabricated by focused irradiation of femtosecond laser beam to induce periodical change of refractive index in silica fibers. The obtained transmission characteristic (Fig. 6) was found to be very stable even after high-temperature annealing below glass transition temperatures (Fig.7). This is a remarkable advantage compared to the conventional method using UV-laser irradiation. Application to the wavelength-division-multiplex optical communication systems is expected.

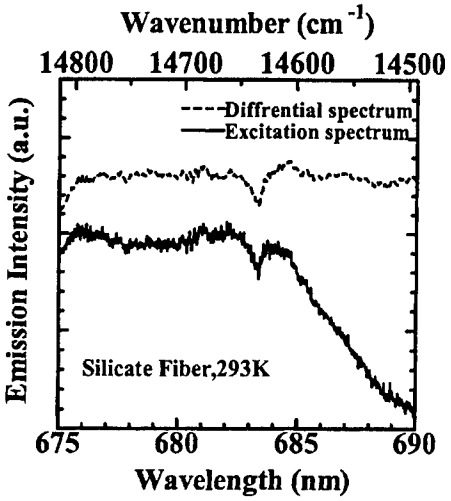


Fig.5 Room-temperature hole-burning characteristic of Sm^{2+}-doped fiber

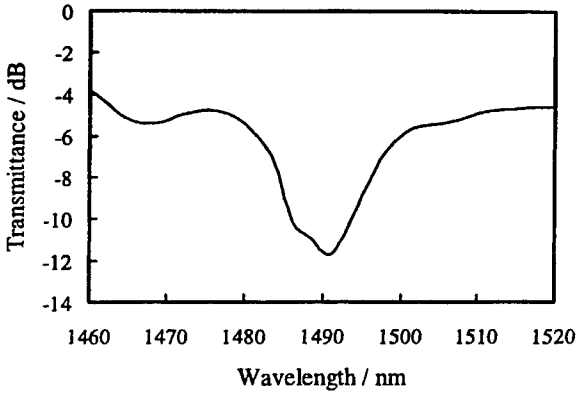


Fig.6 Transmission spectrum of laser-induced fiber grating

Possible Applications

1. High-density optical memories in fibers
2. Wavelength-selective fiber elements
3. Wavelength-division-multiplex optical communication systems

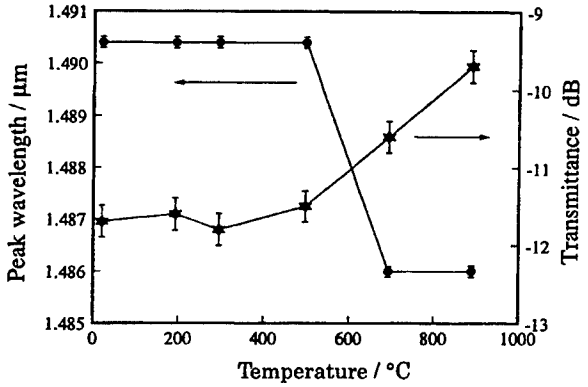


Fig.7 Stability of the fiber grating for annealing

3) Optical memory based on photo-induced valence change and memories [13 – 15]

Reduction of Sm ions by femtosecond laser and application to 4-dimentional optical memories

Outline of Research Results

It has been found that focused irradiation of infrared femtosecond laser within Sm^{3+}-ion-doped glass induces a reduction of the ions (Sm^{3+} to Sm^{2+}) at the focused spot (Fig.8). The mechanism is based on the photo-reduction by multi-photon excitation due to the high peak power of the laser.

High-density optical memories can be realized by using 3-dimensional array of the spots, where absorption/luminescence change is used for reading.

Moreover, "4-dimentional" memories are also available by utilizing the hole-burning effect of the Sm^{2+}-ions at each spot (Fig.9,10), where the memory density reaches $10TB/cm^3$.

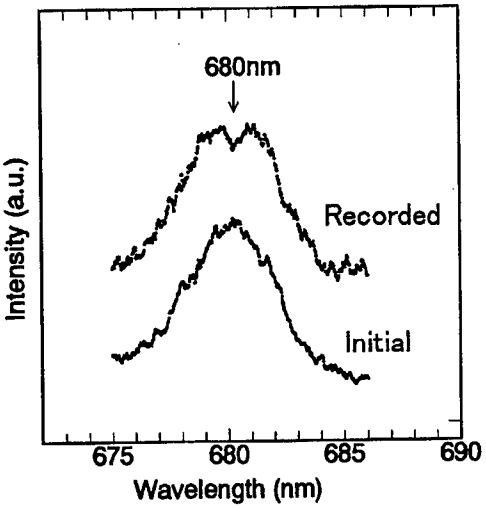


Fig.9 Hole-burning recording characteristic of laser-induced Sm^{2+}-ions in glass

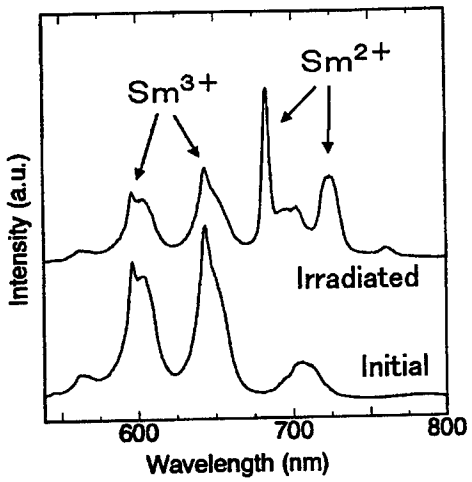


Fig. 8 Change of luminescence spectra with irradiation of femtosecond laser

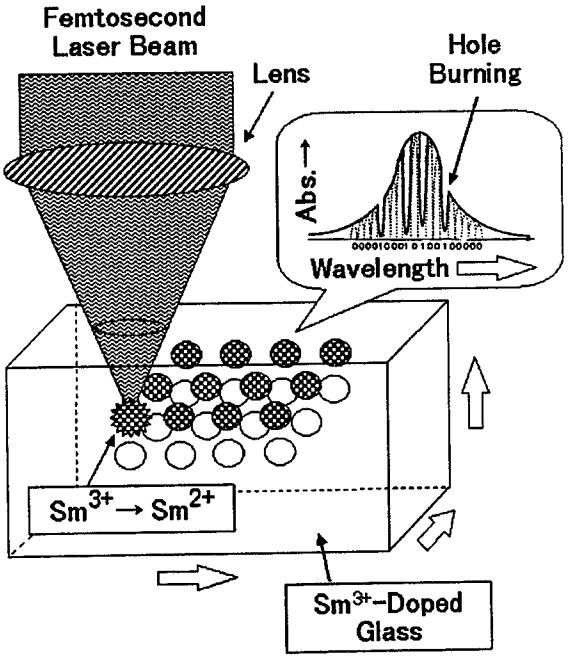


Fig.10 Concept of 4-dimentional ultra high density optical memories

Possible Applications

1. Valance control technique for ion species
2. 4-D ultra high density optical memories

4) Laser-induced crystal growth [16 - 19]

3-dimentional crystal growth within glass by femtosecond laser irradiation

Outline of Research Results

Focused irradiation of femtosecond laser beam within a photosensitive glass containing Ag followed by an annealing has been found to precipitate NaF microcrystals at the focused point (Fig.11).

It is also found that the focused irradiation and scanning of the focused spot within an oxide glass containing Ba and B induces a growth of fiber-like crystal of BaB_2O_4 which is useful as a nonlinear optic material (Fig.12). Second harmonic generation from the crystal has been confirmed (Fig.13).

It seems that this is an unique technique which enables us to form crystalline material at a desired place within glass, and applications to various optical devices are expected.

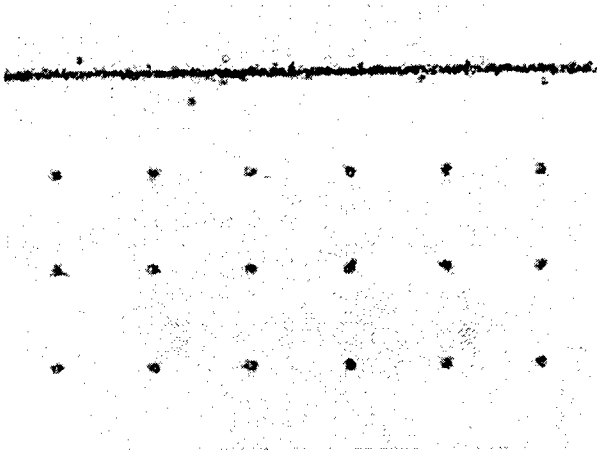


Fig.11 Microcrystals precipitated within photosensitive glass

Possible Applications

1. Laser-induced 3-D crystal growth technique
2. 3-D optical functional devices

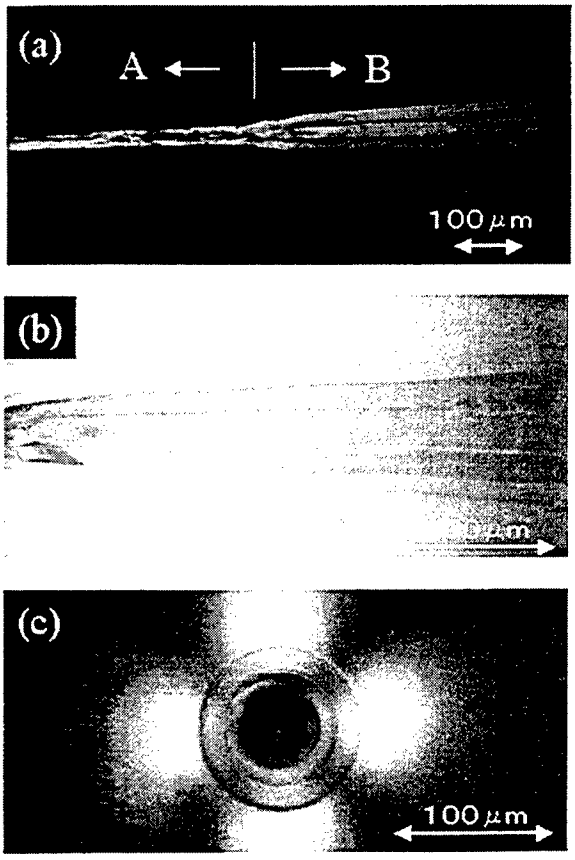


Fig.12 Laser-induced BaB_2O_4 crystal within glass

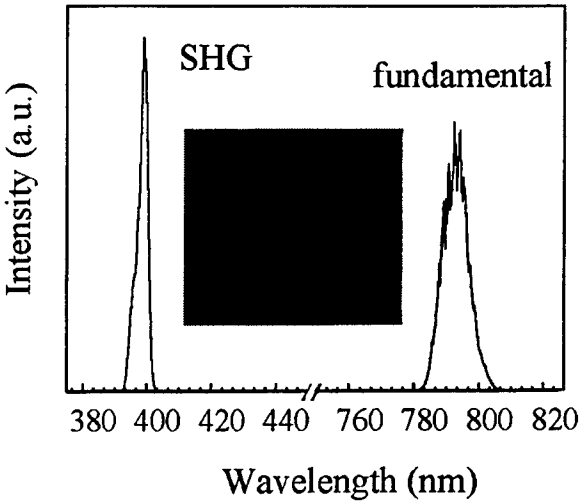


Fig.13 Second-harmonic generation from the BaB_2O_4 crystal

Conclusion

We believe that research results presented here have opened up new possibility in the production of novel functional optical materials and photonic devices, and expect that most of them can be applied to optical communications. However, it is important to point out that the purpose of this book is hopefully to inspire further research and development of active glasses in photonic devices. In this field, new results and discoveries are still being reported frequently at meetings and in journals. The research results presented in here are only a part of our researches in this field.

References

1) R. A. Myers., N. Mukherjee, and S. R. J. Brueck, Optics Letters, **16**, (1991) 1732.

2) E. Snitzer, Physical Review Letters **7**, (1961) 444.

3) E. N. Glezer, M. Milosavljevic, L. Huang, R. J. Finlay, T. H. Her, J. P. Callan, E. Mazur, Optics Letters, **21**, (1996) 2023.

4) P. G. Kazansky, H. Inouye, T. Mitsuyu, K. Miura, J. Qiu, K. Hirao, F. Starrost, Physical Review Letters, **82**, (1999) 2199.

5) K. M. Davis, K. Miura, N. Sugimoto, K. Hirao: Optics Letters **21 (21),** (1996) 1729-1731.

6) K. Miura, J. Qiu, H. Inouye, T. Mitsuyu, K. Hirao: Applied Physics Letters **71**, (1997) 3329-3331.

7) K. Miura, K. Hirao: The Review of Laser Engineering **26 (2)**, (1998) 150-154.

8) K. Miura, H. Inouye, J. Qiu, T. Mitsuyu, K. Hirao: Nuclear Instruments and Methods in Phys. Res. B141, (1998) 726-732.

9) K. Hirao, K. Miura: Journal of Non-Crystalline Solids **239**, (1998) 91-95.

10) K. Miura, J. Qiu, T. Mitsuyu, K. Hirao: Journal of Non-Crystalline Solids **256&257**, (1999) 212-219.

11) K. Nouchi, M. Watanabe, K. Muta, T. Mitsuyu, K. Hirao: Optics Communications **168** (1999) 233-236.

12) Y. Kondo, K. Nouchi, M. Watanabe, P. G. Kazansky, T. Mitsuyu, K. Hirao: Optics Letters **24** (10), (1999) 646-648.

13) J. Qiu, K. Miura, K. Hirao: Japanese Journal of Applied Physics **37**, (1998) 2263-2266.

14) J. Qiu, K. Miura, T. Suzuki, T. Mitsuyu, K. Hirao: Applied Physics Letters **74 (1),** (1999) 10-12.

15) J. Qiu, K. Kojima, K. Miura, T. Mitsuyu, K. Hirao: Optics Letters **24 (11),** (1999) 786-788.

16) Y. Kondo, T. Suzuki, H. Inouye, K. Miura, T. Mitsuyu, K. Hirao: Japanese Journal of Applied Physics **37**, (1998) L94-96.

17) Y. Kondo, T. Suzuki, H. Inouye, K. Miura, T. Mitsuyu, K. Hirao: Proceedings of XVIII International Congress on Glass (The American Ceramic Society, San Francisco, California, 1998) C11, 36-41.

18) Y. Kondo, K. Miura, T. Suzuki, H. Inouye, T. Mitsuyu, K. Hirao: Journal of Non-Crystalline Solids **253** (1999) 143-156.

19) K. Miura, J. Qiu, T. Mitsuyu, K. Hirao: Optics Letters (submitted).

Time-resolved dynamics of plasma self-channeling and bulk modification in silica glasses induced by a high-intensity femtosecond laser

Sung-Hak Cho, Hiroshi Kumagai, Katsumi Midorikawa and Minoru Obara*

Laser Technology Lab. The Institute of Physical and Chemical Research (RIKEN)
2-1, Hirosawa, Wako, Saitama 351-01, Japan
E.mail: shcho@riken.go.jp
**Dept. of Electronics & Electrical Eng. Keio University*

The time-resolved dynamics of plasma self-channeling and refractive index bulk modification in the silica glasses are first observed using a high-intensity femtosecond (110 fs) Ti: sapphire laser (λ_p=790 nm). We propose the new pump-probe measurement to observe the lifetime of both plasma self-channeling and induced refractive index bulk modification. The energy variation of transmitted probe beam, which propagates transversely through the plasma self-channeling is measured. At the pre-breakdown domain, the lifetime of induced plasma self-channeling is 20 ps and structural transition time for forming the refractive index change is 10 ps. At the breakdown domain, however, the lifetime of induced plasma formation is 30 ps and structural transition time for forming the optical damage is 40 ps. We find that the process of refractive index bulk modification is significantly different from those of optical damage. We also measure a wavelength shift (blueshift) of reflected probe beam from the surface of the plasma self-channeling induced by the pump beam. A maximum value of blue wavelength shift is 3 nm when the time delay of probe beam is 2 ps. The expanding velocity of the plasma ionization is calculated from the wavelength shift (blueshift) using the Doppler formula. A maximum velocity of the plasma ionization is calculated to be approximately $6x10^5$ m/s at the delay time of 2 ps.

1. Introduction

Due to the recent remarkable progress in the chirped pulse amplification (CPA) technique [1] with broadband tunable solid-state lasers, it has become an innovative tool to take an advantage of high power ultrashort laser pulses in a wide variety of science and technology fields. The interaction between ultrashort, high-intensity laser lights and transparent solid materials has become a major concern on those application fields since the advent of high-intensity femtosecond lasers [2,3]. When a high-intensity laser beam is focused into the bulk optical transparent materials at higher intensities than the self-focusing threshold, laser-induced solid-density plasma, plasma channeling, and small filaments are produced [4,5]. Plasma self-channeling is an intensity-dependent nonlinear phenomenon, in which a laser beam is tightly focused and guided for the distance longer than the Rayleigh range. It has been interpreted as a counterbalance of the self-focusing due to the Kerr effect and the defocusing effect due to the formation of a low-density plasma [6,7]. Recently, plasma-induced bulk modification by the tightly focused high-intensity laser beams was found to provide a new tool for three-dimensional optical memory and micro-structuring in transparent dielectrics [8-12]. In particular, plasma self-channeling would provide a useful tool to fabricate the double cladding structures and multi-core structures of optical fibers for optical sensor and communication [13].

In the meantime, the studies of the ultrashort optical pulse propagation in transparent media in the nonlinear regime have stimulated great interest in both theoretical understanding and technological applications of the optical materials in three-dimensional imaging [14], optical information coding [15], pulse compression [16, 17], and breakdown studies [18], since the first experimental observation of the refractive index modulation effects in the bulk glass in the 1986 [19] and the optical fibers in 1987 [20]. For example, when the laser intensity is sufficiently low, induced phase modulation refers to the frequency shifts experienced by a weak probe pulse propagating through a medium whose refractive index is modulated by an intense pump pulse. At higher intensities, information on the ionization mechanisms and thus plasma formation or breakdown in the solids induced by the nonlinear interactions is obtainable through reflectivity and transmissivity measurements [21, 22]. Although the observations of the plasma formations and optical damages on the surface of solid target have been reported by many researchers in the past several years with laser pulses [23-25], the time-resolved dynamics of plasma formations and bulk structural changes induced by the interaction between propagating high-intensity pulses and transparent materials have remained unexplored until now.

In our previous works [13,26], plasma self-channeling and refractive index bulk modification in optical fibers

First International Symposium on Laser Precision Microfabrication, Isamu Miyamoto, Koji Sugioka, Thomas W. Sigmon, Editors, Proceedings of SPIE Vol. 4088 (2000) © 2000 SPIE · 0277-786X/00/$15.00

induced by the interaction between high-intensity femtosecond laser beam and transparent materials was demonstrated. However, the time-resolved variations of plasma self-channeling and refractive index bulk modification was not discussed in detail. For satisfactory fabrication of line-shaped refractive index bulk modification structures in transparent materials using plasma self-channeling induced by a high-intensity femtosecond laser, the time-resolved dynamics of nonlinear phenomena, i.e., plasma formation, the generation of color center, and permanent refractive index modification must be determined.

In this paper, we propose a new pump-probe measurement in order to observe the time-resolved dynamics of the plasma self-channeling and induced bulk modification. The lifetimes of the plasma self-channeling and refractive index bulk modification are reported here. In this experiment, bulk silica glasses are used, which enabled one to *in situ* study easily the dynamics of plasma formation and bulk refractive index modification at different time delays, instead of optical fibers used in previous experiments. The results obtained in this experiment will be helpful to understand the physical mechanism of the plasma formation and structural transformation induced by the high-intensity femtosecond lasers in transparent materials.

2. Experimental Setup

The schematic diagram of experimental setup for the time-resolved dynamic of plasma self-channeling and refractive index modification is shown in Fig. 1. The laser used in experiment is a Ti:sapphire oscillator-amplifier laser system (λ_p=790 nm) based on the chirped pulse amplification technique with a 110 fs pulse duration, 1 W average output power, and 1 kHz repetition rate, as a irradiation laser source. The laser beam is divided into the pump and probe one through the beam splitter.

The linearly polarized pump laser beam with a Gaussian profile is focused through a quartz lens with a focal length of 60 mm. It is incident onto the input surface of the optical silica glass (15x15x15 mm) located away from the breakdown point to avoid optical damage at the input end surface. The pump beam is adjusted to induce the plasma self-channeling in bulk silica glass composed of pure silica. The diameter of laser beam on the input surface of silica glass is 100 μm to be coupled with bulk silica glass. The silica glasses (Purity > 99.99%) are provided by the *Tokyo Taisei Glass Co.* The transmitted power is recorded by the optical powermeter connected to the computer. The average energy of the pump beam is ~10 μJ enough to induce plasma self-channeling in bulk silica glass. The induced plasma channeling and plasma-induced bulk modification are observed by the microscope with CCD camera located transversely to the silica glass.

The linearly polarized probe beam with time delay ($\Delta\tau$) is focused through a quartz lens with the focal length of 100~200 mm located transversely to the silica glass. The power of the transmitted probe beam through the plasma self-channeling is recorded by the photodiode connected to the computer with digital memory. Average energy of probe beam is approximately 0.5~1μJ to avoid the generation of plasma formation in the silica glass by focusing the probe

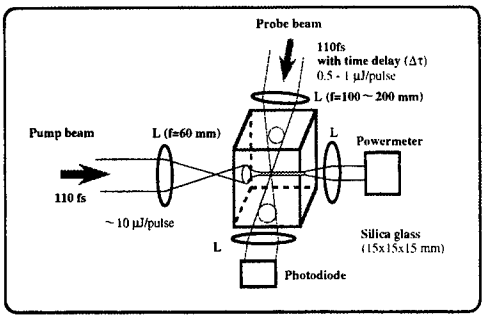


Fig.1 Experimental setup

one. The diameter of the probe beam at the focused spot is adjusted to 15~20 μm, which enables to couple with the induced plasma self-channeling transversely. The time resolution of probe beam is 0.5 ps. The probe beam is adjusted to penetrate transversely through the induced plasma self-channeling, as shown in Fig. 2(b). The energy stability of the probe beam is less than ± 0.75%.

3. Experimental Results and Discussion

Intense ultrashort laser excitation of optically transparent materials causes a change in the refractive index of materials which is dependent on the intensities, which is written as $n = n_0 + n_2 E^2$, and can thus induce self-focusing and plasma formation. Where n_0 is a linear refractive index of material and n_2 is a Kerr coefficient. The self-focusing occurs when the focusing effect exceeds the diffraction of the propagating beam. It is evident that self-focusing in silica glasses occurs at input intensity of $1x10^{12}$ W/cm^2 where n_2 is $3.18x10^{-16}$ cm^2/W in silica one.

In the experiment, the first plasma spot was observed at 60 μm distant from the input surface of the optical silica glass by self-focusing effect at an input intensity of $8x10^{11}$

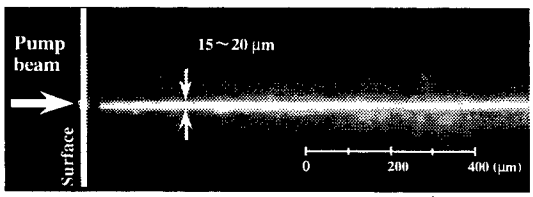


Fig.2. Microscopic side view of plasma self-channeling in the bulk silica glass

W/cm^2 on the input surface of optical glass. The first self-focusing point could be controlled by changing the input angle of the focusing beam to the input surface of optical

glass using the different focal lenses. When input intensity exceeds $1.5x10^{12}$ W/cm^2, an uniform plasma channeling with a diameter of 12~15 μm was observed and reached the length of 9-10 mm from the first self-focusing point in a bulk silica glass (Fig.2).

Some visible refractive index modifications were observed in the center of optical glass after plasma channeling occurred and it proceeded to the deeper distance than the first self-focusing point as the number of laser pulses was increased (Fig.3). It was observed that the process of bulk modification was saturated within $1x10^4$ laser shots approximately. The refractive index modification was formed onto the distance of 9-10 mm with a diameter of approximately 5 μm after laser shot number of $1x10^4$.

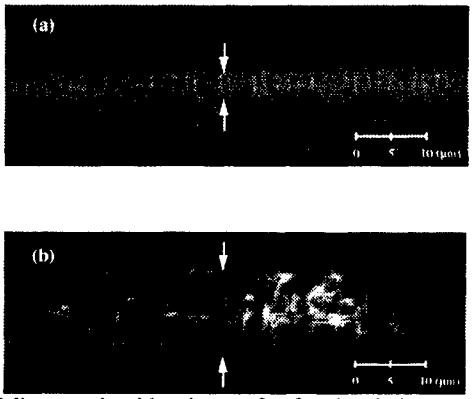


Fig.3. Microscopic side views of refractive index modification and optical damage in a bulk silica glasses. (a) Refractive index modification by the self-channeling at input intensity of $1.5x10^{12}$ W/cm^2. (b) Optical damage excited by input intensity of $5.0x10^{12}$ W/cm^2.

When input intensity exceeded $3.5x10^{12}$ W/cm^2, the plasma induced modification which have cracks, so called the optical damages. Optical damages have the non-uniform diameter of 10~15 μm and have some cracks in modified regions, referred to uniform refractive index modification with a diameter of 5 μm and no cracks. It means that the process of refractive index bulk modification in pre-breakdown domain is different from that of optical damage in breakdown one.

The relationship between time delay of probe beam and energy variation of transmitted probe one during the plasma self-channeling at pre-breakdown regime was shown. The input intensity of pump beam was $1.5x10^{12}$ W/cm^2 on the input surface of the optical glass. The probe beam was focused on the place at where plasma self-channeling occurred. The diameter of focused probe beam in bulk silica glass was 20 μm. The energy of transmitted probe beam was decreased to 95 %, when the time delay of the probe beam was ranging from 0 to 20 ps, approximately. It is suggested that the energy loss of 5% be due to both the reflection or scattering from the low density plasma self-channeling and absorption in plasma formation. And it means that plasma self-channeling occurs for 20 ps in the optical glass. However, when the time delay of the probe beam exceeded 20 ps, the energy of transmitted probe beam was slowly increased to 97% within 10 ps, approximately. It suggests that the lifetime of plasma self-channeling is 20 ps and some structural change, as like refractive index modification occurs within 10 ps. And then, the energy of probe beam became to 97 % and then kept to the stable state after time delay passed over 30 ps. It infers that some refractive index structural transformation is completely done within 30 ps. Refractive index bulk modifications were observed in the optical glass after plasma channeling occurred and it proceeded to the deeper distance. In all cases, any cracks were not observed in the refractive index modification regions. We found that the energy of the transmitted probe beam decreased to 95 % through the plasma self-channeling and to 97% through the formed refractive index bulk modification in our experiment. The maximum value of refractive index increase (Δn) was measured to be $2.1x10^{-2}$.

The relationship between energy variation of transmitted probe beam and propagated distance at different time delays is shown. The focusing point of probe beam with different time delays was moved to the following axis at where plasma self-channeling occurred. In the time delay of 10 ps, the energy of the probe beam was decreased to 95% in the range from 0 to 4 mm. In the time delay of 20 ps, the energy variation of the probe beam was moved onto the deeper distance, ranging from 0 to 7 mm in the bulk glass. When time delay was 30 ps, the distance at where the energy decrease in the probe beam existed from the input surface of silica glass extended to the deeper. When time delay was 40 ps, the energy decrease in the probe beam reached 10 mm at where plasma self-channeling disappeared. It means that the plasma self-channeling was moving onto the deeper optical glass, as the time was passing. And the lifetime of plasma self-channeling was about 20 ps. After the plasma self-channeling disappeared, the increase of transmitted probe beam which reached 98 % of the total energy was observed. It was found that the energy loss of the transmitted probe beam through the plasma self-channeling was higher than that through refractive index bulk modification.

As the same measurement method, the time-resolved dynamics of plasma self-channeling and optical damage at the breakdown regimes is shown. At the pump irradiation of $5.0x10^{12}$ W/cm^2 on the input surface of bulk silica glass, the relationship between the time delays of propagated probe beam and energy variations of transmitted probe beam is described. In this breakdown domain, the energy of the transmitted probe beam was decreased to 30% during plasma self-channeling and it took 30 ps, the lifetime of plasma self-channeling. The transition time of structural

transformation was 40 ps. After the delay time of 70 ps passed, the energy of transmitted probe beam reached 60 % and kept to the stable state. In this case, the optical damage with some cracks was observed in the modified region. The optical damage was the same as that observed. The lifetimes of plasma self-channeling and the transition of structural change in the pre-breakdown regime, was significantly shorter than the plasma formation and optical damage in the breakdown regime. Based on the experimental results of pump-probe measurements, it is found that the process of refractive index bulk modification is significantly different from those of optical damage. The comparison of the time-resolved dynamics of plasma self-channeling and structural change at both the refractive index modifications in pre-breakdown and optical damages in breakdown domain was represented. The density of plasma electron can be calculated by the cutoff frequency (n_c) [21, 22] By considering the transmission properties, the density of plasma self-channeling at pre-breakdown regime would be lower than 1.27×10^{27} [$1/m^3$] and the density of plasma self-channeling in the breakdown regime would be higher than 1.27×10^{27} [$1/m^3$].

In this experiment, we demonstrated the time-resolved dynamics of the plasma self-channeling and structural transformation in both the pre-breakdown regime and breakdown regime in optical transparent glass composed of pure silica. It helps to study easily the nonlinear interaction between high-intensity femtosecond laser beam and bulk glass. In general, the optical silica glass has a high transmission from the UV to IR and a large band-gap of 9.0 eV. At low electric fields of the laser in the optical glasses composed of pure silica, bound electrons do not absorb laser light because the bound valence electron has an ionization potential or band-gap greater than the infrared laser photon energy (1.54 eV). In the meantime, at high fields, multiphoton absorption plays an important role to induce ionization by which a bound electron in an atom absorbs multiphoton simultaneously to produce a free electron. Free electron induced by multiphoton ionization generates repeatedly additional free electrons by the collision with the bound electron and the lattice, leading to a plasma formation in which the free electron density grows exponentially and the increase of plasma temperature. After the laser pulse passed, the generated free electrons were shortly recombined with surrounding ions caused by the plasma rapid quenching.

4. Conclusion

The experimental time-resolved dynamics of plasma self-channeling and refractive index bulk modification in the silica glasses was demonstrated.

References

[1] D. Strickland and G. Mourou, Opt. Comm. **56**, 219 (1985)

[2] R. A. Indik, J. V. Moloney, R. Binder, A Knorr, and S. W. Koch, Opt. Lett. **20**, 2315 (1995)

[3] D. V. D. Linde and H. Schuler, J. Opt. Soc. Am. B. **13**, 216 (1996)

[4] D. M. Mittleman, D. C. Douglass, Z. Henis. O. R. Wood, R. R. Freeman, and T. J. Mcilrath, J. Opt. Soc. Am. B **13**, 170 (1996)

[5] H. E. Bennett, A. H. Guentther, M. R. Kozlowski, B. E. Newnam, and M. J. Soileau Proc. SPIE. **2428**, 469 (1994)

[6] S. C. Rae, Phys. Rev. A. **46**, 2077 (1992)

[7] A. B. Borisov, O. B. Shiryaev, A. McPherson, K. Boyer, and C. K. Rhodes, Plasma
Phys. Control. Fusion. **37**, 569 (1995)

[8] E. N. Glezer, M. Milosavljevic, L. Huang, R. J. Finlay, T. -H. Her, J. P. Callan, and E.Mazur, Optics Lett. **21**, 2023 (1996)

[9] D. Ashkenasi, H. Varel, A. Rosenfeld, S. Henz, J. Herrmann, and E. E. B. Cambell, Appl. Phys. Lett. **72**, 1442 (1998)

[10] K. M. Davis, K. Miura, N. Sugimoto, and K. Hirao. Optics Lett. **21**, 1729 (1996)

[11] S. H. Cho, H. Kumagai, I. Yokota, K. Midorikawa, and M. Obara, SPIE, **3343**, 515 (1998)

[12] S. H. Cho, H. Kumagai, K. Midorikawa, and M. Obara, Technical Report of IEICE, **LQE 99-16**, 53 (1999)

[13] S. H. Cho, H. Kumagai, K. Midorikawa, and M. Obara, Opt. Comm. **168**, 287 (1999)

[14] R. Dorsiniville, P. P. Ho, J. T. Manassah. and R. R. Alfano, "*The Supercontinuum Laser Source*", R. R. Alfano, ed. (Springer-Verlag, New York, 1989), p.375

[15] P. L. Baldeck, P. P. Ho, R. R. Alfano, "*The Supercontinuum Laser Source*", R. R. Alfano, ed. (Springer-Verlag, New York, 1989), p.117

[16] A. M. Johnson and C. V. Shank, "*The Supercontinuum Laser Source*", R. R. Alfano, ed. (Springer-Verlag, New York, 1989), p.397

[17] M. Yamashita and K. Torizuta, Jpn. J. Appl. Phys. **29**, 294 (1990)

[18] D. Du, X. Liu, G. Korn, J. Squier, G. Mourou, Appl. Phys. Lett. **64**, 3071 (1994)

[19] R. R. Alfano, Q. X. Li, T. Jimbo, J. T. Manassah, and P. P. Ho, Appl. Phys. Lett. **11**, 626 (1986)

[20] P. L. Baldeck, R. R. Alfano, and D. P. Agrawal, Appl. Phys. Lett. **52**, 1939 (1988)

[21] B. T. V. Vu, O. L. Landen, and A. Szoke, Phy. Rev. A. **46**, 5089 (1992)

[22] X. Y. Wang and M. C. Downer, Opt. Lett. **17**, 1450 (1992)

[23] G. P. Agrawal, Phys. Rev. Lett. **59**, 880 (1987)

[24] M. N. Islam, L. F. Mollenauer, R. H. Stolen, J. R. Simpson, and H. T. Shang, Opt. Lett. **12**, 625 (1987)

[25] D. Schadt, B. Jaskorzynska, and U. Osterberg, J. Opt. Soc. Am. B. **3**, 1257 (1986)

[26] S. H. Cho, H. Kumagai, I. Yokota, K. Midorikawa, and M. Obara, Jpn. J. Appl. Phys. **37** (1998) L737

Observation of Voids and Optical Seizing of Voids in Silica Glass with Infrared Femtosecond Laser Pulses

Wataru WATANABE*, Tadamasa TOMA*, Kazuhiro YAMADA*,

Junji NISHII**, Ken-ichi HAYASHI*** and Kazuyoshi ITOH*

* *Department of Applied Physics, Graduate School of Engineering, Osaka University, 2-1, Yamada-oka, Suita, Osaka 565-0871, Japan*
E-mail: w-wata@ap.eng.osaka-u.ac.jp

** *Optical Material Division, Osaka National Research Institute, Agency of Industrial Science and Technology, 1-8-31, Midorigaoka, Ikeda, Osaka, 563-8577 Japan*

*** *Planning and Management Development, Research and Development Center, Sumitomo Heavy Industries, Ltd., 63-30, Yuhigaoka, Hiratsuka, Kanagawa, 254-00806 Japan*

Many researchers have investigated the interaction of femtosecond laser pulses with a wide variety of materials. The structural modifications both on the surface and inside the bulk of transparent materials have been demonstrated. When femtosecond laser pulses are focused into glasses with a high numerical-aperture objective, voids are formed. We demonstrate that one can seize and move voids formed by femtosecond laser pulses inside silica glass and also merge two voids into one. We also present clear evidence that a void is a cavity by showing a scanning-electron-microscope image of cleft voids: we clove through the glass along a plane that includes the laser-ablated thin line on the surface and the voids formed inside. The optical seizing and merging of voids are important basic techniques for fabricate micro-optical dynamic devices, such as the rewritable 3-D optical storage.

Keywords: femtosecond laser pulses, glass, voids, manipulation

1. Introduction

Many researchers have investigated the interaction of intense femtosecond laser pulses with a wide variety of materials. The structural modifications both on the surface and inside the bulk of transparent materials have been demonstrated [1-15]. The interaction offers the possibility of materials processing and micromachining. The use of infrared (IR) femtosecond laser pulses enables us to fabricate three-dimensional photonic structures such as waveguides [5-8], gratings [8,9], the coupler [7], and the photonic crystal [10] inside a wide variety of glasses. Using the same technique, permanent optical damage has been created for the 3-D optical data storage in a wide variety of transparent materials including glasses, crystals, and plastics [11-15]. However, the physical mechanisms of the damage responsible for IR photosensitivity have not been elucidated. It was reported that the submicometer-damage was a cavity or void surrounded by densified material [10-12]. Glezer *et al.* polished away samples until the surface level reached the internally structures of the damage and viewed under scanning electron microscope (SEM) and atomic force microscope [12].

In this paper, we demonstrate the experiments of optical move of a void and merger of two voids along the optical axis by translating the focal spot of femtosecond laser pulses [16]. From experimental results we may infer that the voids under the illumination of femtosecond laser pulses are in the melt phase. We also present a clear evidence of voids. We show scanning-electron-micrographs of cleft voids: we clove through the glass along a plane that

First International Symposium on Laser Precision Microfabrication, Isamu Miyamoto, Koji Sugioka, Thomas W. Sigmon, Editors, Proceedings of SPIE Vol. 4088 (2000) © 2000 SPIE · 0277-786X/00/$15.00

includes the laser-ablated thin line on the surface and the voids formed inside.

2. Experiment

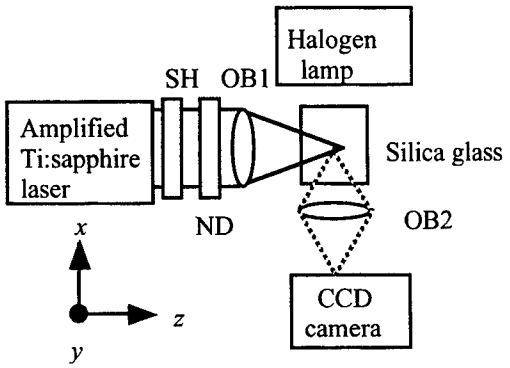


Figure 1 Schematic of experimental setup for creation and in situ observation of voids in silica glass by femtosecond laser pulses; OB1 and OB2 denote objectives. ND and SH denote a neutral density filter and a shutter, respectively.

Figure 1 shows a schematic for experimental setup. Femtosecond laser pulses are focused inside a silica glass to create local structural changes or optical damage. The silica glass sample has a thickness of 3 mm . It was optically polished on both sides for *in situ* observation from the sides. In the experiment, we used 130-fs, 800-nm, 1-kHz pulses from an amplified Ti:sapphire laser and focus the pulses by a microscope objective. The group-velocity dispersion in the optical system was minimized by adjusting the compression grating in the amplifier of the laser system. To create a void, high-numerical aperture (N.A.) objectives were used. The image of the optical damages or voids are observed from the direction perpendicular to the optical axis (y-axis) under optical microscopy. Figure 2 (a) and (b) show the creation of voids for various exposure time and incident energy, respectively. The area of structural changes enlongates with the increase of exposure time and incident energy.

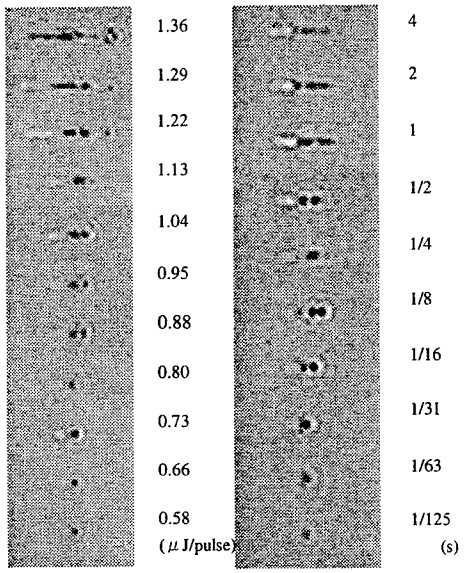
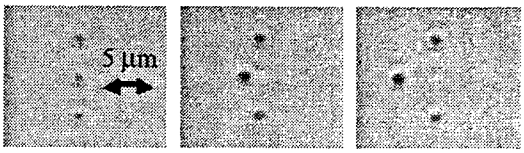


Figure 2 Creation of voids by varying exposure time and incident energy; (a) Incident energy is varied form 0.58 μJ to 1.36 μJ under fixed exposure time (1/125 s), (b) Exposure time is varied form 1/125 s to 4 s under fixed incident energy (0.73 μJ).

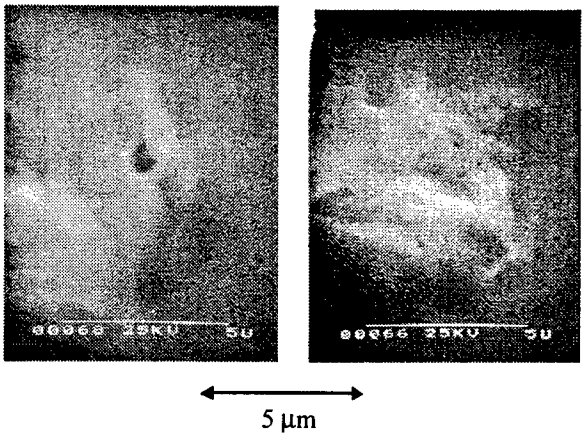
The void can be seized and translated. The focusing objective with N. A. of 0.55 was used and eight successive pulses are normally launched during the exposure time 1 / 125 s in the following experiment. The laser power incident on the focusing objective was reduced to 0.95 μJ/pulse. Figure 3 shows the behavior of a seized and moved void. Left side in the figure coincides with the input of laser pulses. First, for comparison, we created three voids in a plane perpendicular to the optical axis at the depth of 300 μm beneath the surface with the separation of 5 μm. Next, we set the focal point of the objective lens to the middle of voids and translated the sample towards the output plane with a step of 0.5 μm. Figures demonstrate that the void is seized and moved as long as 5 μm towards the incident plane. The visible trajectory after translation implies structural change. This might have connection with refractive index change utilized for the fabrication of waveguides [4-8]. We could not move the void towards the down-stream direction, either normal to the optical axis.



(a) (b) (c)

Figure 3 Sideview of optical seizing and translation of a void. The middle void is translated towards input plane by 5 μm.

To investigate the structural change or geometry of the voids, we took scanning-electron-micrographs of cleft voids. After fabricating a line of void in a glass, we delaminated on the surface a straight thin line by laser ablation along a plane including the line of voids. Figure 4 shows a photograph of SEM image. The image clearly reveals that the optical dark spot was a cavity or a void with a diameter of 0.9 μm. We also see that the region within several micrometers around the void is considered to be changed in phase or distorted by stress.



(a) (b)

Figure 4 Photographed image of a cleft glass with SEM; (a) cross-section including a void and (b) cross-section around void.

To experimentally investigate the thermal effect and thermal stability , the temperature of the sample was raised and kept at 1150 °C for one hour. After the treatment, the structural change was not seen under transmission microscopy; The void cannot be annealed out at 1150 °C, at which is an annealing point of silica glass. This agrees with the result previously reported [14]. Voids are stable with respect to the temperature, which implies the structural change around the void. However, the residual structural change in the trajectory was annealed out. The creation of the void is attributed to plasma formation or thermal dentification of melted region.

3. Conclusion

We demonstrated that we can seize and move voids formed by femtosecond laser pulses inside silica glass and also merge two voids into one. A clear evidence of voids was presented by showing scanning-electron-micrographs image of cleft voids. The voids were controllable with femtosecond laser pulses. This technique may be useful for rewritable 3-D optical storage or dynamical fabrication of optical microstructures inside glasses.

Acknowledgement

The present experiments were conducted at Venture Business Laboratory, Osaka University. The authors thank Dr. T. Nagatomi and Dr. H. Matsuo of Osaka University for help with the SEM observation. We also appreciate the assistance of Dr. K. Kintaka of Osaka National Research Institute, Agency of Industrial Science and Technology with regard to the experiment of the annealing.

References

[1] D. Du, X. Liu, G. Korn, J. Wquier, and G. Mourou: Appl. Phys. Lett., **64**, (1994) 3071.

[2] B. C. Straut, M. D. Feit, A. M. Rubenchik, B. W. Shore, and M. D. Perry: Phys. Rev. Lett., **74**, (1995) 2248.

[3] D. von der Linde and H. Schüler: J. Opt. Soc. Am. B, **13**, (1996) 216.

[4] K. M. Davis, K. Miiura, N. Sugimoto ,and H. Hirao: Opt. Lett., **21**, (1996) 1729 .

[5] K. Miura, J. Qiu, H. Inouye, T. Nitsuyu, and K. Hirao: Appl. Phys. Lett., **71**, (1997) 3329.

[6] K. Hirao and K. Miura: Jpn. J. Appl. Phys., **37**, (1998) L49.

[7] D. Homoelle, W. Wielandy, and A. L. Gaeta, E. F. Borrelli, and C. Smith: Opt. Lett. **24**, (1999) 1311.

[8] K. Hirao and K. Miura: Jpn. J. Non-Cryst. Solids, **239**, (1998) 91.

[9] T. Toma, Y. Furuya, W. Watanabe, J. Nishii, K. Hayashi, and K. Itoh: Opt. Rev. **7**, (2000) 14.

[10] H. -B. Sun, Y. Zu, S. Matsuo, and H. Misawa: Opt. Rev. **6**, (1999) 396.

[11] E. N. Glezer, M. Milosavljevic, L. Huang, R. J. Finlay, T.-H. Her, J. P. Callan, and E. Mazur: Opt. Lett., **21**, (1996) 2023.

[12] E. N. Glezer and E. Mazur: Appl. Phys. Lett., **71**, (1997) 882.

[13] J. Qiu, K. Miura, and K. Hirao: Jpn. J. Appl. Phys. **37**, (1998) 2263.

[14] M. Watanabe, H. Sun, S. Juodkazis, T. Takahashi, S. Matsuo,Y. Suzuki, J. Nishii, and H. Misawa: Jpn. J. Appl. Phys. **37**, (1998) L1527.

[15] J. A. Squier and M. Müller: Appl. Opt., **38**, (1999) 5789.

[16] W. Watanabe, T. Toma, K. Yamada, J. Nishii, K. Hayashi and K. Itoh: Opt Lett (submitted).

Micromachining with high repetition rate femtosecond laser sources

E. BAUBEAU, R. LE HARZIC, C. JONIN, E. AUDOUARD, S. MOTTIN, M. COURBON AND P. LAPORTE.

Laboratoire Traitement du Signal et Intrumentation
Université Jean Monnet UMR CNRS 5516
23 rue du docteur Michelon, F-42023 Saint-Etienne cedex 2.

Ultrashort duration laser sources are considered as a promising tool for new micromachining applications : precise microdrilling and microcutting on various materials. As an illustration of the « non thermal » micromachining, we also paid attention to precious wood. Cutting is achieved without burning, and the cut surface remains undamaged. However, until now, only low-average-power sources are available. An average power level of 10 W appears to be the lowest limit for this type of laser to really become industrial.
We are presently developping such a source based on the use of a 15kHz, 100W copper HyBrID laser as a pump laser. Thus, we intend to reach in a near future a typical drilling rate of one mm per second, for instance, in stainless steel compared with a 50 microns per second drilling rate obtained with presently available KHz and low-average-power sources. Micromachining obtained with our a 1 KHz source will be presented and discussed.

Keywords : Femtosecond, micromachining, non thermal interaction, microdrilling, microcutting

1. Introduction

Femtosecond laser sources have been recently utilized for precise micromachining due to their numerous advantages. Particularly, the femtosecond laser ablation is commonly named non thermal ablation which means that the material exhibits a minimal thermal affected zone (TAZ). Indeed in femtosecond mode, the energy is deposited and transfered to the electrons of the material in time-scale very short compared with the transfer time to the material which allows to avoid thermal effects.
We have essentially studied stainless steel and copper, particularly looking at the effect of the ablated matter depth as a function of the number of shots. We have also performed experiments on precious woods and evidenced the non thermal femtosecond ablation mode.

2. Experimental setup

Experiments have been performed using a 150 fs, 0.5 W average power, 1 KHz Ti:sapphire laser system at 800 nm. The beam is spatially filtered by a 5 mm hole and the micromachining is essentially performed at the image point. The material can be moved on the x, y and z axis with a 1 micron resolution. The x-axis is essentially used for controlling and optimizing the micromachining image point using a 50 mm lens. The y and z axis can be moved at a speed up to 20 mm/s.

3. Results and discussion

We have performed studies on different materials with a special interest on copper samples. Figure 1 shows different machined lines on copper realized at different scan speeds.

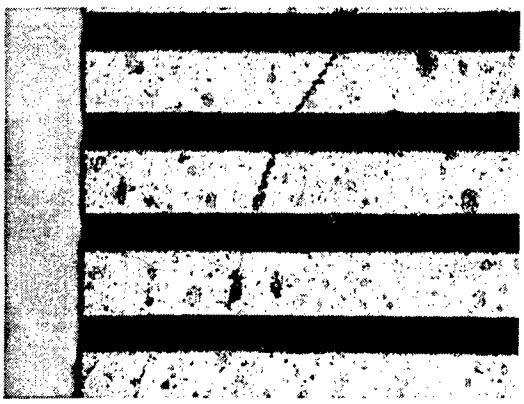


Fig. 1 : Micromachined lines in copper sample. Each line has a width of 100 μm. From the top to the bottom the speed of the sample holder along the z-axis was 1 mm/s.

From these results we have extracted the ablated matter depth as a function of the average number of laser shots (see figure 2).

First International Symposium on Laser Precision Microfabrication, Isamu Miyamoto, Koji Sugioka, Thomas W. Sigmon, Editors, Proceedings of SPIE Vol. 4088 (2000) © 2000 SPIE · 0277-786X/00/$15.00

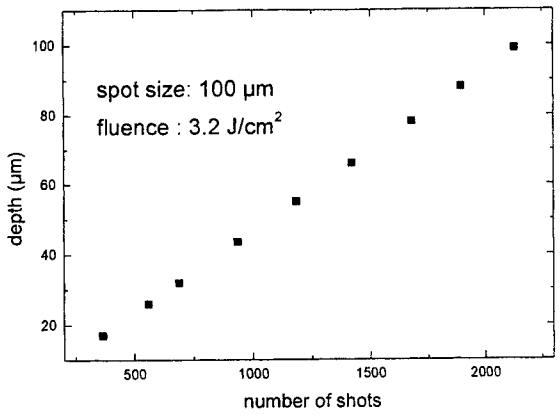


Fig. 2 : Ablated matter depth versus number of shots in copper. The polarization was linear.

The measurement of the depth was performed using a profilometer with a resolution of 1-2 µm. It has to be noticed that the evolution of the depth as a function of the number of shots is linear but only up to a few hundreds of µm. The ablated rate per pulse was found to be 48 nm/pulse in our experimental conditions. The machining was performed at the image point of the hole to obtain a 100 µm diameter hole with a better quality than a 30 µm hole realized at the focus point. At this latter point, the evolution described above is linear only under 100 µm of depth. Although the energy at the focus point is higher (21 J/cm^2) than at the image point (3.2 J/cm^2), we need a lower number of shots to drill the same depth (300 nm/pulse). Unfortunately, an accumulation phenomenon limits the ablation efficiency beyond 100 µm depth at the focus point. We have also studied the polarization effects on etching (see figure 3).

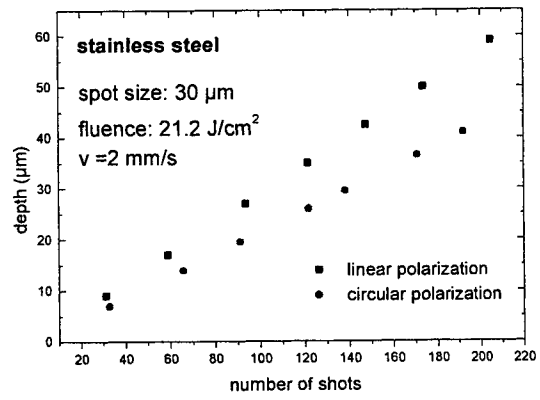


Fig. 3 : Ablated matter depth as a function of the number of shots.

The points represent the depth of different lines obtained in stainless steel. It has to be noticed that the ablated depth is higher using a beam linearly polarized than a circularly one. The material holder is moving along the z-axis and the linear polarization is perpendicular to this axis, thus it appears that the monitoring of the polarization should really increase the ablation efficiency.
We have also compared in the same conditions the ablated matter depth in copper and in stainless steel as is shown in figure 4.

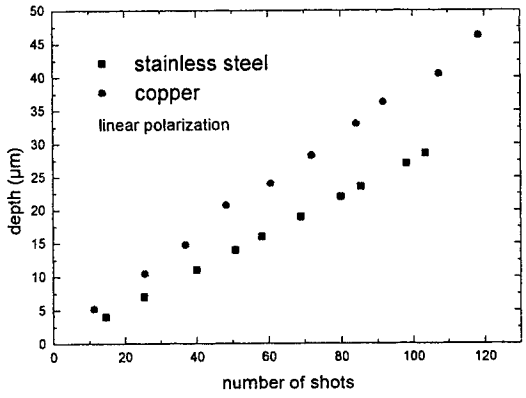
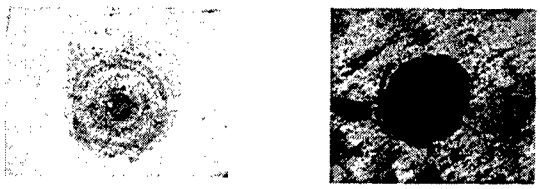


Fig.4 : Comparison between the ablated matter depth versus the number of shots in stainless and copper.

Femtosecond ablation in metals under the plasma threshold can be described using the two temperature model. In this model, we consider that the free electrons are in thermal equilibrium at a temperature T_e greater than the temperature of the lattice T_l. The evolution of T_e and T_l are then described by two coupled heat diffusion equations. The key parameter is the electron/phonon coupling constant , namely g, which determines the electron-phonon energy transfer time τ_r, and then the limit between thermal and non-thermal processes. This coupling value has been widely studied, especially in noble metals such as gold and copper. Typically, for copper, $g=10^{16}$ W/m^3/K [1], and the electron-phonon relaxation time is found to be 4 ps. In transition metals, this constant is an order of magnitude higher. The difference in efficiency displayed in figure 4, for copper and stainless steel can be then explained as follows: g is higher in stainless steel than in copper and thus τ_r is lower than 4 ps. Consequently, the electrons have less time to diffuse into the stainless steel than in copper. Thus the amount of the ablated matter is more important in copper.

If the time width of the laser pulse is greater than τ_r, part of the energy is lost into the lattice. Hence, the material displays a thermal affected zone and the efficiency of the ablation is reduced. Whereas in the femtosecond regime the energy is temporally concentrated (lower than τ_r), then the thermally diffused energy is very reduced and the TAZ is minimum.

Figures 5 a) and b) show the difference between the ns and fs ablation. It has to be noticed that the fluence was 1 J/cm^2 in both cases and at the same wavelength. These conditions are obviously not the best for drilling with ns pulses, but it allows to evidence the difference between the two regimes according to the above model. However a more precise theoretical study of both modes is under development to critically and quantitatively compare ns and fs ablation regimes. Particularly heat affected structural zones around micro-holes can be analyzed by transmission electron microscope (TEM) [2]. This technique will allow us to analyze precisely microstructures and to measure thermal diffusion lengths.

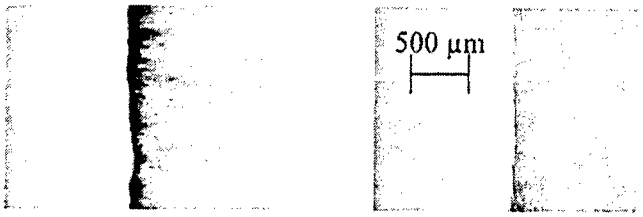


a) nanosecond b) femtosecond

Fig 5 : 50 µm holes in copper.

As the efficiency is optimum in the femtosecond regime, the fluence best conditions for micromachining are achieved near the ablation threshold. Thus to increase the micromachining speed, we think that high repetition rate laser sources with moderate energy is a good choice. We are presently developing a 60 fs, 10 W average power, 15 kHz Ti:Sapphire laser system at 800 nm pumped by a copper HyBrID laser delivering 100 W at 15kHz with a good beam quality (M^2=4) [3].
Besides a commercially 150fs, 5 µJ, M^2<2, 100 KHz repetition rate laser system will be used for low depth machining. It should be a good tool for machining soft materials like silicon and for shallow etching, since it allows to ablate a small quantity of matter per pulse at very high repetition rate (micro-milling). Therefore nice comparisons are expected from the use of very different experimental conditions.

As a conclusion, we mention the case of wood micromachining for which femtosecond laser sources should play an important role. Obviously, ablation of organic materials cannot be described with the same physical model as metals. Intensity-dependent phenomena – namely multi-photon absorption- are the main mechanism to take into account. However, very limited thermal effects are still observed. Preliminary investigations have been performed by Naderi *et al* [4]. We have also observed that the wood surface is not damaged using femtosecond pulses. For instance, the sycamore wood which is very difficult to cut without burning with conventional lasers can be machined with femtosecond lasers without creating a layer of charcoal. Wood cutting with ns and fs pulses is compared in figures 6 a) and 6 b).



a)nanosecond b) Femtosecond

Fig 6 : Sycamore wood cutting

As it is shown in Figure 7, the wood structure is not altered by femtosecond cutting.

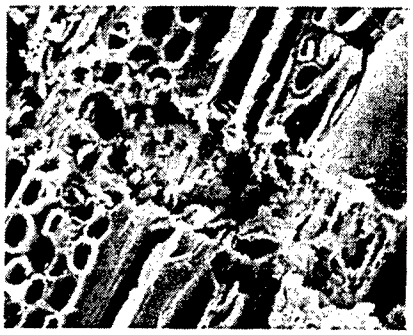


Fig. 7 : SEM image of sycamore femtosecond cutting

References

[1] P. B. Corkum, F. Brunel, N. K. Sherman and T. Srinivasan-Rao, Phys. Rev. Lett, 61,2886 (1988)

[2] A. Luft, U. Franz, A. Emsermann and J. Kaspar Appl. Phys. A, 63, 101(1996)

[3] P. Coutance, G. Naylor and J-P. Pique IEEE J. Quantum Electron., 31, 10 (1995)

[4] N. Naderi, S. Lagace and S. L. Chin Forest Prod. J., 49, 72 (1999)

Transient Light-Induced Refractive Index Change Made by Laser Microfabrication in Nitroaniline-Doped PMMA Film

Kazuhiko YAMASAKI[*], Saulius JUODKAZIS[**], Mitsuru WATANABE[*], Shigeki MATSUO[*], Kenji KAMADA[***], Koji OHTA[***], and Hiroaki MISAWA[*]

[*]Graduate School of Engineering, The University of Tokushima, 2-1 Minamijyosanjima, Tokushima 770-8506, Japan
E-mail: misawa@eco.tokushima-u.ac.jp (Corresponding author: Hiroaki Misawa)
[**]SVBL, The University of Tokushima, 2-1 Minamijyosanjima, Tokushima 770-8506, Japan
[***]Osaka National Research Institute, 1-8-31 Midorigaoka, Ikeda, Osaka 563-8577, Japan

Keywords: PMMA, nonlinear properties, optical memory, laser microfabrication, light-induced damage threshold

We report the observation of high light-induced change in refractive index (recognizable by observation in conventional microscope) in PMMA film doped with an optically non-linear dye 2-nitroaniline $(NO_2(C_6H_4)NH_2$ abbreviated as 2NA). The optically altered micrometer-sized regions were fabricated by single-shot irradiation of 120 fs laser pulses into doped PMMA film using high numerical aperture 1.3 and high magnification ×100 objective lens. The doping of films can be achieved in a wide range of 2NA concentrations (up to 40 wt%) without precipitation. This allows to control a storage time of an optically altered region up to one month by the adjusting the energy of the femtosecond (fs) recording pulse at 800 nm. Typical recording energy was 10-80 nJ/pulse at the point of irradiation. Total recovery of transmission of the PMMA|2NA film was confirmed by optical transmission measurements in microscope. The light induced damage threshold (LIDT) (for permanent damage) was increased more than by 4 times (up to 40 nJ/pulse) when 2NA doping were ca.13 wt%. While the LIDT for transient damage was decreased by 1.5-2 times. Total optical recovery was observed single exponential with decay time of ca. 0.5-1 min for moderate irradiation intensities (0.1×LIDT of permanent damage). The damage induced with at the higher intensities lasts up to month, but the recovery was not total (residual transmission changes were observable).

The phenomenon can be applied for the optical memory, photonic crystal, and micro-mechanical applications. The underlying mechanism of the phenomenon is discussed in terms of anelastic α- and β-relaxation (polymer backbone and side chain relaxation, respectively).

1. Introduction

Polymethylmethacrylate (PMMA) is gaining an interest in the field of optical applications due to its high optical transmission in visible, easy dye-doping, preparation and processing including the laser ablation and controllable photo-modification. A three-dimensional (3-D) optical memory[1] and an optical waveguide[2] have been demonstrated recently. On the part of optical 3-D memory various approaches have been proposed: a bacteriorhodopsin protein-based two-photon absorption (TPA) induced write/read memory,[3] femtosecond (fs) pulse induced micro-explosion recording,[4] photorefractive,[5] photochromic[6] and photopolymer[7] materials have been used as recording media.

Here we demonstrate a novel mechanism of 3-D recording, which is transient with controllable duration of recording (10^{-3}-10^{7} s) made by a single pulse fs-irradiation of PMMA film doped with 2-nitroaniline, $NO_2(C_6H_4)NH_2$. The dye was responsible for TPA of 795 nm illumination and lowered the light induced damage threshold (LIDT) of PMMA. The recovery of optical transmission was explained in terms of viscoelastic α- and β-relaxations of PMMA.

2. Experimental

2-nitroaniline (2NA) was introduced into chloroform solution of PMMA (15 wt.%) then casted over a microscope cover glass to form a film, which was used as recording media. The 2NA doping up to 40 wt.% was precipitation free. Samples were dried in a desiccator at a vacuum of ~10 mm Hg for 24 h. Eventual thickness of the film was ca. 150-300 μm. It was crack free and stable on the yearly scale even after the optical recording. 3-D recording was made by laser

First International Symposium on Laser Precision Microfabrication, Isamu Miyamoto, Koji Sugioka, Thomas W. Sigmon, Editors, Proceedings of SPIE Vol. 4088 (2000) © 2000 SPIE · 0277-786X/00/$15.00

irradiation through an oil-immersion objective (×100 magnification and numerical aperture, NA = 1.3) through the cover glass in order to avoid any oil contact with PMMA film. An irradiation spot (lateral size) can be evaluated as diffraction-limited spot size (diameter of Airy disk) $d = 1.22\lambda/NA$ = 746 nm and the corresponding axial size was $z = 2n\lambda/NA^2$ = 701 nm, where λ = 795 nm is the wavelength of fabrication laser pulse, n is the refractive index at focal point ($n_{PMMA} \approx 1.49$ at 600-800 nm). The sample was translated in the focal plane during irradiation. Every single bit seen as an optically-altered transmission region was recorded in a single shot of 120 fs duration.

3. Results

Permanent optical damage (bit) can be recorded in PMMA film as we reported earlier,[1] when the pulse energy density is higher than LIDT of material. For undoped PMMA, we found it ca. 2.3 J/cm^2 (10 nJ) for 795 nm, 120 fs pulses. This determination was made from an optical transmission, when the bit is recognizable by observation in 100-times magnification, NA = 1.35 objective. The recovery of the transmission of irradiated spot was observed (Fig. 1), when the pulse energy was smaller that 1×LIDT and PMMA film was doped with 2NA. The sequence of snap shots in Fig. 1 allow to trace the recovery of transmission of selected bits *A*, *B* and *C* on a time scale on tens-of-seconds as depicted in Fig. 2. The transmission at the center of the bits showed single-exponential recovery with time constant τ_R = 10-30 s (Fig. 2(a)). More complicated recovery can be observed when the average transmission on a square of 1×1 μm^2 was plotted over time (Fig. 2(b)). It can be seen from Fig. 1 that the bit was enlarging while its transmission was decaying. The increase in average transmission up to 10-15 % was observed at irradiated spot immediately after fabrication in PMMA|2NA-32 wt.% film, when the pulse energy was 12

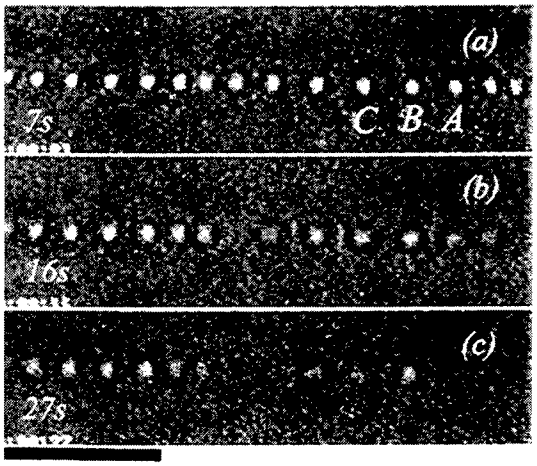


Fig. 1. Time series (a-c) of optical transmission recovery after irradiation of 15 nJ (3.4 J/cm^2) pulses (120fs at 795nm). The film was PMMA|2NA-32wt.% (307μm-thick). Scale bar 7μm.

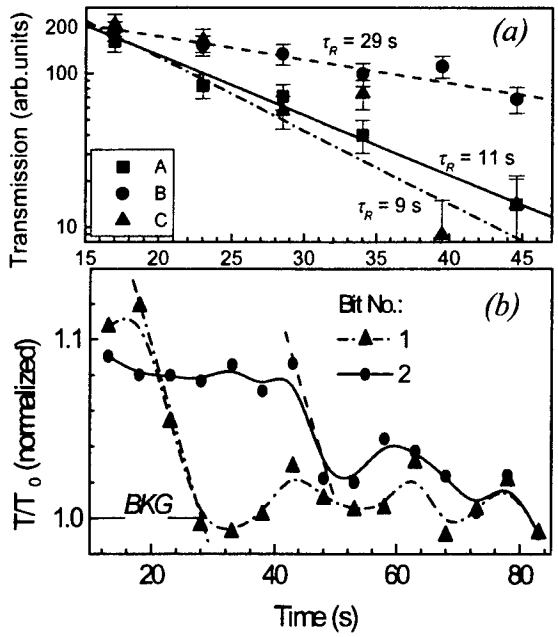


Fig. 2. Time decay of maximum (background subtracted (a)) and average (b) bit transmission. (a) the bits *A*, *B*, and *C* corresponds to those in Fig. 1. (b) averaging was made on 40-by-40 pixels. *BKG* marks the background transmission.

nJ (in terms of energy density 2.7 J/cm^2, the upper limit of intensity can be evaluated using 120 fs pulse duration, 2.3×10^{13} W/cm^2, since the effect of pulse spreading mainly in the objective lens is unknown).

The optical absorption spectrum was found without apparent modifications after the recovery (Fig. 3). The strong absorption band at ca. 400 nm is due to 2NA absorption. The recovery became faster with increasing concentration of 2NA in the PMMA film (Fig. 4). The threshold pulse energy was found slightly decreasing with the increasing density of 2NA. The recovery time at the LIDT was ca. 1s, what allowed to repeat writing/re-writing cycles at 1 Hz pulse repetition rate and no films alteration was observed after all 3 h procedure. This implied that the explanation of the results lies in the light-induced charge and dielectric relaxation.

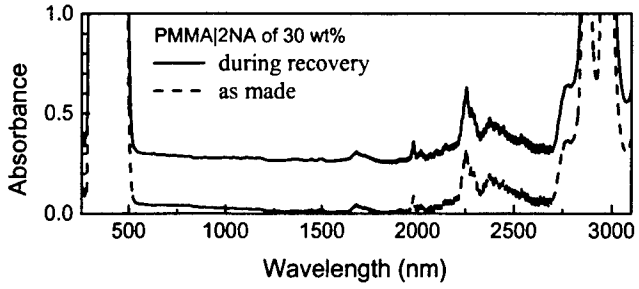


Fig. 3. Absorbtion spectra of fresh PMMA|2NA-30wt.% film (dashed line) and during the recovery (τ_R = 1-3 h) of optical damage (shifted upwards by 0.25). Thickness of film was 157μm.

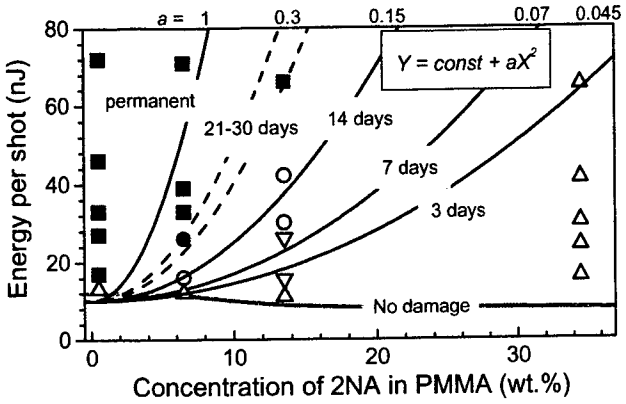


Fig. 4. Summary of the recovery time vs. 2NA concentration and the recording pulse energy. Simulated $Y = Const+aX^2$ dependencies depict observed recovery time. Grey markers and dashed line depicts partial recovery of transmission; solid markers – permanent optical damage.

4. Discussion

Optical alteration of materials is usually considered in terms of refractive index changes, directly related to the local mass-density modifications or in terms of an absorption of optically induced defects, which are, in turn, causing the changes of refractive index via Kramers-Kronig relation.[8] Astonishing high refractive index changes ($> 5\times10^{-2}$) were reported made by microexplosion in silica and sapphire.[9] Indeed, if one is measuring the diffraction efficiency of a grating written by microexplosions and if the absorption is considered negligible the effect of diffraction on thin sinusoidal grating gives overestimated values of refractive index changes. The transmission contrast such as in Fig. 2(a) gives the value of ca. 0.02 for the grating written in silica (similar value would be found in PMMA). We should properly address the refraction, absorption and scattering to get insight into transmission image formation in order to understand the images such as in Fig. 1 (identical images can be observed in silica, sapphire, TiO_2-rutile).

Obviously, when the optically altered volume is of the size comparable with the wavelength of the image forming light (550 nm mid-wavelength of condensor illumination in a microscope) the light scattering is one of the most important factors. To look at a near-field distribution of the light passing through a small sphere of decreased and increased refractive index as compared with the index of sphere's ambience, we carried out numerical simulations according the code developed by Barber and Hill.[10] The program allows to calculate the light intensity inside and outside sphere, when incident plane wave has intensity 1. The central part of the bit was considered of decreased refractive index and the diameter is given by fabrication spot radius of 373 nm. This can be described as a light scattering sphere, which relative refractive index is defined by $m = n/n_0 < 1$, where n is the refractive index of the void-like sphere and n_0 is that of sphere's surrounding. Another

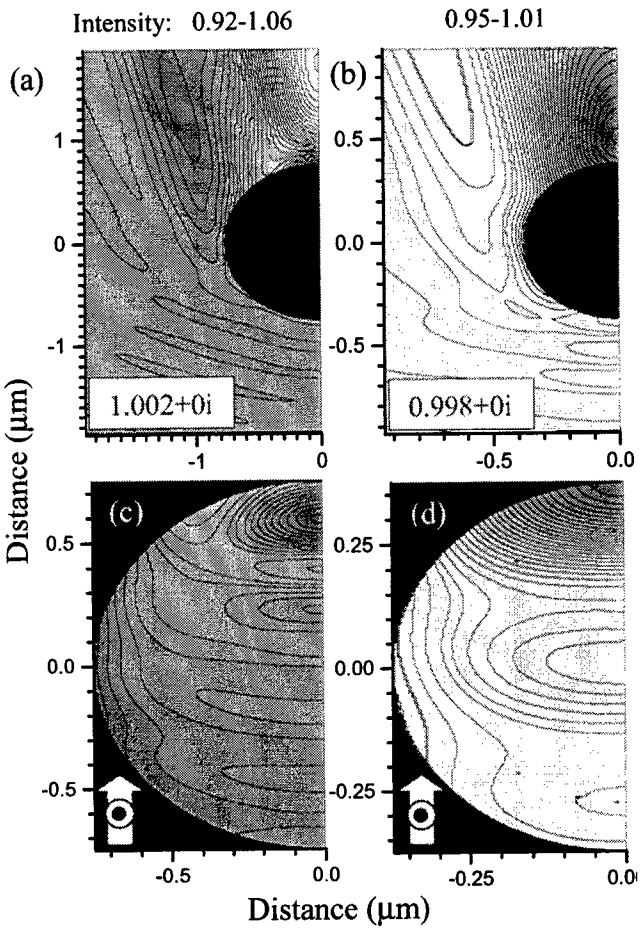


Fig. 5. Near-field intensity distribution of scattering made by spheres of given refractive index and size. Equivalent presentations of densified shell of a bit (a) and void-like center (b). (c,d) internal light fields inside spheres. The intensity of incident plane wave is 1 (polarization and direction of incidence are given by arrow in (c,d)).

sphere considered for calculations was of increased index, $m > 1$, and the diameter was twice larger than that of the void-like sphere's. This simulates the real structure of the bit, which is void-like inside and surrounded by densified shell. In the following part we will show how the employed values of m are justified ($m = 0.998$ for the void-like sphere and $m = 1.002$ for the higher density shell). The results of simulations in Fig. 5 shows, that the center of the sphere with $m > 1$ appears bright centered in transmission (Fig. 5(a)), while the void-like sphere should give an opposite contrast. Also, the larger sphere of $m > 1$ caused larger intensity contrast as compared with that of sphere with $m < 1$. This qualitatively explains the observed transmission of 3-D memory written in PMMA, although the real bit structure was treated simplified as two separate spheres.

To answer the question, what is the refractive index of densified and dilated regions of bit, let us compare our observed recovery time of transmission of 1-100 s with creep compliance data in the experiments of dielectric

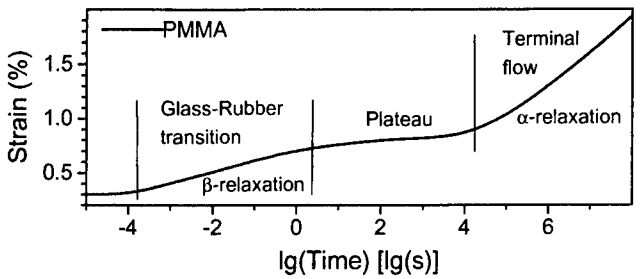


Fig. 6. Strain relaxation in PMMA (reconstructed from ref. 11). 10^6 is ca. 10 days, 10^7 – 100 days.

relaxation. In Fig. 6 the master creep curve is plotted (based on ref. 11). As it can be seen the recovery of 1-100 s (plateau region in Fig. 6) corresponds to the 0.7-0.8% strain. Such a strain is already larger than typical limit of elasticity of ca. 0.2% even in ductile polymers. The strain, as a measure of $\Delta V/V$, there V is the volume, is directly related to the refractive index. Yoldas,[12] derived the relation between porosity and refractive index, which we can adopt for the densified/dilated material:

$$\frac{\Delta V}{V} = Strain \cong 1 - \frac{n_{porous}^2 - 1}{n_{dense}^2 - 1}. \qquad (1)$$

The relation does not depend on the elastic response of material and can be applied to microexplosion altered material. By taking *Strain* = 0.8% (plateau in Fig. 6) we find corresponding refraction index changes of 3.3×10^{-3}. When unperturbed index of film was taken as that of PMMA, namely 1.490. The relative refraction index values of m = 1.002 and 0.998, for the densified and dilated regions can be found. These are the values employed in the modelization of light scattering (Fig. 5). If the absorption needs to be taken into account, the numerical simulations are done with complex refractive index m (the calculations in Fig. 5 were obtained without consideration of absorption). Typical result of absorption on the transmission intensity is the lowered contrast. The direct evaluation of transmission without consideration of scattering is straight forward $I = I_0(1\text{-}R)e^{-ad}$, where R is reflectance, which for the right angle incidence is given by: $R = \frac{(n-1)^2 + k^2}{(n+1)^2 + k^2}$, where $k = \alpha\lambda/4\pi$. (2)

Here, the absorption coefficient can be considered proportional to the strain, since more material is encountered in the light pass in denser region and *vice versa* for dilated one. When pure relaxation mechanism of transmission recovery is considered, the absorption coefficient is α = 0 cm^{-1}. Even then a realistic transmission image can be reconstructed by taking into account light scattering (Fig. 5).

Glass-rubber transition is mainly due to β-relaxation (also known as Johari-Goldstein), i.e. a side chain kinematic movement. At high power of irradiation the temperature can be higher than glass transition of PMMA at T_g = 105°C at irradiation spot (then α-relaxation is involved during cooling and strain release). Are the amorphous polymers responding as a glass or as a rubber is the matter of time and temperature.[13] The temperature control over the processes considered can be expected to follow general dependence of glass-rubber transition, i.e. the time and temperature are acting equivalently on the strain relaxation in polymers. Fig. 2(b) can be explained by glass-rubber transition as well. The plateau region in the transition (Fig. 6) is where entanglement of polymer coils is relaxing. This process does not change the average refractive index as strongly as it does at the faster β-relaxation.

5. Conclusions

We have demonstrated for the first time the 3-D transient optical memory in PMMA|2NA dye doped films. The recovery time is widely varied by the doping concentration and fs-laser pulse energy. The mechanism of optical recovery, most probably, is caused by an anelastic dielectric relaxation, mainly β-relaxation. The phenomenon can find applications in the micro-systems as fluid pumps (driven by strain), optically controlled capacitance (driven by dielectric constant), and temperature sensors (temperature control over transmission). The phenomenon can be expected to be found in other polymers as well.

References

1. K. Yamasaki, S. Juodkazis, M. Watanabe, H. Sun, S. Matsuo, and H. Misawa, *Appl. Phys. Lett.* **76**, (2000) 1000.
2. C. Wochnowski, S. Metev, G. Sepold, *Appl. Surf. Sci.* **154-155**, (2000) 706.
3. Z. Chen, D. Govender, R. Gross, R. Brige, *Biosensors & Bioelectronics* **11**, xv (1996); *BioSystems* **35**, (1995) 145.
4. M. Watanabe, S. Juodkazis, H. Sun, S. Matsuo, H. Misawa, M. Miwa, R. Kaneko, *Appl. Phys. Lett.* **74**, (1999) 3957.
5. Y. Kawata, H. Ishitobi, S. Kawata, *Opt. Lett.* **23**, (1998) 756.
6. D. A. Parthenopoulos, P. M. Rentzepis, *Science* **245**, (1989) 843.
7. J. H. Strickler, W. W. Webb, *Opt. Lett.* **16**, (1991) 1780.
8. P. R. Herman, R. S. Marjoribanks, A. Oettl, K. Chen, I. Konovalov, S. Ness, *Appl. Surf. Sci.* **154-155**, (2000) 577.
9. E. N. Glezer and E. Mazur, *Appl. Phys. Lett.* **71**, (1997) 882.
10. P. W. Barber and S. C. Hill, *Light scattering by particles: computational methods* (World Scientific, Singapore, 1990).
11. N. G. McCrum, B. E. Read, and G. Williams, *Anelastic and dielectric effects in polymeric solids* (Dover Publications, Inc., New York, 1991) ch.8.
12. B. E. Yoldas, *Appl. Optics* **19**, (1980) 1425.
13. G. Strobl, *The physics of polymers* (Springer, Berlin, 1997).

Laser-induced microstructuring of photonic materials: Semiconductors

Jan J. DUBOWSKI

Institute for Microstructural Sciences, National Research Council of Canada Ottawa, Ontario K1A 0R6, Canada
E-mail: jan.j.dubowski@nrc.ca

The laser has become an increasingly important tool, which helps to overcome the limitations of conventional microfabrication technologies, delivering devices capable of performing new and increased numbers of operations within an ever shrinking physical volume. In addition to "classical" applications of lasers such as via hole drilling, trimming or pulsed laser deposition of thin films, there have been new developments in laser-based technologies for the fabrication of advanced micro- and nano-devices. Of particular interest for optoelectronic and photonic applications is the potential for commercial processing of semiconductors and the fabrication of integrated and monolithically integrated photonic devices and circuits.

Keywords: Laser microstructuring, pulsed laser deposition, dry etching, annealing, intermixing, quantum well and dot microstructures, photonic integrated circuits

1. INTRODUCTION

The constantly growing demand for reduced size devices capable of performing new and/or increased number of operations has created strong research in the area of new materials and new materials processing technologies. Historically, the microelectronic industry was the main driving force behind this demand. Recent developments in fiber optics, wireless communications, and multimedia applications have been possible due to the emergence of new technologies for manufacturing advanced optoelectronic and photonic devices. These developments have often taken advantage of the unique features that lasers offer in device manufacturing – a consequence of the tremendous progress in both laser technology and our understanding of the fundamental processes involved in laser-matter interaction.

Numerous high- and medium-power lasers have made a significant contribution to the development of advanced manufacturing technologies. Today, some of the most developed applications that involve lasers as a tool in the manufacturing process of microelectronic and optoelectronic devices are:

- Precision ablation/micropatterning (via hole drilling for printed circuit boards, resistor/capacitor trimming, wire stripping, ink jet nozzle fabrication)
- Marking, scribing (semiconductor and non-semiconductor wafers, solar panels)
- Sub–μm photolithography (248 nm, 193 nm, 157 nm)
- Annealing
  - excimer (a-Si for flat panel displays)
  - non-excimer (quantum well/dot intermixing for integrated photonics)
- Thin film deposition
  - Pulsed laser deposition (high-Tc superconductors)
  - Laser-CVD, laser-CBE (selective area growth)
- Selective doping of semiconductors (GILD)
- Surface processing (planarization, computer hard disk texturing)
- Microwelding (ceramics, glass)
- 3D microstructures (prototyping, Laser-LIGA, MEMS)
- Surface cleaning (sub–μm debris removal)
- Etching (low-damage structuring)

Many of these applications have been discussed at conferences on Laser Applications in Microelectronic and Optoelectronic Manufacturing [1-6], dedicated meetings on Laser Ablation [7-11] and in some books, e.g., [12,13]. Lasers, in addition to offering novel solutions, often become tools of choice because their application leads to cost-effective solutions. As an illustration, the cost of mechanically drilling 200 μm diameter holes during the manufacture of printed circuit boards is about $2 per 1000 holes and it increases dramatically, to almost $18 for a 100 μm diameter hole. This compares with 40 to 80 ¢ per 1000 holes for 100 and 200 μm diameter holes, respectively, when laser drilling is used [14].

This paper reviews the recent advances in the use of lasers for manufacturing and for the investigation of photonic materials and devices. Given the extent of this

First International Symposium on Laser Precision Microfabrication, Isamu Miyamoto, Koji Sugioka, Thomas W. Sigmon, Editors, Proceedings of SPIE Vol. 4088 (2000) © 2000 SPIE · 0277-786X/00/$15.00

rapidly growing activity, it is difficult to present a thorough review. Instead, examples of the most significant achievements will be discussed, with the emphasis on semiconducting materials.

2. LASERS AS TOOLS IN THE INVESTIGATION OF ADVANCED MATERIALS AND MICROSTRUCTURES

Advances in UV laser beam technology, mostly in the development of excimer lasers that took place between 1970 and 1980, and the development of high-harmonic high-power IR lasers (e.g., Nd:YAG at 355 and 266 nm) observed from the beginning of 1990s, have resulted in a rapid increase in the use of various lasers for manufacturing. Fabrication of thin films and precision structuring of materials are the most spectacular applications that have been influenced by these developments. The advantages of using lasers for these applications include:

a) flexibility, i.e., the ease with which a laser-based process can be switched from one material to another
b) clean vaporization (only the target material is heated)
c) direct deposition of complex materials (three and more elements in the target)
d) possibility of forming exotic heterostructures, such as ferroelectric and high-temperature superconductors
e) patterning of materials by direct ablation
f) possibility of low-damage 3D shaping of materials using a reactive (dry) etching approach

In addition to the use of short-wavelength lasers, short-pulse laser processing is a rapidly growing activity due to its potential in precision micromachining. The significant progress observed in this area over the recent 5-6 years has been achieved due to key developments in fs-pulse laser technology [15]. However, fs-pulse laser technology is at the moment relatively expensive and it has to be shown where it could compete with other laser-based technologies for large-scale production of advanced materials and devices, or where the unique features of this technology would justify the high costs of its implementation.

Non-contact processing of materials that can be carried out with any laser-based technology is an attractive feature from the process control viewpoint since it is possible to apply *in-situ* monitoring with a variety of tools.

2.1 Pulsed laser deposition of thin films

Pulsed laser deposition (PLD) is one of the most successful laser technologies that have contributed significantly to the development of new materials and devices. It is a leading technology in fabricating thin oxide films and, especially, high-temperature superconductors. PLD offers extremely high deposition rates, as well as the ability to control deposition rates at a monolayer level per pulse, e.g., [16]. A unique feature of PLD is that it allows deposition of multi-element materials from a single target source, leading very often to the preservation of a target stoichiometry in the thin films that are produced from such target. Thus, in addition to manufacturing capabilities, PLD is an important tool in the investigation of thin film growth mechanisms and the formation of material systems that are not attainable with conventional methods of film deposition. Numerous proceedings from symposia, conferences and books that were published between 1990 and 1999 give a wide-ranging overview of the progress and status in this field [7-12].

An example of a PLD system that utilizes two lasers for independent ablation of different targets is shown in Fig. 1 [16]. The laser beams can be delivered simultaneously to two targets and, if needed, switched between different targets. Pulse energy (fluence), repetition rate and number of pulses delivered per site are computer controlled, which makes it possible to precisely control the amount and rate of growth of the material. In addition to a standard reflection high-energy electron diffraction (RHEED) technique applied during epitaxial growth of semiconducting materials [17], the process of deposition is monitored *in-situ* with a fast-nulling ellipsometer [18]. The system has been used mostly for the fabrication of multiple quantum well (MQW) microstructures of CdTe/CdMnTe [19]. Independent operation of two lasers makes it possible to engineer "superstructures" of CdTe/CdMnTe. An example of such result is shown in Fig. 2. The structure was grown by

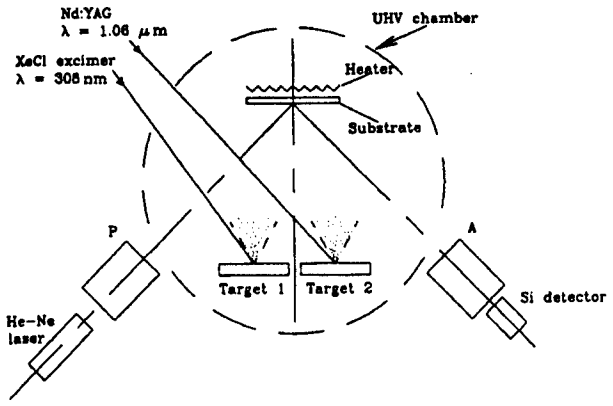


FIG. 1. Schematic diagram of a dual-laser pulsed laser deposition (PLD) system with a fast-nulling ellipsometer implemented for in-situ monitoring of the growth process [16].

ablating CdTe and $Cd_{1-x}Mn_xTe$ ($x = 0.56$) targets with a Nd:YAG laser triggered at 500 Hz and an excimer XeCl laser, which ablated the $Cd_{1-x}Mn_xTe$ target, triggered at a changeable frequency from the range of $0 \leq \omega \leq 60$ Hz. A series of $Cd_{1-x}Mn_xTe$ (50 Å) - CdTe (50 Å) layers was

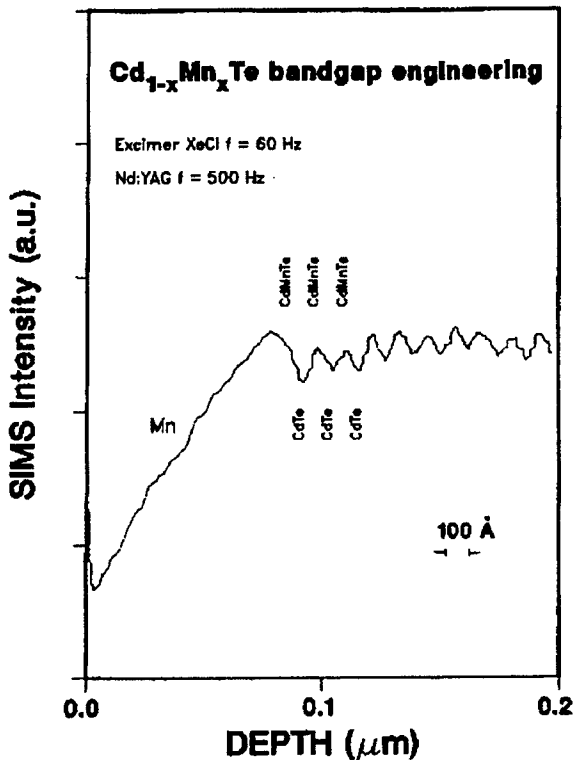


FIG. 2. Secondary ion mass spectroscopy (SIMS) Mn profile in a PLD engineered CdTe/CdMnTe "superstructure" comprising nine CdTe quantum wells and a material with a linearly changing band-gap near the surface [20].

grown first and then a 700 Å thick $Cd_{1-x}Mn_xTe$ material with a gradient of chemical composition from $x \approx 0.30$ to $x = 0$ was formed on top of the structure. This was achieved by maintaining a constant deposition rate of CdTe while vaporization of the $Cd_{1-x}Mn_xTe$ target was gradually phased out as the triggering of the XeCl laser was reduced from 60 to 0 Hz [20]. The dual-laser PLD technique has the potential for controlled doping of semiconductor thin films [21,22]. It has been successfully applied to provide Cd flux, by ablating a metal Cd target, during the epitaxial growth of $Cd_{1-x}Mn_xTe$ films from a $Cd_{0.44}Mn_{0.56}Te$ target [23]. This made it possible to obtain films with $0.44 \leq x \leq 0.70$ by adjusting the ablation conditions of the Cd target. Examples of the use of this technique for non-semiconductor materials include ablation of a Y_2O_3 target with KrF and CO_2 lasers for reduced particulate formation [24] and ablation of Ag and YBCO targets for doping $YBa_2Cu_3O_{7-\delta}$ thin films [25].

In addition to the "laser-only" approach represented in Fig. 1, a combination of PLD with molecular beam epitaxy (MBE) has been explored for gas-phase deposition and fabrication of superlattices, e.g., sawtooth superlattices of $Hg_{1-x}Cd_xTe$ [26], and for N doping of ZnTe [27].

2.2 Laser dry etching

Excimer lasers have recently become tools of choice for sub-μm semiconductor photolithography [28]. One of the attractive features of these lasers is that their high-energy pulses can be used for photoresist-free patterning of materials. This can be realized through direct material ablation or through dry etching upon introducing a reactive gas atmosphere. The idea of a laser-based dry etching (LDE) approach is illustrated schematically in Fig. 3. A comparison with conventional photolithography indicates that LDE leads to the elimination of several processing steps. Required patterns can be achieved by projecting masks made of metallic thin films (e.g., Cr on glass) or stacks of dielectric films. Advanced applications, for instance where utilization of the beam is an important issue, can be realized with phase-shift masks or diffractive element masks. In addition, etching with a tightly focussed beam can be applied for the fabrication of almost arbitrary shape 3D structures (laser carving). The ability to target various sites of the same wafer processed with a laser beam of tunable characteristics also makes possible the fast fabrication (prototyping) of novel microstructures.

Due to the compatibility with a vacuum environment, LDE of semiconductors offers a useful way of integrating patterning with growth for optoelectronic device development. Thus, the process has the potential of providing cost-effective solutions in the manufacture of μm-size microelectronic and optoelectronic devices. An example of a microstructure fabricated in InP using a diffraction-LDE approach [29] is shown in Fig. 4. The result illustrates the strong anisotropy of the process: the shape of the etched features is a reasonable replica of the distribution of the laser beam intensity on the processed surface. Features as small as 0.5 μm can easily be

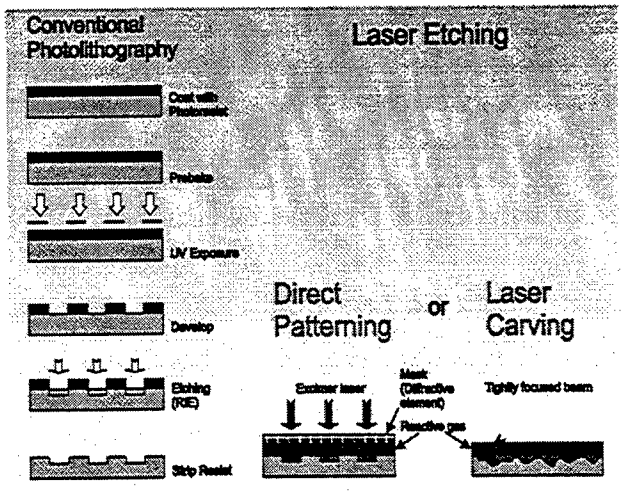


FIG. 3. Patterning by laser dry etching eliminates the several processing steps that are required in conventional photolithography.

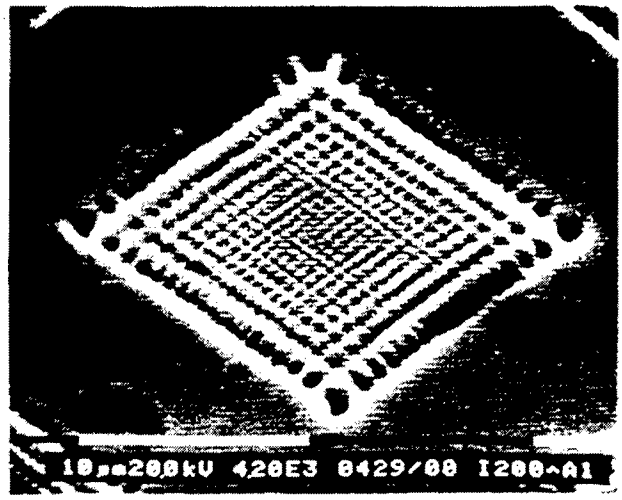


FIG. 4. Patterning of InP with a diffraction-LDE approach. The pattern was formed using 1000 pulses of a XeCl excimer at 71 mJ/cm^2. Processing was carried out in Cl_2/He [29].

distinguished in this figure. In a similar experiment, we were able to fabricate 0.02-μm size features with the LDE technique [30].

An important feature of LDE is that laser pulse energy (fluence) required for structuring in a reactive atmosphere of gases such as Cl_2 or HBr is much smaller than that normally required during direct laser ablation. Consequently, LDE can lead to reduced-damage or damage-free patterning of materials. This issue was addressed specifically in reactive ion etching (RIE) and LDE experiments of InP/GaInAs microstructures [31].

Although substantial effort concerning photo-excited processes and LDE of semiconductors has been documented in the literature [32-44] it remains to be seen whether this method would find its niche in commercial applications. Examples of successful implementation of the LDE technology for device applications include fabrication of InAlAs/InGaAs high-electron-mobility transistors [45], integrated InP microlenses [46] and GaAs/AlGaAs multiple quantum well circular ring lasers [47].

3. MONOLITHICALLY INTEGRATED PHOTONIC DEVICES

Semiconductor lasers are key devices in photonic applications for communications such as in wavelength division multiplexing (WDM) networks. The integration of several semiconductor lasers and, especially, of a single laser with other devices, such as waveguides, modulators, couplers and optical switches require manufacturing technologies capable of addressing a variety of materials. The current approach in manufacturing of such devices relies on the fabrication of hybrids consisting of different materials. This is a practical approach, but it is costly due extensive production requirements. The ability to fabricate multifunctional photonic devices with the same core material, i.e., monolithically integrated photonic devices (MIPD), is an attractive feature with the possibility of overcoming problems related to the hybrid device technology. Non-contact processing and compatibility of high-power IR and UV lasers with materials of extremely different mechanical and optical properties have potential applications for both hybrid and MIPD structures fabrication. This application has also the potential of overcoming the limitations of conventional methods currently applied for manufacturing advanced devices.

A MIPD structure requires different band-gap material within the same wafer. Generally, this can be achieved by growth and/or post-growth processing techniques. The most common growth-related methods are:

a) Growth/Etch/Re-growth
b) Growth on patterned substrates
c) Laser-assisted growth

The basis of each of these methods is selective area epitaxy. The first method has been demonstrated, e.g., for the fabrication of laser/waveguide butt-joints [48,49]. Selective growth on patterned substrates has been investigated, e.g., for GaAs/InGaAs [50] and InP/InGaAs [51,52] microstructures. A 1.55-μm wavelength-selectable microarray of 8 lasers monolithically integrated with a multi-mode interference optical combiner is an example of an advanced photonic device obtained with selective area epitaxy [52]. The use of a laser for selective area epitaxy is based on the ability to change temperature of a wafer at defined areas and/or influence chemical reactions taking place on the growing surface. Depending on the growth process this may change the properties of the grown material from doping to chemical composition levels. Laser-assisted epitaxy has been investigated for materials such as GaAs/AlGaAs [53] and Si [54]. The approach has been demonstrated in successful fabrication of multiwavelength laser arrays based on InP/InGaAsP microstructures [55].

Post-growth processing for manufacturing material with areas of different band-gap takes advantage of the fact that a common active photonic microstructure, such as a semiconductor laser, consists of quantum wells (QW) and barriers that can be intermixed. It has been observed that controlled intermixing between the GaAlAs barrier and GaAs quantum well materials (quantum well intermixing - QWI) can be achieved at relatively low (800-900 °C) temperatures [56]. Direct thermal annealing however does not have the lateral resolution that is required to realize a MIPD concept. Approaches that have been examined to address the lateral resolution issue include [57]:

a) impurity-induced intermixing

b) impurity-free vacancy diffusion
c) ion –implantation-induced intermixing

Since thermal annealing is basic to any QWI technique, the choice of a laser as a heating source is highly attractive due to the ease with which a laser beam can be delivered to a well-defined spot. Thus, selective areas of band-gap shifted material can be achieved within same wafer in a single pressing step. Lasers, such as the KrF excimer (λ = 248 nm), Ar-ion (λ = 514.5 nm) and Nd:YAG (λ = 1064 nm) have been successfully applied for the purpose of demonstrating QWI in microstructures consisting of GaAs/AlGaAs [58-60], InP/GaInAs [61,62] GaInP/AlGaInP [63] and Si/SiGe [64].

3.1 Laser-induced quantum well intermixing for manufacturing MIPDs

The principle of using an IR laser for selective area processing of QW microstructures is depicted in Fig. 5. In this particular case, $Si/Si_{0.70}Ge_{0.30}$ microstructures were processed with a CW Nd:YAG laser. Following a 6 min laser irradiation, a 142 meV blueshift of the band-gap structure was achieved. With the beam focussed to a spot of 0.8 mm diameter it was possible to confine the laser intermixed area to about 2 mm [64]. Processing of GaInAsP/InP QW microstructures with the same laser source led to a significantly better confinement. The results plotted in Fig. 6 illustrate the QW photoluminescence (PL) peak position for such microstructures irradiated for 1 and 4 min. This resulted in maximum blue shifts of 36 and 59

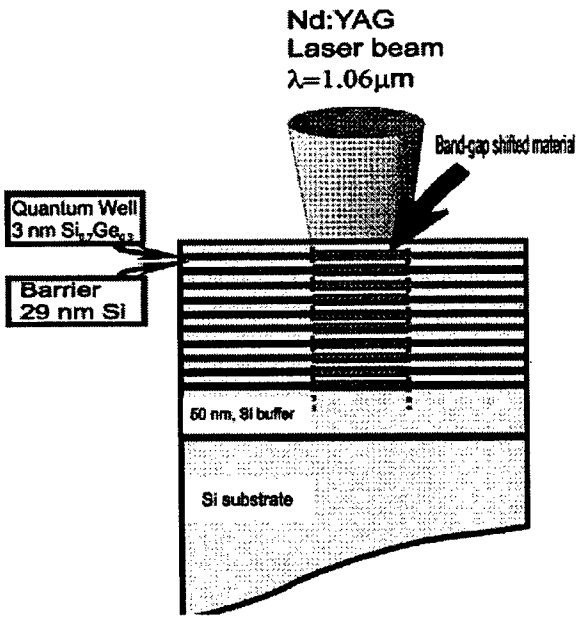


FIG. 5. Schematic illustration of the concept of Nd:YAG laser-induced selective area band-gap tuning in $Si/Si_{1-x}Ge_x$ microstructures [zz].

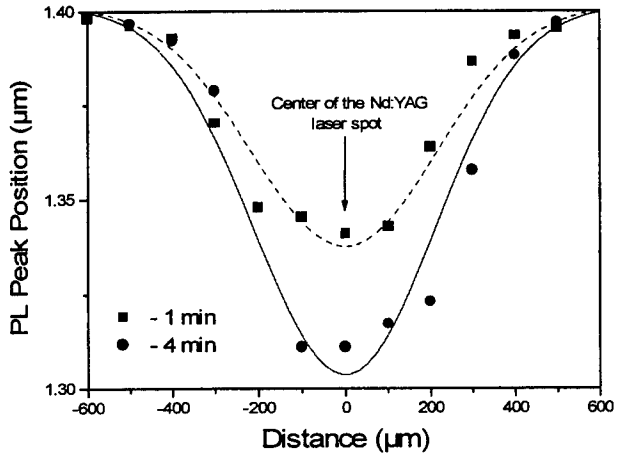


FIG. 6. Two-dimensional profile of the Nd:YAG laser fabricated GaInAsP/InP QWI material. The FWHM of the fabricated structure is about 400 μm, which is about half of the FWHM of a Nd:YAG laser beam used for annealing [62].

meV, respectively [62]. In both cases the spatial profile of the intermixed material can be fitted to a Gaussian curve with a full-width-at-half-maximum (FWHM) of about 0.4 mm. The main reason for the reduced lateral dimension of the QWI material appears due to the less efficient heat dissipation in GaInAsP/InP as compared to that in the $Si/Si_{1-x}Ge_x$ microstructures. However, other parameters such as mechanisms of diffusion and intermixing in these two different material systems have to be taken into account for more accurate interpretation of this result. It is reasonable to expect that dimension of the QWI material could be further reduced if a smaller diameter laser annealing spot and/or reduced annealing time were applied. For instance, the writing of < 100 μm wide lines of the QWI material, blueshifted by 60 meV, has been demonstrated with a beam that was scanned at 20 μm/s [62].

The laser-QWI technique offers the possibility of fabricating material with a continuously changing band-gap. This unique feature can find applications in the fabrication of broad-spectrum light-emitting diodes or dense arrays of multiwavelength lasers. An example of an array of multiwavelength lasers fabricated with the laser-QWI technique is shown in Fig. 7 [65]. This is a truly monolithically integrated photonic device. It consists of 12 broad-area lasers with 500-μm cavity length. Laser A, which emits at ~ 1498 nm, was fabricated from the material that corresponds to the as-grown microstructure. The other lasers, located on the same bar at distances of 1.9 (laser B), 2.4 (laser C) and 3 mm (laser D) from the laser A, emitted at about 1476, 1440 and 1405 nm, respectively. For several laser bars with cavities of 300, 400 and 500 μm, no measurable change in the laser

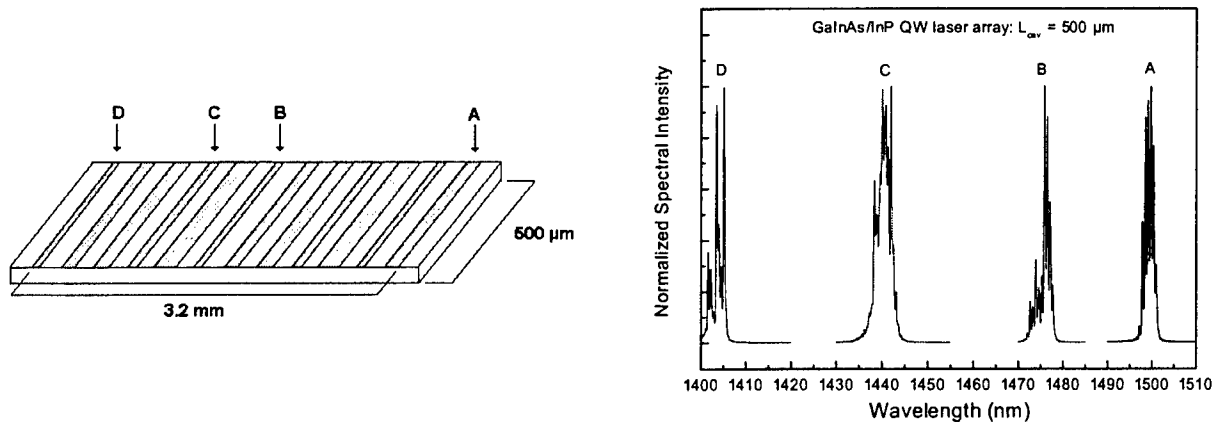


FIG. 7. A schematic drawing illustrating positions of broad area 500 µm cavity lasers on a 3.2 mm long bar (a), and corresponding emission spectra for the indicated lasers (b) [65] .

threshold current density was observed for devices made from the QWI material blueshifted up to 60 nm. Only a slight increase in the threshold current, up to 13 %, was observed for lasers operating at ~ 1400 nm. The increased functionality and/or reduced manufacturing costs of an integrated circuit are key issues addressed by the laser-QWI technology. Clearly, it remains to be shown what would be the maximum allowable blueshift, for a particular material system, without compromising the performance of integrated devices made from such material.

3.2 Laser-induced quantum dot intermixing

There has been a growing interest in the investigation of semiconductor quantum dot (QD) microstructures due to their potential in the fabrication of high gain, low threshold and weak temperature dependent lasers [66]. These features make the QD lasers more desirable than well-established QW lasers. Also, semiconductor QDs have potential as fundamental building blocks of future quantum computers and quantum information processing [67]. In spite of significant progress that has been achieved in recent years, the systematic fabrication of QD microstructures that have well-defined band-gap structure (excited state energy and states spacing like in an artificial atom) has remained an extremely difficult task. The extent of controlling the properties of InAs/GaAs QDs has been increased by introducing the indium-flush technique [68] and *in-situ* annealing [69]. However, post-growth tuning of the QD material properties, if carried out selectively, is a highly attractive technique that could find applications in the fabrication of artificial quantum microstructures and/or photonic band-gap crystals.

Laser-induced intermixing of InAs/GaAs quantum dot (laser-QDI) microstructures has been investigated for selective area tuning of their electronic shell structure. Using a 60 W CW Nd:YAG laser beam, samples were heated up to temperatures near 900 °C. This is a similar approach to that applied for post-growth processing of various QW microstructures. Changing the annealing temperature and irradiation time allows control of the extent of QD intermixing. The effect has a threshold behavior and no significant intermixing has been observed for 30-s irradiation time if temperatures were near 700 °C, or below. Conversely, annealing for 40 s at ~ 850 °C led to blue shifting of the QD ground state by 298 meV, i.e., to the spectral region where the PL signal originated from the InAs wetting layer [70]. Two PL spectra shown in Fig. 8 illustrate the dramatic changes taking place following laser-induced intermixing. The long-wavelength spectrum, which was measured 4 mm away from the laser-annealed spot, corresponds to the as-grown material. Well-resolved QD excited states (n = 1, 2 and 3) with the ground state located at λ_0 = 1078 nm can clearly be seen. The short-wavelength (blue-shifted) spectrum was measured at the center of the laser annealed spot. It can be seen that the position of the ground state observed at λ_0 = 885 nm has been shifted by 251 meV (from λ_0 = 1078). The observation of the QD excited states unambiguously demonstrates that the QDs retained their zero-dimensional density of states even after such intense intermixing conditions. Some indication of the lateral resolution of the laser-QDI process is provided in Fig. 8b which shows the ground state transition (n = 1) as a function of the position on this sample. It can be seen that the most blue-shifted ground state peaks at 880 nm, and its position remains almost unchanged over the distance of 1-1.5 mm, i.e., the distance that approximately corresponds to the size of the laser annealing spot. It can be expected that with smaller laser spot sizes the selectivity of the intermixing process

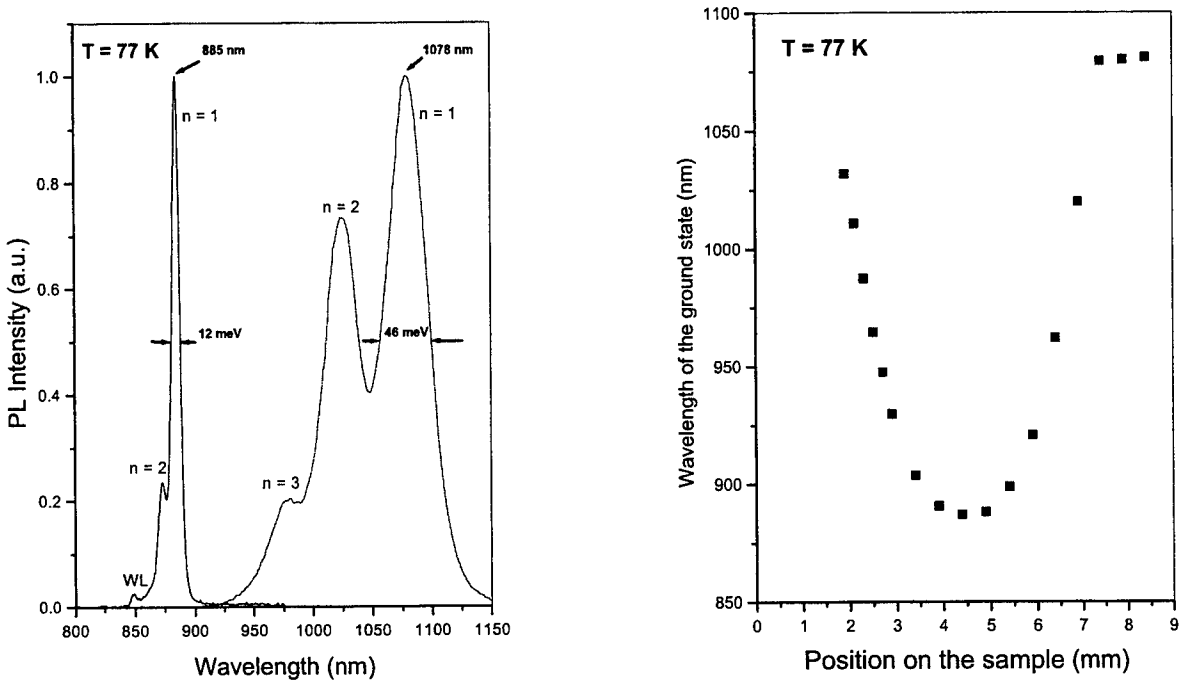


FIG. 8. PL spectra measured at two sites (4 mm apart) on same sample corresponding to the as-grown InAs/GaAs QD material (long-wavelength spectrum) and the laser-QDI material blueshifted by 251 meV (a). Wavelength of the QD ground state (n = 1) plotted as a function of the position on the same sample (b) [70].

could be confined to sub-μm-scale regions. This, in conjunction with the ability to adjust the QD density during the growth process, should make it possible to fabricate arrays of the QDI material, with an individual "pixel" comprising 1 to ~ 100 QD/μm^2.

4. CONCLUSIONS

Continuous advances and development of the laser technology has resulted in many applications, where the laser has been used as a manufacturing tool, offering solutions often unattainable with conventional methods of fabrication. Frequently this has also led to more cost-effective processes such as via hole drilling in manufacturing of printed circuit boards. Pulsed laser deposition has found its niche in investigation of thin films of new materials and novel microstructures. Of particular interest for photonic applications are semiconductors. These materials are pivotal for active (lasers, switches, modulators) elements. They also find applications in fabrication of passive (waveguides) elements of current photonics. Due to the specific requirements concerning the band-gap of semiconductor-made both active and passive devices the process of band-gap engineering that can be realized with the PDL technique, such as shown in Fig. 2, has the potential of providing novel devices and it deserves further attention. One of the most attractive features of laser-based manufacturing technologies is that the laser can process incompatible materials. A direct consequence of this is the possibility of providing less expensive technologies. Also, the laser can become an effective tool for some applications. For instance, it can lead to damage-free patterning (e.g., see Fig. 4) – a feature highly desirable for many applications especially those involving semiconductor materials.

The growing demand for hybrid solutions and monolithically integrated photonic devices has added new possibilities for laser applications. Examples of those possibilities involving post-growth processing (laser intermixing) of semiconductor quantum wells and quantum dots were discussed in this paper. It has been demonstrated that the band-gap structure of Si/Si$_{1-x}$Ge$_x$ and InGaAs/InGaAsP materials can be tuned in excess of 200 meV, i.e., over the range that is essential for fabricating arrays of multiwavelength detectors, lasers and broad-band diodes. The lateral selectivity of this process is sufficient to carry out laser "writing" of band-gap shifted material on μm-scale. Arrays of multiwavelength lasers operating between 1400 and 1500 nm have been fabricated with this technique (Fig. 7). To the best of our knowledge this is the first demonstration of the use of laser-processing technology for the fabrication of a monolithically

integrated photonic device. The idea has recently been examined for laser-induced quantum dot intermixing. Extensive blue shifts (~ 300 meV), reduced inter-sublevel spacing (from ~ 60 to 19 meV) and reduced linewidth of the QD ground state (from ~ 50 to 8 meV) which have not been observed previously confirmed the attractiveness of laser-induced intermixing for device fabrication [70]. In addition to the use of this technique for tuning the properties of as-grown material, potential applications exist in the manufacturing of advanced microstructures such as photonics band-gap crystals and zones of different photonic band-gap crystals monolithically integrated within the same semiconductor chip.

REFERENCES

1. *Laser-induced Thin Film Processing*, J.J. Dubowski, Editor, Proc. SPIE **2403** (1995).
2. *Lasers as Tools for Manufacturing of Durable Goods and Microelectronics*, J.J Dubowski, J. Mazumder, L.R. Migliore, C.S. Roychoudhuri, R.D. Schaeffer, Editors, Proc. SPIE **2703** (1996).
3. *Laser Applications in Microelectronic and Optoelectronic Manufacturing-II*, J.J. Dubowski, Editor, Proc SPIE **2991** (1997).
4. *Laser Applications in Microelectronic and Optoelectronic Manufacturing-III*, J.J. Dubowski, P.E. Dyer, Editors, Proc SPIE **3274** (1998).
5. *Laser Applications in Microelectronic and Optoelectronic Manufacturing-IV*, J.J. Dubowski, H. Helvajian, E.W. Kreutz, K. Sugioka, Editors, Proc SPIE **3618** (1999).
6. *Laser Applications in Microelectronic and Optoelectronic Manufacturing-V*, H. Helvajian, K. Sugioka, M.C. Gower, J.J. Dubowski, Editors, Proc SPIE **3933** (2000).
7. *Laser Ablation for Materials Synthesis*, Editors: D.C. Paine and J.C. Bravman, MRS Proc. Vol. **191** (1990).
8. *Laser Ablation in Materials Processing: Fundamentals and Applications*, Editors: B. Braren, J.J. Dubowski and D.P. Norton, MRS Proc. Vol. **285** (1993).
9. *Advanced Laser Processing of Materials: Fundamentals and Applications*, Editors: R. Singh, D. Norton, L. Laude, J. Narayan, J. Cheung, MRS Proc. Vol. **397** (1996).
10. *Laser Ablation*, Proc. 4th International Conf. on Laser Ablation, Editors: R.E. Russo, D.B. Geohegan, R.F. Haglund, Jr., K. Murakami, Appl. Surf. Sci. **127-129** (1998).
11. *Laser Ablation*, Proc. 5th International Conf. on Laser Ablation, Editors: J.S. Horwitz, H.-U. Krebs, K. Murakami, M. Stuke, Appl. Phys. A69 [Suppl.], **S45-S48** (1999).
12. *Pulsed Laser Deposition of Thin Films*, Editors: D.B. Chrisey, G.H. Hubler, John Wiley & Sons, Inc., New York, 1994.
13. *Laser-Assisted Microtechnology*, S.M. Metev, V.P. Veiko, Springer-Verlag, Berlin Heidelberg, 1994.
14. G. Forest, Laser Focus World, June 1997, p. 105; D. Moser, ESI Inc., private communication.
15. P. Bado, Indust. Laser Solut. Manuf. **15(3)**, 21 (2000).
16. J.J. Dubowski, Mat. Sci. Forum **173-174**, 73 (1995).
17. J.J. Dubowski, D.F. Williams, J.M. Wrobel, P.B. Sewell, J. Le Geyt, C. Halpin and D. Todd, Can. J. Phys. 67, 343 (1989).
18. H.X. Tran, J.D. Leslie, S. Buchanan and J.J. Dubowski, Proc. SPIE **2403**, 116, (1995).
19. J.J. Dubowski, A.P. Roth, E. Deleporte, G. Peter, Z.C. Feng and S. Perkowitz, J. Cryst. Growth **117**, 862 (1992).
20. J.J. Dubowski, Acta Physica Polonica **A80**, 221 (1991).
21. J.M. Wrobel, C.E. Moffit and J.J. Dubowski, MRS Proc. Vol. **285**, 459 (1993).
22. J.M. Wrobel, J.J. Dubowski and P. Becla, Proc. SPIE **2403**, 251 (1995).
23. J.J. Dubowski, J. Cryst. Growth **101**, 105 (1990).
24. S. Witanachchi, K. Ahmed, P. Sakthivel and P. Mukherjee, Appl. Phys. Lett. **66**, 1469 (1995).
25. C.K. Ong, S.Y. Xu and W.Z. Zhou, Rev. Sci. Instr. **69(10)**, 3659 (1998).
26. J.T. Cheung and H. Sankur, MRS Proc. Vol. **191**, 11 (1990)
27. D.H. Lowndes, D.B. Geohegan, A.A. Puretzky, D.P. Norton and C.M. Rouleau, Science **273**, 898 (1996).
28. H.L. Levinson and W.H. Arnold, *"Optical lithography"* in: Handbook of Microlithography, Micromachining, and Microfabrication, Vol. 1, Edited by P. Rai-Choudhury, SPIE Optical Engineering Press, 1997, p.111.
29. M. Prasad, H. Ruda and J.J. Dubowski, J. Vac. Sci. Technol. **B15(6)**, 2046-2051 (1997).
30. J.J. Dubowski, M. Julier, G.I. Sproule and B. Mason, MRS Proc. Vol. **397**, 509 (1996).
31. J.J. Dubowski, B. Rosenquist, D.J. Lockwood, H.J. Labbé, A.P. Roth, C. Lacelle, M. Davies, R. Barber, B. Mason and G.I. Sproule, J. Appl. Phys. **78**, 1488 (1995).
32. M. Hanabusa, Thin Solid Films **218**, 144 (1992).
33. J. Brannon, IEEE Circuits and Device Magazine **13(2)**, 11 (1997).
34. W. Sesselmann, E. Hudeczek and F. Bachmann, J. Vac. Sci. Technol. **B7 (5)**, 1284(1989).
35. F. Foulon and M. Green, Appl. Phys. **A61**, 655 (1995).
36. H. Baumgärtner, W. Jiang and I. Eisele, Appl. Surf. Sci. **106**, 301(1996).
37. X.H. Chen, J.C. Polanyi and D. Rogers, Surf. Sci. **376**, 77 (1997).

38. P. Tejedor and F. Briones, J. Chem. Phys. **101(3)**, 2600 (1994).
39. M.Ishii, T. Meguro, K. Gamo, T. Sugano, Y. Aoyagi, Jpn. J. Appl. Phys. **32(12B)**, 6178 (1993).
40. M.C. Shih, M.B. Freiler, G. Haase, R. Scarmozzino and R.M. Osgood, Jr., Appl. Phys. Lett **61(7)**, 828 (1992).
41. H. Takazawa, S. Takatani and S. Yamamoto, Jpn. J. Appl. Phys. **35(6B)**, L754 (1996).
42. R. Matz, J. Meiler and D. Haarer, MRS Proc. Vol. **158**, 307 (1990).
43. V.M. Donnelly and T.R. Hayes, Appl. Phys. Lett. **57(7)**, 701 (1990).
44. R. Heydel, R. Matz and W. Göpel, Appl. Surf. Sci. **69**, 38 (1993).
45. H. Takazawa, S. Takatani, K. Higuchi and M. Kudo, Jpn. J. Appl. Phys. **35(12B)**, 6544 (1996).
46. R. Matz, H. Weber and G. Weimann, Appl. Phys. A **65**, 349 (1997).
47. C.H. Tsai, J.H. Lee, H.J. Chiang, C.C. Yang, M.C. Shih, B.C. Chen, T.J. Chuang and Y. Chang, IEEE Photonics Technol. Lett. Vol. **10(6)**, 751 (1998).
48. C.A. Verschuren, P.J. Harmsma, Y.S. Oei, M.R. Leys, H. Vonk and J.H. Wolter, Semicond. Sci. Technol. **13**, A169 (1998).
49. R. Gibis, H. Kizuki, P. Albrecht, P. Harde, G. Urmann, R. Kaiser and H. Künzel, J. Cryst. Growth **209**, 463 (2000).
50. A.R. Pratt, R.L. Williams, C.E. Norman, M.R. Fahy, A. Marinpoulou and F. Chatenoud, Appl. Phys. Lett. **65(8)**, 1009 (1994).
51. P.J. Poole, R.L. Williams, C. Lacelle, V. Gupta, J.W. Fraser, B. Lamontagne and M. Buchanan, J. Cryst. Growth **201/202**, 578 (1999).
52. K. Kudo, K. Yashiki, T. Sasaki, Y. Yokoyama, K. Hamamoto, T. Morimoto and M. Yamaguchi, IEEE Photonic Technol. Lett. 2000, **12(3)**, 242 (2000).
53. Q. Chen and P.D. Dapkus, Thin Solid Films **225**, 115 (1993).
54. Y. Suda, M. Ishida and M. Yamashita, J. Cryst. Growth **169**, 672 (1996).
55. R. Iga, T. Yamada and H. Sugiura, Appl. Phys. Lett. **64(8)**, 983 (1994).
56. T.E. Schlesinger and T. Keuch, Appl. Phys. Lett. **49(9)**, 519 (1986).
57. E. Herbert Li, editor, "Selected papers on quantum well intermixing", SPIE milestones series, Vol. **MS 145** (1998).
58. J. Ralston, A.L. Moretti, R.K. Jain and F.A. Chambers, Appl. Phys. Lett. **50**, 1817 (1987).
59. J.E. Epler, R.L. Thornton and T.L. Paoli, Appl. Phys. Lett. **52**, 1371 (1988).
60. B.S. Ooi, C.J. Hamilton, K. McIlvaney, A.C. Bryce, R.M. De La Rue and J.H. Marsh, IEEE Photonics Technol. Lett. **9**, 587 (1997).
61. J.H. Marsh, A.C. Bryce, R.M. De La Rue, C.J. McLean, A. McKee and G. Lullo, Appl. Surf. Sci. **106**, 326 (1996).
62. J.J. Dubowski, S. Charbonneau, P.J. Poole, A.P. Roth, C. Lacelle and M. Buchanan, Proc. SPIE, vol. **3274**, 53 (1998).
63. C.J. Hamilton, O.P. Kowalski, K. McIlvaney, A.C. Bryce, J.H. Marsh, C.C. Button, Electronics Lett. **34**, 665 (1998).
64. J.J. Dubowski, N. Rowell, G.C. Aers, H. Lafontaine and D.C. Houghton, Appl. Phys. Lett. **74**, 1948 (1999).
65. J.J. Dubowski, G. Marshall, Y. Feng, P.J. Poole, C. Lacelle, J.E. Haysom, S. Charbonneau and M. Buchanan, Proc. SPIE **3618**, 191 (1999).
66. S. Fafard, K. Hinzer, S. Raymond, M. Dion, J. McCaffrey, Y. Feng and S. Charbonneau, Science **274(5291)**, 1350 (1996).
67. P. Hawrylak, S. Fafard and Z. Wasilewski, Cond. Mater News **7(4)**, 16 (1999).
68. Z. R. Wasilewski, S. Fafard, and J.P. McCaffrey, J. Crystal Growth **201/202**, 1131 (1999).
69. S. Fafard, Z.R. Wasilewski, C.Ni. Allen, D. Picard, M. Spanner, J.P. McCaffrey and P.J. Piva, Phys. Rev. **B59(23)**, 15368 (1999).
70. J.J. Dubowski, C. Ni. Allen and S. Fafard, submitted for publication.

Micromachining of Transparent Materials by Laser Ablation of Organic Solution

Jun WANG**, Hiroyuki NIINO*, and Akira YABE*

* *National Institute of Materials and Chemical Research, 1-1 Higashi, Tsukuba, 305-8565, Japan*
E-mail: yabe@nimc.go.jp
** *Present address: Taiyo Yuden R&D Center, 5607-2 Nakamuroda, Haruna, Gunma, 370-3347, Japan*

Transparent materials such as fused silica, quartz, calcium fluoride, and fluorocarbon polymer were etched upon irradiation of organic solution containing pyrene with a conventional KrF excimer laser. Threshold fluence for etching was 240 mJ/cm^2 for fused silica. Etch rate remarkably depended on a concentration of pyrene: higher etch rate with the increase of pyrene concentration. It means that pyrene molecules play an important role in this process. The etch rate can be easily controlled through changing a laser pulse number, a laser fluence and a concentration of solution. The mechanism for this process is discussed by cyclic multiphotonic absorption of pyrene in the excited states, thermal relaxation, and formation of super-heated solution. As the results, it is suggested that the process is based on the combination of two processes in the interface between the transparent materials and the liquid: one is a heating process by a super-heated liquid and the other is an attacking process by a high temperature and pressure vapor.

Keywords: micromachining, etching, transparent material, excimer laser, multiphotonic absorption. laser ablation, organic solution

1. Introduction

Laser ablation with pulsed UV lasers such as excimer lasers enabled fine micromachining of a variety of materials including organic polymers. It is indispensable, however, that the material has a significant absorption in the rang of laser lines, because the first process in laser ablation is absorption of photon by the material. Therefore, micromachining of transparent materials such as fused silica and fluorocarbon polymers is not achieved by laser ablation using conventional excimer lasers. Most of recent approaches for such a micromachining are laser ablation by the use of F_2 laser or ultra-short pulsed laser. On the contrary to these studies, we found a new method to etch transparent materials by the use of conventional KrF and XeCl excimer lasers, unexpectedly in the course of mechanistic study on laser ablation of polymer films [1-3].

2. Experimental

Our original study was concerned with laser ablation of polymethylmethacrylate (PMMA) films doped with aromatic organic compounds such as pyrene and benzil [4]. In this study the polymer film which was coated on a fused silica substrate was irradiated with a conventional KrF excimer laser (FWHM 30 ns) (Fig.1(a)). When the sample was once irradiated from the opposite side by an experimental mistake in the dark room, we found unexpectedly that the back surface of a fused silica plate was damaged simultaneously with ablation of the polymer film (Fig.1(b)). This finding is the origin of our processing for transparent materials.

Further pulse irradiation, however, could not extend the etch depth of fused silica because the polymer film was completely ablated after a few pulses. So far as the polymer film is coated on the fused silica plate, the amount of etched

First International Symposium on Laser Precision Microfabrication, Isamu Miyamoto, Koji Sugioka, Thomas W. Sigmon, Editors, Proceedings of SPIE Vol. 4088 (2000) © 2000 SPIE · 0277-786X/00/$15.00

silica is limited to extremely small. Therefore, we set up a new system using an organic solution containing pyrene in stead of a pyrene-doped polymer thin film as shown in Fig. 3. A glass vessel containing an acetone solution of pyrene is attached on the back side of transparent material with O-ring.

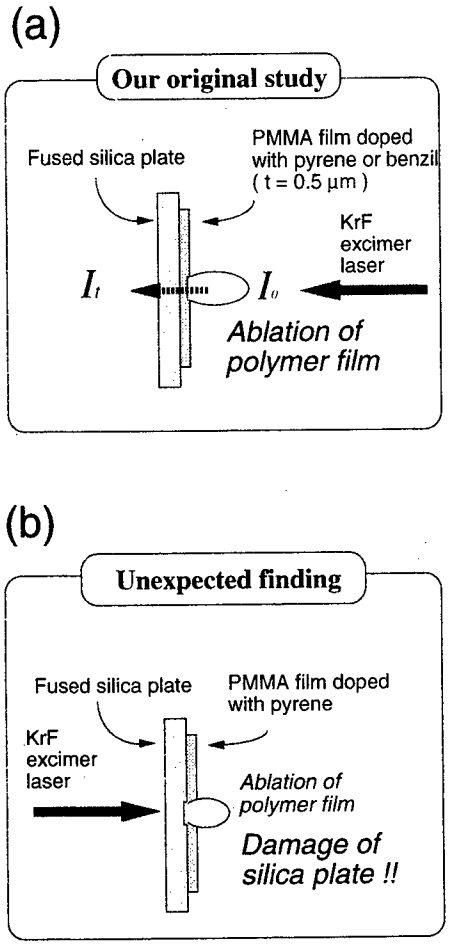


Fig. 1 Schematic diagram for our study on polymer ablation: (a) Original experiment, and (b) Unexpected experiment

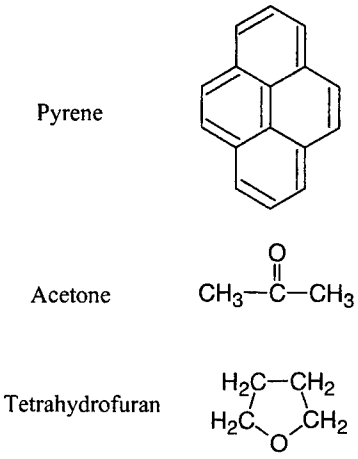


Fig. 2 Chemical formula of chemical reagents used in the processing

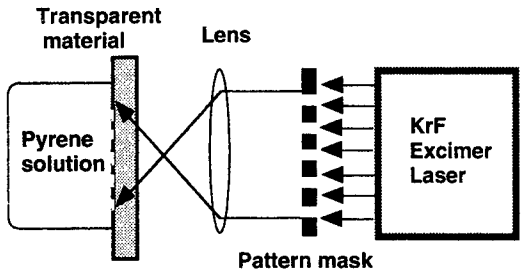


Fig. 3 Experimental setup for micromachining of transparent materials by using organic solution: Laser-Induced Backside Wet Etching

A KrF excimer laser (248 nm, FWHM 30 ns, Lamda Physik, EMG201MSC) and a XeCl excimer laser (308 nm, FWHM 20 ns, Lambda Physik, EMG102MSC) were used as a light source. The intensity of the laser beam was attenuated by a dielectric mirror positioned in front of the laser output. One side of the plate was in contact with acetone solution containing pyrene and the other side was irradiated with the laser at room temperature.

A mask with a square aperture was used to investigate the etch rate. The etched size was about 0.65 mm x 0.65 mm. Etching was carried out with 100 pulses of irradiation with a repetition rate of 2 Hz unless otherwise stated. Depth profiles were determined with a stylus instrument (Talystep, Taylor-Hobson).

A metal stencil mask was used to etch a pattern of 10 μm lines and spaces. The etched pattern was measured by scanning electron microscopy (SEM:DS-720, Topcon).

Transparent materials were a fused silica (SiO_2) plate (Suprasil II, Heraeus) with a thickness of about 0.5 mm and a calcium fluoride (CaF_2, random cut) plate with a thickness of 1 mm, a transparent quartz crystal plate (c-SiO_2, X-cut, 1120) with a thickness of 2.0 mm, and an UV-transparent fluorocarbon polymer film (FEP: fluorinated ethylene-propylene co-polymer), Nitto Denko Co.).

Organic solutions containing pyrene at a concentration of 0.1 to 0.4 mol/dm^3 were prepared by solving pyrene crystallites (Tokyo Kasei Co.) into acetone as solvent.

3. Results

A fused silica plate in contact with an acetone solution of 0.4 mol/dm^3 pyrene was irradiated with 400 pulses of KrF excimer laser at 860 mJ/cm^2. Figure 4 shows scanning electron micrographs (SEM) of the irradiated surface of fused silica. The lines, 10 μm wide and 3.5 μm deep, had well-defined sharp edges without debris and cracks. The etched surface was smooth and debris-free.

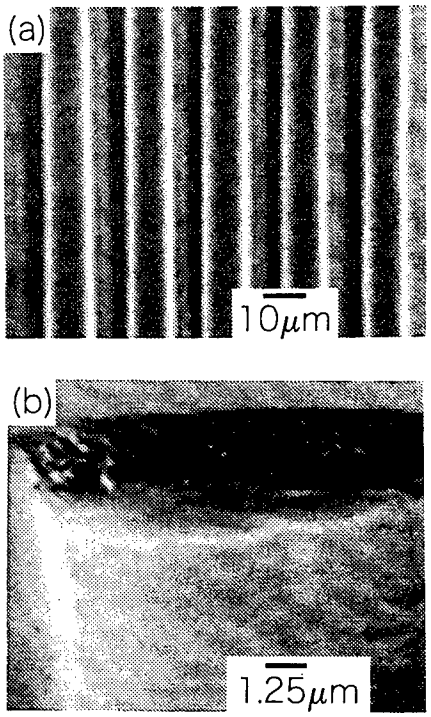


Fig. 4 SEM photographs of the fused silica plate irradiated with 400 pulses with KrF excimer laser at 860 mJ/cm^2, using an acetone solution containing pyrene at a concentration of 0.4 mol/dm^3: (a) top view and (b) magnified view at inclined angle.

Similar irradiations with the KrF excimer laser were carried out for plates of quartz crystal and calcium fluoride. In case of FEP, irradiation was carried out with a XeCl excimer laser unless otherwise noted. SEM photographs of these materials were shown in Figs. 5, 6 and 7.

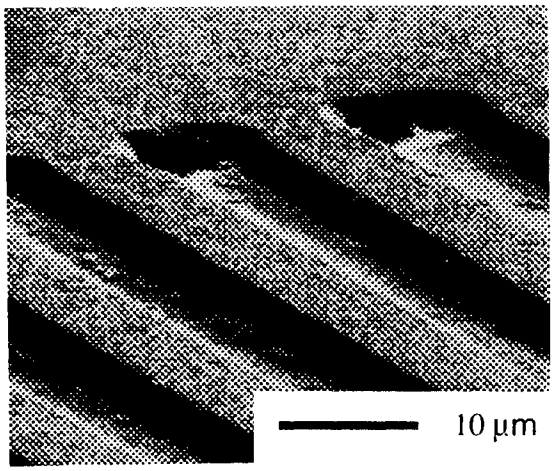


Fig. 5 SEM photograph of quartz crystal irradiated with 400 pulses of KrF excimer laser at 800 mJ/cm^2, using an acetone solution containing pyrene at a concentration of 0.4 mol/dm^3.

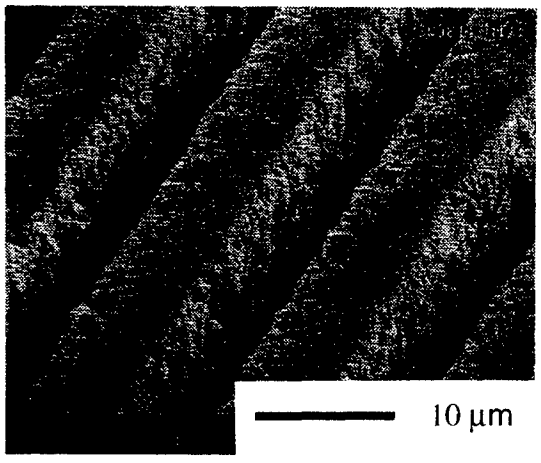


Fig. 6 SEM photograph of CaF_2 irradiated with 500 pulses of KrF excimer laser at 900 mJ/cm^2, using an acetone solution containing pyrene at a concentration of 0.4 mol/dm^3.

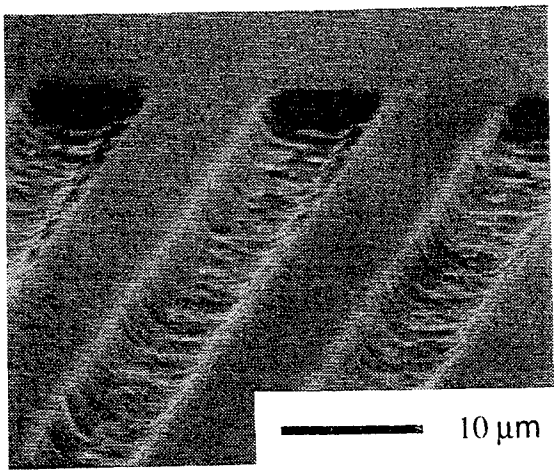


Fig. 7 SEM photograph of FEP irradiated with 400 pulses of XeCl excimer laser at 230 mJ/cm^2, using a THF solution containing pyrene at a concentration of 1.0 mol/dm^3.

Figure 8 shows the relationship between etch rate and laser fluence, where good linear relationships were observed for all the materials. By extrapolation of these lines, threshold fluences were estimated as follows: 240 mJ/cm^2 for fused SiO_2, 330 mJ/cm^2 for crystal SiO_2, 740 mJ/cm^2 for CaF_2, and 45 mJ/cm^2 for FEP. These fluences were remarkably low compared to those given by conventional laser ablation upon direct laser irradiation. For instance, the fluence at 240 mJ/cm^2 in case of f-SiO_2 is about 1/40 lower than that of conventional KrF excimer laser ablation.

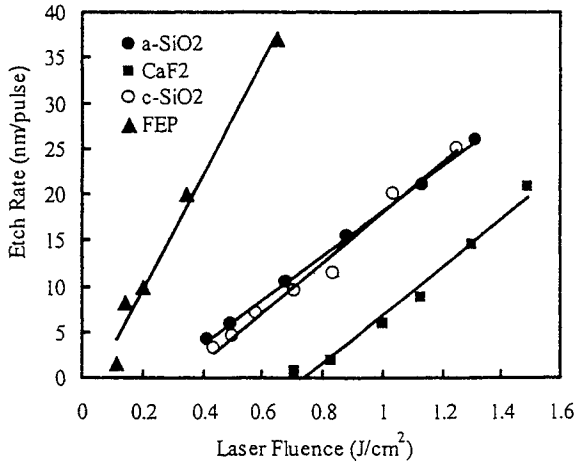


Fig. 8 Plots of etch rate as a function of laser fluence in the irradiation with KrF excimer laser, using an acetone solution containing pyrene at a concentration of 0.4 mol/dm^3.

Figure 9 is plots of etch rate of f-SiO_2 as a function of laser fluence in irradiation with the KrF excimer laser using different concentrations of pyrene in acetone solution. When the concentration of pyrene in acetone increased, the etch rate became higher and the threshold fluence decreased. The solution of 0.4 mol/dm^3 was almost saturated in acetone solvent. If tetrahydrofuran (THF) was used as solvent instead of acetone, 1.0 mol/dm^3 solution was prepared. The threshold fluence of fused SiO_2, using 1.0 mol/dm^3 THF solution decreased to 170 mJ/cm^2.

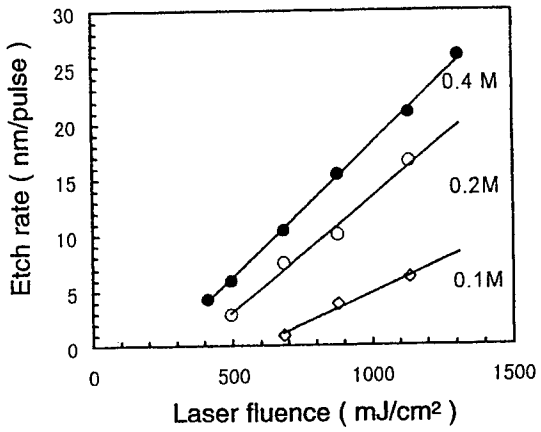


Fig. 9 Plots of etch rate as a function of laser fluence in the irradiation with KrF excimer laser, using acetone solutions at different concentrations.

4. Discussion

The first question, in this processing, is how laser photons are absorbed. It is well known that the transmission of laser is a function of laser fluence in the case of laser ablation of polymer. Recently we reported a method to analyze the nonlinear absorption behavior in laser ablation of polymer doped with pyrene by introducing an absorption coefficient dependent on laser intensity. Similarly to laser ablation of polymer, the absorption coefficients for the solution should be dependent on laser fluence when the solution is irradiated at a high fluence. We estimated corrected absorption coefficients at the threshold fluence (a_{th}) using our previous results. On

the basis of these results, we estimated the penetration depth ($1/a_{th}$) (Fig. 10) for three different solutions as described before in the case of fused SiO_2 (Table 1). As a result, most of laser photons is deposited in a thin solution layer with thickness of around 0.7-2 μm from the surface of silica plate.

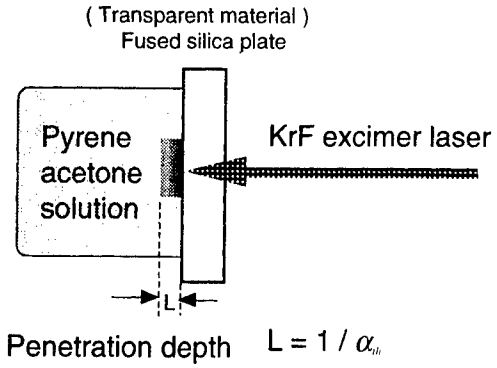


Fig. 10 Laser absorption in Laser-Induced Backside Wet Etching.

The next question is how absorbed laser photons act in organic solution. Although we have not yet studied on primary process of pyrene in solution in the excited states upon laser irradiation, we can refer to a model presented by Fukumura at al. They studied laser ablation of dopant-induced polymer and proposed the model of "*cyclic multiphotonic absorption*" [5,6]. According to cyclic multiphotonic absorption mechanism, each dopant can absorb more than ten photons and the laser energy absorbed by the dopant is converted into thermal energy via rapid nonradiative transition in the excited states, resulting in thermal decomposition of the polymer.

In cyclic multiphotonic absorption, on the assumption that the absorbed laser energy is converted entirely into heat and that the heat diffusion is much slower than the laser pulse duration, we can estimate roughly the maximum temperature of the solution layer at the threshold fluence by using a simple equation:

$$T_{th} = T_0 + a_{th} F_{th} / \rho C$$

where T_{th} is the maximum temperature at threshold, T_0 is room temperature and ρ and C are the density and the heat capacity of acetone, respectively. The results are shown in Table 1. T_{th} is the maximum possible temperature if the liquid is heated to a super-heated state without evaporation The temperature on the surface of fused silica plate in contact with the super-heated liquid will rise to about 2000 K, which is higher than the softening temperature of fused silica (1700 K).

On the basis of these assumption, we imagine a plausible mechanism for our processing as follows (Fig.11). Pyrene molecules in the organic solution absorb the laser energy by cyclic multiphotonic absorption and heat organic solution to generate a super-heated liquid. The super-heated liquid only heat the surface of fused silica but also attack the softened surface with high temperature and pressure vapor. As a result, clusters of SiO_2 must be removed from the bulk plate into liquid phase. After the laser pulse, the irradiated layer cools immediately. This rapid cooling prevents the bulk plate from being thermally damaged.

Table 1 Estimation of maximum temperature (T_{th}) of acetone solution containing pyrene at different concentration upon laser irradiation at threshold: absorption coefficient (α_0), revised absorption coefficient (α_{th}) at etching threshold fluence (F_{th}), and penetration depth ($1/\alpha_{th}$).

Concentrations of pyrene (mol/dm^3)	α_0 (μm^{-1})	α_{th} (μm^{-1})	$1/\alpha_{th}$ (μm)	F_{th} (mJ/cm^2)	T_{th} (K)
0.10	0.20	0.48	2.08	580	1900
0.20	0.39	0.90	1.11	350	2100
0.40	0.78	1.40	0.71	240	2300

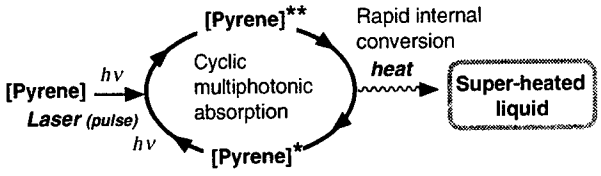


Fig. 11 Plausible mechanism for Laser-Induced Backside Wet Etching.

5. Conclusion

In our processing the role of pyrene molecule is indispensable for efficient etching, because pyrene can absorb cyclically multiphotons and convert UV-laser energy into heat. Pyrene plays a role of molecular heater with enormously high efficiency. Our micromachining process based on this mechanism for pyrene molecule is quite different from the process using aqueous solution containing inorganic compounds such $NiSO_4$[7], CrO_3, and $KMnO_4$[8,9]. In these processing using inorganic solution, remarkably high laser fluence such as 3-10 J/cm^2 was applied and, as a result, it induced microcracking in the etched surface and edge. Compared to these processes, our process enabled fine etching by using effectively UV-laser at low fluence owing to the role of pyrene molecule.

References

[1] J.Wang, H.Niino, and A.Yabe: Appl. Phys.A, **68**(1999) 111.
[2] J.Wang, H.Niino, and A.Yabe: Jpn. J. Appl. Phys., **38**(1999) L761.
[3] J.Wang, H.Niino, and A.Yabe: Appl. Surf. Sci., **154-155**(2000) 571.
[4] J.Wang, H.Niino, and A.Yabe: Jpn. J. Appl. Phys., **38**(1999) 871.
[5] H.Fukumura and H.Masuhara: Chem.Phys.Lett., **221**(1994) 373.
[6] H.Fujiwara, T.Hayashi, H.Fukumura, and H.Masuhara: Appl.Phys.Lett., **64**(1994) 2451.
[7] J.Ikeno, A.Kobayashi, and T.Kasai: Jpn.Soc.Precision Eng. (Seimitsu-Kogakkai-Shi) (Japanese), **55**(1989) 335.
[8] S.I.Dolgaev, A.A.Lyalin, A.V.Simakin, and G.A.Shafeev Quantum Electr., **26**(1996) 65.
[9] S.I.Dolgaev, A.A.Lyalin, A.V.Simakin, and G.A.Shafeev Appl.Surf.Sci., **96-98**(1996) 491.

F2 laser ablation of GaN

Toshimitsu AKANE*, Koji SUGIOKA*, Shintaro NOMURA**,
Kiyotaka HAMMURA*, Kotaro OBATA***, Naoko AOKI***,
Koichi TOYODA***, Yoshinobu AOYAGI*, Katsumi MIDORIKAWA*

*RIKEN (The Institute of Physical and Chemical Research),
2-1 Hirosawa, Wako, Saitama 351-0198, Japan
**Institute of Physics, University of Tsukuba,
Ten-nodai 1-1-1, Tsukuba, Ibaragi 305-8571, Japan
***Department of Applied Electronics, Faculty of Industrial Science & Technology, Science university of Tokyo,
2641 Yamazaki, Noda, Chiba 278-8510, Japan

E-mail: akane@postman.riken.go.jp

Abstract

F_2 laser ablation etching of GaN has been demonstrated. The etching geometry, etching rate and microroughness were investigated, and compared to the case of KrF excimer laser ablation etching. The etching process is consisted of the ablation and hydrochloric acid treatment. Very sharp edge was found along the etched area. The microroughness of etched surface is reduced as the laser intensity increases. The F_2 laser ablation of GaN is thought to be initiated by direct photoionization by single-7.9 eV photon absorption.

keywords: GaN, F_2 laser, KrF excimer laser, ablation, etching, planarization

1 introduction

III-nitride compound semiconductors have difficulty in etching process due to their hardness and chemical stability. Plasma etching [1] [2], reactive ion etching (RIE) [3] [4] have been mainly applied for those materials, however, they might have problem in inducing defects by ion bombardment. Electrochemical [5], electrophotochemical etching in solutions [6], or photochemical etching in gaseous or solutions [7], have been proposed for practical etching methods. Ablative etching is demonstrated to show ultra high etching rate by using YAG:Nd 4ω [8], 2ω [9], and KrF excimer laser [10] [11], Because of its short wavelength (high photon energy), F_2 laser has great potential in lithography for next generation Si-ULSI, and also has potential in intense photochemical excitation in material processing with high resolution.

In this work, we demonstrate F_2 laser ablation etching, and investigate basic etching characteristics.

2 Experimental

The etching process was consisted of the laser ablation and hydrochloric acid treatment. The fluence of F_2 laser (λ = 157.6 nm, τ = 20 ns, Lambda Physik: LPF 105i) was changed from 50 mJ/cm^2 to 2.9 J/cm^2 by changing area size of incident laser. KrF excimer laser was employed for comparison. Single pulse was irradiated to 700 nm-GaN:Mg grown on sapphire substrate in N_2 purging flow. Ni mesh with plenty of 25 μm square holes was set on the samples as a contact mask. Post chemical treatment using 35 %-hydrochloric acid with ultrasonication was undertaken after the laser irradiation. Etched depth was measured by stylus profiler. Surface morphology was observed using conventional optical mi-

First International Symposium on Laser Precision Microfabrication, Isamu Miyamoto, Koji Sugioka,
Thomas W. Sigmon, Editors, Proceedings of SPIE Vol. 4088 (2000) © 2000 SPIE · 0277-786X/00/$15.00

croscope and scanning electron microscope (SEM). Topographic measurement was carried out using tapping mode atomic force microscope (AFM).

3 Results and discussion

Figures 1 shows laser intensity (I) dependence of the etching rate for KrF excimer laser and F_2 laser. For the

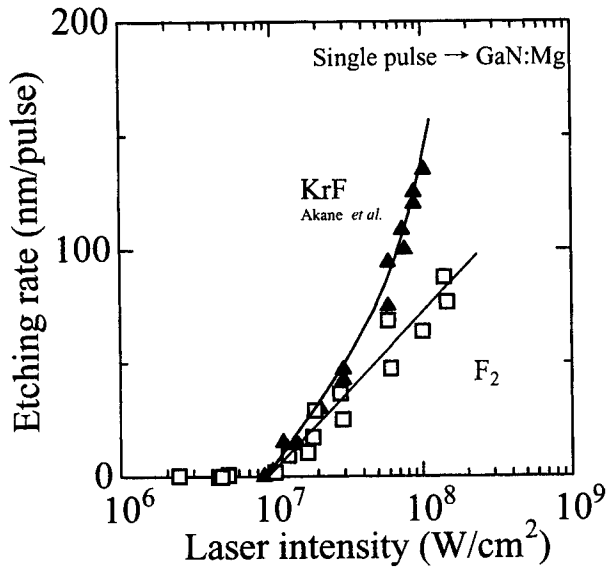


Figure 1: Laser intensity dependence of the etching rate for F_2 laser and KrF excimer lasers.

case of KrF excimer laser etching, acceleration of the etching rate is observed at higher laser intensity [11]. The rate acceleration is caused by temperature rising by the laser irradiation [12]. In contrast, for the case of F_2 laser irradiation, almost no acceleration is confirmed at same intensity range, this means the etching rate is linearly depends upon lnI, i.e., the etching rate is expressed by the Lambert-Beer's law. Thus, F_2 laser realizes less thermal ablation compared to the KrF excimer laser ablation.

AFM images in Fig. 2 are obtained from the samples etched by KrF excimer laser ((a), (b)) and etched by F_2 laser ((c), (d)). The laser intensities are (a) 58.8 MW/cm^2, (b) 88.2 MW/cm^2, (c) 58.8 MW/cm^2, and (d) 100 MW/cm^2. In KrF etched samples (Fig.2 (a) and (b)), geometry degradation at mask edge region is observed. While, well resolved ripple patterns caused by mask edge diffraction, and very sharp mask edges are observed in F_2 laser etched samples (Fig.2 (c) and (d)). Therefore, shorter wavelength is desirable for well-resolved ablation etching.

Figures 3 (a) and (b) are relationship between the average roughness (R_a) and the laser power, for the case of F_2 laser and KrF excimer laser etching, respectively. R_a is evaluated in 5 μm area at the center of etched re-

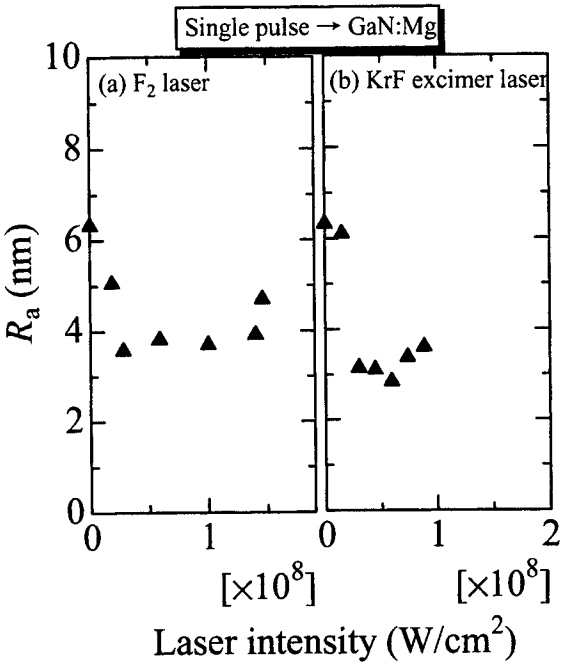


Figure 3: R_a changing as a function of the laser intensity, (a) and (b) are for the case of F_2 laser and KrF excimer laser irradiation, respectively.

gion. R_a is reduced by increase of the F_2 laser intensity (Fig.3(a)), similarly to the case of KrF excimer laser etching (Fig.3(b)). The planarization effect is thought to be the reflection of the temperature rising by the laser irradiation [13]. Ga-rich layer formed at ablated surface by N effusion is thought to act as heat-sink, and lateral heat conduction inside the Ga-rich layer results in thermal decomposition of microroughness at Ga-rich layer/GaN interface. The reduced R_a values are $\sim$ 4 nm and $\sim$ 3.3 nm for F_2 laser and KrF excimer laser etching, respectively. Slightly planarized surface is obtained by KrF excimer laser irradiation, which is thought to be the caused by higher magnitude of temperature rising compared to the case of F_2 laser irradiation.

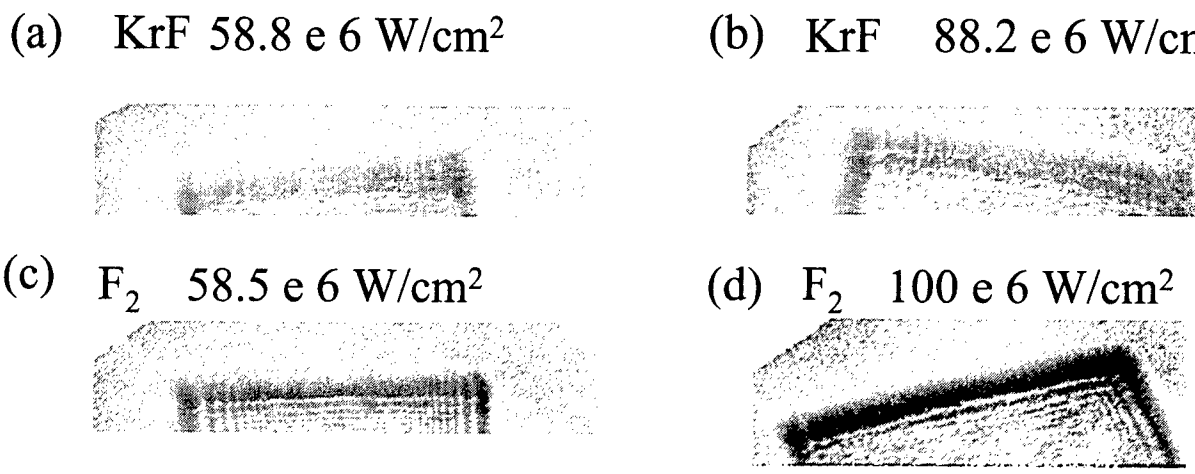


Figure 2: AFM images of laser etchied samples. Images (a) and (b) are taken from the samples etched by KrF excimer laser, (c) and (d) are etched by F_2 laser.

4 conclusion

GaN was successfully etched by F_2 laser ablation and chemical treatment. F_2 laser etched samples exhibited sharp mask edge and mask edge diffraction pattern. The F_2 laser realized less thermal ablation, and resulted in well-defined structure formation. The planarization effect was confirmed in single-pulse F_2 laser etching. In our current work, further pulse irradiation causes severe surface roughening for case of both lasers, however, simultaneous irradiation of both lasers improves surface quality, and realizes extremely sharp etching edge. The single pulse ablation etching using single laser should be proposed for planarization process for finishing of laser diode (LD) cavity mirror.

References

[1] S. A. Smith, C. A. Wolden, M. D. Bremser, A. D. Hanser, R. F. Davis, and W. V. Lampert: Appl. Phys. Lett. **71**, 3631 (1997).

[2] H. P. Gillis, D. A. Choutov, K. P. Martin, S. J. Pearton, and C. R. Abernathy: J. Electrochem. Soc. **143**, L251 (1996).

[3] D. Basak, M. Verdú, M. T. Montojo, M. A. Sánchez-Garcia, F. J. Sánchez, E. Munõz, and E. Calleja: Semicond. Sci. Technol. **12**, 1654 (1997).

[4] J. B. Fedison, T. P. Chow, H. Lu, and I. B. Bhat: J. Electrochem. Soc. **144**, L221 (1997).

[5] S. Yoshida: J. Crystal Growth **181**, 293 (1997).

[6] C. Youtsey, G. Bulman, and I. Adesida: Mat. Res. Soc. Symp. Proc **468**, 349 (1997).

[7] C. Youtsey, G. Bulman, and I. Adesida: J. Elecron. Mat. **27**, 282 (1998).

[8] J. Zhang, K. Sugioka, S. Wada, H. Tashiro, and K. Midorikawa: J. Crystal Growth **189/190**, 725 (1998).

[9] M. K. Kelly, O. Ambacher, B. Dahlheimer, G. Groos, R. Dimitrov, H. Angerer, and M. Stutzmann: Appl. Phys. Lett. **69**, 1749 (1996).

[10] H. Chen, R. D. Vispute, V. Talyansky, R. Enck, S. B. Ogale, T. Dahmas, S. Choopun, R. P. Sharma, T. Venkatesan, A. A. Iliadis, L. G. Salamanca-Riba, and K. A. Jones: Mat. Res. Soc. Symp. Proc. **482**, 1015 (1998).

[11] T. Akane, K. Sugioka, H. Ogino, H. Takai, and K. Midorikawa: Appl. Surf. Sci. **148**, 133 (1999).

[12] V. Srinivasan, M. A. Smrtic, and S. V. Babu: J. Appl. Phys. **59**, 3861 (1986).

[13] . T. Akane, K. Sugioka, and K. Sugioka: Appl. Phys. A **69**, S309 (1999).

Applications of Pulsed Lasers in Low Temperature Thin Film Electronics Fabrication

T. W. Sigmon, D.Toet, P. G. Carey[1], P. M. Smith[2], and P. Wickboldt[2]

Lawrence Livermore National Laboratory
P.O. Box 808, L-395
Livermore, CA 94550 USA
E-mail: sigmon@ieee.org
[1]*Presently at: Applied Materials Corporation 3050 Bowers Ave. Santa Clara, CA 95054 USA*
[2]*Presently at: FlexICs 51 Greenway Dr. Walnut Creek, CA 94596 USA*

For the past several years, our group has focused on the development of polysilicon thin film transistor (TFT) processes having maximum allowable substrate temperatures between 100° to 350°C. These processes are based on excimer laser crystallization of low temperature deposited a-Si thin films combined with low temperature deposited dielectrics and self-aligned gate TFT structures. We have also developed a laser-based, source-drain-gate doping/annealing process. Typical *n*-channel TFT mobilities found are μ_n ~150 cm^2/V-s for the 100°C process and ~400 cm^2/V-s for the 350°C.process. In this paper we describe the basic processes and process physics. We then show results for TFTs fabricated at a variety of maximum substrate temperatures and a-Si deposition techniques.

1. Introduction

Development of Si process technologies enabling the monolithic fabrication of polysilicon thin film electronics at temperatures well below 500°C promises to create opportunities in several new areas of electronics applications. Examples include; *i)* three-dimensional integration of multilayer TFT electronics onto ICs at temperatures low enough to prevent degrading of the underlying circuitry, *ii)* on-panel integration of addressing and switching circuitry in active-matrix flat panel displays and, *iii)* the fabrication of electronics on plastic for low-cost organic light-emitting displays (OLEDs). Although the fabrication of a-Si:H and organic thin film transistors at temperatures well below 450°C has been demonstrated [1,2,3], the current drive and switching performance of these devices (*i.e.*, mobilities ~ 1 cm^2/V-s, sheet resistivities ~) are not adequate for the high drive current requirements of OLED pixels, and the frequency performance required for "on-board" video circuitry.

The foreseen evolution of the flat-panel display industry is toward displays that incorporate increased functionality as part of the display panel. This functionality will be provided by monolithic integration of on-board drivers fabricated in polysilicon thin films. This approach is presently being exploited and relies on crystallization of low temperature deposited a-Si thin films into polysilicon using a pulsed laser [4,5]. For low-cost glass substrates, a 300 - 450°C process provides the needed TFT performance for integration of both *n*- and *p*-channel MOS technology without degradation of the substrate properties. Also, as the development of emissive displays fabricated using OLED pixel material becomes a reality [6], the needed increase in pixel drive current can be implemented by simply replacing the a-Si:H pixel switch transistor with a polysilicon device.

Another direct advantage of low temperature processing, is the ability for fabricating active matrix electronics (pixels, drivers, *etc.*) directly onto plastic substrates for fabricating displays on plastic. For example, polyethylene terephthalate (polyester) is an ideal substrate candidate since it has high optical quality, low cost and is compatable with most semiconductor chemicals. However, it is unable to withstand prolonged temperature exposure above 120°C. With typical processing temperatures of ~250°C for a-Si:H TFTs and 350°C and above for polycrystalline TFTs, this substrate material is eliminated from choice.

Present approaches are attempting to reduce the maximum processing temperature needed to fabricate TFTs to satisfy the requirements of plastic substrates. For a-Si:H TFTs, reduction in the a-Si:H thin film material deposition temperatures has led to severe degradation in important TFT properties, such as mobility. For polysilicon TFTs, pulsed laser crystallization of the silicon is the only technique presently yielding high quality silicon without damaging the underlying plastic substrate.

During the past five years, our group has focused on the development of polysilicon thin film transistor (TFT) processes that result in a maximum substrate temperature of ~100°C. This temperature allows fabrication of high-

First International Symposium on Laser Precision Microfabrication, Isamu Miyamoto, Koji Sugioka,
Thomas W. Sigmon, Editors, Proceedings of SPIE Vol. 4088 (2000) © 2000 SPIE · 0277-786X/00/$15.00

performance polysilicon TFTs directly on low-cost, flexible plastic substrates [7]. Although the effort is focused on developing back-plane electronics for flexible displays, many other applications of this technology are envisioned [8]. Low cost, rugged plastic displays provide the opportunity for a dramatic increase in the variety and utility of military and consumer display products. In fact, the added feature of flexibility may eventually lead to the creation of entirely new display markets. Other advantages when compared to glass include, a reduction in weight of the display as well as decreased breakage during fabrication, increased durability for applications, and lower overall cost. Flexible plastic substrates lend themselves to roll-to-roll processing technologies, potentially enabling the development of large area displays for use in advertising and simulators. As such, laser processing will be directly responsible for the success of these new application areas and products.

The TFT fabrication process is based on pulsed laser crystallization of low temperature deposited a-Si thin-film, combined with a self-aligned, top-gate TFT structure. It incorporates laser-based source-drain and gate doping and annealing processes. The 4 eV photons from a XeCl excimer laser are strongly absorbed in the near-surface region (<10 nm) of the a-Si/polysilicon film. Electrons are excited from the valence band into the direct gap of the a-Si/polysilicon material. By remaining below the ablation threshold for the film, controlled melting of the silicon can be accomplished in a very short time (<10 ns). Using a pulse length in the range of 30 to 50 ns results in deposition of a minimum amount of energy for the process, assuring that the underlying substrate is least affected. The laser energy fluence is chosen to select the final polysilicon microstructure, a parameter important in the fabrication of TFT devices [9]. The laser process effectively shifts the maximum fabrication temperature for the TFTs to that of other steps in the process such as dielectric depositions. This allows TFTs to be fabricated at temperatures as low as 350°C on glass with mobilities approaching that of bulk silicon for use in three-dimensional integrated circuit applications [10].

In the following, we will describe the basic process and physics involved in the laser crystallization. We will then show results for TFTs fabricated for a variety of maximum substrate temperatures and a-Si deposition techniques.

2. Laser crystallization and doping

The laser crystallization and doping processes are carried out using a Lambda Physik XeCl pulsed excimer laser having a full-width at half-maximum (FWHM) of about 35 ns, a double-hump gaussian temporal profile, and a wavelength of λ = 308 nm. The laser beam is passed through homogenizing optics resulting in a top hat spatial profile with better than ±5% intensity variation. The laser beam can be focused from a spot size of 2x2 mm^2 up to 1.2x1.2 mm^2 at the wafer surface. In most of our work, a square beam is stepped across the wafer in a serpentine pattern at pulse repetition rates up to 150 Hz with fixed energy fluence for each scan. Similar homogenizers used in the flat panel display industry are capable of creating rectangular shaped laser beams up to 20 cm wide, allowing a decrease in the laser processing times per substrate.

The wavelength, energy fluence and pulse width of the laser are chosen to optimize the crystallization and doping of the silicon, while minimizing heating of the underlying substrate. At the wavelenghth of 308 nm, the absorption depth of the laser energy for amorphous, polycrystalline, and liquid silicon is on the order of 12 to 15 nm as seen in Fig. 1. The consequence of this very shallow absorption depth is that virtually *all* of the laser energy is deposited into the near surface region of the silicon layer. Figure 1 indicates that laser wavelengths greater than about 360 nm are not suitable for crystallizing thin silicon films since the absorption depth for crystalline (or polycrystalline) silicon increases from about 0.02 μm (20 nm) at λ = 360 nm, to over 0.1 μm (100 nm) at λ = 400 nm. The increase in absorption

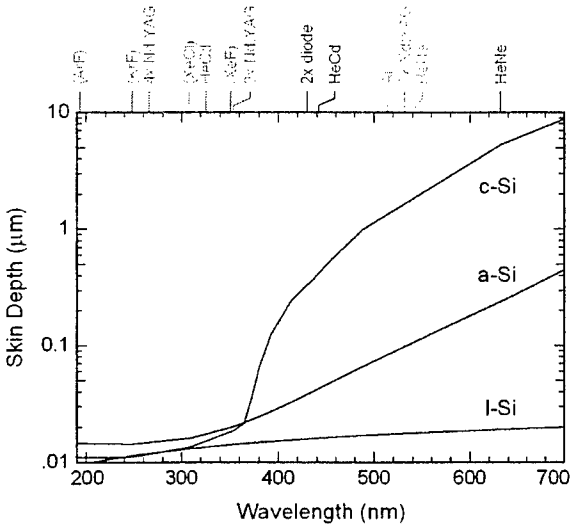


Fig. 1 Absorption (skin) depth for crystalline (or poly), amorphous, and liquid silicon as a function of wavelength for various lasers. For XeCl excimer lasers (λ=308 nm) the skin depth is < 0.015 μm (15 nm) for all three silicon phases which means that virtually all of the laser energy is deposited into the silicon surface region.

depth results in less laser energy being deposited into the thin film silicon layer. By using a short (35 ns) pulse length, the instantaneous power of the laser is high enough (~ 15 MW) to rapidly heat the silicon film to its melting point before sufficient heat can be conducted into the underlying substrate layers.

The crystallization and doping steps are carried out in LLNLs doping and crystallization cluster tool shown in Fig. 2. This cluster tool allows the laser doping deposition and drive-in steps to be integrated without breaking vacuum. For crystallization of silicon on plastic, the laser energy fluence is stepped from 180 to 250 to 330 mJ/cm^2 (for a 90 nm thick silicon layer), with each spot on the sample receiving 3 pulses at each fluence. The final laser energy fluence is chosen to be slightly above the minimum fluence needed to completely melt through the entire silicon film, the full-melt threshold energy, and results in a relatively uniform grain structure for the film. For the doping process, the laser fluence is reduced below the full-melt threshold, with each location receiving 3-5 pulses.

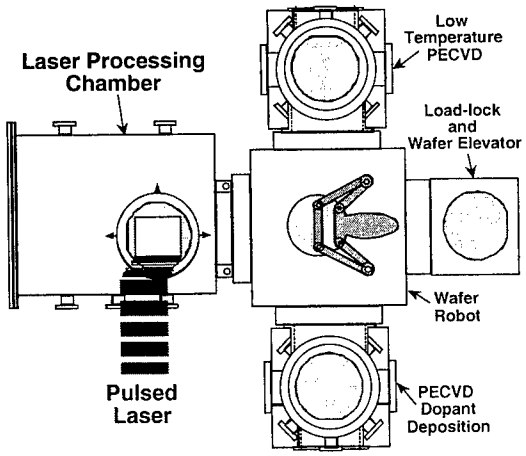


Fig. 2. Laser processing, doping, and PECVD cluster tool.

Using 1-D heat flow simulation and a 35 ns FWHM laser irradiation pulse, the thermal profiles in the silicon and underlying polyester substrate are calculated. An example simulation, shown in Fig. 3, indicates that the silicon surface reaches temperatures in excess of the Si melting point of 1410°C, while the surface of the plastic is heated to approximately 500°C for a time of a few tens of microseconds. This particular simulation was for a 100 nm thick silicon film on a 500 nm barrier oxide on polyester. The laser energy fluence was 480 mJ/cm^2, higher than the full melt threshold energy for this film thickness. Although the polyester surface reaches nearly 500°C for this simulation, the time-temperature product is not sufficient enough to damage the plastic. We have experimentally verified these results using our process [5]. The simulation program predicts lower plastic surface temperatures when thinner silicon layers are used. This results from lower laser energy fluences being required to melt and crystallize thinner films. Similar effects are obtained when using thicker barrier oxides.

3. TFT fabrication

Fig. 4(a)-(d) are schematic cross-sections of the TFT fabrication at various stages in the process. An initial plasma enhanced chemical vapor deposition (PECVD) step

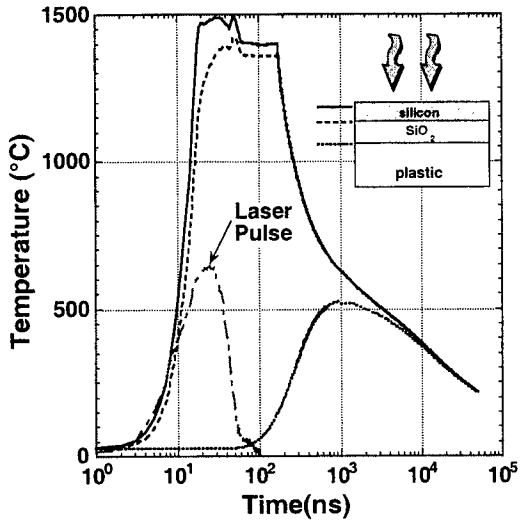


Fig.3. Simulation of the thermal history for the TFT source-drain regions during the laser doping process. The curves match the layers shown in the inset. The XeCl excimer laser pulse intensity units are arbitrary.

is used to deposit a 0.75 μm thick SiO_2 layer on the polyester wafer front and back surfaces. For glass substrates, 100 nm of SiN_x and 500 nm SiO_2 films are deposited. The oxide/nitride layers act both as a contamination barrier between the subsequently deposited silicon layer and the polyester/glass, and as a thermal and stress relief layers for the laser crystallization and doping steps for the polyester. The bottom layer on the polyester also protects it from various processing chemicals and water vapor.

Following deposition of the front and backside oxides, a 90 nm thick amorphous silicon layer is formed using DC magnetron sputtering onto the barrier oxide coated polyester wafer frontside. DC sputtering of the Si avoids the added complexity of a silicon dehydrogenation laser process. Dehydrogenation is normally required to prevent explosive effusion of the excess hydrogen when laser crystallizing low temperature deposited PECVD a-Si:H [11]. For the higher temperature process, we have developed a PECVD process that does not require dehydrogenation [12]. The a-Si layer is then crystallized in the laser crystallization chamber of the cluster tool (see Fig. 2 and Fig. 4a). The multilayer stack, required for fabricating the TFTs, is completed by depositing 100 nm of thick gate oxide in the adjoining plasma chamber of the cluster tool. For the higher temperature process, 130 nm of low pressure CVD SiO_2 is deposited at 300°C. The wafers are then removed from the cluster tool and a 170 nm thick aluminum gate layer is sputter deposited onto this gate oxide in a separate apparatus (Fig. 4b).

The aluminum gate regions are patterned using standard silicon photolithography and wet chemical etching. The oxide overlying the source-drain regions is etched using a two-step dry/wet etch process. Doping of the TFT source-drain regions is carried out using a second

excimer laser step in the cluster tool (Fig. 2). A very thin layer of phosphorous (~30 Å) is deposited onto the surface of the wafer at room temperature using PECVD dissociation of PF_5 diluted with He as the source gas. Following deposition the wafer is transferred into the adjoining chamber where the dopant layer is driven into and simultaneously activated using a silicon melt/regrowth step initiated by the laser. This process is highly effective in doping the source/drain regions, resulting in silicon sheet resistance values of about 700 Ω/□. This step is illustrated in Fig. 4(c). For *p*-channel TFTs, the dopant gas used during the PECVD step is BF_3. We have also demonstrated a laser activated implantation process for this step [12].

The TFT is then photolithographically defined on the silicon layer and dry-etched to produce isolated silicon islands for fabrication of the TFTs. A ~500 nm thick PECVD SiO_2 contact isolation layer is then deposited, patterned, and the metal contact holes are wet-etched. A 800 nm thick Al interconnect layer is sputtered onto the wafer, patterned and wet-etched to complete the TFT structure, shown in cross section in Fig. 4(d). Since the structure is self-aligned, misalignment between the gate and the source-drain levels arising as a result of distortion of the underlying plastic substrate during processing is eliminated.

At this point the wafers are annealed in air at 150°C for 3 hours to improve the TFT device performance and contact resistance values. Although above the maximum polyester softening temperature, this anneal does not noticeably change the flexibility of the plastic. Also, since all of the photolithography steps are completed at this point, there are no concerns about subsequent mask misalignments from changes in the plastic.

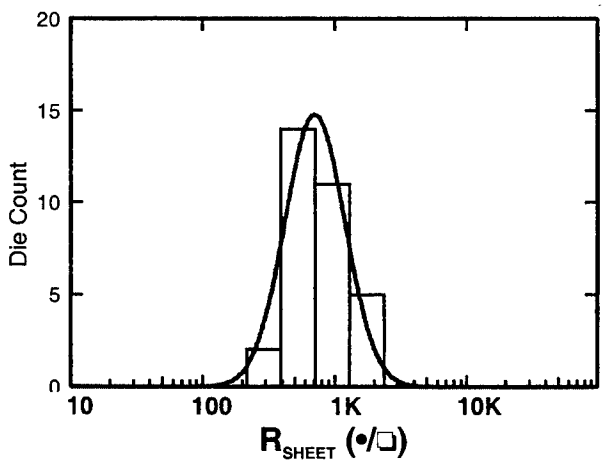


Fig. 5. Histogram of silicon sheet resistance values on a 4 inch diameter polyester wafer. The silicon has been doped by depositing a thin layer of phosphorous using room temperature PF_5 PECVD followed by a laser drive-in step. The gaussian fit to the data is centered at 700 Ω/□.Ω/□.

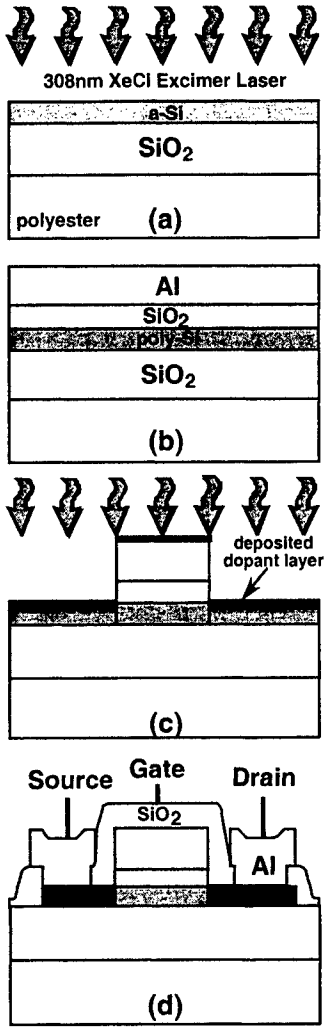


Fig. 4(a)-(d). Schematic cross-sections of LLNL's TFT on polyester or glass process. The laser steps are shown in (a) silicon crystallization and (c) doping.

4. Laser doping results

In Fig. 5 we show a plot of the sheet resistance (R_{SHEET}) values obtained across a 4 inch diameter polyester wafer that has been subjected to the laser doping process. Parametric test structures are measured across the entire wafer allowing the determination of doping uniformity. As seen in the figure, the majority of the data fall in the range from R_{SHEET} = 400-1100 Ω/□, with the distribution centered at ~700 Ω/□. A tighter distribution, centered at even lower values, is obtained by increasing the laser fluence (*i.e.*, melting deeper into the film) and/or the number of laser pulses.

Similar data is obtained for both the Al-gate to Al-interconnect specific contact resistance $R_{c\text{-}sp}$, and the doped silicon to Al interconnect contact resistance. For the Al to Al, the $R_{c\text{-}sp}$ values typically are $3x10^{-6}$ Ω-cm^{-2},

while for *n*-Si-Al $R_{c\text{-}sp}$ is $5x10^{-6}$ Ω-cm^{-2}. We point out that these low values are obtained without the benefit of a contact sintering step (typically ~450°C), a direct result of using polyester for the substrate material. The sheet resistances found for the higher temperature processes are similar.

5. Thin film transistors: low temperature process

As discussed previously, all TFTs fabricated on polyester substrates utilized sputtered, non-hydrogenated a-Si films deposited at room temperature as the starting material. TFTs fabricated using the previously described process exhibit good transistor behavior, with I_{ON}/I_{OFF} current ratios exceeding $5x10^5$ and mobilities greater than 50 cm^2/V-sec. as shown in Fig. 6 and 7 for a TFT with a W/L=100/50 μm gate geometry. We have successfully fabricated TFTs with geometries down to W/L=10/1.5 μm with similar results (W = gate width, L = gate length). I_{ON}/I_{OFF} ratios of this magnitude are sufficient for small display applications, and mobilities of this magnitude are sufficient to make TFTs for driver circuitry directly on the polyester. Reducing the thickness of the silicon layer to 50 nm or below would lead to a reduction in the leakage current (I_{OFF}) of laser crystallized TFTs, while simultaneously making it easier to attain even higher mobilities [13]. We have recently obtained mobilities as

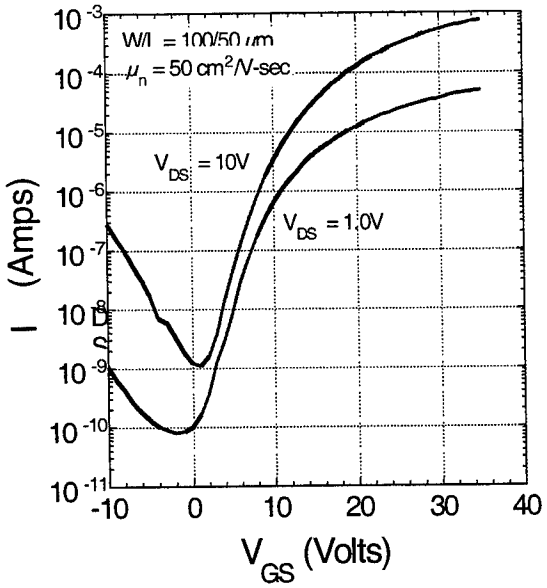


Fig. 6: I_{DS} *vs.* V_G for a W/L=100/50 μm TFT fabricated at 100°C on a polyester substrate. The maximum mobility at V_{DS} = 1.0 V is 50 cm^2/V-sec, and the I_{ON}/I_{OFF} ratios exceed $5x10^5$.

high as 150 cm^2/V-sec. These values represent an improvement over previously reported results, especially in terms of electron mobility and the gate voltages necessary to turn on the TFTs [5]. The improvements are attributed primarily to integration of the critical processing steps, made possible by the cluster tool. These process integration steps are, *i)* silicon laser crystallization followed by gate oxide deposition for improving the silicon/oxide interface, and *ii)* dopant layer deposition followed by laser drive-in for making low sheet resistance source-drain regions.

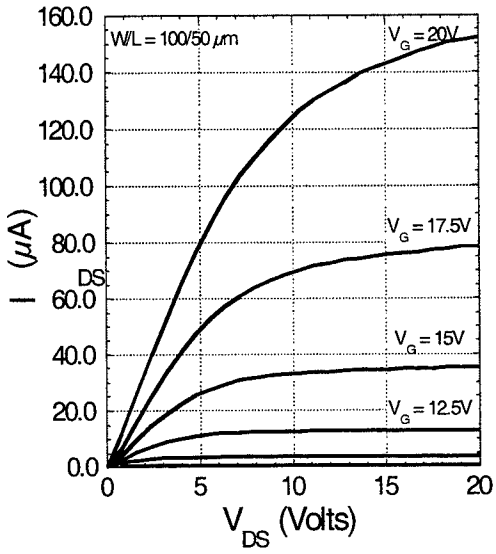


Fig. 7: I_{DS} *vs.* V_{DS} for a W/L=100/50 μm TFT fabricated at 100°C on a polyester substrate. The transfer characteristics indicate that current crowding at the drain is not a problem, resulting from the low contact resistance provided by the laser process.

6. Thin film transistors: medium temperature process

For TFT fabrication at 350°C, both PECVD and sputtered deposited silicon films are used. In the following we discuss results obtained from PECVD films since we have comprehensive experimental results on such films.

Differences in the TFT fabrication processes between the glass and plastic substrates were discussed in **Sect. 1.3** and will not be repeated. Silicon PECVD films, used for the medium temperature process, are deposited to a thickness of 42 nm at a substrate temperature of 350°C from SiH_4. Hydrogen concentrations of < 3 at.% are found for these films using infrared (IR) absorption spectroscopy. In earlier work, we have shown that these films can be laser-crystallized without prior dehydrogenation [14]. The silicon films were crystallized at laser fluences above the full melt threshold (350 mJ/cm^2 for 42 nm thick films), with a pulse-to-pulse overlap of 67%. Several of the films are then partially re-melted using a lower fluence scan (250 mJ/cm^2, 50% overlap), referred to as "full + partial melt" in the following figures. Selection of this melt regime is described elsewhere and will not be repeated in this paper [12]. In Fig. 8 we show I_{DS} vs V_{GS} (gate-sweep) for typical TFTs with a gate width of 10 μm and gate length of 10 μ.m (W/L = 10/10) for both the full-melt

and "full + partial melt" regimes. From such curves, mobility, threshold voltage, subthreshold slope and I_{OFF} are determined for each device. In Figs. 9 through 12 we show distributions of mobility, threshold voltage, subthreshold slope and off current for the two different

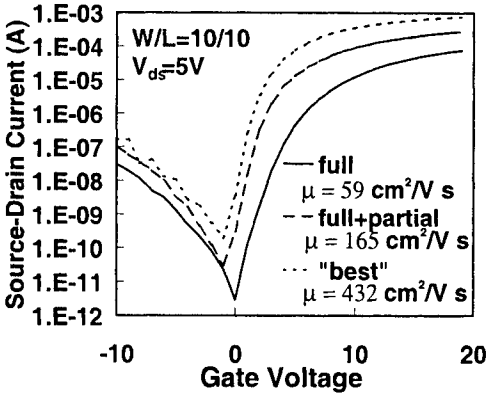


Fig. 8: Transfer characteristics of W/L= 10/10 TFTs made by full melt (solid line) and full+partial melt ELC (dashed line). The dotted line shows the highest mobility TFT.

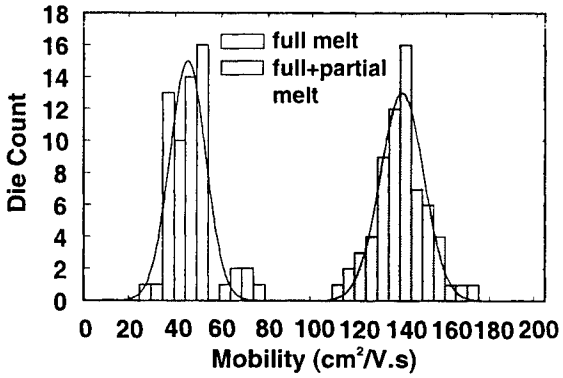


Fig. 9: Histogram of mobility for W/L = 20/40 TFTs measured at V_{DS} of 5 V. A total of 120 devices were measured.

melt processes measured for several wafers.

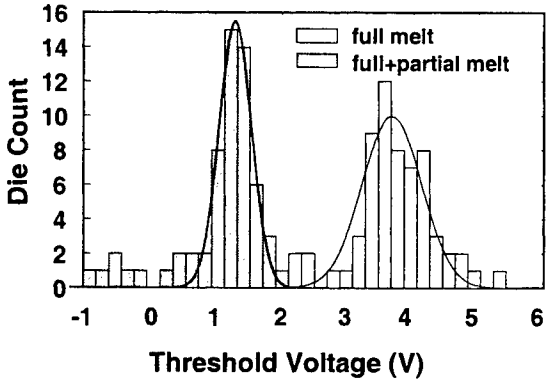


Fig. 10: Histogram of threshold voltage for W/L = 20/40 TFTs measured at a V_{DS} of 5 V. A total of 120 devices were measured.

A total of 60 sets of devices out of 75 on two wafers were measured.

Upon examining Fig. 9, we see that the mobility for the "full + partial melt" TFTs results in an average mobility which is more than twice that of the film not receiving the second laser melt step, while the distribution is only slightly affected. For the full melt case, the medium mobilty is μ_n = 48 cm^2/V s with a FWHM of 18 cm^2/V s and for the full + partial melt case they are 141 and 24 cm^2/V s, respectively. This increase is a direct result of the increase in grain size in the near surface region for the full + partial melt, coupled with only a slight increase in surface roughness above the full melt regime [12].

In Figs. 10 and 11 we plot threshold voltage and subthreshold slope (the slope of I_{DS} *vs* V_G at turn on) for the full and "full + partial melt" cases. In both cases we see significant improvement for the full + partial melt

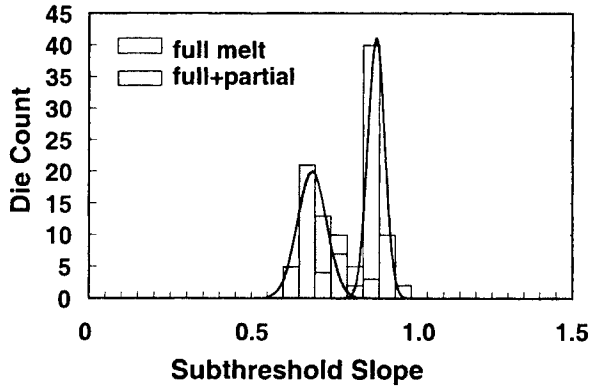


Fig. 11: Histogram of subthreshold slope for the W/L = 20/40 TFTs measured at a V_{DS} of 5 V. A total of 120 devices were measured.

case, with respect to the full melt case. The full-melt threshold and subthreshold slope of 3.5 V and 0.87 V/dec. improve to 1.1 V and 0.7 V/dec., respectively.

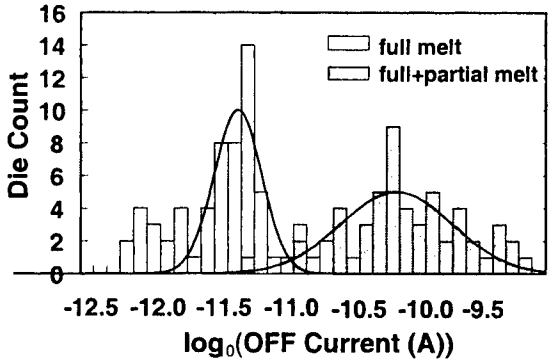


Fig. 12: Histogram of off current for W/L = 20/40 TFTs measured at a V_{DS} of 5 V. A total of 120 devices were measured.

In contrast to the improvement seen for the mobility and threshold, the off currents for the devices does not improve for the "partial + full melt case" as seen in Fig.12. For this parameter, a measure of how well the device turns off a median value of 0.5 pA per μm of gate width for the full melt case, and 5 pA per μm for the "full + partial melt case" are found. It is speculated that this increase is due to the slight increase in the surface roughness seen for the latter [12].

7. Summary

The use of pulsed excimer laser processes for the crystallization of amorphous deposited silicon will be an enabling technology for development of electronics on low temperature substrates such as low cost glass and plastics. Fabrication of TFTs using laser crystallization and doping/annealing capable of driving OLED type displays has been demonstrated. Continued improvement in the distribution of important device parameters such as mobility, threshold voltage, and subthreshold slope will result in laser processing being used for active matrix backplanes, and on-board control and drive electronics. Development of laser doping and annealing insures low on device resistance values insuring switching speeds capable of video rates.

8. Acknowledgments

This work was performed under the auspices of the U. S. Department of Energy at Lawrence Livermore National Laboratory under Contract No. W-7405-Eng-48.

References

[1] T. Sameshima, S. Usui, and M. Sekiya, IEEE Electron Device Lett. 7, 176 (1986).

[2] C. D. Sheraw, D. J. Gundlach and T. N. Jackson, "Flat Panel Displays and Sensors- Principles, Materials, and Processes," Materials Research Society, Vol. 558, pp. 403-408, 1999.

[3] C. S. McCormick, C. E. Weber, J. R. Abelson, and S. M. Gates, Appl. Phys. Lett., Vol. 70, no. 2, pp. 226-7, 1997.

[4] A. Kohno, T. Sameshima, N. Sano, M. Sekia, and M. Hara, IEEE Trans. Electron Dev., Vol. 42, pp. 251-256, 1995.

[5] P. M. Smith, P. G. Carey, and T. W. Sigmon, Appl. Phys. Lett., Vol. 70, no. 3, pp. 342-344, 1997.

[6] See for instance "Flat Panel Displays and Sensors- Principles, Materials, and Processes, Vol. 558, and "Organic Nonlinear Optical Materials and Devices," Vol. 561, Materials Research Society, 1999.

[7] P. G. Carey, P. M. Smith, P. Wickboldt, M. O. Thompson, and T. W. Sigmon, Proc. IDRC '97 Technical Digest, 1997.

[8] N. D. Young, G. Harkin, R. M. Bunn, D. J. McCulloch, R. W. Wilks, and A. G. Knapp, IEEE Electron Dev. Lett., Vol. 18, no. 1, pp. 19-20, 1997.

[9] G. K. Giust and T. W. Sigmon, "Flat-Panel-Display Materials–1998," Materials Research Society, Vol.508, pp. 55-65, 1998.

[10] G. K. Giust and T. W. Sigmon, IEEE Trans. on Elect. Dev., Vol. 45, no. 4, pp 925-932, 1998.

[11] P. Mei, J. B. Boyce, M. Hack, R. A. Lujan, R. I. Johnson, G. B. Anderson, D. K. Fork and S. E. Ready, Appl. Phys. Lett., Vol. 64, no. 9, pp. 1132-1134, 1994.

[12] D. Toet, T. W. Sigmon, T. Takehara, C-C Tsai, and W. R. Harshbarger, in Symp. X

[13] S. D. Brotherton, D. J. McCulloch, J. P. Gowers, M. Trainor, M. J. Edwards, and J. R. Ayres, SID AM-LCD'96 Tech. Dig., pp. 21-24, 1996.

[14] D. Toet, P. M. Smith, T. W. Sigmon, R. Qui, T. Takehara, S. Sun, C-C. Tsai, and W. R. Harshberger, "Flat-Panel-Display Materials–1998," Materials Research Society, Vol.508, pp. 97-102, 1998.

Pulsed laser nitridation of InP

Naoko AOKI[*], Toshimitsu AKANE[**], Koji SUGIOKA[**], Koichi TOYODA[*], Jan J. DUBOWSKI[***] and Katsumi MIDORIKAWA[**]

[**]The Institute of Physical and Chemical Research, 2-1 Hirosawa, Wako, Saitama 351-0198, Japan
[*]Department of Applied Electronics, Faculty of Industrial Science and Technology, Science University of Tokyo, 2641 Yamazaki, Noda, Chiba 278-8510, Japan
[***]National Research Council of Canada, Ottawa, Ontario, K1A 0R6

Nitridation of semiconductor surfaces is attractive for passivation as well as fabrication of new materials. Nitridation of the III-V semiconductors has been mainly reported for GaAs. In this paper, we demonstrate the surface nitridation of InP by KrF excimer laser irradiation in an NH_3 ambient. The laser fluence was fixed at 80 mJ/cm^2 and number of pulses was changed from 500 to 10000. X-ray photoelectron spectroscopy (XPS) analysis of the nitrided samples reveals that the InP surface contains both InN_x and PN_y compounds. Nitrogen content increases with the increase of number of pulses. Near-stoichiometric InN and P_3N_5 are formed by the 2500-pulse irradiation. Aging test reveals that the nitrided samples show anti-oxidation property, which is improved as the number of pulses increases.

Keywords: nitridation, excimer laser processing, InP, XPS, AFM

1. Introduction

Surface passivation or protection of semiconductor materials from oxidation is a very important issue for realizing high performance solid-state devices [1, 2]. Since oxides on InP deteriorate electrical performance, $(NH_4)_2S_x$ treatment, anodic oxidation or Al_2O_3 films have been applied for surface protection and stabilization. There are few reports on nitridation of InP [3] and intensive study is needed to determine chemical bonding state of nitrided surface of InP. In this paper, we demonstrate the nitridation of InP by KrF excimer laser irradiation in an NH_3 ambient. We investigate chemical properties and the stability of laser-formed InN_x films.

2. Experiments

High quality (001) InP wafers were irradiated with a KrF excimer laser (248 nm, 1 Hz, 80 mJ/cm^2) in an NH_3 ambient (760 Torr). Prior to the irradiation, samples were etched in a mixture of HCl (35% water solution), HF (49% water solution), and H_2O (1:1:4) for 3 min at room temperature, which was followed by deionized water rinsing. Morphology of laser-irradiated samples was investigated with an atomic force microscope (AFM). The surface chemistry of both non-irradiated and laser irradiated samples was investigated with an x-ray photoelectron spectroscopy (XPS).

3. Results and Discussion

3.1 Surface morphology

Figure 1 shows the surface morphology of an InP wafer before irradiation (a), and following irradiation with n=500 (b), n=1000 (c), n=2500 (d), n=5000 (e) and n=10000 (f) pulses. It can be seen that up to n=5000 the irradiated samples have a smooth surface described by the average roughness, Ra, equal to about 1 nm. This compares to Ra = 0.3 nm for the surface of a non-irradiated sample. Some obvious surface roughening is observed for the sample irradiated with 10000 pulses.

3.2 XPS analysis

The XPS peak assignment was based on the available literature data [4-6]. After the chemical treatment of InP, the removal of native oxides was confirmed by extinction of peaks at 445.35 eV and 445.9 eV, In_2O_3 and $InPO_4$, respectively, which was observed in the In3*d* scan. Also, the removal of $InPO_4$ was confirmed by the extinction of peaks at 133.5 eV and 134.5 eV in the P2*p* scan.

Figures 2 and 3 show the In3*d* and P2*p* XPS spectra, respectively, of samples irradiated with (i) n=500, (ii) n=1000 and (iii) n=2500. In Fig. 2, the peak around 446 eV corresponds to the In-N bonding. With the increase of n, the InN_x peak intensity increases, and the peak position shifts toward the higher energy side. Therefore, the content of nitrogen (x) is increasing with the increasing number of laser pulses. Near-stoichiometric InN is thought to be

First International Symposium on Laser Precision Microfabrication, Isamu Miyamoto, Koji Sugioka, Thomas W. Sigmon, Editors, Proceedings of SPIE Vol. 4088 (2000) © 2000 SPIE · 0277-786X/00/$15.00

formed at n=2500. Similarly, there are two peaks around 133.4--134.1 eV, which correspond to the spin orbital splitting of the P-N bonding (Fig. 3). As n is increased the peak corresponding to the P-N bonding also increases. At n= 2500, a near stoichiometric P_3N_5 is thought to be formed.

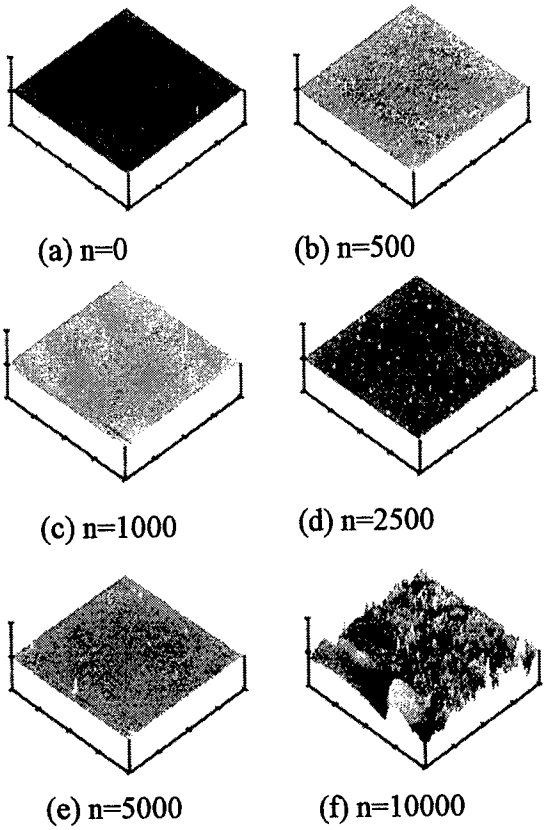


Fig. 1. AFM images of sample surface. The number of irradiating pulses (n) is indicated at the bottom of each image. Scanning region is 20×20 μ m (horizontal) and the vertical range is 100 nm/div.

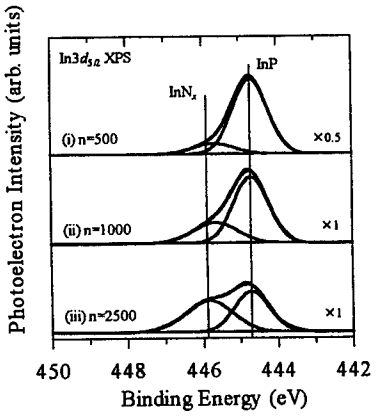


Fig. 2. In3d XPS spectra variation with the number of pulses.

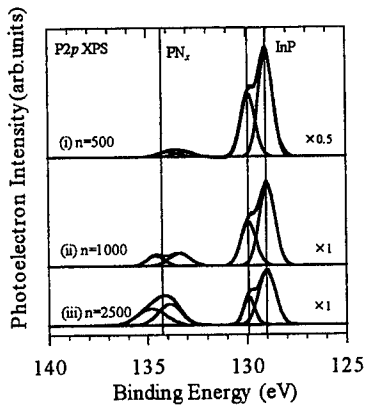
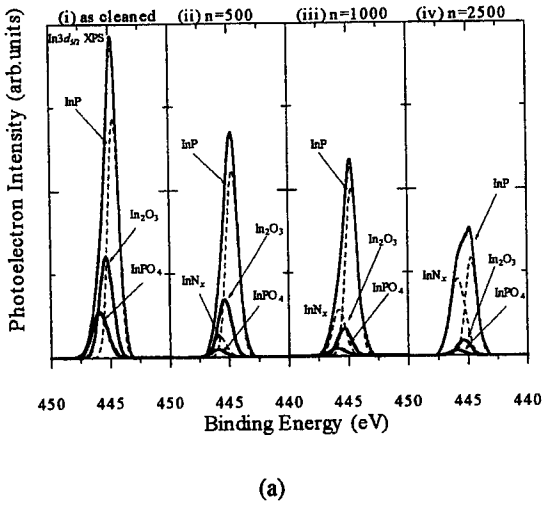
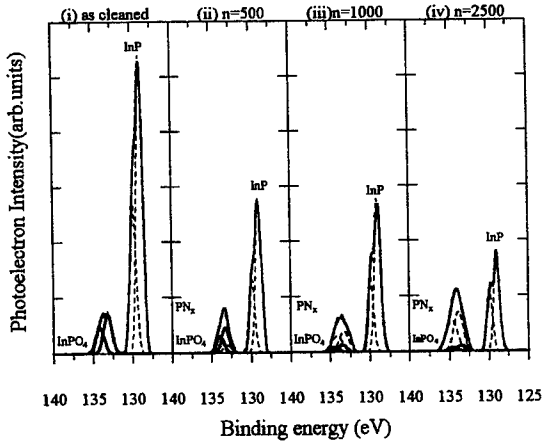


Fig. 3. P2p XPS spectra variation with the number of pulses.



(a)



(b)

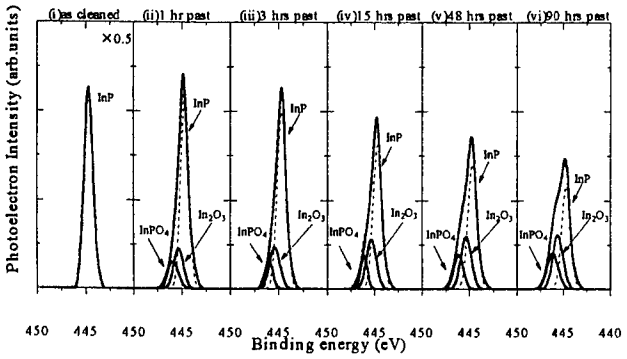
Fig. 4. XPS spectra of InP samples aged for 22 days: (a) In3d XPS spectra; (b) P2p XPS spectra.

3.3 Room temperature aging

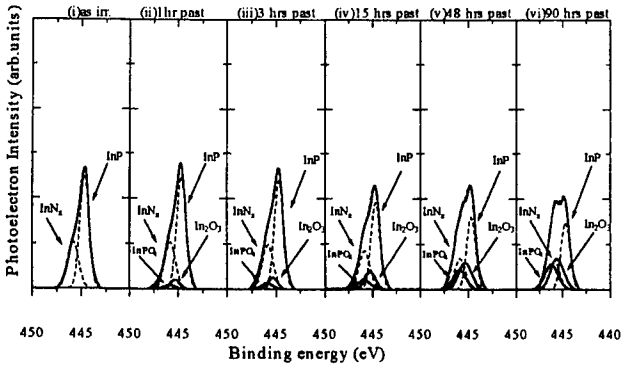
The nitrided samples were aged for 22 days at room temperature in an atmospheric environment. Figure 4(a) and (b) show the In3*d* and P2*p* XPS spectra of aged sample surface. The *n* are (i) 0 (non-irradiated), (ii) 500, (iii) 1000 and (iv) 2500. From Fig. 4(a) and (b), it can be seen that the nitridation suppresses the formation of oxides. This effect is most obvious for the sample irradiated with 2500 pulses.

3.4 Heat-treatment at 200℃

The annealing of nitrided samples was carried out up to 90 hours at 200℃ in an air atmosphere. This experiment was investigated for a fresh sample etched in a HCl:HF:H_2O solution and a sample that was irradiated with 2500 pulses. Figure 5(a) shows the In3*d* XPS spectra of an non-irradiated sample, as a function of the aging time. The In3*d* spectra of a nitrided sample are shown in Fig. 5(b). It can be seen that the intensity of In_2O_3 and $InPO_4$ peaks increases with the annealing time. A comparison between Fig. 5(a) and (b) shows that the oxidation process of the nitrided sample has been significantly slowed down.

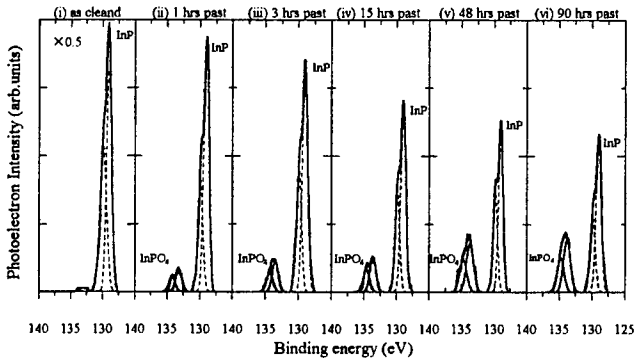


(a)

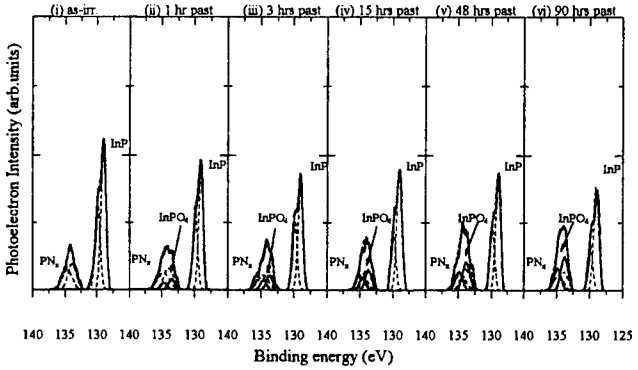


(b)

Fig. 5. In3*d* XPS spectra of heat-treated samples without nitridation (a), and following a 2500-pulse nitridation (b).



(a)



(b)

Fig. 6. XPS spectra of a heat-treated samples: (a) P2*p* XPS spectra without nitridation ; (b) P2p XPS spectra with nitridation.

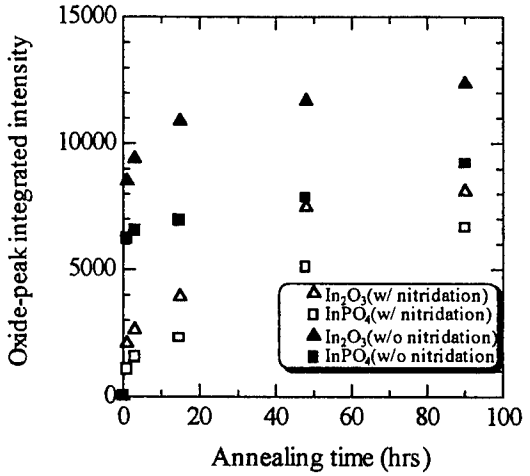


Fig. 7. Peak-integrated intensity of In_2O_3 and $InPO_4$ as a function of the annealing time.

Similarly, Fig. 6(a) and (b) show the P2*p* XPS spectra obtained for (a) non-irradiated and (b) irradiated samples, respectively. The dependence of In_2O_3 and $InPO_4$ integrated peak intensities obtained from the In3*d* scan is shown in Fig. 7. The integrated intensities of oxides sharply increase and saturate for longer annealing time. This result clearly indicates that the laser-induced nitridation of InP leads to a significant suppression of oxide formation at the surface of this material.

4. Conclusions

The nitridation of InP surface has been demonstrated with KrF excimer laser irradiation in NH_3. The XPS spectral analysis shows that the nitrogen content in the surface layer increases with the number of irradiated pulses. Near-stoichiometric InN and P_3N_5 are formed at the surface following the irradiation with 2500 pulses. An InN_x layer fabricated at the surface of InP significantly suppresses the oxidation of InP surface exposed to the air at 200℃.

References

[1] T. Hashizume, Appl. Phys. Lett. **75**, 615 (1999).
[2] G. Hollinger, E. Bergignat, J. Joseph, and Y. Robach, J. Vac. Sci. Technol. A. **3**, 2082 (1985).
[3] J. S. Pan, A. T. S. Wee, C. H. A. Huan, H. S. Tan and K. L. Tan, Appl. Phys. **29**, 2997 (1996).
[4] T. X. Zhao, H. Ji, Q. Liang, X. P. Wang, P. S. Xu, E. D. Lu, J. X. Wu, and C. C. Hsu, J. Vac. Sci. Technol. A. **13**, 1967 (1995).
[5] C. S. Sundararaman, H. Lafontaine, S. Poulin, A. Mouton, and J. F. Currie, J. Vac. Sci. Technol. B. **9**, 1433(1991).
[6] Yoon-Ha Jeong, Jae-Hak Lee, Young-Ho Bae, and Young-Tae Hong, Appl. Phys. Lett. **57**, 2680 (1990).

Molecular Dynamics Simulation of Ablation Process with Ultra-Short Pulsed Laser

Etsuji OHMURA*, Ichirou FUKUMOTO** and Isamu MIYAMOTO*

* *Department of Manufacturing Science, Graduate School of Engineering, Osaka University, 2-1 Yamada-oka, Suita, Osaka 565-0871, Japan*
E-mail: ohmura@mapse.eng.osaka-u.ac.jp
** *The Institute of Physical and Chemical Research, 2-1 Hirosawa, Wako, Saitama 351-0198, Japan*

Ultra-Short pulsed lasers are highly useful tools in the field of microfabrication. In microfabrication, the laser pulse usually is very short in the pico-second or subpico-second range; therefore, it is very difficult to observe the transient material processing phenomena experimentally. Over the years, the authors have conducted molecular dynamics (MD) simulation to study the ablation process with ultra-short pulsed laser irradiation. The MD method has been modified to simulate the laser ablation of metals by updating heat conduction effect by free electrons at each calculation time step. In this paper, a review of the modified MD simulations on ablation and shock phenomena for metal with pico-second laser irradiation is presented.

Keywords: computer simulation, molecular dynamics, ultrafast laser, evaporation, laser shock

1. Introduction

When ultrafast laser is irradiated to the material surface, the vicinity of the surface is melted and evaporated almost instantaneously. Evaporation particles are scattered and deposition is generated around the hole. On the other hand, shock wave propagates in the material and lattice defects, such as dislocations and vacancies are generated. **Figure 1** shows a schematic sketch of laser ablation and shock phenomena.

Femtosecond pulse laser was developed in 1981 by Fork et al. [1] and experimental studies on ultrafast laser ablation were started in about 1985, and many papers have been published especially from 1995. Downer et al. [2] obtained photographic images having 100 fs time resolution of a silicon (Si) surface undergoing melting and evaporation following intense excitation by an 80 fs laser pulse. Pronko et al. [3] studied the threshold fluence of ablation in gold (Au) as a function of pulse width from 10 ns to 100 fs. Stuart et al. [4] measured the pulse-width dependence of damage threshold for homogeneous and multiplayer dielectrics and gold-coated optics at 1053 and 526 nm for pulse durations ranging from 140 fs to 1 ns. Simon and Ihlemann [5] studied the ablation of submicron structures on copper (Cu) and Si by short ultraviolet laser pulses (0.5-50 ps, 248 nm). Momma et al. [6] investigated ablation of steel and Cu plates with thickness of 100 μm to 1 mm by Ti:sapphire laser irradiation of 0.2 to 5000 ps pulses in the intensity range of 10^9 to 5×10^{16} W/cm^2. Rosenfeld et al. [7] measured the timescale for the removal of four dielectric materials (a-SiO_2, c-SiO_2, c-Al_2O_3, c-MgO) from surface irradiated by 120 fs laser with a pulse energy of ca. 50 μJ. Shirk and Molian [8] compared ablation of diamond and CVD diamond with fs-laser and ns-lasers, and studied surface structure with Raman spectroscopy and the relationship between depth per pulse and fluence.

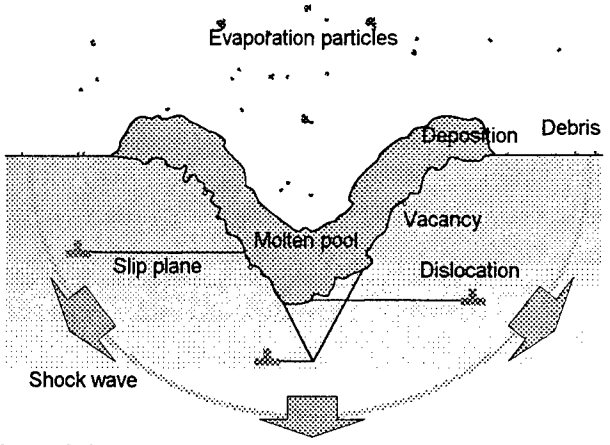


Fig. 1 Schematic sketch of laser ablation and shock phenomena.

On the other hand, Ohmura and Fukumoto started molecular dynamics (MD) simulation of laser ablation in 1993. Their first paper [9] was published in 1994. Laser shock phenomena were reported for the first time in 1995 [10]. In

First International Symposium on Laser Precision Microfabrication, Isamu Miyamoto, Koji Sugioka, Thomas W. Sigmon, Editors, Proceedings of SPIE Vol. 4088 (2000) © 2000 SPIE · 0277-786X/00/$15.00

1997, Ohmura and Fukumoto [11] developed a new MD method for metal, in which heat conduction by free electron is compensated at every time step of MD calculation. This method was named the modified molecular dynamics. And in 1998, three-dimensional MD simulation for Si was presented [12].

In this paper, we present a review of the modified MD simulations on ablation and shock phenomena for metal with ps-laser irradiation [13-16].

2. Evaporation process

In the simulation of ablation, 400 aluminum (Al) atoms per layer and 400 layers in depth, totaling 160,000 atoms were arranged in a square configuration. Snapshots of ablation process caused by laser irradiation of the fourth harmonics of Nd:YAG laser with Gaussian beam whose diameter is about 28 nm are shown in **Fig. 2**, where the average of power density and irradiation time are 5 GW/cm^2 and 6 ps, respectively. The beam diameter is defined here at which the intensity diminishes from its central value by a factor of e^2 which is shown by doted lines in these figures. Absolute value of moved distance of atoms from the initial array in the horizontal direction is shown by a gray scale.

In Fig. 2, the surface rises due to thermal expansion induced by the laser irradiation at first and many small voids are generated in the liquid phase (see Fig. 2 (a)). Then they become larger and larger, and adjacent voids combine each other, which develop into a relatively lager void (Fig. 2 (b)). Finally, the vicinity of surface ejects forming into a relatively large cluster (Figs. 2 (c) to (e)). Then, molten metal becomes spherical by surface tension and deposits around the hole (Fig. 2 (f)). Consequently, circumference of the hole rises higher. Slip planes are generated in the solid phase in the vicinity of surface.

Through these simulations, it was found that there are two types in ablation process, as shown in **Fig. 3**. One is explosive ablation (Fig. 3(a)) and the other is relatively calm ablation (Fig. 3(b)). Explosive ablation occurs when the pulse width is very short. Relatively calm ablation occurs when the pulse width is longer. Pulse width 10 ps is a guidepost of these difference. The photographs of evaporation of Cu with 5 and 50 ps laser irradiations taken by Simon et al. [5] are in good agreement with our results.

3. Evaporation particles

The velocity, size and energy of evaporation particles caused by laser irradiation of uniform intensity distribution were investigated. In this simulation, totaling 160,000 Al

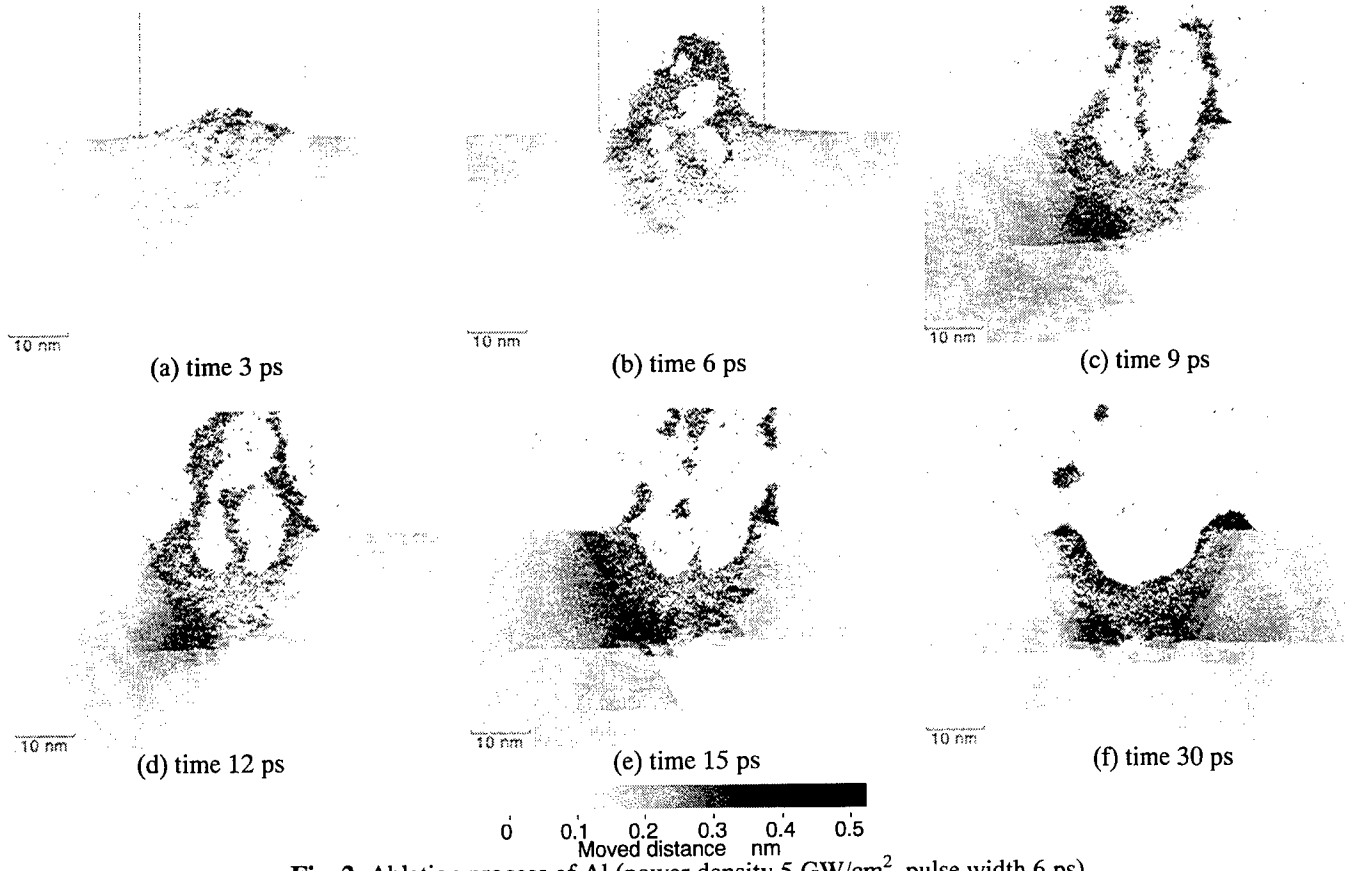
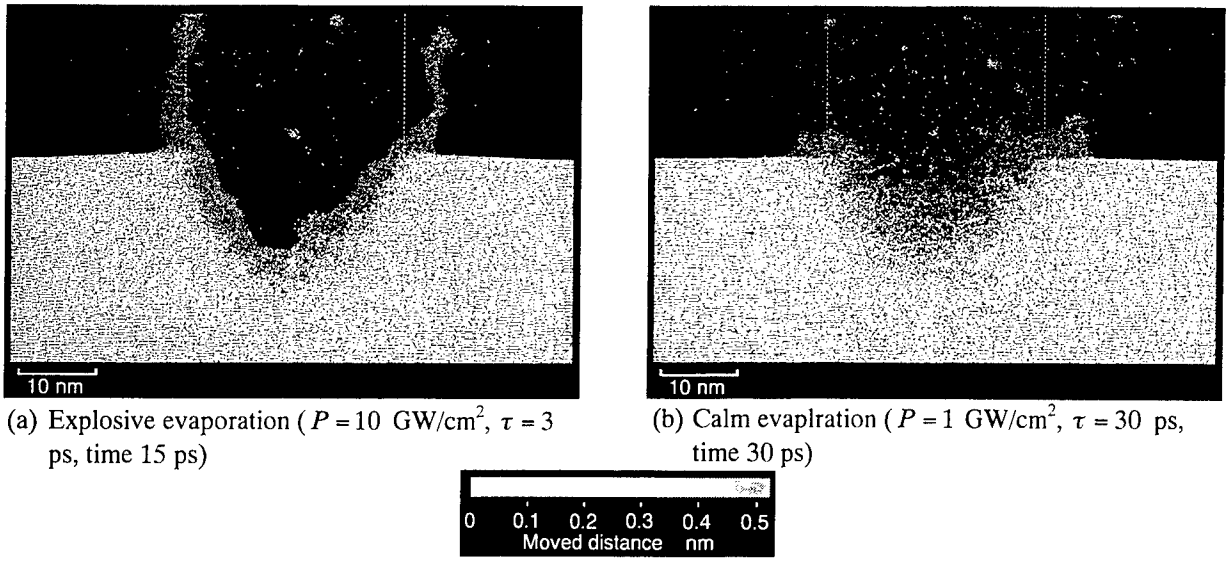


Fig. 2 Ablation process of Al (power density 5 GW/cm^2, pulse width 6 ps)



(a) Explosive evaporation ($P = 10$ GW/cm^2, $\tau = 3$ ps, time 15 ps)

(b) Calm evaplration ($P = 1$ GW/cm^2, $\tau = 30$ ps, time 30 ps)

Fig. 3 Two kinds in ablation process of Al with Gaussian beam (fluence 30 mJ/cm^2)

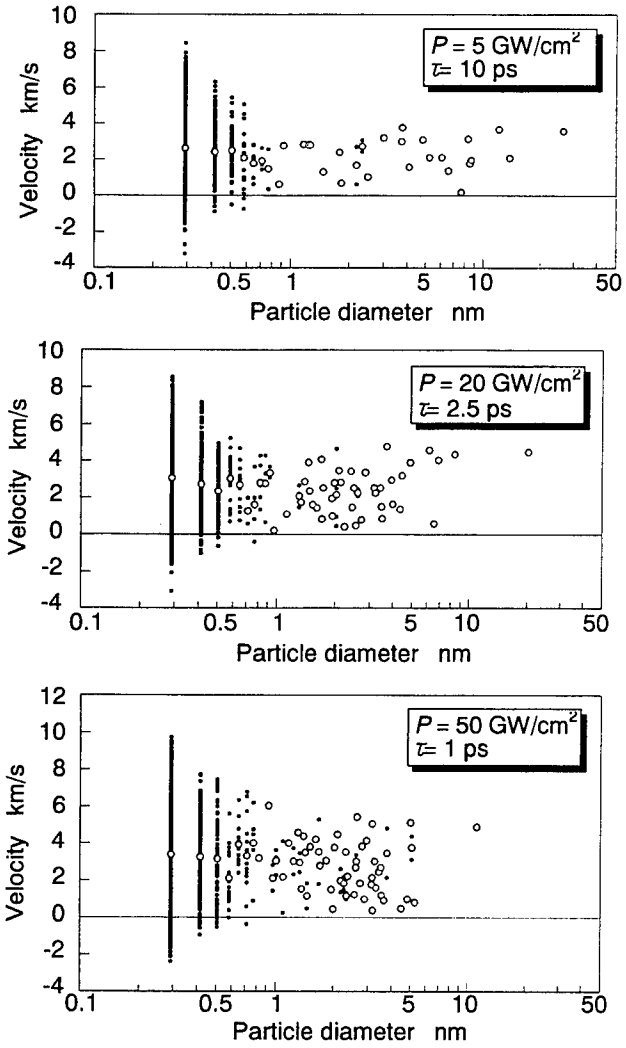


Fig. 4 Relationship between particle velocity and particle diameter (fluence 50 mJ/cm^2)

atoms were also arranged in a square configuration.

Figure 4 shows the relationship between particle velocity in the vertical direction and particle diameter for constant fluence ($F = 50$ mJ/cm^2). Closed circle shows the particle velocity and open circle shows the average velocity of each particle size. The diameter of most particles is less than 1 nm. And the particle velocity is several kilometers per second. As the power density is high, the velocity of evaporated particles becomes relatively large. The influence of power density on the average velocity of the relatively small particles whose size is not more than 1 nm is small, comparing with large particles. Because, small particles are easy to receive the influence of particle collision. Actually, much particles of smaller size come back to the substrate after evaporation, whose velocity is negative.

An example of the velocity distribution of evaporation atoms relating with the height from the initial surface is shown in **Fig. 5**. Velocity increase until the time 10 ps of

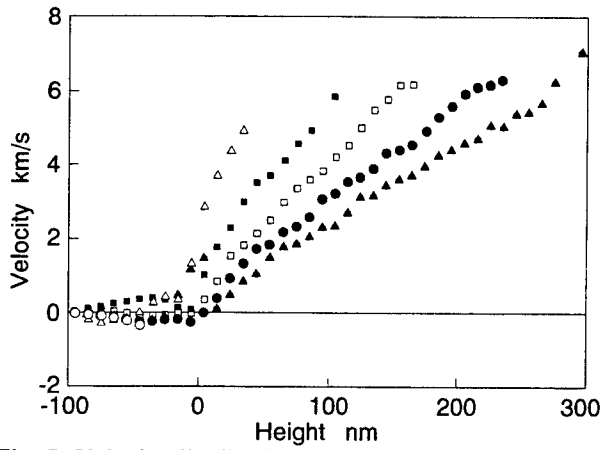


Fig. 5 Velocity distribution of evaporation atoms ($P = 5$ GW/cm^2, $\tau = 10$ ps)

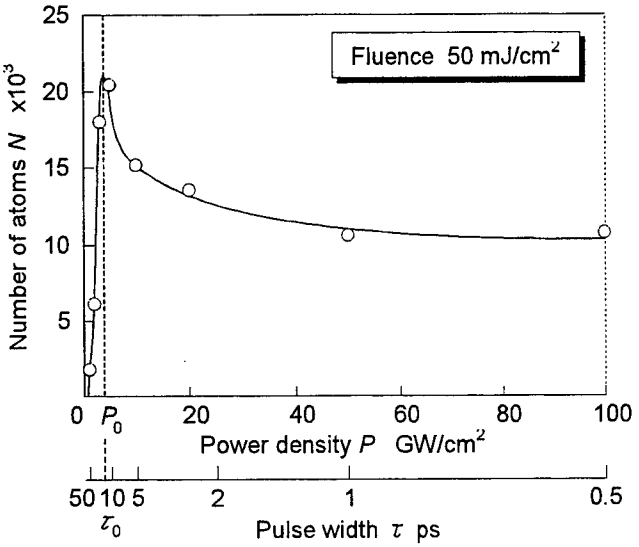


Fig. 6 Relationship between number of evaporated atoms and power density (fluence 50 mJ/cm^2)

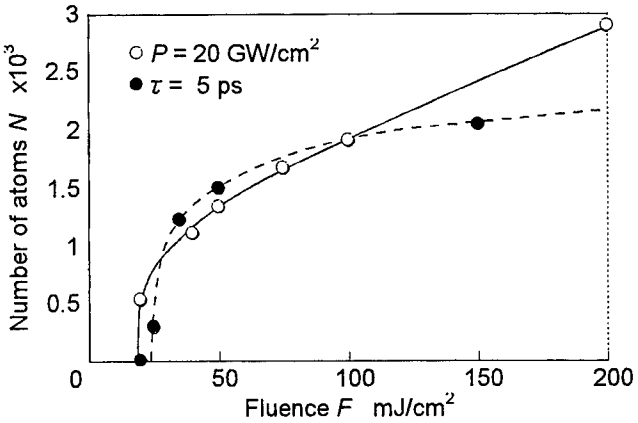


Fig. 7 Relationship between number of evaporated atoms and fluence

pulse end due to the laser absorption, but does not change remarkably after then and particles fly almost constant velocity. The average velocity of particles is proportional to the height from the surface, because particles with higher velocity fly to the higher level.

When the fluence is constant, relationship of the number of evaporated atoms and power density is shown in **Fig. 6**. We can see that there is an optimal irradiance of the laser pulse to evaporate a unit of atoms, that is power density P_0 and pulse width τ_0.

The relationship between number of evaporated atoms and fluence is shown in **Fig. 7**. When the power density is constant, number of evaporated atoms is almost proportional to the fluence, that is irradiation time. Strictly speaking, when the irradiation time is too long, interaction between

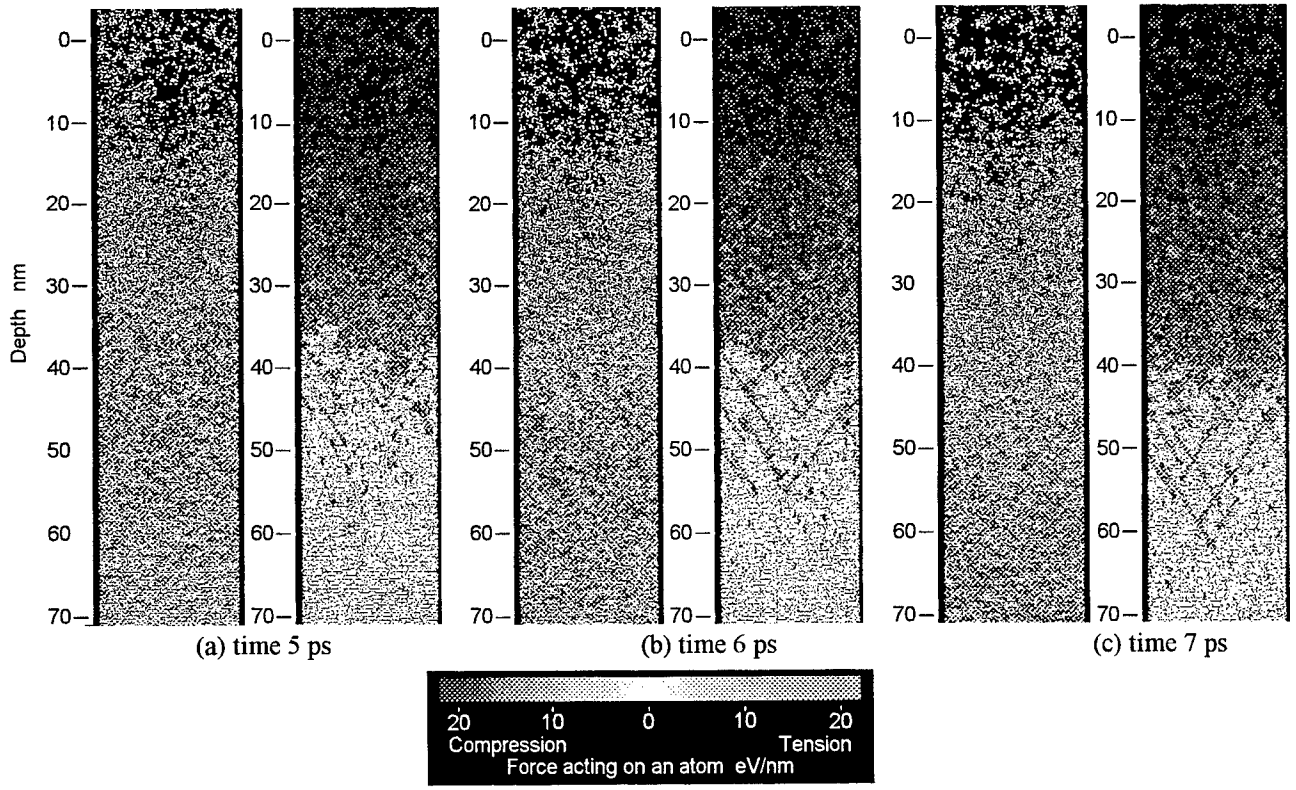
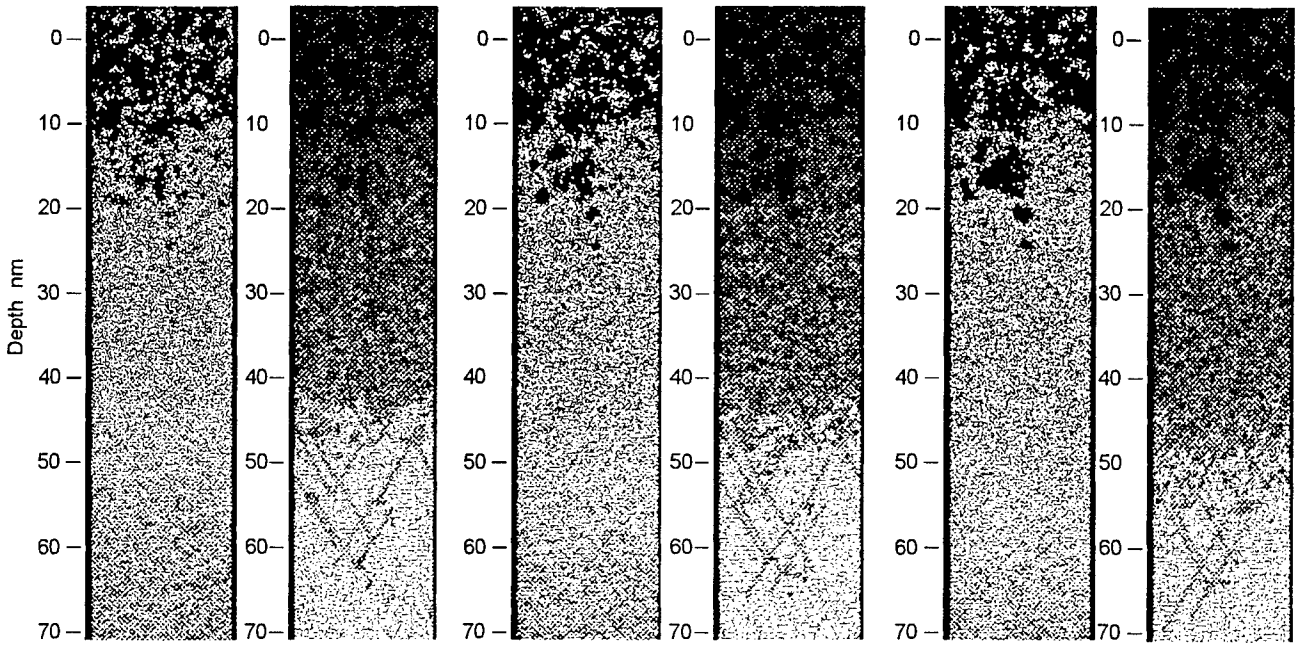


Fig. 8 Stress state of Al atoms (left of each figures) which is shown by a gray scale and disarray of the atom configuration (power density 30 GW/cm^2, pulse width 5 ps)



(d) time 8 ps (e) time 9 ps (f) time 10 ps

Fig. 8 Stress state of Al atoms (left of each figures) which is shown by a gray scale and disarray of the atom configuration (power density 30 GW/cm^2, pulse width 5 ps) (continued)

plasma and laser beam occurs, then the number of the evaporated atoms is not proportional to the fluence. There is a threshold fluence when the pulse width is very short. From this figure, the evaporation threshold fluence is about 20 mJ/cm^2.

When the pulse width is very short, the evaporation threshold fluence can be estimated by a simple model as follows: It is assumed that laser energy is absorbed exponentially. For ultrafast laser, evaporation occurs after laser irradiation stops. Then, evaporation energy is estimated by

$$P\left(1-e^{-\mu d}\right)\tau = \rho d l ,$$

that is, laser energy absorbed in the evaporation depth d. ρ is density and l is latent heat of evaporation. Therefore, evaporation threshold fluence can be estimated by the infinitesimal calculus

$$F \equiv P\tau = \frac{\rho d l}{1-e^{-\mu d}} \rightarrow \frac{\rho l}{\mu}, \quad d \rightarrow 0 .$$

For Al whose absorption coefficient μ is 1.50×10^8 1/m for wave length 266 nm, threshold fluence is 19.4 mJ/cm^2, which is almost equal to the result from Fig. 7.

4. Shock phenomena

In the simulation of shock phenomena, 60 Al atoms per layer and 400 layers in depth, totaling 24,000 atoms were arranged in a square configuration. The stress state of Al atoms and the atomic configuration are shown in **Fig. 8** every 1 ps from 5 ps to 10 ps, when power density is 30 GW/cm^2 and pulse width is 5 ps. The each left figure in Fig. 8 (a)-(f) shows the force acting on an atom in the depth direction which is shown by the gray scale. The each right figure shows the disarray of atomic configuration, that is, generation and movement of dislocations. Dislocations or nucleation of dislocations are represented by black dots and slip planes are shown by gray lines. We can see a shock wave propagating in the material from the each left figure. The propagation velocity of shock wave is equal to the velocity of elastic wave

Figure 9 shows the enlargement of the area from depth 50 nm to 70 nm in Fig. 8. Triangle shows the position of the peak intensity of the shock wave. According to the propagation of shock wave, dislocations are generated and moved in the depth direction. Dislocations moves instantaneously with the velocity of longitudinal wave, when the shock wave propagates. But the usual velocity of dislocation is less than the velocity of transverse wave as well known in the dislocation theory.

Acknowledgement

A part of this study was supported by Grants-in-Aid of Scientific Research from the Ministry of Education, Science and Culture of Japan in 1997, 1998 and 1999.

References

[1] R.L. Fork, B.I. Greene and C.V. Shank: Appl. Phys. Lett. 38, (1981) 671.

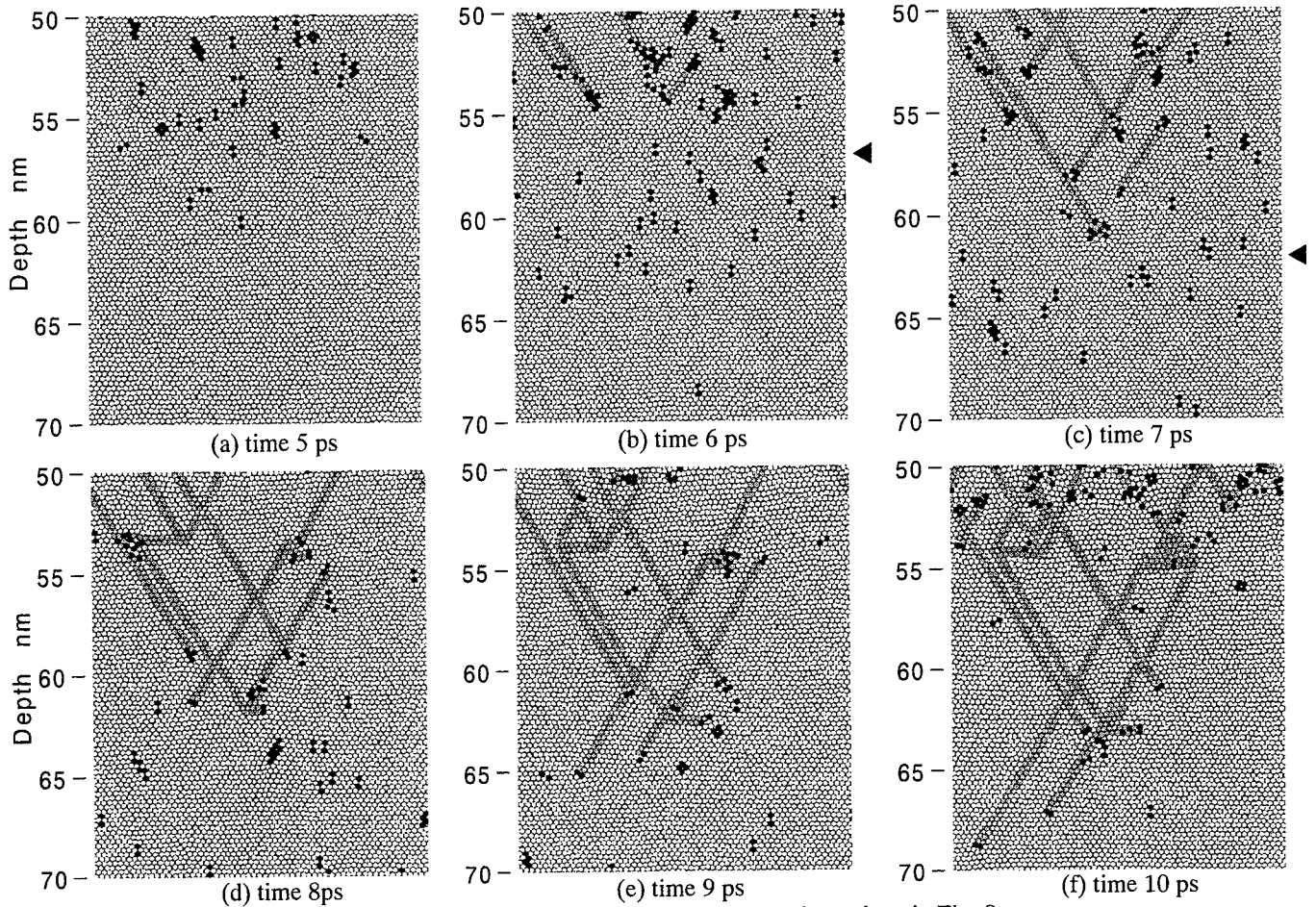


Fig. 9 Enlargement of area between 50 and 70 nm deep in Fig. 8

[2] M.C. Downer, R.L. Fork and C.V. Shank, J. Opt. Soc. Am. B, **2**, (1985) 595.

[3] P.P. Pronko, S.K. Dutta and D. Du: J. Appl. Phys., **78**, (1995) 6233.

[4] B.C. Stuart, M.D. Feit, S. Herman, A.M. Rubenchik, B.W. Shore and M.D. Perry: J. Opt. Soc. Am. B, **13**, (1996) 459.

[5] P. Simon and J. Ihlemann, Appl. Phys. A, **63**, (1996) 505.

[6] C. Momma, B.N. Chichkov, S. Nolte, F. von Alvensleben, A. Tünnermann, H. Welling and B. Wellegehausen: Optics Comm., **129**, (1996) 134.

[7] A. Rosenfeld, D. Ashkenasi, H. Varel, M. Wähmer and E.E.B. Campbell: Appl. Surf. Sci., **127-129**, (1998) 76.

[8] M.D. Shirk and P.A. Molian: J. Laser Appl., **10**, (1998) 64.

[9] E. Ohmura and I. Fukumoto: J. High Temperature Soc., **20**, (1994) 227.

[10] E. Ohmura and I. Fukumoto: Int. J. JSPE, **29**, (1995) 148.

[11] E. Ohmura and I. Fukumoto: Int. J. JSPE, **31**, (1997) 206.

[12] Y. Ishizaka, K. Watanabe, I. Fukumoto, E. Ohmura and I. Miyamoto: Proc. ICALEO'98, Sec. A, (1998) 55.

[13] I. Fukumoto, E. Ohmura and I. Miyamoto: Proc. ICALEO'97, Sec. C, (1997) 150.

[14] E. Ohmura and I. Fukumoto: Int. J. JSPE, **32**, (1998) 248

[15] E. Ohmura, I. Fukumoto and I. Miyamoto: Proc. ICALEO'98, Sec. A, (1998) 45.

[16] E. Ohmura, I. Fukumoto and I. Miyamoto: Proc. ICALEO'99, (1999) 219.

Study of Optical Emission of Plasmas in Ultraviolet and Infrared Laser Ablation of Graphite by Time-resolved Spectroscopy

Tatsuya Shinozaki*,**, Toshihiko Ooie*, Tetsuo Yano* and Masafumi Yoneda*

*Shikoku National Industrial Research Institute, AIST, MITI, 2217-14 Hayashi-cho, Takamatsu, Kagawa, 761-0395, Japan
E-mail shino@sniri.go.jp
**Japan Science and Technology Corporation, 4-1-8 Hon-machi, Kawaguchi, Saitama, 332-0012, Japan

The optical emission spectra of the plasma produced by infrared and ultraviolet laser ablation of graphite in a vacuum were observed. The fundamental output of an Nd: YAG laser was used as the infrared laser. The fourth harmonic output of an Nd: YAG laser and a KrF excimer laser were used as the ultraviolet lasers. The emission intensity of the ionic carbon as well as C_2 and C_3 from the plasma produced by the infrared laser were stronger than that produced by the UV lasers at the same fluences. The C_2 and C_3 emission intensities decreased rapidly with increasing the distance from the target. The emission intensity of atomic carbon at 247.8 nm from the plasma produced by the KrF excimer laser was much stronger than that produced by the other lasers at the same laser fluence, due to the wavelength of the KrF laser being so close to that of atomic carbon's emission line as to raise its electrical state.

Keywords: laser ablation, graphite, carbon plasma, time-resolved spectroscopy, Nd: YAG laser, KrF excimer laser

1. Introduction

Pulsed laser deposition (PLD) is one of the techniques for synthesizing thin films of sp^3 bonded materials such as CNx[1-5] and diamond-like carbon (DLC).[6-13] In order to increase the fraction of the sp^3 bonding in the DLC, UV lasers such as a fourth order harmonic output from an Nd: YAG laser, a KrF excimer laser and an ArF excimer laser were used.[6-9, 12] The fraction of sp^3 bonding of the DLC increased with increasing laser fluence.[9] This is because the C^+ with high kinetic energy in the carbon plume contributes to the sp^3 bonding.[9, 11] More high kinetic energy C^+ is produced by the UV lasers than by the IR and visible lasers at the same fluences. Clusters such as C_2 species do not contribute to the sp^3 bonding of the DLC. The fraction of the cluster increases with increasing laser wavelength.[14]

Influence of the character of the DLC or other films on the laser wavelength was investigated by many researchers.[9, 14] For synthesizing the films by PLD, it is very important to diagnose the ablation plume. There are a lot of diagnostic techniques.[15] However, influence of the carbon plume on the laser wavelength was mainly investigated by a time-of-flight mass spectrometry.[16, 17] By a TOFMS, cluster size and velocity distribution can be measured. However, the time- and spatially-variation of the electronic states of the ionic and atomic carbon and clusters can not be investigated by a TOFMS. They can be investigated by time- and spatially-resolved optical emission spectroscopy.[12,13] However, influence of the character of the carbon plume on the laser wavelength was not investigate.

In this study, the graphite was ablated by the KrF excimer laser (248 nm) and the Nd: YAG laser (266 nm and 1064 nm) to produce carbon plumes. We investigated the dependence of the species, the velocity and the electronic states of the atomic and ionic carbon in the plume on the laser wavelength and fluence by time-resolved spectroscopy.

2.Experiment

Figure 1 shows the experimental setup. A Q-switched Nd: YAG laser (Spectra Physics, GCR-170) and a KrF excimer laser (MPB, AQX-150) were used. The wavelengths of the Nd: YAG laser were set at 266 and 1064 nm, and output energy at 80 mJ and 140 mJ, respectively. The pulse widths were 20 ns and 5ns, respectively. The wavelength of the KrF excimer laser was 248 nm. The energy was set at 100 mJ and the pulse width was 18 ns. The repetition rates of these lasers were set at 10 Hz. Highly oriented pyrolytic graphite (TOYO TANSO, 99.99% purity) was inserted into a chamber, which was evacuated to

First International Symposium on Laser Precision Microfabrication, Isamu Miyamoto, Koji Sugioka, Thomas W. Sigmon, Editors, Proceedings of SPIE Vol. 4088 (2000) © 2000 SPIE · 0277-786X/00/$15.00

less than $5x10^{-7}$ Torr. The laser was focused on the graphite target surface through a 250-mm-focal length lens with an incident angle of 45°. The laser fluence was controlled by varying the beam spot size on the graphite target. The emission from the carbon plume was imaged on the entrance slit of a 0.25-meter spectrometer by a 150-mm-focal length lens. The width of the entrance slit was set at 50 μm. Spatial resolution along the target normal was better than 30 μm. The spectrometer with a gated 1024-chanel intensified charged-coupled device (ICCD) was used. The ICCD had an 8-ns resolution to resolve the temporal variations of the plume spectra. The spectrometer was equipped with 150 and 1200 lines/mm gratings blazed at 300 nm and 250 nm, respectively. Spectral resolution with 1500 and 120 lines/mm grating was more than 0.3 and 2 nm, respectively. The plume was observed at various distances from the target surface. All spectra were accumulated over 20 consecutive laser shots.

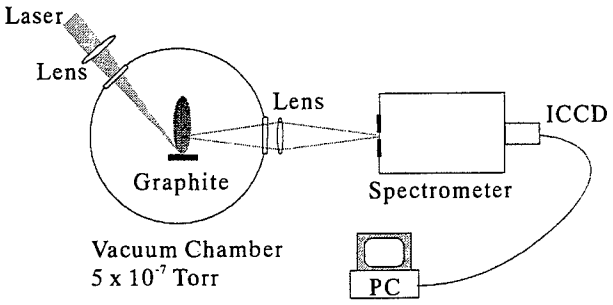


Fig. 1 Schematic diagram of Experimental setup

A signal from the power supply of the Nd: YAG laser was sent as a trigger to a digital delay generator. The signal produced by the delay generator, which was given a suitable delay, was then sent as a trigger to the gate pulse unit of the ICCD. In order to set the timing of the gate pulse of the ICCD, the laser waveform was observed using a photodiode detector. The signal from the gate pulse unit was also observed with a digital oscilloscope.

With the KrF excimer laser, the digital trigger generator gave a laser trigger signal and also the trigger signal for the gate pulse unit, which was suitably delayed from the laser pulse. The time of irradiating the graphite by the laser was defined as 0.

3. Results

In order to investigate the dependence of the spectra from the carbon plume on the wavelengths of the ablation lasers, the 1064-nm, 266-nm and 248-nm lasers irradiated the graphite target at the same fluences of 6 J/cm^2. Figure 2 shows the carbon plume emission spectra produced by the 1064-nm, 266-nm and 248-nm lasers at a distance of 2 mm. C_2 and C_3 emission intensity under the irradiation of the

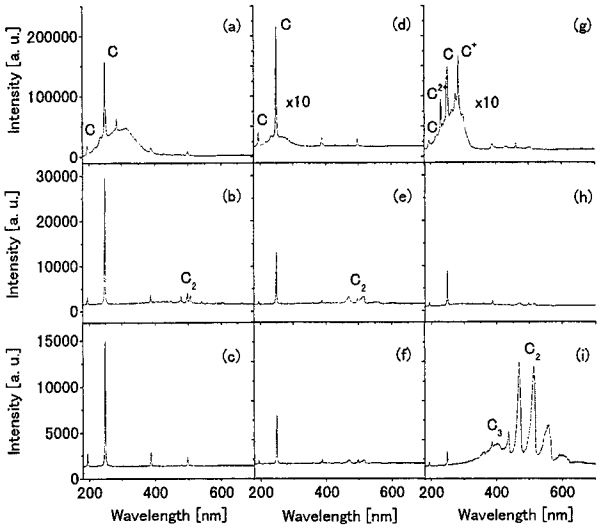


Fig. 2 Carbon plume emission spectra produced by (a, b and c) the 248-nm laser, (d, e and f) the 266-nm laser and (g, h and i) the 1064-nm laser at a distance of 2 mm from the target surface: the spectra were taken at (a, d and g) 50, (b, e and h) 100 and (c, f and i) 500 ns after the onset of the laser pulse. The laser fluences were set at 6 J/cm^2.

1064-nm laser was much stronger than that of the 266-nm and 248-nm lasers. The emission intensity from the ionic carbon was also strong. The C (247.9 nm and 193.1 nm) emission intensities under the irradiation of 248-nm laser were stronger than those of the other lasers.

We investigated the dependence of the spectra from the carbon plume on the wavelengths of the lasers when the fluences were increased. Beam quality of the 248-nm laser is not as good as that of the other lasers and the 248-nm laser beam can not be focused very small. Therefore, the fluence of the 248-nm laser was limited 16 J/cm^2. The optical emission spectrum from the carbon plumes produced by the 248-nm, 266-nm and 1064-nm lasers at a fluence of about 15 J/cm^2 was observed. At a fluence of 6 J/cm^2, C^+, C, C_2 and C_3 emissions could be observed. However, at a fluence of 15 J/cm^2 C_2 and C_3 emissions could not be observed. C, C^+ and C^{2+} emissions could be observed. The strongest C^+ emission was obtained at 426.7 nm ($4f^2F^0$ γ $3d^2D$) by the IR and UV lasers. C^+ emissions at 392.1 nm ($3p^2P^0$ γ $3d^2D$) and 283.8 nm ($2p^2S$ γ $3p^2P^0$) were also strong. The strongest C^{2+} emission was obtained at 229.8 nm ($2p^1P^0$ γ $2p^1D$) with the IR and UV lasers. C^{2+} emissions at 216.4 nm ($3d^1D$ γ $4f^1P^0$) and 465.0 nm ($3s^3S$ γ $3p^3P^0$) were also strong. At fluences of about 15 J/cm^2, the C (247.9 and 193.1 nm) emissions under the irradiation of the 248-nm laser were as strong as those of the 266-nm and 1064-nm lasers.

The temporal variations of the emission intensity of C^+ (283.8 nm), which contributes to sp^3 bonding, at the various

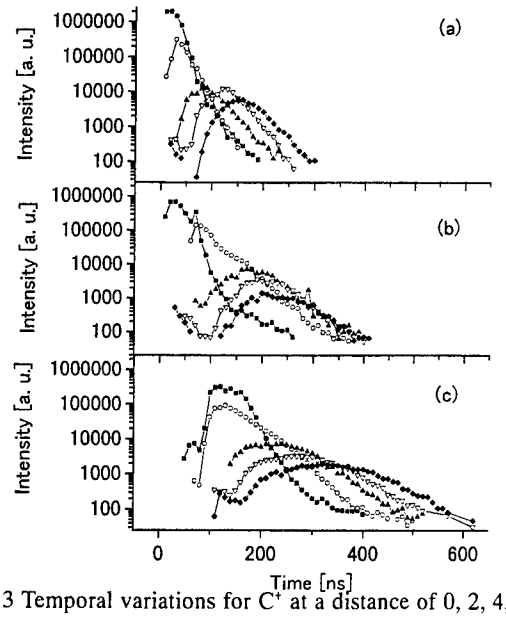


Fig. 3 Temporal variations for C^+ at a distance of 0, 2, 4, 6 and 8 mm from the target surface (a) The 248-nm laser was used at a fluence of 16 J/cm^2. (b) The 266-nm laser was used at a fluence of 14 J/cm^2. (c) The 1064-nm laser was used at a fluence of 19 J/cm^2.

distances from the target are shown in Fig. 3. Near the target surface, the observed emission area was only half as large as at the other points. (Data not shown in Fig. 3) At a distance of 8 mm from the target, the emission intensity was less than 10% of that near the target. Usually, the distance between the target and the substrate under the PLD condition is much longer than 8 mm. Therefore, the most excited ionic and atomic carbon relax to their ground states before deposition.

Table. 1 Most probable velocity of C^+ produced by various lasers.

Laser	Fluence (J/cm^2)	Velocity (10^4 m/s)
Nd: YAG (1064 nm)	125	4.0
	19	3.8
Nd: YAG (266 nm)	30	6.2
	14	6.7
KrF excimer (248 nm)	16	8.6

The most probable C^+ velocities derived by the temporal variations of the emission intensity are shown in Table 1. The C^+ velocity is highly dependent upon the laser wavelength and slightly dependent on the fluence. The C^+ velocity produced by the 248-nm laser at a fluence of 16 J/cm^2 was twice as fast as that by the 1064-nm laser at a fluence of 125 J/cm^2.

4. Discussion

Laser wavelength has various influences on the character of the carbon plume: e.g. species, velocity, temperature and electrical state.

Firstly, the laser penetration depth of the graphite depends on the laser wavelength. The absorption coefficient of the graphite increases with decreasing laser wavelength. That is, the penetration depth using the IR laser is deeper than that using UV laser. Therefore, the amount of graphite removed increases and the initial temperature of the plume decreases with increasing laser wavelength. The plume velocity depends on the initial plume temperature.[15] Therefore, the velocity decreases with increasing laser wavelength.

Secondly, the absorption coefficient of the laser by the carbon plume depends on the laser wavelength. After producing the plume the laser is absorbed by the plume because a nanosecond laser pulse width is longer than the time required to produce the plume. The laser is mainly absorbed by the plume due to inverse-Bremsstrahlung. The absorption coefficient depends strongly upon the laser wavelength.[15] For any given plume condition, the coefficient is proportional to the third power of the laser wavelength. Therefore, the plume temperature increased and the ionization progressed using the 1064-nm laser in spite of the low initial plume temperature. Moreover, the pulse width of the 1064-nm laser was 20 ns, which is four times as long as that of the 266-nm laser. The latter part of the laser pulse was absorbed. Although ionic carbon contributes to sp^3 bonding, the most probable velocity of C^+ is slow with the 1064-nm laser. Therefore, it is difficult to obtain the high fraction sp^3-bonded DLC produced by the 1064-nm laser.

Lastly, there is a special case, when the laser wavelength coincides with the electronic transitions of the atomic or ionic carbon.[7] In this case, one species in the carbon particularly absorbs the laser light. If the atomic carbon transition is coincident with a laser wavelength, the carbon will be ionized or the concentration of only one electrical level will increase. A 248-nm (KrF excimer) laser and a 193-nm (ArF excimer) laser satisfy this condition. The wavelength of the 193 nm is very close to the transition of $3s^1P^0$ γ $2p^{21}D$ (193.1 nm). The wavelength of the 248-nm laser is very close to the transition of $3s^1P^0$ γ $2p^{21}S$ (247.9 nm). Therefore, the concentration of $3s^1P^0$ was high and the emission intensity of transitions of $3s^1P^0$ γ $2p^{21}D$ and $2p^{21}S$ was strong at a fluence of 6 J/cm^2. An Nd: YAG laser (1064, 532, 355 and 266 nm) does not satisfy this condition. In our experiment, the 247.9-nm and 193.1-nm emission intensities were strong when using the 248-nm laser. At a

fluence of 17 J/cm^2, however, this emission intensity became lower than that at a fluence of 6 J/cm^2 because the atomic carbon was excited to the upper level and ionized. Although difference in wavelength between the 248-nm laser and the 266-nm laser is small, the 248-nm laser is superior to 266-nm laser for synthesizing the DLC film.

5. Summary

We investigated the influence of the wavelength on the laser ablation of graphite by means of observing the emission spectra of the carbon plume. The 1064-nm, 266-nm and 248-nm lasers were used. When using the 1064-nm laser, not only the emission from C_2 but also that from the ionic carbon became strong, due to the carbon plume absorbing the laser light by inverse-Bremstrahlung absorption. Therefore, the atomic carbon was ionized.

In PLD, the distance between target and substrate is so long as to relax to ground state most of the atomic and ionic carbon. In order to excite the electric state for sp^3 bonding, collision with the substrate is necessary. The C^+ velocity is important for sp^3 bonding. The C^+ velocity decreased with increasing laser wavelength at the same fluence. The velocity increased slightly with increasing laser fluence.
The wavelengths of the 248-nm laser and the $3s^1P^0$ γ $2p^21S$ transition of the atomic carbon (247.9 nm) are very close. Therefore, the emission intensity from the $3s^1P^0$ γ $2p^21S$ and $2p^21D$ transition was strong at a fluence of 6 J/cm^2. Moreover, the ionization was progressed. Therefore, the 248-nm laser is most suitable for synthesizing the DLC among three lasers (248 nm, 266 nm and 1064nm).

References

[1] C. Niu, Y. Z. Liu and M. Lieber: Science **261** (1993) 334.

[2] Z.-M. Ren, Y.-C. Du, Z.-F. Ying, Y.- X. Qiu, X.-X. Xiong, J.-D. Wu and F.-M. Li: Appl. Phys. Lett. **65** (1994) 1361.

[3] Y. F. Lu, Z. M. Ren, W. D. Somg and D. S. H. Chan: J. Appl. Phys. **84** (1998) 2133.

[4] Y. F. Lu, Z. M. Ren, T. C. Chong, B. A. Cheong, S. I. Pang, J. P. Wang and K. Li: J. Appl. Phys. **86** (1998) 4954.

[5] Y. Aoi, K. Ono and E. Kamijo: J. Appl. Phys. **86** (1999) 2318.

[6] A. A. Puretzky, D. B. Geohegan, G. E. Jellison Jr. and M. M. McGibson: Mat. Res. Soc. Symp. Proc. **388** (1995) 145.

[7] D. B. Geohegan and A. A. Puretzky: Mat. Res. Soc. Symp. Proc. **397** (1996) 55.

[8] A. A. Puretzky, D. B. Geohegan, G. E. Jellison Jr. and M .M. McGibbon: Appl. Surf. Sci. **96-98** (1996) 859.

[9] K. Yamamoto, Y. Koga, S. Fujiwara, F. Kokai and R. B. Heiman: Appl. Phys. A **66**, (1998) 115.

[10] K. Yamamoto, Y. Koga, S. Fujiwara and F. Kokai: Jpn. J. Appl. Phys. **36** (1997) L1333.

[11] V. I. Merkulov, D. H. Lowndes, G. E. Jellison Jr., A. A. Puretzky and D. B. Geohegan: Appl. Phys. Lett. **73**, (1998) 2591.

[12] Y. Yamagata, A. Sharma, J. Narayan and R. M. Mayo, J. W. Newman, and K. Ebihara: J. Appl. Phys. **86**, (1999) 4154.

[13] J. J. Chang, W. McLean, E. P. Dragon and B. E. Warner: *Proc. SPIE Conf. Laser Applications in Microelectronic and Optoelectronic Manufacturing* IV, San Jose, 1999 p. 71.

[14] L. Chen: *Pulsed Laser Deposition of Thin Films*, ed. D. B. Chrisey and G. K. Hubler (John Wiley & Sons, Inc., New York, 1994) Chap. 6, p.182.

[15] D. B. Geohegan: *Pulsed Laser Deposition of Thin Films*, ed. D. B. Chrisey and G. K. Hubler (John Wiley & Sons, Inc., New York, 1994) Chap. 5, p.119.

[16] J. J. Gaumet, A. Wakisaka, Y. Shimizu and Y. Tamori: J. Chem. Soc. Faraday Trans. **89** (1993) 1667.

[17] F. Kokai and Y. Koga: Nucl. Instrum. & Methods B **121** (1997) 387.

[18] W. L. Wiese, J. R. Fuhr and T. M. Deters: *Atomic Transition Probabilities of Carbon, Nitrogen, and Oxygen* (American Institute of Physics New York, 1996) p. 1.

Effects of Repetitive Irradiation in Laser Ablation of Aluminum in Gases Observed by Photoacoustic and Imaging Techniques

Yoshiro ITO*[$], Isamu OGURO*, and Susumu NAKAMURA**

** Department of Mechanical Engineering, Nagaoka University of Technology, 1603-1, Kamitomioka, Nagaoka, Niigata, 940-2188, JAPAN*
[$]Corresponding Author: E-mail: itoy@nagaokaut.ac.jp
*** Department of Electrical Engineering, Nagaoka College of Technology, 888, Nishikatakai, Nagaoka, Niigata, 940-8532, JAPAN*

Effects of irradiating number of pulses of Nd:YAG laser in laser ablation of metals in air have been studied by both photoacoustic and fast-imaging techniques. Photoacoustic detection technique using piezoelectric polymer film revealed the change of coupling among laser radiation, ablated matter, plasma and the target as a function of the laser fluence. Nanosecond imaging technique, where the second harmonic radiation from the same laser was used as illuminating light pulse, showed surface phenomena during and immediately after the ablating laser pulse. Photoacoustic signal intensity as a function of laser fluence was measured at constant pulse energy. It was constant at low fluence, started to increase with fluence at certain threshold, reached a peak and then decreased gradually with increasing fluence. Shapes of the functions were similar but the threshold fluence and the fluence at the peak increased with irradiating pulse number. Imaging observation revealed that a surface layer and/or adsorbed contaminants was ablated by initial few pulses and that material ablation occurred at higher fluence than the surface layer. Ablation of the surface layer caused shock wave and terminated less than 10 pulses while aluminum ablation was accompanied with bright plume and shock wave and affected only slightly by preceding pulses.

Keywords: Laser ablation, Photoacoustic signal, Imaging, Laser pulse number, Surface layer

1. Introduction

Laser ablation process has been applied in precision micromachining of metals, polymers and ceramics. These machining are usually carried out in air or in gas environment by irradiating multiple number of pulses.

We have studied about nanosecond Nd:YAG laser ablation process of metals and ceramics by both photoacoustic detection technique [1-4] and fast imaging technique with nanosecond time resolution [5,6]. Photoacoustic detection technique using piezoelectric polymer film detects acoustic wave propagates into the target and reveal the change of coupling among laser radiation, ablated matter, plasma and the target as a function of the laser fluence. Nanosecond imaging technique, where the second harmonic radiation from the same laser is used as illuminating light pulse, observes surface phenomena including laser-induced plume and surface change.

In this paper, effects of irradiating number of pulses of Nd:YAG laser in laser ablation of aluminum target in air have been studied by both photoacoustic and fast-imaging techniques. Photoacoustic signal intensity as a function of laser fluence was measured at constant pulse energy, i.e., the fluence was varied by changing the laser spot size. It was constant at low fluence, started to increase with fluence at certain threshold, reached a peak and then decreased gradually with increasing fluence. Shapes of the functions were similar but the threshold fluence and the fluence at the peak increased with irradiating pulse number. Imaging observation revealed that a surface layer and/or adsorbed contaminants was ablated by initial few pulses and that material ablation occurred at higher fluence than the surface

First International Symposium on Laser Precision Microfabrication, Isamu Miyamoto, Koji Sugioka, Thomas W. Sigmon, Editors, Proceedings of SPIE Vol. 4088 (2000) © 2000 SPIE · 0277-786X/00/$15.00

layer.

2. Experimental

Detail of the experimental procedure has been given elsewhere [1-6] and only an outline will be described here.

A Q-switched Nd:YAG laser with a second harmonic generator/separator unit was used. Pulse width of the laser was 8 ns (FWHM).

Commercially available aluminum plates of 1mm thick were mechanically polished and used as targets.

The fundamental light was focused onto the target by a plano-convex lens and hit the surface perpendicularly. Distance between the target and lens was varied to change spot size of the beam for adjusting the laser fluence while the pulse energy kept constant.

2.1 Photoacoustic detection [1-4].

The photoacoustic method has been successfully applied to determine the damage thresholds caused by laser irradiation in some materials [7]. We have used a thin piezoelectric film (polyvinilydene fluoride, Kureha Chemical Industry Co., KF piezofilm) of 40 μm thickness. A photoacoustic signal (PAS) was recorded by a digital oscilloscope in pre-trigger mode and then transferred to a personal computer for further processing.

2.2 Nanosecond time-resolved imaging [5, 6].

The fundamental light (1064nm) was used as the ablation beam (Pump Beam) and the second harmonic light (532nm) was used as illuminating light (Probe Beam). The second harmonic light passed through optical delay lines was impinged to the target from a tilted direction.

The ablation phenomenon was taken by the ICCD camera with a gated image intensifier, transferred to a personal computer and then treated by an image-processing program. A band pass filter of 532 nm and a ND filter were placed in front of the camera. The delay time was defined as interval between the rise of irradiated laser pulse detected by a photodiode and the end of the camera gate signal.

The system described above was used for delay times of 5 to 40 ns. For delay times longer than 45 ns, 532 nm light from another Q-switched Nd:YAG laser was used as illumination source and the delay time between two laser pulses was controlled by a digital delay generator.

Geometry of observation is as follows: The second harmonic light passed through the variable optical delay line was expanded by a beam expander and illuminated the irradiated spot along the direction intersecting 60 degrees from the normal direction. Observation direction was at the opposite half plane with an angle 30 degrees from the normal.

3. Results and Discussion

3.1 Photoacoustic signal intensity

Photoacoustic signal (PAS) intensity as a function of laser fluence was measured at constant pulse energy. It was constant at low fluence, started to increase with fluence at a certain threshold, reached a peak and then decreased gradually with increasing fluence. Figure 1 shows the PAS intensity as a function of laser fluence obtained for the first (1st) and hundredth (100th) pulse, respectively. To observe at lower fluence, the results obtained at pulse energy of 40

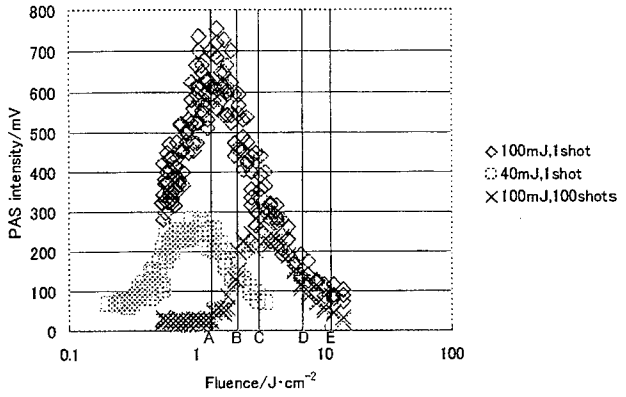


Figure 1. Photoacoustic signal intensity as a function of laser fluence at the first and the hundredth pulse.

mJ and 100 mJ are shown for the first pulse.

The results obtained for the 1st pulse irradiation showed smaller threshold energy fluence and reached the maximum at smaller fluence than those for the 100th pulse irradiation. The signal intensity was larger for 1 pulse than for 100 pulses at all fluence, even though the differences became small at higher fluence region.

Figure 2 shows the PAS intensity at several selected fluences shown in figure 1 as functions of pulse number. At the fluence of 1.3 Jcm^{-2}, **A** in figure 1 where PAS for the 1st pulse reached the maximum and that for the 100th pulse started to increase, the intensity rapidly decreased with pulse numbers less than 10 and remained a small value with further increase in irradiated pulse number. At the fluence of 3 Jcm^{-2}, **C** in figure 1 where the PAS for 100th pulse had the maximum value, the initial decrease of PAS intensity was small and finished within 5 pulses and kept its large values, or showed a slight increase, after that. At higher fluence than **C**, the initial decrease of PAS intensity was small and ended within 5 pulses or so.

We think this initial rapid decrease of the PAS intensity represents the ablation of oxides or other surface layers. Surface of aluminum metal in atmosphere is not metallic but is layers of aluminum oxides and/or hydrides with many adsorbed molecules. We polished the sample surface mechanically only a day before experiment and the samples were cleaned by an ultrasonic cleaner with acetone. But

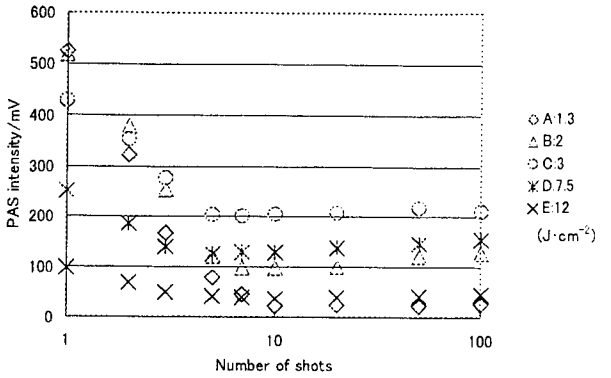


Figure 2. PAS intensity at several selected fluences indicated in figure 1 as functions of pulse number.

we hardly expect that the surface would be free from such oxides and surface contaminant layers. For pulse numbers more than 5 to 10 pulses, the PAS intensity remained nearly constant, or somewhat increased, with further increase in pulse number. These constant intensities should represent the fluence dependence of the ablation of bulk aluminum metal.

These results suggest that the ablation of the surface contaminant layers occur at lower fluence than that of aluminum metal. Its threshold fluence was about 0.3 Jcm^{-2} and most efficient at 1.3 Jcm^{-2}. The threshold of the metal aluminum ablation happened to be nearly the same to this maximum value of 1.3 Jcm^{-2}.

Further decrease of the PAS at higher fluence region might be due to the decrease in irradiated spot area, because, in our experiments, the pulse energy was kept constant and the fluence value was adjusted by changing the irradiated area. Indeed, when we represented the results as specific PAS intensity , i.e., the intensity divided by spot area, it was nearly constant at fluence higher than **A** or **C**.

3.2 Time-resolved imaging

We carried out the time-resolved imaging measurement for the 1st, 5th, 10th and 100th pulse at several fluences. An example of the image obtained is shown in figure 3. A black-and-white double line in the figure shows the front of expanding shock wave accompanied with laser ablation plume. Change of the surface at laser irradiated area is also seen in the figure. The results of the imaging observation are summarized as follows:

(1) At low fluence of 0.85 Jcm^{-2}, an image of shock wave was observed for the 1st pulse but not for the 100th pulse. The irradiated area turned to black after the 1st pulse and it partly became brighter after 100th pulse.

(2) Darkening of irradiated area was observed at all fluence after the 1st pulse but it became brighter after less pulse number as the fluence increased.

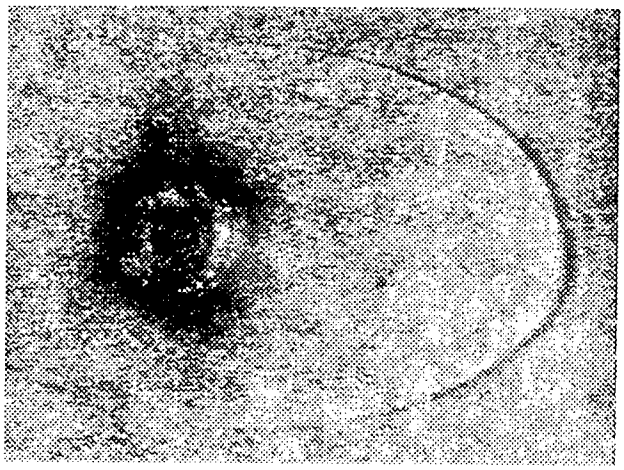


Figure 3. Typical image obtained by our imaging measurement for aluminum target irradiated in air at the 100th pulse. Delay time is 500 ns and laser fluence is 7.5J/cm^{-2}.

(3) Bright image of plasma appeared partly in irradiated area at **A** of 1.3 Jcm^{-2} where spatial distribution of laser intensity was high. The plasma covered the whole area at fluence higher than **C** of 3 Jcm^{-2}.

(4) At fluence higher than **A**, growth of a shock wave was observed at all pulse numbers but its growth speed depended on pulse numbers, especially at lower fluence.

(5) Much higher fluence, higher than **D** of 7.5 Jcm^{-2}, we observed a jet-like plasma formation **[5,6]** and we saw little difference in time evolution of it due to pulse numbers.

Figure 4 shows the plots of shock wave front height with time at **A** and **D**. This shock wave image represents the growth of laser-induced plume **[5]**. At **A**, the speed of shock wave was faster for the 1st pulse than that for the 100th pulse. Lower the fluence, the difference were larger. At **D**, there was little difference between the two cases. Higher fluence than **D**, time evolution of the shock wave was unchanged with irradiated pulse numbers.

3.3 Ablation of surface layers and bulk metal

The result (1) suggested that selective ablation of surface layer occurred and no ablation of aluminum metal did at this low fluence. This is in good agreement with the results of the PAS measurement. The other results also support our assumption that the initial decrease of PAS shows the ablation of surface layers and residual signals correspond to metal ablation process.

At fluence higher than **C**, there was only a little effects due to irradiated pulse numbers. As the fluence becomes high, the contribution of ablation of surface layers becomes less, because enough amount of energy to ablate both the surface layers and the metal under them would be supplied by a pulse.

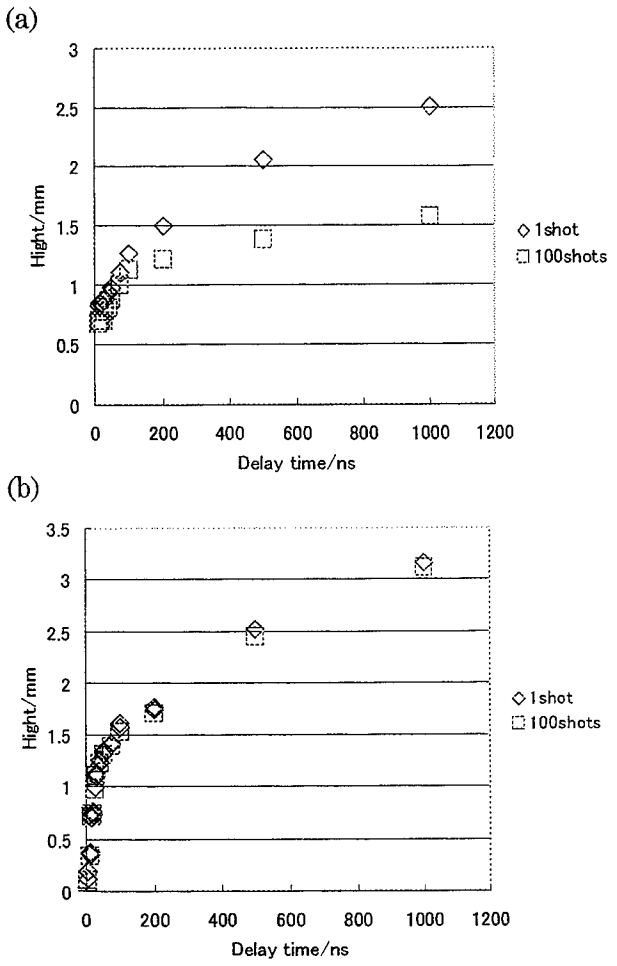


Figure 4. Plot of the height of shock wave front with time for the first and the hundredth pulse at fluence (a) **A** of 1.3 Jcm^{-2} and (b) **D** of 7.5 Jcm^{-2}. Target is aluminum and is irradiated in air.

The darkening of laser irradiated area may due to photo-anodizing of aluminum but is not clear at present.

The photoacoustic signal represents coupling between incident laser light and target material. At low light intensities, it corresponds to the amount of absorbed energy, or part of absorbed energy converted to thermal energy. At higher light intensity as in our case, there should be large contribution from reaction of the ejected mass to the PAS.

4. Conclusion

Effects of repetitive pulse number in laser ablation of aluminum have been studied by photoacoustic and imaging techniques. PAS intensities varied with fluence and shapes of the variation were similar but the threshold fluence and the fluence at the peak increased with irradiating pulse number. Imaging observation revealed that a surface layer and/or adsorbed contaminants was ablated by initial few pulses and only a week shock wave was generated. Ablation of bulk material occurred at higher fluence than the surface layer. Aluminum ablation was accompanied with bright plume and shock wave and affected only slightly by preceding pulses.

Acknowledgments

This work is partly supported by Grants-in-Aid for Scientific Research from the Ministry of Education, Science, Sports and Culture of Japan (11650736, 11305053 and 10558082).

References

[1] Ito, S. Nakamura, and F. Hirakawa, Photoacoustic measurement of the energy absorption of pulsed Nd:YAG laser at Cu and Al surfaces. *Photoacoustic and Photothermal Phenomena, III, Springer Series in Optical Sciences.* Ed. D. Bicanic, Springer-Verlag, Berlin, Heidelberg, pp. 702-704, 1992

[2] Y. Ito, M. Kametani, J. Imai and S. Nakamura, Interaction between intense Nd:YAG laser pulse and a metal. *Beam-Solid Interactions-Fundamentals and Applications*. Editors, M. A. Nastasi, N. Herbots, L.R. Harriott, R.S. Averback, MRS Proc. **279**, MRS, Pittsburgh Pennsylvania, pp. 743-748, 1993

[3] S. Nakamura, J. Imai, and Y. Ito, Photoacoustic measurement of energy absorption in pulsed Nd:YAG laser processing. Proceedings of ICALEO'93, LIA Vol.**77**, pp. 145-151, 1994

[4] Y. Ito, M. Murayama, Y. Fukuzawa, and S. Nakamura, Interaction of high power laser pulses on aluminum measured by photoacoustic methods: Effects of wavelength. Proceedings of ICALEO'97, LIA Vol. **83**, Part 1, Sec. A, pp. 131-138, 1997

[5] Y. Ito, T. Shimizu, I. Oguro, and S. Kijima, Jet-Like Plasma Formation in Laser Ablation of Metals Observed by Nanosecond Imaging Technique in Gases. Proceedings of ICALEO'99, LIA Vol. **87**, Part 2, Sec. E, pp. 61-70, 2000

[6] Y. Ito, I. Oguro, Y. Fukuzawa and S. Nakamura, Nanosecond laser ablation of metals in gases observed by photoacoustic and imaging techniques Proceedings of High Power Laser Ablation 2000, Proc. of SPIE, **4065**, (in press)

[7] E. Matthias, R. W. Dreyfus, From laser induced desorption to surface damage , in *Photoacoustic, Photothermal and Photochemical Processes at Surfaces and in Thin Films*, edited by P. Hess, Springer-Verlag, Berlin, pp. 89-128, 1989 and references therein.

Ultra-Short Pulsed Laser Microstructuring of Diamond

Michael SHIRK*, Pal MOLIAN*, Cai WANG**, Kai Ho**, and Ajay MALSHE***

*Mechanical Engineering Department, ** Physics Department,
Iowa State University, Ames, IA 50011, USA, E-mail:molian@iastate.edu
***Mechanical Engineering Department, University of Arkansas, Fayetteville, AR 72708, USA

Precision microfabrication of diamond has many applications in the fields of microelectronics and cutting tools. In this work, an ultra-short pulsed Ti: Sapphire laser was used to perform patterning, hole drilling, and scribing of synthetic and CVD diamonds. Scanning electron microscopy, atomic force microscopy, profilometry, and Raman spectroscopy were employed to characterize the microstructures. A tight-binding molecular dynamics (TBMD) model was used to investigate atomic movements during ablation and predict thresholds for ablation. The ultra-short pulsed laser generated holes and grooves that were nearly perfect with smooth edges, little collateral thermal damage and recast layer. The most exciting observation was the absence of graphite residue that always occurs in the longer-pulsed laser machining. The ablation threshold for ultra-short pulsed laser was two orders of magnitude lower than that of longer-pulsed laser. Finite-difference thermal modeling showed that ultra-short pulses raised the electron temperatures of diamond in excess of 100,000 K due to multiphoton absorption, absence of hydrodynamic motion, and lack of time for energy transfer from electrons to the lattice during the pulse duration. TBMD simulations, carried out on (111) and (100) diamond surfaces, revealed that ultra-short pulses peel carbon atoms layer-by-layer from the surface, leaving a smooth surface after ablation. However, longer pulses cause thermal melting resulting in graphite residue that anchors to the diamond surface following ablation.

Keywords: femtosecond laser, diamond, micromachining, molecular dynamics, cutting tool, electronics

1. INTRODUCTION

Diamond fabrication has been an ongoing effort for centuries, and has grown from art to science. Ralchenko and Pimenov [1] recently reviewed the processes needed to shape diamond: cleaving, sawing, polishing, bruiting, and grinding. It should be noted that most of these processes have not changed significantly over the years. Recent developments are electrical discharge machining (EDM) and laser machining to form fine structures on polycrystalline diamond [1]. EDM has been used to make dies, gears, and microdrills, among other shapes from polycrystalline diamond. Since diamond is an insulator, either the surface must be converted to graphite or a metal coating must be applied in order to make it conductive for EDM. In laser machining, a Q-switched Nd:YAG laser in the fundamental (1064 nm) and frequency-doubled (532 nm) mode, or an ultraviolet (193-351 nm) excimer laser is used. Diamond has a large optical band-gap, around 5.2 eV, which prevents it from readily absorbing photons below 227 nm. Therefore, a laser must create optical damage in the material in the form of color centers and phase changes or the diamond must have defects and microvoids, then light absorption can be enhanced.

Diamond machining with a laser is usually performed in either oxygen or air, which reduces the formation of recast layer because the carbon reacts with oxygen upon vaporization to form carbon dioxide. The Q-switched Nd:YAG laser is by far the most popular laser used in the diamond industry today to polish diamond surfaces and to etch structures onto the surface. However, the nanosecond pulsed Nd:YAG laser leaves some undesirable effects such as large heat affected zone, large tolerances, limited aspect ratio, and adverse effects on optical and electrical properties. Femtosecond pulsed laser ablation is new a technology that has potential to overcome many of these problems and will enable the generation of fine-scale, high-performance devices (tools, windows, thermal spreaders) manufactured from diamond and other engineering materials [2].

Femtosecond pulsed lasers create a new spectrum of laser-material interactions because of their extreme intensity ($>10^{12}$ W/cm^2) and short pulse duration (10^{-15} s). The assumptions used in conventional nanosecond or longer pulsed laser ablation, such as the Beer-Lambert Law for absorption and thermal equilibrium of the electrons and lattice, are not valid for femtosecond pulses. The time scales for laser interaction with the surface is essential for understanding the mechanisms of material removal and phase transition in diamond under intense laser radiation. For nanosecond or longer pulses, the electrons excited by the photons can transfer their kinetic energy to the lattice and reach thermal equilibrium with the lattice during the laser

First International Symposium on Laser Precision Microfabrication, Isamu Miyamoto, Koji Sugioka, Thomas W. Sigmon, Editors, Proceedings of SPIE Vol. 4088 (2000) © 2000 SPIE · 0277-786X/00/$15.00

pulse, since the pulse duration is longer than the electron-ion relaxation time which is about 10^{-12} sec. Therefore, laser ablation using nanosecond pulses can be treated as a thermal process. In the case of femtosecond laser pulses, the laser energy is transferred to the electrons in a short time interval of only a few hundred femtoseconds. This is shorter than the electron-ion relaxation time, thus, the energy deposited from the laser pulse will remain in the electron system and the lattice is not thermally equilibrated with the electrons.

2. MODELING

Based on the above considerations, we have designed a computer simulation using finite-difference scheme (FDS) and tight-binding molecular dynamics (TBMD) model to investigate laser ablation of diamond as a function of pulse width. The FDS model was formulated to predict the electron temperatures through the Fermi-Dirac distribution function, and the ion temperatures through the kinetic energy of the ions. Diamond's thermal properties are dominated by phonon modes. Therefore, the thermal conductivity and heat capacity of the electrons were evaluated using the Fermi-Dirac statistics. The density of states was first determined by calculating the number of valence electrons per volume, and then used to determine the heat capacity (C) for the temperatures within the expected range. Thermal conductivity (K) was then estimated using the relation $K = 1/3\ C v l$ where v is the electron velocity (a quantity determined from the band structure of diamond), and l is the mean-free-path length of an electron (the distance that an electron can travel, on an average, before undergoing a scattering event). These properties were then used to predict the electron temperature distributions. The FDS model incorporated intensity-dependent absorption of the laser light by the electrons and predicted the thermal profiles within the electrons from the start of a laser pulse to one picosecond. For nanosecond pulses, the electronic temperature was set equal to the lattice temperature. For femtosecond pulses, the lattice was allowed to evolve freely with an initial temperature of 300 K. The electron and lattice temperatures obtained in FDS were then used in tight-binding molecular dynamics (TBMD) simulations to evaluate the dynamics of ablation events. TBMD was chosen for this work because it is a computationally efficient means of studying the structures, dynamics and electronic properties of complex systems at the atomic level TBMD used a temperature-dependent tight-binding potential to describe the interaction between carbon atoms. This potential provides an accurate representation of the electronic band structures, cohesive energies, elastic constants, and phonon frequencies of crystalline carbon [3]. Simulations were performed with an initial geometry of a 12-layer slab with 24 atoms per layer arranging in the (2 x1) π-bonded chain reconstructed structure. The boundary conditions were periodic in the directions parallel to the surface. The top and bottom surfaces were left unbounded. The data were correlated with FDS model to estimate ablation threshold. TBMD simulations were also used to evaluate the phase transition mechanism during laser machining of diamond.

3. EXPERIMENTAL WORK

In addition to modeling, an 825-nm wavelength, 120-fs pulse, 1 kHz Ti:Sapphire laser was used to perform laser ablation experiments on chemical vapor deposited and on single crystal diamonds in order to verify the model predictions. The 95% Gaussian beam with a 12-mm diameter circular beam profile, was focused onto the surface of the diamond which was mounted on a four axis micropositioner in a vacuum chamber at pressures of less that 10^{-4} torr. The diameter of the focused spot was 100 μm as determined by beam analysis. An electronic shutter was then used to control the exposure time and a quarter wave plate/Brewster window combination was used to control the pulse energy. Ablated samples were then characterized using micro-Raman spectroscopy, atomic force microscopy (AFM), and scanning electron microscopy (SEM).

4. RESULTS AND DISCUSSION

Figures 1 is an SEM image of a hole drilled in CVD diamond using 120 fs pulses. Notice the fine scale features visible around the edges of the holes. The ablation was a very clean process with no evidence of recast layer, collateral damage, or other undesirable effects. The same effects were found true for single crystal diamond. Figure 2, a hole ablated in single crystal diamond and characterized using AFM, shows a nearly perfect 100-μm diameter hole. The edge of the hole is a rapid transition from the flat, pristine diamond surface to a steeply-sided, smooth-edged hole. There is no evidence of recast or collateral damage. Figure 3 shows an AFM image of a groove ablated in single-crystal type IIA diamond. This was made by slowly translating the sample as the laser ablated at 1 kHz. However it is apparent that the base of the groove is not as smooth as the edges, a factor that would be expected due to irregularities in the beam profile. Micro-Raman spectrum, shown in Figure 4, shows pure diamond surface after laser ablation Previous studies using long-pulsed lasers have shown significant peak broadening and even elimination of

the diamond peak [4]. It is clear that the ultrashort pulses create very chemically pure, defect free surfaces, as is desirable for most applications.



Fig.1. SEM image of a hole in CVD diamond

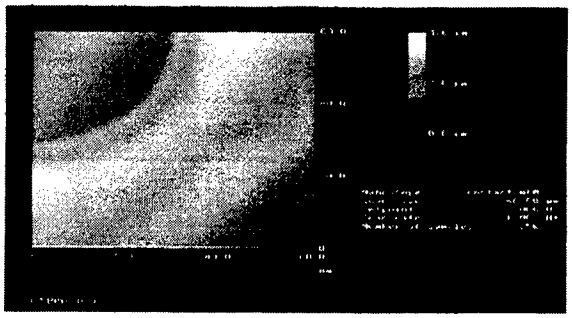


Fig.2. AFM image of a hole in single crystal diamond

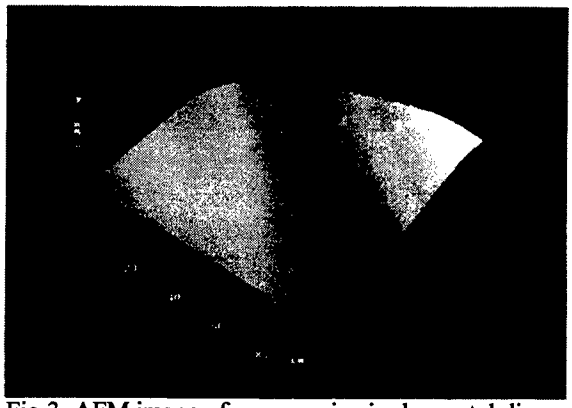


Fig.3. AFM image of a groove in single crystal diamond

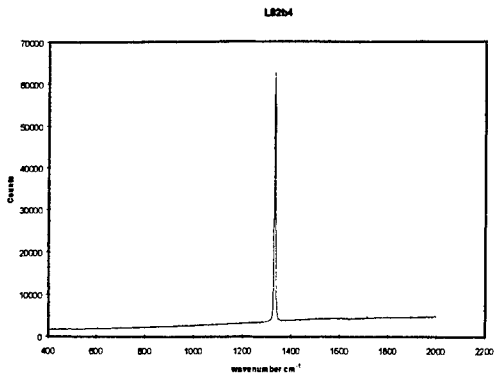


Fig.4. Raman spectrum of CVD diamond ablated surface

Atomic simulations show that the length of laser pulse is crucial in laser ablation of diamond. Finite-difference methods predict that the electron temperature decays exponentially with depth. The electron temperatures for 120-fs pulse length at a depth of 50 nm were 20,000 K and 140,000 K for the pulse energy fluences of 1.3 J/cm^2 and 6.4 J/cm^2 respectively. Such high-temperatures were attributed to multiphoton absorption, absence of hydrodynamic motion, and lack of time for energy transfer from electrons to the lattice during the pulse duration. TBMD simulations showed that the electron temperature thresholds for atomic movement occurrence were 15,000 K for (111) surfaces, 25,000 K for (100) surfaces, and 60,000 K for bulk diamond. A correlation with finite-difference model predictions of 120-fs laser ablation showed that threshold energy fluence for diamond ablation was 0.02 J/cm^2 and 0.05 J/cm^2 for (111) and (100) surfaces respectively. For the 23-nsec pulsed laser ablation, the electron-lattice equilibrium temperatures to initiate ablation were estimated at 2500 K for (111) and 4000 K for (100) at energy fluences 5 J/cm^2 to 10 J/cm^2 respectively.

The stability of the different surfaces determines the ease with which diamond is ablated. The (111) is the cleavage plane that requires less energy to create. The (100) surface requires more energy to create. TBMD simulations are shown in Figures 5 through 8. For nanosecond pulsed ablation, the structure of (111) surface was stable at electron-lattice equilibrium temperatures below 2500 K (simulation period was 10 ps). Similarly, the (100) surface retained its original structure until 4000 K for nanosecond pulses. In femtosecond pulsed simulations, graphitization began to occur when the electron temperature was 15,000 K for (111) and 25,000 K for (100) surfaces (the simulation

period was 500 fs). TBMD showed that phase transition from diamond to graphite has occurred for both nanosecond and femtosecond pulses but the evolution of graphitization was different. For ns-pulses, the graphitization occurred vertically; i.e. graphite-like regions penetrate into the bulk with the formation of diamond-graphite interfaces perpendicular to the surface before the system turns into graphite sheets completely. For fs-pulses, the graphitization followed a layer-by-layer process, making the removal of transformed graphite layers easy. The energy required to convert diamond to graphite is also lowest along the (111) plane because it is only necessary to break one bond per two atoms on the surface. When these bonds break, the six-membered puckered rings quickly flatten leaving graphite. Since the π bonding between planes of graphite is rather weak, these planes are easily removed during ablation. In the (100) surface, the same change occurs along the (111) plane, except at higher temperatures. This caused an increase in restriction on the movement of the plane, thereby increasing the energy required. Bulk diamond was extremely stable with regard to electronic excitation, and TBMD showed that atomic motion occurred in this case at extreme temperature, 60,000 K. TBMD model predictions were correlated very well with experimental findings, confirming threshold energy fluence and the absence of phase transition.

In summary, the femtosecond laser removes more material and leaves a very clean cut. It peels atoms from the diamond surface in a layer-by-layer fashion through a non-thermal mechanism, leaving a smooth, graphite-free diamond surface.

ACKNOWLEDGEMENTS

The authors would like to thank the Division of Design and Manufacturing, National Science Foundation for the support under the grant DMI-9622518

REFERENCES

1. V. G. Ralchenko, and S. M. Pimenov, *Handbook of Industrial Diamonds and Diamond Films,* 983-1021 (New York: Marcel Dekker, Inc.), 1999
2. M. D. Shirk, P. A. Molian, and A. P. Malshe, J. Laser App. **10**, 64-70 , 1998.
3. M. S. Tang and C. Z. Wang, Phys Rev B **53,** 979-982 1996.
4. R. Windholz and P. A. Molian J. Mater. Sci. **32**, 4295-4301, 1997.

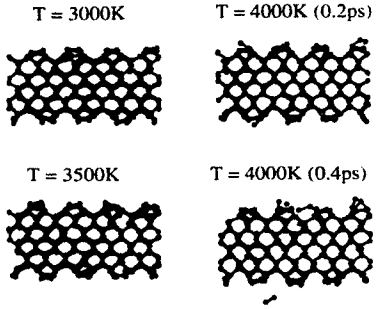


Fig.5. (100) diamond at 4000 K (nanosecond pulse)

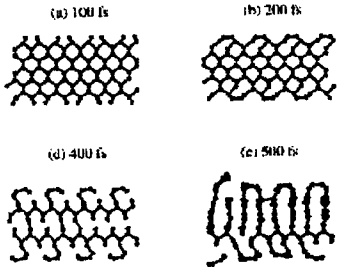


Fig.6. (100) Diamond at 25,00 K (femtosecond)

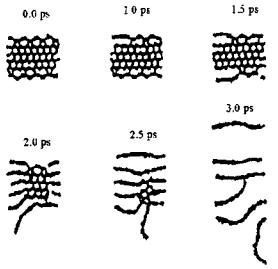


Fig.7. (111) diamond at 2500 K (nanosecond)

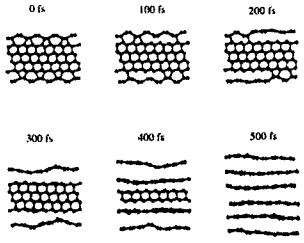


Fig.8. (111) surface at 15,000 K (femtosecond)

Effects of Laser Pulse Shape on Jet-like Plasma Formation in Laser Ablation of Metals under Atmosphere at High Fluence : Observation by Nanosecond Imaging Technique

Satoshi KIYOKU* , Yuichi KUROSAKI* , Isamu OGURO , Susumu NAKAMURA and Yoshiro ITO*[§]**

** Department of Mechanical Engineering, Nagaoka University of Technology,*

1603-1,Kamitomioka, Nagaoka, Niigata, 940-2188, JAPAN

[§]Corresponding Author: E-mail: itoy@nagaokaut.ac.jp

*** Department of Electrical Engineering, Nagaoka College of Technology,*

888, Nishikatakai, Nagaoka, Niigata, 940-8532, JAPAN

We have developed a nanosecond imaging technique, where fundamental radiation of a Nd:YAG laser was used as ablating beam while the second harmonic radiation from the same laser was used as illuminating light pulse, to study surface phenomena during and immediately after the ablating laser pulse. Using this system, we observed the ablation phenomena of metals in air and found that, at fluence higher than about 10 J/cm^2, there appeared jet-like plasma growing towards incident laser beam at velocities of as high as 10^5 ms^{-1} in addition to the laser induced plume. The jet grew during the laser pulse and when the pulse terminated, its rapid growth stopped. In this paper, we investigated the effects of laser pulse shape on this jet-like plasma. We found that appearance of the jet became later and its growth continued longer as pulse width increased. Growth speed of the jet depended on the pulse shape, even though the jet grew up to similar height at the end of the pulse. Our results showed that, even though a laser parameter in laser ablation was usually represented as the fluence, the controlling parameter for the jet growth was temporal change of laser power.

Keyword: Laser ablation, Imaging, Metal, Pulse shape, Plasma

1. Introduction

When a high power laser pulse is irradiated to a target, the target material becomes high temperature and high pressure state, and neutral atoms, molecules, ions, clusters and electrons which compose constituents of the matter are explosively released with a bright spark. This explosive delamination process is called laser ablation. By focusing a laser pulse to a tiny spot, we can easily get high laser density at the spot to achieve the laser ablation locally. Therefore, sharp etching with only slight heat damage left around the irradiation part is possible. The ablation process has already found some applications in microelectronics and medical fields and is expected as one of promising fine fabrication techniques. Laser ablation process is, however, very complicated, non-linear process and there are many still to be made clear, such as the effects of pulse width and laser fluence.[1]

We have observed the laser ablation phenomenon by an imaging system which has a nanosecond time resolution and found a jet-like plasma which grows very high-speed along the laser incidence direction at high fluence[2-5]. In this paper, we will report about effects of laser pulse width on the jet-like plasma formation as well as plume growth at the same laser fluence.

2. Experimental

Detail of the experimental procedure has been given elsewhere [2,3,5] and only an outline will be described here. A Q-switched Nd:YAG laser, Powerlite 8000 (Comtinuum, Co.) with a second harmonic generator/separator unit was used. Light from the laser contains both converted second harmonic radiation and fundamental radiation. Both of the second harmonic and the fundamental radiation separated by the separation apparatus were used in this experiment. The fundamental light (1064nm) was used as the ablation

First International Symposium on Laser Precision Microfabrication, Isamu Miyamoto, Koji Sugioka, Thomas W. Sigmon, Editors, Proceedings of SPIE Vol. 4088 (2000) © 2000 SPIE · 0277-786X/00/$15.00

beam (Pump Beam) and the second harmonic light (532nm) was used as illuminating light (probe Beam). The fundamental light was focused onto the target by a plano-convex lens and hit the surface perpendicularly. The second harmonic light passed through optical delay lines was impinged to the target from a tilted direction.

Distance between the target and lens was varied to change spot size of the beam for adjusting the laser fluence while the pulse energy kept constant, 100 mJ in this experiment. Laser fluence was adjusted to be 10 J/cm^2. Different pulse width was obtained by adjusting a Q-switch delay time of the laser. This usually caused changes in pulse energy, too. So, a beam attenuater was used to keep the pulse energy constant. Laser pulse shape was monitored by combination of a fast photodiode and a digital oscilloscope. Pulse width, which is usually represented by its FWHM value, were measured to be 8, 13 and 23 ns, respectively. But their full widths (FW), from the rise to the end of the trace, showed smaller differences with each other: 35, 55 and 70 ns, respectively.

Aluminum (1050) plates of 1mm thick were mechanically polished and used as targets. Each pulse was shot on a fresh surface, i.e., each photo represents a single pulse event.

The ablation phenomenon was taken by the ICCD camera with a gated image intensifier, transferred to a personal computer and then treated by an image-processing program. The delay time was defined as interval between the rise of irradiated laser pulse detected by a photodiode and the end of the camera gate signal.

The system described above was used for delay times of-5 to 40 ns. For delay times longer than 45 ns, the second laser (Surelite I) was used as illumination source and the delay time between two laser pulses was controlled by a digital delay generator (DG 535, Stanford Research Inst., Co.).

Geometry of observation is important in reading the images and is illustrated schematically in figure 1 with a typical image obtained. The second harmonic light passed through the variable optical delay line was expanded by a beam expander and illuminated the irradiated spot along the direction intersecting 60 degrees from the normal direction. Observation direction was at the opposite half plane with an angle 30 degrees from the normal. A band pass filter of 532 nm and suitable neutral density filter were placed in front of the camera. The gate width of camera was 3 ns and was monitored by a digital oscilloscope.

The white picture in the figure shows jet-like plasma growing perpendicular to the surface. Its shadow projected against the sample surface is clearly observed. Boundary of the shadow is clearer than bright plasma image itself, which allows us to determine its height precisely from simple geometric calculation shown in the figure. Shadow length is elongated than actual plasma height and thus is measured easily. Actual plasma height H is calculated by

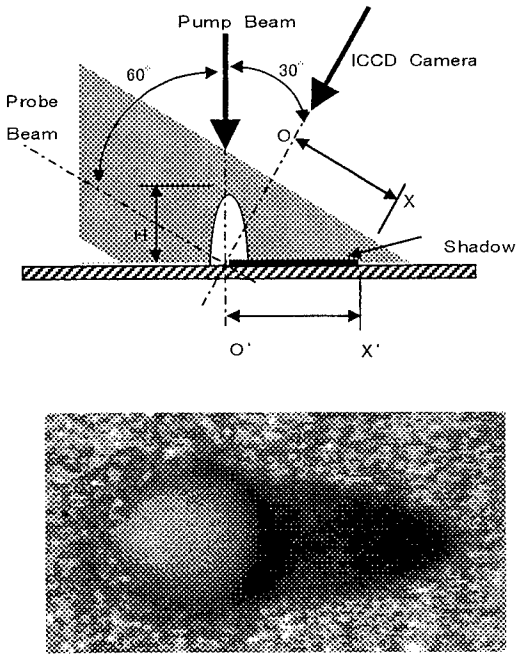


Fig. 1. Geometry of beams and observation.
Above: Geometry of ablating and illuminating beam and observation direction.
Below: A typical image obtained. Sample is Al, laser fluence is 10J/cm^2, and delay time is 50ns in air.

$$H = OX \tan 30^\circ / \cos 30^\circ ,$$

where OX is the shadow length measured on the display.

3. Results and Discussion

Fig.2 shows the example of observed images. The above of the figure are images observed at the delay time of 15ns, and the below are those at 50ns. Pulse width is 8 ns, 13 ns, and 23 ns from left to right.

At delay time of 15ns, the difference in growth of jet-like plasma is clearly seen. The jet-like plasma had already appeared in the shortest pulse case (a): it grew as high as 0.7mm. In (b), it seems that the jet-like plasma just started to grow, even though its height was not able to estimate from the image. In the longest pulse case (c), we cannot see any bright image assignable to the jet. At delay time of 50 ns, in the image for the shortest pulse width (d), growth of the jet already stopped and its shadow stared to thin out. Furthermore, closer look reveals that an additional shadow, which was possibly be that of ablated aluminum plume**[2,3]**, was growing inside the shadow. In (e), the growth of the jet had almost stopped, and the shadow of plume had appeared at inside of it. In the image for the longest pulse width (f), the growth of jet-like plasma still continued. The height of the jet-like plasma was almost the same for three pulse widths at delay time of 50 ns.

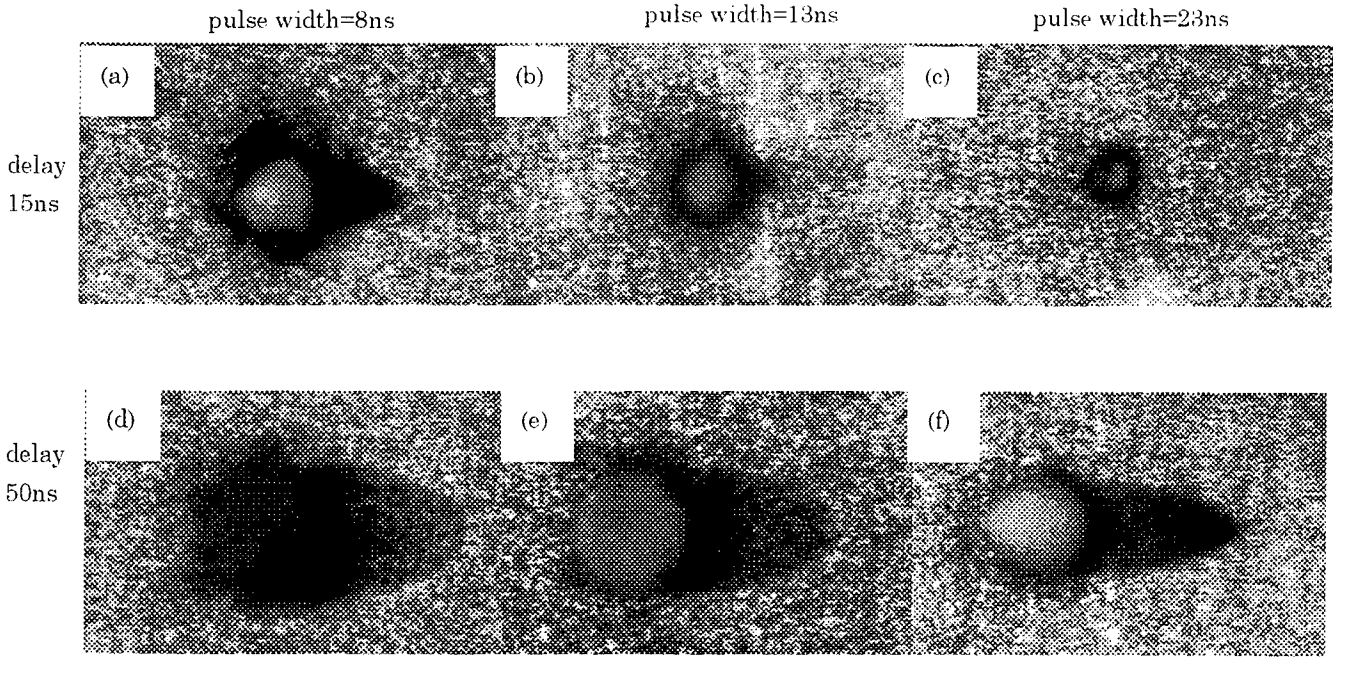


Fig.2. Time resolved images of jet-like plasma for three pulse widths.
Above: delay time=15ns (a)pulse width=8ns ; (b)pulse width=13ns ; (c)pulse width=23ns
Below: delay time=50ns (d)pulse width=8ns ; (e)pulse width=13ns ; (f)pulse width=23ns

We consider that this jet-like plasma should be laser induced breakdown plasma of air initiated by electrons supplied from the target**[2,3]**.

In images at longer delay times, the shadow of jet-like plasma was gradually thinned and, instead, a shadow showing a shock wave front appeared as shown in figure 3. There was no clear difference in images of shock waves later than 100 ns for three pulse widths.

Figure 4 shows plots of observed height of jet-like plasma and shock wave with delay time. From this figure we summarize following characters of the jet-like plasma.

(1) Shorter the pulse width, earlier the jet starts.
(2) Shorter the pulse width, faster the growth speed of it.
(3) The plot shows an S-character shape.
(4) End point of fast growth corresponds to the end of laser pulse, i.e., full width of the pulse.

Earlier than 10ns, the height seems constant because shadow of the jet is buried under a black image of laser irradiated spot so that precise determination of its length is difficult, as you can see in the figure 2 (c). The jet-like plasma changed its temporal behavior according to the laser pulse shape. Because the pulse energy and fluence were kept constant, the peak power was inversely proportional to the pulse width. Therefore, we think the growth of the jet-like plasma is controlled by laser power distribution.

After the end of the pulse, the jet-like plasma stopped its

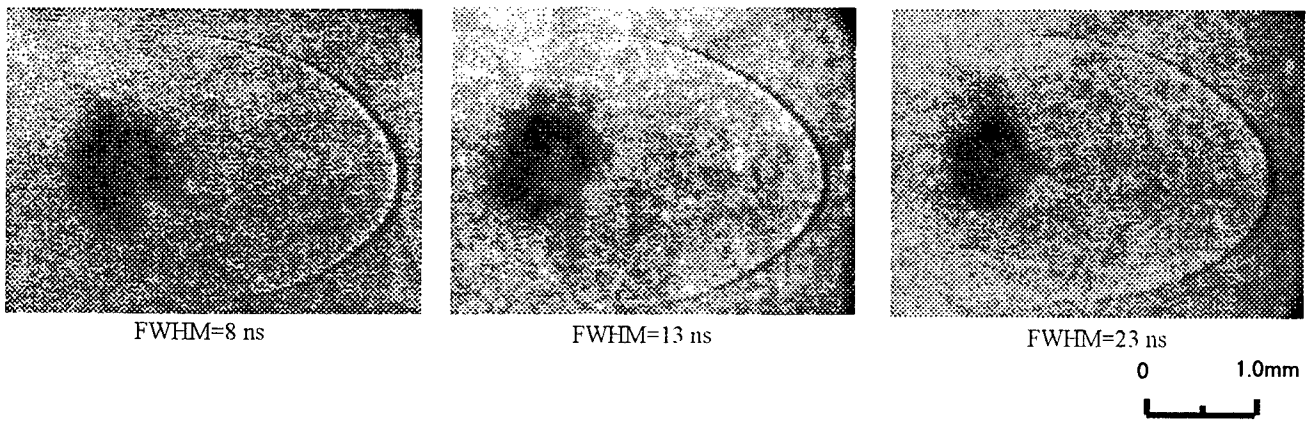


Fig.3. Image of shock wave dues to plume observed at delay time of 500 ns.

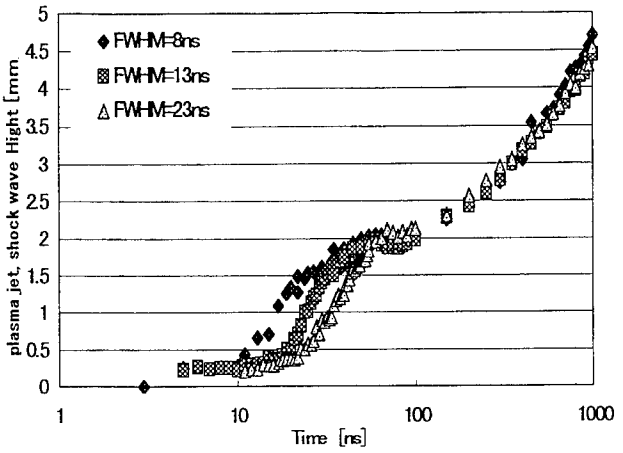


Fig.4. Growth of jet-like plasma and shock wave for three pulse width with time. Target is aluminum and laser fluence is 10J/cm^2

fast growth and remained nearly equal height until 100 ns or so. In this stage, the shadow slightly expanded to lateral direction and was thinning rapidly and the boundary of the shadow changed into a black-and-white double line representing a shock front usually seen in a shadowgraph. This suggests that the fast growth of the jet would not be driven by plasma pressure but by laser light filed itself. The growth speed of the jet were a bit smaller than 10^5 ms^{-1}.

Inside of the thinning shadow, we could sometimes observe another shadow growing slower than the jet. It seems that this shadow, which we think due to the laser induced plume of aluminum, eventually catch up with the preceding shock-wave due to the jet-like plasma and continue to grow later than 1000 ns. This growth is shown as the second growing stage in the figure, which appears later than 100 ns. Growths of these shock-waves (plume) seem almost the same for examined three pulse widths. Shock-wave front expanded both in axial and lateral directions. The growth speed of this part is order of 10^3 ms^{-1}, which is in good agreement with plume expansion speed in air reported previously. The similar value is obtained in our experiments at lower fluence than the threshold of the jet-like plasma formation**[2,4,5]**. This would suggest that the pressure, mass and temperature of the plume are nearly the same for these three cases because their behavior seems quite similar in our observation.

Assuming that this is true, the difference in pulse width causes little effect on laser ablation of the target materials, so long as the pulse energy is the same. The jet-like plasma formation should cause decoupling of pulse energy to the target materials due to its generation process and absorption by the plasma, but it seemes that the amount of laser energy transferred to the target is nearly the same for three pulse width examined.

Commonly used laser parameters describing the laser ablation processes are laser wavelength and laser fluence. Most of the researchers might notice that laser pulse shape sometimes affect results but, in most of the studies so far, different pulses were supplied from different lasers and thus accompanied with other parameter changes as well.

Our results on the jet-like plasma have shown the effects of pulse shape without other change of parameters. Behavior of the plume driven shock wave, however, suggests that the laser fluence would be considered as a good laser parameter for describing the plume when the pulse width changes by factor of 2 or 3 in a few tens of nanosecond range.

4. Conclusion

The jet-like plasma formation in laser ablation of aluminum in air showed distinctive dependence on temporal laser pulse shape even though the fluence and total pulse energy were same. The results suggested that the jet was driven by laser light field and not by pressure of the plasma. Laser induced plume observed after the jet showed little dependence on the pulse shape. Our results have shown the effects of pulse shape without other change of parameters and suggested that the laser fluence would be considered as a good laser parameter to describe nanosecond laser ablation.

Acknowledgments

This work is partly supported by Grants-in-Aid for Scientific Research from the Ministry of Education, Science, Sports and Culture of Japan (11650736, 11305053 and 10558082).

References

[1] For example, B. Dieter, *Laser Processing and Chemistry, 2nd Ed.* Springer-Verlag, Berlin, Heidelberg, 1996

[2] Y. Ito, T. Shimizu, I. Oguro, and S. Kijima, "Jet-Like Plasma Formation in Laser Ablation of Metals Observed by Nanosecond Imaging Technique in Gases." Proceedings of ICALEO'99, LIA Vol. **87**, Part 2, Sec. E, pp. 61-70, 2000

[3] Y. Ito, I. Oguro, Y. Fukuzawa and S. Nakamura, "Nanosecond laser ablation of metals in gases observed by photoacoustic and imaging techniques" Proceedings of High Power Laser Ablation 2000, Proc. of SPIE, **4065**, (in press)

[4] Y. Ito, S. Kijima, T. Shimizu "Observation of the laser ablation process with nanosecond time resolution." Proceedings of 1998 Fall meeting of the Japanese Society for Precision Engineering, 406 (in Japanese)

[5] Y. Ito, S. Nakamura, I. Oguro "Laser ablation of aluminum." Proceedings of Annual Meeting of the Japan Society of Electrical Machining Engineers, 1999, 111 – 114 (in Japanese)

Molecular Dynamics Analysis on Physical Phenomena of Metal with Evaporation Induced by Laser Irradiation

Ichirou FUKUMOTO[*], Etsuji OHMURA[**], Alexei ZHIDKOV[*], Akira SASAKI[*], Takayuki UTSUMI[*] and Isamu MIYAMOTO[**]

[*] *Advanced Photon Research Center, Kansai Research Establishment, JAERI, 25-1 Mii-minami, Neyagawa Osaka 572-0019, Japan*
E-mail: fukumoto@apr.jaeri.go.jp

[**] *Department of Manufacturing Science, Graduate School of Engineering, Osaka University, 2-1 Yamada-oka, Suita, Osaka 565-0871, Japan*

Recently, ultra-short pulsed lasers with high peak power have been developed, and their application to the materials processing is expected for a tool of precision microfabrication. During surface generation process with laser ablation, lattice defects such as dislocations, vacancies, grain boundaries, are also generated beneath the surface. Lattice defects influence the quality or accuracy of materials processing, therefore it is important for laser precision microfabrication to elucidate the generation mechanism of them. In this paper, laser ablation phenomena of metal were analyzed using the modified molecular dynamics method, which has been developed by Ohmura and Fukumoto. Main results obtained are summarized as follows: (1) The shock wave induced by the Gaussian beam irradiation propagates radially from the surface to the interior. (2) A lot of dislocations are generated near the surface by the propagation of shock wave. (3) Many grains are generated in the resolidification process after the end of laser pulse. They are metastable and some crystal-orientations of them change to one of the base metal and the grain boundaries disappear in the cooling process.

Keywords: laser precision microfabrication, computer simulation, molecular dynamics, fusion, evaporation, shock wave, dislocation, grain boundary

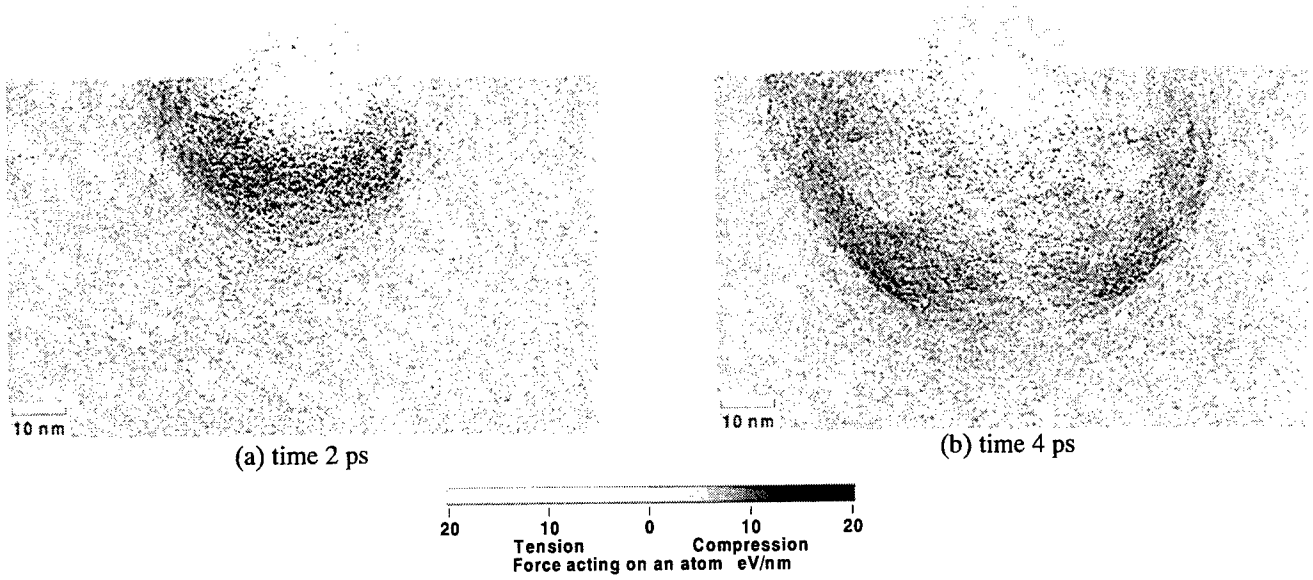
1. Introduction

Recently, the ultra-short pulse CPA (chirped pulse amplification) laser with high peak power has been developed, and it is being expected as a powerful tool of laser precision microfabrication. When the surface is ablated due to laser irradiation with a high peak power, shock wave is generated and propagates to the interior of the target from irradiation spot. It also induces the generation of a lot of dislocations in the material. On the other hand, many grain boundaries must be generated in the liquid phase in the rapid cooling process. Since such lattice defects influence the quality or accuracy of micro processing, it is important to clarify the mechanisms of their generation. Because they are generated in the microscopic area momentarily inside the target, it is very difficult to observe the generation process experimentally. Therefore, many theoretical or numerical analyses of the laser ablation phenomena have been performed. In this paper, the microscopic shock phenomena and resolidification processes are analyzed through the molecular dynamics (MD).

2. Simulation methods

In the present simulation, laser is assumed to be the fourth harmonics of Nd:YAG laser (wave length 266 nm) with the pulse duration of ps order. Mono-crystalline aluminum (Al) is chosen as the target material, and Morse potential [1] is applied to the interatomic potential. Analysis area is the Al (111) plane, and 400 atoms per layer in the direction of surface and 400 layers in the depth, totaling 1.6×10^4 atoms are arranged in a square configuration. The details of the configuration method of initial atomic array and the photon absorption model were described in Refs. [2] and [3]. The modified MD method [4], in which heat conduction by free electrons is compensating at every time step of MD calculation, is also applied in this paper.

First International Symposium on Laser Precision Microfabrication, Isamu Miyamoto, Koji Sugioka, Thomas W. Sigmon, Editors, Proceedings of SPIE Vol. 4088 (2000) © 2000 SPIE · 0277-786X/00/$15.00



(a) time 2 ps (b) time 4 ps

Fig. 1 Stress state of Al atoms during Nd:YAG (4ω) laser irradiation, which is shown by a gray scale. Average power density and pulse duration are 200 GW/cm^2, 1.5 ps, respectively.

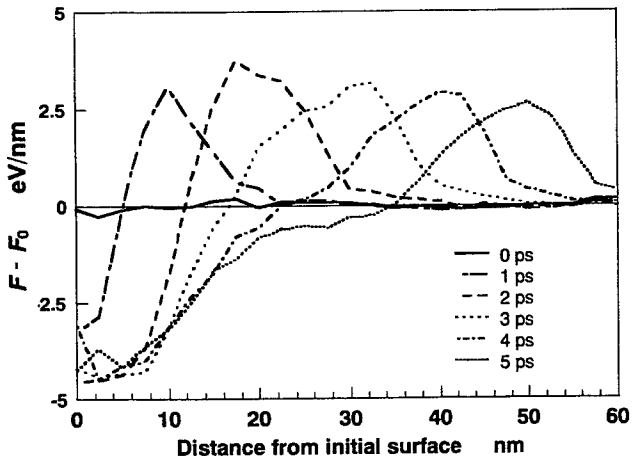


Fig. 2 Transition of shock wave at every 1 ps since irradiation starts. Irradiation conditions are the same as Fig. 1.

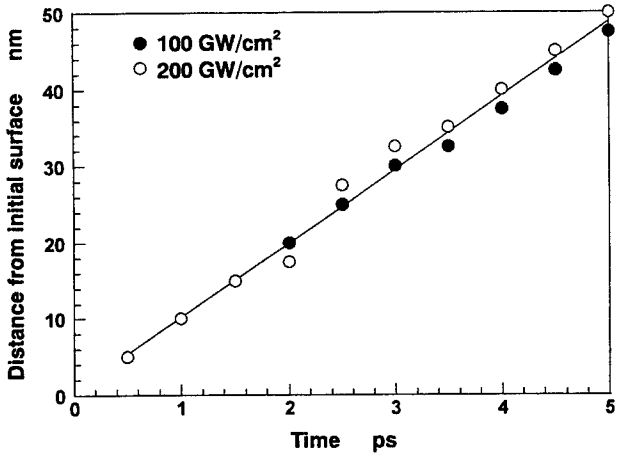


Fig. 3 Transition of the peak intensity position of shock wave at every 0.5 ps since irradiation starts. Irradiation conditions are the same as Fig.1.

3. Propagation of shock wave

Microscopic stress states of Al atoms due to Gaussian beam irradiation of pulse duration 1.5 ps and average intensity 200 GW/cm^2 are shown in **Fig. 1**. In these figures, the force acting on an atom in the direction of width is shown by a gray scale. We can see the compressed area generated circlewise at 2 ps (Fig.1 (a)) and spreads out radially inside the material (Fig.1 (b)). **Figure 2** shows the transition of the average stress states of Al atoms on a circle drawn in the analysis area, whose center is set at the beam center irradiated to the initial surface, at every 1 ps after irradiation start. The average stress state is evaluated by the difference between the mean of the force acting on an atom on the circle F and the mean value of all Al atoms in the initial state F_0, and $F - F_0 > 0$ means compression. Compressed area propagates from the irradiation spot to the interior as a shock wave, whose shape is seen as a triangle. The transition of peak intensity position of the shock wave from irradiation spot is shown in **Fig. 3**. The result in the case of average power density 100 GW/cm^2 and pulse duration 3 ps is also shown in Fig. 3. A straight line is one obtained by the method of least squares. Propagation velocity of the shock wave, which is given by the gradient of this line, does not depend on irradiation conditions but is equal to the elastic wave velocity of Al.

4. Generation of dislocations

The crystal state of Al atoms in Fig. 1 are shown in **Fig. 4**. In these figures, gray lines show the slip planes with an edge dislocation, which is shown by a black dot, at the end of each one. Black dots show the atoms in liquid phase, that is, group of them show the molten pool. The semicircles shown by solid lines are the peak intensity position of the shock wave. And, the semicircles of the dotted line show the position where $F - F_0 = 0$ in Fig. 2. The vicinity of irradiated area melts at first then ejects explosively. At the same time, a shock wave is generated and propagates to the interior, and many dislocations are generated from the solid-liquid interface by propagation of the shock wave. The dislocations are moved tangentially by the shock wave with the velocity of longitudinal wave of the material. After the shock wave has passed, the dislocations move at the lower velocity than traverse wave.

5. Grain boundaries generation

Ablation and resolidification processes of Al with the laser irradiation of uniform power intensity 100 GW/cm^2 and pulse duration 0.5 ps are shown in **Fig. 5**. In Figs. 5(a) and Fig. 5(b), evaporation occurs violently and many small particles are ejected from the surface. We can see some small voids in the liquid phase in Fig. 5(a). Heat is conducted to the interior, then remarkable thermal expansion occurs and some small voids and many slip planes are generated in the liquid phase and solid phase, respectively (Fig. 5(c)). Voids in liquid phase become larger during ablation process, as shown in Fig. (d), they remain since then as we can see in Fig. 5(f). On the other hand, nucleation of grain starts in Fig. 5(d), some grain boundaries become clearly in Fig. 5(e). But they are metastable, therefore some crystal-orientations of them change to one of base metal and they disappear in the cooling process. It is thought that the voids and the grain boundaries in resolidificated layer, which are shown in Fig. 5(f), remain as lattice defects.

6. Conclusions

The shock phenomena accompanied with laser ablation and resolidification processes in liquid phase are simulated through the modified MD. Obtained results are summarized as follows:

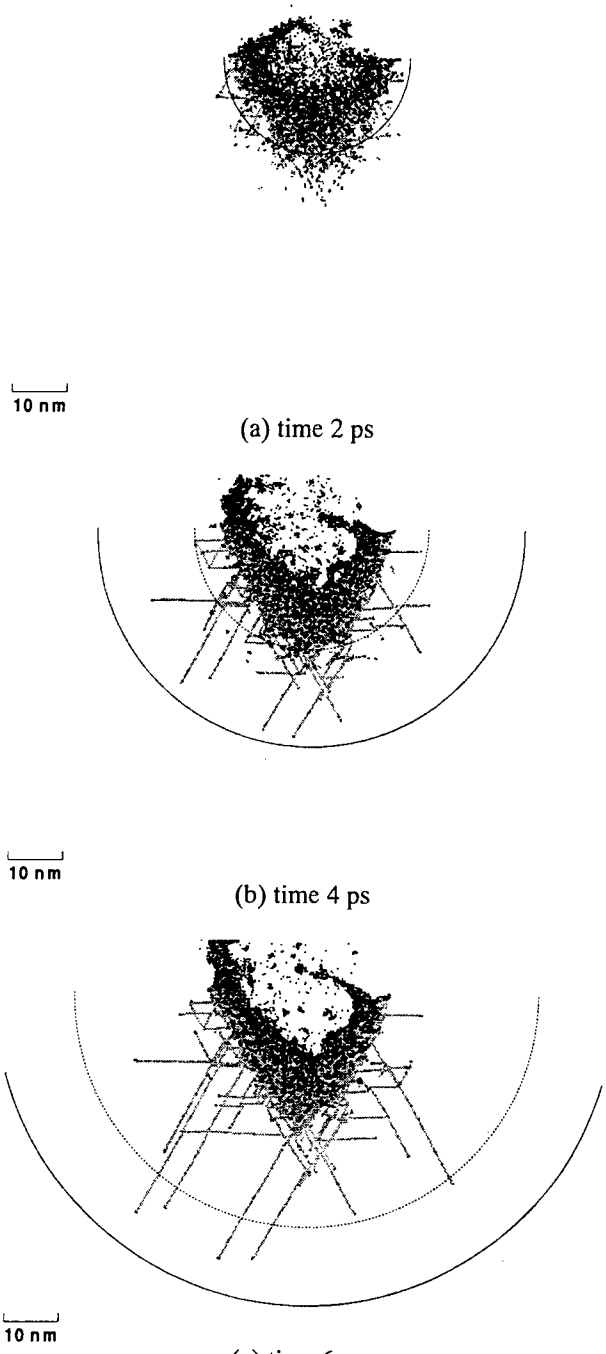


Fig. 4 Propagation of shock wave, shown by a semicircle of a solid line, and behavior of slip planes in the material. Irradiation conditions are the same as Fig.1.

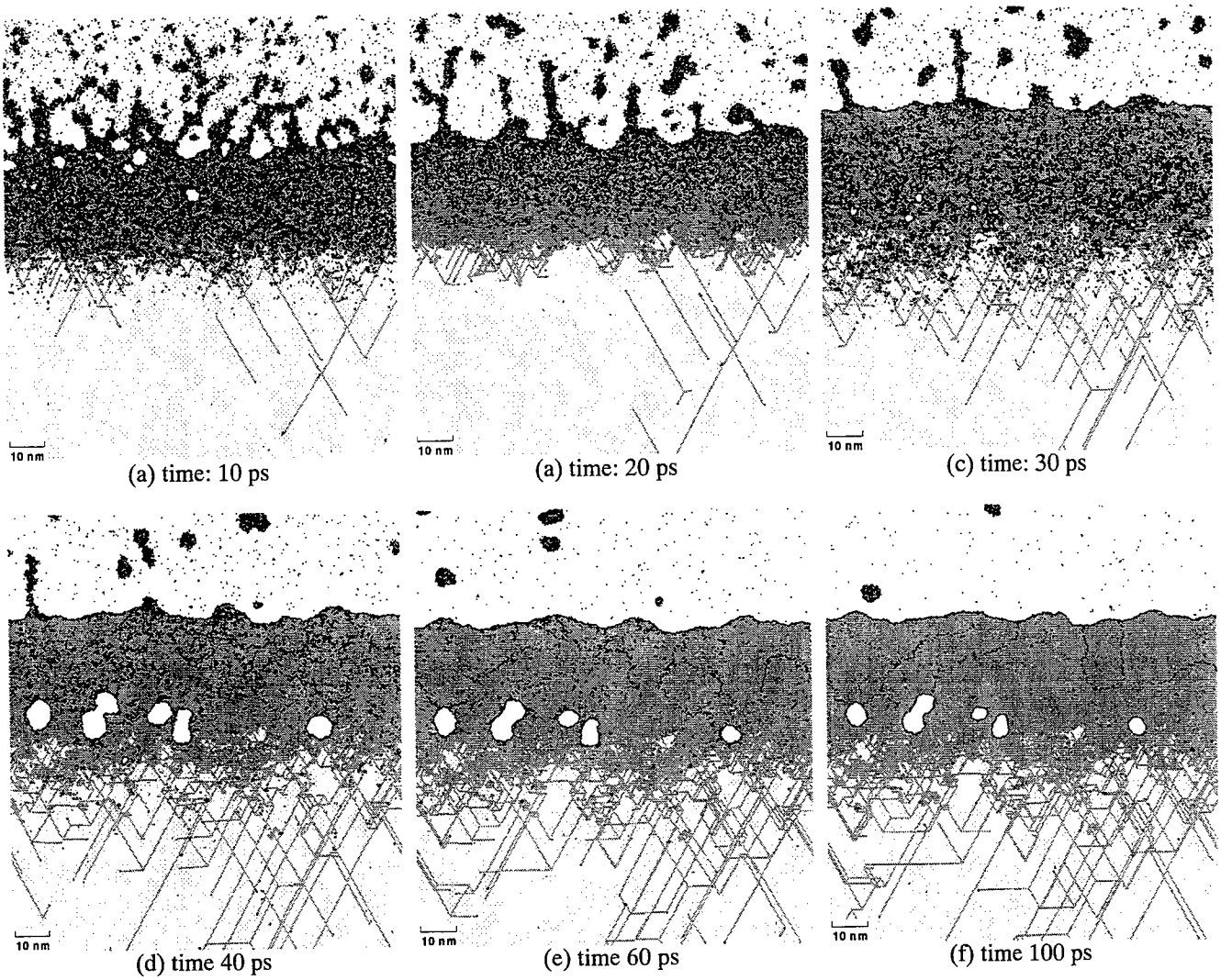


Fig. 5 Ablation and resolidification processes of Al with the laser irradiation of power intensity 100 GW/cm^2 and pulse duration 0.5 ps. Slip planes with an edge dislocation at the end, voids and grain boundaries can be seen.

(1) The shock wave induced by the recoil pressure due to laser ablation propagates radially from the irradiation spot to the interior of the target. The propagation velocity of the shock wave is almost equal to the speed of the longitudinal wave of the target.

(2) A lot of dislocations are generated from solid-liquid interface by the propagation of shock wave. Dislocations move with the shock wave with the longitudinal wave velocity. After the shock wave passes, the velocity of dislocations is not larger than that of the traverse wave.

(3) Many grains are generated in the resolidification process. Some crystal-orientations of them change to one of base metal and the grain boundaries disappear in the cooling process, but others remain as the lattice defects.

Acknowledgement

A part of this study was supported by Grants-in-Aid of Scientific Research from the Ministry of Education, Science and Culture of Japan in 1997, 1998 and 1999.

References

[1] L. A. Girifalco and V. G. Weizer: Phys. Rev., **114**, (1959), 687.

[2] E. Ohmura and I. Fukumoto: J. High Temperature Soc., **20**, (1994), 227. (in Japanese)

[3] E. Ohmura and I. Fukumoto: Int. J. JSPE, **30**, (1996), 128.

[4] E. Ohmura and I. Fukumoto: Int. J. JSPE, **31**, (1997), 206.

Novel Technology for Laser Precision Microfabrication of Hard Materials

Koji Sugioka and Katsumi Midorikawa

RIKEN - The Institute of Physical and Chemical Research
Wako, Saitama 351-0198, Japan
E-mail: ksugioka@postman.riken.go.jp

Hybrid laser processing for precision microfabrication of hard materials, in which interaction of a conventional pulsed laser beam and another medium on the material surface leads to effective ablation, is reviewed. The main role of the medium is to produce strong absorption of the ns-laser beam to the materials. Simultaneous irradiation of the UV laser beam with the VUV laser beam possessing extremely small laser fluence performs accurate ablation of the hard materials such as fused silica, crystal quartz, sapphire, GaN, SiC, etc. (VUV-UV multiwavelength excitation process). Metal plasma generated by the laser beam effectively assists high-quality ablation of transparent materials, leading to submicron grating fabrication and high-speed hole drilling of glass materials (laser-induced plasma-assisted ablation (LIPAA)). The detailed discussion includes ablation mechanism of hybrid laser processing and comparison of advantages and disadvantages with F_2 laser ablation.

Keywords: hybrid laser processing, hard material, precision microfabrication, micromachining, ablation, VUV laser, fused silica, multiwavelength excitation, laser-induced plasma, F_2 laser.

1. Introduction

Development of precision microfabrication techniques for hard materials such as fused silica and GaN is strongly desired in various industrial fields. Although pulsed laser ablation is quite attractive for high-quality and high-efficiency microfabrication of various kinds of materials, conventional UV, visible or IR lasers often induce severe damage and cracks to the hard materials. So far, two kinds of approaches were attempted to overcome these problems. One is use of novel lasers such as vacuum ultraviolet (VUV) and femtoseond (fs) lasers. Herman et al. reported F_2 (157nm) laser ablation of fused silica for the high-quality surface patterning [1]. Varel et al. reported high-quality channel drilling of fused silica by fs laser ablation [2]. However, it is well known that such lasers have many difficulties for practical use at the moment, due to small pulse energy, unreliability, unstability, high photon cost, etc. If conventional pulsed lasers in UV, visible, or IR ranges can be utilized for the processing, great advantage is obvious. Recently, hybrid-laser ablation has been proposed as another approach for high-quality ablation of fused silica. That is, another medium is introduced into the conventional ns-laser ablation system. The main role of the medium is to produce strong absorption of the ns-laser beam to the materials. Wang et al. developed laser-induced backside wet etching (LIBWE) for micropatterning of transparent materials, in which one side of the substrate is in contact with an acetone solution containing pyrene and the other side is irradiated with KrF excimer laser [3]. Sugioka et al. reported that simultaneous irradiation of the VUV laser beam possessing extremely small laser fluence with the UV laser beam has performed accurate ablation of the hard materials (VUV-UV multiwavelength excitation process) [4-13]. Zhang et al. reported the surface patterning and high-speed channel drilling of fused silica and related glass materials by laser-induced plasma-assisted ablation (LIPAA) using an IR (1.06 μm, 6 ns), visible (532 nm, 6 ns) or UV (266 nm, 6 ns and 248 nm, 34 ns) laser [14-17]. Thus, hybrid laser processing opens up new avenues for precision microfabrication of hard materials.

In the present paper, precision microfabrication of the hard materials by hybrid laser processing developed by us ((1) VUV-UV multiwavelength excitation process and (2) LIPAA) is reviewed. The detailed discussion includes ablation mechanism of hybrid laser processing and comparison of advantages and disadvantages with the conventional laser processing using the F_2 laser.

First International Symposium on Laser Precision Microfabrication, Isamu Miyamoto, Koji Sugioka, Thomas W. Sigmon, Editors, Proceedings of SPIE Vol. 4088 (2000) © 2000 SPIE · 0277-786X/00/$15.00

2. VUV-UV multiwavelength excitation process

2.1 Concept

Figure 1 shows a schematic illustration of the concept of multiwavelength excitation process. In this process, VUV and UV laser beams are directed to a substrate at the same time. The energy density of VUV laser is as small as several tens mJ/cm^2, which is 1 - 2 orders lower in magnitude than that of single wavelength laser ablation using an F_2 laser. The energy density of simultaneously irradiated UV laser beam is the order of 10^0 J/cm^2 which is comparable to that of single wavelength ablation. For micropatterning of solid surfaces by this process, the unpatterned VUV beams are irradiated to a broad area and only the UV laser irradiation area should be localized, as shown in Fig. 1. The contrary scheme, i.e., patterned irradiation of the VUV beam with unpatterned irradiation of the UV beam, is also possible.

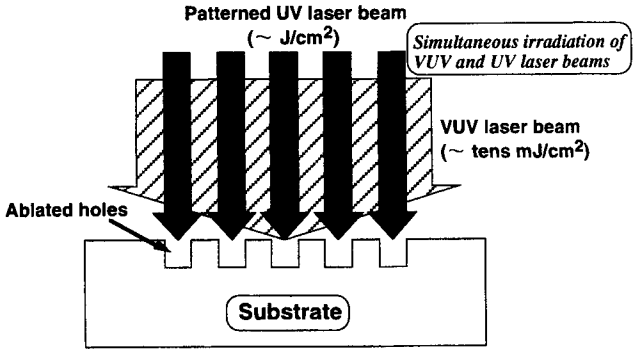


Fig. 1. Schematic illustration of concept of multi-wavelength excitation process.

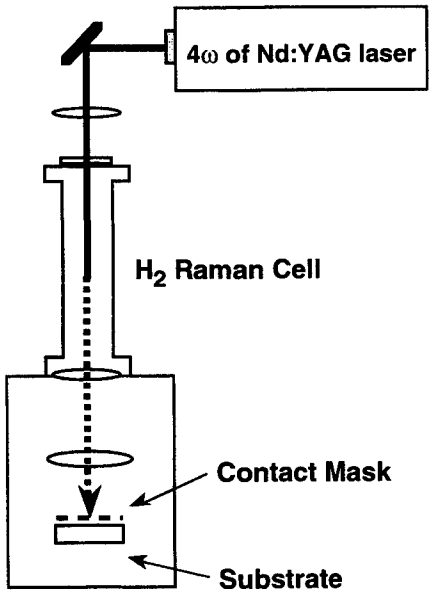


Fig. 2. Schematic illustration of experimental setup for multiwavelength excitation process using a VUV Raman laser.

2.2 Ablation using VUV Raman laser

The VUV Raman laser, based on high-order anti-Stokes Raman scattering of a fourth harmonic of a Q-switched Nd:YAG laser (a 266 nm wavelength and an 8 ns pulse width) in a Raman cell filled with hydrogen gas at 4 atm., was used in our initial experiments. Figure 2 shows a schematic illustration of experimental setup for ablation of the hard materials using the VUV Raman laser. Figure 3 shows output characteristics of the VUV Raman laser when a 100 mJ pulse of the fourth harmonic of Nd:YAG laser is incident to the Raman cell. The VUV Raman laser simultaneously radiates fifteen discrete wavelengths from the 133 nm 9th-order anti-Stokes beam to the 594 nm 5th-order Stokes beam including the pump beam of a 266 nm wavelength whose energy is the largest and accounts for about 45 % of total energy of the output beams. The pulse energy of anti-Stokes lines exponentially decreases with increase of the order and drops to less than 1 mJ in the VUV region. The VUV beams has a tophat-like shape, although the 266 nm wavelength beam has a Gaussian-like shape [18]. For the multiwavelength laser ablation, the laser fluence was calculated by totaling pulse energy of each wavelength component.

In the experiment, all wavelength components emitted

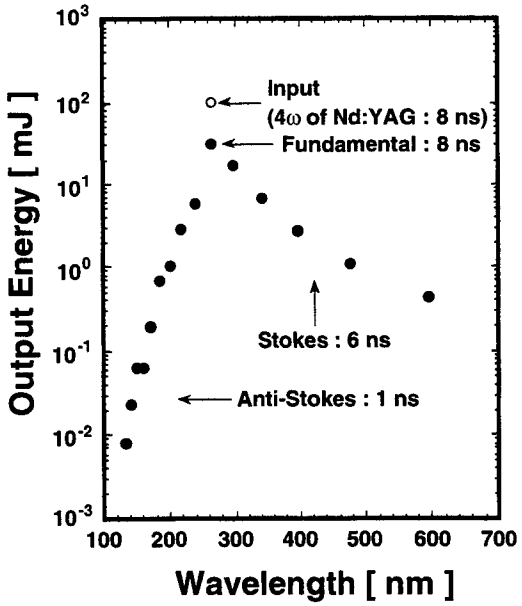
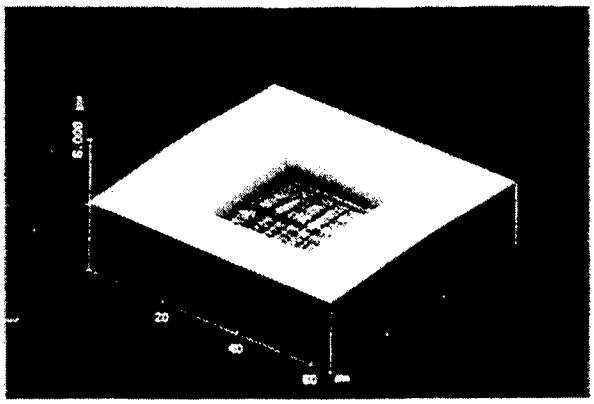
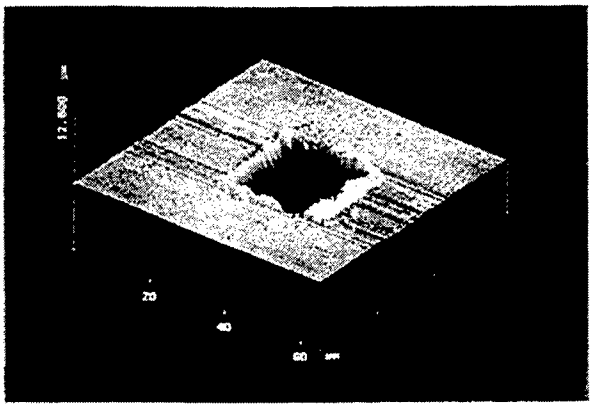


Fig. 3. Output characteristics of the VUV Raman laser.



(a) VUV Raman laser



(b) 266 nm laser

Fig. 4. AFM images of ablated 6-H SiC.

from the VUV Raman laser were directed to the substrates placed in a vacuum chamber with pressure less than $8x10^{-5}$ Torr using an MgF_2 lens at the same time. In this case, a Ni mesh with 25x25 μm^2 apertures was put on the sample surface as a contact mask for the micropatterning. The irradiated area at the sample surface and the repetition rate of the laser pulses were set at about 1 mm in diameter and 1 Hz, respectively.

Figure 4 shows atomic force microscope (AFM) images of single-crystal 6H-SiC ablated by (a) simultaneous irradiation of multiwavelength components emitted from the VUV Raman laser and (b) the only 266 nm wavelength beam, followed by chemical treatments using HCl: H_2O_2:H_2O and HF:H_2O. The laser fluence of 266 nm laser beam and number of laser pulses were 1.06 J/cm^2 and 60 pulses, respectively. The fluence of VUV laser beams for multiwavelength irradiation was estimated to be ca. 20 mJ/cm^2. For the sample ablated by the multi-wavelength irradiation, a well-defined pattern corresponding to the contact mask pattern used was created. Neither cracks nor distortion took place at the edge region, and little debris was deposited on the circumference. The flat bottom almost corresponding to the original surface and the flat walls as well as the sharp edges were obtained. The etching rate was estimated to be as large as 35 nm/pulse. On the other hand, for the sample ablated by the only 266 nm beam, the ablated pattern was distorted, and the edges showed undesirable swelling. In addition, the ablated surface seems to be somewhat roughened.

This novel ablation technique was applied to precision microfabrication of the other hard materials such as fused silica, crystal quartz, sapphire, lithium niobate, SiC, and GaN. For every material, well-defined micropatterns with no cracks, no distortion, and little debris deposition were fabricated similarly to the case of SiC. Microanalysis using photoluminescence and Raman spectroscopy indicated that ablated surfaces of SiC and GaN had little deterioration of crystallinity.

2.3 F_2-KrF excimer laser multiwavelength ablation

The VUV Raman laser used in our initial experiments is unstable for practical use, since it simultaneously radiates fifteen different wavelengths from VUV to visible ranges and its pulse energy in VUV region is too small. As a next step, we demonstrate a new technique of dual-beam ablation of fused silica by multiwavelength excitation process using F_2 laser and KrF excimer laser in nitrogen atmosphere for approaching practical application.

The schematic diagram of the experimental setup for the ablation of fused silica using the dual laser beams was shown in Fig.5. KrF excimer laser beam (248nm) was focused on the front side of the substrate surface through a contact Ni mask (an array of 25x25 μm^2) using a fused silica lens as an ablation beam. F_2 laser beam (157 nm) was directed on the rear side of substrate surface using an MgF_2 lens as an excitation beam. A pulse generator was

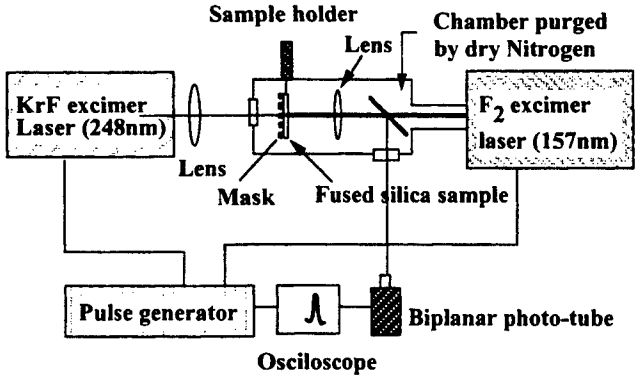
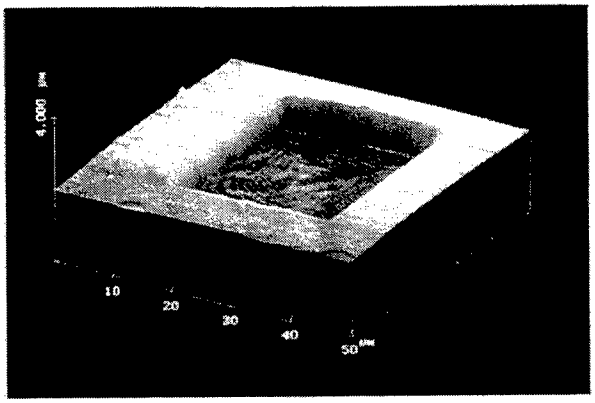
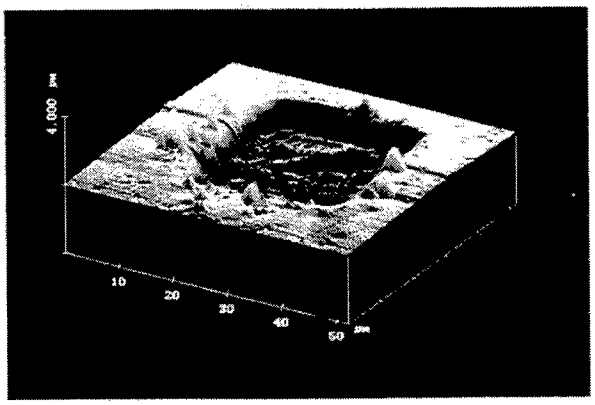


Fig. 5. Schematic illustration of experimental setup for F_2 - KrF excimer laser multiwavelength excitation process.



(a) F_2 - KrF excimer lasers



(b) KrF excimer laser

Fig. 6. AFM images of ablated fused silica.

used to trigger two laser systems for controlling irradiation timing of two beams. At 157 nm wavelength, about 60% of F_2 laser beam can reach the front side of the substrate, since the thickness of fused silica used is as thin as 150 μm. The repetition rate of both KrF excimer and F_2 lasers is 1 Hz in order to exclude effects arising from heating of sample. In the whole experimental process, the F_2 laser fluence on the front surface was constantly kept at 60 mJ/cm^2. The ablation chamber was continuously purged by dried nitrogen gas during the process.

Figure 6 shows AFM images of fused silica ablated by (a) dual beams using F_2 and KrF excimer lasers and (b) KrF excimer laser. The high-quality ablation with well-defined structures without debris deposition around the ablated area takes place for the dual beams. In detailed observation, regular ripple structures appear on the ablated surface. This pattern was formed by diffraction of KrF excimer laser at edge of the mask, suggesting that the ablated surface structure reflected the spatial energy distribution of the laser beam. Therefore, it is deduced that there is little thermal influence during the process. Additionally, it was confirmed in another observation that the quality was comparable to single wavelength ablation using F_2 laser. On the other hand, single KrF excimer laser causes roughness at ablated surfaces, distorted patterns, and much debris deposition.

2.4. Mechanism

The above results indicate that the ablation quality can be drastically improved by simultaneous irradiation of VUV laser beams with small laser fluence. In order to investigate the role of VUV beams, we measured absorption of fused silica to KrF excimer laser beam induced by simultaneous irradiation of F_2 laser beam.

Figure 7 shows pulse forms of KrF excimer laser beam transmitted through the fused silica (a) without and (b) with simultaneous irradiation of F_2 laser beam from the opposite side of KrF excimer laser irradiation. The vertical axes represent beam intensity in an arbitrary unit. The fused silica has no absorption to the KrF excimer laser beam without the F_2 laser irradiation. However, it is quite obvious that beam intensity is reduced by the irradiation. This means that simultaneous irradiation of F_2 laser induces a large absorption to the fused silica by KrF excimer laser beam. This phenomenon may be explained as the excited state absorption (ESA) induced by coupling of KrF excimer and F_2 laser beams. In order to discuss ESA in a current case, the band structure of fused silica is illustrated in Fig. 8. The energy gap and the electron affinity are 9.0 eV and 0.9 eV, respectively. Therefore, electron excitation from valence band to conduction band by F_2 laser (7.9 eV) is impossible. However, the absorption edge of the fused silica used is around 170 nm (7.3 eV), which is ascribed to

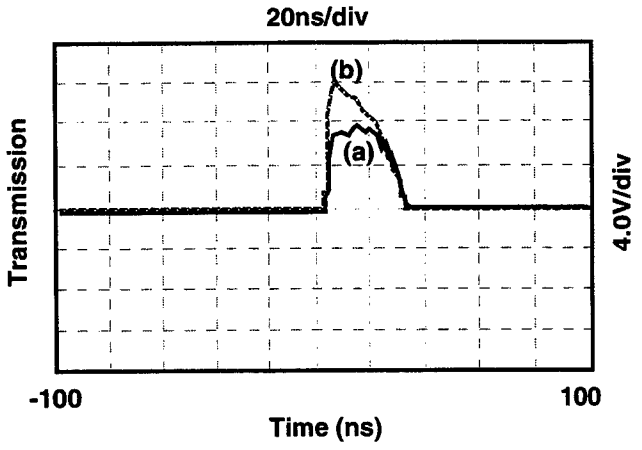


Fig. 7. Pulse forms of KrF excimer laser transmitted by fused silica (a) with and (b) without simultaneous irradiation of F_2 laser .

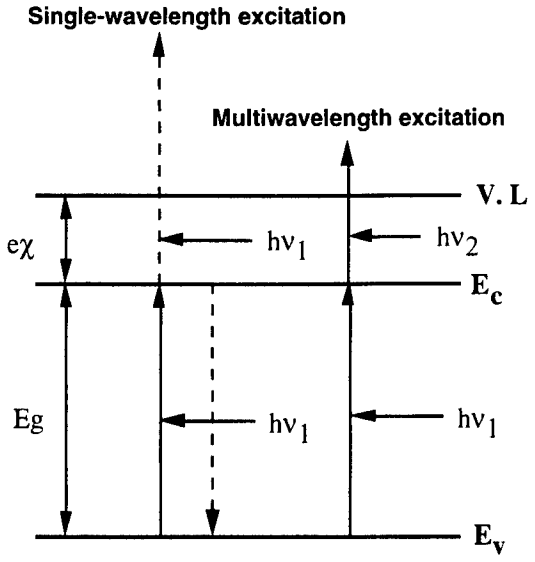


Fig. 8. Band structure of fused silica and electron excitation processes.

impurities and defects. Thus, the fused silica has absorption to the F_2 laser beam, so that electrons can be excited from the valence band to the defect levels. The electrons trapped at the defect levels are easily raised beyond the vacuum level by photons of more than 2.6 eV, which corresponds to a 477 nm wavelength. Accordingly the excited state may strongly absorb single photon of KrF excimer laser. Thus, electrons excited by F_2 laser are raised beyond vacuum level by KrF excimer laser irradiation, leading to Si-O bond scission and finally causing effective ablation.

On the other hand, the mechanism for wide band-gap semiconductors such as SiC and GaN is thought to be different, because such materials have strong absorption even to the UV beam due to their band-gaps of 3 - 4 eV. Namely, a single photon of the UV laser beam is sufficient to directly excite electrons from the valence band to the conduction band. However, the excited electrons in semiconductors cannot contribute to bond scission unlike insulators, since they are not self-trapped. In this case, the bond scission is only possible by cascade excitation through localized electron states ascribing to defects [19]. In the meanwhile, a single photon of the VUV laser beam can directly excite electrons from the valence band to the vacuum level and induce photo-ionization, since the photon energy is larger than sum of the band-gap and electron affinity (5.5 - 7.5 eV). Then, the large laser fluence of the simultaneously irradiated UV laser beam can be used efficiently to eject the ionized species.

2.5. Advantages

The multiwavelength excitation process presented here has many advantages compared with the conventional single wavelength laser ablation. Comparison of features between the multiwavelength excitation and single wavelength processes is summarized in Table I. That is, quite small fluence of the VUV laser for the multi-wavelength excitation process results in reduction of photon cost as well as extension of processing area leading to increase of throughput. Additionally, the ablated patterns are determined by the UV laser beam. Therefore, difficulty in using VUV optics and projection systems is eliminated. Furthermore, unstable pulse-to-pulse energy and spatial nonuniformity of the VUV laser beam are not sensitive for high-quality ablation.

Table I. Comparison of the multiwavelength excitation ablation with F_2 laser ablation.

Process	Advantage	Disadvantage
F_2 laser ablation	Simple setup.	High photon cost. Small processing area. VUV projection system and optics. Speckle noise. Pulse-to-pulse unstability.
Multiwavelength excitation ablation	Low photon cost. Large processing area. UV projection system. Insensitive to unstable VUV pulse.	(Complicate setup.)

3. Laser-induced plasma-assisted ablation

3.1. Experimental scheme

The multiwavelength excitation process using the UV laser combined with the VUV laser has many advantages

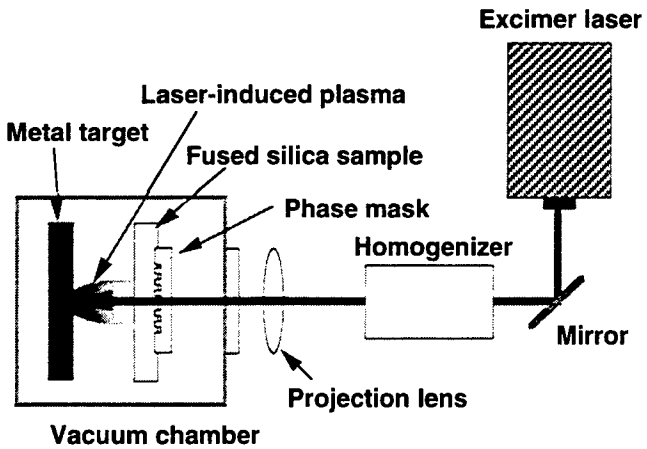


Fig. 9. Schematic illustration of experimental apparatus for LIPAA using a KrF excimer laser and a phase mask.

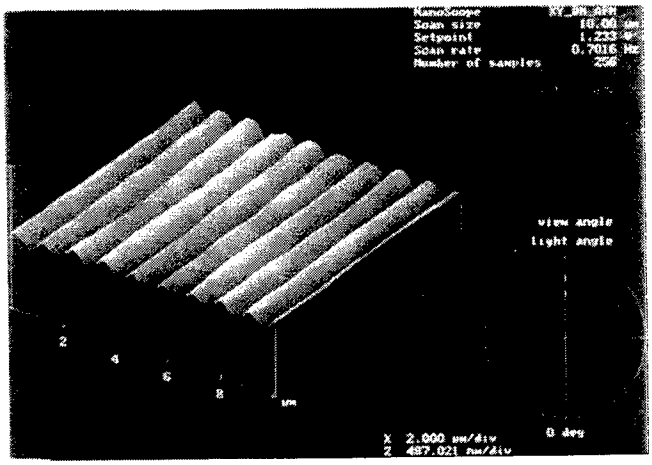


Fig. 10. AFM image of grating structure fabricated in fused silica by LIPAA using a KrF excimer laser and a phase mask (the distance between the sample and the target : 200 μm).

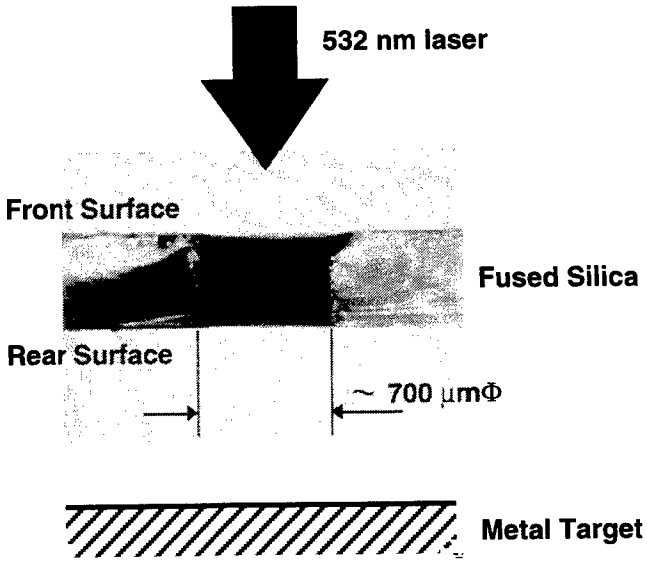


Fig. 11. Optical microscope photograph of a cross section of the through hole fabricated in 0.5-mm-thick fused silica by LIPAA (the distance between the sample and the target : 1.5 mm).

compared with the conventional single wavelength laser process as mentioned above. However, if only the conventional UV, visible or IR laser can be utilized for microfabrication of fused silica and the related glass materials, greater advantage is obvious for practical application. Recently, we have developed another hybrid laser processing of the glass materials by laser-induced plasma-assisted ablation (LIPAA) [13-15]. The most important feature of this technique is that the single conventional pulsed laser can lead to an effective ablation of the transparent materials by coupling of the laser beam to plasma generated from a metal target by the same laser.

Figure 9 shows a schematic illustration of the experimental apparatus for LIPAA. The KrF excimer laser of a 248 nm wavelength and a 34 ns pulse width is homogenized by using a couple of 5x5 microlens arrays (fly's eye type homogenizer). The homogenized beam is projected to the fused silica substrate placed in the vacuum chamber using a single fused silica lens. Since the fused silica has no absorption in a UV range, the laser beam goes through the substrate and then is absorbed at a metal target surface (typically Ag) placed behind the substrate with a distance of a few hundreds μm ~ a few mm. The repetition rate of laser irradiation is kept constant at 1 Hz. Due to interaction of plasma generated from the target and the laser beam, significant ablation takes place at the rear surface of substrate. In this experiment, a phase mask with a 1.065 μm period designed for the KrF excimer laser beam is kept in contact with the front surface of substrate for direct microfabrication. One of advantages of this technique is that the mask is not affected by debris deposition since ablation takes place at the reverse side of substrate. Instead of the excimer laser, the other pulsed IR and visible as well as UV lasers can be used. For micropatterning, a mask projection method is also available.

3.2. Fabrication of micrograting

Figure 10 shows an AFM image of grating structure fabricated on the fused silica substrate by using the experimental setup shown in Fig. 9 at the laser fluence of 1.3 J/cm^2 and 40 pulses. Well-defined and clean micrograting structure was formed without any severe damage. A period of the grating is about 1.06 μm, which well agrees with that of the mask used. The cross-sectional profile of the grating has a sine-wave-like structure with a depth of a few hundreds nm and a smooth surface. Thus, the present technique is very attractive for precision microfabrication of fused silica. Additionally, various microstructures such as Fresnel-zone pattern and micro-trench can be formed by the mask projection method using fundamental (1.06 μm), 2ω (532 nm), or 4ω (266 nm) of Q-switched Nd$^+$:YAG laser.

3.3. High-speed hole drilling

Fabrication of a through hole in glass materials is also possible by LIPAA. In this experiment, a 532 nm wavelength beam of a 6 ns pulse width was used. The laser beam was incident on the sample placed in the vacuum chamber through an aperture of 5.0 mm in diameter and a focus lens. Figure 11 shows a optical microscope photograph of a cross section of the through hole fabricated

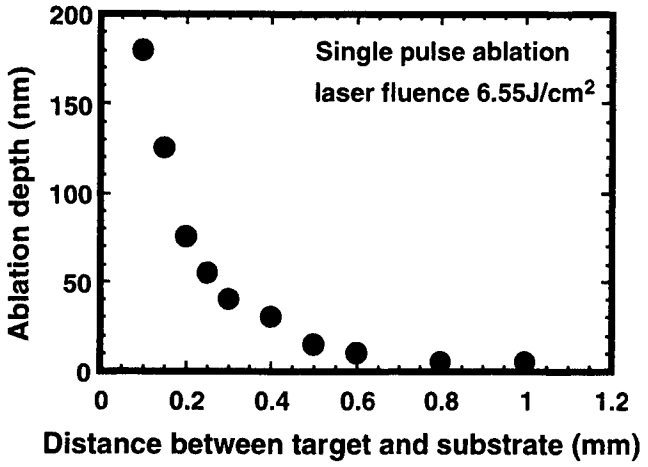


Fig. 12. Dependence of ablation depth on the distance between the sample and the target for LIPAA using a single pulse irradiation.

in 0.5-mm-thick fused silica at laser fluence of 7.7 J/cm^2 and 300 pulses. The diameter of fabricated hole is about 700 μm. Here we define that the rear surface corresponds to the side attacked by the laser-induced plasma and the front surface is the side where the laser beam is incident. A well-defined hole without large cracks was basically formed. The hole-drilling of Pyrex glass was also demonstrated and an almost similar result was obtained.

Lee et. al. have applied the LIPAA process in the air using a fundamental beam of Q-switched Nd:YAG laser for scribing of sapphire wafers which are used as substrates for blue LED and LD based on GaN [20]. By scanning the tightly focused laser beam, the wafer can be scribed in any shape.

Thus, the LIPAA is quite attractive for not only surface micropatterning but also high-efficiency micromachinning of transparent materials.

3.4. Mechanism

Although the mechanism of this technique is complicate and still unknown, we consider that ablation proceeds by combination of three processes, that is, influence of species in the plasma to the sample surface, plasma heating, and metal film deposition. In order to discuss the mechanism, dependence of ablation depth on the distance between the sample and the target was examined as shown in Fig. 12. In this experiment, a fourth harmonic of Nd:YAG laser of a 266 nm wavelength and a 6 nm pulse width was used. The laser fluence was set at 6.55 J/cm^2 and an only single pulse was supplied. At the distance shorter than 0.6 mm, significant ablation takes place even by single pulse irradiation, and the ablation depth exponentially increases with decreasing the distance. This fact suggests that the laser-induced plasma can directly contribute to ablation below this significant distance and its influence increases with decreasing the distance. We suppose the following two possibilities as the plasma direct interaction, i.e., (I) charge exchange between ions or electrons in the plasma and the sample surface, or (ii) transfer of kinetic or potential energy of ions, electrons and radicals in the plasma to the sample surface. Here, the kinetic energy of species are typically in the range of a few eV to several hundreds eV, so that the velocities are estimated to be $10^3 \sim 10^4$ m/s for ions and radicals and $10^5 \sim 10^6$ m/s for electrons, respectively. Therefore, the length of flight during the laser pulse duration of 6 ns is calculated to be several $\sim$ several tens μm for ions and radicals and several hundreds μm $\sim$ several mm for electrons, respectively. By taking account of the above experimental result, this estimation indicates that electrons in the plasma is mainly attributed to this process. The extremely large ablation depth at the distance shorter than several tens μm may be due to contribution of ions and radicals. The plasma heating may be also possible, since it causes large change in optical properties of the substrate such as absorption coefficient. On the other hand, at the distance longer than 0.6 mm, ablation does not take place by single pulse irradiation, while it was confirmed that additional pulse irradiation induced ablation. In this case, absorption of the laser beam to the metal thin film deposited on the substrate surface by preceding laser pulse is thought to be dominant mechanism.

4. Conclusion

Precision microfabrication of hard materials such as fused silica has been demonstrated by two kinds of hybrid laser processing, i.e., VUV-UV multiwavelength excitation process and LIPAA.

Simultaneous irradiation of the VUV and UV beams presents direct microfabrication of fused silica with well-defined patterns, little debris deposition, and little thermal damage. The mechanism is attributed to the excited-state absorption, that is, ablation takes place by strong absorption of the uv laser beam to the excited-state formed by the VUV beam irradiation. The novel ablation technique presented in this paper gives some advantages to precision microfabrication of not only fused silica but also the other hard materials such as crystal quartz, sapphire, lithium niobate, SiC and GaN.

In the meanwhile, LIPAA of another hybrid laser processing of glass materials, in which only the single conventional UV, visible, or IR laser led to an effective ablation of the transparent materials by coupling to plasma generated from a metal target by the same laser, was demonstrated. LIPAA realized surface micropatterning and high-speed hole drilling for the glass materials.

Finally, we conclude that novel ablation techniques by hybrid laser processing have great potential for precision

microfabrication of the hard materials for practical applications.

References

[1] P. R. Herman, K. Beckley, B. Jackson, K. Kurosawa, D. Moore, T. Yamanishi, and J. Yang: Proc. SPIE Vol. **2992**, (1997) 86.

[2] H. Varel, D. Ashkenasi, A. Rosenfeld, M. Wahmer, E. E. B. Campbell: Appl. Phys. A**65**, (1997) 367.

[3] J. Wang, H. Niino, and A. Yabe: Appl. Phys. A**68**, (1999) 111.

[4] K. Sugioka, S. Wada, A. Tsunemi, T. Sakai, H. Takai, H. Moriwaki, A. Nakamura, H. Tashiro, and K. Toyoda: Jpn. J. Appl. Phys. **32**, (1993) 6185.

[5] K. Sugioka, S. Wada, H. Tashiro, K. Toyoda, and A. Nakamura: Appl. Phys. Lett. **65**, (1994) 1510.

[6] K. Sugioka, S. Wada, H. Tashiro, K. Toyoda, Y. Ohnuma, and A. Nakamura: Appl. Phys. Lett. **67**, (1995) 2789.

[7] K. Sugioka, S. Wada, Y. Ohnuma, A. Nakamura, H. Tashiro, and K. Toyoda: Appl. Surf. Sci. **96-98**, (1996) 347.

[8] J. Zhang, K. Sugioka, S. Wada, H. Tashiro, and K. Toyoda: Jpn. J. Appl. Phys. **35**, (1996) L1422.

[9] K. Sugioka, S. Wada, H. Tashiro, and K. Toyoda: Appl. Surf. Sci. **109/110**, (1997) 179.

[10] J. Zhang, K. Sugioka, S. Wada, H. Tashiro, and K. Toyoda: Appl. Phys. A**64**, (1997) 367.

[11] J. Zhang, K. Sugioka, S. Wada, H. Tashiro, and K. Toyoda: Appl. Phys. A**64**, (1997) 477.

[12] J. Zhang, K. Sugioka, S. Wada, H. Tashiro, and K. Toyoda: Appl. Surf. Sci. **127-129**, (1998) 793.

[13] J. Zhang, K. Sugioka, and K. Midorikawa: Appl. Phys. A70, (2000). (in press).

[14] J. Zhang, K. Sugioka, and K. Midorikawa: Opt. Lett. **23**, (1998) 1486.

[15] J. Zhang, K. Sugioka, and K. Midorikawa: Appl. Phys. A**67**, (1998) 499.

[16] J. Zhang, K. Sugioka, and K. Midorikawa: Appl. Phys. A**67**, (1998) 545.

[17] J. Zhang, K. Sugioka, and K. Midorikawa: Appl. Phys. A**69**, (1999) S879.

[18] H. Moriwaki, S. Wada, H. Tashiro, K. Toyoda, A. Nakamura, A. Kasai, and A. Nakamura: J. Appl. Phys. **74**, (1993) 2175.

[19] N. Itoh: Nucl. Instr. Meth. B**122**, (1997) 405.

[20] J.-M. Lee, J.-H. Ho,and T.-K. Yoo: Proc. SPIE Vol.**3933**, (2000). (in press)

Novel Results of Laser Precision Microfabrication with Excimer Lasers and Solid-State Lasers

Uwe STAMM, Michael FIEBIG, Sergei GOVORKOV, Eric MAYER, Rustem OSMANOV, Michael SCAGGS, Evgeni SLOBODCHIKOV, Alexander WIESSNER and Dirk BASTING

[a]*Lambda Physik AG, Hans-Böckler-Straße 12, D-37079 Göttingen, Germany*
[b]*Lambda Physik Inc., 3201 West Commercial Blvd, Fort Lauderdale, FL 33309, USA*
Tel: +49 551 69380 Fax: +49 551 68691 e-mail: randd@lambdaphysik.com

Over the last decades laser technology has found the way into various industries. For microfabrication specifically excimer lasers have developed to powerful manufacturing tools because of their short UV wavelengths as well as the progress in excimer laser technology. More recently the development of pulsed medium-power diode-pumped solid-state lasers has opened the way to new micromachining applications related to the available superior beam quality. Here we review technological achievements in both industrialized excimer lasers and diode-pumped Nd:YAG lasers for microfabrication . Data are presented for industrial 308 nm excimer lasers with energy stability better than 1 % (sigma) at 300 W average power. Using the latest technology in 157 nm excimer lasers applications of processing of "difficult" materials are presented. Finally we review results on studies of microdrilling of metals and ceramics using a newly developed 10 kHz diode-pumped solid-state laser at wavelengths 1064 nm, 532 nm and 355 nm.

Keywords: excimer laser, diode-pumped solid-state UV laser, 157 nm laser, F_2 laser, TFT annealing, micromachining, microdrilling

1. Introduction

The revolutionary progress in semiconductor, communication and information industries based on electronic and photonic technologies demands for the development and enhancement of various microfabrication techniques to support micro- and nano-technologies. The trend for "smaller size and higher speed" is evident in integrated microchips for computers, micro-optics and micro-electro-mechanical systems (MEMS). Biotechnology and medicine as well require micro- and nano-technological approaches. Ultraviolet excimer lasers and diode-pumped solid-state lasers play an important role in the development of the corresponding laser precision microfabrication techniques.

In the present paper we give a short review on new technological achievements in

1. High power ultra-stable 308 nm excimer lasers for application in thin film transistor (TFT) liquid crystal display (LCD) manufacturing and high precision microfabrication,
2. 157 nm lasers and their application in processing of difficult materials,
3. Micro-drilling of metals and ceramics by newly developed diode-pumped solid-state lasers.

2. High power industrial 308 nm excimer lasers with ultra-stable energy

Applications as polycrystalline-silicon thin film transistor annealing and ink-jet nozzle drilling have been the main driving applications for higher average power and better pulse-to-pulse and long term energy stability for industrial excimer lasers. In strategic alliance for the TFT LCD manufacturing application, Japan Steel Works (annealer), MicroLas (optics) and Lambda Physik (laser) have developed a 308 nm excimer laser annealing system several years ago[1]. The 308 nm wavelength has been shown to be well matched to the annealing process and gives significant advantage with respect to the optics lifetime in the annealing system. While the early systems have been used for process development and small scale manufacturing of active matrix LCDs, today TFT annealing systems are on the production floor. The necessary yield for high volume production sets stringent demands onto the energy stability of the laser. Increasing sizes of the displays

First International Symposium on Laser Precision Microfabrication, Isamu Miyamoto, Koji Sugioka, Thomas W. Sigmon, Editors, Proceedings of SPIE Vol. 4088 (2000) © 2000 SPIE · 0277-786X/00/$15.00

require higher pulse energy and higher average output power.

We have developed the third and are developing the fourth generation of industrial lasers for excimer laser annealing (Lambda Physik's LAMBDA STEEL). Both generations differ in the output energy and average power available from the laser. In figure 1 the output power of both lasers is shown versus repetition rate. While the LAMBDA STEEL 670 is operated at 670 mJ, the LAMBDA STEEL 1000 allows operation at 1 J pulse energy. With operational repetition rates of up to 300 Hz, the LAMBDA STEEL 1000 is the first industrial 300 W excimer laser in the world.

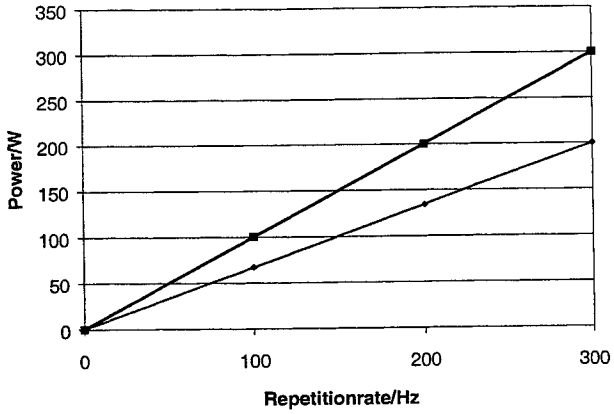


Fig. 1 Output power versus repetition rate for the LAMBDA STEEL 1000 (upper) and LAMBDA STEEL 670 (lower) curve.

Significant progress has been made in the improvement of pulse-to-pulse energy stability of both laser models. In figure 2 various measures of the pulse-to-pulse energy stability are given. The upper diagram shows the sigma value of the energy distribution for a continuous operation of the laser over 40 million pulses with the same gas fill. Energy stability sigma is around 0.5 %. The second diagram gives the normalized deviation of the maximum pulse energy and minimum pulse energy from average pulse energy for the same period of operation taken always over 6000 pulses. The maximum energies deviate by around 2 % from average, minimum pulse energies are 2-3 % smaller than the average pulse energy. The graphics at the bottom gives the distribution of the output pulse energy in absolute values. Peak-to-peak energy stability is about 4 %. Accordingly, the LAMBDA STEEL laser is the most stable industrial high power excimer laser in the world. Its application in TFT annealing and microfabrication should allow for a new quality in the production process.

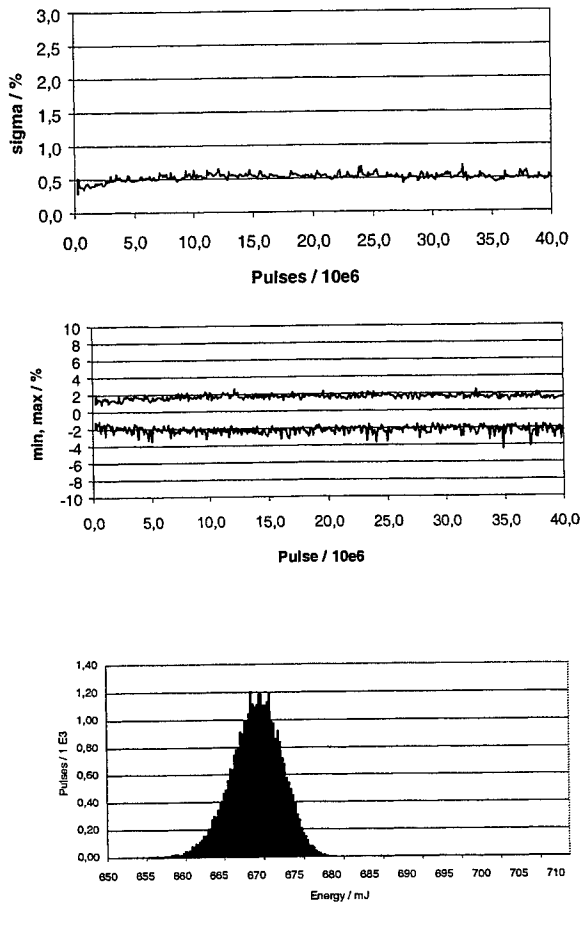


Fig. 2 Energy stability of the LAMBDA STEEL 670. Upper graph: energy stability sigma, middle: relative maximum and minimum energy deviations from average (6000 pulses sampled), bottom: distribution of pulse energies.

3. High performance 157 nm lasers in micro-processing of materials

Fluorine lasers, emitting at 157 nm, deliver the shortest commercially available laser wavelength. The gain medium excitation is similar to that used in excimer lasers, but the molecular laser transition gives an emission with a photon energy of 7.9 eV. During the last years, a lot of progress has been made in 157 nm laser technology at Lambda Physik. Advances in gas discharge and laser tube design (NovaTube® and DuraTube® technology) coupled with clean-room assembly standards have produced robust, cost effective, industrial-standard fluorine lasers (F_2 lasers). The development has been driven by both the need for reliable industrial 157 nm sources for micromachining of difficult, i.e. transparent materials, as well as the microlithography roadmap having included 157 nm technology. According to

the SIA-Roadmap, the 157 nm wavelength of the F_2 laser emission will be used for chip production with critical dimensions of 100 nm down to the 70 nm node [2].

Fluorine lasers are today available at various energy, repetition rate and power levels. The size of the lasers ranges from small portable air-cooled units to large size high power systems. Operating output parameters of different Lambda Physik laser models are summarized in table 1.

Table 1 Output parameters of different Lambda Physik fluorine lasers

	Optex	LPF 202	LPF 205	LPF 220	NovaLine F1030
Power	0.3 W	1.0 W	2.5 W	6.0 W	10.0 W
Repetition Rate	200 Hz	20 Hz	50 Hz	200 Hz	1000 Hz
Energy	1.5 mJ	50 mJ	50 mJ	30 mJ	10 mJ

The next generation of industrial fluorine lasers is under development at Lambda Physik aiming for 20 W output power at 2 kHz repetition rate [3]. Experimental data from the development laboratory are shown in figure 3.

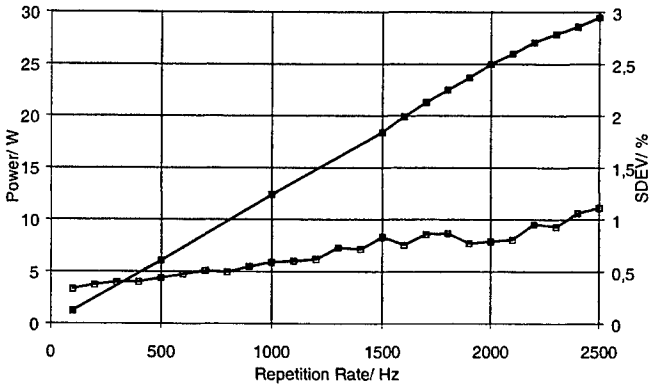


Fig. 3 Output power and energy stability of an industrial 157 nm laser currently under development at Lambda Physik.

We have investigated laser ablation of several materials, such as glass, PTFE/Teflon, and quartz/fused silica. In the experiments, we used an industrial Lambda Physik NovaLine F600 with 10 mJ stabilized pulse energy at pulse repetition rates of up to 600 Hz. In our studies, in addition to the 157 nm wavelength, the NovaLine F600 laser was operated at 193nm to compare the ablation quality. The fluence was adjusted to 6.5 J/cm^2 by laser discharge voltage or external attenuation. The pulse duration of the F600 was 8-15 ns for both wavelengths.

A mask imaging system projected de-magnified illumination patterns onto samples with an objective lens. This method offers well-defined ablation fluences, and a potential order of magnitude improvement in resolution (1-5 μm) over high intensity focal point machining. It also offers optical precision between features and well-defined edges between ablated and unexposed zones.

Since laser radiation at 157 nm is strongly absorbed by oxygen and water vapor, the beam path from the output coupler to the lens was evacuated. A proprietary nozzle design purged the beam path from the objective lens to the sample. The samples were machined by imaging the metal mask with the aperture of known dimensions; computer controlled stages perform the motion control of the sample.

3.1. Micromachining of glass

Glasses are widely used for manufacturing of visible optics and chemical handling equipment (lenses, lens arrays, microfluidic plates, etc). At the given fluences of this study, we were unable to machine glass to any appreciable resolution at wavelengths of 248 nm or above. Therefore, in figure 4 we show ablation results at the commonly employed ArF excimer wavelength of 193 nm, and in comparison results at the F_2 wavelength of 157 nm.

The figures show good and similar results for both wavelengths. In both cases there were 500 pulses applied at a fluence of 6.5 J/cm^2. While the ablation rate was an order of magnitude lower for 157 nm, the surface quality is smoother. Therefore, applications requiring excellent surface quality for blind holes may find 157 nm fluorine laser processing advantageous.

3.2. Processing of fused silica / quartz

Fused silica as well as natural quartz have the benefit of low thermal expansion and a high melting point. Since it can be optically polished, it is used as a substrate material for a variety of optical components in applications, such as displays, fiber optics, and micro-optical components. A comparison of laser ablation of fused silica at 193 nm and 157 nm is shown in figure 5. Working at 193 nm creates a lot of thermal damage, microcracking, and chipping. The 157 nm results show clean blind holes with no thermal damage to the material; there is no microcracking and only a small amount of redeposition or distorted material at the edge of the hole.

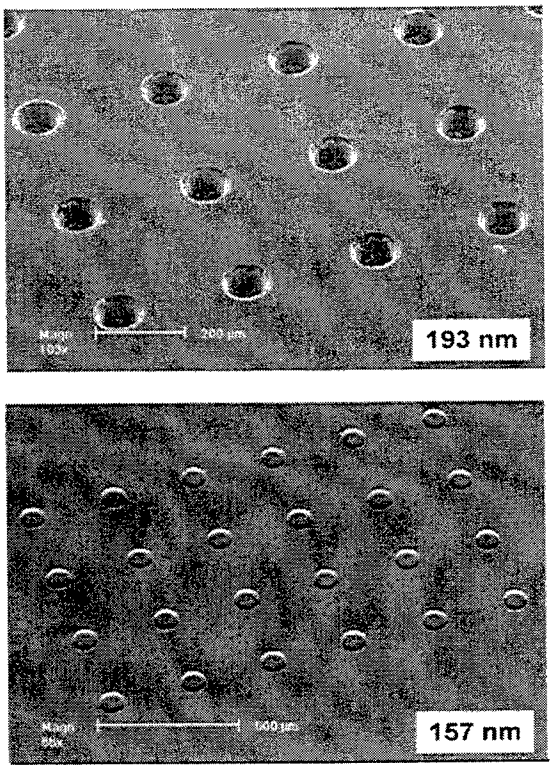


Fig. 4 Blind holes in glass, processed at 193 nm (upper) and 157 nm (lower)

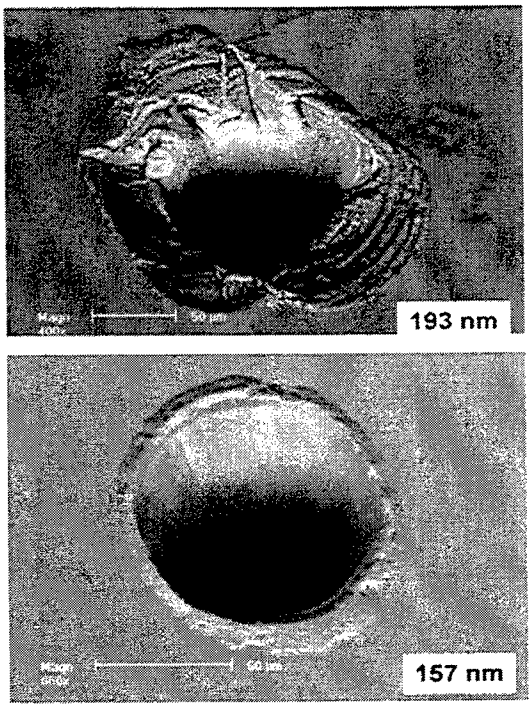


Fig. 5 Fused silica, processed at 193 nm (upper) and 157 nm (lower)

3.3. Ablation of PTFE/Teflon®

PTFE is a mechanically, electrically, and chemically stable material. It is used in the life sciences for catheters, implants, etc. Its electrically insulating properties make it the material of choice for the electronics industry. For example, it is used as a high-voltage insulator between conductive layers in multi-layer chips and circuit boards.

Due to Teflon's absorption characteristics, longer wavelengths can only machine with high fluence by thermally overloading the material or through multi-photon absorption. Even at 193 nm PTFE can not be effectively machined. Figure 6 shows the differences in results, obtained from 193 nm, and 157 nm ablation of PTFE.

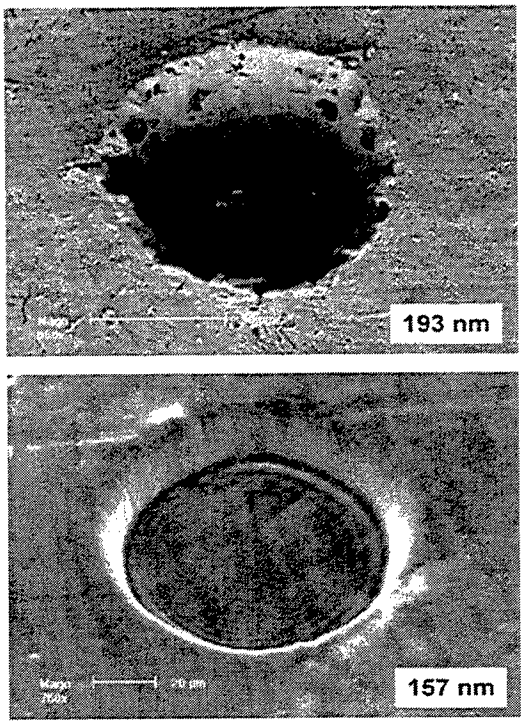


Fig. 6 PTFE, processed at 193 nm and 157 nm

At 193 nm an ablation with acceptable result is possible, but the edge quality and the walls are still of low quality. Micromachining at 157 nm produces very clean results with no evidence of debris or thermal damage. The edges are well defined and sharp, and the bottom surface is very smooth. The ring pattern with an approximate 10 μm period of undulation can be seen on the bottom surface. The pattern is suspected to be caused by diffractive interference in the illumination.

4. Michromaching with UV solid-state lasers

Q-switched short-pulse (10 ns) all-solid-state lasers offer excellent beam quality and high power in combination with industrial robustness. These qualities make them potentially efficient sources for high throughput manufacturing of microstructures with characteristic sizes of 10 μm to several 100 μm.

In investigations of microdrilling of materials as stainless steel, titanium, aluminum and ceramics, we utilized amplified all-solid-state system consisting of side-pumped, q-switched Nd:YAG oscillator (Lambda Physik's Gator2000) followed by diode-pumped amplifier. The oscillator produced 15 nsec pulses in TEM_{00} beam with an average power of 10 W at 1064 nm and nominal repetition rate of 10 kHz. The amplifier output was 28 W at the fundamental wavelength, and 15 W and 10 W at the second and third harmonic wavelength correspondingly. Quality of the amplified beam was better than 1.2 times of diffraction limit.

We investigated drilling rates achievable in dependence of the thickness of the samples as well as the wavelength of the laser. A more detailed discussion of the results of these experiments is given elsewhere [4].

Figure 7 shows laser fluence dependence of the average ablation rate for two different values of thickness of stainless steel samples. In 50 μm-thick foil, ablation can be considered a surface ablation, since the beam diameter at the surface (20 to 30 μm) is comparable to the sample thickness. Fast material removal begins at approximately 10 J/cm^2, with ablation rate reaching roughly 1 μm per pulse. Consistently with the previous works, ablation rate increases only slightly as the laser fluence is increased by more than order of magnitude above this threshold.

For thickness of the sample increased to 0.87 mm, the minimum laser fluence required to penetrate entire sample increases to 100 J/cm^2, i.e. ten times the threshold value for the thin sample. Apparently, at lower laser fluence, ablation terminates at a certain depth, due to attenuation of the beam in the column of vapor and plasma that fill the hole. As the sample thickness approaches 1 mm, ablation rate becomes strongly wavelength-dependent. At the similar laser fluence, UV laser beam provides almost an order of magnitude faster drilling than IR beam. For clear comparison, Fig.3 shows the maximum ablation rates that we observed at laser fluence of 30 to 40 times of surface ablation threshold, at three different wavelengths.

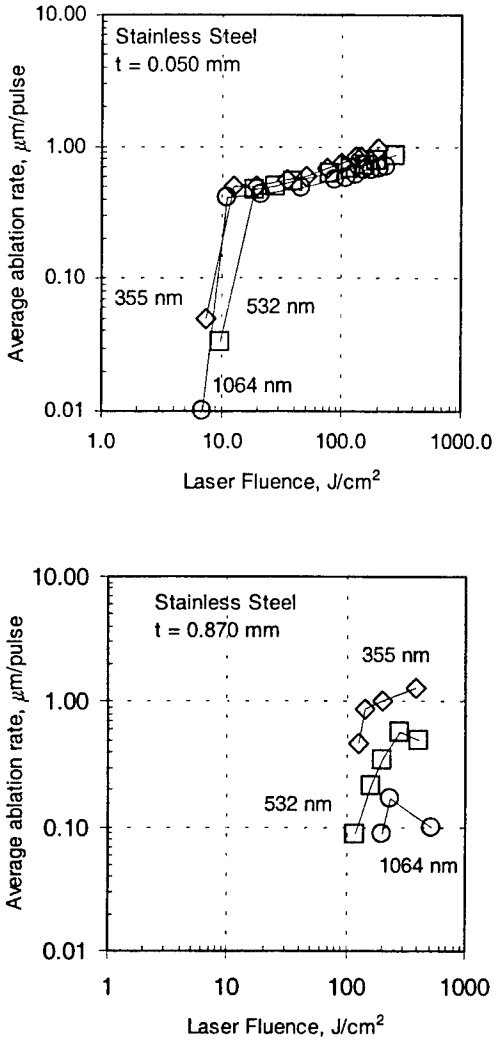


Fig.7 Ablation depth per pulse in stainless steel at three laser wavelengths: 1064 nm (circles), 532 nm (squares), 355 nm (diamonds). Sample thickness: top: 50 μm; bottom: 870 μm.

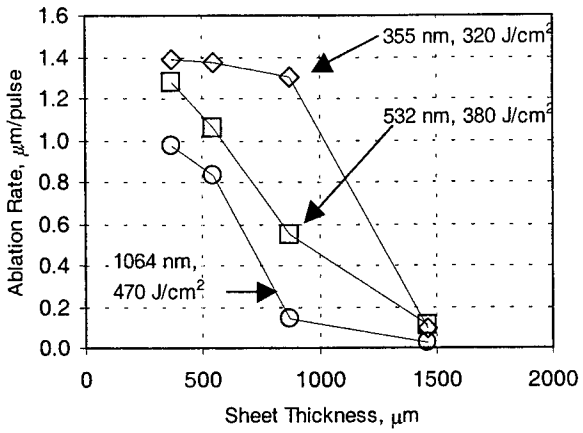


Fig.8 Comparison of average ablation depth per pulse versus sample thickness at three laser wavelengths. Note sharply increasing difference in rates for samples thicker than 0.5 mm.

We found that the wavelength dependence of average ablation rate is remarkably strong for the high aspect ratio holes. Our conclusion is that shorter wavelength allows drilling significantly higher aspect ratio holes at a higher speed for the sample thickness exceeding 1 mm. Using the third harmonic the ablation rate are almost an order of magnitude higher than as compared to the IR laser output. This wavelength dependence is so strong because the beam has to penetrate thick layer of dense plasma, which is not present in drilling thin foils due to three-dimensional plume expansion.

5. Conclusions

We have summarized novel technological developments as well as results on precision microfabrication with excimer lasers and solid-state lasers. The unique properties of the laser sources described in the paper will open the field for new applications in industry.

References

[1] J. Shida, S. Ishizaka, N. Kobayashi, O. Kato, "Crystallization of a-Si films by excimer laser annealing method", JSW Technical Review No. 17.

[2] R. Harbinson, International SEMATECH's 157 nm Lithography Workshop, 15-17 February 1999, Phoenix, AZ, USA.

[3] K. Vogler, U. Stamm, I. Bragin, F. Voß, S. Govorkov, G. Hua; J. Kleinschmidt, R. Pätzel, "Advanced F2 lasers for microlithography", *SPIE Microlithography 2000*, 27 February – 03 March 2000, Santa Clara, CA, USA.

[4] S. Govorkov, E. Slobodchikov, A. Wiessner, D. Basting, "High-throughput micromachining of steel and ceramics with solid-state UV laser", SPIE Proceedings of *Photonics West*, 22 – 28 January 2000, San Jose, CA, USA.

Excimer laser microfabrication and micromachining

Malcolm GOWER

Exitech Ltd, Hanborough Park, Long Hanborough, Oxford OX8 8LH, United Kingdom
E-mail: m.gower@exitech.co.uk

Reports in 1982 of polymers ablated and etched by excimer laser radiation mark the founding of laser microfabrication and micromachining as technologies that in the intervening period has matured into a manufacturing process used by a diverse range of industries. This paper describes some of these industrial applications.

Keywords: Micromachining, excimer lasers, laser ablation, industrial applications, MEMS

1. Introduction

Excimer lasers are proving to be highly successful for fabricating industrial components with feature sizes in the range between 0.05 – 1000μm[1-4] (see Fig 1). As well as providing a 15 year, 5 generation extension to optical lithography as used in the manufacture of silicon chips, excimer lasers are used for microfabricating many of the critical features in a wide variety of the electronic and telecommunication components that are enabling the current vast explosion in internet-based communications. This paper describes the *'state of the art'* for some of these excimer laser microfabrication applications.

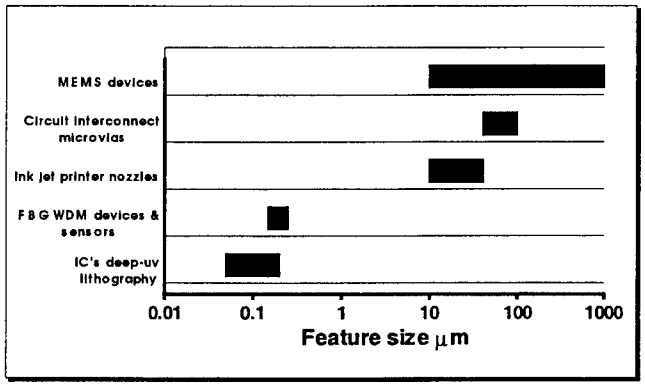


Fig 1. Critical feature size ranges of excimer laser microfabricated components

2. Developments in deep-uv lithography

At single-pulse fluences below the threshold for material ablation, KrF and ArF excimer lasers are now the light source of choice for performing the lithography step crucial to the mass production of large memory size *integrated circuits* (IC's), *microprocessors* and *application-specific IC's* (ASIC's). Their short wavelength allows ever-smaller (down to 130nm) and greater densities of devices to be replicated. To achieve such small features the performance of the stepper cameras used to replicate the circuit patterns from masks onto photoresist-coated silicon wafers has had to improve enormously in a very short time. Higher optical resolution using shorter wavelengths of illumination and increasingly larger numerical aperture imaging lenses has enabled smaller circuit features to be produced. Enlarging the image field diameter of the lens has also allowed larger area chips to be fabricated.

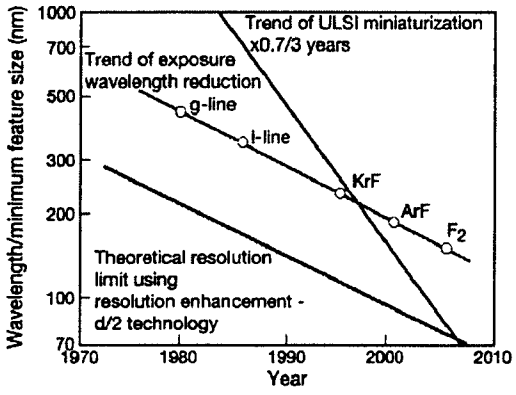


Fig 2. Source wavelength and CD for photolithography
Courtesy of S Okazaki, Hitachi Ltd

Fig 2 shows the technology trends for photolithography light sources and design rule *critical dimensions* (CD) as used in

First International Symposium on Laser Precision Microfabrication, Isamu Miyamoto, Koji Sugioka, Thomas W. Sigmon, Editors, Proceedings of SPIE Vol. 4088 (2000) © 2000 SPIE · 0277-786X/00/$15.00

this industry. It is now believed F_2 lasers producing radiation at 157nm will follow 193nm ArF lasers and be the favored light source for producing circuit features in the 60-100nm range required in 2004. Currently there is intensive R&D activity aimed towards developing suitable 157nm process tools and and associated technologies including high-power line-narrowed laser sources, transmissive optical materials, coatings, imaging lenses, masks, pellicles and photoresists.

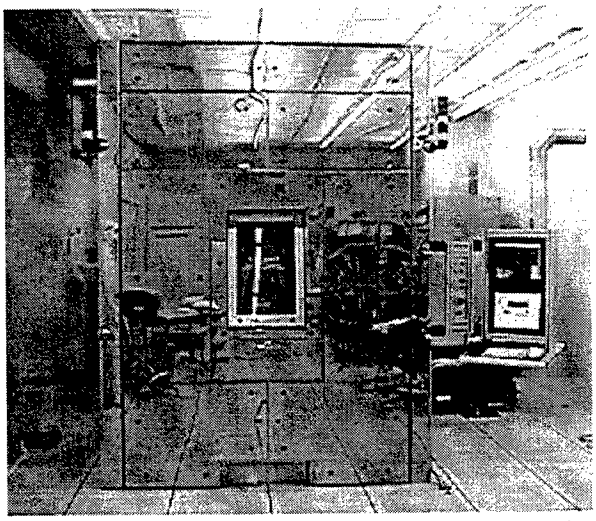


Fig 3. Exitech 157nm Microstepper. *Courtesy of International Sematech*

Fig 3 shows a small field F_2 laser Microstepper being used to carry out resist and other materials characterisation and development issues at 157nm. Fig 4 shows high resolution 1:1 and isolated 130nm and 120nm lines imaged in 248nm resist using such a 157nm exposure tool.

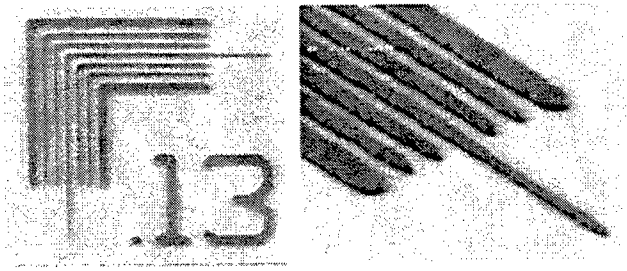


Fig 4. (a) 130nm and (b) 120nm 1:1 and isolated lines imaged in Shipley XP-98248-S resist using the 157nm Microstepper in Fig 3. *Courtesy of International Sematech.*

3. Excimer laser drilling of microvia holes in circuit interconnection packages

Almost as important as the rapid improvements in speed and memory of IC's are the parallel developments in interconnection packaging made during the last 20 years. So speed, power and area (real estate) are not compromised, packages on which chips are mounted for connection to other devices have had to keep pace with the rapid advances made in IC's. There are now more than a dozen generic types of chip interconnection packages which include *multichip-modules* (MCM's), *chip-scale-packages* (CSP's) like *ball-grid-arrays* (BGA's), *chip-on-boards* (COB's), *tape-automated-bonds* (TAB's). Generally these consist of multilayer sandwiches of conductor-insulator-conductor with electrical connection between layers made by drilling small holes (vias) through the dielectric and metal plating metal down the hole. Such blind via holes provide high-speed connections between surface-mounted components on the board and underlying power and signal planes while minimizing valuable real estate occupation. For example, due to difficulties in soldering IC's with greater than ~200 pins, peripheral lead mounting packages like TAB's must be made larger than the chip. By placing microvia connections in the package at the base of the chip instead of around its periphery, a BGA is no larger than 20% the size of the chip.

Drilling microvias by ablation was first investigated in the early 1980's using pulsed Nd:YAG and CO_2 lasers[5,6]. Excimer lasers led the way in applying it to volume production when the Nixdorf computer plant of Siemens introduced polyimide ablative drilling of 80μm diameter vias in MCM's - as used to connect silicon chips together in high-speed computers[7]. Fig 5 shows the Siemens MCM and the KrF laser drilled microvias in the acrylic resin-polyimide dielectric material. Other mainframe computer manufacturers such as IBM rapidly followed suite and installed their own production lines for this application[8].

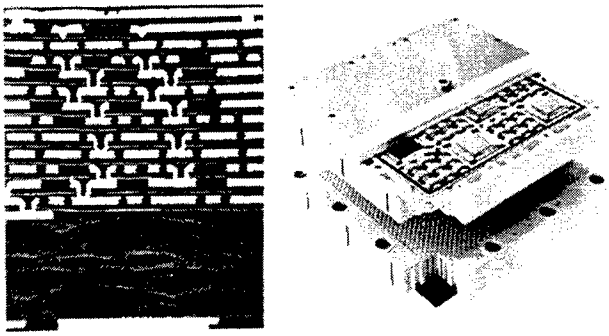


Fig 5. KrF laser drilled microvias in MCM's. (a) Cross-section of 14-layer copper-plated MCM showing 80μm diameter microvias; (b) Populated and assembled MCM package board. *Courtesy of Siemens AG, Germany*

With fewer process steps than other methods, laser-drilling

is regarded as the most versatile, robust, reliable and high-yield technology for creating microvias in thin film packages. Trillions of vias have now been drilled with excimer lasers at yields >99.99% whose *mean time between failure* (MTBF) has been logged at >1,000 hours.

Interconnection densities on rigid and flexible *printed circuit and wiring boards* (PCB's, PWB's and FPC's) are also increasing - driving the requirement for drilling ever-smaller vias in these packages[9]. Thus there is a demand for an ever-increasing packing density of interconnections - for example mountings in current mobile phones and camcorders have around 1200 interconnections/cm^2. Such packages have much lower fabrication costs than MCM's and the current common practice is to mechanically drill the vias. However as diameters decrease to < 100μm it is generally recognized pulsed CO_2 and/or Q-switched Nd:YAG lasers will displace mechanical drills - for such low cost packages excimer lasers are too slow and their running costs are too high. For these boards, holes must be drilled at speeds of several hundred per second at costs of <1¢/1,000 holes. At present excimer lasers are only used to drill microvias in high-value packages such as MCM's and BGA's[10].

4. Excimer laser drilling of ink jet printer nozzles

Inkjet printers comprise a row of small tapered holes through which ink droplets are squirted onto paper. Adjacent to each nozzle, a tiny resistor rapidly heats and boils ink forcing it through the orifice. Increased printer quality is achieved by simultaneously reducing the nozzle diameter, decreasing the hole pitch and lengthening the head. 600 dots-per-inch (dpi) printers typically have 300 nozzles each of 28μm input diameter.

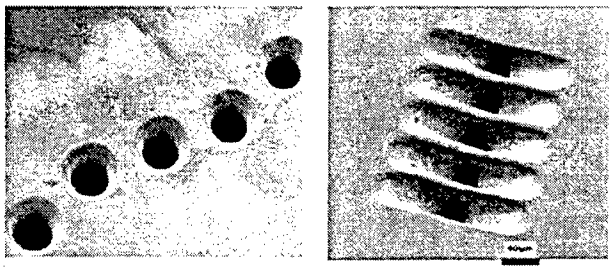
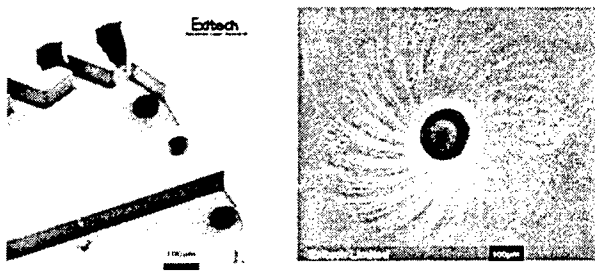


Fig 6. KrF laser-drilled ink jet printer nozzles in polyimide (a) 30μm diameter nozzle array; (b) Nonlinear tapered nozzles to aid laminar flow

Excimer laser drilling of nozzle arrays allows manufacturers to produce higher performance printer heads at greater yields. At average yields of >99%, excimer laser mask projection is now routinely used for drilling arrays of nozzles each having identical size and wall angle[11]. Figure 6(a) shows an excimer laser drilled nozzle array in a modern printhead while Fig 6(b) shows nozzles with nonlinear tapers to aid the laminar flow of the droplet through the orifice. More advanced printers sometimes use piezo-actuators. Rather than being constrained to give shapes characteristic of the process, excimer laser micromachining tools with appropriate CNC programming can readily engineer custom-designed reverse-tapered, $2^1/_2$D and 3D structures. Fig 7(a) shows an array with ink reservoirs machined behind each nozzle while Figure 7(b) shows an example of a rifled tapered hole which spins the droplet to aid its accuracy of trajectory.



(a) (b)

Fig 7. KrF laser-micromachined nozzle structures in polyimide

Figure 8 shows a KrF laser-based tool used for production drilling of ink jet printer nozzles. Mask projection is used to drill all the nozzles in an array simultaneously. The reproducibility of excimer laser drilling allows hole diameter tolerances of ±1μm to be achieved in volume production.

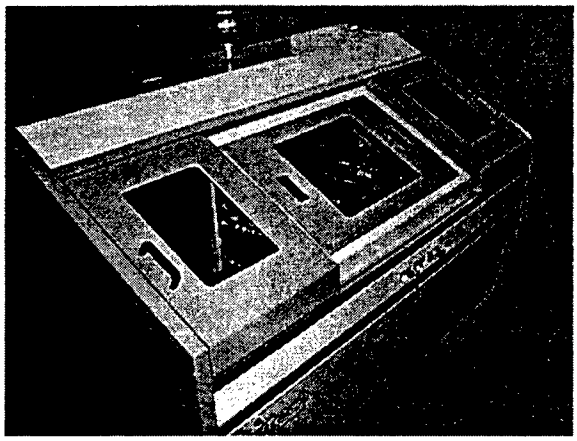


Fig 8. Exitech M6000 ink jet printer nozzle drilling tool

5. Excimer laser micromachined biomedical catheters

As in microelectronics and its associated technologies, the drive for increasing miniaturization with improved device functionality is crucial to the rapid progress being made in the biomedical industry[12]. Precision microdrilling with excimer lasers is routine when making delicate probes used for analyzing *arterial blood gases* (ABGs)[13]. ABG sensors measure the partial pressures of oxygen (PaO_2), carbon dioxide ($PaCO_2$) and hydrogen-ion concentration (pH) used for monitoring the acid-base concentration essential for sustaining life. In intensive care units, ABG results are used to make decisions on patient's ventilator conditions and the administration of different drugs. The use of fiber-optic sensors for ABG analysis provide clinical diagnostics at the patient's bedside without the need for taking blood samples and doing remote analysis[14].

Fig 9(a) shows an example a ABG catheter for monitoring blood in prematurely borne babies. The hole at the side of the PVC bilumen sleeving tube through which blood is drawn is machined using a KrF laser. In this case the clean cutting capability of the laser provides the necessary rigidity that prevents kinking and blockage of the tube when inserted into the artery.

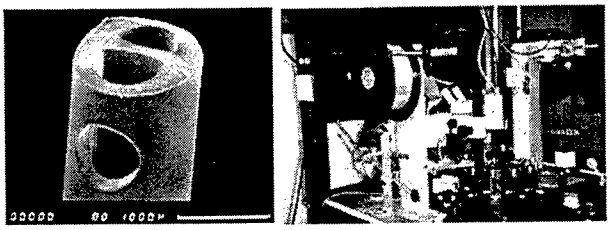


Fig 9. Excimer laser manufacture of blood gas sensor (a) KrF laser-drilled hole in side of PVC bilumen catheter; (b) Automated reel-to-reel fibre hole-drilling system

More important components of this catheter are the PaO_2 and $PaCO_2$ sensors. These consist of a spiral of up to five ~50x15μm rectangular holes machined in a 100μm diameter acrylic (PMMA) optical fiber with an ArF laser. The holes are filled with a reagents whose optical transmission depend on the PaO_2 and $PaCO_2$ levels of the surrounding blood. Using a fully-automated workstation shown in Figure 9(b) that has computer-controlled reel-to-reel fiber feeding and laser-firing, all five holes shown in Figure 10(a) are drilled in the fiber. By spatially-multiplexing a single excimer beam into five smaller ones, holes are drilled simultaneously through the fiber.

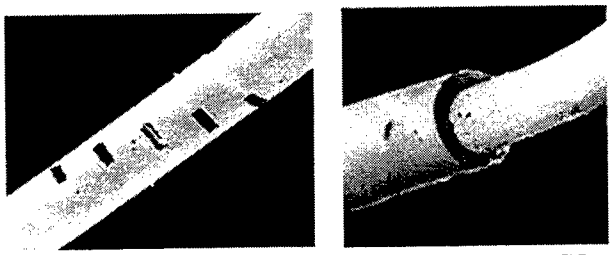


Fig 10. (a) ArF laser-drilled holes in PaO_2 and $PaCO_2$ acrylic fibres; (b) KrF laser-stripped insulation from pH-sensor wire

Preferential excimer laser etching of plastics compared to metals is applied to the stripping of insulation from 100μm diameter wires prior to soldering connections. The process relies on the threshold for excimer laser ablation of the polymer being much lower than for damaging the copper or silver core. As shown in Fig 10(b), excimer lasers are used to cleanly strip away the polyurethane insulation sleeving of wires which form the pH resistivity sensor in the ABG catheter above. Such pulsed laser wirestripping is also in widespread use for preparing connection wires to computer hard-disk reader heads.

6. Excimer laser writing of Fiber Bragg Gratings

As a means of greatly increasing the bandwidth for data transmission through optical fibers, *wavelength division multiplexing* (WDM) of signals is currently experiencing extremely rapid growth in the telecommunications sector. Early single-mode fibers were designed to have zero dispersion at 1.3μm - the best source wavelength at the time. With ensuing improvements to laser diodes at longer wavelengths, modern fibers are designed to operate in the region of lowest attenuation in silica at 1.5μm. To double the bandwidth of older fibers, both wavelengths can be copropagated in the fiber. Until 1994, WDM for data transmission was limited to just these two channels at rates up to 2.5Gb/sec/channel. In current communication systems this has expanded to 16 channels and is expected to rise to ~40 wavelengths within a year. With single-channel capacity also rising to ~10Gb/sec, WDM is enabling a single fiber to carry rates of ~160Gb/sec. Key parallel developments which are making WDM technology so successful are (a) stable output at specific wavelengths from DFB laser sources (b) erbium-doped fiber-amplifiers for signal regeneration without electronic conversion (c) external modulators for reducing crosstalk between signals at closely spaced wavelengths (d) *fiber Bragg gratings* (FBG's) for efficient separation (demultiplexing) of closely spaced wavelengths.

FBG's are manufactured by exposing the fiber core through the side cladding with a spatially-modulated intensity distribution from a uv laser - sometimes 2^{nd}-harmonic cw Ar^+, but increasingly pulsed 193 and 248nm excimer and 266nm 4th-harmonic Nd:YAG or Nd:YLF lasers[15,16]. Although not yet fully understood, it is believed that the uv light breaks oxygen-vacancy defect bonds in the (germanium or cerium) doped core. Liberated electrons migrate and retrap at other color center sites leading to permanent intensity-dependent changes of ~1% to the refractive index. The most simple and popular method for producing the intensity modulation is to use the pattern created by the interference between ±1 diffracted orders from a transmission phase mask designed to suppress light in the 0th-diffracted order. When the mask is placed close to the side of the fiber at average illumination intensities of 10-20W/cm^2, gratings can be recorded in a few minutes depending on the photosensitivity of the fiber used. For reflectivity at 1.5μm wavelengths, the FBG pitch needs to be 0.5μm. As shown in Figure 11(b), FBG's several millimeters in length can produce reflection filters with bandwidths <100GHz (≤ 0.8nm).

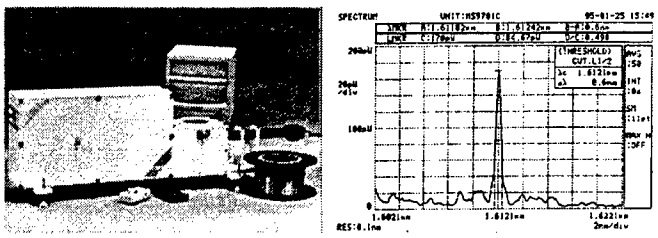


Fig 11. (a) Exitech MA500 proximity mask aligner for writing FBG's; (b) 0.6nm bandwidth reflection peak at 1.6μm of 248nm written FBG

FBG's can be used for other signal management operations in telecommunications. Due to the wavelength variation of refractive index, normally different wavelengths will travel at different speeds in the silica core which because its increasing bandwidth with distance adds noise to the signal. By reflecting different wavelengths from different regions, a chirped FBG in which the grating period changes along its length can be used to compensate for this dispersion. This application is important both for long-haul communications when nonlinear two-photon dispersion effects become important, and when using low-loss 1.5μm wavelengths in older 1.3μm fibers. By allowing each propagating wavelength to experience similar amplification characteristics in wide-band WDM operation, FBG's can be used to flatten the gain from fiber-amplifiers. In addition, FBG's can act as frequency and mode-selective mirrors for erbium fiber and diode lasers, narrow-bandwidth transmission filters and wavelength-selective taps for network monitoring. FBG's can also be used as optical sensors for the remote detection of local stress, strain and temperature in engineering and medical environments. A change in one or more of these properties changes the period of the FBG which in turn modifies its reflection properties for laser diode probe sources. Reflected wavelength shifts of <1pm at 1.5μm correspond to grating optical length changes of $<10^{-6}$% induced by local strain and temperature fluctuations of <1μstrain and <0.1^{o}C respectively. Their small size, corrosion resistance, chemical inertness, electrical nonconductivity and immunity to electromagnetic interference make FBG's ideal for embedding in civil engineering structures like buildings, bridges and dams; transportation systems like aircraft, trains and boats; military systems like sonar arrays; terrestrial intruder alarms and medical catheters.

7. Excimer laser microfabrication of Micro-Electro-Mechanical Systems

'Micro-electro-mechanical systems' (MEMS) bring together mechanical, electrical and optical technologies to create an integrated device that employs miniaturization to achieve high-complexity in a small volume[17]. This generally involves fabricating mm-μm size structures with μm-nm tolerances. The success of microengineering comes from miniaturization and its consequences: high-sensitivity, short-measurement times, low-energy consumption, good-stability, high-reliability, self-calibration and testing. Microsensors detecting local parameters like pressure, flow, force, acceleration, temperature, humidity, chemical content etc, have in the last decade been engineered into the engine and performance management systems of cars and aircraft. They also provide the key to electromechanical microcomponents such as ink jet printer heads, gas chromatographs, gyroscopes, galvanometers, microactuators, micromotors, micro-optics etc. Devices like implantable drug delivery systems containing sensors, valves and control system with power source capable of operating for many years are being developed.

Examples of the types of surfaces that can be structured by excimer laser ablation are shown in Figure 12. Blazed grating and pyramid-like structures can be readily fabricated on surfaces by mask-dragging techniques[18].

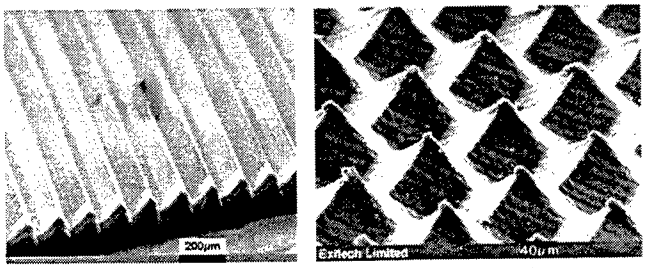


Fig 12. KrF laser produced surfaces in polycarbonate produced using mask-dragging techniques. (a) Blazed grating (b) Pyramids

Such methods can be used for making micro-optical surfaces like those shown in Fig 13. The 'black' anti-reflective property of the 'moth's-eye' type of surface machined on the CsI crystal shown in Fig 13(a) is being used to prevent ghost images in very large infrared optical telescopes. The microlens array shown in Fig 13(b) is used for shaping beams from laser diodes. Each lenslet in this array has a focal length of 1mm.

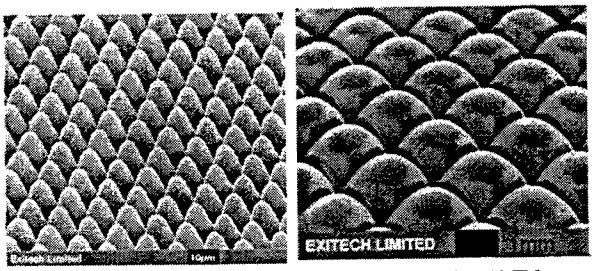


Fig 13. Micro-optical surfaces fabricated by KrF laser micromachining and orthogonal mask-dragging. (a) Cesium Iodide far-infrared optical crystal (b) Polycarbonate

Adaption of silicon lithography and etch batch-processing as developed by the semiconductor industry is currently the dominant MEMS fabrication method. However being restricted to just one material (silicon) surface and bulk etched in only 3 directions- along (110), (100) and (111) crystallographic-planes, other more flexible micromachining methods including pulsed uv-laser ablation are being evaluated for MEMS. The perceived advantages of uv-laser micromachining are many: (i) few processing steps, (iii) highly-flexible CNC programming of shapes for engineering prototyping, (iii) capable of serial and batch-mode production processing, (iv) no major investment required in large clean-room facilities and many expensive process tools, (v) can be applied to a wide range of polymers, ceramics, glasses, crystals, insulators, conductors, piezomaterials, biomaterials, non-planar substrates, thin and thick films, (vi) compatible with lithographic processes and photomask making. An example of a MEMS device fabricated by excimer laser micromachining is the biochip.

Recent advances in personal healthcare and environmental monitoring have led to the development of different diagnostic devices that can perform a variety of analysis functions. The applications of such diagnostic 'chips' is widespread and includes food and water supplies, drug delivery systems, personal drug administration, DNA analysis, blood monitoring, cell sorters, pregnancy testing, etc. One of the most researched areas has been the so-called biofactory-on-a-chip comprising compact discrete devices for micro-monitoring chemical analysis in the environment and medical areas.

Because of the inherent bioincompatibility of silicon, in general biomedical sensors must be fabricated from other materials. Because many biodegradable or compound materials are not well-suited to conventional chemical and plasma etching processing laser machining of these devices is becoming ever more important. A biochip manufactured using laser technology is shown in Fig 14.

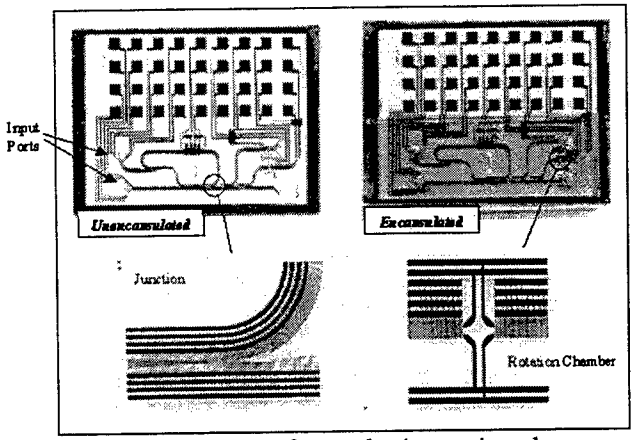


Fig 14. Biochip manufactured using excimer laser micromachining

This device consists of a multilevel layout of $2^1/_2$D laminations of gold electrode conveyor tracks, channels and chambers sandwiched between insulating polymer layers. The process of manufacture has been presented elsewhere[19]. In general an excimer laser is used both to ablate a gold layer to leave behind 10μm wide electrodes as well as to machine the interconnect microvia holes in a dielectric polymer layer. Using the process of travelling-wave dielectrophoresis, a simple low voltage AC power supply applied to the electrode structure controls the sample

fluidic motion. Microchannels for transporting the sample from the inlet ports to the analysis sites are excimer laser micromachined (see Fig 15).

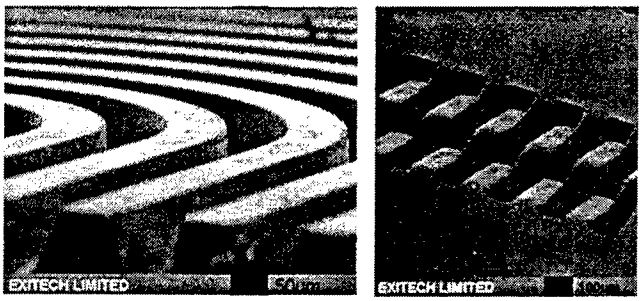


Fig 15. KrF laser micromachined microfluidic channels in polyester

When connected to external power and optical recognition devices the overall dimension of the chip is 55mm x 40mm. With such a laser-based micromachining method all steps are carried out using the same tool obviating the need for any additional processing steps. Hence there is great flexibility in the design of the chip layout.

Flat and ramped channels such as those shown in Fig 16 are being used for securing small cylindical objects like fiber optic cable.

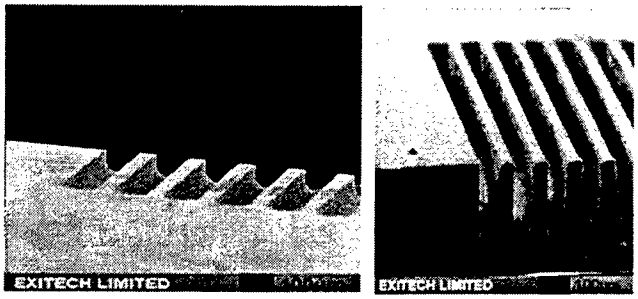


Fig 16. KrF laser micromachined fiber holders in polyester

As illustrated in Fig 17, controlled 3D-structuring of materials by excimer laser etching[18] can produce the basic building blocks of bridges, diaphragms, pits, holes, ramps, cantilevers, etc needed for microengineering devices like gyroscopes, galvanometers, gas chromatographs, microactuators, micromotors, etc.

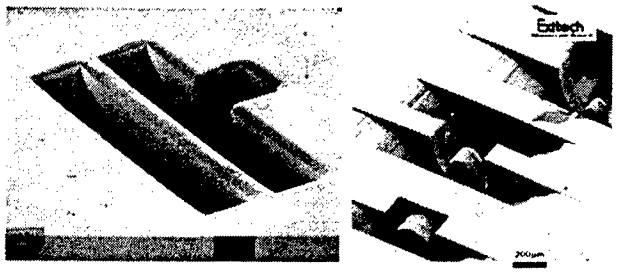


Fig 17. KrF laser-machined 3D-structures in polycarbonate using Exitech M7000 CNC micromachining system. (a) Beam structure (b) Ramps, channels and bars

Half-tone masks comprising of variable dot size and density features can be used to produce images on a workpiece having a grey intensity scale – in a similar fashion to images printed in newspapers. This grey scale can be used to control the excimer laser etch depth. As shown in Figure 18, such masks can be used to produce structures like diffractive optical elements (*DOE';s*) that have $2^1/_2$D topography.

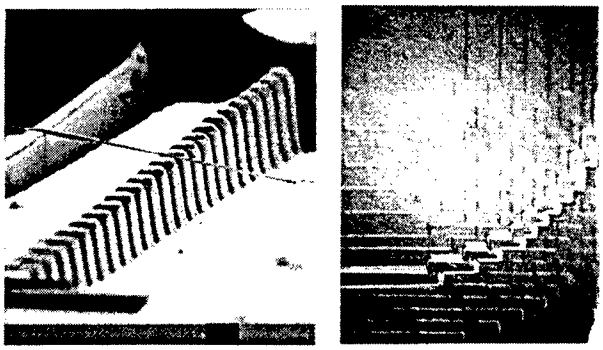


Fig 18. (a) Descending column staircase and (b) part of 8-level diffractive optical element. Produced using half-tone masks to control feature depth.

Fig 19 shows examples of uv-laser micromachined 3D-structures in polymers which when used with the LIGA (from the German acronym: *lithographie galvanoformung abformung*) process of electroforming, can be replicated in metal - a process now known as Laser LIGA[20]. Once a master has been made by excimer laser micromachining such methods allow high volumes of replica parts to be manufactured at low unit costs.

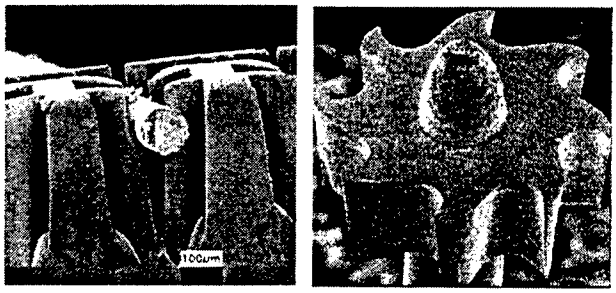


Fig 19. MEMS devices fabricated by excimer laser micromachining. (a) KrF laser machined 100μm fiber clamp (b) 470μm diameter, 130μm height nickel intravascular. *(b) Courtesy of Rutherford Appleton Laboratory*

Already recognized by government-supported initiatives in Japan and the European Union, laser micromachining will be a key manufacturing tool in emerging nanotechnologies[21].

The economic advantages of mass production at low unit cost is of the highest importance and will open up many new industrial application areas for excimer lasers.

8. Acknowledgements

It is a pleasure to thank P Rumsby, N Rizvi and J Fieret of Exitech Ltd who have made many contributions to the original experimental material contained in this paper.

References

1. M C Gower '*Industrial applications of pulsed lasers to materials processing*', in 'High-Power Laser Ablation' SPIE **3343**, 171 (1998)
2. M C Gower. '*Excimer lasers: current and future applications in industry and medicine*' in 'Laser Processing in Manufacturing', eds R C Crafer & P J Oakley, Chapman & Hall, (1993)
3. D J Elliott '*Ultraviolet laser technology and applications*', Academic Press (1995)
4. W W Duley '*UV lasers – Effects and applications in materials science*', Cambridge University Press (1996)
5. S D Allen, M Bass and M L Teisniger '*Comparison of pulsed Nd:YAG and pulsed CO_2 lasers for hole drilling in printed circuit board materials*', CLEO '82 Conference Summary
6. M N Watson. '*Laser drilling of printed circuit boards*', Circuit World, **11**, 13 (1984)
7. F Bachman. '*Excimer lasers in a fabrication line for a highly integrated printed circuit board*'. Chemtronics **4**, 149 (1989).
8. J R Lankard & G E Wolbold. '*Laser ablation of polyimide in a manufacturing facility*'. Appl Phys. **A54**, 355 (1992)
9. H Holden. '*Microvia PCB's:the next generation of substrates & packages*', Future Circuits International **1**, 71, (1997)
10. R S Patel, T F Redmond, C Tessler, D Tudryn and D Pulaski, '*Via production benefits from excimer laser tools*', Laser Focus World (Jan 1996)
11. C Rowan. '*Excimer lasers drill precise holes with higher yields*', Laser Focus World (Aug 1995)
12. A South. '*Miniaturization of Medical Products: The Development Challenge*'. Medical Device Technology, **9**, 30, (1998)
13. M C Gower. '*Excimer lasers for surgery and biomedical fabrication*' in Nanotechnology in Medicine and the Biosciences, eds R R H Coombs & D W Robinson, Gordon & Breach (1996)
14. R S Gifford & D J Bartnik. '*Using optical sensors to measure arterial blood gases*', Optics & Photonics News, **9**, 27, (Mar 1998)
15. R Kashyap, '*Fiber Bragg Gratings*', Optics and Photonics Series, Academic Press (1999)
16. A Othonos and K Kalli '*Fiber Bragg Gratings, Fundementals and applications in telecommunications and sensing*', Artech House, (1999)
17. A B Frazier, R O Warrington and C Friedrich '*The Miniaturization Technologies: Past, Present and Future*', IEEE Trans. on Industrial Electronics, **42**, No5, 423 (1995)
18. E C Harvey & P T Rumsby. '*Fabrication techniques and their application to produce novel micromachined structures and devices using excimer laser mask projection*' in 'Micromachining and microfabrication process technology III' SPIE **3223**, 26, (1997)
19. R Pethig, J P H Burt, A Parton, N H. Rizvi, M S. Talary and J A. Tame, '*Development of Biofactory on a chip technology using excimer laser micromachining*', J. Micromech. Microeng., **8**, 57 (1999)
20. W Bacher, W Menz and J Mohr, '*The LIGA Technique and its potential for Microsystems – A Survey*', IEEE Trans. on Industrial Electronics, **42**, No5, 431 (1995)
21. P McKeown. '*Nanotechnology*'. Emerging Technology Series: New and Advanced Materials, UN Industrial Development Organization **1** (1997)

High efficient microdrilling of silicon wafer using excimer laser

Shinsuke ASADA , Tomokazu SANO and Isamu MIYAMOTO

Department of Manufacturing Science, Gradient School of Engineering, Osaka University, 2-1, Yamada-oka, Suita, Osaka 565-0871, Japan
Phone:+81-06-6879-7535 Fax:+81-06-6879-7534
E-mail:asadarr@mapse.eng.osaka-u.ac.jp

Drilling rate of thin silicon wafer of 50μm thickness was determined as a function of beam diameter and laser fluence of KrF excimer laser with a pulse width of approximately 30ns FMHW. Analysis of drilling process indicated that decreasing beam diameter and laser fluence enhanced the drilling rate with improved quality of the drilled hole .The extent of debris and molten particles ejected from the hole was also reduced as the laser fluence was decreased. The drilling rate, approximately 0.6μm per pulse at beam diameters larger than 100μm, increased significantly as the beam diameter decreased especially below 20μm, reaching approximately as large as 4μm per pulse at 10μm in diameter under constant laser fluence. On the other hand, only very small increase in drilling rate was observed as the laser fluence was increased. A simple formula was derived where the drilling rate is proportional to the fourth root of the laser fluence and inversely proportional to the square root of the beam diameter, assuming that the silicon is removed in a liquid state out of the hole.

Keywords: microdrilling, excimer laser, silicon, drilling rate

1. Introduction

Short pulse lasers enable precision material processing due to limited heat diffusion in target during the pulse duration. Nano second pulse lasers like excimer laser or Q-switched YAG laser have been applied to material processing including drilling, marking and patterning, because they are of the shortest pulse length without any complex and expensive equipments like pico or femto second pulse lasers. Although a large number of drilling experiments have been carried out so far, most experiments were made with beam diameters lager than 100μm.

In this paper, the effects of diameter and fluence of laser beam on the drilling rate are systematically analyzed in KrF excimer laser drilling of thin silicon wafer. The mechanism of drilling thin silicon wafer is discussed, and a simple formula is drived based on a melt ejection model.

2. Experimental setup

Percussion drilling of silicon wafer in air was carried out using KrF excimer laser (wavelength 248nm, pulse width 30ns FMHW) with mask projection method. Circular holes with different diameters were drilled with the beam diameters from 7μm to 200μm. The experiments were performed in the fluences below 30J/cm^2 at 5Hz. Silicon wafers with thickness of 20, 30 and 50μm were drilled in a surface of (111). The drilling rate in terms of average removal depth per pulse was determined from the number of pulse needed to drill through the wafer with given thickness. Scanning electron microscope was used to observe the shape of the drilled hole and the range of the debris deposition.

3. Results and discussion

3.1 Appearance of drilled hole

The surface appearance of the drilled hole is shown in **Fig. 1(a)(b)**. On the edge of the drilled hole molten area is observed. Around the hole both droplets of molten silicon with diameters of several micrometers and debris consisting of fine particles with nano-order sizes are deposited.

Debris is deposited in a fine circular area around the drilled hole as shown in **Fig 1(c)**. In **Fig. 2** the range of the debris deposition is plotted against pulse energy for different beam diameters. It is seen that the range of the debris deposition is proportional to the cubic root of incident pulse energy regardless the beam diameter. The extent of the blast wave driven by the laser-induced plasma R is given by [1]

$$R = \left(\frac{E}{P}\right)^{\frac{1}{3}} \qquad (1)$$

where E is incident laser pulse energy and P atmospheric pressure. The extent of the debris deposition is proportional to the cubic root of the incident pulse energy, since the debris deposited on the target surface driven by the force resulted from the cooling wave of the plasma after the pulse. On the other hand the droplets deposit almost radially from the hole, but the deposition range is random. This is because

First International Symposium on Laser Precision Microfabrication, Isamu Miyamoto, Koji Sugioka, Thomas W. Sigmon, Editors, Proceedings of SPIE Vol. 4088 (2000) © 2000 SPIE · 0277-786X/00/$15.00

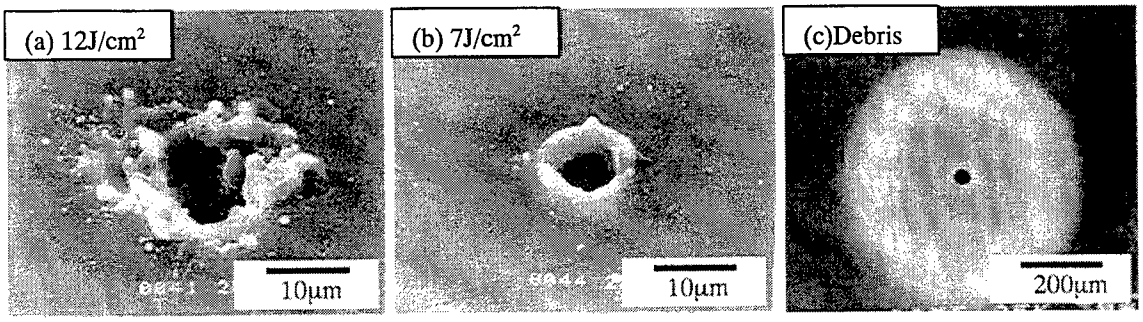


Fig. 1. Percussion drilling of 50μm thick silicon with KrF excimer laser (τ=30ns, λ=248nm), beam diameter 10μm and fluence: (a)12J/cm², (b)7J/cm², (c)Debris deposition.

droplets, which are more heavier particles than debris, is less affected by the cooling wave.

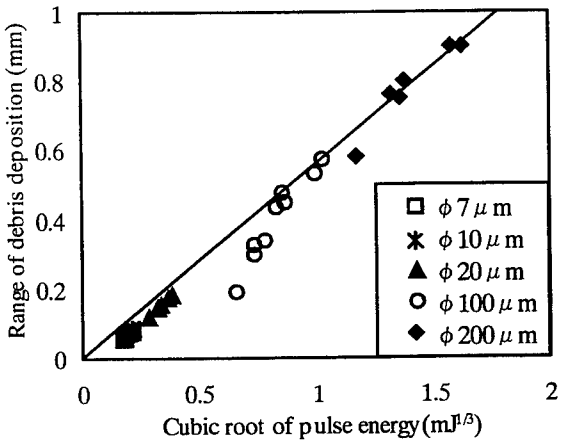


Fig.2. The range of debris deposition as a function of pulse energy at different beam diameters.

3.2 Drilling rate

Experimental drilling rate is plotted against laser fluence for different beam diameters in **Fig. 3**. Little increase in drilling rate is observed as the laser fluence is increased at any beam diameters. Similar tendency was observed in drilling of metal by using YAG laser [2]. At higher laser fluences, molten zone around the drilled hole becomes larger and the opening part of the hole becomes more irregular in shape as shown in **Fig. 1**. When the laser fluence is increased, the excess deposited energy produces more amount of molten material which is difficult to be sustained stably.

On the other hand, the drilling rate depends strongly on the beam diameter, as seen in **Fig. 4** where experimental drilling rate is ploted vs. beam diameter at a constant fluence 12J/cm². The drilling rate is almost constant of approximately 0.6μm per pulse at beam diameters larger than 100μm. At beam diameters smaller than 100μm, however, the drilling rate increases, as the beam diameter decreases. Especially, it increases rapidly at beam diameters below 20μm, reaching approximately up to 4μm per pulse, which is as large as 7 times larger than the value for beam diameters larger than 100 μm. Such a strong dependence of drilling rate on the beam diameter has not been reported so far, because most laser drilling experiments have been carried out at beam diameters lager than 100μm as aforementioned.

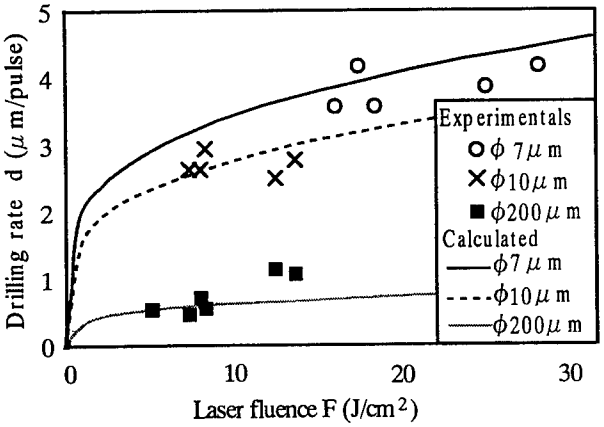


Fig.3. Relationsip between drilling rate and laser fluence at different beam diameter. Dots are experimental values and lines are values calculated by **eq.(7)**.

3.3 Drilling mechanism of silicon

In this section, the mechanism of the laser drilling is discussed to account for the experimental data shown in **Figs. 3 and 4**. In the previous report, the authors discussed the effect of laser absorption in laser induced plasma on the drilling rate at different beam diameters [3]. According to the experimental result in the previous report, the absorption coefficient of the plasma decreased at beam diameters laser than 100μm due to radial diffusion of the plasma. However such a significantly change in the absorption coefficient corresponding to **Fig. 4** was not observed. This indicates

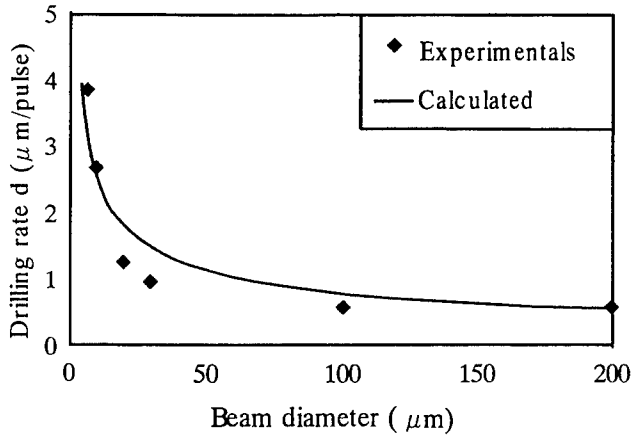


Fig.4. Relationsip between drilling rate and beam diameter at constant laser fluence 12J/cm^2. Dots are experimental values and lines are values calculated by **eq.(7)**.

that the decrease in the laser absorption in plasma is not considered to be a main cause to increase the drilling rate as seen in **Fig. 4.**

Droplets and debris deposited around the hole evidence that silicon is removed by melt ejection and evaporation. Then the drilling rate U is given by

$$U = U_M + U_E \qquad (2)$$

where U_M is the drilling rate by melt ejection and U_E the drilling rate by evaporation. Melt ejection rate U_M can be much larger than U_E, because latent heat of melting is much smaller than that of evaporation. Thus the silicon increased to be drilled by only melt ejection for simply, then the drilling rate is related to laser fluence and beam diameter as follow.

Molten layer formed in the irradiated zone is driven radially outside by the evaporation recoil pressure as shown in **Fig. 5.** The flow velocity of the molten layer V is related with laser fluence F to which the recoil pressure is proportional to the F.

$$F \propto \Delta P = \frac{1}{2}\rho V^2 \qquad (3)$$

where ρ is the density of silicon and ΔP the evaporation recoil pressure over the atmospheric pressure. Assuming uniform plane heat source moves in a direction perpendicular to the heat source plane at velocity U, steady temperature distribution given by

$$T(z) = \frac{q}{\rho c U}\exp\left(-\frac{Uz}{\kappa}\right) \qquad (4)$$

where q is power density of the absorbed laser , c specific heat and κ thermal diffusivity and z distance from the heat source. Then the thickness of the molten layer δ is given by

$$\delta = \frac{\kappa}{U}\ln\left(\frac{T_M}{T_E}\right) \qquad (5)$$

where T_E is evaporation temperature and T_M molten temperature of silicon. The drilling velocity U driven by the radial flow of at velocity V is given by [4]

$$\pi r^2 U = 2\pi r \delta V \qquad (6)$$

where r is radius of laser beam. Assuming that drilling rate per pulse d is proportional to drilling velocity U, d is given by

$$d = kF^{\frac{1}{4}} r^{-\frac{1}{2}} \qquad (7)$$

where k is a constant, determined by atmospheric pressure, material specific and pulse condition. As a result drilling rate d is finally proportional to the fourth root of the laser fluence and inversely proportional to the square root of the beam radius.

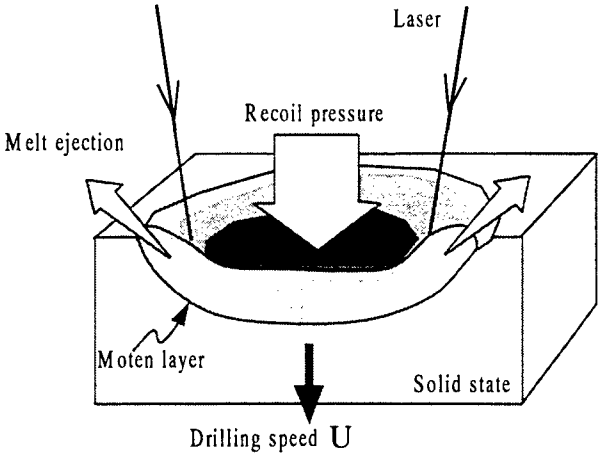


Fig.5. Schematic diagram of melt ejection of silicon from molten layer on laser irradiated area.

Equation (7) indicates that drilling rate tends to saturate against laser fluence because of fourth root low. With increasing laser fluence, temperature of the molten silicon increases and lateral heat conduction can not be neglected. Therefore, molten zone around the drilled hole becomes larger at higher laser fluences as aforementioned. On the other hand, this equation also indicates that the drilling rate has strong dependence on beam diameter due to inverse relationship. Solid lines in **Figs. 3 and 4** are the calculated values from **Eq.(7)**. Good agreements are observed between experimental and calculated values in a wide range. It is found that the simple model can be applied in a wide range of beam diameter and laser fluence.

The drilling experiments were also carried out using copper and polyimide. The experimental drilling rate is plotted against beam diameter at constant fluences in **Fig. 6.** Drilling rate of polymide, which evaporates without melting, is almost constant regardless beam diameter. On the other hand copper is seen to behave like silicon. This is thought to be because copper has a wide temperature range of liquid phase. These results evidence that strong dependence of drilling rate on beam diameter is caused by melt ejection.

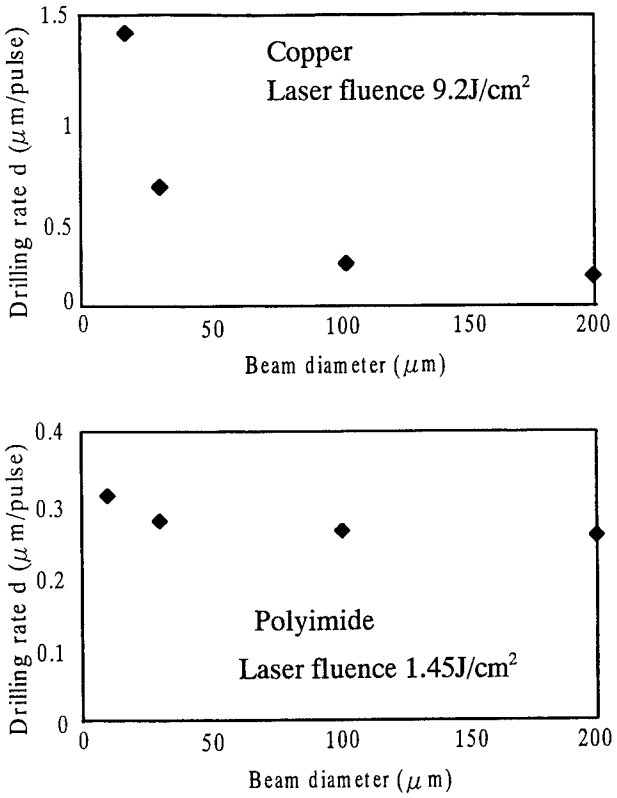


Fig.6. Relationship between drilling rate and beam diameter at constant fluences about 50μm thick copper and polyimide.

4.Conclusion

Drilling rate in thin silicon wafer using KrF excimer laser was investigated as a function of diameter and fluence of laser beam. The conclusion obtained this study can be summarized as follows.

1. The drilling rate at constant fluence increases rapidly below 20μm in diameter reaching approximately up to 4μm per pulse. On the other hand it little depends on laser fluence.
2. A simple formula of drilling rate was derived as a function of diameter and fluence of laser beam in a wide range based on melt ejection process.
3. At higher laser fluence, the opening part of the hole becomes wider and more irregular in shape. Because excess fluence increases temperature of molten silicon and lateral heat conduction.

References

[1] Miyamoto, et al., Proceedings of ICALEO'94 (1994)pp 240-248.
[2] Sergei V.Govorkov, et al., Proceedings of SPIE '00 (2000) pp 365-370.
[3] H. Maruo, I. Miyamoto and T. Ooie, Proceedings of LAMP'92 (1992) pp 293-298.
[4] M.von Allmen, J.Appl.Phy.47 (1976) pp.5460-5463.

Micro-machining using Femtosecond Lasers

H. K. TÖNSHOFF, A. OSTENDORF, S. NOLTE, F. KORTE and T. BAUER

Laser Zentrum Hannover e. V.; Hollerithallee 8; 30419 Hanover, Germany;
Phone: +49-511-2788-215; Fax: +49-511-2788-100; E-Mail: ba@lzh.de;

Femtosecond laser systems have been proved to be effective tools for high precision micro-machining. Almost all solid materials can be processed with high precision. The dependence on material properties like thermal conductivity, transparency, heat- or shock sensitivity is strongly reduced and no significant influence on the remaining bulk material is observed after ablation using femtosecond laser pulses. In contrast to conventional laser processing, where the achievable precision is reduced due to a formed liquid phase causing burr formation, the achievable precision using femtosecond pulses is only limited by the diffraction of the used optics. Potential applications of this technique, including the structuring of biodegradable polymers for cardiovascular implants, so-called stents, as well as high precision machining of transparent materials are presented.

Keywords: micro-machining, micro-structures, femtosecond laser pulses, ultrashort laser pulses, stents, biodegradable polymers

1. Introduction

Following the growing need for miniaturisation in industrial applications, various micro-machining processes, like photolithography, electrical discharge machining (EDM) or micro-cutting have been established in the past. However, nearly all of those processes are optimised for a few special materials. Many high-tech applications require materials, which are not machinable with conventional techniques, e.g. very hard materials (diamond, sapphire) or materials, which must not be heat-affected during the structuring process (bio-degradable polymers, amorphous metals, Shape Memory Alloys)[1].

Machining with femtosecond laser pulses (1 fs = 10^{-15} s) can overcome this lack of machining processes for sophisticated materials. Femtosecond laser pulses offer great flexibility in structuring work pieces with high precision on micrometer scale, while avoiding thermal influence within the bulk material. The variety of machinable materials comprehend almost all solid materials, including transparent or highly heat conducting solids (glass, polymers, copper).

In contrast to conventional laser material processing, ablation with ultrashort pulses leads to a direct transition of the material into plasma, resulting in a 'cold' ablation without heat-affected material. Therefore, the structural size is not limited by thermal or mechanical damages, e.g. cracks, burrs and debris, but only determined by the diffraction limit of the used optical system [2].

The present and rapid development of fs-laser sources makes compact and reliable laser systems with sufficient average power output available right now. Future systems are designed to be even more compact and reliable. Therefore, femtosecond lasers have set off to enter industrial operation [2,3].

2. Short-pulse ablation

Conventional laser micro-machining processes are typically based on pulsed laser sources like excimer lasers or frequency converted Nd:YAG lasers, which provide laser pulses of 10-30 ns duration. While being irradiated, the material is heated up to the melting temperature and thus vaporised. Due to the long pulse duration, heat conduction and diffusion effects take place, which influence the surrounding material. Besides thermally initiated effects like shock-waves or stresses direct thermal influences can occur [Fig.1b].

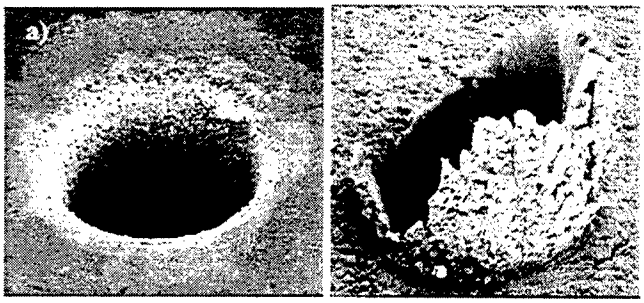


Fig.1: Thermal influences on drillings in stainless steel with 80 µm diameter: (a) using 120 fs laser pulses, (b) using 13 ns laser pulses

Therefore, micro-cracking, burr formation as well as debris can be observed using ns-laser pulses.

First International Symposium on Laser Precision Microfabrication, Isamu Miyamoto, Koji Sugioka, Thomas W. Sigmon, Editors, Proceedings of SPIE Vol. 4088 (2000) © 2000 SPIE · 0277-786X/00/$15.00

The ablation with femtosecond laser pulses consists of the following two steps: First, the irradiated laser energy is absorbed inside the surface layer by bound and free electrons, which leads to excitation and ionisation of the material. Therefore, the electrons are heated up to very high temperatures up to ~10^5 K (10 eV). As this happens within some femtoseconds, the energy is only deposited into the electron subsystem during this period.
Second, the rapid absorption effect is followed by energy transfer to the atomic subsystem. The overheated electrons transfer the energy to the lattice, which leads to bond breaking and material expansion. Thermal diffusion effects are negligible due to the short interaction time of some picoseconds. Therefore, the ablation occurs without the formation of burrs or heat- or shock-affected zones [Fig.1a].
The theoretical background of fs-ablation has already been discussed in detail [4,5,6]. The described processes for the ablation of metals is similar to those of other solids (semiconductors, dielectrics and isolators). In metals the absorption is carried out by free electrons due to inverse bremsstrahlung (linear absorption). The electron density can be considered constant during the interaction time with the laser pulse.
For other materials, where no free electrons are present (semiconductors, dielectrics, polymers, etc.), the laser radiation is deposited due to interband transitions, multiphoton and electron-impact absorption. In this case, the electron density changes during the laser pulse.

3. Applications

Ultrashort laser pulse material processing combines minimal collateral damage of surrounding material with very high precision and broad spectra of feasible materials. The meaning of these advantages will be highlighted with several specific medical and technical applications presented in the following.

3.1 Structuring of biodegradable polymers

Apart from direct use of fs-lasers in medicine for surgery, for example the correction of myopia like LASIK (laser assisted in situ keratomileusis) [7], the structuring of medical implants, e.g. coronary stents, is a promising application with growing industrial interest [8].
Coronary stents are used as an minimally invasive treatment of arteriosclerosis, as an alternative for bypass operations. Since the requirements of medical implants (e.g. burr-freeness, x-ray opacity) are very strict, just a few materials are commonly used. Today, typical materials used for stents are stainless steel or shape memory alloys. For these materials chemical post-processing techniques have been developed to achieve the required properties. However, these materials are not optimal in several medical aspects (e.g. risk of restenosis, limited bio-compatibility etc.).

New approaches favour stents for temporary use only, which necessitate bioresorbable materials like Mg-base alloys or special bio-polymers [Fig. 2a]. Other materials, like tantalum, show improved x-ray visibility [Fig. 2b]. For these materials, no established post-processing technique is available. Furthermore, most of them show strong reactions to thermal load. Therefore, it is essential to avoid influences on the remaining material in order to keep the specific material properties. Femtosecond pulse laser material processing meets the requirements of these sophisticated materials.



Fig 2: Prototypes of stents made of: (a) bio-resorbable polymer, (b) tantalum

3.2 Machining of Diamond

According to the availability of high-quality synthetic chemical–vapour deposited (CVD) diamond, this unique material is being used increasingly. Diamond has advantageous mechanical, thermal and optical properties, which makes diamond a superior base for electro-optical devices like sensors. However, machining is still a problem due to its very high hardness and its natural faceted surface structure.
The surface roughness, which can be about 20-50µm, has to be improved in order to achieve optical surfaces or allow sufficient contact of electrodes. Fig 3a shows treated (left part) and natural surface of the CVD sample (right part). Although excimer lasers can be used for surface smoothing, they are more favourable, since they produce a graphitised surface layer.

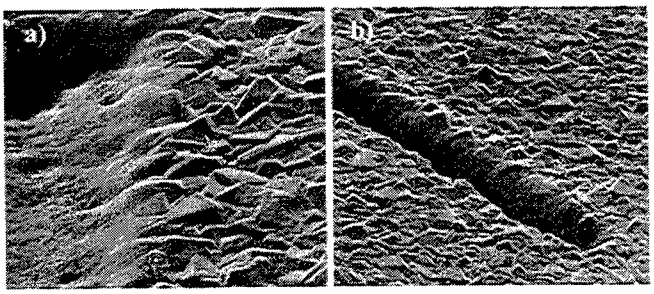


Fig. 3: Machining of diamond: (a) surface smoothing, (b) cutting of CVD- sample

Fig. 3a shows an example, where femtosecond pulses from a Ti:sapphire laser were used for smoothing the surface. The smoothing has been carried out under an angle of incidence

of 45°, using a fluence of 10 J/cm². In this case, no graphitisation of the surrounding area has been observed, neither for smoothing nor for cutting [Fig. 3b] .
When using diamond or glass like Pyrex as a base material for Printed Circuits, vias for electronic contacts are required. Conducting lines on the waver, which are in the vicinity of these holes, must not be affected by the machining process. Drilling of diamond or glass cannot be done mechanically on a micrometer scale, while drilling with conventional lasers induces thermal stress, which causes cracks in the glass near to the exit of the hole. Drillings using fs laser pulses shows very good results regarding desired geometry, process quality and induced damage [Fig. 4].

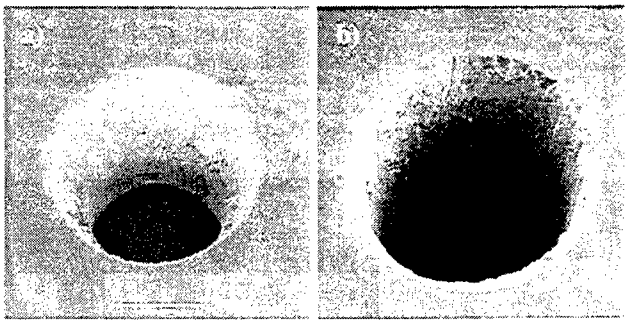


Fig. 4: (a) Drilling of glass with conical entrance, diameter 700μm
(b) Drilling in diamond, diameter 80 μm

Even combinations of conic or pyramidal entrances and cylindrical holes can be machined [Fig. 4b].

3.3 Metallic microstructures

The machining of metallic structures in the micrometer range can be performed successfully using fs-laser pulses. One promising application is the machining of acceleration grids, to be used in streak camera tubes [Fig.5].

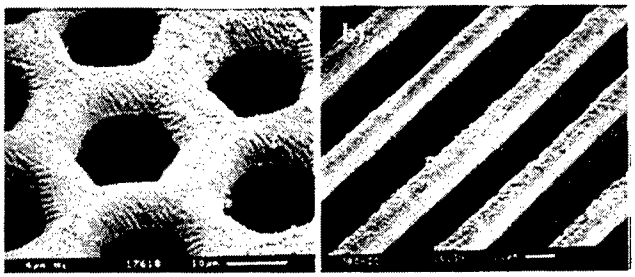


Fig. 5: Fs- machined acceleration meshes: (a) Hexagonal mesh with structural periodicity of 20μm, (b) grid mesh. Overall structure size of both meshes: 11x8mm²

Acceleration grids have to be highly transmitting for electrons, and still have to generate an electric field being as homogeneous as possible. This can be fulfilled by generating grids with many thin struts. However, theses fine struts are likely to be deformed by mechanical or thermal stress.
Using ultrashort laser pulses for the structuring, despite of the small structural size, no burrs or deformation due to thermal load is present. The achieved transmission ratio of the grids is about 60 %.
Even sub-wavelength structures can be generated either by combining the femtosecond laser with a scanning near-field optical microscope (SNOM) [10] or by making use of the well defined threshold of the femtosecond ablation process [11]. In this case, when choosing the peak fluence to be slightly above the ablation threshold, only the central part of the spatial Gaussian beam profile ablates the material. This enables one to overcome the diffraction limit and to produce sub-wavelength holes.

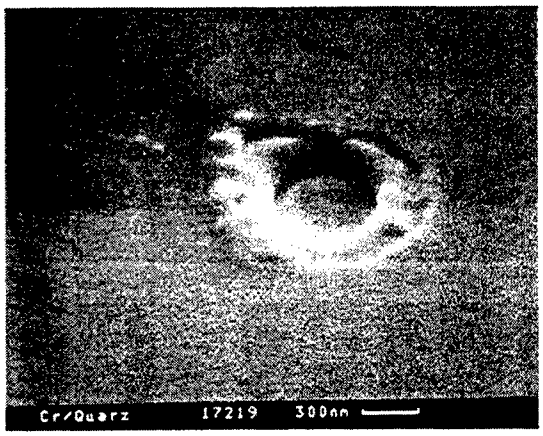


Fig. 6: Drilling in a chrome film using a microscope objective for machining at a central laser wavelength of 780 nm

Fig. 6 shows a hole drilled in a chrome film on a quartz carrier. These techniques allow the fabrication of sub-micrometer structures, for example for the repair of lithographic masks.

4. Conclusions

Femtosecond lasers are capable of minimally invasive machining of various materials with very high precision. Machining of sophisticated materials like diamond, glass or biodegradable polymers has been detailed as well as the machining of micrometer and sub- micrometer sized structures in metals. It can be expected, that fs-lasers will be used increasingly in several micro-machining applications.

5. Acknowledgement

This work was financed by the German ministry of Education and Research (BMBF, 13N7053) and by the European Community (BE97-4841 / BRPR-Ct89-0694). Special thanks to Dr. N. Rizvi, Exitech Ltd., Dr. C. Momma,

Cortronik GmbH and Dr. J Howorth, Photek Ltd. for their co-operation.

6. References

[1] B.C. Stuart, M.D. Feit, S. Herman, A. M. Rubenchik, B. W. Shore, M. D. Perry, J. Opt. Soc. Am. B. **13**, 459 (1996)

[2] R. Mellish, S.C.W. Hyde, N. P. Barry, R. Jones, P. M. W. French, J . R. Taylor, C. J. van der Poel, A. Valster, Appl. Phys. B **65** (1997) 221

[3] C. Hönninger, I. Johannsen, M. Moser, G. Zhang, A. Giessen, U. Keller, Appl. Phys. B **65** (1997) 423

[4] F. Korte, S. Nolte, B. N. Chichkov, T. Bauer, G. Kamlage, T. Wagner, C. Fallnich, and H. Welling: Appl.Phys A **69**, S7-11 (1999)

[5] S. Nolte, C. Momma, H. Jacobs, A. Tünnermann, B. N. Chichkov, B. Wellegehausen, J. Opt. Soc. Am B. **14**, 2716 (1997)

[6] B. N. Chichkov, C. Momma, S. Nolte, F. von Alvensleben, A. Tünnermann, Appl. Phys. A **63** (1996) 109

[7] H. Lubatschowski, G. Maatz, M. Rudolf, A. Heisterkamp, U. Hetzel, H. Welling, W. Ertmer, Graefe's Arch. Clin. Exp. Opthalmol. 238, 33-9, Jan. 2000

[8] C. Momma, U. Knop, S. Nolte; Progr. in Biomed. Res. (Feb. 1999) 39

[9] A. Rosenfeld, M. Lorenz, R. Stoian, D. Ashkenasi; Appl. Phys. A **69** pp. 373-376 (1999)

[10] S. Nolte, B. N. Chichkov, H. Welling, Y. Shani, K. Lieberman, H. Terkel; Optics Letters **24**,13, July 1999

[11] D. Strickland, G. Mourou, Opt. Commun. **56**, 219 (1985)

Micromachining with Ultrafast Lasers

*K. Shihoyama, *A. Furukawa, **Ph. Bado, **A. A. Said
*Hoya-Continuum, 23-2 Sakamachi, Shinjuku-ku Tokyo 160, Japan
** Clark-MXR, Inc. 7300 W. Huron River Dr. Dexter, Michigan, USA
E-mail: phbado@cmxr.com

Conventional laser machining is based on continuous-wave or long-pulse lasers. With these lasers, thermal diffusion limits the accuracy and the reproducibility of the machining process. Laser-matter interaction is fundamentally different in the ultrafast (femtosecond) regime. This discovery has opened the way for generalized fine laser micromachining.
Keywords: Micromachining, laser, ultrafast, workstation, HAZ

1. INTRODUCTION

Machining materials with lasers – a technology first introduced in the early 1970's– is now used routinely in many industries. Laser *micro*machining is a more recent development. First demonstrated in the 1980's, micromachining with lasers is an evolving technology. Initially laser micromachining was based on continuous-wave or long-pulse lasers. With these "conventional" lasers, the heat transferred from the laser beam to the work piece introduces numerous restrictions that limit the precision and the quality of the machining process. In other words, laser micromachining is... well, not so *micro*, but rather coarse by today's standards. Machinists have learned ways to minimize the negative effects associated with heat transfer through various types of pre- and post-processing. These additional steps considerably increase the complexity and the cost of the machining operation.

Most machining techniques deposit heat into the material that is being machined. This heat does not stay localized where it was deposited, but moves away in a characteristic time, the so-called "heat diffusion time", which is of the order of a few picoseconds.

In the early nineties, scientists at the University of Michigan, in a group headed by Professor Gerard Mourou, discovered that the transfer of heat from the laser beam to the work piece could be defeated using ultrafast laser pulses instead of standard long-pulse lasers. Additionally, they found that machining with ultrafast laser pulses is very precise and highly deterministic. These discoveries opened the way for fine laser micromachining.

Before looking at some samples that were machined with ultrafast pulses, let's first take a closer look at the way laser beams of differing pulsewidth interact with matter. To make this complex science reasonably understandable, we have simplified or ignored many issues. We arbitrarily divide the physics of how light interacts with materials into two time regimes - one in which the laser pulse is either very, very short (called ultrafast or ultrashort) and another in which the laser pulse is not so short (which we call "long"). Ultrafast, or ultrashort, means that the laser pulse has a duration that is somewhat less than about 10 picoseconds - usually some fraction of a picosecond (femtosecond). "Long" means that the pulse is longer than about 10 picoseconds, that is, longer than the heat-diffusion time. These long pulse lasers may be continuous, quasi-continuous, or Q-switched, but in any case they are all generating long pulses compared to the heat-diffusion time.

2. MACHINING WITH LONG PULSE LASERS

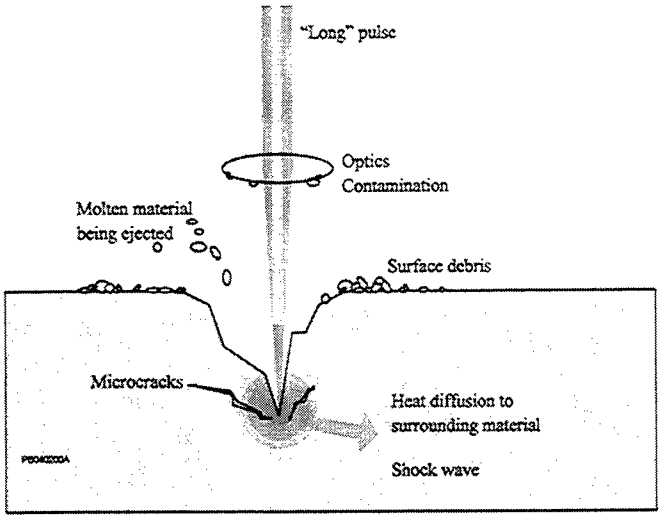
The most fundamental feature of material interaction in the long pulse regime is that the heat deposited by the laser in the material diffuses away from the work zone *during* the pulse duration, as shown in Figure 1. Technically speaking, the laser pulse duration is longer than the heat diffusion time. There are several reasons why heat diffusion is detrimental to the quality of the machine part:

- Heat diffusion reduces the efficiency of the micro-machining process. It "sucks" energy away from the work spot, leaving less energy available to remove material.
- Heat-diffusion reduces the temperature at the focal spot (the machining spot), clamping the working temperature not much above the melting point of the material. Consequently, the material is removed by depositing a lot of energy into the melted material, causing it to boil. Drops of molten material are ejected away from the work zone. These drops ultimately fall back onto the surface and contaminate the sample. Removal of these contaminants may be difficult. These droplets may also contaminate the beam delivery optics. With long pulse laser machining, it is very difficult to go much above the melting point because the energy moves away from the machining spot as fast as it deposited by the laser.
- Heat-diffusion reduces the accuracy of the micro-machining operation. Typically, heat diffuses away from the focal spot (and there is plenty of heat because the process is inefficient!), melting an area that is larger than the laser spot size. Thus, while the minimum laser spot size might be in the range of one micron, in many materials it is difficult to create features with dimensions much smaller than a few tens of microns.
- Heat-diffusion affects a large zone around the machining spot. This zone is referred to as the "heat affected zone" or HAZ. The heating (and subsequent cooling) waves

First International Symposium on Laser Precision Microfabrication, Isamu Miyamoto, Koji Sugioka, Thomas W. Sigmon, Editors, Proceedings of SPIE Vol. 4088 (2000) © 2000 SPIE · 0277-786X/00/$15.00

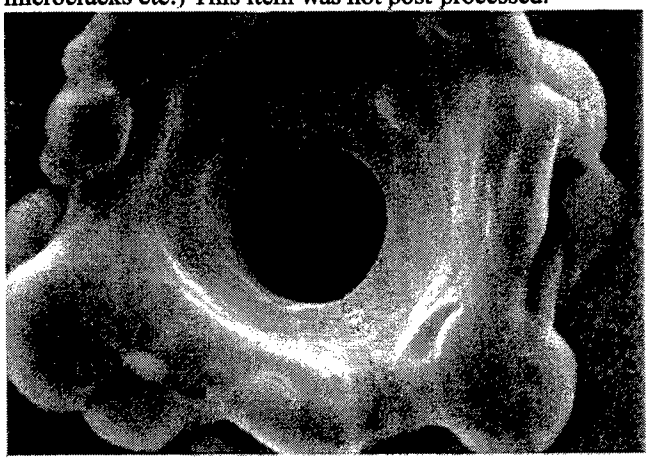
that propagate through the HAZ causes mechanical stress and can create microcracks in the surrounding material as shown in figure 2. These defects are 'frozen' when the material cools. In subsequent routine use, these cracks may cause premature device failure. A closely related phenomenon is the formation of a recast layer of material around the hole. This resolidified material often has a physical and/or chemical structure that is very different from the original material. This recast layer may be mechanically weak and it may break away from the unheated core material after some time.

Figure 1: Light-matter interaction in the long-pulse regime



Clearly, when micromachining with long laser pulses heat diffusion dominates the material removal process. This is associated with undesirable phenomena. Reducing, or eliminating, heat diffusion is therefore highly desirable.

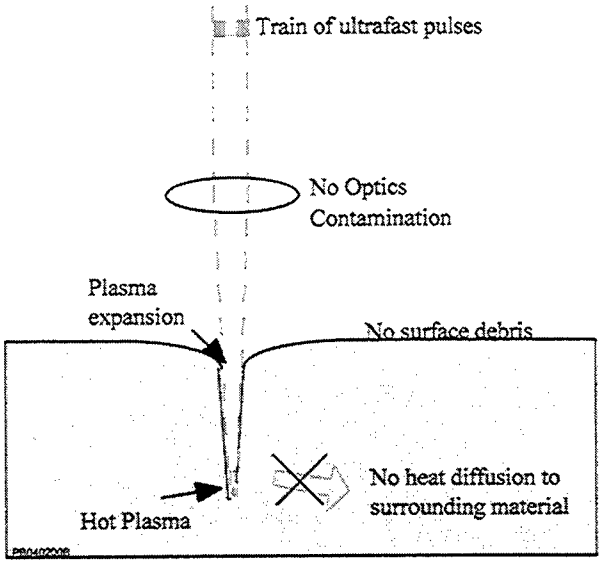
Figure 2: Long-pulse machining of a copper alloy aperture. This piece clearly shows heat-related effects (HAZ, recast, microcracks etc.) This item was not post-processed.



3. MACHINING WITH ULTRAFAST PULSE LASERS

The most fundamental feature of laser micromachining with ultrafast pulses is that the heat deposited by the laser into the material does not have time to move away from the work spot during the time the laser pulse is illuminating the material. The duration of the laser pulse is shorter than the heat diffusion time.

Figure 3: Light-matter interaction in the ultrafast-pulse regime



This regime has numerous advantages:

- The energy does not have time to diffuse away, thus the efficiency of the machining process is high.
- Because the deposited energy does not have time to move away from the focal spot it just piles up. As a result, the temperature rises almost instantly past the melting point of the material. In the time duration of the pulse the material temperature quickly rises well beyond even the evaporation point. The temperature climbs into the plasma regime.
- Ultrafast lasers deliver incredible intensity levels. They can easily deliver hundreds of Terawatts per square centimeter at the work spot. No materials can withstand the forces at work at these power densities. Consequently, ultrafast laser pulses can machine anything.
- The plasma created by ultrafast laser pulses expands outward, away from the work surface in a highly energetic gas plume. The internal forces that previously held the material together are vastly insufficient to contain this hot gas expansion. Consequently, there are no droplets that condense onto the surrounding material. Rather, material re-deposition, is there is any, is in the form of a very fine powder which can be easily removed.

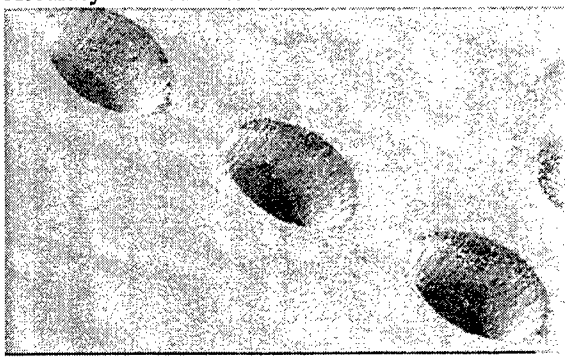
Additionally, since there is no melt phase, there is no splattering of material onto the surrounding surface. Very little post-processing, if any, is required.

- Most of the energy deposited by ultrafast laser pulses is carried away by the expanding plasma. Consequently, very little heat is left behind to produce a heat-affected zone (HAZ). The shock effects associated with heat wave propagation, microcracks for example, are avoided even for brittle material like ceramics.

Finally we would like to briefly mention three very important additional advantages associated with ultrafast pulse machining

- The interaction of ultrafast laser pulses with matter is highly reproducible. This makes for high quality micromachining with very reproducible results, shot-after-shot. All laser pulses (long or short) interact with a material through its free-electrons. The abundance, or absence, of free electrons determines the ultimate repeatability of the machining process. In metals, where free electrons are plentiful, the machining process is reproducible (but secondary effects, such as heat-diffusion, may create additional limitations). In materials with few free-electrons such as semi-conductors, dielectrics, and ceramics, the machining threshold is poorly defined, and the reproducibility of the process problematic. This limitation is eliminated if the laser pulse itself creates the required free-electrons. Ultrafast lasers with their huge peak power are excellent generator of free-electrons through multiphoton ionization. Consequently they can reproducibly machine very all materials.

Figure 4: These three 100-micron diameter holes were machined in stainless steel as part of a reproducibility study. Accuracy was found to be of the order of 1 %.



- Using ultrafast pulses you can micromachine *inside* transparent materials. Standard lasers are unable to machine transparent materials; the beam just propagates straight through the material. But ultrafast lasers generate peak powers so high that transparent materials can be machined through non-linear absorption as shown in figure 5.

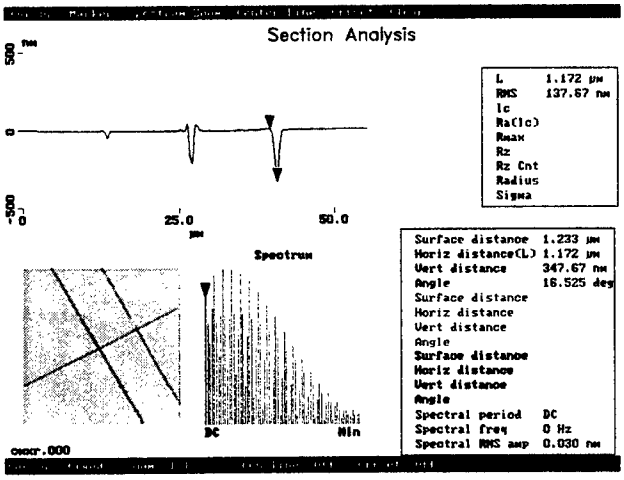
Figure 5: Using an HCC/Clark-MXR workstation, we engraved 2 letters 300-micron below the surface of a sapphire plate. The letters are approx 100-micron tall.

- You can machine sub-micron features. The accuracy of the ultrafast pulse machining process is such that you can machine features that are better than the classical theoretical diffraction limit, using only the "tip" of the laser beam.

Figure 6: A high-quality submicron hole micromachined in silicon



Figure 7: Trenches micromachined in silicon

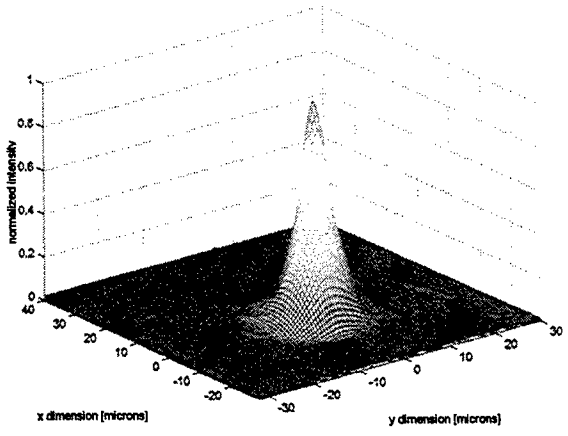


4. SOME UNIQUE ULTRAFAST MACHINING CASE STUDIES

Dielectrics micromachining with ultrafast pulses offer some unique opportunities. For example, when machining glass with a Clark-MXR Model RS-2001 Ultrafast Workstation, you can not only ablate the material but also physically modified it *without* ablating it. For example, you can change its index of refraction.

Large localized refractive index changes have been observed in a wide variety of glasses. This localized effect allows for the fabrication of two-dimensional or three-dimensional photonic structures through a direct-write process, by translation of the sample with respect to the focal point. This idea has been applied to the fabrication of optical waveguides in silicate, borosilicate, chalcogenide and fluoride glasses. The manufacturing threshold was found to vary with the glass formation. Adjusting the focal spot and the laser intensity allows the fabrication of waveguides that are by design single mode (as shown below), or multimode. The quality of the resulting waveguides is excellent. Due to the deterministic nature of the ultrafast pulse-matter interaction you can generate waveguides with walls that are well defined and optically smooth. The internal scattering losses are low.

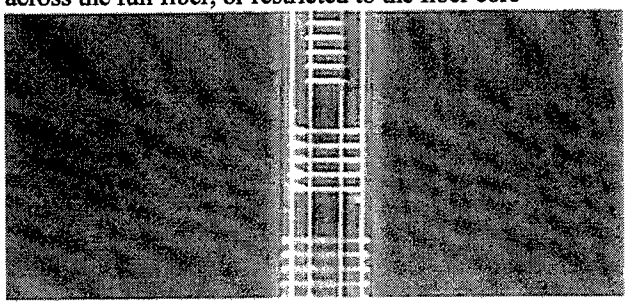
Figure 8: Profile from a single-mode waveguide manufactured by direct-write with femtosecond pulses



Scanning the laser spot or translating the sample along an axis perpendicular to the propagation direction of the incident light beam provides the most flexibility for writing planar patterns. You can produce complex structures such as 3D-waevguides, Y-junction splitters, couplers, and long period gratings.

One of the most exciting developments associated with the femtosecond direct-write approach is its capability to write active waveguides, *i.e.* waveguides that exhibit gain when activated by the appropriate source. We have used one of our ultrafast micromachining workstations to directly-write active waveguides deep inside Nd-doped glass substrates. Note that our manufacturing approach is compatible with all doped glasses, including those designed to operate at long (infrared) wavelengths.

Figure 9: This photography shows a series of gratings written in a single mode fiber. The gratings can be imprinted across the full fiber, or restricted to the fiber core



5. IN SUMMARY...

Ultrafast pulse lasers can machine any material (and/or locally change their chemical or physical properties). The process generates no contamination to the surrounding material, no melt zone, no microcracks, no shock wave, no delamination, and no recast layer. It is highly reproducible, it can be used to create sub-micron features, and it can machine features inside transparent materials.

This new technology is however not perfect. The technology that makes these laser pulses ultrafast does not produce very high average power. Consequently the throughput is often low. Additionally, the technology is complex. So far its commercial acceptance has been limited to the microelectronics industry, and for the foreseeable future ultrafast machining will be restricted mainly to applications that cannot be addressed with traditional machining technologies.

Hoya Continuum and Clark-MXR are addressing these issues in an effort to provide turned-key solutions including complete workstations, more powerful ultrafast sources, and machining know-how needed to implement this new and exciting technology.

Figure 9: HCC/Clark-MXR ultrafast workstation



A Technique of Microfabrication Suitable for Machining Submillimeter Wave Components

W.Y. LIU [1], D.P. STEENSON [2], M.B.STEER [3]

University of Leeds, Leeds, LS2 4AJ, United Kingdom
Email: 1) flute@ieee.org, 2) d.p.steenson@leeds.ac.uk, 3) m.b.steer@ieee.org

Abstract - **This paper reports a novel methodology of microfabrication particularly suitable for machining sub-millimeter wave components. The proposed technique entails the use of a positive photoresist (known as EPON SU-8 ™) in realization of E-plane components, in addition to other 3-D polymer structures such as rectangular waveguides. Because the micro-structure fabricated with the said photoresist can be less than ten microns thick, a high-Q E-plane circuitry of negligible substrate thickness can be lithographically processed to attain minimal dielectric loss. On the other hand, a planar whisker can be glued onto the E-plane circuits, enabling electrical contact of the small-diameter devices to be formed.**

But realizing non-planar structures with parametric variation in thickness is not lithographically trivial, adding the fact that the waveguide flanges can only be machined mechanically at the time of this writing. As such, the authors suggest that an oversized waveguide channel and standard flange interfaces be first mechanically milled onto a metal block. The components to be processed with the said photoresist are then directly fabricated onto the oversized waveguide channel, in such a way that their interfaces to other standard waveguides can be maintained without loss of geometrical accuracy.

In this paper, the basic fabrication procedures are first described, with formulae given on some design criteria. Laser Direct Imaging as applied to processing of SU-8 based submillimeter wave components are discussed, with particular reference given to the technical considerations as found from our recent experimental evidence. Measurements will be given to further substantiate this presentation.

I. Introduction

Miicromachining are now gaining attention in the field of terahertz engineering. Waveguides and other non-planar transmission lines are commonly in use for this frequency band. But mechanically machining components operating at frequencies higher than 150 Ghz is not technically easy. As such, some current micromachining techniques are being employed in production of submillimeter wave components. The considerations of high-frequency transmission typically include, but not limited to, a) transmission losses and b) feasibility of integrating active devices. Although waveguide is a low-loss transmission medium, it is also an inflexible medium for integrating active devices. One solution to this problem is to incorporate a printed circuit containing the active device(s) into the E-plane of the waveguide. In so doing the devices to be integrated can be wire-bonded directly to the E-plane printed circuit, which connects the waveguide through a waveguide-to-finline transition. Figure 1 shows an example of E-plane circuits commonly used in submillimeter wave applications.

Among a handful of the micromachining techniques, the most commonly employed is perhaps silicon-etching. In silicon-etching, micro-features are 2-dimensionally etched until the full waveguides are structurally formed. Silicon-etching can be employed to form the rectangular waveguide structures. But etching a non-orthogonal structure, such as an horn with a parabolic surface, is not as straightforward as milling by a numerically controlled machine.

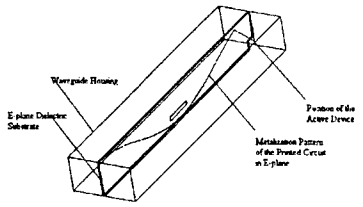


Figure 1. An Example E-plane Circuit

A few years back, some authors [1] have suggested the use of an ultra-thick photoresist (known as SU-8) to lithographically fabricate a waveguide for submillimeter wave frequencies. SU-8 is a photosensitive epoxy that can be hardened when exposed to ultra-violet light for sufficiently long. Therefore, it is possible to lithographically fabricate small micro-features. But because SU-8 is not a conducting material, the fabricated structure needs be coated with a layer of good conductor. The problem of this technique is that the said photoresist can be structurally deformed by heat before it is exposed to ultra-violet light. In addition, this technique has not addressed the issue of standard waveguide flanging and the feasibility of integrating active devices into a waveguiding system.

First International Symposium on Laser Precision Microfabrication, Isamu Miyamoto, Koji Sugioka, Thomas W. Sigmon, Editors, Proceedings of SPIE Vol. 4088 (2000) © 2000 SPIE · 0277-786X/00/$15.00

This paper presents a technique of microfabrication that is also based on the said photoresist, SU-8, but which tackles the problems previously discussed. Certain formulae are given to justify some design criteria. Finally, we discuss the feasibility of the use of Laser Direct Imaging to speed up fabrication of printed waveguides.

II. Technical Considerations

As mentioned earlier, one of the typical concerns of realization of submillimeter wave components is minimization of transmission losses. The transmission losses can be caused by waveguide discontinuities, dielectric losses and skin effect. The source of waveguide discontinuities can be surface roughness, and the thickness of the E-plane dielectric substrate. If x-axis is the axis along the substrate surface, the surface roughness can be expressed as effective surface profile , given as

$$\delta(x)_{eff} = \sqrt{\frac{1}{X_p}\int_0^{X_p} \delta(x)dx} \tag{1}$$

where x_P is the periodicity along the x-direction. The higher the operating frequency is, the more critical the surface roughness becomes. Processing SU-8 does not require surface treatments in general. An optically smooth surface is guaranteed if the hot-plate baking the SU-8 sample is not under mechanical disturbance.

As mentioned earlier, the transmission loss of the waveguide is directly associated with the thickness of the E-plane dielectric substrate. In general, the attenuation is given by:

$$\alpha = K\left(\frac{s}{\lambda}\right) \text{ Nepers / mm} \tag{2}$$

where S is the substrate thickness of the E-plane circuit, λ is the guide wavelength and K is a proportional constant. In other words, if the E-plane is made with SU-8, the thickness the SU-8 substrate should be minimized.

By skin effect, the RF current is concentrated in a layer directly below the conductor surface. In flat, infinitely thick conductors, the current density J is given by $J(x) = J_o \exp(-x(i+j)/\delta)$. is the skin depth given as

$$\delta = \sqrt{\rho \pi f \mu} \tag{3}$$

where μ is the permeability of the conductor material. f is the operating frequency. In general, the skin depth is smaller for higher operating frequencies. For a good conductor, one micron in thickness is equivalent to a few skin-depths at submillimeter wave frequencies.

III. Microfabrication Technique

Our micromachining technique entails two parts: a) microfabrication of rectangular waveguide housing; b) microfabrication of the E-plane printed circuits that are to be embedded into the waveguide housing of part a). What follows is a description of the basic fabrication procedures for the waveguide housing and the E-plane printed circuits.

a) Microfabrication Procedures of Waveguides

This section presents the procedures required to fabricate an SU-8 based waveguide for sub-millimeter applications. In realization of 3-D polymer structures such as rectangular waveguides, it is possible to lithographically process the waveguide features directly onto an oversized waveguide channel of a metal block. In so doing, we can use the depth of the oversized channel to control the SU-8 layer thickness, thus avoiding any inaccuracy in thickness due to inaccurate spin speed of the spinner and premature melting by heat. The support of the concave oversize channel also eliminates the need for an ultra-thick photoresist as opposed to the technique proposed in [1]. In addition, since the metal block itself has been machined with all the standard waveguide flanges, the fabricated waveguide can still be connected easily to other components through the standard flanges.

Basic Procedures of Processing a SU-8 Based Waveguides

Step 1. Mill a metal block with the required standard flange interfaces and an oversized waveguide channel (so called pocket). See figure 2.1.

Step 2. Apply the SU-8 photoresist onto the oversized waveguide channel until the SU-8 photoresist is just full, as shown in figure 2.2.

Step 3. Pre-bake the whole metal block together with the SU-8 photoresist as done in step 2, until the SU-8 liquid becomes sufficiently runny. Then let it cool down until the SU-8 photoresist changes to solid. With a solid SU-8 photoresist structure embedded into the oversized waveguide channel, expose 2-D waveguide features to ultra-violet light for around 6 minutes, using a photomask. Then post-bake the SU-8 filled metal block for a few minutes to further harden the sample. Finally, remove unwanted SU-8 patterns with SU-8 developer for around a few ten minutes. After this step, the required waveguide features will be structurally formed, as shown in figure 2.3.

Step 4. Hardbake the newly developed waveguide structure for at least one hour to completely harden the waveguide structure. Then, sputter a layer of good conductor onto the inner lining of the waveguide channels.

S-parameters of the SU-8 based waveguide have been measured. The S11, which is used to determine the electrical reflection of transmitted signal, was found to be

below -20 dB for the whole W-band, indicating that the waveguide discontinuity problem is insignificant.

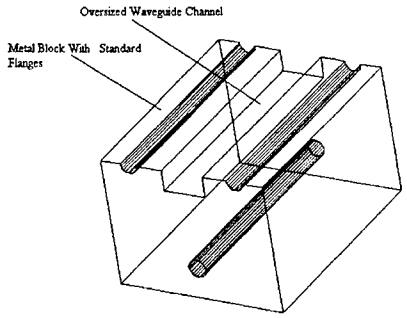


Figure 2.1 A Metal Block, with An Oversized Waveguide Channel

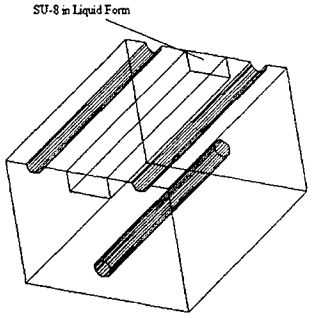


Figure 2.2 Oversized Waveguide Channel Filled with SU-8

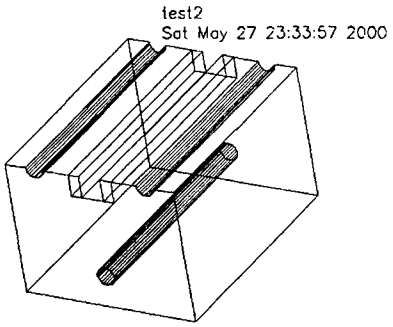


Figure 2.3. Metal Block with the Required Waveguide Channel

b) Microfabrication Procedures of E-plane Components

This section presents the procedures necessary to process an E-plane component using SU-8, which is to be incorporated into the waveguide realized in part a. As discussed in section II, the thickness of the dielectric backing S should be minimized. The layer for this E-plane dielectric support will be realized by spinninh on SU-8 at high speed onto a smooth surface. The metalization on printed circuits of the E-plane is to be thickened to around one micron.

Basic Procedures of Processing a SU-8 Based E-plane Circuits

Step 1. First evaporate a thin layer of silver as a sacrificial layer to one side of a glass slide. This thickness of the sacrificial silver layer is not important. Then evaporate the metalization pattern of the printed circuit directly onto the surface of sacrificial layer done in Step 2, preferably in gold or copper. See figure 3.1.

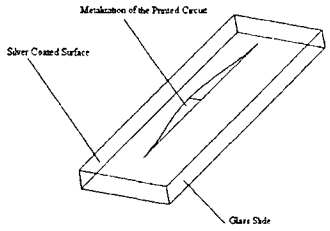


Figure 3.1. A Glass Slide with Metalization Pattern On the Silver Coated Surface

Step 2. Spin on SU-8 onto the surface with the metalization pattern. The thickness of the SU-8 layer should be minimized to no more than 50 microns, thus minimizing the attenuation as given in (3). See figure 3.2.

Step 3. Pre-bake the sample obtained from Step 3 at 100 degree C for around 10 minutes. Then, expose the wanted area to ultra-violet light for about 2 minutes, using a mask. Following the UV light exposure, post-bake the sample for another 10 minutes at 100 degree C. By soaking the sample to the SU-8 developer, the unexposed SU-8 photoresist will be developed away, leaving the sample as shown in figure 3.3.

Step 4. Soak the sample into iron III nitride solution to etch away the silver sacrificial layer and to remove the glass slide.

The measured S-parameters, as shown in figure 3.4 in the end of the paper, suggest that the E-plane circuits realized with this technique are of very low transmission loss and suffers from very little discontinuity problem. The measured S21 (or S12), which indicates the loss between two ports, is no more than 0.6 dB, whereas the S11 (or S22) is below -15 dB for the whole band.

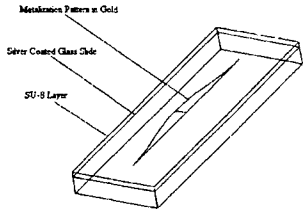


Figure 3.2 Metalization Pattern, topped with an SU-8 layer.

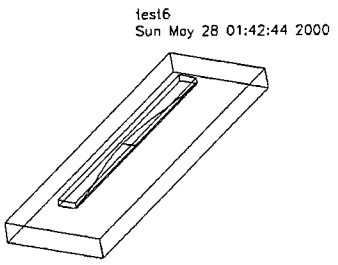


Figure 3.3. The Appearance of the Sample after Step 3

III. Feasibility of Fabrication by Laser Direct Imaging

Laser Direct Imaging, LDI, is currently being used for production of printed circuit boards. In LDI, the laser directly raster-scans the metalization pattern onto the photoresist covering a copper-clad substrate, without the need for a photo-mask. Since the metalization patterns of waveguides are not much different from those of high-resolution printed circuits, it appears the working principal of LDI can similarily be applied to production of printed waveguides. This appears to be particularly true if the LDI system is based on an ultra-violet laser. Experiment has been done to investigate the feasibility of using LDI on processing of SU-8, based on our home-made visible laser. Our experimental evidence suggests that production of waveguides by direct laser writing is technically possible with minor considerations. What follows are the considerations about application of LDI to microfabrication of submillimeter wave components, according to our findings.

Feature sizes drawn by current LDI systems may be down to 50 microns. In terms of the wavelength requirements, this resolution may be adequate for submillimeter wave applications. Due to the bitmap nature of the LDI images and other raster effects, however, surface roughness can be generated in the waveguide housing, which affect the transmission efficiency when the operating frequency is high.

Before exposure to ultra-violet light, any thermal effects can deform the SU-8 sample. Direct writing of the metalization pattern by LDI can thermally shock the pattern if the laser generates heat to the SU-8 sample.

One solution to this problem is to use a transparent sheet as a thermal isolation layer to protect the SU-8 sample from pre-mature deformation. At the time of this writing, the photosensitivity of femtosecond laser in SU-8 has not been identified. But femtosecond laser can eliminate heat flow to surrounding material, as opposed to other longer pulsed laser. Therefore, imaging with femtosecond laser can potentially avoid the problem of premature thermal deformation of the SU-8 sample.

IV. Conclusions

This paper has demonstrated, with measured S-parameters , a feasible technique of microfabrication of millimeter wave and submillimeter wave components, with a positive photoresist, known as SU-8. Our experimental evidence also suggests that the working principal of laser direct imaging can be applied to microfabrication of waveguide using SU-8.

V. Acknowledgement

The authors wish to acknowledge Mr. T. Mosley's help in machining the metal blocks.

VI. References

1) C.E.Collins, R.E. Miles, G.M. Parkhurst, J.W. Digby, H. Kazemi, J.M Chamberlain, R.D. Pollard, J.J. Cronin, S. Davies, J.W. Bowen, D.P. Steenson, "Use of novel Photoresists in The Production of Submillimeter Wave Integrated Circuits", SPIE International Society for Optical Engineering, pp. 108, July 20-23,1998

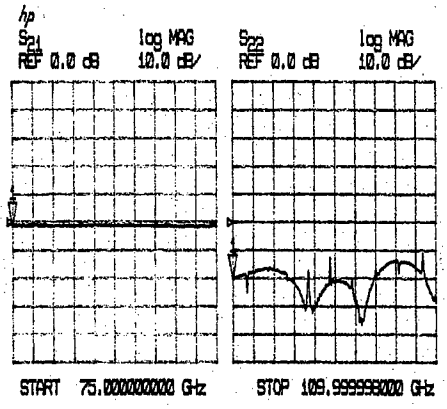


Figure 3.4. Measured Performance of An Example E-plane transition Realized with The Said Technique

Laser via-hole drilling of printed wiring board

Toshiharu Okada

Production Engineering Laboratory, Matsushita Electric Industrial Co., Ltd.
2-7 Matsuba cyo, Kadoma city, Osaka, Japan
E-mail: okada@labo.ped.mei.co.jp

In these few years, telecommunication appliances, for example cellular mobile telephone and mobile computer, have been becoming smaller and lighter. In addition they have been equipped with higher performances. Stepping with that progress, the technologies about integrated circuits, electrical components, battery and display devices that are used in those equipment mentioned before have been developing successfully. In the field of multi-layer printed wiring board, many efforts have been made to drill smaller size via holes in order to minimize the size of wiring pattern. Especially laser micro drilling technology that has been expected to be able to overcome the conventional mechanical drilling technology has been spread rapidly into the factory mainly in Japanese market since 1996. As a result, the typical size of the via hole diameter has become 100 to 200 micrometer from 300 to 400 micrometer and the structure of multi-layer has been changed from through-hole structure to inner via hole structure.
Laser micro hole drilling technology nowadays including the "ALIVH", which is the name of the printed wiring board that Matsushita has developed, and the survey of the next generation laser drilling technology will be presented.

Key ward: laser drilling, via-hole, printed wiring board, ALIVH, CO_2 laser, YAG laser, THG

1. Introduction

In these several years, mobile telecommunication equipment has spread widely in the market. Especially the cellular phone has rapidly increasing in number. Figure 1. shows the change in the market size of cellular phone in the world [1]. In 1998 the market grew at 53.8% and it has continued to grow at about 6% per year.

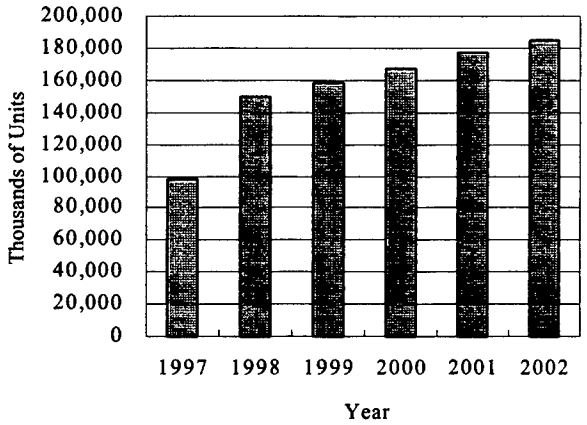


Figure 1. World wide market of cellular phone
(2000~2002:predicted)

Figure 2. shows the growth of Japanese market[2]. It also showed the big growth at 30% in 1998 and has been growing at 10-20% every year.

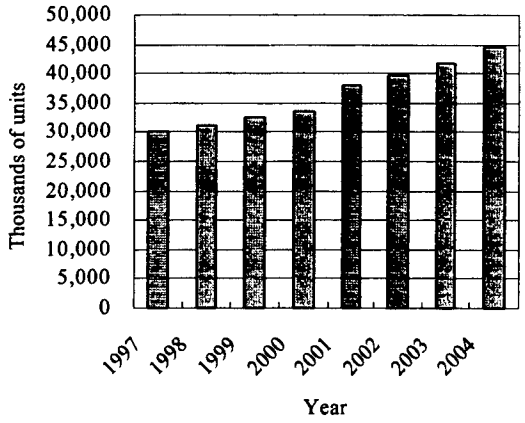


Figure 2. Japanese market of cellular phone
(2000~2004: predicted)

Towed by the expansion of the cellular phone market, the sales of multi-layered printed wiring board(PWB) with high packaging density has also grown rapidly. Figure 3. shows the worldwide market of multi-layered PWB with high packaging density[3]. In 2003 the revenue will be expected to become $3 billion. And 27.5% of the total revenue will be occupied by cellular phone use.

In order to meet the consumer's requirement for lighter and smaller mobile equipment, the development of higher packaging density PWB has been pushed forward by the

First International Symposium on Laser Precision Microfabrication, Isamu Miyamoto, Koji Sugioka, Thomas W. Sigmon, Editors, Proceedings of SPIE Vol. 4088 (2000) © 2000 SPIE · 0277-786X/00/$15.00

manufacturers in Japan. According to the improvement in the wiring density, smaller size via-holes drilling technology

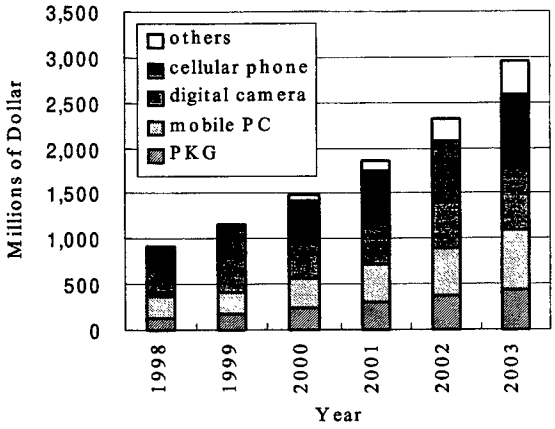


Figure 3. World wide market of high packaging density multi-layered PWB (2000~2003 : predicted)

has been needed. Laser via-hole drilling technology has been able to be the substitute for conventional mechanical drilling method.

The advantages of laser via-hole drilling compared to another two processes are the drilling speed, flexibility for the variety of wiring pattern, and the ability to drill relatively smaller diameter via-holes.

Matsushita Electric Industrial started to develop the laser via-hole drilling technology in 1991 concurrently with the development of our innovated PWB dubbed "ALIVH" (Any Layer Inner Via Hole). ALIVH has been into the market since 1996 and has represented an epoch-making advance in the development of PWB up to the present.

This paper presents the development of CO_2 laser drilling technology for ALIVH and discusses the post-CO_2 laser drilling technology for next-coming higher packaging density PWB.

2. Development of CO_2 laser via-hole drilling technology for ALIVH

2.1 Features of ALIVH structure

Figure 4. shows the conventional through hole structure and the ALIVH IVH(Inner Via Hole)structure. Conventional through hole structure multi-layered PWB do not permit mounting of components on top of through hole, so down-sizing is restricted. In addition, because through holes become obstacles for wiring design, the length of wires is hard to minimize.

On the other hand, ALIVH IVH structure does not have any through hole. Instead, the arbitrary layers are electrically connected only by IVH. Thus the high density mounting of components, which was impossible with the conventional through hole structure, has become a reality. Packaging density of ALIVH has become higher by

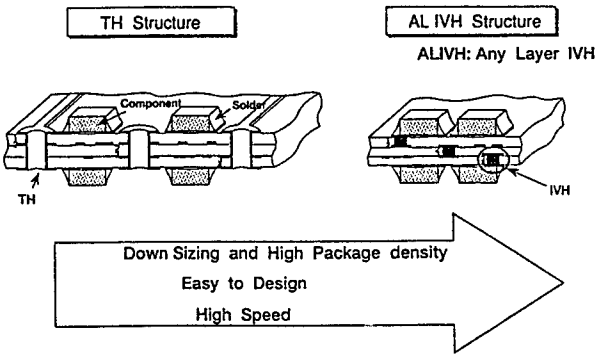


Figure 4. Conventional through hole structure and ALIVH IVH structure

approximately 30 to 50%. The more, due to the any layer IVH structure, wiring capability has been greatly improved. Total designing time has been able to be reduce by 20 to 50%.

2.2 The main subjects for developing ALIVH

Figure 5. shows three main subjects for developing ALIVH. Laminates material is Matsushita's original non-woven aramid with epoxy resin. The base material made of non-woven aramid is lighter and stronger compared to commonly used woven glass material. Another advantage of this material is that the laser energy threshold is lower than that of woven glass material. Aramid is very easy to drill by CO_2 laser, and this is one and important reason for us to adopt the material.

Inner via holes of ALIVH are processed with CO_2 laser drilling method. CO_2 laser drilling could drill under 200 micron diameter holes with much higher speed compared to mechanical drilling even in 1993.

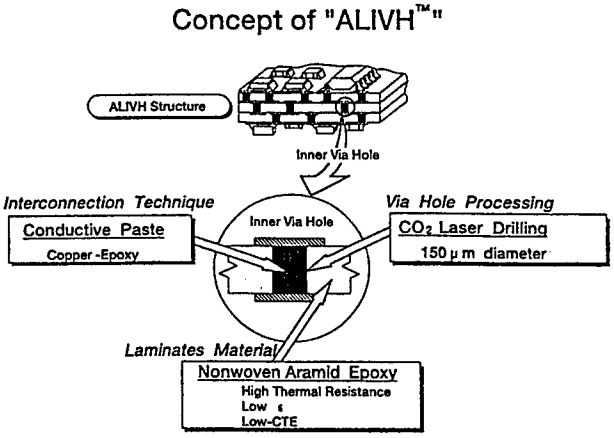


Figure 5. Concept of ALIVH development

Conductive paste has been developed for interconnection, as a replacement for conventional copper plating. By filling via holes with this conductive paste and laminating the multi-layers by the stack method, ALIVH structure has been completed.

2.3 The main feature of laser via-hole drilling technology

Figure 6. shows the schematic illustration of laser via-hole drilling equipment for ALIVH. Three main features of laser drilling equipment for ALIVH are the drilling speed, small size drilled holes, and laser irradiation positioning accuracy. In order to get the high speed laser drilling, Matsushita have been the first to develop the CO_2 laser scanning units with galvanometer scanner and large size scan lens made of ZnSe for via-hole drilling. To improve the productivity per unit area, we have taken two scanning units on a laser drilling equipment at the first stage of our development, and we could double the productivity.

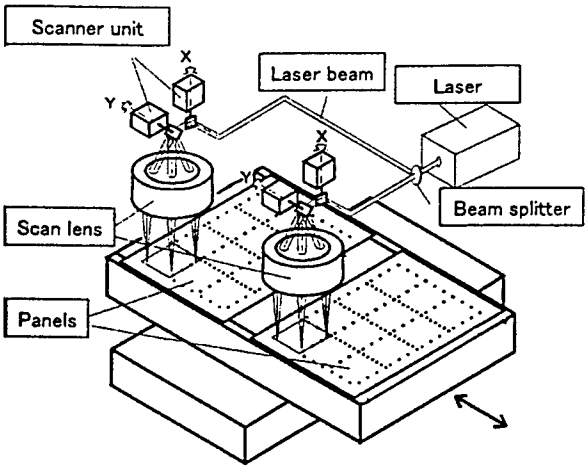


Figure 6. Schematic illustration of laser via-hole drilling equipment

Figure 7. shows the cross section and ray trace of the scan lens. In case of designing the scan lens, we have to consider that the laser beam should be irradiated perpendicular to the substrate. If not, the circularity of the via-holes changes in place and we cannot get the uniform and small diameter via-holes. We have accomplished the via-holes circularity of over 90% and the small via-hole diameter of about 100 micron using scan lens with 101.6mm focusing length.

When we use the galvanometer scanning units in order to position the laser beam, we cannot expect the absolute positioning accuracy without correcting the error caused by optical distortion, laser beam miss-alinement, and slight rotation between 2-axis galvanometer coordinates and 2-axis X-Y stage coordinates. Figure 8. shows the schematic illustration of the error collecting method. Positioning error are measured by the inspection equipment exclusively developed for ALIVH and according to the results of measurement it is corrected numerically.

Figure 9. is an example of position error spread diagram. Each dot shows an error from the correct position. Positioning error is within 30 micrometer.

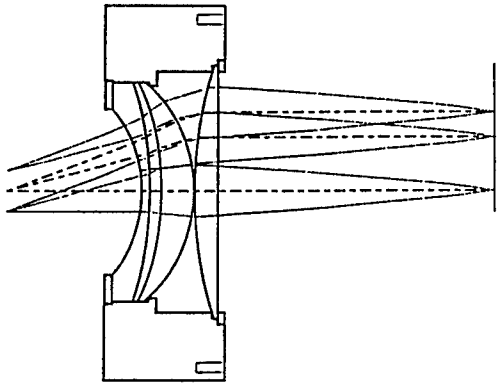


Figure 7. Cross section of the scan lens

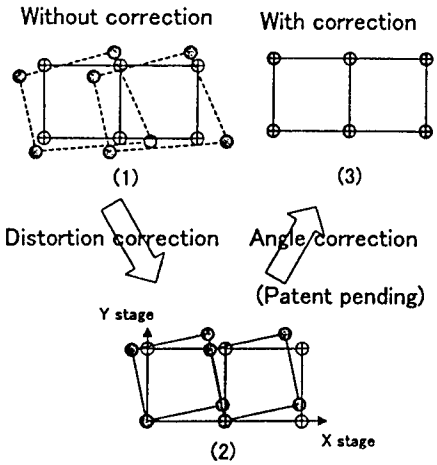


Figure 8. Schematic illustration of the error correcting method

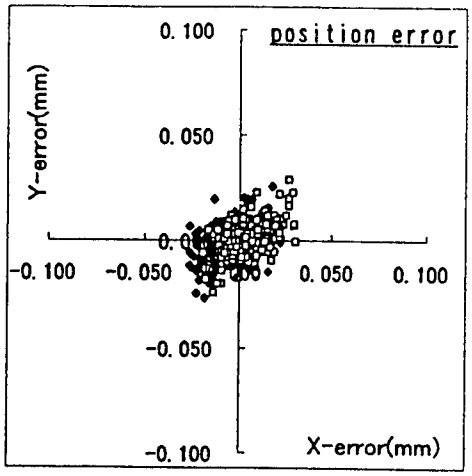


Figure 9. Positioning error spread diagram of laser drilled via-holes

The mass production of ALIVH has started in 1996. Now, ALIVH has occupied the 60% of cellular phone market.[4] And a number of laser via-hole drilling equipment have been operating continuously almost 24 hours a day and over 300 days a year. The equipment for mass production have been provided several functions to keep the process stable. The processing dust collector is important to keep the surface of substrates clean. Laser pulse monitoring unit is also important to keep watching if the output power of laser oscillator changes or not.

CO_2 laser via-hole drilling technology has already become the standard manufacturing process of the PWB industry within an amazingly a short period. It took just 4 years since the first mass production of laser via-hole drilled PWB started.

On the other hand, the packaging technology of Integrated Circuit (IC) has made remarkable progress within these 4 years. Chip Size Package (CSP), Ball Grid Array (BGA) and Multi Chip Module (MCM) have already been realities. And the market requires the PWB industry to meet much higher wiring density for IC packaging. And thus, much smaller via-hole diameter has been needed inevitably. Figure 10. shows the predicted via-hole diameter from year 2000 to 2010.[5] Via-hole diameter will reach 25 micrometer with laser drilling as well as with photo process, and 100 micrometer with mechanical drilling.

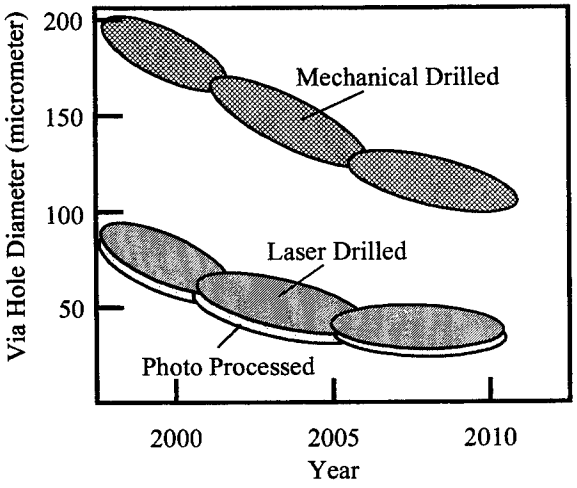


Figure 10. Predicted via-hole diameter in high packaging density PWB

3. Post-CO_2 laser via-hole drilling

The ordinary wavelength of CO_2 laser is 9.3 micrometer or 10.6 micrometer. So it is not suitable for drilling via-holes under the diameter of 50 micrometer. Figure 11. shows the calculated CO_2 laser beam focusing spot diameter assuming the mask imaging optics. Using 0.5 mm diameter mask, it is possible to make under 50 micrometer image, but it's not practical. So we need shorter wavelength laser which can be focused smaller than CO_2 laser .

We can find out that kind of laser in the group of solid-state lasers and excimer lasers. In this paper solid-state laser that is suitable for focusing applications will be discussed.

Figure 12. shows the optical transparency vs. wavelength for

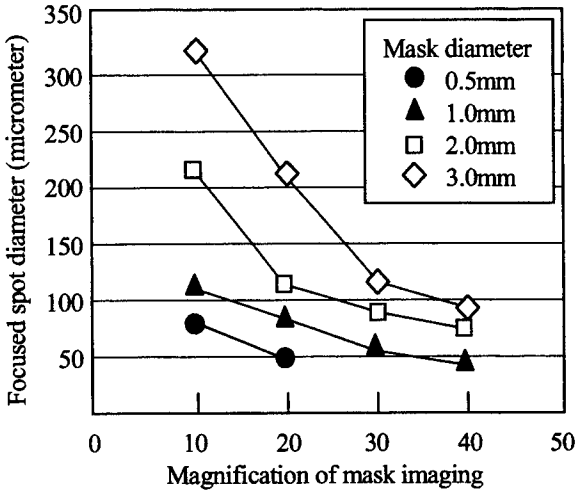


Figure11. Calculated focused spot size of CO_2 laser as a function of mask imaging magnitude

various kind of resin films. According to this figure, laser beam absorption for most films seems to increase at and under the wavelength of Third Harmonics of YAG laser (THG-YAG). (Wavelength of THG-YAG is 355nm.)

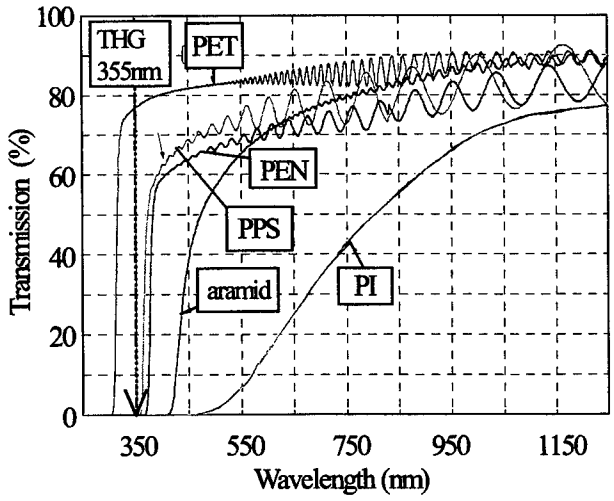


Figure 12. Optical transmission as a function of wavelength for several kind of resin films

THG-YAG laser drilled via-holes on polyimide film with 100,200,300 μm hole space is shown in Figure 13. A hole's diameter is 50 micrometer, and the Hear Affected Zone(HAZ) observed is small.

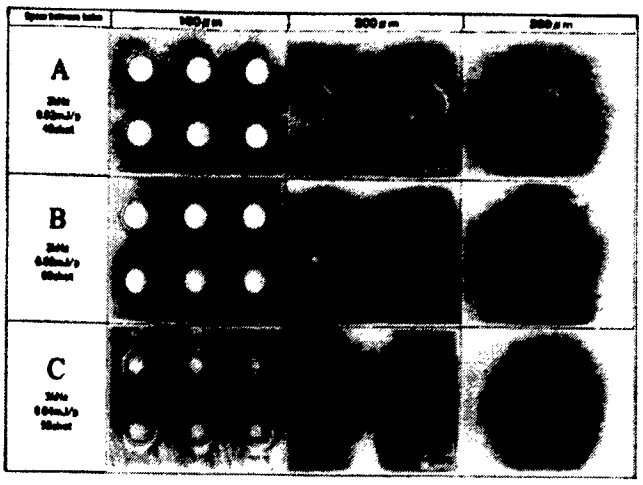


Figure 13 . THG-YAG laser drilled via-holes on PI film

The aspect ratio (taper) of THG-YAG laser drilled blind holes as a function of the number of laser irradiation is shown in Figure 14. and Figure 15. Shorter wavelength laser is likely to absorb on the surface of the substrate and not to penetrate into the material, so it needs a number of laser shots in order to drill a hole. This is the disadvantage to be solved to improve the productivity of shorter wavelength laser via-hole drilling process.

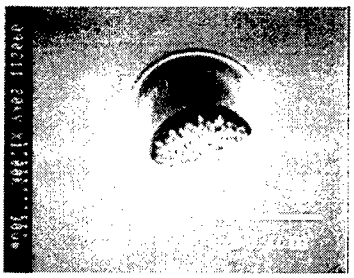


Figure 14. Blind via-hole on epoxy resin by THG-YAG laser drilling

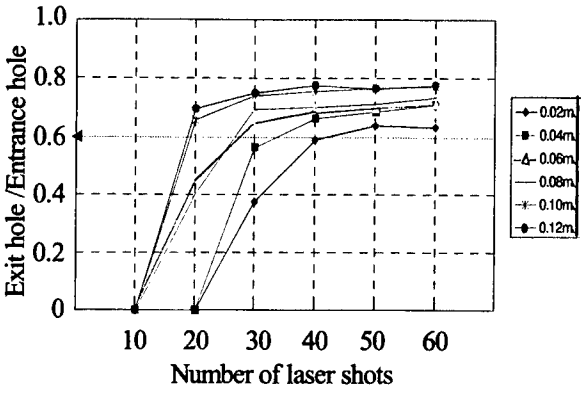


Figure 15. Ratio of exit hole diameter by entrance hole diameter as a function of the number of laser shot

The pulse duration of typical THG-YAG is about 10 to 100 ns. In this pulse width condition, a portion of the laser drilling is likely to be the thermal process.
When the mode of laser beam is kept good, laser beam can be focused to the small spot and the intensity becomes higher enough to cause the ablation process. But once the mode has been degraded, laser beam cannot be focused enough. So that HAZ around the drilled hole is enlarged. Figure 16. shows the effect of THG-YAG laser beam mode on HAZ around the drilled hole.

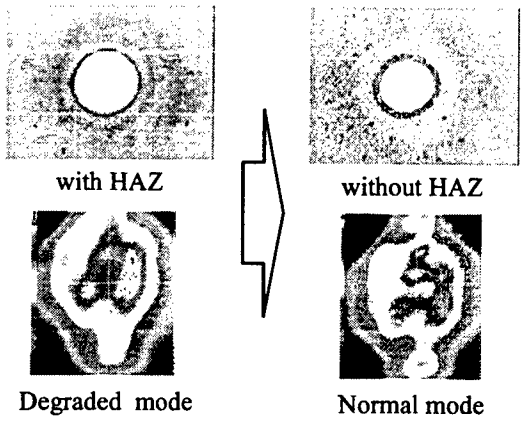


Figure 16. Effect of laser beam mode on HAZ around the via-hole

Femto-second laser has still been in scientific region, but it's ultra-short laser pulse scarcely generate the HAZ around the drilled hole. If we need to get the via-holes with best quality, ultra-short pulse laser drilling must be one of the best process. Figure 17. shows the femto-second laser trepanning process. In this case, the substrate has been trepanned around to cut off after four times round pass. And the HAZ

around the hole does not find at all.

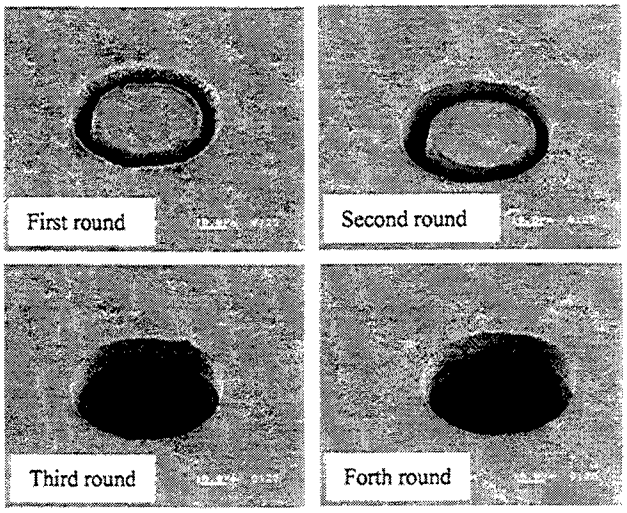


Figure 17. Process of laser trepanning with Ultra-short pulse solid-state laser

Figure 18. shows the trepanning results on the material of woven glass with epoxy. We can also see the drilled hole with good quality.

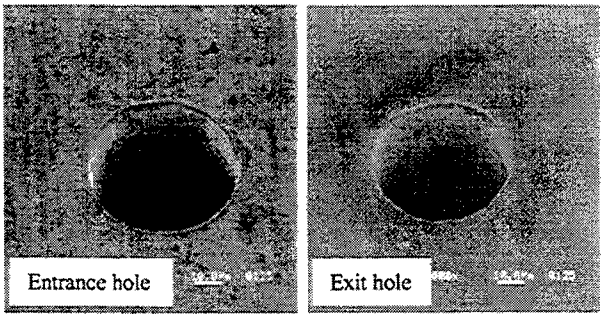


Figure 18. Trepanning on glass-epoxy substrate with ultra-short pulse laser

4. Summary

Matsushita Electric Industrial has developed the original any layer inner via-hole PWB ALIVH and CO_2 laser via-hole drilling technology concurrently. ALIVH has already been mass-produced and has been applied mainly for cellular phone. CO_2 laser via-hole drilling technology has spread widely into the Japanese PWB industry and has been established the position as the standard PWB process.
Japanese market has gone a head in putting the higher packaging density multi-layered PWB to the use of cellular phone. Higher packaging density PWB has been introduced into 73% of cellular phones.
In north America and Europe, down-sizing of cellular phone seemed not to have been investigated eagerly, and higher packaging density PWB has not been widely spread into the market.
In the north American market, higher packaging density PWB has been introduced only 15% of cellular phones.
In European market, they have been introduced only 16% of cellular phone.
But nowadays, internet access with cellular phone has been taken as a matter of course. And the next year, cellular phone will be used as the visual data terminal. In that case, cellular phone must be equipped higher performance than before and higher performance PWB will be needed necessarily.
In the following few years, CO_2 laser via-hole drilling technology for multi-layered PWB is expected to spread in the world. And it will depend on the improvement of productivity whether post-CO_2 laser via-hole drilling technology would be succeed as well as CO_2 laser drilling or not.

Reference

[1] World wide electronics market research '99
Fuji Kimera Co., Ltd.
[2]Communication equipment marketing research '99
Fuji Kimera Co., Ltd.
[3]Electronics Technology, June 2000, pp.19
[4] Electronics Technology, June 2000, pp.24
[5] Electronics Mounting Society, June 1999, pp.90
(Electronics Mounting Technology Load-map 2010

Present Status of Excimer Laser Exposure Apparatus

Akiyoshi Suzuki

Optics Research Division 4, Optics Technology Research Center, Canon Inc.
20-2,Kiyohara-Kogyodanchi, Utsunomiya-shi, Tochigi-ken, 321-3292, Japan
E-mail: akiyoshi@cks.canon.co.jp

One of the most important technical driving forces for IC manufacturing is lithography. IC manufacturing equipment is required to work in severe full-time operation, such as 24 hours a day and 7 days a week. KrF laser, however, has established its status, and has proven the applicability of excimer laser itself.

The transition from super high pressure mercury lamp (i-line: 365nm) to KrF laser was a natural trend, because the resolution is improved proportionally with shorter wavelength. Practical resolution is now said to attain half the wavelength, using high NA optics and imaging "tricks", such as phase shifting masks, oblique illumination, etc. At present, 130nm resolution is pursued using a KrF laser and a projection lens whose NA is nearly 0.7.

ArF laser lithography is also under extensive development. In the initial stage, it has proven 120nm resolution with an NA 0.6 projection lens, and now aims at 100nm resolution of 4G-bit DRAM as the next generation. The light source development always comes first in lithography, and F2 laser technology is now paid much attention.

Keywords: microlithography, excimer laser, KrF laser, ArF laser, F2 laser, resolution, semiconductor manufacturing,

1. INTRODUCTION

Laser microlithography has been paid much attention since the age of contact printing. Practical KrF micro-lithogrpahy was first presented by V. Pol in 1987 [1]. It took, however, nearly ten years that KrF laser lithography was introduced in real production.

Microithography involves wide variety of technologies, such as optical systems, resists, optical materials and light sources. The development of super-resolution technology might have postponed the age of KrF lithography, but it is true that each basic technology was far from maturity at the start of 1990s. The ten years were devoted to develop not only the exposure apparatus, but also many peripheral items like lasers and resists.

This paper deals with the background of the laser microlithography, and explains the contemporary status for each laser exposure system.

2. Background of laser microlithography

There exist various items that promote the remarkable progress of semiconductor industry, and microlithography is recognized as one of the most important technical driving forces. In semiconductor industry, ITRS (International Technology Roadmap for Semiconductor) committee proposes the target specification for the next ten years to come. Fig.1 shows a part of the recent ITRS roadmap. There has been a golden rule that the technology node of fine patterns has been reduced 70% per 3 years, but its acceleration is now discussed.

Year	1999	2000	2001	2002	2003	2004	2005	2008
Technology Generation	180			130			100	70
DRAM								
Half pitch	180	165	150	130	120	110	100	70
Contacts	200	185	170	150	145	140	130	100
Overlay (m+3 σ)	65	58	52	45	42	38	35	25
CD control(3σ)	18	17	15	13	12	11	10	7
MPU								
Half pitch	230	210	180	160	145	130	115	80
Gate length(in resist)	140	120	100	90	80	70	65	45
Gate length(post etch	140	120	100	90	80	70	65	45
Contacts(in resist)	230	210	180	160	145	130	115	80
CD control(3σ)	14	12	10	9	8	7	6	4
ASIC (SoC)								
Half pitch	230	210	180	160	145	130	115	80
Gate length(in resist)	180	165	150	130	120	110	100	70
Gate length(post etch	180	165	150	130	120	110	100	70
Contacts(in resist)	230	210	180	160	145	130	115	80
CD control(3σ)	23	21	19	16	15	13	12	7
Minimum feature size	90	80	70	65	55	50	45	33

(unit: nm)

Fig.1 ITRS Lithography Roadmap('99)

First International Symposium on Laser Precision Microfabrication, Isamu Miyamoto, Koji Sugioka, Thomas W. Sigmon, Editors, Proceedings of SPIE Vol. 4088 (2000) © 2000 SPIE · 0277-786X/00/$15.00

The key factor for fine line patterning is the development of exposure apparatus including lasers. Three major items of exposure apparatus are resolution, overlay (alignment) accuracy and cost of ownership (throughput). Above all, resolution capability always comes first. Though KrF laser system gives expensive cost, the strong requirement for higher resolution has made its introduction possible.

Resolution capability is known to be expressed through the well known Rayleigh's equations. Minimum resolution linewidth RP and depth of focus DoF can be expressed as follows:

$RP=k_1 \lambda /NA$

$DoF=k_2 \lambda /NA^2$

where λ is exposure wavelength, NA is the numerical aperture of the projection optics and k_1 and k_2 are proportional constants which correspond to process parameters. The royal way to enhance resolution is to make the value of λ/NA smaller, and it shows the direction of larger NA and shorter wavelengths

		Resolution (nm)									
	NA	250	200	180	150	130	110	100	90	80	70
KrF	0.60	0.60	0.48	0.44	0.36	0.31	0.27	0.24	0.22	0.19	0.17
	0.65	0.65	0.52	0.47	0.39	0.34	0.29	0.26	0.24	0.21	0.18
	0.70	0.70	0.56	0.51	0.42	0.37	0.31	0.28	0.25	0.23	0.20
	0.75	0.76	0.60	0.54	0.45	0.39	0.33	0.30	0.27	0.24	0.21
	0.80	0.81	0.64	0.58	0.48	0.42	0.35	0.32	0.29	0.26	0.23
ArF	0.60	0.78	0.62	0.56	0.47	0.40	0.34	0.31	0.28	0.25	0.22
	0.65	0.84	0.67	0.61	0.50	0.44	0.37	0.34	0.30	0.27	0.24
	0.70	0.91	0.72	0.65	0.54	0.47	0.40	0.36	0.33	0.29	0.25
	0.75	0.97	0.78	0.70	0.58	0.50	0.43	0.39	0.35	0.31	0.27
	0.80	1.03	0.83	0.74	0.62	0.54	0.46	0.41	0.37	0.33	0.29
F2	0.60	0.96	0.76	0.69	0.57	0.50	0.42	0.38	0.34	0.31	0.27
	0.65	1.04	0.83	0.75	0.62	0.54	0.46	0.41	0.37	0.33	0.29
	0.70	1.11	0.89	0.80	0.67	0.58	0.49	0.45	0.40	0.36	0.31
	0.75	1.19	0.96	0.86	0.72	0.62	0.53	0.48	0.43	0.38	0.33
	0.80	1.27	1.02	0.92	0.76	0.66	0.56	0.51	0.46	0.41	0.36

Fig.2 Table of k_1 factors

Fig.2 is the table of k_1 values, which can be considered as a normalized linewidth. Several years ago, the practical k_1 value was considered as 0.6, but it now approaches 0.4 owing to the progress of resists. In KrF system, NA value is now going up to 0.7 or larger. The comparison of Fig.1 and 2 shows the status of each laser. It explains the natural demand for ArF and F2 lasers.

In excimer laser microlithography, ordinary optical glass materials cannot be used by absorption. Fused silica and CaF2 are the only material for optical system. Fig.3 shows the optical material for microlithography. The constraint of the optical material gives serious effect for compensating chromatic aberration of the optical system. In DUV region, the development of materials is always the key.

There are three major factors that lead excimer lasers to microlithography.

The first factor is short wavelength, and it is easy to explain through the Rayleigh's equation.

The second is high output power in DUV region. Illumination intensity of the excimer apparatus, however, is not so high at the wafer plane when it is compared to i-line apparatus. The reason why the same throughput is achieved with KrF apparatus depends on the appearance of chemically amplified resist with high sensitivity. The typical sensitivity of i-line resist is 2000J/m², whereas that of KrF is 100J/m². KrF microlithography has become possible with the combination of the resists.

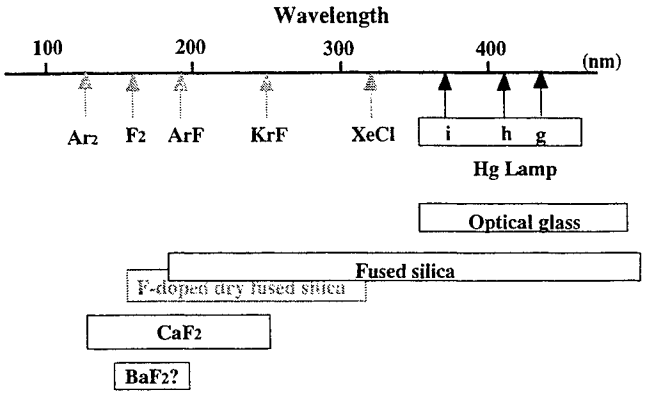


Fig.3 Lasers and optical materials

The third is spectral line narrowing capability. The chromatic aberration problem was solved by line narrowing of lasers. In KrF, focus sensitivity to wavelength is nearly 0.14um/pm[2]. Considering the depth of focus is below 1um, the requirement for FWHM must be less than 1pm, which matched the line narrowing capability of KrF lasers well.

The establishment of excimer laser microlithography involves such unexpected system matching. It is natural that it took ten years to find its full possibility for practical use, because IC manufacturing equipment is required to work in severe full-time operation, such as 24 hours a day and 7 days a week.

3.KrF Exposure Apparatus

KrF exposure apparatus is now the main manufacturing tool in recent semiconductor production. KrF lasers have demonstrated their applicability to microlithography field.

KrF laser microlithography has several advantages over other excimer laser exposure system.

The greatest advantage is high transparency of fused silica. Its transparency is over 99.9%/cm, which is higher than those of various i-line glasses. The efficiency of KrF optical system is high, and the thermal aberration caused by the absorption of the exposure light is almost neglegiable. As a result, KrF exposure system is very stable by nature.

The second point is the matching of chromatic aberration of the optical system and spectral line narrowing capability of lasers. The FWHM of i-line exposure system is 10nm, whereas that of KrF is nearly 0.5pm. In the design of i-line optical system, chromatic aberration must be balanced in the 10nm range by mixing the various kinds of glasses with different dispersion. The balancing is critical according to the material constraint. In KrF system, line narrowing technology has solved such critical compensation.

Stability to environment is another advantage. Chemical contamination is not prominent in the spectral range over 220nm.

Fig. 4 shows the recent exposure results of KrF exposure apparatus[3], FPA-3000 EX6 (NA 0.65) and FPA-5000 ES2 (NA 0.68). It shows over 0.5um depth of focus for 150nm L&S patterns with NA 0.65 and 0.68. As resolution limit, 120nm patterns are resolved with NA 0.68 optics. The continuous effort to extend KrF lithography has opened new possibility using double exposure method [4], and 55nm isolated gate pattern generation was reported recently[5].

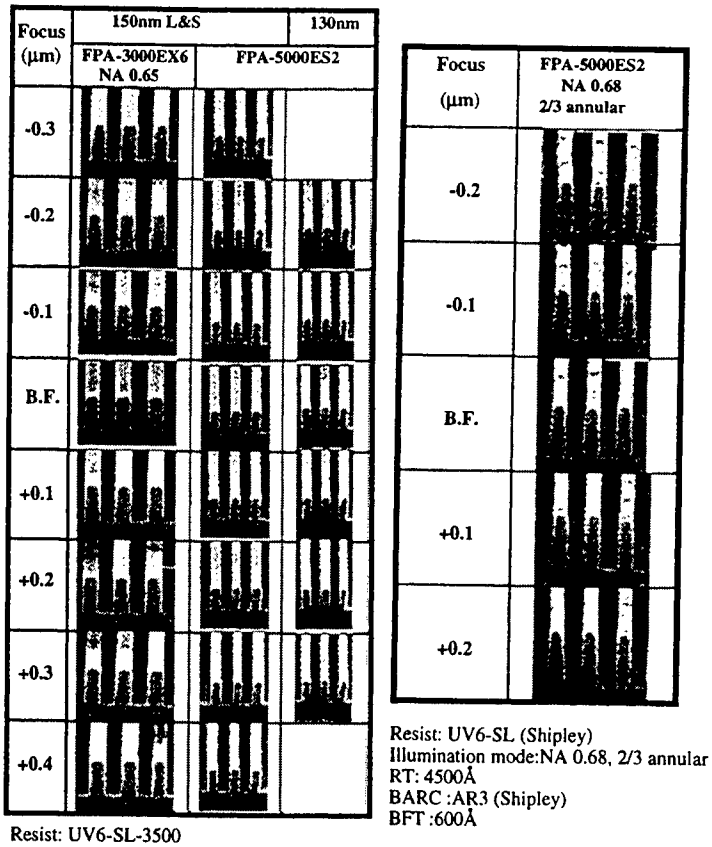


Fig.4 Exposure results of recent KrF apparatus

In order to achieve higher resolution, super-resolution technology, such as modified illumination or phase-shifting masks, is indispensable. Accordingly, the requirement for projection optics is getting severer [6]. Wave Front Engineering (WFE) is introduced to minimize and optimize the aberrations by using Zernike polynomials. It is applied not only to the optical design, but also to the manufacturing phase. The wave front aberration is monitored with a phase measurement interferometer (PMI), which has a special laser with the same wavelength of the exposure light. In addition to PMI, various lasers are used for checking the surface accuracy, homogeneity, birefringence of elementary components of optical system. T

It is natural to assume that KrF microlithogrpahy can extend its region beyond 130nm or finer with higher NA because of its intrinsic advantage. The completion of practical WFE has made the extension possible.

4. ArF Exposure Tool

4-1. Background

ArF laser microlithography exists on the extrapolation position of KrF system. Its resolution target is 130nm to 100nm technology node. ArF system can be constructed in the similar way of KrF system as shown in the early Japanese work [7], though it contains symptoms of specific issues in VUV region. The new items below 200nm are optical material and environmental control.

There are two major issues for optical material, one is durability, and the other is the development of new optical material. Because the photon energy goes higher, the durability of optical material has been taken much attention from the beginning, and been studied for a long period [8]. The main issues of fused silica, which is the main material in KrF microlithography, are the change of transmittance and the material damage caused by ArF laser exposure.

Wet fused silica which has high hydrogen concentration was demonstrated to suppress the generation of color centers such as E' center, and to show good transmittance with durability.

For ArF laser exposure, a new damage phenomenon called compaction was found. Compaction makes the densification of fused silica in the exposure area of high intensity, and induces extra stress. Considering the life time of the optical system, the energy concentration in projection optics is calculated minutely to ensure its peak energy value less than $1J/m^2$/pulse. Compaction has strong correlation to the peak energy of laser pulses. Pulse stretching and higher repetition rate are, therefore, effective to suppress the damage of the optical system. As for the damage of fused silica, further study is now under investigation [9].

In order to compensate chromatic aberration, the development of CaF_2 has been done extensively. The

dispersion of fused silica at 193nm is about three times larger than that at 248nm. For a refractive system with fused silica, the requirement for FWHM is assumed 0.2 to 0.3pm. The line narrowing capability of laser matched the requirement from the optical system at 248nm. In ArF system, however, the predicted difficulty for line narrowing accelerated CaF2 development. Fluoride crystals have higher band gap, which makes both the transmittance and the durability higher in DUV region. The optical specifications for homogeneity, stress birefringence and the size of CaF2 are now almost sufficient for lithographic use. The stable supply of CaF2, however, will be a key issue for ArF and future F2 laser microlithography.

4-2. Development of ArF exposure apparatus

The first full-field ArF exposure tools were announced in 1999 [10,11], and they are now being used for developing ArF specific processes. Progress in optical materials, the preliminary research for compaction and line narrowed laser made it possible to adopt the same type of optics as that of the KrF exposure apparatus, though there had been many arguments regarding projection optics configuration. The specifications of the ArF scanning exposure apparatus, FPA-5000 AS1, are NA 0.6, 1/4X magnification, exposure area 26x33mm^2, and equivalent throughput as that of the KrF scanner [3].

In the ArF wavelength region, oxygen absorption spectrum has still discrete distribution, which makes it possible to select the adequate wavelength with little absorption.. In addition, the development of high quality CaF2 enabled the adoption of the same configuration of projection optics as that of the KrF exposure apparatus Tight purging capability is equipped with chemical contamination effect below 200nm taken into account

Aiming at 130nm resolution, the NA of the projection optics was selected 0.6 through the hypothesis of k_1=0.4 of contemporary KrF resists. From the table in Fig.2, NA 0.60 of ArF system is almost equivalent to NA 0.77 of KrF system. In order to apply WFE to the ArF projection optics, an interferometer using the exposure wavelength is necessary. A special laser for PMI measurement was developed to make the accurate evaluation of the aberrations possible. The manufacturing technology for ArF projection optics has become sufficient for the 130-100nm generations.

Fig. 5 shows the exposure results of FPA-5000 AS1. The process condition was PAR-710 resist with a thickness of 4000 Å, and 1600 Å BARC was used. In Fig.5, CD (Critical dimension) values of horizontal and vertical patterns for 9 points in a shot are plotted simultaneously. ±10% CD-DOF for 130 nm L&S in the exposure field was 0.6um with 1/2 annular illumination.

Fig.6 shows the SEM pictures of 120nm. Features down to 120 nm are resolved under the conventional illumination with σ 0.75. In addition, nearly 0.8 um DOF is obtained for 120 nm L&S with 1/2 annular illumination. The DOF of 120nm L&S for NA 0.68 KrF apparatus is only 0.3um, which shows the advantage of reducing the λ /NA value.

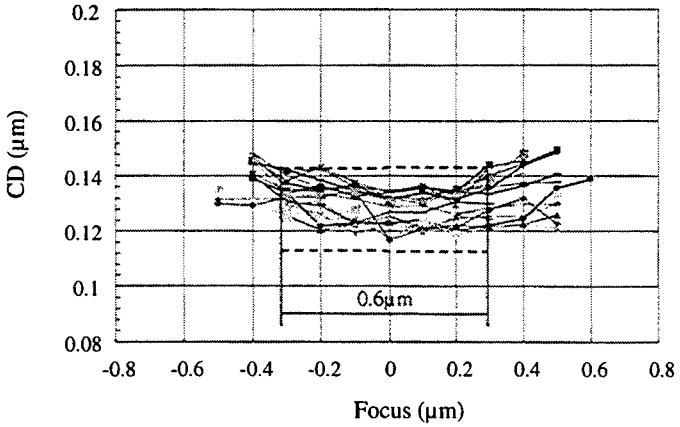


Fig.5 CD DoF of 130nm L&S (ArF NA 0.60)

Other items were also investigated. Image field deviation (IFD) in full field was 90 nm and astigmatism was 59 nm. Dynamic distortion was controlled to 5 nm in the scanning direction and to 17 nm in the slit direction. IFD and distortion results are almost equivalent to the latest data of KrF apparatus, which exemplifies that technology for KrF has been successfully transferred to ArF apparatus.

According to the experiments, thermal aberration was correctable with conventional software controls, since the absolute value was very small Absorption of heat by optical materials appears as thermal expansion and refractive index change. Since these two are balanced with each other for CaF2 in the region of ArF, most of thermal aberration is considered to come from fused silica. The influence of heat absorption was minimized due largely to the progress of fused silica and coatings. The illumination intensity is expected to increase with the introduction of 2 kHz lasers, but the controllability of the thermal aberration will lead to future productivity enhancement.

The practical history of ArF laser exposure apparatus, however, has just started. It is necessary to make further technical challenges to ArF-inherent issues. Exposure tools are required to provide higher NA with improved quality. The progress of optical material and resist performance is necessary. At the final stage, the cost of ownership (CoO) will be a key issue. Since the main portions of CoO consist of lasers and tool costs, total system optimization is necessary.

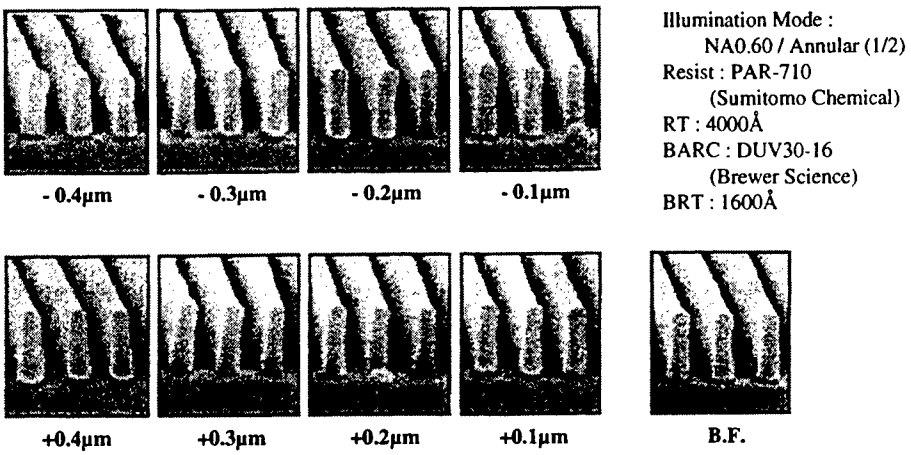


Fig.6 SEM of 120nm L&S (ArF NA 0.60, 1/2 Annular Illumination)

5. F2 laser microlithography

F2 laser has the wavelength which is on the law of 20% shrinkage of lithographic generation change. The resolution target is 100nm to 70nm technology node. F2 laser microlithography, however, is not the simple extension of the former system because there exist many new items to challenge, such as environmental control, optical material, resists, pellicles and so forth [12]. In addition to this, the allowable time for development is limited according to the acceleration of ITRS roadmap.

Environmental control is an specific issue of F2 laser microlithography, since strong absorption spectra exist at 157nm for oxygen, water and hydrocarbons. The projection optical system, cannot be used in the evacuated condition in order to homogenize the heat generated by the absorption of exposure light. Though 157nm belongs to VUV region, the exposure apparatus must be used in the gaseous conditions. Nitrogen or helium is an adequate gas for purging. The level of purging for oxygen and water must be controlled on the order of ppm. Hence, strong purging is necessary for the optical paths and the handling region of reticles and wafers.

In addition, chemical contamination is much severer at 157nm. Electrostatic discharge is also necessary because of the removal of humidity. These factors have the exposure apparatus designed in quite a different way from KrF and ArF age.

In VUV region, oxides cannot be used due to absorption, and the fluorides are the only candidates for both bulk and coating optical material. Narrow selection of material offers serious constraint to the optical design.

CaF2 is the only candidate for bulk material at present. It is very difficult to compensate chromatic aberration with a single material. In order to conquer this difficulty, several countermeasures are being developed, such as catadioptric system design, the search for second crystal (BaF2) and the ultra-line-narrowed laser. For a refractive system which uses only CaF2, its requirement for FWHM is 0.2pm. For a refractive system which uses both CaF2 and BaF2, the requirement is 0.5pm, and that for catadioptric system is 1pm. The development of BaF2 has just started, but the data is not sufficient at present. The decision of the projection optics will determine the whole specification and future possibility of the exposure apparatus, and there remain a little time for us to determine the final selection.

Technological situation of F2 laser microlithography has made great progress since 1999. F-doped fused silica and F2 laser are the two main topics.

As for the optical material, CaF2 development was on the extrapolation position of ArF situation. The transmittance of CaF2 has attained 99.5%/cm, which is almost equivalent to that of fused silica at 193nm. Though further improvement is necessary for efficiency and thermal aberration, the applicability of CaF2 is within our scope.

The appearance of F-doped dry fused silica solved the problem of mask substrate with low thermal expansion, and has activated the development of F2 laser microlithography. Wet fused silica in KrF and ArF cannot be used in 157nm because of the absorption of oxygen. Dry fused silica was used instead, and doping of fluorine has solved the transmission problem.

F2 laser was another topic. FWHM by simple line selection was first said to be 17pm [12], but now is recognized 0.6pm according to the resolution improvement of spectrometers[13]. Considering the influence to projection optics, this change of figures shows the importance of VUV metrology. These inventive steps will lead the development of F2 laser microlithography with accelerating speed.

The development of F2 laser microlithography has only a short history yet. The important peripheral technologies, such as resists and pellicles are still left unsolved. At 157nm, strong absorption constrains the selection of organic materials for resists and pellicles. Hard pellicles using F-doped fused silica are developed instead. As we experienced in KrF and ArF system development, strong collaboration is necessary to solve these technical issues.

6. Summary

Excimer laser microlithography has established its status, and is still growing. 250nm resolution was its introduction, and F2 exposure system is going to challenge 70nm technology node. The systematic combination between lasers, exposure tool, optical material and resists helped one another, and has formed a new technology region. Line narrowed lasers, CaF2 and chemically amplified resists are typical examples of systematic optimization. In addition, line narrowing capability can suppress the chromatic aberration, which makes it easy to introduce WFE to projection optics.

As excimer laser microlithography expands its status, its responsibility for future generation becomes severer. In microlithography, light source always comes first. Changing wavelength, however, needs much challenge and cost. The effective development will be required more intensively, searching the optimum system configuration for the future system.

References

[1] V.Pol, J.H.Bennewitz, G.C.Escher, M.Feldman, V.A.Firtion T.E.Jewell, B.E.Wilcomb and J.T.Clemens: Proc.SPIE 633 *Optical Microlithography V*, (1986) 6

[2] R.W.McCleary, P.J.Tompkins, M.D.Dunn, K.F.Walsh, J.F.Conway, R.P.Mueller: Proc. SPIE 922 *Optical/ Laser Microlithography* (1988) 396

[3] N.Sano, K.Takahashi, H.Nakano and A.Suzuki: Proc. SPIE *Optical Microlithography XIII* (2000) to be published

[4] A.Suzuki, K.Saitoh and M.Yoshii: Proc. SPIE 3679 *Optical Microlithography XII*(1999) 396

[5] M.Fritze, J.Buurns, P.Wyatt, P.Davis, D.Astrofi, A.Curtis, D.Preble, H-Y. Liu, J.Shaw, N.Sullivan, R.Brandom and M.Mastovich: Proc. SPIE *Optical Microlithography XIII* (2000) to be published

[6] C.Progler and D.Wheeler: Proc. SPIE 3334 *Optical Microlithography XI*(1998) 256

[7] M.Sasago, Y.Tani, M.Endo and N.Nomura: Proc. SPIE 1264 *Optical/Laser Microlithography* (1990) 466

[8] M.Rothschild, R.B.Goodman, M.A.Hartney, M.W.Horn, R.R.Kunz, J.H.Sedlacek and D.C.Shaver: J.VacSci Technol. B10(6) Nov/Dec (1992) 2989

[9] R.W.Morton, R.L.Sandstrom and G.M.Blumenstock: Proc. SPIE *Optical Microlithography XIII* (2000) to be published

[10] J.Mulkens, J.M.Stoeldraijer, G.Davis, M.Dierichs, B.Hemskamp, M.H.Moers, R.A.Geore, O.Roempp, H.Glatzel and C.Wagner: Proc. SPIE 3679 *Optical Microlithography XII* (1999) 506

[11] S.Mori: Proc. SPIE 3679 *Optical Microlithography XII* (1999) 522

[12] T.M.Bloomstein, M.W.Horn, M.Rothschild, R.R.Kunz, S.T.Palmacci and R.B.Goodman: J.Vac.Sci.Technol. B15(6) Nov/Dec (1997) 2112

[13] K.Vogler, S.Govorkov, G.Hua, F.Voss, E.Bergmann, U.Stamm and R.Paetzel: Proc. *The first International Symposium on 157nm Lithography* (2000) to be published

Local annealing of shape memory alloys using laser scanning and computer vision.

Moustapha HAFEZ*, Yves BELLOUARD**, Thomas SIDLER*, Reymond CLAVEL** and René-Paul SALATHE*

*Institut d'Optique Appliquée, Département de Microtechnique, Ecole Polytechnique Fédérale de Lausanne, BM, 1015 Lausanne, Switzerland
Email: moustapha.hafez@epfl.ch
Email: thomas.sidler@epfl.ch

**Institut des Systèmes Robotiques, Département de Microtechnique, Ecole Polytechnique Fédérale de Lausanne, BM, 1015 Lausanne, Switzerland

A complete set-up for local annealing of Shape Memory Alloys (SMA) is proposed. Such alloys, when plastically deformed at a given low temperature, have the ability to recover a previously memorised shape simply by heating up to a higher temperature. They find more and more applications in the fields of robotics and micro engineering. There is a tremendous advantage in using local annealing because this process can produce monolithic parts, which have different mechanical behavior at different location of the same body. Using this approach, it is possible to integrate all the functionality of a device within one piece of material.
The set-up is based on a 2W-laser diode emitting at 805nm and a scanner head. The laser beam is coupled into an optical fiber of 60µm in diameter. The fiber output is focused on the SMA work-piece using a relay lens system with a 1:1 magnification, resulting in a spot diameter of 60µm. An imaging system is used to control the position of the laser spot on the sample. In order to displace the spot on the surface a tip/tilt laser scanner is used. The scanner is positioned in a pre-objective configuration and allows a scan field size of more than 10 x 10 mm^2. A graphical user interface of the scan field allows the user to quickly set up marks and alter their placement and power density. This is achieved by computer controlling X and Y positions of the scanner as well as the laser diode power.
A SMA micro-gripper with a surface area less than 1mm^2 and an opening of the jaws of 200µm has been realised using this set-up. It is electrically actuated and a controlled force of 16mN can be applied to hold and release small objects such as graded index micro-lenses at a cycle time of typically 1s.

Keywords: Laser scanning, local annealing, tip/tilt scanner, monolithic structures, and micro-robotics.

1. Introduction

Monolithic shape memory alloy (SMA) micro-devices are highly interesting and efficient tools for manipulation and assembling of complex micro-systems as well as smart actuators or sensors in themself. Their basic idea is to integrate all functions of a device, like actuating part, flexible hinges, fixation parts, biasing elements etc. into the same piece of material, avoiding therefore reliability detrimental difficult high precision assembling and handling. As from the shape change point of view, the shape memory effect is not reversible, the main problem in developing monolithic devices is to be able to generate reversible motion [1, 2]. We propose a new solution to this problem, consisting in local annealing of material at selected places of the monolithic device. This means that only certain selected regions will exhibit a shape memory effect and the remaining non annealed material will have an elastic behaviour only and can be used e. g. as pull back springs to provide a reversible motion on cooling.
A high brightness diode laser with fiber beam delivery, in conjunction with a compact tip-tilt scanner present an efficient method for controlled local heating down to a volume of 10^{-3} mm^3 of thin sheet materials like SMA, even in complicated structures.

First International Symposium on Laser Precision Microfabrication, Isamu Miyamoto, Koji Sugioka, Thomas W. Sigmon, Editors, Proceedings of SPIE Vol. 4088 (2000) © 2000 SPIE · 0277-786X/00/$15.00

The proposed system consists of an optical scanning head with a 2W diode laser (λ = 805 nm) with fiber beam delivery (60µm core diameter step index fiber), a compact single mirror tip-tilt scanner, collimating and focussing lenses with unity magnification ratio and a CCD camera based computer image acquisition and scanner control system. The whole optical system is mounted on a small (300x500 mm) tabletop sized and easily transportable breadboard.

2 Optical set-up

The figure 1 shows the basic optical set-up of the system. A fiber pigtailed diode laser delivering up to 2 W of optical power out of a 60µm core diameter step index fiber is collimated by the lens L1 and conveyed via the dichroic mirror M1 (high reflectivity at 805 nm and 45 °) and the scanner mirror M2 to the focussing optics. The magnification ratio is given by the focal length of the collimating and focussing lens and can be adapted to a specific application. For the present purpose, a unity magnification ratio results in a round laser spot of approximately 60 µm diameter and intensity of the order of 17 kW/cm^2 on the workpiece.

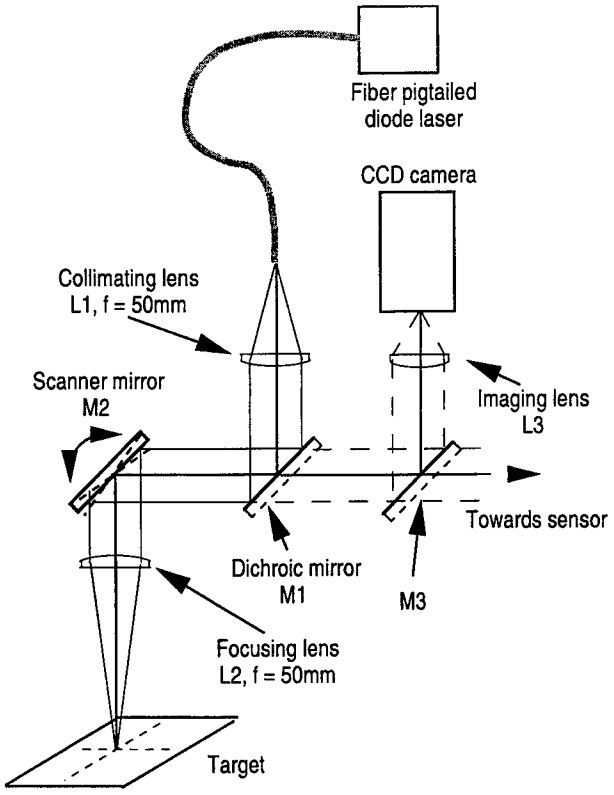


Figure 1 Optical set-up for the local annealing system.

A compact single mirror tip-tilt scanner is used for the displacement and precise positioning of the laser spot on the workpiece. This scanner has a mirror surface of 30x40 mm^2, a tilt range of ±3.5° (±60 mrad), with a repeatability of better than 50µrad, leading to a spot pointing precision of the order of 3µm (50 mm focal length focussing lens). The settling time for maximum deflection angle is less than 10 ms. The complete scanner (without electronics) fit in a volume of 30x40x50 mm^3 [3]. The scanner is in a pre-objective configuration. As the vision system sees the scene across the scanning mirror, it points already to the working point of the diode laser. Therefore, a high magnification ratio for the image can be foreseen, permitting an easy and precise aiming control. The computer vision system is coupled to the scanner control and permits to address with mouse control or, corresponding to computer controlled predefined patterns, any point in the target field of 6x6 mm^2. The scanner head could also be equipped with sensor channels for e. g. on line acquisition of a temperature signal with an IR detector (via an other dichroic mirror M3).

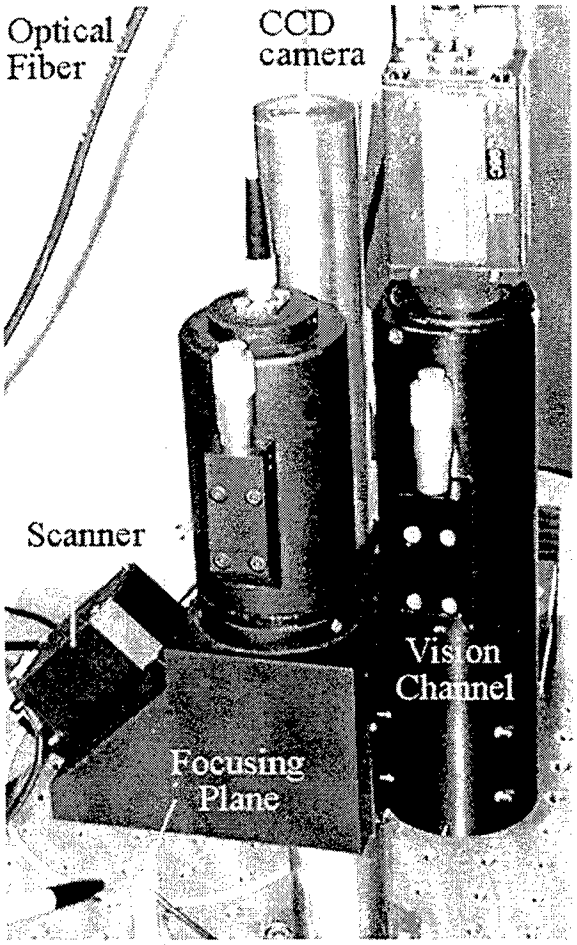


Figure 2 Photograph of the optical system

Figure 2 shows a photograph of the complete optical system. In the actual system a simple achromatic doublet lens is implemented as focussing lens, but for more critical applications, a new scan lens (based on a Cook triplet) has been developed, which guarantees a constant spatial resolution all over the entire scan field, without the severe drawbacks of very strong chromatic aberrations of usual F-Θ lenses which exclude practically a correct image acquisition.

3 Computer vision system

A computer vision system based on a CCD camera and a PC is used for precise control of the position and scan of the laser spot on the workpiece [4]. The image of the sample is seen via the scanner mirror with adequate enlargement and is therefore always centred on the pointing direction of the scanner. A visible diode laser light pen for visualising the pointing direction can be foreseen, but as the CCD camera is also sensitive to the diode laser wavelength, even the laser spot itself at low power can be used for high precision aiming means. The enlargement factor for the vision system is given essentially by the focal length of the imaging lens L3 (see figure 1) and can be adapted to the specific need. Any point of the scan field of 6x6 mm^2 can be addressed either directly by mouse control (e. g. for teach-in of specific patterns) or by more advanced computer control. Arbitrary scan patterns can be introduced by teach-in or by CNC control via the PC. A single mirror tip-tilt scanner in a 90° beam deviation configuration presents systematic image deformations resulting from the scan principle itself, but also from the scan lens aberrations. These systematic image distortions do not alter the scanner precision and repeatability and can be exactly measured experimentally and introduced into a correction matrix for automatic correction during CNC controlled scanning, e. g. when predetermined geometrical patterns must be followed.

4 Local laser annealing of a micro-gripper

Local annealing was applied to a complex mechanical structure, consisting of the micro-gripper shown in figure 3. The key idea is to select and anneal the place where a shape memory or superelasticity is desired and to let the remaining parts non-annealed. With this method different mechanical states as well as active and passive parts can be introduced within a single piece of material. This method can be applied on SMA films, cold rolled sheets, cold drawn wires or other materials which have been work-hardened. The annealing process then reduces the amount of internal stress. The mechanical behaviour of a cold-rolled sheet before and after annealing in a furnace is shown in figure 3.

In order to obtain a reversible motion of the micro-gripper, the following process has been applied: The gripper is cut out of a non-annealed work-hardened SMA-sheet by a pulsed Nd-YAG fundamental mode Slab laser (minimal kerf width ≈ 20μm). The as cut gripper is placed in the local annealing system and local annealing of the shaded area of the figure 3 is performed by irradiating with the diode laser (laser power approx. 1.5 W) the concerned areas. The heating time is of one second and the maximum monitored temperature on the actuating part was about 550° whereas the bias spring only heated up to about 100°C. At room temperature, the gripper arm is then deformed out of its elastic domain in order to define the open position. By controlled heating of the whole structure (e. g. with a Peltier element) to a temperature of about 60°C, the gripper closes now, due to the recovery force generated by the phase transformation in the annealed part. During cooling, (to approx. 10°C), when the actuating part has returned to the martensite state, the elastic bias spring can pull the arm back in its open position.

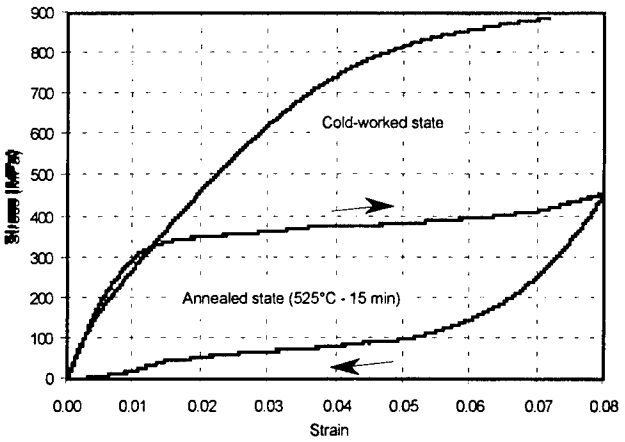


Figure 3Stress-strain behaviour of a cold rolled sheet before and after annealing (in a furnace).

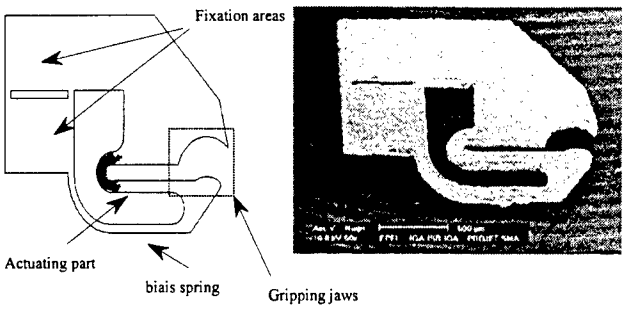
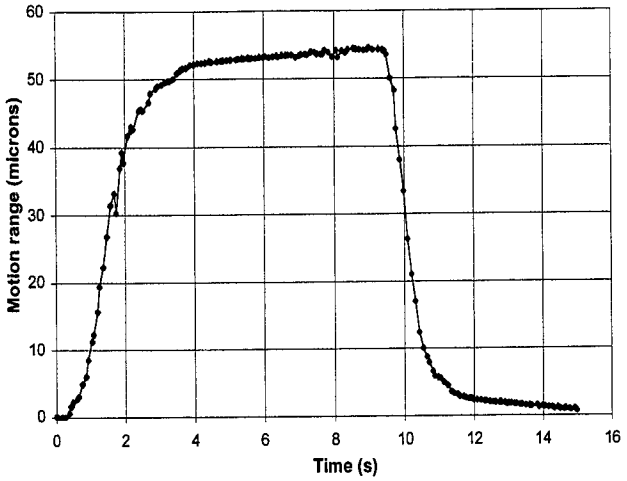


Figure 4 SMA micro-gripper, design and realisation (the black area represents the locally annealed region). Overal dimensions: 1.4 x 1.8 mm.

The figure 5 shows the diagram of a complete cycle of the movement of the gripper. The main advantages of the local laser annealing are the freedom to choose the parts to be annealed (with a spatial resolution of less than 100μm), no particular design restrictions, contactless technology (no delicate handling problems) and suitability for MEMS technology and MEMS fabrication environment (clean



room, vacuum chamber, etc.).

Figure 5 Diagram of a complete temperature cycle of the micro-gripper, hot temperature is about 60°C, cold temperature about 10°C. The total mechanical amplitude is 55 μm.

5 Conclusions

A table-top local laser annealing system has been presented, based on a fiber pigtailed high power diode laser (Pmax = 2W), an optical head comprising a compact tip-tilt scanner and a computer image acquisition and scanner control system, permitting the local annealing of monolithic SMA devices with a spatial resolution of less than 100 μm. The application of the system to the realisation of a micro-gripper used for micro-robotic handling of small graded index lenses has beem shown.

References

[1] Y. Bellouard, R. Clavel, R. Gotthardt, T. Sidler, J.-E Bidaux, "A new concept of Monolithic Shape Memory Alloy Micro-Devices used in Micro-Robotics", Actuators 1998, Bremen, Germany, June 17 -19, 1998, pp. 499-502.

[2] Y. Bellouard, T. Lehnert, T. Sidler, R. Gotthardt, R. Clavel, "Monolithic Shape Memory Alloy Actuators: A New Concept for Developing Smart Micro-Devices", Material Research Society (MRS), Fall Meeting Conference Symposium on Smart Materials, Vol. 604, Boston, 1999, to be published.

[3] Hafez M., Sidler, T., Salathé R.P., Jansen G., and Compter J.C. "Design, simulations and experimental investigations of a compact single mirror tip/tilt laser scanner" Mechatronics (accepted on the 17th of September 1999).

[4] Y. Bellouard, A. Sulzmann, J. Jacot, R. Clavel, "Design and highly accurate 3D displacement characterization of monolithic SMA micro-gripper using computer vision", SPIE, Microrobotics and Microsystems Fabrication, 16-17 Oct. 1997, vol. 3202, pp. 2-11.

Virtual Engineering helps to get laser adjustment industrially accepted

Burkhard MÜLLER

Chair of manufacturing technology, University of Erlangen-Nuremberg, Egerlandstr. 11, 91058 Erlangen, Germany
E-mail: B.Mueller@lft.uni-erlangen.de

Laser adjustment allows a new process chain for fast, cost-efficient and highly precise assembly. It can be done without the usually very elaborate exact positioning of the jointing parts since after joining the components are adjusted into the desired position by laser forming. In order to make this new process chain possible an actuator can be joined between the bearer and the relevant functional element. This actuator enables the functional element to be moved into the desired position by conversion of laser energy. After the adjustment it remains in the assembly.
For simple adjustment tasks an intuitively controlled design process can lead to solutions to an actuator design. As far as more complex tasks are concerned, like e.g. adjusting the 7 relevant degrees of freedom of all optics in electro-optical transducers, new design principles are necessary.
After elucidating the process principle this paper presents the demands imposed on such actuators. Founded on the basic actuators, the integral approach to the actuator design is presented with its complete mathematical description being the basis of the computer-aided procession of all actuator-specific data. Thus it becomes possible to solve the inverse problem of the requirements made on geometry.

Keywords: Laser forming, Micro forming, Modelling, Simulation, Laser adjustment

1 Introduction

Laser adjustment is a further development of laser forming. It uses the specific characteristics of laser forming as a contact-free, non-resilient and easily automatizable method to cause little deformations. The laser forming process is based on an inhomogeneous temperature field, which is created by laser radiation. The thus obstructed thermal expansion leads to a plastic deformation. Detailed descriptions of the mechanisms and of possible fields of application are given in [1].

The interaction between laser parameters, material parameters and geometry can lead to different temperature fields. In figure 1 the 4 essential mechanisms are presented, namely the internal stress-point mechanism, the temperature-gradient mechanism (TGM), the buckling mechanism and the upsetting mechanism. A decisive distinguishing feature is the difference in temperature between top side and underside of the sheet metal. If this difference is significant, one of the two first-mentioned mechanisms occurs. If the difference in temperature is only little, either the buckling or the upsetting mechanism is predominant.

Both the temperature-gradient mechanism and the upsetting mechanism are very suitable as adjustment processes since a reliable process control is possible. The other two mechanisms are applied in the field of rapid prototyping but it is more difficult to control them in a closed loop for adjustment purposes.

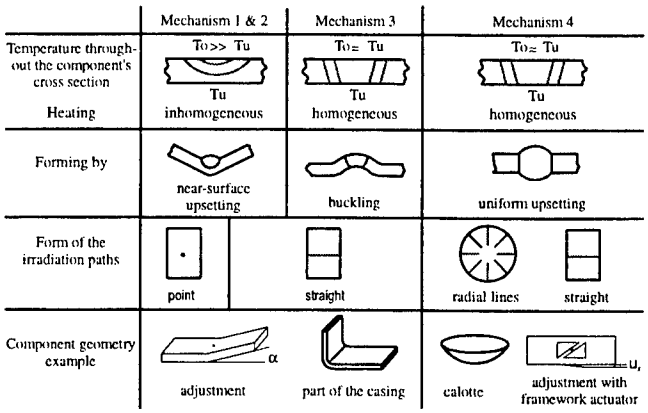


Fig. 1 Laser forming mechanisms

Some exemplary solutions are presented in [2,3]. With all these applications the adjustment has to be carried out in a closed loop.

For laser adjustment special irradiation positions are required. A fast closed loop and thus an effective application of this technology is only possible by means of specially

First International Symposium on Laser Precision Microfabrication, Isamu Miyamoto, Koji Sugioka, Thomas W. Sigmon, Editors, Proceedings of SPIE Vol. 4088 (2000) © 2000 SPIE · 0277-786X/00/$15.00

fitted actuators. At present they are designed in an iterative process on the basis of fundamental actuator geometries [4]. However, for complex tasks with both several directions and degrees of freedom which are independent of each other it is not possible to meet the required short production cycles without effective computer assistance. In order to be able to use the possibilities of CAD also for the design of actuators, functions are needed which enable a direct implementation into the world of CAD.

2. Requirements on actuators

Irrespective of the fact whether the actuator is a component specially suited to laser forming or a conventional bearer, it has to fulfil some basic requirements. They can be divided into economic and technical requirements. The economic requirements are basically determined by the use of low-cost materials and semifinished products but also by actuator geometries, which due to a fast adjustment process reduce production time and thus production costs.

The thermal inertia determines significantly the production time. The inhomogeneous temperature field leads to an uneven thermal expansion and displacements, which obstruct the measurement of the actual value in the closed loop. The thermal inertia can be influenced by material, geometry and process. Materials with higher thermal conductivity directly reduce the thermal inertia. The actuator's geometry determines the distances which are relevant for the temperature balance. That way, adjustment on the basis of the out-of-plane effects is considerably faster than that based on in-plane shortening since in the out-of-plane case the temperature gradient is balanced out substantially faster than in the in-plane case. Influence can also be exerted by means of process changes. Thus the heat transport into the surroundings can be improved considerably by means of an active cooling by gases or liquids. However, a homogeneous temperature field is only hard to achieve that way.

The technical requirements on the actuators are determined by the number of the necessary degrees of freedom, the maximum and minimum adjustment area and the accessibility of the forming sections for the laser beam.

An additional requirement, which is already well-known from the conventional manufacturing chain, is the thermal and mechanical stability of the components. A reversible or irreversible maladjustment of functional elements in the components' whole field of application must not occur. Also the mechanical stability under load with vibration and acceleration forces, which is required due to normal strain, must not obstruct the system's function.

3. Drafts of complex actuator systems

For the draft of actuator systems an exact description of the basic actuators is necessary. A basic actuator is defined as the minimum unit, which by means of laser irradiation leads to a controlled displacement or bend.

3.1 Basic actuators

Figure 3 shows the four basic types: the bridge and angle actuator with possible displacement in positive x-direction, the double-bridge and angle actuator with bead, which allow a displacement both in positive and negative x-direction.

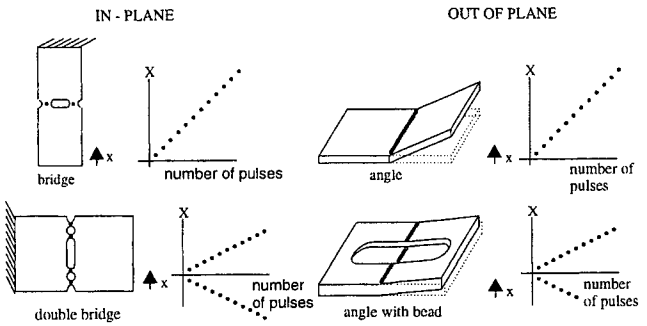


Fig. 3 Basic actuators

3.2 Description by means of kinematic chains

The links between the individual basic types, the adjustment object and the frame are represented in the bar model. The basic actuators can – depending on the effect they use – be regarded either as joints in the out-of-plane case or as guide for the in-plane case. Thus it becomes possible to describe the whole actuator by means of a bar model as a multi-body system with n partial bodies. The coordinate system describes the inertial position coordinates of a single partial body.

On suitable examination the actuators can be regarded as an open chain or as a tree structure. For the recursive description of the actuator's orientation the process of Denavit-Hartenberg [5,6] can be applied, which is well-known from robot kinematic. With this method, a base B_i is assigned to each bar. The relative position of base B_i to base B_{i-1} is described by the Euler angles Ψ and υ and the line segments u_i and v_i. Angle ψ_i is the angle between the 1-axis of base B_{i-1} and the 1-axis of base B_i with the 3-axis of base B_{i-1} serving as rotational axis for determining the angle. Angle υ_i results from a rotation of base B_{i-1} around the new 1-axis of base B_{i-1} until the 3-axes of the bases i-1 and i coincide. The segment lines u_i and v_i are perpendicular to each other. The length of the linking straight line of the generally curved joint axes i-1 and i is designated as v_i. The

distance between the intersection of this linking straight line and base B_{i-1} is u_i.

Each angle in the actuator, be it a forming edge, which was produced by the manufacturing process of the actuator or presents a position of the laser beam in the out-of-plane basic form, can be described by a rotational matrix T_i.

With rigid forming edges the angles ψ and υ are fixed, when applying the out-of-plane basic form the angles have to be described by $\psi + C_i \cdot n_i$ respectively by $\upsilon + C_i \cdot n_i$. C_i is the transfer coefficient, which depends on the process parameters and the detail geometry, and can be taken from a knowledge basis. Variable n_i serves to describe the number of laser pulses at the spot i.

$$T_{i-1,i} := \begin{bmatrix} \cos\psi_i & -\sin\psi_i & 0 \\ \sin\psi_i & \cos\psi_i & 0 \\ 0 & 0 & 1 \end{bmatrix} \cdot \begin{bmatrix} 1 & 0 & 0 \\ 0 & \cos\vartheta_i & -\sin\vartheta_i \\ 0 & \sin\vartheta_i & \cos\vartheta_i \end{bmatrix}$$

Rigid bars, which connect only two active elements, are described by the translational vector t_i whereas with active bars it has to be distinguished between two assembling positions. If the active axis coincides with the rotational axis i-1, u_i has to be replaced by $u_i - C_i \cdot n_i$; if this is not the case, v_i has to be expressed by $v_i - C_i \cdot n_i$.

$$t_{i-1,i} := \begin{bmatrix} v_i \cos\psi_i \\ v_i \sin\psi_i \\ u_i \end{bmatrix}$$

The rotational matrices T_i and the translational vector t_i are combined in the matrix D_i. Considering the formulae presented in [5] the total matrix for the actuator can be drawn up.

$$D_{i-1,i} := \begin{bmatrix} T_{i-1,i} & t_{i-1,i} \\ 0 & 1 \end{bmatrix} \qquad D := D_{0,1} \cdot \ldots \cdot D_{n-1,n} := \begin{bmatrix} T & t \\ 0 & 1 \end{bmatrix}$$

Vector t describes the coordinates of the actuator's end point. This end point coincides with the intersection point of actuator and adjustment object.

$$t := \sum_{k=1}^{n} \left[\prod_{i=0}^{k-1} T_{i-1,i} \right] t_{k-1,k} \qquad T := \prod_{i=1}^{n} T_{i-1,i}$$

The 3x3 partial matrix T of the total matrix D describes the rotation of base i in relation to base 0 and thus the rotation of the intersection point of actuator and adjustment object.

By way of illustration figure 4 shows an actuator with three bars, an active angle and a rigid angle. At base B_0 the actuator is connected with the surroundings. At base B_3, e.g. a mirror can be fixed. Rotational axis 2, where the laser forming is carried out, is essential for the actuator's movement behaviour. All the other rotational axes and bars provide the ambient structure in order to fulfil the constructive constraint. Points P_1, P_2 and P_3 are to lie on a straight line with P_3 representing the connection to the surroundings and thus coinciding with B_0. The other constraints concern the adjustment area, which has to cover the range from -0.75° to +0.75° in relation to α and β. As minimum step size and thus final precision 0.1° is required.

If nothing else is stated, in the following the numerical values given in the table are assumed:

Variable	i = 1	i = 2	i = 3	i = 4
ψ_i	$\frac{1}{2}\pi - \arctan(\frac{4}{5})$	$\arctan(\frac{4}{5})$	$n_3 \cdot C_3$	$n_4 \cdot C_4$
υ_i	0	$^1/_2\pi$	0	0
u_i	0	0.5	0	0
v_i	$\sqrt{5^2+4^2}$	0.5	2.5	0

By laser forming at rotational axis 2 angle ψ is changed by a value which is dependent on process parameters and detail geometry but independent of kinematic. Due to the process presented above the resulting displacement of base B_3 can be inferred directly from the matrix D. The rotation of base B_3 is possible by use a rotational axis 3; besides angle α also angle β can be influenced by laser irradiation at this axis, figure 4.

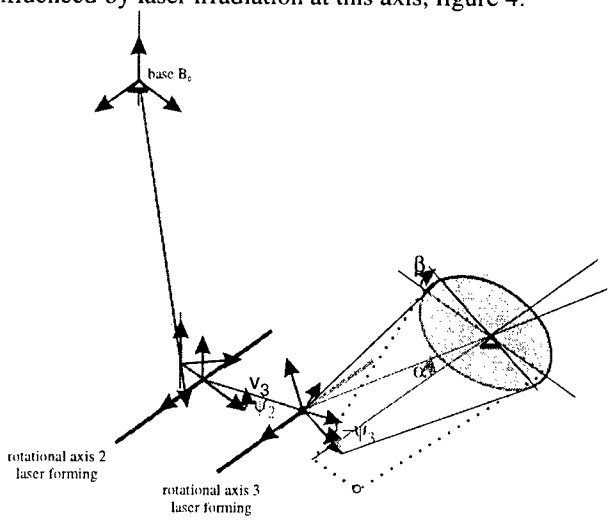


Fig. 4 Kinematic chain for an actuator

3.3 Discussion of the movement behaviour of a simple actuator

Let's have a closer look at the actuator shown in figure 4 to elucidate the possibilities of this method. With irradiation at position 1, i.e. at rotational axis 2 in positive ψ-direction, the following Denavit-Hartenberg matrix results from it.

$$D = \begin{bmatrix} 0 & 0 & 1 & 4 \\ \cos(n_1 C_1) & -\sin(n_1 C_1) & 0 & 2.5\cos(n_1 C_1) + 5.5 \\ \sin(n_1 C_1) & \cos(n_1 C_1) & 0 & 2.5\sin(n_1 C_1) \\ 0 & 0 & 0 & 1 \end{bmatrix}$$

Parameter n_i indicates the number of laser pulses at the corresponding position, constant C_1 is the transfer constant

for the basic type used here. From the geometrical relationships of the intersection point of actuator and adjustment object in relation to the fixation of the adjustment object in the space the angles α and β can be determined directly from the matrix.

$$\alpha = \arctan(0.625 \sin(n_1 C_1 - n_2 C_2))$$

$$\beta = \sin(n_1 C_1 - n_2 C_2)\cos(n_3 C_3 - n_4 C_4) + \cos(n_1 C_1 - n_2 C_2)\sin(n_3 C_3 - n_4 C_4)$$

Hereby the following assignment has to be taken into consideration for all permissible irradiation positions 1 to 4

Position 1; index 1 ⇒ rotational axis 2; positive ψ_2

Position 2; index 2 ⇒ rotational axis 2; negative ψ_2

Position 3; index 3 ⇒ rotational axis 3; positive ψ_3

Position 4; index 4 ⇒ rotational axis 3; negative ψ_3

The angles α and β, which result from the laser forming, set the required two-dimensional result space. By linear combination of the actuator's four reactions resulting from the different irradiation position a point field has to be set, which meets the requirements of minimum point distance <= 0.1° and size of target space >= 0.75°. Figure 5 illustrates the size of that space depending on the parameter bar length v_3, see fig. 4. It can be seen that with a bar length of v_3 = 5 mm an almost linear behaviour can be achieved with all four irradiation positions with simultaneous equivalence of the size of space in α and β. Reducing the length v_3 to just 2.5 mm improves linearity but also has the effect that the size of space in α-direction does not meet the requirements any more. In the fictitious case here with the bar length v_3 = 10 mm the minimum step size, which can be achieved by laser adjustment with a pulse in α-direction, is above the tolerance range.

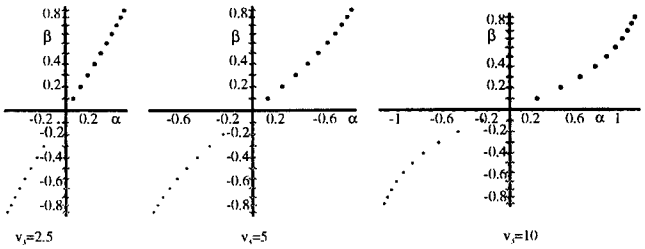


Fig. 5 Transfer behaviour of the actuator illustrated in fig. 5

Due to the initialized representation of the actuator's geometry it is possible to determine its behaviour, i.e. amount of degrees of freedom, position of the irradiation points, size of the adjustment space and minimum step size.

4. Conclusion and outlook

The method described here to model actuators as kinematic ones with the Denavit-Hartenberg matrices description enables an integration in a CAD-system. For the complete description of the exemplarily presented actuator the 16 parameters illustrated in table 1 are sufficient. By systematically varying these parameters the total of all actuators can be represented by three bars and two active angles. However, due to the parameterization this method is not in the least restricted to the presented simple actuators but e.g. also actuator systems for the seven degrees of freedom of all optics can be designed independently in a computer-aided design process. Since the kinematic chain contains information about all relevant constraints, like amount of degrees of freedom, adjustment area and possible precision, the result space can not only be set completely but also a computer-aided selection of optimum solutions is possible.

For generating completely new actuator geometries future works will deal with the implementation of the solution presented here in a commercial CAD-system. Founded on the problem raised by the designer the system independently suggests solutions. For generating these solutions optimization algorithms are used. On the basis of a knowledge acquisition and classification of available actuator types a data basis is created, which serves as a component catalogue both for the optimization of the kinematic chain and for the detailed interpretation.

5. References

[1] Vollertsen, F.: Mechanisms in Laser Forming. In: Geiger, M.; Vollertsen, M. (editors): Laser Assisted Net shape Engineering I, Bamberg: Meisenbach (1994). 345 - 360

[2] Verhoeven, E. C. M.; de Bie, H.F.P.; Hoving, W.: Laser Adjustment of Reed Switches: Micron Accuracy in Mass Production. In: Geiger, M.: Otto, A. (Hrsg.); Laser in der Elektronikproduktion & Feinwerktechnik, LEF'99. Bamberg: Meisenbach (1999) 169 - 179

[3] Vollertsen, F.; Geiger, M.: Laserstrahljustieren mechatronischer Komponenten. In: Jüptner, W. (Hrsg.): Laser – Von der Wissenschaft zur Anwendung. Strahltechnik Bd. 10. BIAS Verlag, Bremen 1997, 309 - 320

[4] Geiger, M.; Huber, A.; Müller, B.; Basic Actuator Geometries for the Laser Adjustment Process. In: McKeown, P.; Brinksmeier, E. (editors); 1st international conference and general meeting of the European society for precision engineering and nanotechnology. Bremen: BIAS (1999) 526 - 529

[5] Pfeiffer, F.; Reithmeier, E.: Roboterdynamik, Eine Einführung in die Grundlagen und technische Anwendungen. Stuttgart: Teubner 1987

[6] Denavit, J.; Hartenberg, R.S.: A Kinetic Notation for Lower-Pair Mechanisms Bases on Matrices, ASME J. Appl. Mech., 215 - 221, 1955

High-resolution contact lithography by excimer lasers*

Huang Huijie, Lu Dunwu, Du Longlong, Zhao Yongkai, Yuan Cailai, Jiang Baocai, Wang Runwen

Shanghai Institute of Optics and Fine Mechanics, Chinese Academy of Sciences
PO Box 800-216, Shanghai 201800, China
Email: ldwsiofm@mail.shcnc.ac.cn

High-resolution contact lithography was conducted by both 248-nm KrF and 193-nm ArF excimer lasers on PMMA resist. The resist thickness is about 0.5 μm. Resolution of 0.5-μm lines and spaces was obtained on PMMA resist after KrF excimer laser exposure and subsequent wet development. No self-developing photoetching was observed. However, with ArF excimer laser as the exposure light source, resolution of 0.3-μm lines and spaces was obtained on the same resist by direct photoetching under high exposure dose, as well as under lower exposure dose combined with subsequent conventional wet developing process.

Keywords: high-resolution lithography, contact lithography, excimer laser, 248-nm lithography, 193-nm lithography, self-developing

1. Introduction

DUV excimer laser lithography has been becoming the mainstream technology in high-density integrated circuit fabrication. The promising laser sources are 248-nm KrF, 193-nm ArF, and even 157-nm F_2 excimer lasers [1].

Contact lithography is a simple and expedient way to investigate the imaging characteristics of new light source as well as photoresist. In addition, this technique is most economical for low-volume device manufacturing, such as productions of holographic gratings.

In this paper, we report here our high-resolution contact lithography experiments with KrF and ArF excimer lasers. 0.5-μm lithographic resolution was obtained by KrF excimer laser, and 0.3-μm lithographic resolution by ArF excimer laser. The photoresist used in our experiments is PMMA.

2. Experimental setup

Fig.1 shows the schematic illustration of experimental setup. The KrF excimer laser used in this setup is developed by ourselves [2], and the ArF excimer laser is a Lambda Physik Model LPX110i. Table 1 gives the parameters of the two excimer lasers. A 2.6^X 1-dimensional Galilean telescope is added following the laser as a beam expander to form uniform illumination. A square homogeneous beam cross section is obtained through a square aperture. In order to obtain good results, the wafer coated with PMMA resist is held in close contact with a chromium quartz mask.

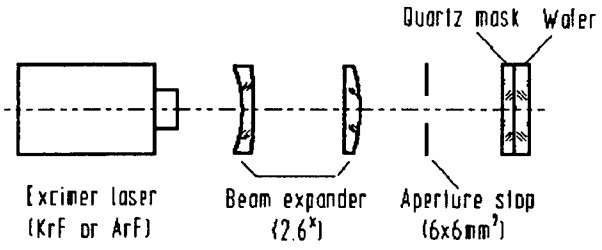


Fig.1 Experimental setup for contact lithography

Table 1 Primary parameters of excimer lasers

Excimer laser	Wavelength	Pulse duration (FWHM)
KrF	248.3 nm	22 ns
ArF	193 nm	17 ns

* This work is supported by the National Natural Science Foundation of China (NSFC), Grant No. 69878029.

First International Symposium on Laser Precision Microfabrication, Isamu Miyamoto, Koji Sugioka, Thomas W. Sigmon, Editors, Proceedings of SPIE Vol. 4088 (2000) © 2000 SPIE · 0277-786X/00/$15.00

3. Experimental details and results

Our experiments were carried out on PMMA resist. PMMA is chosen as the photoresist, since it is one of the most excellent resists for its fine line resolving power and has been used as the resist for electron beam, x-ray, and DUV light source [3,4]. The resist in our experiments is Model XHR-EP-3 DUV sensitive PMMA developed by Wuxi Chemical Engineering Design and Research Institute in China. After spin-coated on the wafer surface, the PMMA film is prebaked for 30 minutes at 165°C. The thickness of PMMA film is about 0.5 μm. The developer is the solution of methyle isobutyl keton (MIBK) and isopropyl alcohol (IPA) in the ratio of 2:1. The developing time and the temperature are 1 minute and 10°C respectively.

At first, lithography using KrF excimer laser was conducted. Resolution of 0.5-μm lines and spaces was patterned on the wafer surface after KrF excimer laser exposure and subsequent wet development, as shown in Fig.2. The exposure dose is about 5 J/cm^2. No self-developing photoetching was observed even if the exposure dose was increased to about 12 J/cm^2. The KrF excimer laser operated at a repetition rate of 1 Hz, and the single pulse energy is about 10 mJ within a 6×6-mm^2 area. The power density on the mask surface is about 1.3 MW/cm^2.



Fig. 2 Photograph of 0.5-μm resolution patterns obtained by KrF excimer laser contact lithography

Secondly, contact lithography by 193-nm ArF excimer laser was carried out. Resolution of 0.3-μm lines and spaces was obtained on the same resist by direct photoetching under high exposure dose, as well as under lower exposure dose combined with subsequent conventional wet developing process. The ArF operated at 1-Hz repetition rate, and the single pulse energy is about 25 mJ within the 6×6-mm^2 area. This gives a peak power density of about 4.1 MW/cm^2. The exposure dose is 3.5 J/cm^2 for self-developing lithography and 300 mJ/cm^2 for wet development lithography, respectively.

We measured the patterned PMMA resist layer using a Digital Instruments Model Dimension 3100 atomic force microscope (AFM). Fig. 3a shows the directly photoetched patterns, and Fig. 3b the patterns with wet development lithography. Some build up can be observed in Fig. 3a. For practical use, the debris must be purged away by some proper methods before subsequent processes. Fig. 3c is the 3-dimensional profile of 0.3-μm lines and spaces of Fig. 3b.

4. Discussions and conclusions

High-resolution contact lithography was demonstrated. PMMA resist used in our experiments is suitable for sub- and sub-half-micron lithography in DUV spectral region.

High-resolution direct contact lithography is more easily achieved with ArF excimer laser than that with KrF excimer laser, because 193-nm wavelength light has higher photon energy and higher absorption coefficient than 248-nm KrF excimer laser[5]. If some sensitized chemical reagent had been added to PMMA, the direct photoetching would have happened with KrF excimer laser.

Another factor, that direct photoetching did not happen in our experiment, is probably that the power density of the KrF excimer laser is less than that of ArF excimer laser.

References

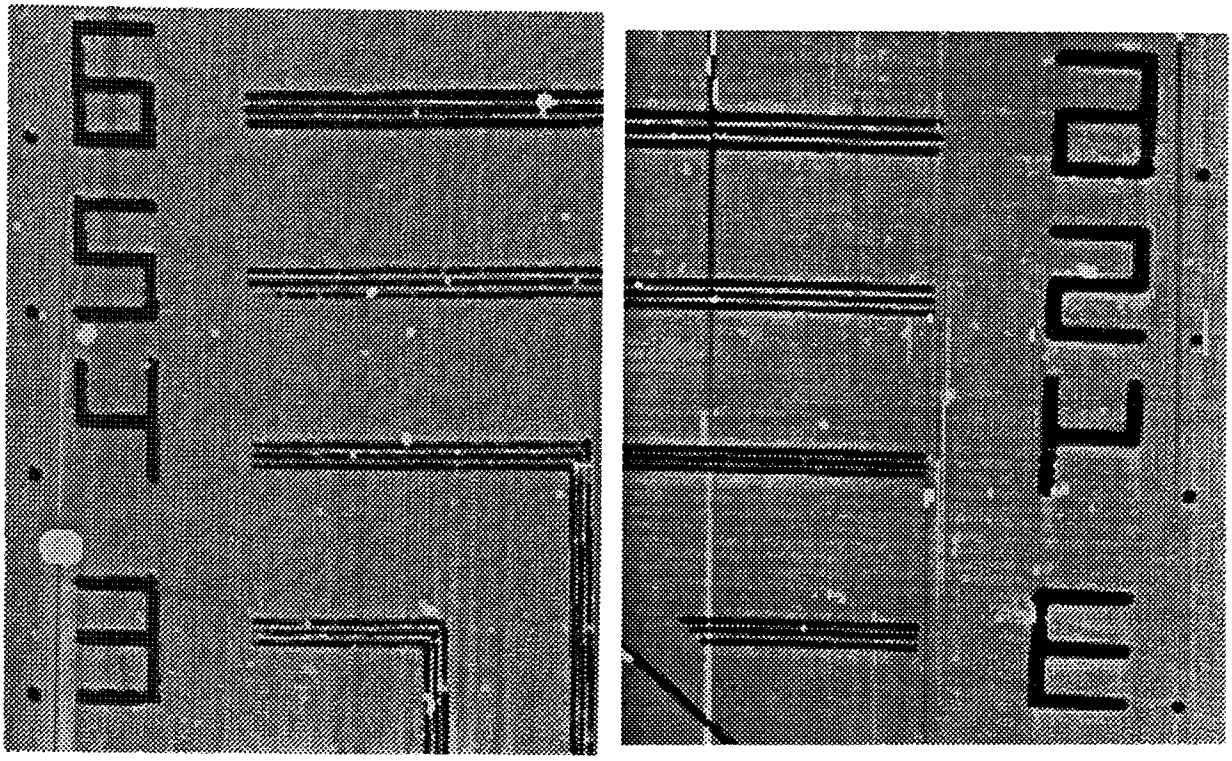
[1] Pieter "Pete" Burggraaf, "Optical lithography to 2000 and beyond", *Solid State Technology*, **42(2)**, pp.31-41, 1999.

[2] Dunwu Lu, Huijie Huang, Yu Yan, Longlong Du, Ruichang Gao, "Halfmicron excimer laser lithography using a 1:1 broadband catadioptric lens with a half circle field", *Proc. SPIE*, **3051**, pp.972-976, 1997.

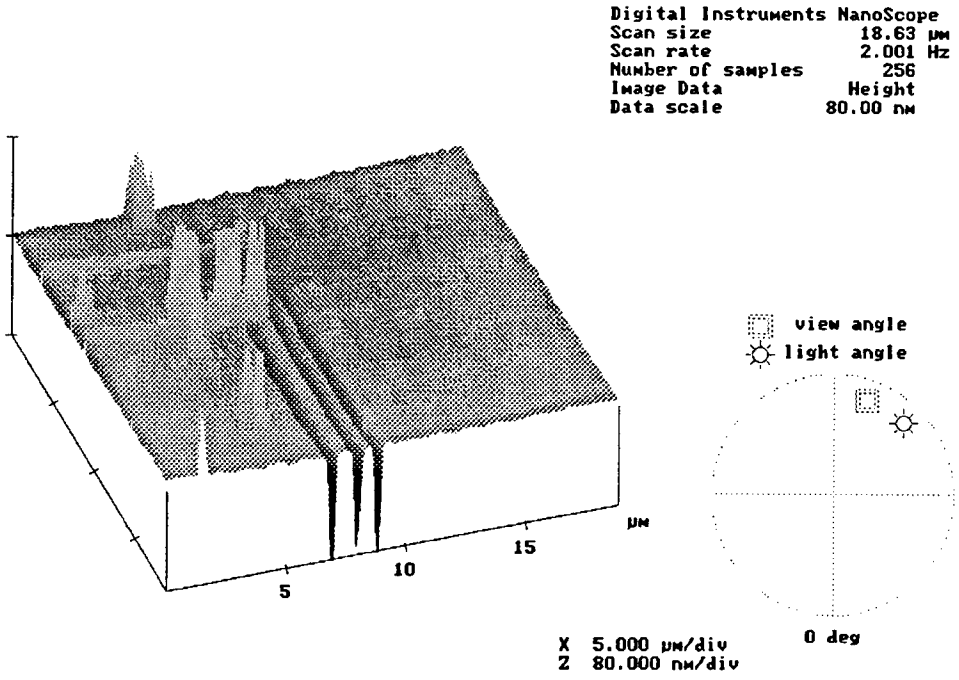
[3] S. Rice and K. Jain, "Direct high-resolution excimer laser photoetching", *Appl. Phys.*, **A33**, pp.195-198, 1984.

[4] Y. Kawamura, K. Toyoda, and S. Namba, "Deep UV submicron lithography by using a pulsed high-power excimer laser", *J. Appl. Phys.*, **53(9)**, pp.6489-6490, 1982.

[5] Y. S. Liu, H. S. Cole, H. R. Philipp, and R. Guida, "Photoetching of polymers with excimer lasers", *Proc. SPIE*, **774**, pp.133-137, 1987.



(a) (b)



(c)

Fig. 3 AFM images of 0.3-µm resolution patterns obtained by ArF excimer laser contact lithography, where (a) directly photoetched patterns, (b) patterns from conventional lithography, and (c) 3-D profile of 0.3-µm lines and spaces of (b).

Inorganic-organic hybrid material for lithography

Lin PANG, Yingbai YAN, Guofan JIN, Minxian WU

State Key Laboratory of Precision Measurement Technology and Instruments, Department of Precision Instruments, Tsinghua University, Beijing, 100084, P.R.China
E-mail:pangl@ntl.pim.tsinghua.edu.cn

Tetraethoxyorthosilicate and methacryloxypropyl trimethoxy silane are used to form inorganic and organic networks, respectively. Photosensitive agent is added to initiate free-radical cross-linking polymerization of unsaturated carbon bonds and thus makes the material act as a negative tone photoresist. Developed in dilute base solution, microoptical element, such as lenses and gratings, were fabricated by contact copy with UV-exposure. Shrinkage effect is investigated after optical elements obtained. Compared with the mask, the spacing of the exposed areas in sol-gel film shrinks, and the shrinkage rate is about 20%.

Key words: photosensitive, microoptical element, solgel, inorganic-organic

1. Introduction

In fabricating microoptical elements, generally, a photoresist layer must be used to transfer the pattern of photomask into the substrate. The properties of photoresist and its adherence to the substrate would influence the quality of the transferred pattern. Moreover, the processing needs complex instruments to transfer the pattern, such as reactive ion etching etc., which not only increase the capital cost but also lead to the enhance of the error. To simplify technology, inorganic-organic composite recording material via sol-gel route was proposed to fabricate mocrooptical elements. Photoresist is not needed to act as transition layer, which would avoid distortion in the transfer of pattern in the fabrication of elements.

The hybrid sol-gel method has been widely used in the fabrication of microstructural optical components for various applications. Because of its low optical loss, simple processing, and the properties of tailored at the molecular lever for a particular application, the method has attracted attention of those material scientists and photonics device engineers who seek to take advantage of the appealing optical properties.[1,2,3] In the processing, photo-induced polymerization was employed in the branch of the chain in the hybrid sol-gel material, the shrinkage cause by the polymerization must affect the fidelity of the pattern during the transfer of the mask. The exposure causes the enhancement of molecular weigh in exposed areas and the molecular shift between the exposed areas and unexposed ones, which result in the real-time relief. This effect would exert impact on the deepening of the relief and expanse of the transition region during the development. The study about the shrinkage of the spacing is significant to fabricate optical element with accuracy feature.

In the paper we report our present experimental results and the shrinkage of spacing in fabricating optical element in the hybrid sol-gel glass. The process of composing the hybrid sol-gel material was presented in section 2. In section 3, the fabrication of elements in solgel material was

First International Symposium on Laser Precision Microfabrication, Isamu Miyamoto, Koji Sugioka, Thomas W. Sigmon, Editors, Proceedings of SPIE Vol. 4088 (2000) © 2000 SPIE · 0277-786X/00/$15.00

given, followed by the investigation of the shrinkage of the spacing in section 4. Finally, the mechanism of those effects was discussed.

2. Preparation of inorganic-organic hybrid material

A silicon oxide matrix was synthesized by hydrolysis and polycondensation actions. The silicon oxide network was formed from tetraethoxyorthosilicate (TEOS) and 3-methacryloxypropyl trimethoxy silane (MAPTMS) with a molar ratio of 10:1, which were dissolved in adequate volume of alcohol, and then hydrolyzed by 0.1M hydrochloric acid solutions.

The addition of MMA can both intensify the network and adjust the property of material. The quantity of MMA would directly influence the transmittance of the hybrid material in the UV wavelength range.

After the solution was prepared, it was aged at room temperature for one week. The prepared composite was made photosensitive by a photoinitiator. The photoinitiator forms free radicals during UV exposure, which leads to free-radical cross-linking polymerization of unsaturated bonds and thus makes the material act as a negative tone photoresist. The photoinitiator, benzoin, was added to the hybrid sol-gel material solution in a molar ratio of 1:100. Films derived from sol were dip-coated on borosilicate glass substrate. Because organically modified silicate glasses tolerate stress relaxation more effectively than do glasses derived from traditional silica sources, like tetraethoxyorthosilicate, film could be deposited in one step in thickness ranging from 2 to 15μm. Film thickness varies linearly with dip-coating speed in some speed range.[4] After precision dip-coating, film were immediately heated (prebaked) in air at 100°C for 2 min to remove the solvent and improve the adhesion of the sol-gel material to the substrate.

The films were illuminated by a 100W mercury UV lamp with a diffuser, placed at 20 cm for some time through a contact mask. After exposure the films were developed with base solution and investigated by an interference microscope.

3. Fabrication of optical elements in hybrid material

The contact mask, which was used in UV exposure, contained array of lenses. The films with thickness of 0.4μm were exposed to UV light for 30min. After exposed the films were developed in a dilute solution of NaOH in water for ~1min, In Fig.1, the central part and rim in one unit of the array of lenses were shown respectively. The shift of interference fringes was ~1.7, and the relief depth was ~0.4μm, which is the thickness of the film.

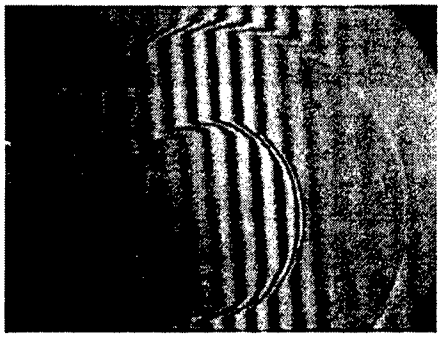


Fig.1.(a)

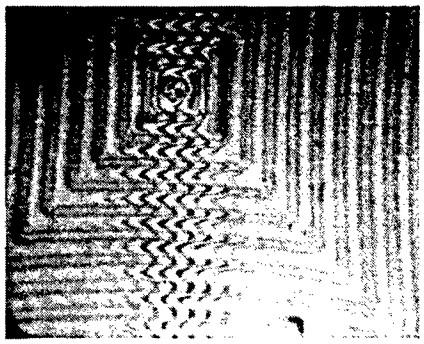


Fig.1.(b)

Fig.(1). (a). Interferogram of the central part in one unit of the array of lenses. (b). Interferogram of the rim of the array.

To investigate the quality of the transfer of the mask, binary mask with dark width of 21μm and transparent width of 8μm was used to UV light. The process of fabrication is the same above. Fig.2 shows the experimental results. From

Fig.2 (a), it can be seen that there is sidewall adjacent to the ridge of the relief, which can be seen more manifest in the Fig.2 (b). From the shift of interference fringes of ~ 6, and the relief depth was ~ 1.6μm.

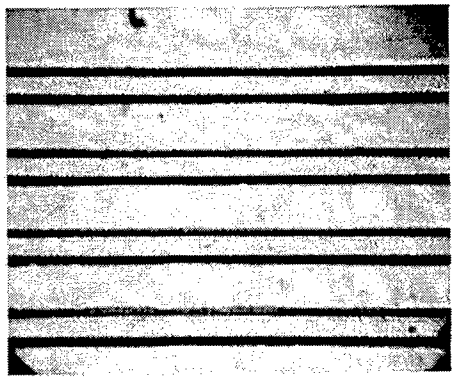


Fig.2. (a)

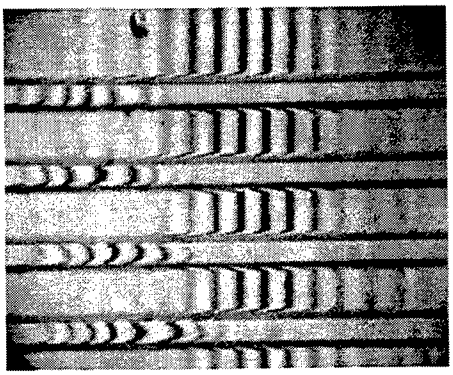


Fig.2.(b)

Fig.2. (a) Microphotograph of a binary grating with 29-μm spacing. (b) Interferogram of the binary grating.

4. Shrinkage of the spacing

From the microphotograph (Fig.2), it can be seen that the sidewall of the relief is not so vertical as expected, but trapeziform in the cross-section. The above width of the trapeziform is regarded as the width of the relief. The slope side of the trapeziform is known as transition region, which corresponds to the quality of the elements. In the experiments, the films with thickness of 2.0μm and binary mask were used to investigate the shrinkage. Experimental data are shown in Table 1.

Table 1 Relation between shrinkage percentage and exposure time

Exposure Time (min)	22	31	60	120
Shrinking Percentage (%)	22.0	31.3	25.6	8.8

The shrinking percentage was obtained as the ratio of the width of difference between the width of exposed areas and that of the above side of real-time relief, and exposed width. There was some errors arising from distinguish of the boundary between the above side and the transition region. Table 1 shows that the shrinkage is independent on he exposure dose. The shrinkage can be formed during the initial exposure.

5. Discussion

Compared to other negative optical material, such as DCG, the inorganic-organic sol-gel material is of very strong shrinkage effect. The reason for this is the incompact structure in sol-gel material besides its free radical polymerization, which is of more shrinkage than the cross-linking in DCG during exposure. The degree of polymerization in the sol-gel material is low, which causes the molecules to move easily, and irregular accumulated molecules cause a large lap between the molecules. To decrease the shrinkage effect, some measures should be taken in the composition of the materials, by increasing the degree of linear polymerization and filling the lap between the molecules.

In this paper, new sensitive hybrid solgel material is

composed. With the material and contact copy, some preliminary experiments and application with this process have been reported. Of course, a more extensive and more systematic studies of the process should be undertaken.

Acknowledge

Authors acknowledge supports a grand from China Postdoctoral Science Foundation as well as a grant for fundamental research from school of machine and engineering of Tsinghua University.

References

1. J.T.Rantala, P.Ayras, R.Levy, S.Honkanen, M.R.Descour, N.Peyhambarian, "Binary-phase zone-plate arrays based on hybrid solgel glass", Opt.Lett. 23, (1998),1939-1941.
2. S.I.Najafi, T.Touam, R.Sara, M.P.Andrews, M.A.Fardad, "Sol-gel glass waveguide and grating on silicon", J.Lightwav Tech. 16, (1998),1640-1646.
3. P.Muller, B.Braune, C.Becker, H.Krug, H.Schmidt, "Fabrication of monolithic refrative optical lenes with organic-inorganic nona-composites: Relations between composition and mechanical and optical properties", SPIE, 3136, (1997),462-469.
4. Lin Pang, Hui Wei, Bo Chen, Lurong Guo," Fabrication of sol-gel optical element with dichromated gelatin as photoresist", SPIE,Vol.3557, (1998),5-7.

The Etching Characteristics of the PDP Barrier Rib Pastes by Focused Ar^+ laser and Nd:YAG laser

Min-young Ahn, Kyoung-cheol Lee, Hong-gyu Lee, Cheon Lee

Department of Electrical Engineering, Inha University, 253 YongHyun-dong, Nam-ku, Inchon 402 - 751, KOREA
E-mail : chnlee@inha.ac.kr

The paste dried and hardened on glass substrate for fabrication of the PDP(Plasma Display Panel) barrier rib was selectively etched using focused Ar^+ laser(λ=514 nm)and Nd:YAG laser(λ=266, 532 nm) beam. A barrier rib was composed of mixtures which were made from organic gel, glass powder and ceramic powder. Using a second harmonic Nd:YAG laser (λ=532 nm), the threshold laser fluence was about 6.5 mJ/cm^2 for the barrier rib samples softened at 120 °C. The thickness of 180 μm of the sample was completely removed without any damages on the glass substrate by laser fluence of 19.5 J/cm^2. In order to increase the etch rate of the barrier rib materials, samples were heated on a hot plate during the laser irradiation. The etch rate at the hot plate temperature of 200 °C was roughly 4.2 times faster than that of room temperature.

Keywords : PDP barrier rib paste, Ar^+ laser, Nd:YAG laser, heating effect, etch rate

1. Introduction

The interest in PDP (Plasma Display Panel) has been extended since it is an attractive method for fabricating large area HDTV(40 to 60 inch diagonal screen). The display construction consists of anode and cathode electrodes which are formed on the front and rear pieces of glass, and barrier ribs are utilized to form the individual pixels and prevent discharge in adjacent cells(cross talking)[1]. Several methods of the barrier rib formation have been developed as screen-printing, sand blasting, mechanical pressing, lift-off, etc. These methods have some problems including difficulties of large area alignment, low productivity, expensive cost and so on. Recent work has shown the potential to be applied laser to PDP devices, as ITO(indium tin oxide) used in transparent electrodes of PDP and PR(photoresist) used in etching process are patterned by laser writing system[2-4]. Thus, an attempt was made to develop a barrier rib manufacturing process using the laser patterning system in this study. In advance, we carried out investigations those were necessary to increase a throughput.

2. experiment

PDP barrier rib materials were patterned using CW(Continuous Wave) type Ar^+ laser which of wavelength is 514 nm, and pulse type(repetition rate of 10 Hz) Q-switched Nd:YAG laser which of fundamental wavelength is 1064 nm. SEM(Scanning Electron Microscope) was used in observation of etched depth, width, and cross-sectional profile of barrier rib materials by laser patterning.

2.1 experimental equipment

In this study, PDP barrier rib materials were patterned by using Ar^+ laser(514 nm, CW) and Nd:YAG laser which can generate the fundamental wavelength at 1064 nm or its harmonics(532, 266 nm). These harmonics were achieved by specific modules easily plugged onto the optical head of laser. Ar^+ laser beam was focused using a 20 × microscope objective lens. Second harmonic(λ=532 nm) and fourth harmonic(λ=266 nm) beams of Nd:YAG laser were focused using lenses with focal length of 200 mm which were made of BK7 and fused silica, respectively. Figure 1 shows the schematic diagram of PDP barrier rib fabrication system using Nd:YAG laser. Samples were fixed on a xyz-motorized stage controlled by personal computer. Then samples were irradiated with focused Nd:YAG laser or Ar^+ laser beam. To increase the etch rate of the sample we heated the substrate with a resistive heater. And in order to increase the throughput we generated multi-beams with a metal mask between the sample and the focusing lens. The metal mask was manufactured by wire cutting which was a simple and

First International Symposium on Laser Precision Microfabrication, Isamu Miyamoto, Koji Sugioka, Thomas W. Sigmon, Editors, Proceedings of SPIE Vol. 4088 (2000) © 2000 SPIE · 0277-786X/00/$15.00

cheep method of a metal patterning. A line and a space of the metal mask were 90 μm and 270 μm, respectively.

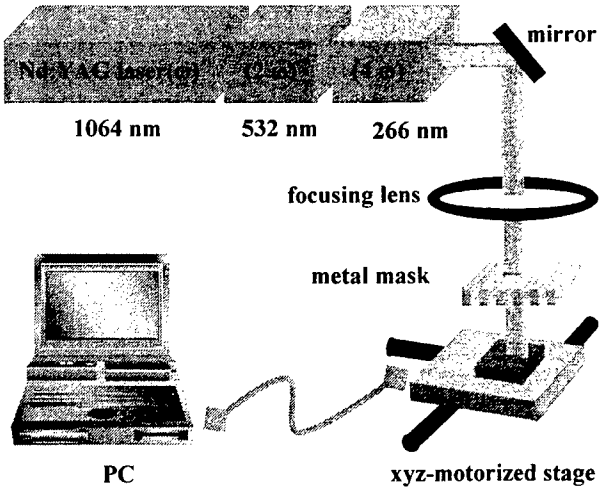


Fig. 1. The schematic diagram of a PDP barrier rib fabrication system by Nd:YAG laser

2.2 samples

Product percentages of the PDP barrier rib paste used for samples in this study are shown in table 1. We made two type samples of 180 μm thickness. Which of one is only dried below 120 °C and the other is hardened below 565 °C. Each sample was made by 13 times screen printing with the paste.

Table 1. Product percentages of the PDP barrier rib paste for samples in this study

	Product percentage
Lead Compounds	50 %
Aluminum Oxide	27 %
Chrome Compounds	5 %
ETC	18 %

3. Results and discussion

3.1 Etching of PDP barrier rib materials using Nd:YAG laser

When second harmonic(532 nm) of Nd:YAG Laser was used, the etching threshold fluence for the PDP material was 6.5 mJ/㎠ and the printed paste(thickness of 180 μm) on the glass substrate was removed clearly at a laser fluence of 19.5 J/㎠. The etch rate of dried sample is higher than that of hardened sample as illustrated Fig. 2. The etch rate increases with increase of the laser fluence. But when fourth harmonic(266 nm) of Nd:YAG laser was used, the etch rate of sample was very low at any laser fluence. It was considered that absorption rate of the sample by Nd:YAG laser at wavelength of 532 nm was higher than that of 266 nm.

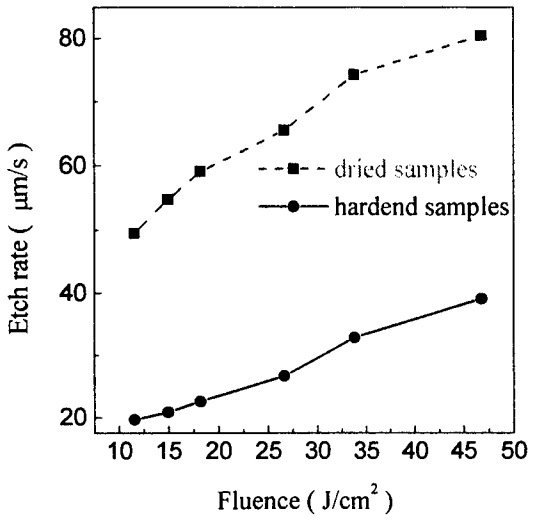
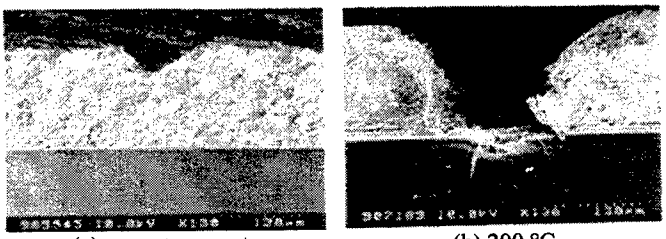


Fig. 2. The etch rate of PDP barrier rib materials according to laser fluence and properties of the sample using Nd:YAG laser(532 nm, beam scan speed of 200 μm /s).

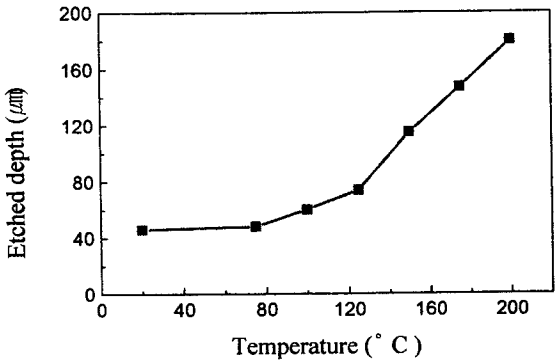
3. 2 Increase in etch rate of the PDP barrier rib material by heating effect

It is necessary to rise etch rate of the PDP barrier rib material in order to increase the throughput of the fabrication process. So we set a resistive heater on the xyz-motorized stage shown in figure 1, and irradiated Nd:YAG laser(532 nm) on the sample. As a result, etch rate of sample increase clearly above heating temperature of 100 °C with Nd:YAG laser(532 nm) fluence of 97.5 J/cm², beam scan speed of 200 μm/s. Figure 3 shows the etched depth according to rising heat temperature. Figure 3(a) is a cross sectional SEM image showing the etched depth at room-temperature. Figure 3(b) is a cross sectional SEM image showing the etched depth at 200 °C . And etched depth as a function of heating temperature is plotted in figure 3(c). PDP barrier rib paste consists of solid powder, organic and inorganic gel. In typical firing process of PDP barrier rib paste, the first step from 110 °C to 130 °C removes the organic gel, the second step from 320 °C to 340 °C does the inorganic gel. The third step of 565 °C

corresponds with the softening point of glass and adhere between solid powder in the paste and the substrate[5]. In case of using samples dried below 120 °C, organic gel still remained in the paste. This remainder was removed by substrate heating. Vacant sites and distortions in the paste were formed. As these results, the printed layer had many defects and then, became to be fragile. This imperfection of the structure compared to the sample without heat treatment allowed the effective etching by the subsequent laser beam irradiation[2].



(a) room-temperature (b) 200 °C



(c)

Fig. 3 Cross-sectional SEM images showing the etched depth as a function of heating temperature at (a) room-temperature and (b) 200 °C (Nd:YAG laser at 532 nm, fluence of 97.5 mJ/cm^2, scan speed of 200 μm/s). (c) The etched depth as a function of heating temperature.

3.3 Etching of PDP barrier rib materials using Ar^+ laser

Figure 4 is a cross-sectional SEM image of PDP barrier rib sample etched by Ar^+ laser(514 nm). PDP barrier rib paste printed on the glass substrate was etched clearly without any damage of substrate at Ar^+ laser power density of 32 MW/cm^2 and scan speed of 200 μm/s. When Ar^+ laser power density is insufficient, the paste can not be evaporated and pilled up around the laser beam where the laser intensity is low. Assist gas jets at a side of focusing position could be answer about the sediment problem[6-7].

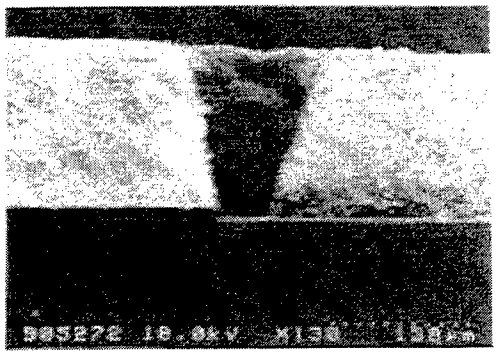


Fig. 4 A cross-sectional SEM image of PDP barrier rib sample etched by Ar+ laser (laser power density = 32 MW/cm^2, beam scan speed of 200 μm/s)

3.4 Formation of PDP barrier rib using multi-beam of Nd:YAG laser

In order to increase the throughput we set a metal mask between the sample and focusing lens as illustrated in figure 1 and generate multi-beam of Nd:YAG laser(532 nm). There are 32 % loss of laser fluence with the mask. Figure 5 is the SEM image that shows a cross-sectional profile of PDP barrier rib etched by multi-beam of Nd:YAG laser using a metal mask. With laser fluence of 2.86 J/cm^2 and beam scan speed of 200 μm/s, PDP barrier ribs of 10 lines are formed with one laser beam scan using the metal mask

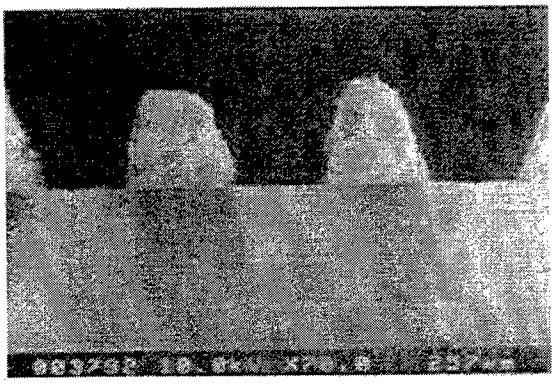


Fig. 5 A cross-sectional SEM image of PDP barrier rib sample etched by multi-beam of Nd:YAG laser using metal mask (laser fluence of 2.86 J/cm^2, beam scan speed of 200 μm/s)

4. Conclusion

This paper presented a method of PDP barrier rib fabrication using focused Ar^+ laser and Nd:YAG laser. In case of using Nd:YAG laser(532 nm), the etching

threshold fluence for the PDP barrier rib material was 6.5 mJ/cm^2 and the printed paste(thickness of 180 μm) on the glass substrate was removed clearly with laser fluence of 19.5 J/ cm^2. In order to increase the etch rate, samples were heated on the resistive heater. As a result, The etch rates were 65 μm/s and 270 μm/s at room temperature and 200 °C, respectively. To raise the throughput we generated multi-beams of Nd:YAG laser using a metal mask between the sample and focusing lens. In this way, 10 lines of PDP barrier rib were formed by one laser beam scan with laser fluence of 2.86 J/cm^2, beam scan speed of 200 μm/s.

5. Reference

[1] H. Fujii, et al, "A sandblasting process for fabrication of color PDP phosphor screens", SID Digest 1992, pp 728-731

[2] K.C. Lee, M.Y. Ahn, C. Lee, SPIE Meeting, vol. 3898, pp. 208-215, december 1999.

[3] O. Yavas, M. Takai, Journal of Applied Physics, vol. 85, no. 8, pp. 4207-4212, April 1999.

[4] O. Yavas, M. Takai, Applied Physics Letters, vol. 73, no. 18, pp. 1558-2560, November 1998

[5] T. K. Williams, A. S. Shaikh, "Thick film materials system for plasma displays", Asia Display 1995, pp.553-556

[6] Farooq K, Kar A, Journal of Applied Physics, vol. 83, no. 12, pp. 7467-7474, June 1998

[7] W O'Neill, W M Steen, Journal of Physics D-Applied Physics , vol. 28, no.1, pp. 12-18, January 1995.

Thermomechanical mechanisms of laser cleaning

Vadim P. VEIKO, Elena A. SHAKHNO, Sergey V. NIKOLAEV

Laser Applications Engineering and Applied Ecology Department,
St.Petersburg Federal Institute of Fine Mechanics (Technical University)
14 Sablinskaya str., 197101, St.Petersburg, Russia
E–mail: veiko@lastech.ifmo.ru
Phone/Fax: +7.812.2333406

Keywords: substrate, particle, absorption, thermal enlargement, heat transfer

The physical mechanisms of dry and steam laser cleaning of the surface are investigated theoretically.

At dry laser cleaning particles are removed from the surface due to inertial force that caused by particles and/or substrate thermal expansion by light absorption and thermal conduction. The condition of complete particle removal, when it does not return to the substrate, is defined. The considered physical mechanism of dry laser cleaning is propagated to multipulse regime.

The physical mechanisms of steam laser cleaning are proposed to be caused by liquid layer vaporization near the particle surface due to substrate and/or particle light absorption and non–uniform action of vapor pressure to the particles. The evaluated thresholds of dry and steam laser cleaning are in a good agreement with known experimental data.

1. Introduction

The problems of laser cleaning of solid surface attract attention of many investigators now (for instance [1, 2]). Laser cleaning is used for removal of particles of different sizes and materials and films of soiling substances from solid surfaces. There are dry and steam laser cleaning methods, they are based on pulse laser heating of solid surafce, dry and in presence of liquid layer on it, correspondingly. The laser cleaning methods are free from shortcomings, which are peculiar to other methods, such as technological complication, necessity of washing and drying, shortcomings of oecological features. In the cases, when dry laser cleaning turns out to be not enough effective, steam laser cleaning is used.

The physical mechanism of dry laser cleaning of the substrate surface is supposed to be connected with fast thermal enlargement of particles and/or substrate by nanosecond laser pulses action. Thermal enlargement creates the cleaning force overcoming the adhesion force, binding the particles and the substrate surface [1].

Our investigations of before–evaporation regimes of the laser induced front transfer (LIFT) [3] let use the physical models of solid film tearing–off from the donor substrate for description the dry laser cleaning process.

The physical mechanism of steam laser cleaning of the surface is supposed to be connected with liquid layer heating by heat transfer from the substrate and with liquid vaporization by volume [1]. We tried to concretize the physical picture of this process, pointing out influence of particle absorption the process, and defining unevenness of vapor pressure distribution at the particle surface as the cause of the cleaning force appearance.

2. Dry laser cleaning

2.1. The cleaning force

By laser action, the substrate and/or particles being at it absorb radiation. Substrate or particles heating can be caused (depending on their optical properties) as by direct light absorption, as by heat transfer from the absorbing substrate to the particles or from the absorbing particles to the substrate (Fig.1). It should be noted that in the last case heating of the substrate zone under the particle is not effective because of radial thermal diffusion. If the particles are transparent or semi–transparent, the substrate absorption depends on different optical effects in particles: multi–reflection, size depended effects etc.

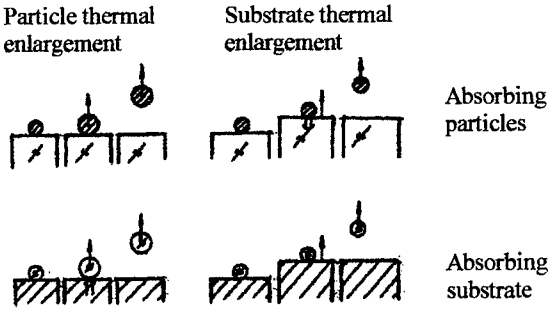


Fig.1. Illustration of the physical mechanisms of dry laser cleaning.

By particle and/or substrate heating the particle mass center displacement $\delta = \delta_s + \delta_p$ takes place:

$$\delta_{s(p)} = \int_0^{h_{s(p)}} \alpha_{s(p)} T_{s(p)} dy_{s(p)} \qquad (1)$$

First International Symposium on Laser Precision Microfabrication, Isamu Miyamoto, Koji Sugioka, Thomas W. Sigmon, Editors, Proceedings of SPIE Vol. 4088 (2000) © 2000 SPIE · 0277-786X/00/$15.00

δ_S and δ_p are partial displacements caused by substrate (s) and particle (p) enlargement correspondingly, α_S, α_p, h_S, h_p, T_S, T_p are linear coefficient of thermal enlargement, thickness and temperature increasing from the initial value of the substrate (s) and particle (p) correspondingly. Coordinate axes y_S and y_p are directed from the substrate (s) and particle (p) surfaces into them normally to the substrate surface. The coefficient k defines the connection between thermal enlargement of the whole particle and its mass center displacement and changes from 0 to 1. Thermally small particles ($h_p \le \sqrt{a_p \tau}$, a_p is particle thermal diffusivity, τ is pulse duration), i.e. up to micron size metal particles or lesser dielectric particles, are heated almost uniformly by their thickness and $k \approx 0.5$. By thermally large absorbing particles, thermal energy concentrates in their upper part and mass center displacement almost is absent, i.e. $k \approx 0$. By thermally large transparent particles heated from the substrate, thermal energy concentrates in their lower part and $k \approx 1$.

Acceleration of the particle mass center bound with its thermal displacement causes the intertial force $F_0 = md^2\delta/dt^2$, m is the particle mass. Value of this force can be obtain by comparison of equations (1) with energy balance equations:

$$A_{S(p)} q dt = \int_0^{h_{S(p)}} \rho_{S(p)} c_{S(p)} dT_{S(p)} dy_{S(p)} \qquad (2)$$

q is incident radiation power per surface area unit, A_S, A_p, ρ_S, ρ_p, c_S, c_p are effective absorption coefficient, density and heat capacity of the substrate (s) and particle (p) corerspondingly. Effective absorption coefficient of some object is defined here as ratio of power received by the object due to radiation absorption and also due to thermal transfer, to power of the incident radiation at it.

Obtained value of inertial force is:

$$F_0 = m \frac{dq}{dt} \left(\frac{\alpha_S A_S}{\rho_S c_S} + k \frac{\alpha_p A_p}{\rho_p c_p} \right) \qquad (3)$$

During the pulse front edge, $dq/dt > 0$ and the force F_0 ($F_0 > 0$) presses the particle to the substrate surface. During the back edge, $dq/dt < 0$ and the force $|F_0|$ ($F_0 < 0$) acts as a cleaning force, tearing–off the particle from the substrate surface. Particle tearing–off occurs, if cleaning force exceeds the adhesion force F_a.

2.2. Surface cleaning condition

The cleaning force disappears after pulse finishing, but the adhesion force remains. The teared–off particle will not return to the substrate, if its kinetic energy after finishing its and substrate's enlargement exceeds the work of particle moving to infinity against adhesion force:

$$\frac{m u_*^2}{2} > \int_{z_*}^{\infty} F_a dz \qquad (4)$$

z is the distance between the particle lower surface and the substrate surface, u is particle mass center velocity, z_* and u_* are z and u values in the moment of the particle and surface enlargement finishing.

Let us consider the peculiar cases of dry cleaning.

2.2.1. Absorbing particles and/or absorbing substrate enlargement

Particle moving from the substrate starts at the moment of pulse back edge beginning t = 0. The equation of its movement is:

$$m \frac{d^2 x}{dt^2} = -F_a(z) \qquad (5)$$

x is the distance between the particle mass center and the initial placement of the substrate surface. The correlation between coordinates x and z is:

$$\frac{dx}{dt} = \frac{dz}{dt} + \frac{d\delta}{dt} \qquad (6)$$

The initial conditions: $z = z_0$, $dz/dt = 0$ by $t = 0$. The initial distance between the particle and substrate z_0 is defined in [1] as atomic separation.

Deciding approximately the equation (5) together with cleaning condiiton (4), we obtain the value of the cleaning force $|F_0|$, which is necessary for complete particle removal. For enough large values of $F_a(z_0)/m$ (particle size is $d << 10\ \mu$) it is:

$$|F_0| > \frac{3}{2} F_a(z_0) + \frac{2}{3} \frac{z_0}{n-1} \frac{m}{\tau_1^2} \qquad (7)$$

τ_1 is pulse back edge duration.

The number n depends on the kind of adhesion force: $F_a \sim 1/z^n$. For Van der Waals forces n = 2–3 [1].

Correspondingly, the cleaning condition for laser intensity ε is:

$$\varepsilon > \frac{3}{8} \frac{F_a(z_0)}{m} \frac{b\tau^2}{\frac{\alpha_S A_S}{\rho_S c_S} + k \frac{\alpha_p A_p}{\rho_p c_p}} + \varepsilon_{th} \qquad (8)$$

$b = \frac{2\tau_1}{\tau}$ is a coefficient defining the temporal shape of the pulse, ε_{th} is a threshold intensity:

$$\varepsilon_{th} = \frac{2}{3} \frac{\frac{z_0}{(n-1)b}}{\frac{\alpha_S A_S}{\rho_S c_S} + k \frac{\alpha_p A_p}{\rho_p c_p}} \qquad (9)$$

2.2.2. Transparent particles enlargement

If the particles are transparent and the substrate is absorbing one, but the thermal enlargement coefficient of

the particle is much more than the same of the substrate ($\alpha_p >> \alpha_S$), the cleaning force is caused by particle enlargement due to its heating from the substrate. By this, substrate enlargement is almost absent. Particle enlargement, in this case, is stopped by pulse back edge beginning (t = 0) due to thermal contact interruption by particle separation from the substrate. Therefore the values u_* and z_* in the cleaning condition (4) are defined in the moment t = 0. Calculated intensity value, which is necessary for complete cleaning is:

$$\varepsilon > \frac{\rho_p c_p}{k\alpha_p A_p}\tau\sqrt{\frac{z_0}{2(n-1)}\frac{F_a(z_0)}{m}} \qquad (10)$$

2.3. Dry laser cleaning in the multipulse regime

In spite of developed idea about the nature of the adhesion force, its concrete value is difficult to define due to indefinites of particle shape, its real contact area with substrate and other factors. Therefore we shall use the experimentally defined value of the adhesion force per unit area of the particles section: $P = \rho_p dF_a/m$.

The P value depends on materials properties, particles shape and a number of other factors, and is about ~ 10^6 N/m^2. Analysing the above given cleaning conditions (8, 10), one can show, that the calculated values of P, by which cleaning takes place, are much less than the real values. In practice, the multipulse regime is used, the number of pulses is about $N \approx 100$ [1]. The physical mechanism of the process seems to be following. The partial particle tearing–off, i.e. decreasing of its contact area with the substrate, occurs by each pulse. By this, adhesion force decreases each time by some value ΔF_a. The partial relaxation occurs between the pulses. So, adhesion force decreases by value $(1-\beta)N\Delta F_a$ after the N–th pulse ($\beta < 1$ is relaxation coefficient, it supposedly increases by laser repetition rate f decreasing, particle size d increasing and depends on materials of the substrate and particles and particles shape). If $(1-\beta)N\Delta F_a = F_a$, the particle is removed from the substrate after the N–th pulse. From (8) and (10) one can obtain values of P and d by which cleaning takes place:

– by thermal enlargement of adsorbing particles and/or adsorbing substrate:

$$\frac{P}{d} < \frac{8}{3}(1-\beta)N\rho_p\left(\frac{\alpha_S A_S}{\rho_S c_S} + k\frac{\alpha_p A_p}{\rho_p c_p}\right)(\varepsilon - \varepsilon_{th}) \qquad (11)$$

ε_{th} is threshold intensity (13);

– by thermal enlargement of transparent particles:

$$\frac{P}{d} < 2(1-\beta)N\rho_p\left(\frac{\varepsilon}{\tau}k\frac{\alpha_p A_p}{\rho_p c_p}\right)^2\frac{n-1}{z_0} \qquad (12)$$

Table 1. Calculated and experimentally measured [1] values of threshold intensity for dry laser cleaning of quartz substrate from Cu and Al particles for different wavelengths λ (n = 2, b = 1 assumed).

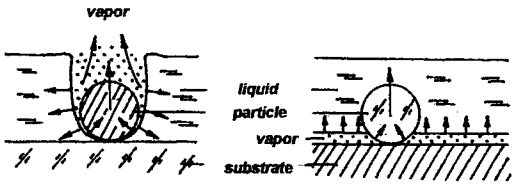
		ε_{th}, mJ/cm^2		
		λ = 286 nm	λ = 532 nm	λ = 1064 nm
Cu	calc.	23.8	26.9	63.2
	exp.	20	40	80
Al	calc.	18.3	25.2	27.9
	exp.	10	30	40

3. Steam laser cleaning

By steam laser cleaning of the substrate surface it is covered by thin layer of liquid. The particles and the liquid layer are removed from the substrate surface by laser pulse action. The physical mechanism of the cleaning process defines by the way of heat transfer to the evaporating liquid.

3.1. Absorbing particles at the transparent substrate

The upper part of the particle heats first of all by its light absorption. Liquid above the particle's top also heats and evaporates due to heat transfer from the heated particle top, its evaporation is like micro–explosion. By this, the particle top becomes free from the liquid. Then the particle heats into, and liquid, which is adjoining to the heated particle surface, heats and thin layer of it evaporates. Appeared vapor pressure pushes off the liquid from the particle surface in the evaporation region. As a result, the heat transfer from the heated particle to the liquid decreases and evaporation decreases or ends. Therefore effective evaporation occurs only in the narrow region at the particle surface near the isotherm of liquid boiling temperature T_{ev}. So, the vapor canal forms around the particle suface. It broadens up and depends in time and vapor pressure is maximum in its lower part (Fig.2a).



a) b)

Fig.2. Illustration of the physical mechanisms of steam laser cleaning:
a — absorbing particle, b — absorbing substrate

The action of vapor pressure at the particle depends on position of the effective evaporation region. When it is situated near the particle's upper part, the vertical projection of the force of vapor pressure F_n (normal to the substrate surface) is directed down, to the substrate surface and presses the particle to it. During vapor canal development, the effective evaporation region transfers to the lower part of the particle. By this, F_n becomes directed

up, and if $F_n > F_a$, it pushes the particle up from the substrate surface.

Threshold intensity ε_{th} of steam laser cleaning ε_{th} in considered case can be evaluated as laser intensity value, which is necessary for heating of the whole particle to the temperature T_{ev}:

$$\varepsilon_{th} = \frac{\rho_p c_p d(T_{ev} - T_0)}{\overline{A}_p} \qquad (13)$$

$\overline{A}_p$ is average absorption coefficient of the particle regarding influence of the angle of incidence, T_0 is the initial temperature.

The shape of the particles and their position relatively the substrate surface considerably influence the efefctiveness and possibility of cleaning. Naturally, removal of the particles, which maximum area section is near the substrate surface (like hemisphere lying at the plate surface), is difficult: the force F_n is always directed down. Presence of some particles of such kind explains the observed efefct of noncomplete cleaning [1].

3.2. Transparent particles at the absorbing substrate

Heating of the absorbing substrate causes heating and explosion–like evaporation of the liquid near the substrate surface. By this, vapor pressure acts the lower part of the particle, therefore the force F_n is directed up. By $F_n > F_a$ the particle is removed from the substrate surface (Fig.2a).

The threshold intensity in this case can be defined as laser intensity value, which is necessary for substrate surface heating up to the temperature T_{ev}:

$$\varepsilon_{th} = \left(\rho_S c_S \sqrt{a_S} + \rho_l c_l \sqrt{a_l}\right) \frac{(T_{ev} - T_0)\sqrt{\pi\tau}}{2A_S} \qquad (14)$$

ρ_l, c_l, a_l are density, thermal capacity and thermal diffusivity of the liquid correspondingly, a_S is thermal diffusivity of the substrate.

3.3. Absorbing particles at the absorbing substrate

In this case, the substrate surface near lower part of the particle is situated in its shadow and does not absorbs laser radiation. Liquid in this region can heats by heat transfer as from the particle top, as from irradiated substrate zone. The criterion of the prevailing thermal transfer way is $\varphi = \overline{A}_p \sqrt{a_p} / \left(A_S \sqrt{a_S}\right)$. If $\varphi > 1$ liquid in the shadow region heats basically from the particle (see p.3.1). If $\varphi < 1$ — from the substrate (cleaning mechanism is like that considered in p.3.2).

Let us calculate threshold intensity for steam cleaning of NiP substrate from 1 μ Al particles by using isopropanol alcohol as luquid for cleaning (T_{ev} = 355 K) and wavelength λ = 248 nm. In this case $\varphi > 1$ and assuming $\overline{A}_p = (1 - R)/2$ (R is reflectivity by normal incidence) and T_0 = 20°C, one can obtain: ε_{th} = 32.6 mJ/cm^2. Experimentally measured value for the same conditions [1] is 30 mJ/cm^2.

4. Conclusion

The worked out physical mechanisms of dry and steam laser cleaning of the surface show the following regularities.

Characteristics of dry laser cleaning processes considerably differ for case of adsorbing particles and/or adsorbing substrate and for case of transparent particles by its heating from the substrate. In particular, there is some threshold intensity in the first case, and it is almost absent in the second case. Threshold intensity value depends on physical properties of the particles and substrate materials, particle size and temporal shape of the pulse. Calculated values of threshold intensity are in a good agreement with experimental data. Dry cleaning effectiveness depends on optical and thermal properties of the substrate and particles and coefficients of their thermal enlargement. In particular, the effective cleaning of the substrate from thermally large particles is possible, if radiation is absorbed by the substrate. For thermally small particles can be used radiation absorption as by the substrate, as by the particles. If radiation is absorbed by small particles (≤ 0.1 μ), cleaning effectiveness increases by particle size increasing, by larger sizes of the particles it decreases, since quantity of thermal energy received by the lower part of the particle is unsufficient and since relaxation increases. Cleaning effectiveness increases by laser pulses repetition rate.

The physical mechanism of steam cleaning is connected with prevalent action of vapor pressure to lower part of the particle surface. The regularities of the steam laser cleaning are different for the substrate and particles materials with differ thermal and optical properties. Depending on their correlation, liquid evaporation is caused its heating by the particles or by the substrate. There are threshold intensities in both cases. In the first case, it is proportional to the particle size, in the second case — to $\tau^{1/2}$. The steam laser cleaning effectiveness is considerably depends on particle shape.

5. References

[1] Y.F.Lu, W.D.Song, Y.Zhang, T.S.Low. Proceedings of SPIE, **3550**, (1998), pp.7.

[2] J.Boneberg, M.Mosbacher, V.Dobler, P.Leider, N.Chaoui, J.Siegel, J.Solis, S.N.Afonso. The EOS/SPIE International Symposia on Industrial Lasers and Inspection, Munich, Germany, 1999.

[3] V.P.Veiko, A.I.Kaidanov, H.A.Kovachki, E.A.Shakhno. Proceedings of SPIE, **1856**, (1993), pp.11.

N2 Laser Stereo-Lithography

Saburoh SATOH*, Takao TANAKA*, Nobuya HAYASHI*

and Chobei YAMABE*

*Department of Electrical and Electronic Engineering, Faculty of Science and Engineering,
Saga university, 1 Honjyo-machi, Saga, 840-8502, Japan
TEL:+81-952-28-8655, FAX:+81-952-28-8651
E-Mail : satoh@esp.ee.saga-u.ac.jp

A number of pulsed and/or continuous wave lasers are applied in stereo-lithography. In particular, the He-Cd laser and Ar ion laser with a wavelength of 325nm and 351/364nm respectively are used as ultraviolet (UV) light source. Disadvantages of these lasers include inefficient output energy, which is less than 0.1%, large machine size, insufficient output power, and they are very expensive. In the near future, these lasers are expected to increasingly lack the requested performance for higher speed stereo-lithography systems. Moreover, there will be growing demands for lower cost apparatus.

For the laser stereo-lithography, the N2 laser with cylindrical tube has been adopted to achieve a lower cost type UV light source. Because of its excellent output efficiency, it is expect to downsize the power supply and laser head, and allows air-cooling. Moreover we adopt an optical fiber system for its optics, because the N2 laser output beam divergence has an excessive,

In view of this, attempts were made to develop a special design cylindrical tube as the UV light source. This paper reports the fundamental characteristics of this laser.

Key words: stereo-lithography, UV light source, N2 laser, cylindrical tube, optical fiber system

1. Introduction

A number of pulsed and/or continuous wave lasers are applied in stereo-lithography[1)-4)]. In particular, the He-Cd laser and Ar ion laser with a wavelength of 325nm and 351/364nm respectively are used as ultraviolet (UV) light source. Disadvantages of these lasers include inefficient output energy, which is less than 0.1%, large machine size, insufficient output power, and they are very expensive. In the near future, these lasers are expected to increasingly lack the requested performance for higher speed stereo-lithography systems[5)]. Moreover, there will be growing demands for lower cost apparatus.

On the other hand, excimer laser, a high peak pulsed power laser with UV light emission, is considered an appropriate UV light source for semiconductors and/or photochemical processes[6)]. A XeCl excimer laser (308nm) annealing for liquid crystal display panel is currently being put to practical use[7)]. XeCl excimer laser has a disadvantage because it employs only pulse laser. Its output efficiency is however over 1% which is the highest level amongst UV-lasers. Moreover it is easy to set the laser output power over 100W. To apply excimer laser for stereo-lithography, we propose a new concept for the mask type optical system.[8)-9)]

Because of its easy operation, a N2 laser and an excimer lamp can realize lower-cost stereo-lithography equipment. In view of this, attempts were made to develop a special design cylindrical N2 laser tube and excimer lamp as the UV light source[10)].

This paper reports the fundamental characteristics of this laser.

First International Symposium on Laser Precision Microfabrication, Isamu Miyamoto, Koji Sugioka,
Thomas W. Sigmon, Editors, Proceedings of SPIE Vol. 4088 (2000) © 2000 SPIE · 0277-786X/00/$15.00

Table 1. Characteristics of different lasers and excimer lamp

	Lasers				Lamp XeCl
	Ar	He-Cd	XeCl	N2	
Continuous/ pulse	Continuous	Continuous	Pulse 2kHz	Pulse 1kHz	Continuous
Wave length (nm)	364 351	325	308	337	308
Output power (mW)	100-500	20-40	1400	50	250
Input power (kW)	10-20	0.6-0.8	0.2	0.3	0.02
Cooling	Water	Air	Air	Air	Air
Optical system	Galvanomirror	Galvanomirror	Mask	Fiber	Fiber

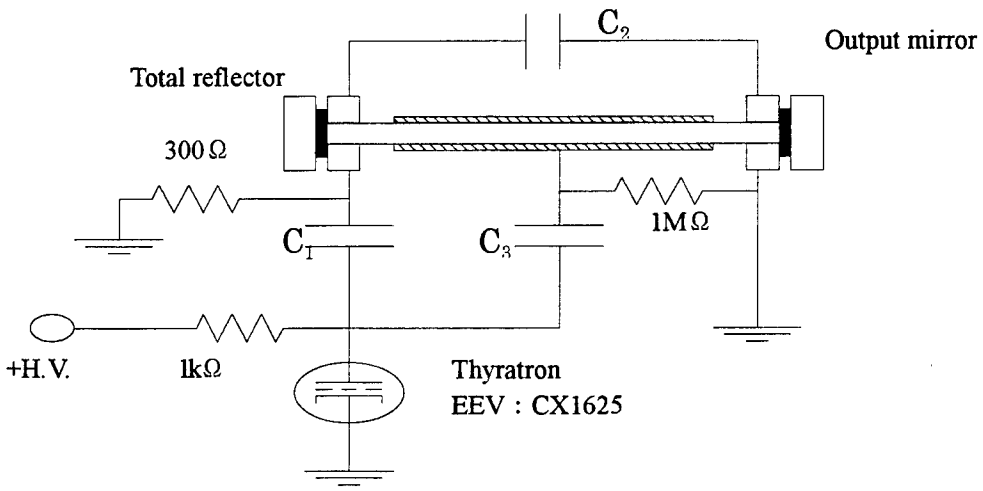


Fig. 1 Electric circuit and laser tube of N2 laser

2. Stereo-Lithography Technology

Stereo-lithography is a technology for creating 3 dimensional (3D) high precision models with photochemical reaction which locally cures liquid resin with UV-light. The 3D model is pre-designed with a computer aided design (CAD) system, converted to counter data which indicates each cross section pattern, after which, UV-laser functions as a point pattern-maker on the surface of the liquid resin. In this resin, photosensitive material (photoinitiator) reacts to the UV-light, polymerizes the surrounding molecules, and finally expands to a huge molecule. With UV laser, only a thin layer of liquid resin surface is cured, which makes it necessary to create layers one by one, successively.

Table 1 shows a comparison of the characteristics of several kinds of lasers and an excimer lamp. The Ar ion laser and the He-Cd laser are conventional lasers for stereo-lithography. The XeCl excimer laser is a typical laser for industrial use, which has a low output power but sufficient

repetition rate. We are currently developing the XeCl excimer lamp and the N2 laser. These lamp and laser are expected to downsize the power supply and lamp/laser head, and allow air-cooling because of its excellent output efficiency and its easy operation. And moreover, these will be expected to be low-cost apparatus.

On the other hand, if a conventional optical system with the He-Cd laser and a galvanomirror were applied to its optics, it would be impossible to achieve the maximum power and efficiency by the excimer lamp and the N2 laser. Because these lamp and laser are easy to operate but output beam divergences have an excessive, we adopt an optical fiber system for its optics.

3. Experiment and Result

Figure 1 shows a N2 laser and an exciting electric circuit. Its cylindrical tube was made from alumina (Al_2O_3) of 3mm in bore diameter and 150mm in length. To perform corona discharge inside the laser tube as a preionization, out side of the laser tube of 100mm in length was covered with a copper thin sheet named an auxiliary electrode, which connected to a capacitor C3. Both ends of the tube were terminated with mirror flanges, which hold the discharge electrodes simultaneously and connected to a main capacitor C1 and peaking capacitors C2. Both mirrors also could be aligned easily. The pure N2 gas was used at a pressure of 1.3 kPa.

When C1 and C3 was charged and Thyratron was fired, high dv/dt voltage was applied to the auxiliary electrode because of its small capacitance, and corona discharge occurred inside the laser tube as an effective preionization. After the C2 voltage was gradually increased, the main discharge and the laser emission were performed.

The optical system consisted of an UV achromatic objective lens LMU-10X-308nm (OFR Inc.), an optical UV-fiber SC200/250 (FUJIKURA Ltd.) with a core/clad diameter of 0.2/0.25 mm and length of 2 m, and a X-Y plotter MP5300 (GRAPHTEC Inc.) controlled by a personal computer. The sample resin was "ADEKA LASCURE HS-660" produced by CMET Inc., whose absorption depth was 0.1mm at a He-Cd laser of 325nm and was 0.2mm at a N2 laser of 337nm. The N2 laser UV light was irradiated on the surface of the resin as a parameter of the laser energy density. After post curing the object with off-focused XeCl excimer laser EMG50E (Lambda Physik Inc.), the thickness and weight were measured with a micrometer and a chemical balance weight measure.

Finally, we tried to make a 3D article based on the above fundamental results. It was set that the curing depth was 0.15 mm, and the UV light energy density from the end of the fiber was less than 20 mJ/cm^2. After a layer was solidified, the object was submerged by several mm into the liquid resin, immediately raised up, and set at the next position to which 0.15 mm was added from the previous setting position with the Z axis table controlled by a personal computer. Finally, the object was washed with alcohol to remove the non-cured resin and dried by off-focused excimer laser beam in the post curing process.

Figure 2 and 3 show the output characteristics of the N2 laser and the output power from fiber at repetition rate of 100 Hz. UV emissions increased with the applied voltage. Compared with the operating pressures, UV emission at 1.3 kPa was the maximum at the applied voltage of 13 kV. It was supposed that discharge uniformity improved at this gas pressure and higher applied voltages.

On the other hand, UV emission per pulse slightly decreased when the repetition rate increased over 100 Hz. The maximum UV emission per pulse of 90 μJ at 100 Hz and the maximum average power of 50 mW at 1000 Hz were obtained.

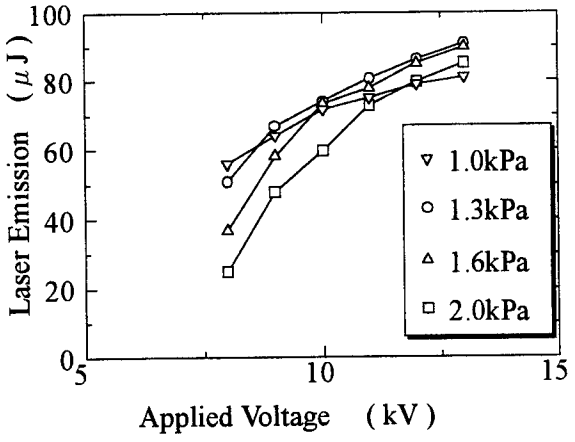


Fig. 2 Output characteristics of N2 laser as parameter of gas pressure

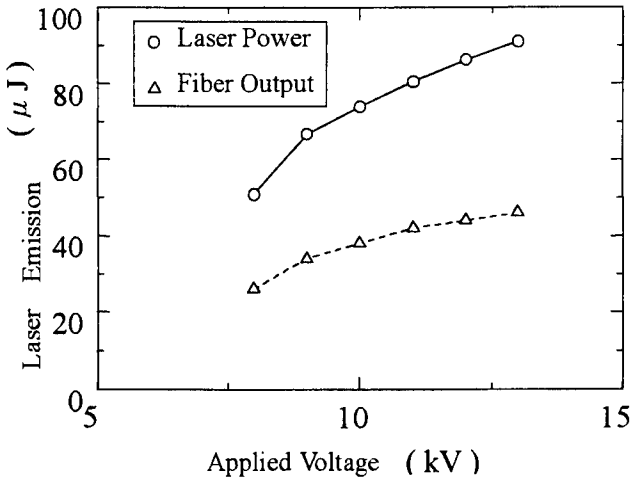


Fig. 3 Output characteristics of N2 laser and output power from fiber

4. Conclusion

A N2 laser has been adapted to achieve a lower cost UV light source in laser stereo-lithography. The excellent output efficiency and easy operation of the N2 laser allow down sizing of the power supply and laser head, and air-cooling. Moreover to realize the maximum output power and efficiency, an optical fiber system is adopted for its lithography optics.

In this experiment, a new type cylindrical laser tube with a bore diameter of 3mm and length of 150mm was examined. With laser operation, UV emissions increased with the applied voltage and indicated the maximum output power at a pressure of 1.3 kPa. The emission per pulse also slightly decreased when the repetition rate was over 100 Hz. The maximum UV emission per pulse of 90 μ J at 100 Hz and maximum average power of 50 mW at 1000 Hz were obtained.

In the next study we will investigate the conditions in which the N2 laser is the most useful for stereo-lithography from the point of accuracy, curl and distortion to construct 3D articles, and for lower cost apparatus.

Acknowledgment

We would like to express our thanks to SMET Inc. for supplying "ADEKA LRASCURE HS-660" and Dr. T. Goto, at Toshiba but now at BELL TECHNO Inc. with whom we held the discussions. This study was partially supported by a Grant-in-Aid for Scientific Research from the Ministry of Education, Science, Culture and Sports.

References

1) C.Decker: *J. Polym. Sci.*, Polym. Chem. Ed., **21**, pp.2451, 1983.
2) J.P.Fouassier, P.Jacques, D.J.Lougnot, and T.Pilot : *Polym. Photochem.*, **5**, pp.57, 1984.
3) M.A.Williamson, J.D.B.Smith, P.M.Castle, and R.N.Kauffman : *J. Polym. Sci.*, Plym. Chem. Ed., **20**, pp.1875, 1982.
4) C.E.Hoyle, M.Trapp, and C.H.Chang : "Laser initiated polymerization : The effect of pulse repetition rate," *Polym. Mater. Sci. Eng.*, **57**, pp.579-582, 1987.
5) P.F.Jacobs : *Rapid Prototyping & Manufacturing*, Nikkei BP (1993).
6) T.Goto, K.Kakizaki, S.Takagi, N.Okamoto, S.Satoh, S.Kosugi, and T.Ohishi : "5 kHz high repetition rate and high power XeCl excimer laser," *Rev. Sci. Instrum.*, **66**, pp.5162-5164, 1995.
7) T.Tanaka and N.Konishi : *OYO BUTURI*, **63**, pp.1034, 1994(in Japanese).
8) S.Satoh, K.Yokogawa, J.Shimada, S.Ihara, M.Ishimine, C.Yamabe, and T.Goto : "A fundamental study on stereo-lithography with KrF excimer laser," *KATAGIJYUTU*, **11(13)**, pp.62-62, 1996 (in Japanese).
9) S.Satoh, K.Yokogawa, M.Ishimine, S.Ihara, and C.Yamabe : "A study on mask type stereo-lithography with XeCl excimer laser," *Rev. Laser Engineering*, **26**, Special Supplement for APLS'98 , pp.121-124, 1998.
10) S.Satoh, T.Tanaka, S.Ihara, and C.Yamabe : "Excimer lamp stereo-lithography," *Proceeding of SPIE – Laser applications in microelectronic and optoelectronic manufacturing V-*, **3933**, pp.1-8, 2000.

Hole Drilling of Glass Substrates with a Slab Waveguide CO_2 Laser

Yoshikazu YOSHIDA*, Yuji KOBAYASHI**, Tiejun ZHANG**,
Hiroyoshi YAJIMA***, Yuji HASHIDATE***, and Hiroshi OGURA***

*Mechanical Engineering, Toyo University, 2100 Kujirai, Kawagoe, Saitama, 350-8585, Japan.
E-mail: zen@eng.toyo.ac.jp
**Mechanical System Engineering, Yamanashi University, 4-3-11 Takeda, Kofu, Yamanashi, 400-8511, Japan.
***Matsushita Research Institute of Tokyo Inc., 3-10-1, Higashimita, Tama-ku, Kawasaki, Kanagawa, 214-8501, Japan.

Using 30 – 1000 μs pulses and 9.3 μm wavelength from a CO_2 slab waveguide laser, focused to a spot size of 130 μm, we have produced holes in synthetic quartz, soda-lime glass, and Pyrex glass substrates. In the three types of substrates, the mass removal per pulse increases almost linearly with the pulse energy used to vary the pulse interval. The removal rates of the three substrates are almost the same. We examine the effect of the pulse interval on the hole structure and the pile-up around the hole in single- and multiple-pulse hole drilling. The deformation in the pile-up region can be accounted by the melting walls of the hole. Moreover, we examine the effect of pulse energy on the inclination of the hole walls. A multiple-pulse hole shaping technique is effective in decreasing the height coefficient of the pile-up region and the angle of inclination.

Keywords: Laser micro-machining, Hole drilling, Slab waveguide laser, Glass.

1. Introduction

To achieve high speed and high information transfer in radio communication systems, wide-band millimeter-wave radio systems have been actively developed. To realize these systems, the authors propose a multi-chip module structure where GaAs active circuits are flip-chip mounted on multi-layered circuits, which are fabricated on a low-cost silicon substrate.[1] However, substrates require a low dielectric constant and low-loss materials for operating in the millimeter wave frequency bands. From the point of view of low-loss characteristics, glass is better than silicon.

Micromachining of quartz glass is rather difficult compared to that of silicon substrate. Further, miniaturization and multi-layering of the chips require flatness and verticality of < 1 μm accuracy. Substrates have reduced their size so much that glass fabrications by conventional machining techniques such as sand blasting and ultrasonic machining have become too costly and difficult. Reactive ion etching (RIE) is the most popular method of micromachining for glass. However, RIE requires a photolithography process and its etching rate of glass is lower than that of silicon. Recently, much attention has been paid to pulsed laser as a powerful tool for micro-patterning and drilling of substrates. Over the past decade, pulsed CO_2 lasers are well known to be capable of precision materials processing for polymeric and ceramic substrates.[2] Recently, direct writing of a micro-optical structure on quartz glass by a high precision laser was demonstrated using a pulsed CO_2 slab waveguide laser.[3] The mechanism of hole drilling is mainly due to the melting effects by infrared rays. Therefore, the melting region is larger around the hole and the hole accuracy is low.

Many beam parameters (energy, duration of the laser pulse, number of laser pulses, focused beam size, etc.) must be considered for obtaining the given hole dimensions. We have used

First International Symposium on Laser Precision Microfabrication, Isamu Miyamoto, Koji Sugioka,
Thomas W. Sigmon, Editors, Proceedings of SPIE Vol. 4088 (2000) © 2000 SPIE · 0277-786X/00/$15.00

a CO_2 slab waveguide laser to demonstrate that the height of the pile-up around a hole is dependent on the type of glass substrate used, the pulse duration, and the number of laser pulses.

2. Experimental

A Sealed, pulsed RF, slab waveguide CO_2 laser (DIAMOND™ 84I, Coherent Inc) operating at 9.3 μm is used as a light source. Power density is 5×10^{10} W/m^2. In this experiment, the laser pulse energy is controlled by an optical attenuator; the pulse energy is controlled by an internal pulse generator. The beam is focused onto the substrate using an aspheric lens of 88.9 mm focal length and producing a spot diameter of ~130 μm. The pulse rises in power towards a quasi-cw level of ~500 W from 30 μs to 100 μs and then is held constant from 100 μs to 1000 μs. The desired laser pulse repetition rate can be selected from 1 Hz to 20 kHz. Pulse energy is in direct proportion to the pulse interval.

Synthetic quartz, soda-lime glass, and normal Pyrex glass substrates are employed in our experiments. They are device assembly substrates used for practical applications.

3. Results and discussion

3.1 Defocusing

The beam-focusing conditions influence the hole profile to a large degree. Figure 1 presents the hole diameter and the taper angle of the hole in quartz glass at constant radiant energy but at different focus locations with respect to the front surface of the substrate. The walls melt slightly due to heat conduction when the light flux propagates parallel to them. However, in practical hole drilling applications, irradiation by a diverging beam of sufficient density causes extensive melting of the walls.

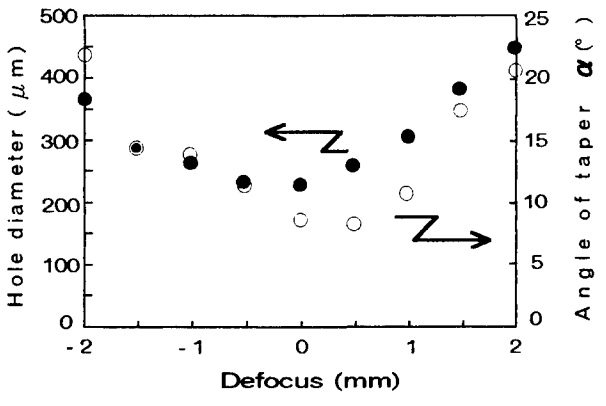


Fig.1 Hole diameter and taper angle of a hole in quartz glass for different focus locations on the front surface of the substrate.

3.2 Single-pulse hole drilling

With respect to the laser machinability, we have compared three types of glass substrates for laser-pulse hole drilling. Figure 2 shows hole depth per single pulse versus pulse interval. The depth increases almost linearly with the pulse energy. It is found that the speed of material removal increases with the local irradiance. The removal rates of the three types of glass are very similar.

Scanning electron micrographs (SEM) of the holes in the three types of glass substrates are shown in Fig.3 at a pulse interval of 1000 μs. These are the surfaces where the laser first strikes. Gaussian beams tend to form round holes with diameters roughly equal to the beam diameter near the surface. There is a pile-up around every hole, which is mainly due to the melt displacement toward the outer rim. On the exit surface, a similar pile-up can be observed. In Fig.3(c), debris outside of the pile-up is observed. During the early stages of hole formation, its diameter changes only slightly, while its depth grows linearly with time due to evaporation from the entire irradiated area. Then the combination of intensive hole-wall melting and liquid-phase ejection slows down of the rate of depth increase. Comparing the three substrates, the soda-lime glass produces much larger amounts of sputter around the hole and micro cracking is evident in the surrounding area on the front surface. Moreover, large cracks have formed on the rear surface of the soda-lime glass. In the soda-lime glass, the

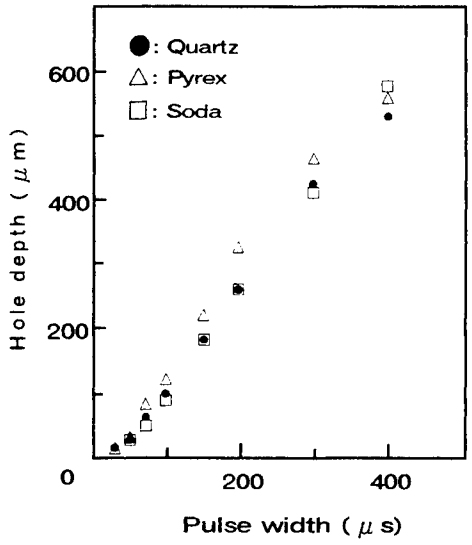
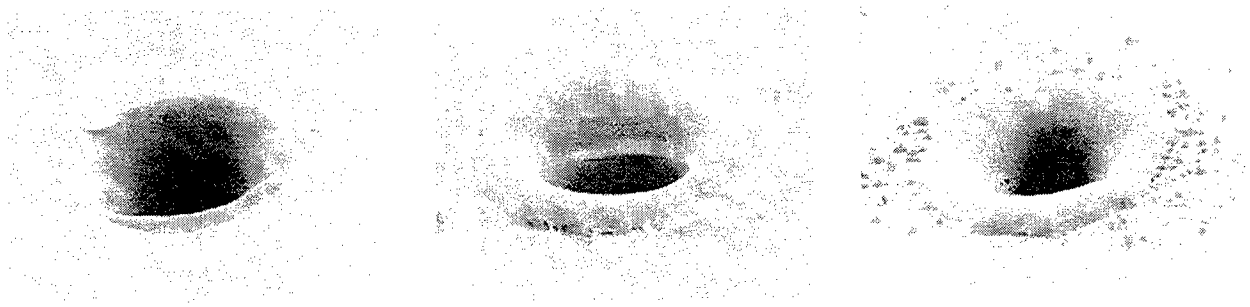


Fig.2 Hole depth per single pulse versus pulse interval.



(a) (b) (c)

Fig.3 Scanning electron micrographs of the holes from the laser input surface. (a) Synthetic quartz, (b) Pyrex glass and (c) Soda-lime glass.

residual stress is expected to be larger than quartz glass because of its high thermal expansion coefficient and large mass of molten glass created due to its low melting point.[3] We have shown that the three types of substrates have similar mass removal rates, and so the higher-pile-up created in soda-lime must be caused by melt displacement toward the outer rim.

Figure 4 shows the height coefficient of pile-up versus the pulse interval. The height decreases with increasing pulse interval. The decrease of the height is due mainly to melting effects. However, the height saturates at an interval above 400 μs. In the cases of soda-lime and Pyrex, they saturate around 1.5×10^{-5}. In the case of quartz, it saturates around 5×10^{-6}. At over 400 μs, the pulses are too long to promote material removal by vaporization and increased melt depths. It is found that signs of micro cracking are present in the pile-up area. Allcock et al[4] reported a material removal mechanism in soda-lime glass using a TEA-CO_2 laser. They have concluded that micro cracking occurs due to residual stresses left within the substrate upon cooling.

Figure 5 shows the angle of inclination versus the pulse interval. The angle decreases with increasing pulse intervals up to 300 μs and is mainly due to Gaussian beams. It then saturates around 10° beyond 700 μs. The saturation is probably due to the point of focus. It is seen that the hole depth and diameter have a nonlinear relationship with the pulse energy. The longer the pulse, the larger the melt volume and, therefore, the larger the hole-size scatter. In addition, long pulse durations (more than 0.8 ms) adversely affects a large region, where structural changes occur, as well as the appearance of defects, such as cracks, on the hole surface as a result of the increase of the heat-affected layer.

With respect to laser machinability, quartz is the best of the three used in this experiment. A small fraction of the liquid phase remains on the walls after the end of the laser pulse. It is very important to understand the vaporization kinetics and the hydrodynamic rejection of the liquid-phase material. In these conditions, the precision of single-pulse hole drilling usually does

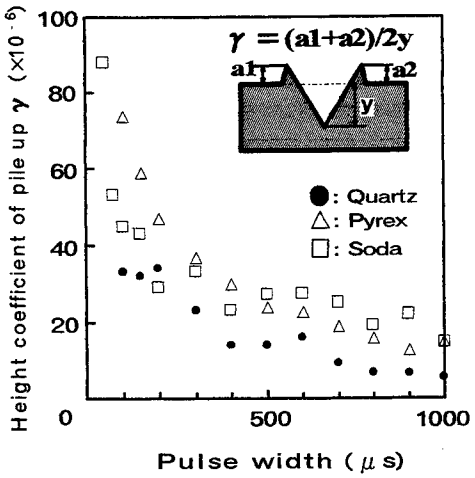


Fig.4 Height coefficient of pile-up versus pulse interval.

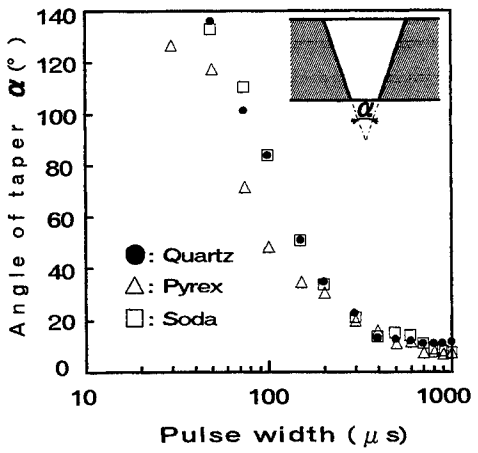


Fig.5 Angle of inclination in hole wall versus pulse interval.

not reach saturation. In single-pulse material treatment, the hole-size scatter is determined first and foremost by the instability of the laser-pulse parameters. The most efficient way of increasing the laser drilling precision is to use the multiple-pulse treatment technique.[5]

3.3 Multiple-pulse hole drilling

The technique of multiple-pulse hole drilling shapes the hole by means of applying a train of identical laser pulses at a given energy and duration. Figure 6 shows the height coefficient of pile-up versus the number of laser pulses. The angle decreases in height with increasing irradiation number from 1 to 3. The decrease in height is due mainly to melting effects. However, the height is minimized around 2×10^{-6} at 6 or 7 pulses.

Figure 7 shows the angle of inclination versus the number of laser pulses. The angle decreases with increasing irradiation number up to around 20 and then it saturates. In the cases of 100 and 400 μ s, they saturate at around 7° . In the case of 1000 μ s, it saturates at around 4.5° . A hole can form in a 0.5 mm thick quartz glass at an interval above 400 μ s by single pulse. Multiple-pulse processing at an interval of 100 μ s allows the hole depth to grow gradually due to the layer-by-layer vaporization by each pulse. At 1000 μ s, the height monotonically rises beyond 7 pulses. This is evidence that thermal conduction melting outside the beam is occurring, defining a heat affected zone of several tens of microns wide. The existence of a minimum value is affecting the heating and destruction of the walls. This trial shows that good results are possible using multi-pulse technology.

4. Conclusions

Material removal in hole drilling is basically connected with the disintegration of the substance in the irradiated zone and the subsequent motion of the melting material and debris. We have examined the pile-up around the hole and the inclination of the walls at various pulse energies. Using pulsed CO_2 laser, material is removed by surface evaporation and hydromechanics where heat conduction is not negligible. We have concluded with the following:

(1) Glass having a lower melting point and a larger thermal expansion coefficient is not feasible for precision hole drilling.

(2) In single-pulse hole drilling, there is a limitation on the precise hole shape because of the liquid-phase residue in the hole after the pulse.

(3) In multi-pulse hole drilling, an optimum number of pulses exist for precise hole formation.

Future work will include further testing of other glasses and lens systems, aiming toward smaller beams, greater material removal depth, and higher accuracy.

References

[1]H.Ogura et al.: MWE'99 Microwave Workshop Digest(1999)357.

[2]W.R.Wrenner: Circuit manufacturing (May, 1977)29.

[3]H.J.Baker et al.: Proc. AHPLA'99(Osaka,Japan,1999.11)

[4] G.Allcock, P.E.Dyer, G.Elliner, and H.V.Snelling: J.Appl.Phys., **78**(1995)7295.

[5] S.M.Metev and V.P.Veiko: "Laser-Assisted Microtechnology" (Springer-Verlag, Berlin, 1994)p.157.

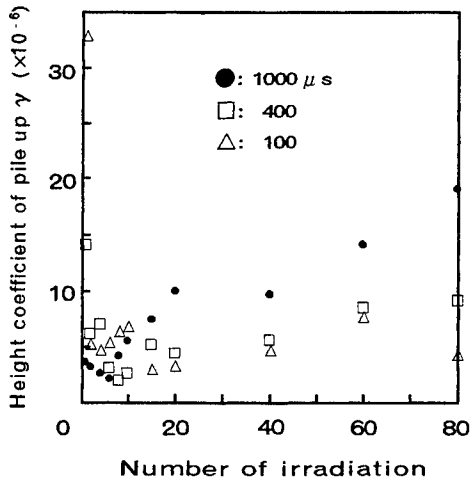


Fig.6 Height coefficient of pile-up versus number of laser pulses in quartz.

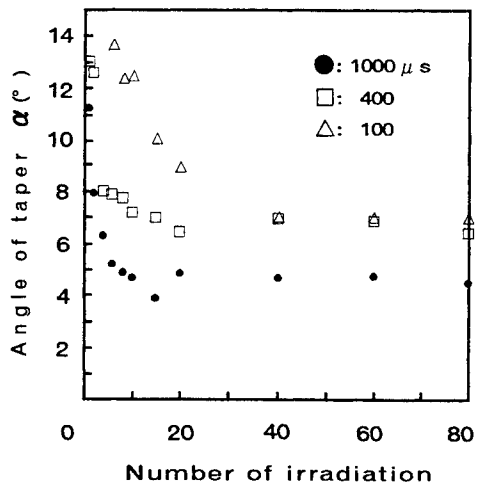


Fig.7 Angle of inclination versus number of laser pulses in quartz.

High Repetition Rate ArF Excimer Laser for Microlithography

*Osamu WAKABAYASHI, **Tatsuo ENAMI, **Ken ISHII,
**Katsutomo TERASHIMA, *Yasuo ITAKURA, *Takayuki WATANABE,
**Takeshi OHTA, *Ayako OHBU, *Hirokazu KUBO, **Hirokazu TANAKA,
*Satoshi ANDOU, **Takashi MATSUNGA, **Hiroshi UMEDA, *Toru SUZUKI,
*Akira SUMITANI and *Hakaru MIZOGUCHI

*Laser Research Dept., Research Div., Komatsu Ltd.,
1200 Manda, Hiratsuka, Kanagawa 254-8567, Japan
E-mail: osamu_wakabayashi@komatsu.co.jp
**Excimer Laser Dept., Electronics Div., Komatsu Ltd.,
400 Yokokura-shinden, Oyama, Tochigi 323-8558, Japan

ArF excimer lasers are the light source of choice for the next generation of microlithographic tools enabling structures below the 130nm technology node. For these lithographic mass production lines Komatsu successfully developed an ArF excimer laser, named "G20A", which has a 2kHz pulse repetition rate, 10W average power and 0.5pm (FWHM) spectral bandwidth.

G20A has three significantly improved important items: (1) the high resolution line narrowing module, (2) the high power and high repetition rate solid state pulse power module, and (3) the Xe added laser gas yielding an improved overall laser performance.

ArF laser spectra were determined with our newly developed high-resolution spectrometer. The instrument function of the spectrometer was measured with a 193nm coherent light source jointly developed with the University of Tokyo.

The laser gas composition is one key parameter of excimer laser performance. The deteriorating effect of impurities on ArF performance is e.g. ten times larger than on KrF performance. We observed that added Xe gas, however, has a beneficial effect on the pulse energy and the energy stability at high repetition rates.

Experimental results of a currently developed 4 kHz ArF laser are also reported.

Keywords: lithography, ArF, excimer laser, high repetition rate, xenon, impurity, metrology, spectrum

1. Introduction

This paper reports key technologies and performances of high repetition rate ArF lasers developed by Komatsu.

ArF excimer laser lithography is moving from R&D to mass production thus requiring that performance and durability of ArF lasers match the KrF laser standard. Especially, the ArF laser durability, which directly effects the cost of operation of the laser device, has to be improved in order to allow the industrial usage of ArF lithography.

Earlier, we already reported the billion level durability of our ArF laser [1]. In addition, high repetition rate ArF lasers are required for next generation, high NA, high throughput scanners. The performance of high repetition rate ArF lasers, however, is very sensitive to various factors such as characteristics of electrical components, optical elements and gas conditions.

Chapter 2 describes the modular G20K laser system, chapter 3 Komatsu's original ArF laser key technologies that significantly improve performance, reliability and quality of the ArF laser. Chapter 4 and 5 finally present laser performance data at 2kHz and 4kHz repetition rate, respectively.

2. ArF excimer laser system

A schematic of the laser light source is shown in Fig. 1. The excimer laser includes a monitor module(MM) which monitors the laser beam quality, a line narrowing module (LNM) which limits the oscillation bandwidth and a pulse power module(PPM) which generates fast electrical pulses

First International Symposium on Laser Precision Microfabrication, Isamu Miyamoto, Koji Sugioka,
Thomas W. Sigmon, Editors, Proceedings of SPIE Vol. 4088 (2000) © 2000 SPIE · 0277-786X/00/$15.00

causing gas discharges and thus providing the laser gain in the laser chamber. In the next chapter, technical points of these components are discussed.

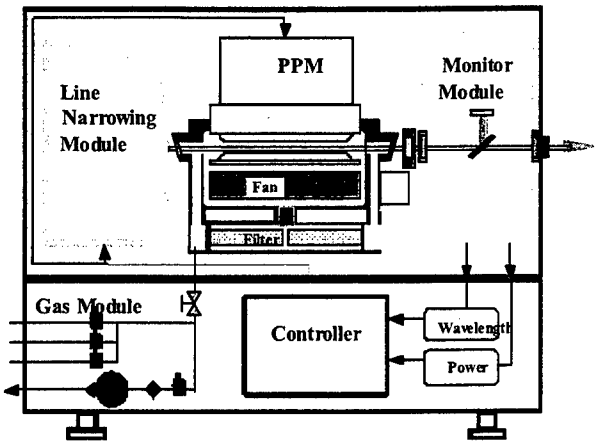


Fig. 1 Schematic diagram of excimer laser

3. ArF laser key technology

Komatsu developed several original key technologies providing high precision, durable laser devices. Main technologies are presented in this chapter.

3.1 RF pre-ionization based chamber[2]

A radio frequency electric discharge through a dielectric medium has uniform and long range characteristics, because the dielectric layer acts as a stabilization impedance of the electric discharge and the distributed circuit (RF pre-ionization). Therefore an initially uniform electron distribution can be produced and the output stability of excimer lasers using RF pre-ionization is consequently very high. This technology also enables higher repetition rate operation.

3.2 Solid state switch pulsed power technology [2]

An all solid state pulsed power supply, combining a saturable reactor and a solid state switch, has been developed. The lifetime of this pulsed power supply surpasses ten billion pulses because its components do not degrade. In addition, the power supply has a higher stability than supplies using thyratron switches, thus providing lower pulse-to-pulse energy fluctuations.

3.3 High resolution line narrowing and monitor modules[1]

The narrow spectral bandwidth of the excimer laser oscillation is obtained using a high-resolution line-narrowing module that includes several dispersive elements such as prisms and a high-resolution diffraction grating. CaF_2 optical elements are used to further increase the laser durability. Moreover, a new LNM design with decreased optical path is adopted in order to increase the output energy.

The laser is equipped with a monitor module that measures the spectral bandwidth, the central wavelength and the output energy. In addition, these laser parameters are stabilized by a feedback control system.

The permanent absorption of UV-light of optical elements used for wavelength selection and monitoring changes their optical characteristics. This problem can be reduced by using materials with ultra-violet resistance and a small UV-absorption. In addition, drifts of the optical MM wavelength calibration elements are monitored in real time using an atomic light source as absolute wavelength standard. The high accuracy absolute-wavelength stability is further guaranteed by a feedback control of the calibration unit.

3.4 Gas contamination control[4]

Impurities of the laser gas greatly effect the performance of the ArF laser as we discovered during a fundamental research cooperation with Kyushu university [3]. We therefore propose to add Xe gas to the laser gas in order to stabilize and to enhance the ArF laser performance. As we noted, gases like O2, CO2, and Xe added to ultrahigh purity gas increased the laser output power in case of the ArF laser [1]. For example, Fig.2 shows the change of the laser pulse energy using high purity gas with and without added Xe or O2. As in actual exposure, a burst mode was chosen with blocks of 500 pulses emitted at 1000Hz and separated by 0.2s rest intervals. Without any Xe or O2 added the ArF laser clearly shows "spiking": the initial pulse energy gradually decreases during about 100 pulses and fluctuates

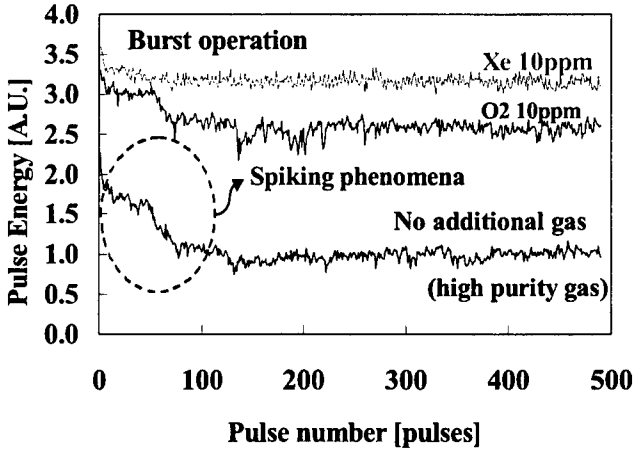


Fig. 2 Additional gas Effect on ArF laser burst chataristics

then around a constant value. The spiking is due to the fact that deteriorated discharged laser gas circulates in the laser chamber and returns to the electrodes not fully regaining its original quality. Adding 10 ppm of O2 increased the laser

energy by a factor of 2.5 but the "spiking" remained. Adding 10ppm of Xe increased the laser energy by a factor of 3 and the spiking nearly disappeared. Consequently, it is important to reduce contamination sources inside the laser chamber. Komatsu has developed a magnetic bearing technology that avoids contamination caused by mechanical contacts of fan rotating components with the laser chamber. The greatly improved energy stability assured the development of the ArF laser for mass production [3].

3.5 Spectral measurement by 193nm coherent light source and spectrometer[1]

An accurate measurement of the spectrum of the ArF laser is very important for exposure tools equipped with a refractive system. Komatsu has therefore developed a 193nm coherent light source (193CLS) in cooperation with Tokyo University.

Fig. 3 shows a schematic of the 193CLS used to measure the instrument function of our high-resolution spectrometer. The 193CLS light source contains a seeder, an amplifier, and a wavelength conversion unit. The seeder is a single mode, CW diode laser. The pulsed amplifier is a Ti:sapphire ring laser. The amplified light subsequently passes through a wavelength conversion unit generating the fourth harmonic at 193.4nm. The spectral bandwidth at 193.4nm is smaller than 0.01pm and the output energy at 1 kHz is 1mW. Fig.4 shows that the measured instrument function of our developed spectrometer has a FWHM of only 0.06pm. All

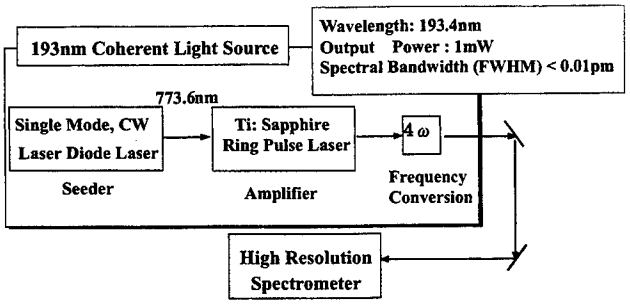


Fig. 3 Optical arrangement for providing 193nm coherent light source to measure the instrument function of the spectrometer

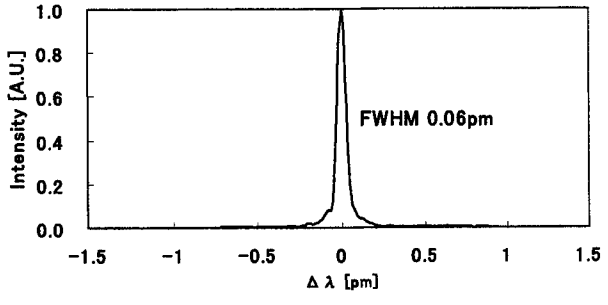


Fig. 4 Instrument function of our developed high resolution spectrometer

ArF laser spectra have been analyzed performing deconvolution of the convoluted spectra with this measured instrument function.

Hence, the developed 193CLS light source contributes also significantly to the mass production of our high quality ArF excimer lasers.

4. Features and performance of 2kHz ArF excimer laser; G20A[5]

For the ArF laser we improved and optimized the high-repetition rate technologies being originally developed for our 2 kHz KrF laser [5]. Though components are basically identical with those used for the KrF laser, some advanced technologies were introduced and the LNM was redesigned due to the wavelength difference and to the need for a PPM with higher output power.

Laser chamber, system controller and gas module, which also proved their reliability, are interchangeable with the KrF laser.

Fig.5 shows the spectrum of our ArF G20A laser. The deconvoluted spectral bandwidth (FWHM) is 0.34 pm and the spectral purity is 0.85 pm. These values are better than those of current KrF lasers.

The second feature is high repetition rate and high power. Fig. 6 shows the dependency of the output power and it's

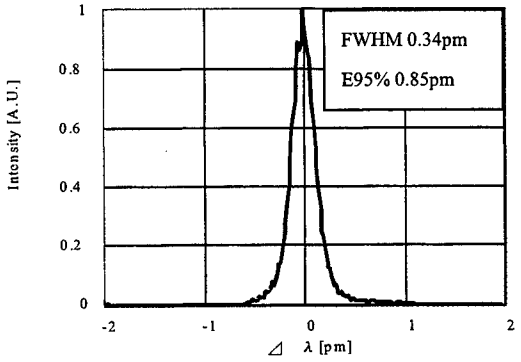


Fig. 5 Spectrum of the 2kHz ArF laser (G20A)

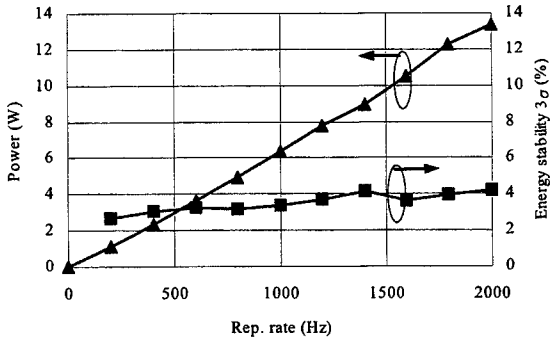


Fig. 6 Dependency of power and stability on oscillation

stability (3 σ) on the oscillation frequency. As can be seen an output power over 10 W with an energy stability better than 5 % (3 σ) is obtained at 2 kHz. However, compared to the KrF laser the input power of the ArF laser has to be 1.5 times larger due to its smaller cross section for stimulated emission and the shorter excited dimer's lifetime. Therefore, the development of a solid state PPM providing high power and repetition rate is indispensable to achieve high energy with better stability. As our results show, our development of an improved PPM succeeded.

The third feature is a better energy stability and a long gas lifetime obtained by adopting a suitable laser gas for ArF. Fig. 7 shows the trend of the gas pressure and of the energy stability for one gas fill of Xe added and of conventional gas. The gas lifetime improves by a factor of five and the

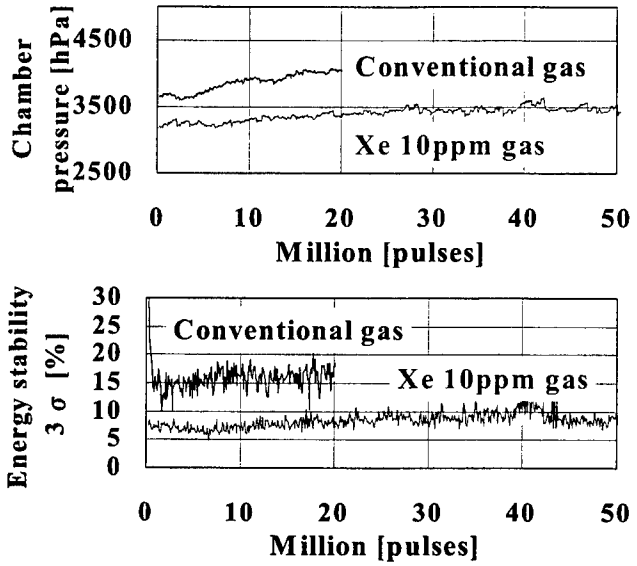


Fig. 7 Trends of gas pressure and energy stability for one gas fill

Table 1 Performance of 2kHz ArF laser(G20A)

Items	G20A
Repetition Rate	2000Hz
Output Power	10W
Pulse Energy	5mJ
Energy Stability(3 σ)	<10%
Energy Dose Stability	<±0.3%(50 pulses window)
Bandwidth(FWHM)	<0.5pm
Spectral Purity(95%E)	<1.3pm
Wavelength Stability	<±0.05pm (50 pulses avg.)
Pulse Duration(TIS)	>30ns

energy stability by 0.5 using the developed Xe added gas. The fact that this gas is expected to be the world standard endorses the advanced technology invented by Komatsu.

The performance of the ArF excimer laser G20A is summarized in table 3. Performances including spectral bandwidth and pulse energy stability fulfill exposure usage requirements. Hence, G20A is ready for lithographic mass production.

5. Results of 4 kHz ArF laser operation

Ultra-high repetition rate technology is very demanding. The most important point is to control the discharge repeatability in order to maintain output energy and stability. Fig. 8 shows experimental results for different repetition rates. On one hand, the output power linearly increases with higher repetition rates, yielding 20W at 4kHz. On the other hand, the energy stability deteriorates being about 2 times larger at 4kHz compared to 2 kHz. We suppose, however, that the energy stability at 4kHz can be improved by adjusting the laser gas circulating speed and reducing its fluctuation, as well as by a further optimization of PPM parameters for high repetition rate operation.

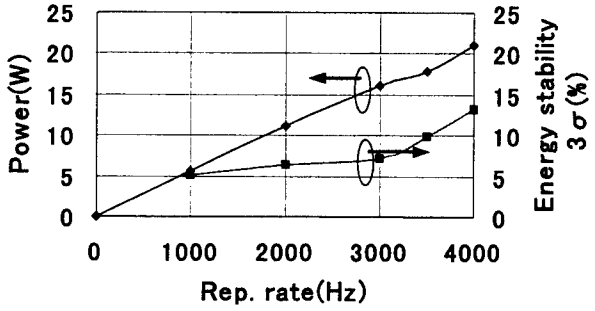


Fig. 8 Experimental result of 4 kHz operation

6. Conclusion

We have established ArF key technologies that improve performance, durability and quality of ArF lasers. In conclusion, the 2 kHz ArF laser (G20A) employing the above-mentioned technologies has proven to fulfill requirements of next generation microlithography mass production tools. A 4 kHz ArF laser is currently under development indicating that 5 kHz or higher versions could be realized in the near future.

References

[1] O. Wakabayashi et al.: Proc. SPIE, **3679**,(1999) 1058.
[2] T. Enami et al.: Proc. SPIE, **3334**,(1998) 1031.
[3] A. Sumitani et al: SPIE's 25th Ann. Intl. Symp. On Michrolithography, (2000) [4000-511].
[4] K. Kataoka et al.: Jpn.J.Appl.Phys., **83**,(1999) 6735.
[5] T.Enami et al: SPIE's 25th Ann. Intl. Symp. On Michrolithography, (2000) [4000-512].

High power second harmonic generation with free running Nd:YAG slab laser for micro-machining applications.

Sébastian Favre, Thomas Sidler, René-Paul Salathé

Institute of Applied Optics (IOA), Swiss Federal Institute of Technologies (EPFL), BM 4.111, CH-1015 Lausanne EPFL, Switzerland
Email: sebastian.favre@epfl.ch

Abstract: Frequency doubled Nd:YAG lasers represent an attractive alternative to other laser tools for many material processing applications, but frequency doubling with pulsed Nd:YAG lasers has been performed until now only with pulses of tens of nanoseconds. In material processing with longer pulses (10-1000 µs), such as encountered in typical 1.06 µm industrial Nd:YAG applications, the laser-material interaction is different and, in particular, higher material ablation rates are performed. Furthermore, the green light material processing permits a better focusability and a higher absorption in most materials. However, frequency doubling with long pulse lasers is much more difficult and less efficient up to now. The main problems are the generation of a fundamental 1.064 µm beam of high quality necessary for the non-linear process, and the low damage threshold of the non linear materials in the long pulse regime. Therefore, a zigzag slab laser, which has a high beam quality and an inherently linear polarisation of the beam, is an ideal candidate for non-linear processes.

The optical damage threshold in the non-linear materials is the main limiting parameter. The 140 W instantaneous power obtained for a 200 µs pulse duration in extra-cavity configuration allows us to finely process sheets up to 300 µm thick.

Keywords: Micro-Machining, Micro-Cutting, Harmonic Generation, Material Interaction, High-brightness laser.

Introduction:

Frequency doubled and tripled Nd:YAG laser represent an attractive alternative to eximer lasers for many material processing applications. Although the available pulse energies are typically less than eximer laser, the high beam quality permits a very good focusing property (spot of diameter down to some micrometers), resulting in intensities largely sufficient for material processing application such as direct-write machining sources.

Most of extra-cavity second harmonic generation (SHG) with Nd:YAG lasers have been performed so far with Q-switch lasers (pulses of several nanoseconds) as this type of laser can easily deliver the peak powers necessary to achieve good conversion efficiencies. For this mode of operation efficiencies of more than 65% have been reported[1]. The main problem for harmonic generation is in the generation of a powerful fundamental wave with a high beam quality, which can provide the high intensity narrow beam of low divergence, necessary by the non-linear process.

However, typical industrial applications are based on free running Nd:YAG lasers with pulses of 10-1000 µs duration since the material ablation rate is much higher in this region. The higher absorption of most materials at the second harmonic wavelength would permit to achieve higher yields or open up new possibilities for processing some difficult materials (with, e.g., high I.R. reflection).

But frequency doubling with long pulse lasers is more difficult and less efficient and no results have been reported so far for free-running Nd:YAG lasers. At our knowledge, we report first results on extra-cavity long pulse second harmonic generation with KTP (potassium titanyl phosphate [$KTiOPO_4$]), LBO (Lithium Triobate [LiB_3O_5]) and MgO:$LiNbO_3$ (Lithium Niobate) as non-linear crystals.

Set-up:

Figure 1 shows the experimental set-up. A free running zig-zag slab laser (active medium with parallelepiped geometry) with extra-cavity electro-optic shutter has been used as light source.

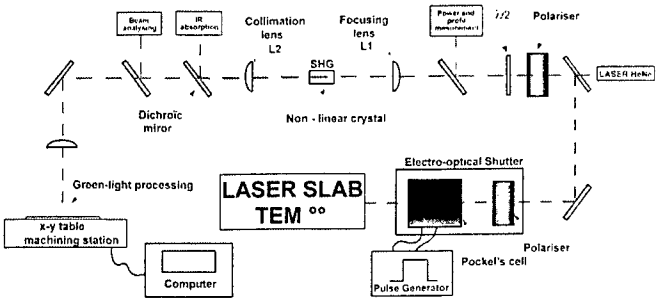


Fig. 1. Experimental Set-up

The laser radiation is directed via two mirrors, a half-wavelength plate and a dielectric polariser on to lens L1. The half-wave plate and polariser allow to precisely control the pulse power without changing neither pump energy nor beam shape. Polariser and half-wave plate, can be interchanged: for constant polarization on the non-linear crystal, the polariser is placed after the half-wave plate, whereas for constant power, the polariser precedes the half-wave plate. The light is focused onto the crystal by lens L1, re-collimated by lens L2 and directed onto the machining place. The dichroic mirror eliminates the remaining IR beam. All the experiments were done with the non-linear crystal on a Peltier element temperature stabilised holder or in a precision micro-heater. These holders are placed on a stage with two rotational and two translationnal degrees of freedom, permitting the fine adjustment of the crystal angles and to control the exact interaction location on the crystal for damage determination.

The SLAB laser with a zigzag propagation and triple passage allows us to obtain a gaussian fundamental mode beam ($M^2 \approx 1.6$) resulting in a high intensity focal spot, with low divergence (long Rayleigh range), best suited for the limited angular acceptances of the non-linear crystals. An other advantage of the slab laser is the linearly polarised output (ratio > 400:1), which avoids the problems of polarisation losses of typical ROD lasers. As the laser is working in a quasi-fundamental mode, we observe a damped spiking with 8 to 10 times higher peak power at the leading edge of the pulse than the average pulse peak power. These first high power spikes can lead to crystal damages. In order to avoid these spikes, we implemented an extra-cavity electro-optical shutter consisting of a Pockels-cell followed by a polariser. This procedure permits, with minimal losses and a rise time of less than 1 µs, the generation of purely rectangular shape pulses with a controlled width from 10 to 1000 µs. Figure 2 shows the original pulse with spiking and the resultant rectangular shaped pulse. For the shutter off state, the residual transmission is less than 0.08%.

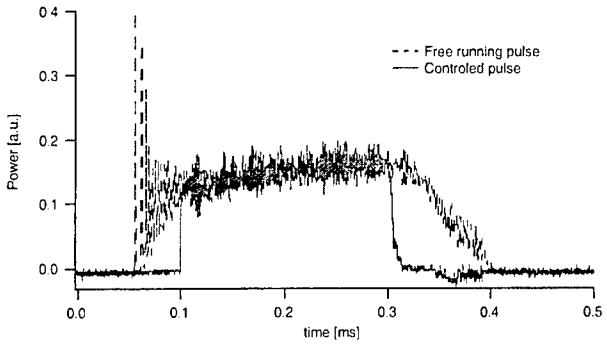


Fig. 2. Controlled pulse shape with optical Shutter

The laser is operated at a low repetition rate in order to prevent excessive thermal loading of the non-linear crystal, leading to thermal lensing and resulting in the degradation of the beam quality and also of the conversion efficiency.

Efficiency:

The second harmonic power conversion efficiency for a 10 mm long KTP crystal is shown in figure 3 as a function of incident intensity.

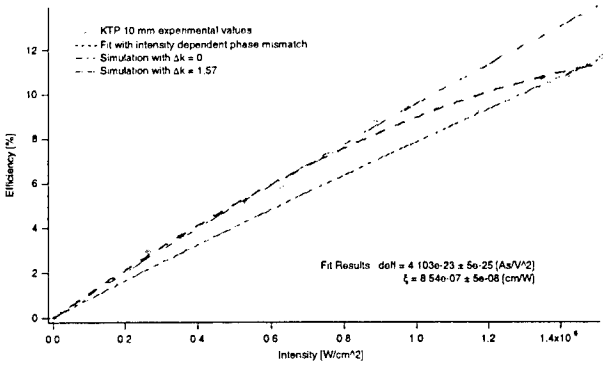


Fig. 3. Efficiency results for KTP 10 mm length with the exact analytical solution and with a fit with intensity dependence phase mismatch

As the efficiency increases not linearly with intensity and begins to saturate, the experimental behavior can not be approximated in single way by the use of the linear low conversion efficiency approximation like in the theoretical plane wave approximation and the exact formula must be used.

$$\eta = \frac{P_{2\omega}}{P_{\omega}} = \tanh^2\left\{\sqrt{l^2 KI \frac{\sin^2\left(\frac{\Delta k\ l}{2}\right)}{\left(\frac{\Delta k\ l}{2}\right)^2}}\right\} \quad with \quad K = 2\left(\frac{\mu_0}{\varepsilon\varepsilon_0}\right)^{\frac{3}{2}}\left(\frac{2\pi c}{\lambda_{\omega}}\right)^2 d_{eff}^2$$

For the different non-linear materials, different effects are predominant and the slightly sub-linear behavior is probably angular phase-mismatch due to the beam degradation and/or thermal phase-mismatch and it can be related in the both cases to the absorption and the resulting heat deposition in the non-linear medium. As this effect is intensity dependant, a heuristic intensity dependent phase-

mismatch has been introduced, $\Delta \mathbf{k} = \xi \mathbf{I}$, which also includes the limited length of coherence caused by the divergence of the laser beam, as well as the angular and thermal deviations of the crystal compared to its position of ideal phase match.

The fit results give $d_{eff} = 4.1\ 10^{-23}\ AsV^{-2}$, $\xi = 8.54\ 10^{-5}$ m/W. The non-linear coefficient d_{eff} is in good agreement with manufacturers data and theoretical values which typically are on the range between $1.93\ 10^{-23}$ and $4.63\ 10^{-23}$ AsV^{-2}). The heuristic phase match parameter of $\xi = 8.54\ 10^{-5}$ m/W indicates that for our configuration (l = 1 cm), a phase mismatch of $\Delta\phi = 0.425$ is introduced at an intensity of 1 MW/cm^2. We suspect that the origin of this phase mismatch could be of thermal nature, but have no evidence at the moment on the detailed mechanism.

Damages:

The optical damage threshold in the non-linear materials ultimately limits the second harmonic generation efficiency with long pulse lasers. This damage is due to the high intensity involved in the non-linear process, and the damage threshold is significantly lower with long pulses than with Q-switch pulses with nano-seconds time duration. The phenomenon is essentially of statistical nature and in our domain of long pulses duration, the crystals suffered of thermally induced fracture on its output face.

The damage is defined as any visible change in the laser-irradiated site by measurement of the transmitted light. In our case, all damages are catastrophic pertinent and occur in KTP with the presence of a plasma and a acoustic sound emission. Coated and uncoated crystals show within fluctuations related to the statistical nature of the damage process, the same damage threshold. There is also no evidence that the AR coating has any influence on the damage threshold.

Different non-linear materials show different threshold intensities at which the damage occurs, these thresholds depend also on the manufacturers. With the exception of $LiNbO_3$, all the other crystals were damaged at the output surface. We noticed that the threshold for surface damage is lower than for bulk material damage and damage is produced only in the presence of generated green light[3]-[4]. As shown in figure 4, the intensity and the pulse duration of the generated green light were the most important parameter for evaluating the damage threshold. Although the $LiNbO_3$ has an exceptionally high non-linear coefficient, it was eliminated, due to its low optical bulk damage threshold.

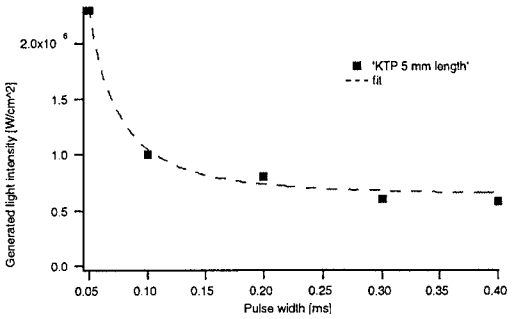


Fig. 4: Optical damage versus pulse duration and green light

Results:

Figure 5 shows the best conversion efficiency and the power of the second harmonic wavelength as a function of the incident fundamental intensity we obtained with a 15 mm length KTP crystal. During our experiments, we obtain approximately the same efficiency for SHG with KTP and LBO crystals. The maximum second harmonic conversion efficiency we obtained without optical damage with a 15 mm long crystal was of 14.6 % with LBO and 17.4 % with KTP. This allows us to obtain up to 145 W of instantaneous power and pulses energies at $\tau_p = 200$ µs of respectively 32.4 mJ and 29.0 mJ, but at different input conditions.

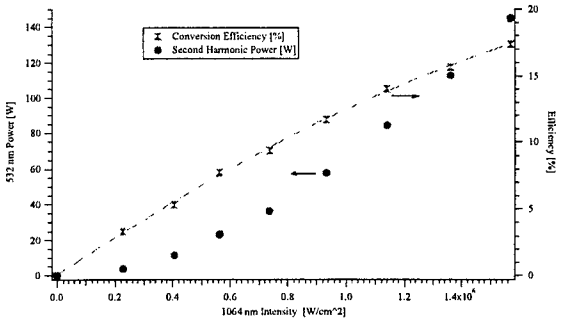


Fig. 5. Conversion efficiency and second harmonic power versus Intensity for 15 mm length KTP crystal

In both cases, longer crystals could not increase the efficiency, the length being ultimately limited by the walk-off effect[2] for KTP and the beam divergence for LBO.

With such second harmonic pulse energies, we was able to process materials up to 300 µm thick with a kerf width down to 15 µm for fine sheets. These conditions allowed us to cut with high precision micro-grippers in memory shape alloy as shown in figure 6 and 7, which are used in robotics manipulation of micro-lens of 200 µm diameter.

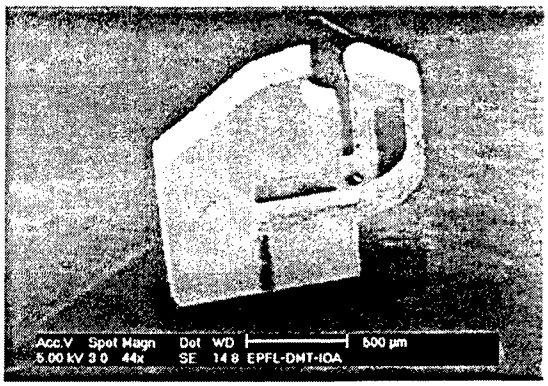


Fig 6. Micro-gripper

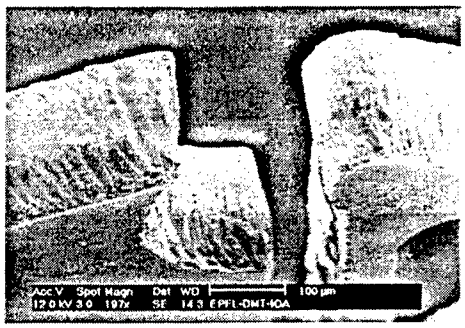


Fig 7. Detail of the roughness

Conclusions:

A maximum conversion efficiency of 14.6 % has been obtained with 15 mm long KTP crystal and 17.4 % with a 15 mm long LBO crystal.

The conversion efficiency as a function of intensity shows a sublinear behavior with respect to the ideal phase matched case at intensities above 1 MW/cm^2.

For long pulse frequency doubling of 200 µs in KTP crystals with Nd:YAG laser, catastrophic optical damage appears at approximately 1 MW/cm^2 for second harmonic intensity and no evidence has been found that the damage threshold originates from the antireflex coating of the crystals.

References:

[1] W. Koechner, "Nonlinear Device" in Solid-State Laser Engineering, 4th edition, E.D. Springer-Verlag, chap. 10, 1996

[2] J.P. Fève, B. Boulanger and G. Marnier, "Experimental Study of Walk-off Attenuation for type II SHG in KTP", IEEE Journal of Quantum electronics, Vol 31, N° 8, 1995.

[3] R. Blachman, P.F. Bordui, M.M Fejer, "Laser-induced photochromic damage in KTP", Appl. Phys. Lett. 64 (11), 1994.

[4] R. Blachman, P.F: Bordui, M.M Fejer, "Laser-induced photochromic damage in potassium titanyl phosphate", *Appl. Phys. Lett*, Vol 64, N° 11, March 94, pp. 1318 - 1320

Efficient high-pulse-energy green beam generation by intracavity-frequency-doubling of a quasi-cw laser-diode-pumped Nd:YAG laser

Susumu Konno, Yoko Inoue, Tetsuo Kojima, Shuichi Fujikawa, and Koji Yasui

Advanced Technology R&D Center, Mitsubishi Electric Corporation
8-1-1 Tsukaguchi, Amagasaki, Hyogo 661-8661,Japan
Tel:81(Japan)-6-6497-7110,Fax:81(Japan)-6-6497-7288
E-mail: konno@lap.crl.melco.co.jp

50-mJ green and 12-mJ UV pulse beam were generated at 1-kHz repetition rate. Intracavity-frequency-doubling of a quasi-cw laser-diode-pumped Nd:YAG laser was used as a green beam source. CLBO($CsLiB_6O_{10}$) crystal was used for 4th harmonic generation.

Key Words: Laser diode, SHG, FHG, Quasi-cw, Intracavity-frequency-doubling

1. Introduction

With the recent development of high power laser diodes and high quality frequency conversion crystals, various high average power green beam sources were developed based on intracavity-doubled diode-pumped Q-switched Nd:YAG lasers[1-3]. In industrial applications, intracavity-doubling scheme is advantageous because of it's high efficiency. Although high pulse energy green beam sources has been demanded in both scientific and industrial fields, pulse energies of intracavity-doubled Nd:YAG lasers were limited less than 20mJ/pulse. Since, upper state lifetime of Nd:YAG crystal is too short for efficient generation of Q-switched pulse at low repetition rate. Quasi-cw pumping is one of the most promising approach to overcome this problem.

Solid-state UV lasers are akso attractive in the field of precision material processing applications. Fourth harmonics of IR solid-state lasers have potential market in the field of electronic circuit boad processing, because of it's high absorption coefficient for various polymers.

In this work, we report an intracavity doubled diode-pumped Nd:YAG laser, with 50-mJ 532-nm beam, at 5.4% electrical-to-optical conversion efficiency, at a repetition rate of 1kHz. We also obtained 12mJ 4th harmonic beam with a CLBO ($CsLiB_6O_{10}$) crystal. Diffusive reflector pumping configuration was used for efficient pumping. Quasi-cw diode pumping was used for efficient generation of high pulse energy Q-switched IR beam at 1kHz repetition rate.

2. Experiment

2.1 Second harmonic generation

Figure1 shows the schematic cross section view of the pump module[4]. The pump module contains sixteen quasi-cw laser diodes (60W peak power) and employs a diffusive reflector[4]. The laser-diodes are operated at 1kHz repetition rate with 200-μs-long pulse width. In Fig.1, we show the resonator configuration used for the green beam generation.

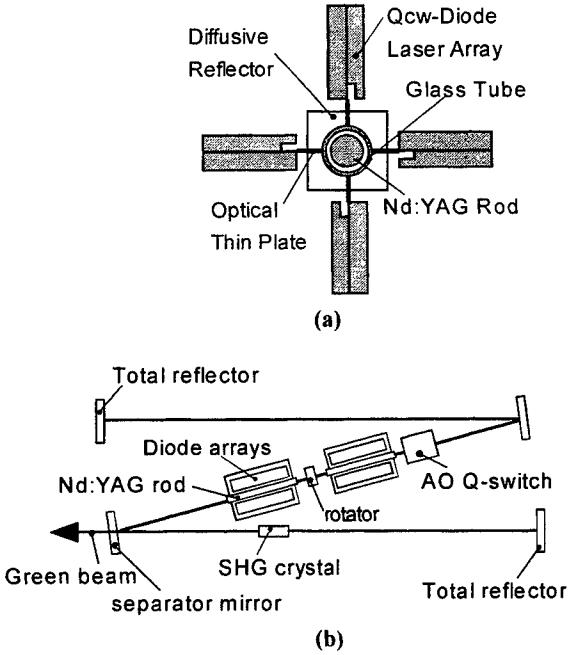


Fig.1 Schematical view of the **(a)**pump module, and **(b)**Resonator configuration.

The 2.8-m-long z-shaped resonator was folded by a harmonic separator mirror and a total reflector. An acousto-optical Q-switch was placed in the resonator for Q-switching

First International Symposium on Laser Precision Microfabrication, Isamu Miyamoto, Koji Sugioka,
Thomas W. Sigmon, Editors, Proceedings of SPIE Vol. 4088 (2000) © 2000 SPIE · 0277-786X/00/$15.00

operation. An SHG crystal (LBO(LiB_3O_5)) was placed in one arm of the resonator for the second harmonic generation. The green beam was extracted in one direction from the harmonic separator mirror.

In Fig.2, we compare the laser performances of Q-switched IR(T=40%) and Q-switched SHG operation.

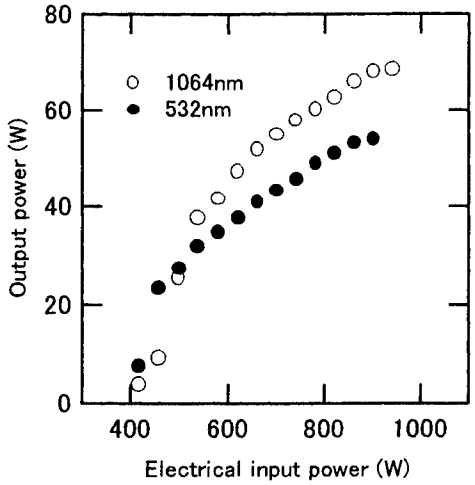


Fig.2 Q-switched SHG and IR output power.

The laser was operated at 1kHz repetition rate. The maximum green average output power of 53W was obtained at 880W total electrical input power into the laser diodes, corresponding to the maximum green pulse energy of 53-mJ, and the electrical efficiency of 6%. The ratio of the green output to the Q-switched IR output is more than 80%. The estimated beam quality was M^2=10.

2.2 Fourth harmonic generation

We also demonstrated fourth harmonic generation of the 50-mJ,1-kHz green laser. The experimental setup is shown in Fig.3. The green beam extracted from the green laser is focused into a 15mm long type-I CLBO crystal by a lens. The CLBO crystal was used at 140 degree. Generated 4th harmonic beam was separated from the green beam with two separator mirrors as shown in fig.3 [6].

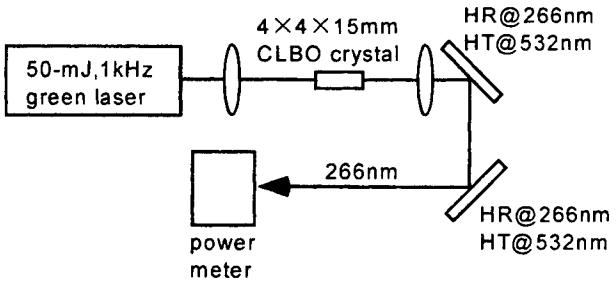


Fig.3 Experimental setup for 4th harmonic generation.

We show the UV output power as a function of the incident green power in Fig,4. The maximum UV output power of 12W was obtained with green incident power of 40W, corresponding to the conversion efficiency of 30%.

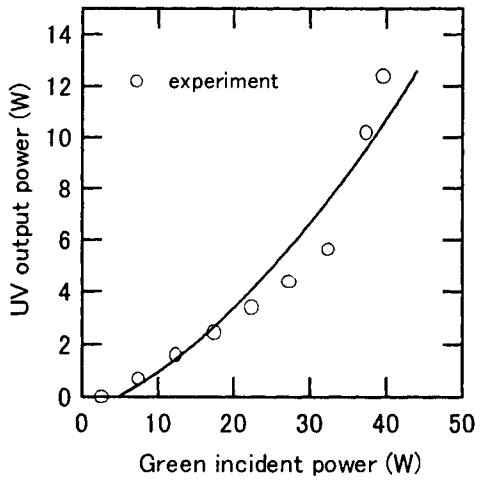


Fig. 4 UV output power as a function of green incident power.

3. Summary

We have enhanced the electrical efficiency of a high-pulse-energy green laser by intracavity frequency doubling of a quasi-cw laser-diode pumped Nd:YAG laser. The highest green pulse energy of 53mJ was generated at a repetition rate of 1kHz, with 5.4% electrical efficiency. We have shown that the electrical efficiency of high-pulse-energy green laser systems could be enhanced to be comparable with those of conventional high-repetition, intracavity-doubled green lasers.

References

[1] Jim J.Chang, Ernie P. Dragon,Chris A. Ebbers, Isaac L. Bass, and Curt W. Cochran, Digest of Conference on Advanced Solid State Lasers, (Optical Society of America, Washington D.C., (1997),p.300

[2] S.Konno, T.Kojima, S.Fujikawa, and K.Yasui, Opt.Lett.**25**,105-107 (2000).

[3] B.J Le Garrec, G.J. Raze and M.Gilbert, Opt.Lett.**21**,1990-1992 (1996).

[4] S.Fujikawa, T.Kojima, and K.Yasui, J. sel. Topics Quantum Electron. vol.3,No.1,40-44 (1997).

[5] K.Yasui, Appl.Opt.**35**, 2566-2569 (1996).

[6] T.Kojima, S.Konno, S.Fujikawa, K.Yasui, K.Yoshizawa, Y.Mori, T.Sasaki, M.Tanaka, and Y.Okada, Opt.Lett.**25**, 58-60 (2000).

Ultrafast Fiber Lasers: Alternative Light Sources for Industrial Material Processing

Gregg SUCHA and Heinrich ENDERT

IMRA, America, Inc. , 1044 Woodridge Ave., Ann Arbor, MI 48105, USA
E-mail: hendert@imra.com ; gsucha@imra.com

The development of ultrashort pulse laser technology will have a strong impact on the advancement of laser machining. Ultrashort laser pulses can reduce the heat-affected zone and the shock-affected zone, resulting in much cleaner cuts, and therefore higher precision. However, acceptance of ultrafast technology is hindered by the cost and complexity of ultrafast lasers. In this paper, we describe recent progress in fiber-based ultrafast laser technology which promises to be sufficiently rugged and low-cost to enter the industrial arena. We also discuss results of micromachining using a sub-nanosecond laser pulses from a new Yb:fiber-based laser system.

Keywords: micromachining, femtosecond, ultrafast, fiber laser, ablation, cladding-pumped

1 Introduction

A growing number of industrial laser users are becoming interested in using ultrashort laser pulses for specialized commercial applications ranging from micromachining and materials processing, to high-performance instrumentation and metrology. "Ultrashort" or "ultrafast" pulses are incredibly short bursts of laser energy, lasting only about 1 picosecond (10^{-12} sec) or less. These pulses are many thousands of times faster than pulses from conventional industrial lasers, which commonly generate nanosecond pulsewidths. Because they are so fast, ultrashort pulses have unique capabilities, enabling applications which simply cannot be done with the present generation of industrial lasers. For example, ultrashort laser pulses have the ability to cleanly ablate any material with a minimum of thermal or shock damage to the surrounding material. In many cases, this results in cleaner cuts when compared with other lasers.

Ultrafast fiber lasers, promise to revolutionize micromachining. The higher precision, reduced heat-affected zone (HAZ) and reduced shock-affected zone (SAZ), are all by now well documented.[1] In spite of these possibilities, ultrafast lasers have not yet been widely adopted into the micromachining industry. This is true despite the fact that ultrafast lasers which can perform micromachining have been commercially available for several years. The reason for this lag in acceptance is the high cost and complexity of ultrfast laser systems. The systems are very complex, requiring a highly-trained operator; and they are also very susceptible to environmental conditions, requiring frequent adjustment. These current generations of ultrafast lasers simply are not suitable for use on the factory floor, unlike current generations of design-hardened industrial lasers.

With the promise of improvements in micromachining, there is great incentive to develop new generations of femtosecond technology which will be compact, robust, low-mainenance, and easy to operate. High-power fiber laser technology is considered as a prime candidate for transforming ultrafast lasers from a scientific tool into an industrial tool. Indeed, such systems have already been produced at the low-power end—ultrafast fiber laser systems are now commercially available which are compact, turnkey, and require no maintenance. These are penetrating into OEM markets, which was unthinkable a few years ago.

2 High power fiber lasers

Fiber lasers are similar to their solid-state counterparts in many ways. As with solid-state lasers such as Nd:YAG, optical fibers can be doped with impurities such as Neodymium (Nd), Erbium (Er), or Ytterbium (Yb), which provide optical gain when pumped by a light source (e.g., laser diodes). However, doped-fibers provide certain advantages over solid-state laser crystals. First of all, fibers are flexible and can be rolled up into a tight space or spooled, making it possible to construct fiber lasers in a very compact package. Another advantage is that the laser light is confined to the core of the fiber, providing a well-controlled beam shape. Also, thermal management is easier because the long, thin fiber has much more surface area per unit volume than a bulk laser crystal. Finally, many kinds

First International Symposium on Laser Precision Microfabrication, Isamu Miyamoto, Koji Sugioka, Thomas W. Sigmon, Editors, Proceedings of SPIE Vol. 4088 (2000) © 2000 SPIE · 0277-786X/00/$15.00

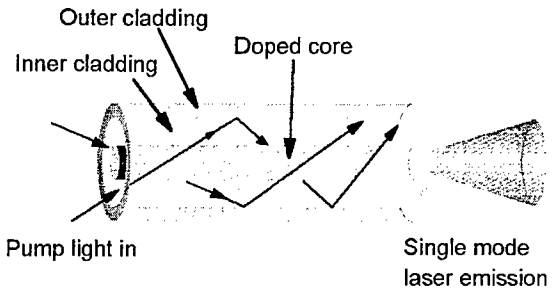


Figure 1. Double-clad fibers make it possible to launch 10's of watts of optical power from inexpensive, broad-strip diodes. (see Ref. 2)

of fiber optic devices are rugged enough for difficult applications (for example, even deployment in harsh undersea conditions in telecommunications cables). These features have made fiber lasers useful in a number of industrial applications outside of telecommunciations such as thermal printing, marking, and materials processing.

Fiber lasers have had a reputation for being low in power compared with solid-state lasers. This was due to the fact that previous generations of fiber lasers required single-mode pumping; and single-mode pump diodes are limited in power to only a few hundred milliwatts. In the last few years however, fiber lasers with much higher output powers have been developed and are being offered as commercial products. The breakthroughs in higher power have come thanks to a variety of developments. The first breakthough is the technique of cladding pumping. As shown in Figure 1, double-clad fibers are designed to provide single-mode waveguiding in the core (for the signal) and multimode waveguiding in the inner cladding (for the pump).[2] This structure makes it possible to use high-power diode bars and arrays as pump sources, which can provide 100's of Watts of pump light. Cladding pumped fiber lasers are capable of generating significant amounts of power, especially when using highly efficient Yb-doped fibers. Researchers have recently demonstrated that they can obtain over 100 Watts of CW power from a Yb-doped fiber laser.[3]

In another major technological development, researchers have been able to scale up the fiber core diameter from the standard 8 microns up to 25, 50, and even 100 microns. This in turn, facilitates scaling up the output power by many times. By careful design, even these large-core, multimode fibers can transmit optical pulses in only a single transverse mode,[4] giving high quality beam profiles, which are essential for precision applications such as micromachining. In addition to high average powers, high pulse energies can also be obtained. Researchers have recently shown that they can design Q-switched fiber lasers which produce up to 3 millijoules of energy in a 100 ns pulse, making them comparable in performance to industrial Q-switched YAG lasers.[5] The peak power levels generated by these lasers (~50 kW) are limited by the damage threshold of the fiber.



Figure 2. CVD diamond cut using a 750ps fiber-amplified, microchip laser. Note the absence of graphitization in areas surrounding the cut.

Large-core fibers have enabled a new generation of short pulse lasers which operate in the sub-nanosecond regime. At IMRA America (Ann Arbor, MI) researchers have amplified pulses from a Q-switched microchip laser in a large-core Ytterbium-doped fiber. The output pulses (250 microjoules, sub-ns duration) are interesting for different micromachining applications, and actually give superior processing performance with tested materials. This system depends critically on new, proprietary technology,

developed at IMRA, to protect the fiber from the very high peak power levels (>300 kW) which would otherwise damage it. It also depends on propagating the pulse in a single mode in the large core fiber. Figure 2 shows the result of cutting a square hole in a thin CVD diamond substrate using 800 ps pulses from this laser system.[6] The amount of graphitization surrounding the cut is greatly reduced compared with conventional Q-switched YAG lasers.

3 Ultrafast fiber lasers

Fiber lasers are well-suited to ultrafast applications as they have a large amplification bandwidth, so that they can also be mode-locked to generate ultrashort pulses. In commercial systems, Erbium-doped fibers serve as the gain medium for ultrafast fiber lasers, providing short pulses at wavelengths near 1560 nm, and in some cases at the second harmonic, 780 nm. These simple systems have output powers ranging from 10's to 100's of milliwatts. In one particularly rugged design (IMRA Femtolite) single-mode diode pumping and polarization control result in highly stable operation, even with a change in environmental temperature of a ±15° C, which is a much larger range than for most ultrafast lasers.

It is possible to obtain higher average powers from ultrafast fiber lasers by using Yb-doped fiber, due to the higher gain and higher power efficiency. To take advantage of Yb:fiber, the wavelength of the ultrashort pulses must lie somewhere in the wavelength range of 1030-1060 nm. This can be accomplished by Raman shifting the pulses from an Er:fiber laser from 1560 nm out to near 2100 nm, and then frequency doubling in a nonlinear crystal of periodically poled Lithium niobate (PPLN). These pulses are then injected into a length of Yb:fiber, and are amplified to average power levels of 0.5-1.0 Watts, which makes this comparable to solid-state ultrafast laser systems.[7]

Scaling up the power for ultrafast fiber lasers beyond this level is not quite so simple. Because ultrashort laser pulses have such high peak powers (10's of Megawatts), nonlinear optical effects in the fiber's core can "shred" an optical pulse, resulting in very distorted pulse profiles with ringing, pedestal, and prepulse, if the system is not designed properly. These effects can wipe out many of the advantages provided by clean, ultrashort optical pulses. Therefore special techniques are required to overcome the problems which are unique to amplifying high-power ultrashort pulses. The most commonly employed technique is chirped pulse amplification (CPA). Here, a short pulse is stretched in time (by a factor of ~1000) to lower the peak power. After being amplified, the pulse is recompressed to its original length of less than 1 ps. This has been applied in solid-state, ultrafast lasers for several years. The CPA technique can also be applied to ultrafast fiber lasers in which a stretched pulse is amplified in a gain fiber and then recompressed to very short duration. Lasers systems based on this technique (see Fig. 4) afford tremendous flexibility

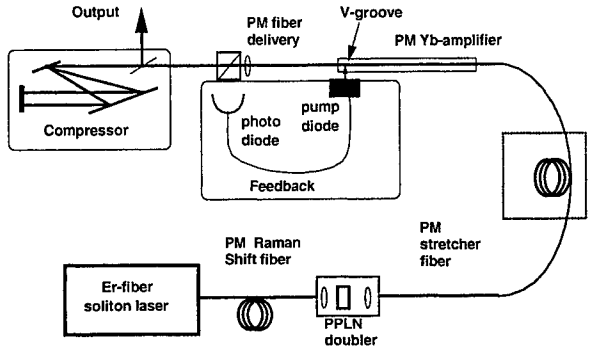


Figure 3. Ultrashort pulses at 1550 nm from an Er:fiber laser can be Raman-shifted, and then frequency-doubled to 1030 or 1064 nm, making them compatible with Yb- or Nd-doped amplifiers. After amplification in a cladding-pumped Yb-doped fiber, the output power is about 0.5-1.0 Watts.

in terms of repetition frequency (1 Hz to 1 MHz) and pulse energy. At the "low" end of repetition rate scale, FCPA systms are capable of producing energies of 100 microjoules, at repetition rates of 5 kHz, with pulsewidths of 250 fs.[8] At the high end, they have been shown to generate up to 13 Watts of average power at 50 MHz.[9]

Another promising new technique is parametric chirped pulse amplification (PCPA), which uses a parametric amplifier pumped by a fiber-amplified microchip laser (Figure 5).[10] The parametric amplifier crystal consists of Periodically-poled Lithium Niobate (PPLN) which provides very high nonlinearity and engineerable phase matching. One of the chief advantages of this system is that the parametric amplification produces very high gain (~80 db) in a single stage, thus eliminating the need for complex multi-stage, or multi-pass amplification. Such systems can provide 10's of microjoules, and appear to be scalable to 100's of microjoules, using the pump-source desribed earlier (i.e., a Yb-fiber amplified microchip laser).

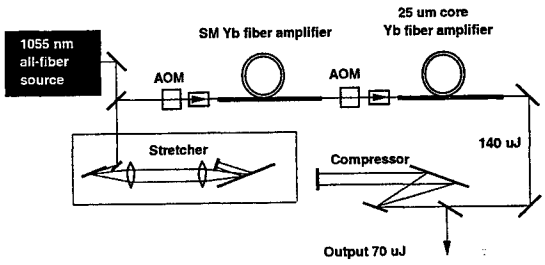


Figure 4. Ultrafast FCPA laser system using 1055 nm all-fiber source, and large-core Yb:fiber amplifier in the last stage. Pulse energies of 100 microjoules are generated.

Additionally, by adding a solid-state amplifier to the pump source, as shown in Figure 5, the PPLN crystal can be pumped with several millijoules of energy.[11] In this configuration, the PCPA systerm produces pulses with over 1 mJ of energy, and duration of 1.5 ps.

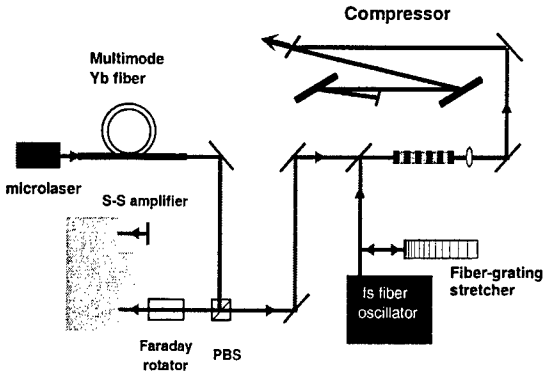


Figure 5. Parametric chirped pulse amplification (PCPA) provides high gain in a single stage. Pumped by mJ pulses from an amplified microchip laser, and injected by a femtosecond fiber laser oscillator, the system can be built very compactly, and provide millijoules of pulse energy.

4 Summary

Recent advances in fiber-based laser technology show promise as industrial laser systems of the future. In contrast to early technology, current fiber lasers can generate 10's of watts of average power; while 100 W lasers, and even kilowatt fiber lasers are under development.

In addition to CW fiber laser applications, the combination of fiber technology with ultrafast laser techniques is creating completely new application opportunities, which will qualify the ultrafast laser world for real industrial solutions. In particular, it is now becoming increasingly clear that ultrafast laser technology would be a valuable tool in various industries such as microelectronics, automotive, textiles, telecommunications, and medical device manufacturing. In spite of nearly 1000 installed scientific ultrafast amplified systems worldwide, and the great promise of ultrafast lasers though, industrial customers are only beginning to pay attention. The main "show-stoppers" are the complexity, size, and fragility of most ultrafast lasers, and the need for a specialist to operate them. However, due to the fiber-based architecture, ultrafast fiber lasers can be shrunk and put in packages of reasonable size. Clearly, advances are being made to make ultrafast lasers rugged, compact, reliable, and easy to use. Fiber-based laser technology, with its many advantages, is one of the new promising alternatives to solid-state lasers.

[1] P. S. Banks, et al., "Femtosecond micromachining," *Conference on Lasers and Electro-optics (CLEO),* San Francisco, CA, paper CFD-2 (1998).

[2] G. Sucha and H. Endert, "Fiber lasers have advantages," *Industrial Laser Solutions,* Jan. 2000.

[3] V. Dominic, et al., "110 W fiber laser," *Conference of Lasers and Electro-optics (CLEO),* Baltimore, MD, paper CPD-11 (1999).

[4] M. E. Fermann, "Single-mode excitation of multimode fibers with ultrashort pulses," *Opt. Lett.*, **23**, 52 (1998).

[5] H. L. Offerhaus, et al., "Multi-mJ, mulit-Watt Q-switched fiber laser," *Conference on Lasers and Electro-optics (CLEO),* Baltimore, MD, paper CPD-12 (1999).

[6] N. H. Rizvi, P. T. Rumsby, M. C. Gower, "Laser Micromachining -- New Developments and Applications," *Proc. SPIE*, Vol. 3933, Photonics West, San Jose, CA, (2000).

[7] M. E. Fermann, M. L. Stock, A. Galvanauskas, A. Hariharan, G. Sucha, D. Harter, and L. Goldberg, "Highly efficient low-noise Yb femtosecond fiber laser," *Conference on Lasers and Electro-optics (CLEO),* San Francisco, CA, paper CMQ2 (2000).

[8] G. C. Cho, et al., "100 microjoule and 5.5 Watt Yb-fiber femtosecond chirped pulse amplifier system," *Conference on Lasers and Electro-optics (CLEO),* San Francisco, CA, paper CMW2 (2000).

[9] A. Galvanauskas, M. E. Fermann, "13-W average power ultrafast fiber laser," *Conference on Lasers and Electro-optics (CLEO),* San Francisco, CA, paper CPD3, (2000).

[10] A. Galvanauskas, et al, "Parametric chirped pulse microamplifier based on engineerable quasi-phase-matched $LiNbO_3$," *Ultrafast Phenomena XI*, Springer Series in Chemical Physics, Vol 63, Springer-Verlag, Berlin, 1998, p. 60.

[11] A. Galvanauskas, A. Hariharan, and D. J. Harter, "Diode pumped parametric chirped pulse amplification system with mJ output energies," *Ultrafast Phenomena XII,* (accepted).

Evaluation of characteristics of VUV optical materials irradiated by F_2 Laser

Yasuo ITAKURA, Fumika YOSHIDA, Youichi KAWASA, Akira SUMITANI, Osamu WAKABAYASHI and Hakaru MIZOGUCHI

Research Center, Research Division, Komatsu Ltd., 1200 Manda, Hiratsuka, Kanagawa 254-8567, Japan
E-mail: yasuo_itakura@komatsu.co.jp

The F_2 Laser (wavelength 157nm) is becoming the most promising candidate of light source for next generation optical micro-lithography below the 100nm-technology node. We have developed VUV optics evaluation system, which is able to measure the transmittance between DUV and VUV region right after laser irradiation and the temporal transmittance during 157nm-laser irradiation. This system structured by Ni-plated Aluminum and stainless steal. The inside of chamber is purged any laser light absorption gas away with high purity nitrogen gas during the irradiation. Using this system, we can measure the characteristics of the irradiated sample without exposing to the air or other contamination sources. So this system had $\pm 0.5\%$ accuracy result in repeated measurement. In the in-situ transmittance measure system, the transmittance can be monitored during F_2 laser irradiation. And we evaluated characteristics of VUV optical materials in the early period of F_2 laser irradiation by this in-situ transmittance measure system.

Key words: F_2 Laser, VUV optics, transmittance

1. Introduction

The semiconductor lithography technology keeps being made minutely, and is accelerating rapidly. According to achieving of the design rule of 100nm or less and making to high throughput, the light source for lithography is demanded to make higher repeatability and to make shorter wavelength. F_2 laser (wavelength 157nm) lithography has emerged recently as a candidate of post-ArF excimer laser lithography. As peripheral technology, the optical materials used in this wavelength are demanded to be with high permeability and durability. To develop optical materials operatively, the evaluation at realistic condition is indispensable. Comprehensive research and development related to 157-nm optical materials evaluation has been done by SEMATECH and MIT Lincoln Laboratory.[1] Komatsu started F_2 laser research in 1997 and proved the technical feasibility of 800Hz operation in 1998.[2] In 1999, we got a research fund from MITI and succeeded in developing of 2000Hz 14W F_2 laser.

However, it is not yet clear how the laser characteristics relate to the radiation damage of materials.

The purpose of this research is to examine how the laser characteristics, such as power density, repetition rate and pulse profile influence the VUV optical materials.

In this work, we present an evaluation system to determine the transmittance of calcium fluoride substrates and the coatings as well.

2. Apparatus

The F_2 laser oscillation device was developed, and the evaluation system of optical materials used in the laser was constructed.

The VUV optical materials evaluation system consists of four units: a F_2 laser, a real time monitoring in-situ transmittance measurement unit, an in-situ VUV spectrophotometer, and a high precision VUV

First International Symposium on Laser Precision Microfabrication, Isamu Miyamoto, Koji Sugioka, Thomas W. Sigmon, Editors, Proceedings of SPIE Vol. 4088 (2000) © 2000 SPIE · 0277-786X/00/$15.00

spectrophotometer. Figure 1 shows the construction of the system. F_2 laser can be operated with 14W@2000Hz at 30kV and with a total gas pressure of 4200hPa. Real time monitoring in-situ transmittance measurement unit consists of a vacuum chambers system, F_2 laser light deliver optics, F_2 laser pulse energy sensors and a sample transfer stage.

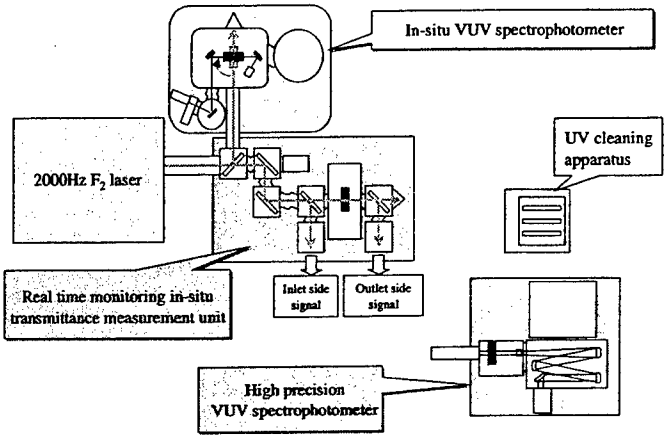


Fig.1 VUV optical materials evaluation system

The vacuum chambers system keeps chamber pressure at about 100hPa by high purity nitrogen gas and vacuum pump during irradiation. This system structured by Ni-plated Aluminum and stainless steal. F_2 laser light deliver optics leads the laser light to the sample with two total reflection mirrors. Part of the pulse energy is sent to the energy sensor by setting up the CaF_2 substrate before and behind the sample to be irradiated. SXUV photodiodes made by the IRD inc. was used as the energy sensor. By using short-pass filter, the energy sensor detected every pulse energy without extra red light. The sample transfer stage is set up for moving the sample in the chamber without exposing to atmosphere.

This unit showed $\pm 2\%$ repeated stability.

In-situ VUV spectrophotometer has a structure which enable us to measure the sample directly after the irradiation without atmosphere exposition. In the spectrophotometer part, the range of the wave length which can be measured is 130-300nm due to the light source with D_2 lamp. The angle of incidence to the sample of the inspection light was set to 0° for transmittance, and 7.5° for reflectivity. In-situ VUV spectrophotometer showed $\pm 0.5\%$ repeated stability.

In high precision VUV spectrophotometer, transmittance in 157.6nm can be measured in $\pm 0.1\%$ repeated stability.

The range of the wave length which can be measured is 120-200nm in the vacuum(2.7×10^{-3}Pa) by the light source with D_2 lamp. The preprocessing is important in the optical material evaluation. The UV cleaning apparatus was introduced as a pretreatment equipment because more important when evaluate optics at highly accuracy.

3. Results and discussion

3.1. Transmittance measurement of no court substrate

Because of the high photon energy (E=7.9eV), crystal materials such as calcium fluoride should be used as optical materials for F_2 laser. As for this calcium fluoride, various grades are being put out by lots of makers, and the laser tolerance is greatly different according to the manufacturing method and mixed impurities. The transmittance of excimer grade calcium fluoride substrates provided by different makers was measured by real time monitoring in-situ transmittance measurement unit. The result is shown in Figure 2.

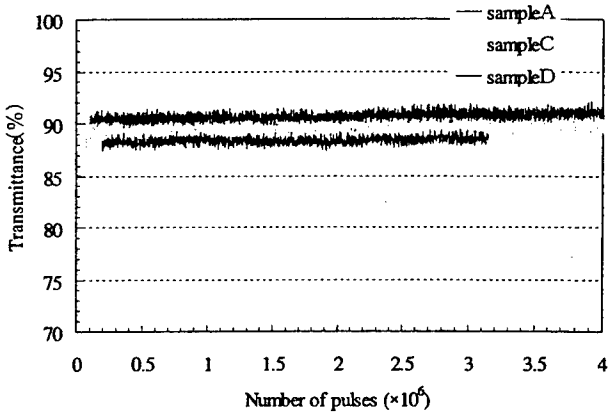


Fig.2 CaF_2 in-situ 157nm transmittance

Theoretical transmittance of the calcium fluoride substrate in 157.6mn is 90.7%(NIST data used). Substrate A showed almost similar to the theoretical value, substrate C showed a value of 89.5% and substrates D showed a value of 88.5%. We recognized that the difference in transmittance existed between substrates in the state before irradiation. The decrease in transmittance caused by 4Mpls F_2 laser irradiation was not observed.

The spectrum transmittance characteristic evaluation of the no court calcium fluoride substrate was also executed with the in-situ VUV spectrophotometer. Figure 3 shows the

spectrum transmittance characteristic before and after the F_2 laser irradiation of each substrate. It become clear that the difference of transmittance characteristic of each substrate in the wavelength area shorter than 190nm was initial existent already. Substrate D suffered most from the irradiation. Transmittance supposed in each case after F_2 laser irradiation. It is guessed that substrate D has a character different from substrate A and B.

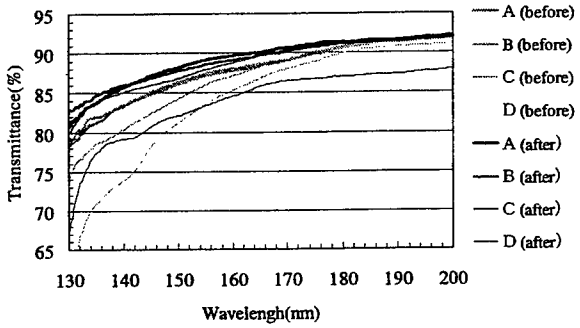


Fig.3 VUV transmittance of CaF_2 substrates from different makers.

In addition, the substrate coating with a partial reflection film of 30% was measured. The spectrum transmittance before and after the F_2 laser irradiation was investigated with the in-situ spectrophotometer. Figure 4 shows the spectrum transmittance characteristic.

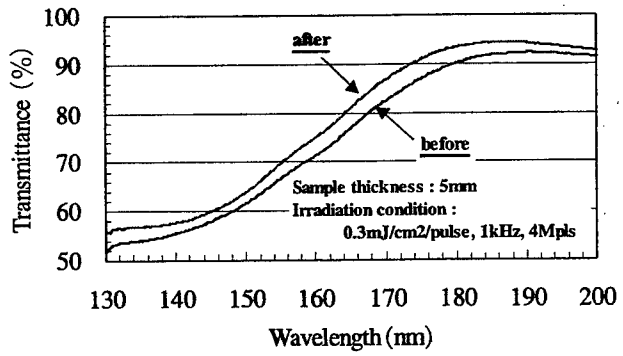


Fig.4 VUV transmittance of coating substrate

It was observed that the transmittance increased 3% or more with the F_2 laser irradiation. 30 minutes later, a decrease in transmittance of about 0.5% was found it keep the substrate remain inside with N_2. This shows that transmittance of the coating substrate changes in a very short time compared with the no court substrate, and it is more sensitive to the environment than the no court substrate. In other words, the surface state of a coating substrate is of greater responsive than a no court substrate and exists adsorb moisture and organism in atmosphere easily. Reflectivity decreased by about 1% after laser irradiation. About this phenomenon, the thickness of the coating film changes as a result of laser irradiation, and it is possible to read to a decrease in reflection characteristic.

3.2. Cleaning effect

Transmittance of optical materials are also greatly influenced by the preprocessing. It is notable that the influence by the difference of the preprocessing is also responsible for the transmittance loss by the irradiation described above. Thus, the effect of cleaning was evaluated to various no court substrate transmittance with the high precision VUV spectrophotometer. Three kinds of cleaning method (wiping with methanol, UV cleaning and the F_2 laser irradiation) was tested. The results are shown in Figure 5.

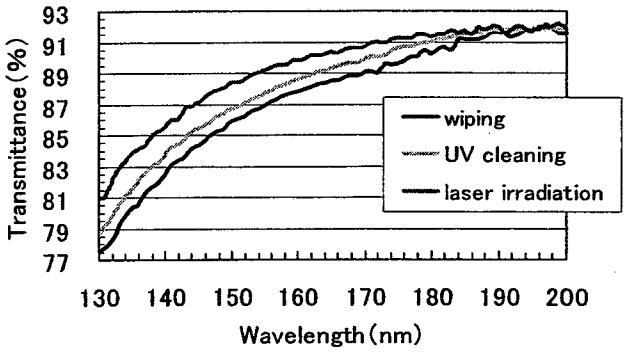


Fig.5 Cleaning effect by each cleaning methods for sample A

Table Cleaning effect by each cleaning methods for sample A

	Transmittance(%)
wiping	87.5
UV cleaning	88.2
laser irradiation	89.7

The transmittance rise due to us irradiation was confirmed in 157.6nm though the effect of the UV cleaning was hardly

seen in 193.4nm (ArF laser wavelength). This result showed that the methanol wiping has little cleaning effect of in the wavelength area shorter than 190nm. It is suggested that using methanol and paper might pollute the substrate surface. As for substrate transmittance in 157.6nm, it was shown that the result of further rise was obtained, and F_2 laser irradiation was the most effective one. According to the result mentioned above, UV cleaning is insufficient to do an accurate evaluation of an optical material for the F_2 laser. It became clear that the cleaning by F_2 laser light irradiation is indispensable to evaluate an optical material for F_2 laser accurately.

4. Conclusion

A new VUV optical materials evaluation system was developed. The system consists of a latest F_2 laser, a real time monitoring in-situ transmittance measurement unit, an in-situ VUV spectrophotometer, and a high precision VUV spectrophotometer.

For CaF_2 substrates, transmittances were measured directly after the 157nm laser irradiation. Transmittances at 157nm varied clearly with each CaF_2 samples. Since samples may be affected by atmosphere contaminates, therefore in-situ measurement system is indispensable.

High precision VUV spectrophotometer was used to examine the cleaning effect of optical surfaces due to the F_2 laser irradiation. According to the different cleaning methods test, transmittances arranged in a order of methanol wipe < UV cleaning < F_2 laser irradiation. The F_2 laser irradiation turned out to be the most effective method as a measurement preprocessing.

5. Acknowledgment

This work was performed under the management of Association of Super-Advanced Electronics Technologies (ASET) in the Ministry of International Trade and Industry (MITI) Program of Advanced Semiconductor Equipment Technology supported by New Energy and Industrial Technology Development Organization (NEDO).

References

[1] M. Rothchild and A. K. Bates 157nm Lithography workshop, 63, (1999)

[2] S. Nagai et al. Extended abstracts(The 46th spring meeting,1999);The Japan society of applied physics and related societies, p740,28p-YB-5

Laser processing system for micro drilling of printed circuit boards

Junichi Nishimae, Yukio Satoh, Tetsuo Kojima, Tsukasa Fukushima*

Advanced Technology R&D Center, Mitsubishi Electric Corporation,
8-1-1 Tsukagichi-Honmachi, Amagasaki, Hyogo, Japan
E-mail: nishimae@lap.crl.melco.co.jp
**Nagoya Works, Mitsubishi Electric Corporation, 5-1-14 Yata-Minami, Higashiku, Nagoya, Aichi, Japan*

Two laser processing systems for micro drilling of printed circuit boards and/or LSI packages are presented. One is a pulsed CO2 laser system and the other is a LD-pumped THG-YAG laser system, both are now commercially available.

Keywords: micro drilling, printed circuit board, package, CO2 laser, LD pumped YAG, THG

1. Introduction

Today, there is a large market for high-performance and miniaturized electronics such as mobile phone. The market demand has driven the development of high-density mounting technology such as Build-up Multi-layer (BUM) printed circuit boards, Chip Size Packaging (CSP) of LSI and so on. Over the past few years, several kinds of laser processing system have been adopted to drill a large number of small size micro-via or through holes on the substrates for BUM and/or CSP.

The excimer laser forms micro-holes of very good quality, because its short pulse causes less thermal damage to the substrate [1]. However, the photon cost of the laser is too high for mass production. The TEA-CO2 laser also forms micro-holes of good quality and the photon cost is bearable [2]. However, its pulse repetition rate is insufficient to recent high-speed scanners, so the throughput with flexible scanning optics is limited relatively low. Near infrared and visible laser does not match with the spectral absorption of the major materials of the substrates. Thus, the mainstream of the present laser micro-drilling system employs a pulsed CO2 laser of high repetition rate and a flexible high-speed scanning optics.

We have developed a unique CO2 laser micro-drilling system. The CO2 laser operates at high repetition rate up to 4kHz and emits gain-switching short pulses like a TEA-CO2 laser, so that the system can provide both the high-quality processing and high throughput. In the case of a CO2 laser system, the minimum size of the micro-hole is limited to several tens of microns by diffraction. The increasing demand for higher density requires a reliable high-power UV source of low photon cost. We have been developing a LD pumped Nd:YAG laser with frequency conversion technique for the UV source.

This paper presents the pulsed CO2 laser micro-drilling system and the LD pumped THG-YAG laser system, both are now commercially available.

2. Light source

2.1 CO2 laser

Figure1 shows the schematic construction of the CO2 laser. The optical axis, the gas flow direction and the discharge are perpendicular to each other. The transverse gas flow replaces the active medium for each pulse, which ensures the pulse operation at high-repetition rate free from any thermal hysteresis. High-frequency high voltage is applied to the electrodes covered with glass. The excitation discharge through dielectric insulator is maintained stably even at high power density and high-repetition rate.

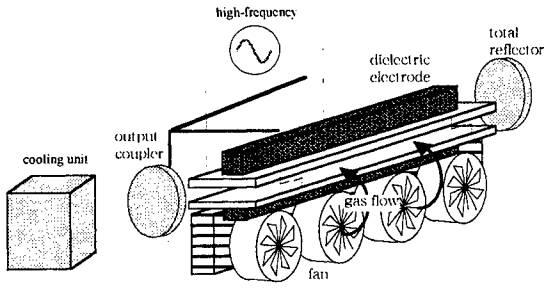


Fig. 1 Schematic construction of the CO2 laser

The discharge power through dielectric insulator is proportional to the carrier frequency of the applied voltage, so we have developed a direct switching 2MHz MOS-FET inverter for the power supply [3]. Since the inverter does not use a transformer, the inductance of the discharge circuit is so low that high power discharge (applied voltage 6kV, peak current 60A) is achieved.

First International Symposium on Laser Precision Microfabrication, Isamu Miyamoto, Koji Sugioka,
Thomas W. Sigmon, Editors, Proceedings of SPIE Vol. 4088 (2000) © 2000 SPIE · 0277-786X/00/$15.00

The basic specification of the laser is shown in table1. The rated repetition frequency is 4kHz. Figure2 shows the schematic pulse profile of the laser. By controlling the discharge duration, the laser emits variety of pulses from 400ns gain switched pulse to 15μs quasi-cw flat top pulse. This unique feature enables the laser to form high-quality micro-holes on various substrates with high throughput.

Table 1 Specification

carrier freq.	2MHz
wave length	9.3μm
transvers mode	TEM00
average output	100W
pulse energy	100mJ
pulse duration	1~15μs
repetition freq.	4kHz

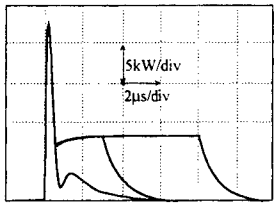


Fig. 2 Schematic pulse profile

2.2 LD pumped YAG laser

Figure3 shows the schematic configuration of the LD-pumped THG-YAG laser utilizing frequency conversion technique. The YAG rod converts the LD pump power to 1.064μm IR, the SHG crystal converts the IR to 532nm green power and finally the THG crystal mixes the IR and green power into 355nm UV power. Figure4 shows the cross-section of the pumping module. The laser diodes (LD) are closely coupled to the pumping cavity having diffusely reflecting inner surface [4]. This configuration provides a compact pumping module and ensures efficient and uniform excitation of the YAG rod. Because of the efficient and uniform excitation, high output power of good beam quality is stably obtained.

An acousto-optical Q-switch was used for Q-switching operation. Average UV output power of 5W is obtained at a repetition rate of 5kHz. The oscillating transverse mode is a low order multi-mode.

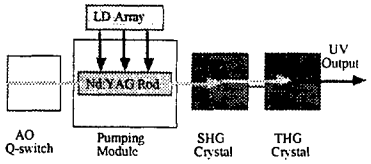


Fig.3 Schematic configuration of LD-pumped THG-YAG laser

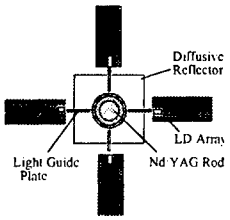


Fig.4 Cross-section of pumping module

3. System performance

Figure5 shows the schematic configuration of the laser micro-drilling system. The laser beam emitted by the oscillator illuminates the pinhole mask, then the processing lens forms an image of the pinhole onto the work-piece (substrate). Double axis scan mirrors shift the position of the image rapidly up to 1000points/s. The scanning area is limited by the view angle of the processing lens typically 50mm x 50mm square. The work-piece is placed on the fast and precise mechanical table with vacuum chuck, and then repetitive step and scans process the whole work-piece. A microscopic CCD digital video camera with an efficient image-processing unit is equipped for alignment and process optimization. Loader and unloader units for automatic processing are available. The PC/NC controller installed with a friendly user-interface supervises the whole system.

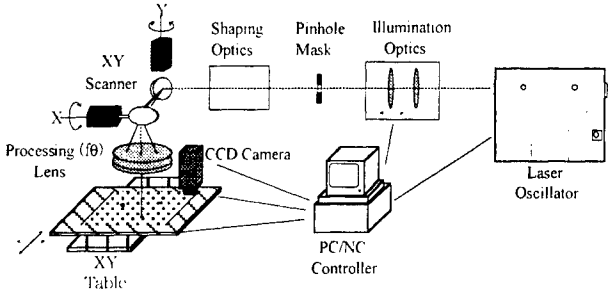


Fig.5 Schematic configuration of laser micro-drilling system

Figure6 is a photograph of the laser micro-drilling system. The CO2 laser system and the UV-YAG laser system have almost the same external appearance except for the oscillator. Both systems are now commercially available as our product. sFigure7 shows the cross-section of a sample micro-via formed by the CO2 laser system. The material of the substrate is glass-epoxy (FR4), the thickness of the substrate is 50μm, and the diameter of the via-hole is 100μm. It is shown that a smooth side-wall is formed in a composite material with little thermal damage.

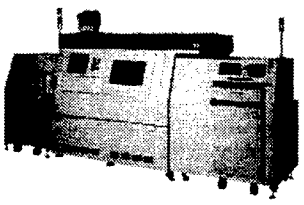


Fig.6 Appearance of laser micro -drilling system



Fig.7 Cross-section of micro-via formed by CO2 laser

When the diameter of the micro-hole is relatively large (>100μm), the CO2 laser system is favorable. The focusing ability of the CO2 laser is good enough to form a micro-hole of diameter larger then 100μm. In the process of large holes, high power and high pulse energy is required to achieve high throughput. On the other hand, the UV-YAG laser system is favorable to the process of small holes (<50μm). The

process of small holes does not require so high power or energy but good focusing ability of the light source. So the UV-YAG laser is promising as a light source for micro-drilling system of next generation.

We have developed and keep on developing both the CO2 and UV-YAG laser processing system for micro-drilling of printed circuit boards utilizing our original laser technology, control & information technology and so on. The laser micro-drilling system will be an indispensable tool for future industry.

References

[1] T.Yamamoto et.al., Proc. ICALEO '97, vol. 83f Section E-31, Nov. 17-20 (1997)

[2] J. Morrison, IPC Printed Circuits Expo, S15-3 March 9-13, (1997)

[3] 岩田,他, 電気学会研究会資料, EDD-98-88 (1998)

[4] S.Fujikawa, T.Kojima, and K.Yasui, J. sel. Topics Quantum Electron. vol.3,No.1,40-44 (1997).

Development of the enhanced concurrent in-line inspection system for CO_2 laser drilling machine

Hideaki NAGATOSHI*, Kazuhide ISAJI*, Tsutomu SUGIYAMA*,
Hidehiko KARASAKI* and Makoto KATO**

* Matsushita Industrial Equipment Co., Ltd.,
3-1-1 Inazu-cho, Toyonaka, Osaka 561-0854, Japan
** Advanced Technology Research lab. of Matsushita Electric Industrial Co., Ltd.,
3-10-1 Higashimita, Tama-ku, Kawasaki 214-8501, Japan

Summary

The performance of the concurrent in-line inspection system in CO_2 laser drilling process has improved by the defect pattern estimation algorithm. The optical detection principle of the system is based on the relationship between the reflected laser intensity from the bottom copper foil in via-hole and the area size of the exposed copper surface.

The principle and the advantage of the enhanced concurrent inspection system was described. Using the improved concurrent inspection system, the etched hole diameter and defect of PWB can be examined. This function has a capability to substitute AOI function. As a result, reliability and throughput in PWB drilling process has been improved.

Keywords: in-line inspection, CO_2 laser, drilling, PWB, AOI, via-hole

1. Introduction

The high-density interconnection technology, especially using BGA (ball grid array), CSP (chip size package) and MCM (Multi-chip module), was led to manufacture light-weight and high-performance electric products such as cellular phones. For example in personal cellular phone, ASIC-CPU and RAM/ROM IC's, data bus-lines were designed with precision spacing rule and located at the second layer using interstitial via-hole. For IMT-2000 cellular phone, the number of the data bus-lines and the pincount of the ASIC-CPU will be estimated double and triple of a current model, respectively. As a result, the density of via-hole will increase more and more. Therefore, reliability and throughput in drilling process will become more important performance for PWB manufacturing.

In 1998, we developed the CO_2 laser via drilling machine with the concurrent in-line inspection monitoring using in-process monitoring technology [1-4]. This machine had the unique designed optical system, using telecentric scan lens, galvanometric scanners and the concurrent in-line inspection system. And this inspection system, which was worked by the polarization of laser light, had the capability of estimating the bottom area of exposed copper foil in the drilling process at real time. In 1999, the CO_2 laser drilling system was improved by process feedback system, named "Active control" [5]. Active control system was realized the improvement of the throughput over 25% in drilling process for glass-cored epoxy substrates.

In this paper, the capability of the enhanced concurrent in-line inspection system to substitute the AOI (automatic optical inspection) function was described.

2. Principle of concurrent in-line inspection system

2.1 Outline of principle

Buildup multilayer PWB has a structure with inner layer copper foil. The via-hole processing is a former process to connect the inner layer copper foil with the surface. According to CO_2 laser drilling process progresses, the copper foil of the inner layer is gradually exposed. The reflected light from the inner layer copper foil is intensified with increasing in the area of the exposed copper foil. Using this result, the concurrent in-line inspection system is executed the hole inspection simultaneously with the drilling process [1].

Figure 1 shows the relation between changing of the processed hole diameter, and the measured intensity of the reflected laser light. In Fig. 1, the relation between intensity of reflected light and the processed hole diameter is almost linear proportional relation. Therefore, using to the

First International Symposium on Laser Precision Microfabrication, Isamu Miyamoto, Koji Sugioka, Thomas W. Sigmon, Editors, Proceedings of SPIE Vol. 4088 (2000) © 2000 SPIE · 0277-786X/00/$15.00

measurement of the reflected light intensity, the concurrent inspection system can be estimated the processing hole diameter.

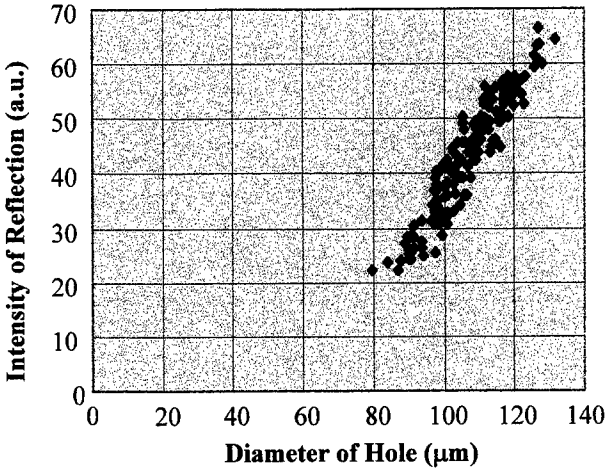


Fig. 1 Reflected intensity and diameter of via-holes

2.2 System configuration

The concurrent in-line inspection system is composed of the optical isolation unit to separate out incident light for drilling PWB and the reflected light from the PWB, the optical sensor to detect the incident light, the optical sensor to detect the reflected light, and some optical components. Figure 2 shows the schematic diagram of the basic optical system [1].

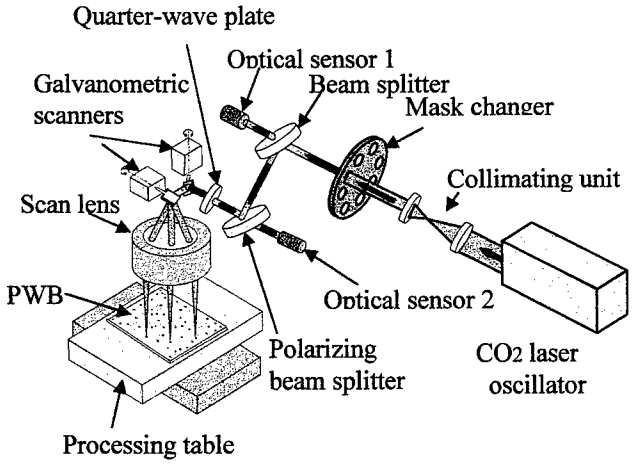


Fig.2 Schematic diagram of optical systems

The output laser light from CO_2 laser oscillator is shaped and optimized according to the processing hole diameter by the collimating unit and the mask changer. The laser light is passed to the beam splitters and the quarter-wave plate. After that, the laser light to be irradiated to the PWB is positioned by the galvanometric scanners and the scan lens, and the PWB is drilled.

The reflected laser light from the PWB is detected by the optical sensor 2. Moreover, a part of the incident light is led to the optical sensor 1 and detected.

When the concurrent in-line inspection system inspects the hole, the following various compensation processing are carried out to improve the detection accuracy of the incident light and the reflected light.

First, in this system, the intensity of both the reflected light and the incident light are detected, and the reflected light is normalized by the incident light. This process compensates the CO_2 laser output variation. Secondly, the deviation of the reflected light intensity at the each position in the scanning area is compensated. Thirdly, the optical sensor to detect the laser light intensity is heated by the laser light led to the sensor, and the gain drift and 0 drift appear to the output signal. The change in the sensor power output caused by the sensor temperature of optical sensors and surrounding temperature is compensated.

In order to drill the designed hole diameter, we can decide the threshold value which related the hole diameter based on the reflected light intensity data compensated by the mentioned contents.

3. Algorithm for defect pattern estimation

3.1 Outline

Two methods of via-hole processing in the buildup PWB are well known. The first one (conformal mask method) is the method that the PWB is adhered the copper foil to the surface, many etched holes are patterned to the surface copper foil, and the hole is drilled by irradiating laser light to removed position. The second method (image mask method) is the method of irradiating the laser light directly to the resin on the surface of the PWB.

The concurrent in-line inspection system estimates the diameter of the bottom of the hole in the via-hole processing. However, for the conformal mask method, the irradiated laser light is partially reflected from the copper foil on the surface. Then, it is thought that the etched hole diameter and the location accuracy of the etched hole can be estimated by measuring the reflected light intensity from the copper foil on the surface.

3.2 Experiment

In the experiment, the optical system shown in Fig. 2 was used for measuring the reflected light intensity. In PWB for experiment, four kinds of hole diameters, 60, 120, 160 and 220 μm, were prepared. There were 2000 holes for one of etched hole diameters. The laser light of one pulse per one hole was irradiated and the reflected light intensity from the conformal mask was measured. All etched hole on PWB was similarly measured. In addition, as assuming the case without the hole, the laser light was irradiated one pulse to the place without etched hole, and measuring the reflected light was repeated for 2000 times.

As measurement result, the reflected light distribution is shown in Fig. 3. The reflected light intensity is shown in the

horizontal axis, the detection frequency was shown in the vertical axis.

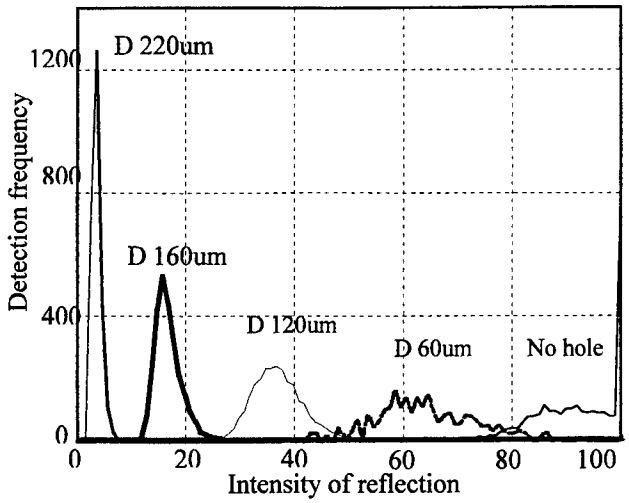


Fig. 3 Relationship of intensity of reflection and frequency

In the case of large etched hole diameter, irradiated laser light is absorbed almost at the resin of the etched hole. Therefore, the reflected light intensity is weak. In the case of small etched hole diameter, irradiated laser light is not absorbed almost at the resin of the etched hole. Therefore, the reflected light intensity is strong. In the case of no hole, irradiated laser light is reflected from the surface copper foil on the PWB.

In next, the change of reflected light intensity from via-hole was measured increasing the number of laser pulse. It is shown in Fig. 4. The reflected light is intensified with increase in the number of laser pulse. The reflected light intensity of the first pulse depends on the etched hole diameter, as shown in Fig. 3. The reflected light intensity is intensified by increasing the bottom area of the inner layer copper foil with plural laser pulse irradiations.

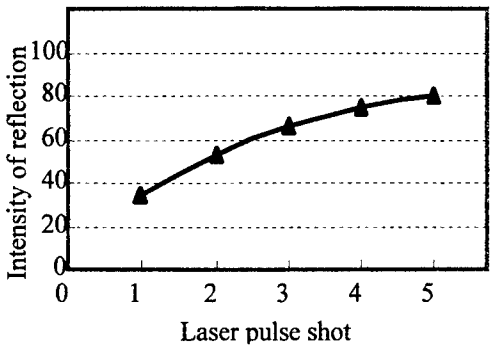


Fig. 4 Transition of reflected light intensity

3.3 Algorithm

To examine the etched hole diameter and defect of PWB using the reflected light intensity, block diagram as shown in Fig. 5 were developed. The reflected light intensity detected with optical sensor 2 is calibrated with the temperature compensation data and the scanning position compensation data. Incident light intensity detected with optical sensor 1 is also calibrated with the temperature compensation data. After calibration process, the reflected light is normalized with incident light.

The diameter of etched hole is basically estimated by the normalized reflected light intensity shown in Fig. 1. However, an observed reflected light intensity has been diverged as shown in Fig. 3. Therefore, to estimate the etched hole diameter from the measured reflected light intensity, the upper bound and the lower bound of the reflected light intensity according to the hole diameter are set. The hole by which the reflected light intensity exceeds the upper bound or the lower bound is recorded as NG hole.

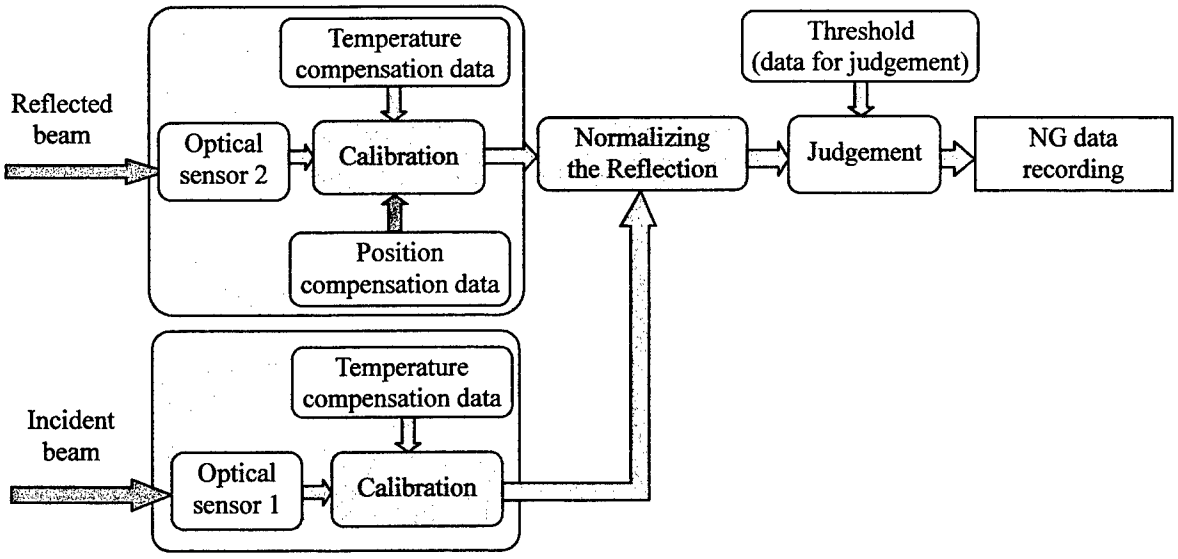


Fig. 5 Control block diagram of algorithm for defect pattern estimation

3.4 Defect pattern

There are many types of defects at etched hole of PWB.

The hole diameter which is smaller or larger than the designed etched hole diameter, is judged by comparing the reflected light intensity with the upper bound or lower bound. In the case of exceeding the upper bound threshold of the reflected light intensity, the etched hole diameter is smaller than the designed hole diameter. In the case of exceeding the lower bound threshold of the reflected light intensity, the etched hole diameter is larger than the designed hole diameter. "No hole" by mis-etching is easily detected.

In the case of misaligned etched hole from the right position, the irradiated laser light does not hit the etched hole and the intense reflected light is detected. That is similar to the small situation of the etched hole diameter.

Using the plural pulses, the misalignment of the inner layer copper foil can be detected. In the case of misaligned inner layer copper foil, the exposed bottom copper foil is small. Therefore, the change in the reflected light intensity become small compared with that of Fig. 4.

Defect patterns that can be detected with this system is shown in Fig. 6.

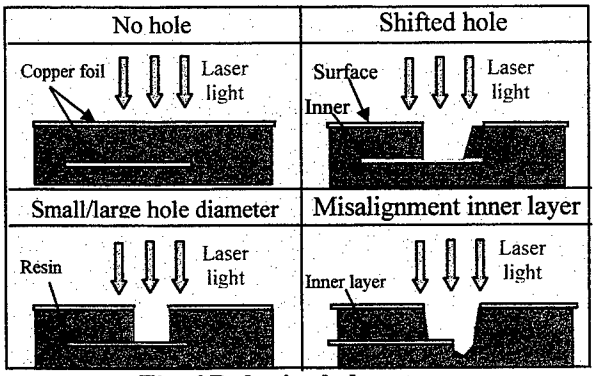


Fig. 6 Defective hole pattern

3.5 High throughput processing

As the above-mentioned, this concurrent in-line inspection system can work as laser drilling and inspection defective holes at the same time. Therefore, additional time for the inspection is ignored.

In the conventional via-hole processing, desmear process and hole inspection process by AOI are required after laser drilling. AOI process time is typically needed 40 seconds. However, in our system as shown in Fig. 7, only desmear process is required. As a result, tact time in the entire via-hole processing with using this system is shortened and the high throughput processing can be achieved.

The significance of our laser drilling machine, the AOI system is not required and tact time can be reduced, was confirmed.

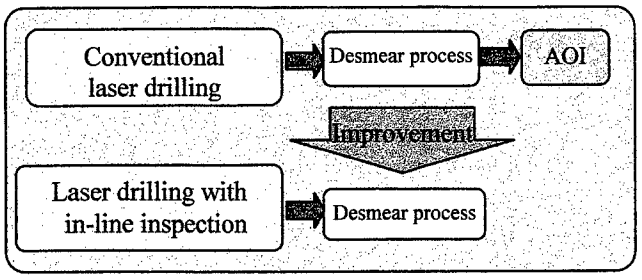


Fig. 7 Process of laser drilling and inspection

4. Conclusion

The improved concurrent in-line system was described. The optical detection principle of the system is based on the relationship between the reflected laser intensity from the bottom copper foil in via-hole and the area size of the exposed copper surface. The improvements were carried out by the development of algorithm for defect pattern estimation. Using the system, the etched hole diameter and misalignment could be detected. As a result, the capability of the enhanced concurrent in-line inspection system to substitute the AOI function was confirmed.

Reference

[1] H.Karasaki et. al.; ICALEO'98 proceedings G-50

[2] H.Karasaki et. al.; 5th Symposium on Micro-joining and Assembly Technology in Electronics '99 pp203-208

[3] H.Karasaki et. al; Proceedings of 45th laser material processing conference, JLPS, pp131-138

[4] M.Kato et. al.; Lase '99 Proceedings.

[5] K.Isaji et. al.; Electronic circuits world convention 8 proceedings. CD-ROM

Laser Micro Processing Unit and Its Application

Kenshi FUKUMITSU and Tomonori OIE

Electron Tube Division,#2,Hamamatsu Photonics K.K.
314-5,Shimokanzo,Toyooka-Village,Iwata-Gun,Shizuoka 438-0193,Japan
E-mail:fukumitu@etd.hpk.co.jp

This is the report for compact laser micro processing unit excimer laser emploied featuring very fine process with high accuracy.

This unit consists of objective lens, of which magnification is 10 to 80, used for both processing and observation. It makes possible high energy density resulting 0.5μm resolution at 248nm, accurate positioning and compact size.

Applications

1) Removing upper metal layer of LSI in order to inspect pattern of the bottom layer.
2) Creating fine geometrical pattern on PET fiber cloth in order to apply new function such as better dyeing and adhesiveness.
3) Creating 100μm dia. hole to artificial blood vessel made of polyurethane tube with 2mm inner dia. in order to have similar mechanical property to real blood vessel.

Keywords:exicimer laser,Microfabrication,LSI,PET,polyurethane

1. Introduction

Excimer Laser Micro Processing Unit features fine resolution in micron order level because the excimer laser emits high energy photon so that the processing is done by using abrasion phenomenon without generating heat. This unit is used for processing of PCB, machining of micro machine and so on. In fact, it is confirmed to process many kinds of material such as metal, resin and ceramics.

In the development of large processing unit for industrial use, large processing area and high frequency pulsing of laser have been main development points in order to get high throughput and low running cost. However, the miniaturization and fine processing were main development concepts of this unit. The "Excimer Laser Micro Processing Unit" having 0.5um resolution has been developed by redesigning optics and downsizing oscillator leading to the best ability of excimer laser. [1]

This report describes the construction and features of "Laser Micro Processing Unit C4540", which has separate laser oscilator from processing part, and "IC laser Ablator L5910", which has everything in one box. The application examples are also introduced.

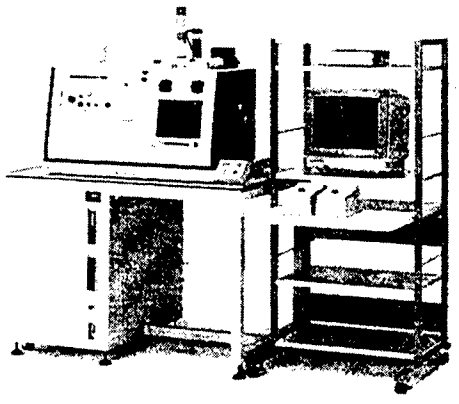


Fig.1 IC Micro Ablator L5910

First International Symposium on Laser Precision Microfabrication, Isamu Miyamoto, Koji Sugioka, Thomas W. Sigmon, Editors, Proceedings of SPIE Vol. 4088 (2000) © 2000 SPIE · 0277-786X/00/$15.00

2. Background of Development

Excimer laser radiates ultraviolet (UV) light from 193nm to 351nm, so that it can process with 0.5um resolution in theory. However, approximately 2um is the actual limit of existing unit because of the difficulty of optical design and selection of optical material in UV range. While the lithography system already has quarter micron resolution. In order to achieve same resolution with processing unit, the unit has been developed by looking at following points mainly:

1) Improvement of reduction projection lens.
2) Establishment of the technology for efficient radiation of laser.
3) Increasing laser energy density at process point.
4) Improvement of ease of use and establishment of safety.

Fig.1 shows appearance of "IC laser Ablation unit L5910"

3. Construction of the Unit

Fig.2 shows example of construction inside. The unit consists of following 6 blocks.

1) The beam shaping optics to optimize laser beam shape and power distribution.
2) The mask and adjustable slit to determine process pattern.
3) Projection lens to project mask pattern on the sample.
4) Multiple stage to adjust the process position of sample.
5) Microscope to adjust process point and to observe sample.
6) Controller for whole system including excimer laser oscillator and gas supplier.

The table 1 shows the each part consisted and its function. In order to get performance of the lens, the beam shaping optikal system has beam expander, homogenizer, attenuator and so on depending on the purpose of process. The lenticular is used for homogenizer because it can regulate the uniformity and beam shape at the same time. In order to achieve large adjustable range and high durability, the dielectric multi layer coating optics is used for attenuator.

The optical system is de-magnifying projection by mask imaging method. The reason of adopting mask-imaging method is that the pattern process is the majority of processing by excimer laser. The sample is irradiated by excimer laser beam, illumination light for mask and illumination light for observation. Finite optical system is adopted so that all of light are on the same axis. Thus, it is not necessary to use image formation lens .

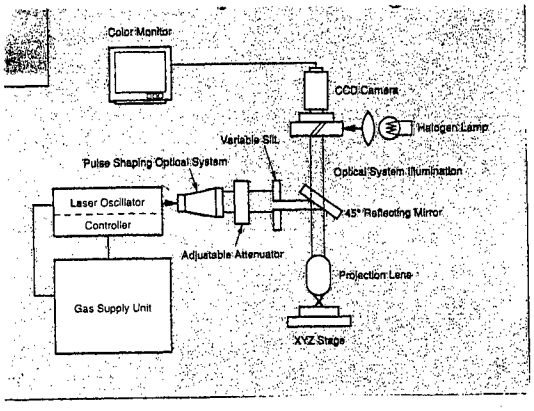


Fig2. Example of construction inside.

Table 1 Construction of Laser Micro Processing Unit

Part		Function
Processor	Beam shaping optics	Homogenize the laser beam and adjust divergence to de-magnifying lens.
	Mask	Select mask, which has processing pattern, or adjustable rectangular slit.
	Illumination of mask	Project mask pattern on sample with visible light and display it on the monitor.
	De-magnifying lens	De-magnify the mask pattern on the sample by mask imaging method.
	Multi axis stage	Align the sample to any desired position. It can be automated by combining with image processor.
Observation Part	Microscope Optics	Observe the sample through de-magnifying lens. Align the processing position and adjust the focus.
	Monitor for camera	Display the sample image taken by CCD camera on the monitor to show lines and for image processing.
Controller	Computer	Control the stage and laser oscillator. Picking up piston from the image and calculation for correction can be possible.
Gas Supplier	Supplier	Unit chassis and cabinet for gas cylinder of laser gas. It is controlled automatically.
	Safety	Gas leak detector, seismograph and anemometer are equipped.

4. Features

The greatest feature of this unit is high resolution. Table-2 shows basic characteristics of objective lens in excimer micro processing unit and magnification of the lens used in microscope for general use. There is a variety of magnifications from 10 to 80 times. The theoretical limit of resolution at 193nm is 0.15um and 0.15um resolution was actually achieved by test at 248nm. Similar resolution to microscope lens can be obtained at the around of processing area without distortion. The magnification of the observation optics including CCD camera to get the image on

the monitor is 7300 times maximum.

Color aberration is taken into account for these lenses so that the laser beam is also focused on if the processing part is in focus on the monitor. Besides, since the unit has illumination light for mask, mask pattern and its position is displayed on the monitor with bright visible light. Therefore, it is possible not only to align processing area but also to adjust the slit size on the monitor.

Table 2 De-magnifying lens for Excimer Laser

For Excimer Laser					For Microscope
Magnification	NA	Resolution (um)	Processing Resolution (um)	Working Distance (mm)	Magnification
					×5
×10	0.2	0.62	2	10	×10
					×20
×22	0.28	0.44	2	23	
					×40
×55	0.5	0.24	1	8	
×80	0.65	0.19	0.5	2	
					×100

- The resolution is the one when using KrF laser (248nm).
- Processing resolution differs at different material.

The accuracy of position is also important as well as that of processing so high magnification of observation system and laser beam alignment system are indispensable. They make possible automated position alignment by image processing.

The magnification of standard lens employed in "IC laser ablator L5910" is 55 times so the line width of mask pattern is 550um when processing with 10um line width. The mask with 550um line width can be easily made by etching metal. Besides, it is possible to keep energy density low at the mask so the mask made of organic material can be made by this unit. The necessary energy density at the processing part is determined by the material so the power of laser oscillator can be less than 1/30 when using 55 times lens compared with 10 times lens in order to get same energy density. With "IC laser ablation system", more than 30J/cm2 of energy density can be obtained from less than 10mJ laser.

Thus, the bigger magnification of lens gives an advantage not only for the ability of processing, but also for reliability of laser, damaging of mask, life time of optical parts and so on.

5. Applications

Here are three example of application using excimer laser micro processing unit.

Fig.-3 is the picture of LSI after removing upper metal pattern by IC laser ablator L5910. The upper metal pattern was taken away with the area of 30x30um after removing polyimide and 1um thickness SiN film. Then, middle metal layer was removed with 10x10um area to observe the bottom metal pattern. It can be clearly observed that there is no damage made to the bottom Al layer.

The LSI has laminate construction as shown on the figure and there are more than three layers even only for metal layer. The YAG laser cutter has been used for LSI analysis, however, IR laser doesn't have processing selectivity so it damages to lower pattern. Therefore, it can't be used for latest LSI processing, thus, the excimer laser is used because of good selectivity.

The technology to remove specified isolation layer or metal pattern layer in order has been strongly required for failure analysis of LSI. The excimer laser is widely used for advance treatment of prober, EB tester, emission microscope. [2] [3]

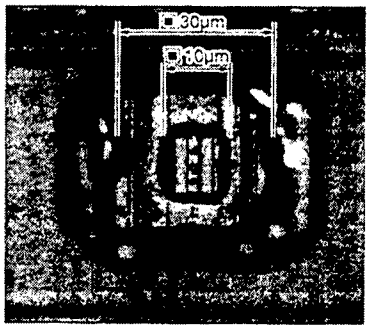


Fig.3 LSI after removing upper metal pattern.

Fig.-4 is the example of modified surface of PET fiber after the excimer laser (KrF) is irradiated. It is well known that irradiating laser modifies the surface structure of resin and creates geometrical pattern.[4] The purpose of tis experience is to develop the fabrics having new characteristics such as better dyeing and adhesiveness by irradiating laser to the fiber.

The size of micro structure such as groove or fold is 0.5-2um so the influence given when creating microstructure can be studied by irradiating excimer laser with same size as micro structure or a few times bigger to the one peace of approx. 20um dia fiber. It is believed that it helps to discover the mechanism of generating microstructure or boundary effect not only for fibers but also other resins.

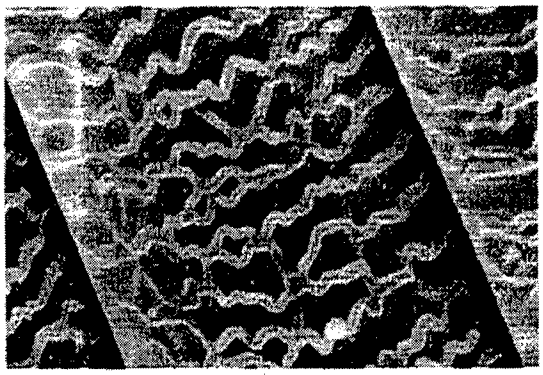


Fig.4 Typical example of irradiated PET surface

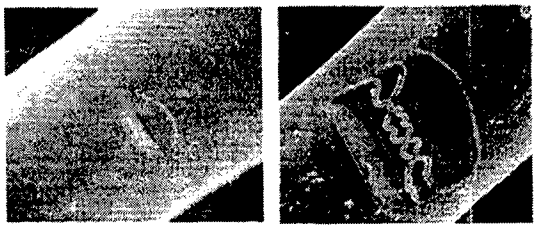


Fig.5 Example of small area irradiation

Fig.-6 is the example of processing of the polyurethane tube (2mm inner dia., 100um wall thickness), making 100um dia. micropores with 200um distance in between longitudinal axis and each 60deg, 30deg and 15deg angle to circumference, in order to create artificial vessel.[5] The micropores having sharp edge are lined up precisely. It is possible to modify mechanical characteristic of tube similar to that of real vessel.

In order to confirm the function of pores, the ingrowth of cell through pores has been observed as shown on Fig.-7 It is clearly seen endothelialization through 100um pores processed to 30um thickness polyurethane tube. Verification test for compliance match is now being fabricated.

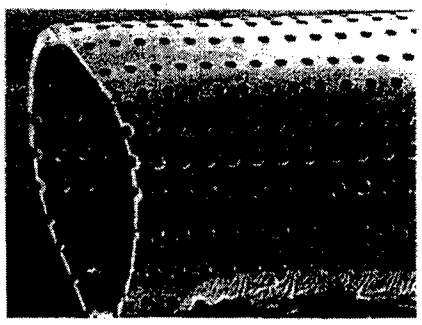


Fig.6 Example of processing of the polyurethane tube



Fig.7 The ingrowth of cell through pores

6. Ending

"IC laser ablation unit L5910" small excimer laser inside is a desk top size unit so it is easy to installation.

However, the processing the this unit features is being replaced by "IC ablator L7270", which employs ultra violet solid state laser oscillator, because it is now possible to achieve 3rd and 4th harmonics of solid state laser with good stability. Therefore, the excimer laser type is shifting to shorter wavelength model, ArF (193nm), for processing of glass or resin, which 193nm beam is required. Further more, development of KrF(157nm) model is being planned.

At the end, we thank to Dr.Y.Nakayama and Dr.K.Mizoguchi for the data of applications.

References

[1]T.Oie,T.Wakuda,and K.Fukumitsu:Reports on Topical Meeting of the Laser Society of Japan .,RTM-97-15,(1997)33-38

[2]T.Ueki,S.Nakamura,and Y.Komine:European Symposium on Reliability of Electron Devices,Failure Physics and Analysis(ESREF1999)

[3]T.Sekiguchi,K.Akagi,M.Yamawaki,N.Nakayama,T.Funatsu,and M.Harigaya;NEC Reports Vol.49 No3(1996)243-247

[4]K.Mizoguchi,S.Okubo,M.Ishikawa,A.Ouchi,Y.Koga,and T.Oie:Proceeding of Symposium on Process of Dyeing in Wakayama(1998)

[5]T.Matsuda,Y.Nakayama:Journal of Biomedical Materials Research,Vol.31(1996)235-242

Micro Materials Processing with High Power Diode Lasers

Friedrich BACHMANN*, Reiji TAKAHASHI**, Susumu FUJISHIMA**

* *ROFIN-SINAR Laser GmbH, Galileo-Galilei-Str. 10, D-55129 Mainz, Germany, e-mail: f_bachmann@compuserve.com*

** *ROFIN-Marubeni Laser K.K., Sun-Intelligent Building 4F, 3162 Sakai, Atsugi-shi, Kanagawa-ken, 243 Japan*

High power diode lasers gain considerable interest for materials processing applications, since they are very efficient, easy to use, reliable and almost service free. In contrast to conventional lasers, state-of-the-art high power diode lasers consist of a high number incoherently coupled individual semiconductor lasers, which are combined to one unit by use of semiconductor technology, micro-mechanics and micro-optics. A power range from 10 W until up to 8 kW can be covered. This paper describes the technology of diode lasers in the range between 30 and 150 W. The diode lasers have already successfully entered the industrial manufacturing area. As applications of lasers in this power range soldering and polymer welding are described in more detail.

Keywords: diode lasers, materials processing, micro processing, laser soldering, polymer welding

1. Introduction

Diode Lasers are widely used in communication, computer and consumer electronics technology. These applications are based on systems, which provide power in the milliwatt range. Since a few years high power diode laser systems are available, with a power range from a few ten watts up to several kilowatts. Their basis, however, are in principle still the milliwatt lasers mentioned above, which are integrated into a compact system and combined by semiconductor technology, as well as mechanical and optical micro-technology. In the low power range up to 150 W diode lasers can be used for micro materials processing, e.g. micro soldering or polymer welding, whereas for the classical laser materials processing area, e.g. surface treatment, welding or brazing laser systems up to 8 kW are offered on the market.

2. Diode Laser Technology [1], [2]

From a traditional diode laser element typically only a few milliwatts can be extracted from a pn-transition. To increase the power, several single elements are integrated into one semiconductor element, which has a size of about 10000 µm x 600 µm x 115 µm, where 600 µm is the resonator length in this case; this may be as long as 2 mm in todays high power lasers. This unit is called a "laser bar". The special shape of the light generation area leads to special light emitting characteristics, which shows a high divergence in the direction of the pn-transition ("fast axis"), and a lower divergence, but a wide emitting "stripe" in the pn-plane ("slow axis"), leads to a Gaussian profile in one direction and - at least theoretically - a top hat in the other. (for details see [1], [2])

Even if these laser bars show electrical to optical efficiencies of 40 to even above 50%, considerable amount of heat must be removed through the small footprint if power resp. current is increased further; therefore, the laser bar must be mounted onto a special water-cooled heat sink, which removes the excess heat and, thus, prevents the bar resp. the mirror facets from thermal destruction.

The fast axis light is collimated by cylindrical micro-lenses to get a parallel beam; the slow axis light can also be collected by micro-lens arrays or by sophisticated beam re-rangement concepts, e.g. a beam tilt unit [3] which is described in detail elsewhere [1].

For further increase of power, several of the assemblies consisting of the laser bar, the heat sink and the micro-optics for beam forming can be stacked on top of each other. In low power laser systems (see §3) only four or five assemblies are stacked to reach about 150 W with a good beam quality of ca. 50 to 80 mm mrad[1)], whereas for higher power up to 35 may be stacked on top of each other, delivering up to 1 kW from one stack, but at the expense of beam quality, which is typically in the range of 200 to 300 mm mrad in the multi-kilowatt-systems (see [1],[2]). Fig. 1 shows a unit, in which four heat-sinks and laser bars are stacked and the beam is formed to a quadratic shape by use of the beam tilt unit [3].

1) Since the Beam-Parameter-Product (BPP) is in most cases different in the slow and the fast axis direction (see above), these values correspond to the geometric average: $\langle BPP \rangle = \sqrt{BPP_{fast} * BPP_{slow}}$

First International Symposium on Laser Precision Microfabrication, Isamu Miyamoto, Koji Sugioka, Thomas W. Sigmon, Editors, Proceedings of SPIE Vol. 4088 (2000) © 2000 SPIE · 0277-786X/00/$15.00

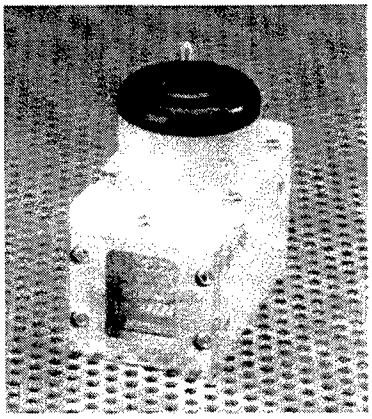


Fig. 1:
Stacked diodes with beam tilt unit (micro prism facettes are visible in the rectangular front window) and water absorber cartridge (cylindrical unit on top)
Foto: DILAS Diodenlaser GmbH

3. Diode Laser Systems for Micro Materials Processing

The basic unit shown in fig. 1 is integrated in diode laser systems which provide up to 150 W with a beam quality, which is sufficient for most precision micro materials processing applications. A typical system for industrial use is shown in fig. 2. The system delivers a spot with a size of 0,6 mm x 1,2 mm at a working distance of 84 mm. The laser head including the optical tubus is as small as 186 mm x 50 mm x 71 mm (length x width x height) and the weight is only 1,2 kg. Therefore, the laser head can be easily integrated into processing systems.

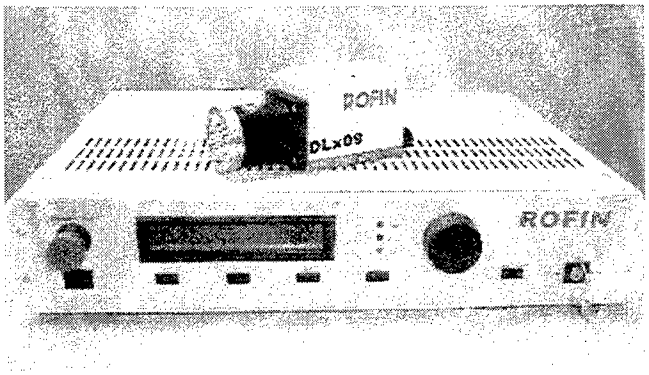


Fig. 2: Industrial diode laser system for micro materials processing up to 150 W (cooling unit is not shown)

For those applications, where the rectangular beam shape is disadvantageous or where the space is even too small for the above mentioned laser head, fibre coupled units are available. By special micro-optical components, e.g. the beam tilt unit [3], the emitting stripes of the diode laser bar can be rearranged in such a way, that a quadratic beam with identical divergencies in x- and y-direction is generated. Such a beam can be coupled into an optical fibre with a high efficiency. Fig. 3 shows a 30 W fibre coupled unit[2)] with a 400 µm diameter 0,22 N.A. step index fibre and working head, which will be described in more detail later.

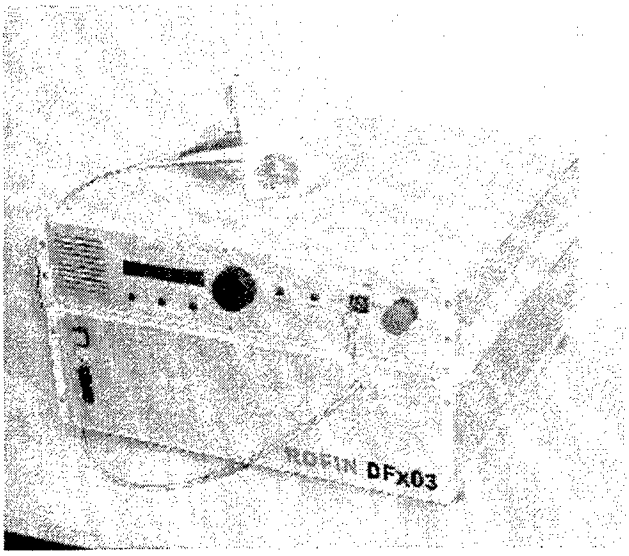


Fig 3: Fibre coupled table top diode laser system for micro materials processing (30 W; 400 µm diam. 0.22 NA SI-fibre)

The result of micro materials processing with lasers is in many cases sensitive to the laser power, which is absorbed from the work piece. The absorbed power, however, depends not only from the incident laser power, but also from the surface conditions, from the relative velocity of the work piece and the laser spot etc. Too high power for a fraction of a second may overheat the work piece for a short time and lead to a fatal damage of the part. To minimise such a risk an on-line control unit is offered for power control. This unit, which is shown in fig.4 consists of a pyrometer, which measures the thermal radiation from the irradiated surface as well as a camera for positioning and visual process control. The pyrometer signal, which is proportional to the temperature at the surface of the work piece is analysed by a computer and the result is fed back into a control loop for the laser power, so that the laser power will automatically reduced, if the temperature becomes too high and vice versa.

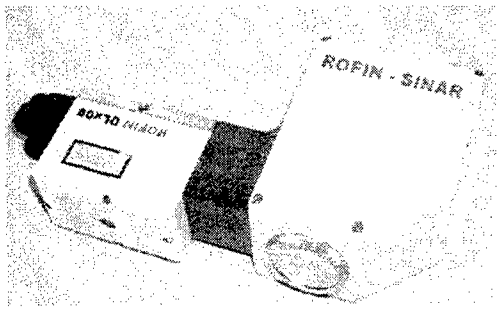


Fig. 4: Working head with a direct coupling to a 90 W (up to 150 W available) laser head; fibre coupling is also possible (see fig.3)

2) Financial support from the EC for the development of this system in frame of the BRITE-EURAM project "POLYWELD" (project number BE 97-4625 BRPR-CT98-0634) is gratefully acknowledged

4. Micro-Applications of Diode Lasers

4.1 Soldering

The miniaturisation of the electronic components, which leads to a higher pitch, i.e. distance and size of the connector leads are decreasing. Thus, for such components, which cannot be soldered by mass flow soldering technique e.g. for thermal reasons, manual soldering used so far becomes more and more difficult. Laser soldering as an alternative method has been developed several years ago in the early 80's, preferably using pulsed low power NdYAG lasers; laser soldering is advantageous over conventional soldering technologies, since it does not need any mechanical contact, provides a good accessability to tiny parts and is very good to control in terms of power and positioning; besides the dimensional reasons mentioned above, these features make laser soldering especially attractive, if components have to be soldered, which are sensible against electrostatic discharges (ESD) or sensitive against thermal load. However, the relatively high cost of operation and the rather large size of the NdYAG laser head prevented integration in existent soldering systems and thus large scale application so far. High power diode lasers in the power range of 30 to 150 W as described above rule out these disadvantages. The high efficiency and the long lifetime of the diodes[3] makes the high power diode laser a very attractive tool for soldering applications. Furthermore, the power of the diode laser can be controlled very accurately, much better than that is possible for the pulsed NdYAG laser; this can be used either by careful definition of a power track for the weld cycle, or - even more convenient - by pyrometer feedback control.

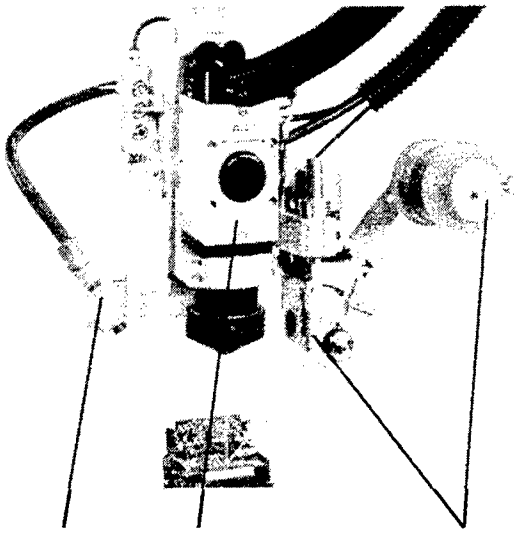


Fig. 5: Typical set-up for diode laser soldering [5];

A typical set-up of a commercially available soldering system is shown in Fig. 5 [5]. It consists of the diode laser, which is aligned to the solder pad, a wire feed system and - optionally - by a pyrometer for the measurement of the surface temperature in the solder region: in this photograph, an off-axis pyrometer is used, but on-axis integrated system, as described in section 3 is of course also possible.

4.2 Polymer Welding

Similar to laser soldering, polymer welding has been performed earlier by use of NdYAG or CO_2 lasers [6]. And also, the same is true as for soldering: The break through of this technique is going on by use of high power diode lasers!

Polymer materials are normally transparent in the near infrared spectral region, where high power diode lasers typically emit, but coloured and black polymers can absorb diode laser radiation. The thermo-mechanical behaviour of polymers, however, differs considerably from the behaviour of metals: whereas metals show a clear transition at certain temperature from the solid to the liquid state and from the liquid to the vapour phase, thermoplastic polymers start melting at so called glass temperature and slowly reduce viscosity with increasing temperature up to the melting point. At higher temperatures polymers rather start decomposing than they vaporise. Duroplastic or elastomeric materials normally do not show any softening behaviour when heated, but decomposition or charring, and thus, are not suited for laser welding. The viscosity of the heated polymers is still high compared to melted metals; moreover, thermal conductivity of polymers is much lower, than that of metals.

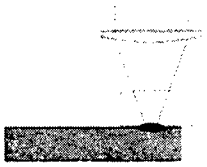


Fig. 6:
typical configuration for polymer welding [7]

For these reasons, the ideal configuration for polymer welding is the overlap weld of a layer, which is transparent for the laser and a layer, which is strongly absorbing (i.e. in a few tenths of a millimeter) the laser light, as is shown in the sketch in fig. 6: The laser radiation is absorbed in the bottom layer, which is heated beyond the glass and melting temperature, but of course not above decomposition temperature. The heat is then transferred by heat conduction from the absorbing layer to the non-absorbing layer, which thus, is also melted, if the melting temperatures are in the

3) Properly manufactured semiconductor elements typically do show degradation instead of sudden failure; therefore as a criterion for lifetime of diode lasers, the time after which the maximum specified output power has decreased by 20% is defined. Technically, the current is increased during this time to maintain output power. Under this definition today typical lifetimes exceed 10.000 hours. It must, however, be mentioned, that the lifetime depends from the actual parameters of use and can exceed the above number considerably [4]

same range. If the layers are sufficiently pressed together, the melted material from the two layers is mixed and thus, forms a reliable joint after cool down.

One of the very first industrial applications of diode lasers for polymer welding is the hermetic seal of the electronic car key, which is shown in fig. 7 [7]. The most interesting in that part is, that it not only demonstrates a successful use of high power diode laser in an industrial manufacturing environment, but also shows, that even layers, which show the same colour to the human eye – black – can be welded together with the method described

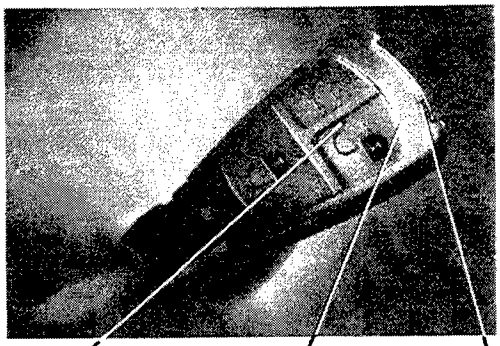


Fig. 7: Laser welded electronic key [6], Laser power ca. 40 W; welding speed ca. 10 m/min

above: whereas the body is blackened by carbon black and thus is absorbing over a wide range from the visible to the infrared, the lid is made black by pigments, which are also absorbing in the visible, but which are transparent at the laser wavelength. In that way, the ideal set-up for polymer welding as proposed in fig. 6 is realised: the top layer is transparent for the laser, whereas the bottom one is heated at the interface region and melted by the diode laser.

4. Conclusion

High power diode lasers have already entered the industrial manufacturing floors for low power and high power (up to several kilowatts) applications ([1], [2]). Whereas in the high power range surface treatment, heat conduction welding and brazing seem to be most attractive, in the range of lower laser power micro processing applications as high precision soldering and polymer welding have been successfully demonstrated and implemented in manufacturing lines. However, the lower beam quality of diode lasers compared to NdYAG or CO_2 lasers still excludes diode lasers from those applications, which require high power density above 10^6 W/cm². Therefore ambitious research projects have been launched to exploit the diode laser technology not only into the classical laser applications but even more into those novel applications, where the modular concept, i.e. the fact, that the high power diode laser consists of many separate individual laser sources, are advantageous [8]. This strategy will lead to a bright future of diode lasers and a wide, new laser market in the next few years.

5. Acknowledgement

I would like to express my great thanks to the Fraunhofer Institut für Lasertechnik (ILT) in Aachen, Germany, Dr.P.Loosen, D.Hänsch, Prof.R.Poprawe, H.Pütz, and U.-A.Russek, and to M.Flament and S.Reinl of Dilas Diodenlaser GmbH, who performed experiments, permitted the use of the results, graphics and photographs in this paper and also helped me very much by their interpretations, discussions and consulting.

The funding of the European Community in frame of the POLYWELD-Project under Contract No. BE 97-4625 BRPR-CT98-0634 is gratefully acknowledged.

6. Literature

[1] F.Bachmann, *"High Power Diodes and Applications"*; AHPLA Conference, Osaka, Oct. 1999; SPIE Proc. Vol. 3888 p. 394 (1999)

[2] F.Bachmann, *"High power kW-range diode lasers for direct materials processing"*; to be presented at XIII. International Symposium On Gas Flow & Chemical Lasers - High Power Laser Conference, Florence, Italy, September 18 - 22, 2000; to be published (2000)

[3] Patent No. DE 195 00 513 C1, Dilas Diodenlaser GmbH, Mainz, Germany

[4] F.Bachmann, *"High power diode lasers for materials processing – actual status and future aspects"* LAM-2000 ConferenceSt.Petersburg, Russia, August 23-25, 2000; to be published

[5] Company brochure MTA Automation AG, Brügg, Switzerland

[6] R.Klein, *"Bearbeitung von Polymerwerkstoffen mit infraroter Laserstrahlung"*; Thesis RWTH Aachen, Germany, 1990

[7] By courtesy of Fraunhofer-Institute for Laser Technology, Aachen, Germany

[8] F.Bachmann, *"Present status and future aspects of high power diode laser materials processing under the view of the German national research project"* Photonics West 2000 (LAMOM-V), San Jose, CA, USA, Jan 14 to 28, 2000; to be published in SPIE Proceedings Vol. 3933 (2000)

UV laser ablative shaping of optical surface using ArF laser

Takahisa JITSUNO*, Keiu TOKUMURA** and Hisashi TAMAMURA***

*Institute of Laser Engineering ,Osaka University , 2-6 Yamada-oka, Suita, Osaka 565-0871, Japan
e-mail: jitsuno@ile.osaka-u.ac.jp
**Nalux Co.Lted. 2-1-7 Yamazaki, Shimamoto-chyo, Misima-gun, Osaka 618-0001,Japan
***Sony/Tektronix Co. 5-9-31 Kitashinagawa, Shinagawa, Tokyo 141-0001, Japan

A new scheme for phase control of optical components using laser ablation shaping (LAS) has been developed. The surface shape of optical plastic material coated on a glass plate is ablated using 193 nm laser light to control the transmission wave front. The surface shape is monitored *in situ* and corrected to attain the desired aberration level. The irradiation fluence is about 40 mJ/cm^2, and the ablation depth per pulse is about 0.01 μm per pulse for UV-cured resin. A wave front aberration of 3.0 λ is reduced to 0.17 λ in the case of flat surface shaping. In the case of spherical surface generation, an aberration of 2.5 λ is reduced to 0.2 λ. Increase in surface roughness is kept within the acceptable levels. This scheme has been applied to the fabrication of micro-optical elements for the collimation of laser diode (LD) or single mode optical fiber (SMF). In the case of LD lens, micro-collimate lens was placed at the output surface of LD, and the wave-front error was measured with Shack Hrtmann wavefront sensor. In the case of SMF, small lens was formed directly at the output surface with uv-cured resin. The laser beam was focused to 250 μm in radius for micro-fablication. The wave-front distortion was decreased from about 15 λ to less than 2 λ in mm size lens.

Keywords : laser ablation, ArF laser, optical phase control, micro-optics, laser ablative shaping

1. Introduction

Precise optical components are very important for high performance optical system. However, the fabrication of precise optical components such as lens, mirrors or windows is difficult in conventional polishing or casting process. Recently some new fabrication schemes are developed using ion beam milling [1] or magnetic fluid[2]. However, even in such new schemes, the fabrication of precise optical components becomes very critical when the size of the optical components is smaller than 1 cm. Nevertheless, the optical component must be used combined with the optical source or other optical components. In this sense, optical components must have desirable shape for obtaining a good optical performance combined with other optical system.

We have proposed the method of laser ablative shaping (LAS) of optical components using a very short wavelength laser (ArF excimer laser: λ =193 nm)[3][4]. In this scheme, the ArF laser beam is irradiate on to the surface of the optical plastic material coated on a glass plate to ablate the surface for the control of the transmitting or reflecting wavefront. This process was made under the measurement of a wavefront sensor, and the process was controlled by a computer. We obtain very good control of transmitted wavefront for flat surface and spherical lens generation [4]. This should be the first report on the shaping of refractive optics using laser ablation to attain the accuracy level required for use in precise optics.

We also applied LAS scheme to control the wavefront of micro-optical components such as micro-lens for the collimation of laser diodes (LD)[5] or single mode optical fibers (SMF). In this application, the plastic micro-lense was coupled with the light source (LD or SMF), and the phase of the output beam was measured and corrected so as to obtaining a well collimated beam. In this scheme the coupling error of lens with the light source is easily compensated, and the output beam is in a very good alignment condition for the light source.

In this paper, we report on the fabrication of phase error correction of precise optics using an ArF excimer laser in a non contact shaping scheme. In section 2, the experimental method and the experimental results of the processing with direct beam irradiation in 5 cm size elements are described. The application of LAS scheme to LD and SMF are given in section 3. Discussion and conclusions are included in section 4.

First International Symposium on Laser Precision Microfabrication, Isamu Miyamoto, Koji Sugioka, Thomas W. Sigmon, Editors, Proceedings of SPIE Vol. 4088 (2000) © 2000 SPIE · 0277-786X/00/$15.00

2. Processing with direct beam irradiation

The schematic of the LAS system is shown in Fig.1. This system consists of a phase-shift interferometer (Olympus, KIT-201), an ArF excimer laser (Lambda Physik, Compex 201), a precise X-Y stage (Physik Instruments, resolution: 0.1 μm) and computers for the control of the stage and calculation of the wavefront. Due to the poor beam quality of the ArF laser, a uniform part of the output beam is selected using a 4.5-mm-diameter aperture. This beam is projected directly onto the work piece for ablative shaping. A variable beam attenuator is used to control the laser intensity. We chose PMMA and UV-cured resin materials because of the good ablation uniformity under ArF laser irradiation. We observed a highly uniform surface after ablation. However, optical plastics are very poor materials and cannot be used in precise optics because of the bulk nonuniformity of the index, the index change due to humidity absorption and the strong birefringence induced by stress. To overcome these disadvantages, we used a very thin layer of UV-cured resin coated onto a glass substrate. If the thickness of the resin is reduced from 5 mm to 50 μm, the bulk nonuniformity, index change and the stress birefringence are reduced by less than 1/100 the original values, a level which is acceptable for practical application to precise optics. We fabricated this hybrid glass-plastic plate using the replica method[4].

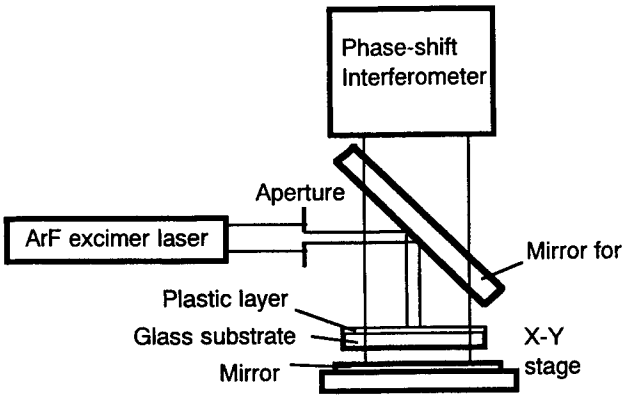


Fig. 1. Schematic of the laser ablative shaping (LAS) system

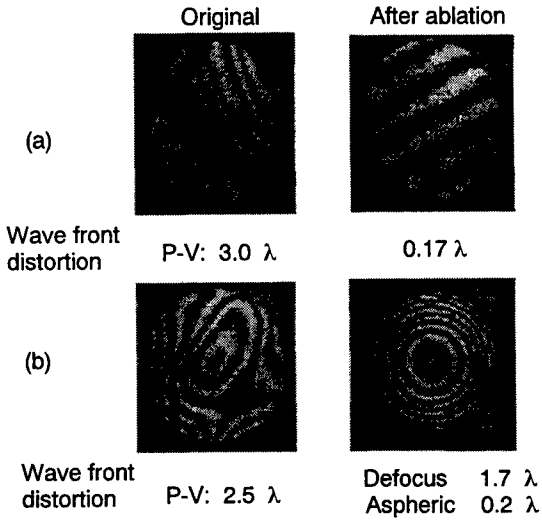


Fig. 2 Correction of transmitted wavefront. (a) flat and (b) spherical surface.

At the start of the process, the wavefront of the substrate is measured using the interferometer. This wavefront is compared with the desired shape (in this case, flat or spherical), and the computer generates a map of the number of pulse shots to be directed on the substrate. The ArF laser is operated at 17 Hz. During the laser pulse irradiation, the X-Y position of the substrate is controlled by the computer. After laser pulses irradiation, the wavefront is measured again. These procedures are repeated until the phase error reaches an acceptable level. Normally, this feedback loop is repeated 2 or 3 times for obtaining the desired results. The experimental results of LAS are shown in Fig. 2. In this case, 5-cm-diameter substrates of hybrid glass-plastic plates are used for flat and spherical surface generation. The fluence of the irradiating laser pulse is 45 mJ/cm2. This fluence is chosen because the surface roughness is minimum at this fluence level. The scan increment is 0.36 mm in the X and Y directions. The position of the substrate is moved point to point by this increment after the shot of laser pulses decided from the phase map. The wavefront distortion at the starting period was 3.0 λ for flat surface generation, and 2.5 λ for spherical surface generation. The final wavefront distortion for the flat surface was 0.17 λ over 90% of the area. In the case of a spherical surface, the aspherical component was also less than 0.2 λ. The surface roughness was almost the same before and after ablation.

3. Processing with focused beam irradiation

3.1 Micro-lens for laser diode

Since LAS has been demonstrated as a useful scheme to fabricate precise optics, the most important field of application of LAS is in the micro-optics fabrication[5]. In conventional optical fabrication technologies including magnetic fluid scheme, the fabrication of high accuracy micro-lens is a very difficult subject. On the other hand, LAS seems to be very easy to apply

to the micro-lens fabrication because we can change the size of laser beam as we want. We chose single mode laser diode as the light source for this demonstration. We designed a micro-lens for visible (λ= 670 nm) single mode LD, and fabricated this lens with casting process of optical plastic. This lens consists two cylindrical lenses in orthogonal direction and curvatures of these lenses are 1.26 and 1.79 mm in radius. This lens was mounted on to the LD and the wavefront of the output beam was measured with a Shack-Hartmann wavefront sensor. This wavefront sensor was used because the aberration level of the output beam was as large as 40 λ, which is too large aberration to measure with interferometers. In the case of the micro-lens fabrication, irradiation beam was focused on to the phase correction plate placed as shown in Fig. 3. An example of phase correction of LD beam is shown in Fig. 4. The original aberration of 30 λ was reduced to 4 λ after the correction of phase. This insufficient correction of aberration was come from the surface deterioration due to a large ablation depth. In this correction, the ray at the peripheral area consists larger aberration as compared with the central area, and new peripheral rays are appeared after the correction. This problem will be suppressed when the initial aberration level is reduced by the improved design of micro-lens.

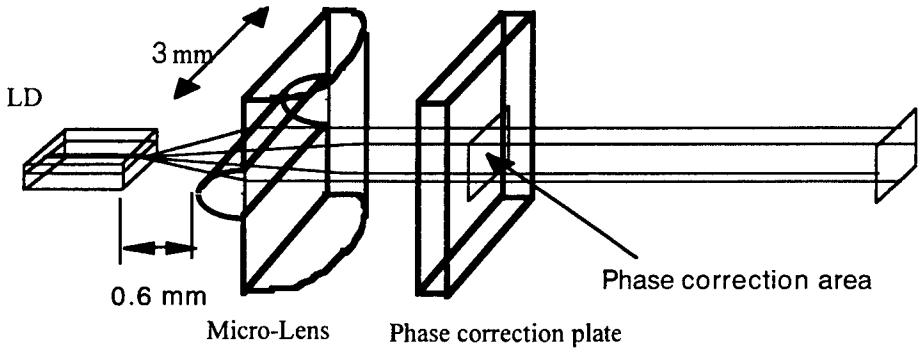
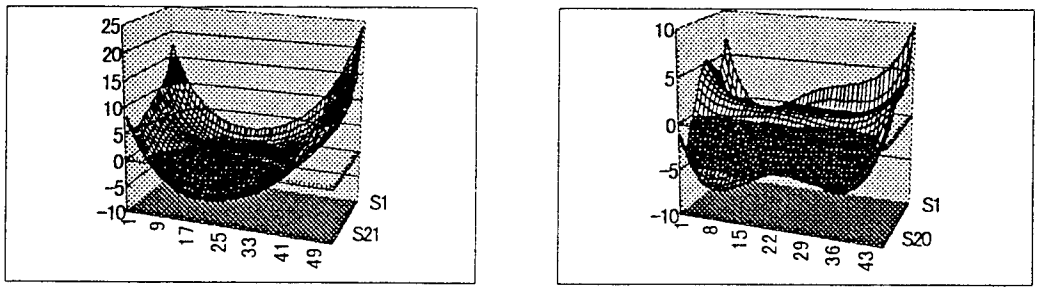


Fig. 3. Schematics of phase correction of laser diode (LD) light.



(a) Original wavefront
PV(λ): 30.5 RMS(λ): 4.7
Beam size : 1.79 x 0.93

(b) After correction
PV(λ): 13.3, RMS(λ): 2.1

Fig. 4 Correction of wavefront of LD light. (a) Original and (b) after correction.

3.2 Micro-lens for single mode optical fiber

In the field of optical fiber application, the fiber connection is a troublesome problem. Conventional single mode connectors require very high accuracy components and the cost of this connector is not cheep enough. We also have many problems when we want to couple light sources such as LD or lasers with SMF or to use balk optics such as polarizers or filters between SMFs. For avoiding this problem, we tried to apply LAS scheme to the SMF connection. A micro-lens for the collimation of SMF light has been fabricated directly on the end surface of SMF. A simple tube was attached to the end of fiber and a small amount of UV-cured resin was injected on the end surface of the fiber. This resin forms a small lens by the

surface tension, and is cured by UV light. We can measure the aberration of this micro-lens using the light through the fiber, and this aberration can be corrected by LAS. In the case of SMF lens, the initial aberration of 15.4 λ was reduced to 2.2 λ. This aberration level is not enough for the direct application of this method to the mail line of fiber network, this connector will be applicable to the fiber connection at the local aerial network (LAN) or the fiber to the home (FTTH).

4. Discussion and conclusions

In the case of direct beam irradiation, the aberration level of after phase correction was low enough for many applications. However, in the case of focused beam irradiation, the level of phase correction is not high enough; the surface of ablated area was deteriorated due to the increase of surface roughness. The actual reason of this deterioration is not clear as yet. We are now trying to improve the surface roughness by changing the polarity of the irradiation beam and the beam pattern on the surface. A very critical dependence of surface structure after the ablation with a slight amount of change in polarization has been observed. We will find the mechanism in which the surface roughness is affected during LAS process in focused beam irradiation.

References

[1] S. R. Wilson, D. W. Reicher, C. F. Kranenberg, J. R. McNeil, P. L. White, P. M. Martin and D. E. McGready, "Ion beam milling of fused silica for window fabrication", in Laser- Induced Damage in Optical Materials; 1990, SPIE Proc. Vol. **1441**, The Society of Photo-Optical Instrumentation Engineers (P.O. Box. 10, Bellingham, Washington D.C. 98277) (1990) pp. 82-86.

[2] I. V. Prokhorov, W. I. Kordonski, L. K. Gleb, G. R. Gorodkin and M. L. Levin, "New high-precision magnetorheological instrument-based method of polishing optics", OSA OF&T workshop digest, **24**, (1992) p. 134.

[3] T. Jitsuno, K. Tokumura, N. Nishi, N. Nakashima, M. Nakatsuka and S. Nakai, "UV laser ablative figuring of precise optics," in Conference on Laser and Electro-Optics (CLEO)'95, Vol. 15 of 1995 OSA Technical Digest Series (Optical Society of America, Washington, D.C., 1995) paper CTuK3, (1995) pp.132-133 .

[4] T. Jitsuno, K. Tokumura, N. Nakashima and M. Nakatsuka,"Laser ablative shaping of plastic optical elements for the phase control", Appl. Optics, **38**, (1999) pp.3338-3342.

[5] K. Tokumura, T. Jitsuno, M. Nakatsuka, G. Y. Yoon and H. Tamamura, "UV laser ablative figuring of precise optics", AHPLA'99, SPIE, **3885**-36, Suita, Osaka, Nov. 1-5, (1999).

Non-lithographic coherent array of ultrafine particles on an irradiated material using Nd:YAG laser - Influence of the laser fluence on the microstructure -

Yuji KAWAKAMI and Eiichi OZAWA

Nano Particle Division, Vacuum Metallurgical Co., Ltd.
516, Yokota, Sanbu-machi, Sanbu-gun, Chiba 289-1297, Japan
E-mail : BYR17073@nifty.ne.jp

A non-lithographic coherent array of ultrafine tungsten particles (150 - 500 nm diameter) is self-assembly arranged around a laser-irradiated mark on a tungsten substrate. Single and poly-crystal tungsten substrates were irradiated by a Q-switched Nd:YAG laser under low pressure in an inert gas atmosphere. We studied the effect of the laser fluence on the morphology of the coherent arrays. Scanning electron microscopy (SEM) and transmission electron microscopy (TEM) were used for these observations. The spacing of the coherent array increases with increasing laser fluence. For a 10.5 J/cm^2 irradiation, many droplets and peeling of the surfaces induced by rapid thermal expansion of the tungsten surface were observed. The recrystallization texture on the surface was also confirmed by TEM observations. This suggests that the irradiated surface layer was partially recrystallized during laser irradiation. We concluded that coherent arrays are related to the laser fluence, the crystal surface structure, and the crystal growth. The recrystallization of the slightly melted tungsten on the top surface induced by the repeated laser irradiation plays a vital role in the formation of the array. If we can produce a coherent array of ultrafine tungsten particles with a higher aspect ratio, it may have potential applications for the emission cathodes of field emission displays (FED) and microelectronic devices.

Keywords: non-lithographic coherent array, ultrafine particles, Q-switched Nd:YAG laser, tungsten, single crystal, recrystallization, field emission display (FED)

1. Introduction

It is well known that a laser induced periodic surface structure (LIPSS) has been produced on various kinds of material surfaces over the past thirty years. Metals (Al alloy, brass, Ni_xP_{1-x}, iron) [1-4], semiconductors (Si, Ge, GaAs) [2, 5-7], polymers [8], and recently, multilayer materials [9], inorganic materials [10], superconductors [11], diamond crystals and microclusters [12] were used as the target materials in the study of laser ablation. Some researchers have observed the LIPSS and ripple patterns on irradiated materials like a silicon single-crystal surface using CO_2, Nd:YAG, and excimer lasers. Almost all the researchers have tried to understand the formation of the periodic surface ripples related to the optical characteristics of the used laser beam. Based on their discussions, the periodic ripples were related to the number of laser shots and not to one or the incident wavelength. The first pulse causes only a rough surface while subsequent pulses create periodic ripples [13]. The ripples depend on the incident wavelength, polarization, and the angle of incidence. The ripple spacing is calculated from Rayleigh's diffraction condition as stated in Eq. (1) [1, 3, 5-7].

$$\Lambda = \lambda/(1 \pm \sin\theta) \quad (1)$$

where Λ is the ripple spacing, λ is the laser wavelength, and θ is the angle of incidence relative to the surface normal.

Some researchers considered that the ripple spacing is related to the polarization (*p*-polarized incident beam) of the incident laser beam [1-3, 5-8]. In this case, the ripple direction should be perpendicular to the polarization of the normal incident beam and parallel to the plane incident beam at $\theta \geq 45°$ [5]. The ripple spacing of the incident beam at $\theta \geq 45°$ was calculated from $\lambda / \cos\theta$[5]. For a polyethersulfone (PES) film, the spacing is several times larger than the laser wavelength, and thermal processes on the etched surface play a significant role in the microstructure formation [8].

First International Symposium on Laser Precision Microfabrication, Isamu Miyamoto, Koji Sugioka, Thomas W. Sigmon, Editors, Proceedings of SPIE Vol. 4088 (2000) © 2000 SPIE · 0277-786X/00/$15.00

When the laser beam was circularly polarized, no ripples were observed [6]. In a recent report on inorganic materials using an ArF excimer laser for geometric surface modification, the influence of polarization was not confirmed. In the single crystalline CaF_2 case, the structure of the laser-irradiation marking depended on the crystal surface structure [10]. The LIPSS induced on metallic surfaces does not necessarily depend on the laser light polarization or wavelength. A more important factor seems to be the characteristics of the material and its molten bath rather than those of the laser [4].

We have previously reported that a new coherent array of ultrafine tungsten particles of about 700 nm in diameter was discovered around the laser-irradiated mark on the (100) orientation surface of a single crystal tungsten substrate [14-16]. These arrays were coherently arranged in several directions like a two-dimensional crystal structure. On the other hand, the ripples were arranged only in one direction. This experimental result seems to indicate that the coherent array of particles is not related to only the laser characteristics as former researchers considered. We tried to clarify whether the angle of incident and the polarization were related to the formation of the coherent array. The formation of the coherent array patterns were not affect by the polarization with the p- and s-polarized beams. For a high angle of incidence, we did not find the coherent array under the conditions of Refs. 14 and 15 [14-15]. We also confirmed two types of arrays, namely, a cubic system and a hexagonal one [14-16]. Recently, we have also produced a coherent array of ultrafine tungsten particles of about 150 nm in diameter with a spacing at 640 nm [17].

In this study, we have used the second harmonic (532 nm) wavelength of a short-pulse Nd:YAG laser in order to clarify the effect of the laser fluence on the spacing of the array on the single-crystal tungsten.

2. Experimental procedure

The apparatus (Chamber; ULVAC Materials Technology Co., Ltd., Chiba, Japan) used in the experiments is schematically illustrated in Fig. 1. The laser was a Q-switched Nd:YAG laser (Spectra-Physics, CA, INDI-50, maximum energy: 580 mJ at 1064 nm, 220 mJ at 532 nm) which had a full width at half-maximum of 4.5-5.5 ns at 532 nm. The incident beam was polarized using a 1/4 λ plate and a 1/2 λ plate, so that the beam was *p*-polarized at 532 nm. The beam was introduced to the chamber through a fused silica window (CVI Laser Corporation, NM) and focused with a BK7 glass lens (CVI Laser Corporation, NM) on the tungsten surface. The shot numbers were 2400 pulses at 20 Hz in the same region. The laser fluences were 2.6, 5.2, and 10.5 J/cm^2. The angles of incidence, θ, were 4° and 10°.

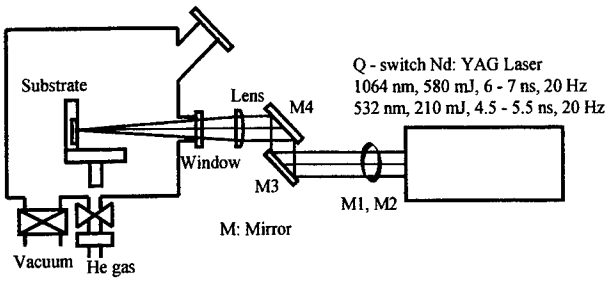


Fig. 1 Schematic diagram of the experimental apparatus.

A process chamber was first evacuated to 1×10^{-4} Pa and then high purity helium gas (99.9999 mass%) of 4 kPa was introduced. Specimens were single-crystals of tungsten with mirror-polished (100) -, (110) -, and (111) orientation surfaces (Metal Crystals & Oxides, Ltd., Cambridge, England, 99.99 mass%) and a mirror-polished poly-crystal tungsten (Furuchi Chemical Co., Ltd., Tokyo, Japan, 99.99 mass%). They also were cleaned in acetone and petroleum benzine using a ultrasonic wave cleaner before the laser irradiation.

A scanning electron microscope (SEM; JEOL, Ltd., JSM-6300F, Tokyo, Japan) was used for the surface observations. The cross section of the array was also observed by transmission electron microscopy (TEM; JEOL, Ltd., JEM-4000EX, Tokyo, Japan).

3. Results and discussion

Figures 2(a), 2(b), and 2(c) show SEM microphotographs around the laser-irradiated mark on the (111)-orientation single crystal tungsten surface, which show the influence of the laser fluence at 2.6, 5.2, and 10.5 J/cm^2, respectively. The particle array structures in Figs. 2(a) and 2(b) are clearly visible. The ultrafine particles of about 380 - 500 nm are coherently arranged with spacing at 595 nm (Fig. 2(a)) and 683 nm (Fig. 2(b)). In case of the higher laser fluence, we could not find the array but saw many droplets and peeling of surface layer induced by thermal expansion of the tungsten, as depicted in Fig. 2(c). The spacing calculated from Eq. (1) was 453 or 644 nm. These values are very different from the ones obtained from the experimental results. In the case of the 17.4 J/cm^2 laser fluence at 1064 nm and 5.2 J/cm^2 laser fluence at 532 nm, the spacing of the coherent array was also different from the calculated spacing [14-17]. That is, the surface patterns depend on the effect of the laser fluence rather than the wavelength of the laser.

Figure 3(a) shows a SEM microphotograph around the laser-irradiated mark on the (100)-orientation single crystal tungsten surface. The ultrafine particles of about 150 nm (radius of curvature; 70-80 nm) are coherently arranged like a two-dimensional hexagonal system with a spacing at 640 nm. Figure 3(b) shows a

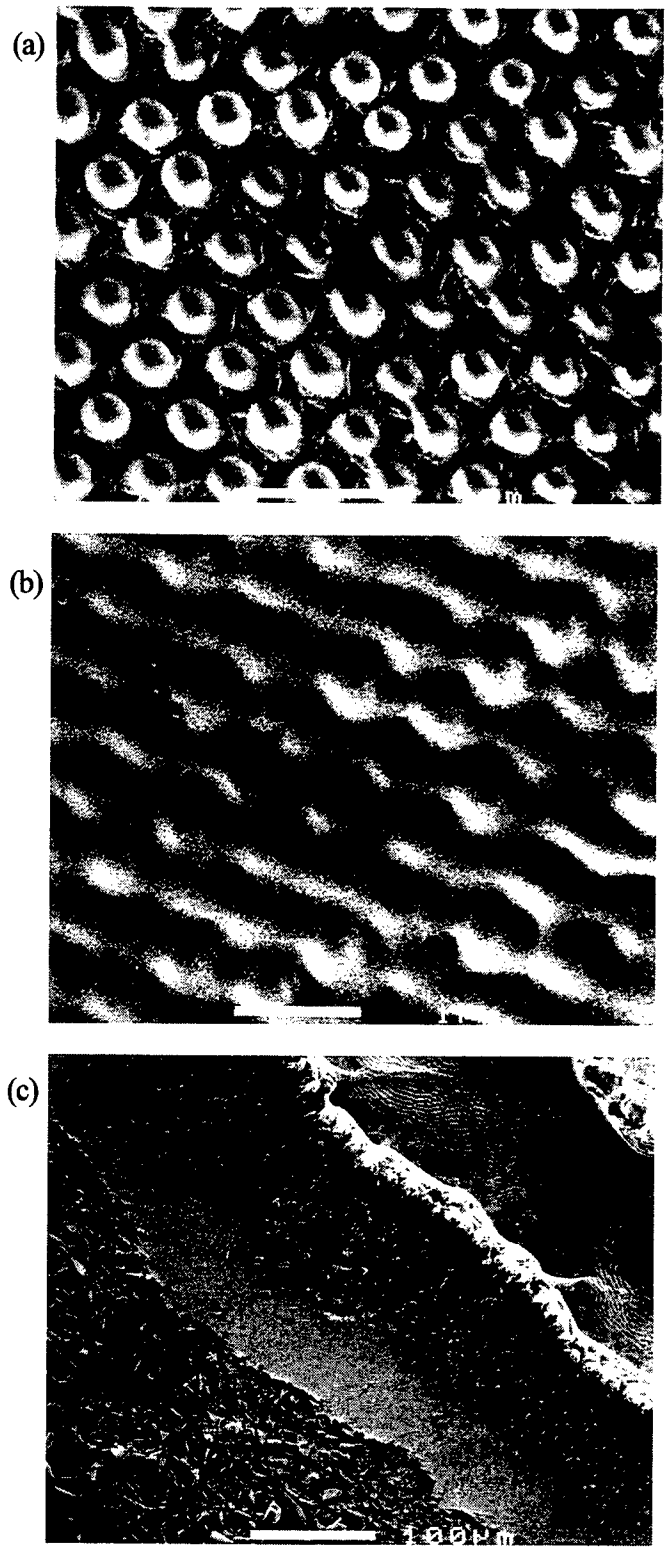


Fig. 2 SEM microphotographs around the laser-irradiated mark on the (111)-orientation single crystal tungsten surface (θ = 10°). (a) 2.6 J/cm^2, (b) 5.2 J/cm^2, (scale bar = 1 μm), (c) 10.5 J/cm^2 (scale bar = 100 μm).

cross-sectional TEM image of the ultrafine particle in Fig. 3(a). The particles composed of the coherent array seem to grow from the matrix surface as if they rise continuously from the base material, because we cannot see any grain boundary between the particles and the matrix surface. From this experimental result, we concluded that the formation of so many protuberances is related to a kind of crystal growth and the factors that control their formation are the laser fluence, the crystal surface structure preferential growth direction of the crystal, cooling rate and its direction, etc. Anyway, the recrystallization of the slightly melted tungsten on the top surface induced by the repeated laser irradiation plays a vital role in the formation of the array.

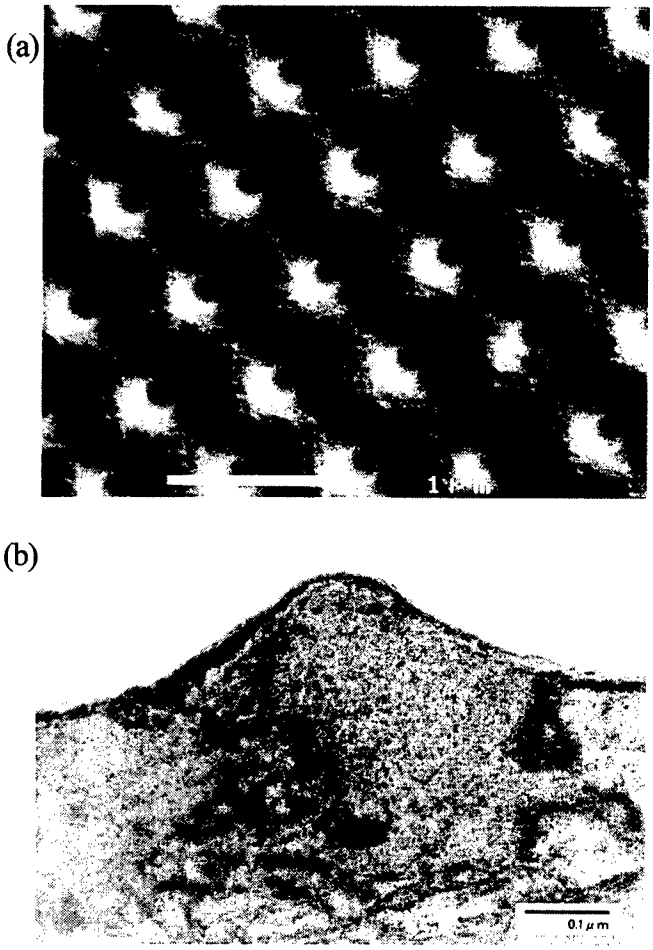


Fig. 3 (a) SEM microphotograph around the laser-irradiated mark on the (100)-orientation single crystal tungsten surface (5.2 J/cm^2, θ = 4°), (scale bar = 1 μm), (b) Cross-sectional TEM image of the ultrafine particle in Fig. 3(a)

In order to clearly understand the formation mechanism of the array of particles, we should study it in more detail. The rapid solidification of the molten tungsten induced by the laser beam

should also be considered [14-17]. The laser fluence seems to be a very important factor for inducing the coherent array, since the spacing of the array was changed by the intensity of the laser fluence. The effect of the surface structure, crystal growth (dendrite), surface tension (surface energy), thermal effect, and shock wave should be carefully considered [17].The formation mechanism of a Coulomb crystal [18], which is formed from the Coulomb potential energy due to the charge between the particles, might also be considered.

4. Conclusion

In summary, we could form a different spacing array of about 150-500 nm-sized ultrafine particles using the second harmonic (532 nm) wavelength of the short-pulse Nd:YAG laser irradiation. These two-dimensional coherent arrays cannot be explained based only on the laser's characteristics such as the wavelength, incident angle, and polarization as previously done. The interesting points are as follows: (1) the ultrafine tungsten particles of about 150-500 nm were coherently arranged in several directions, (2) the spacing of the array was changed by the intensity of the laser fluence and in the case of the 10.5 J/cm^2 laser fluence, many droplets and peeling of surface layer are observed, and (3) the recrystallization texture on the surface was confirmed for the ultrafine particle. A much more detail discussion is necessary to understand this phenomenon. Such a coherent array of ultrafine particles may have a significant potential for widely diversified industrial applications ranging from emission devices of a field emission display (FED) and microelectronic devices.

This work has been supported by the R&D Institute for Photonics Engineering (RIPE) entrusted from the Advanced Photon Processing and Measurement Technologies Program of the New Energy and Industrial Technology Development Organization (NEDO) of Japan.

References

[1] A. K. Jain, V. N. Kulkarni, D. K. Sood, and J. S. Uppal: J. Appl. Phys., **52**, (1981) 4882.
[2] H. M. van Driel, J. E. Sipe, and Jeff F. Young: Phys. Rev. Lett., **49**, (1982) 1955.
[3] N.R.Isenor: Appl. Phys. Lett., **31**, (1977) 148.
[4] A. Dauscher, V. Feregotto, P. Cordier, and A. Thomy: Appl. Surf. Sci., **96-98**, (1996) 410.
[5] J. F. Young, J. E. Sipe, J. S. Preston, and H. M.van Driel: Appl. Phys. Lett., **41**, (1982) 261.
[6] M.Oron and G.Sørensen: Appl. Phys. Lett., **35**, (1979) 782.
[7] P. M. Fauchet and A. E. Siegman: Appl. Phys. Lett., **40**, (1982) 824.
[8] H. Niino, M. Shimoyama, and A. Yabe: Appl. Phys. Lett., **57**, (1990) 2368.
[9] G. K. Giust and T. W. Sigmon: Appl. Phys. Lett., **70**, (1997) 3552.
[10] K. Ohsawa and H. Tokura: J. Jpn. Soc. Precision Eng., **64**, (1998) 121.
[11] I. Kawayama, J. J. Dubowski, H. Nishikawa, and T. Kawai: Appl. Surf. Sci., **143**, (1998) 313.
[12] A. M. Ozkan, A. P. Malshe, T. A. Railkar, W. D. Brown, M. D. Shirk, and P. A. Molian: Appl. Phys. Lett., **75**, (1999) 3716.
[13] Z. Ball and R. Sauerbrey: "*Laser Ablation and Desorption*" ed. by J. C. Miller and R. F. Haglund, (Academic Press, San Diego, CA, 1998), Vol. 30, pp.341.
[14] Y. Kawakami, E. Ozawa, and S. Sasaki: Appl. Phys. Lett., **74**, (1999) 3954.
[15] Y. Kawakami, S. Sasaki , and E. Ozawa: J. Jpn. I. Met., **63**, (1999) 1105.
[16] Y. Kawakami, S. Sasaki, and E. Ozawa: "*Surface Modification Technologies*" ed. by T. S. Sudarshan, K. A. Khor, and M. Jeandin (ASM International, Materials Park, Ohio, 1999), Vol. 13, pp.345.
[17] Y. Kawakami and E. Ozawa: Appl. Phys. A (2000) (in press).
[18] J. H. Chu and Lin I.: Phys. Rev. Lett., **72**, (1994) 4009.

Kinetic study of nanofabrication on gold films by atomic force microscope tips under laser irradiation

B. Hu, Y. F. Lu[1], Z. H. Mai, W. D. Song, W. K. Chim

Laser Microprocessing Laboratory
Department of Electrical Engineering and Data Storage Institute
National University of Singapore
10 Kent Ridge Crescent, Singapore 119260

Recently, scanning probe microscope (SPM) has become a promising technique for nanofabrication. In this paper, we present a novel method of nano-fabrication, namely, nano-fabrication by atomic force microscope (AFM) tips under laser irradiation. The SPM was operated as an AFM. During imaging and nano-fabrication, the AFM is in constant force mode. The tip is fixed with the sample moving via a tube scanner. Nano-lithography software controls the scanner motion in x and y directions. The SPM has an open architecture allowing an external laser beam incident on the tip at an incident angle between 0 to 45°. A vertical polarized Nd:YAG pulsed laser with a pulse duration of 7 ns was focused on the tip. An electrical shutter was introduced to switch the laser irradiation. Alignment between the laser beam and the tip was performed under a high-power charge coupled device (CCD) microscope. Nano-fabrication was carried out on gold films deposited on n-type Si substrates using the physical deposition method. The kinetics of the nanostructure fabrication has been studied. Craters were created in air ambient under different laser pulse numbers, pulse energies and tip force. The feature size of the craters, which are in the nanometer scale, increases with the pulse number, pulse energy and the tip force. This technique has potential applications in the high-density data storage.

Keywords: laser; scanning force microscope; nanofabrication; kinetics; gold thin film.

1. Introduction

Laser-induced processing of materials has been regarded as a promising and expending field for both science and engineering since the invention of laser. This field has been intensively investigated and found great useful in many areas, such as microelectronics and magnetic. Laser as a tool, not only makes manufacturing cheaper, faster, cleaner and more accurate but also opens up entirely new technologies and manufacturing methods that are not simply available using standard technologies. However it is restricted to micrometers and sub-micrometers due to the diffraction of laser light. In response to the challenges in nanofabrication, a novel technology that combines laser and SPM was developed and has been studied extensively [1-3]. Nanostructures on gold films have been fabricated by direct writing using laser assisted scanning tunneling microscope (STM) and AFM in vacuum and in air ambient respectively [4-10]. This technology is important for a number of future technical applications such as high-density data storage, mask production and reparation for semiconductor industry.

In this paper, we will describe nano-fabrication on gold films using AFM in combination with laser. The setup of our experiments, sample preparation and experimental methods will be discussed. The experimental results show that the tip-enhanced laser irradiation can be effectively used in nano-fabrication.

2. Instrumentation and experimental methods

Figure1 shows the schematic diagram of the experimental setup. A commercial SPM (Model Autoprobe CP, Park Scientific Instruments) was used. The SPM works as either an STM or AFM. It has an open architecture that allows a pulsed laser beam incident directly onto the surface of the tip and the sample. In the experiment, the SPM was operated as an AFM, working in

[1] Email: eleluyf@nus.edu.sg, Fax: +65-779-1103

First International Symposium on Laser Precision Microfabrication, Isamu Miyamoto, Koji Sugioka, Thomas W. Sigmon, Editors, Proceedings of SPIE Vol. 4088 (2000) © 2000 SPIE · 0277-786X/00/$15.00

constant force mode. On-axis CCD microscope with a 3500× zoom provided a real-time, color video view of the surfaces of the tip and the sample. Commercial Si tips were used in the study. The length of tips is about 3 μm and the radius of curvature is 12 nm. A Q-switched pulsed Nd:YAG laser was used. The frequency-doubled pulsed laser has a vertical polarization. The pulse duration is 7 ns and the maximum repetition rate is 10 Hz. The output energy is adjustable. We introduced an electrical shutter to switch the laser on and off and a 20 cm Plano-convex lens to provide focusing of the pulsed laser. The focused laser beam was introduced to the tip-sample gap from the front side of the probe head. Alignment of the focused laser beam to the tip-sample gap was performed under the optical CCD microscope by observing the diffraction light from the tip. The incident angle of the external laser beam is adjustable between 0 ~ 45°. We controlled the incident angle to be about 0°, so as to reduce direct incidence of the laser beam on the sample surface and to prevent the laser-induced damage to the cantilever as well. AFM images were taken using the same tip after fabrication. The fabrication and imaging process were controlled by nanofabrication software.

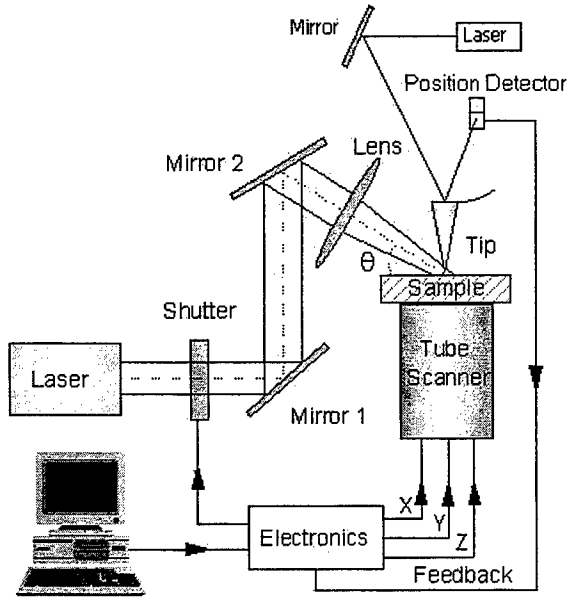


Fig. 1 Schematic diagram of the experimental setup.

Gold films were used in the study. The films were deposited on n-type Si substrates by physical vapor deposition (PVD) method. STM imaging on the gold films showed the grain size of the gold films is approximately 30 nm. A step between the film surface and the substrate surface, which was used to measure the thickness of the gold films, was created using mechanical mask. The film thickness is 50 nm.

3. Results and discussion

Figure 2 shows an AFM image of a 2×2 dot array created at 1 to 4 laser pulses respectively as labeled in the figure. The laser intensity is about 80 MW/cm^2. AFM image was taken immediately after the fabrication with the same tip. The depths of the pits were measured as the peak-to-valley height of the pits in the direction normal to the laser incidence. Considering the roughness of the sample surface, we measured the depth from both sides of the pits and used their mean value as the "measured depth". These pits have different measured depths ranging from 4 to 10 nm, and diameters from 28 to 40 nm. Protrusion was observed around the dots, which implied a thermal mechanism. The enhanced near field at the tip apex locally heats the gold film underneath the tip. And the tip force easily creates a dot on the softened sample surface. During our experiment, the tips did not show any severe distortion or wear and was in good working condition.

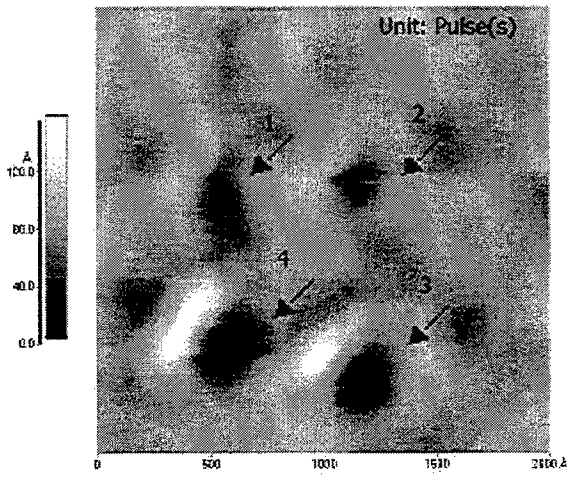


Fig. 2 An AFM image of a 2×2 dot array created on gold film at 1 to 4 laser pulses, at laser intensity of 80 MW/cm^2

The relationship between measured depth and the pulse number under different laser intensity is shown in Fig.3. The measured depth increases with laser pulse number steadily at first. After several pulses, the curve shows a tendency to saturate.

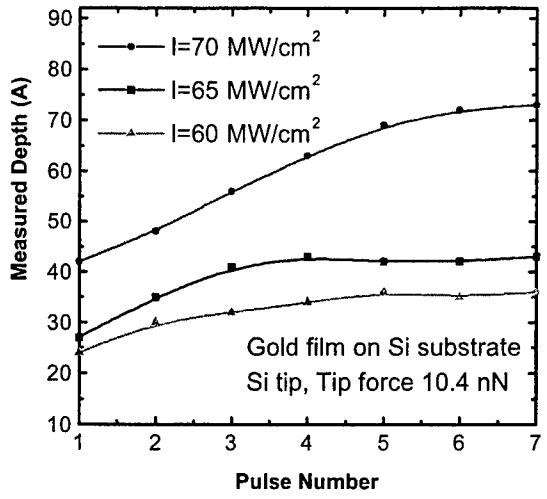


Fig. 3 Relationship between measured depth of the pits and laser pulse number

Under laser irradiation, the tip acts as a receiving antenna to collect incident laser energy and then as a transmitting antenna to form an enhanced field underneath the tip apex. This field decays rapidly at a small distance. Only when the laser irradiation illuminates the tip apex, an enhanced near field can be introduced to affect the sample surface (Fig. 4(a)). After several laser pulse shots, a crater with outburst is created. The tip sinks to the sample surface to maintain the tip force in constant. Thus laser irradiation is prevented from reaching the tip apex, resulting in the reduction of the near field. As the field affects the sample surface less, the curve saturates.

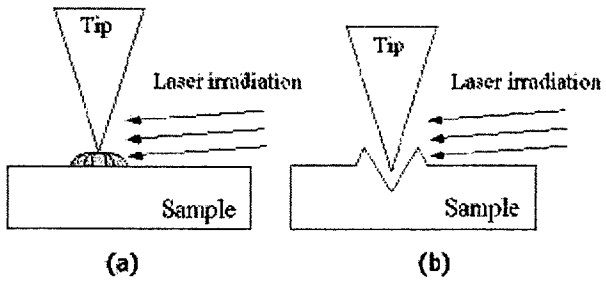


Fig. 4 Schematic diagram of the tip status under laser irradiation (a) At the beginning of pulsed laser shots (b) After several pulsed laser shots

The dependence of measured depth on laser intensity is shown in Fig. 5. The curve has a linear relationship between measured depth and laser intensity, which is coincident with our result of nano-fabrication by a STM tungsten tip under the same circumstances. In the STM case, the laser beam is almost in parallel with the sample surface, so that the heating effect on the sample surface can be neglected. Curve A shown in Fig. 6 has a linear relationship between pit depth and laser intensity as well. The thermal expansion of the tip was calculated versus laser intensity, as shown by curve B in Fig. 6. Comparison between the curves A and B shows that laser-induced thermal expansion cannot be neglected for nanosecond pulsed laser and the mechanism is based on thermal mechanical indention with the laser heated STM tips [5]. Similarly, we deduce that the AFM tip expends at the laser irradiation and penetrates into the sample surface.

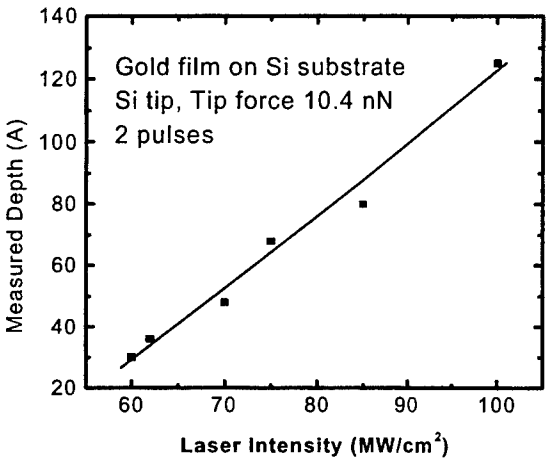


Fig. 5. Dependence of measured depth of the pits on laser intensity by fabrication with AFM tips

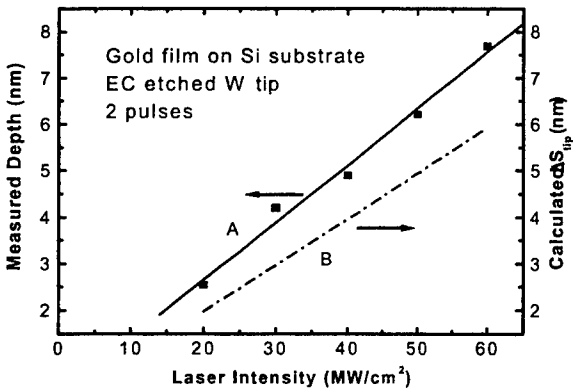


Fig. 6 Dependence of measured depth of the pits on laser intensity by fabrication with STM tip

The relationship between the measured depth and the tip force is shown in Fig. 7. The measured depth increases with tip force. The dependence is almost linear. The dots

were still observed when the tip force is below zero that an attractive force is applied. This could be another evidence that mechanical contact took place: the tip extends and penetrates into the sample surface.

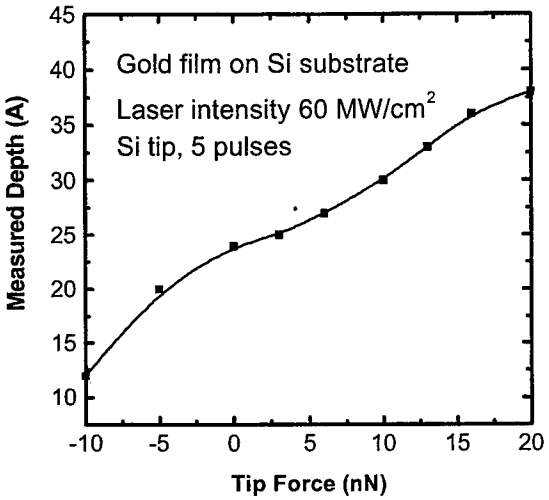


Fig. 7 Relationship between measured depth of the pits and tip force

We also made a ditch using the pulsed Nd:YAG laser, as is shown in Fig. 8. In order to obtain this continuous line, the scan rate of the tube scanner must be slow enough. The laser repetition is 9 Hz and the scanning speed is 0.08 Hz, laser intensity is 90 MW/cm^2. The width of the line is about 100 nm; the measured depth is about 11 nm.

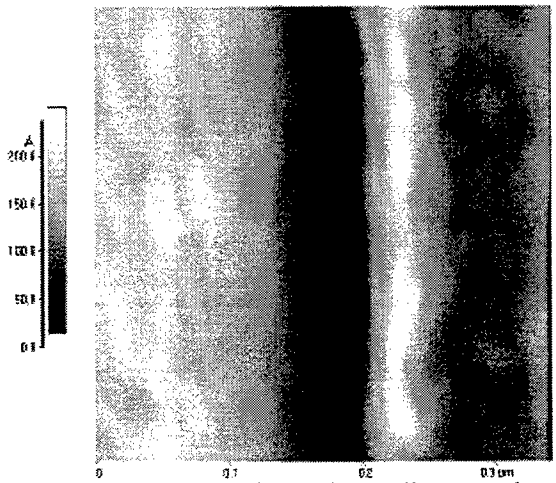


Fig. 8 An AFM image of a continuous line created on gold film

4. Conclusions

The nanofabrication process under Si AFM tips in air ambient was investigated. A 2×2 dot array was created using a Nd:YAG pulsed laser that has a duration of 7 ns and a maximum repetition of 10 Hz. The crater-like pits were measured 28 to 40 in sizes and 4 to 10 in measured depths. The relationship between the feature size of the craters and several considerations were investigated that the size of the pits increases with the pulse number, pulse energy and the tip force. The fabrication is based on field enhancement near the tip apex and mechanical indentation of the tip under laser irradiation. The experiments show that laser combined field enhancement underneath an AFM tip can be effectively used to fabricate on gold films in nanometer scale.

Acknowledgement

The authors would like to thank Ms. H. L. Koh and Mr. Y. W. Goh for their kind help in the installation and maintenance of the facilities in our experiments.

References

1. S. T. Yau, D. Saltz and M. H. Nayfeh, J. Opt. Soc. Am. B 2, 1538 (1985).
2. L. Arnold and W. Krieger, J. Vac. Sci. Technol. A, 35, 7774 (1987).
3. Z. H. Mai, Y. F. Lu, W. D. Song and W. K. Chim, Appl. Surf. Sci. 154-155, 360 (2000).
4. P. H. Cutler, T.E. Feuchtwang, T. T. Tsong, Y. Kuk, Nguyen and A. A. Lucas, Phy Rev. B 35, 7774 (1987).
5. Li, Y. Z., L. Vazquez, R. Piner, R. P. Andres and R. Reifenberger, Appl. Phys. Lett. 54, 1424 (1989).
6. J. Jersch and K. Dickmann, Appl. Phys.Lett. 68, 868 (1996).
7. A. A. Gorbunov and W. Pompe, Phys. Status Solidi A 145, 333 (1994).
8. J. Jersch, F. Demming and K. Dickmann, Appl. Phys. A: Mater. Sci. Process. 64, 29 (1997).
9. J. Boneberg, H.-J. Munzer, M. Tresp, M. Ochmann and P. Leiderer, Appl. Phys. A: Mater. Sci. Process. 67, 381 (1998).
10. Y. F. Lu, Z. H. Mai, Y.W.Zheng and W. D. Song, Appl. Phys. Lett. 76, 1200 (2000).

Laser Surface Annealing of Ni-Base Super Alloy for Enhancement of Material Performance in Hydrogen Environment

Akio HIROSE, LIU Liufa and Kojiro F. KOBAYASHI

Department of Manufacturing Science, Graduate School of Engineering, Osaka University, 2-1 Yamadaoka, Suita, Osaka 565-0871, Japan
E-mail: hirose@mapse.eng.osaka-u.ac.jp

In the present work, laser surface annealing has been applied to an age-hardened Ni base super alloy Inconel 718 using a 2.5kW CO_2 laser to improve its performance in hydrogen environment. Laser surface annealing can produce a locally solutionized zone at the surface of Inconle 718. In the solutionized zone the age precipitates of γ' and γ" are dissolved in the matrix, and thereby the hardness of the solutionized zones is reduced to below 250Hv from approximately 450Hv of the aged base metal hardness. The surface softened zones having several hundred micro meters in depth can be obtained without melting the treated zone by controlling the laser parameters, i.e. the defocus distance and traverse speed. Having much greater ductility than the aged base metal in hydrogen environment, the surface softened zones can effectively prevent hydrogen induced cracking, which tends to occur at the surface of a stress concentrated region. In the present case, the ductility of the surface annealed specimen is almost twice that of the base metal in a tensile test under a 29.4MPa hydrogen atmosphere at room temperature with hydrogen pre-charging. Since a controlled laser irradiation can precisely and locally anneal the surface of a stress concentrated region where hydrogen induced cracking is liable to occur, a sacrifice of strength of the structure caused by the surface softening is negligible.

Keywords: Ni base super alloy, Inconel 718, laser surface annealing, local solutionizing, hydrogen induced cracking.

1. Introduction

An age-hardened Ni-base superalloy, Inconel 718, is strengthened by homogeneously precipitated γ' and γ" phases [1]. This alloy has high strength at moderate temperature, good creep and fatigue resistance [1]. However, since the alloy is fairly sensitive to hydrogen embrittlement, preventing cracking or failure induced by hydrogen embrittlement is important in using the alloy under environment including hydrogen, for example, in a liquid hydrogen fueled rocket engine [2-4].

The alloy in the solution treated state is expected to be less sensitive to hydrogen embrittlement, because its strength and hardness are significantly lower than those in aged state. However, the solutionized alloy may not be suitable for use as a structural material because of its low strength. Generally, hydrogen-induced cracking often occurs in stress concentrated regions in the structure. Thus, if only the stress concentrated region can be softened by locally annealing, hydrogen cracking can be effectively prevented with little sacrifice of strength of the structure. A laser beam is feasible as a heat source for this local annealing because of its high controllability and high energy density.

From this point of view, in the present work a 2.5kW CO_2 laser was applied to surface annealing of Inconel 718. First, the laser process parameters that provided surface solutionized zones without melting the surface were obtained. Next, an effect of the surface softening on hydrogen embrittlement of Inconel 718 was investigated by means of a tensile test under a high pressure hydrogen environment using the laser surface solutionized specimens.

2. Experimental procedure

Two commercial heats of Inconel 718 whose chemical compositions are listed in Table 1 were used in this work. Inconel 718A and 718B were supplied as a 4mm-thick plate and a 10mm-diameter bar, respectively. Heat treatments for the alloys are solution annealing of 3.6ks at 1243K-oil quench-

Table 1 Chemical compositions materials used.

	Ni	Cr	Fe	Nb+Ta	Mo	Ti	Al	Co	Mn	Si	Cu	C
Inconel 718A	52.55	18.50	18.40	5.12	3.02	0.98	0.42	0.43	0.15	0.08	0.04	0.04
Inconel 718B	52.57	18.47	18.40	5.14	2.95	0.99	0.39	0.34	0.16	0.08	0.04	0.04

First International Symposium on Laser Precision Microfabrication, Isamu Miyamoto, Koji Sugioka, Thomas W. Sigmon, Editors, Proceedings of SPIE Vol. 4088 (2000) © 2000 SPIE · 0277-786X/00/$15.00

ing and two-step aging of 28.8ks at 993K-28.8ks at 894K-air cooling. The materials subjected to only the solution annealing are denoted as solution materials. The materials subjected to the solution and the two-step aging treatments are denoted as aged materials.

A 2.5kW CO_2 laser was employed to anneal the surface of the aged Inconel 718A plates. Before the laser processing, the surface of the plates was polished using #400 emery paper and cleaned with acetone. The surface was irradiated by the laser beam at a constant laser power of 2.5kW. Traverse speeds were varied from 3.33 to 250mm/s. The positions of the focal point were also varied, namely 10, 20, 30 and 40mm above the surface (denoted as Df=10, 20, 30 and 40mm, respectively). The depths of the laser annealed regions were measured on polished and etched cross-sections with an optical microscope. Vickers hardness measurements of the laser annealed regions were made on the cross-sections from the surface to the bottom at every 100μm using a load of 1.96N. Transmission electron microscopy (TEM) observations were performed using a 200kV transmission electron microscope.

The tapered bar specimen of Inconel 718B shown in Fig. 1 was used for the hydrogen embrittlement test. The middle 10mm of the specimen was subjected to the laser surface annealing treatment. One side of the specimen was clamped in a jig and rotated at a constant speed. The rotating specimen was irradiated by the laser beam using a laser power of 2.5kW and Df=20mm. Thus, a single-track laser solutionized zone was produced. A laser solutionized zone of 10 mm in length was made by ten overlapping tracks, each track overlapping a previous track by 1mm.

The hydrogen embrittlement tests were performed on the solution, aged and laser surface annealed specimens. The specimens were tensile tested in an autoclave under a hydrogen atmosphere of 29.4MPa pressure at room temperature using a cross head speed of 1.67×10^{-3}mm/s. There were two cases of treatments for the specimens before testing, namely with and without hydrogen pre-charging. The hydrogen pre-charging was carried out under a hydrogen pressure of 25MPa for 7.2ks at 800K. Thus hydrogen was absorbed into the specimen by the hydrogen pre-charging.

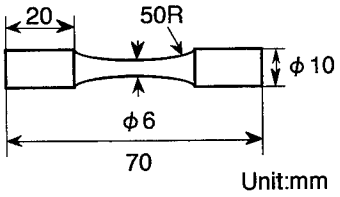


Fig. 1 Shape of hydrogen embrittlement test specimen.

3. Results and discussion

3.1 Hardness distribution and microstructure

In the laser surface annealing, too much heat input resulted in surface melting. As mentioned later, to obtain surface solutionized zones without melting the surface, laser parameters, namely defocus distance and traverse speed in the present case, should be properly selected. Figure 2 shows a typical laser surface solutionized zone (LSSZ) produced on the Inconel 718 alloy surface. TEM observations revealed that the superlattice reflections due to the presence of the age precipitates [5, 6]

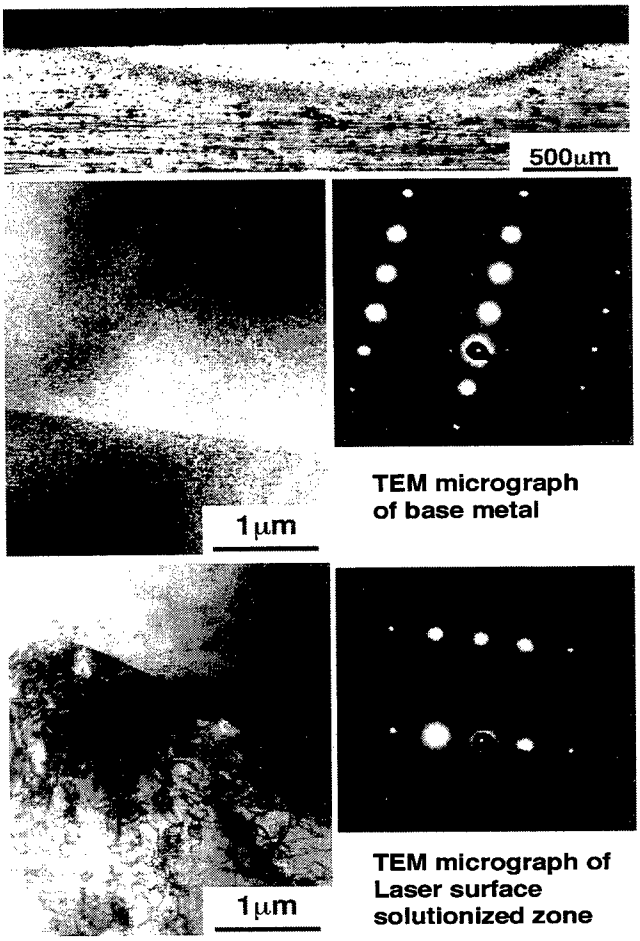


Fig. 2 Microstructures of laser surface solutionized zone (Defocus distance: 20mm, traverse speed: 16.7mm/s).

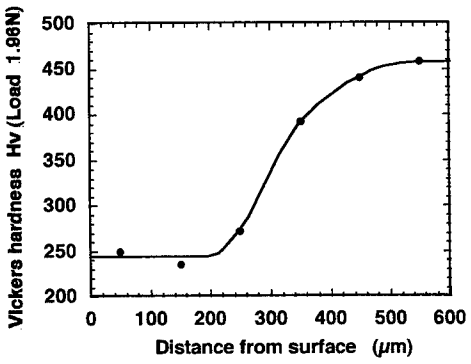


Fig. 3 Hardness distribution across the laser surface solutionized zone.

were not observed in the LSSZ. Hence, in this region, the age precipitates are found to be dissolved in the matrix owing to heating and subsequent rapid cooling by the laser annealing.

Figures 3 shows the hardness distribution across the LSSZ presented in Fig. 2. The hardness of the surface region whose depth was approximately 250μm was reduced to below 250Hv from 450Hv of the base metal hardness. This surface softened region coincide almost exactly with the lightly etched LSSZ in Fig. 2. Thus, the softened regions could be produced at the surface of the aged Inconel 718 without melting by laser surface annealing.

3.2 Optimum laser process conditions

Figure 4 shows depths of the melted and solutionized zones plotted against traverse speed for different values of Df. The LSSZ without melting were obtained in certain ranges of traverse speed, which were 167 to 250mm/s for Df=10mm, 16.7 to 50mm/s for Df=20mm, 6.67 to 16.7mm/s for Df=30mm and below 3.33mm/s for Df=40mm. Lower traverse speeds than these ranges resulted in formation of the surface melted zones except for Df=40mm where no melted zone was produced in this experiment. With higher traverse speeds than these ranges, no visible solutionized zones were obtained. Figure 4 also includes a map indicating the laser process conditions that provide the LSSZ without melting. Too small Df or too low traverse speed results in too much heat input into the surface regions, causing melting the surface. In contrast to this, too large Df or too high traverse speed results in insufficient heat input to produce LSSZ. The proper ranges of traverse speed for producing the surface solutionized zones shift to slower speeds with increasing Df. Laser process conditions to obtain desirable depths of the LSSZ can be selected using the map in Fig. 4.

3.3 Hydrogen embrittlement test

Figures 5 show the tensile strengths obtained in the tensile tests without hydrogen pre-charging. While the tensile strength of the solution specimen was somewhat lower in a hydrogen atmosphere than in air, hydrogen had no effect on the tensile strengths of the aged and surface solutionized specimens. The strength of the surface solutionized specimen was approximately 13% lower than that of the aged specimen. This is caused by the surface softened zone of the former. However, in an actual structure, the volume of the softened region will be negligibly small in comparison with the volume of the structure. Therefore, a sacrifice of strength of the structure caused by the surface softening will be also negligible.

Figure 6 shows the ductility obtained in the tensile tests with and without hydrogen pre-charging. In the tests without hydrogen pre-charging, the ductility in a hydrogen atmosphere was significantly lower than in air for all three kinds of the specimens. However, while the reduction of the surface solutionized specimen was equivalent to that of the aged one in air, the former was 1.5 times the latter in a hydrogen atmosphere. This value corresponded to that of the solution specimen. Thus sensitivity of the surface solutionized specimen to hydrogen embrittlement was comparable with that of the solution specimen. In all the three specimens, fracture initiated at the specimen surfaces in a hydrogen atmosphere. This means that sensitivity of the surface regions to hydrogen embrittlement governs the fracture of the specimens. Therefore, the softened surface region in the surface solutionized specimen

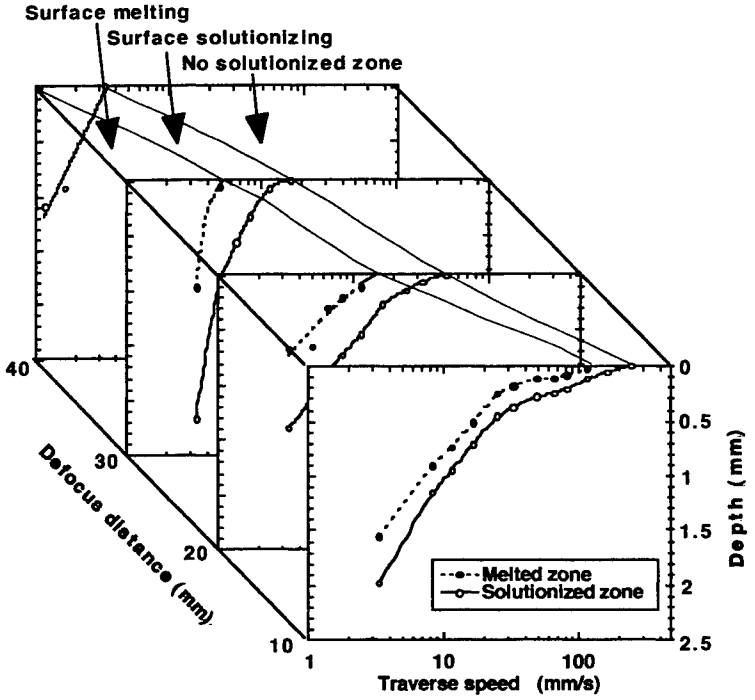


Fig. 4 A diagram describing laser surface annealing of Inconel 718.

should lead to higher resistance to hydrogen embrittlement than in the aged specimen.

In the tests without hydrogen pre-charging, hydrogen insufficiently diffuses into the specimen center. In the structures under corrosive service conditions, hydrogen will be absorbed beyond the surface softened region. Therefore, hydrogen pre-charged tensile tests were carried out to investigate if the surface softening is effective to hydrogen embrittlement when hydrogen is absorbed to the specimen center. In Fig. 6 the ductility of the aged and surface solutionized specimens with hydrogen pre-charging is also indicated. In this experiment, the laser surface solutionized specimen treated with a traverse speed of 25mm/s was used. The reduction of the surface solutionized specimen was almost twice that of the aged specimen. This value is comparable to that in the tensile test without hydrogen pre-charging, while hydrogen pre-charging significantly reduced the ductility of the aged specimen. In the aged specimen, the fracture was initiated in the vicinity of the specimen surface. However, in the laser surface solutionized specimen, the fracture initiation site was inside the specimen. Since the surface solutionized region is softer and thereby less sensitive to hydrogen embrittlement than the specimen inside, the initiation of hydrogen cracking in the surface region can be prevented. This delay of the crack initiation causes the increase in the ductility of the surface solutionized specimen.

It is revealed from these results that laser surface annealing effectively improve the resistance to hydrogen embrittlement in Inconel 718. Since a controlled laser irradiation can precisely and locally solutionize the surface of a stress concentrated region where hydrogen induced cracking is liable to occur, laser surface annealing can prevent such cracking in Inconel 718.

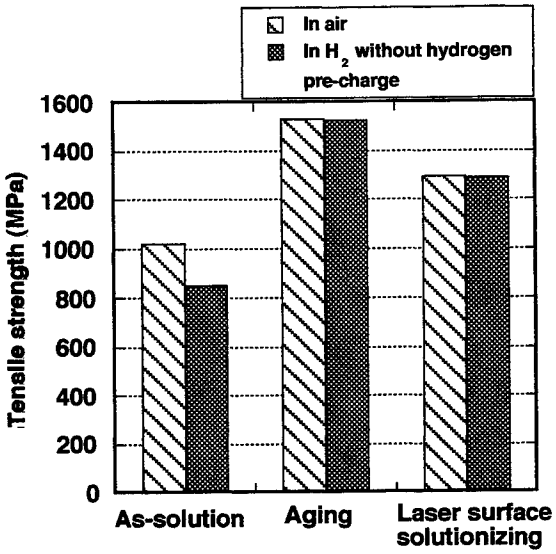


Fig. 5 Tensile strength obtained in the tensile tests without hydrogen pre-charging.

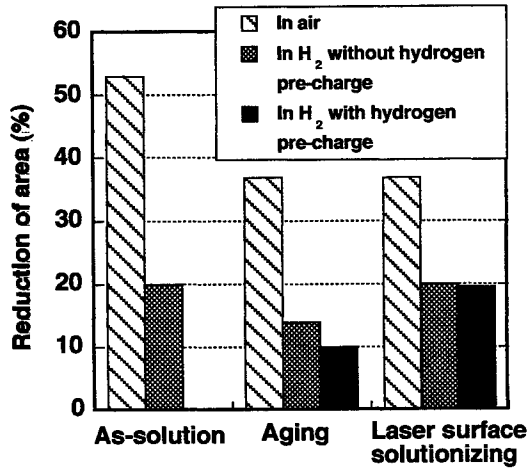


Fig. 6 Ductility obtained in the tensile tests with and without hydrogen pre-charging.

4. Conclusions

1) In laser surface annealing of Inconel 718, selecting proper laser parameters, defocus distance and traverse speed, could produce surface solutionized zones, where the age precipitates of γ' and γ'' were dissolved in the matrix, without melting the treated zones. The hardness of the surface solutionized zone decreased to below 250Hv from 450Hv of the aged base metal.
2) The depths of the surface solutionized zones increased with the defocus distance. The surface solutionized zone with more than 1mm in depth was obtained without melting in a defocus distance of 40mm and a traverse speed of 3.33mm/s. A process map indicating the laser parameters to provide surface solutionized zones without melting was obtained.
3) In hydrogen embrittlement tests both with and without hydrogen pre-charging, the surface solutionized specimens showed higher ductility than that of the aged specimens under a 29.4MPa hydrogen atmosphere at room temperature. This is because the surface solutionized zones are less sensitive to hydrogen embrittlement than the aged base metal.

References

[1] "*Superalloys Source Book*" edited by M. J. Donachie, Jr, (ASM, Metal Park, Ohio, 1984) pp. 47-400.
[2] S. Fukuyama, K. Yokogawa, M. Araki, Y. Koyari, H. Aoki and Y. Yamada: J. Soc. Mater. Sci. Jpn., **38**, (1989) pp. 539-545.
[3] S. Fukuyama, K. Yokogawa, M. Araki, Y. Koyari and Y. Yamada: J. Soc. Mater. Sci. Jpn., **40**, (1991) pp. 736-742.
[4] S. Fukuyama, K. Yokogawa, Y. Yamada and T. Iida: Tetsu to Hagane, **78**, (1992) pp. 860-869.
[5] M. Sundararaman, P. Mukhopadhyay and S. Banerjee: Metall. Trans., **23A**, (1992) pp. 2015-2028.
[6] Ya-fang Han, P. Deb and M. C. Chaturvedi: Metal Sci., **16**, (1982), pp. 555-561.

Research on Laser Texturing Process and Surface Quality Control

Jianfeng Jiang*, Yonghui He**, Yonggen Yan**, Wansheng Zhao***, Yaohuan Xu**

*School of Electronics & Information Technology, ShangHai JiaoTong University, China
E-mail: jiangjfhit@yahoo.com
**Technical Center, ShangHai BaoSteel Group Corp., ShangHai, China
***Mechanical Engineering Department 421#, Harbin Institute of Technology, China

The needs to quantity and quality of cold-rolled steel sheets demanded its fine surface quality. Some efficient methods of surface measurement are introduced to construct a surface quality controlling system. Through theoretical analysis and large amount of experiments, the basic relationship between surface topography and process parameters can be established and the optimal parameters can be got to instruct to obtain more ideal surface of roller and steel sheet.

Keywords: laser texturing, surface quality control, 3D topography measurement, optimization of process

1. Introduction

The needs to quantity and quality of cold-rolled steel sheets are gained as the rapid growing of automobile and household appliance industry. Steel sheets are demanded not only having good physical performances but also having fine surface micro-topography characteristics, which affects directly the performances of application. However, topography of steel sheet's surface comes from that of textured roller. Thus, it is very important to control the texturing process in order to control the surface quality in turn.

2. Laser-textured surface measuring and quality controlling system

Aiming at the special measuring conditions of roller and steel sheet, which have rough surface and large range of measurement, we design our own measuring devices based on the scanning white light interferometry(SWLI) method[1] and the triangular light beam scanning method(TLBS).

As shown in Fig.1, the laser-textured surface quality measuring and controlling system can be constructed based on these two profilers. On the one hand, the surface characteristic parameters can be got through measurement of

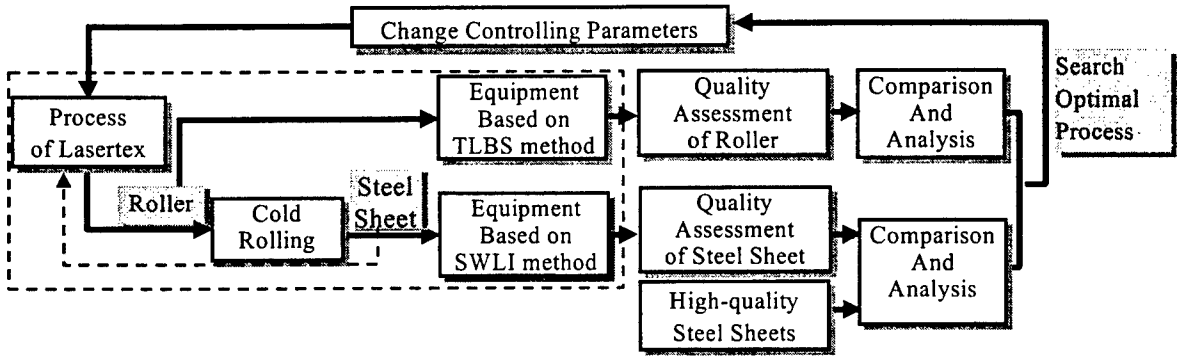


Fig.1 Constituent of laser texturing surface quality measuring and controlling system

First International Symposium on Laser Precision Microfabrication, Isamu Miyamoto, Koji Sugioka, Thomas W. Sigmon, Editors, Proceedings of SPIE Vol. 4088 (2000) © 2000 SPIE · 0277-786X/00/$15.00

laser-textured roller's surface. According to theoretic deduction and experiments, the corresponding relationship between process parameters and topography will be acquired to get optimal parameters and ideal surface of textured roller. On the other hand, after cold-rolled process, the surface characteristic parameters can also be got through measurement of topography of steel sheet's surface based on the SWLI profiler. Next, the comparison and analysis between excellent surface and them can be applied to find gap and deduce inversely to the surface of roller. Moreover, laser-texturing process can be instructed through analysis and application of the optimal process parameters. Obviously, this kind of idea meets the future trend of the development of surface topography measurement, namely measurement instructs machining.

3. Requirements of topography of laser-textured roller and steel sheets

3.1 Requirement of topography of cold-rolled steel sheet

The most instance of laser-textured steel sheets is to used as the shell of high-grade automobile and electric appliance. So it is demanded fine visual effect and its surface must has fine lacquer quality. In order to prolong the operating life, it still should have fine wear-resistance and scratch-resistance quality. In addition, fine deep-punching quality is also required in the process of molding manufacture, especially punching.

As for the fine lacquer quality, it is demanded that the fluctuation of surface should change frequently and there is large quantity of craters to contain paint. That is to say, the surface should have big peak-value density, such as value of PPI(Peaks Per Inch) or PC(Peaks Count), from the point of quantification. The bigger the value of PPI, the better the lacquer quality and the greater the bounding capacity between the film coating and the base material.

Fine wear-resistance and scratch-resistance quality demand fine lubricating property of surface, which requires that the surface should hold large amount of pits to contain lubricant and to collect small pieces of metal particles in order to avoid scratching the surface. Besides, the regular and isolated distribution of craters does good to improve the deep-punching quality. During the process of deep punching, the lubricant hold in craters will take effect to lubricate. But when the pressure rising at some position, lubricant will be pushed away, which will affect the lubricating effect. Therefore, related isolated distribution does good to make lubricant hold enclosed state under pressure and form a buffer between steel sheet and tool to insure the lubricating effect in stressed zone.

To sum up in a word, the requirements to laser-textured steel sheet can be concluded as large quantity and isolated distribution of craters.

3.2 Requirements of topography of laser-textured roller

In fact, the laser-texturing process is very complex and involves several disciplines such as thermotics, hydromechanics, metallurgy etc. Fig.2 shows the schematic figure of it and Fig.3 shows the section of crater formed.

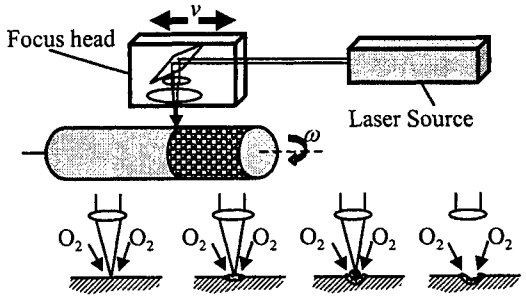


Fig.2 Schematic diagram of laser texturing process

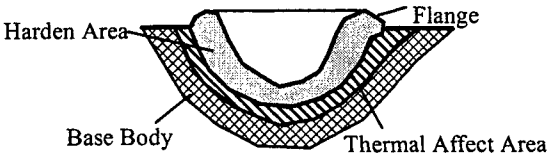


Fig. 3 Cross section figure of crater processed by laser texturing

As shown in Fig.4, in the course of rolling, the rigid convex flange embeds the steel plate and a concave pit will be formed on the surface of plate. Part of the plate's surface material will flow into the crater of roller under pressure and the related convex boss will be formed. Apparently, the topography of steel sheet will be isolated circular concave pit around regular-arranged convex flange and fits for the requirements of steel sheets mentioned above. In addition, this kind of shape benefits to improve rolling condition. On the one hand, the friction between roller and steel sheet is

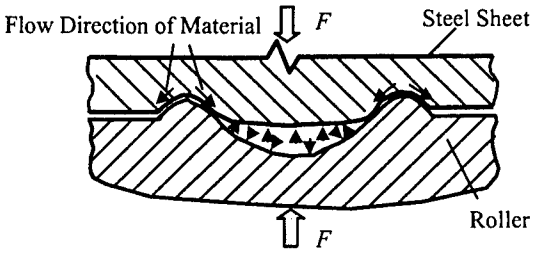


Fig.4 Relationship between laser textured roller and steel sheet when rolling

increased due to occlusion between them, which reduces the possibility of sliding and even abrasion. On the other hand, the lubricant in isolated crater will not be easy to flow away although there is pressure between roller and plate. Keeping fine lubricant condition even under high-pressure make the surface of roller and plate separate and does good to the rheology of plate when rolling and avoids adherence between roller and plate.

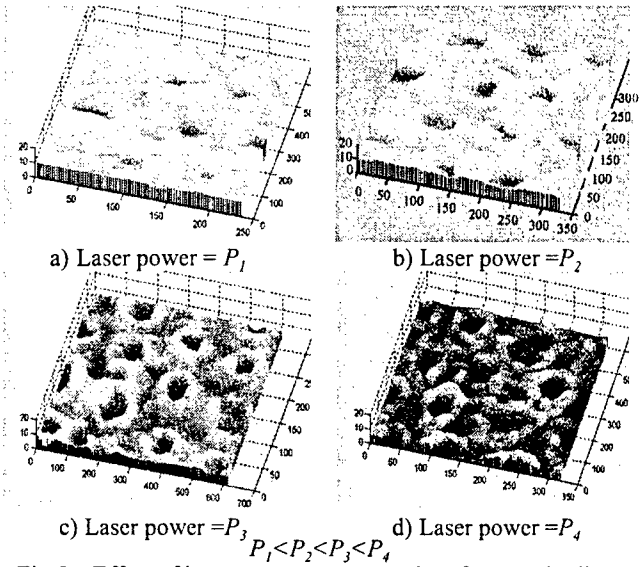
In conclusion, the requirements to the crater of laser-textured roller can be specified as follows: regular and isolated distribution of craters; big value of R_a; suitable height and width of flange outside of crater; high hardness and wear resistance of flange.

4. Surface quality control of laser-textured roller

4.1 Effect of process parameters to topography of roller

Because controlling of topography of laser-textured roller should be realized through changing process parameters of laser texturing, the effects of these parameters to machining must be understood clearly. The laser-textured process parameters include mainly laser power, laser pulse waveform (pulse width, peak pulse power), group frequency, rotary speed of roller, shifting speed of focusing head etc. In addition, the aided gas has also some effect on the machining result.

Fig.5 shows the 3D surface topography of laser-textured roller under condition of different *LP* with $P_1<P_2<P_3<P_4$. As shown in Fig.5-a) and Fig.5-b), it is obvious that the depth of crater and the height of flange is lower when the *LP* is lower. The shape of crater is apparently not ideal and the roughness is small. When the *LP* is increased, the depth and height of flange will increase and the shape of crater becomes relatively ideal as shown in Fig.5-c). But if the *LP* is increased continuously, the gasification phenomenon becomes more seriously. And the flange is decreased and even not to be formed as shown in Fig.5-d). Thus, the adjustment of laser output power should be appropriate.



a) Laser power = P_1 b) Laser power =P_2

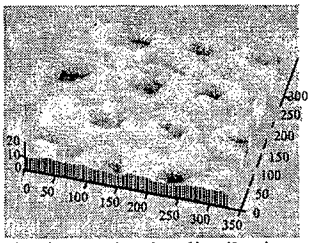
c) Laser power =P_3 d) Laser power =P_4

$P_1<P_2<P_3<P_4$

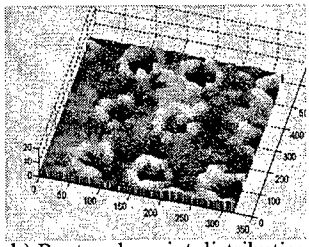
Fig.5 Effect of laser power to topography of textured roller

There are definite relationships among laser power (*LP*), pulse width (*PW*) and peak pulse power (*PPP*). Under the condition of constant value of the *LP*, the *PPP* will be decreased if the *PW* is increased. So the *PPP* should be controlled within definite range. If it is too high, gasification phenomenon caused by application of laser beam on roller will be serious and flange will be relatively lower and even not formed under the condition of same depth of crater. In order to stack flange around concave pit as high as possible, the *PPP* should be reduced and the surface can reduce to be gasified.

Fig.6 shows the 3D surface topography under condition of different pulse frequency with the same laser power and the frequency of $f_1>f_2$. Thus, if the *LP* is the same, the smaller the width of pulse, the bigger the peak pulse power. The result is that the gasification phenomenon becomes serious and the shape of crater will be not ideal. Fig.6-b) shows that the shape of the flange is not perfect. So the selection of pulse frequency, pulse width and laser pulse and the coordination of them are very important and also very complex. We need to acquire the optimal parameters through theoretic analysis and large amount of experiments



a) Diamond point distribution Laser pulse frequency = f_1



b) Rectangle point distribution Laser pulse frequency = f_2

Fig. 6 Topography of roller under different points distribution and laser pulse frequency

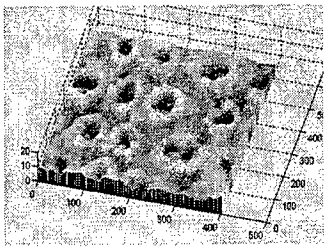
on the base of ideal 3D surface topography of roller.

The group frequency (*GF*) can be defined as the laser pulse number acted on the surface of roller. Improvement of pulse number, therefore, can be applied to improve energy density on unit area.

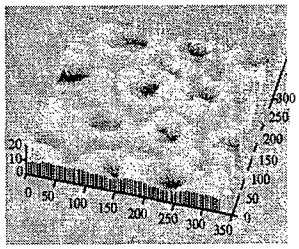
The rotary speed of roller and focusing head shifting speed will affect the distribution regularity and the degree of regularity of craters on the surface of roller directly. The controlling precision can be guaranteed by the precision of machine body and numeric system.

In order to increase the height of flange, the blowing of aided gas can be used to diffuse the molten metal. The conditions of aided gas include pressure, direction and type. The pressure must be controlled within a range. Low pressure will have little effect, but over pressure will lead to splashing of melt metal and stack them outside of crater. The direction of blowing will also affect the textured surface. An acute angle between direction of airflow and rotation of roller seems to result in ideal crater and high value of roughness, and an obtuse angle, however, will lead to serious splashing of melt metal. In addition, the type of aided gas also has effect on machining result. Under the condition of same laser parameters and with the blowing of oxygen, the depth of crater will increase but the flange will be low, which results in shallow crater and high flange on the surface of steel sheet. With blowing of hydronitrogen, roughness, however, will be decreased and the gasification phenomenon will be reduced apparently and the flange will be increased.

Fig.7 shows that the effect of aided gas's pressure to 3D topography of roller with $P_1<P_2$. It is obvious that decreasing pressure can increase the height of flange.



a) Pressure of aided gas = P_1



b) Pressure of aided gas = P_2

Fig.7 Effect of aided gas pressure to 3D topography of roller

4.2 Methods to improve quality of laser-texturing

To sum up mentioned analysis above, the following methods can be applied to control the surface quality of laser-textured roller: properly selecting *LP*, *PW* and *PPP* to control the shape of crater; precisely controlling the speed of roller and focus head shifting to control distribution of crater; properly selecting type of aided gas and direction of it to control surface topography.

But the process of laser texturing is actually a very complex one. So it is difficult to create a definite mathematical model between machining process and surface topography and to control the shape of crater precisely through selecting proper process parameters. The feasible means is to adapt the mode of experiment proof combined with theoretic analysis. Under the instruction of laser-texturing theory, different surface topography under different process parameters can be acquired through large amount of process experiments. Through comparison and analysis of them, the optimal process parameters can be got and set to texture ideal surface topography of roller.

5. Conclusion

In conclusion, it is very important to measure the surface 3D topography of roller and steel sheet, because it provides a means to embody the machining quality and instruct machining process in turn. Through theoretic analysis and experiment can we acquire optimal process parameters to improve surface quality of steel sheets.

References

[1] Jianfeng Jiang, Yonghui He, Wansheng Zhao. Non-contact high-precision surface three dimensional profiler. Proc. of SPIE, Denver,1999, Vol.3784, pp.362

Thermohydrodynamics Analysis on the Mechanism of Bump Formation in Laser Texturing

Etsuji OHMURA*, Rina MURAYAMA* and Isamu MIYAMOTO*

* *Department of Manufacturing Science, Graduate School of Engineering, Osaka University, 2-1 Yamada-oka, Suita, Osaka 565-0871, Japan*
E-mail: ohmura@mapse.eng.osaka-u.ac.jp

Laser texturing on a hard disk for a computer has been already used practically, but the mechanism of bump formation has not been elucidated yet. The purpose of this study is to elucidate the mechanism of bump formation in laser texturing by thermohydrodynamics analysis. Latent heat of evaporation, movement of gas and liquid interface, evaporation recoil pressure, Marangoni force that depends on temperature gradient and the surface tension are considered. The VOF (Volume of Fluid) method is used for the analysis of behavior of the free surface. Obtained results are as follows: (1) The downward flow is generated in the molten pool by the evaporation recoil pressure, and then it induces the outward flow in the radial direction. (2) After laser irradiation is stopped, the downward flow at the center of the molten pool and the outward flow in the radial direction are kept. Therefore, the center of the molten pool surface is lowered and the surface rises around the hole, that is, a bump is formed. (3) When the temperature coefficient of surface tension is negative, Marangoni force is most effective to the surface rise when the resolidification starts outside of the bump.

Keywords: computer simulation, thermohydrodynamics, laser texturing, bump, evaporation recoil pressure, molten metal flow

1. Introduction

Laser texturing of a hard disk for a computer is one of the most popular industrial applications of laser precision microfabrication [1]. In this technology, a short pulse YLF laser is irradiated to the CSS zone of a hard disk and many fine bumps are formed. CSS zone is the area where the magnetic head lands when a hard disk stops. The height of bumps is about 10 to 20 nm. Elucidation of the bump formation mechanism is indispensable for reliability improvement of laser texturing.

It may be guessed that molten metal flow accompanied with evaporation due to laser irradiation will be deeply concerned with the bump formation. There are many subjects that should be solved in the modeling and numerical calculations when such melting phenomena are analyzed. One of them is treatment of the free surface of molten metal. Purposes of this study are as follows: (1) Mathematical modeling of molten metal flow accompanied with evaporation due to laser irradiation. (2) Establishment of numerical calculation method by applying the VOF method [2] to thermohydrodynamics analysis of free surface problem. (3) Elucidation of bump formation mechanism in laser texturing, paying attention to the evaporation recoil pressure and Marangoni force.

2. Method of analysis

2.1 Analysis model

Considering the estimation results of physical quantities concerned with evaporation [3], the present analysis model can be expressed by **Fig. 1**. The model is axisymmetric. The r axis is taken in the direction of radius and the z axis is taken in the direction of depth. Fundamental equation in the solid phase is heat conduction equation. Fundamental equations in the molten metal are the equation of continuity

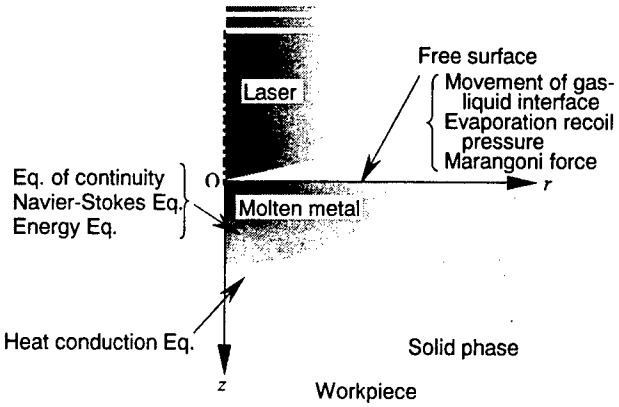


Fig.1 Analysis model

First International Symposium on Laser Precision Microfabrication, Isamu Miyamoto, Koji Sugioka, Thomas W. Sigmon, Editors, Proceedings of SPIE Vol. 4088 (2000) © 2000 SPIE · 0277-786X/00/$15.00

$$\frac{1}{r}\frac{\partial ru}{\partial r}+\frac{\partial v}{\partial z}=0, \tag{1}$$

Navier-Stokes equations

$$\frac{\partial u}{\partial t}+u\frac{\partial u}{\partial r}+v\frac{\partial u}{\partial z}=-\frac{1}{\rho}\frac{\partial p}{\partial r}+\eta\left[\frac{1}{r}\frac{\partial}{\partial r}\left(r\frac{\partial u}{\partial r}\right)+\frac{\partial^2 u}{\partial z^2}-\frac{u}{r^2}\right], \tag{2}$$

$$\frac{\partial v}{\partial t}+u\frac{\partial v}{\partial r}+v\frac{\partial v}{\partial z}=-\frac{1}{\rho}\frac{\partial p}{\partial z}+\eta\left[\frac{1}{r}\frac{\partial}{\partial r}\left(r\frac{\partial v}{\partial r}\right)+\frac{\partial^2 v}{\partial z^2}\right] - g\beta(T-T_M), \tag{3}$$

and energy equation

$$\rho c\left(\frac{\partial T}{\partial t}+u\frac{\partial T}{\partial r}+v\frac{\partial T}{\partial z}\right)=\frac{1}{r}\frac{\partial}{\partial r}\left(Kr\frac{\partial T}{\partial r}\right)+\frac{\partial}{\partial z}\left(K\frac{\partial T}{\partial z}\right) + Q, \tag{4}$$

where u and v are velocity in the r and z directions, respectively, and t is time, p pressure, η kinetic viscosity coefficient, ρ density, c specific heat, g gravitational acceleration, β coefficient of cubical expansion, T temperature, T_M melting point and Q heat generation per unit volume per time.

At the free surface, the movement of gas and liquid interface is expressed by

$$q+K\frac{\partial T}{\partial n}=\rho l_B\frac{\partial R}{\partial t}, \tag{5}$$

where R is radius of curvature at gas and liquid interface and $\partial/\partial n$ is inner normal derivation. Evaporation recoil force is given by

$$f_V=\dot{m}_V v_T, \tag{6}$$

and Marangoni force, which depends on temperature gradient, is given by the following equation [5]:

$$\frac{\partial T}{\partial s}\frac{\partial \gamma}{\partial T}=\mu\frac{\partial u_S}{\partial n}, \tag{7}$$

where γ, μ are surface tension coefficient, viscosity coefficient, respectively, $\partial/\partial s$ is tangential derivation and subscript S shows that its value is taken on surface.

2.2 Treatment of free surface

As approach to treat free surface in numerical fluid dynamics, MAC method and VOF method are known well. In MAC method, marker particles are put on the free surface. Geometry change of free surface can be understood by following the movement of marker particles. But MAC method may be complicated when we treat the movement of gas and liquid interface accompanied with evaporation and decrease of volume. Therefore, in this study, we apply the VOF method. In VOF method, the function F is defined, that means the volume fraction of liquid phase physically. And its transport equation is given by

$$\frac{\partial F}{\partial t}+\frac{\partial Fu}{\partial x}+\frac{\partial Fv}{\partial y}=0 \tag{8}$$

for incompressible-fluid.

By the way, VOF method was proposed to analyze flow of fluid at an uniform temperature. In our problem, there is temperature distribution in the molten pool. Therefore we must derive the energy equation considering the function F.

If we take an arbitrary closed surface in the fluid contains free surface, the equation

$$\rho c\frac{\partial}{\partial t}\int_V FT dV=\int_S FK\nabla T dS-\rho c\int_S FT\boldsymbol{u}\cdot\boldsymbol{n}dS \tag{9}$$

is derived from the energy conservation law. That is, energy increase in the region V is equal to the inflow energy from boundary S, which is given by the sum of heat conduction and enthalpy transportation. Considering Gauss theorem, we obtain

$$\int_V\left[\rho c\frac{\partial FT}{\partial t}-\nabla\cdot(FK\nabla T)+\rho c\nabla\cdot FT\boldsymbol{u}\right]dV=0. \tag{10}$$

Here V is arbitrary, and then the integrand must be zero, therefore, the equation

$$\rho c\frac{\partial FT}{\partial t}+\rho c\nabla\cdot FT\boldsymbol{u}=\nabla\cdot(FK\nabla T) \tag{11}$$

is obtained. Transport equation of the function F is expressed by

$$\frac{\partial F}{\partial t}+\nabla\cdot F\boldsymbol{u}=0, \tag{12}$$

as shown in Eq. (8). Accordingly, the energy equation considering the function F is obtained as

$$F\frac{\partial T}{\partial t}+F\boldsymbol{u}\cdot\nabla T=\frac{1}{\rho c}\nabla\cdot(FK\nabla T). \tag{13}$$

In numerical computations, the staggered mesh is used here and the above-mentioned equations are approximated by the finite difference equations.

3. Analysis results and discussions

3.1 Transition of surface profile

Figure 2 shows the change of surface profile of aluminum due to the laser irradiating condition shown in **Table 1**. The z axis is magnified 40 times of the r axis. Maximum temperature reaches boiling point at time about 10 ns. Center of the surface becomes hollow in concave after evaporation stats. The average velocity of the movement of gas and liquid interface in about 5 ns before stopping laser irradiation is about 9 m/s, which is relatively large. This is caused by both evaporation and evaporation recoil pressure, and effect of the latter is more remarkable. We cannot see the surface rise around the hole during laser irradiation. The center of surface continues to descend downward until the time 55.35 ns when resolidification of the molten metal is

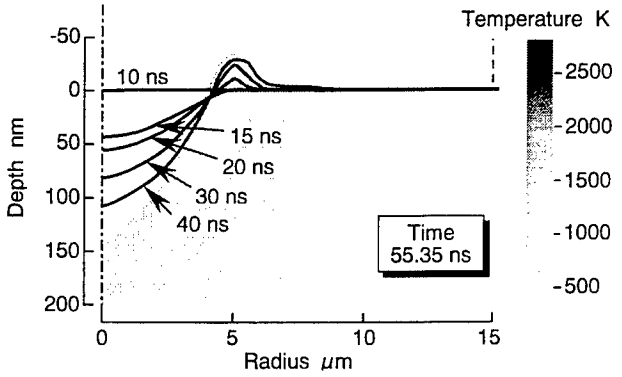


Fig. 2 Transition of surface profile

Table 1 Laser irradiation condition

Laser power	425 W
Pulse width	15 ns
$1/e^2$ radius	15 μm
Absorptivity	0.3

completed. The bump is formed after stopping laser irradiation.

3.2 Transition of molten metal flow

Temperature distribution and flow of molten pool at time 15, 30 and 45 ns are shown in **Fig. 3**. Temperature is shown by the gray scale. The dots show the grid points whose temperature is above melting point. Velocity of flow is shown by a vector. The length of a segment is magnitude of the velocity. During laser irradiation, the downward flow is generated in the molten pool by the evaporation recoil pressure, and then it induces the outward flow in the radial direction. On the other hand, the outward flow is generated at the surface area of radius 5 to 6 μm from the center of the laser beam, because the temperature gradient is steep at this area and Marangoni force is the largest. The surface rise around the hole during laser irradiation is very small, because it is compensated with the mass loss by evaporation.

After laser irradiation is stopped, the evaporation recoil pressure does not occur of course, but the downward flow at the center of the molten pool and the outward flow in the radial direction are kept. Therefore, the center of the molten pool surface is still lowered. The downward velocity of the gas and liquid interface is about 2.3 m/s, which is about one fourth of the velocity in evaporation period. The outward flow forms a semi-doughnut-shaped rise around the hole, that is, the bump is formed, because evaporation does not occur now. Marangoni force acts to draw the surface of the molten pool in the radial direction, because the temperature coefficient of surface tension for aluminum is negative. Therefore Marangoni force is most effective to the surface rise when the resolidification starts outside of the bump. The surface generation process accompanied with evaporation above mentioned is shown schematically in **Fig. 4**.

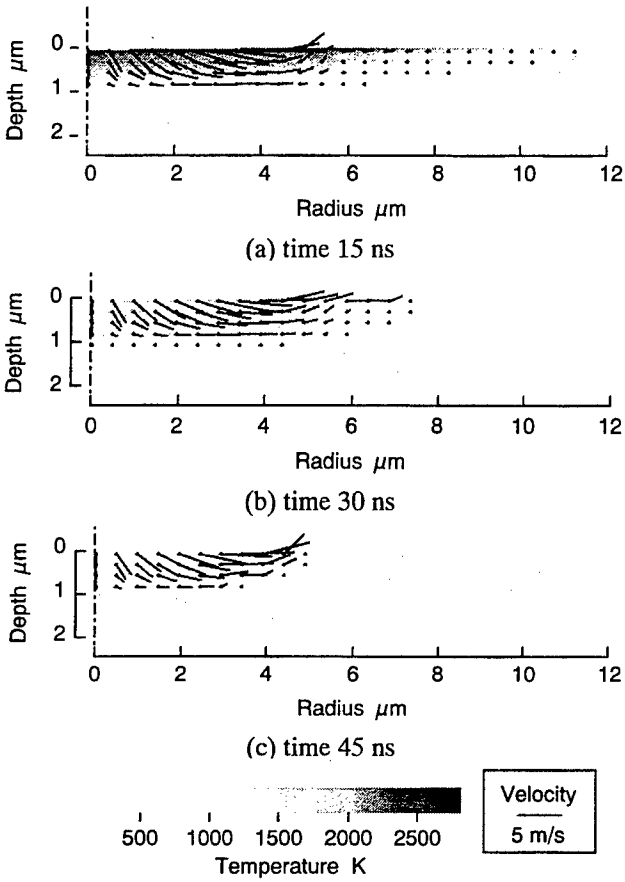


Fig. 3 Transition of molten metal flow

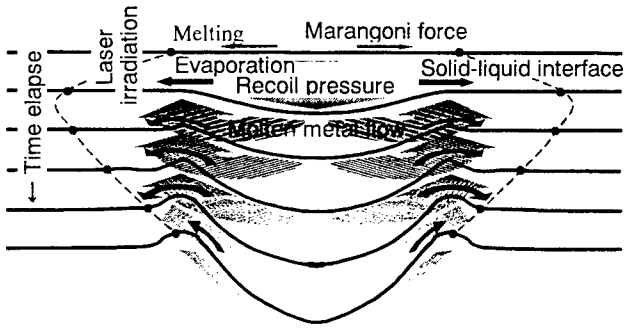
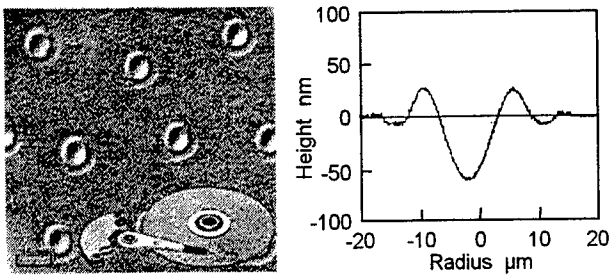


Fig. 4 Schematic sketch of transition of surface profile

3.3 Effect of Marangoni force

Figure 5 shows an optical microscopic photograph of bumps on a hard disk and a measured result of the surface profile obtained by AFM. In this case, the bumps are generated on a NiP film on aluminum substrate. Therefore, the target material is not pure aluminum, but the surface profile is almost the same as the present analyzed result. Strictly speaking, we can see a small concave round the remarkable semi-doughnut-shaped surface rise and a very small surface rise around the concave.



(a) (b)

Fig. 5 Laser texturing on a computer hard disk (a) and surface profile by AFM (b)

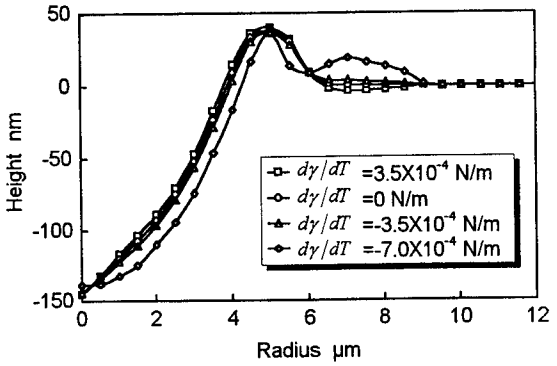


Fig. 6 Change of surface profile under various $\partial\gamma/\partial T$

Using various values for the temperature coefficient of surface tension $\partial\gamma/\partial T$, the thermohydrodynamics analyses were carried out. The results on surface profile and transition of bump height are shown in **Figs. 6** and **7**, respectively. When $\partial\gamma/\partial T$ is positive, a small concave is generated around the bump, because the inward flow at the surface, where the temperature gradient is large, is induced by the Marangoni force. When $\partial\gamma/\partial T$ is negative, a small surface rise is generated around the bump because of the outward flow caused by Marangoni force. Especially, it is remarkable when $\partial\gamma/\partial T$ is -7×10^{-4} N/m K, which is two times of $\partial\gamma/\partial T$ in the previous analysis, and the surface profile looks like the AFM profile in Fig. 5 (b). As shown in Fig. 7, Marangoni force has an effect to lower the bump height when $\partial\gamma/\partial T$ is negative.

4. Conclusions

One mathematical modeling of molten metal flow accompanied with evaporation due to laser irradiation was proposed. Applying VOF method to thermohydrodynamics analysis of free surface problem, numerical calculation method was established. Through these mathematical modeling and numerical calculation method, bump formation mechanism in laser texturing was elucidated as follows:.

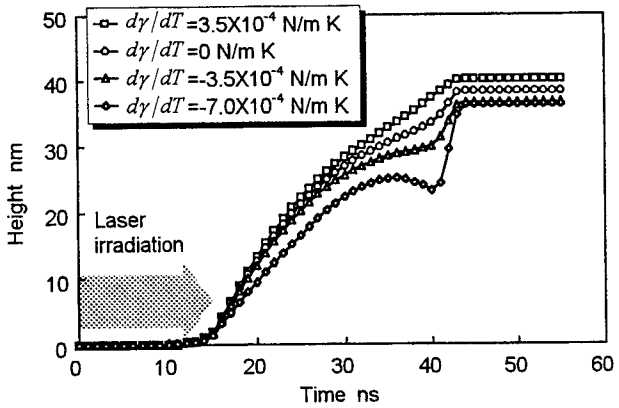


Fig. 7 Transition of bump height under various $\partial\gamma/\partial T$

(1) The downward flow is generated in the molten pool by the evaporation recoil pressure, and then it induces the outward flow in the radial direction. The surface rise around the hole during the laser irradiation is very small, because it is compensated with the mass loss by evaporation.

(2) After laser irradiation is stopped, the evaporation recoil pressure does not occur, but the downward flow at the center of the molten pool and the outward flow in the radial direction are kept. Therefore, the center of the molten pool surface is still lowered and the surface rises in a semi-doughnut shape around the hole, that is, the bump is formed.

(3) The Marangoni force that acts to draw the surface of the molten pool in the radial direction, when the temperature coefficient of surface tension is negative. Therefore Marangoni force is most effective to the surface rise when the resolidification starts outside of the bump.

Acknowledgements

A part of this study was supported by Grants-in-Aid of Scientific Research from the Ministry of Education, Science and Culture of Japan in 1997, 1998 and 1999.

References

[1] P. Baumgert, D.J. Krjnovich, T. A. Nguyen and A. C. Tam: IEEE Trans. on Magnetics, **31**, (1995) 2946.

[2] C. W. Hirt and B.D. Nichols: J. Comp. Phys., **39**, (1981) 201.

[3] E. Ohmura, H. Hayashi and I. Miyamoto, Int. J. JSPE, 32, (1998) 196.

[4] M. I. Cohen: Material Processing, Laser Handbook, Vol. 2 (F. T. Arecci and E. O. Schulz-Dubois, eds.), North-Holland Publ. Co. (1972) 1577.

[5] V.V. Semak, J.A. Hopkins, M.H. McCay and T.D. McCay: Proc. of ICALEO'94 (1994) 641.

[6] T.R. Anthony and H.E. Cline: J. Appl. Phys., **48**, 9 (1977) 3888.

Micromachining with a Frequency Converted Diode-Pumped Nd:YAG Laser

Kevin HARTKE*, Kevin KING**, Dave FARSON***, Kevin ELY*

*EWI, 1250 Arthur Adams Dr., Columbus OH 43221
E-mail: kevin_hartke@ewi.org
** Cutting Edge Optronics, St. Louis, MO 63301
*** Ohio State University, Columbus OH 43210

Laser ablation with a Q-switched diode-pumped Nd:YAG laser was used to produce grooves in H-13 tool steel and 6061 aluminum specimens. The relationships between laser wavelength, power and travel speed and the material removal rate, groove depth and quality were studied. Nondimensional relationships between the process and material variables and groove area and depth were found. The material removal rate was found to be significantly higher for the aluminum material. However, no significant increase in material removal or groove quality was found for the shorter wavelength laser energy. Significant recast was observed in grooves having a depth/width ratio larger than approximately 1 and all grooves had some amount of recast material remaining as a burr at the top edges.

Introduction

As diode-pumped solid state laser technology continues to be rapidly developed, these lasers offer significant advantages as an energy source for micromachining. They are relatively efficient compared to lamp-pumped Nd:YAG lasers and thus require less cooling and have smaller laser cavities for equivalent output power than lamp-pumped lasers. Due to lower thermal distortion, the beam quality is high so small focus spot sizes can be obtained, which allows faster machining with better feature definition. When pulsed at high peak power, they can be effectively frequency-doubled to produce 0.532 μm radiation.

In this study, grooves were machined in H-13 tool steel and 6061 aluminum specimens using a diode-pumped Nd:YAG laser, with and without frequency conversion. Comparisons are made between the effectiveness of machining (material removal rate and depth) with the fundamental and frequency-doubled wavelengths. The quality of the machined features is assessed qualitatively.

Experimental Setup and Procedure

For machining at the fundamental wavelength, a laser system having the configuration sketched in Figure 1 was used. The laser used dual pump-heads, each with a single Nd:YAG rod and multiple diode laser bars for pumping. The cavity included an electro-optic Q-switch and an aperature for improving mode quality. The average power of the linearly polarized output beam was adjusted using a rotating extra-cavity polarizing element and the beam was converted to circular polarity before being delivered to the work piece. Further optical elements in the beam delivery system were the same as for the frequency-doubled system and are discussed below. The frequency-doubled laser used a similar cavity design to that shown in Figure 1, but with one pump-head and an acousto-optic q-switch. As shown in Figure 2, the output beam was cleaned by aperturing, expanded with a telescope, apertured again and then focused onto the work surface. For both systems, the external and internal beam apertures ensured that $M^2 \approx 1$, so the focused spot diameter d_s could be estimated using the relation

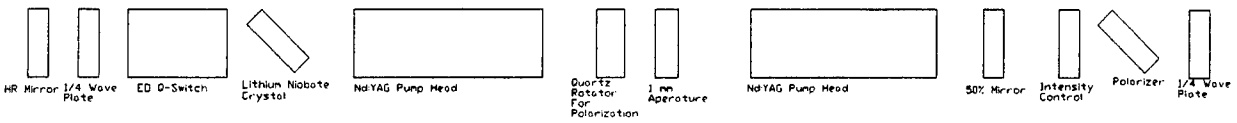


Figure 1. E-O Q-switched laser cavity design.

$$d_s = \frac{4}{\pi}\lambda\frac{D}{f} \qquad (1)$$

where λ is wavelength (1.06 μm or 0.532 μm), D is beam diameter at the focusing optic (6 mm) and f is lens focal length (50 mm). The spot sizes calculated from (1) are 12 mm for λ = 1.06 μm and 6 μm for λ = 0.532 μm.

To assess the independent effects of selected process input parameters (pulse frequency, pulse time and

First International Symposium on Laser Precision Microfabrication, Isamu Miyamoto, Koji Sugioka, Thomas W. Sigmon, Editors, Proceedings of SPIE Vol. 4088 (2000) © 2000 SPIE · 0277-786X/00/$15.00

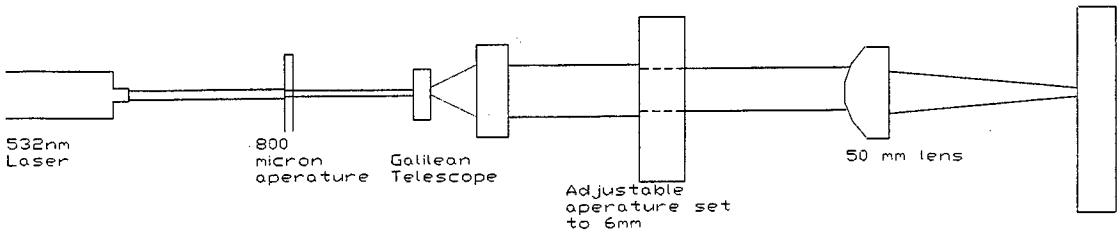


Figure 2. Beam delivery optics (used for both 0.532 and 1.06 μm laser systems).

travel speed), they were varied individually over the ranges shown in Table 1. Note that the pulse time was constant at 15 ns irrespective of pulse frequency for the E-O Q-switch laser but varied approximately linearly with pulse frequency for the A-O (frequency-doubled) laser. The average power values shown were measured with a power meter prior to processing at each setting. In all tests, grooves were produced using 5 passes at the selected settings.

Table 1. Processing Parameters.

λ μm	Pulse Freq. kHz.	Pulse Time ns	Travel Speed mm s^{-1}	Avg. Power W
1.06	0.5 - 2	15	4 - 13	0.4 – 1.6
0.532	5 - 9	35 - 45	4 - 13	0.7 – 1.0

Results

The micromachined grooves were cross sectioned and measured. The resulting groove dimensions are tabulated in Table 2.

Discussion

Inspection of the data allows one to conclude that the aluminum was much more easily machined than the steel. For comparable process travel speed and average power, groove depths and area were both two to three times as large for the aluminum. The effect of laser wavelength is somewhat more difficult to assess since the spot size and travel speeds varied substantially in the trials at the two wavelengths.

To compare the effects of process parameters and material properties more effectively, non-dimensional correlations were made between the groove dimensions and process and material parameters. This analysis was carried out using the well-known Buckingham Pi technique [1]. An attempt was made to identify the simplest correlations that produced an acceptable fit to the data.

In the case of groove area, the simplest relationship that produced a significant linear fit to the data involved nondimensional parameters that have been previously applied to weld cross sectional area [2]. An expression nondimensional groove area, labeled Ch because it was introduced by Christensen [3] is

Table 2. Beam Delivery system design.

Pulse Freq KHz.	Travel Speed in/min	Power kW	Area per Pass μm^2	Depth per Pass μm
	Tool Steel λ = 1.06 μm			
1	20	0.8	291.6	7.242
1	30	0.8	81	2.442
1	10	0.8	283.4	8.648
1	20	0.6	119	3.89
1	20	1	281	7.158
2	20	1.6	276.8	8.732
0.5	20	0.4	58	1.944
	Tool Steel λ = 0.532 μm			
7	80	0.8	79.4	3.766
7	120	0.8	44	2.152
7	40	0.8	213.4	10.8
9	80	0.72	57.2	2.69
5	80	0.92	80.8	2.98
7	80	1.0	178	5.544
7	80	0.7	31.6	2.318
	Aluminum λ = 1.06 μm			
1	20	0.8	633.4	14.98
1	30	0.8	367.4	9.6
1	10	0.8	754.6	24.792
1	20	0.6	456.6	12.91
1	20	1	680.4	16.138
2	20	1.6	1477.2	36.25
0.5	20	0.4	246.4	6.994
	Aluminum λ = 0.532 μm			
7	80	0.8	291.8	13.49
7	120	0.8	223.6	8.482
7	40	0.8	570.6	35.104
9	80	0.8	281.4	15.806
5	80	0.8	288.6	10.468
7	80	1.0	524.8	17.006
7	80	0.7	106.4	7.2

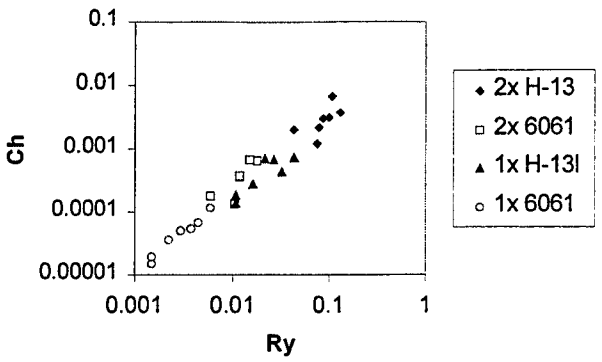


Figure 3. Correlation between nondimensional groove area (Ch) and nondimensional process heat input (Ry).

$$Ch = S^2 \cdot A \cdot \alpha^{-2}$$

Where S is travel speed, A is groove cross sectional area removed per pass (measured area divided by 5) and α is thermal diffusivity of the material as shown in Table 1. An expression for nondimensional laser energy input, labeled Ry because it was first introduced by Rykalin is

$$Ry = P_{av} \cdot S \cdot \alpha^{-2} \cdot H_{sl}^{-1}$$

where P_{av} is average power and H_{sl} is enthalpy of melting of the material. A log-log plot showing the correlation between these two parameters is shown in Figure 3. Although there is significant scatter in the data ($R^2 = 0.94$) it is evident that the general linear trend of the data is well-expressed by the correlation

$$Ch = 0.053 * Ry^{1.21}.$$

A second correlation was found for the depth data. The nondimensional depth was expressed as D/r_s where D is depth per pass (measured depth divided by 5) and r_s is focus spot radius. It was correlated to duty cycle T_{on} / T, phase change temperatures T_{lv} / T_{sl}, phase change enthalpies H_{lv} / H_{sl}, and nondimensional energy input $P_{av} / S \cdot \alpha^2 \cdot \rho$ where T_{ON} is pulse time (s), T is time between pulses (s), H_{lv} is enthalpy of vaporization, T_{lv} is boiling temperature at atmospheric pressure, T_{sl} is melting temperature and ρ is the density of the solid material. The regression-fit relation among these variables was found to be

$$D/r_s = 100 \, (T_{on} / T)^{0.57} (T_{lv} / T_{sl})^{4.67} (H_{lv} / H_{sl})^{0.88} (P_{av} / S \cdot \alpha^2 \cdot \rho)^{0.85}.$$

The correlation coefficient for the linear fit to the log data was 0.92. The correlation is displayed graphically in Figure 3, which plots measured dimensionless depth against the values predicted from (3).

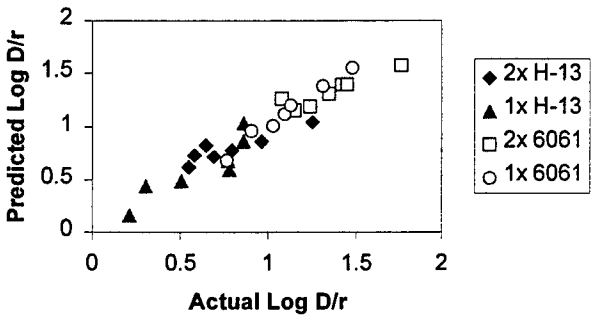


Figure 4. Correlation between measured nondimensional groove depth and that predicted by Eq. (5).

To determine if laser wavelength had an effect on machining, the residual errors to a linear curve fit to the log data were examined. There was no clear difference between the machining results obtained at the two wavelengths. This leads to a conclusion that there was no significant difference in the efficiency of material removal at the two wavelengths used in the trials.

An additional set of tests were run to determine the maximum aspect ratio of grooves that could be produced in aluminum. Grooves were machined using 0.532 μm energy at the lowest travel speed setting shown in Table 3. The grooves produced by 20 machining passes were approximately 300 μm deep and 15 μm wide, a depth/width ratio of 29. A typical groove cross section is shown in Figure 5. Some un-removed material (recast) was observed in the bottom of the grooves. Additional

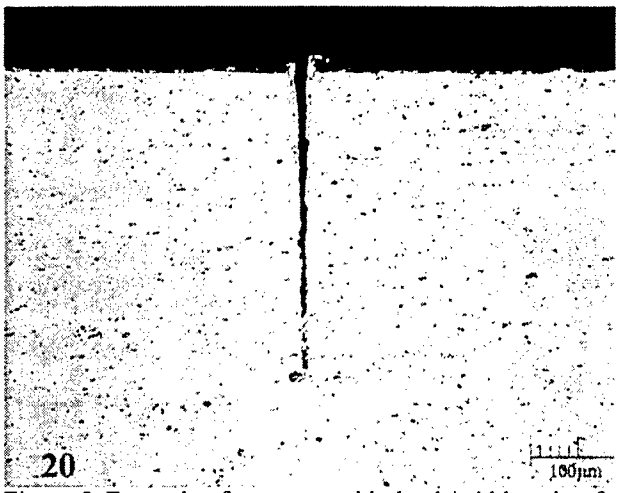


Figure 5. Example of a groove with depth/width ratio of 20 produced in aluminum material with 0.532 μm laser

passes did not increase groove depth but did remove some of the recast.

Conclusions

Micromachining of grooves in tool steel and aluminum using a diode-pumped solid state laser. Both

the fundamental (1.06 μm) and freqnency-doubled (0.532 μm) wavelengths were used. It was found that the aluminum material was machined much more effectively than the tool steel. It was also noted that a significant amount of recast remained in grooves when the depth/width ratio was more than approximately 1. Nondimensional correlations to the data revealed that there was no significant difference in machining effectiveness between the fundamental and frequency doubled wavelengths.

References

[1] E.R.G. Eckert, R. Drake: "*Analysis of Heat and Mass Transfer*", (McGraw Hill, NY, 1972).
[2] P.W. Fuerschbach: Weld. J., **75,** (1996) 24.
[3] N. Christensen, V. Davies, K. Germundsen: Brit. Weld. J., **12**, (1965), 54.

High-Precision Micro Cutting of Ceramics with Short-Pulsed Solid-State Lasers

Joachim RADTKE, Tobias ABELN, Michael WEIKERT and Friedrich DAUSINGER

Institut fuer Strahlwerkzeuge (IFSW), University of Stuttgart,
Paffenwaldring 43, 70569 Stuttgart, Germany
E-mail: radtke@ifsw.uni-stuttgart.de

This contribution will present results for high-precision cutting of technical ceramics with short-pulsed solid-state lasers in fundamental and frequency-doubled wavelength. On the basis of ample experiments, a surprising absorption behaviour of some ceramics in the case of irradiation with high intensity will be discussed. Furthermore, the influence of wavelength and process gas on cutting speed and quality is demonstrated. The investigations resulted in a process strategy with multiple passing over of the kerf suited for remarkably improving process velocity and quality. Finally, structures applicable for nozzles and spinnerets are shown.

Keywords: micro cutting, ceramic, short-pulsed, solid-state laser, laser-machining.

1. Introduction

In the case of ceramics, conventional processes cannot meet the increasing requirements with regard to reduced dimensions and tolerances. Furthermore, there is a demand for non-circular shaped holes which cannot be adequately fulfilled by conventional techniques. For this reason, the interest of industry in precise laser machining of ceramics has constantly grown.

Up to now, CO_2-lasers have almost exclusively been used for laser processing of ceramics in industrial applications. In the case of micro machining, mainly excimer lasers have been taken into account. The wavelengths emitted by both types of lasers are strongly absorbed in ceramics, which is not expected for solid-state lasers.

2. Absorption behaviour of ceramics

Regarding the interaction of laser beam and bulk material, there is an essential distinction between pure and homogeneous ceramics and technical ceramics. Furthermore, there is a difference in absorption phenomena at high and low intensity.

2.1 Low temperature, low intensity absorptivity

In literature, for pure ceramics some data of optical properties can be found [1]. The degree of reflection is lower than in metals and much more of the incident light is penetrating into the bulk material. In metals, penetrating radiation is completely absorbed in a surface layer of a thickness an order of magnitude smaller than the wavelength. Fig. 1 depicts the optical penetration depth in case of some ceramics. It is remarkable that the behaviour of these ceramics is totally different from those of metals in the spectral range between 0,5 and 10 µm. The penetration depth is even up to three orders of magnitude larger than the wavelength in this so-called transmission window.

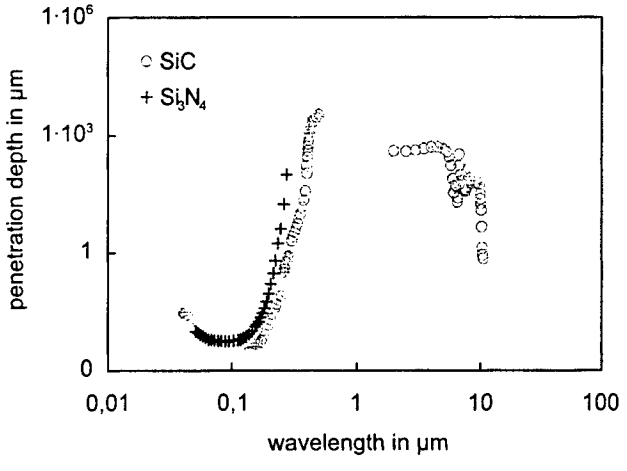


Fig. 1: Absorption length l_α in pure and homogeneous SiC and Si_3N_4 depending on wavelength.

As laser ablation is a thermal process, the penetration depth has a decisive influence. Depending on the incident fluency, a certain maximum of optical penetration should not

First International Symposium on Laser Precision Microfabrication, Isamu Miyamoto, Koji Sugioka, Thomas W. Sigmon, Editors, Proceedings of SPIE Vol. 4088 (2000) © 2000 SPIE · 0277-786X/00/$15.00

be exceeded to reach temperatures required for laser ablation. Neglecting heat conduction, it is possible to calculate achievable surface temperatures in dependence on optical penetration depth and fluency. In case of pure ceramics only a deficient heating is to be expected because of the optical penetration depth in the range of 1 mm.

2.2 High temperature, high intensity absorptivity

Despite of what could be deduced from Fig. 1 and the calculations, ceramic materials can be machined with Nd:YAG-lasers quite efficiently [2]. An explanation for this surprising observation was found by investigating the high temperature optical behaviour of various ceramics with a calorimetric set-up [3]. Fig. 2 shows results for technical Si_3N_4 and AlN. Besides a more or less pronounced trend of decreasing penetration depth, both materials show a dramatic increase in reflectivity starting at a temperature depending on material composition. In [4], this effect was connected with the high temperature chemistry of these materials causing a decomposition in gaseous and liquid metallic components, mainly. From this we can conclude that in case of energy density values high enough to heat the surface within pulse duration to decomposition temperature, the ceramic material starts to show optical behaviour like metals.

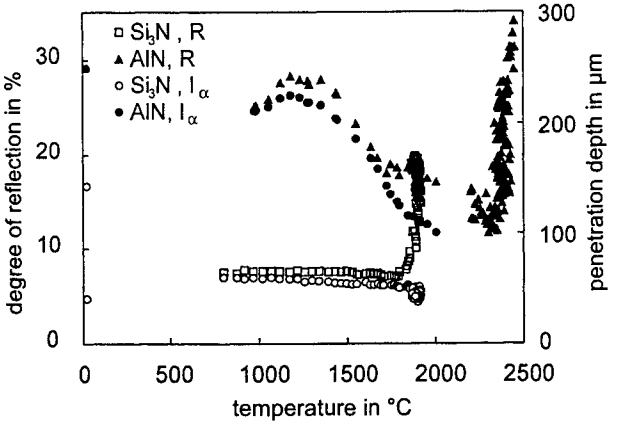


Fig. 2: Reflectivity R and absorption length l_α of technical AlN and Si_3N_4 at high temperature.

3. Ablation behaviour of ceramics

In ceramics, the change to metallic behaviour described above is limited to the hot interaction zone, the surrounding bulk material remains semi-transparent. The change to metallic behaviour however, should not be necessarily permanent as transmission experiments with picosecond laser pulses turned out at the General Physics Institute in Moscow. The results of these experiments are shown in Fig. 3. At first, initial transmission through a thin ceramic plate was measured at an intensity too low for ablation. Afterwards transmission was measured during ablation with an intensity of 10^{12} W/cm^2 and finally with low intensity after ablation. During ablation, a transmission an order of magnitude smaller than the initial value was measured for both ceramics. In case of AlN, the degree of transmission remained at a low level after ablation whereas the value of Al_2O_3 nearly approached the initial value. An explanation for the decrease of transmission during ablation is plasma shielding which was confirmed in further experiments [5]. On the other hand, the permanent decrease of transmission for AlN could not be explained. For this reason, it should be supposed that a highly absorbing layer is formed during irradiation with lasers of high intensity. In case of AlN, this layer kept the optical properties after ablation, but lost them for Al_2O_3.

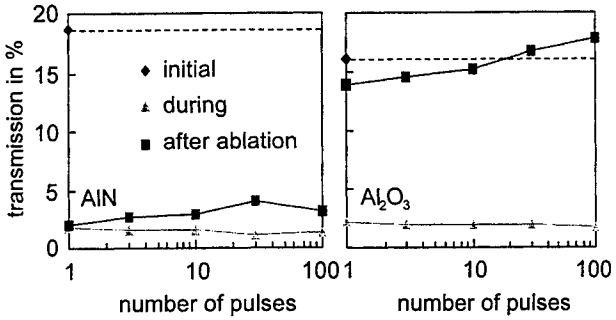


Fig. 3: Transmission of laser light through thin ceramic plates.

According to the Hirschegg Model for drilling with short-pulsed lasers [5] also two tools acting during the cutting process can be assumed for the special process technique described below. The primary one is the laser beam which is responsible mainly for the deepening of the kerf in the direction of its propagation and feed direction. The secondary tool is a laser induced plasma which acts primarily in radial directions, widens the kerf and smooths the cutting edge.

4. Processing technique

As we have shown in several publications [5-7] for drilling, a breaking up of the process in a multitude of ablation steps (the so-called helical drilling) is suitable to enhance accuracy. We adapted this technique to the high-precision micro cutting of complex geometries. In contrast to conventional cutting which is essentially a through drilling followed by the cutting procedure, the so-called laser-machining reaches the breakthrough after multiple passing over of the kerf. While penetrating the workpiece, the focal position, the pulse energy and to some extend the energy per section can be varied. An increase of accuracy is reached by shortening the pulse duration and minimizing the focal diameter which leads to reduction of ablated material per pulse.

The performance data of the diode pumped solid-state laser system used in the investigations are shown in Tab. 1

Table 1 Data of the diode pumped Nd:YAG-laser

wavelength	repetition rate	pulse duration	pulse energy	focal diameter	energy density
1064 nm	1 kHz	12 ns	8 mJ	19 µm	2822 J/cm^2
532 nm	1 kHz	12 ns	5 mJ	11 µm	5261 J/cm^2

4.1 Influence of process strategy

Fig. 4 depicts cutting kerfs and edges in Si_3N_4. The thickness of the sample is 1 mm. To compare the results of the different strategies it is helpful to define the effective feed rate by the ratio of instantaneous feed rate to number of passes. Although the instantaneous feed rate is different (1,2 mm/min for the single pass and 6 mm/min for five passes), the effective feed rate is the same and also the resulting processing time is equal.

In case of the conventional cutting technique, there is a lot of recast material remaining in the kerf. Whereas for the laser-machining nearly no recast material is observed. Furthermore, the cutting edge is even smoother than for a single passing. One possible explanation for this could be the better removal of the ablated material due to the small ablated volume per pulse in laser-machining.

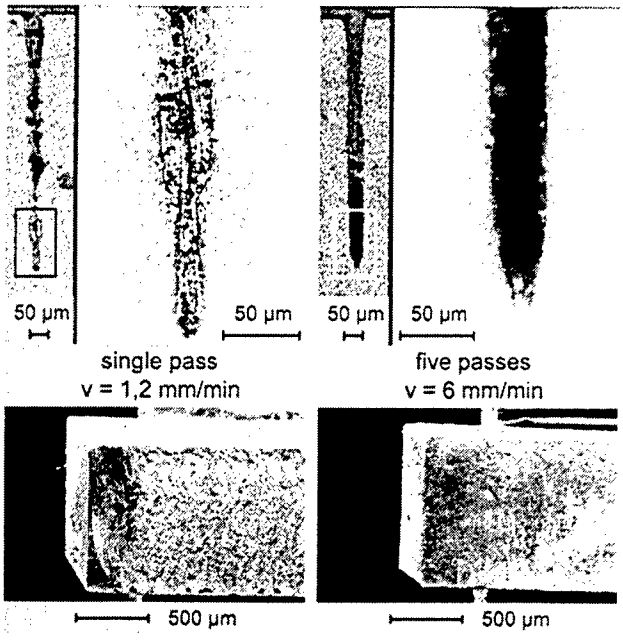


Fig. 4: Kerfs (above) and cutting edges (below) in Si_3N_4 with conventional cutting technique (left) and laser-machining (right) at same effective feed rate (v_{eff} = 1,2 mm/min, λ = 532 nm).

Further on, laser-machining not only offers an improvement in process quality but also in process efficiency as demonstrated in Fig. 5. By all means, the effective feed rate is kept constant for the comparison of the results. For both wavelengths the achievable kerf depth, which corresponds to the cutable material thickness, can be increased by raising the number of passes. This is another advantage of the small ablated volumes per pulse in laser-machining.

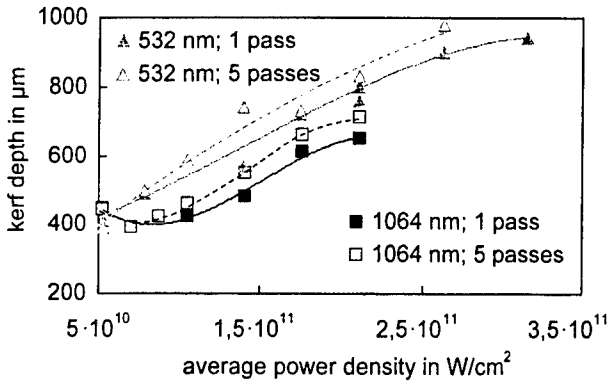


Fig. 5: Influence of process strategy on process efficiency at same effective feed rate (Si_3N_4, v_{eff} = 2,4 mm/min).

The same results have been obtained for oxide ceramics like Al_2O_3 or ZrO_2.

4.2 Influence of wavelength and process gas

The influence of process gas on process efficiency is shown in Fig. 6 for Al_2O_3 and different wavelengths. At 1064 nm and for a material thickness of 800 µm, it is possible to increase the feed rate by 100% from about 1 mm/min to more than 2 mm/min by using helium as process gas. This can be attributed to smaller shielding effects of the laser induced plasma, in comparison to a processing without helium. Due to less plasma interaction at shorter wavelengths it is even possible to achieve a 50% higher feed rate in the second harmonic than in the basic wavelength without gas. No remarkable increase in feed rate at higher material thickness could be attained with helium as process gas for a wavelength of 532 nm.

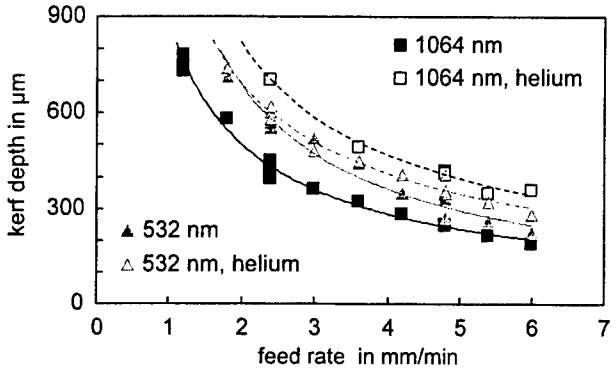


Fig. 6: Influence of wavelength and process gas on cutting speed (Al_2O_3, single pass, E = 2,1·10^{11} W/cm^2).

Apart from process efficiency it is important to consider the process quality. In Fig. 7 SEM-pictures of typical cutting edges are depicted for Al_2O_3. Best results are obtained by

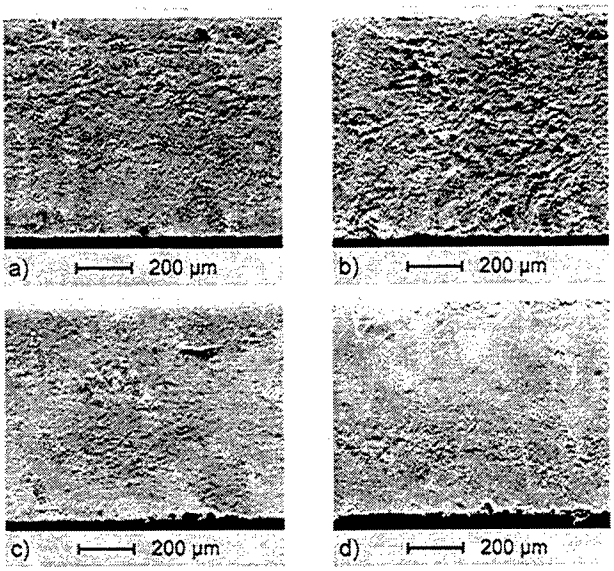


Fig. 7: Typical cutting edges in Al_2O_3 (laser-machined a) $\lambda = 532$ nm, b) $\lambda = 532$ nm with helium, c) $\lambda = 1064$ nm, d) $\lambda = 1064$ nm with helium).

laser-machining without process gas at 1064 nm. The flank is quite homogeneous, nearly without any redeposited material on it. Quality gets worse by using helium - a redeposited layer with low roughness is formed which is partly cracking off. In the second harmonic also a good quality of the cutting edge is possible without process gas. The use of helium is not sensible for reasons of quality as well as process efficiency.

4.3 Applications

An application demonstrating the possibilities of laser-machining is presented in Fig. 8. A so-called trilobal geometry in Al_2O_3 with a thickness of 0,4 mm was produced. The width of the legs is 100 µm and the length is about 300 µm. The cast taken from this complex geometry shows a very smooth surface of the flank and good constancy in shape. The detail on the right depicts the sharp edge at the exit.

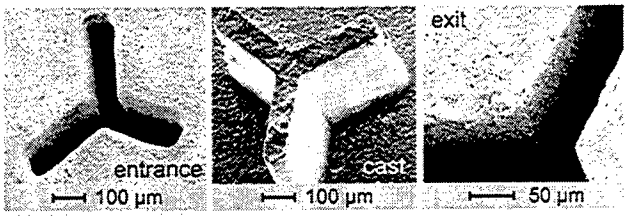


Fig. 8: Laser-machining of a trilobal geometry for spinnerets (under contract of CeramTec AG).

As a matter of principle, nearly any geometry can be produced by laser-machining. For this reason, an application in ceramic nozzles and spinnerets is conceivable. A prototype of a ceramic spinneret in ZrO_2 is depicted in Fig. 9. The dimensions of the star are nearly the same as for the trilobal, the material thickness to be cut is about 600 µm.

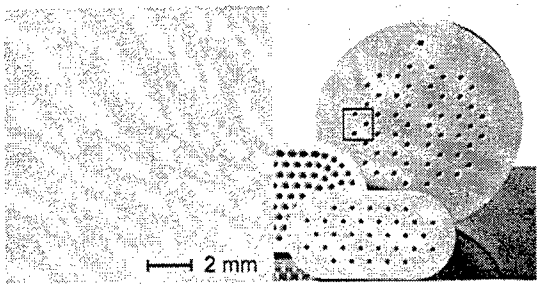


Fig. 9: Prototype of a laser-machined spinneret.

5. Conclusions

Diode pumped solid-state lasers offering pulse energies beyond several mJ at pulse duration near to 10 ns allow to produce complex geometries of high aspect ratio and unprecedented accuracy in combination with the laser-machining process.

References

[1] E. D. Palik: *Handbook of Optical Constants of Solids.* Orlando: Academic Press, 1985.

[2] E. Meiners: *Abtragende Bearbeitung von Keramiken und Metallen mit gepulstem Nd:YAG Laser als zweistufiger Prozeß.* Stuttgart: Teubner, 1995.

[3] S. V. Garnov, V. I. Konov, O. G. Tsarkova, F. Dausinger, A. Raiber: *High temperature measurements of reflectivity and heat capacity of metals and dielectrics at 1064 nm.* SPIE Proceedings, Vol. 2966, 1997.

[4] A. Raiber: *Grundlagen und Prozeßtechnik für das Lasermikrobohren technischer Keramiken.* Stuttgart: Teubner, 1999.

[5] F. Dausinger, T. Abeln, D. Breitling, J. Radtke, V. Konov, S. Garnov et al.: *Drilling of ceramics with short-pulsed solid-state lasers.* LaserOpto **31** (1999) No. 3, pp. 78.

[6] F. Dausinger, T. Abeln, M. Beck, W. Jaschinski, J. Radtke, G. Spiecker: *Bohren von Keramik.* In: F. Dausinger et al. (ed.): Proc. of Stuttgarter Lasertage (SLT '99). Stuttgart: FGSW, 1999, pp. 33.

[7] T. Abeln, J. Radtke, F. Dausinger: *High Precision Drilling with Short-Pulsed Solid-State Lasers.* In: P. Christensen, P. Herman, R. S. Patel (ed.): Proc. of the Laser Microfabrication conference ICALEO '99. Orlando (Fl): Laser Institute of America (LIA), 2000, pp. 195 (LIA Vol. 88).

Acknowledgement

The authors wish to thank the Federal German Ministry of Education and Research (BMBF) for funding of the underlaying projects 13 N 7052 and 13 N 7054.

Laser-Micro-Caving of Steel with Solid-State Lasers

Tobias ABELN, Joachim RADTKE, Michael WEIKERT
and Friedrich DAUSINGER

Institut fuer Strahlwerkzeuge (IFSW), University of Stuttgart, Paffenwaldring 43, 70569 Stuttgart, Germany
E-mail: abeln@ifsw.uni-stuttgart.de

In this contribution a technique will be presented using a cw solid-state laser for high precision micro-machining of steel which avoids recast layers and burr formation. This processing technique gets rid of the detrimental melt production by using oxidizing for material removal. The produced oxide chips can be removed from the structure completely by compressed air. No processing chemicals are necessary like in etching techniques. Other advantages of this method are sharp edges without any burrs, smooth bottoms in the structure ground and a small heat affected zone compared to material removal by melting.

Keywords: Laser-Micro-Caving, solid-state laser, steel, oxidation, machining.

1. Introduction

The economical potential of laser micro-machining has already been shown in numerous application fields. The laser is utilized mainly for marking, trimming, drilling, cutting and welding. An increasing interest in high-precision ablation of metallic materials can be observed. When removing the material by melting and vaporizing with standard pulsed lasers, however, the aim of high accuracy and resolution can not be fulfilled due to recast layers and burr formation. In view of this, a technique using a cw solid-state laser for high precision micro-machining of steel which avoids these flaws will be discussed.

2. Processing principle

The principle of Laser-Micro-Caving (LMC) is a laser induced spatially defined oxidation process on a steel surface. To start this process, the steel has to be heated above a certain temperature, which depends on the thermal properties and alloying elements of the material. The surface temperature of the irradiated zone is further increased by the exothermal reaction of the oxidation process.

Due to the lower melting temperature of iron oxide compared to the melting point of iron an oxide melt can be produced without melting the base material. This is the main reason for reaching the excellent precision of this processing technique. A disadvantage is the low processing speed limited by diffusion in the oxide layer.

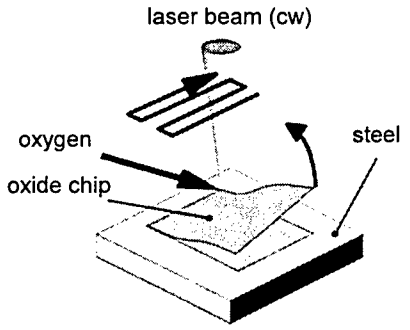


Fig. 1: *Principle of Laser-Micro-Caving (LMC)*

The shape of the cross-section and the formation of the interaction zone are leading to the assumption that recoil pressure of evaporating oxide forms a shallow cave which can be regarded as the onset of a keyhole (as is well known in laser welding). This mechanism deepens the ablation depth to some extent and accelerates it by keeping the oxide layer (which has to be transversed by diffusion) shallow. Too heavy vaporization makes the process instable, however, and causes melting of the base material.

The limitation of the vapor pressure is the reason why a cw solid-state laser is used for the investigations. Using pulsed systems with high peak powers the process gets more instable. Furthermore, to stabilize the mentioned oxide transformation, it is necessary to supply the oxygen at low pressure. When processing with appropriate parameters, the pro-

First International Symposium on Laser Precision Microfabrication, Isamu Miyamoto, Koji Sugioka, Thomas W. Sigmon, Editors, Proceedings of SPIE Vol. 4088 (2000) © 2000 SPIE · 0277-786X/00/$15.00

duced oxide layer lifts off from the bulk material as a chip (Fig. 1).

The lift off is due to a temperature profile occurring in the interaction zone during the cooling process. This mechanism is known from laser bending of metal foils [1]. The bending mechanism of the oxide chip is comparable to the temperature gradient mechanism (TGM). Due to rapid heating a steep temperature gradient develops. The thermal expansion at the upper side is converted into an elastic and plastic compressive strain. Owing to the asymmetry of the temperature field during heating and cooling the plastic strains are not cancelled during cooling. So after cooling the upper layer of the chip is shorter than the lower layer resulting in a bending angle which bends the oxide towards the laser beam [2].

The detachment of the chip is facilitated by the boundary between the oxide and the bulk material.

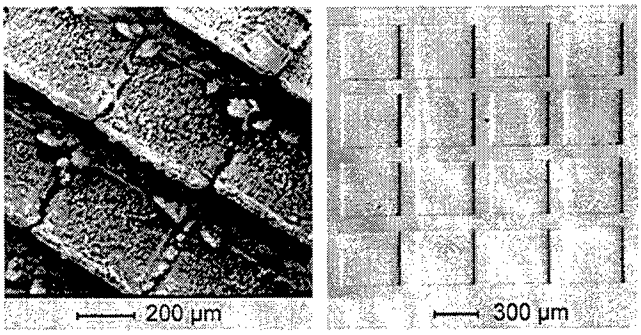


Fig. 2: Structure after Laser-Micro-Caving (LMC) (left); Structure after cleaning by compressed air (right)

In contrast to the well known technique for macroscopic laser machining [3][4][5] the LMC process does in general not form an oxide chip after each laser scan but oxide plates in the dimension of the irradiated surface area. That is why the oxide has to be removed after processing the structure as a whole (Fig. 2). An explanation for this behavior could be the small focus diameter of about 40 µm, which is capable to produce only a small oxide volume.

3. Experimental results

3.1 Minimal oxide volume for detachment

Results concerning the necessary aspect ratios and cross-sections leading to an oxide detachment are shown in Fig. 3. Beside the volume of the oxide chip the aspect ratio of the groove has a great influence on the detachment procedure.

At high aspect ratios (depth/width), that means the groove is very deep, no detachment can be observed. In this case the bending forces are not strong enough to overcome the forces at the interface to the bulk material. For unalloyed steels and aspect ratios smaller than 0.5, a cross-section up to 1.5 mm² and a length larger than about 0.5 mm are required for removing the oxide chip by bending. Processing alloyed steels with the same parameters an oxide detachment can not be observed. This is probably caused by the different shape of the cross-section (Fig. 4).

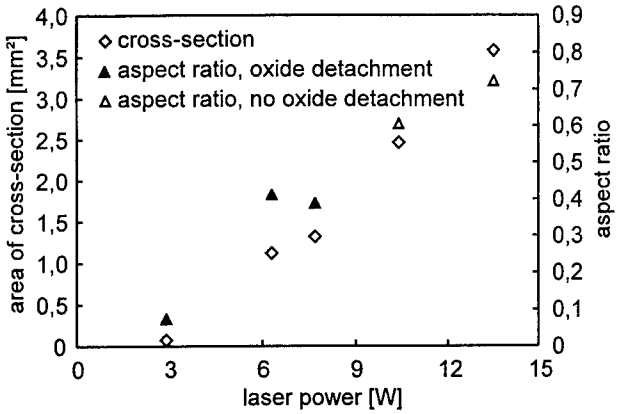


Fig. 3: Area of cross-section and aspect ratio leading to oxide detachment (C 45, v = 180 mm/min, single passage)

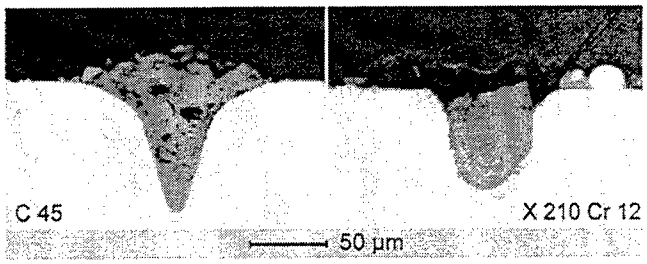


Fig. 4: Cross-sections of an unalloyed and an alloyed steel (P = 14 W, v = 180 mm/min)

In case of unalloyed steels the cross-section is V-shaped. For alloyed steels the distribution of this area is U-shaped leading to higher required forces for detachment caused by the larger interaction areas between oxide and bulk material and the steeper flank angles. Therefore, the cross-section for an oxide detachment has to be higher working with alloyed steels. This is achievable carrying out the ablation process by multi passing the ablation area with a certain overlap of the tracks. So the oxide volume gets high enough for detachment by itself.

The different shapes of the cross-section could be caused by the Marangony effect which leads to a different formation of the melt flow in the interaction zone.

3.2 Influence of processing parameters on ablation behavior

Investigations referring to the material properties like the influence of alloy constituents on ablation behavior revealed that an increased content of carbon causes a high ablation rate, and a high portion of chromium leads to a low surface

roughness. Examinations concerning the processing parameters have shown that a low surface roughness of the structures can be obtained by rising the scan speed or reducing the laser power at a constant scan speed [6].

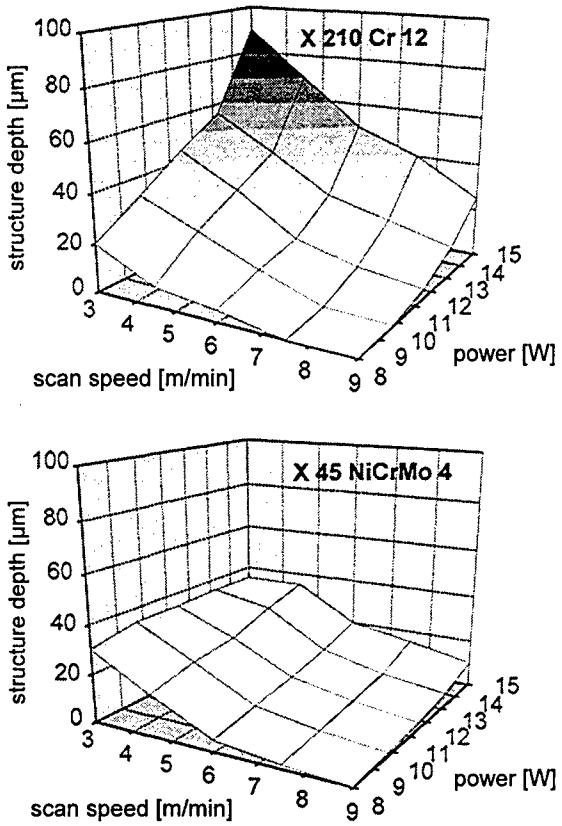


Fig. 5: Influence of alloys, scan speed and laser power on structure depth

The comparison of the results using the steels X 210 Cr 12 and X 45 NiCrMo 4, depicted in Fig. 5, confirms the relationships mentioned above. The diagrams show the structure depth referring to a variation of scan speed and laser power.

A comparison regarding the chip formation for these two alloyed steels in dependence on scan speed and laser power is shown in Fig. 6. In the diagrams indicates the grey color an ablation by melt, the black color that the oxide chip lifts off and the light one that the oxide chip does not detach. At first sight the X 45 NiCrMo 4 seems to be better suited for a high process stability because of the large black area. On the other hand the structure depth can not reach values deeper than 40 µm (Fig. 5) and the surface roughness is of about two times higher. So the higher alloyed steel is, despite the smaller process window, better suited for Laser-Micro-Caving. Advantages are mainly the higher process efficiency caused by a much higher ablation volume, the small surface roughness and the possibility to vary the structure depth in a wide range.

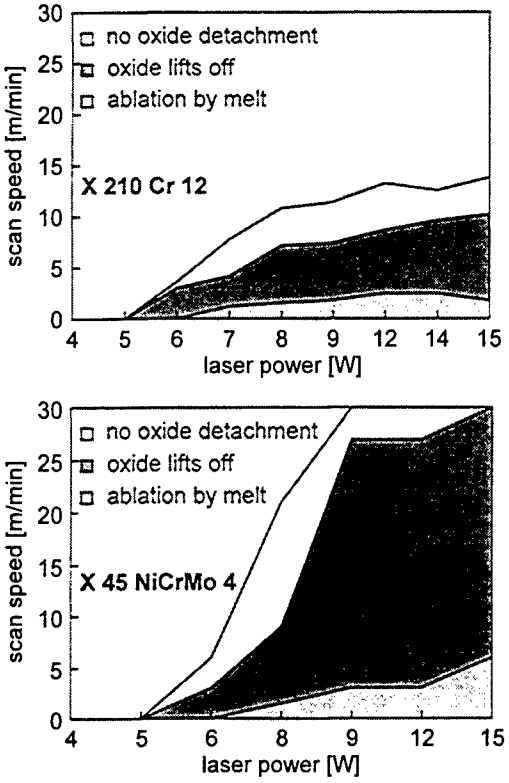


Fig. 6: Influence of alloys, scan speed and laser power on chip detachment

In addition to these parameters, the overlap of the laser tracks has a strong influence on the surface quality. Depending on the kind of steel and the laser parameters, there exists an optimum value, which leads to a low surface roughness. Numerous experiments lead to the rule of thumb that the optimum value of the sidestep is the third to the fifth part of the focus diameter for all investigated unalloyed and alloyed steels.

4. Applications

The capability of producing microstructures in steel without any dross of melt and flank angles in the range of 80° up to 90° allows to apply the Laser-Micro-Caving in a wide range of technical applications. Because of the easy chip removal by a short gas blow, there is no further mechanical or chemical cleaning process necessary. Moreover, this uncomplicated cleaning process allows to cave three-dimensional structures with high geometric quality. As an example, Fig. 7 depicts a pyramid structure with an overall depth of 126 µm. The dimensions of the single steps are 18 µm in height and 18 µm in width.

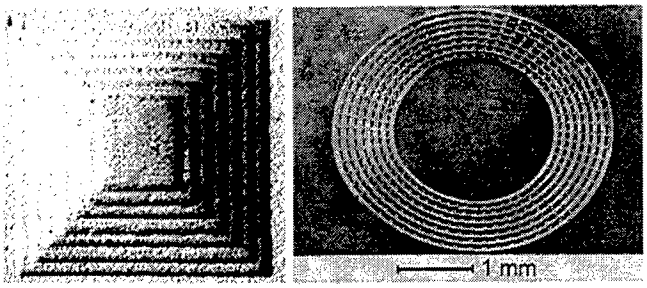


Fig. 7: 3D-laser-caving of steel (size: 400 x 400 µm²) (left); Galvanic moulded structure made of Ni-Co (in cooperation with Robert Bosch GmbH) (right)

An interesting technical application of such micro-caved surfaces is the galvanic moulding of micro structures. To produce big volumes of micro parts, it is necessary to transform the serial process of LMC to a parallel one. The process of Laser-Micro-Caving can be used for rapid tooling of a mould. With this tool, it is possible to generate a high number of micro structures. Fig. 7 shows such a moulded part with a diameter of 3.5 mm. In the same way, it is conceivable to use the laser caved mould for an injection moulding process. These techniques might become a cost efficient method for producing components of micro-systems.

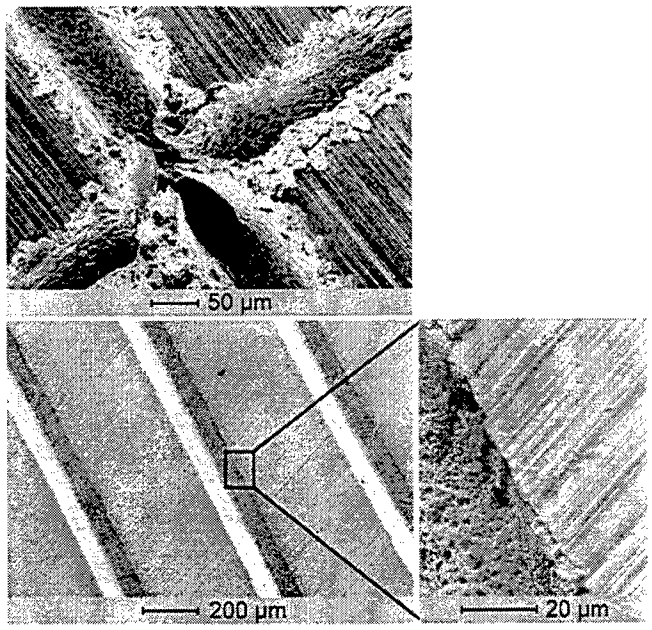


Fig. 8: Grooves processed by melt expulsion (above) and Laser-Micro-Caving (below)

Another application of the Laser-Micro-Caving is the engraving of steel plates and cylinders in the printing and embossing industry. The advantages for the manufacturers of printing cylinders are a remarkable reduction of chemical waste compared to the conventional etching technology and the possibility to produce structures by the so called „computer to plate" technology [7]. In the packing equipment industry, these micro structured surfaces can be applied for embossing paper or plastic foils to get special decorative effects or to protect products from copying.

One important advantage of micro-machining is the ability to improve the functional properties of macroscopic systems. As an example, laser engraved grooves are depicted in Fig. 8. Using this grooves in a slide bearing, an oil pad will be built up. Because of this lubrication oil film, friction and wear can be remarkably reduced. In contrast to the grooves processed by melt expulsion the magnification on the right demonstrates once again that there is no melt in the structure and the edge radius is smaller than 1 µm. Some small plates broke out at the edge, due to a hardening process by grinding and polishing the surface before the laser-machining process.

References

[1] Raiber, A.; Dausinger, F.; Hügel, H.: Laserbearbeitung in der Mikrotechnik. wt-Produktion und Management 86, 1996.

[2] Vollertsen, F.: Mechanisms and models for laser forming. In: Geiger, M. et al. (ed.): Proc. of the 26th International CIRP Seminar on Manufacturing Systems LANE '94. Bamberg: Meisenbach, 1994, pp. 345 - 359.

[3] Eberl, G.; Hildebrand, P.; Hügel, H.; Meiners, E. et al.: Laserspanen, eine neue Technologie zum Abtragen. Laser und Optoelektronik 25 (1993) Nr. 3, pp. 80 - 87.

[4] Beyer, E.; Eberl, G. et al.: Laser caving: Rapid progress in an advanced technology. In: Geiger, M.; Vollertsen, F. (ed.): Proc. of the 26th Intern. CIRP Seminar on Manufacturing Systems LANE '94. Bamberg: Meisenbach, 1994, pp. 477 - 490.

[5] Penz, A.; Fazeny, S.; Schuoecker, D.: Machining and modeling of high-quality reliefs in steel with pulsed CO2-laser radiation. In: Dubowski, J.; Dyer, P. (ed.): Laser Applications in Microelectronic and Optoelectronic Manufacturing III. SPIE, 1998, pp. 209 - 220 (Proc. SPIE Vol. 3274).

[6] Abeln, T.; Raiber, A.; Dausinger, F.; Hügel, H.: Laser-Micro-Caving (LMC) – a tool for high precision ablation of steel. Geiger, M. et al. (ed.): Proc. of the 30th Intern. CIRP Seminar on Manufacturing Systems LANE '97. pp. 877-885. Bamberg: Meisenbach, 1997.

[7] Meiners, E.: Mikrostrukturierung von Makrooberflächen – Laseranwendungen in der Druckformenherstellung. In: Dausinger, F. et al. (ed.): Proc. of the 6th Europ. Conf. on Laser Treatment of Materials ECLAT'96, Vol. 2, 1996, pp. 663 - 674.

Laser joining of micro components with fibre lasers and diode lasers

A. Gillner, L. Bosse, T. Kramer, A. Olowinsky, M. Wild

Fraunhofer-Institute for Laser Technology ILT
Steinbachstraße 15, 52074 Aachen, Germany
e-mail: gillner@ilt.fhg.de

The production of microsystems and miniaturized devices often requires joining technologies, which meet the demands of ultra clean manufacturing. Especially for optical and medical products low pollution and distortion joining processes are necessary to guarantee the quality and the function of the device.
For this applications laser welding with fibre lasers at laser powers of up to P = 10 W and focus dimensions < 30 μm have been used for welding micro mechanical devices. At intensities $I > 10^6$ W/cm² welding depths of 100 μm can be achieved with minimized pollution of the parts and smooth and clean apperance of the surface of the welds. For joining polymers and dissimilar materials high power diode lasers have been used providing even better conditions regarding pollution of the joining partners. By using material adapted laser wavelengths the heating of the material can be concentrated to the inner joining area of an overlap material joint. With this technique, thermoplastic polymer compounds and silicon glass compounds have been joined with low temperature and no influence on the quality of the parts with joining widths of less than 100 μm.

Keywords: Joining, fibre lasers, diode lasers, pollution, polymer welding

1. Introduction

Micro systems technology require packaging and interconnection technologies which meets the demands of flexible production with still small lot sizes and, in contrast to micro electronics applications often with different materials. Additionally depending on the application of the micro parts the joint has to withstand high temperatures, aggressive fluids and mechanical forces constantly without degradation and negative long time effects. The laser technology offers appropriate solutions for packaging and interconnection using processes, which have been approved for a long time in fine mechanics and joining applications. With new developments laser joining can be used also for packaging and assembly of micro parts made from silicon, glass and polymers with low heat input , low distortion and low pollution. In table 1 different joining technologies are listed in comparison to laser joining. As it can bee seen from the table, laser joining is especially suitable for applications at high temperatures and harsh atmospheres and surroundings, such as sensors and other electric components for the use in automotive parts.

Technology	Temperature range	Advantages / Disadvantages	Application
Adhesive Bonding	< 100° C	+ low cost - selective process	-low temperature sealing - optoelectronics
Soldering	< 200° C	+ low cost + large quantity - long time instability	electronic interconnection
Bonding	< 600° C	+ fast - restricted material choice - selective	chip interconnection
Resistance Welding	< 1500° C	+ fast + all materials - selective	connector packaging
Laser Welding	> 1500° C	+ fast + all materials	- packaging - joining differentmaterial

First International Symposium on Laser Precision Microfabrication, Isamu Miyamoto, Koji Sugioka, Thomas W. Sigmon, Editors, Proceedings of SPIE Vol. 4088 (2000) © 2000 SPIE · 0277-786X/00/$15.00

The main advantage of laser joining is the high precision and the long term stability of the joint. Especially in joining optoelectronic components a joining technology is required, which does not influence the optical quality of the subcomponents by splashes or recondensation of evaporated solubles from adhesives. But also laser joining has to be improved with respect to higher quality and smaller welding geometry. First attempts have been made to reduce the size of the weld spot with the aim of increasing the assembling accuracy. A newly developed joining technology for pig-tailing laser diodes uses a laser based assembling system, where a covar ferule is welded to a holder and the distortions are corrected by subsequent laser bending pulses [1]. Sub-micron accuracy is achieved for fibre pigtailing where displacement shifts for round parts can be minimised by using three weld spots simultaneous, which are positioned symmetrical around the axis of the part.

In electronic production laser beam micro-welding can also be used as an alternative joining technique to the well known soldering process, for example to contact leads [2].

2. Laser joining processes

Laser soldering is used, when the temperature load on the component has to be minimized and the accessibility to the soldering position is restricted. In comparison to other selective soldering processes like plasma and micro flame soldering the processing times are much shorter, so that the technology can be integrated into a high speed assembly line. Especially, due to the availability of high power diode lasers laser soldering has a strong increasing market with reasonable investment costs and low maintenance efforts.

Due to the minimizing of the size of the products laser soldering is used especially for small soldering geometries and short soldering times. [5]. Another application is soldering at high temperatures for lead free solders, where other soldering technologies fail.

Due to the small size of diode lasers and the used micro optics new technologies in assembly lines can be realized. In figure 2 system is shown, where laser optics and gripping systems are combined in a common tool as a so called pick-and-joining-tool. This system is equipped with 4 diode lasers at a power of P = 40 W each, linked to the head via 600 μm optical fibres. The focusing optics contains a vario optics to allow the variable set up of illumination length and width. With this system

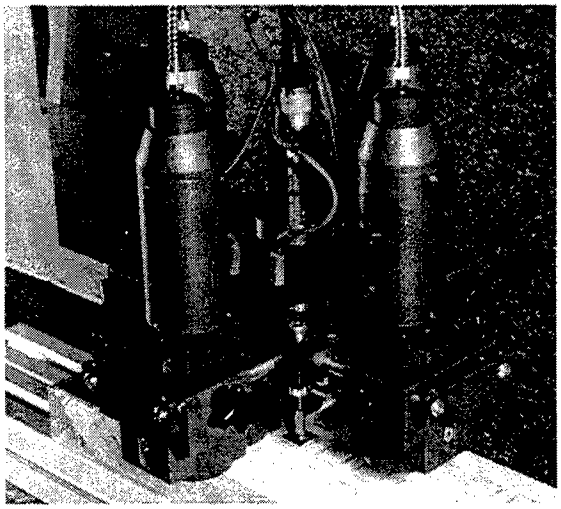


Fig. 2: Pick-and-Joining-Tool for laser soldering electronic components

components can be picked, positioned and joined at the same time. Applications can be found in the assembly of electronic components on MID-parts and parts where the position has to be fixed with an accuracy of < 10 μm.

To ensure a high reproducibility several sensor devices are included in the pick-and join-head. For the determination of the part position a camera is included, which looks through the gripping device and allows position accuracies < 100 μm. Furthermore for process control a pyrometric sensor can be included to measure the temperature in the interaction zone during heating the solder paste. In Fig. 3 a typical time dependent temperature signal for soldering is shown.

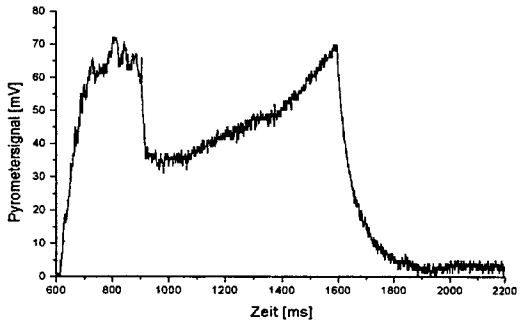


Fig. 3: Pyrometric temperature signal for soldering process

Laser beam welding is widely used as a common joining technology in fine mechanics applications. Applications can be found in the assembly of

electron beam guns for CRTs, razorblades, dental products and a large number of consumer parts with high quality. Due to new developments for laser beam sources with better beam quality the application field for laser beam micro joining has been moved to geometries < 100 μm with accuracies of sometimes less than a few μm.

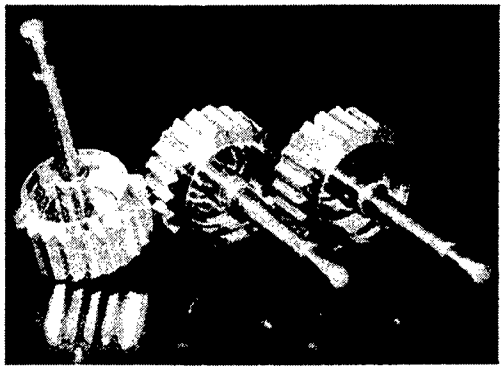


Fig. 4: Laser welding examples from watch industry

Especially for the assembly of electronic parts and sub-components laser beam welding is used for the packaging of high power electronic components. [3]. In figure 4 and 5 two examples from the watch-industry and the electronic-industry are shown.

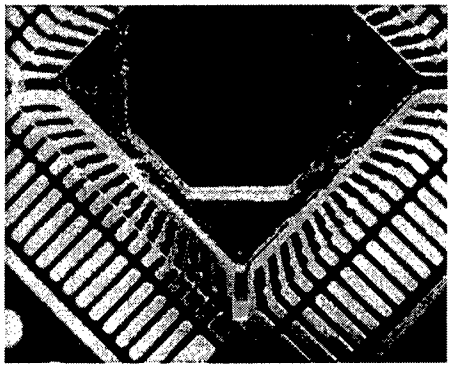


Fig. 5: Laser welding examples from electronic industry (laser welded lead frame)

With new fibre lasers, laser beam welding can be further improved to smaller joining geometries and lower heat input. Fibre lasers offer fokus geometries < 20 μm at P = 10 W, which is enough to weld steel parts with low distortion and low pollution. These requirements are strongly increasing in electronics and fine mechanics as well as for medical products. Part distortions < 10 μm can be achieved .

As a special technology among the laser welding processes the laser assisted bonding can be seen. [4]. It is used for joining silicon and glass components where Nd:YAG radiation is transmitted through the glass part and absorbed on the silicon surface at the interface between two parts. At this interface the joining process by production of melt, hydrogen bridges and adhesion is performed. In Fig. 6 the principle set up of the laser bonding process is shown.

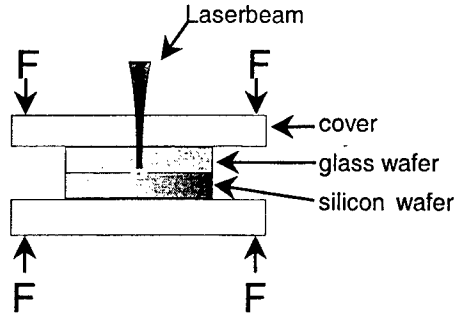


Fig. 6: Principle set up of laser bonding process

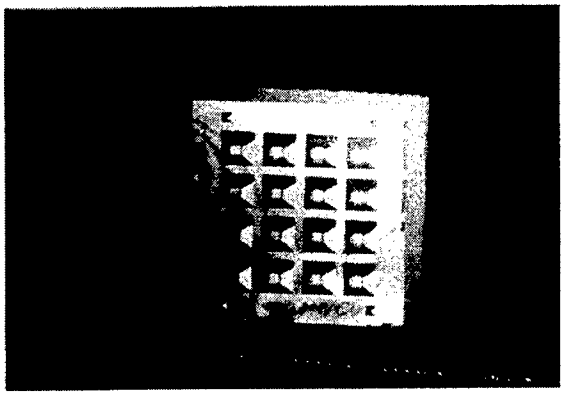


Fig. 7: Laser bonded silicon micro cavities

Figure 7 shows an example with the sealing of a silicon cavity. The main advantages of this technology in comparison to the widely used anode bonding process is

- low heat input
- selective bonding geometries
- joining under gases and fluids
- low influence on pre-processed wafers and enclosed components

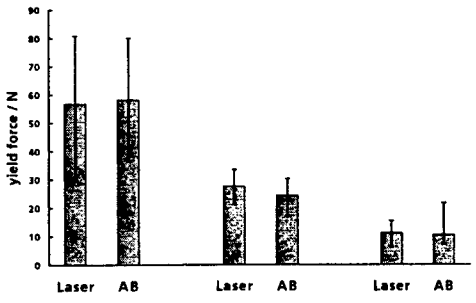


Fig.8: Yield force of laser bonded silicon compound for 3 different joining areas

The application of this technologies can be found in the assembly of sensors and micro system components as well as the assembly of micro fluidic parts with biological components for biological essays.

With respect to the various applications this technology can also be perfomed at low and high pressure and even under fluids. The achievable joining forces are similar to conventional anodic bondic process (Fig. 8).

A similar processing principle is used for welding polymer parts. Both joining partners are fixed together with a minimum gap < 50 μm and is pressed tightly together. The laser beam transmits through one of the joining partners and is absorbed at the second joining partner which is pigmented by special ingredients, like carbon and absorbing dies. By heat conduction both partners are heated up simultaneously and a melt bet-ween the parts in the interaction zone is produced. The applications for this technology can be found mostly in the packaging of electronic components and parts from automotive supplier industry. By using an online temperature control with a pyrometric measurement this process can be used also for temperature sensitive components with high process safety. Fig. 9 shows an example for an electronic locking system for the automotive industry.

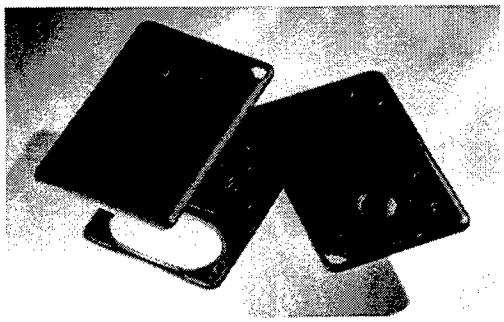


Fig. 9: Laser welded polymer locking system

3. Conclusion

Laser micro joining offers a large variety of different packaging technologies for micro system assembling. Laser welding and bonding is suitable for thin metal foils and micro wires from low temperature materials, like gold and silver to high temperature materials, like tungsten. Also silicon-glass compounds and LIGA-Components can be joined with the following advantages:

- high local selectivity
- small fusion zone
- low heat input
- no adhesives
- short processing time
- low investment costs

For fine mechanics applications laser joining can be used without almost any preparation, but in micro systems packaging the parameters and the joining conditions have to be well adapted to perform a high quality joint. This process can be supported by integration of temperature control and special clamping and materials handling devices. In future further developments will lead to a reduction of joining geometries in the μm-range to obtain micrometer packaging technologies.

References

[1] B. Valk, R. Battig, O. Anthamatten, *Laser Welding for Fiber Pigtaling with Long term Stability and Submicron Accuracy*, Optical Engineering, **34** 9 (1995).

[2] M. Geiger, M. Glasmacher, H.-J. Pucher, *Laserstrahl-Mikroschweißen als alternatives Fügeverfahren zur Lead-Kontaktierung,* Tagungsband SMT/ASIC/HYBRID 94, VDE-Verlag 1994

[3] W.Hoving, *"Laser Micro-welding in the Electronics Industry"*, Proc. Of the 6th International Welding, Symposium of the Japan Welding Society, 19-21 November 1996, Nagoya, Japan, pp. 267-272.

[4] F. Legewie, A. Gillner, R. Poprawe, *Selective sealing and bonding of silicon-glass compounds and LIGA-components by laser beam welding*, MICRO-MAT '97, to be published

[5] A. Gillner, *Laser welding and brazing for high temperature packaging and interconnection,* Proc. HITEN '97, to be published

Pulsed Nd-YAG laserwelding of titanium ear implants

Jan GEDOPT, Erwin DELARBRE

Vito, Materials Technology, LCV, Boeretang 200, 2400 Mol, Belgium
E-mail : jan.gedopt@vito.be
Phone: +32.14.33 57 44, Fax : +32.14.32 11 86

Three different prototypes of ear implants have been successfully produced using Nd-YAG laserwelding.
The prototypes differ in use and dimensions.
This presentation will deal with the latest developed ear implant, i.e. a box containing special electronics inside.
The implant has to be He leak tight, the weld penetration should be between 50 and 65% of the cover in order to be sure to avoid damage of the electronics in the box and the temperature should not exceed 100°C during welding. Furthermore no sharp edges and no surface contamination or oxidation is allowed.
Pulsed Nd-YAG welding proved to be a fabrication technique who allowed satisfying those conditions. Through an appropriate choice of pulse energy, pulse time, pulse frequency, overlap and an external cooling device we succeeded to fulfil all those requirements.
Special devices have been developed and are used to position the boxes adequately in front of the laser beam. During the welding a copper heat sink was used to eliminate the developed heat, and at the same time this was used to keep a good contact between the cover and the rest of the box.
In the development phase the internal temperature during the welding cycle has been measured. With an appropriate choice of pulse frequency, pulse time, the internal temperature could be limited to about 80°C. XPS measurements have also been performed on dummies in order to control the eventual formation of a titanium deposit during welding.
Finally 30 implants have been welded successfully, and they will now be used for further medical tests, first on animals and later on human beings.

Keywords: laser, welding, implants, titanium, Nd-YAG

1. Introduction

A method for laser welding of parts used in ear implants has been developed.

In a previous project a laserwelding technique for the fabrication of two different types of ear implants has been developed, one with a diameter of 11 mm a height of 3.85 mm and a wall thickness of 0.4 mm and a second type with dimensions 2.55 by 1.5 mm with a wall tickness of 0.2 mm). Both are cochlear ear implants containing a magnet inside a welded titanium box.

The new type is much more sophisticated than the previous ones. In order to reduce the size and the efficiency the electronic that produces signals going to the ear nerves is contained in the implant. The implant has a diameter of 18.7 mm, a height of 3.8 mm and a wall thickness of 0.2 mm

2. Demands to the implants

The electronic is contained in a box made of the titanium alloy Ti6Al4V to be compatible with the human body.
The box has to satisfy the following conditions:

- He leak tightness better than 5.10^{-8}mbar.l/sec (MIL-STD-883D)
- Welding depth between 50 and 75% of the wall thickness
- Maximum inside temperature during welding lower than 100°C
- No sharp edges
- No surface contamination
- No evaporation of titanium during welding.
- No moisture into the box.

3. Optimization of process parameters

The boxes that have been welded only contained a low value magnet inside, but the new type contains very

First International Symposium on Laser Precision Microfabrication, Isamu Miyamoto, Koji Sugioka, Thomas W. Sigmon, Editors, Proceedings of SPIE Vol. 4088 (2000) © 2000 SPIE · 0277-786X/00/$15.00

expensive electronics that is very sensitive to heat input, contamination and the presence of moisture.

A pulsed Nd-YAG laser (400W Lumonics) has been used for the welding experiments.

The final welding is performed with a pulse length of 15 ms, an energy of 2J, a frequency of 3Hz, 120 steps/min and a welding time of 6 min (720 steps). The overlap of 2 pulses is at least 50%. A lens with a focal length of 80 mm has been used for welding the implants.
With those parameters it is possible to fulfil the above requirements.

However, in order to succeed other precautionary measures are necessary. To reduce the gap between the cup and the case a special holder has been fabricated who allows pressing the cover against the box. Furthermore, to keep the temperature below 100°C in the box, a special holder and a copper piece positioned onto a titanium holder, to prevent surface contamination of the box, is used as a heat sink to take away the produced heat. To prevent the laserbeam from hitting directly the electronics a special design is necessary. This design is schematically represented below:

4. Laserwelding under a controlled atmosphere

The implants to be welded are first put into a container that is vacuum pumped during 4 hours to eliminate moisture, and consequently filled with very pure argon and sealed before introducing the container into a glove box in which welding is performed.

The glove box is completely filled up with argon at a low overpressure, in order to prevent air to enter the glove box and to contaminate the implants. After entering the container with the implants in the glove box; the glove box is washed at least during twelve hours with argon to reduce the moisture content. The relative humidity could be reduced to 4%, which corresponds with a dew point of approximately –30°C. During welding argon is blown in the weld spot to prevent surface oxidation.

The use of a container than contains several implants permits welding of a large number of implants without the necessity to open the glove box and to wash it for 12 hours each time an implant has to be welded.

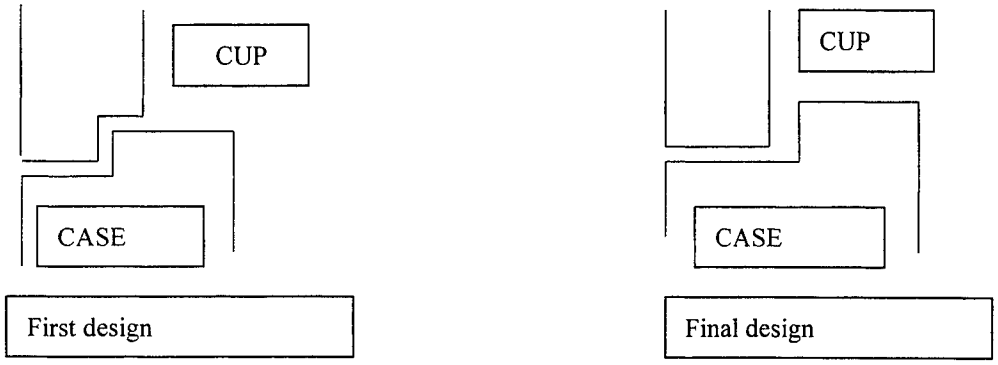


Fig. 1 Design of the box

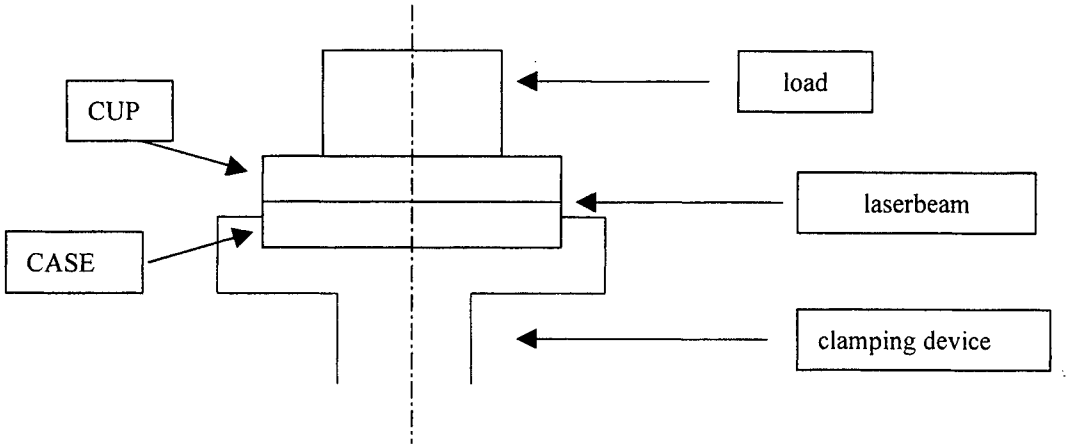


Fig. 2 Schematic view clamping device

The laser light is directly brought in the glove box, by means of a sealed extension tube. The use of a direct-coupled laser instead of a fiber coupled laser results in a smaller weld spot, due to the smaller beam size. The optics are fixed to this extension tube and for the positioning a high resolution CCD camera is used for positioning and controlling of the welding cycle.

5. Qualification controls of the welded implants

The following examinations have to be performed and will be discussed: visual inspection, He-leak tests, mechanical vibration tests, mechanical pressure tests, temperature cycling, weld characterisation, temperature measurement, contamination.

6. Examination of surface contamination

As explained before care has to be taken in order to avoid all external contamination. The clamping devices are chosen in a way not to contaminate the implants. The welding gasses have to be inert and very pure in order to avoid surface contamination. The clamping devices are cleaned before each use. Finally gloves are used to handle the specimens. XPS (a surface analyzing technique) has been used to analyze the surface on possible contamination and oxidation. No traces of contamination or oxidation could be found on the specimens. XPS has also been used to analyze the surface of a dummy placed into the box before and after welding in order to control if during welding titanium has evaporated and being deposited onto the surface of the dummy. Since titanium conducts electrical current the deposition of it onto the electronics inside the box could cause the malfunctioning of the sophisticated electronics.

7. He-leak tightness

The specimens where tested following the specifications of MIL-STD/833D. Therefore it is necessary to leave some room for gasses into the box corresponding to the dimensions of the box. The welded specimens are put under He pressure for at least 2 hours at a pressure of 5.2 bar. After that they have to be leak tested within 15 min.

The laserwelds were sound, but some implants showed leaks caused by the throughputs for the connection of the electrodes.

8. Control of the welding temperature

The control of the temperature during the welding process has been controlled by means of 3Pt-100 thermocouples placed inside the box at the place of the weld bead. The maximum temperature that has been measured didn't exceed 80°C, and further this temperature peak lasted only a few seconds. This confirmed the expectations that the welding did not damage the electronics.

9. Resistance against mechanical deformation

The resistance against deformation is another important topic. An external pressure exercised onto the cover of the box could bring the box into contact with the electronics, with a risk of damaging it. Special care has to be taken to avoid this, as well during the manipulation stage as during implantation and use. A second test is a mechanical vibration test. The welded boxes are subjected to this test and He-leak tested before and after to see if the weld is damaged during those tests.

10. Characterisation of the weld

Metallographic examination has been performed to control the weld penetration and the width. Originally the weld width should not exceed 300µm since it was expected that the thickness should increase. In practice it was noticed that the weld had a width of 420µm, but on the other hand the radius decreased by 20µm. When the weld width was decreased to 300 µm the weld depth decreased also to 120 µm, which was not acceptable. Therefore, a weld width of 420 µm is accepted with a weld depth of around 160µm. This is schematically represented in the figure below.

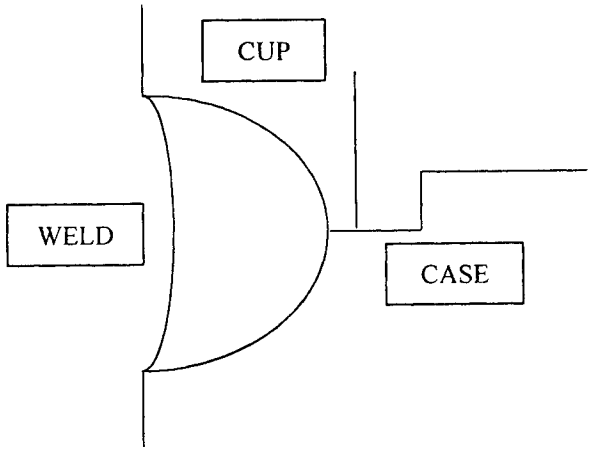


Fig. 3 Schematic view of the weld

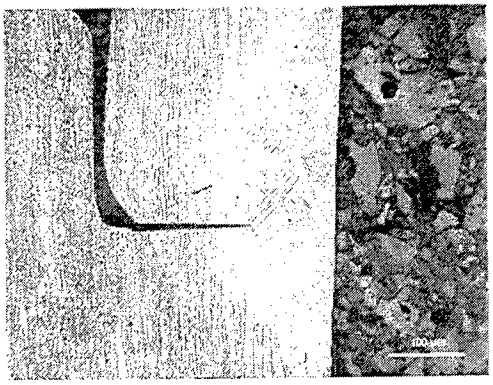


Fig. 4 Metallographic examination box

Results Finally 30 implants have been produced as prototypes and are actually tested on animals. In the photographs below the complete apparatus is shown with a detail of the welded box itself.

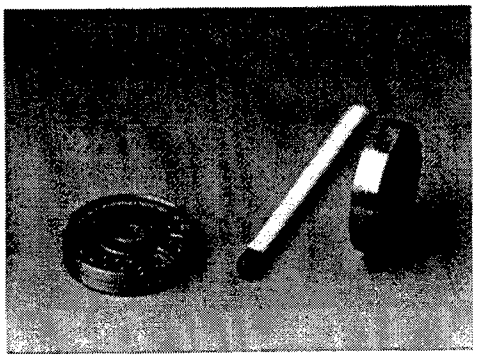


Fig. 5 View of a welded implant

Acknowledgement

We wish to express our gratitude to Cochlear Technology Centre Europe (before Philips Hearing Implants) to allow the publication of those results.

A compact, multi-sensor laser scanning head for processing and monitoring micro-spot welding

Moustapha HAFEZ[*], Karin JULLIARD[*], Sylvain GROSSMANN[*], Lino OLIVETTA[*], Thomas SIDLER[*], René-Paul SALATHE[*], Hans-Peter SCHWOB[**], Toon BLOM[***], and Willem HOVING[***]

[*]*Institut d'Optique Appliquée, Département de Microtechnique, Ecole Polytechnique Fédérale de Lausanne, BM, 1015 Lausanne, Switzerland*
Email: moustapha.hafez@epfl.ch
Email: thomas.sidler@epfl.ch
[**]*Lasag Industrial Lasers, Thun, Switzerland.*
[***]*Philips Centre for Manufacturing Technology,5600 MD Eindhoven, The Netherlands.*

Abstract: In order to improve the reliability of micro-spot welding of metal parts in production such as e. g. in electron guns for TV picture tubes, real-time information about the evolution of the welding process should be available to allow on-line modification of the laser parameters. Such information can be derived from a set of sensors that are mounted on a laser-scanning head. Different sensors are used to monitor the optical fiber output power to determine the evolution of temperature during the spot welding process, to measure plasma emission and back-reflected laser light. A vision channel and a CCD camera are used to control the position of the laser spot on the parts to be processed.
The compact scanning head is composed of a tip/tilt laser scanner, a collimating lens and a focusing lens. The scanner is fast steering, with a bandwidth of 700Hz, and can tilt by ±3.5° with a repeatability better than 50μrad. The settling time for maximum deflection is less than 10ms. The scanning lens is a newly developed focusing lens designed to replace commercial cumbersome scanning lenses such as F-θ lenses, which have large volume, weight and price. This lens is based on the well-known Cooke triplet design and guarantees a constant shape of the spot all over the scan surface and is specially well suited for high power beam delivery. The scan field achieved by the system is limited to 25mm x 25mm. The laser used for this application is a pulsed Nd:YAG laser delivered by an optical fiber to the optical head. However, the system can be adapted to different types of lasers.
Laser micro-spot welding on copper substrate has been performed in the frame of the Brite-Euram project MAIL. Smaller tolerances (a factor of 2 less) on the spot diameters were obtained in the case of a sensor controlled operation compared to the case where sensor control is not used.

Keywords: Compact head, micro-spot welding, multi-sensors, tip/tilt scanner, new focusing lens.for material processing applications.

1. Introduction

Many material processing applications use fiber optical beam delivery of the laser power to the processing equipment. Fiber beam delivery has become a standard technique in recent years for processes such as welding, which require relatively low beam quality but highly uniform beams. This is mainly due to the ease of manipulation and the high flexibility of optical fibers in light guiding. A further advantage of fiber delivery is its tendency to circularise and depolarise the beam, leading to a near flat top-hat beam profile with high reproducibility. These properties are of prime importance for reliable industrial process control in various laser materials processing applications. Moreover, fiber beam delivery leads to more compact beam handling systems. In fact, diverse applications are restricted with a limited volume of space. Therefore, the need for more compact high precision manipulators and measuring systems is also increasing. A compact, multi-sensor laser scanning head for processing and monitoring micro-spot welding is presented in this paper. In order to improve the reliability of micro-spot welding of metal parts in production such as e. g. in electron guns for TV picture tubes, real-time

First International Symposium on Laser Precision Microfabrication, Isamu Miyamoto, Koji Sugioka, Thomas W. Sigmon, Editors, Proceedings of SPIE Vol. 4088 (2000) © 2000 SPIE · 0277-786X/00/$15.00

information about the evolution of the welding process should be available to allow on-line modification of the laser parameters. The optical head proposed is based on fiber optical beam delivery of the laser power. The main modules are a tip/tilt high-power laser scanner to control the laser spot position and a set of Silicon and Germanium sensors to monitor and control the micro-spot welding process. For more than two decades, galvanometer scanners have been the usual solution for laser scanning systems [1]. In order to scan in two directions, two rotating scanners must be used. One of the mirrors must be larger to allow the scan of the laser beam generated by the rotation of the other mirror. The tip/tilt scanner used in this system has a single mirror that achieves the two degrees of freedom in rotation and can steer large beams up to 25 mm in diameter. The design principles of this scanner are presented in [2].

1. Set-up

The optical head is based on a pre-objective laser scan system. In this configuration, the tip/tilt scanner is placed before the focusing optics (see Fig. 1).

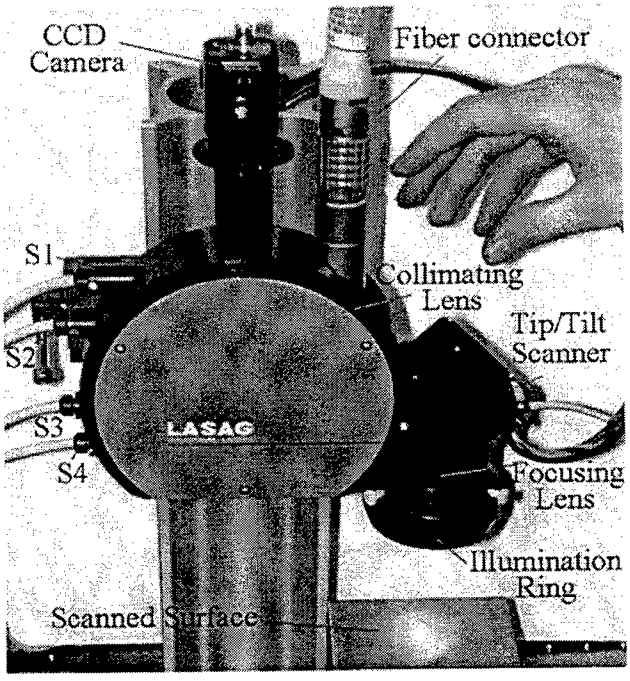


Figure 1- Compact multi-sensor laser scanning head. S1 is the temperature sensor composed of two photodiodes (Si and Ge) in a sandwich configuration. S2 is the plume sensor, S3 detects the back-reflected light of Nd:YAG on the irradiated part, and S4 is the monitoring sensor for the laser to detect pulse shape.

The optical fiber is fixed on the head by means of the fiber connector. The laser beam is collimated by a first lens and is then steered and accurately positioned by the scanner. The focusing lens has been designed to replace commercial cumbersome scanning lenses such as F-θ lenses, which have large volume, weight and price. This new lens guarantees a constant shape of the spot all over the scan surface and is specially well suited for high power beam delivery. A ring composed of 20 LEDs emitting at a wavelength of 620 nm is fixed around the lens and is used to illuminate the working plane as indicated in Fig.1. This configuration provides a homogeneous and optimised illumination for the vision module. The CCD camera is mounted on the system to monitor the working plane, as e. g. for aim and shoot applications. A set of Silicon and Germanium sensors are mounted on the optical head to determine the evolution of temperature, the plasma, the back reflected light and the pulse shape during the spot welding process. The laser source used in the experiments is a pulsed Nd:YAG laser 150/220W (Lasag SLS 200) and the optical fiber has a fiber core diameter of 200 μm.

2. Single mirror tip-tilt scanner

In order to construct a compact high performance scanner, the different components must be carefully optimized. In this sense, the moving part, essentially the mirror and the actuators must be designed to minimal inertia for maximum motor force and mechanical stiffness. Moving magnet linear motors arranged in a push-pull, pure torque delivering configuration are used as actuators. A cone-ball bearing with a (half) sapphire ball glued to the moving part and a POM cone on the stationary part assumes a minimum friction and maximum rigidity suspension.

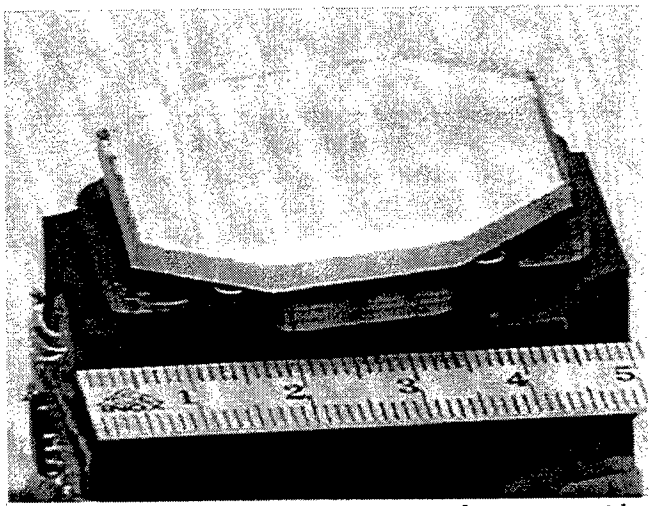


Figure 2- Compact single mirror tip-tilt scanner with housing removed. The overall dimensions of the scanner are 30x40x50 mm.

The figure 2 shows the scanner with removed outer housing, the mirror and the motor coils can clearly be seen. Two preload fixed holding magnets take the mirror securely in place even in an upwards down configuration and hold the rotation around the mirror axis fixed, leaving only the two desired tip and tilt rotations free. As no elastic restoring force is present, the scanner can only be used in a closed control loop configuration. The actual mirror position is measured with a laser light pen reflected by the back mirror surface and falling onto a 2-dimensional position sensitive detector (PSD), yielding the two electrical position signals for the closed loop control.

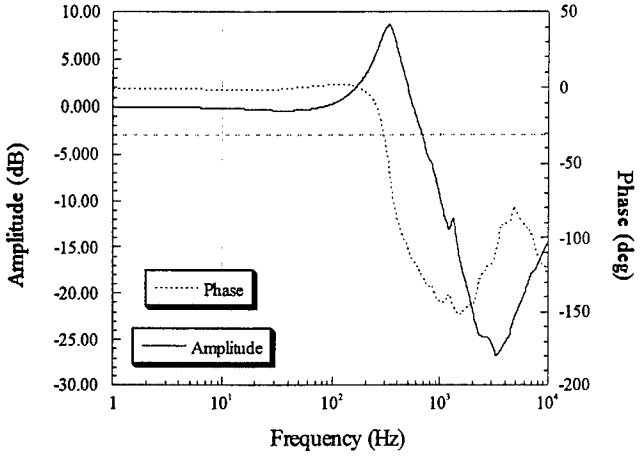


Figure 3- Closed loop frequency response of the single mirror tip-tilt scanner.

The figure 3 shows the closed loop response for the scanner and the figure 4 the response to a step input, for both axes. The maximum settling time for a full-scale step input remains less than 10 ms, permitting thus e. g. high cadence spot welding.

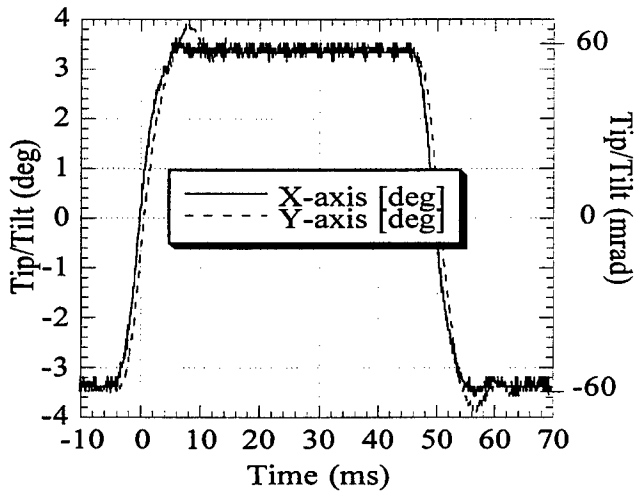


Figure 4- Step response of the single mirror tip-tilt scanner for maximum deviation, in x and y direction.

3. Scanner optics

Pre-objective laser scan systems are found in industries ranging from graphic arts to semiconductor manufacturing. They are found in devices as diverse as laser engravers and document scanners. In this configuration, the head is placed before the focusing optics. Pre-objective scanning requires flat-field lenses such as "F-Theta" lenses. What makes such laser scan lens unique is the combination of a flat image plane, a wide angular field, and a linear relationship between input scan angle and the displacement of the laser focus on the target field. The scanning spot will therefore, move along the scan line at a uniform velocity. In addition, laser scan lenses are designed with an external aperture stop, apodized pupil illumination, and for operation in monochromatic light [Melles Griot]. However, the drawbacks for such lenses are their high price, their bulky design and the high chromatic aberrations causing difficulties with vision systems.

The new lens guarantees a constant shape of the spot all over the scan surface (see figure 5). This feature is extremely important in material processing applications because the shape of the weld spot determines the quality of the process. The focusing lens has a focal length of 100 mm and can reach a scan field of 25mm x 25mm..

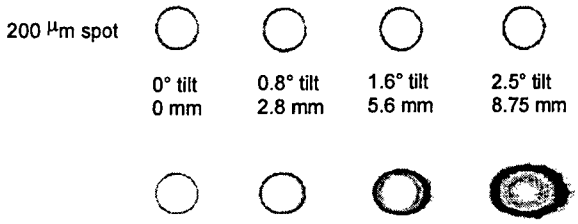


Figure 5 – Laser spot simulations. The four spots on the upper row are the result of a 200µm core diameter fiber output imaged with the new triplet lens, at different locations of a flat scan field.. The new lens guarantees a constant shape all over the surface. The first spot to the left is the centre of the scan field. The mirror is then tilted by 0.8°, which causes a displacement of the spot on the surface of 2.8mm. The four spots on the lower row are the spots using a standard doublet lens. The distortion of the spot increases as it leaves the centre of the scan field. This is due to the scan line curvature typical for pre-objective scanning.

4. Sensors and process monitoring.

Based on the different signals measured by the set of sensors, a classification, an off-line control or a closed

loop feedback control can be used to monitor the quality of spot welds. The output signals of the different sensors are indicated in Fig. 6. The amplitude of the signals indicated in Volts depends on amplifier gain "K_n" of each sensor and the energy transmission coefficient "τ_n" along the different optical paths of the sensors. Therefore the different amplitudes can only be compared to each other if each sensor is multiplied by its relative $K_n\tau_n$ product. The laser pulse duration in this case is 4.5 ms with a flat-top shape as determined by the laser monitoring sensor (S4).

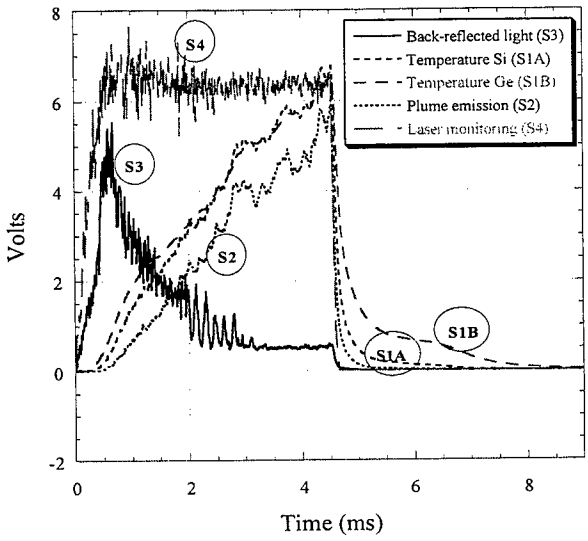


Figure 6- Output signals of the back-reflected Nd:YAG light, Si and Ge temperature sensor, the plasma detection signal, and the laser monitoring signal.

The reflected Nd:YAG light on the working sample that returns back in the optical head as indicated by sensor (S3) reaches a peak value at the melting point of the material that is processed. The amplitude of the signal drops then significantly, due to the molten pool that forms into a cup scattering the reflected light and hence reducing the amplitude of the back-reflected light in the head.
On the other hand, the plume sensor has a different behavior as its amplitude increases with time during the laser pulse. The amount of plume detection is also an important information to determine the quality of spot welds.

5 Laser spot welding

Laser micro-spot welding has a wide variety of applications in micro-mechanics and electronics such as e. g. in automatic fabrication of electron guns for TV picture tube and printed circuit boards with solder joints. A European project entitled "Multi-Sensor Assisted Intelligent Laser processing (MAIL)" has been run successfully in the frame of an international collaboration with several partners. The aim of the project was to improve the reliability of micro-spot laser welding of metal parts in production, by the development of a self-learning real-time feedback control system. The basic problem of this technology is how to attain the part per million (PPM) defect level needed for wider industrial applications. The two main defect sources are the position tolerances of the products and the variation in their surface conditions. That is why the compact scanner developed in this work represents a key module in this application for the aim and shoot system that recognizes the joint position and adjusts the actual laser spot position. The scanner is mounted on a multi-sensor real time monitoring optical head to be able to control on line the quality of the spot weld. Active control of the weld pool temperature with a Ge-detector e. g. results in an important improvement of the reproducibility of copper welds and at least two times less dispersion in the final weld diameter.

Acknowledgment

The activities have been performed in the framework of the three Brite-Euram projects: AMULET (Accurate manipulation using laser technology), MAIL (Multi-sensor assisted intelligent laser processing), and SLAPS (Self-tuning and user-independent laser material processing units) sponsored by the European Community and the Swiss Government (OFES).

References

[1] Montagu J. I., "Galvanometric and resonant low-inertia scanners" in Optical scanning, edited by Marshall G. F. (Marcel Dekker, Inc., New York, 1991), Vol. 31, pp. 525-613.

[2] Hafez M., Sidler, T., Salathé R.P., Jansen G., and Compter J.C. "Design, simulations and experimental investigations of a compact single mirror tip/tilt laser scanner" Mechatronics (accepted on the 17th of September 1999).

[3] Hoving, W., "Accurate manipulation using laser technology" SPIE proceedings Europto series: Lasers in Material Processing, Vol. 3097, pp. 284-295, Washington, 1997.

New Interferometric Method to Measure the Complete Geometry of the Keyhole

Muhammad Muddassir GUALINI*, Hans STEINBICHLER**

*Pakistan Institute of Lasers and Optics, P.O. Box 1384, Islamabad, Pakistan
E-mail: optica97@isb.comsats.net.pk

**Steinbichler Optotechnik GmbH, Am Bauhof, 4 – 83115 Neubeuren, Germany
E-mail: Steinbichler@steinbichler.de

PulsESPI, combined with an innovative beam deliver device, may enable obtaining a very accurate control sensor to determine with improved accuracy some of the laser material processing parameters like the geometry of the keyhole and cutting kerf in real time.

Keywords: Lasers, Laser Material Processing, Sherography, PulsESPI, Holography, Keyhole, Cutting Kerf, CCD, FRAMESplus

1. Introduction

We discuss a possible innovative sensor to measure several Laser Material Processing (LMP) parameters in real time, like keyhole geometry, seam weld track and joint width and thickness. Many mathematical models have been introduced insofar to describe LMP procedures. Modeling should not be confined to its theoretical results [1] but be essential to set the laser process parameters. Measuring and monitoring systems shall have enough accuracy to interact with the model results and provide real time information to correct errors generated by several factors, like mathematical approximations of the model and limits of the device. Misalignments introduced by the laser work handling mechanical tolerances, unexpected non-uniformity of the material morphology may contribute to alter the expected results.

The development of new LMP methods, especially the fabrication of micro-components, requires also extremely precise and accurate real time controls.
The above discussion justifies the quest of new, complex and more precise and accurate devices. Instruments that monitor and measure in real time laser material processing parameters for procedures from cutting to ablation, from soldering to welding and heat transformation hardening. An ideal device shall monitor without contact, with very high response-speed and good accuracy, all the geometrical components of the weld, cutting kerf and surface quality and flatness of hardened materials. Optical devices using laser sources and generating interferometric optical fringes can match the required qualities.

2. Devices measuring LMP parameters.

Current optical devices do not show a high level of accuracy but their performances are accepted. Systems, based on interferometric fringes analysis appear more accurate but limited by the presence of hot keyhole plasma, while they perform better measuring cutting kerf, surface quality and flatness of laser hardened materials.

2.1 Optical non-interferometric methods.

Majority of optical systems is based on direct detection of the keyhole or cutting kerf by a solid state CCD camera. An interesting device [2] exploits the information provided by spatially distibuted intensity of electromagnetic radiation emitted by the process under control. The system consists of a high-speed camera mounted on the housing of the focusing laser optic. The camera optical path is aligned with the laser beam path. The device detects the light intensity variations across the keyhole or cutting kerf along the x and y-axis and with the help of a proper algorithm correlates the intensities with the z-axis. The system is mainly suitable for keyhole welding of thin blanks. Electromagnetic noise, mechanical and thermal instabilities may also influence the measurements, although partially compensated by the high-speed data collection (image recording > 2900 frames/second).

An infrared, processing monitor is used during surface transformation hardening procedures [3]. There is a linear relationship between the DC monitor output and the achieved hardness and case depth. The same device can track "changes in surface quality or flatness of the part

First International Symposium on Laser Precision Microfabrication, Isamu Miyamoto, Koji Sugioka, Thomas W. Sigmon, Editors, Proceedings of SPIE Vol. 4088 (2000) © 2000 SPIE · 0277-786X/00/$15.00

that is being treated" [3] but vibrations and thermal effects, like schlieren, may limit the accuracy.

2.2 Interferometric methods.

These are interesting because optical fringes are generally multiples of $\lambda/2$, λ is the source wavelength. Lasers increase the fringes contrast and resolution thus enabling to use digital techniques to analyze and interpret them, without compromising resolution and accuracy of the measure. Furthermore these devices offer a very large response bandwidth thus ensuring real time measurements.

Several laser-based methods to generate interferometric fringes are available [4]. Besides classical interferometers (i.e. Michelson, Farby-Perot, Twymann-Green) fringes can be produced using speckle, holography and shearography. Sheargraphy has been proposed to monitor in real time the weld track and the generation of surface porosity [5, 6]. Conventional interferometers require mirror-like surfaces for good fringe resolution. CW and pulsed holography give best results when surfaces are temporarily white coated in order to ensure a uniform reflectivity so that fringes are generated with almost the same intensity contribution of the two separated beams. Sensitivity to misalignments and mechanical vibrations are limits of conventional interferometers and holography, CW and pulsed. This is a serious problem for their application in LMP where Electro-mechanical actuators are source of vibrations.

When a highly coherent laser beam impacts a surface its natural reflection and unevenness generate a set of back-reflected beams interfering with the main beam. The result is a granular beam on the impacted surface [7]. Off plane variations of the surface influence shape and distribution of the "speckle grains" thus enable to correlate this change with the geometrical variations generated by deformations or vibrations. ESPI has as very large response bandwidth and the possibility to quantify geometrical deformations, while shearography enables to detect surface defects, generated by strain deformations. Pulsed-ESPI has attracted our interest due to its characteristics that appear superior to shearography and will be described in the next sections.

3. The proposed device

The sensor exploits an interferometric principle known as Pulsed-ESPI. The laser light back reflected from the keyhole surfaces generates the fringes. The sensor can be divided in three parts, each of them discussed here below. The first is the laser projector that produces the optical phenomenon to be exploited. The second is the transmitting optic that projects the laser beam into the keyhole and detects the back-reflected signal into the CCD camera. Third is the optics and electronic receiving system, including also the fringe analysis software. See figure 1.

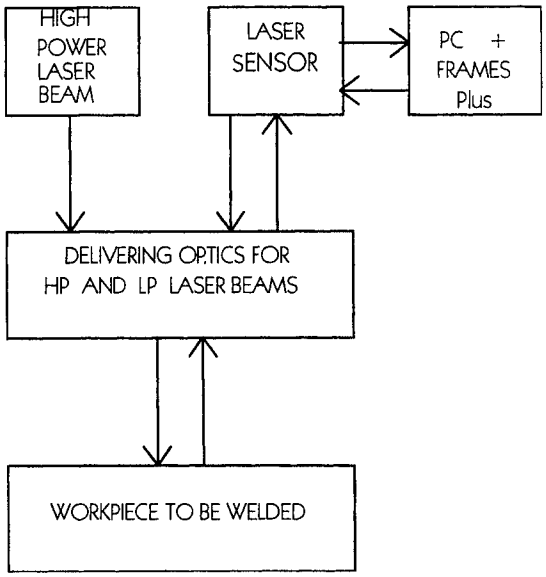


Fig. 1 Block Diagram Of the Innovative Device.

3.1 The projector configuration

Methods that enhance the accuracy of the above-described system are basically ESPI (Electronic Speckle Pattern Interference), Puls-ESPI, and TV-Shearography. 3-D ESPI requires 3 laser sources. TV-Shearography has good accuracy and less sensitivity to vibrations but thermal effects and depth of focus may be a limiting factor. Puls-ESPI requires a high energy Ruby laser but given the very small dimensions of the keyhole (maximum 20-mm depth by 0.1-mm diameter) a green Nd:YAG DPSS or a blue pulsed semiconductor laser maybe also considered. Puls-ESPI combines the advantages of conventional Pulsed Holography and ESPI. Fringes can be recorded in few nanoseconds thus the sensor is less sensible to thermal schlieren and low frequency vibrations. The investigating beam in Puls-ESPI is transmitted through optics while the reference beam is transmitted through fiber optic and this fits in the configuration of the beam delivery system that we have adopted. Puls-ESPI enables to obtain a full picture of the laser process geometry, measuring also contour profiles of the seam joint before and after welding. Live-display of fringes keyhole in 3-D is obtained using *FRAMESplus* software. A fringe image of a cylindrical hole on a metal sheet is stored in the PC. This hole has the diameter fitting in the minimum waist of the keyhole, derived from any theoretical model available. The effective keyhole geometry will be then detected as a deformation of the original cylinder, given the micrometric dimension of the measure.

3.2 The transmitting optics

The transmitting optics is a double inclination flat mirror that deflect, the High Power (HP) and Low Power (LP) laser beams with different inclinations as visible in Figure 2.

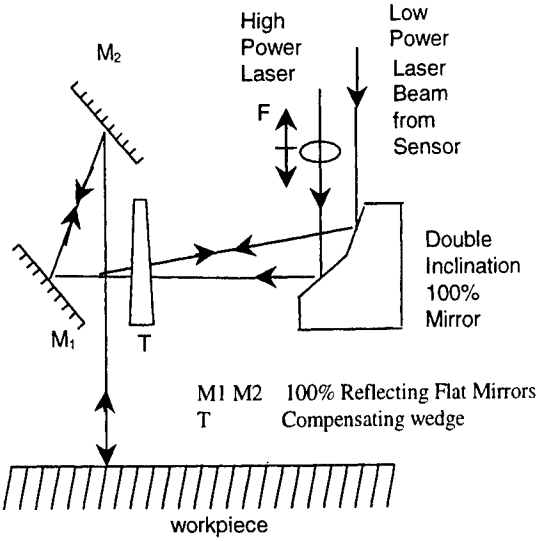


Fig. 2 The transmitting optics

M_1, M_2 act as a roof (penta) prism but with a wider error acceptance angle (10' of arc), this enables the LP and HP beams to mix avoiding optic aberrations. The wedge compensating optics acts to correct the inclination of the LP beam. The LP back reflected beam follows the same path. This design can be particularly appreciated working with HP CO_2 laser beams. The laser head formed by M_1, M_2 can rotate around the optical axis. A third reflecting mirror (not visible in figure 2) introduces another axis of freedom without disturbing the alignment, LP and HP beams [8]. A conventional lens focuses the HP laser beam. LP and HP depth of focus can be adjusted simultaneously or independently, accordingly to the application. The focusing lens of the LP is not shown since it is assumed integrated in the zoom lens assembly of the CCD camera.

3.3 Sensor Mathematical Model

A specific mathematical model for PulsESPI does not exist yet. We are developing software to be interfaced with the LMP models available for simulation of the process. Development and description of this model is beyond the scope of the present work, nonetheless we underline some cardinal points here below. A first approach is to correlate the models of ESPI and pulsed holography [7, 9], then we intend developing the relation given by M. L. Vest [10] and here reproduced:

$$I = |\mathbf{M}_T|^2 = J_0^2(\mathbf{K}\bullet\mathbf{A}-\mathbf{K}\bullet\mathbf{A}_R) \qquad (1)$$

where $\mathbf{M}_T$ is the characteristic function of the specific setup, $\mathbf{K}$ is the sensitivity vector, which is related to the illumination conditions, $\mathbf{A}$ and $\mathbf{A}_R$ are amplitude vectors of the object and the reference beams while J_0 is the zero order Bessel function.

From literature [7, 9] we have for the off plane displacement measure, Δ_z:

$$\Delta_z = N\,[\,\lambda/(1+\cos\theta)], \qquad N = 0, \pm1, \pm2, \pm3,\ldots \qquad (2)$$

where λ is the laser wavelength of the PuslESPI projector and $\theta \equiv \Sigma_i^{\infty}\theta_i$ the angle of the illuminating beam. In the proposed setup $\theta \equiv \Sigma_i^{\infty}\theta_i \approx 90°$ therefore (1) reduces to:

$$\Delta_s|_{PulsESPI} = N\,\lambda, \qquad N = 0, \pm1, \pm2, \pm3,\ldots \qquad (3)$$

While for the double pulse holography applied to a component in movement we have to consider that the virtual images of the hologram (reconstructed on the CCD plane) are modulated by a fringes system described by the square of the zero order Bessel function. The following relation may express thus the characteristic function, M_T:

$$\mathbf{M}_T = J_0\{(\mathbf{K}\bullet\mathbf{A})^2-(M_R)^2-2(\mathbf{K}\bullet\mathbf{A})M_R\cos\phi_R]^{1/2}\} \qquad (4)$$

being M_R the modulation depth of the illuminating beam and ϕ_R the associated phase shift.

3.4 Advantages of the proposed device

The proposed solution has the following advantages and innovations:

1. Higher accuracy. It works on fringe detection and not on direct pixel sensitivity.
2. Improved behavior against thermal schlieren and vibrations induced by the work handling.
3. Improved flexibility. No misalignments or cumbersome positioning systems.
4. The field of view of the CCD camera is not affected by the diffraction introduced by any small aperture.
5. Real time measure of the LMP parameters like weld depth, joint width and thickness.
6. Measurements can be recorded and stored for comparison with theoretical models.

3.5 Disadvantages of the proposed device

1. High output power of the PulsESPI laser source
2. Effects of plasma glare [11] (drilling, cutting and welding) and metals high temperature electromagnetic emission (surface alloying and transformation hardening)
3. Thermal Schlieren, for example inside the keyhole
4. Necessity of narrow band filters [11]

3.5 Results on a simulated keyhole

Fig 3 shows a hole in a metal plate. Figure 4 shows the corresponding fringes obtained with a 1D-ESPI setup using the 532 nm wavelength of a Nd:YAG frequency doubled. The hole has a diameter of 3.5 mm in a 4 mm aluminum plate. Reference frame is the plate before drill.

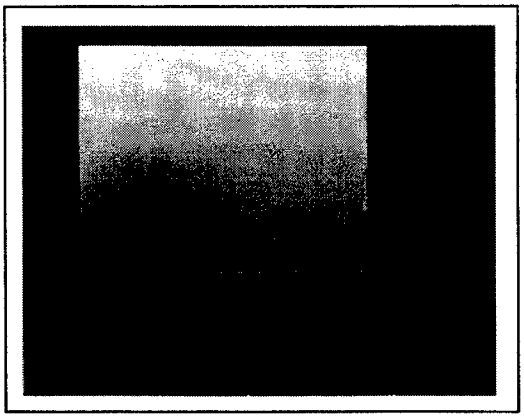


Fig. 3 Simulated keyhole



Fig. 4 Fringes filtered by *FRAMESplus*

4. Conclusions

Early work on a hole with 1D-ESPI is an encouraging result for further developments on real keyhole during laser welding sessions. Work is in progress to carry these tests with PulsESPI. Also the development of a suitable model for PulsESPI is in progress. Once the experimental side will prove satisfactory we will revert to the selection of the best mathematical model of keyhole welding and, finally confront the results between the predicted and measured keyhole. The last step will be to define the algorithms to realize a universal adaptive control for laser material processing and implement it.

5. Acknowledgments

The authors are particularly thankful to Engineer Iftikhar and Mr. Mazhar Ishaque for the drawings and typesettings, to Miss Tanja Boheme for the great support in handling and coordination of e-mail messages, to Mr. Sixt and Engelsberger for the practical and experimental work. Finally to Dr. Ashraf Atta and Dr. Sheik Shahdin to have allowed the production of some ,early work of the Laser Group directed by them.

6. References

[1] W. M. Steen, Laser Material Processing, Springer-Verlag, 1991

[2] P. Abels, S. Kaierle, C. Kratzsch, R. Poprawe, W. Schulz, Universal Coaxial process control system for laser material processing, Proceedings ICALEO'99, San Diego, Ca

[3] Z. Xu, C.B. Reed, Keng H. Leong, Real Time Monitoring of Laser Surface Hardening of Ferrous Alloy, Proceedings ICALEO'99, San Diego, Ca

[4] J.T. Luxon, D.E. Parker, "Industrial Lasers and their Applications", Prentice-Hall, (1985)

[5] M. M. S. Gualini, Proceedings ISAM'99

[6] M. M. S. Gualini, Proceedings ICALEO'99, San Diego, Ca

[7] M.M.S. Gualini, *Proc. 1st International Symposium on Mechanical Vibrations, Islamabad, 1998,* pp. 90

[8] M. M. S. Gualini, Proceedings ICALEO'99, San Diego, Ca

[9] M.M.S. Gualini, *Proc. 1st International Symposium on Mechanical Vibrations, Islamabad, 1998,* pp. 224

[10] C.M. Vest, *Holographic Interferometry*, J. Wiley & Sons, 1979, pp. 215

[11] W. Steen, private communication 27/05/2000 by e-mail.

Micro soldering using a YAG laser - On lead-free solder -

Sumio Nakahara, Tatsuya Kamata, Noriyuki Yoneda,
Shigeyoshi Hisada, and Takeyoshi Fujita

Department of Mechanical Engineering, Kansai University,
3-3-35 Yamatecho, Suita, Osaka 564-8680, Japan
E-mail nakahara@kansai-u.ac.jp

Solderability of conventional Sn-37Pb solder pastes and Pb-free alloys (Sn-43Bi and Sn-2Ag-5Bi-0.5Cu) were examined on micro soldering using a YAG laser. Experiments were performed in order to determine the range of soldering parameters of a laser power density and an irradiation time for obtaining an appropriate wettability based on a visual inspection by a Japanese Industrial Standard. And the laser soldering processes were monitored by measuring temperature change inside solder joint (solder and Cu pad) and on a surface of a chip component. Next joining strength of chip components for surface mounting soldered on printed circuit board (glass epoxy) was tested on application thickness of solder paste (0.2, 0.3, and 0.4 mm). In addition, joining strength characteristics at different power density and materials were examined around thermal shock test by the gas phase method. As a result, characteristics of Sn-Ag-Bi-Cu (Pb-free) solder paste are equivalent to that of Sn-Pb solder paste.

Key Words: laser soldering, lead-free solder, joining strength, strength evaluation, and YAG laser

1. Introduction

Soldering technology is central to junction technique, which is itself vital to production engineering in the electronic industry. Micro-soldering, a small-scale junction technique, is in particular attracting considerable attention, as a result of the contemporary trend in the electronics industry aiming at the realization of high density surface mounting of printed circuit boards. At the present stage of technological development, improving the reliability of micro-soldering technique is a major goal.

The essential characteristics of the laser soldering method are two: ease of focusing the input beam on the prescribed portion of the target, with good accuracy of positioning; and ease of control of the input energy required by process (in the case of CW lasers, by controlling the output power and irradiation time).

Thus, in the laser soldering method, heat effects around the work juncture point can be kept to a minimum by determining the optimum irradiation condition of the laser (i.e. with regard to output power and irradiation time). On account of these merits, there is now a steadily increasing trend towards applying the laser soldering method to the soldering of electronic parts very sensitive to heat damage, such as those in FPIC (Flat Package Integrated Circuit). Although laser soldering technology does not yet have a long history, a long and effective future as a micro-soldering technique in the production of high density mounting of IC and LSI may be predicted for it.

Recently, lead and its compounds in the most common solder such as 63Sn37Pb have been demonstrated to be highly toxic. For environmental reasons there has been a push to develop lead-free solder alloys to find alternatives to Pb-bearing solders in the United States, Europe, and Japan.

In this paper, two lead-free solder alloys were studied to establish its feasibility for potential applications in the electronics industry. For comparison eutectic material 63Sn 37Pb was used as a standard solder alloy.

Here we have experimentally determined the range of soldering parameters of a laser power density and an irradiation time for obtaining an appropriate wettability based on a visual inspection by a JIS. In addition heat effects on the soldered junction were examined when a laser beam

First International Symposium on Laser Precision Microfabrication, Isamu Miyamoto, Koji Sugioka,
Thomas W. Sigmon, Editors, Proceedings of SPIE Vol. 4088 (2000) © 2000 SPIE · 0277-786X/00/$15.00

irradiated solder paste printed onto an electronic circuit substrate. The temperatures of small portions of the substrate and of the solder were measured using thermocouples. Next joining strength of chip components for surface mounting soldered on printed circuit board was tested on application thickness of solder paste. In addition, joining strength characteristics at different power density and materials were examined around thermal shock test by the gas phase method.

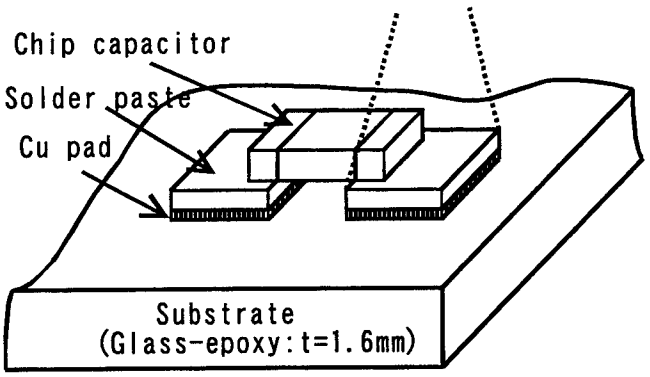


Fig.1 Sample form of laser soldering

2. Experimental

The YAG laser beam with multi-mode passes through an aperture of diameter of 3.5 mm, is bent to 90 degree by a prism, is focused using condenser lens of focal length of 48.5 mm, and irradiated onto the surface of the sample by means of defocus. At this point, the irradiation beam spot diameter is 2.8 mm. The laser beam is irradiated over the entire surface the 2 x 2 mm^2 area of solder paste.

Irradiation time is controlled by means of a mechanical shutter inside the laser resonator. The mechanical shutter has response time of 50 msec when it is operated by a microcomputer. A copper pad printed onto a substrate of glass reinforced epoxy being etched to a size of 2 x 2 mm^2, as shown in Fig.1, the Sn-37Pb solder pastes and Pb-free alloys (Sn-43Bi and Sn-2Ag-5Bi-0.5Cu) are printed by means of a metal screen to form a layer of a thickness of 0.2, 0.3, and 0.4 mm on the copper pad. Chromel-alumel thermocouples (K type) of a wire diameter of 0.05 mm are applied to the surface of substrate sample, and the increase in temperature in each portion of the sample is measured.

The contact point of the thermocouple is brought into contact with the surface of solder paste and with the surface of the copper. Figure 2-1 shows the sample used in the experiment to examine the heat effect on the chip capacitor. Here the thermocouples are applied to the chip capacitor with a small amount of bond. The laser irradiation is done only on the side of the solder paste that adheres to the chip capacitor.

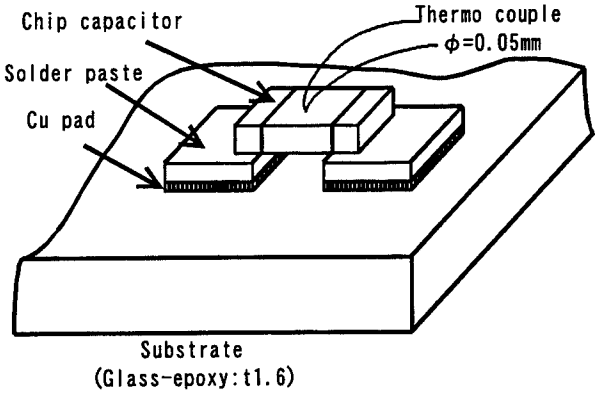


Fig. 2-1 Chip Capacitor

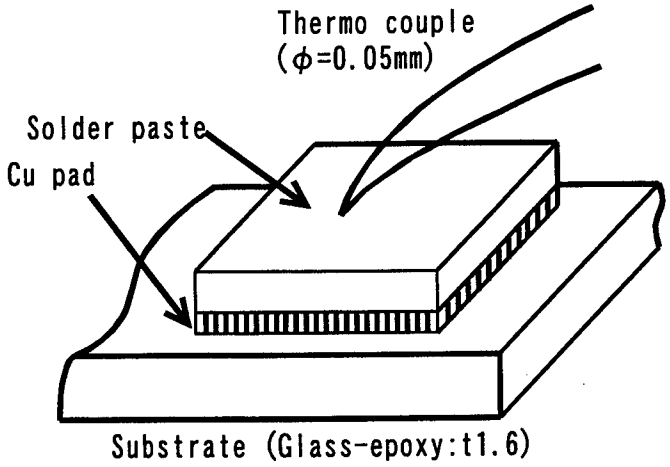


Fig. 2-2 Solder

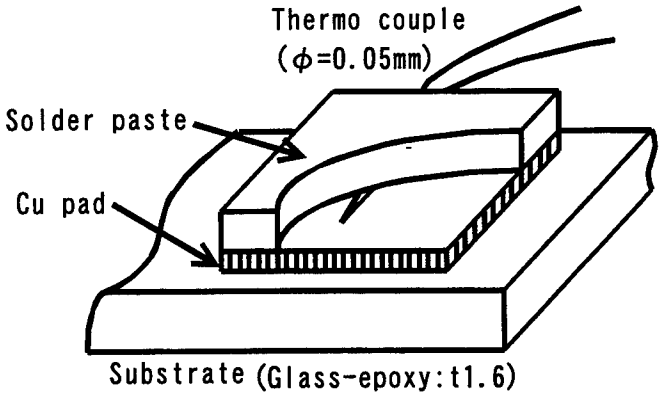


Fig. 2-3 Cu Pad

In order to record the temperature high-speed changes during irradiation, the electromotive power of the thermocouple is transformed using an A/D converter and is recorded by the microcomputer as temperature data. Argon gas as an assistant gas is blown at 10 *l*/min onto the soldering area, in order to keep the samples in an atmosphere of inactive gas, which removes materials evaporating from solder paste in the soldering area, thus avoiding any laser irradiation power loss that these might cause. The rise in temperature in each part of the sample is measured before, during, and after irradiation.

3. Experimental Results and Discussion

Figure 3 shows the temperature change of a copper pad, solder and a chip capacitor caused by the laser power density of 500 W/cm^2 and the irradiation time of 0.2 sec. It may be assumed that when the surface of the copper pad was irradiated by the laser at the power setting shown, once the copper reached the melting point of the solder, all the solder present upon it melted, and soldering was successfully completed.

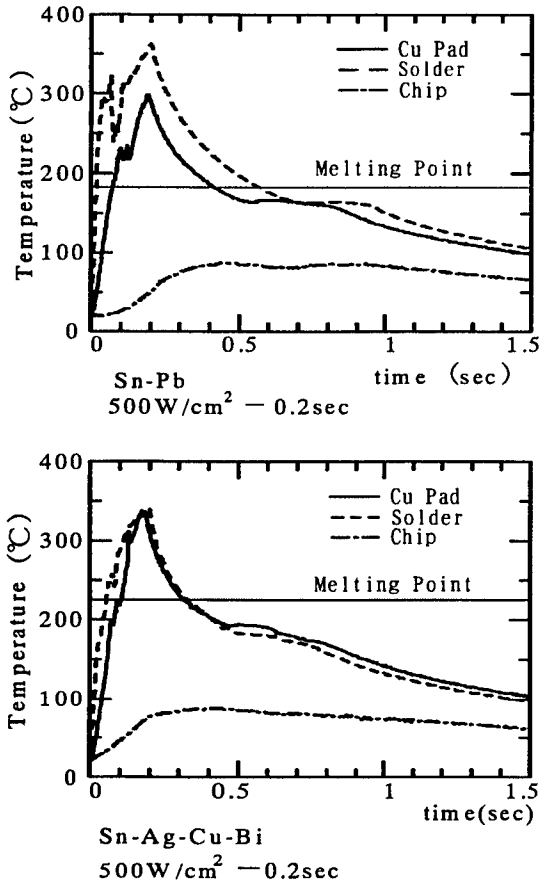


Fig. 3 Temperature change measured using thermocouple as shown Fig. 2.

It can be seen that the solder melts in irradiation conditions such that the temperature of the surface of copper pad reaches the melting point of the former in Fig. 3. The greater laser energy is required when the laser irradiation power is lower, and the irradiation time longer. Heat effects on the substrate are decreased for higher power densities of laser irradiation and for shorter times of irradiation. Useful increase of irradiation power does, however reach a limit, the reason being that the solvent in solder paste evaporates instantaneously during brief rapid heating. It is, therefore, concluded that an understanding of the material properties of the solder paste is important, and decisions concerning conditions for optimal heat input are necessary if the heating condition is to be made to conform to the property.

One of the methods that evaluate solderability is that contact angle of wetting is measured and from this the properties of the solder connection are estimated. Contact angle is defined as shown in Fig. 4. The reliability that made a decision according to the information of contact angle of the solder connection are examined in laser irradiation time range of 0.1 to 2.0 sec, and laser power densities of 200 to 500 W/cm^2 as shown in Fig. 5. Judgments of evaluating the solder connection for the contact angle and visual inspection are according to JIS (C 0054).

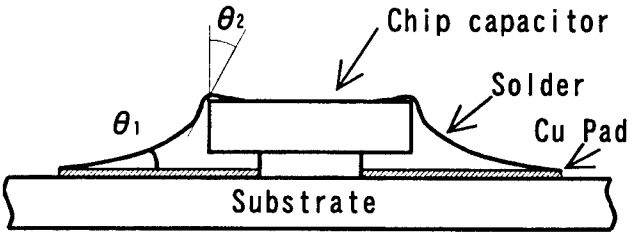
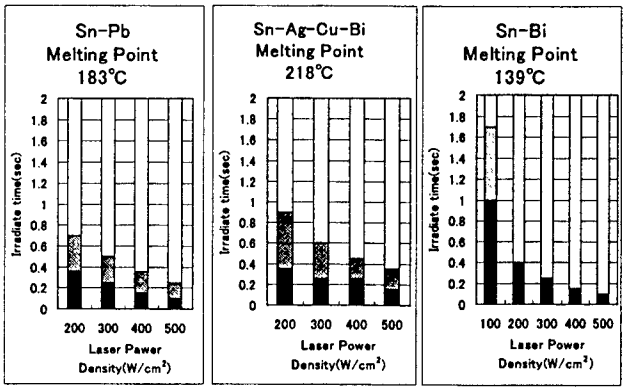


Fig. 4 wetting angle θ



■Non joint ■Satisfied joint □Defective Appearance

Fig.5 Results of visual inspection test

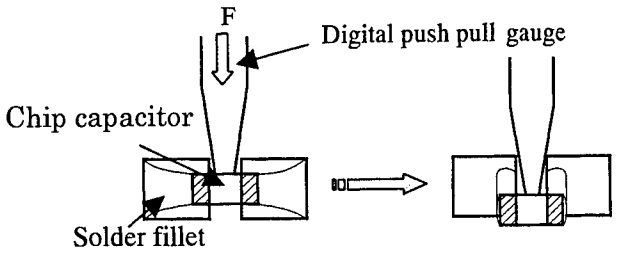


Fig. 6 Outline of joint strength test

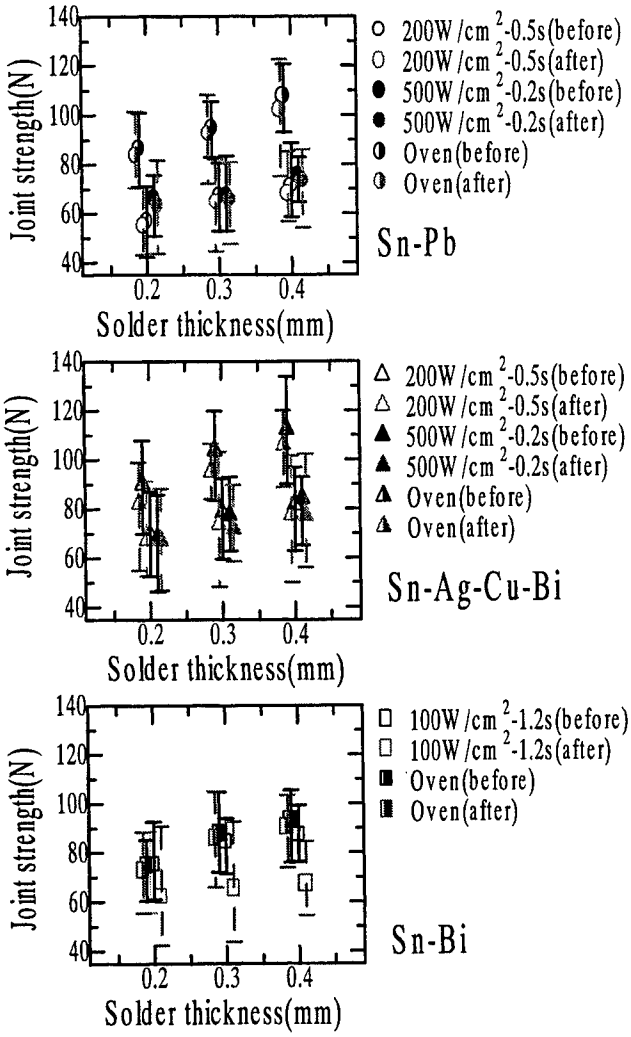


Fig. 7 Strength of solder joint
(before): before thermal shock test
(after) : after thermal shock test
Oven : conventional reflow method
W/cm2: laser power density

For the reliability tests, soldered test boards were loaded by thermal shock between –55 and +125 C. The test was followed by using MIL standard, MIL-STD-883C. The duration of one cycle was 20 minutes. The holding time under the atmospheres at the lower and upper temperatures was 10 minutes. No power was provided to the electronic component during the temperature cycling. On solder joints of chip components (2 x 1.25 x t0.5 mm) additionally the shear forces (push-off force F) as shown in Fig. 6 were determined with a force gauge before and after thermal shock test. The influence of laser power densities, thickness of printed solder paste, and heating process on the strength of the solder joints were compared as shown in Fig. 7. The results show that the joint strengths increase with increasing the printed solder thickness. The highest values are reached for Sn-Ag-Cu-Bi, followed by Sn-Pb and Sn-Bi.

Summary

YAG laser soldering system was constructed capable of transmitting laser beam to the working point and controlling laser power density and irradiation time. The laser soldering was operated successfully without any thermal damage on chip components and the substrate. Based on these results it can be concluded that Sn-Ag-Cu-Bi is suitable for use as alternative solder to Sn-Pb standard alloys.

Acknowledgment

This work is partly supported by the aid of Kansai Univ. Special Research Grants: Grant-In-Aid for Joint Research on Priority Areas in 1999 and also by a Grant-in-Aid for Scientific Research from the Ministry of Education, Science and Culture, B (2)-12450105.

References

[1] L. Dorn, F. Herbert, S. Jafari, and T. Schubert: Trans. ASME, J. Manufacturing Sci. Engr., 119, (1997) 786-790.

[2] I. Fidan, R. P. Kraft, L. E. Ruff, and Stephen J. Derby: IEEE Trans. Components, Packaging, Manufacturing Technology – Part C -, **21**, (1998) 172-181.

[3] J.H. Lee, Y. H. Lee, and Y.S. Kim: Scripta Mater., **42**, (2000) 789-793.

[4] W. Ren, Z. Qian, M. Lu, S. Liu, and D. Shangguan: J. Electronic Packaging, **121**, (1999) 271-274.

[5] R. S. Whitelaw, R. W. Neu, and D. T. Scott: J. Electronic Packaging, **121**, (1999) 99-107.

[6] T. E. Wong, L. A. Kachatorian, and H. M. Cohen: Trans. ASME, J. Electronic Packaging, **121**, (1999) 186-190.

[7] X. Q. Shi, W. Zhou, H. L. J. Pang, Z. P. Wang: Trans. ASME, J. Electronic Packaging, **121**, (1999) 179-185.

Plasma Behaviors in Laser Cutting

Hideyuki HORISAWA*, Masataka TAMURA** and Seiichiro KIMURA**

* *Department of Precision Mechanics, School of Engineering, Tokai University, 1117 Kitakaname, Hiratsuka-shi, Kanagawa 259-1292 Japan*
email: horisawa@keyaki.cc.u-tokai.ac.jp
** *Power and Industrial Systems Research And Development Center, Toshiba Corporation, 2-4 Suehiro-cho, Tsurumi-ku, Yokohama 230-0045 Japan*

Behaviors of the plasma, the emission intensity, distribution, source and species were evaluated using a high-speed video camera, a color CCD camera, and a spectrum multi-channel analyzer. It was found that a strong blue radiation from iron atoms of workpiece, nitrogen molecules or ions of a gas jet, when the cut surface quality was not acceptable. As cutting speed increased, plasma formation region where a laser beam was focused was more extended. It was found that flow speeds of molten material at bottom in which the plasma was induced became slower than those of top and middle points. Also, scattering angles of molten material droplets at a bottom exit of a kerf became larger and, at the same time, reattachment of molten material at the bottom was observed. Moreover, it was found that additional branches of the flows of molten material with smaller and darker droplets were formed intermittently, and that parts of the branches of the flowing droplets were being attached as dross to the bottom edges. From these results, it was confirmed that the plasma formation (region) and sizes and angles of striations (cut surface quality) were strongly correlated. Possibilities of the in-process evaluation of the cut surface quality by monitoring the plasma sizes and/or brightness in laser beam cutting were discussed.

Keywords: Laser cutting, Plasma formation, Plasma behavior, High-speed camera, Cut surface quality

1. Introduction

Laser cutting is a thermal process that results in higher quality and precision than other thermal processes. In the cutting process, a focused laser beam impinges on material surface and melts and/or evaporates the irradiated point, and at the same time a coaxial gas jet to the laser beam is ejected to the point blowing the molten and/or vaporized material off through a cutting kerf. It has been observed that a strong electromagnetic wave and a pressure wave (acoustic wave) are emitted from the cutting point of the workpiece during the cutting process [1 – 4]. Especially gaseous substances emitting visible lights of the electromagnetic wave are often termed as "plasma", which is a term generally used for gaseous luminous substances. However, there have been little efforts for identification of their species, behaviors, and mechanisms of their formation [4]. It is assumed for sources of the emission of this type to be; 1) workpiece (solid state, liquidized state (molten material, or molten metal in most cases), vaporized state (atom, molecule), plasma), 2) a gas jet (atom, molecule, plasma), and 3) surrounding atmosphere, etc. From these points, the light emitted from a cutting point must be containing significant information relating to a state of the point, such as chemical species, temperature, density, etc. It is therefore very important for an acquisition of the state of the cutting point to observe and to measure characteristics of the plasma precisely.

In this study, characterization of the plasma induced in laser cutting was performed. First of all, radiative behaviors of the plasma for various cutting conditions were observed, and then, investigations of the emission mechanisms were performed through measurements of the emission intensity, position, and identifications of possible species of radiation. Also, a correlation between the radiative phenomena and cutting performance, such as cutting speed and cut surface quality, were investigated. Moreover, possibilities of in-process monitoring of laser cutting using the emission signals from the cutting point were discussed.

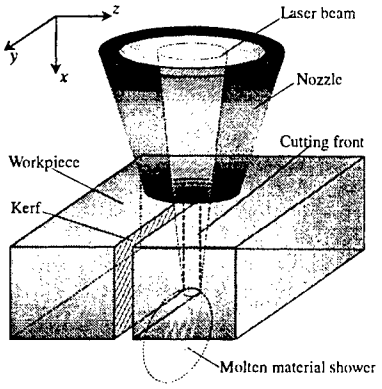


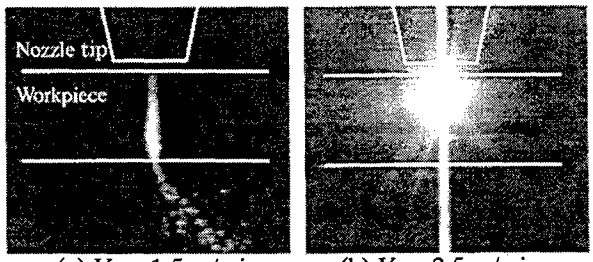
Fig.1 Schematic drawing of laser cutting.

2. Experimental

In this study, a 6 kilo-watt CO_2 laser machine (Nippei Toyama with Fanuc C6000B) was used. The workpiece used in study was stainless steel (SUS316L) of 8 mm thick, and a focal point of a laser was set at the bottom surface. A

First International Symposium on Laser Precision Microfabrication, Isamu Miyamoto, Koji Sugioka, Thomas W. Sigmon, Editors, Proceedings of SPIE Vol. 4088 (2000) © 2000 SPIE · 0277-786X/00/$15.00

convergent-divergent nozzle of ϕ3.2 mm in diameter was used, and nozzle-workpiece distance was kept constant, 1.5 mm. In general laser cutting, suitable conditions of laser pulses, i.e. pulse energy, frequency, duty factor, are selected for preferable cutting conditions of workpieces [1 – 3]. However, in this study, laser beam conditions in each cut were set constant, laser power: P_L = 6 kilo-watts (continuous wave), cutting speed: Vc = constant, feed pressure of a gas jet: Ps = constant, to observe and to characterize dynamic behaviors of plasma itself induced in laser cutting. Nitrogen gas was used for a coaxial gas jet to a laser beam, and the maximum feed pressure was set ~ 1.3 MPa. In this experiment, observations of emission intensity, position, distribution, and behavior of plasma induced at a cutting point were performed using the highspeed video camera (PHOTRON : Fastcam-ultima-uv (40500 fps, 24.6 μsec/frame)), the color CCD camera (SONY : CCD-V700 (30 fps, 100 μsec/frame)), and the spectroscopic multichannel analyzer (HAMAMATSU: PMA-50) for various cutting conditions of laser power: P_L, cutting speed: Vc, and feed pressure of a ges jet: Ps.



(a) Vc = 1.5 m/min (Fine quality cutting) (b) Vc = 2.5 m/min (Poor quality cutting)

Fig.2 Color CCD camera images of laser cutting (View direction: -y (30 fps, 100 μs/f), Laser power: P_L = 6 kW (CW), Nitrogen gas jet: P_s = 1.3 MPa, Workpiece: SUS316L(t:8mm), Vc: Cutting speed).

3. Results and Discussion

3.1 Characteristics of Plasma Emission

Color CCD camera images of a cutting front and induced plasma viewed from – y direction are shown in Fig.2. As shown in Fig.2(a), an orange radiation was observed in a cutting kerf of a workpiece and also under the kerf exit when the cutting condition, i.e., laser power, cutting speed, focusing point, feed pressure of a gas jet, etc., was in a range of preferable (higher) quality cut surface. It was confirmed from the spectroscopic diagnostics that the orange light is irradiated from surface of molten material. On the other hand, when the cutting condition was not in a good range, i.e., the cut surface quality was not acceptable, a strong blue radiation was observed inside a cutting kerf of a workpiece as shown in Fig.2(b),. It was found from the spectroscopic diagnostics and possible atoms, molecules or ions which may exist at the cutting point, that the blue light is irradiated from iron atoms of workpiece, nitrogen molecules (N_2: 1st Positive System and 2nd Positive System) or ions (N_2^+: 1st Negative System) of a gas jet [4 – 6].

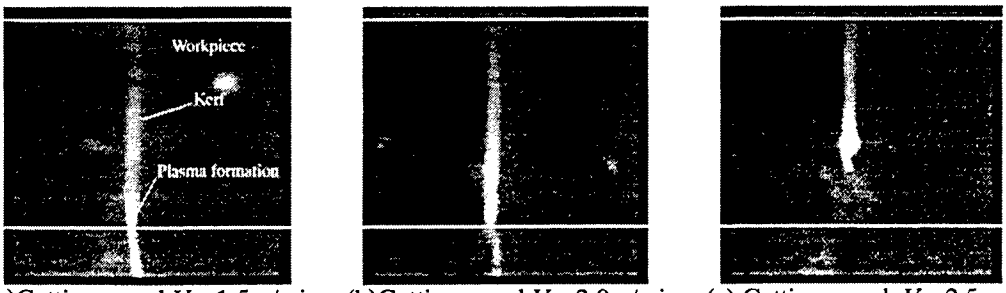
3.2 Plasma Behaviors in a Cutting Kerf

Photos of plasma behaviors in a laser cutting kerf observed with the highspeed video camera from – y direction are shown in Fig.3 (Cutting speed: Vc = 1.5 m/min, (b) Vc = 2.0 m/min, (c) Vc = 2.5 m/min). From Fig.3, it can be seen that the radiative sources are roughly divided into three types as follows; 1) plasma induced inside a cutting kerf (at a cutting front or cut surfaces), 2) molten material running downwards inside a cutting kerf, and 3) molten material scattering out of a cutting kerf. In a case of Fig.3(a) Vc = 1.5 m/min, no reattachment of molten material, or dross, at bottom edges of a kerf exit was observed, and the cut surface quality was the best among the whole conditions in this experiment. In Fig.3(a), it can be seen that a small bright spot, or plasma, is induced at the bottom of a cutting front in which a laser beam is focused. In this case, it was found that flow speeds of molten material at top, middle and bottom in a kerf were almost same, ~ 11 m/sec. Also in this case, the flow of molten material concentrated into the size less than the kerf width below the kerf exit, and the flow speed estimated was about the same as the flow speed inside the kerf.

In the case of faster cutting speed condition, Fig.3(b) Vc = 2.0 m/min, a little reattachment of molten material at bottom edges of the kerf exit was observed, though the cut surface quality was not very low. In this case, it can be seen that a range of plasma formation around which a laser beam is focused is more extended than the case of Fig.3(a), and also that two bright points are induced vertically. It was found from the pictures that flow speeds of molten material at top and middle points inside a kerf were constant, ~ 11 m/sec, while the flow speed at bottom in which the plasma was induced became slower, ~ 2 m/sec. Also it was observed that at the bottom exit of the kerf the flow of molten material is spreading intermittently. With much faster cutting speed, Fig.3(c) Vc = 2.5 m/min, through penetration of cutting was no longer possible after cutting a few centimeters, and at the same time a strong blue radiation as shown in Fig.2(b) was observed. In Fig.3(c), plasma is induced at a higher position in depth, or around a middle point, inside a kerf, and its emission intensity is stronger than Fig.3(a) and (b) cases. Also it was observed from the pictures that flow speed of molten material was about the same, ~ 11 m/sec, in region from top to the point in which the plasma was induced inside a kerf. However, at the plasma formation region the flow speed of molten material became extremely slow and the molten material flow was standing. At the kerf bottom exit, wider scattering of the molten material with increasing the cutting speed was also observed.

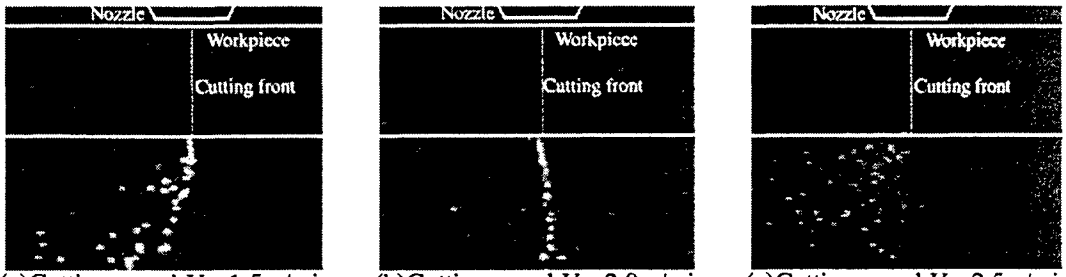
3.3 Motion of Molten Material Scattering at a Kerf Exit

Color CCD camera images of scattering molten material below a bottom exit of a kerf observed from – z direction (see Fig.1) for the same conditions as Fig.3 are given in Fig.4, in which cutting speeds are (a) Vc = 1.5 m/min, (b) Vc = 2.0 m/min, and (c) Vc = 2.5 m/min, respectively. In Fig4(a), Vc = 1.5 m/min, each droplet of molten material is larger, emitting stronger light, and its scattering angle is likely constant, compared to other cases, Fig.4(b) and (c). On the other hand, it was found that as cutting speed increases, as Fig.4(b) Vc =



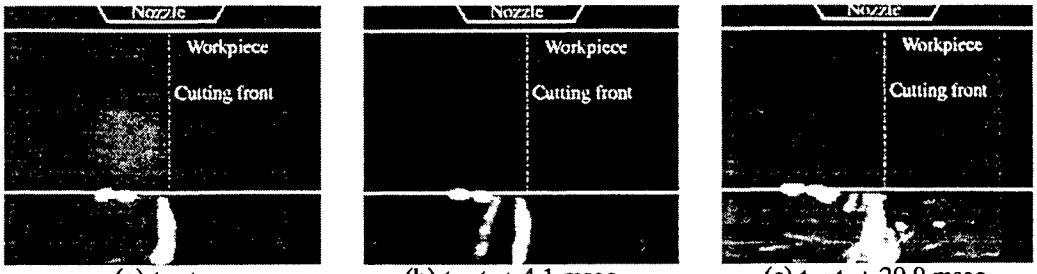
(a)Cutting speed:Vc=1.5m/min (b)Cutting speed:Vc=2.0m/min (c) Cutting speed: Vc=2.5 m/min

Fig.3 Highspeed camera images of laser cutting (View direction: -y (13500 fps, 74 μs/f), Laser power: P_L = 6 kW (CW), Nitrogen gas jet: P_s = 1.3 MPa, Workpiece: SUS316L(t:8mm)).



(a)Cutting speed:Vc=1.5m/min (b)Cutting speed:Vc=2.0m/min (c)Cutting speed:Vc=2.5m/min

Fig.4 Color CCD camera images of laser cutting (View direction: -z (30 fps, 100 μs/f), Laser power: P_L = 6 kW (CW), Nitrogen gas jet: P_s = 1.3 MPa, Workpiece: SUS316L(t:8mm)).



(a) $t = t_0$ (b) $t = t_0$ + 4.1 msec (c) $t = t_0$ + 20.9 msec

Fig.5 Highspeed camera images of laser cutting (Process of dross formation) (View direction: -z (13500 fps, 74 μs/f), Laser power: P_L = 6 kW (CW), Nitrogen gas jet: P_s = 1.3 MPa, Cutting speed: Vc = 2.0 m/min, Workpiece: SUS316L(t:8mm)).

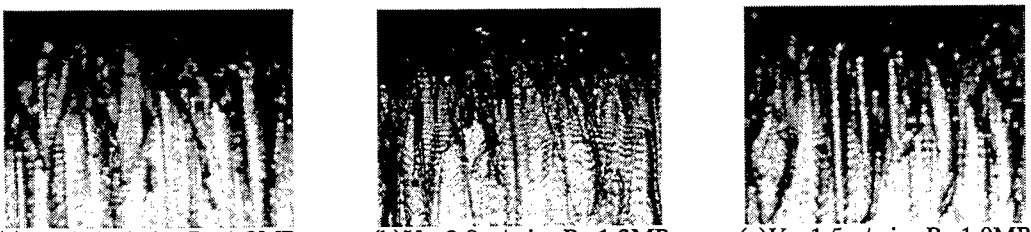
2.0 m/min and (c) Vc = 2.5 m/min, both size and brightness of the molten material droplets decrease and their scattering range become wider. It was confirmed that scattering angles of molten material droplets to +/– y and z directions at a bottom exit of a kerf become larger and, at the same time, reattachment of molten material at bottom edges of a kerf is observed.

In order to ascertain this phenomena temporally and spatially, observations with the highspeed video camera from – z direction were performed. Some examples of the photos for cutting speed of Vc = 2.0 m/min are given in Fig.5. It was shown from the photos that most of the molten material is flowing down from a bottom of a cutting front. Also, it was found that additional branches of the flows of molten material with smaller and darker droplets are formed intermittently, as shown in Fig.5(b), and that parts of the branches of the flowing droplets are being attached as dross to the bottom edges of a kerf exit. Moreover, in Fig.5(c), several branches are being formed and scattering angle of the molten material is larger. From these results, it was confirmed that formation of the branches of molten material flow, dross formation (dross reattachment to the kerf bottom edges), and increase of the scattering angle of the molten droplets below a cut kerf are closely correlated.

3.4 Correlation between Plasma Behavior and Cut Surface Quality

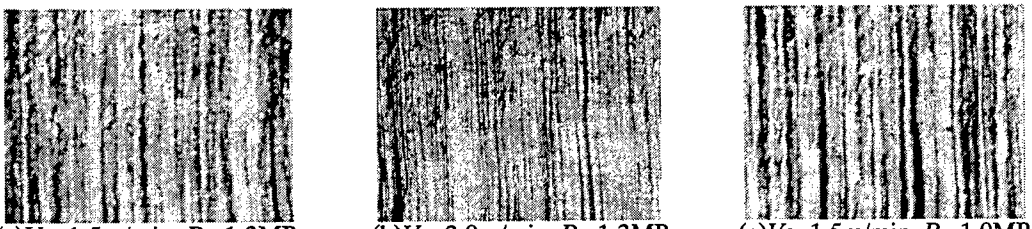
Images of cut surface taken by the optical microscope for various conditions are given in Figs.6 ~ 8 (Fig.6: top edge of a cut surface, Fig.7: middle surface, Fig.8: bottom edge; (a) Vc = 1.5 m/min, Ps = 1.3 MPa (dross free or no dross reattachment), (b) Vc = 2.0 m/min, Ps = 1.3 MPa (dross reattachment), (c) Vc = 1.5 m/min, Ps = 1.0 MPa (dross reattachment)). In all cases, striations formed during cutting were observed on cut surfaces. At middle surface, Fig.7, intervals of the striations were smaller, or surface roughness estimated was smaller, while at top and bottom edges, the surface roughness was larger. Also, similar values for the surface roughness of top and middle positions were observed.

On the other hand, it was found that both sizes and angles, or drag angles, of striations at bottom sections were different in each case. In (a) Vc = 1.5 m/min, Ps = 1.3 MPa (dross free



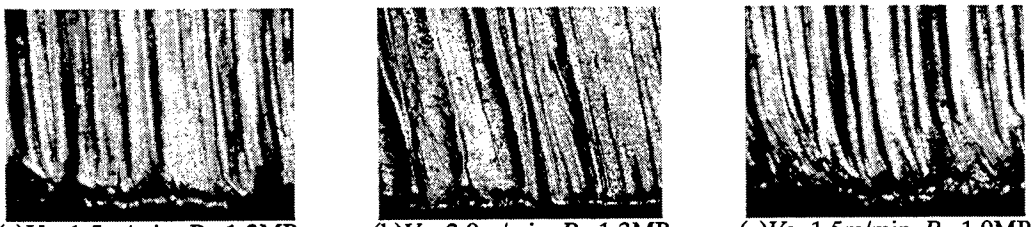
(a)Vc=1.5m/min, P_s=1.3MPa (b)Vc=2.0m/min, P_s=1.3MPa (c)Vc=1.5m/min, P_s=1.0MPa

Fig.6 Photos of laser-cut surface (upper edge) (Laser power: P_L = 6 kW (CW), Workpiece: SUS316L(t:8mm)).



(a)Vc=1.5m/min, P_s=1.3MPa (b)Vc=2.0m/min, P_s=1.3MPa (c)Vc=1.5m/min, P_s=1.0MPa

Fig.7 Photos of laser-cut surface (middle) (Laser power: P_L = 6 kW (CW), Workpiece: SUS316L(t:8mm)).



(a)Vc=1.5m/min, P_s=1.3MPa (b)Vc=2.0m/min, P_s=1.3MPa (c)Vc=1.5m/min, P_s=1.0MPa

Fig.8 Photos of laser-cut surface (lower edge) (Laser power: P_L = 6 kW (CW), Workpiece: SUS316L(t:8mm)).

or no dross reattachment), striations are almost vertical, and the surface roughness is smaller, or cut quality is preferable, except the positions of plasma formation or bottom edges (see Fog.3(a)). While in a faster cutting speed condition, (b) Vc = 2.0 m/min, Ps = 1.3 MPa (dross reattachment), striations at the bottom edges are not vertical but inclined about 15 degrees from a vertical line, and this bottom area corresponds to a region of plasma formation in Fig.3(b). Similar trend was found in a much faster cutting speed condition, (c) Vc = 1.5 m/min, Ps = 1.0 MPa (dross reattachment)). In conditions of this study, it was found that the plasma formation region expands with increase of the cutting speed. As cutting speed increases, a delay or a curvature of a cutting front bottom becomes significant, and then a laser beam impinges on the curved surface. It was found that the plasma formation becomes more significant due to this impingement of the beam on the surface [4].

From these results, it was confirmed that the plasma formation (region) and sizes and angles of striations, or local surface roughness (cut surface quality), are strongly correlated, and that the sizes of the plasma formation region corresponds to the surface roughness, or quality. Therefore, by monitoring the plasma sizes and/or brightness in laser beam cutting, the in-process evaluation of the cut surface quality could be possible.

4. Conclusions

Behaviors of the plasma, the emission intensity, distribution, source and species were evaluated using a high-speed video camera, a color CCD camera, and a spectrum multi-channel analyzer. From the results, it was confirmed that the plasma formation (region) and sizes and angles of striations, or local surface roughness (cut surface quality), are strongly correlated, and that the sizes of the plasma formation region corresponds to the surface roughness, or quality. Therefore, by monitoring the plasma sizes and/or brightness in laser beam cutting, the in-process evaluation of the cut surface quality could be possible.

References

[1] G. Chryssolouris, *Laser Machining: Theory and Practice*, Spinger-Verlag, New York, 1991.

[2] Japan Laser Processing Soc., *Laser-Setsudan no Genjo to Shorai-Gijutsu* (in Japanese), Japan Laser Processing Soc., Osaka, 1996.

[3] F. O. Olsen, "Laser Cutting Theory," *Proc. 4th Nordic Laser Material Processing Conference*, pp.77 – 88, 1993.

[4] Horisawa, H., Ashizawa, H., and Yasunaga, N., "Plasma Characterization in Laser Cutting", *Proc. SPIE Vol.3888*, pp.82-89 (2000).

[5] R. W. B. Pearse, and A. Gaydon, *The Identification of Molecular Spectra (4th Edition)*, Chapman and Hall, London, 1976.

[6] A. R. Strignav, and N. S. Sventitskii, *Tables of Spectral Lines of Neutral and Ionized Atoms*, IFI/Plenum, New York, 1968.

Fundamental Study about Molten Metal of Laser Cutting

*Takashi FUSHIMI, Hiromasa NAKAJIMA, *Hideyuki HORISAWA, Shigeru YAMAGUCHI, **Nobuo YASUNAGA and *Tomoo FUJIOKA*
**Department of physics, School of Science, Tokai University 1117 Kitakaname, Hiratsuka-city, Kanagawa 259-1292, Japan*
E-mail: 9jspm017@keyaki.cc.u-tokai.ac.jp
***Department of Precision Mechanic School of Engineering, Tokai University 1117 Kitakaname, Hiratsuka-city, Kanagawa 259-1292, Japan*

This study, the action of molten metal in the kerf using oxygen an a assist gas was observed with the high speed digital CCD camera. The ejection of molten metal is changed direction in every 2ms. Case of the optimum condition speed cutting (1800mm/min), The molten metal moves straight down to bottom of the kerf. Case of the high speed cutting (2800mm/min), Case of the mass of molten metal stays in the kerf, dross the appeared underneath workpiece. And case of ejection angle is over the 45 degree, dross appeared underneath the workpiece. Mass molten metal and small molten metal is every pulsed.

Keyword: assist gas, dross, ejection, molten metal, laser cutting,

1.Introduction

Laser cutting is the most widely used of all laser machining processes. In laser cutting, a laser beam penetrates through the entire thickness of the workpiece and advances parallel to the surface of the workpiece. Depending on the phase of material removed, laser cutting is divided into two types: sublimation and fusion cutting. In the case of laser fusion cutting, the material is melted at the erosion front and ejected from the kerf with the assist gas jet. [1] However, through cutting of thick metal can more frequently face technical difficulties like generation of rough cut-surface and dross formation compared to the thin mild steel sheet. It is also well known that a narrow kerf is created during laser through cutting process, resulted in a complicated interaction among laser light, gaseous medium and melted metal. Though the laser through cutting can perform with better quality than the gas cutting and the plasma cutting, one of the reasons why it has not been widely used can be attributed to less information in order to predict laser cutting performance. [2-3]

One of the key issues to improve the surface quality laser cutting process, should be properly to understand molten metal behavior in the kerf, since the origin of surface roughness and dross formation is thought to be action of molten metal. However study of action of molten metal which has very little progress. [4] The objective of this study is to observe dross formation in kerf using oxygen of assist gases. Transient action of molten metal in a kerf was experimentally observed with a high-speed digital CCD camera at a maximum full frame rate of 40500 frames per second.

2 Experimental set up

A schematic diagram of the experiment is shown in Fig.1.

Experimental condition is shown in Table.1.

(1) Laser source

The experiments were done with a transverse flow type CO_2 laser, which is a commercial product of the AMDA (model LCF644). A maximum output power level of the laser apparatus is 2kW with a M^2 value of 2.5. As a focusing lens, we used a single ZnSe plano-convex lens with a focal length of 127 mm (5.0 inches). The laser beam diameter at a focal point is approximately 120 μ m. The center of laser beam was located at slightly inside of cutting edge (700~800 μ m) of the steel so that an erosion front can be observed.

(2) Assist gas and nozzle

A diameter of the nozzle mouth is 2.0mm. The between nozzle and workpiece is 1.5mm. A maximum pressure of assist gas can increase up to 0.4MPa. In the case of dross-free with oxygen as an assist gas, scanning speed is between 500mm/min and 3000mm/min. The pressure of an assist gas is constant 0.15Mpa.

First International Symposium on Laser Precision Microfabrication, Isamu Miyamoto, Koji Sugioka, Thomas W. Sigmon, Editors, Proceedings of SPIE Vol. 4088 (2000) © 2000 SPIE · 0277-786X/00/$15.00

(3) Diagnostics

Transient motion of molten metal was observed with a high-speed digital CCD camera, (PHOTRON model Fastcam-ultima). A maximum frame rate of the CCD camera reaches 40500 frames per second. However, a reduced frame rate at 27000 frames per second was used throughout the experiments, since we need the full frame data transfer for better image resolution. The image on the CCD plane has threes times as coefficient of magnification to an original object. The brightness was adjusted into the ND filters in front of the high-speed digital CCD camera.

The height of camera axis was set in the same surface of metal sheet. The view was obtained perpendicular to the axis along the scanning direction.

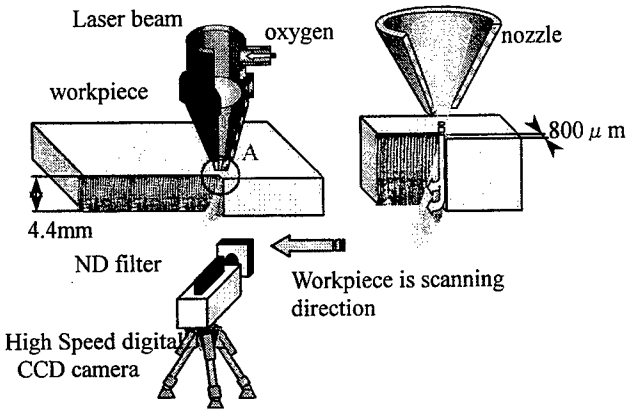


Fig.1 Schematic view of experiment

Table.1 Experimental condition

	Condtion A	Condtion B	Condtion C
Laser power	1500(W)	1500(W)	1500(W)
Scanning speed	600(mm/min)	1500(mm/min)	2800(mm/min)
Assist gas	0.15MPa	0.15MPa	0.15MPa
	Dross	Dross Free	Dross
	ExcessOxygen	Balance	Lass Oxygen

3 RESULTS

Figure 2 represents the conditions A cutting.

These photographs represented as typical actions of molten metal were picked up with a increment of every 5.8 ms, while the digital camera captured each frame with a much shorter increment of every 37 μ s. The molten metal moves straight down to bottom of the kerf. The molten metal moves straight down to bottom of the kerf. When the molten metal moves the kerf, erosion front is pulsed. When the ejection of molten metal at the direction of moved workpiece, dross is appeared underneath the workpiece.

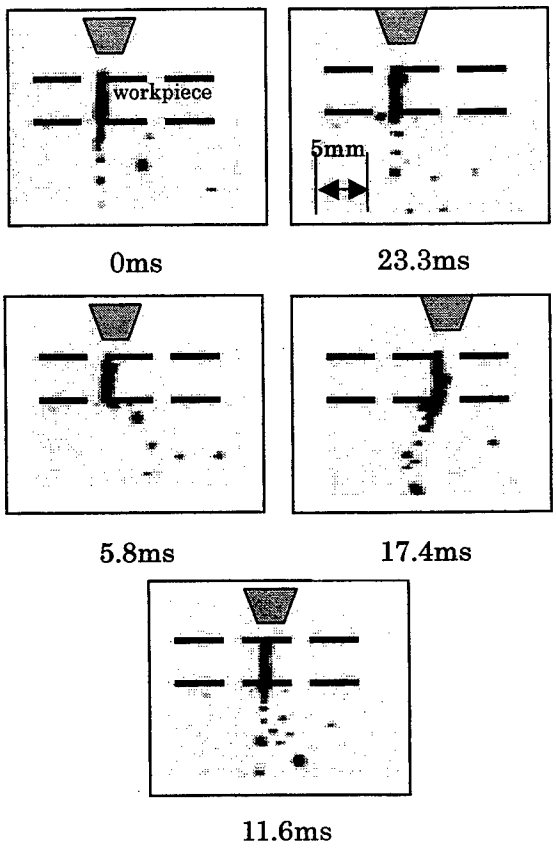


Fig.2 High speed photographs of an erosion front (conditions A)

Figure 3 represents the cutting under conditions B cutting. These photographs represented as typical actions of molten metal were picked up with a increment of every 0.11 ms, while the digital camera captured each frame with a much shorter increment of every 37 μ s Consecutive molten metal ejection is occurred. A mass of molten metal is regularly formed at the top of the kerf and it move to straight down to bottom every 600 μ s. A mass of molten metal is formed every 600 μ s.

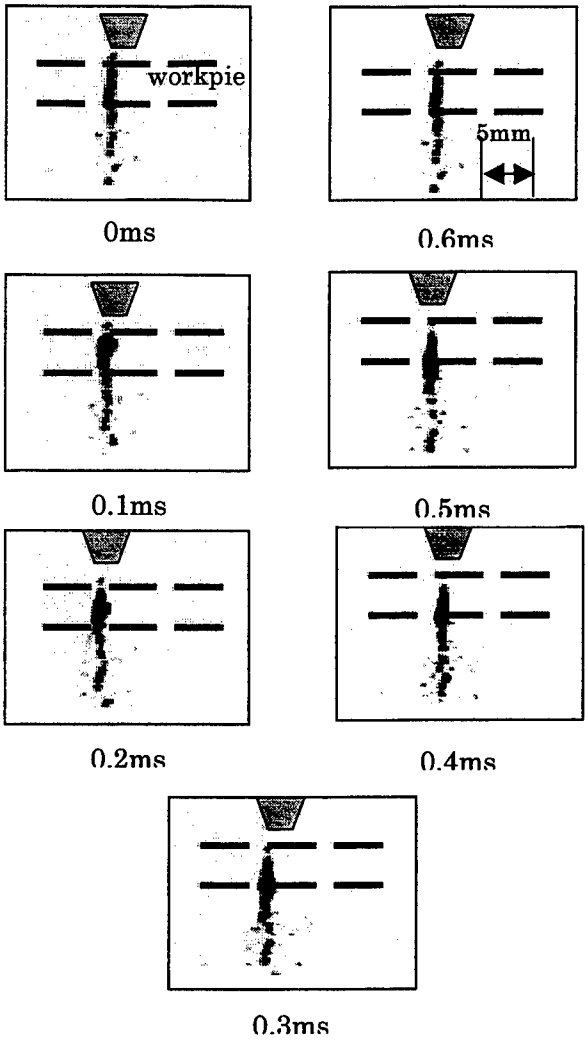


Fig.3 High speed photographs of an erosion front (conditions B)

Figure 4 represents conditions C cutting. These photographs represented as typical actions of molten metal were picked up with a increment of every 2.6 ms, while the digital camera captured each frame with a much shorter increment of every 37 μ s. The molten metal at the angle 30° down to bottom of the kerf maybe due to lower temperature in molten metal compared to conditions A.C. The with a higher viscosity molten metal mostly ejected toward the scanning direction of moved workpiece. The ejection angle of molten metal is every 2600 μ s. The part of molten metal moved at the bottom of workpiece.

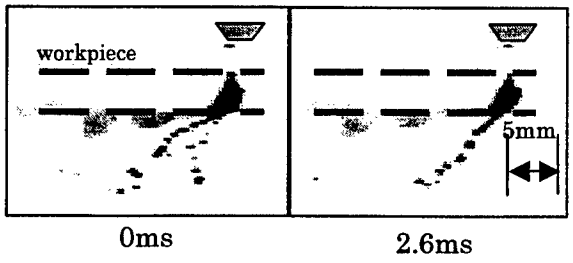


Fig.4 High speed photographs of an erosion front (conditions C)

4 SUMMARY

Case of the mass of molten metal stays in the kerf, dross the appeared underneath workpiece. And case of ejection angle is over the 45 degree, dross appeared underneath the workpiece. Mass molten metal and small molten metal is every pulsed.

References

[1] Frederick F. Ling "*Laser Machining*" p160, George Chryssolouris, New York, 1991

[2] Tohru MURAI "*Trend of Laser Cutting Technology*" JAPAN WELDING SOCIETY Vol. 66, No.7, 524, July, 1997

[3] H.jorgensen, Lyngby, D.Kechemair, Arcueil, and F.O.Olssen, Lyngby "*On-line detection of the cut quality during CO_2 Laser beam cutting*" INTERNATIONAL BEAM TECHNOLOGY GONFERENCE Vol.135, P172-177 1991

[4] Frederick F. Ling "*Laser Machining*" p47, George Chryssolouris, New York, 1991

Fundamental study about CO_2 Laser Welding of Titanium Aluminide Intermetallic Compound

[a]Gaku kuwahara, [a]Shigeru Yamaguchi, [a]Kenzo Nanri, [b]Masanori Ootani, [b]Masato Testuka, [b]Sachio Seto, [c]Mikiya Arai and [a]Tomoo Fujioka

[a]Department of Physics, School of Science, Tokai University, 1117, Kitakaname, Hiratsuka-City, Kanagawaken, 259-1291, Japan
[b]Department of Metallurgical Engineering, School of Engineering, Tokai University,
[c]Materials Tech. Dept., R&E Div. Aero-Eigines & Space, Ishikawajima-Harima Heavy Industries Co., Ltd, 3-5-1, Mukodai, Tanashi-City, Tokyo,181, Japan

Titanium aluminide intermetallic compound is attracting attentions as heat-resistant and high-specific strength material in the next generation, especially, it is promising material in the field of aerospace components. Conventional machining process including welding, however, can be hardly applied due to its very low ductility. The objective of this study, as a first stage, is to find out paying attention to crack and hardness the fundamental good conditions of the bead-on-plate welding of TiAl intermetallic compound using CO_2 laser irradiation. In the experiment, we used the casting gamma titanium aluminide contained iron, vanadium and boron with a thickness of 2 mm. We carried out bead-on-plate laser welding in the titanium aluminide material in inert gas environment filled with argon. We measured fused depth, Vickers hardness, transverse crack numbers and so on as major parameters of welding speed from 1000 to 4600 mm/min and initial temperature of specimen from R.T. to 873 K with a beam spot size of 0.5 mm and an output power of 1.5 kW. In addition, the specimens were analyzed by Electron Probe X-ray Micro Analyzer, Energy Dispersive X-ray Spectroscopy and X-ray Diffractometry. As a result of experiments, transverse crack-free welding was achieved, when initial temperature was at 873 K. In every condition, the value of Vickers hardness of fused zone increased compared with base. We think the reason of it is an increase of α_2 (Ti_3Al) phase, which is caused by rapid cooling, taking in Oxygen, fine structure and so on.

Keywords : CO_2 laser, bead-on-plate welding, TiAl, intermetallic compound, argon gas

1. Introduction

Intermetallic compound is defined as two or more kinds of metallic atoms combined with the constant population ratio. Many intermetallic compounds exhibit even more attractive characteristics than face of any other materials. Among these, TiAl intermetallic compound has excellent characteristics. The advantages are follows; First is light weight whose specific gravity of TiAl corresponds to only a half of that with Ni-supper-alloy. Second is high specific strength in high temperature. The strength of TiAl is compatible with Ni-supper-alloy. More over with regard to high-specific strength, the higher temperature becomes, the higher strength of TiAl up to 1000 [K]. Thus, TiAl can be promising materials in the field of aerospace and jet engine components, in the next generation.

The establishment of the suitable methods with joining two TiAl plates together, is one of the crucial issues to put a TiAl to practical use. It is possible to join two TiAl plates together with the diffusion welding. Actually however, the diffusion welding is not suited to join the parts of complicated shape and/or thin plate. In case of joining of thin plate or complicated shape, in general, melting junction method is hoped, because that method has versatile and flexibility. Laser welding is one of good candidates, in addition, it has some advantages. The laser welding is useful in many fields, because a laser beam is the most controllable and flexible heat source. Using laser welding of TiAl, for example, TiAl is prevented oxidation than other welding methods, by high speed processing ability of the laser welding. Therefore we decided that we would achieve laser welding of TiAl intermetallic compound. It has been reported that the TiAl added Mo to improve ductility were welded by the CO_2 laser [1], [2], [3].

It is comfirmed the atomosphere of the laser welding is very important by past experimental result. Laser welding using a vacuum chamber seems to be an alternative method. However, in this case, the apparatus can be so bulky if a laser welding of large materials is demanded, resulting in less flexibility.

First International Symposium on Laser Precision Microfabrication, Isamu Miyamoto, Koji Sugioka, Thomas W. Sigmon, Editors, Proceedings of SPIE Vol. 4088 (2000) © 2000 SPIE · 0277-786X/00/$15.00

The objective of this study, as a first stage, is to find out paying attention to crack and hardness the fundamental good conditions of the bead-on-plate welding of TiAl intermetallic compound using CO_2 laser irradiation.

2. Experiment

2. 1. Material

Specimens used in the experiments were TiAl compound that had been precision casting and then done HIP (Hot Isostatic Pressing) treatment. Fe, V and B were tailored to improve the performance of cast [4]. The specimens were processed 60 mm long, 25 mm wide and 2 mm thick and the 60th surfaces were polished by the emery paper(#600). The chemical composition of specimen is shown as Table.1.

Table 1. Chemical composition of cast TiAl-Fe-V-B

	Al	Fe	V	B	O	N	Ti
At%	45.9	1.27	1.24	0.31	0.12	0.03	Bal

2. 2. Setup

The experiments were performed with a commercially available CO2 laser, AMADA LCF644. A maximum laser output power of reaches 2 kW. Laser beam quality corresponded to a M^2 factor of 2.5. A schematic drawing of the experimental setup is shown in Fig.1

The laser beam was focused just on the specimen's bottom by a single plano-convex lens with a focal distance of 254 [mm], beam spot diameter on the specimen surface was 0.44 mm. The laser power in the experiments was kept constant at 1.5 [kW].

The specimens were placed inside the shielding box, whose dimension was $16.5 \times 17 \times 9$ cm^3. A metal plate with a small slit was attached on the top-face of the shielding box, as a lid for the prevention of the air-invasion. The slit, whose width was set to be 10 mm, was used as a laser beam inlet window.

The atmosphere of the box was replaced by an Ar gas to minimize the influence of oxidation. The Ar gas was supplied by a shield gas nozzle. The beam axis and the flow direction of the shield gas were set to be met at an angle of 55 degree to the surface of specimen. The shield gas nozzle made of Cu was 4 mm in diameter. The flushing time for gas exchange was 10 minutes at a flow rate of 5 L/min. During the laser irradiation, on the other hand, flow rate was increased to 10 L/min to reduce of the plume effect.

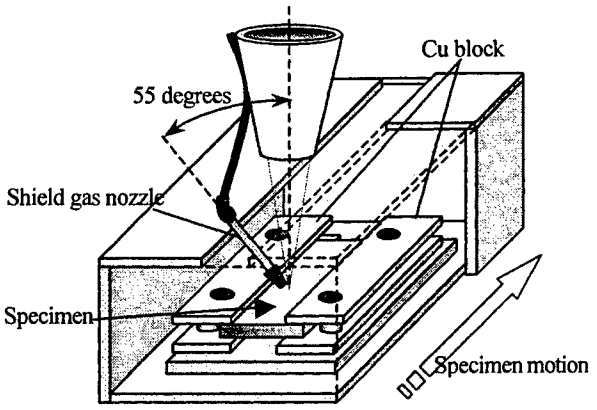


Fig. 1 Schematic drawing of experimental setup

The specimen was heated in advance by a heater to make up for low ductility and to prevent transverse crack. The temperature of the specimen was monitored using thermocouple and was controlled by a digital temperature controller. The initial temperature of specimens was varied from room temperature to 873 [K]. The welding speeds which is relevant to cooling rate were varied from 1000 mm/min to 4600 mm/min.

The welding conditions were shown in table 2.

Table 2. Welding condition

Out put power	[kW]	1.5
Welding speed	[mm/min]	1000~5000
Initial temperature	[K]	R.T., 573, 673, 873
Shield gas flow rate	[L/min]	10

2. 3. Evaluation method

After the laser irradiation, the specimens were evaluated as follows. Transverse and vertical cracks of the specimens were observed by visible dye penetrant inspection. And we measured average Vickers hardness of melted zone from the surface to1mm under the surface (every 0.2mm increment). In addition, the specimens were analyzed by Energy Dispersive X-ray Spectroscopy (EDX), Electron Probe X-ray Micro Analyzer (EPMA) and X-ray Diffractometry (XRD).

3. Result and discuss

3.1. penetration depth

Welding speeds that could allow full bead-on-plate welding were 3000 [mm/min] or less at an initial temperature of 873 [K], 2600 [mm/mm] or less at an initial temperature of 673 [K], and 2000 [mm/min] or less at an initial temperature of 300 [K].

3. 2. Transverse crack

In each initial temperature, relationships between the number of cracks and the welding speed were shown as Fig. 2. The number of cracks decreased with increasing initial temperature. It was possible to obtain crack-free bead-on-plate welding, when initial temperature was 873 [K]. Moreover, the crack frequency depended on the welding speed too, at reduced initial temperatures of 300 [K], 573 [K] and 673 [K].

The transverse crack is probably caused an appearance of non-equilibrium phase because of rapid cooling around 1400 [K]. We assume that this non-equilibrium which is hard

similarly to martensite in steel's quenching. And very poor ductility of TiAl might affect the number of cracks.

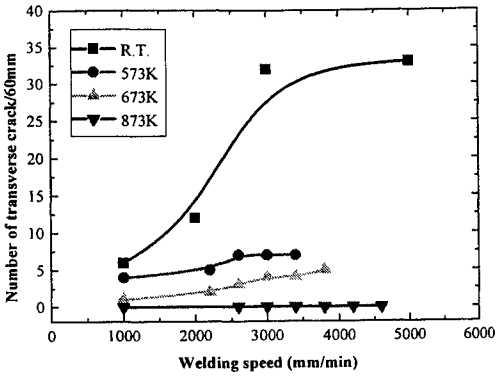


Fig. 2 relationship between welding speed and the number of cracks

And vertical crack is confirmed in case that the width of bead is wide due to low welding speed.

3.3. Hardness

Fig. 3 shows the average Vickers hardness of melted zone. In
case of any initial temperatures, value of Vickers hardness is higher than base metal's value (about 350 Hv). We were interested in two points in this figure. First point is when initial temperature is 875 [K] the value of hardness is the second to R.T. Other is, in all initial temperature, the lines of the value of Vickers hardness have valley.

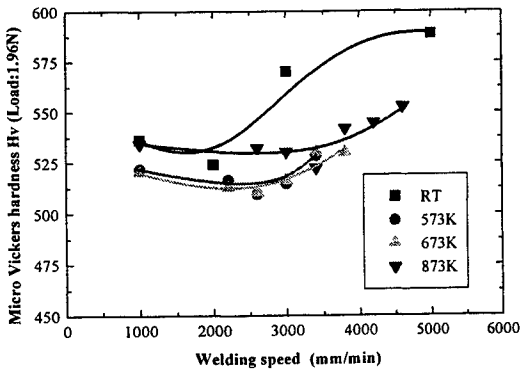
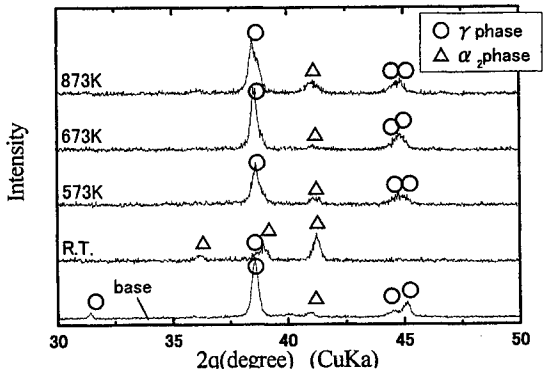


Fig. 3 Average Vickers hardness

In each temperature with a welding speed of 3000 mm/min, the results of XRD analysis are shown as Fig.4. In this figure the open circle shows TiAl phase and open triangle shows Ti_3Al phase. The intensity of Ti_3Al were increased than base metal. In addition, the intensities of Ti_3Al phase correspond to the value of Vickers hardness (refer to Fig. 3). Therefore we supposed that the increase of hardness was caused by an appearance of Ti_3Al phase, because Ti_3Al is harder than TiAl phase.



Welding speed : 3000 mm/min

Fig.4 result of ERD analysis

The increase of Ti_3Al (α_2) phase can be attributed to following two reasons; First is rapid cooling around 1400 [K] because it is eutectoid transformation temperature. It is reported that the order from α(Ti) phase to α_2 is easy in supersaturation.[2][5] .Second is an influence of taking in Oxygen, because Oxygen act as an element stabilization of a phase[4],[6]. Namely, the increase of hardness caused more storongly rapid cooling when cooing rate was fast, and taking in Oxygen when cooling rate was slow.

3.4. Result of EPMA and EDX analysis

As a result of EDX analysis (R. T. 3000 mm/min), there were not a big difference of the concentration of Ti, Al, Fe and V in the points of base metal, boundary face and melted zone.

On the other hand, result of EPMA analysis shows a possibilities of decrease of Al. Additionally, it is comfirmed that the melted zone exhibited fines structure compared with base metal. This fine structure, as might be expected, resulted in the increase of hardness too.

4. Conclusion

TiAl-Fe-V-B intermetallic compound was welded by CO2 laser irradiation whose output power was constant as 1.5 kW.

We could achieve bead-on-plate welding with no transverse crack, with raised initial temperature at 873 [K]. The number of cracks decreased with increasing of initial temperature and decreasing welding speed.

The average Vickers hardness, on the other hand, increased than the value of base and were not dependent on initial temperature compared with the number of cracks. We

supposed that the increase of hardness was caused by an appearance of Ti_3Al phase. The increase of Ti_3Al (α_2) phase can be attributed to rapid cooling around 1400 [K] and an influence of taking in Oxygen.

Reference

1. A. HIROSE, Y. ARAI, K. KOBAYASHI, "Microstructure and crack sensitivity of laser-fusion zones of Ti-46 mol% Al-2mol % Mo alloy", *Journal of Materials Science.* **30**, pp.970-979, 1995
2. Akio Hirose, Yoshihiro Arita and Kojiro F. Kobayashi, "Microstructural Change of TiAl Intermetallic compound during Laser Fusion Processing and Mechanical Properties of the Fusion Zone", *J. Soc. Mat. Sci.,Japan.* **44**. pp. 1145-1150, 1995.
3. Akio Hirose and Kojiro F. Kobayashi. "Joining of Ti-Base Advanced Materials", *Japan light metal welding*, **35**. pp. 535-542, 1997.
4. Sachio Nishikiori, Kenji Matsuda and Yukiya Nakagawa, "Effect of dissolved Oxygen content on microstructure and room temperature tensile properties of cast TiAl-Fe-V-B Alloy", *The Journal of the Iron and Steel Institute of Japan.* **83**, pp. 647-652, 1997.
5. E. L. Hall and Shyh-Chin Huang, *Acta Metall.* 38, 539,1990
6. T. Ahmed and H.M.Flower, *Mater Scie Eng*, A152, 1992

Effect of Nozzle Shape on Surface Integrity in Micro Cutting with Pulsed YAG Laser

Yasuhiro OKAMOTO*, Yoshiyuki UNO* and Naoki MIYANAGI**

* *Department of Mechanical Engineering, Okayama University, 3-1-1 Tsushimanaka, Okayama 700-8530, Japan*
E-mail: okamoto@mech.okayama-u.ac.jp
** *Hitachi Construction Machinery Co., Ltd., 650 Kandatsu, Tsuchiura, Ibaraki 300-0013, Japan*

YAG laser has widely been used for precision micro machining in many fields. However, adhesions of dross and spatter to the base material due to high energy beam machining lead to the deterioration of the surface integrity. It is important to understand the assist gas flow from the tip of a convergent nozzle in order to improve the surface integrity, since material is mostly removed away by the gas flow spouted in the same direction of the laser beam.

In this paper, effects of the nozzle shape on assist gas flow and the machined results were experimentally analyzed using the Schlieren method. There exists an unstable region in which the pressure on the workpiece changes periodically, and the region becomes wider with the reduction of the exit diameter. The pressure on the workpiece increases with an increase of the exit diameter, which makes the dross height smaller. However, it is necessary to select the nozzle shape according to the demand of the surface integrity, because the consumption of the assist gas increases and the kerf width becomes wider with an increase of the exit diameter. Moreover, it was pointed out that a kind of nozzle with a convex curve on inner wall of nozzle led to better surface integrity.

Keywords: YAG laser, dross generation, nozzle shape, assist gas flow, Schlieren method, Mach shock disk

1. Introduction

YAG laser has widely been used for precision micro machining in many fields, because it has the benefits of the possibility to focus the laser beam in a small spot. However, in YAG laser beam machining, material is melted or vaporized by the absorbed heat and is partly removed by the pressure of vaporization. This scattered material adheres as spatter, which can be prevented by a coat of an anti adhesive agent, to the base material again. On the other hand, melted material is mostly carried away downward by the assist gas flow spouted coaxially along the axis of the laser beam. Unfortunately, it is impossible to carry away completely, and the part of melted material adheres to the exit side as dross, which leads to the deterioration of the surface integrity in micro cutting. Therefore, the assist gas flow has a great influence on the generation of dross. The assist gas flow spouted from the nozzle tip is generally a complicated supersonic underexpanded jet [1], in which the pressure and the flow rate vary in every point. In the case of setting a workpiece under the nozzle, the flow becomes more complicated, since a vortex ring appears on the workpiece. Moreover, it is considered that the gas flow changes remarkably before and after the laser beam penetrates the workpiece completely. Therefore, it is important to understand the assist gas flow spouted from the tip of a convergent nozzle in order to improve the surface integrity. In this paper, the effects of nozzle shape on the assist gas flow and the machined results are experimentally analyzed using some kinds of nozzles with different shapes.

2. Experimental procedures

Fig.1 shows the schematic diagram of experimental setup. The pulsed Nd:YAG laser pumped by the Xenon flush lamp was used in this study. The focal length is 50 mm, and the laser beam pattern is single-mode, which is suitable

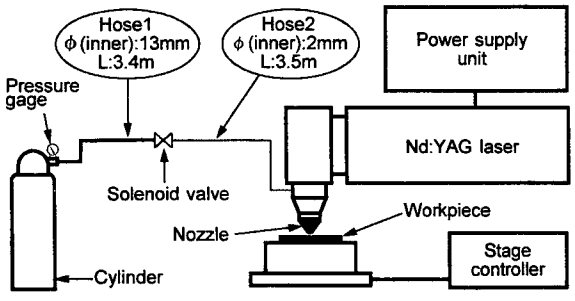


Fig.1 Schematic diagram of experimental apparatus

First International Symposium on Laser Precision Microfabrication, Isamu Miyamoto, Koji Sugioka, Thomas W. Sigmon, Editors, Proceedings of SPIE Vol. 4088 (2000) © 2000 SPIE · 0277-786X/00/$15.00

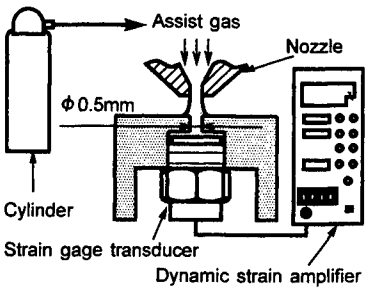


Fig.2 Measurement method of pressure on the workpiece

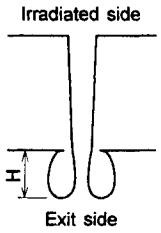
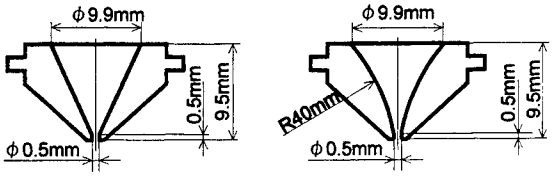


Fig.3 Definition of dross



(a) Nozzle type : N (b) Nozzle type : N_R

Fig.4 Shape of nozzle

for precision cutting. Stainless steel SUS304 (in JIS specification) of 0.15 mm in thickness was used as a workpiece, which was set on the X-Y stage. The cutting experiment was carried out controlling the feed of stage. Oxygen was used as the assist gas, whose pressure was varied from 98 kPa to 1568 kPa. The gap distance between the nozzle tip and the workpiece surface was kept to be 1 mm. Besides, the Schlieren method was used in order to visualize the assist gas flow.

The pressure on the workpiece was measured as shown in Fig.2. The strain gage transducer was set under the penetrated hole of 0.5 mm in diameter, and its output was recorded as the pressure on the workpiece. In this paper, this pressure is expressed as Pw (the pressure on the workpiece), while the pressure at the exit of the cylinder is expressed as Pc (the cylinder gas pressure).

Fig.3 shows the schematic cross section of the workpiece after the laser beam cutting. The top of the figure is the irradiated side, and the bottom is the exit side. In this study, the distance H between the top of dross and the matrix is defined as the height of dross, which is determined by the average of ten measurements.

Fig.4 shows the shapes of the nozzle discussed in this paper. The nozzle (a) is a conventional nozzle. This type with 0.35, 0.5 and 0.75mm in exit diameter are employed. The nozzle (b) is a new designed nozzle, which has a convex curve of 40 mm on the inner wall. In this paper, (a) is expressed as the nozzle N, and (b) is expressed as the nozzle N_R.

3. Assist gas flow from the convergent nozzle

Fig.5 shows the Schlieren photographs of the assist gas flow using a convergent nozzle with 0.5mm in exit diameter.

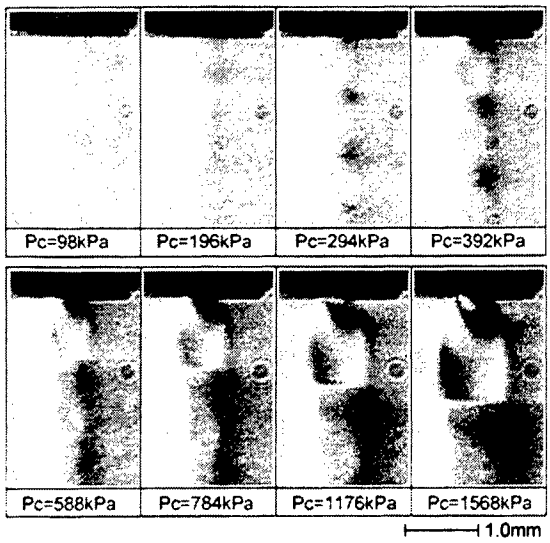
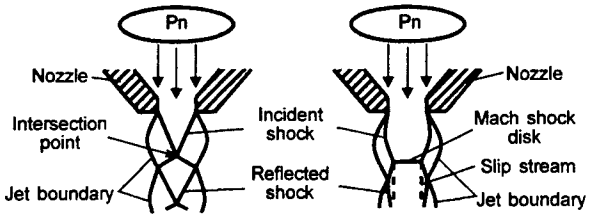


Fig.5 Schlieren photographs of the assist gas flow



(a) P_n / P : small (b) P_n / P : large

Fig.6 Difference of gas flow near the exit of nozzle

The assist gas flow at 98 kPa is a parallel flow. On the other hand, for more than 196 kPa, that is the supersonic underexpanded jet, which is an unstable flow. Moreover, the form of the gas flow at low pressure is different from that at high pressure. It is caused by the ratio of Pn (the pressure of assist gas at the exit of the nozzle) to P (the atmospheric pressure)[2]. As shown in the Fig.6 (a), the shock wave intersects at the center axis when the ratio Pn / P is small. On the other hand, normal Mach shock disk (MSD) is formed when the ratio Pn / P is large as shown in the Fig.6 (b). In this case, it corresponds when the cylinder gas pressure is more than 392 kPa. The critical ratio for changing from the flow type with an intersection point to that with MSD is approximately 3 (around 294 kPa) judging from the Schlieren photographs in Fig.6. Around the critical pressure, the assist gas flow is extremely unstable because of the transitional point of the gas flow type (a) to (b).

Fig.7 shows the schematic illustration and the Schlieren photographs of the impinging gas flow on the workpiece under the similar condition as the actual machining when the workpiece is located just under the nozzle. The upward flow appears in the vortex ring around the center axis. The position of MSD is determined by the balance between the upward force of the flow in the vortex ring and the

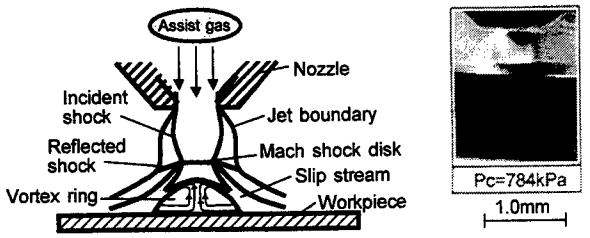


Fig.7 Schematic illustration and Schlieren photograph of impinging gas flow on the workpiece

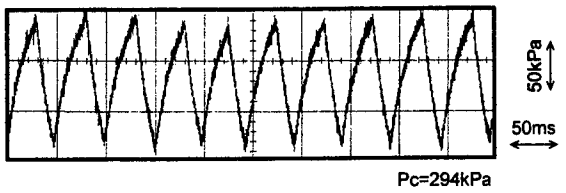


Fig.8 Vibration of the pressure on the workpiece

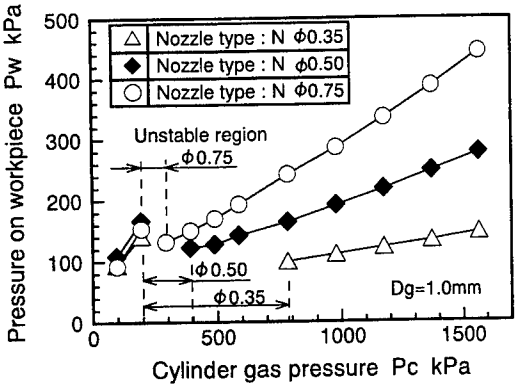


Fig.9 Relationships between the pressure on the workpiece and the cylinder gas pressure using three kinds of nozzles different in the exit diameter

downward force of the cylinder pressure. Therefore, the flow under the nozzle is unstable and tends to be influenced by the various factors. It is considered that the flow changes dynamically because of its instability, once the balance is lost.

Fig.8 shows the vibration of the pressure on the workpiece under the condition in which the gap distance was 1.0 mm and the cylinder gas pressure was 294 kPa. In this case, the pressure on the workpiece varied regularly with 120 kPa in amplitude and 50ms in frequency, and the sound was generated regularly. It is considered that the effective energy is lost. On the other hand, this vibration is generated only in this case with the penetrated hole. The reason is considered as follows. As mentioned before, the gas flow tends to be affected by the various factors when an obstacle is under the nozzle. Especially in this case, the intersection point and MSD are generated at the same level of the workpiece surface that has a penetrated hole. When,

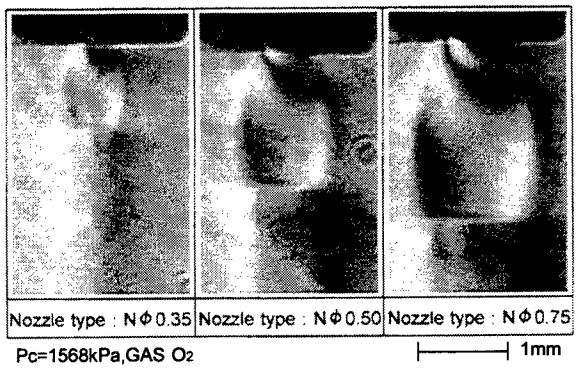


Fig.10 Schlieren photographs of the assist gas flow using three kinds of nozzles different in the exit diameter

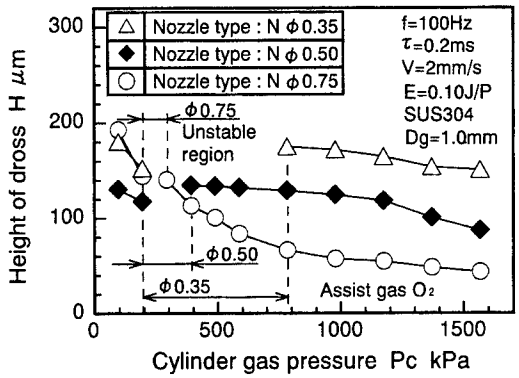


Fig.11 Relationships between the height of dross and the cylinder gas pressure using three kinds of nozzles different in the exit diameter

the balance of force is lost, and MSD repeatedly appeared or disappeared. Therefore, the pressure on the workpiece changes periodically. In this study, the region of vibration of the pressure on the workpiece is expressed as the unstable region. This fluctuation of the assist gas flow leads to irregular dross generation.

4. The effect of nozzle shape

Fig.9 shows variations of the pressure on the workpiece with the cylinder gas pressure using three kinds of nozzles different in the exit diameter. As can be seen from the figure, the pressure on the workpiece increases with an increase of the exit diameter after the unstable region. On the other hand, for the nozzle with a large exit (0.75 mm in diameter), the unstable region is from 200 kPa to 300 kPa, while for the small exit nozzle (0.35 mm in diameter), it is from 200 kPa to 800 kPa. Consequently, the unstable region becomes wider with the reduction of the exit diameter. It is considered that the difference of the unstable region by the nozzle might be caused by the difference of the position of the intersection point and MSD.

Fig.10 shows the Schlieren photographs of the assist gas flow using each nozzle. As shown in the figure, the distance

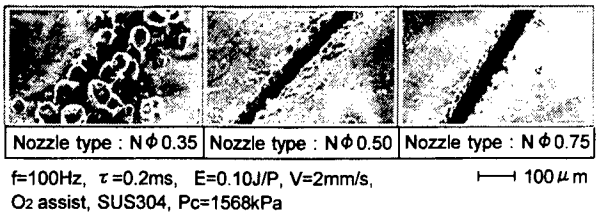


Fig.12 SEM micrographs of dross using three kinds of nozzles different in the exit diameter

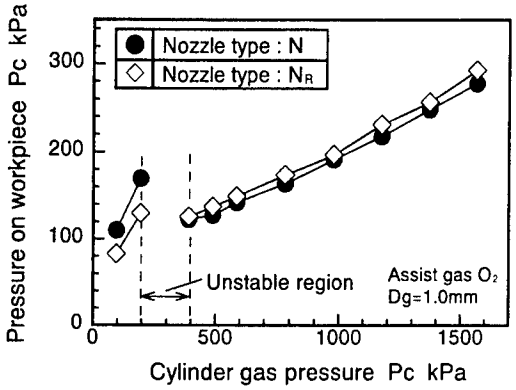


Fig.13 Relationships between the pressure on the workpiece and the cylinder gas pressure using nozzle N and NR

from the tip of the nozzle to MSD becomes longer with an increase of the exit diameter. Consequently, the position of MSD differs by the exit diameter of the nozzle even under the same cylinder gas pressure. Therefore, it is considered that the difference of the balancing condition might cause the difference of the unstable region by the exit diameter as shown in the Fig.9.

Fig.11 shows the relationships between the height of dross and the cylinder gas pressure. Under the same cylinder gas pressure condition, the height of dross becomes smaller with an increase of exit diameter. Fig.12 shows SEM (scanning electron microscope) micrographs of dross using the nozzle with a different exit diameter. As shown in the figure, the larger diameter nozzle leads to the suppression of dross generation, since the pressure on the workpiece increases with an increase of the exit diameter as mentioned before. However, it is necessary to select the nozzle shape according to the demand of the surface integrity, because the consumption of the assist gas increases and the kerf width becomes wider with an increase of the exit diameter.

Next, the newly designed nozzle NR with a convex curve of 40 mm on the inner wall of the nozzle was investigated. Fig.13 shows the relationships between the pressure on the workpiece and the cylinder gas pressure. As shown in the figure, the pressure on the workpiece using the nozzle NR is larger than that using the conventional nozzle N. Fig.14 shows the relationships between the height of dross and the cylinder gas pressure. The height of dross using the nozzle NR is smaller than that using the nozzle N, since the pressure

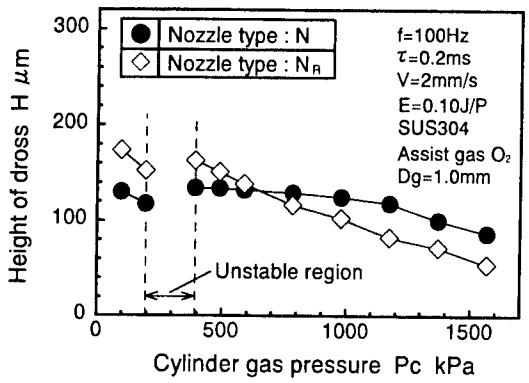


Fig.14 Relationships between the height of dross and the cylinder gas pressure using nozzle N and NR

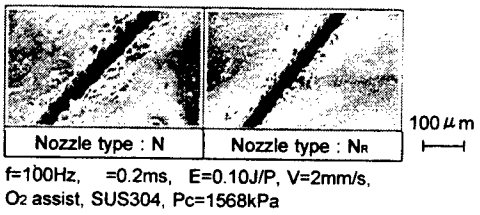


Fig.15 SEM micrographs of dross using nozzle N and NR

on the workpiece using the nozzle NR is larger. Fig.15 shows SEM micrographs of dross using the nozzle N and NR. As shown in the figure, the height of dross using the nozzle NR is smaller than that using the nozzle N. These results show that the nozzle with convex curve of 40mm on inner wall leads to better machining results.

5. Conclusions

Main conclusions obtained are as follows:

(1) There exists an unstable region in which the pressure on the workpiece changes periodically and dross is generated irregularly.

(2) A convex curve of 40 mm on inner wall of nozzle leads to a reduction of dross height.

(3) An unstable region and dross height becomes smaller with an increase of the exit diameter. However, it is necessary to select the nozzle shape according to the demand of the cost and the surface integrity, because the consumption of the assist gas increases and the kerf width becomes wider with an increase of exit diameter.

References

[1] J.Fieret and B.A.Ward: Circular and Non-circular Nozzle for Gas Jet Assist in CO_2 Laser Cutting, Culhan Laboratory, (1986) 47.

[2] I.Ichimatsu: Engineering thermodynamics, Shokabo, (1989) 380 (in Japanese).

A method to evaluate Nd:YAG laser microscopic spot welding process using reflected laser power

Seo-jeong Park,Ryuichi Honma and Isamu Miyamoto

Department of Manufacturing Science,Graduate School of Engneering,
Osaka University, 2-1,Yamada-Oka,Suita,Osaka565-0871,Japan
Phone:+81-06-6879-7535 Fax:+81-06-6879-7534
e-mail : psj@mapse.eng.osaka-u.ac.jp

Abstract.

A system consisting of 11 photodiode sensors from 0 to 90 degree with respect to the workpiece surface has been developed to detect the angular distribution of the reflected laser intensity. Spot welding process in thin copper sheet using pulsed Nd:YAG laser was experimentally analyzed by detecting angular distribution of reflected laser beam with time resolution. Spot welding was performed with pulse duration of 1 ms on a phosphorus copper thin sheet with thickness 250 μm in atmospheric condition. The change in the contour of the molten pool was investigated by time-resolved angular distribution of the reflected laser beam and penetrating time at a sampling frequency of 40 KHz. The laser beam passing through the thin sheet was also detected; the penetration time through the thin sheet was approximately 0.6 ms at an incident power density of 2.7×10^6W/cm^2. The reflectance determined by integrating angular distribution of the reflected laser intensity was approximately 85% at the beginning of the pulse and then decreased with time. It is also shown that this system can be used for monitoring the quality of the lap welding of thin sheet metals.

Keywords: pulsed YAG laser, spot welding, reflected laser power, thin metals, angular distribution.

1. Introduction

It is important to investigate the change in the shape of molten pool while laser irradiates on work surface to understand the spot welding process. How the surface of molten pool is changed and how deep key-hole is in spot welding are the elements to determine the welding quality.

Since molten pool in pulsed laser welding fluctuates, the reflected beam exhibits variable angular distribution. A system to measure the reflected beam from the surface of molten pool has been developed in this experiment, and the angular distribution of the reflected beam was measured with time of resolution.

The objectives of this study are (1) to describe the system measuring the newly developed monitoring using reflected laser beam, (2) to evaluate the welding process in the thin copper sheet and (3) to propose an in-process monitoring method using reflected beam obtained from the measurement of angular distribution.

2. Experimental set up

Figure1 shows a schematic picture of the experiment system. Spot welding was performed using pulsed Nd:YAG laser with pulse width of 1 ms on a thin sheet of phosphorus copper of 250 μm in thickness without shielding gas. The incident YAG laser beam was condensed by a lens of focal length of 150 mm (f: 150) on the thin sheet.

The intensity distribution of laser beam measured on the workpiece showed Gaussian distribution with a $1/e^2$-diameter about 400 μm. Silicon photo-diode with a high sensitivity to YAG laser wavelength was used to measure the intensity of the incident and the reflected laser beam. The incident beam passed through 45-degree mirror was measured by sensor P (in). The spatial distribution of the reflected beam was detected by 10 sensors arranged between 0 and 82degrees with respect to the work surface. The laser beam reflected back through the condensing lens

First International Symposium on Laser Precision Microfabrication, Isamu Miyamoto, Koji Sugioka,
Thomas W. Sigmon, Editors, Proceedings of SPIE Vol. 4088 (2000) © 2000 SPIE · 0277-786X/00/$15.00

was measured by sensor P (90). The signal detected by P (90) corresponds to the laser power reflected in a range between 82 and 90 degrees. The laser beam passing through the workpiece was also detected by the penetration sensor. The sensitivity of 12 sensors was calibrated carefully. Incident, reflected and passed laser intensity was detected simultaneously at a sampling frequency of about 40 KHz. Analog signal was transformed into the digital signal by A/D converter.

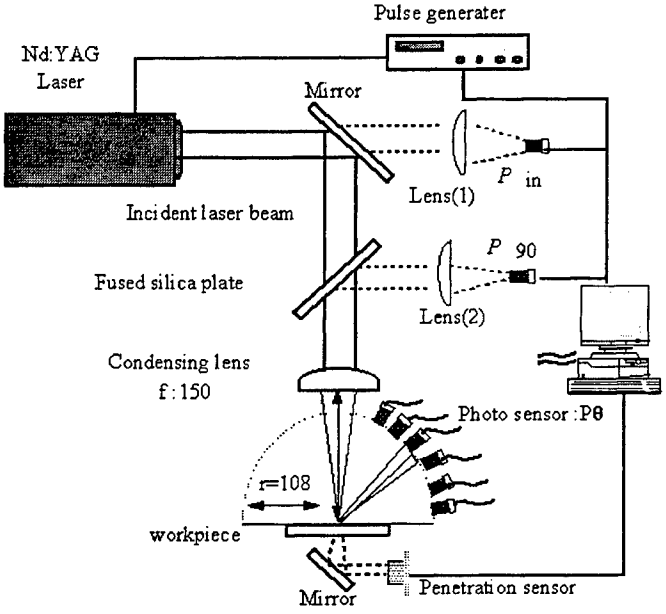


Fig.1 Experimental Setup.

3. Results and discussion.

3.1 Angular dependence of reflection.

The reflectance of YAG laser beam to the phosphorus copper was measured at room temperature, and was approximately 90%. Before discussing the angular distribution of the reflected beam in spot YAG laser welding, the reflectance of workpiece was determined from the signal obtained by using the system developed in this study.

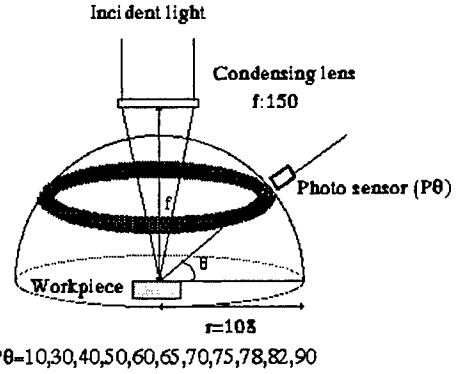


Fig.2 coodinates of the system and photo-sensor.

Assuming that the laser beam reflects axi-symmetrically, the reflectance R is calculated by

$$R = \frac{2\pi r^2}{W_0}\int_0^{\frac{\pi}{2}} P_\theta \cos\theta d\theta \text{ ----------(1)}$$

where W_0 is the incident beam power and Pθ is the reflected beam power per unit area at angular θ at radius r.

Figure 3 shows total power of the reflected beam and the incident beam power W_0. In this case, the incident laser power W is as low as approximately 100W. The workpiece was not melted at all at this experimental condition. No reflection was detected by sensors other than P (90). The reflectance thus determined was in a range between 85% and 88%, which is very close to the reflectance at room temperature.

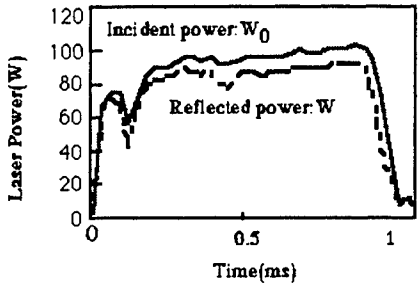


Fig.3 Incident and reflected power for polished phosphrus copper at low power level.

Figure 4 shows **(a)** the incident laser power, **(b)** the reflected intensity at different angular zone, **(c)** an appearance (SEM) of copper surface of laser irradiated zone and **(d)** the direction of the reflected beam when the incident power was relatively low, approximately 1.2KW. In this picture, the reflection intensity to given angle is given by the length of the arrow. The penetration signal was not detected in this power level. The reflected power detected by the

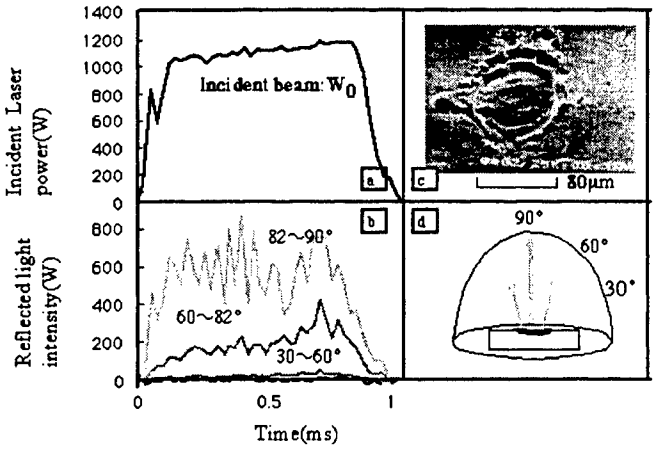


Fig.4 Experimental results obtained at laser power of 1100W. (a)A waveform of incident beam power. (b)A waveform of the reflected beam power. (c)SEM picture of surface of molten pool. (d) Direction of the reflected beam.

sensor P (90) was predominant, where as in 60~80degrees, the intensity of the reflected beam was approximately 200W. The intensity of reflected beam in 0~60degree was very weak. The proportion of the laser power reflected between 82 and 90 degrees (inside condensing lens) was 56%, and 60~82 degrees 18% and 0~60 degrees under 1%. The averaged reflectance determined by equation (1) was approximately 75%.

Figure 5 is an example of penetrated spot welding at incident power of 4000W. The penetration signal was detected at approximately 0.6 ms, showing that the key-hole opened at this time. This result indicates that averaged drilling speed in the pulse welding is approximately 0.4m/s. **Figure 5 (c)** shows that key-hole was closed after the laser pulse finished. **Figure 5(b)** shows the intensity distribution of the reflected beam from each angle. **Figure 5 (d)** shows the intensity and direction of the reflected laser beam.

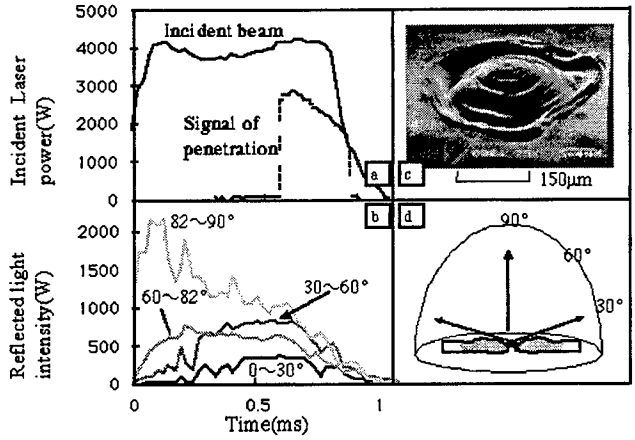


Fig.5 Experimental results obtained at laser power of 4000W. (a)A waveform of incident beam power. (b)A waveform of the reflected beam power. (c)SEM picture of surface of molten pool. (d) Direction of the reflected beam.

Figure 6 shows the reflectance determined by integrating the angular distribution of reflected beam intensity shown in **Fig.5**. The reflected power in 0~70degrees is also shown in the figure. The reflectance begins to decrease around 0.6ms at which key-hole penetrates the sheet. The reflected power in a range between 0 and 70degrees was increased during the key-hole was deepened until 0.6ms.

The average value of reflectance was 65%. Compared with the reflectance of the phosphorus copper measured at room temperature, it is remarkable decrement due to the laser beam passed through the key-hole.

Figure 7 shows the reflected ratio at different angular regions plotted against incident laser power. Data points are averaged values determined from five to ten experiments.

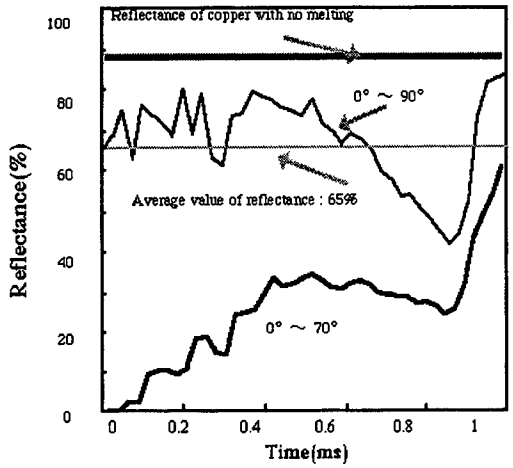


Fig.6 The time change in reflected intencity.

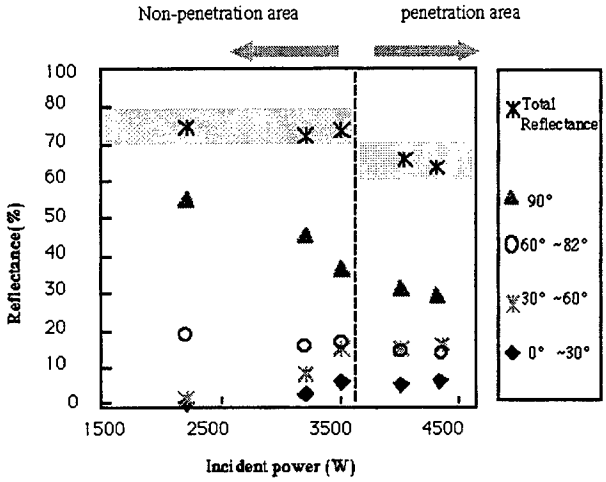


Fig.7 Proportion of reflected power plotted against incident power.

When the incident power was less than 3500W, the penetration signal was not detected by the penetration sensor. Then the reflectance was almost constant in a range from 70% to 80%. However, as the incident power was increased, the reflected beam intensity tends to decrease in the high angles. On the contrary, the reflected beam intensity in lower angles increased resulting in little change in the reflectance in non-penetration area.

When the incident power was over 3500w, the reflectance decreased down to 60% level. As the incident power was increased, the intensity of the reflected beam was increased a little in high angular distribution and decreased a little in low angular distribution. Consequently, one can recognize whether the workpiece is penetrated or not in terms of the reflectance.

3.2 Reflection in lap welding.

The distribution of the reflected laser beam was examined in lap joint which consists of the upper workpiece

of 65μm in thickness and the lower workpiece of 250μm in thickness. The angular distribution of the reflected beam intensity was detected at the incident laser power of 1200W and 2200W.

Figure 8 (a) shows experimental result for lap welding with gap width of 25μm at 1200W, which corresponds to the power density of 0.84×10^6 W/cm^2. The intensity reflected between 85.2 and 90 degrees keeps larger value until 0.2~0.3ms. After 0.3ms, the intensity of the reflected beam at lower angles was increased gradually. One can see that the lower the reflecting angle is, the later the beginning time of the reflectance increment becomes later. It should be noted that the intensity of the reflected beam between 85.2 and 90degrees showed significant increase again at 0.8ms.

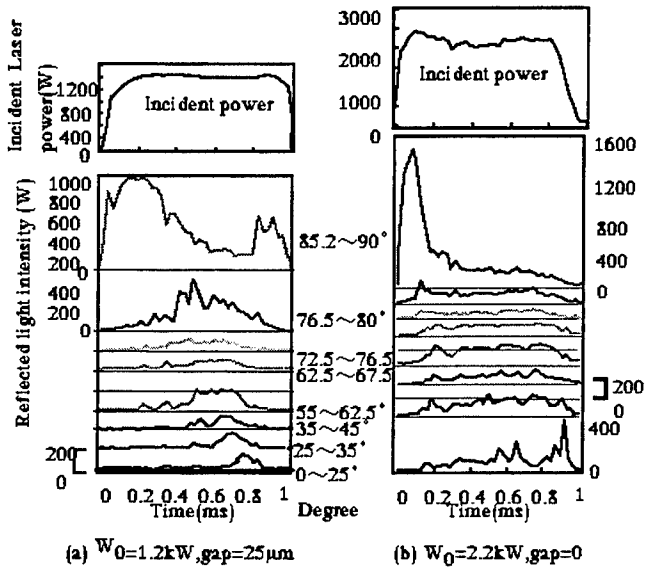


Fig.8 Variation of reflected laser beam at each angle.

Figure 9 shows the welding process deduced based on the change in the intensity distribution presented in **Fig. 8 (a).** The increase in the reflection at 0.8ms indicates that the upper sheet was molten down to expand the key-hole diameter. So that the laser beam was reflected by the lower sheet having flat surface. As shown in SEM picture, enough molten pool was not formed in the lower sheet, and thus two workpiece were not well bonded. **Figure 8 (b)** shows experimental result in lap welding with no gap width at the power of 2.2KW, which corresponds to the power density of 1.55×10^6 W/cm^2. The intensity of the reflected beam between 85.2 and 90degrees keeps larger value until the key-hole was established. After molten pool was formed, the intensity of the reflected beam keeps constant value.

The schematic picture based on **Fig. 8 (b)** is shown in **Figure 10**. No secondary increase in the reflection at 85.2~90degrees was observed, indicating that the weld pool was formed to weld the upper workpiece and the lower workpiece successfully as seen in SEM photograph.

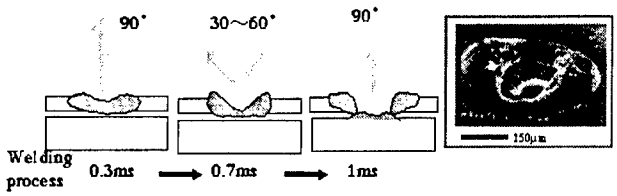


Fig.9 Illustration of welding process corresponding to Fig.8(a).

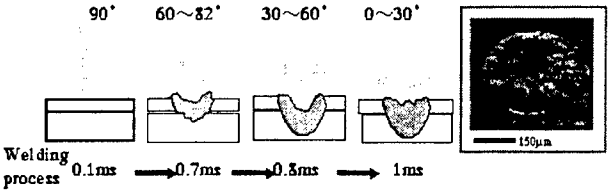


Fig.10 Illustration of welding process corresponding to Fig.8(b)

4. Conclusion

The results obtained in this study are summarized as follows:

1. A system has been developed to determine time resolved angular distribution of the reflection in spot YAG laser welding of thin sheet, by which the surface state of the molten pool can be discussed.
2. The reflectance was determined by integrating the angular distribution of the reflected beam intensity.
3. The intensity of the reflected beam was increased at lower angles during key-hole was deepened.
4. The system can be used to monitor the spot welding quality.

References

[1] E. Fogarassy, S. Lazare " Laser Ablation of Electronic Materals", Eupopean Materals research Socity Monographs, Vol. 4.

[2] Tsukihara, Ichikawa, Kojima and Kimura " An approach to Monitor YAG Laser welding process using its Refected Laser power", Sectin c-ICALEO 1998, pp 93~101

[3] V. Semask, J.A. Hokins and M.H. McCay " A technique for Melt pool oscillation Monitoring during Laser spot welding", Section-C-ICALEO 1997, pp 11~20

[4] Jurgen Griebsch, Helmut Hugel, Frich Dausinger, Marius Jurca "Laser Ablation of Electronic Materials", Eupopean Masterials research Society Monographs, Vol. 4

Selective Laser Sintering with Heat of Formation by Using Reactive Materials

Takayuki KAMITANI*, Osamu YAMADA** and Yoji MARUTANI*

* *Department of Information Systems Engineering, Faculty of Engineering, Osaka Sangyo University, 3-1-1 Nakagaito, Daito, Osaka 574-8530, Japan*
E-mail: kamitani@ise.osaka-sandai.ac.jp
** *College of General Education, Osaka Sangyo University, 3-1-1 Nakagaito, Daito, Osaka 574-8530, Japan*

ABSTRACT

In this paper, we propose a new method of fabricating 3-D models of the high-temperature structural materials such as ceramics by selective laser sintering (SLS). To save the laser energy, we adopted the combustion synthesis which is the exothermic reaction between the raw materials. By adding chemical reaction heat to laser heat, the particles of the products of the reaction were bonded together by relatively low laser energy. The combinations of the raw materials and the laser scanning conditions for solidifying the products and laminating the solidified layers were investigated experimentally. Since burning in the furnace is unnecessary in the proposed method, it is possible to fabricate the models in a short time.

Keywords: selective laser sintering, combustion synthesis, heat of formation, layered manufacturing, rapid prototyping

1. Introduction

Metal and ceramics are widely used in the mechanical parts required the strength and the heat resistance. Ceramics are also used as the casting molds. Metal models are generally fabricated by cutting, milling, electrical discharge machining (EDM), casting, etc. Ceramics models are mostly fabricated by pouring the ceramics slurry into the molds and sintering at high temperature.

In recent years, selective laser sintering (SLS)[1], three dimensional printing (3DP)[2], fused deposition modeling (FDM)[3], and laminated object manufacturing (LOM)[4] have been developed as the methods of fabricating 3-D models of the ceramics and the metal directly from CAD data like the stereolithography[5].

In any of these conventional methods, since the powders or the sheets of the materials are connected temporarily by the binder, sintering at high temperature near the melting points above 1000°C is required to connect the materials together firmly. Therefore, the fabrication takes for a long time and a high degree of skill about burning process is required.

There is a method of fabricating the models directly by heating and fusing the metal powder sprayed on the laser beam spot. However, laser power of more than 500W is necessary even in the case of Co alloy having the melting point of 1200°C[6]. It is difficult to apply this method to the ceramics models which has to be sintered by keeping the materials at high temperature for a long time.

In this paper, we propose a new method of fabricating the 3-D models of high-temperature structural materials by using combustion synthesis[7] induced by laser heating. In this method, the synthesis of the compounds and the fabrication of the 3-D models progress simultaneously. By adding the chemical reaction heat to laser heat, the fabrication of the 3-D models of the heat-resistant inorganic materials such as the ceramics can be realized with low laser energy. Since the proposed method dispenses with sintering in the furnace, the knowledge and the skill about the process are unnecessary and the models can be fabricated in a short time. The principle of this method and the experiments are described in the following chapters.

2. Principle

Generally, combustion means the chain-reacting chemical reaction between an element and oxygen with the generation of heat and luminescence. In the case of using the element near oxygen in the periodic table instead of oxygen, similar reaction often occurs. The former which is the oxidation reaction and the latter are known as oxidative combustion and nonoxidative combustion, respectively.

The method of producing the compounds as the condensate by these combustion reaction is called combustion synthesis[7]. The combustion synthesis is a highly efficient method of obtaining the compounds, because it advances to spontaneously after the ignition and the compounds are synthesized in a few seconds. In the oxidative combustion, ceramics such as Al_2O_3 is obtained.

First International Symposium on Laser Precision Microfabrication, Isamu Miyamoto, Koji Sugioka, Thomas W. Sigmon, Editors, Proceedings of SPIE Vol. 4088 (2000) © 2000 SPIE · 0277-786X/00/$15.00

Table 1 Combinations of the tested materials and their chemical reaction formulas.

No.	Raw materials (molar ratio)	Chemical reaction formula	Heat of formation	Products	Melting point of the products
①	CuO: 10%, Cu: 84%, Al: 6%	$0.3CuO+2.7Cu+0.2Al=3.0Cu+0.1Al_2O_3$	38.8kJ/mol	Cu Al_2O_3	Cu: 1084°C Al_2O_3: 2054°C
②	Ti: 33%, Al: 33%, TiAl: 34%	0.5Ti+0.5Al+0.5TiAl=TiAl	37.7kJ/mol	TiAl	TiAl: 1460°C
③	Ti: 43%, Al: 43%, TiAl: 14%	0.75Ti+0.75Al+0.25TiAl=TiAl	56.5kJ/mol	TiAl	TiAl: 1460°C
④	Ti: 50%, Al: 50%	Ti+Al=TiAl	75.3kJ/mol	TiAl	TiAl: 1460°C
⑤	Mo: 33%, Si: 67%	$Mo+2Si=MoSi_2$	118.4kJ/mol	$MoSi_2$	$MoSi_2$: 2027°C

The nonoxidative combustion by using N, C, B, and Si produces the nonoxide ceramics which are nitride, carbide, boride, and silicide, respectively. In the case where Al is used, the intermetallic compound termed alminide is produced. In this study, we adopted the reaction heat of the combustion synthesis to solidify the materials having high melting points with low laser energy.

Fig.1 shows the sequence of fabricating the 3-D model. Some kinds of powders are mixed uniformly and are spread thin. The beam of infrared laser is scanned over the layer of the powders. The powders in the scanned area are bonded together and are connected to the solidified layer beneath the powder layer while synthesizing the compounds. By repeating the powder spreading and the laser scanning, a 3-D model is fabricated.

In this method, it is necessary that the material only in the scanned area solidifies stably and the layers are connected firmly.

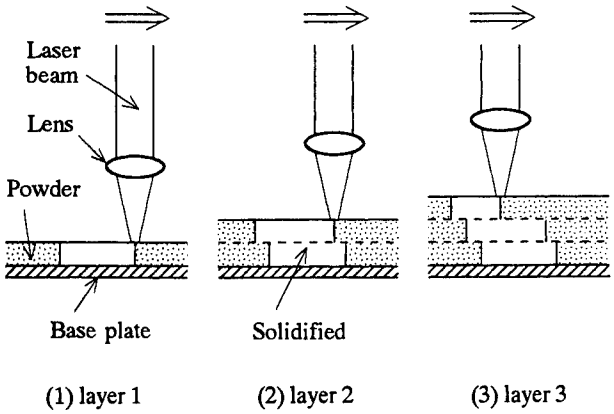


Fig. 1 Sequence of fabricating the 3-D model.

3. Experiments

3.1 Stability of solidification

Cermet of Cu and Al_2O_3, intermetallic compound TiAl, and ceramics $MoSi_2$ were selected as the structural materials of the models. Especially, TiAl and $MoSi_2$ are known as the promising high-temperature structural materials. Tested materials and their chemical reaction formulas are shown in Table1. Particle sizes of the raw materials were CuO: 1-2μm, Cu: 15μm, Al: 27.6μm, Ti: 45μm, TiAl: 40μm, Mo: 1.5μm, and Si: 2-3μm.

In the combustion synthesis, the product which is inert substance is sometimes added to the raw materials for the purpose of controlling the heat of formation[7]. The inert materials in Table1 are Cu of material ①, and TiAl of material ② and ③. These materials were investigated whether or not the combustion reaction was limited in the scanned area.

Fig.2 shows the experimental apparatus. Output beam of CO_2 laser (SYNRAD Co.: Model 48-1-28, wavelength: 10.6 μm, TEM00 mode) is focused on the raw materials. To simplify the scan, the vessel is rotated by a motor. Spot size of the beam is 117μm at the calculated value.

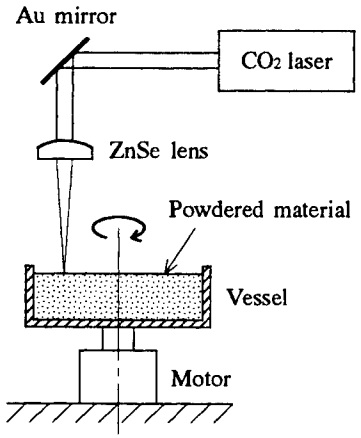


Fig. 2 Experimental system.

The raw material was spread with the thickness of 3mm and scanned from the above by the laser. Fig.3 shows the state of the material during laser scanning. The material in the irradiated area incandesced and sparked, and turned black after the irradiation.

Fig.4 shows the experimental results. Reactions are classified into the next 3 states by the scanning condition of the laser and the constitution of the raw material.

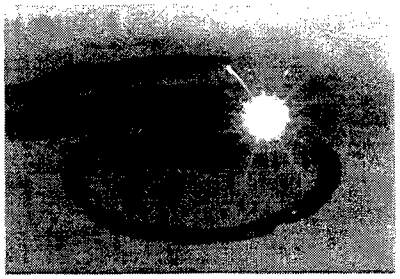


Fig. 3 Material during laser scanning.
(material ③, laser power: 4W, scanning speed: 1.65mm/sec)

(1) The materials only in the scanned area were solidified.
(2) The whole materials were burned out by the chain reaction.
(3) The powders in the irradiated area were scattered by the excess laser power.

Increment of the supplied energy [W/mm/sec] makes the reaction move from (1) to (3). Material ④Ti+Al is easy to burn out by the chain reaction. Solidified objects made from material ② and ③ that the product TiAl was mixed previously were significantly brittle. Accordingly, material ①Cu+Al+CuO and ⑤Mo+Si solidify stably and firmly.

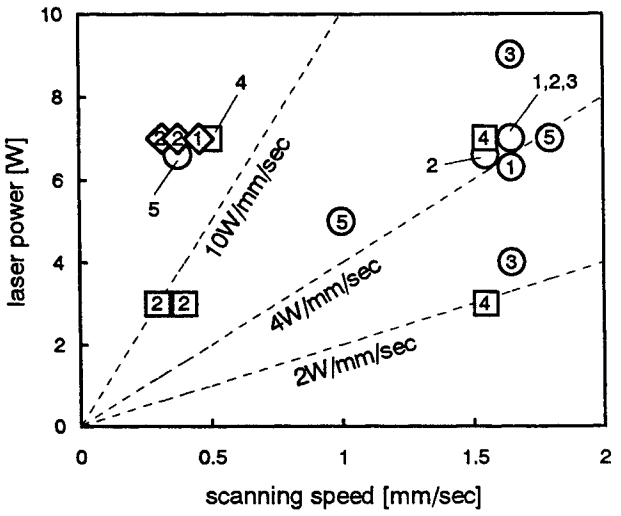


Fig. 4 Relationship between the scanning condition and the stability of the solidification.
(The numbers in the symbols show the material numbers.
○: The materials only in the scanned area were solidified.
□: The whole materials were burned out.
◇: The powders in the irradiated area were scattered.)

To know the effect of the reaction heat, the same solidification experiment as the above was done by using Fe powder (particle size: 50μm, melting point: 1535°C). In the case of the reactive materials, the materials could be solidified with the laser power of a few [W]. On the other hand, to solidify the Fe powders with the scanning speed of 1mm/sec, not less than 10W was required. This indicates that the combustion reaction plays a part which reduces the external energy required for the solidification.

3.2 Fabrication of layered models

Lamination experiment was done by using material ① and ⑤. Since the solidified depth was not less than 0.3mm in the above solidification experiment, this experimental condition was set as the following:

laser power: 7W
scanning speed: 1.65mm/sec
layer thickness: 0.2mm

However, in this condition, the layers did not connect each other and unified object could not be fabricated. On the other hand, when the supplied energy [W/mm/sec] was increased, burning out by the chain reaction was occurred.

We attempted to add an inert binder to the raw reactive materials and connect the particles with the combustion synthesis and the assistance of the binder. In this case, it is thought that the binder material reduces the reactivity of the total system. For this reason, we considered that the reactivity of the raw materials themselves have to be high in the case of using the binder. Material ④Ti+Al was selected as the reactive raw materials and the glass powder (particle size: 100μm, softening point: 550°C) which was easy to obtain was used as the binder. The mixed material was spread with the thickness of 3mm as paragraph 3.1. In the case that the material ④ : glass powder weight ratio was 1:1, even if the supplied energy was about 2W/mm/sec (laser power: 3W, scanning speed: 1.55mm/sec), the materials burned out by the chain reaction. To reduce the reactivity further, the ratio was changed to be 1:2. In this ratio, the solidification reaction stabilized, but the solidified object was porous and fragile. To strengthen the solidified object, the ratio was chosen to be 1:3. As a result, the solidified object became dense and rigid. The materials could be solidified with the laser power of not less than 2W. On the other hand, in the case of only the grass powder, not less than 3W was needed for the solidification. This indicates that the reaction heat assists the melting of the binder.

Next, we tried to fabricate the layered models by using this mixed material of 1:3 weight ratio. For the purpose of fabricating the freeform models, CO_2 laser marker (Sunx Co.: LP-110) was used as the laser scanning system. Wavelength of the laser beam is 10.6μm. Mode of the beam is TEM00. Spot size of the beam is 110μm at the theoretical value. Based on the solidified depth at 2W/mm/sec in this mixing ratio, experimental condition is maintained as the following:

laser power: 6W
scanning speed: 3mm/sec
layer thickness: 0.5mm
the number of layers: 8 layers

Fig.5 shows an example of the layered model. In this example, there are two intersecting ovals in cross-section. The connectivity between the layers and between the ovals are firm enough.



Fig. 5 An example of the layered model.

4. Conclusions

We have proposed the new method of fabricating 3-D models of the high-temperature structural materials with low laser energy by using the exothermic reaction and have done some fundamental experiments. Since the combinations of the tested materials were significantly reactive, the top of the solidified layers could not be heated to the melting point by the laser to avoid burning out. In this way, it is not easy to connect the layers only the reactive materials.

We are planning to try to melt the top of the solidified layers through the use of the raw materials having a slightly lower reactivity than the tested materials. In the case, the required laser energy becomes larger than that of this time, but it is expected that the laminated models can be fabricated without the binder.

References

[1] I. Lee, A. Manthiram, and H. L. Marcus: *Solid Freeform Fabrication Proc., Austin, 1995*, pp.46.

[2] S. Michaels, E. M.Sachs, and M. J. Cima: *Proc. of the 4th Int. Conf. on Rapid Prototyping, Dayton, 1993*, pp.25.

[3] T. F. McNulty, F. Mohammadi, A. Bandyopadhyay, D. J. Shanefield, S. C. Danforth, and A. Safari: Rapid Prototyping J., **4**, (1998) 144.

[4] B. B. Mathewson, W. S. Newman, A. H. Heuer, and J. D. Cawley: *Solid Freeform Fabrication Proc., Austin, 1995*, pp.253.

[5] T. Nakai, and Y. Marutani: Trans. of IEICE, **J71-D** (1988) 416.

[6] W. Koenig, T. Celiker, and H. J. Herfurth: *Proc. of the 2nd European Conf. on Rapid Prototyping and Manufacturing, Nottingham, 1993*, pp.303.

[7] O. Yamada: J. of Science and Industry, **65**, (1991) 460.

Observation of Nanoparticle Formation Process by Two-Dimensional laser induced fluorescence, UV Rayleigh scattering and Re-Decomposition Laser Induced Fluorescence methods

Junichi Muramoto, Takahiro Inmaru, Yoshiki Nakata, Tatsuo Okada and Mitsuo Maeda

Graduate School of Information Science and Electrical Engineering, Kyushu University, 6-10-1 Hakozaki, Higashi-Ku, Fukuoka, 812-8581, Japan
E-mail: okada@ees.kyushu-u.ac.jp

We have investigated the formation process of nanoparticles in the laser ablation plume by different laser imaging spectroscopy techniques, such as Two-Dimensional laser induced fluorescence (2D-LIF), UV Rayleigh scattering (UV-RS), and Re-Decomposition LIF (ReD-LIF). Clusters, which are hardly observed by the UV-RS method due to their small size, are observed by the ReD-LIF method. The dynamics and formation processes of the nanoparticles, which are synthesized in the Si or ZnO ablation plume, is presented.

Keyword: Laser Ablation, Nanoparticle, Imaging Spectroscopy

1. Introduction

Pulse Laser Ablation (PLA) method can be used to fabricate the nanoparticles [1 – 5]. The formation process of the nanoparticles during PLA method have been investigated by different imaging techniques, such as Two-Dimensional laser induced fluorescence (2D-LIF) method, UV Rayleigh scattering (UV-RS) method and so on. We have already reported the temporal changes of the distributions of the Si atoms and the Si nanoparticles in ablation plume by the 2D-LIF and UV-RS methods [6 – 8]. Moreover, to visualize the clusters, which were hardly visualized by UV-RS method due to their small size, has been developed. A new laser imaging spectroscopy is termed as "Re-Decomposition LIF (ReD-LIF)" method. In the ReD-LIF method, the cluster is vaporized into atoms by irradiating another laser beam, and then the vaporized atoms are measured by LIF method.

In this article, we report the Si nanoparticle formation process, which was observed *in-situ* by the 2D-LIF, UV-RS, and ReD-LIF methods. Further, we also report the condensed nanoparticle formation process observed by the UV-RS method when a ZnO target was ablated.

2. Experiment

The experimental setup is shown in Fig. 1. A target, which was a Si wafer or a ZnO sintered pellet (99.9 %wt), was placed on a rotating holder. A KrF excimer laser (Lambda Physik EMG201 MSC) beam was focused on the target surface with a fluence of about 2.6 J / cm^2 (40 mJ @ 1.5 mm^2). A pressure of an ambient He and O_2 gas was in the range from 0.1 Torr to 10 Torr. The ambient gas was changed after each ablation. For the measurement, a probe laser was delivered from a frequency doubled optical parametric oscillator (OPO: Quanta-Ray MOPO-730) when the Si target was used. The probe laser beam was sheeted and directed into the plume. In the 2D-LIF method, the wavelength of the probe laser was tuned on the Si resonance

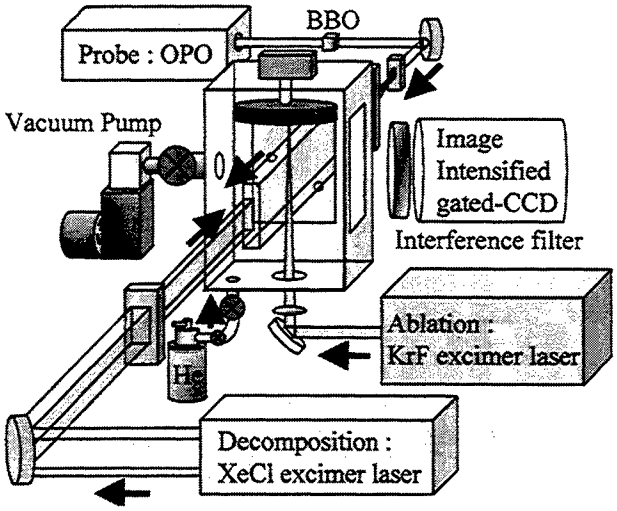


Fig. 1 Experiment setup.

First International Symposium on Laser Precision Microfabrication, Isamu Miyamoto, Koji Sugioka, Thomas W. Sigmon, Editors, Proceedings of SPIE Vol. 4088 (2000) © 2000 SPIE · 0277-786X/00/$15.00

line of the $3p\,^3P_2 - 4s\,^3P_2$ transition, which is at 251.61 nm. In the UV-RS method, the wavelength of the probe laser was detuned off the resonance line. The LIF and RS light was detected by a gated and image-intensified CCD camera (ICCD: Hamamatsu C2925 and C5895) with an interference band-pass filter. When the ZnO target was ablated, the probe laser beam was delivered from a XeCl excimer laser (Lambda Physik EMG201) for the UV-RS method.

In the ReD-LIF method, a XeCl excimer laser beam was used as a decomposition laser. The decomposition laser beam passed in the region, which was also illuminated by the probe laser beam. The delay time between the decomposition laser and the probe laser beam was critical and had to be properly set. Based on the experimental result, the optimized delay time was estimated at 10 μs.

3. Result

3.1 Si nanoparticle formation process

Fig. 2 shows the temporal changes of the Si atom and Si nanoparticle distributions observed by the 2D-LIF and UV-RS methods. The pressure of the ambient He gas was 10 Torr. Scales on the left-hand side indicate the distance from the target surface, and shaded areas indicate the region illuminated by the probe laser beam. The time after the ablation is shown at the left-bottom in each image. The spherical-shaped images were observed at the time before 0.9 ms, when the wavelength of the probe laser beam was tuned on the resonance line of Si atoms. The spherical-shaped images show the Si atom distributions. An invisible area was also observed in the central region of the distribution of Si atoms. At the delayed time after ablation, the anchor-shaped images were observed in the previously invisible area. The anchor-shaped images were even observed when the wavelength of the probe laser beam was detuned off the resonance line of the Si atom, and therefore these images were considered as the Si nanoparticle distribution.

It is thought that the Si clusters, which were hardly visualized by UV-RS method due to their small size, existed in the invisible area of the Si distribution. Figure 3 shows the result observed in the ReD-LIF method. The energy of the decomposition laser beam was 75 mJ. The pressure of the ambient He gas was 10 Torr. The time after the ablation was shown at the left bottom in each image. The scale at the left-hand side shows the distance from the target. The shaded and striped area on the scale shows the illuminated region by the probe and decomposition laser beam, respectively. At 0.11 ms after ablation, the central region of the Si atom distribution was not visualized, the formation process of the Si nanoparticle might not have

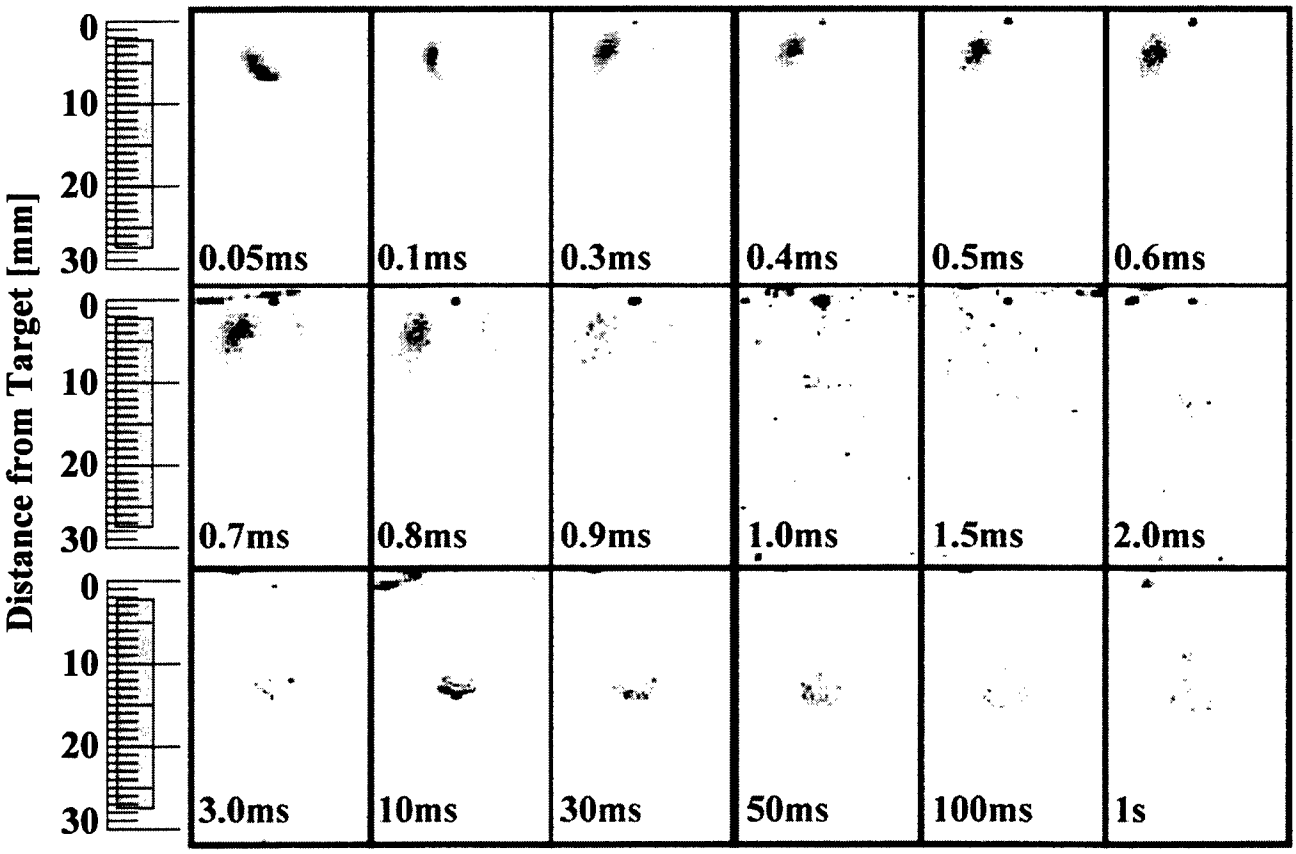


Fig. 2 Temporal changes of Si atom and nanoparticle distribution observed by 2D-LIF and UV-RS method

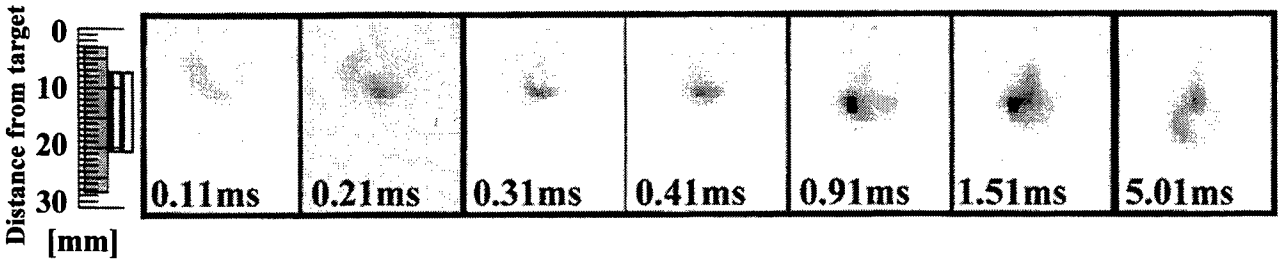
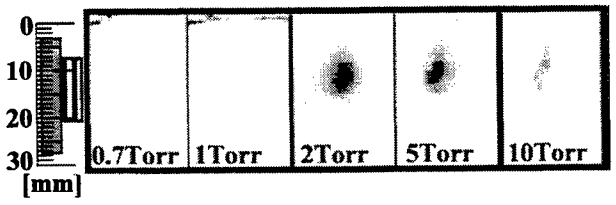


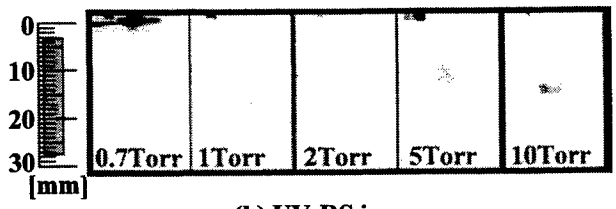
Fig. 3 Result of the ReD-LIF method

sufficiently progressed. However, Si_2 molecules were clearly observed in the ablation plume at about 0.2 ms after ablation by LIF method [6]. The ReD-LIF signal was observed at 0.21 ms after the ablation. After 1.51 ms, the ReD-LIF signal was observed even at peripheral area of the anchor-shaped distribution of the Si nanoparticle observed by UV-RS method. These observations were consistent with the result of the previous reports. Under these specific experimental conditions, the noticeable clustering was started at the time around 0.2 ms after the ablation.

Figure 4 (a) shows the ReD-LIF images observed at a different pressure of the ambient He gas. The pressure of the ambient He gas is indicated at the left bottom in each image. The time after ablation was fixed at 10.01 ms. For comparison, the UV-RS images are shown in Fig. 4 (b). The ReD-LIF images were observed at the pressure of the ambient He gas with 2 Torr and above. On the other hand, the UV-RS images were observed at the pressure of the ambient He gas with 5 Torr and above. Based on the observation of the deposition on the substrate by using an electron microscope, the Si nanoparticles were observed when the pressure of the ambient He gas was around 2 Torr [9].



(a) ReD-LIF image



(b) UV-RS image

Fig. 4 (a) ReD-LIF and (b) UV-RS images at different pressure of ambient He gas

3.2 Nanoparticle Formation process in ZnO ablation plume

Figure 5 shows the nanoparticle formation process in the ZnO ablation plume observed by the UV-RS method. The pressure of the ambient O_2 gas was 10 Torr. The XeCl excimer laser was used as the probe laser beam. No image was observed at the time after ablation with 0.2 ms and below. After 0.3 ms the condensed nanoparticles were observed, and then the nanoparticle formed anchor-shaped image. Since the similar behavior of the condensed nanoparticle was also observed when the Si target was ablated, it is believed that the dynamics in the nanoparticle formation process does not depend on the kind of the target.

4 Summary

The nanoparticle formation processes in the ablation plume, when the Si or ZnO targets were ablated, was observed by the 2D-LIF, UV-RS and ReD-LIF method. In 2D-LIF and UV-RS method, the temporal changes of the Si atom and nanoparticle distributions were observed. The Si atoms condensed into nanoparticle at the central region of the distribution. The cluster, whose size was too small to be visualized by UV-RS method, existed in the central region of the Si atom distribution. The clusters were visualized by the ReD-LIF method. The condensation of nanoparticles in the ZnO ablation plume was also observed by the UV-RS method. Since the anchor-shaped images were also observed at delayed time after ablation, it is thought that the dynamics of the nanoparticles was not governed by the composition of the target. We have already observed the different distribution of the nanoparticle when the other ambient gases were used [7]. For further understanding of the condensation dynamics, development of the visualization method for an ambient gas flow is now in progress.

Acknowledge

This work was supported in part by the Grant-in-Aid for Scientific Research from the Ministry of Education, Science, Sports and Culture, and Foundation for Advancement of

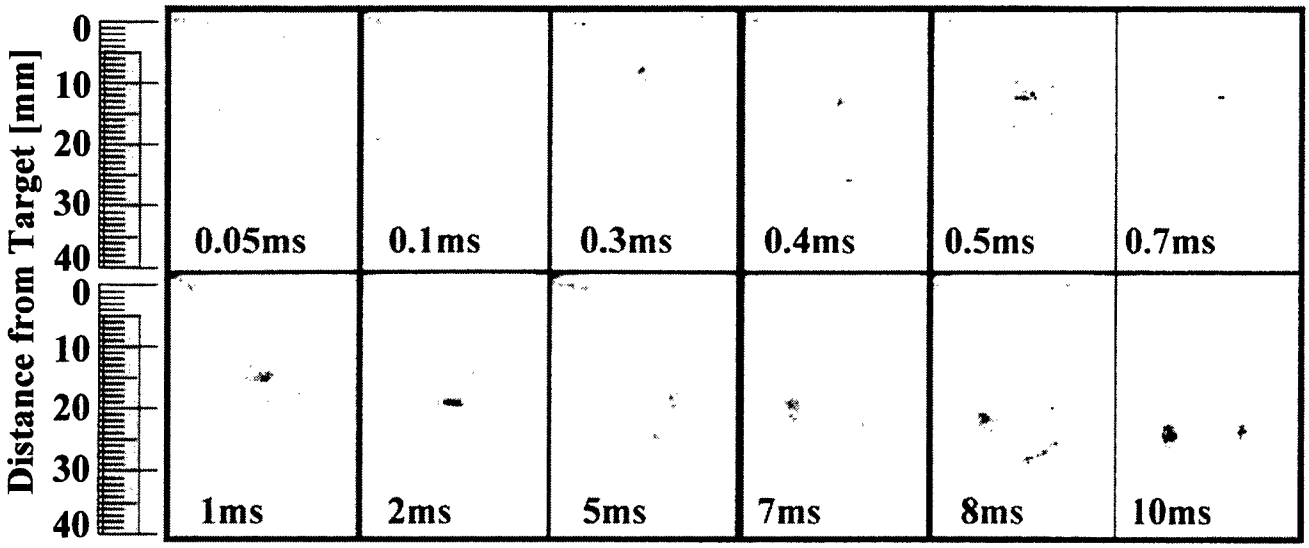


Fig. 5 UV-RS images in ZnO ablation plume

International Science. Junichi Muramoto also acknowledges the Japan Society for Promotion of Science for Young Scientists for the research fellowship.

References

[1] E. Werwa, A. A. Seraphin, L. A. Chiu, C. Zhou and K. D. Kolenbrander, Appl. Phys. Lett. 64, 1821 (1994).
[2] Y. Yamada, T. Orii, I. Umezu, S. Takeyama and T. Yoshida, Jpn. J. Appl. Phys. 35, 1361 (1996)
[3] T. Yoshida, S. Takayama, Y. Yamada and K. Mutoh, Appl. Phys. Lett. 68, 1772 (1996).
[4] T. Makimura, Y. Kunii, N. Ono and K. Murakami, Jpn. J. Appl. Phys. 35, L1703 (1996).
[5] P. Melinon, P. Keghelian, B. Prevel, V. Dupuis, A. Perez, B. Champagnon, Y. Guyot, M. Pellarin, J. Lerme, M. Broyer, J. L. Rousset and P. Delichere, J. Chem. Phys. 108, 4607 (1998).
[6] J. Muramoto, Y. Nakata, T. Okada and M. Maeda, Appl. Surf. Sci. 127-129, 373 (1998).
[7] J. Muramoto, T. Inmaru, Y. Nakata, T. Okada, M. Maeda, Appl. Phys. A 69 [Suppl.], S239 (1999).
[8] J. Muramoto, Y. Nakata, T. Okada, M. Maeda, Jpn. J. Appl. Phys. 36, L563 (1997).
[9] Q. Li, T. Sasaki, N. Koshizaki, Appl. Phys. A 69, 115 (1999).

Influence of laser fluence on the synthesis of carbon nitride thin films by nitrogen-ion-assisted pulsed laser deposition

J. P. Zhao, Z. Y. Chen, T. Yano, T. Ooie, M. Yoneda, and J. Sakakibara

Shikoku National Industrial Research Institute, AIST, MITI, 2217-14 Hayashi-cho, Takamatsu, Kagawa 761-0395, JAPAN
E-mail: zhao@sniri.go.jp

Carbon nitride films were deposited by pulsed Nd:YAG laser ablation of graphite with assistance of nitrogen ion beam bombardment. The nitrogen to carbon (N/C) atomic ratio, surface morphology and bonding state of the deposited carbon nitride films were characterized by X-ray photoelectron spectroscopy (XPS), Fourier transform infrared (FTIR) spectroscopy and atomic force microscopy (AFM). The influence of laser fluence on the synthesis of carbon nitride films was investigated. The N/C atomic ratio of the carbon nitride films can reach the maximum at the highest laser fluence. XPS and FTIR analyses indicated that the bonding state between the carbon and nitrogen in the deposited films was influenced by the laser fluence during deposition. The carbon-nitrogen bonding of C-N, C=N together with very few C≡N were found in the films. Results indicated that the laser fluence also had critical effect on the surface morphologies of the carbon nitride films.

Keywords: carbon nitride, pulsed laser deposition, ion-beam-assisted deposition, bonding state, surface morphology

1. Introduction

A continuing interest in carbon nitride materials has persisted since the theoretical calculation of their structures and properties by Liu and Cohen [1] and others [2,3]. Considerable efforts have been made to realize and understand the structures and properties of the predicted metastable crystalline C_3N_4 phases (α-, β-, cubic, etc.). Some experimental results on the synthesis of crystalline C_3N_4 confirmed by transmission electron diffraction patterns have been reported [4,5]. In most of those reports, the deposited carbon nitride films were mainly composed of the amorphous phase in which small crystallites embedded. While claims of crystallinity remain unresolved, there have been interesting results of studies of the mechanical and tribological properties of amorphous carbon nitride films which suggest that they are a promising material for applications such as protective coatings for magnetic media [6].

When carbon bonds with nitrogen, a number of bonding hybridization are possible: sp, sp^2 and sp^3. The local structural property that distinguishes potentially superhard and dense C_3N_4 phases from softer, low-density material is the carbon coordination: hard materials require sp^3-bonded carbon in the C_3N_4 network, while sp^2-bonded carbon will lead to much softer materials. Due to its high reactivity, atomic nitrogen is believed to play a major role in the synthesis of nitrides. Hence, nitrogen ion beam assisted deposition has been widely used in producing carbon nitride thin films. In this study, the low energy nitrogen ion beam assisted pulsed laser deposition (PLD) was applied to

First International Symposium on Laser Precision Microfabrication, Isamu Miyamoto, Koji Sugioka, Thomas W. Sigmon, Editors, Proceedings of SPIE Vol. 4088 (2000) © 2000 SPIE · 0277-786X/00/$15.00

synthesize the carbon nitride films. Due to both of carbon species that produced by laser ablation of graphite and nitrogen ions have hyperthermal kinetic energies, the method that we used in present study possesses potential advantages for the synthesis of the metastable material. The purpose of this work is to synthesize the carbon nitride films by using the ion-beam-assisted PLD and try to understand the effect of laser fluence on the structure and bonding of the synthesized carbon nitride films.

2. Experiment

Carbon nitride films were deposited in a ion-beam-assisted PLD system with a background pressure of less than 1×10^{-6} Torr. The pressure during film deposition was about 4×10^{-4} Torr. The experimental setup is schematically shown in Fig. 1. The fouth harmonic output from a Nd:YAG laser with a wavelength of 266 nm were used for the ablation of highly oriented pyrolytic graphite (HOPG) target with an incident angle of 45°. The laser repetition rate was 10 Hz and the pulse width was 10 ns. The HOPG target was rotated by an external motor to provide a fresh surface for each pulse. Si(100) wafer was used as substrate for deposition. The substrate was irradiated by a low energy nitrogen ion beam generated from a 3 cm ion source (Ion Tech, Inc.) during carbon species deposition. The ion beam had a current density of about 0.8 mA/cm^2 and an incident angle normal to the substrate surface. The energy of the nitrogen ion beam was only 63 eV, which was much lower than those used in many studies [7,8]. Such low ion energy was used in order to prevent the possible structure and stress relaxation induced by ion bombardment, which have been thought to promote the formation of sp^2 bonded carbon. The substrate temperature was controlled at about 540°C during the film deposition. The distance between the target and the substrate was 35 mm.

The synthesized carbon nitride films were subject to a series of characterization including X-ray photoelectron spectroscopy (XPS), Fourier transform infrared (FTIR) spectroscopy and atomic force microscopy (AFM), in order to examine the chemical composition, bonding state and surface morphology of the films. XPS measurements were carried out using a Mg Kα 1253.6 eV X-ray source with an energy resolution of 0.8 eV. FTIR measurements were done on a Perkin Elmer FTIR 2000 spectrometer.

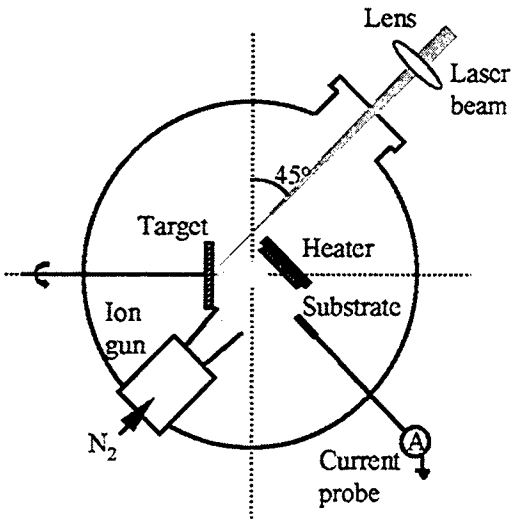


Fig. 1 Schematically experimental setup.

3. Results and Discussion

Although it is possible to change the laser fluence by using optical filter, the method that we used in present work is to simply adjust the laser beam from focus to unfocused position. That is, we obtained larger fluence by focusing the laser beam in smaller irradiation spot. Figure 2 shows the N/C atomic ratio in the synthesized carbon nitride films evaluated with XPS as a function of the laser fluence. As the laser fluence was reduced, the N/C atomic ratio first sharply decreased to the minimum at about 8.7 J/cm^2, and then slightly increased as the laser fluence reduced further. The dependence of the deposition rate of the carbon nitride films on the incident laser fluence is shown in Fig. 3. The deposition rate changed with the laser fluence in the opposite manner as that of N/C atomic ratio. Due to the very low ion energy, we could not expect a significant sputtering effect during the film deposition. Therefore, the arriving ratio of carbon to nitrogen species on the substrate surface determined the final N/C atomic ratio in the carbon nitride films. The larger deposition rate induced by the larger laser beam size corresponds to the higher C/N arriving ratio, therefore, the lower N/C atomic ratio in the films. This could be confirmed in Fig. 4, which shows the relationship between the N/C atomic ratio and the size of craters on the

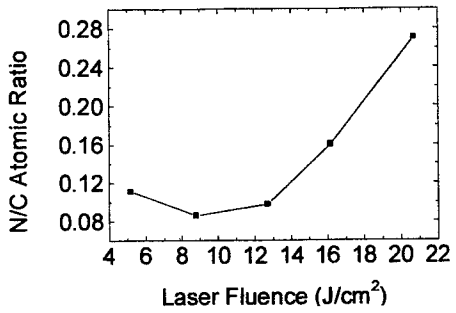


Fig. 2 N/C atomic ratio as a function of laser fluence.

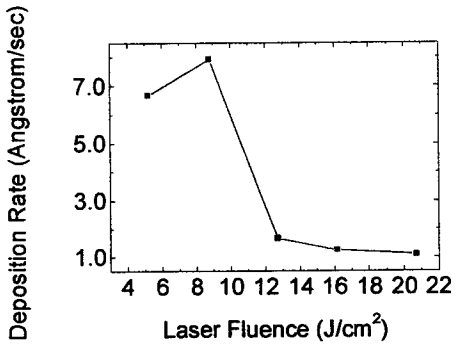


Fig. 3 Deposition rate as a function of laser fluence.

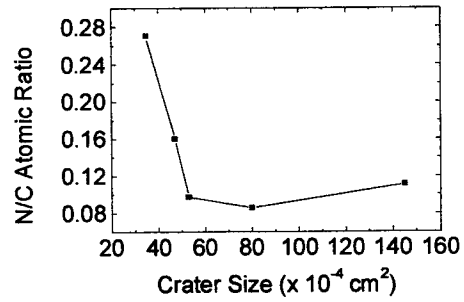


Fig. 4 Relationship between N/C atomic ratio and crater size.

HOPG target generated by the laser irradiation with different fluences. In addition, we noticed that the N/C atomic ratio increased at the laser fluence lower than 8.7 J/cm^2 though the crater size increased, as shown in Figs. 2 and 4. This could be attributed to the reduced total mass of the carbon species generated by the low fluence laser irradiation. Although the crater size generated at this low laser fluence became larger, the low energy density of the irradiation was not sufficient to evaporate a large amount of carbon species for deposition, which can be confirmed by the reduced deposition rate as shown in Fig. 3. Hence, the C/N arriving ratio reduced and the N/C atomic ratio of the film increased.

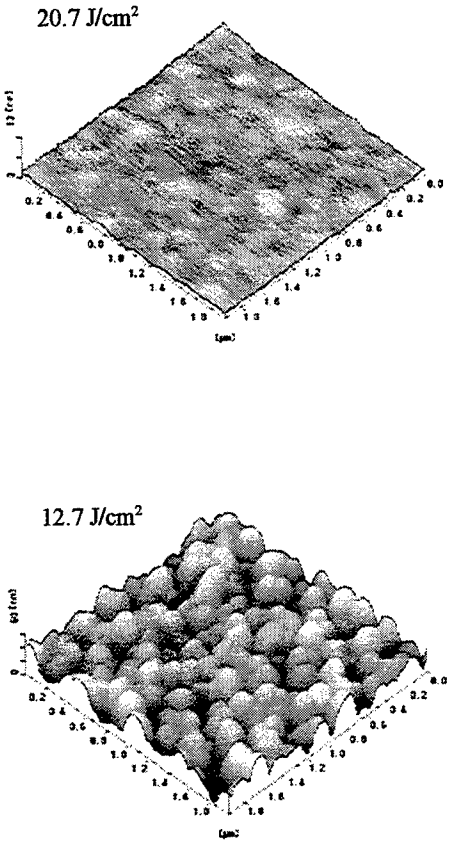


Fig. 5 AFM morphologies of the carbon nitride films.

In addition, we cannot exclude the possible effect of laser fluence on the plasma dimension and distribution, which could also influence the arriving ratio of carbon to nitrogen and the final N/C atomic ratio.

Figure 5 shows AFM images of the surface morphologies of the carbon nitride films deposited at two typical laser fluences of 20.7 and 12.7 J/cm^2, respectively. Although both films show the column-like surface structure with regular domed topes, the smoothness and compactness of the film deposited at higher laser fluence are much better than that of the film deposited at lower laser fluence. This can be attributed to the different kinetic energies of the carbon species produced at different laser fluence. The high energy carbon species resulting from the high fluence laser irradiation would considerably enhance the surface mobility of the depositing atoms, which then improved the surface morphologies of the films.

The corresponding C 1*s* and N 1*s* core level spectra of

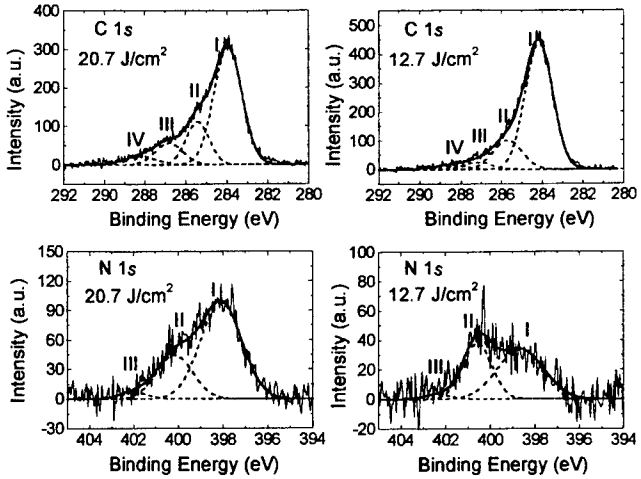


Fig. 6 C 1*s* and N 1*s* core level spectra of the carbon nitride films. C 1*s*: (I) C-C, (II) sp^2 C-N, (III) sp^3 C-N and (IV) C-O; N 1*s*: (I) sp^3 C-N, (II) sp^2 C-N and (III) N-O.

the two films are shown in Fig. 6. It can be seen that not only the nitrogen content decreased obviously at low laser fluence, the relative ratio of sp^3 C-N (C_3N_4 phase) to sp^2 C-N ($C_5N \sim C_2N$ phase) reduced significantly. Therefore, it could be concluded that the laser fluence had critical influence on the bonding state between carbon and nitrogen atoms. The FTIR spectra that shown in Fig. 7 give the same results as those of XPS studies. That is, with higher laser fluence, the stretching bands of C-N single bonds (C_3N_4 phase) became dominant. However, the stretching bands of C=N double bonds ($C_5N \sim C_2N$ phase) predominated at lower laser fluence. No obvious C≡N triple bonds related band was observed in the FTIR results. According to these results, we therefore proposed that the high kinetic energy resulting from the high laser fluence would promote the formation of sp^3 hybridized carbon and corresponding C_3N_4 phase.

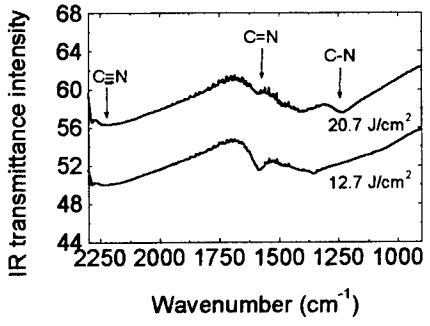


Fig. 7 FTIR transmission spectra of the carbon nitride films.

4. Conclusions

Carbon nitride films were synthesized by low energy nitrogen ion beam assisted pulsed laser deposition. The N/C atomic ratio, surface morphology and the bonding state between carbon and nitrogen were found to be obviously influenced by the laser fluence. The high laser fluence was proposed to promote the formation of desired sp^3 hybridized carbon and C_3N_4 phase in the carbon nitride films.

References

[1] A. Y. Liu and M. L. Cohen: Science, **245**, (1989) 841.

[2] A. Y. Liu and R. M. Wentzcovitch: Phys. Rev. B, **50**, (1994) 10362.

[3] D. M. Teter and R. J. Hemley: Science, **271**, (1996) 53.

[4] C. Liu, Y. Z. Lu, and C. M. Lieber: Science, **261**, (1993) 334.

[5] K. M. Yu, M. L. Cohen, E. E. Haller, W. L. Hansen, A. Y. Liu, and I. C. Wu: Phys. Rev. B, **49**, (1994) 5034.

[6] H. Sjostrom, S. Stafstrom, M. Boman, and J. E. Sundgren: Phys. Rev. Lett., **75**, (1995) 1336.

[7] X. M. He, L. Shu, W. Z. Li, and H. D. Li: J. Mater. Res., **12**, (1997) 1595.

[8] J. Vlček, K. Rusňák, V. Hájek, and L. Martinů: J. Appl. Phys., **86**, (1999) 3646.

Preparation of Metal Oxide Thin Films Using Coating Photolysis Process With ArF Excimer Laser

Tetsuo TSUCHIYA, Akio WATANABE, Yoji IMAI, Hiroyuki NIINO, Akira Yabe, Iwao YAMAGUCHI, Takaaki MANABE, Toshiya KUMAGAI and Susumu MIZUTA

National Institute of Materials and Chemical Research, 1-1 Higashi, Tsukuba, 305-8565, Japan
E-mail: tsuchiya@nimc.go.jp

The preparation of metal oxide thin films have been developed using the metalorganic(MO) compounds coating photolysis process with ArF excimer laser irradiation at room temperature. The effect of the starting materials and irradiation method on the product films was investigated by FT-IR, UV, XRD and SEM. It was found that metal acetylacetonates or metal 2-ethylhexanoate was effective as the starting materials. When using metal acetylacetonates as the starting materials, crystallized TiO_2, In_2O_3 and ZrO_2 were obtained with ArF laser irradiation at 50 mJ/cm^2 at a repetition rate of 5 Hz for 5 min. When using Zn-acac, Fe, Sn, or In 2-ethylhexanoate as the starting material, a two-step process consisting of both preliminary weak (10mJ/cm^2) and sufficiently strong irradiation(50mJ/cm$_2$) was found to be effective for obtaining crystallized ZnO, Fe_2O_3, SnO_2 and In_2O_3 films. In addition, crystallized complex oxide thin films such as ITO, $PbTO_3$ and $PbZrO_3$ were successfully obtained from the metal acetylacetonates or metal 2-ethylhexanoate using MO coating photolysis process. Patterned metal oxide thin films were also obtained by the ArF laser irradiation through the photomask, followed by leaching with solvents. The crystallization mechanism was discussed from the point of view of the photochemical reaction and photothermal reaction.

Keywords: ArF excimer laser, Metalorganic compound, Metal oxide thin films, Crystallization, Patterning

1. Introduction

For electronics or optical information processing which will be the core technologies of the twenty-first century, it is essential to integrate highly functional metal oxide thin films into devices or systems. For this reason, many investigations have been carried out by various methods. In many cases, however, many devices or systems, which include materials such as semiconductor silicon or organic materials, are sensitive to heat treatment. Therefore, satisfying both conditions of being able to integrate metal oxide thin films at low temperature and being able to pattern are very important requirements. Recently, in order to decrease of the deposition temperature, the laser assist process adapted to various processes such as laser ablation[1], sol-gel[2], sputtering[3] and CVD[4] has been reported. On the other hand, we have developed a new method of depositing metal oxide thin films from a metalorganic precursor using the coating photolysis process with ArF laser [5-6] and have reported that simple oxides such as TiO_2, In_2O_3, SnO_2, ZrO_2 and ZnO films have been successfully prepared by the coating photolysis process using ArF laser irradiation at room temperature. The coating photolysis process using a metalorganic compound is advantageous over other techniques with respect to the accuracy in composition control and simplicity. This also opens the possibilities of direct patterning for electronic device. In this paper, we discuss some experimental results, the merits of this technique and the formation mechanism of the metal oxide thin films.

2. Experimental

A schematic diagram of the process is shown in Fig. 1 The precursor solutions were spin-coated on quartz or silicon substrates at 2000-6000 rpm[5-6]. The metalorganic films were then dried at 150-200℃ in air for 10 min to eliminate the solvent and were then irradiated at repetition rates of 10-50 Hz with an unfocused ArF laser (Lambda Physik,

First International Symposium on Laser Precision Microfabrication, Isamu Miyamoto, Koji Sugioka, Thomas W. Sigmon, Editors, Proceedings of SPIE Vol. 4088 (2000) © 2000 SPIE · 0277-786X/00/$15.00

Compex 110). The laser fluence on the films, monitored by a laser power meter (Scientech, 38-2UV5), was adjusted to 10～50 mJ/cm^2.

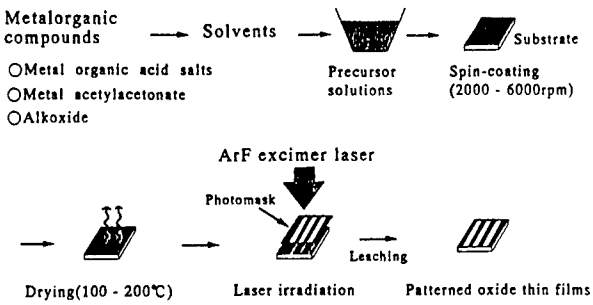


Fig. 1 Schematic diagram of the process.

3. Results and Discussion

3.1 Relation between starting materials and photolysis

First, we have investigated the relation between starting materials and photolysis. All of the starting materials tested were irradiated by ArF laser irradiation at a fluence of 50 mJ/cm^2 and at a repetition rate of 5 Hz for 5min. The results of the crystalline phases identified by XRD and IR of the films derived from the starting materials are summarized in Table 1. When using Titanium-naphtenate, photolysis was not observed. When using Ti-tetraisopropoxide, changes in the IR spectrum were observed, however, the product was amorphous based on the XRD measurement. On the other hand, when using Ti-di-n-butoxide(bis-2,4-pentanedionate):Tiacac, Bis(2,4-pentanedionate)-Ti oxide(Ⅱ):TiOacac and Ti-2-ethyl-1-hexaolate as the starting material, rutile phase TiO_2 was obtained using the ArF laser irradiation. Fig. 2(b) shows the XRD patterns of the TiO_2 film prepared by the coating photolysis process.

From the above studies, it was proven that metal acetylacetonates and metal alkoxides with long carbons chain could be used as the starting materials in metalorganic compounds[5-6]. According to the IR measurements before and after the ArF laser irradiation, the IR absorption spectrum due to TiOacac, Tiacac and 2-ethyl-1-hexaolate completely disappeared. Hence, no organic components were found to be present in the film after the ArF laser irradiation.

Since the UV absorption of an organic compound depends on the organic group, the UV absorption effect of organic groups on the photolysis was investigated using Tiacac and TiOacac. According to the UV measurements of the Tiacac and TiOacac, the absorbance of the TiOacac film at 193nm is stronger than that of Tiacac film. This means that TiOacac can be easily decomposed by ArF laser irradiation. As a matter of fact, TiO_2 (rutile) was obtained at a fluence of 10mJ/cm^2 using TiOacac, whereas TiO_2 (rutile) was barely obtained at a fluence of 30mJ/cm^2 using Tiacac. From the above results, the metal oxide thin films prepared by ArF laser irradiation was found to be strongly dependent on the starting materials used.

Table 1 The results of the crystalline phases identified by XRD and IR for the films derived from verious starting materials.

Starting materials	Product	
	XRD	IR
Ti-naphtenate	Amorphous	Many groups
Ti-tetraisopropoxide	Amorphous	Small OH
Ti-di-n-butoxide(bis-2,4-pentanedionate)	Rutile	None
Bis(2,4-pentanedionate)-Ti oxide(Ⅱ)	Rutile	None
Ti-2ethyl-1- hexanolate	Rutile	None

In the case of using a thermal process, rutile TiO_2 was obtained above 700℃. On the other hand, Sato et. al. reported that the anatase phase was transformed into the rutile phase with XeCl laser irradiation at a fluence of 80 mJ/cm^2 for 60min[7], where the transition of anatase to rutile was explained by a photothermal reaction. Therefore, in order to determine whether the decomposition observed in this study was caused by a photothermal effect or a photochemical effect, anatase TiO_2 films prepared by thermal treatment at 500 ℃ was be irradiated by ArF laser irradiation at a fluence of 50 mJ/cm^2 and at a repetition rate of 5 Hz for 5min. However, no phase transformation from anatase to rutile was observed. Therefore, the formation of rutile phase would be attributed to not only a photothermal reaction but also a photochemical reaction of the organic compounds during the coating photolysis process.

Irradiations were also carried out with In, Sn and Zr-acac, and crystallized In_2O_3, SnO_2 and ZrO_2 films were also obtained successfully by ArF laser irradiation.

3.2 Two-step irradiation method

In the case of organic acid salts such as Fe 2-ethylhexanoate were spin coated on the quartz substrate, the ablation of the iron 2-ethylhexanoate was observed by ArF laser irradiation at a fluence of 50 mJ/cm^2. In order to prevent such ablation, the two-step irradiation method was developed. That is, at the first step, the Fe 2-ethylhexanoate was irradiated with the ArF laser at 10 mJ/cm^{2}at a repetition rate of 50 Hz for 0.5 min, and in the second step, the laser power was raised to 50 mJ/cm^2 at a repetition rate of 10 Hz for 5 min. Fig. 2(b) shows the XRD pattern of the product obtained by ArF laser irradiation. The peaks were assigned to γ-Fe_2O_3. It is very surprising that γ-Fe_2O_3 was directly obtained by ArF laser irradiation without further treatment

because the simple heating of iron 2-ethylhexanoate up to 500 ℃ gives α-Fe_2O_3 and γ-Fe_2O_3 which are considered to be metastable.

When using In, Sn and Pb- 2-ethylhexanoate, crystallized In_2O_3, SnO_2 and PbO films were also successfully obtained by ArF laser irradiation.

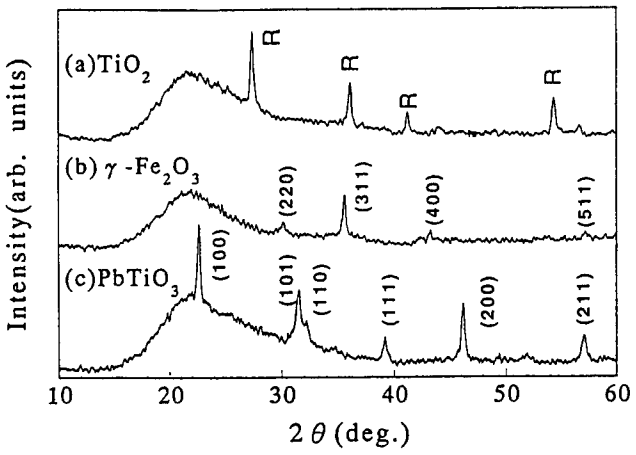


Fig. 2 XRD patterns of (a)film obtained by spin-coating Ti-2-ethylhexanolate and irradiation by an ArF laser at a fluence of 50 mJ/cm^2 for 5 min at a repetition rate of 10 Hz, (b)film obtained by spin-coating Fe-2-ethylhexanoate and irradiation by an ArF laser; the first laser irradiation was at a fluence of 10 mJ/cm^2 with a repetition rate of 50 Hz for 0.5 min, and a second laser irradiation was performed at a fluence of 50 mJ/cm^2 with a repetition rate of 10 Hz for 5 min. (c)$PbTiO_3$ film obtained by spin-coating lead -2-ethylhexanoate and Ti-2-ethylhexanoate and irradiation by an ArF laser; the first laser irradiation was at a fluence of 10 mJ/cm^2 with a repetition rate of 50 Hz for 0.5 min, and a second laser irradiation was performed at a fluence of 50 mJ/cm^2 with a repetition rate of 10 Hz for 5 min .

3.3 Preparation of complexes oxides

The preparation of an oxide compound consisting two or more metallic elements such as $PbTiO_3$ and $PbZrO_3$ has been investigated using the coating photolysis process. Fig. 2 shows the XRD pattern of the product obtained by ArF laser irradiation. When using Pb-2-ethylhexanoate and Ti-2-ethyl-1-hexaolate as the starting materials, the $PbTiO_3$ perovskite phase with the pyrochlore phase were obtained by ArF laser irradiation at 50 mJ/cm^2 with a repetition rate of 10 Hz for 5. On the other hand, a single phase of $PbTiO_3$ perovskite was successfully obtained using the two-step irradiation method consisting of both preliminary weak and subsequently strong irradiation as shown in Fig. 2(c). $PbZrO_3$ was also obtained by the coating photolysis process using the two-step irradiation method.

3.4 Direct patterning

Another advantage of this method is that the patterned metal oxide thin films are obtained by ArF laser irradiation through the photomask followed by leaching the unirradiated part with solvents as shown in Fig. 1. In this study, the grid of width 20 μ m was used for the photomask.

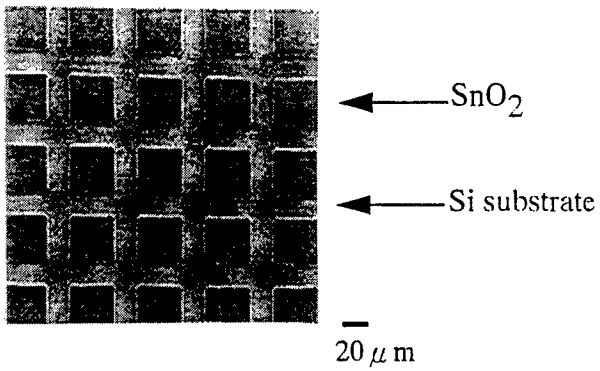


Fig. 3 SEM photograph of the patterned SnO_2.

Fig. 3 shows the SEM photographs of the patterned SnO_2 films on a Si substrate obtained by this method. The dark areas show the SnO_2 films and the bright areas are the Si substrates. The square of the patterned SnO_2 films are 45 μ m. The widths of the line spaces are 20 μ m. The edge of the patterned SnO_2 is sharp. These results can be considered to clearly demonstrate possibility of preparing the fine patterning of the metal oxide thin without a etching process using a halogen gas.

4.Conclusion

In this study, it has been shown that crystallized metal oxide films such as TiO_2, In_2O_3, ZrO_2, ZnO, SnO_2, and Fe_2O_3 can be obtained by ArF laser irradiation using metal acetylacetonate complexes and metal 2-ethylhexanoates. An oxide thin film containing two or more metallic elements such as $PbTiO_3$ also has been successfully prepared. Furthermore, it was found that the present method could be applied to the fine patterning of the metal oxide thin films.

Acknowledgements

The authors express their sincere thanks to Dr. T. Sasaki and Dr. N. Koshizaki, National Institute of Materials and Chemical Research, for their helpful discussions and their help with the profilometer measurements.

5.References

[1]H. Tabata, T. Kawai, S. Kawai, O. Murata, J Fujioka and S. Minakata, Appl. Phys. Lett. 59 (1991) 2354.

[2]A. Ando, T. Katayama, M. Shimizu and T. Shiosaki, Jpn. J. Appl. Phys. 31 (1992) 3001.

[3]X. M. Lu, S. Zu, W. S. Hu, Z. G. Liu and Y. N. Wang, Appl. Phys. Lett. 66 (1995) 2481

[4]Y. Yamazaki, T. Hioki, H. Funakubo, K. Shinozaki and N. Mizutani, Mater. Res. Bull., 30(9)(1995) 1081.
[5]T. Tsuchiya, A. Watanabe, Y. Imai, H. Niino, I. Yamaguchi, T. Manabe, T. Kumagai and S. Mizuta : Jpn. J. Appl. Phys. 38 7B (1999) L823.
[6]T. Tsuchiya, A. Watanabe, Y. Imai, H. Niino, I. Yamaguchi, T. Manabe, T. Kumagai and S. Mizuta : Jpn. J. Appl. Phys. 38 10B (1999) L1112.
[7]H. Sato, S. Nishio, S. Kato, K. Marumo, A. Matsuzaki, and R. Yoshida: Bull. Chem. Soc. Jpn., 69, (1996) 3381.

Preparation of Conducting Polymer Thin Films by UV Laser-Assisted Deposition

Satoru NISHIO, Motoyoshi OKUMURA, Yoshiaki TAKETANI, Akiyoshi MATSUZAKI and Hiroyasu SATO

Laser Photo Chemistry Research Group, Department of Chemistry for Materials, Faculty of Engineering, Mi'e University, Kamihama-cho, Tsu, Mi'e, 514-8507, Japan
E-mail: nishio@chem.mie-u.ac.jp

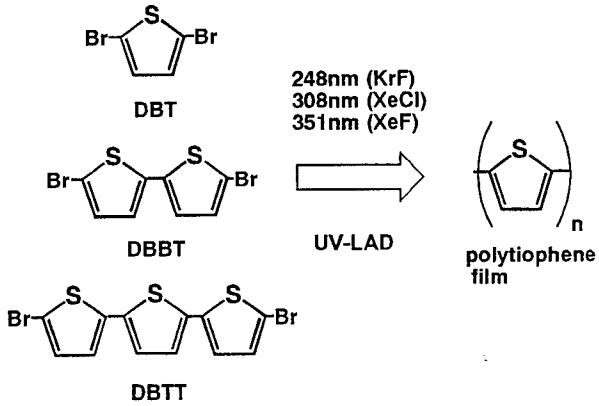
UV Laser-Assisted Deposition (UV-LAD) of three kinds of thiophene related compounds, 2,5-dibromothiophene (DBT), 5,5'-dibromo-2,2'-bithiophene(DBBT) and 5,5'''-dibromo-2,2':5',5''-terthiophene (DBTT) with 248 (KrF), 308 (XeCl) and 351nm (XeF) beams enabled us to obtain polythiophene thin films with highly oriented fibrous structure called laser induced periodic structure (LIPS). The conductivities of the films from DBBT with a 308nm beam and from DBTT with a 351nm beam have reached to the order of 10^{-3} and 10^{-1} Scm^{-1}, respectively, by doping with iodine after the UV-LAD process. FT-IR, XPS and UV-vis. spectra show that, although sulfur atoms are eliminated to some extent, polymerization basically occurs at α positions of the thiophene related compounds by elimination of halogen atoms.

Keywords: polythiophene, thin film, excimer laser, UV-LAD, LIPS

1. Introduction

In recent photopolymer science and technologies, various UV beams have been employed as a new tool for precision processing such as microscopic polymerization or modification of polymers. [1-3] Especially, the excimer laser is considered to be excellent for the photochemical reaction and microscopic processing making good use of its high reaction selectivity and spatial control. Along such a trend, we have tried to prepare polythiophene thin films from several thiophene derivatives such as 2,5-dichlorotiophene (DCT), 2,5-dibromothiophene (DBT) and 2,5-diiodothiophene (DIT) as reactants by UV laser-assisted deposition (UV-LAD) with some excimer laser beams. [4, 5] In these cases, however, only 193 and 248nm could be employed for preparation because of their absorbance band less than 250nm, resulting in formation of films with considerable defects such as elimination of sulfur atoms owing to damaging by the excess energy of photons. It is necessary, therefore, to apply longer wavelength for the purpose of preparation of better defined polythiophene.

In this report, in addition to DBT, 5, 5' - dibromo-2, 2'-bithiophene (DBBT) and 5,5'''-dibromo-2,2':5',5''-terthiophene (DBTT) with maximum absorption peaks at 320 and 360nm, respectively, were synthesized to employ as starting materials for preparation of polythiophene films by UV-LAD with 308 and 351nm as well as with 248nm as shown in Scheme 1.



Scheme 1 Preparation of polythiophene films by UV-LAD of various thiophene derivatives.

First International Symposium on Laser Precision Microfabrication, Isamu Miyamoto, Koji Sugioka, Thomas W. Sigmon, Editors, Proceedings of SPIE Vol. 4088 (2000) © 2000 SPIE · 0277-786X/00/$15.00

2. Experimental

The experimental setup for UV-LAD is described in our previous paper.[4, 5] The reactants DBBT and DBTT were synthesized in Dimethylformamide (DMF) from starting materials, 2,2'-bithiophene(BT) and 2,2':5',2"-terthiophene (TT), respectively, following the conventional method. [6] DBT, DBBT or DBTT was deposited by sublimation onto a quartz or KBr substrate under irradiation of an unfocused excimer laser beam in a reaction chamber evacuated below 10^{-3}Torr. 248(KrF), 308(XeCl), and 351nm(XeF) laser beams at the fluence of 10 - 20 $mJcm^{-2}pulse^{-1}$ were applied for the film preparation. Substrate temperature was kept between 200 and 240 K with liq. N_2 during film preparation. After preparation, the substrate was heated up to 380K to get rid of unreacted monomers. The films prepared by UV-LAD of DBBT at 308nm and DBTT at 351nm were doped with iodine by exposing them with iodine vapor in a glass cell after film preparation.

Surface morphology, structure and physical properties of the films prepared by UV-LAD were studied by atomic force microscopy (AFM), FT-IR, ultra violet-visible spectroscopy (UV - vis.), X-ray photoelectron spectroscopy (XPS) and electric conductivity measurements. Hereafter we will use such an abbreviated mark for each film as DBBT(308) for the film prepared by UV-LAD of DBBT with a 308nm beam.

3. Results and discussion

Every film prepared by UV-LAD has an oriented structure consisting of numerous fibers. This structure is often observed in surface modification of polymers with polarized excimer laser beams and called laser induced periodic structures (LIPS). [1,2] As an example, AFM image of a surface morphology of DBBT(308) is shown in Fig. 1.

Table 1 shows the C_{1s} peak position and relative abundance of bromine and sulfur atoms against carbon atoms (Br/C and S/C, respectively) of each film obtained by XPS measurement together with those for α-terthiophene (3T) as a reference. For DBBT(248), the values Br/C and S/C are 0.06 and 0.15, respectively, meaning that 76% of bromine and 35% sulfur atoms are eliminated. These values are not so different from those for DBT(248). Assuming a complete α, α'-bonded polymer, it consists of 7 - 8 thiophene ring units considering from the Br/C ratio. Smaller value of S/C ratio compared to that of 3T (0.23), however, suggests partial bond breaking of thiophene rings.

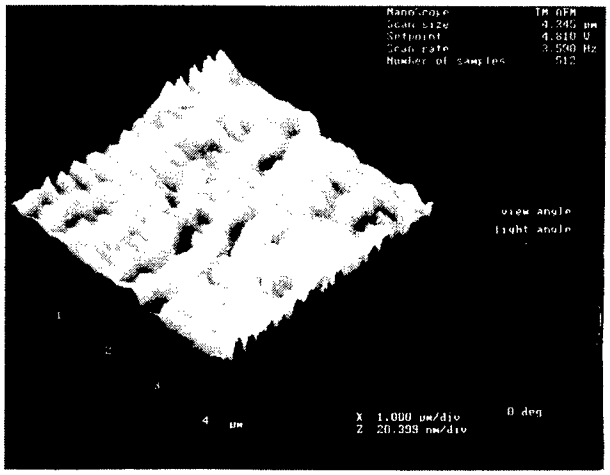


Fig. 1 AFM image of a surface morphology of DBBT(308).

Table 1 Br/C, S/C and C_{1s} peak positions by XPS measurements for each film prepared by UV-LAD together with those of α-terthiophene (3T). In parentheses are also listed the elimination ratio of Br and S atoms against the reactants.

Sample	Br/C	S/C	C_{1s} peak Position(eV)
DBT(248)	0.14 (0.72)	0.15 (0.35)	285.0±0.1
DBBT(248)	0.06 (0.76)	0.15 (0.35)	284.2±0.1
DBBT(308)	0.07 (0.72)	0.17 (0.26)	284.1±0.1
DBTT(248)	0.11 (0.34)	0.15 (0.35)	284.1±0.1
DBTT(351)	0.14 (0.16)	0.18 (0.22)	284.0±0.1
3T		0.23 [a]	284.3

[a] Sulfur atoms are eliminated, to some extent, during XPS measurement, resulting in smaller value (0.23) compared with theoretical one (0.25).

This structural disorder must impede the development of π-conjugated system. The result that C_{1s} peak position for DBBT(248) is slightly lower (284.2eV) than that for 3T (284.3eV), indicates that the π-conjugation length of the film is a little longer than that of 3T. As for DBBT(308), although the elimination ratio for bromine atom is 0.72, nearly equal to those for DBT(248) and DBBT(248), we obtain 0.26 for sulfur atom. The C_{1s} peak position of DBBT(308) is 284.1eV, slightly lower than that for DBBT(248). This means that UV-LAD with longer wavelength restrains the elimination of sulfur atoms,

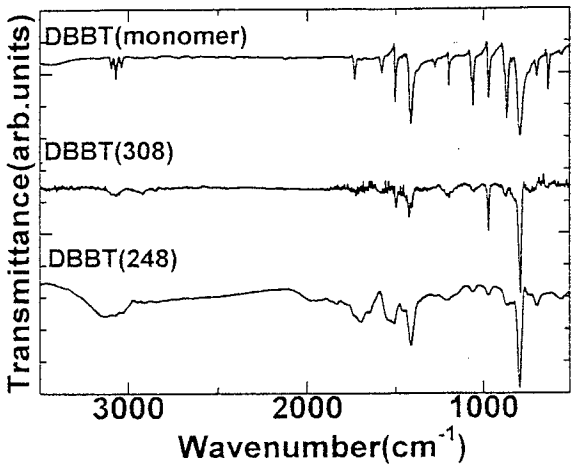


Fig. 2 FT-IR spectra for DBBT(248) and DBBT(308) together with that of DBBT monomer.

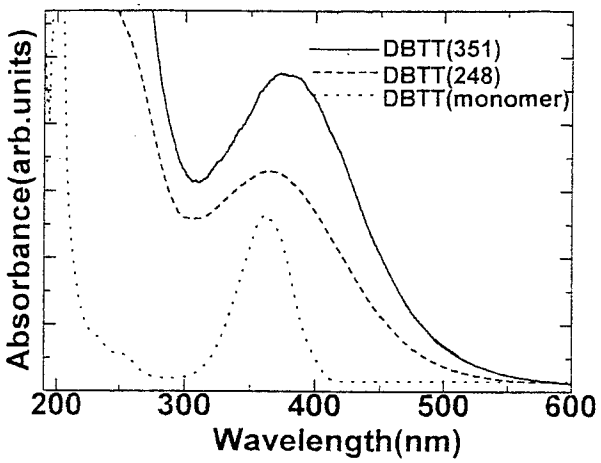


Fig. 3 UV-vis. spectra for DBTT(248) and DBTT(351) together with that of DBTT monomer.

resulting in obtaining the film with better developed π-conjugated system.

FT-IR spectra of DBBT(248) and DBBT (308) are shown in Fig. 2 together with that of DBBT monomer. Peaks around 1510, 1430 and 1210cm^{-1} ascribed to thiophene rings are detected clearly in the spectra for DBBT(308). Peaks around 1000cm^{-1} are assigned to C-H in-plane bending.[7-9] Presence of a peak at 794cm^{-1} assigned to C-H out-of plane bending vibration related to ß-H (H at 3 or 4 position) of thiophene[7-9] suggests that polymerization occurs predominantly at α and α' positions of DBBT by eliminating halogen atoms. For DBBT(248), on the contrary, broadening of the peaks related to thiophene rings and a new peak around 1700cm^{-1} can be observed. This peak is assigned to CO stretching of carbonyl groups formed through reaction of radicals created in the photochemical processes with oxygen atoms in the reaction chamber or those in air, suggesting that structural defects also exist in the films. These defects may come from bond breaking of thiophene rings as well as from the link missing in polymerization. Peak intensity ratio between symmetric (1430cm^{-1}) and anti-symmetric (1510cm^{-1}) stretching vibration of thiophene ring gives us the information on the average conjugation length of the polymer.[7] According to such an analysis, average conjugation lengths n for DBBT(248) and DBBT(308) are estimated to 4 and 5 respectively. Here we define n as conjugation length, which corresponds to the number of thiophene unit cells connecting each other with sp^2 hybrid orbitals of carbon atoms $(C_4H_2S)_n$.

These results described above suggest that UV-LAD with longer wavelength enable us to obtain better defined polythiophene. So we tried to perform UV-LAD with 351nm for DBTT with an absorption band around 350nm.UV-LAD with 248nm for DBTT was also carried out for comparison. From XPS results as shown in Table 1, although the elimination ratio for bromine atom of DBTT(351) is 0.16, smaller than those of DBT(248) and DBBT(308), the value S/C is 0.18, meaning that only 22% of sulfur atoms are eliminated. This value is most excellent among all the samples we prepared, indicating that longer wavelength is of use for preparation of better defined polythiophene by UV-LAD. The C_{1s} peak position of DBTT(351) (284.0eV) suggests better developed π-conjugated system of this film.

According to the FT-IR measurement for DBTT(248) and DBTT(351), extremely sharp peaks at 1500, 1450, 1240 and 1000cm^{-1} assigned to thiophene ring were detected for DBTT(351), though those for DBTT(248) were weak and broad. From peak intensity ratio between symmetric (1430cm^{-1}) and anti-symmetric (1510cm^{-1}) stretching vibration of thiophene ring, we estimated the average conjugation lengths to be 5 and 8 for DBTT(248) and DBTT(351), respectively.

The UV-vis. spectra for the films prepared by UV-LAD of DBTT(248) and DBTT(351) are shown in Fig. 3, together with the reactant monomer (DBTT). The spectrum for DBTT was measured by dissolving each monomer in methanol. Broad shape of the spectrum for each film suggests that the film consists of several components with different π-conjugation length. Although the maximum peak

position of the spectrum for each film is not so different from that for the reactant, band edge of each film shifts to longer wavelength region. The optical band gap of DBTT(351) is estimated to be 2.5eV by Mott plot. [10] Although this value is larger than those for polythiophene prepared, for example, by chemical method reported by Kobayashi et al. (2.0eV) [11], it is much more excellent than that of DBT(248) (3.1eV) [5] and not inferior to those for the plasma-polymerized thiophene films (2.5-3.1 eV).[12]

Finally, the effect of electron acceptor on the electric conductivity for DBBT(308) and DBTT(351) was investigated by doping them with iodine after film preparation. Drastic increase in the conductivity was observed immediately after beginning of the doping for each film. The conductivities of DBBT(308) and DBTT(351) have reached to the order of 10^{-3} Scm^{-1} and 10^{-1} Scm^{-1}, respectively. The latter value is more than three orders higher than those of polythiophene film prepared by plasma polymerization. [11]

4. Conclusion

Polythiophene thin films were prepared by UV Laser-Assisted Deposition (UV-LAD) of some thiophene derivatives with various excimer laser beams. UV-LAD of three kinds of thiophene related compounds, 2,5-dibromothiophene (DBT), 5,5'-dibromo-2,2'-bithiophene (DBBT) and 5,5'''-dibromo-2,2':5',5''-terthiophene (DBTT) with 248 (KrF), 308 (XeCl) and 351nm (XeF) beams enabled us to obtain polymerized films with highly oriented fibrous structure called laser induced periodic structure (LIPS). FT-IR, XPS and UV-vis. spectra show that, although sulfur atoms are eliminated to some extent, polymerization basically occurs at α positions of the thiophene derivatives by elimination of halogen atoms. For DBBT(308) and DBTT(351), the average conjugation length have been estimated to be corresponding to that of thiophene oligomers consisting of 5 and 8 thiophene units, respectively. The conductivities of DBBT(308) and DBTT(351) have reached to the order of 10^{-3} and 10^{-1} Scm^{-1}, respectively by doping with iodine after the UV-LAD process.

Acknowledgements

This work is a part of the project of Institute for Fundamental Chemistry, supported by Japan Society for the Promotion of Science - Research for the Future Program (JSPS-RFTF96P00206).

References

[1] H. Hiraoka and S. Lazare: Appl. Surf. Sci., **46,** (1990) 264.

[2] H. Hiraoka, W. Y. Y. Wong, T-M. Wong, C-T. Hung, W-C. Loh and F. M. Lee: J. Photopolym. Sci. Technol., **10,** (1997) 205.

[3] A. Yabe and H. Niino: J. Photopolym. Sci. Technol., **10,** (1997) 159.

[4] S. Nishio, S. Okada, Y. Minamimoto, M. Okumura, A. Matsuzaki and H. Sato: J. Photochem. Photobiol. A. Chem., **116,** (1998) 245.

[5] S. Nishio, M. Okumura, S. Okada, Y. Minamimoto, Y. Taketani, A. Matsuzaki and H. Sato: J. Photopolym. Sci. Technol., **11,** (1998) 347.

[6] P. Bauerle, F. Wurthner, G. Gotz and F. Effenberger: Synthesis, November, (1993) 1099.

[7] Y. Furukawa, M. Akimoto and I. Harada: Synth. Met., **18,** (1987) 151.

[8] S. Hotta, W. Shimotsuma and M. Taketani: Synth. Met., **10,** (1984/85) 85.

[9] M. Akimoto, Y.Furukawa, H. Takeuchi, I. Harada, Y.Soma and M.Soma: Synth. Met., **15,** (1986) 353.

[10] N. F. Mott and E. A. Davis: "*Electronic Processes in Non-Crystalline Materials, 2nd ed.*", (Clarendon Press, Oxford, 1979), Chap. 6.

[11] M. Kobayashi, J. Chen, T. C. Chung, F. Moraes, A . J. Heeger: F. Wudl, Synth. Met., **9,** (1984) 77.

[12] K. Tanaka, K. Yoshizawa, T. Takeuchi, T. Yamabe and J. Yamauchi, Synth. Met., **38,** (1990) 107.

Nanosatellites and MEMS Fabrication by Laser Microprocessing

Henry Helvajian*[1], Peter D. Fuqua, William W. Hansen, and Siegfried Janson
Laboratory Operations, The Aerospace Corporation
MS:M2-241 PO, Box 92957 Los Angeles, California 90009 , USA
**E-mail: Henry.helvajian@aero.org*

By definition Nanosatellites are space systems that can weigh 1-10 kg and can perform unique missions (e.g. global cloud cover monitoring, store-and-forward communications) acting either in constellation of distributed sensor-nodes or in a many-satellite platoon that flies in formation. The Aerospace Corporation has been exploring the application of microelectronics fabrication and advanced packaging technology to the development of a mass-producible nanosatellite. Particular attention is being directed at M^3 (Micromachining/MEMS/Microsystems) technology which appears to be important in the integration and manufacturing of these satellites. Laser direct-write processing techniques are being applied for rapid prototyping and to specific 3D fabrication steps where conventional microelectronics fabrication techniques fall short. In particular, a laser based technique has been developed that combines the rapid prototyping aspects of direct-write and the low cost/ process uniformity aspects of batch processing. This technique has been used to develop various fluidic components and a microthruster subsystem in a photostructurable glass/ceramic material.
Keywords: nanosatellites, MEMS, laser 3D fabrication, photostructurable glass,

1. Introduction

Microelectronics, miniaturization and batch processing techniques have revolutionized the consumer electronics industry mostly in the way components, systems and major assemblies are designed, manufactured and sold. These keystone disciplines have also engendered development of new technologies or processing approaches, namely MEMS (microelectromechanical system), microsystems and micromachining or sometimes labeled as M^3. These new microengineering disciplines have found successful application areas in many industries, from household-appliances, communications, automobiles and human health care and medicine (-- one estimate of potential world market >10B $US by 2004)[1]. In contrast, there has been little application of M^3 technology to the aerospace industry. These findings engender a modicum of surprise despite the fact that microengineering technologies enable functionality at reduced mass and volume; features that are eagerly sought after by any aerospace systems design engineer.

Nearly eight years ago, The Aerospace Corporation, in a series of papers and presentations, presented the concept of the mass-producible, 1kg class, nanosatellite (nanosat)[2]. Figure 1 shows a conceptual design of the nanosatellite. To first order the design is an exercise in integrated packaging technology. However, not apparent in the figure is the need for material processing technologies that go beyond silicon materials and planar microelectronic fabrication techniques. Nanosatellites can do viable space missions if sufficient functionality can be incorporated in the 1kg mass. Systems engineering studies show that this becomes possible via the implementation of microengineering/M^3 technologies[3]. Various possible missions comprise a large number (~1000) of nanosats in low earth orbit constellations, a smaller number of nanosats flying in formation[4] and solitary nanosats conducting inspecting missions on larger satellites. Regardless of the mission, the development of an integrated-package nanosatellite and its concomitant manufacturing line becomes cost prohibitive unless mass-production approaches are incorporated in the design and large numbers of nanosatellites are produced. To arrive at the end goal of a fully-integrated, mass-producible, 1kg class nanosatellite, The Aerospace Corporation is taking a dual path approach in its research and development efforts. First, develop a near term experimental space platform using standard microfabrication techniques and second, explore a wide range of microengineering technologies that would lead to the development of a fully integrated nanosatellite. The experimental space platform, called the Picosat, has been built and was successfully launched into space in February 2000.[5] Two 250 g mass picosatellites were tethered together by a 33 m graded fiber at an orbital altitude of 670 km[6]. Figure 2 shows the two Picosat flight units with each unit having dimensions of 7.5cm x 10 cm x 2.5 cm. The data from both Picosats was directly transmitted to ground stations for analysis. The Picosat represents a first attempt at developing a disposable, semi-mass producible, space platform for experimental testing. A series of picosat missions are planned to test and validate microengineering

[1] * person to whom correspondence should be addressed

First International Symposium on Laser Precision Microfabrication, Isamu Miyamoto, Koji Sugioka, Thomas W. Sigmon, Editors, Proceedings of SPIE Vol. 4088 (2000) © 2000 SPIE · 0277-786X/00/$15.00

technologies for use on the nanosatellite. The second set of picosatellites have recently been launched (Minotaur)[7]

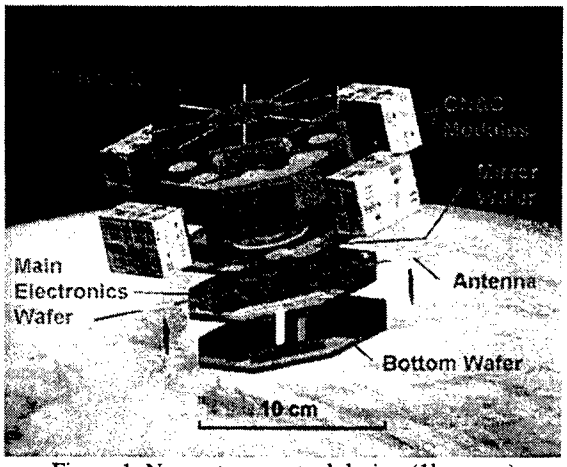
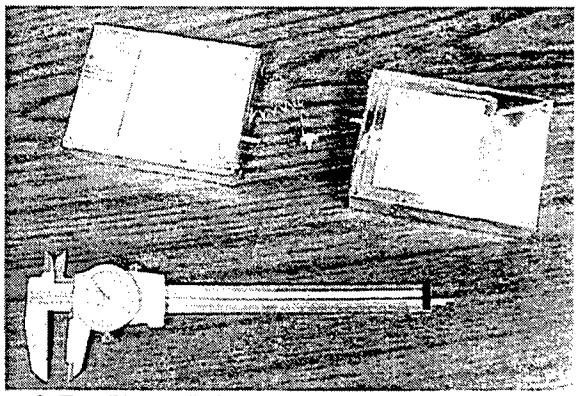


Figure 1: Nanosat conceptual design (1kg mass)


Figure 2: Two Picosat flight units with disassembled 30 m tether (Courtesy of E. Y. Robinson, The Aerospace Corporation)

In evaluating material processing technologies for the development of the nanosatellite, The Aerospace Corporation has identified several capabilities that are deemed important[8]. There is a need for rapid prototype processing. This capability reduces net development cost by enabling selective microfabrication of key structures and the quick evaluation of numerous nanosat subsystem designs without resorting to extensive processing at a foundry. Other important capabilities include microfabrication in true 3 dimensions (3D), processing at an embedded interface and processing materials other that silicon. The nanosat, which, appears as a layered sandwich of processed wafers, could include non-silicon wafers (e.g. glass, ceramic, diamond, metal). Therefore, material processing tools that can inherently process a variety of materials is beneficial to rapid prototyping. The laser is one such tool. It can process a variety of materials and it is the only tool that can put down material, remove material and simultaneously serve as a process diagnostic.

A laser direct-write microfabrication technique has been developed at The Aerospace Corporation that incorporates the main of the advantages of direct-write processing (e.g. maskless processing and true 3D processing) with the ease and cost-effective aspects of batch processing (i.e. parallel processing nominally provides process uniformity over a wafer scale)[9]. This technique has been applied to the fabrication of true 3D microfabricated components in glass/ceramic materials[10]. In general, serial material processing techniques like direct-write offer significant flexibility in materials processing. Modifications and alterations in the fabrication or design, in some cases, can be accommodated in near real-time. However, laser direct-write processing is essentially serial in nature and therefore a time intensive fabrication process. For example, the use of laser ablation to micro-fabricate simple holes can be costly if millions of holes are to be cut out. On the other hand, batch processing techniques are ideal for this case. Using a sequence of mask lithography, bake and etch processing steps, any number of holes can be fabricated cost effectively. Taking this example further, batch processing approach becomes costly and not even viable if the holes are to have true 3D shapes (e.g. hourglass) rather than standard 2.5D (i.e. cylindrically extruded shapes as typically achieved from 2D masking and etching operations).

It is possible to take the advantages of laser direct-write processing and merge it with that of batch processing if the direct-write segment is utilized only for volumetric patterning of the material and not for material removal. The patterning can include any complex shape that the direct-write tool can fashion. The resulting impregnated pattern can then be chemically batch processed to either remove the exposed or non-exposed regions. A key aspect of this merged process is the material. It must be made of photolytically active ingredients that, upon exposure, can either resist or be dissolved. Even though various polymers have this property (e.g. chemical resist technology used in microelectronics) there are only a handful of "engineered" materials that can be photoactivated and also have material properties suitable for space systems application.

Certain glass and ceramic materials find use in space systems. Their dielectric properties and resistivity to caustic chemicals (i.e. for use in propellant cavities) are two reasons for their use. Current techniques for the fabrication of microstructures in glass and ceramic materials include micro-milling, masking-patterning and chemical etching and laser ablation. Neglecting for the moment the differences in machining quality and given that short pulse laser ablation (i.e. femtosecond) is found to be more proficient than long pulse laser ablation (i.e. nano and microsecond), all the techniques have the main drawback of process throughput. Fortunately, there is a class of photostructurable glass/ceramic materials that incorporate photoactivators that permit patterning. Furthermore, these materials have the unique property of controlled de-vitrification (i.e. crystallization) at low temperatures. As a consequence, a programmed bake process can convert the patterned material from a glass state into a full ceramic

state[11]. There are over 5000 varieties of these glass/ceramics that go by various generic names such as photositalls, photocerams and pyrocerams but the most successful commercialization in the USA is in tableware and is sold under the trade name CorningWare™. Donald Stookey of Corning Corporation is credited with doing initial research on photositalls (ca 1948)[12]. Currently there are two manufacturers that make photositalls suitable for microfabrication applications. Foturan™ manufactured by the Schott Corporation and PRG-3 Photoceram manufactured by HOYA Corporation. To our knowledge the fabrication of microstructures in these photositalls is currently done by a UV lamp lithography step using a mask followed by a hydrofluoric acid (HF) chemical etch process[13].

In this paper we present the development of a laser microengineering process whereby both the direct-write and batch processing techniques are implemented to fabricate true 3D microstructures in the photositall Foturan. Our technique differs from the UV lamp exposure process in that we use a focused, high repetition rate, pulsed laser to volumetrically pattern the glass. We have measured, for selected UV laser wavelengths, the required photon dose for exposure, the resulting impact of the dose on the chemical etch efficiency between exposed and unexposed areas[14] and the minimum photon dose required to trigger high efficiency chemical etching (i.e. exposed rates)[15]. In the latter investigation we have identified a non linear dependence on the laser fluence. Based on the information from these investigations we have fabricated numerous true 3D microstructure patterns either as solitary units, in large arrays or as interconnected pattern assemblies that function as a complex micro-fluidic device. We also have successfully patterned embedded channels within a 3mm thick wafer. These embedded channels are intended to connect fluidic reservoirs and save a sealing step in packaging or to undercut supported microstructures. The developed 3D laser microfabrication technique has been integrated with a rapid prototype direct-write patterning microstepper that is controlled by CADCAM software. Using this facility we have microengineered several prototype microthruster systems that are designed to maintain attitude control of a 1kg class nanosatellite[16]. The microthruster impulse and thrust efficiency have been experimentally measured[17]. One particular design flew in space on a recent NASA Shuttle mission, STS-93 in July 1999[18].

2. The Fabrication Process

Photositalls function via a three step process; an illumination step, a ceramization step and a preferential isotropic etching step[19]. For Foturan, the photosensitive character arises from trapped Ce^{3+} (admixture CeO_2) and Ag^+ (admixture Ag_2O) ions that are stabilized by Sb_2O_3 in lithium aluminosilicate.[20] Using the conventional linear absorption model, Ce^{3+} can be photoionized to form Ce^{4+} and a free electron at photon energies near 3.97 eV (318 nm). The free electron neutralizes a nearby Ag^+ ion (i.e. $Ag^+ + e^- \rightarrow Ag^o$) leaving a latent image of the absorption event. In the ceramization step, migration and local clustering of the Ag^o nuclei lead to formation of lithium silicate crystals. In a 5% solution of HF these crystals etch 20-40 times faster than the unexposed amorphous material. An aspect that is critical to the surface finish of the final microstructure or the degree of ceramization is the growth rate of the crystals and the maximum bake temperature. Both growth rate and phase of the lithium silicates can be controlled during the bake step. A low temperature (~600 C) bake results in multi-phase crystals that dissolve in HF acid, while a high temperature bake (>700 C) forms a true ceramic phase that is resistant to HF. Figure 3 shows data from X-ray diffraction analysis of two processed samples: an exposed but not baked sample (Top: glassy-amorphous state) and a sample that has undergone a programmed bake sequence for ceramization (Bottom).

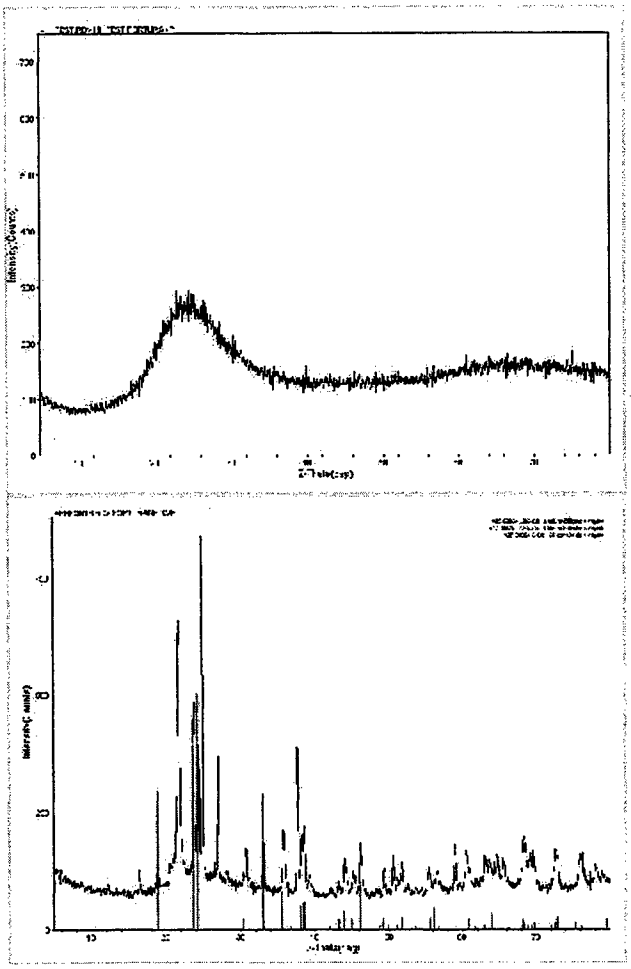


Figure 3: X-ray 2Θ scans of amorphous (exposed but not baked) sample (top); and crystalline (exposed and baked) (bottom). The identified bands in the bottom scan are for lithium silicate.

The Aerospace microfabrication process utilizes the wavelength dependence of the UV absorption to control the

volume of material that is exposed. By changing the laser wavelength from 248nm (OD=3.0) to 355 nm (OD=0.1) it is possible to vary the penetration depth of the laser light from less than 100 microns to over a mm. During exposure we also control the incident laser fluence and the applied dose (i.e. number of laser shots). Finally, great care is taken to control the shape of the laser beam, the focal volume and the depth of focus (i.e. confocal parameter $b=2\pi\omega_o^2/\lambda$, where ω_o is the beam radius at waist and λ is the wavelength). All these controls insure against thermal runaway damage within the focal volume region and also permit better precision in the depth of exposure. Figure 4 shows that for a constant laser fluence the exposure depth depends on the number of shots applied. This data suggests that by controlling the laser shot number (i.e. for constant fluence) the material can be made to "cut" to a predetermined depth.

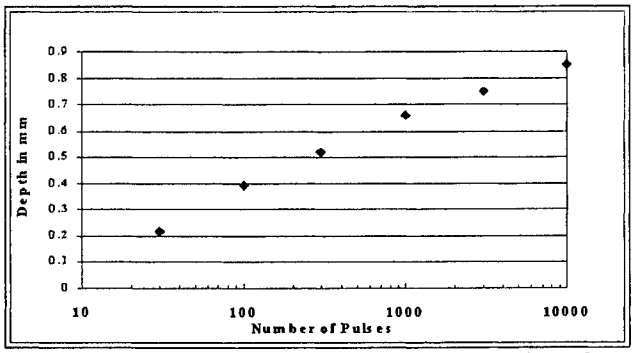


Figure 4: Etch depth versus number of laser pulses (266 nm) for constant per pulse laser fluence and constant etch protocol.

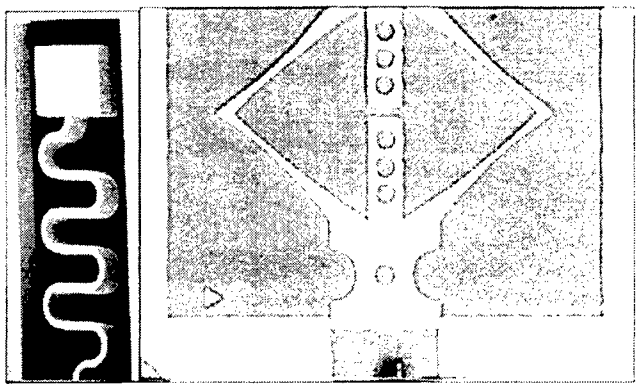
The aforementioned controls are integrated with an XYZ micro-stepper that is accurate to 5 microns over 100 mm XY translation and an automated system that can transfer one of four incident laser wavelengths to the sample surface. Three individually selectable microscope objectives can be used to focus the laser beam unto the sample (5X, 10X and 20X). Two high repetition lasers "feed" the exposure tool. A 2kHz excimer laser (Potomac Photonics SGX1000) and a 1kHz diode seeded Nd-Yag laser (Continuum HPO-1000). Automated fast shutters flag on/off the various laser beams and power meters are used for average power readings. Local dose control can be set through software commands to the stepper motor speed parameter or via burst-commands to the laser. For a multi-color exposure process, the various wavelength patterns are drawn separately, as layers, using AutoCAD™ software. The DXF output of the AutoCAD software is converted to machine control language using a translator program. All or any selected number of wavelength specific layers can be run automatically.

We have used this in-house developed direct-write laser exposure tool to fabricate various microstructures including resonant beams, springs and fluidic channels in glass or ceramic materials. This capability enables the development of ceramic or glass based MEMS. We have fabricated free standing structures and microstructures that are true 3D patterned. Figure 5 shows two free standing structures that can be used for prototyping resonant microstructures and springs, while in Figure 6 a prototype design for a 4-way fluidic mixing and passthrough device is shown. The etched pattern utilized four DXF-layers. In Figure 7 we show a similar device that has been transformed into full ceramic state. Feature resolution of better than 20 microns can be maintained during the glass to ceramic transformation process.

Early experimental results from our laboratory suggested that a critical dose of UV light is necessary to *form a connected etchable network of lithium silicate crystals*. This hypothesis could be cast in the equation shown below,

$$D_c \ \alpha \ F^m(r,z)N$$

where D_c defines the critical dose for *forming a connected etchable network of lithium silicate crystals*, F is the fluence (J/cm^2) with radial dependence, r, and depth dependence z and power dependence m. N is the number of laser shots.


Figure 5: SEM of a free standing meander spring(200 μm deep, 80 μm wide and 4 mm long) with proof mass (left) and an optical microscope photograph of a bow-spring loading a piston, 10 mm long with bow tapering to 80 μm wide (right).

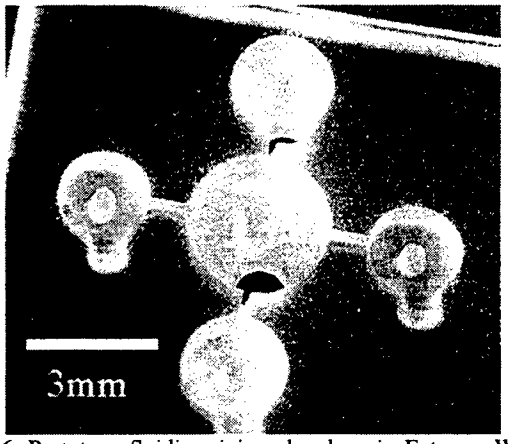


Figure 6: Prototype fluidic mixing chambers in Foturan. Wafer is 1mm thick.

To test this hypothesis an experiment was devised that used a pulsed diode seeded Nd-Yag system operating on the 3rd and 4th harmonics to irradiate 1 mm thick Foturan samples with a known spot size. The analysis consisted of precisely measuring the etch depth (for 266nm irradiation) and hole diameter (for 355nm irradiation) as a function of the number of laser pulses with a proven Gaussian profile. Both the hole depth and diameter define a boundary region where the material is barely exposed, but has not developed a connected network of crystals to promote etching. This region is easily identifiable in cross section scanning electron microscope (SEM) pictures in which the images show isolated crystals. For a Gaussian spatial distribution, it is possible to derive the total irradiated laser fluence (and dose) at the boundary region presuming there is measurement of the irradiated laser pulse energy.

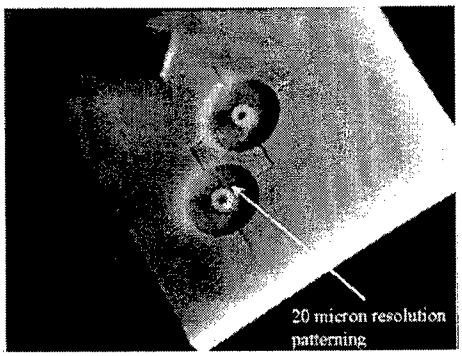


Figure 7: Prototype fluidic device patterned and etched and then converted into ceramic state.

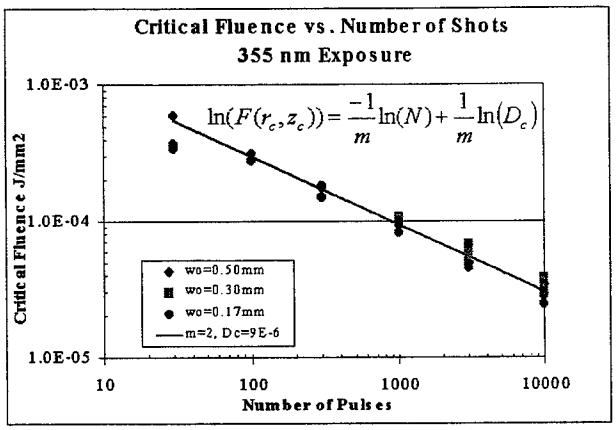


Figure 8: Non-linear exposure process, data for 3 spot sizes (0.5, 0.3, and 0.17 mm) are plotted. The results for 266 nm are similar but not shown[21].

In our experiment, the spot size on the sample was measured using a knife edge on a translation stage and in front of a power meter. The results which could be fit to an *erfc* function corroborated a Gaussian spatial energy distribution profile with a defined spot size ω_0. Consequently, by measuring laser power and number of laser shots administered per sample, it is possible to derive the laser fluence and the irradiated total dose at the boundary regions. Figure 8 plots this derived fluence as a function of laser shot number on a log-log scale. The fit is for m=2. The result indicates a squared dependence on the laser fluence. We can not yet experimentally prove whether the non-linear fluence dependence results from a photoabsorption process (i.e. via a true sequential two photon process or a process that involves a long lived intermediate state and some form of energy pooling) or is merely a consequence of the required density of etchable sites. Further experiments are underway in our laboratory to elucidate the underlying non linear mechanism in the photolytic process. Regardless, these results are surprising but they enable the laser to microfabricate embedded structures. By regulating the dose to near the measured critical value and by appropriately shaping the laser focal volume we have microfabricated embedded stacked channels. Figure 9 shows two rectangular stacked channels that were exposed from the same side. Note that there is no exposure above and below each channel and also none in between. The material is only exposed in the volume region where the administered laser dose is above a critical value.

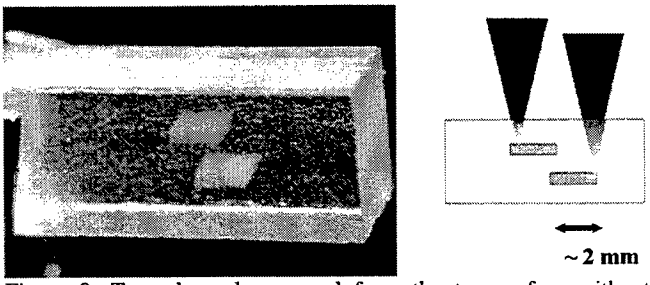


Figure 9: Two channels exposed from the top surface without inducing any exposure in between. This post-baked Foturan clearly shows which regions have been exposed.

This capability for embedding microchannels or microstructures has numerous applications. Specifically, it reduces a potential wafer bonding step in a micro-fluidic application and enables the selective undercutting of supported structures. An embedded exposure does not necessarily lead to an embedded cavity. The length and aspect ratio of any embedded microcavity structure will strongly depend on getting the etchant into the exposed region and removing the byproducts.

3. Microthruster Applications

Microthrusters (1-10mN force) are used for propulsion and attitude control in small space satellites. Smaller microthrusters in the 10 - 1000μN class can also be used for dynamic suppression/damping of vibrations in extended space structures. Microthruster propellants can be a high pressure gas, a liquid, a sublimating solid or a chemically reactive solid. Regardless of the type of propellant, the efficient use of the limited supply is always a paramount issue to space system designers, because spacecraft lifetime is usually dictated by the availability of the onboard propellant. This concern becomes more acute for pico and nano satellites (≤1kg class) because of the overall limited size and volume. Regardless of the microthruster type,

microthrusters typically have mesoscopic (cm to mm-scale) dimensions (e.g. fuel tank volume), microscopic (micron-scale) segments (e.g. fuel lines) and even nanoscopic (nanometer-scale) structures (e.g. surface coatings). The large dynamic range in dimension over which a material must be processed places a constraint on the accuracy of fabrication tools when developing an *integrated* microthruster. For example, an integrated ion propulsion system would require the fabrication of a fuel tank (cm-scale) that is "co-fabricated" with an array of field emitter tips (nanometer scale). For numerous materials, laser processing offers one approach to bridging this wide dynamic range of precision processing. By implementing high fluence techniques like laser ablation with medium fluence techniques like direct-write volumetric patterning and low fluence techniques that lead to surface texturing, it is possible to use a laser to co-fabricate cm scale structures with nanometer scale structures.

Using the laser direct-write technique discussed above, we have developed several prototype microthrusters. First, a bi-directional cold gas microthruster (1mN class) was developed in which one key element of the unit was the precise microfabrication of the hour-glass shape exit nozzle[22]. The hour-glass shape is easy to profile with an appropriate f-number (f/#) objective lens and the setting of the laser dose to initiate exposure within both the focussing and diverging focal volume. As a consequence, the hour-glass shape can be fabricated from one side of the glass/ceramic wafer and uses only one pulse from a 10ns Nd-Yag laser operating in the third harmonic. No trepanning operations are required.

Another type of microthruster has been developed which essentially is an array of individually addressable microsolid thrusters[23]. It is a stack of three wafers comprising of two silicon wafers sandwiching a glass ceramic wafer. The bottom wafer contains a patterned array of resistors that act as igniters, the middle wafer contains an array of fueled micro-chambers that have been fabricated using the laser direct-write volumetric patterning technique and the top layer is a patterned array of SiN membranes that are designed to contain the rising combusting gas pressure to a predetermined value. The advantage of the thruster design is its ease of fabrication and the ability to simultaneously make a large number of one-shot microthrusters on wafer scale dimensions. Figure 10 shows a picture of an assembled 15 "one-shot" microthruster array on a US penny. The per pixel thrust provided is measured to be 80mN on average and roughly 60W of power is released during the roughly 0.4 msec combustion event[24]. The glass/ceramic fuel layer plays an important role in this microthruster design. The firing of one microchamber must not induce fratricide to an adjoining chamber. With a brittle material like single crystal silicon, there is the potential for cleaving and near-neighbor ignition as a result of the shock wave from the micro explosion. However, by using a glass/ceramic material for the fuel container, we expect to get a more robust device and reduce the potential for near-neighbor fratricide. Measurements done in our laboratory show that the modulus of rupture (MOR) of the vitreous glass state is 60 N/mm^2 and increases to 98N/mm^2 after partial ceramization. The near term goals for the digital thruster program are to fly an experiment on a suborbital rocket (i.e. Scorpius)[25] and a follow-on Picosat mission.

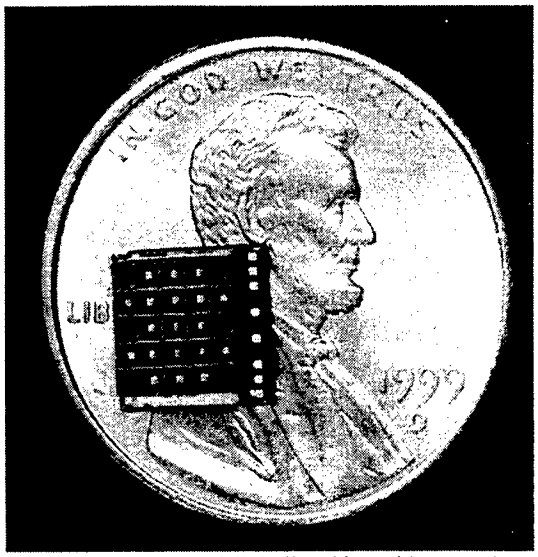


Figure 10: A (3x5) array of digitally addressable microthrusters (the four side holes are used for alignment during assembly). Thruster coupon flew on US/NASA Shuttle mission STS-93 and was tested for mechanical survivability using an inert propellant.

4. Discussion

The direct-write laser material processing technique, as presented, is an attempt to merge the advantages of direct-write processing (i.e. flexibility) with that of batch processing (i.e. process throughput). The technique works as a merged process because of the unique photo-absorptive and low temperature devitrification properties of the photositall material Foturan. In this case a glass/ceramic material can be volumetrically "micro-machined" in three dimensions without resorting to laser ablative or micro-milling operations, alleviating high residual stresses, and without resorting to multiple mask step operations, obviating the high cost of multiple mask development. Although photositalls are a unique class of materials, some thought should be given to the "engineering" of materials for laser direct-write patterning and batch process etching applications.

For space systems development, the types of materials that would be preferred commonly have robust mechanical properties (e.g. to withstand the rigors of launch and survive in the harsh UV and charged particle environment of space). Furthermore, in most terrestrial applications, there is a particular advantage in choosing materials that can also serve as substrates for electronics or photonics. The commercially available photositalls can fulfil some of these

requirements but certainly not all. But consider this: With the advent of polymer electronics and the growing trend for direct-write deposition of electronic components[26], it will not be long before direct-write electronics technology is available (though clearly not with the e-h mobilities possible in semiconductors). Direct-write photonics may require a longer development period but is possible. Regardless, lasers, in general, will play a role in direct-write material processing[27]. The key is developing a laser direct-write capability to micro-process a substrate material that permits co-fabrication of micromechanical, microfluidic, electronic and photonic components. The resulting device would be a true direct-write processed microsystem. In this regard, developing an "engineered" substrate for laser processing is crucial. The "engineered" substrate material must be such that, upon wavelength specific laser excitation, the material is altered in a fashion that can be further processed either chemically, or via a much reduced fluence laser ablation/desorption process. The latter processing approach would use very large area (>> cm) low fluence lasers to selectively remove material, somewhat mimicking a standard batch process but employing an environmentally-friendly dry mass-removal processing step. A step in this direction is the work of Sujioka et al. on multistep laser processing of GaN laser ablation/etching where it was shown that the simultaneous radiation of laser wavelengths (157nm and 248nm) significantly increased the quality of the etched pattern[28]. Developing a special substrate for laser direct-write processing will require a better understanding of the laser material interaction phenomena.

In The Aerospace Corporation process we have focused on the development of a non-ablative laser microfabrication technique that can be applied to photostructurable glass ceramic materials. These materials can be used in the design of microsystems where the intrinsic properties, common to most glasses, and the unique properties of ceramics are found to be important. The Aerospace Corporation applications have been in the development of microthrusters for nanosatellite applications. Our technique has been used to fabricate arrays of 3D microstructures on or within a wafer with resolution near 20 microns. Both semi-ceramic and full ceramic components have been microfabricated without loss of resolution. Currently, the resolution of the technique is not limited by the laser or the chemical etch process but by the chromophore (i.e. trapped charge) doping density set by the glass manufacturer. It would be a valuable exercise to process a photositall glass manufactured with a higher chromophore doping density and explore the feasibility of fabricating microstructures on the micron or submicron level.

Our results do not shed light on the fundamental exposure process or the extent to which the host material in the glass (i.e. SiO_2) is "solarized" by the UV laser and how this solarization effects lithium silicate crystal growth. These are subjects of ongoing work at The Aerospace Corporation.

5. Summary

Future space architecture designs include missions for satellites with mass ranging from 1-10 kg (i.e. nanosatellites). For these missions to be viable and cost effective, these nanosatellites must be designed and fabricated using mass-production concepts. Laser material processing has specific advantages over other processing techniques. In particular, its versatility in processing of numerous materials and its non-intrusive in situ processing nature. Laser direct-write processing has special advantages in rapid prototyping applications and if the direct-write techniques could be used to "sensitize" the material with the pattern, it is conceivable that the laser direct-write approach can also be used during manufacturing. The Aerospace Corporation has developed such a technique for the volumetric patterning of glass/ceramic materials which are subsequently batch processed using a wet chemical. The technique has been used to fabricate various microthrusters which are now undergoing space testing.

5. Acknowledgements

The authors would like to acknowledge contributions from various Aerospace Corporation staff. Dave Taylor and Meg Abraham for general discussions, Ernie Robinson for the data on the Picosat project, Joe Uht and Nathan Presser for the SEM pictures and Paul Adams for the X-ray diffraction analysis. The laser material processing development project was supported by The Aerospace Corporation, Corporate Research Initiative Program.

---

[1] S. Marshall in Micromachine Devices Vol. 2 No. 8, pp. 6-11, Vol. 2 No.11, pp. 5-7, 1997; Other studies by SPC Systems Planning Corporation (1994, 1997); SRI Consulting (1994, 1997); SEMI (1996); NEXUS (1994, 1997); Intelligent Microsensor Technology (1996); Samsung & MRI (1996, focused on inertial sensors).

[2] S. W. Janson, "Mini-, Micro-, and Nanosatellite Concepts" in Micro- and Nanotechnology for Space Systems: an Initial Evaluation, H. Helvajian and E. Y. Robinson Eds., (Aerospace Press, El Segundo, CA.) Monograph 97-01, pg. 67,1993; S. Janson, H. Helvajian and E. Y. Robinson, " The Concept of 'Nanosatellite' for Revolutionary Low-Cost Space Systems," Proceedings of 44th Congress of the International Astronautics Federation (Graz, Austria, 16-22 Oct. 1993); H. Helvajian ed., Microengineering Technology for Space Systems, (Aerospace Press, El Segundo, CA.) Monograph 97-02, 1995

[3] S. W. Janson, "Mass-Producible Silicon Spacecraft for 21st Century Missions", Paper AIAA 99-4458, Proceedings AIAA Space Technology Conference & Expo 28-30 September 1999, Albuquerque, NM, USA.

[4] J. E. Pollard, C.C. Chao and S. W. Janson, "Populating and Maintaining Cluster Constellations in Low-Earth Orbit", AIAA-99-2871, 1999.
[5] "A Big Future for Tiny Birds" Business Week, March 20,2000.
[6] S. L. Hast , N. J. Ho, C. H. Ouyang, and D. S. Oltrogge "The Ground Station Pre-flight Operation Plan for The DARPA-Aerospace PICOSAT Project" Aerospace Report No. ATR-2000(1967)-1, 2000.
[7] D. A. Hinkley, "DARPA-Aerospace PICOSAT Project: Compliance Data Package for MSII.1 Flight" Aerospace Report TOR-2000(1967)-1, 2000.
[8] H. Helvajian and S. W. Janson "Microengineering Space Systems" pg. 29 in Microengineering Aerospace Systems, H. Helvajian Ed. (AIAA Press, Reston VA and The Aerospace Press, El Segundo CA) 1999.
[9] W. W. Hansen, S. W. Janson and H. Helvajian " Direct-Write UV Laser Microfabrication of 3D Structures in Lithium Alumosilicate Glass" Proc. of SPIE Vol. 2991, pg. 104, 1997.
[10] P. Fuqua, S. W. Janson, W. W. Hansen, and H. Helvajian " Fabrication of True 3D Microstructures in Glass/Ceramic Materials by Pulsed UV Laser Volumetric Exposure Techniques", Proc. SPIE Vol. 3618, pg. 213, 1999.
[11] A. Berezhnoi "Glass-Ceramics and Photo-Sitalls" Plenum Press, NY 1970.
[12] S D. Stookey "Pyroceram, Codes 9606, 9608, 1st Report, Corning Glass Works, Corning , NY, May 1957.
[13] D. Hulsenberg, R. Bruntsch, K. Schmidt, F. Reinhold, "Micromechanische Bearbeitung von Fotoempfindlichem Glas" Silikattechnik, Vol. 41, (1990) 364; http://www.mikroglas.com.
[14] W. W. Hansen, S. W. Janson and H. Helvajian " Direct-Write UV Laser Microfabrication of 3D Structures in Lithium Alumosilicate Glass" Proc. of SPIE Vol. 2991, 1997 pg. 104.
[15] P.D. Fuqua, D. P. Taylor, H. Helvajian, W. W. Hansen, M. H. Abraham, "A UV Direct-Write Approach for Formation of Embedded Structures in Photostructurable Glass-Ceramics" in *Materials Development for Direct-Write Technologies*, edited by D.B. Chrisey, D.R. Gamota, H. Helvajian, and D.P. Taylor, (Mater. Res. Soc. Proc. **624** Pittsburgh, PA, 2000), in press
[16] S. W. Janson and H. Helvajian " Batch-Fabricated Microthrusters for kilo-gram class Spacecraft 1998 IEEE Aerospace Conference, Paper 093c Mar 21 - 28, Snowmass Village, CO,
[17] D. H. Lewis Jr., S. W. Janson, R. B. Cohen and E. K. Antonsson, "Digital Propulsion" Sensors & Actuators A Vol. 80(2000) pg. 143.
[18] D. G. Sutton . R. S. Smith, P. Chafee, S. Janson, L. Kumar, N. Marquez, J. Osborn, B. Weiller, L. Weideman " MEMS Space Flight Testbed" AIAA paper 99-4604 Proceedings of AIAA Space technology Conference Sept. 1999;
[19] A. Berzhnoi, "Glass-Ceramics and Photositalls" Plenum Press (New York, 1970).
[20] D. Hulsenberg, R. Bruntsch, K. Schmidt, F. Reinhold, "Micromechanische Bearbeitung von Fotoempfindlichem Glas" Silikattechnik, Vol. 41, (1990) 364; T.R. Dietrich, W. Ehrfeld, M. Lacher, M. Krämer, B. Speit, "Fabrication Technologies for Microsystems Utilizing Photoetchable Glass", Microelectronic Engineering 30 (1996) 497-504
[21] P.D. Fuqua, D. P. Taylor, H. Helvajian, W. W. Hansen, M. H. Abraham, "A UV Direct-Write Approach for Formation of Embedded Structures in Photostructurable Glass-Ceramics" in *Materials Development for Direct-Write Technologies*, edited by D.B. Chrisey, D.R. Gamota, H. Helvajian, and D.P. Taylor, (Mater. Res. Soc. Proc. **624** Pittsburgh, PA, 2000), in press
[22] H. Helvajian, S. W. Janson, "Batch-Fabricated Microthrusters: Initial Results", AIAA-96-2988 (1996); S. W. Janson and H. Helvajian " Batch-Fabricated Microthrusters for kilo-gram Class Spacecraft", Proceedings of the GOMAC '98 Conference "Micro-Systems and Their Applications" March 16-19, 1998, Arlington VA.
[23] D. Lewis, S. Janson, R. Cohen and E. Antonsson "Digital MicroPropulsion", Sensors and Actuators A: Physical, 2000, 80(2), pp. 143-154; S.W. Janson, H. Helvajian, and K. Breuer, "MEMS, Microengineering and Aerospace Systems," AIAA paper 99-3802, 30th AIAA Fluid Dynamics Conference, Norfolk, VA, June 1999.
[24] D. Lewis, S. Janson, R. Cohen and E. Antonsson, "Digital MicroPropulsion" Proceedings of the IEEE MEMS'99, Jan. 1999,
[25] J. V. Berry, R. E. Conger, J. R. Wertz "The Sprite Mini-Lift Vehicle: Performance, Cost and Schedule Projections for the First of the Scorpius Low-Cost Launch Vehicles, 13th Annual AIAA/USU Conference on Small Satellites, Logan, Utah, August 1999.; http://www.design.caltech.edu/micropropulsion/index.html.
[26] *Materials Development for Direct-Write Technologies*, edited by D.B. Chrisey, D.R. Gamota, H. Helvajian, and D.P. Taylor, (Mater. Res. Soc. Proc. **624** Pittsburgh, PA, 2000) in press.
[27] D. Chrisey, "Matrix Assisted Pulsed Laser Evaporation Direct-Write (MAPLE_DW)", in *Materials Development for Direct-Write Technologies*, edited by D.B. Chrisey, D.R. Gamota, H. Helvajian, and D.P. Taylor, (Mater. Res. Soc. Proc. **624** Pittsburgh, PA, 2000), in press Mater. Res. Soc. Proc. **624**; H. Helvajian " Laser Material Processing: A Multifunctional In - Situ processing Tool for Microinstrument Development" in " Microengineering for Space Systems" The Aerospace Press Monograph 97-02 (1997) pg. 67.
[28] K. Sugioka, S. Wada, K. Toyoda, "Ablation of Wide Band-Gap Materials by Multi-Wavelength Irradiation using a VUV Raman Laser", Applied Surface Sci. Vol. 109/110 pg. 179, 1997.

Microgroove Fabrication with Excimer Laser Ablation Techniques for Optical Fibre Array Alignment Purposes.

Kris Naessens, An Van Hove, Thierry Coosemans, Steven Verstuyft, Luc Vanwassenhove, Peter Van Daele and Roel Baets.

Ghent University – IMEC, dept. of Information Technology
Sint-Pietersnieuwstraat 41, B-9000 Gent, Belgium
E-mail: kris.naessens@intec.rug.ac.be

Abstract.

Currently, an ever increasing need for bandwidth, compactness and efficiency characterizes the world of interconnect and data communication. This tendency has already led to serial links being gradually replaced by parallel optical interconnect solutions. However, as the maximum capacity for the latter will be reached in the near future, new approaches are required to meet demand. One possible option is to switch to 2D parallel implementations of fibre arrays.
In this paper we present the fabrication of a 2D connector for coupling a 4×8 array of plastic optical fibres to RCLED or VCSEL arrays. The connector consists primarily of dedicated PMMA plates in which arrays of 8 precisely dimensioned grooves at a pitch of 250 μm are introduced. The trenches are each 127 μm deep and their width is optimized to allow fixation of plastic optical fibres.
We used excimer laser ablation for prototype fabrication of these alignment microstructures. In a later stage, the plates can be replicated using standard molding techniques.
The laser ablation technique is extremely well suited for rapid prototyping and proves to be a versatile process yielding high accuracy dimensioning and repeatability of features in a wide diversity of materials. The dependency of the performance in terms of quality of the trenches (bottom roughness) and wall angle on various parameters (wavelength, energy density, pulse frequency and substrate material) is discussed.
The fabricated polymer sheets with grooves are used to hold optical fibres by means of a UV-curable adhesive. In a final phase, the plates are stacked and glued in order to realize the 2D-connector of plastic optical fibres for short distance optical interconnects.

Keywords: 2D parallel fibre connector, optical interconnect, laser ablation, optical alignment structures.

1. Introduction.

A number of technologies are at our disposal for fabrication of microstructures: LIGA (German acronym for lithography, electroforming and molding), deep proton lithography and standard processes from the micro-electronic manufacturing technology. In general these fabrication methods suffer from low throughput, severe environmental requirements and high cost. Injection molding and embossing allow mass fabrication in a very fast way but due to expensive master tools (matrix), these technologies are unsuitable for fabrication of components in small or moderate amounts.
The last decade, excimer laser ablation has acquired the reputation of being a reliable technology for fabrication of microstructures. This non-resist technique does not require clean-room facilities, can be applied on a broad range of materials and is potentially fast since it allows parallel processing by means of mask patterns. It is therefore extremely suited for prototyping, proof-of-principle and fabrication of micro parts in small amounts or in applications where conventional tools (e.g. mechanical drilling) become too bulky and are not accurate enough.
Typical applications for laser ablation are via-drilling in printed circuit boards, removal of short cuts in electronic circuitry, wire stripping, fabrication of waveguides, micro-lenses and alignment structures in polymers, tissue removal in medical oriented applications [1,2,3,4,5]...

First International Symposium on Laser Precision Microfabrication, Isamu Miyamoto, Koji Sugioka, Thomas W. Sigmon, Editors, Proceedings of SPIE Vol. 4088 (2000) © 2000 SPIE · 0277-786X/00/$15.00

In this paper we focus our attention on alignment structures and investigate the feasibility of the technique for optical interconnect applications with plastic optical fibres.
For short-distance purposes as e.g. chip-to-chip interconnect within racks, POF (Plastic Optical Fibre) can be a very valuable alternative for glass fibre based solutions. Due to its higher numerical aperture and core size in comparison to glass fibre, POF provides enhanced coupling efficiency and relaxed alignment tolerances. In addition, the fibre is very flexible, allows easy end-facet preparation with a hot-knife technique and is a basically low cost solution. The fact that POF has a higher loss than glass fibre is of little importance since we consider interconnect distances that vary between a few centimeter and 1 meter. However, at this moment only 1D connectors (MT-like ferrules) are commercially available while the ever increasing need for higher bandwidth begs for 2D solutions. In this paper we demonstrate the fabrication of such a connector with laser ablation and report on our first results.

2. The 2D POF connector concept.

FIG. 1 illustrates the concept of this 2D connector. It consists of a number of stacked polymer plates (thickness slightly smaller than 250 micron) with U-grooves in which POFs are fixed at a pitch of 250 micron.

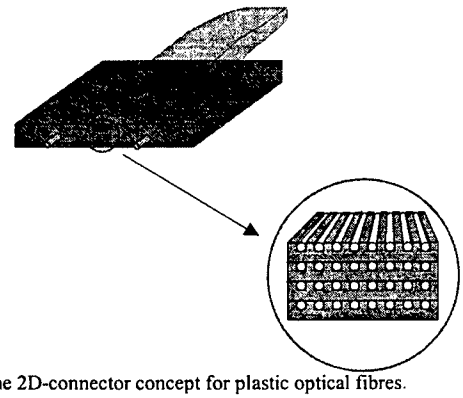


FIG. 1: The 2D-connector concept for plastic optical fibres.

We chose a trench geometry as surface profile for plastic optical fibre alignment since the open upper side allows rather easy insertion of the fibre and the depth of the grooves, defined by the diameter of the fibres (125 micron), is within the limits of what one can achieve with excimer laser ablation by aperture or mask imaging.
Around the stack of grooved plates (this is called the ferrule) a structure containing alignment features for coupling to other ferrules or to transceivers is added. These features can be e.g. alignment pins as shown in FIG. 1. In this paper we focus on the fabrication of the ferrule.

3. Fabrication of the fibre alignment structure.

The alignment structure consists of 8 grooves at a pitch of 250 μm, each having a length of 10 mm and a depth of 127 μm. The latter ensures that there is enough space for the UV-curing glue to cover a fibre with a nominal diameter and allows a little tolerance on the fibre diameter.

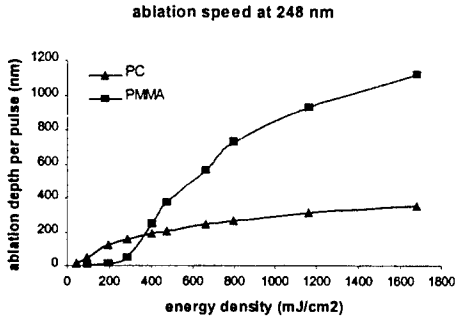


FIG. 2: Ablation characteristics of PMMA and PC at 248 nm, derived from the depth of ablation for 50-pulse holes (70 μm).

The choice of the substrate material and the excimer wavelength has been based on experiments with the polymers polymethylmethacrylate (PMMA) and polycarbonate (PC), and two common excimer wavelengths: the ArF transition at 193 nm and the KrF transition at 248 nm. For both wavelengths and materials, we made the grooves in two ways which we will call the 'moving aperture' and the 'hybrid mask method. The first approach uses a single square aperture of 800μm as mask geometry, which is scanned along the substrate, ablating grooves of 160 μm (demagnification 5) width sequentially. The latter method uses a more complex mask that is imaged onto the substrate. The mask pattern consists of 4 grooves, each of length 2.5 mm and is designed for the same demagnification as mentioned above. Due to the limited field of the projection lens we were not able to further increase the area of the mask. Therefore it was still necessary to scan the pattern along the substrate surface. However, the scanning time is much shorter since several grooves are ablated at the same time and the length of the groove pattern on the mask is longer (2.5 mm versus 800 μm). Since our laser ablation set-up does not include a homogenizer, the scanning improves the smoothness of the grooves due to averaging of the spatial intensity distribution of the laser pulses.

PMMA has a rather low absorption coefficient which allows the pulse to penetrate deeper into the material (higher ablation rate) but which is also responsible for the higher threshold of the pulse intensity as illustrated in FIG. 2.
After ablation of the grooves, a cleaning step with water and pressurized air was performed.
The experiments were carried out with a Lumonics Pulse Master 848 (suitable for both KrF and ArF gas mixtures) and by means of an optical set-up as in FIG. 3. A Molectron J3 pyroelectric joulemeter, put at far distance from the image plane, was used for energy density measurements.

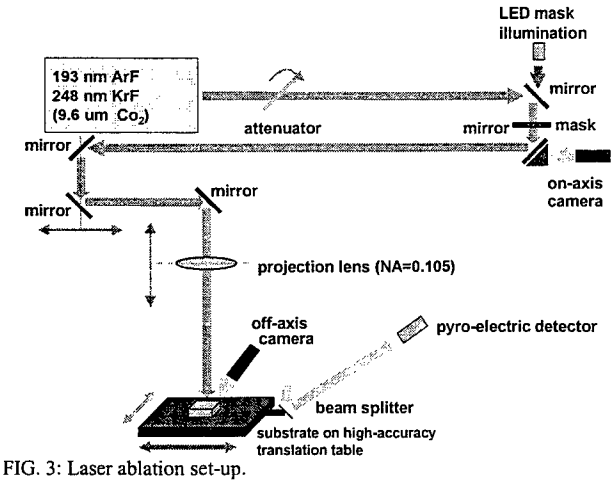


FIG. 3: Laser ablation set-up.

4. Fabrication procedure of the 2D ferrule.

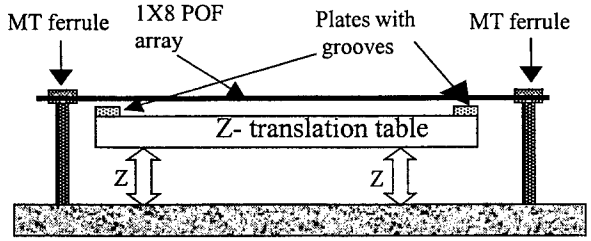
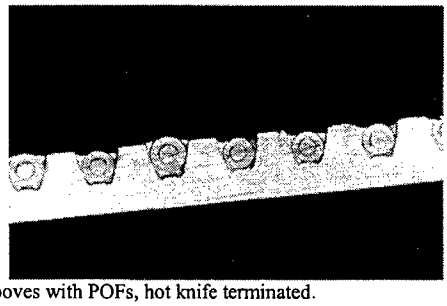


FIG. 4: Setup for fixing the POFs in the grooves.

The fabrication of the ferrule can be divided in three main steps: ablating the grooves, introducing the POFs in the grooves, and finally stacking the plates with grooves. The production of the grooves has been discussed in detail in paragraph 3. The fixation of the POFs is performed as follows: a 1 X 8 array is stretched and roughly aligned by means of two standard MT™ ferrules (FIG. 4). Then the plates with grooves are pushed against the POFs in such a way that the fibres are now laying in the grooves. Finally the POFs are fixed with UV-curing glue and the complete plate with fibres is cut with a knife at 110 °C. A plate with POFs can be seen in FIG. 5. The POFs are prototype fibres (POFs with an outer diameter of nominally 125 μm and a core of 63 μm are not yet commercially available) with a relatively high non-uniformity of the diameter (115-135 μm). This will strongly influence the precision on the position of the fibres.


FIG. 5: Grooves with POFs, hot knife terminated.

The following step in the assembly of the ferrule is the stacking of the substrates. If the plates are stacked at a pitch of 250 μm, one obtains a 2D POF ferrule with a pitch of 250 μm in 2 directions. In order to perform this stacking, a method called "virtual" alignment is developed.



a. The first plate is looked at with 2 cameras.


b. The corners of the plate are aligned on the crosshairs of the cameras.



c. The plate is moved over an exact distance of 250μm.

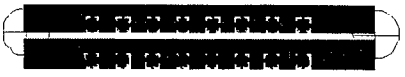

d. The second plate is aligned on the crosshairs. In this way the plates are positioned at a pitch of 250μm. After this step the plates are glued together.

FIG. 6: 'Virtual' alignment.

The principle of this technique is based on two key elements: the use of two independent movable cameras and the use of a translation table with sub-micron precision. The method is explained with an example in FIG. 6: two plates are stacked at a pitch of 250μm. This procedure can easily be expanded to stack several plates. This method neither uses a mask nor a master tool, but it creates a kind of "virtual" mask on which the plates are aligned. Hence it is a flexible and versatile technique for the assembly of prototypes.

5. Experimental results.

A. Laser ablation of the grooves.

A number of parameters are at our disposal to fabricate the grooves: energy density of the pulses, pulse frequency, substrate material, fabrication method (as mentioned above) and number of passes of the aperture or mask over the substrate. We performed a number of tests in which we fabricated grooves of nominally 100 μm for different values of the upper parameters. Depth and roughness of the grooves were measured by a Wyko and a SEM was used to look at the profiles. We will here summarize our conclusions.

- Influence of the wavelength and material type.

We ablated PMMA and PC with 193 nm as well as 248 nm excimer laser irradiation.
For PMMA we observed an ablation rate which is about 280 nm/pulse for 193 nm at 270 mJ/cm^2. At the KrF wavelength, where we were able to reach higher energies, etch rates as fast as almost 1 μm per pulse were obtained at a far higher energy density level (623 mJ/cm^2). However, the benefit of higher etching speed is accompanied by a higher roughness of the bottom as illustrated in FIG. 7.

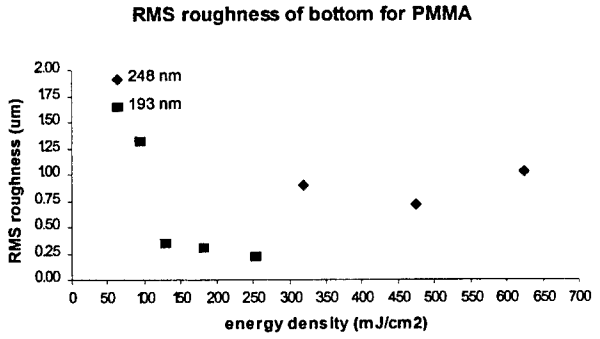


FIG. 7: PMMA ablation characteristics with the hybrid mask method.

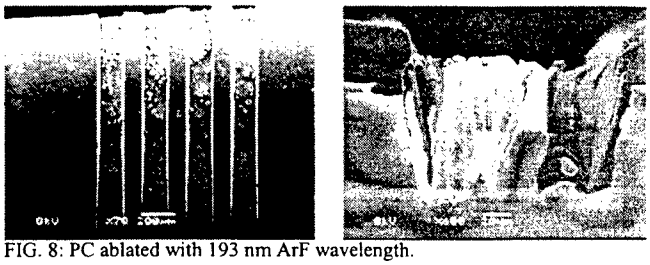


FIG. 8: PC ablated with 193 nm ArF wavelength.

The case for PC is even worse: ablation at 193 nm resulted in a very rough structure, which is totally unsuitable for alignment purposes (FIG. 8). The cone like structure on the bottom increases as the energy density and/or frequency is raised. At 248 nm, it ablated well with speeds up to 240 nm/pulse for 680 mJ/cm^2. The RMS roughness stayed well below 0.3 μm.

- Influence of pulse frequency and energy density.

Naturally, increasing the energy density speeds up the ablation process and for both materials we observed a better surface quality for energies much higher than the threshold values.

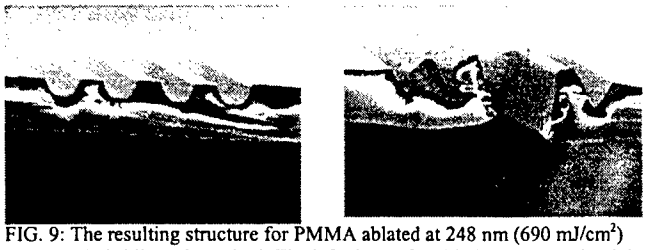


FIG. 9: The resulting structure for PMMA ablated at 248 nm (690 mJ/cm^2) with the 'hybrid' mask method. The left picture for ablation at 5 Hz, the right one for ablation at 50 Hz.

However, at these energies, if one increases the frequency as well, deformation of the groove structure can occur, as we observed for PMMA at 248 nm (FIG 9, right).

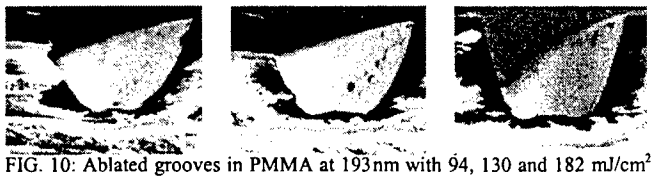


FIG. 10: Ablated grooves in PMMA at 193nm with 94, 130 and 182 mJ/cm^2 respectively.

- Influence of the fabrication method.

We varied the number of times that the mask scans over the substrate, keeping the total number of pulses fired in the

grooves constant. FIG. 11 summarized the results: for the aperture method, more passes (up to 5) speed up the ablation process; for the hybrid mask approach, the gain in speed by increasing the number of scans is rather little. This can be explained by the steepness of the exposed surface, which undergoes ablation: in the hybrid mask method this angle is much smaller than in the case of the moving aperture. Thus the energy density at this surface remains higher and ablation still takes place without much loss of speed.

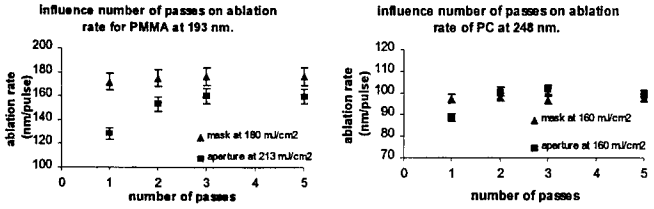


FIG 11: Influence of the number of passes to fabricate the grooves.

Based on these results, we chose PMMA as substrate material and used the ArF wavelength for the fabrication of the grooves with the 'hybrid mask' method (FIG. 12). In this way we were able to produce the full alignment structure of 8 grooves each 10 mm long in only 20 minutes. The pulse frequency was 20 Hz and the energy density 270 mJ/cm^2. The resulting grooves had a wall angle of approximately 78 degrees and a bottom RMS roughness of 0.33 μm.

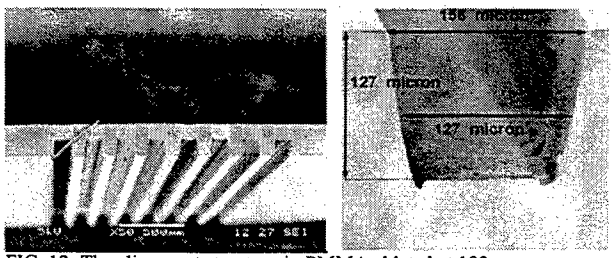


FIG. 12: The alignment structure in PMMA ablated at 193 nm.

B. Realization of the ferrule.

A 4X8 POF array (FIG. 13) was realized using POFs with a core diameter of 63μm and a cladding diameter specified at 125 μm. In order to evaluate the assembly method the position of the POF cores was measured. The precision of these positions is defined by two factors: first the position of the POFs in the grooves and second the quality of the stacking procedure. The pitch between adjacent fibres in one plate is mainly influenced by the position of the POFs in the grooves: we found an overall average of 249 μm with a standard deviation of 10 μm (FIG. 14). This value indicates that the grooves are made at an exact pitch but that the POFs themselves are not always in the right position in the groove. A large part of this error is caused by the varying POF diameter. We calculated the average Y position of a row of POFs in one plate and a standard deviation of 10 μm was found here as well.

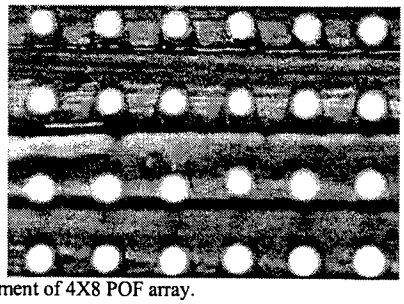


FIG. 13: Fragment of 4X8 POF array.

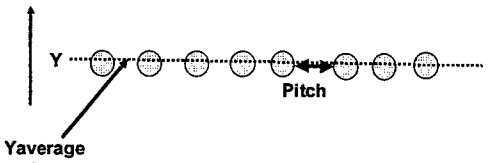


FIG. 14: Position of POFs in grooves.

In order to evaluate the stacking procedure we looked at the Y pitch: the distances between the average Y position lines of the different POF rows (FIG. 15). Values between 237 and 259 μm were found with an average of 246 μm. Part of the large spread of the results can be explained by a non-optimized gluing procedure. A similar calculation for the X direction revealed values between 242 and 256 μm with an average of 249 μm.

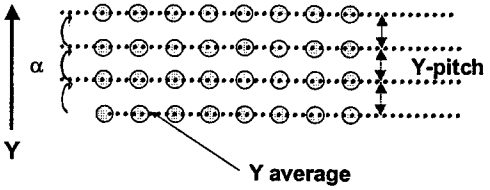


FIG. 15: Parameters related to stacking.

6. Conclusions.

We developed 2D ferrules with promising characteristics for the use in 2D connectors for parallel POF-based optical links. We investigated and evaluated several techniques for the production of these ferrules: laser ablation, hot knife cutting and 'virtual' alignment. Experiments revealed good average results but suggested that a further effort has to be performed

in order to increase the uniformity of the results, especially with respect to the alignment of the POFs in the grooves in spite of the micron accuracy of the trenches.
However, as an overall conclusion we can state that the above mentioned techniques are adequate for the assembly of prototype 3D connectors.

7. Acknowledgements.

The authors would like to thank the Flemish IWT for equipment support as well as the Belgian DWTC project IUAP-13 and IWT-ITA project VLSI-Photonics, and the European Community ESPRIT project OIIC.

8. References.

1 Xiaomei Wang, James R. Leger and Robert H. Rediker,Appl. Opt. **36**, p. 4660-4663 (1997)

2 N. A. Vainos, S. Mailis, S. Pissadakis, L. Boutsikaris, P. J. M. Parmiter, P. Dainty and T. J. Hall, Appl. Opt. **35**, p. 6304-6319 (1996)

3 S. Mihailov and S. Lazare, App. Opt. **32**, p. 6211-6218 (1993)

4 B. L. Booth, J. L. Hohman, K. B. Keating, J. E. Marchegiano and S. L. Witman, SPIE 1377 Excimer Laser Materials Processing and Beam Delivery Systems, p. 57-63 (1990)

5 M. Stiller, SPIE 1377 Excimer Laser Materials Processing and Beam Delivery Systems, p. 73-78 (1990)

Fabrication of Ce:YIG film for electric and magnetic field sensor by pulsed-laser deposition and laser-induced forward transfer (LPM2000)

Yoshiki Nakata*, Yuko Tashiro*, Tatsuo Okada*, Mitsuo Maeda*
Sadao Higuchi**, Kiyotaka Ueda*

*Kyushu University, 6-10-1 Hakozaki, Higashi-ku, Fukuoka, 812-8581 Japan
E-mail: nakata@ees.kyushu-u.ac.jp
**Central Research Institute of Electric Power Industry, Komae, Tokyo, 201-8511 Japan

Ce-doped yttrium iron garnet (Ce:YIG) thin films were deposited for the first time by pulsed-laser deposition (PLD) on gadolinium gallium garnet (GGG(111)) substrates. Well crystallized film was obtained at high substrate temperature (~ 900 ℃) and in low Ar gas pressure (~ 50 mtorr). A Faraday rotation angle was wavelength dependent, and the largest value was 4.2×10^4 deg/cm at 420 nm. The control of the charge state of Ce ion is necessary for crystallization. The deposited Ce:YIG films were transferred by laser-induced forward transfer (LIFT) process to obtain a thick film.

Keywords: laser ablation, pulsed-laser deposition, thin film, Ce:YIG, laser-induced forward transfer

1 Introduction

A surge sensor system is needed for high power line. Ce-doped yttrium iron garnet (Ce:YIG, $Y_{3-x}Ce_xFe_5O_{12}$) is a promising material as using Faraday effect [1,2]. Ce:YIG, in which a part of Y in YIG ($Y_3Fe_5O_{12}$) is substituted by Ce, shows larger Faraday rotation angle compared with YIG. For an application as small sensors, Ce:YIG has to be formed in a film with good crystallinity, high optical transmittance and large Faraday rotation angle. On the other hand, pulsed-laser deposition (PLD) is a powerful technique for the deposition of a variety of thin films, especially for oxides. YIG thin film has been fabricated by PLD with good crystallinity [3]. In this experiment, Ce:YIG was deposited on GGG(111) substrate by PLD for the first time. The crystallinity, transmittance and Faraday rotation angle of the thin films, which were deposited in various temperature and pressure, were measured. To obtain thick film for larger Faraday rotation angle, the stack deposition by laser-induced forward transfer was attempted for the first time.

2 Setup

A Ce:YIG ($Y_{3-x}Ce_xFe_5O_{12}$, x=0.6) sintered target was ablated by an KrF excimer laser with an ablation fluence of 4 J/cm^2 and an energy of 50 mJ in a chamber filled with an oxygen or Ar gas. GGG(111) substrate on a SiC heater was placed 45 mm below the target, and the temperature was monitored by a radiation thermometer. The crystallinity and the surface morphology of the deposited film was measured by a x-ray diffractometer (XRD) and an optical microscope. The transmittance was measured by a spectrophotometer.

3 Characteristics of Ce:YIG films

Fig. 1 shows the x-ray spectrum of Ce:YIG films deposited on GGG(111) substrate under different Ar

First International Symposium on Laser Precision Microfabrication, Isamu Miyamoto, Koji Sugioka, Thomas W. Sigmon, Editors, Proceedings of SPIE Vol. 4088 (2000) © 2000 SPIE · 0277-786X/00/$15.00

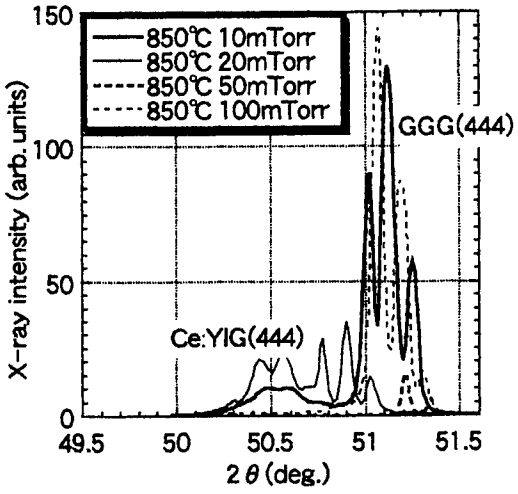


図 1: XRD spectra of Ce:YIG films deposited on GGG(111) substrate. Temperature was 850 ℃ in the deposition and the ambient gas was Ar.

gas pressure. The temperature during deposition was 850 ℃. The XRD spectra at around 2θ = 51 degree is from GGG(111) plane, and the three peaks correspond to the fine structure of the Cu-Kα x-ray spectrum. On the other hand, the peaks around 2θ = 50.5 degree is from Ce:YIG (111). The crystallized Ce:YIG films were obtained only at lower Ar gas pressure.

The crystallization of Ce:YIG thin film is summarized in Fig. 2 for different Ar gas pressure and temperature. The good crystallinity was obtained at lower Ar gas pressure and higher temperature. On the other hand, no crystallized film was obtained with the deposition under oxygen gas atmosphere with the oxygen gas pressure ranging from 10 to 400 mtorr, and between 750 and 850 ℃ temperature. This may be explained on the basis of chemical substitution. Ce atoms have to be substituted in the yttrium site with a charge state of 3+ to have a crystallinity. When the film is deposited under high Ar gas pressure or low temperature, the ablation plume is confined in a smaller volume [4,5], and Ce atoms stay for a long time in the gas phase before reaching to a substrate, and are oxidized to CeO_2 by the oxygen originated from the target. As a result, most Ce atoms incorporated into the film with a charge state of 4+. Further, when the atmospheric gas was oxygen, Ce atoms were easily oxidized, therefore no crystallization was obtained.

Fig. 3 shows the transmittance spectrum of the

mTorr / ℃	Vacuum	10	20	50	100	200
900	—	—	◎	◎	○	○
850	—	◎	◎	×	×	—
800	◎	×	×	Crystallized ◀		Amorphous ▶
750	×	×	—	◎	○	×

図 2: Summary of crystallinity of Ce:YIG films deposited on GGG(111) substrate deposited in Ar ambient gas.

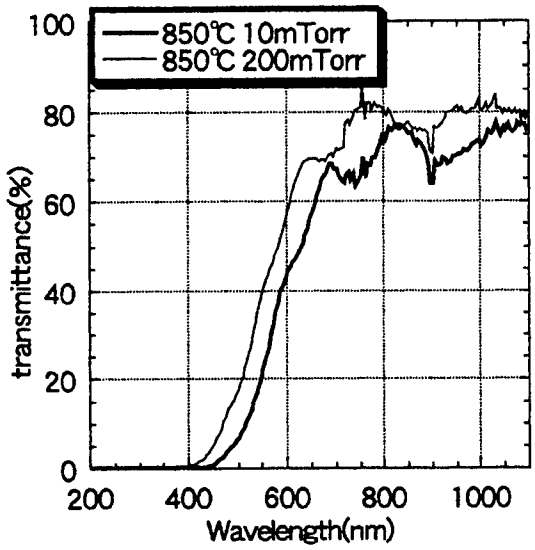


図 3: Transmittance spectra of Ce:YIG thin films deposited at 850 ℃.

Ce:YIG film deposited at different Ar gas pressure. The cut off wavelength where the transmission reduced to zero, shifted to the longer side at lower gas pressure. The color of the film deposited at 10 mtorr of Ar was dark green, and at 200 mtorr was brown. To our experience, all dark green films were crystallized.

Fig. 4 shows the Faraday rotation angle as a function of wavelength at an applied magnetic field of 3000 Oe. The rotation angle was very small for a noncrystallized film deposited at 850 ℃ and at the Ar gas pressure of 50 mtorr. In crystallized film, the rotation angle positively peaked at about 430 nm, and became negative at wavelength longer than 850 nm. Similar behavior has been reported with the film deposited by rf sputtering [7]. The maximum value was 4.2 degree/μm at 420 nm with the film deposited at 900 ℃ and an Ar gas pressure of 20 mtorr. No apparent Faraday rotation was observed for the films

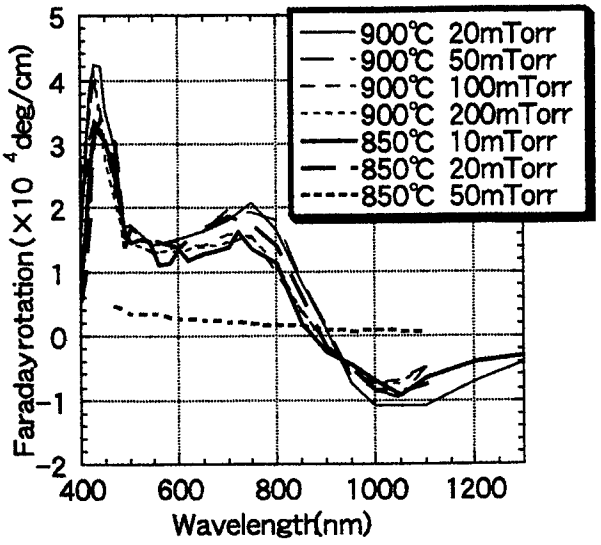


図 4: Faraday rotation angles of Ce:YIG thin films.

deposited at lower than 800 ℃. Therefore, to enlarge the Faraday rotation angle, it is important to control the crystallinity, in other words to control the charge state of Ce. It may be possible to monitor the charge state in the PLD process by laser-induced fluorescence (LIF) or two-dimensional laser-induced fluorescence (2D-LIF) [4-6], in which the behavior of Ce, CeO and CeO_2 are monitored.

4 Fabrication of film by LIFT

Laser-induced forward transfer (LIFT) is a technique for the fabrication of thin film, particularly spatially localized thin film. In the past investigations, micron-sized single stratum thin films has been deposited by LIFT [8-10]. For the electro-optic device application, thick film is needed to obtain a large Faraday rotation angle. In this investigation, the stacking of Ce:YIG thin film by LIFT was firstly tried.

Fig. 5 shows the experimental setup for LIFT. Two Ce:YIG thin film, deposited on GGG at 950 ℃ and at Ar pressure of 200 mtorr for 4 hours by conventional PLD, were used. The color of the films was between dark green and brown, so they were crystallized in part. The donor film was ablated from the backside by a second-harmonic wave of YAG (532nm) through an objective lens. The ablation energy was 100 mJ, and the fluence was about 6 J/cm^2 on the GGG substrate of the donor film. The ejected film was deposited on a acceptor film faced to the donor film. The deposition was done in vacuum condition, and with 5 shots of ablation.

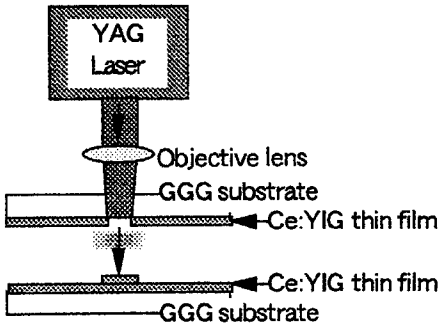


図 5: Setup for LIFT.

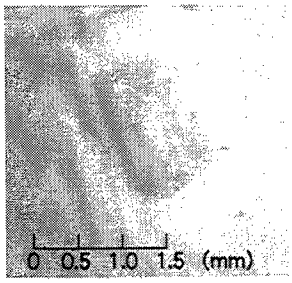


図 6: Surface of the deposited film.

Fig. 6 shows the picture of the deposited film observed with an optical microscope and CCD camera. In visual, the deposited film seems silver and different from that of donor film, which shows the difference of crystallinity or composition. On the other hand, the ablated region on the donor film is clear. The deposited region is well confined, not splashed. No ejection of the donor film was obtained with one shot of ablation laser at 100 mJ. On the other hand, at 170 mJ the film was ejected from donor film but deposition was hardly obtained on the acceptor film.

Fig. 7 shows the transmittance of the acceptor film, and that of the deposited region. The transmittance decreased with the deposition by LIFT. This is because of the increase of the thickness, and the change of the composition of the deposited film.

Fig. 8 shows the x-ray spectra of the acceptor and deposited films. In both, the broad spectra from Ce:YIG are seen. There is some difference at around 2θ=50.5 degree, and this shows some decrease in crystallinity of the deposited film. The ablation fluence, the wavelength of the ablation laser in LIFT should be optimized to obtain a well crystallized stacking film.

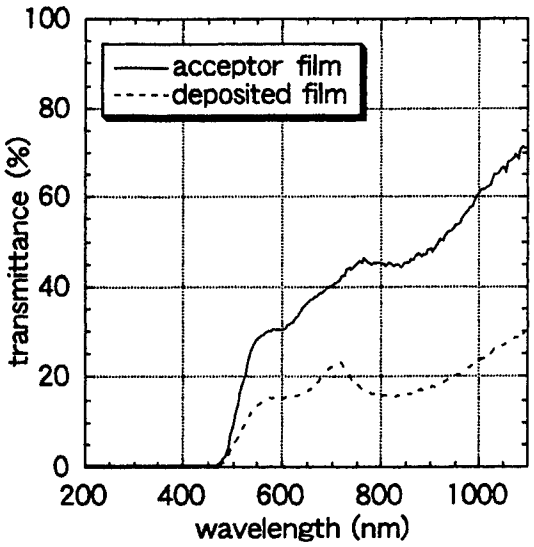


図 7: Transmittance spectra of Ce:YIG thin films of acceptor film and made by LIFT.

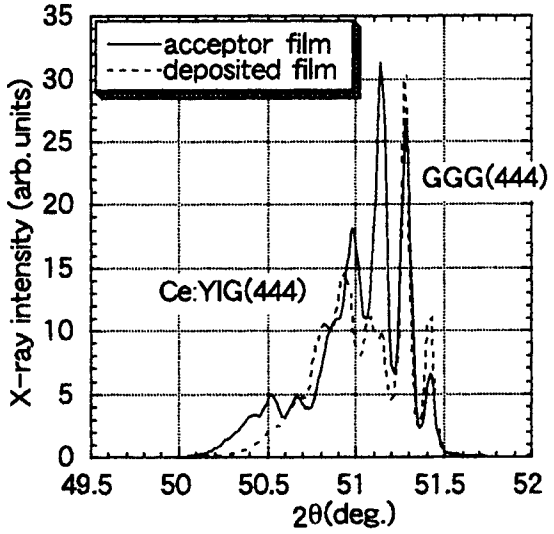


図 8: XRD spectra of Ce:YIG films of acceptor film and the film deposited by LIFT.

5 Conclusion

For an electro-optic sensor, Ce:YIG films were successfully deposited on GGG(111) by PLD for the first time. The charge state of Ce is needed to be 3+ for crystallization, and crystallization is needed for large Faraday rotation angle. This can be achieved by using Ar gas instead of oxygen gas in PLD process. To monitor the charge state of the Ce atoms, LIF and 2D-LIF will be useful. LIFT was attempted for the first time to stack the Ce:YIG film, and partially crystallized film was obtained.

Acknowledgement

The SEM observation was performed at the Engineering Branch of the Center of Advance Instrumental Analysis of Kyushu university.

References

[1] G. Diankov, V. Tassev and M. Gospodinov: Proc. SPIE - Int. Soc. Opt. Eng. **3052**, (1996) 390.

[2] T. Bosselmann: Proc. SPIE - Int. Soc. Opt. Eng. **3099**, (1997) 305.

[3] P.C. Dorsey, S.E. Bushnell, R.G. Seed and C. Vitoria: J. Appl. Phys. **74**, (1993) 1242.

[4] Y. Nakata, G. Soumagne, T. Okada and M. Maeda: Appl. Surf. Sci. **127-129**, (1998) 650.

[5] Y. Nakata, H. Kaibara, T. Okada and M. Maeda: J. Appl. Phys. **80**, (1996) 2458.

[6] J. Muramoto, Y. Nakata, T. Okada and M. Maeda: Appl. Surf. Sci. **127-129**, (1998) 373.

[7] T. Shintaku, A. Tate and S. Mino: Appl. Phys. Lett. **71**, (1997) 1640.

[8] Y. Nakata, T. Okada: Appl. Phys. A **69**, (1999) S275.

[9] T. Okada, Y. Nakata, J. Muramoto and M. Maeda: Proc. SPIE - Laser Applications in Microelectronic and optoelectronic Manufacturing III **3274**, (1998) 246.

[10] J. Bohandy, B.F. Kim, F.J. Adrian: J. Appl. Phys. **60**, (1986) 1538.

Electroosmotic Flow Control in Micro Channels Produced by Scanning Excimer Laser Ablation

Frank WAGNER and Patrik HOFFMANN

Institute of Applied Optics, BM, Swiss Federal Institute of Technology Lausanne, CH – 1015 Lausanne EPFL, Switzerland
E-mail: Patrik.Hoffmann@epfl.ch

Excimer laser ablation of a scanned substrate can be used for prototyping of lab-on-a-chip microfluidic channels [1]. Here, the relationship between the wetting properties of the channels and the irradiation conditions is described. The wetting properties are quantified by electroosmotic flow measurements in channels, produced with different conditions of scanning ablation. The observed variations can be explained in terms of a competition between a direct and an indirect redeposition pathway for the debris.

Keywords: Micro machining, surface modification, microfluidics, electroosmotic flow.

1. Introduction

Excimer laser ablation of polymers is well known to produce high quality structures in nearly all polymers, as it was first described in 1982 [2]. As mentioned recently by Rossier *et al.* [3], a drastic increase in hydrophilicity of ablated micro channels in poly(ethylene terephthalate) (PET) can be achieved by scanning the substrate. This makes excimer laser ablation a versatile tool for rapid prototyping of micro fluidic systems, as for example lab-on-a-chip devices.

In such devices, a sample solution (usually aqueous) is injected, pumped, separated and eventually analyzed by electrochemical means. Channels for these applications need to meet special requirements in their surface properties in order to optimize the efficiency of the final device. We have already investigated in detail the influence of the irradiation conditions on the surface structure of the channel floor and of the ramps, forming at the beginning and at the end of the channels [4]. We also observed an enhanced redeposition of debris in the channel, depending on the conditions during the ablation [5].

In this paper, we show how the scanning ablation parameters influence the electroosmotic flow in PET micro channels. Further we propose an explanation for the observed effect.

2. Scanning ablation

In order to produce micro channels, which are longer than the beam width on the sample, one can imagine two modes of fabrication. (i) One can drill one rectangular hole using a common mask projection technique, stop the laser, move the substrate, drill the next hole in contact with the first one and so on. This mode of channel fabrication will be called "static ablation". (ii) Alternatively, the substrate can be moved with the appropriate speed v while it is irradiated by the laser, in order to produce channels of the required depth d_{tot}. Further on, we will refer to this method as "scanning ablation".

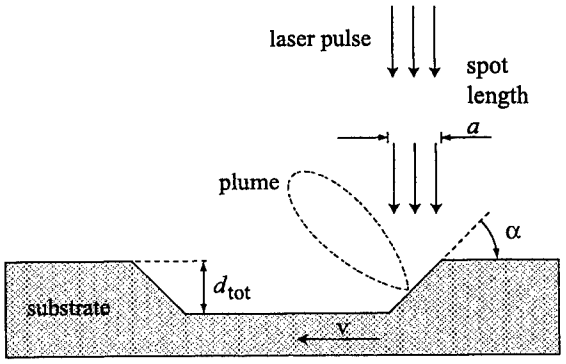


Fig. 1 Schematic diagram showing the parameters of scanning ablation

When using scanning ablation, ramps form at the beginning and at the end of the channels during the fabrication. Only the end ramp is irradiated. The angle α, that it forms with the original sample surface, is given by the depth of the channel d_{tot} and the length of the irradiated spot a in the scanning direction (Fig. 1), i.e. $\alpha = \arctan(d_{tot}/a)$. The depth of the channel can be expressed by $d_{tot} = n \times h(\Phi)$, where n is the number of pulses used in static ablation for one hole, and $h(\Phi)$ the ablated thickness per pulse at fluence Φ. Given the pulse repetition rate f, n and a, the appropriate scan speed v can be derived: $v = f \times a / n$.

First International Symposium on Laser Precision Microfabrication, Isamu Miyamoto, Koji Sugioka, Thomas W. Sigmon, Editors, Proceedings of SPIE Vol. 4088 (2000) © 2000 SPIE · 0277-786X/00/$15.00

3. Experimental

3.1 Substrates and laser

Two types of substrates were used: (i) Biaxially stretched poly(ethylene terephthalate) (PET) foil, in which one stretching direction dominated over the other (thickness 100 μm, Melinex S, ICI). (ii) Amorphous unstretched PET (thickness 500 μm, Mylar, Goodfellow).

These two substrates were irradiated with a standard ArF excimer laser (193 nm, 20 ns, LPX 205, Lambda-Physik) as already described [4].

3.2 Channel production

We used n = 200 pulses and a width of 40 μm for all channels. The channel length between the two reservoirs was 15 mm. The reservoirs were drilled by static laser ablation. In both substrates, we produced 38 μm deep channels by using different spot lengths a and scanning speeds v. This resulted in a change of the ramp angle α during the ablation (Table 1).

Table 1 Corresponding values for the spot length a (μm) and the ramp angle α (degrees).

a (μm)	1000	500	200	100	50
α (°)	2.0	4.3	11	22	42

For the stretched samples we used holes of 1000 μm times 40 μm that we drilled completely through the sample as reservoirs. After channel and reservoir fabrication by laser ablation, the samples were laminated with a poly(ethylene) (PE) on PET lamination at 130°C in order to close them.

In the unstretched substrates, the use of through-drilled holes led to insufficient quality of the electroosmotic measurement data, because the reservoir volume / channel volume ratio became too high. Therefore, for this kind of substrate, the channels were first drilled, then laminated and finally the lamination was opened by the laser. A drop of solution placed on the openings of the lamination then represents the reservoir. Measurements (< 3min.) were carried out directly after placing the drops, so that concentration changes due to solvent evaporation can be neglected.

In the stretched samples, the static structure, developed perpendicularly to the main stretching direction [6]. Its amplitude and period are about 3 μm. We produced two series of channels in the stretched substrate; in one series, we aligned the structure with the channel direction ("longitudinal" series) and, in the other series, the structure was perpendicular to the channel direction ("transversal" series). As recently described, the static structure transforms to the scanning structure for $\alpha \geq 11°$ [5]. This leads to a smoother channel surface in the micron range. As expected, the channels in the unstretched substrate did not show any structure in the micron range.

In all three series, the debris contribution became important for $\alpha \geq 22°$ and added nanometer scale roughness and porosity to the channels [5].

3.3 Electroosmotic flow measurement

The electroosmotic flow was measured using Huang's current monitoring method [7]. We placed drops (10 μl) of phosphate buffer (pH = 7.2, Sigma) in each reservoir. The total salt concentration of the buffer in the two reservoirs differed slightly (10 mMol/l, 8 mMol/l). While applying the electric field that induced the electroosmotic flow, the resistivity of the channel was monitored by measuring the electrical current. The resistivity of the channel at a given time depends on the percentage of the channel filled with the low resistivity (high concentration) buffer and the percentage of the channel filled with the high resistivity (low concentration) buffer. The measurement of the channel resistivity as a function of time thus indicates the motion of the interface formed by the two liquids.

For all measurements, we applied a driving electrical field of 20 kV/m and all cited literature values are converted to this value for better comparison. The measured electrical current was about 4 μA and hence heating effects can be neglected.

4. Results and discussion

4.1 General observations

The electroosmotic flow velocity in the channels varied as a function of the ramp angle by about 25% in all three series (Fig. 2). In almost all cases the maximum flow velocity was reached at $\alpha = 4.3°$ and was approximately as high as the value for fused silica capillaries (10×10^{-4} m/s [7]). All the data represented in Fig. 2 resulted from laminated channels. This PE-lamination is identical for all channels and thus smoothes the flow velocity data. This means that the observed variations are lower than the variations that would be observed if all four walls of the channels were ablated surfaces.

No significant differences could be found between the longitudinal and the transversal series. In other words, the orientation of the micrometric structure has no measurable influence on the electroosmotic flow in our experiments.

Comparing our values ($\alpha = 2°$) with the value published by Roberts *et al.* [8], we observe in absence of the micrometric structure a slightly faster electroosmotic flow. In more detail the values of the longitudinal and transversal series of 8.3×10^{-4} m/s and 8.5×10^{-4} m/s respectively are in excellent agreement with the value of Roberts *et al.* (8.4×10^{-4} m/s), whereas the value of the series without structure of 9.9×10^{-4} m/s is 18% higher. However, in order to confirm this value, further investigations are necessary.

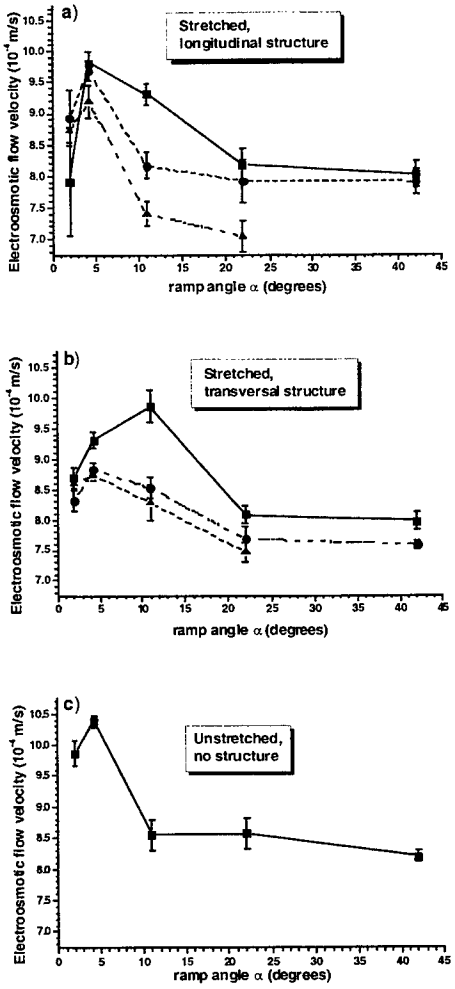


Fig. 2 Electroosmotic flow velocity (@ 20 kV/m) as a function of the ramp angle α. Figures **a** and **b** show the series produced in the stretched substrate. Figure **c** shows the series produced in the unstretched substrate. (For further details see experimental section.) Different curves in one graph correspond to channels produced or analyzed on different days. The standard errors for 3 pairs of drops and 4 measurements per drop pair in the same channel are indicated.

4.2 Explication of the maximum

The maximum flow velocity, observed in all substrates around $\alpha = 4.3°$, can be interpreted in terms of variations in the ζ-potential of the channels. As we always used the same buffer, variations in the ζ-potential are directly related to variations in the surface charges or polarity of the channel surfaces. These surface properties also determine the water wetting behavior of the polymer and of the ablated polymer.

Lazare *et al.* reported a decreasing O/C-ratio in XPS measurements after static ablation of PET at 193nm wavelength [9]. This is in good agreement with their observation that the water contact angle increases, from 68° on unirradiated PET to 105° on the ablated surface. This data indicates clearly that PET has a low ζ-potential compared to clean fused silica, that is wetted by water (contact angle = 0°, [10]), and that static ablation further decreases the ζ-potential.

However, the ζ-potential of channels produced by scanning ablation is determined by the debris. The debris can be more or less charged or composed by polar reaction products, which are formed during the collisions of the ejected ablation products with oxygen in air [11].

In the case of static ablation, collisions with the ambient gas are the main reasons for redeposition of the debris on the substrate [12]. The left part of Fig. 3 shows water condensed by breathing out near a statically ablated rectangular hole. It impressively shows how the debris, which is caused by this *indirect* redeposition mechanism, renders the unwettable native PET (zone A) wettable (zone B). We see that zone B is covered by a thin film of water indicating a high-energy surface as for example fused silica. The form of the outer border of the wetted region in Fig. 3 corresponds very well to the form of the debris pattern, as also observed after excimer laser ablation of polyimide (PI)

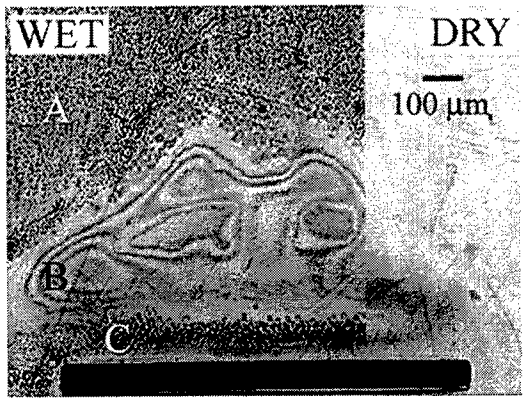


Fig. 3 Optical microscope image of water condensed by breathing out near a statically ablated surface in PET (200 pulses, 1000 mJ/cm^2, depth 38 µm). **Zone A:** non-wetting native PET. The dark dots are water droplets. **Zone B:** wetted surface because of redeposition by collision; we see a thin film of water. **Zone C:** non-wetting surface because of PLD-like direct redeposition. We see once more droplets of water. On the right side (dry image) we see only the main debris hill.

[13].

However, in scanning excimer laser ablation with high ramp angles we need to consider a second deposition pathway for the debris in the channels. This is a kind of "self-PLD" (PLD – pulsed laser deposition), where the substrate (channel floor) is approaching more and more the target (end ramp) for higher ramp angles [5]. Obviously, the angular density distribution in our case will not obey the simple $\cos^n(\theta)$-relation [14], as it does in PLD. The two main reasons for this are (i) the presence of the air and (ii) the irradiation of a relatively large rectangular surface, i.e. the inclined ramp. Nevertheless, it is reasonable to assume that inclining the irradiated surface with respect to the channel

floor strongly enhances the direct deposition of ablation products on the channel floor. This means that this kind of debris deposits on the channel floor without collisions with the oxygen-containing atmosphere. In consequence, this kind of debris will have a low ζ-potential.

For static ablation we can also observe in Fig. 3 (left part) a small region (zone C) directly at the border of the ablated surface where this kind of debris determines the surface properties, and the water cannot wet the surface. The comparison with the dry image shows that the borderline between zone B and C crosses the middle of the main debris hill, which has a homogenous surface topography as measured by AFM [15]. Thus, the wettability contrast between zones B and C, as described above, is due to a difference in chemical composition of the surfaces. In consequence, the non-wetting behavior of zone C cannot be attributed to a roughness effect [10].

Though, the maximum electroosmotic flow velocity appears at the ramp angle where we have the most redeposition by collision and still negligible PLD-like redeposition in the channel. The increase in electroosmotic flow velocity with increasing the ramp angle from $\alpha = 2.0°$ to $\alpha = 4.3°$, is caused by a change of the indirectly redeposited debris pattern. Miotello *et al.* have shown that the gas dynamic effects tend to result in a debris pattern, that is rotated with respect to the ablated shape [13]. Thus, little debris is deposited near to the short side of an ablated rectangular surface (Fig. 3). This effect will be more important for the spot of 40 μm × 1000 μm ($\alpha = 2.0°$) than for 40 μm × 500 μm ($\alpha = 4.3°$). Thus the usage of the 500 μm long spot enhances indirect redeposition at the short side of the rectangle, i.e. in the channel.

For $\alpha \geq 11°$, the PLD-like redeposition process becomes more and more important. The debris with low ζ-potential, deposited by this mechanism thus decreases the electroosmotic flow velocity.

5. Conclusions and Outlook

We showed that the electroosmotic flow in excimer laser ablated micro fluidic channels in PET varies with the ramp angle α. We obtained in stretched and unstretched PET-foils, i.e. with and without micrometric structures, a maximum flow velocity at a ramp angle of $\alpha = 4.3°$. The flow velocity, at this maximum, is comparable to the electroosmotic flow in fused silica.

The existence of the maximum flow velocity at $\alpha = 4.3°$ is attributed to the competition of two different debris redeposition mechanisms. The indirect redeposition occurs because of collisions of the ejected material with the surrounding gas molecules and deposits material with a high ζ-potential. The direct redeposition is a kind of PLD-mechanism. A part of the ablated material is directly ejected in the direction of the channel floor and forms material with a low ζ-potential on it. Direct redeposition becomes important at $\alpha = 11°$ and is dominant at $\alpha \geq 22°$. The existence of these two redeposition mechanisms was pinpointed by the water wetting experiment of the surroundings of a statically ablated rectangle in PET.

Finally, all electroosmotic flow velocities were measured in channels with a PE on PET lamination. This means that about a quarter of the channel walls is identical in all channels. Thus the variations in the ζ-potential of the ablated surfaces are higher than 25%. The ζ-potential values, of ablated surface and lamination, will be determined in the near future, by applying the formula of Andreev *et al.* [16].

6. Acknowledgements

This work was done in collaboration with the Laboratory of Electrochemistry of the Swiss Federal Institute of Technology Lausanne (EPFL). Especially we acknowledge François Bianchi for installing the electroosmosis setup and valuable discussions on the subject. Our thanks also go to the Swiss Federal Institute of Technology Lausanne (EPFL) for funding this work.

References

[1] J.S. Rossier, M.A. Roberts, R. Ferrigno and H.H. Girault: Anal. Chem., **71**, (1999), 4294-4299.
[2] Y. Kawamura, K. Toyoda and S. Namba: Appl. Phys. Lett., **40**, (1982), 374-375.
[3] J.S. Rossier, P. Bercier, A. Schwarz, S. Loridant and H.H. Girault: Langmuir, **15**, (1999), 5173 - 5178.
[4] F. Wagner and P. Hoffmann: Appl. Surf. Sci., **154-155**, (2000), 627-632.
[5] F. Wagner and P. Hoffmann: Appl. Phys. A, **69**, (1999), S841-S844.
[6] E. Arenholz, V. Svorcik, T. Kefer, J. Heitz and D. Bäuerle: Appl. Phys. A, **53**, (1991), 330.
[7] X. Huang, M.J. Gordon and R.N. Zare: Anal. Chem., **60**, (1988), 1837-1838.
[8] M.A. Roberts, J.S. Rossier, P. Bercier and H. Girault: Anal. Chem., **69**, (1997), 2035.
[9] S. Lazare and R. Srinivasan: J. Phys. Chem., **90**, (1986), 2124-2131.
[10] F.M. Fowkes: *"Contact Angle, Wettability, and Adhesion"* (American Chemical Society, Washington D.C., 1964).
[11] H. Niino and A. Yabe: Appl. Phys. Lett., **60**, (1992), 2697.
[12] S. Küper and J. Brannon: Appl. Phys. Lett., **60**, (1992), 1633.
[13] A. Miotello, R. Kelly, B. Braren and C.E. Otis: Appl. Phys. Lett., **61**, (1992), 2784.
[14] S. Lazare and V. Granier: Chem. Phys. Lett., **168**, (1990), 593.
[15] F. Wagner and P. Hoffmann: to be published, (2000).
[16] V.P. Andreev, S.G. Dubrovsky and Y.V. Stepanov: J. Micro. Sep., **9**, (1997), 443 - 450.

Three Dimensional Micro-Assembling Technique Applying Laser Trapping

Daisuke SAWAKI* , Junich IKENO** , Osamu HORIUCHI*** , Toshio KASAI**

*Graduate school, Toyohashi University of Technology, 1-1 tenpaku-cho, Toyohashi, Aichi, 441-8580, Japan
E-mail: sawaki@premac.tutpse.tut.ac.jp
**Saitama University, 255 Shimo-Okubo, Urawa, Saitama, 338-8570, Japan
***Toyohashi University of Technology

A new manipulation technique using Q-Switched laser beam was developed in this research. By using which, we could trap a fine particle in the air with relatively lower laser output. In order to clarify the possibility of the application of this method in micro-machining, the assembly experiments were conducted and the experimental results showed that the three dimensional microstructure from fine particles can be realized by this technique.

1. Introduction

In recent years, the realization of micro-machine and micro-device with elements having various functions integrated becomes more and more necessary. If a new micro-machining technique which can manufacture material and shape at the same time is developed, the highly functional parts with less space can be expected. In this research, a new concept is considered by arranging the fine particles in three dimension according to the design of material and shape of the parts, and then sintering to strength the structure. However, to fulfill this task, the three dimension manipulation and micro-assembly technique of fine particles is indispensable. The laser trapping technique was suggested to manipulate fine particles in water with optical radiation pressure by Ashkin in 1970[1]. Since the manipulation is non-contact, the following advantages can be obtained: 1) Complex manipulation with high degree of freedom. 2) High speed manipulation without vibration. 3) Manipulation of multiple particles at the same time. On the other hand, the manipulation is considered difficult in the air because the surface tension is very big between the base plate and fine particles. However, considering the environment of micro-machining, the manipulation in the air is desirable to meet the requirements of high degree of freedom and stability. Hereby, this research proposed a new method on trapping the fine particles in the air and developed a new micro-machining technique by assembling three dimensional micro-structure from fine particles with laser beam.

2. Experiments on Trap of Fine Particles with Laser Beam

2.1 Trapping principle of fine particles with optical radiation pressure

The generation of optical radiation pressure can be explained by geometrical optics in case the optical wavelength is shorter than the diameter of fine particle to be trapped[2]. The generation of radiation pressure with an optical beam going through a fine particle is shown in **Figure 1**. When beam "a" goes into a fine particles, an optical radiation pressure " Fat" happens at the orthogonal direction of the interface. Then, when the beam goes out from the fine particle, the optical radiation pressure "Fa0" happens. The total force is "Fa" . As for the beam "b" , force "Fb" happens. The total force "F" of "Fa" and "Fb" is in the direction which always makes the center of fine particle according to the focal point of laser beam. Hence, the trapping of fine particles with laser light becomes possible. Shown in

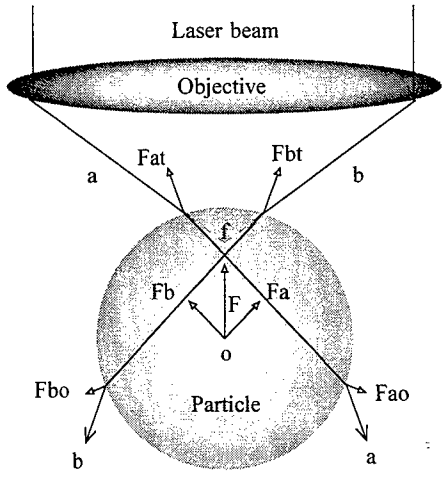


Fig.1 Qualitative view of particle trapping

First International Symposium on Laser Precision Microfabrication, Isamu Miyamoto, Koji Sugioka, Thomas W. Sigmon, Editors, Proceedings of SPIE Vol. 4088 (2000) © 2000 SPIE · 0277-786X/00/$15.00

Table 1, the optical radiation pressure acting on silica fine particles caused by YAG laser light were calculated. Silica fine particles are transparent for YAG laser light, and laser light irritates from the upper of fine particles which are put on the optical axis. In case the position of focal point is from the upper part of fine particles to the lower part of particles, the calculation result is shown in **Figure 2**. Axis Z illustrates the position of focal point (Z=r/R, r means the distance between center of particle and focal point , R means the radius of particle), where +1.0 and -1.0 mean the top and bottom of fine particles respectively. Axis X shows the force acted on silica fine particles with the gravity force included. On this axis, the minus value means the force points downwards and the plus value means the force points upwards. When the output of laser is 14mW and focal point is on the upper part of fine particle, the total force from two directions offsets. When focal point is set at Z=0.75 with an output of 20mW, it is calculated that silica fine particles can be levitate into the air with optical radiation force.

2.2 Experimental apparatus

The configuration of experimental system is illustrated in **Figure 3**, It is mainly consisted of three parts, laser oscillator, beam scanner and light accumulating part. The details of each are as follows:

1)Q-switched YAG laser (Lee Laser 818TQ, λ=1.06μm, maximum output 18W, beam Mode TEM$_{00}$) is applied in Laser oscillator.

2)Laser beam scanning part is constructed by two pieces of galvano mirror to realize horizontal laser scanning on X-Y surface which is orthogonal to optical axis. It is possible to scan the laser beam focal pointed by objective with high speed and at a resolution of 0.17μm.

3)Microscope is applied in the light accumulated part (Nikon X2-TI-EPI), YAG laser beam irradiates into the microscope, with the optical axis being the same as that of illumination. The bright field objective (CF IC EPI Plan×50) is utilized. The aberration between visible light and YAG laser light has been removed through modification. The fine particles are observed in three-dimension space with CCD cameras arranged on the upper and side locations.

Table 1 Conditions of calculation

YAG laser power	~20mW
Polarization	Circularly polarized light
Objective	N.A.=0.8
Particle	SiO_2(φ8.0μm)
Refractive index	n=1.4
Enviroment	Air
Refractive index	n=1.0

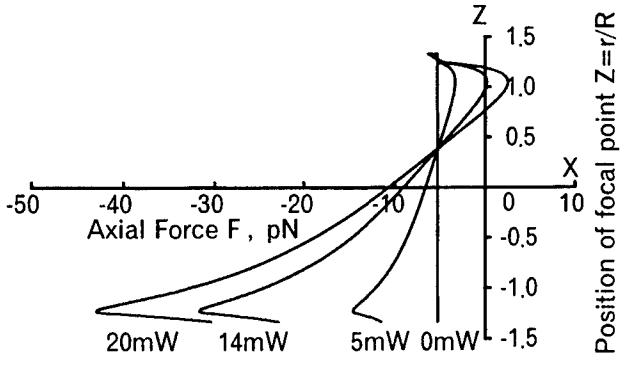


Fig.2 Relation between axial force and focal point

2.3 Experiments on trap of fine particles

The trapping experiments were conducted in the air. The experimental results showed the output of laser must be more than 2W, which is 2 digits larger than that of calculation. It is supposed that the reason lies on the attractive force between the base plate and the fine particle caused by the moisture in the air. To overcome this force instantly, it is necessary to raise the peak output of laser light. Hereby the experiment was conducted by using Q-switch, whose condition is shown in **Table 2**. The focal point was set at the upper part of the fine particle. The experimental result showed that it is possible to trap a fine particle at a low output under 120mW. The trapped fine particle is shown in **Figure 4(a)**, the fine particle was trapped in three dimension for the first time. And, when the focal point is set at the base plate, it can also be observed that the fine particle, shown in **Figure 4(b)**, was levitated about 1μm high. However, according to the optical radiation theory, the particle should be pushed onto the base plate when the focal point is set lower than the center of silica fine particle. Although the mechanism has not been clarified by now, this experiment confirmed the fine particles in the air can be manipulated

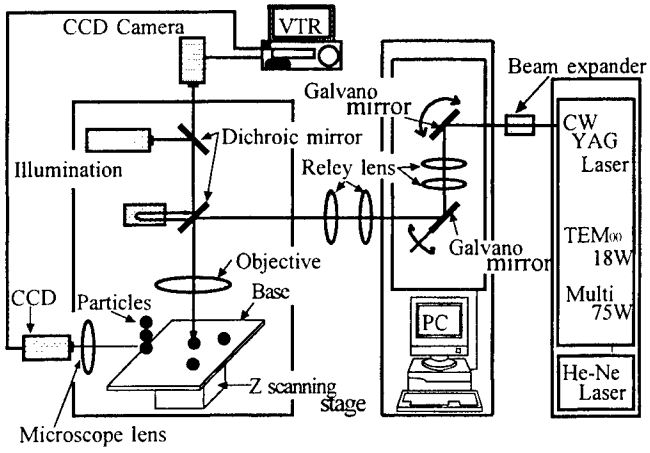


Fig.3 Configuration of experimental system

by laser beam, which makes the assembly of micro-structure by laser beam possible.

3. Assembly of Three Dimensional Micro-Structure

3.1 Principle of assembly technique

The principle of assembly method is shown in **Figure 5**. Laser light is irradiated on a fine particle, shown in **Figure 5(a)**, to detach the fine particle from the base plate. Then Z stage is lowered to levitate fine particle to a certain assembly height in **Figure 5(b)**. **Figure 5(c)** shows that the fine particle is moved horizontally. Finally, in **Figure 5(d)**, the stage is raised to complete the assembly. According to this procedure, the assembly of three dimension micro-structure can be conducted.

3.2 Experiment of assembly in vertical direction

A series of consecutive photos of experiments are shown in **Figure 6(a)-(d)**. Silica fine particle (2) trapped in the air is shown in **Figure 6(a)**. In **Figure 6(b)**, the stage was lowered and particle (2) was transported to the position higher than particle(1) by vertical manipulation. **Figure 6(c)** illustrates the transportation of particle (2) to the top of (1) by horizontal manipulation. And finally, in **Figure 6(d)**, the stage was raised until two particles contacted. With the same procedure repeated, particle (3) and (4) were assembled in **Figure 6(e)**. Therefore a vertical assembly was completed.

3.3 Experiment of assembly in horizontal direction

If two fine particles adsorb each other by the surface tension force, the assembly in horizontal direction may be also possible. Hereby, the assembly experiments in horizontal direction were conducted, shown in **Figure 7(a)-(e)**. **Figure 7(a)** and **(b)** show particle (2) was assembled to the side of vertical assembled silica fine particle (1). Similarly, silica (3) was assembled. Furthermore, in **Figure 7(d)** and **(e)**, fine particle (4) was manipulated under (2) and (3). At this time, although part of the laser beam is disturbed by particle (2) and (3), manipulation still remains possible. Hence the more complex formation can be expected.

Table 2 Experimental conditions

Laser power	120mW
Q-sw repetition rate	35kHz
Objective	N.A.=0.8
Particle	SiO_2(ϕ 8.5μm)
Refractive index	n=1.4
Enviroment	Air
Refractive index	n=1.0

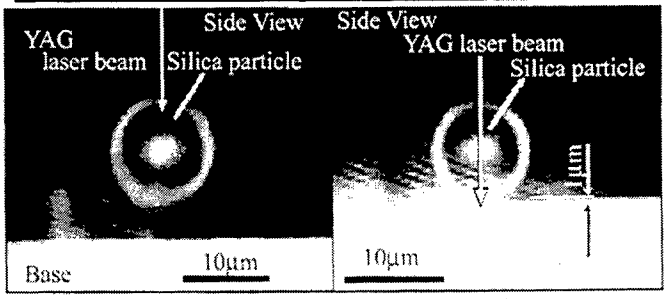


Fig.4 Trapped silica particle in the air

3.4 Assembly of micro-structure in three dimension

After the basic assembly in vertical and horizontal directions was confirmed, the micro-structure in three dimension was conducted. Shown in **Figure 8**, the tetrahedron was assembled by 220 silica fine particles. Therefore, a three dimensional micro-structure was realized through the laser trapping technique developed in this research.

4. Conclusions

The three dimensional manipulation technique of fine particles in the air and the assembly technique of micro-structure have been developed in this research. The following conclusions were obtained.

1) By using Q-switch, a fine particle can be easily trapped in the air, with an average of laser output under 120mW.
2) The fine particle was levitated 1μm high when the focal point of laser beam was set at the surface of base plate, lower than center of the particle. This phenomenon was difficult to be explained by the conventional theory.
3) The assembly of fine particles was supposed, and the assembly in vertical and horizontal direction succeeded in the experiments.

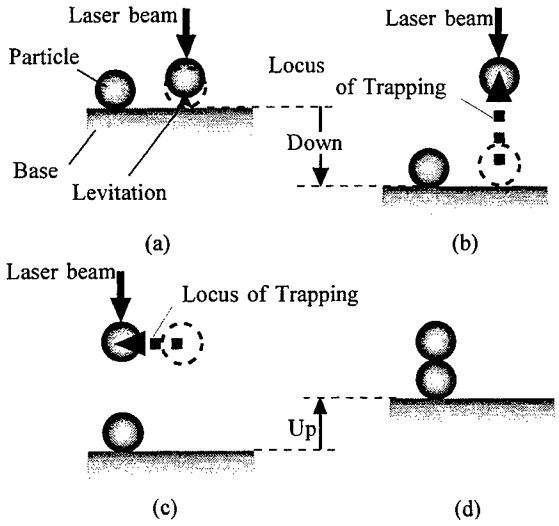
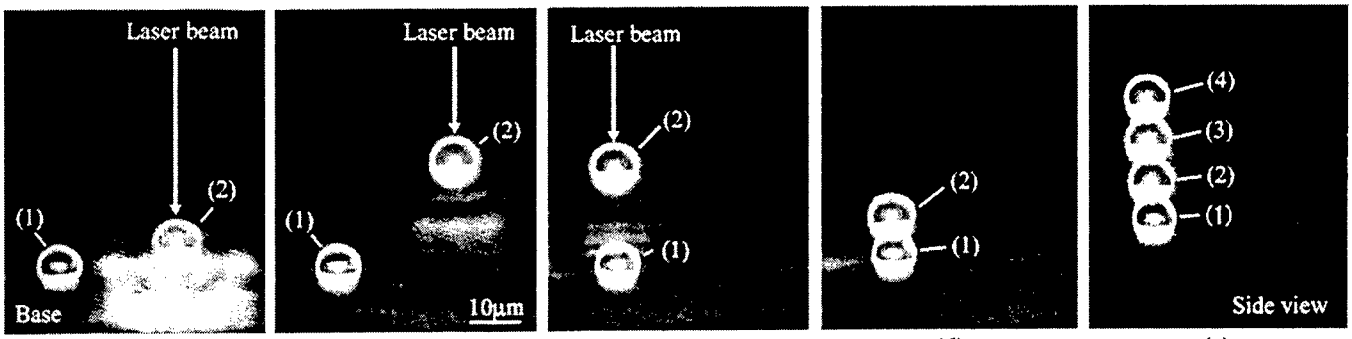
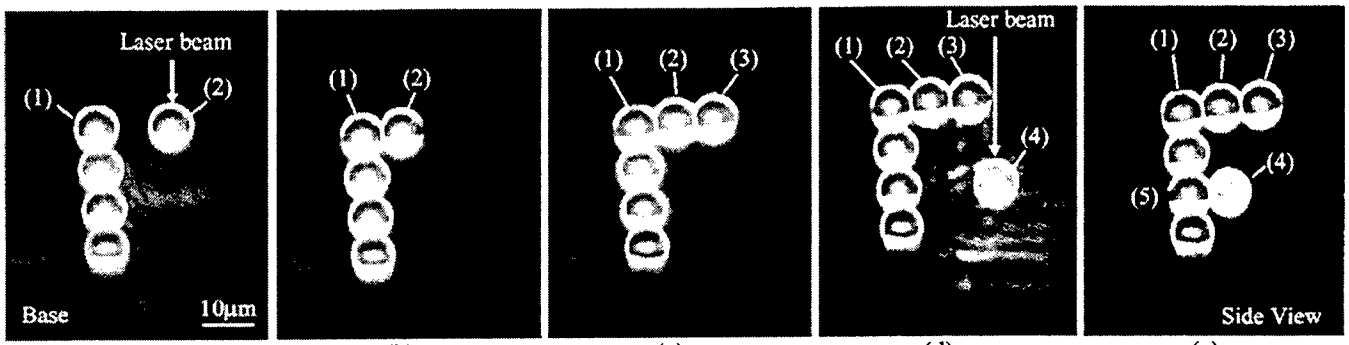


Fig.5 Procedure of micro-assembly technique by laser beam



(a) (b) (c) (d) (e)

Fig.6 Silica particles assembled vertically



(a) (b) (c) (d) (e)

Fig.7 Silica particles assembled horizontally

4) The assembly of three dimensional micro-structure is considered possible by using the technique developed in this paper.

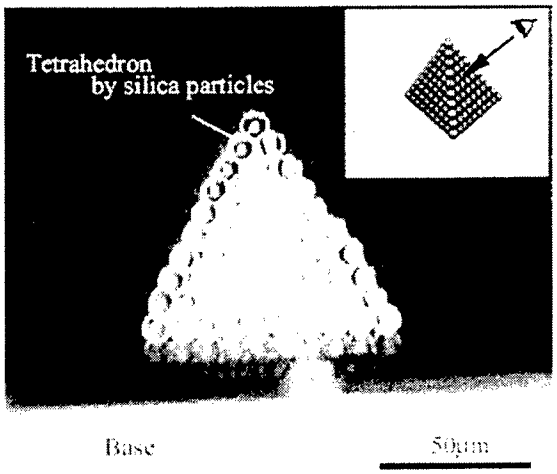


Fig.8 3-D micro-structure with a tetrahedron

-References-

1)A.Ashkin, Physical Review Letters, 24-4(1970),156.
2)A.Ashkin, Biophysical Journal, Vol.16(1992),569-582.

Advanced Laser Microfabrication of Photonic Components

Peter R. HERMAN*, Kevin P. CHEN*, Paul CORKUM, Andrei NAUMOV**, Sandy NG*, and Jie ZHANG***

**Department of Electrical and Computer Engineering, University of Toronto, 10 King's College Rd., Toronto, ON, M5S 3G4, Canada*

***Steacie Institute for Molecular Sciences, 100 Sussex Drive, Rm 2083, Ottawa, ON, K1A 0R6, Canada*

The powerful transition from electronic to photonic systems in today's internet-driven communication industry is driving the development of processes to miniaturize and integrate optical components. New processing and packaging technologies are now required that can precisely shape and assemble transparent optical components to sub-wavelength accuracy. Laser microfabrication technology is beginning to play a role here. Our groups are exploring two extremes in laser technology – ultrafast lasers and very short wavelength F_2 lasers – to microstructure optical surfaces and to profile refractive-index structures inside transparent glasses. In this paper, we compare photosensitivity responses, spatial resolution, and processing windows for the deep-ultraviolet and ultrafast laser approaches, and discuss prospects for laser printing and trimming of optical waveguide components and circuits.

Keywords: photosensitivity, refractive index, ultrafast lasers, F_2 lasers, optical waveguides

1 Introduction

High-speed optical-fiber communications and the unrelenting demand for Internet "bandwidth" are revolutionizing today's communication industry as played out by the increasing emphasis on photonics versus electronics technologies. This powerful transition is spurring industry to miniaturize and to integrate optical components into highly functional optical circuits much like the planarization and integration of electronic components on silicon or germanium wafers four decades earlier. New processing and packaging technologies are now required that can precisely shape and assemble transparent optical components to sub-wavelength accuracy. Laser microfabrication technology has a significant role to play in analogy with the wide use of lasers in lithography, trimming, repair, and inspection of today's semiconductor electronic chips. For photonics, applications are reserved only for light sources that interact strongly with transparent materials. Our groups are exploring two extreme laser approaches to shaping structures in glasses: ultrafast (UF) and deep-ultraviolet (UV) laser processing.

Past laser micromachining studies [1] by University of Toronto groups provided head-to-head comparisons of UV F_2-laser and UF (1 ps) laser approaches, and introduced a new UF-laser processing mode called *burst machining* [1,2]. Delivered fluence was key to driving strong absorption mechanisms that permit smooth sculpting of surfaces by coupling sufficient energy per unit volume to heat, melt, and ablate fused silica irrespective of absorption channels. Laser-glass interaction mechanisms, ablation morphologies, and processing windows were discussed and compared. The use of these lasers to control and to profile refractive index change was also briefly examined [1]. The present invited paper expands on these preliminary refractive-index studies and compares processing rates for far UV and UF laser approaches in processing glass materials.

Refractive-index profiling with ultraviolet lasers (193, ~250nm) [3,4] is a relatively new processing technology of commercially importance to the photonics industry for fabrication of fiber Bragg and long-period gratings. Interest is also expanding to laser trimming, for example, to correct phase errors in arrayed waveguide gratings [5,6]. We examine the extension of such techniques to record short-wavelength light from the F_2 laser. The 157-nm photons promise faster and stronger photosensitivity responses without the need for enhancement techniques [7]. The F_2 laser drives strong linear interactions in both germanosilicate and pure silica glasses and waveguides, and induces refractive-index changes in the range of $\sim 10^{-4}$ to $>10^{-3}$. Such index values are practically useful for writing Bragg or volume gratings and are extensible to shaping and trimming two-dimensional optical circuits. The 157-nm photon also approaches the bandedge defect states in pure fused silica. Here, the photosensitivity response is found to be orders–of-magnitude stronger and more rapid compared with that provided by traditional UV lasers (193 or 248 nm) [8,9]. To date, there has only been speculation as to the underlying physical mechanism [3,4]: color centers, compaction and stress relief.

UF lasers drive fundamentally different interactions that lead also to useful refractive index changes in

First International Symposium on Laser Precision Microfabrication, Isamu Miyamoto, Koji Sugioka, Thomas W. Sigmon, Editors, Proceedings of SPIE Vol. 4088 (2000) © 2000 SPIE · 0277-786X/00/$15.00

transparent glasses [10,11,12]. We describe optical waveguides formed with 50-fs pulses of 800-nm light at 1-100 kHz repetition rates. This contrasts sharply with the 15-ns duration and 100-Hz rates of the 157-nm F_2 laser. UF laser-matter interaction dynamics is not fully understood, however, as in F_2-laser induced index changes, there are several proposed contributing factors, for example, multiphoton ionization, field ionization, electron avalanche, *microexplosion* [11], compaction, and color centers [10].

The present paper summarizes a comprehensive study of photosensivity of various grades of glasses. We compare photosensitivity responses, spatial resolution, and processing windows for the deep-UV and UF laser approaches, and discuss prospects for printing and trimming optical waveguides and circuits in glass materials. Processing rates are comparable for the two laser classes and show that accumulated fluence is the key to the magnitude of the induced refractive-index change. We also present evidence of a thermal role for UF processing that enhances photosensitivity responses for repetition rates $\geq$ 10 kHz; an analogous *burst machining* effect was described previously [1,2] that provides crack-free ablation of transparent glasses.

2 Experiments

A commercial F_2 laser (Lambda Physik, LPF220i) provided deep UV light at 157-nm wavelength. Pulses of ~20-mJ energy and ~15-ns duration were formed in a 20×7-mm^2 beam with ~3-mrad by ~1-mrad divergence. Apertures and lenses were used to provide uniform exposure and to control fluence. A sealed processing chamber was flushed with 1-atm argon gas for vacuum-ultraviolet transparency. The laser was operated at 100 Hz repetition rate.

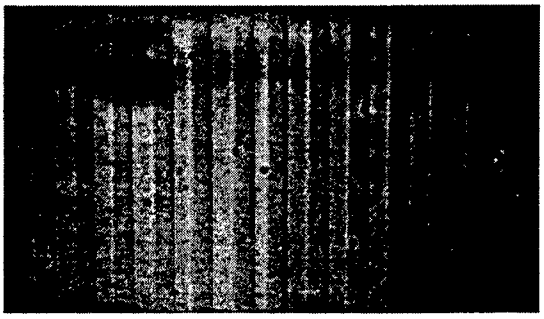


Fig. 1 Optical microscope side view of a fused silica window after 157-nm laser exposure with 180,000 pulses at ~84 mJ/cm^2 fluence. A volume grating of 140-μm period was formed deep (~1mm) into the glass.

The UF laser consisted of an Ar^+-pumped Ti:sapphire oscillator, a stretcher, a regenerative amplifier (Coherent RegA 9050), and a single grating compressor. The output pulses had a maximum energy of 1.5 μJ at 800 nm and a pulse width of 50 fs. The repetition rate was variable up to 250 kHz. A 10X microscope objective focussed the beam to a 3-μm diameter spot size. Samples were mounted on x-y stages driven by 0.1-μm step-size stepper motors and scanned along the optical axis.

Samples consisted of uv-grade fused silica cover slips and windows (Corning 7940), polished fused silica blanks, 3% GeO_2-doped planar waveguides (PIRI SMPWL) and single-mode optical fibers (SMF28). Samples were exposed to various fluence values and a wide range of pulse numbers, and then evaluated by a range of techniques as described below to assess the laser-induced refractive index change.

3 Photosensitivity Responses

3.1 Fused Silica with 157-nm Radiation

A proximity amplitude mask was used to form volume-gratings (140-μm period) in various grades of fused silica glasses. Fig. 1 shows the side view of a polished fused silica window (Corning 7940; 1200-ppm OH) after 157-nm exposure with 180,000 pulses at ~84 mJ/cm^2 fluence. A ~1-mm deep volume grating is clearly formed in the 2-mm thick sample. This penetration is in keeping with an absorption coefficient of α_{157} ~ 10 cm^{-1} at 157-nm wavelength.

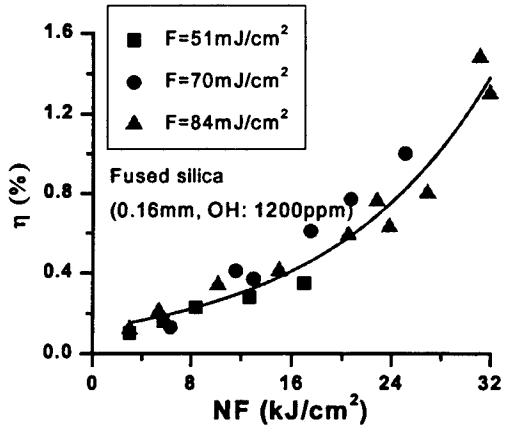


Fig. 2 The increase of diffraction efficiency as a function of accumulated laser fluence for volume gratings formed in 160-μm thick fused silica (1200-ppm OH) by 157-nm exposure. The laser fluence per pulse was 51, 70 and 84 mJ/cm^2, and the pulse number was varied from 6.0x10^4 to 3.6x10^5 at a laser repetition rate of 100Hz.

To characterize refractive index changes, wet-fused silica (OH: 1200 ppm; α_{157} = 26 cm^{-1}) cover slips of thickness d = 0.16 mm were radiated with 157-nm light. The first-order diffraction efficiency was measured for a HeNe laser in samples exposed to F = 51-84 mJ/cm^2 fluence and pulse number in the N = 60,000 - 360,000 range. Results are plotted in Fig. 2 as a function of accumulated fluence, *NF*.

The clustering of the data about a single line shows that index changes are controlled by accumulated fluence, *NF*, for the current processing range. This offers advantages in concentrating finite laser energy to increase fluence and processing speed, or reducing fluence for larger area exposure at slower rates.

Data in Fig. 2 were applied in a numerical model to assess the volume index change, $\Delta n\ e^{-\alpha d}$. An exponential index profile was inferred (α = 26 cm^{-1}) by stacking several plates together and noting the index fall-off from sample to sample. Results of the refractive-index change are shown in Fig. 3 as function of *NF*. Surface compaction on the scale of 10's of nm was also noted by stylus profilometry on the laser-irradiated surface. The surface index change follows a universal material compaction response of $\Delta n \sim (NF)^{0.70}$, a single-photon response that greatly exceeds the two-photon volume compaction response of $\Delta\rho \sim (NF^2)^{0.53}$ reported [6] for 193-nm exposure of fused silica. Overall, 157-nm laser-induced compaction and refractive index changes are approximately three orders of magnitude faster than reported for 193- or 248-nm lasers [5,6]. For 157-nm laser radiation, an absolute index changes of 4.2 x 10^{-4} is available in an ~400-μm thick surface layer after a 60-min exposure (at 100 Hz). Such index change can provide useful phase correction for a wide range of applications in shaping and trimming optical components made with pure silica.

3.2 Germanosilicate Waveguides with 157-nm Radiation

Germanium doping of fused silica provides a controlled increase in refractive index to define the waveguide cores of optical fibers and planar circuits. Such doping also lowers the bandgap from ~9.1 eV to values comparable with the 7.9-eV photon energy of the F_2 laser. Strong absorption in thin layers is promising for directly accessing strong and rapid photosensitivity responses on scale lengths commensurate with waveguide geometries of ~10 μm. For these reasons, 157-nm laser radiation is an ideal candidate for fabricating photonic components and circuits inside germanosilicate fiber and planar waveguides [1,7].

Here, we survey results of 157-nm photosensitivity studies on planar and fiber waveguides. Standard telecommunication fibers (SMF 28) and silica-based cladless planar waveguides (PIRI SMPWL) were examined. The planar waveguide consisted of an 8-μm thick GeO_2-doped (3%) core layer grown over 20-μm of fused silica, all on a silicon substrate. Because germanosilicate is much more photosensitive (>10X) than the fused silica cladding, index changes were assumed to be dominant in the waveguide core.

Fig. 4 shows the effective index change observed in planar waveguides as a function of accumulated laser fluence. The single-pulse fluence was ~7.5 mJ/cm^2. Index values were inferred from prism-coupled angle changes using HeNe laser probe light. The 157-nm induced index change had an unsaturated value of $4x10^{-3}$ for the zeroth mode for both virgin and H_2-loaded samples. However, a total fluence of only 8 kJ/cm^2 was required for the hydrogen loading case compared with ~22 kJ/cm^2 for the untreated case. This 3-fold enhancement offered by hydrogen loading is modest in comparison with order of magnitude enhancements seen with longer wavelength exposure [13], and attests to the strong interaction offered by 157-nm radiation.

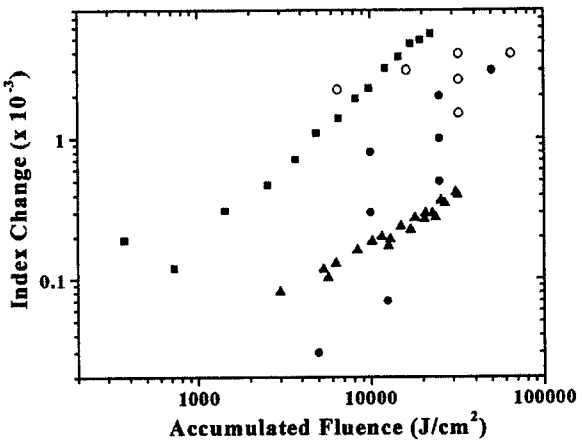


Fig. 3 Comparison of deep UV and UF laser induced index changes in fused silica and germanosilicate glasses: ▲ F_2-laser on pure fused silica, F_2-laser on GeO_2-doped (3%) fused silica, ○ UF-laser on fused silica (10-100 kHz), and ● UF-laser on fused silica (1 kHz) from [12]. See text for further details.

Since effective index is a weighed average of the refractive index for the mode profile, the peak index change in the photosensitive layer is expected to be higher than in Fig. 4. This is further born out by the ~2-fold strong index change noted for the fundamental mode in both waveguide types of Fig. 4. This discrepancy can be accounted for by applying a simple step-profile model of index change. Results suggest a 157-nm penetration depth of ~4μm for the largest laser exposures. The calculated peak index changes are plotted in Fig. 3 as a function of accumulated fluence for the case of non-H_2 loaded planar waveguides. Index changes as high as 0.005 are noted, and overall responses are more than an order of magnitude higher than for the case of pure fused silica. Further, this index change is strong and rapid compared with longer-wavelength exposure of similar germanosilicate waveguides (3% GeO_2) without H_2-loading techniques. For example, responses are an order of magnitude faster than with 193-nm radiation, and follow a single-photon response in comparison with inferred two-photon responses [14].

A rapid 157-nm photosensitivity response was also found [7] for standard telecommunication fiber (Corning

SMF-28). Fig. 5 shows an optical microscope picture of coupled 633-nm HeNe-laser light scattering from a long-period grating (140-μm period). The scattering light is mainly visible from one side of the fiber suggesting a non-uniform index-change profile. This is consistent with a small penetration depth (~4 μm) as inferred above from the mode measurement results for the planar waveguide.

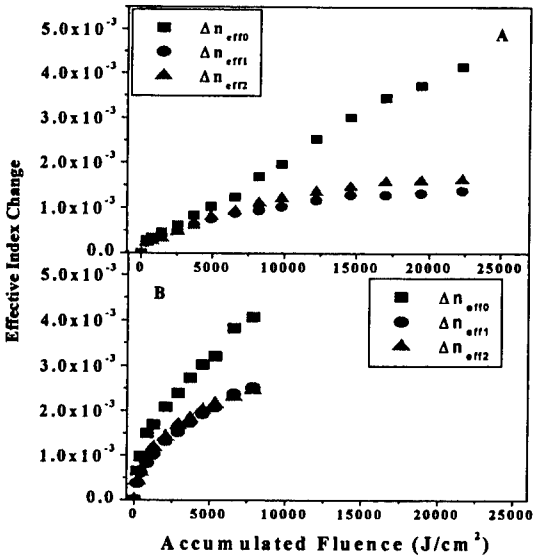


Fig. 4. Effective index change as functions of accumulated laser fluence in 3% Ge-doped planar waveguides: (a) without H_2 loading, and (b) loaded with H_2 at 105 bar for 10 days. Three modes are noted for the 633-nm probe laser.

The transmission spectrum of a similar long-period fiber grating with 304-μm period is shown in Fig. 6 for the case of a H_2-loaded sample (at 100 bar for 10 days). A ~20-dB loss peak is noted at the 1.58-μm telecommunication band. This response developed with 2,700 pulses at ~1.8 mJ/cm^2 fluence – or with only ~4.75-J/cm^2 total fluence. For 248-nm KrF lasers, a >300-fold larger total fluence is required to develop the same strength loss peak. F_2-laser radiation clearly drives strong material responses in germanosilicate glasses.

3.3 Fused Silica with UF Lasers

We are currently studying the effects of varying pulse energy, repetition rate, scan speed, and focus diameter on the induced index change and the quality of waveguides to define a processing window for UF laser writing of good quality optical waveguides.

Waveguides were written by focusing the laser beneath the surface of the sample and translating the sample along the laser axis. Fig. 7 shows the obvious difference in quality between 100 kHz and 10 kHz waveguides under similar fluence and accumulated fluence conditions. For 100 kHz repetition rate, there is noticeably more damage.

UF-laser induced index changes were inferred from



Fig. 5. HeNe laser light scattered from long period grating (Λ=140-μm) inscribed in a Corning SMF-28 fiber by the 157-nm F_2 laser

numerical aperture (NA) measurements of 650-nm light coupled into the waveguides with 0.10 NA optics. Light exiting the waveguides was collected by a 32x microscope objective (0.30 NA), passed through a pinhole at the image plane, and recorded with a CCD detector placed ~6 cm from the image plane. Intensity profiles were captured and analyzed with *NIH Scion* imaging software to determine the beam width (FWHM) and NA. The effective index modulation, Δn, was found using

$$NA = \sqrt{2 \cdot n \cdot \Delta n}\,, \qquad (1)$$

where n is the bulk refractive index.

A maximum index change of ~5 x 10^{-3} was measurable, limited by heavy waveguide losses and poor coupling efficiency for waveguides damaged as shown in Fig. 7 (top). The measurement technique had a minimum sensitivity of ~1 x 10^{-3}, limited by the weak waveguiding. This index-change range is ideally suited for defining single-mode waveguides with mode profiles matching standard telecommunication fiber waveguides. Preliminary results of measured index changes are shown in Fig. 3 for 10 and 100 kHz repetition rates. Also shown for comparison purposes are index changes as reported by Gaeta and coworkers [12] using 100-fs pulses at 1-kHz repetition rate. Accumulated fluence was based on total exposure within one confocal beam parameter. Results fall into a similar range with the F_2-laser results, the accumulated fluence being key to the total achievable index change.

Preliminary results suggest further that higher repetition rates (10 kHz) induce 2-fold or higher index changes than with 1-kHz rates. This may be due to the accumulative heating effects for weak thermal transport. The thermal diffusion scale length, L_{th}, for laser pulse separation time, t, is determined from

$$L_{th} = \sqrt{4 \cdot D \cdot t} \qquad (2)$$

where D is the thermal diffusion coefficient. For fused silica, one finds scale lengths of 6 μm and 60 μm for repetition rates of 100 kHz and 1 kHz, respectively. Comparison with the ~3-μm focused diameter of the laser

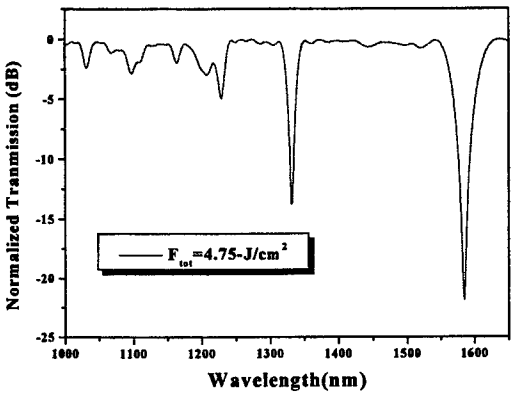


Fig. 6. Transmission spectrum of a long period grating (Λ=304-μm) formed in hydrogen loaded SMF-28 fiber with the 157-nm F_2 laser.

suggests that absorbed laser energy is not dissipated between pulses for the higher repetition rate case and accumulated heated effects are therefore present that can enhance the refractive index change. Our group has identified similar heating effects in UF-laser burst machining of fused silica. Accumulated heating effects appear responsible for the elimination of microcracks that would otherwise form at slower repetition rate [1,2]. An accumulated heating effect also appears to underlie the microexplosion effects in Ref. [11].

4 Comparison between UV and UF Processing

The glass response to UV laser light has been more extensively studied. The 157-nm photon provides near bandedge absorption, very much like a single photon response. The UF interaction entails many more physical mechanisms – multi-photon ionization, field ionization, electron avalanche – to couple light into transparent material before phonon relaxation, thermal transport and other physical processes leave a permanent mark on the local refractive index. Compaction and color center processes are both clearly at play in the F_2-laser photosensitivity process in glasses. Similar roles have also been suggested for UF-laser induced refractive index changes [10,11].

Irrespective of the differing laser approaches, index changes in Fig. 3 shows similar orders of magnitude effects for both laser approaches. Accumulated fluence is the key control factor suggesting that total absorbed laser energy will define the index change. The F_2 laser induces an index change of 0.0001 to 0.0004 in pure fused silica for an accumulated fluence range of 3 to 30 kJ/cm^2. The response is improved more than 10-fold to Δn = 0.005 in germanium-doped fused silica, a much stronger absorber of 157-nm light. Similar index changes – Δn = 0.001 to 0.005 – are also noted for fused silica with the UF laser, whose light is fundamentally transparent to the material. The larger point-to-point scatter for the UF case is due to the NA measurement technique, which is very sensitive to the waveguide quality. The UF-laser process is also intrinsically more sensitive to repetition rate, single-pulse fluence, and pulse number, and may therefore be more challenging to control unlike the F_2-laser approach.

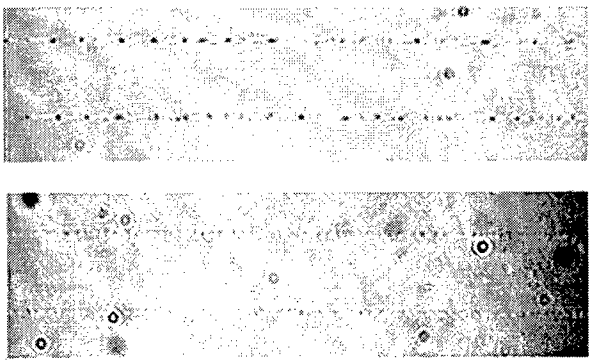


Fig. 7. CCD optical microscope image of waveguides written inside bulk fused silica by 100-kHz (top) and 10-kHz (bottom) repetition rate UF-laser pulses with 1-μJ per pulse energy. Scan speeds were 200 and 20 μm/s, respectively, to deliver identical accumulated fluence. Waveguides are spaced 50 μm apart.

Index changes in the range of 1 - 5 x 10^{-3} are useful for a wide range of photonics manufacturing applications. An accumulated fluence of 20 kJ/cm^2 can be delivered rapidly for tightly focused UF laser sources, and form waveguides at scan speeds ~1 mm/s for high repetition rate systems. Excimer and F_2 lasers offer much higher power (10's W) than UF lasers (<1 W) and are therefore better suited to high volume applications, especially those where large area coverage is required such as in printing two-dimensional optical circuits. The UF laser is more suited to direct-write processing, a slower process but one that offers more flexibility in patterning and trimming applications. The UF laser has one substantial advantage over UV lasers – the internal structuring of three-dimensional index profiles in transparent glasses. This presents interesting prospects for shaping novel three-dimensional photonic structures for optical telecommunication applications. Further extension to frequency doubling and tripling offers tighter focal geometries such that sub-micron feature sizes similar to that provided by UV excimer lasers can also be exploited. Well defined features of ~500-nm size are required for 1.55-μm wavelength Bragg structures. The fine control of index

changes available from both laser classes will serve many niches as the current practice of UV-laser printing of fiber-based devices expands to two- and three-dimensional integrated structures.

5 Conclusions

Two extreme approaches in index profiling of transparent glasses have been examined in this paper. Deep-UV nanosecond lasers and 50-fs near-infrared laser light have been shown to induce index changes of 1 to 5 x 10^{-3}, a useful range for commercial purposes. The 157-nm F_2-laser offers strong photosensitivity responses in fused silica and low-concentration germanosilicate glasses in comparison with that available with traditional UV sources. UF lasers is another promising approach offering similar photosensitive responses. One key observation is that accumulated fluence is a common control parameter in both laser approaches. A total exposure of ~20 kJ/cm^2 appears necessary to reach a ~10^{-3} index change without damage to the glass structure. Such exposures are realizable in practical time frames, ~100 ms for the UF laser and several minutes for the UV laser. Both lasers are now commercially available and offer attractive prospects for shaping photonic components in fused silica and related glasses.

Acknowledgements

The authors gratefully acknowledge financial support from the National Research Council, the Natural Sciences and Engineering Research Council, Photonics Research Ontario, and the Canada Foundation for Photonics Innovation.

References

[1] P.R. Herman, R.S. Marjoribanks, A. Oettl, K. Chen, I. Konovalov, S. Ness, *Applied Surface Science*, **154** (2000) 577.

[2] P.R. Herman, A. Oettl, K.P. Chen, R.S. Marjoribanks, Laser micromachining of transparent fused silica with 1-ps pulses and pulse trains, SPIE Proc. 3616 (1999) 148.

[3] Raman Kashyap, Fiber Bragg Gratings (Academic Press, CA, 1999).

[4] A. Othonos, "Fiber Bragg Gratings," *Review of Scientific Instruments*, vol. 68, pp. 4309-4341, 1997.

[5] K. Takada, T. Tanaka, M. Abe, T. Yanagisawa, M. Ishii, K. Okamoto, Electron. Lett. 36 (2000) 60.

[6] J. Gehler, F. Knappe, Opt. Fiber Comm. Conf. (OSA 2000), paper WM9-1.

[7] P.R. Herman, K. Beckley, and S. Ness, 157-nm Photosensitivity in germanosilicate and fused-silica glasses, Conf. on Lasers and Electro-Optics, San Francisco, CA, 4-8 May 1998.

[8] M. Rothschild, D.J. Ehrlich, D.C. Shaver, *Appl. Phys. Lett.* **55** (1989) 1276.

[9] D.C, Allan, C. Smith, N.F. Borrelli, T.P. Seward III, *Opt. Lett.* **21** (1996) 960.

[10] K.M. Davis, N. Sugimoto, K. Hirao, *Opt. Lett.* **21** (1996) 1729.

[11] E.N. Glezer, M. Milosavljevic, L. Huang, R.J. Finlay, T.-H. Her, J.P. Callan, E. Mazur, *Opt. Lett.* **21** (1996) 2023; E.N. Glezer, E. Mazur, *Appl. Phys. Lett.*, **71**, (1997) 882.

[12] D. Homoelle, S. Wielandy, A.L. Gaeta, N.F. Borrelli, C. Smith, *Opt. Lett.* **24** (1999) 1311.

[13] P. Lemaire, R.M. Atkins, V. Mizrahi, W.A. Reed, *Electron. Lett.* **29** (1993) 1191.

[14] J. Albert, B. Malo, K.O. Hill, F. Bilodeau, D.C. Johnson, S. Theriault, *App. Phys. Lett.* **67** (1995) 3529.

Laser Processing of Convex Structures in Chalcogenide Glasses

Tamihiro Gotoh and Keiji Tanaka

Department of Applied Physics, Faculty of Engineering, Hokkaido University
Sapporo 060-8628, Japan
phone : +81-11-706-6634 fax : +81-11-716-6175
e-mail : tgotoh@eng.hokudai.ac.jp

Micron-scale convex deformations can be produced in two kinds of chalcogenide glasses only by exposures to focussed cw laser beams. In covalent compounds such as As_2S_3 the deformation is formed through the so-called giant photoexpansion phenomenon, and in Ag-containing chalcogenide glasses it is made through photoinduced accumulation of Ag^+ ions. These phenomena are promising for fabrication of micro optical components.

Keywords: convex structure, chalcogenide glasses, giant photoexpansion, photostructural change, photoinduced ion accumulation, microlens, gratings

1. Introduction

Many kinds of laser processing techniques have been known so far [1], while the development is still limited in scope. For instance, we can produce concave or hole structures using intense cw or pulsed light sources such as CO_2 and excimer lasers. However, only a few techniques are available for the laser fabrication of *convex* structures, and in addition, most of the techniques need after-treatments such as etching processes.

We here report two direct processes which can produce micro-convex structures in chalcogenide glasses. One process is the so-called giant photoexpansion in covalent chalcogenide glasses [2], and the other is the photoinduced accumulation of Ag^+ ions in Ag-containing chalcogenide glasses [3]. These processes can form convex deformations with diameters of $\geq$ 0.2 μm and heights of $\leq$ 5 μm only by light exposures. Light sources needed are small cw lasers such as He-Ne lasers. In the present work, typical characteristics of the two processes obtained using As_2S_3 and Ag-As(Ge)-S are reported. These processes are promising for the direct production of a variety of thermally-erasable optical elements such as microlenses, gratings, and relief holograms. Produced patterns can also be employed as masters for replicas.

2. Experimental

Two kinds of chalcogenide glasses were employed in the present study. One is a typical covalent glass, As_2S_3, and the other is ion-conducting glasses, Ag-As(Ge)-S. As_2S_3 films were prepared by vacuum evaporation, and then annealed at the glass transition temperature ~200 °C. $AgAsS_2$ films were obtained through the photodoping process from evaporated Ag and AsS_2 films [4], and then annealed for stabilization at ~150 °C. $Ag_{60}Ge_{13}S_{27}$ films were prepared by co-evaporation [5]. Polished melt-quenched samples were also examined.

Laser processing and pattern evaluation were done as follows: As_2S_3 and $AgAsS_2$ samples were exposed to light beams emitted from a He-Ne laser (λ = 633 nm, $\hbar\omega$ = 2.0 eV) of 2 mW at room temperature, unless otherwise specified. The light beam was focussed using microscope objective lenses. $Ag_{60}Ge_{12}S_{28}$ samples were illuminated by evanescent blue light (λ = 473 nm, $\hbar\omega$ = 2.6 eV) obtained

First International Symposium on Laser Precision Microfabrication, Isamu Miyamoto, Koji Sugioka,
Thomas W. Sigmon, Editors, Proceedings of SPIE Vol. 4088 (2000) © 2000 SPIE · 0277-786X/00/$15.00

from fiber probes for a scanning near-field optical microscope (SNOM). Surface deformations were evaluated using an atomic force microscope (AFM) and a Nomarski-type optical microscope.

3. Results and discussion

3. 1 Giant photoexpansion

Figure 1 shows an AFM image of a 50 μm-thick As_2S_3 sample exposed for 10 s to a light beam focussed by a microscope objective of 100×. The beam diameter at the sample surface was ~ 2 μm so that the power density was estimated at 5×10^4 W/cm^2. We see in the figure that the illuminated region expands convexly. The height of the deformed region is ~ 600 nm, which corresponds to ~ 1.5 % of the sample thickness, and the diameter is ~ 2 μm being comparable with the light-spot size.

Mechanisms of this phenomenon still remain to be studied [6]. It is demonstrated that this photoeffect enhances at low temperatures to 20 μm [7], which manifests that the phenomenon is athermal, i.e. it being a kind of photoelectro-structural processes [2]. In more detail, the phenomenon is assumed to be caused by photoexpansion and photoinduced fluidity. That is, it is known that the photoexpansion (of ~ 0.5 % at room temperature) is inherent to illuminated regions in As_2S_3 [8]. Then, when the light-spot size is smaller than the penetration depth of light (~ 1cm for 633 nm light) and the film thickness, we can envisage an illuminated cylindrical volume, which tends to expand. However, sideward expansion of the volume is suppressed by unilluminated regions, and it will be converted to a free expansion at the illuminated surface through the photoinduced fluidity [9]. As a result, the prominent expansion appears through this volume effect.

This process can make a variety of convex deformations with diameters of 2 - 100 μm and heights of < 20 μm only by light exposures. It is suitable for fabricating micro-circular deformations. Linear expansions can be produced by moving light spots. Produced deformations are stable at room temperatures, while these can be erased by annealing at ~ 180 °C. Applications of these structures to microlenses and so forth have been demonstrated previously [10].

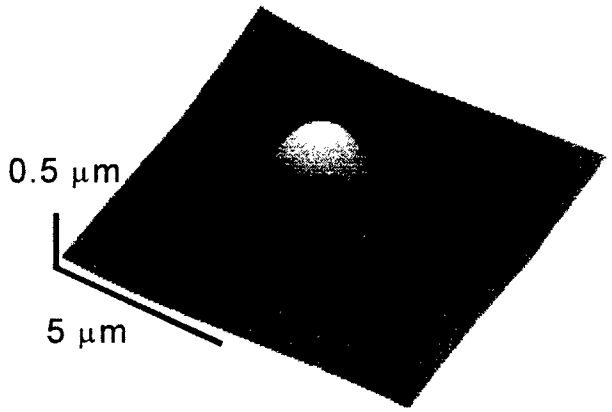


Fig. 1 An AFM image of a 50 μm-thick As_2S_3 sample after an exposure for 10 s to 2.0 eV light of 1.8 mW.

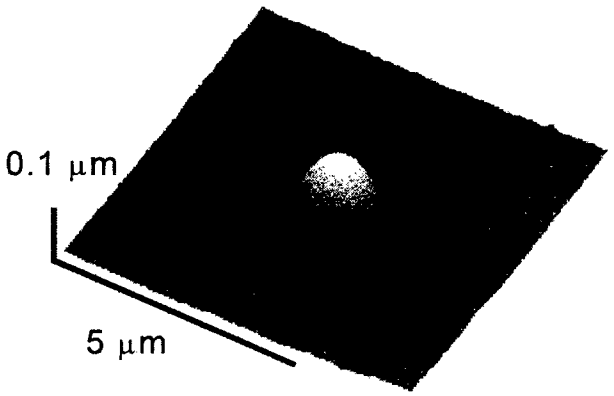


Fig. 2 An AFM image of a 1 μm-thick $AgAsS_2$ sample after an exposure for 60 s to 2.0 eV light of 0.2 mW.

3.2 Photoinduced ion accumulation

Figure 2 shows an AFM image of a 1 μm-thick $AgAsS_2$ film after an exposure to the focussed light beam for 60 s. We see a circular convex structure at the illuminated region. The diameter of the convex structure is nearly the same with that of the focussed beam spot, ~ 2 μm, and the height is ~120 nm, which amounts to ~12 % of the sample thickness. The deformation is stable, at least, for a half year at room temperature in the dark. On the other hand, the deformation can be erased with an annealing treatment at the glass transition temperature, ~ 150 °C.

Ambient light will also erase the structure.

This phenomenon is assumed to be caused through a photoinduced chemical modification process [11]. When $AgAsS_2$ is illuminated with light, electrons and holes are photoexcited, and the holes diffuse toward unilluminated regions. The illuminated region is then negatively charged, and in response, Ag^+ ions in the unilluminated region migrate to the illuminated region. This Ag^+-ion accumulation causes the photoexpansion with the photoinduced fluidity. Actually, as will be reported elsewhere [12], the Ag concentration in illuminated region increases by ~ 3 at.%, which is quantitatively consistent with the observed volume expansion. In addition, we see in Fig. 2 that the peripheral of the expansion is slightly hollowed, which signifies the Ag depletion.

It has been demonstrated that the expanded structure shown in Fig. 2 works as a microlens. Actually, when the expansion was inspected using an optical microscope, transmitted light was found to be focussed at 2 μm above the structure. This focal length is quantitatively reasonable. The focal length f can be estimated as $f = r^2 / 2(n-1)\Delta L$ [2], where r and ΔL are the radius and the height of the deformation, and n is the refractive index of the expanded medium. Putting $r = 1$ μm, $\Delta L = 0.12$ μm, and $n = 3.0$ (the refractive index of $AgAsS_2$ [13]), we obtain $f \approx 2$ μm, which is consistent with the observed focal length.

Minimal deformations in lateral dimensions can be produced by using evanescent light obtained from the SNOM fiber probes. $Ag_{60}Ge_{12}S_{28}$ films were utilized in this experiment, since it has been known that in Ag-rich glasses prominent accumulation of Ag^+ ions occurs through the photo-surface deposition process [14].

Figure 3 shows a typical result. The obtainable beam diameter by this SNOM probe is ~ 0.2 μm [15]. The input light intensity into the fiber is ~ 0.1 mW, and the output intensity from the probe is estimated at ~ 1 nW. Shorter exposure times are preferred here, and accordingly, blue light has been employed [5], which gives an exposure time of 2 s. The expansion is circular with a diameter and a height of 0.2 μm and 20 nm. In this result, we also see the hollow structure around the expansion

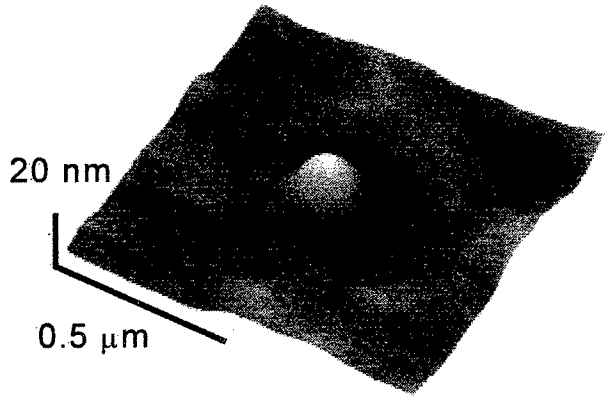


Fig. 3 An AFM image of a 0.5 μm thick $Ag_{60}Ge_{12}S_{28}$ sample after an exposure for 2 s to 2.6 eV evanescent light of ~ 0.1nW.

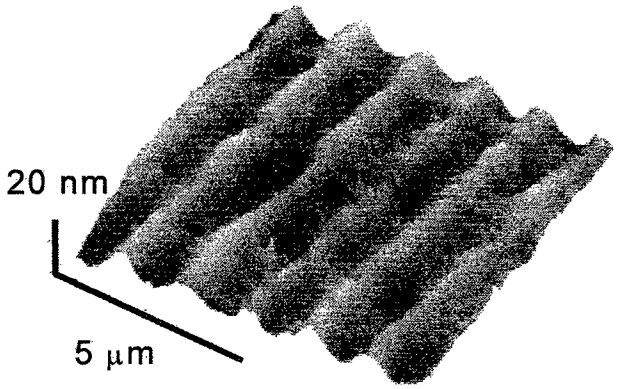


Fig. 4 An AFM image of a grating pattern fabricated on a 1 μm-thick $AgAsS_2$ film for 2 hours light exposure.

Grating structures can be produced with this ion-accumulation phenomenon. Figure 4 shows an AFM image of a grating pattern fabricated on a 1 μm-thick $AgAsS_2$ film, which is exposed to two-beam interference fringes of the 2.0 eV light for 2 h. The fringe spacing of the grating is ~ 1.4 μm and a modulation amplitude is ~ 10 nm.

4. Comparison

Figure 5 compares the expansion height made through the giant photoexpansion (3.1) and the photoinduced ion accumulation possess (3.2) as a function of the light-spot size. As an absolute value, the photoexpansion can produce higher expansions over varied spot diameters. The volume effect is essential for the giant photoexpansion, and accordingly it appears only in thick samples. On the other hand, the ionic process appears only for spot diameters smaller than 5 μm, which may correspond to the diffusion length of the Ag^+ ions [16]. However, the fractional change reaches to 12 %. At low temperatures, the giant photoexpansion becomes greater [7], while the photoinduced ion accumulation disappears [12].

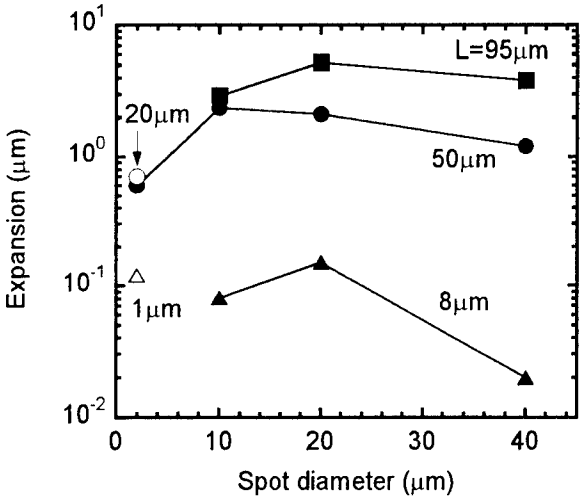


Fig. 5 The deformation height as a function of the light-spot size. The sample thickness is varied from 1 to 95 μm. Closed symbols and open symbols are the data of As_2S_3 and $AgAsS_2$, respectively.

5. Final remarks

The volume expansion phenomena described in the present work have some advantages. First, the phenomena can be induced only by mild laser light in a variety of chalcongenide glasses. For instance, blue laser light can produce the giant photoexpansion in as GeS_2 [2]. Second, the present phenomena are athermal, and accordingly precise patterns can be produced. In thermal phenomena, heat conduction precludes precise pattern control. Third, these laser processing can be used under any circumstances, such as in the air.

Acknowledgements

The authors would like to thank Dr. T. Kawaguchi for providing samples. The present work is partially supported by Grants-in-Aid for Scientific Research from Research Fellowships of the Japan Society.

References

[1] Y. Yoshida: "*The Physics and Technology of Microfabrication*" (Shokabo, Tokyo, 1998) pp.163. [in Japanese]

[2] H. Hisakuni and K. Tanaka, Appl. Phys. Lett., **65,** (1994) 2925.

[3] N. Yoshida and K. Tanaka, J. Appl. Phys., **78**, (1995) 1745.

[4] A. V. Kolobov and S. R. Elliott, Adv. Phys., **40**, (1991) 625.

[5] T. Kawaguchi, S. Maruno and K. Tanaka, J. Appl. Phys., **73**, (1993) 4560.

[6] K. Tanaka, Phys. Rev. B, **57**, (1998) 5163.

[7] K. Tanaka: "*Physics and Applications of Non-Crystalline Semiconductors in Optoelectronics*" ed. by A. Andriesh and M. Bertolotti, (Kluwer Academic Publishers, Netherlands, 1997) pp.35.

[8] H. Hamanaka, K. Tanaka, A. Matsuda and S. Iijima, Solid State Commun., **19**, (1976) 499.

[9] H. Hisakuni and K. Tanaka, Science, **270**, (1995) 974.

[10] H. Hisakuni and K. Tanaka, Opt. Lett., **20**, (1995) 958.

[11] N. Yoshida and K. Tanaka, J. Appl. Phys., **78**, (1995) 1745.

[12] T. Gotoh and K. Tanaka, Phys. Rev. B, to be submitted.

[13] A. Zakery, A. Zekak, P. J. S. Ewen, C. W. Slinger and A. E. Owen, J. Non-Cryst. Solids, **114,** (1989) 109.

[14] S. Maruno and T. Kawaguchi, Jpn. J. Appl. Phys., **33**, (1994) 6470.

[15] Data sheets of SNOM (Seiko Instruments Inc.)

[16] Y. Kawamoto and M. Nishida, Phys. Chem. Glasses, **18**, (1977) 19.

Laser ablation process of quartz material using F2 laser

Takahisa JITSUNO*, Hironari MIKATA*, Keiu TOKUMURA**,
Nobu KUZUU***, Naoyuki KITAMURA****, Yoshizo KAWAGUCHI*****

*Institute of Laser Engineering ,Osaka University , 2-6 Yamada-oka, Suita, Osaka 565-0871, Japan
e-mail: jitsuno@ile.osaka-u.ac.jp
**Nalux Co.Lted. 2-1-7 Yamazaki, Shimamoto-chyo, Misima-gun, Osaka 618-0001,Japan
***Department of Applied Physics, Fukui University, 3-9-1 Bunkyo, Fukui 910-8507, Japan
****Osaka National Industrial Research Institute, AIST, MITI, 1-8-31 Midori-oka, Ikeda, Osaka 563-8577, Japan
*****Chugoku National Industrial Research Institute, AIST, MITI, 2-2-2 Hiro-Suehiro, Kure, Hiroshima 737-0197, Japan

An investigation on the laser ablative shaping (LAS) of the quartz glass has been made experimentally. F2 laser laser was used as the laser light source for efficient ablation of quartz material. The output beam of F2 laser was focused on to the surface of quartz plate. The ablation rate was about 10 micron m/pulse at the irradiation fluence of 2 J/cm^2. A uniform ablation of quartz plate has been demonstrated using F2 laser. The waveform of incident and transmitted laser light was measured by high speed photo-tubes to observe the time dependence of the absorption. The measured waveform indicates that the absorption was small at the leading edge of the laser pulse, and a strong absorption was induced at the end of laser pulse due to the excited state absorption. These phenomena are quite similar to both in F2 and ArF laser light. We have developed a simple model in which the instantaneous absorption is proportional to the absorbed energy prior to the moment. The calculated absorption was in good agreement with the measured wave-form. The change of transmittance in UV and VUV region was measured after the irradiation of F2 laser for samples of different concentrations of impurities.

Keywords : laser ablation, F2 laser, quartz glass, ablation rate, absorption coefficient, excited state absorption

1. Introduction

In the field of optical fabrication, the quartz glass is a very important material because it has very high transmittance in wade range of spectrum (from near IR to VUV region), high thermal resistivity, suitable hardness, high uniformity, and high chemical stability. The importance of the quartz glass have been largely increased recently for the application in VUV laser lithography. However, this quartz glass is usually shaped by optical polishing because the hardness of quartz glass is high. In the polishing process, a long process time and skillful techniques are necessary to control the surface shape.

On the other hand, we have developed a new scheme to control the surface shape of optical elements using laser ablation[1]. In this scheme, we used optical plastics coated on the glass plate as the ablation surface, and ArF excimer laser (193 nm wavelength) was used as the light source. This scheme is called laser ablative shaping (LAS). LAS process was very effective to reduce the optical aberration of optical elements in transmission or reflected wavefront without any contact with the surface of material.

However, the wavelength of ArF laser is too long for the LAS process of quartz glass because the photon energy of 193 nm laser light is 6.4 eV which is much smaller than the band gap energy of about 9 eV of quartz glass. We have investigated the LAS process for quartz glass using ArF and F2 lasers [2]. Although the wavelength of F2 laser is not enough short because the photon energy is 7.9 eV, F2 laser is the shortest wavelength laser which can provides reliable repetitive output.

In this paper, the surface ablation of the quartz glass by F2 laser ablation are presented. The transformation of laser pulse waveform due to pass through the silica glass, and the change of spectral transmittance by laser expose are also described.

2. Experimental setup and surface processing

The F2 laser system [Lambda Physic 'COMPex 102'] was filled with the laser gas containing F2 and He up to 2.6 atoms. In the case of charged voltage of 30 kV, the laser pulse had about 6 mJ output energy and about 10 ns duration in full-width-half-maximum. Figure 1 shows a schematic optical arrangement for the laser ablation process with the F2 laser. The laser beam was focused by a MgF2 lens of 20 mm in focal length. All optical passes were substituted the air by nitrogen gas because the laser light at 157 nm wavelength is largely absorbed by the oxygen in the atmosphere [3].

First International Symposium on Laser Precision Microfabrication, Isamu Miyamoto, Koji Sugioka,
Thomas W. Sigmon, Editors, Proceedings of SPIE Vol. 4088 (2000) © 2000 SPIE · 0277-786X/00/$15.00

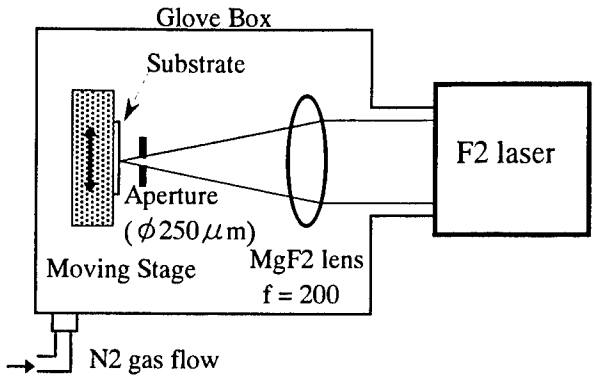


Fig.1 Schematic arrangement of the laser ablation process with F2 laser.

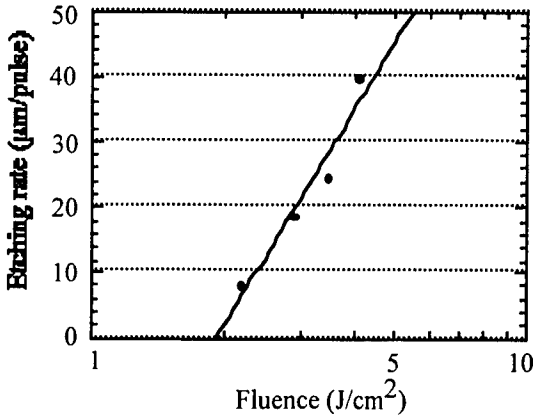


Fig.2 Dependence of the ablation depth on the fluence.

The laser beam pattern changes its intensity on the focal point because the laser oscillation was temporally and spatially multi mode, and fringes were observed on the ablated track of the quartz glass. A uniform part of the focal pattern was selected with 250 mm aperture.

To measure the ablation rate, the ablated depth vs. the irradiation fluence (shown in Fig. 2) or the number of shots was observed. The ablated depth was measured with increasing the number of shots. It was a linear function to the number of shots and to the fluence. A flat surface process was made by scanning the substrate with X-Y stage. The processed surface and its vertical profile are shown in Figs. 3 and 4. Although a uniform ablation was obtained, the surface roughness was large as a few μm. This surface roughness was produced due to a nonuniform beam pattern of the irradiation beam and the debris deposited on the surface during the process. These problems will be improved using the beam homogenizer and the gas jet flow.



Fig.3 Processed surface by scanning irradiation (×50).

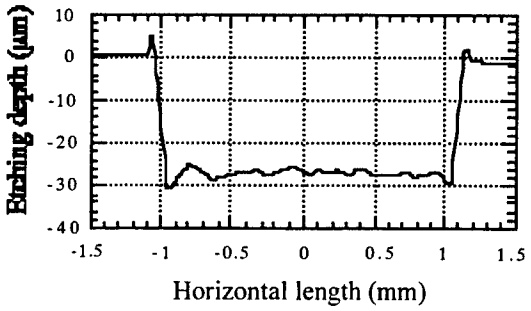


Fig.4 Vertical profile of scanned surface.

3. Deformation of transmitted pulse waveform

As described above, flat surface ablation of quartz glass have been made using F2 laser light. However, the surface roughness of the ablated area was highly degraded due to the increase of small ripples in wade range of spatial frequencies. This ripple may be originated in the ablation process of quartz glass by F2 laser light. The photon energy of F2 laser is smaller than the band gap energy of quartz glass (SiO_2), and the ablation process must be a non-linear process. To improve the LAS process of quartz glass, we must know the ablation mechanism. For this purpose, we measured the transient absorption at 157 nm by measuring the pulse shape through the quartz sample. The experimental arrangement is shown in Fig. 5, and the input and the output pulses waveforms were observed in front of the focusing lens and downstream of silica sample, respectively, as shown in Fig.5. The pulse waveforms were measured with two biplanar photo-tubes and a digital oscilloscope. The irradiation fluence was adjusted by shifting the sample against the focal point of the lens. The signal of the transmitted waveform was compared with the input pulse waveform. The input and the output pulse was in good agreement at low fluence. With increasing the fluence, the waveform of output pulse deviates from the incident waveform as shown in Fig. 6(a). This phenomena are quite similar in the case of ArF laser light.

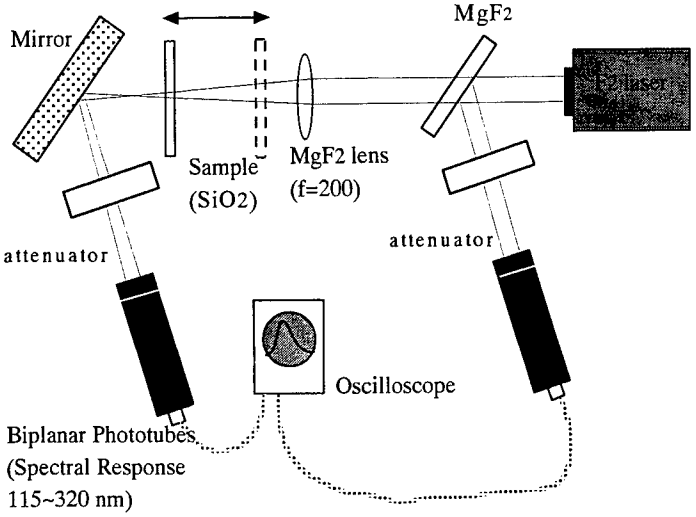
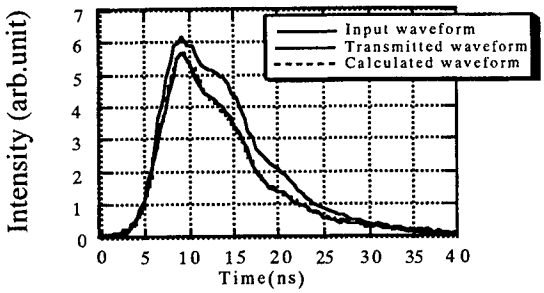
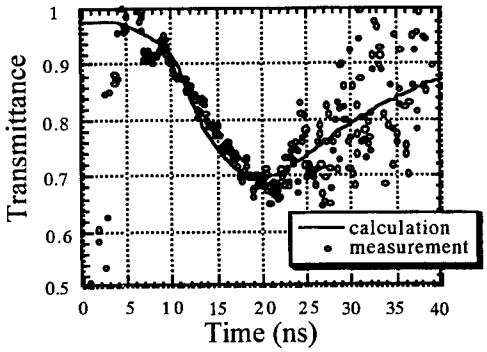


Fig. 5 Experimental arrangement for the measurement of the input and transmitted waveform.



(a) Waveform



(b) Transmittance

Fig. 6 Measured and calculated waveforms.

This phenomena was understood that the transient absorption depends on the fluence of F2 laser. These results indicates that the absorption of quartz glass for laser light is very small at the beginning of the irradiation, and it increases rapidly in time by increasing the fluence. It suggests the importance of excited state absorption. We constructed a model as following to understand the transient absorption.

$$\alpha(x,t) = A\int_0 (I(x,t) - I(x+\Delta x,t))\cdot \exp(-\tau\cdot t)dt, \quad (1)$$

$$\frac{dI(x,t)}{dx} = -\beta\cdot I(x,t)^2 - \alpha(x,t)\cdot I(x,t), \quad (2)$$

where A is a fixed number, α is absorption coefficient, β is two photon absorption coefficient [4] and $1/\tau$ is a life time of excited state. In these equations, the absorption coefficient α is given as a function of absorbed energy prior to the time period. The integral term of the incident fluence I(x,t) in Eq.(1) means that new absorption was generated due to the absorbed energy in unit length Δx. It is also assumed that the absorption is decreased with a life time τ. At the parameters of A : 3555 $\times 10^9$, β : 0.1 cm/W and $1/\tau$: 16.7 ns, the transient absorption was calculated by using these equations. Figure 6 (b) shows the instantaneous ratio of the output pulse to the input pulse, and the transient absorption calculated by Eq.(1). The results from Eq.(1) could fit to the experimental plots. In the processing of the quartz glass with F2 laser, therefore, the excited state absorption is important on the ablation mechanism.

4. Spectral transmittance

There are many kinds of quartz glass with different compound elements and with different optical performances. At 157 nm wavelength, for example, the quartz glass has the transmittance of 0 to 40 %/cm [5]. We compared with the spectral transmittance of five quartz glasses with different elements as shown in Table 1. One example of the measured results for 10000 pulses exposing at 1.5 mJ/cm^2 fluence and for 36000 pulses at 4 mJ/cm^2 are shown in Fig. 7 (a) and (b). At low fluence, a weak increase of transmittance (so called bleaching) was observed. However, at the higher fluence, a broad spectrum absorption has been observed as shown in Fig. 7 (b).

Table 1 Summary of content in different samples of silica glass.

sample	OH ($10^{18}cm^{-3}$)	Cl ($10^{18}cm^{-3}$)	SiH ($10^{18}cm^{-3}$)	H_2 ($10^{18}cm^{-3}$)
ED-A	7.1 (90ppm)	<0.1	n.d.	n.d.
ED-H	3.2 (40ppm)	<0.1	n.d.	n.d.
ED-B	<0.1	<0.1	1.0	n.d.
ED-C	<0.1	31 (1000ppm)	n.d.	n.d.
ES	93 (1200ppm)	1.2	n.d.	1.8

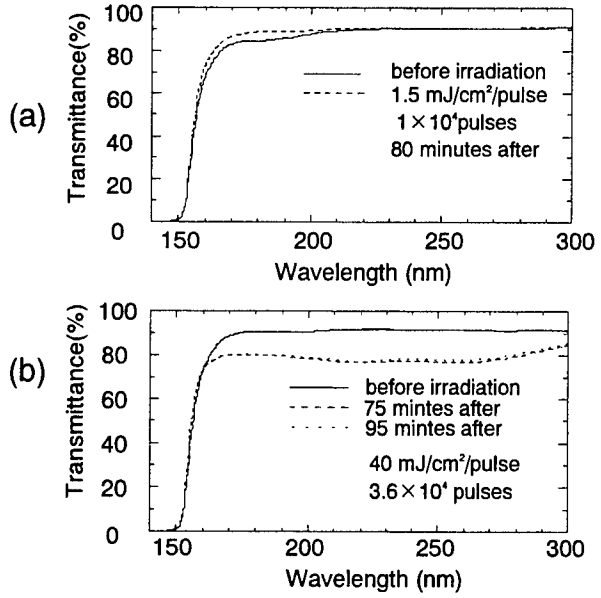


Fig. 7 VUV transmission change of quartz glass with F_2 laser irradiation..
(a) at 1.5 mJ/ cm^2, and (b) at 40 mJ /cm^2.

5. Summary

We tried to shape the surface of quartz glass by scanning irradiation using F_2 laser. A uniform plane ablation has been achieved although the surface roughness was still large. This shows the future possibility of laser ablation by VUV laser for processing the optical elements. The waveform measurement of the transmitted laser light through the silica glass shows very strong absorption in the latter part of the irradiated pulse. To investigate the reason for this phenomena, we calculated with a simple model that absorption coefficient increased in proportion to the amount of energy absorbed prior to the moment, and its result was in very good agreement with the measurement. As the result, the latter part of the waveform decreases because the laser light is absorbed by the excited state witch was generated by the early part of laser pulse and which declines in a life time. This indicates that the ablation process contains not only the multi-photon absorption but also excited state absorption. This phenomena is a non-linear one which is greatly depends on the fluence and the photon energy. Because photon energy is large in F_2 laser, the generation of the color center is also remarkable. The knowledge obtained through this experiment is very important to achieve uniform ablative shaping (LAS) of the quartz glass. We will investigate the interaction of F_2 laser light and quartz glass using time and spectrum resolved absorption measurement in the next step.

6. Acknowledgement

The authors would like to thank Yamaguchi Nippon Silica Glass CO., LTD. for the preparation of samples of different kinds of impurities.

References

[1] T. Jitsuno, K. Tokumura, N. Nakashima and M. Nakatsuka,"Laser ablative shaping of plastic optical elements for the phase control", Appl. Optics, **38**, (1999) pp.3338-3342.
[2] H. Mikata, T. Jitsuno, K. Tokumura, S. Motokoshi and M. Nakatsuka, "F2 laser ablation process of silica glass", AHPLA'99, SPIE, **3885**, Suita, Osaka, Nov. 1-5, (1999) pp.57-64.
[3] K.Watanabe, Edward C.Y. INN, and Murray Zelikoff, "Absorption Coefficients of Oxygen in the Vacuum Ultraviolet", J. Chem. Phys., **21**, (1953) pp. 1026-1030.
[4] Robert K. Brimacombe, R. S. Taylor and K.E.Leopold, "Dependence of the nonlinear transmission properties of fused silica fibers on excimer laser wavelength", J.Appl.Phys., **66**, (1989) pp. 4035-4039.
[5] N.Kuzuu, "ArF-excimer-laser induced absorption in soot-remelted silicas", LASER-INDUCED DAMAGE IN OPTICAL MATERIALS, SPIE, **2714**, BOULDER, COLORADO, (1995) pp. 41-51.

Optical Diagnostics in Laser-induced Plasma-assisted Ablation of Fused Quartz

M.H. Hong, K. Sugioka*, Y.F. Lu, K. Midorikawa* and T.C. Chong

Laser Microprocessing Laboratory, Department of Electrical Engineering and Data Storage Institute, National University of Singapore, 10 Kent Ridge Crescent, Singapore 119260
Email: dsihmh@dsi.nus.edu.sg
** Laser Technology Laboratory, RIKEN-The Institute of Physical and Chemical Research, Wako, Saitama 351-01, Japan*

A wideband and ultrafast phototube is applied to diagnose laser-induced plasma-assisted ablation of fused quartz. It is found that signal waveform is closely related to laser fluence and target-to-substrate distance. For the distance less than a threshold, below which quartz ablation takes place even by single pulse irradiation, there are three peaks detected. Signal analyses show that the first peak is attributed to laser scattering, the second and third ones to Ag target and quartz substrate ablation. It confirms that there is a direct influence of target plasma on substrate ablation. The third peak moves forward and overlaps with other peaks as the distance decreases and laser fluence increases. Peak amplitude and its arrival time of the quartz plasma are used to characterize the ablation dynamics. Signal variation with pulse number shows that at a higher distance, there are only two optical peaks attributed to laser scattering and target ablation in the first pulse. While by further pulse irradiation, the peak for quartz ablation is recorded. It is due to Ag thin film deposited on quartz rear side surface after the first pulse irradiation. As the distance increases further, the peak for quartz ablation moves to the right and finally disappears because of no thin film deposited.

Keywords: signal diagnostics, laser-induced plasma-assisted ablation, laser plasma interaction, fused quartz, plasma substrate interaction

1. Introduction

Fused quartz is one of the most important materials in various industrial applications due to its high hardness, high thermal stability and high transparency in the visible wavelength region. It is highly desirable to develop a sophisticated microfabrication technique for this material to manufacture phase shift masks, optical waveguide devices and UV optics [1,2]. With a wide energy bandgap around 9 eV, fused quartz is transparent to most laser sources. Though F_2 and vacuum-ultraviolet (VUV) Raman lasers have been successfully applied in the microfabrication of fused quartz [3,4], these technologies have disadvantages of high photon cost, poor beam quality and complicated setup. Recently, K. Sugioka et al. proposed a highly potential laser ablation scheme for transparent hard materials microfabrication by UV and visible lasers [5,6]. With an aid of laser-induced plasma from a metal target ablation, fused quartz can be drilled through or patterned. However, the quartz ablation is highly dynamic. In the nanoseconds time scale, there are target ablation with plasma generation as well as complicated interactions among laser light, target plasma and quartz substrate. Detail mechanism on the laser ablation is still unclear. In this paper, an ultrafast phototube is applied to diagnose optical signals generated during the laser-induced plasma-assisted laser ablation of fused quartz. Signal analyses of laser light scattering and plasma generation from both metal target and quartz substrate ablation are carried out. Signal variation as a function of laser fluence, pulse number and target-to-substrate distance is studied for a better understanding of mechanisms behind this dynamic process.

2. Experimental setup

Figure 1 shows experimental setup for the optical signal diagnostics of pulsed laser-induced plasma-assisted ablation of fused quartz. A KrF excimer laser (Lambda Physik, LPX 100) was used as a light source. It has a wavelength of 248 nm and a pulse duration (FWHM) of 23 ns. Laser beam went through a beam splitter. 5% of its energy was reflected into an energy meter to monitor its output. The other part of laser energy was focussed onto a Ag (99.99%) target in ambient air by a quartz lens with a focal length of 150 mm. Laser fluence was tuned by varying laser output energy.

First International Symposium on Laser Precision Microfabrication, Isamu Miyamoto, Koji Sugioka, Thomas W. Sigmon, Editors, Proceedings of SPIE Vol. 4088 (2000) © 2000 SPIE · 0277-786X/00/$15.00

Optical-graded fused quartz (Viosil, 0.5 mm thick, Shinetsu Quartz Co. Ltd.) was used as substrate, which was placed in front of the Ag target and adjusted by a micrometer with a target-to-substrate distance from 0.2 to 2 mm. Before the laser irradiation, it was ultrasonically cleaned with acetone and ethanol, followed by rinse with DI water. Since it is transparent, the laser light goes through the substrate first and then ablates the Ag target. Plasma generated from target ablation interacts with quartz rear side surface and later part of incident laser light, which induces significant ablation on the quartz surface. An ultrafast phototube (Hamamatsu R1328U-53) with a photocathode diameter of 1 cm was applied to capture optical signals generated during the laser ablation. Its spectral response is from 185 to 650 nm with rise time and fall time of 60 and 55 ps, respectively. It detects scattered laser light and plasmas generated from both target and substrate ablation at a same time. Optical signal recorded was sent to a digital oscilloscope (Lecroy LC 534A, bandwidth 1 GHz and sampling rate 2 GS/s) with a time resolution of 1 ns. Synchronous output of laser controller was sent to the oscilloscope as a trigger signal for the signal detection. Digitized signal was then sent to a PC for data storage and further processing. A narrowband interference filter, which only allows 248 nm laser light passing through, was inserted in front of the phototube to distinguish the scattered laser light from the plasmas. The phototube was kept at 5 cm away from laser spot on the Ag target at a detection angle of 90° with respect to target normal. Its center was kept in the same level of the target surface and optical signals were sensed from the upper half of the phototube.

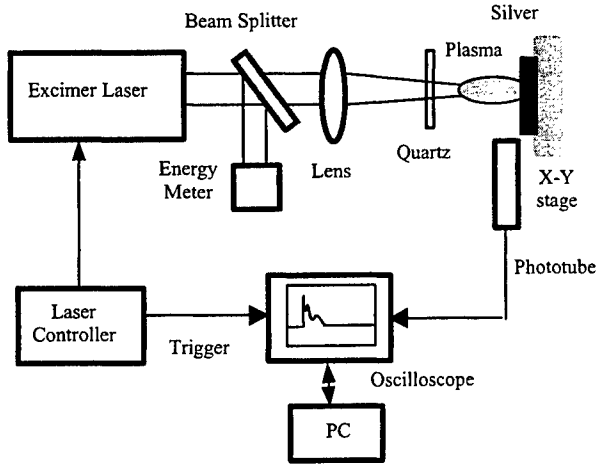


Fig. 1 Experimental setup for the optical diagnostics of pulsed laser-induced plasma-assisted ablation of fused quartz.

3. Results and discussion

Figure 2 shows the optical signals captured at the first pulse of laser irradiation for a laser fluence of 7.2 J/cm^2 and target-to-substrate distances of 0.22, 0.54, 0.79 and 1.95 mm, respectively. It can be found that there are two peaks in an optical signal for the distance of 1.95 mm. Microscopy observation of target and substrate surfaces before and after the laser ablation showed that the Ag target was ablated with the laser irradiation while morphology of quartz surface didn't change. It was also observed in the experiment that the second peak disappeared after the signal passing through a 248 nm filter. Therefore, it can be concluded that the first peak is attributed to the laser light and the second one to plasma generated from the target ablation. Since the phototube was placed out of reflection plan of the incident laser beam. The first peak is attributed to light scattering during the laser ablation. While for the distance of 0.79 mm, there is another peak following the target plasma in the optical signal. Surface morphology comparison showed that both the target and substrate were ablated with the first pulse of laser irradiation. It means that this new peak is attributed to the quartz ablation. As the distance reduces further, its peak amplitude increases greatly and the peak position moves to the left and overlaps with the other peaks. Optical emission spectrum analyses also confirm that the third peak is attributed to the quartz ablation with its emission spectral lines detected [7]. Since the quartz substrate is transparent to the laser light, its ablation is resulted from the aid of target ablation-induced plasma.

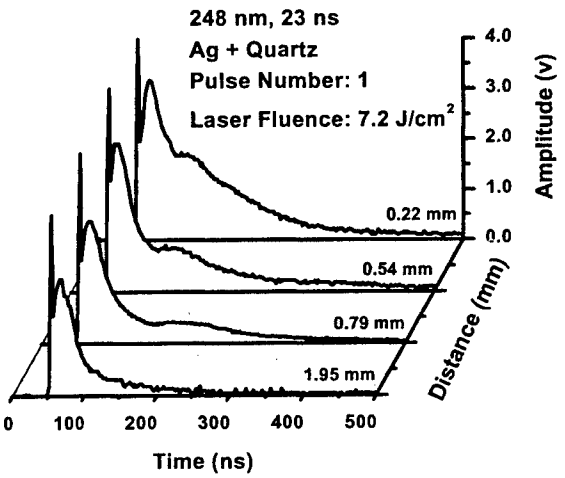


Fig. 2 Optical signals captured during the first pulse of laser ablation at a laser fluence of 7.2 J/cm^2 and target-to-substrate distances of 0.22, 0.54, 0.79 and 1.95 mm.

To analyze the peak distributions, the optical signals were deconvoluted into three different profiles. Since the laser light is in a form of pulse, it is fitted by the following equation:

$$f_1(t) = A \times [1 - exp(-\frac{t - t_o}{\tau_1})]^p \times exp(-\frac{t - t_0}{\tau_2}) \quad , \qquad (1)$$

where A, p, t_0, τ_1 and τ_2 are fitting parameters. Meanwhile, laser ablation of solid materials produces a plasma which

has a strongly forward-peaked distribution along a direction normal to the substrate surface. Since there are strong collisions among plasma species at early stage of laser ablation, plasma generated behaves like a nozzle source. Besides plasma expansion, there is also a large center-of-mass motion. Therefore, plasma time-of-flight (TOF) spectrum is often described as a shifted Maxwell-Boltzmann distribution [8]:

$$f_2(t) = \frac{B}{t^4} \times exp[\frac{-(m/2kT_o)(L_f - v_d t)^2}{t^2}] \quad , \qquad (2)$$

where B is a fitting parameter, m the mass of ablated species and k the Boltzmann constant. T_o represents the characteristic temperature of the distribution. L_f stands for plasma flight distance from the substrate surface and v_d is the center-of-mass velocity.

The above equations were used to fit the optical signal shown in Fig. 2 for the target-to-substrate distance of 0.22 mm. Fitting result is illustrated in Fig. 3. Peak amplitude and its arrival time are applied to characterize laser light scattering and plasma generation. It was noted in the calculation that for the target ablation, the plasma flies toward the substrate, while plasma for the substrate ablation flies in the opposite distance, from the substrate to the target. It can be observed from Fig. 3 that the target plasma appears at a delay time of 5 ns after the starting of laser irradiation. Time for the laser interaction with target plasma is around 20 ns. It is defined as the time interval between laser pulse termination and starting of the plasma profile [9]. Since the target plasma flies outward at a high speed, it could reach the substrate rear side surface in a time delay less than 20 ns. Generation of the substrate plasma implies that the target plasma may interact with the later part of incident laser light at the quartz surface, which induces the latter ablation even with the first pulse of laser irradiation.

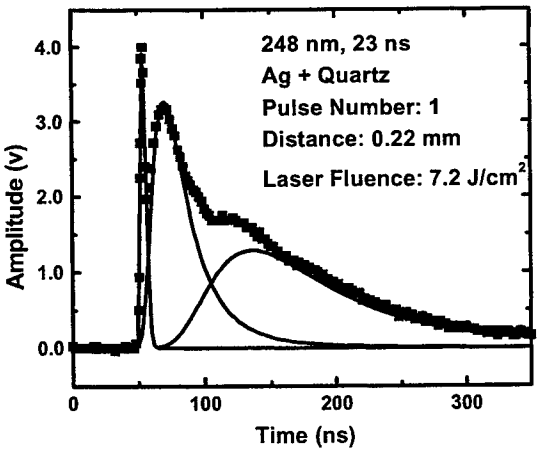


Fig. 3 Signal fitting for the first pulse of laser ablation at a laser fluence of 7.2 J/cm^2 and a target-to-substrate distance of 0.22 mm.

Figure 4 presents the peak amplitude and peak arrival time for the substrate plasma as a function of target-to-substrate distance during the first pulse of laser irradiation. Laser fluence applied was 7.2 J/cm^2. It is clear that the plasma peak amplitude reduces while its peak arrival time increases with the distance. For the distance higher than 1.75 mm, the substrate plasma disappears. It means that there is no laser-induced plasma-assisted ablation of the quartz substrate. This is because the target plasma reaches the substrate rear side surface at a time delay higher than 20 ns. The target plasma interaction with incident laser light finishes before it reaches the substrate surface. Therefore, it can be estimated that the target plasma is flying outward at a speed around 8.75×10^4 m/s during the laser ablation at a laser fluence of 7.2 J/cm^2.

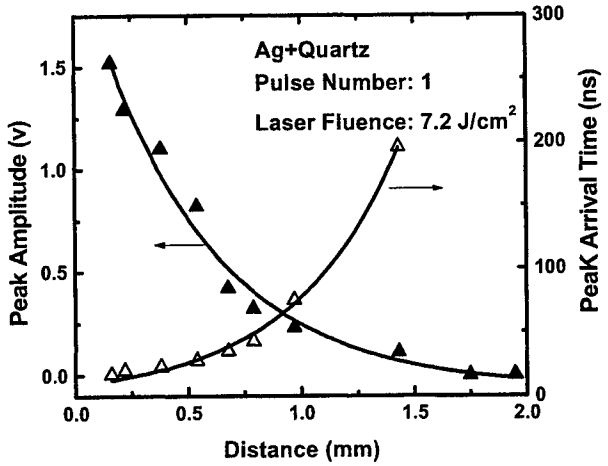


Fig. 4 Peak amplitude and its arrival time for the substrate plasma as a function of target-to-substrate distance at a laser fluence of 7.2 J/cm^2 during the first pulse of laser ablation.

Figure 5 shows the peak amplitude and peak arrival time for the substrate plasma as a function of laser fluence at a target-to-substrate distance of 0.25 mm during the first pulse of laser irradiation. It can be observed that the plasma peak amplitude increases greatly with laser fluence. Meanwhile, its peak position moves to the left at a higher laser fluence. It is because there is a stronger laser ablation of the Ag target at a higher laser fluence, which induces a higher dynamic target plasma. It enhances the interaction between incident laser light and the target plasma and results in the stronger quartz ablation. It can also be observed that there is no substrate ablation at a laser fluence of 1.2 J/cm^2. From the experimental results, threshold fluence for the quartz ablation with the first pulse of laser irradiation can be estimated to be 1.4 J/cm^2 for the target-to-substrate distance of 0.25 mm. At this fluence, time for the laser interaction with the target plasma is around 10 ns. Therefore, speed of the target plasma can be calculated as 2.5×10^4 m/s.

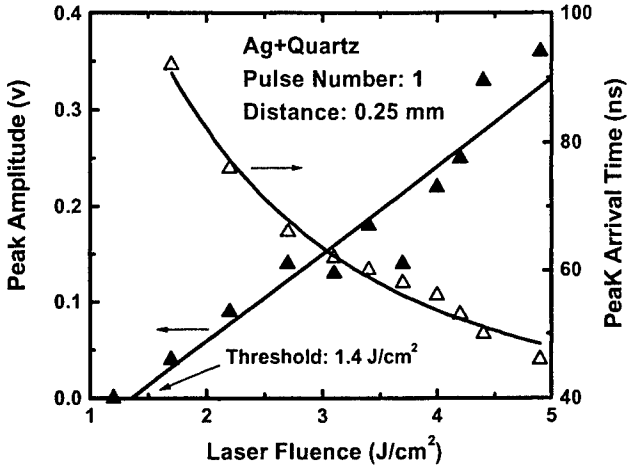


Fig. 5 Peak amplitude and its arrival time for the substrate plasma as a function of laser fluence at a target-to-substrate distance of 0.25 mm during the first pulse of laser ablation.

Based on the previous discussion, it can be concluded that the quartz ablation at the first pulse of laser irradiation depends on the Ag target ablation and complicated interactions among incident laser light, target plasma and quartz rear side surface. For a high target-to-substrate distance, the target plasma reaches the quartz surface after the laser plasma interaction terminates. Though there is no the quartz ablation at the first pulse of laser irradiation, target plasma species deposit on the quartz rear side surface and form a metal thin film. It modifies the light absorption characteristics for the quartz surface, which induces the quartz ablation with further pulse irradiation. Figure 6 shows the peak amplitude of the substrate plasma as a function of pulse number at a laser fluence of 4.4 J/cm^2 and target-to-substrate distances of 0.25 and 0.78 mm. For the distance of

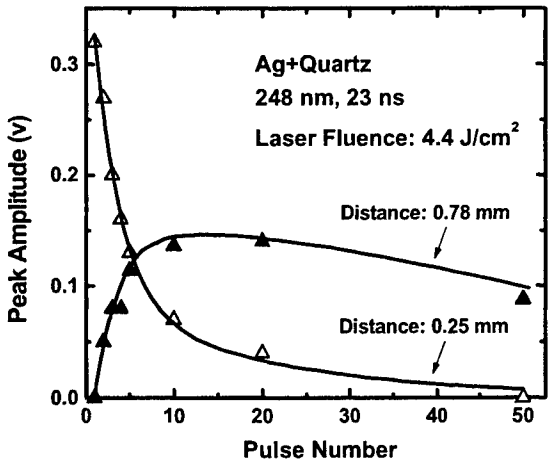


Fig. 6 Peak amplitude of the substrate plasma as a function of pulse number at a laser fluence of 4.4 J/cm^2 and target-to-substrate distances of 0.25 and 0.78 mm.

0.25 mm, the peak amplitude at the first pulse is the highest and reduces gradually to zero with pulse number. This is because the quartz substrate is ablated and a through hole is formed after 50 pulses of laser irradiation. While for the distance of 0.78 mm, the peak amplitude is zero at the first pulse and starts to increase with the second pulse of laser irradiation. It is due to Ag thin film deposition on the quartz rear side surface at the first pulse. It enhances the quartz light absorption ability and induces its ablation at the second pulse. As pulse number increases, quartz ablation is stronger at the first several pulses and then reduces gradually as more and more quartz materials are removed.

4. Conclusions

Optical diagnostic during laser-induced plasma-assisted ablation of fused quartz shows that the signal captured is attributed to laser light scattering and plasmas generated from both metal target and quartz substrate ablation. It can be concluded from signal analyses that quartz ablation is resulted from target ablation and dynamic interactions among target plasma, incident laser light and quartz rear side surface. For the distance lower than a threshold, quartz is ablated even at the first pulse of laser irradiation due to laser interaction with target plasma at the quartz surface. As the distance increases, there is no quartz ablation at the first pulse while it occurs with further pulse irradiation due to metal thin film deposition. Threshold distance is around 1.75 mm for a laser fluence of 7.2 J/cm^2. Quartz ablation is also closely related to laser fluence. For laser fluence higher than a threshold, the ablation occurs at the first pulse. Threshold fluence is about 1.4 J/cm^2 for the distance of 0.25 mm. Plasma speed at the early stage of laser ablation is also estimated.

References

1. K.O. Hill, B. Malo, F. Bilodeau, D.C. Jhonson and J. Albert, Appl. Phys. Lett., **62**, (1993) 1035.
2. K.M. Davis, K. Miura, N. Sguimoto and K. Hiro, Opt. Lett., **21**, (1996) 1729.
3. P.R. Herman, K. Beckley, B. Jackson, D. Moore and T. Yamanishi, SPIE, **2992**, (1997) 86.
4. K. Sugioka, S. Wada, H. Tashiro, K. Toyada and A. Nakamura, Appl. Phys. Lett., **65**, (1994) 1510.
5. K. Sugioka, J. Zhang and K. Midorikawa, SPIE, **3822**, (1999) 6.
6. J. Zhang, K. Sugioka, and K. Midorikawa, Opt. Lett., **23**, (1998) 1486.
7. M.H. Hong, K. Sugioka, Y.F. Lu and K. Midorikawa, to be published.
8. Q.Z. Qin, Z.H. Han and H.J. Dang, J. Appl. Phys., **83**, (1998) 6082.
9. Y.F. Lu, M.H. Hong and T.S. Low, J. Appl. Phys., **86**, (1999) 2899.

A laser method for marking bar codes on glass substrates

Hirotoshi Hayakawa

YASKAWA ELECTRIC CORPORATION Research Laboratory, 2-1 Shiroishi Kurosaki Yahatanishi
Kitakyushu Fukuoka, 806-0004, Japan
E-mail:hh@yaskawa.co.jp

A method that uses a Nd:YAG laser was developed to mark bar codes on glass substrates. In this method, bar codes are created by a combination of laser deposition and laser trimming; a film for the black bars of the bar code is deposited on the glass substrate, and part of the deposited film is trimmed to expose the white bars of the code. The resulting bar code has high contrast and high resolution. The measured transmission coefficient of the black bars was 2%. When the transmission coefficient was less than 70%, the bar codes were identified at an acceptable level, i.e. the code identification rate was at least 70%, with an average of 91%. The bar code was impossible to identify when the transmission coefficient was 78%. The laser power tolerance of the film deposition for code identification was about ±50% at optimum laser power.

keywords: Nd:YAG laser, marking, bar code, 2-D matrix symbol, glass substrate

1. Introduction

Code marks, such as bar codes and two-dimensional (2D) matrix symbols on glass substrates, are used in the electronics industry to mark products, such as liquid crystal displays (LCD) and plasma display panels (PDP), during production. Recognized code data of the code marks are utilized to find optimum treatment of each process in the industry. For practical application, bar codes and symbols require the following properties: high resolution, stable quality, low damage to substrate, thermal- and chemical-proof, particle-free marking process, and low manufacturing cost. Several marking methods to the glass substrate have been developed, such as direct marking methods that use CO_2 laser or UV laser irradiation[1], inner marking methods[2], and plasma assist machining methods[3]. The advantages of direct marking methods are low cost and chemical-proof marks. The disadvantages are that the code marks are not visible and the marked substrates are structurally weak. The advantages of laser deposition marking methods that use a Nd:YAG laser are that the marks are visible and are thermal- and chemical-proof. The disadvantages are that the resulting code marks do not have high enough contrast or resolution and that a high concentration of particles is generated during the marking process[1]. Laser transfer marking methods that use a Nd:YAG laser have many advantages, such as high contrast and resolution, because the code marks are marked by using a low laser power [1), 4)]. However, the stability of the quality is strongly dependent on the laser power, because adhesion of the codes and the symbols on the glass substrates depends on the laser power as well. Furthermore, the method requires accurate substrate setting mechanism for marking, so that the gap between the glass substrate and transfer material is stable and constant.

To solve the most drawbacks of the above-mentioned methods, I developed a marking method that involves two processes; laser deposition and laser trimming. This method was then used to mark bar codes and 2D matrix symbols. The results show that the marked bar codes and symbols have high properties on code identification.

First International Symposium on Laser Precision Microfabrication, Isamu Miyamoto, Koji Sugioka,
Thomas W. Sigmon, Editors, Proceedings of SPIE Vol. 4088 (2000) © 2000 SPIE · 0277-786X/00/$15.00

2. Fundamentals of the developed marking method

Figure 1 shows a schematic of the developed marking method for bar codes and 2-D matrix symbols.

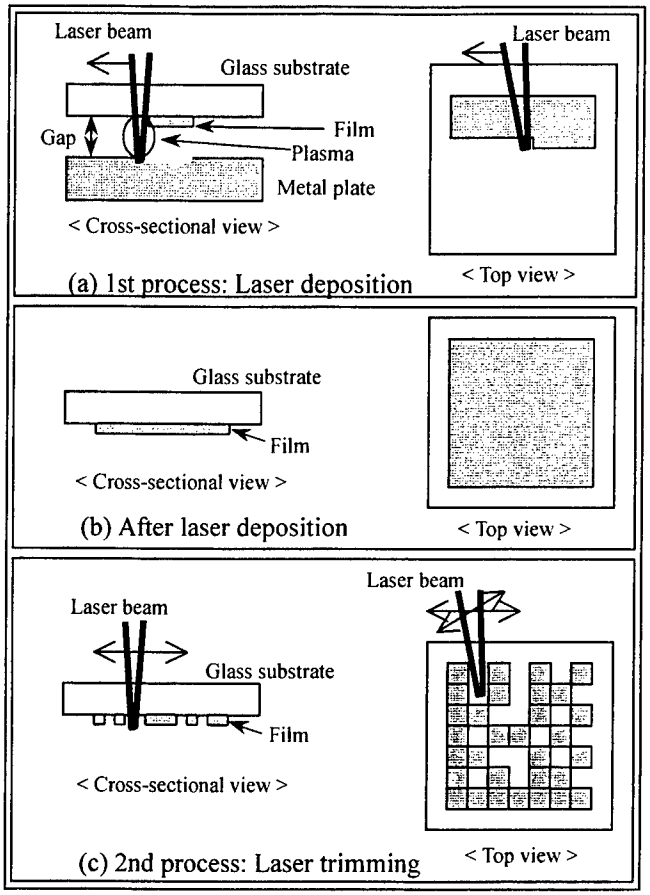


Figure 1 Developed marking method for marking bars codes and symbols on glass substrates.

In the laser deposition, first, a glass substrate is placed on a metal plate with the fixed gap between the substrate and plate. Then, the surface of the metal plate is irradiated with the laser through the glass substrate, thus creating plasma in the gap. This plasma then deposits as a film on the glass substrate. The laser beam acts as a raster, and thus a film is deposited on the substrate wherever the laser scans. In the laser trimming, the metal plate is removed, and part of the film is removed, or trimmed, by laser irradiation. Thus, the black segments of a symbol or bar code are made by the laser deposition process, and the white segments by the laser trimming process. The developed marking method differs from conventional marking methods in that the conventional marking methods, the black segments are marked at the point of laser irradiation on the glass substrate by machining, deposition, or transfer, whereas in the developed marking method, a film is made on the marking object, which is a glass substrate.

3. Experimental

Laser power of Nd:YAG laser marker was measured a function arc lamp current for pumping at continuous-wave (CW) irradiation and pulse irradiation. The relationship between the laser power and the arc lamp current was determined.

Bar codes on sodium glass substrates with a stainless steel plate were made by the developed marking method. The gap between the glass substrates and the stainless steel plate was 60 μ m. In the laser deposition, films were deposited on a glass substrates at a raster scanning with 50 μ m pitch, with arc lamp current from 11 to 16 A, and at a Qsw frequency of 3kHz. The transmission coefficient of the deposited films was measured by using the measurement system shown in Figure 2.

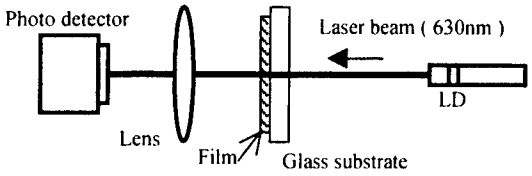


Figure 2 System used to measure the transmission coefficient of a deposited film

The relationship between the transmission coefficient of the film and the code identification performance of marked bar codes was determined by using various marking conditions: arc lamp current from 11A to 16A, and Qsw frequency of 2,3,4 and 8kHz. A bar code scanner with a 630nm wavelength laser diode (LD) was used for the code identification. Code identification rate was defined as the number of successful identifications of 500 times reading on the same bar code.

4. Results and Discussion

Figure 3 shows the laser power as a function of the arc

lamp current for CW and Qsw frequency. The laser power increased with increasing arc lamp current and increasing frequency. The increase of the laser power was relatively linear between 11A and 18A.

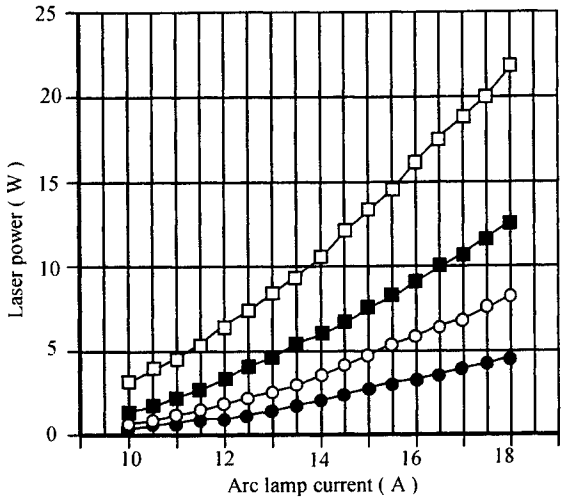


Figure 3 Laser power versus arc lamp current at various Qsw frequency. □ : CW, ● : Qsw = 1kHz, ○ : Qsw = 2kHz, ■ : Qsw = 4kHz.

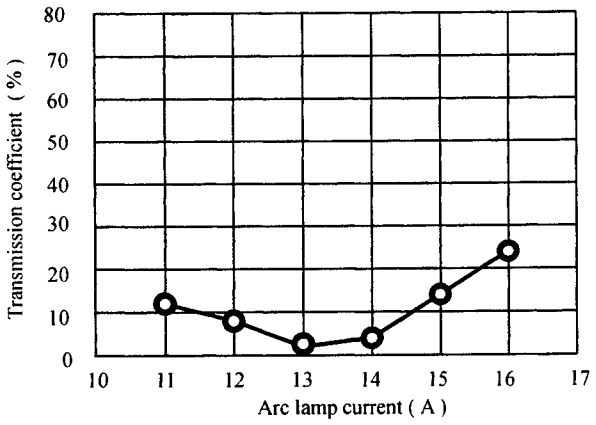


Figure 4 Transmission coefficient of the deposited film as a function of the arc lamp current used in the marking.

Figure 4 shows the transmission coefficient of the films as a function of the arc lamp current used in the marking. The maximum transmission coefficient was 25% at 16A, and the minimum was 2% at 13A. When the current exceeded 14A, the transmission coefficient increased probably due to the mode fluctuation of the Nd:YAG laser. The energy density of the laser beam decreases as the laser beam spot diameter increases, and thus the thickness of the films marked with a current over 14A is thinner than that of films marked with a current of 13A.

Figure 5 shows the relationship between the transmission coefficient of the black bars and code identification rate of the bar codes. The bar codes were made at various lamp currents (11,12,13,14,15 and 16A) and Qsw frequencies (2,3,4 and 8kHz).

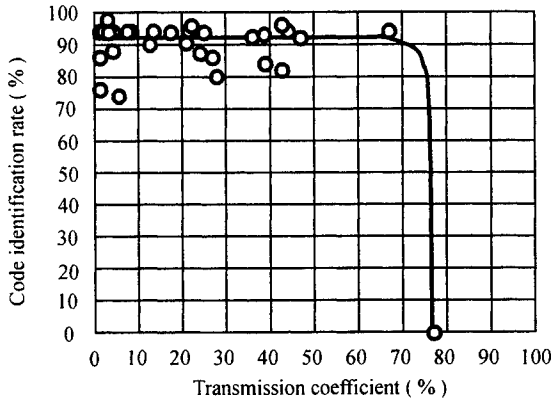


Figure 5 Code identification rate versus transmission coefficient of the marked black bars.

When the transmission coefficient was less than 70%, the bar codes were identified at an acceptable level, i.e. the code identification rate was at least 70%, with an average of 91%. The bar code was impossible to identify when the transmission coefficient was 78%, corresponding to bar codes marked using the lowest laser power i.e., arc lamp current of 11A at a Qsw frequency of 2kHz. The range of laser power resulting in an identifiable bar code was 2.5W to 10W. The tolerance of the laser power was ±50% at a Qsw frequency of 4kHz. In conventional marking methods, this level of tolerance can not be achieved. This level of tolerance shows that the developed marking method is effective for marking by using a YAG laser with mode fluctuation.

Figure 6 shows a representative photograph of a bar code made with the developed marking method. The width of the narrow bars was 0.2mm and that of the wide bars was 0.5mm.

The white narrow bars were formed by scanning three lines with the laser beam. The high contrast of this bar code makes the code easy to identify. Although a bar code in which the narrow bars were 100 μ m wide was successfully marked, the code could not be identified because it was below the detection limit of the bar code scanner.

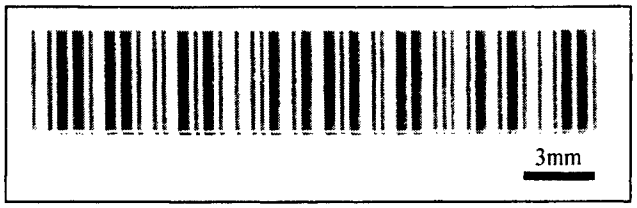


Figure 6 Photograph of a marked bar code on a glass substrate.

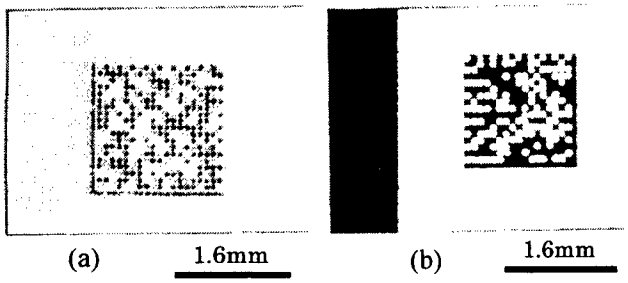


Figure 7 CCD images of marked 2-D matrix symbols on a glass substrate.
(a) Laser deposition marking method
(b) Developed laser marking method

Figures 7(a) and (b) show CCD images of 2-D matrix symbols marked by a conventional laser deposition marking method and by the developed laser marking method, respectively. The symbol created by conventional laser deposition has low contrast because the boundaries between the white and black segments are indistinct. The reason for these indistinct boundaries is that during deposition of the film, a area of the deposited film for the black segments is wider than the laser beam spot diameter. The film thickness of the black segments is thinner at the boundaries. In contrast, the symbol created by the developed laser marking method has high resolution and high contrast. In the developed laser marking method, the same result, namely, high resolution and high contrast, is expected when a coated film on the glass substrate is irradiated with the laser.

Compared with conventional methods, the developed method produces highly stable code identification due to the high contrast and high resolution of the marked codes. The developed laser marking method was applied to marking equipment for bar codes in a display panel manufacturing line.

5. Conclusion

The developed marking method successfully produced marked bar codes that have stable quality for code identification due to high contrast and high resolution, and have wide tolerance of laser power.

Reference

1) Tatsuya Nakano, Monthly Bar Code, Vol.11, No.5, 16 (1998)

2) Ken-ichi Hayashi, Proceedings of 45th Laser Materials Processing Conference, 23, (1998)

3) Jie Zhang, Koji Sugioka and Katsumi Midorikawa, Proceedings of 45th Laser Materials Processing Conference, 1, (1998)

4) Nikkei Mechanical, No.532, 49 (1999-1)

Photo-induced refractive-index changes in filaments formed in glasses with femtosecond laser pulses

Kazuhiro YAMADA*, Tadamasa TOMA*, Wataru WATANABE*,
Junji NISHII** and Kazuyoshi ITOH*

*Department of Applied Physics, Graduate School of Engineering, Osaka University
2-1, Yamadaoka, Suita, Osaka, 565-0871 Japan
E-mail: yamada@fermat.ap.eng.osaka-u.ac.jp

**Optical Material Division, Osaka National Research Institute
Agency of Industrial Science and Technology
1-8-31, Midorigaoka, Ikeda, Osaka, 563-8577 Japan

Recently, the structural modifications of glass by focusing femtosecond laser pulses have been demonstrated. We present photo-induced structural changes in silica glass with femtosecond laser pulses. We investigated the relationship between the formation of filaments and local refractive index changes in silica glass. *In situ* observation revealed the coincidence between the location of filament and that of refractive index change. The observation also showed that the region of refractive index change elongates toward the upstream direction of laser pulses with the exposure time. The region of refractive index change was several hundred-micron long and the diameter was smaller than two microns. The length of the region was dependent on the numerical aperture of focusing lenses. The refractive index change was confirmed to be as large as 0.01 by three different methods. We fabricated a 2-mm waveguide by translating the sample along the optical axis.

Key words: femtosecond laser pulses, filament, refractive index change, waveguide, micro-fabrication

1. Introduction

Over the past three decades, many researchers have investigated the fabrication of Bragg grating in Ge-doped silica glass with UV radiation [1]. Recently, the structural modifications of dielectrics by focusing intense femtosecond laser-pulses have been demonstrated [2-4]. The large increase (> 0.01) in the refractive index was obtained in the region of glass damaged by femtosecond laser pulses [5]. The infrared photosensitivity allows the fabrication of three-dimensional photonic structures or devices by translating the sample with respect to the focal point. Although the physical mechanisms responsible for infrared photosensitivity are still under investigation, this technique has been applied to the three-dimensional optical storage [6-10], waveguides in a wide variety of glasses [11-13], gratings [14-16], couplers [13], and photonic crystals [16].

Self-focusing of ultrashort laser pulses in transparent materials has close connections with the induction of refractive index change [5] and 3-D microstructuring [17]. The filament formation has been reported to lead to the crystallization of silver nanoperticles in silver-doped glass [18]. The filamentation is also applied to bulk modification in optical fibers [19]. In this paper, we investigate the relationship between the filament and the refractive index change in silica glass that are induced by femtosecond laser pulses. *In situ* observation of the filament and the region of refractive index change shows that the region moves toward the incident direction of laser pulses with the exposure time. We also observe that the location of filament coincides with the region of refractive index change. The region has the length of several hundreds of microns and the refractive index change is confirmed to be 0.8×10^{-2} by the two of three different methods. The present study suggests a special technique that allows fabrication of low-loss straight waveguides and small Bragg reflectors.

2. Experiments

Figure 1 shows the optical setup. We focus the laser pulses inside a sample of silica glass; a cube of 3 × 2 × 20 mm. The sample is commercially-available fused-silica glass. The 4-sides of the sample are optically polished for *in situ* observation. In the experiment, we used 130-fs pulses intensified by Ti:sapphire regenerative amplifier. The

First International Symposium on Laser Precision Microfabrication, Isamu Miyamoto, Koji Sugioka,
Thomas W. Sigmon, Editors, Proceedings of SPIE Vol. 4088 (2000) © 2000 SPIE · 0277-786X/00/$15.00

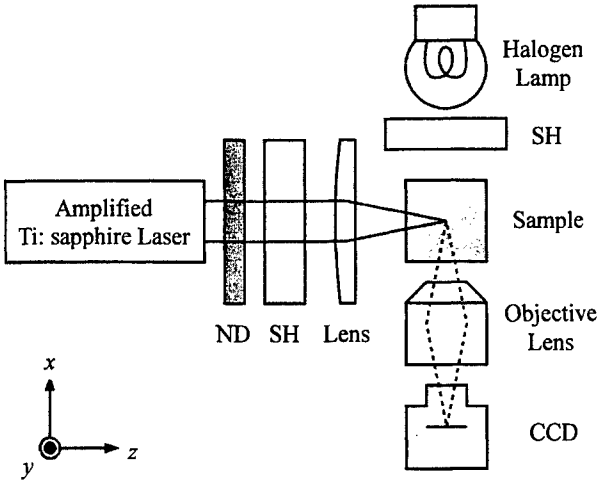


Figure 1 Schematic of the optical setup for *in situ* observation of a filament and the region of refractive index change in silica glass: ND, neutral density filters; SH, shutter.

wavelength was 800 nm and the repetition was 1-kHz. We minimized the pulse duration at the focal point by adjusting the compression grating in the amplifier of the laser system. This minimization is achieved by obtaining the strongest supercontinuum in the far field.

We observed the temporal behavior of filament formation and then the photo-induced refractive-index change. We will use in the following the term "filament" to refer to the region where the laser pulses are localized due to self-trapping and are partly scattered thereof by the process of Rayliegh scattering. We can thus observe the filament without illumination. When we observe the resultant refractive-index change, we illuminate the region of interest by a halogen lamp.

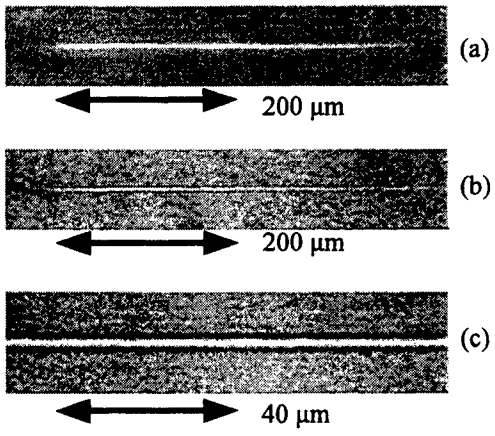


Figure 2 Relationship between the filament and the region of refractive index change: (a) photograph of the filament; (b) the region of refractive index change; (c) expanded view of the region of refractive index change.

Figure 2 shows the relationship between the filament and the region of refractive index change. Fig. 2(a) shows the microscopic side view of a single filament under excitation by ultrashort laser pulses. The laser beam was focused by single lens that has a focal length of 100 mm (0.01-NA). Fig. 2(b) shows microscopic side view of the same region where the refractive index change was induced by the excitation of laser pulses. The region was exposed to the laser pulses for 2 min.. Fig. 2(a) and (b) show that the region of refractive index change spatially coincides with the location of the filament. Fig. 2(c) shows the expanded view of the region of refractive index change. The figure shows that the profile is quite smooth.

Figure 3 shows the trans-illuminated microscopic images of refractive index change induced by a single and multiple filaments. The incident energy of laser pulse was varied under the condition of fixed exposure time (2 min.). When the incident energy is lower than 0.7 μJ/pulse, the filament is not observed nor is the refractive index change induced. In the range of 0.7-2.3 μJ/pulse, a single filament is generated and the refractive index change is also induced in the same region as the filament. In the range of 2.3-10 μJ/pulse, multiple filaments are generated and the refractive index change is induced in the same region as each filament. The result is shown in Fig. 4(a). Generation of multiple filaments in glass has already been reported by Steinberg [20]. Beyond the pulse energy of 10 μJ/pulse, granular structures that are seen in Fig. 4(b) were observed around the "linear focal" point where the laser pulses with the reduced energy would be

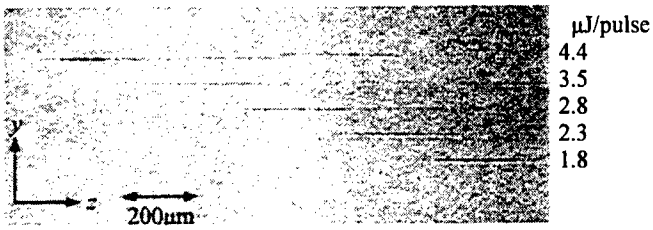


Figure 3 Variations of the resultant refractive-index change for different incident energies of laser pulses.

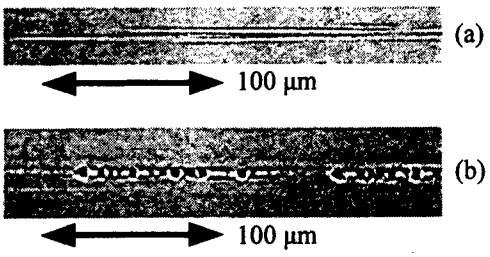


Figure 4 Trans-illuminated microscopic photographs of (a) refractive index change induced by multiple filaments and (b) granular structures.

focused without self-focusing. These structures were similar to that described by Ashkenasi [17]. We observed that when the incident energy was increased, the head of the filament moved to the upstream direction. We can ascribe this effect to the self-focusing of the ultrashort pulses.

Figure 5 shows the dependence of the region of refractive index change on exposure time under the fixed incident-energy condition (1.9 μJ/pulse). The exposure time is varied from 0.25 min. to 30 min.. To our knowledge, we first observed the fact that when the exposure time is increased, the region of refractive index change elongates toward the upstream direction. This direction of elongation coincides with that of the movement of the granular structure as reported by Ashkenasi [17]. The elongation almost saturated after approximately 30 min.. The region is 500 μm long and the diameter is 1.7 μm. As far as we know, this is the smallest diameter of the core created by ultrashort laser pulses.

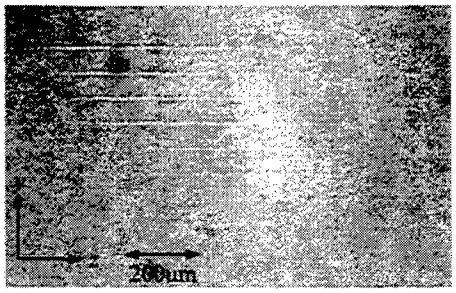


Figure 5 Variations of the resultant refractive-index change generated by single filament for different exposure time.

We estimated the refractive index change by three different methods; the focusing method [21], the Sénarmont compensator arrangement and the coherent filtering method. The coherent filtering method employs the Schlieren arrangement. The results are tabulated in Table 1. If we neglect the results of the focusing method that is based on the geometrical optics, we may adopt the value of 0.8×10^{-2} for the maximum change of refractive index.

Table 1 The refractive index changes estimated by the three methods.

Method	Calculated index change
Focusing method	1.4×10^{-2}
Sénarmont compensator	0.82×10^{-2}
Schlieren method	0.85×10^{-2}

We investigated the formation of filament and the refractive index change by using focusing lenses with various NA. The results are tabulated in Table 2. The column of incident energy indicates the range of incident pulse energy where a single filament is formed. The column of length of the filament indicates the length of the formed single filament. When the pulses with 1.1 μJ/pulse were incident through a lens with NA of 0.05, the length of the filament was 400 μm. Lower the NA, longer the length of the region of refractive index change was. The saturation time was also dependent on NAs. The maximum index change and the diameter did not depend on NAs. When NA was longer than 0.44, the strong optical damage occurred and no filaments were generated.

Table 2 Summary of the resultant refractive-index change for the various NAs of the focusing lens.

Numerical aperture	Incident energy	Length of the filament	Saturation time
0.05	1.1-2.3 μJ	400-500 μm	30 min.
0.1	0.9-2.0 μJ	120-200 μm	10 min.
0.3	0.3-0.5 μJ	20-40 μm	5 min.
0.44		No filaments	

We conducted a thermal treatment of the sample with the refractive index change. The sample was treated at 1150°C for 1 hour. The treatment temperature was a little bit higher than the annealing point of silica glass. We took 4 hours to raise the temperature and took 19 hours to cool down to the room temperature. We observed through a microscope that the region of refractive index change was annealed out. This result implies the presence of stress in the sample before the thermal treatment.

We fabricated a waveguide with a length of 2 mm by translating stepwise or continuously the sample along the optical axis. We coupled light from a He-Ne laser 633-nm to the waveguide. We used a microscope objective with NA of 0.13 to couple the light. Due to the round shape of the end of the refractive index change, the maximum coupling was achieved by the beam of NA=0.13. We coupled 2-mW light and could not observe the scattered radiation from the guided light. We may conclude that we can fabricate waveguides with low loss propagation by using the method described in this paper.

3. Conclusion

We investigated the relationship between the formation of filament and local refractive-index change in silica glass that were induced by near-infrared femtosecond laser-pulses. *In situ* observation revealed that the location of filament coincides with that of the refractive index change. We also showed that the region of refractive index change elongates toward the incident direction of the laser pulses with the exposure time. The region of refractive index change in silica glass was length of the several hundred-micron and the diameter was smaller than 2 microns. The length was dependent on the numerical aperture of the focusing lens. The

refractive index change in silica glass was confirmed to be 0.8×10^{-2} by the two of three different methods. The present technique may be suited for the fabrication of small optical microstructures and devices inside glasses such as low-loss waveguides and Bragg reflectors.

Acknowledgement

The present experiments were conducted at Venture Business Laboratory, Osaka University. The authors thank Dr. Kintaka of Osaka National Research Institute, Agency of Industrial Science and Technology for his assistance regarding the experiment of annealing.

References

[1] K. O. Hill, Y. Fujii, D. C. Johnson, and B. S. Kawasaki, "Photosensitivity in optical fiber waveguides: application to reflection filter fabrication," Appl. Phys. Lett., **32,** (1978) 647.

[2] D. Du, X. Liu, G. Korn, J. Wquier, and G. Mourou, "Laser-induced breakdown by impact ionization in SiO_2 with pulse widths from 7 ns to 150 fs," Appl. Phys. Lett., **64,** (1994) 3071.

[3] B. C. Straut, M. D. Feit, A. M. Rubenchik, B. W. Shore, and M. D. Perry, "Laser-induced damage in dielectrics with nanosecond to subpicosecond pulses," Phys. Rev. Lett., **74,** (1995) 2248.

[4] D. von der Linde and H. Schüler, "Breakdown threshold and plasma formation in femtosecond laser-solid interaction," J. Opt. Soc. Am. B, **13,** (1996) 216.

[5] K. M. Davis, K. Miiura, N. Sugimoto and H. Hirao, "Writing waveguides in glass with a femtosecond laser," Opt. Lett., **21,** (1996) 1729.

[6] E. N. Glezer, M. Milosavljevic, L. Huang, R.J. Finlay, T.-H. Her, J.P. Callan, and E. Mazur, "Three-dimensional optical storage inside transparent materials," Opt. Lett., **21,** (1996) 2023.

[7] E. N. Glezer and E. Mazur, "Ultrafast-laser driven micro-explosions in transparent materials," Appl. Phys. Lett., **71,** (1997) 882.

[8] J. Qiui, K. Miura, and K. Hirao, "Three-dimensional optical memoryusing glasses as a recording medium through a multi-photon absorption process," Jpn. J. Appl. Phys., **37,** (1998) 2263.

[9] M. Watanabe, H. Sun, S. Juodkazis, T. Takahashi, S. Matsuo,Y. Suzuki, J. Nishii and H. Misawa, "Three-Dimensional Optical Data Storage in Vitreous Silica," Jpn. J. Appl. Phys., **37,** (1998) L1527.

[10] J. A. Squier and M. Müller, "Third-harmonic generation imaging of laser-induced breakdown in glass," Appl. Opt., **38,** (1999) 5789.

[11] K. Miura, J. Qiu, H. Inuye, T. Nitsuyu, K. Hirao, "Photowritten optical waveguides in various glases with ultrashort pulse laser," Appl. Phys. Lett., **71,** (1997) 3329.

[12] K. Hirao and K. Miura, "Writing waveguides in silica-related glasses with femtosecond laser," Jpn. J. Appl. Phys., **37,** (1998) L49.

[13] D. Homoelle, W. Wielandy, and A. L. Gaeta, E. F. Borrelli, and C. Smith, "Infrared photosensibvity in silica glasses exposed to femtosecond laser pulses," Opt. Lett., **24,** (1999) 1311.

[14] K. Hirao and K. Miura, "Writing waveguides and gratings in silica and related materials by femtosecond laser," Jpn. J. Non-Cryst. Solids, **239,** (1998) 91.

[15] T. Toma, Y. Furuya, W. Watanabe, J. Nishii, K. Hayashi, and K. Itoh, "Estimation of the Refractive Index Change in Glass Induced by Femtosecond Laser Pulses," Opt. Rev., **7,** (2000) 14.

[16] H. -B. Sun, Y. Zu, S. Matsuo, and H. Misawa, "Microfabrication and characteristics of two-dimensional photonic crystal structures in vitreous silica," Opt. Rev., **6,** (1999) 396.

[17] D. Ashkenasi, H. Varel, A. Rosenfeld, S. Henz, J. Hermann, and E. E. B. Cambell, "Application of self-focusing of ps laser pulses for three-dimensional microstructuring of transparent materials," Appl. Phys. Lett., **72,** (1998) 1442.

[18] Y. Kondo, T, Suzuki, H. Inouye, K. Miura, T. Mitsuyu, and K. Hirao, "Three-dimensional microscopic crystallization in photosensitive class by femtosecond laser pulses at nonresonant wavelength," Jpn. J. Appl. Phys., **37,** (1998) L94.

[19] S. -H. Cho, H. Kumagai, I. Yokota, K. Midorikawa, and M. Obara, "Observation of self-channeled plasma formation and bulk modification in optical fibers using high-intensity femtosecond laser," Jpn. J. Appl. Phys., **37,** (1998) L737.

[20] G. N. Steinberg, "Filamentary Tracks Formed in Transparent Optical Glass by Laser Beam Self-Focusing. I. Experimental Investigation," Phys Rev., A **4,** (1971) 1182.

[21] D. Marcuse, "Refractive index determination by the focusing method," Appl. Opt., **18,** (1979) 7.

Laser Surface Cleaning --- Basic Understanding, Engineering Efforts and Technical Barriers

Y.F. Lu[1], W.D. Song, M.H. Hong, Z.M. Ren and Y. W. Zheng

Laser Microprocessing Laboratory,
Department of Electrical Engineering and Data Storage Institute,
National University of Singapore, 10 Kent Ridge Crescent, Singapore 119260

Laser cleaning as a new cleaning technique has emerged in order to effectively remove contaminants from solid surfaces. Two types of laser cleaning techniques have been developed recently, relying on pulsed laser heating of the surface without or with the presence of a thin liquid coating. Laser cleaning was demonstrated both theoretically and experimentally to be an effective cleaning technique for removing contaminants from solid surfaces without damage. For dry laser cleaning, two cleaning models were established for removal of particles from substrate surfaces from the viewpoint of energy and force. For steam laser cleaning, a cleaning model was established for removal of particles from substrate surfaces with a thin liquid layer by taking Van der Waals force, capillary force, cleaning force, and chemical bonding into account. The models not only explain the influence of incident direction, wavelength, fluence on cleaning efficiency, but also predict the cleaning thresholds. The experimental results show that the laser cleaning efficiency increases with increasing fluence and pulse number, but does not depend on the repetition rate. The surface cleanliness can be monitored in real time by acoustic, electric and optical means. Applications of laser cleaning to clean magnetic slider surface, magnetic media surface, silicon wafer and IC mold surface will also be addressed. Engineering efforts and technical barriers of laser cleaning will be discussed in detail.

KEYWORDS: Laser cleaning, cleaning model, cleaning mechanisms, cleaning applications.

1. Introduction

As semiconductor and microelectronics device fabrication technology advances toward higher densities and smaller circuit dimensions, contamination control becomes one of the most critical problems in the industry.[1,2] Similarly, in the disk drive industry, head flying height has been continually reduced to increase the recording density. This implies that tiny particles on the slider or disk surfaces can damage both the slider and disk surfaces and hence lead to the failure of the disk drive system. The removal of contaminants from optical surfaces is a major concern as the contaminants on these surfaces can absorb and scatter light which degrades the optical throughput and stray light rejection. Thus, the cleanliness of solid surfaces becomes a highly critical issue.

Consequently, there have been significant efforts to develop effective techniques to remove surface contaminants,[1,2] such as high-pressure jet; mechanical wiping and scrubbing; etching and ultrasonic cleaning. Some of them such as ultrasonic cleaning require the immersion of a sample into a liquid bath, which has a number of serious drawbacks. Firstly, it is widely known that wet techniques could add contaminants due to insufficient cleaning and filtering of the liquid at the submicron level. Secondly, the usage of hazardous chemicals and solvents becomes undesirable for environmental and industrial reasons such as causing cancers in humans and depleting ozone layer. Other problems associated with the wet techniques are rinsing/drying difficulties and incompatibility with other processes. Hence, dry cleaning techniques have emerged in order to overcome these drawbacks.

[1] Y.F. Lu: Email: eleluyf@nus.edu.sg; Telephone: 65-8742118; Fax: 65-7791103

First International Symposium on Laser Precision Microfabrication, Isamu Miyamoto, Koji Sugioka, Thomas W. Sigmon, Editors, Proceedings of SPIE Vol. 4088 (2000) © 2000 SPIE · 0277-786X/00/$15.00

Recently, laser cleaning was demonstrated to be an efficient cleaning method for removal of particulate and organic film contamination from solid surfaces.[3-20] Two types of laser cleaning have been reported in the literature, relying on pulsed laser heating of the solid surfaces without or with the presence of a thin liquid coating. We shall refer to these two types as dry laser cleaning and steam laser cleaning, respectively. For dry laser cleaning, particles can be ejected from particulate-contaminated surfaces by short-pulse laser irradiation. The proposed mechanism of the ejection is fast thermal expansion of the particle and/or solid surfaces, which induces large cleaning force to overcome the adhesion force between particles and solid surfaces.[16-20] Another mechanism is laser ablation of particles as particulate materials have small ablation threshold than that of the solid surfaces.[9] The laser cleaning of organic film contaminants is considered due to laser photo-ablation and thermal-ablation of the contaminants.[7] For steam laser cleaning, the proposed mechanism is assumed to be the momentum transfer from the laser-heated and suddenly evaporating liquid film to the particles on the solid surfaces.[3-5] Compared with wet cleaning, it has several advantages such as dry process without using organic solvents, area-selective cleaning and cleaning samples on line. The following will focus on science and engineering in laser surface cleaning. The cleaning models, cleaning efficiency and several industry applications will be discussed in detail.

2. Removal of film-type contaminants

The mechanisms of laser-induced removal of thin film contaminants are laser photo-ablation and thermal-ablation.[7] If the binding energies of molecules of thin film contaminants are within the range of photon energies of laser irradiation, photo-decomposition or photo-ablation is possible. For example, the photon energy of a KrF excimer laser is 5 ev. This energy can break the O-O, H-H, O-H, C-C, C-H, N-H chemical bonds. When superfluous energy is irradiated, simultaneous thermal-ablation will occur.

2.1 IC packages

Plastic packaging of IC devices has been extensively applied in the wafer backend industry. IC components are generally placed into the cavities of a mould. Molding component liquefied by heat and pressure is then forced into the cavities. It solidifies and finally gives a sturdily encapsulated device. However, plastic encapsulation is by no means a perfect process. During the IC packaging, molding compound leaks out and forms flashes on IC package surfaces. It will greatly influence next packaging processes, such as plating and bending. In the worst case, it will even cause scrap of the whole IC package. Therefore, deflash of the IC packages is one of the critical processes in the manufacturing. Medium blasting, water jet shooting and chemical etching are conventional techniques in IC packaging lines. We found that laser cleaning can be used to remove those flashes from IC package. The cleaning efficiency of laser-induced removal of film-type contaminants is defined as the ratio of thickness of film removed and total thickness of the film. For laser cleaning of IC package, the cleaning efficiency is shown in Fig. 1. It is found that the cleaning threshold is about 100 mJ/cm^2 and the cleaning efficiency increases with increasing laser fluence.

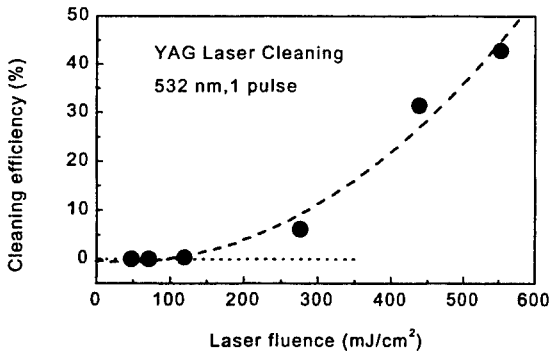


Fig. 1 The cleaning efficiency.

Figure 2 shows a typical optical micrograph of IC package surfaces before and after laser cleaning. It is observed that flashes on IC package surfaces have been removed by laser irradiation.

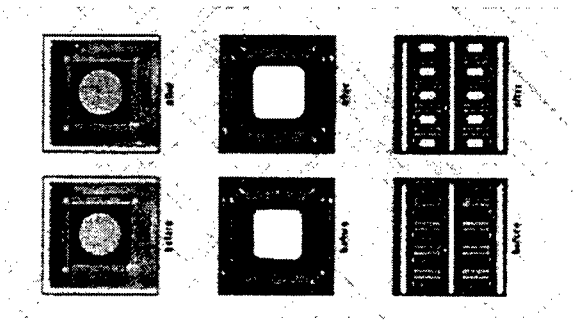


Fig. 2 The typical optical micrograph of IC package surface before and after laser cleaning.

2.2. IC mould

Traditionally, surface contaminants such as oil, grease, wax and other organic and inorganic compounds on IC mold are removed from the surfaces by injecting a substance called melamine into the empty molds, exposing it to intense heat and pressure to liquefy the substance, and then letting it solidify. During this process, the contaminants react with the melamine compound and bond to its surface of the solidified melamine compound. Once solidified, the melamine compound is thrown out. However, this method has a number of shortcomings such as long time processing, low cleaning efficiency and containing toxic fumes being harmful to human beings. We demonstrated that laser cleaning is a good cleaning method to remove these contaminants from IC mold surfaces.

Figure 3 shows a typical optical micrograph of an IC mold with and without laser cleaning. In Fig. 3, the top half surface of the IC mold are processed by excimer laser irradiation, whilst the bottom one retain the contaminated originals. The experimental result shows that grease and wax contaminants on IC mold surfaces can effectively be removed by laser irradiation.

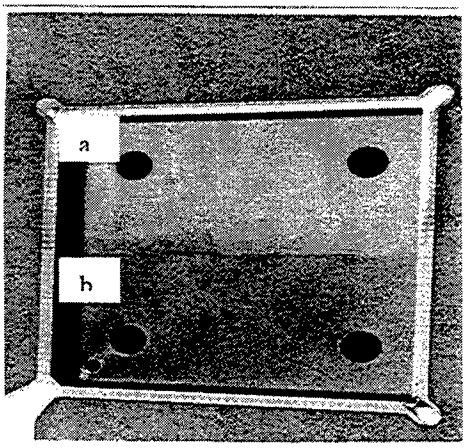


Fig. 3 The optical micrograph of IC mold with (a) and without (b) laser cleaning.

2.3 PCB

Resin contaminants around holes are produced in manufacturing of printed circuit board (PCB). Usually, these contaminants are removed by inserting PCB into chemical solutions and letting them react with the chemical solutions. Although this method is widely used in industry, it has some drawbacks such as waste chemical solutions processing. We also found that resin contaminants around holes in PCB can be effectively removed by laser cleaning. Figure 4 shows typical optical micrograph of PCB surfaces before and after laser cleaning.

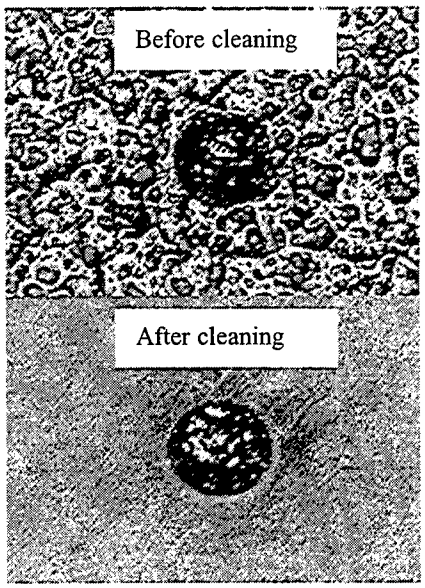


Fig. 4 The typical optical micrograph of PCB surfaces before and after laser cleaning.

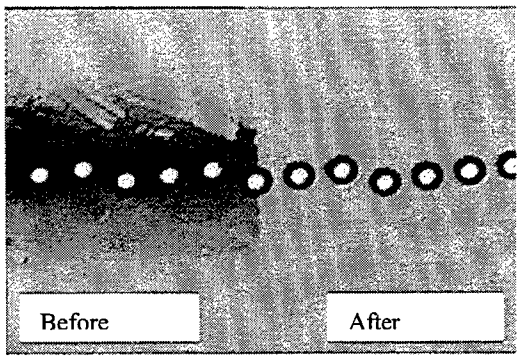


Fig. 5 The typical optical micrograph of flexible circuit surfaces before and after laser cleaning.

2.4 Flexible circuit

Carbon contaminants on Kapton substrate surfaces are produced in manufacturing of flexible circuit. Usually, these contaminants are removed by plasma etching. We found that laser cleaning can be used to effectively remove these contaminants from the surfaces. Since Kapton substrate is almost transparent to green light, a YAG laser with a wavelength of 532 nm is good cleaning source without damage to the substrates.

Figure 5 is typical optical micrograph of flexible circuit surfaces before and after laser cleaning. It is seen that contaminants on Kapton surfaces have been removed by laser cleaning.

3. REMOVAL OF PARTICLES

3.1 Theory and experiment

3.1.1 Dry laser cleaning

Several important forces exist and can cause strong adhesion of a tiny particle on a solid surface.[1] These include Van der Waals force, capillary force, and electrostatic forces, which easily exceed gravitational forces on small particles. For a dry system, a capillary force will not be taken into the consideration while calculating the adhesion force of particles on substrate because there is no liquid film layer between the particulates and substrate (assuming negligible atmospheric moisture). In a dry system, Van der Waals force predominates for tiny particles with a particle size less than a few microns and electrostatic forces predominate for large particles, i.e. greater than about 50 microns in size.[1] In semiconductor, disk drive and other microelectronic industries, particles are usually much smaller than 50 μm, Van der Waals force is dominant adhesion force for these tiny particles on dry solid surfaces. Therefore, the adhesion force between a tiny particle and a solid surface F is

$$F = \frac{hr}{8\pi z^2} + \frac{h\delta^2}{8\pi z^3} \tag{1}$$

where r, h, δ and z are the particle radius, the material-dependent Liftshitz-Van der Waals constant, the radius of the adhesion surface area and the atomic separation between the particle and surface. Typical values of h range from a low value of ~ 0.6 eV for polymer/polymer interaction to a large value of ~ 9.0 eV for gold/gold interaction. For Van der Waals-bonded crystals, the atomic separation z is approximately 4 angstroms.[1,2]

Due to the short pulse laser irradiation, there is a rapid increased in temperature of a particle and/or substrate. This increased in temperature will indirectly generate a cleaning force. The cleaning force per unit area f is [16-20]

$$f = \gamma E \Delta T \tag{2}$$

where γ and E are the linear thermal expansion coefficient and the elastic modulus of the particle and/or substrate, respectively. The ΔT is temperature rise of the particle and/or substrate.

Since cleaning forces induced by laser irradiation depend on temperature distribution in a substrate or a particle, it is needed to know the temperature distribution in order to calculate the cleaning force. When a pulsed laser irradiates a substrate surface, the temperature distribution in the substrate can be described by the one-dimensional heat equation. The temperature at any point inside the substrate $T(x,t)$ is a function of depth below the substrate surface x and time t, and is governed by the one-dimensional heat equation [21,22]

$$\rho c \frac{\partial T(x,t)}{\partial t} = k \frac{\partial^2 T(x,t)}{\partial x^2} + (1-R)\alpha I_0 \exp(-\alpha x) \tag{3}$$

where ρ, c, K, R, α and I_0 are density, specific heat, thermal conductivity, reflectivity, absorption coefficient of the substrate material and laser intensity on the substrate surface, respectively.

If the cleaning force (per unit area) exceeds the adhesion force (per unit area), the particle may be detached from the substrate surface. Therefore, the cleaning condition will be cleaning force (per unit area) larger than the adhesion force (per unit area).The particle removal condition can be also derived from the viewpoint of energy is[23-25]

$$\frac{8R^{\frac{1}{2}}E}{15(1-\sigma^2)}[Ls - f(\tau) + Lp_0]^{\frac{5}{2}} + \frac{1}{2}\times\frac{4}{3}\pi R^3 \rho\left(\frac{df}{dt}|\tau\right)^2 \geq F_s[Ls - f(\tau) + Lp_0] + \frac{AR}{6\varepsilon_0} \tag{4}$$

where R, E, σ and ρ are the radius, elastic modulus, Poisson coefficient and density of a particle, respectively. And Ls, Lp_0, f(t), τ, F_s, A and ε_0 are the maximum expansion, the initial deformation parameter, particle dislocation function, laser pulse duration, , the total surface adhesion force, the Hamaker constant and the least distance between a particle surface and a substrate surface, respectively. The first item in the left side of above equation is the elastic deformation potential energy after irradiation, the second item in the left side is the kinetic energy of the particle. The first item of the right side of above equation is the work of adhesion force while the particle recovers from

deformation at time instant τ to "point contact", the second item of the right side is the adhesion energy of "point contact".

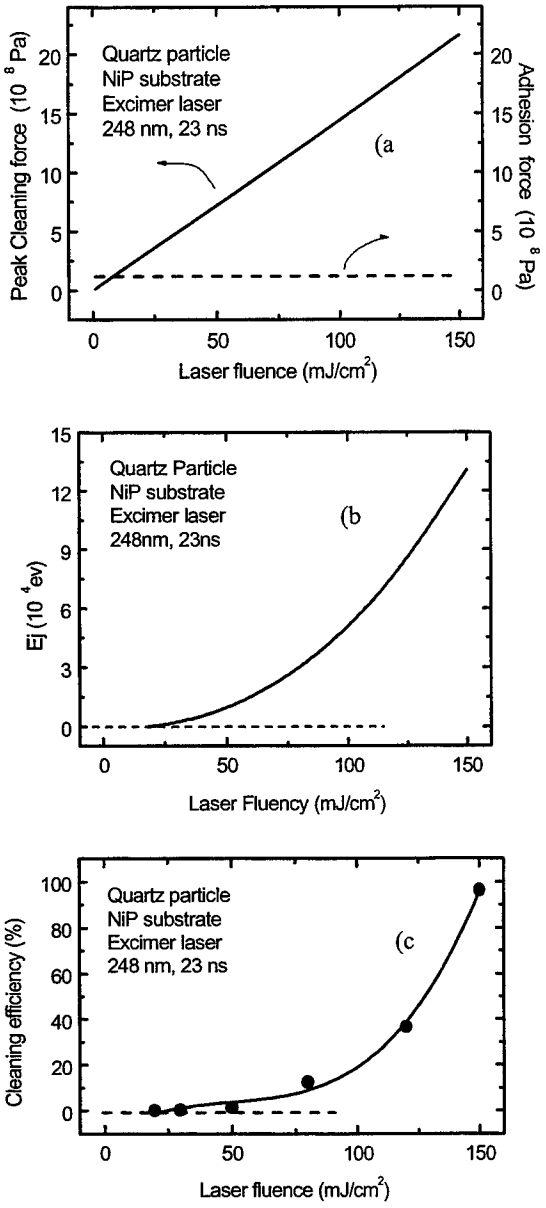


Fig. 6 The peak cleaning force (a), ejecting energy (b) and cleaning efficiency (c) at different laser fluences.

If we define ejecting energy Ej as the left part of Eq. 4 subtracting the right part, the particle removal condition can be expressed as

$$Ej > 0 \qquad (5).$$

Figure 6 shows the peak cleaning force, ejecting energy and cleaning efficiency at different laser fluences. It indicates that both peak cleaning force and ejecting energy increase with increasing laser fluence. The theoretical cleaning thresholds predicted by the cleaning models from the viewpoint of force and energy are 10 and 20 mJ/cm^2, respectively. The experimental threshold as shown in Fig. 1(c) is about 16 mJ/cm^2, which is close to theoretical thresholds. Therefore, the experimental results can be explained and predicted by theoretical analyses.

3.1.2 Steam laser cleaning

For a wet system, a capillary force and Van der Waals force will act to hold a tiny particle. The adhesion force between a tiny particle and a solid surface F is [1-3]

$$F = \frac{hr}{8\pi z^2} + \frac{h\delta^2}{8\pi z^3} + 4\pi\gamma r \qquad (6)$$

where γ is the liquid surface tension.

For laser with enough intensity irradiating on a solid surface coated by non-absorption liquid film, a sheet of liquid near the liquid/substrate interface can be superheated through thermal diffusion. According to energy conservation, the pressure of stress wave at the vapor/liquid interface is[26-27]

$$P = [2\rho c(P_v - P_\infty)vf)]^{1/2} \qquad (7)$$

where ρ, c, P_v, P_∞, v and f are the liquid density, transmit speed, vapor pressure inside the bubble, ambient liquid pressure, expansion velocity and volume fraction of vapor, respectively. The cleaning force caused by this pressure can be obtained by Eq. (7). The threshold of laser cleaning is defined as the laser fluence at which the cleaning force is equal to the adhesion force.

Figure 7(a) shows the cleaning force at different laser fluences together with the adhesion force. It indicates that the cleaning force increases with an increase of laser fluence and theoretical cleaning threshold is 27.5 mJ/cm^2 for removal of 1 μm alumina particles from IPA coated NiP surface. Figure 2(b) shows laser fluence dependence of cleaning efficiency for removal of 1 μm alumina particles from NiP surface coated with IPA film. It is found that the cleaning threshold is about 30mJ/cm^2 and the cleaning efficiency

increases rapidly with laser fluence, which are close to theoretical analyses.

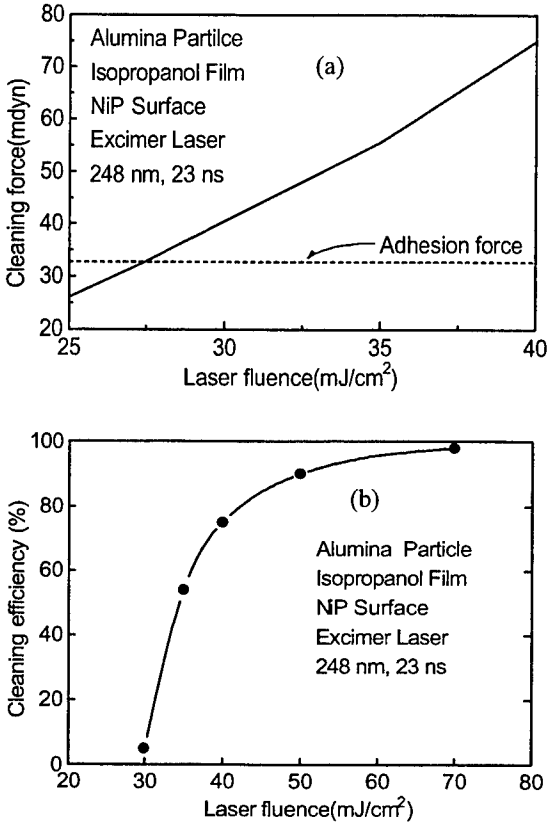
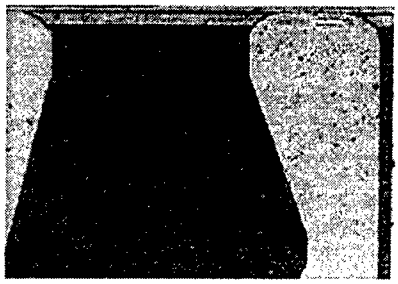


Fig. 7 The cleaning forces (a) and cleaning efficiency (b) as a function of laser fluence.

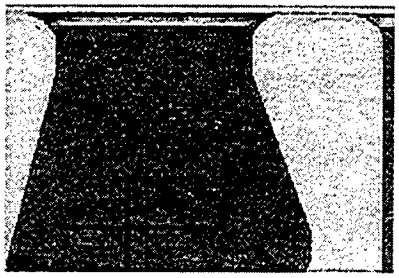
3.2 Applications in disk drives

In a hard disk drive, head flying-height has been continually reduced to increase the recording density. At present the flying height is about or below 0.1 μm, this implies that even submicron particles can damage both the slider and disk surfaces, hence lead to failure of the disk drive system. Thus, the cleanliness of disk and slider surfaces becomes very critical. Above discussions indicate laser cleaning being an efficient cleaning method for removal of particles from solid surfaces. The following shows that laser cleaning can be used in hard disk drive industry. Figures 4 shows optical micrographs of laser cleaning of magnetic sliders. It was found that particulate contaminants on slider surfaces have been efficiently removed by laser cleaning.

Figure 9 shows AFM profiles of disk surface with and without laser cleaning. Comparing both AFM profiles at the uncleaned and the cleaned areas, it is clear that laser irradiation can efficiently remove submicron particles from the disk surface. For example, the particles with only 0.2 μm in radius observed from the AFM profile have been removed by laser cleaning.



Before laser cleaning



After laser cleaning

Fig. 8 The optical micrographs of laser cleaning of magnetic sliders.

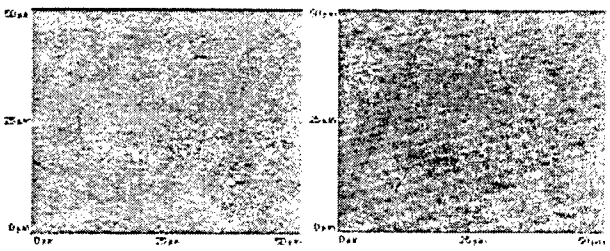


Fig. 9 AFM profiles of the disk surface at the uncleaned area and the cleaned area at a laser fluence of 150 mJ/cm², a pulse number of 100 and a repetition rate of 10 Hz.

4. Monitoring of laser cleaning

For laser-induced removal of film-type contaminants from solid surfaces, an acoustic wave will be generated due to laser ablation of contamination. The

acoustic wave generated is consisted of ultrasonic and sonic components. With a microphone nearby, the acoustic waves can be detected. Figure 10 shows acoustic waves captured during KrF excimer laser irradiation of IC mould at laser fluence of 400 mJ/cm^2. The signals were recorded at the 1st, 5th and 10th pulses of the laser irradiation. Microphone was placed about 25 cm away from laser spot on the substrate. It is found that surface texture did not change during the laser cleaning while contamination on the surface was completely removed as shown in Fig. 3. It can also be observed from Fig. 10 that the acoustic waves reduce gradually with pulse number and finally disappear after ten pulses. Since variation of the acoustic waves is closely related to the contamination levels on substrate surfaces, the acoustic wave detection can be applied to monitor the laser cleaning in real time. The signal peak-to-peak amplitude can be selected as a characteristic parameter to correlate with cleaning efficiency. Acoustic wave detection is a sensitive signal diagnostic technique, which can reflect removal of contamination in a thin layer of nanometers.[28-29]

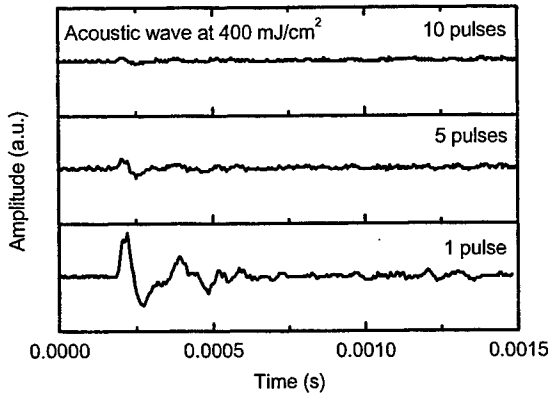


Fig. 10 Acoustic waves recorded during laser cleaning of IC mould surfaces at 400 J/cm^2.

Laser ablation of contamination materials is one of the important mechanisms for laser cleaning. Since threshold fluence for organic contamination ablation is much lower than that for solid substrates. With a proper selection of laser parameters, organic contamination can be removed without damage of substrate surface. During laser cleaning of the contamination, plasma is generated above the substrate surface. As the cleaning continues, concentration of surface contamination reduces gradually. The plasma becomes smaller and finally vanishes when all the contamination is removed. Plasma consists of charged and neutral particles. From classical electrodynamics, fast moving charged particles emit out an electric field. With a tiny metal probe nearby, an electric signal can be detected. Variation of the electric signal reflects dynamics of the laser cleaning in real time. Figure 11 shows the electric signals detected during the excimer laser cleaning of grease contamination on a copper substrate. Laser fluence was 0.54 J/cm^2. It is much lower than ablation threshold for copper substrate 1.3 J/cm^2. There is no substrate ablation during the surface cleaning. Probe distance was set as 2.5 mm. The electric signals were recorded at pulse numbers of 1, 2, 3, 4, 5, 10, 50 and 100, respectively. It is clear that there is a nanosecond negative peak in the electric signal. As pulse number increases, both the peak amplitude and width reduce gradually. It implies that charged particle emission decreases as the cleaning proceeds. The electric signal vanishes completely after fifty pulses. Microscopy observation of the substrate surface after the laser processing shows that the organic contamination on the substrate has been completely ren..... It is clear that the signal variation is closely related to the laser cleaning process. Therefore, the electric signal detection of plasma-induced electric field can also be applied to control the laser cleaning in real time.[30]

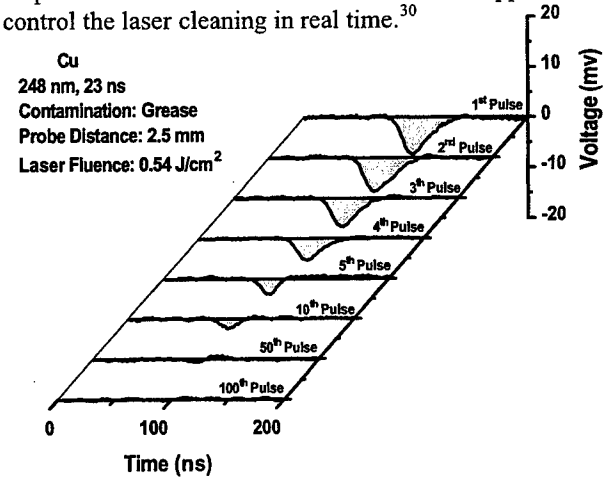


Fig. 11 Electric signals detected during the excimer laser cleaning of grease contamination from copper substrate for a laser fluence of 0.54 J/cm^2 and pulse numbers from 1 to 100.

As mentioned above, the mechanism of laser-induced removal of organic contaminants is direct laser ablation of the contaminants, relying on the photochemical and photophysical properties of the organic contaminants and the physical properties of the substrates. Since laser ablation of contaminants will

result in an acoustic wave, hence acoustic wave can be used to monitor the laser cleaning process of organic contaminants. However, laser cleaning of particulate contaminants cannot be monitored by acoustic wave generation, as laser cleaning of particles does not involve laser ablation of contaminants. Therefore, there is a need to find an alternative method to monitor the laser cleaning process of particulate contaminants. We found that a laser based airborne particle counter is able to detect particles that are being ejected from the substrate surfaces upon irradiation of laser.

5. Future efforts and barriers

Laser cleaning has the potential for very wide applications. On can easily consider the applications for cleaning package covers; flexible circuits; paint, oil and grease from metals; printed circuit board (PCB) and lead wires of electronic components; magnetic heads and slider surfaces; magnetic media surface; semiconductor wafer and IC circuits; deflash of IC packages; glass surfaces for optical applications (lenses, CD-ROM), glass surfaces for display applications; window glass for high building; medical equipment.

Technically, laser cleaning is feasible for most industrial applications. There are a few factors, however, limit the commercialization of this technology. Usefully, laser equipment are expensive, especially for those with UV lasers and optics. High initial investment for laser cleaning to replace conventional one is required. Consumables such as laser gas and flash lamps add on the operation costs. Therefore, much effort is required to reduce the cost of the lasers and equipment and to find applications with reasonably high value-added. Besides economic issues of laser cleaning, in-depth understanding of laser-material interactions is essential. Since laser irradiation induces photothermal and photochemical reactions on the surface. Some side effects, such as thermal damage and photochemical decomposition on substrate surface, need to be avoided. Although high laser fluence usually increases cleaning efficiency, it can also cause surface damages on the substrate. Much effect is required to find a balance between high cleaning efficiency and low side effects.

Laser cleaning still faces limitation to clean large substrate with high speed. Most lasers have limited laser power and beam spot size. In order to clean a large surface, the laser beam must be scanned over the surface. It is therefore surface consuming and limiting the throughput of the cleaning process. Safety is also a concern in laser cleaning. Laser gases, laser light and cleaning products are potential hazardous in the production environment. Further study is required to make sure all these hazardous can be under control.

Design of laser Optics is also of great importance in laser cleaning. For example, excimer laser has very complicated modes in the laser beam. The propagation of excimer laser beam is difficult control. The beam profile is changing with the propagation distance. The beam profile also depends on individual lasers. Beam homogenizer is commonly used in industrial applications with a drawback of large energy loss. Better optics design is required to achieve good homogenity and low energy loss.

6. Conclusions

Dry and steam laser cleaning was demonstrated to be an efficient cleaning tool for removing particles and thin film contaminants from solid surfaces both theoretically and experimentally. Cleaning models were established for laser-induced removal of particles from solid surfaces by taking adhesion forces and cleaning force into account both for dry and steam laser cleaning. Laser cleaning forces are induced by fast thermal expansion of particles and/or solid surfaces irradiated by laser for dry laser cleaning and by evaporating liquid film heated by laser irradiation for steam laser cleaning, respectively. With increasing laser fluence, the difference between the cleaning force and the adhesion force increases, resulting in easier removal of particles from substrate surfaces or a higher cleaning efficiency. Comparing theoretical and experimental thresholds, the same trends for both theoretical and experimental cleaning thresholds were observed. The theoretical cleaning thresholds are quite close to those of the experimental cleaning thresholds. Therefore, the theoretical analysis can successfully predict and explain the experimental results. The mechanism of laser-induced removal of organic contaminants is laser photo-ablation and thermal-ablation. The film-type contaminants on IC package, IC mould, Printed Circuit Board and flexible circuit can be effectively removed by laser cleaning. Laser cleaning process can be monitored by acoustic wave, electric field signal and particle counter.

REFERENCES

1. K.L. Mittal, *Particles on Surfaces*, vol.1, Plenum Press, New York, pp.3-400, 1988.

2. K.L. Mittal, *Particles on Surfaces*, Marcel Dekker,, New York, pp.1-45, 405-417, 1995.
3. W. Zapka, W. Ziemlich, and A.C. Tam, "Efficient pulsed laser removal of 0.2 μm sized particles from a solid surface," Appl. Phys. Lett., pp. 2217-2219, 1991.
4. K. Imen, S.J. Lee and S.D. Allen, " Laser-assisted micron scale particle removal," Appl. Phys. Lett., 58(2), pp. 203-205, 1991.
5. A.C. Tam, W.P. Leung, W. Zapka and W. Ziemlich, "Laser-cleaning techniques for removal of surface particles," J. Appl. Phys. 71(7), pp. 3515-3523, 1992.
6. J.D. Kelley and F.E. Hovis, " A thermal detachment mechanism for particle removal from surfaces by pulsed laser irradiation," Microelectronic Engineering 20, 159-170, 1993.
7. Y.F. Lu, M. Takai, S. Komuro, T. Shiokawa and Y. Aoyagi, "Surface cleaning of metals by pulsed-laser irradiation in air," Appl. Phys. A 59, 281-288, 1994.
8. H.K. Park, C.P. Grigoropoulos, W. P. Leung and A.C. Tam, "A Practical excimer laser-based cleaning tool for removal of surface contaminants," IEEE Transactions on Components, Packaging, and Manufacturing Technology Part A, 17(4) 631-643,1994.
9. Y.F. Lu, W.D. Song, M.H. Hong, B.S. Teo, T.C. Chong and T.S. Low, " Laser removal of particles from magnetic head sliders," J. Appl. Phys., 80(1), pp. 499-504, 1996.
10. K. Mann, B. Wolff-Rottke and F. Muller, " Cleaning of optical surfaces by excimer laser radiation," Appl. Surf. Sci., 98, pp. 463-468, 1996.
11. R. Oltra, O. Yavas, F. Cruz, J.P. Boquillon and C. Sartori, " Modelling and diagnostic of pulsed laser cleaning of oxidized metallic surfaces," Appl. Surf. Sci., 98, pp. 484-490, 1996.
12. D.A. Wesner, M. Mertin, F. Lupp and E.W. Kreutz, " Cleaning of copper traces on circuit boards with excimer laser radiation," Appl. Surf. Sci., 98, pp. 479-483, 1996.
13. M. Afif, J.P. Girardeau-Montaut, C. Tomas, M.Romamd, M. Charbonnier, N.S. Prakash, A. Perez, G. Marest and J.M. Frigerio, " In situ surface cleaning of pure and implanted tungsten photocathodes by pulsed laser irradiation," Appl. Surf. Sci., 98, pp. 469-473, 1996.
14. I. Gobernado-Mitre, J. Medina, B. Calvo, A.C. Prieto, L.A. Leal, B. Perez, F. Marcos and A.M. de Frutos, " Laser cleaning in art restoration," Appl. Surf. Sci., 98, pp. 474-478, 1996.
15. J.B. Heroux, S. Boughaba, I. Ressejac, E. Sacher and M. Meunier, " CO_2 laser-assisted removal of submicron particles from solid surfaces," J. Appl. Phys. 79(6), 2857-2862, 1996.
16. W.D.Song, Y.F.Lu, K.D.Ye, C.K. Tee, M.H. Hong, D.M. Liu and T.S.Low, "Cleaning force in laser cleaning of silicon substrate", SPIE Vol.3184, 158(1997).
17. Y.F.Lu, W.D.Song, B.W. Ang, M.H.Hong, D.S.H.Chan and T.S.Low, "A theoretical model for laser removal of particles from solid surface", Appl. Phys. A65, 9(1997).
18. Y.F.Lu, W.D.Song, K.D.Ye, Y.P.Lee, D.S.H.Chan and T.S.Low, "A cleaning model for removal of particles due to laser-induced thermal expansion of substrate surface", Jpn. J. Appl. Phys., 36(10A), L1304(1997).
19. Y.F.Lu, W.D.Song, K.D. Ye, M.H.Hong, D.M. Liu, D.S.H.Chan and T.S.Low, " Removal of submicron particles from nickel-phosphorus surfaces by pulsed laser irradiation", Appl. Surf. Sci. 120, 317(1997).
20. Y.F.Lu, W.D.Song, C.K. Tee, D.S.H.Chan and T.S.Low, "Wavelength effects in dry laser cleaning of particles on solid surfaces", Jpn. J. Appl. Phys. Part 1, No.3A, 840(1998).
21. D. Bhattacharya, R.K. Singh and P.H. Holloway, " Laser-target interactions during pulsed laser deposition of superconducting," J. Appl. Phys. 70(10), 5433-5439, 1991.
22. J.R. Ho, C.P. Grigoropoulos and J.A.C. Humphrey, " Computational study of heat transfer and gas dynamics in the pulsed laser evaporation of metals," J. Appl. Phys. 78(7), 4696-4709,1995.
23. Y.F.Lu, Y.W. Zheng, W.D.Song, "An energy approach to the modelling of particle removal by pulsed laser irradiation", Appl. Phys. A68, 569-572, 1999.
24. Y.F.Lu, Y.W. Zheng, W.D.Song, "Characterization of ejected particles during laser cleaning", J. Appl. Phys. 87(1), 549-552, 2000.
25. Y.F.Lu, Y.W. Zheng, W.D.Song, "Laser induced removal of spherical particles from silicon wafers", J. Appl. Phys. 87(3), 1534-1539(2000).
26. Y.F.Lu, Y. Zhang, W.D.Song, D.S.H.Chan, "A theoretical model for laser cleaning of mic roparticles in a thin liquid layer", Jpn. J. Appl. Phys. Part 2, No.11A, Vol.37, L1330-L1332, 1998.
27. Y.F. Lu, Y. Zhang and W.D. Song, "Laser cleaning of tiny particles in a thin liquid layer and its theoretical model", Appl. Surf. Sci., 139, 140-144, 1999.
28. Y.F. Lu, M.H. Hong, S.J. Chua, B.S. Teo, and T.S. Low, "Audible Acoustic Wave Emission in Excimer Laser Interaction with Materials", J. Appl. Phys., 79(5), 2186-2191, 1996.
29. Y.F. Lu, Y.P. Lee, M.H. Hong and T.S. Low, "Acoustic Wave Monitoring of Morphology Change during Excimer Laser Interaction with Copper Surfaces", Appl. Surf. Sci. 119, 137-146,1997.
30. Y.F. Lu, and M.H. Hong, "Electric signal detection at the Early stage of the laser ablation in the ambient air", J. Appl. Phys., 2812-2817, 1999.

Laser Processes for Precise Microfabrication of Magnetic Disk-Drive Components

Andrew C. TAM
IBM Corp., Almaden Research Center
650 Harry Rd., San Jose, CA 95120-6099

The technique of laser micro-processing has recently found several important and widespread applications in the manufacturing of disk-drive components. Examples provided here include the cleaning of surface contaminants, the formation of "nano-bumps" on disk surfaces for controlled surface texturing or for making glide height standards, and the micro-bending of magnetic head sliders for flight-height controls. Short-pulsed laser irradiation at suitable wavelength, fluence, and incidence direction can be used to clean off particulate and organic-film contaminants from surfaces of critical components, for example, the slider and the disk. Controlled disk texturing is needed to alleviate the problem of "stiction" which occurs when the disk stop spinning and the super smooth slider comes into stationary contact with the super smooth disk. A compact laser operating at high pulse repetition rate can be used to produce a low-stiction racetrack composed of typically a million nano-bumps. This can be done both for NiP/aluminum disks, or for glass disks. Single isolated bump with a specified height for providing height-standard can also be tailor-made. Very recently, we have developed a "laser curvature adjust technique" and implemented it into production of magnetic head sliders. Here, microscopic adjustments of the curvature of air bearing surface of sliders can be produced by suitable laser scribing at the back side of the ceramic slider.

Keywords: Laser cleaning, Laser texturing, Laser micro-bending, Disk-drive manufacturing

1. Introduction

Data-storage density in disk-drives continues to increase dramatically, now doubling every year. The present data density in production disk-drives (mid-2000) is 1.5×10^{10} per sq-inch, corresponding to a data-bit size of typically 800 x 50 nm. Such unprecedented rapid technology advances pose many manufacturing challenges, sometimes solvable only by developing new manufacturing processes. To enable the data-density increase, the read-write sensors on the magnetic head slider must fly closer and closer to the disk in order to write and read smaller data bits. The so-called "fly height" is currently at about 20 nm and decreasing. Hence, surface cleanliness is very important, the disk surface as well as the slider Air-Bearing Surface (ABS) facing the disk must be extremely smooth, and the slider ABS curvature must be painstakingly controlled as this affects the fly height. This situation continues to open up needs for new manufacturing processes, providing new opportunities for laser micro-processes based on selective pulsed localized heating.

The interest in adopting laser materials processing in hi-tech manufacturing is enhanced by the fast advances in "industrial" laser sources, particularly, the diode-pumped Nd-doped solid-state lasers. These compact, "turnkey" lasers provide high repetition rate, high reliability, and good beam-quality. As cost continues to drop for these solid-state laser sources, both for the fundamental output in the infrared (IR) and harmonic outputs in the green or ultraviolet (UV), more manufacturing applications will surely continue to arise. The energy per pulse is typically 10 μJ or less. However, the good beam quality permits tight focussing, producing optical energy density or fluence at the focussed spot up to several Joule per sq-cm. Since thermal diffusion is very limited because of the short pulse width, typically tens of nsec, the incident laser fluence is adequate to cause a variety of localized surface modifications. Hence, such a high pulse-repetition-rate laser is ideally suitable for materials processing using the "moving spot" process.

Some examples of recent applications of laser processing in the disk drive manufacturing is given here, in order of increasing fluence: laser cleaning at low fluence (typically 0.1 J/cm^2), laser texturing and bump formation on metal or glass surfaces at intermediate fluence (typically 1 J/cm^2), and laser micro-bending of ceramics at high fluence (typically >2 J/cm^2).

First International Symposium on Laser Precision Microfabrication, Isamu Miyamoto, Koji Sugioka, Thomas W. Sigmon, Editors, Proceedings of SPIE Vol. 4088 (2000) © 2000 SPIE · 0277-786X/00/$15.00

2. Laser Cleaning of Surface Contaminants

Laser cleaning has been of interest for over ten years in the micro-electronics and data-storage industry for the removal of sub-micron particulates and organic contaminant films, especially for cases where conventional cleaning means are inadequate. We have developed laser cleaning (LC) processes based on the use of short-pulsed UV laser irradiation. The laser source can be an excimer laser, or a harmonic Nd:YAG laser. Various mechanisms for the action of removal of particles and film-contaminants from surfaces are possible, and these can generally be categorized into "dry LC" and "steam LC" process types. Dry LC operates in the absence of any liquid film on the surface; its cleaning action can be based on thermo-acoustic shock, photothermal bond breaking, thermal vaporization, or gas breakdown and plasma effects. Steam LC operates in the presence of a micron-thick liquid film condensed onto the surface just before the pulsed laser irradiation. Its cleaning mechanism is based on the explosive vaporization of the liquid film. We have developed practical tooling for industrial application of LC [1], and have studied the physical basis for the removal of microscopic particles from the surface [2].

Steam Laser Cleaning is a powerful technique for the removal of submicron particulates, requiring significantly lower laser fluence for the cleaning action compared to dry LC. A liquid film of micron thickness is explosively vaporized (EV) to boost the particulate removal. EV occurs because of the rapid superheating of the liquid film, made possible when short-pulsed laser of duration on the order of 10 nsec is used. The laser heating can be due to strong substrate absorption only, strong film absorption only, or partial absorption by the substrate and by the film. The case of strong substrate absorption (caused by UV laser for many materials) is of special interest, since this produces the strongest pressure transients at the liquid/solid interface (where it is most effective for the removal of surface particles), and hence provides effective cleaning for a wide variety of particles, whether absorbing or not. An inclined angle of incidence onto the surface produces better LC results compared to normal incidence [3]. The reasons include: (1) The inclined irradiation can more readily reach the particle/solid interface and also heat up the sides of the particles, producing a more desirable location of the transient heating and pressure surge for the particle ejection. (2) The effective fluence on the background surface is reduced by a "cosine" factor, resulting in less likelihood of surface damage.

For the general case of surface contaminants composed of a variety of organics and particulates, we have found that a combination of steam LC and dry LC is usually most effective for the best cleaning action. A few cycles of steam LC and dry LC (done with various incident angles) may be necessary, and the laser fluence must be carefully controlled to avoid substrate damage but yet produce the cleaning effect. Based on these considerations, we have designed and constructed a practical LC tool [1] for cleaning delicate disk-drive components like magnetic head sliders and disks. This LC tool provides several important features: choice of dry LC and/or steam LC, capability to translate and rotate the part being cleaned, controlling the laser beam shape, incident direction, and fluence, and fast scanning of the laser beam by a galvo mirror. A "LC cycle" is defined here as a full area scanning of the sample done by fast galvo scanning of the laser spot in one direction as the sample is translated slowly in the perpendicular direction; the laser pulse repetition rate must be sufficiently fast to permit adequate pulse-to-pulse overlap. If a vapor (usually water mixed with a little isopropanol to enhance wetting) is made to condense on the surface in between laser pulses, it is called a "steam LC cycle". Otherwise, it is a "dry LC cycle".

We have performed experiments on the effectiveness of the LC tool [1] using 248 nm UV laser irradiation typically at a laser fluence of 110 mJ/cm^2 and incidence angle of about 50 degrees. For particulate contamination, for example, 1-μm sized alumina particles on a polished chromium surface, we observed that a few steam LC cycles followed by a few dry LC cycles produce the best results, usually complete removal of all particulates. However, if only dry LC cycles are used, only incomplete cleaning is produced. These results confirm earlier observation [4] that micrometer-sized particles are much more readily removed by steam LC rather than dry LC under the same irradiation conditions. On the other hand, organic films or smears are effectively removed either by dry LC or by steam LC when the UV laser photon can cause photochemical decomposition of the film materials. While steam LC cycles alone can produce good LC action for particles, we usually prefer at least 1 dry LC cycle at the end to ensure that any organic contaminants, however small in amount, condensed onto the surface during the steam LC cycles are removed in the final cycle. Hence, the LC tool is usually operated with the use of steam LC cycles followed by dry LC cycles at various incidence angles, using suitable fluences as appropriate for each cleaning situation.

3. Laser micro-melting to produce nano-bumps

The disk surface and the slider ABS that "flies" on the disk must have smoothness on the order of 1 nm or better, in order to support very high density recording, with magnetic bit length being 50 nm and shrinking. However, supersmooth surfaces tend to stick together when they come into resting contact (when power is turned off and the slider is permitted to rest on the disk near the inner diameter). In this case, the slider can stick onto the disk with strong adhesion force at longer resting times, especially in the presence of lubricant or other organic films on the surface. This can cause significant damages when the disk is made to start to spin again. This is the problem of "stiction", which can be solved by producing a racetrack near the inner diameter with highly controlled roughness for the landing and take-off of the slider. The roughness must be enough to overcome stiction, but not excessive because this will cause too much wear and tear during slider landing and take-off. We discovered that a compact laser source operating at high pulse repetition rate of over 100 kHz is ideally suited to produce the "laser-textured landing zone" required to alleviate the stiction problem in contact start/stop disk-drives. This technique of forming the contact start/stop (CSS) zone on the disk is called "Laser Zone Texturing" [5,6], first put in production in 1994, and is now an industry standard.

There are 2 kinds of disk substrates in common use. One is a Nickel-Phosphorous (NiP) plated aluminum substrate, and the other is aluminosilicate glass substrate. The NiP is an amorphous metal film of thickness about 10 μm, and its surface is easily polishable to an ultra-smooth finish. NiP disk substrates are commonly used in server and desktop disk drives. Glass substrates are even more polishable to ultra-smoothness, and are commonly used in mobile drives.

We have found that ultra-smooth bumps of diameter ranging from 0.05 mm to 0.002 mm, and of bump height from tens of nm down to a few nm, can be produced on NiP by focussed pulsed laser heating. A diode-pumped Nd:vanadate laser operating at or above 100 kHz pulse repetition rate, with pulse energy on the order of a few μJ, is ideal for such an application. Since the laser pulse width is short, typically tens of ns, each pulse produce an isolated heated spot on the amorphous NiP coating. The laser fluence is adjusted such that the heated and molten NiP pool has the proper diameter and surface tension gradient such that there is slight lateral flow of liquefied NiP before it solidifies again, producing the permanent bump on the disk surface without any volume gain.

By rotating and translating the disk while the pulsed laser beam is shuttered on, an array of bumps located in an annulus is produced in a few seconds. The total number and locations of the bumps can be controlled precisely. This bumps are typically spaced a few tens of μm apart. This bump array forms the CSS zone as a narrow racetrack near the ID of the disk. The magnetic head slider can rest on hundreds of such bumps on the CSS zone instead of on the supersmooth disk surface, thus reducing drastically the stiction force between the slider and the disk surface. This laser texturing technique is clean, solvent-free, precise, economical, and much better than conventional abrasive-texturing techniques,, and is now widely adopted in the industry. The process reproducibility is impressive, as all the bumps on a disk, and from disk to disk, can be "tuned" to specific heights with reproducibility within a fraction of a nm (one standard deviation). Up to date, about a billion disks have been laser-textured worldwide, with each disk having close to a million bumps.

Single bumps for "height standards" in the range of a few nm to hundreds of nm can also be made [7]. Height standards are needed in various micro-mechanical device fabrications. For the disk-drive industry, standard protrusions or bumps on a "reference disk" is needed to calibrate the fly height of magnetic head sliders. Such calibration bumps were conventionally made by some kind of deposition technique. The laser-melting method we developed for texturing can be used or adapted for making calibrated single bumps. If a single laser pulse as used in the texturing is used, a single bump of the same height is obtained. A more flexible method is a "multi-pulse bump buildup" technique whereby a lower fluence is used, and the bump height is built up by repeated pulsing at the same location till the desired bump height is reached. By careful control of the fluence, bump height can be increased at about 1 nm/pulse.

We have also shown [8, 9] that ultrasmooth glass disk surface can also be textured. Here, the microscopic spot heating to form the bumps are done using microsecond pulses obtained by acousto-optic modulation of a stabilized waveguide carbon dioxide laser. This pulse train is focussed onto a moving glass disk and produces up to a million bumps in a few seconds to provide the textured landing zone. Bump heights in the range of a few nm to a hundred nm can be made. Bump formation here is due to localized softening and expansion of the glass, rather than lateral flows as in the NiP case. There is a positive volume gain in the glass bump formation.

4. Laser Curvature Adjust Technique

The fly height of the magnetic head slider on the disk surface is established by dynamic equilibrium between the downward loading force from the slider suspension and the uplifting force from the air bearing generated between the disk and the flying slider. The curvature (crown) of the slider air bearing surface (ABS) is an important parameter that determines the uplifting force, so slider curvature control has become very important as fly height continues to be reduced. The "crown" of a slider is defined as the maximum separation between the cylindrical fit to the ABS and the imaginary flat plane defined by the leading and trailing edges of the slider. Typical crown values are measured in nm, while the slider size is about 1 mm x 1 mm, so the slider crown is truly microscopic, but yet it is important to control the crown values. Crown varies from slider to slider because of variations in the surface stresses from slider to slider. What we observed was that surface stress can be modified by scanning a focussed pulsed laser beam on the slider back side (opposite to the ABS), producing a line or track of microscopic surface-modification or ablation of the ceramic material. This laser-scribed line causes a reduction of the compressive stress on the surface, thus causing the ABS to become more convex, i.e., increase in crown. The most interesting fact is that by proper laser scribing a line, composed of overlapping spots about 20 μm in diameter on the back side, we can produce a crown change of typically 1 nm at the ABS. Interestingly, this provides exactly the proper magnitude of crown control that is needed.

We have designed and implemented in manufacturing the Laser Curvature Adjust Technique (LCAT) tool [10]. As in the technique of laser zone texturing for NiP disks, we utilize a Nd:vanadate Q-switched laser operating at 100 kHz or above as the laser source for scribing marks or lines on the back side of the sliders. The laser pulse energy is on the order of 10 μJ, and the pulse duration on the order of 100 nsec. The short pulse duration is needed in order to limit thermal diffusion, i.e., although the peak temperature at the irradiated spot is sufficiently high to cause melting or ablation of the ceramic material, it is much lower just some tens of micrometers away in order that the read/write elements are not damaged. The Nd: Vanadate laser beam passes through proper shutters, attenuator, and beam-shaper to provide the proper beam diameter, and is then directed to a 2-dimensional scanning galvo mirror. A large-field scan lens is positioned one focal length away from the galvo mirror to provide telecentric scanning of the scribing beam at the back side of the sliders. An optical monitor is used at the slider ABS to monitor the crown before and after a first installment of laser scribing is done. The optical monitor is based on the measurement of the degree of convergence or divergence of probe laser beams reflected from the ABS. A convex surface (positive crown) produces divergence in the reflected beams, while a concave surface (negative crown) produces convergence in the reflected beams. We use the optical monitor to control the total number of laser scribed lines on the back side of the slider, such that the desired target crown value is reached for each slider. Using this "close-loop control" LCAT process, many millions of sliders have been manufactured with crown controls within a few nm.

5. Conclusions

Several new applications of pulsed laser micro-processing have been developed for the manufacturing of disk drive components. Matured applications that have been extensively implemented in the industry include the laser zone texturing technique, the production of standard calibration bumps, and the fine tuning of slider curvatures using the LCAT process. One reason for the successful reception of the new laser processing techniques is that compact, efficient, low-cost, and turn-key laser systems (particularly the diode-pumped solid-state lasers with fundamental or harmonic outputs) have become available in the past few years, providing reliable low-cost solutions for laser micro-processing. Another reason is that new requirements (e.g., smaller dimensions, cleaner devices, tighter clearances) for component continue to arise as the technology moves so rapidly, opening up new opportunities for laser micro-processing.

6. Acknowledgments

I would like to thank many colleagues, in particular, Peter Baumgart, Costas Grigoropoulos, Dongsik Kim, Wing P. Leung, Hee K. Park, Chie C. Poon, Iraj Pour, Tim Strand, Xianfan Xu, and Werner Zapka for their valuable contributions to the work reviewed in this paper.

References

[1] H. K. Park, C. P. Grigoropoulos, W. P. Leung, and A. C. Tam: IEEE Trans. Comp. Packag. Manufac. Technol., **17A**, (1994) 631

[2] H. K. Park, D. Kim, C. P. Grigoropoulos, and A. C. Tam: J. Appl. Phys., **80**, (1996) 4072
[3] A. C. Tam and W. Zapka: "Laser cleaning of a delicate (easily laser-damaged) surface", IBM Tech. Discl. Bull, **35** (1992), 70
[4] A. C. Tam, W. P. Leung, W. Zapka, and W. Ziemlich: J. Appl. Phys. **71**, (1992), 3515
[5] P. Baumgart, D. J. Krajnovich, T. A. Nguyen, and A. C. Tam: IEEE Trans. Mag., **31** (1995), 2946
[6] A. C. Tam, I. K. Pour, T. Nguyen, D. Krajnovich, P. Baumgart, T. Bennett, and C. P. Grigoropoulos: IEEE Trans. Mag. **32** (1996), 3771
[7] T. Strand, A. C. Tam, P. Baumgart, and J. Colonia: IEEE Trans. Mag. **34** (1998) 1786
[8] A. C. Tam, J. Brannon, P. Baumgart, and I. K. Pour: IEEE Trans. Mag. **33**, (1997) 3181
[9] J. Brannon, R. White, A. C. Tam, and P. Baumgart: IEEE Trans. Mag., **34**, (1998) 1789
[10] A. C. Tam, C. C. Poon, L. Crawforth, and P. Lundquist: "New Laser Curvature Adjust Technique (LCAT) for fine adjustment of the crown and camber of magnetic head sliders", Insight (Published by International Disk Drive Equipment and Materials Association, U. S. A.), May/June (2000) 8-12

Optical Radiation Pressure Micromachining Using a Small Particle

Hiroki SHIMIZU*, Takashi MIYOSHI*, Satoshi KIYONO**

* Department of Mechanical Engineering and Systems, Graduate School of Engineering, Osaka University, 2-1 Yamada-oka, Suita, Osaka 565-0871, Japan
E-mail miyoshi@mech.eng.osaka-u.ac.jp
** Department of Mechatronics Graduate School of Engineering, Tohoku University, Aoba-yama 01, Aoba-ku Sendai, 980-8579, Japan

This paper presents a new micro-machining using optical radiation pressure induced by incident laser light, which is based on laser trapping technology. In order to verify the feasibility of our proposed new micro-machining, we construct the experimental system and carry out the fundamental experiments. As a result, we found that the proposed micro-machining will make it possible to remove effectively the surface up to the depth of several nm using the particles trapped by the optical radiation pressure, even if the pressure force is as small as 0.1nN.

Keywords: micromachining, laser trapping, optical radiation pressure mechanochemical polishing, diamond grain

1.Concept of optical radiation pressure micro-machining

Nowadays, there are many micro-machining processes, for example, fine electro-discharge machining[1], micro-lathe machining[2] and the application processes of semiconductor technology such as photo-lithography[3], etching, etc.. But, these micro-machining processes can't satisfy all the requirements in production of the micro-machine parts.

So, we proposed a new micro-machining using optical radiation pressure. The concept of proposed micro-machining is as follows: When the laser light focused by the objective lens is irradiated to the small dielectric particle such as spherical silica, the incident laser light induces the radiation pressure force on the small dielectric particle. It is known as laser-trapping technology[4][5], the particle is dynamically trapped and manipulated by the optical radiation pressure force. The trapping force is considered to be as small as pN to nN of less than atomic force.

As shown in Fig.1, if the laser trapped particle is moved, rotated or oscillated by the optical radiation pressure, the micro-machining which removes the amount of atomic order, namely the depth of cut is as small as several nano meter, will be able to be performed.

2.Experimental method

2.1Experimental system and procedure

In order to verify the feasibility of our proposed micro-machining, the fundamental experiments are carried out according to the following experimental method.

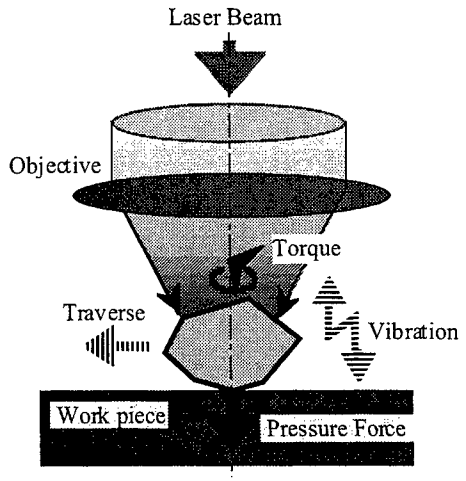


Fig 1 Concept of optical radiation pressure micro-machining

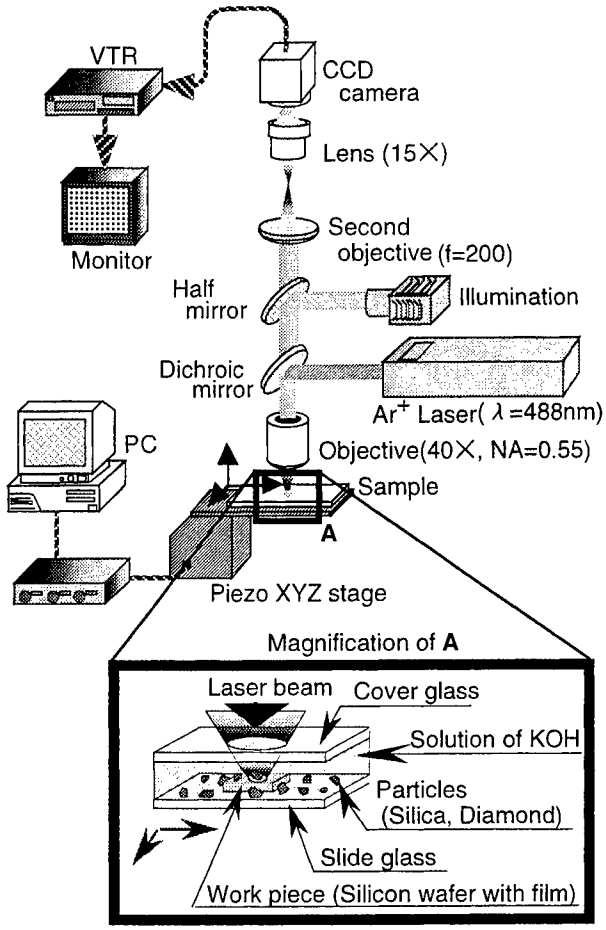


Fig 2 Schematic diagram of optical radiation pressure micro-machining system

Fig.2 shows the experimental system for performing the optical radiation pressure micro-machining. This system consists of laser trapping unit and microscopic observation unit. The Ar+ laser (λ = 488 mm) is used as trapping laser source and this laser beam is focused by the objective lens of which NA is 0.55. The detail around the workpiece in the experimental system is shown in the magnification of A in the Fig. 2 .

The workpiece is placed on the slide glass. The solution of KOH is used as machining fluid, which is filled between the slide glass and the cover glass to promote the chemical action. The machining particle in this solution are dispersed over the workpiece surface. One of the particles is trapped by the incident laser focused on the workpiece.

The trapping force induced by incident laser are predicted in the order of pN to nN from the results of our simulation of the trapping force for the spherical object shape.

In this experiment, the machining particle is trapped in stable position and the workpiece put on the slide grass is moved by

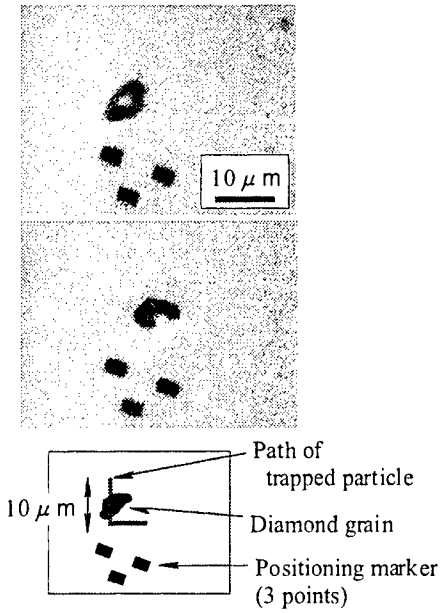


Fig 3 Experimental view of rotating diamond grain

the piezo actuator: thus relative movement between particle and workpiece is realized. By using computer controlled piezo XYZ stage, It makes a particle moving repeatedly with a constant path on the workpiece. The trapped particle, its movement, and operation of this experiment are directly observed by the microscopic unit of which magnification is 600 × on CCD and recorded by VTR.

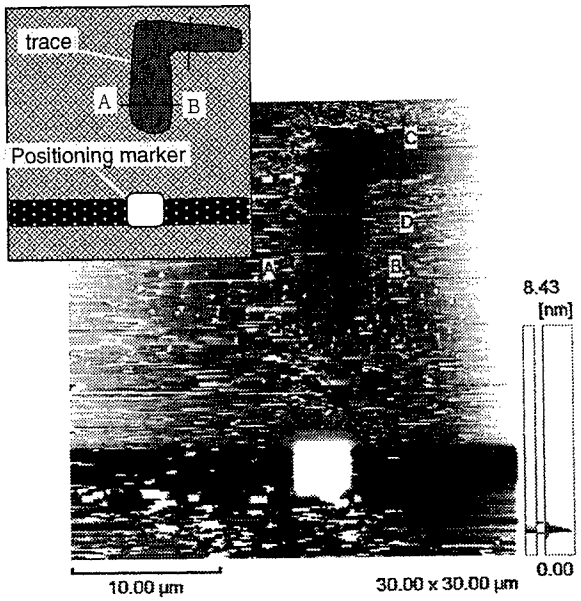
Fig. 3 shows the view of machining experiment obtained by CCD camera. Irregular shape object placed upper position is a laser trapped diamond grain. Diamond grain is given not only relative movement to silicon wafer but rotating movement.

2.2 Experimental conditions

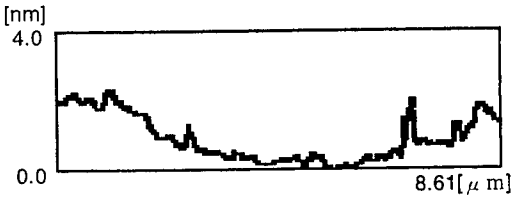
We used the silicon wafer as a workpiece. As a machining tool, one is irregular shaped diamond grains whose size are about 1 to 10 μm and the other is spherical silica particles whose diameter are 5μm.

Table 1 Experimental condition

	non-rotating diamond grain	rotating diamond grain	silica sphere
Size of particle	6.5×3.0μm	6.0×2.5μm	5.0μm (diameter)
Number of trace	200 times	50 times	100 times
Traverse speed	14.5μm/s	4.4μm/s	14.5μm/s
workpiece	silicon wafer	silicon wafer	hydrocarbon film
trapping laser	Ar^+ laser λ=488nm 100mW (objective lens output)		
Machining fluid	solution of KOH (pH11)		

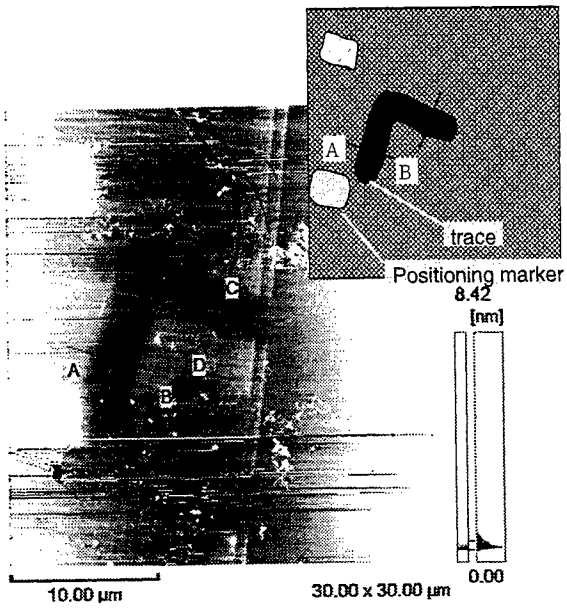


(a) AFM observation image of workpiece surface

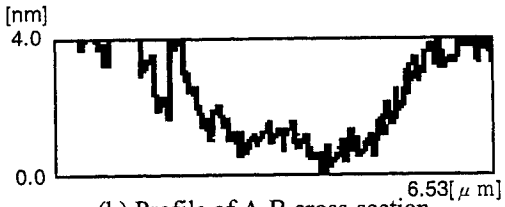


(b) Profile of A-B cross-section

Fig 4 Experimental results for the case of non-rotating diamond grain



(a) AFM observation image of workpiece surface



(b) Profile of A-B cross-section

Fig 5 Experimental results for the case of rotating diamond grain

Laser power is 100mW at the output side of objective lens and laser spot size is about 4μm diameter at the beam waist . The beam waist position is adjusted at a few microns near the workpiece surface, in order to induce the trapping force pressing the particle against the workpiece surface.

Details of the experimental conditions are shown in Table1.

3. Experimental results and Discussion

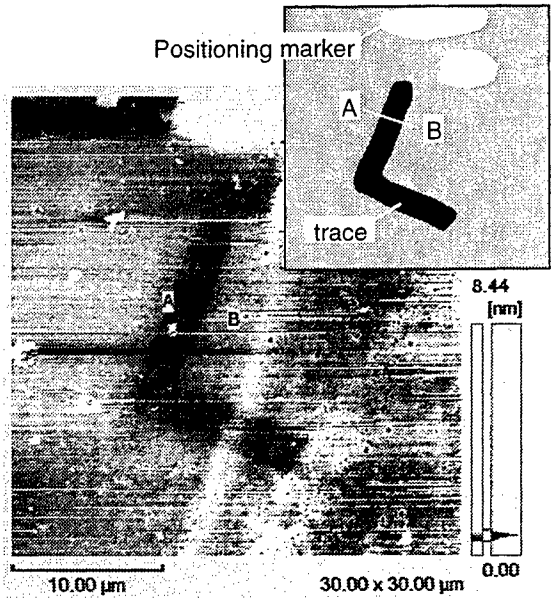
First, we verified the motion controllability of laser trapped particles. As a result, the diamond grain with non-spherical irregular shape is not easily trapped with stability comparing with the spherical particles, however, some of the irregular shape particles are stably trapped and rotated. It is considered that the non-spherical and asymmetrical particles shape causes its rotation. The rotation ratio is up to 300r.p.m. at high speed.

Next, we performed the machining experiments . Fig.4 and Fig.5 show the machining experimental results obtained by AFM observation for the case of non-rotationg diamond grain and rotating diamond grain respectively.

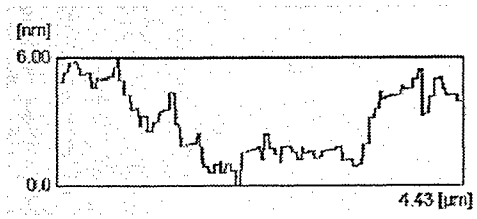
The rectangular bright parts in Fig.4(a) and Fig.5(a) mean positioning markers which allow us to find the machining areas and the moving traces of the machining particles. The traces which look like hook are observed nearby the markers in both Fig.4(a) and Fig5(a). The positions and the shapes of those traces conform to moving path of the particles. This fact shows that the trapped particle's movement fabricates those traces on the surface of silicon wafers. In non-rotation case, the particle is trapped and moved with keeping long side of 6.5μm horizontally. So it is predicted that the width of latelal side of the trace is differ from longitudinal side. In practice, the width of trace is about 3μm in lateral side and about 5μm in longitudinal side respectively. This fact shows that the shape of grain is closely related to the shape of machining trace.

While, in rotation case, the width of trace is almost same value of 4μm in both lateral and longitudinal sides. the trace width is seen to be equal to the average grain diameter.

The cross-sections of the traces are shown in Fig.4(b) and Fig.5(b). The groove depths are very small to be about 1 ~ 2 nm and 3 ~ 4 nm respectively . The groove in rotation case is



(a) AFM observation image of workpiece surface



(b) Profile of A-B cross-section

Fig 6 Experimental results for the case of silica sphere

about twice as deep as that in non-rotation case, in spite of smaller number of trace and lower traverse speed. This result suggest that rotationg diamond grain is more efficient than non-rotating diamond garin in our proposed micro-machining method.

Next, we carry out the machining experiment using a silica sphere as machining tool and hydrocarbon film as workpiece surface. Hydrocarbon film as thick as 100nm is formed on the silicon wafer by the irradiation of electron beam and will be able to easily machined due to the lower hardness. Fig. 6 shows the results of machining experiment obtained by AFM observation. The groove is estimated to be about 3μm in width and 3~4 nm in depth. From this result, when the workpiece surface is not so high in mechanical strength, even the laser torapped silica sphere with low hardness will be able to be used as a machining tool.

4. Conclusions

We proposed a new micro-machining technology based on laser trapping. In order to verify the feasibility of our proposed method, we performed the fundamental experiment. The results obtained in this paper are summarized as follows:

(1) The laser trapping force which is as small as 0.1 nN enables stably trapping of the spherical particle. Furthermore, that force enables not only to stably trap the rotating diamond grain but also to freely control the position of the rotating grain.

(2) By traversing the laser trapped particles such as a diamond grain on the silicon wafer and a silica sphere on the hydrocarbon film, we observed the grain trace with the depth of several nano meter by the use of AFM. This fact suggests the feasibility of the optical radiation pressure micro-machining.

References

[1] T.Masuzawa et al.: "Wire Electro-discharge Grinding for Micro Machining", Ann. CIRP, 34, 1, (1985) 431.
[2] K.Okano, T.Waida, T.Suto, J.Mizuno and T.Kobayashi: "Micro-grinding of Micromachine Parts", Proc. Int. ABTEC(Abrasive Technology) Conf., Seoul, (Nov.1993) 100.
[3] T.Sato : "Micromachining of 3-dimensional Microstructure by Etching", J. of JSPE, 61, 10, (1995) 1369.
[4] A.Ashkin: "Acceleration and trapping of particles by radiation pressure", Phys.Rev.Lett., 24, (1970) 156.
[5] A.Ashkin, J.M.Dziedzic, J.E.Bjorkholm and S.Chu: "Observation of a single-beam gradient force optical trap for dielectric particles", Opt Lett, 11, (1986) 288.

Micropeak Array in the Scribe Line on a Wafer

Teiichirou CHIBA, Ryuusuke KOMURA and Akira MORI

Research Center, Research Division, Komatsu Ltd., 1200 Manda, Hiratsuka, Kanagawa 254-8567, Japan
E-mail: teiichirou_chiba@komatsu.co.jp

Small dot matrix marking on a silicon wafer has been performed using an second-harmonic generation (SHG) laser of yttrium aluminum garnet (YAG), liquid-crystal-display (LCD) mask, and projection optics. A marked image was obtained after laser irradiation through the pattern on the LCD mask. The each dot is a square with sides of 3.6 μm, the pitch of each dot is 4.5 μm and the height (not the depth) of each dot is approximately 0.5 μm. The topography of each dot is unique, and features a central peak and peripheral depression. We have named this topography "micropeak" and have proposed a hypothesis for the micropeak formation mechanism, based on the density of liquid silicon and the congelation of molten silicon. In this report, micropeaks were formed in the scribe line on a wafer covered with oxide layers. Without being torn, these oxide layers were pushed up by micropeak generation and rose. Silicon particle scattering around the laser irradiation area was prevented completely. Clear dot images were observed through the transparent oxide layers. The conditions for clean marking by laser irradiation greatly depend on the thickness of the oxide layers.

Keywords: laser marking, silicon wafer, scribe line, thin film structure

1. Introduction

In semiconductor manufacturing, silicon wafers have identification numbers, and production control systems record each wafer's manufacturing history in host computers. However, since these systems have recently became unmanageably large and the host computer loads keep increasing, system simplification is required.

Therefore we propose to store some of the processing information on the silicon wafer itself by laser marking instead of it storing in the host computer. Marks are applied between wafer processing steps, and the recorded information can be read at any step in the process. As a result, the host computer's transactions and storage size will decrease. In this method, we also propose a scribe line between device dies on the wafer surface as the marking site, because this area does not have device patterns and is almost bare silicon to enable each device die to be easily cut off after all processes are complete.

Oxide was deposited on the scribe line area during wafer processing steps. Laser marking on the scribe line should be considered as a laser process of a silicon substrate with multi layer surface structure. The research on laser processing of a multi layer structure substrate has been progressed in the field of solar batteries, liquid crystal panels [1] and information recording. [2] In those researches, the thermal distribution in layer structures formed by laser irradiation was calculated and process optimization was discussed. Maydan [3] showed that front and back laser irradiations have the same efficiency for metal film removal from metal deposited-glass substrates, and the glass substrate prevents the deposition of the removed material on the object lens in back irradiation. Biancos [4] showed that back irradiation for the α-Si/TCO layer through the glass substrate was more efficient than direct front irradiation. This was caused by absorption differentials of air/target and glass/target interfaces.

We have previously proposed "micropeak" technology, by which very small peaks are formed on the silicon wafer. [5] [6] In this study, we examined the formation of "micropeak" on a wafer surface covered with oxide layers without surface fracture, by laser irradiation through the transparent surface oxide layers, in the same way as the back irradiation process above. In particular, the influence of the oxide layer thickness on laser irradiation conditions was examined and discussed.

2. Experimental Set up

The experimental configuration of laser marking is depicted in Fig. 1. A Q-switched second-harmonic generation (SHG) laser of yttrium aluminum garnet (YAG) was operated with a pulse width of 90 ns, wavelength of 532 nm, and repetition rate in the range from 1 to 1000 Hz. The pulse energy was varied continuously by a variable beam attenu-

First International Symposium on Laser Precision Microfabrication, Isamu Miyamoto, Koji Sugioka, Thomas W. Sigmon, Editors, Proceedings of SPIE Vol. 4088 (2000) © 2000 SPIE · 0277-786X/00/$15.00

ator and measured with a thermopile laser power detector, and then the irradiation energy density on the target surface was calculated. Energy density is within the range 1-10 J/cm^2 and has 5 % error, which mainly arises from the pulse-to-pulse energy instability. A laser beam was expanded and collimated, then incident on the liquid-crystal-display (LCD) mask. The uniformity of the laser beam intensity on the LCD mask was better than ± 5 %. The displayed mask pattern is demagnified onto the target surface with a ratio of 1/100. This projection system also has a confocal auto-focusing function, and the projection lens is actuated to the best focal point by piezoelectric positioner.

The reading system has an objective lens with 1/10 magnification, a light-emitting diode (LED) lighting source and a conventional machine vision system. [7]

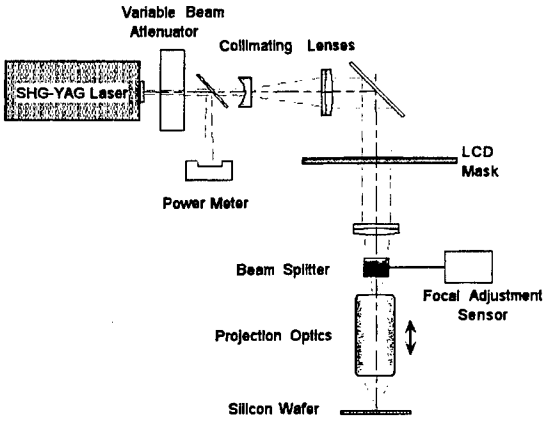


Fig. 1 Experimental configuration.

The marking dot and surface film shape were observed with a scanning electron microscope (SEM) and a transmission electron microscope (TEM). For TEM observation sample preparation, carbide and metal were deposited on the sample surface to prevent sample breakdown, then the sample was thinned by the focused ion beam (FIB) method. The determination of chemical elements in the surface layers was also carried out by energy dispersive spectroscopy (EDS).

The scribe line surface structure on a dynamic random access memory (DRAM) chip sample is shown in Fig. 2. Figure 2(a) is a cross-sectional SEM micrograph of the scribe line. The line area width is approximately 80 μm. Figure 2(b) is the magnified image of the surface layer structure. The total layer thickness is 1 μm. Figure 2(c) shows results of the EDS analysis of the surface layer. Only silicon and oxygen were detected, and each layer comprised silica.

Moreover, silicon wafer substrates covered with oxide film of various thicknesses were prepared in order to examine the influence of film thickness on marking conditions. Samples were prepared by thermal oxidation of the bare silicon wafer, and the surface oxide thicknesses were 1460, 4400 and 9150 Å.

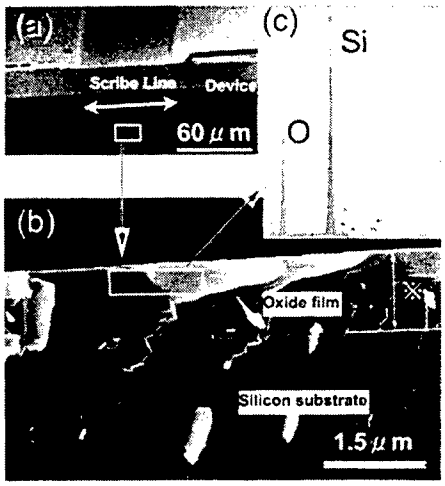


Fig. 2 Cross-sectional SEM views of scribe line area: (a) whole scribe line. (b) surface oxide magnified image. (c) EDS analysis result inside white window in (b).

3. Results

3.1 Laser marking on a scribe line

Figure 3(b) shows a mark on a scribe line, with the laser irradiation conditions of 1.60, 1.44 and 1.28 J/cm^2 single pulses, respectively, and the minimum energy density required for visible marking was 0.6 J/cm^2. This is a bright-field optical image obtained by the machine vision system.

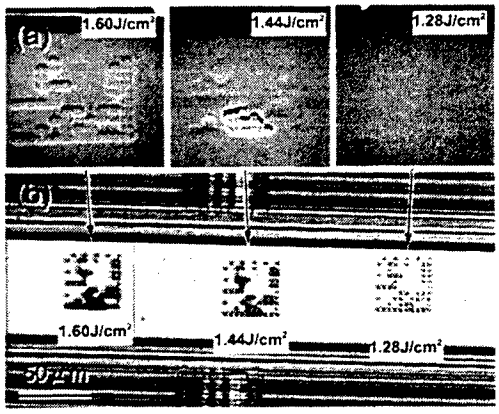


Fig. 3 Laser markings on the DRAM chip scribe line. (a) SEM view for each irradiation condition. (b) Optical image obtained by machine vision system.

The marking patterns consist of the "micropeaks" which are squares with sides of 3.6 μm, and the peaks are arranged 10 x 10 two dimensionally with 4.5 μm intervals. These markings are Data Matrix 2D-code patterns of ID Matrix Ltd., and cosist of 6-digit numbers.

Figure 3(a) shows magnified mark images for each condition. The sample was tilted and observed by SEM. The oxide film was damaged with an energy density of 1.44 J/cm^2 or more, while no damage occurred at 1.28 J/cm^2. These results show that this marking process has an energy density range within which it is possible to make clean marks without oxide film damage. Furthermore, swelling of the oxide film surface corresponding to micropeak formation was observed at 1.28 J/cm^2. Figure 4 shows the schematic process of the micropeak forming under an oxide film and pushing it up. As a result, projections with good visibility can be formed under oxide film.

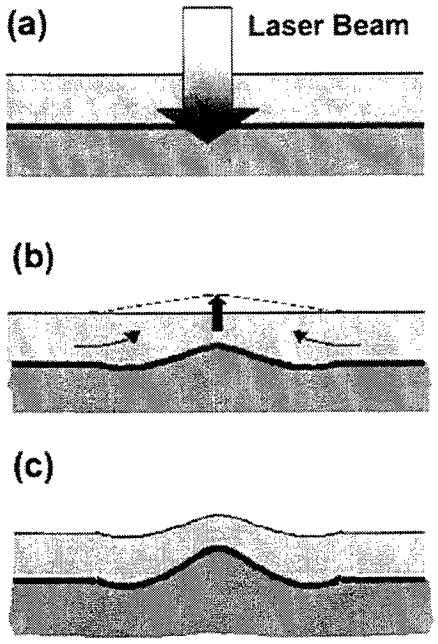


Fig. 4 Micropeak formation.

3.2 Laser marking with various film thicknesses on a substrate

The marking condition dependence on the oxide film thickness is shown in Fig. 5. The horizontal axis is laser irradiation energy density, and the vertical axis is oxide film thickness. The symbols for each thickness show the energy density ranges from the minimum value for obtaining of an optically clear marking image to the maximum value for the marking without inducing surface film cracks. The energy ranges for marking in film thicknesses of 1460 and 4400 Å were small, while the one for a thickness of 9150 Å was wide. However, the energy range for marking was not proportional to the film thickness.

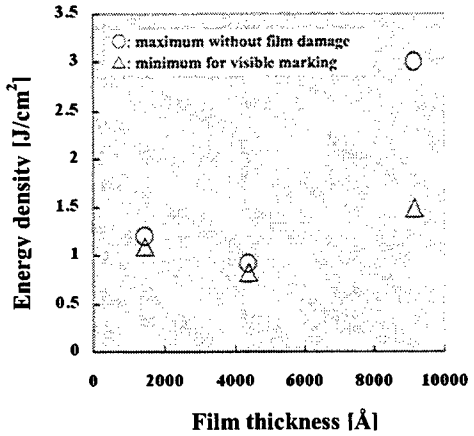


Fig. 5 Influence of oxide film thickness on marking conditions.

Figure 6 shows magnified dot images produced with the minimum irradiation energy density to induce surface oxide film cracks. Figure 6 (a) is for the case of a film thickness of 1460 Å. The cracks propagated radially from the dot center. Figure 6 (b) is for the case of a film thickness of 4400 Å. A plate-shaped oxide film fracture occurred.

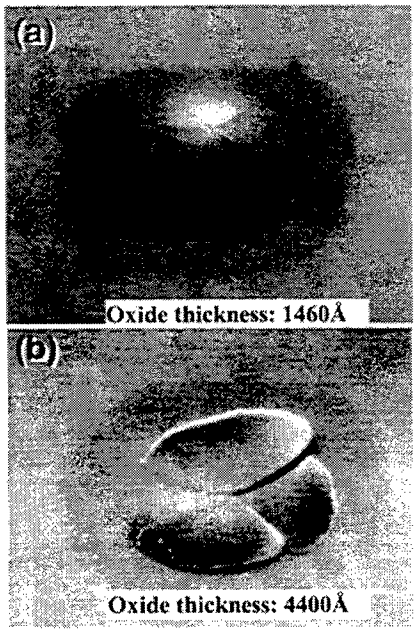


Fig. 6 SEM views of surface oxide film cracks:
(a) 1460Å film, radial crack propagation.
(b) 4400Å film, plate-shaped fracture.

Figure 7 shows the cross-sectional image of a micropeak formed with slightly less energy density to induce an oxide film crack. The arrow shows the oxide layer. The white layer on the oxide is a protection film for FIB, and the lower gray layer is the silicon substrate. The upheaved dot center substrate does not have any significant defect, and was confirmed to be single crystalline from the electron diffraction pattern. Furthermore, the oxide layer transform along the upheaved silicon substrate shape can be observed.



Fig. 7 TEM cross-sectional image of "micropeak" under oxide film.

4. Discussion

4.1 Influence of surface oxide film thickness influence

In Fig. 6(a), the 1460-Å-thick film was pushed up and the surface crack spread radially from the dot center. The oxide film was amorphous silica, and these findings suggest that the film was warmed by thermal conduction from the silicon substrate heated by laser irradiation, and then may have deformed plastically over the glass transformation temperature. On the 4400 Å film, the surface oxide was removed. At this thickness the internal stress due to micropeak formation remains the same, but laser irradiation may not have sufficient heat capacity to produce surface oxide glass transformation over the entire dot area. As a result, the surface oxide could not deform plastically, and plate-shaped fracture occurred.

The results for the 9150-Å-thick film suggest that the surface oxide film of a thickness between 4400 and 9150 Å has the strength to resist the internal stress due to micropeak formation.

Furthermore, additional preheating with smaller pulse train irradiation just before the marking pulse expanded the energy density range without surface film fracture in a film of 1460 Å thickness. One explanation is that preheating prompted surface oxide glass transformation. However, in a more than 4400-Å-thick oxide film, preheating did not have this effect. Consequently it is difficult to mark a silicon substrate covered with oxide film with a thickness of around 4400 Å.

4.2 Influence of film material

The minimum energy densities required to induce film surface damage were 1.44 J/cm^2 for a 1-μm-thick oxide film on the scribe line and 3.10 J/cm^2 for the 9150-Å-thick thermal oxide on the silicon substrate. The thermal oxide layer required twice the energy density required by the scribe line film though the film thicknesses were approximately the same, because the oxide on the scribe line, deposited by chemical vapor deposition (CVD), has a lower melting point than thermal oxide.

The minimum energy densities required for visible marking were 0.6 J/cm^2 for the scribe line of an oxide film and 1.4 J/cm^2 for the thermal oxide. This can be explained by the difference in the silicon substrate / oxide film interface strength. The CVD-deposited oxide film has less film and interface strength, and thus has less resistance to the rising of the silicon substrate during marking dot formation.

5. Conclusion

Laser marking of the scribe line was achieved with a DRAM device chip. Micropeaks, small projection marking dots, were formed in the scribe line covered with oxide films without surface fracture. Since the silicon substrate rose and pushed up the surface oxide film during marking dot formation, the marking conditions depended on several factors, including surface oxide film thickness, film strength and interface strength. We presumed that the surface film thickness of the scribe line changed during the process in semiconductor manufacturing, and examined the influence of film thickness on marking conditions. Visible markings without surface fracture were obtained except with the film thickness of around 4000 Å. We will continue the investigation of the optimization of multi layer laser marking, and generalize this technology.

References

[1] O. Yavas and M. Takai: Appl. Phys. Lett., **73**, (1998) 2558.
[2] A. Medvid, M. Knite, J. Kaupuzs and V. Frishfelds: Proc. SPIE Int. Soc. Opt. Eng., **3055**, (1997) 58.
[3] D. Maydan: Bell Syst. Tech. J., **50**, (1971) 1761.
[4] N. Bianco, B. Morrone and O. Manca: Heat Technol., **15**, (1997) 49.
[5] A. Mori and T. Chiba: Semicon Japan 99, SEMI-Technology Symp. 7-57.
[6] T. Chiba, R. Komura and A. Mori: submitted to Jpn. J. Appl. Phys.
[7] T. Okamoto, K. Bedrosian: Densizairyo, **35**, (1996) 103 [in Japanese].

Matrix Assisted Laser Transfer of Electronic Materials for Direct Write Applications

R.C.Y. AUYEUNG*, H.D. WU*, R. MODI**, A. PIQUÉ, J.M. FITZ-GERALD, H.D. YOUNG*, S. LAKEOU*, R. CHUNG† and D.B. CHRISEY

Naval Research Laboratory, Code 6372, Washington DC 20375
**SFA Inc., 9315 Largo Drive West, Largo, MD 20774*
***George Washington University, Department of Mechanical and Aerospace Engineering, Washington DC 20052*
†Geo-Centers, Inc., 1801 Rockville Pike, Rockville, MD 20852

A novel laser-based direct-write technique, called Matrix Assisted Pulsed Laser Evaporation Direct Write (MAPLE-DW), has been developed for the rapid prototyping of electronic devices. MAPLE-DW is a maskless deposition process operating under ambient conditions which allows for the rapid fabrication of complex patterns of electronic materials. The technique utilizes a laser transparent substrate with one side coated with a matrix of the materials of interest mixed with an organic vehicle. The laser is focussed through the transparent substrate onto the matrix coating which aids in transferring the materials of interest to an acceptor substrate placed parallel to the matrix surface. With MAPLE-DW, diverse materials including metals, dielectrics, ferroelectrics, ferrites and polymers have been transferred onto various acceptor substrates. The capability for laser-modifying the surface of the acceptor substrate and laser-post-processing the transferred material has been demonstrated as well. This simple yet powerful technique has been used to fabricate passive thin film electronic components such as resistors, capacitors and metal lines with good functional properties. An overview of these key results along with a discussion of their materials and properties characterization will be presented.

Keywords: direct write, laser forward transfer, matrix assisted pulsed laser evaporation (MAPLE), matrix assisted pulsed laser evaporation direct write (MAPLE-DW), rapid prototyping, electronics devices.

1. Introduction

There is a strong need in industry for rapid prototyping and manufacturing of passive electronic components on various substrates in the mescoscopic regime (micron to mm range). This capability is required in order to fabricate smaller and more versatile electronics devices, to iteratively measure the performance of circuits too difficult to model and to quickly design and test circuits without a time-consuming photolithographic mask process.

Direct-write technologies provide a flexible, maskless and efficient technique for depositing a wide variety of materials under ambient conditions which can be easily integrated into a CAD/CAM system. Direct-write methods do not compete directly with photolithography in manufacturing sub-micron size components, but are intended to supplant current surface mount technologies in the mesoscopic regime.

Various direct-write technologies have been developed in the last few years. Some of these techniques include micropen, inkjet, plasma spray, focused ion beam, e-beam and other liquid microdispensing approaches. Laser-based direct-write techniques[1] include Laser Induced Forward Transfer (LIFT), laser CVD, laser particle guidance and Matrix Assisted Pulsed Laser Evaporation Direct Write (MAPLE-DW).

In this paper, the principles of the MAPLE-DW technique will be described and results from some of the fabricated structures will be presented.

2. Background

Ever since the invention of the laser in 1960, much research has been directed towards the interaction of laser

First International Symposium on Laser Precision Microfabrication, Isamu Miyamoto, Koji Sugioka, Thomas W. Sigmon, Editors, Proceedings of SPIE Vol. 4088 (2000) © 2000 SPIE · 0277-786X/00/$15.00

radiation with materials. Its high coherence, directionality and brightness properties make laser radiation ideal for materials processing applications. These same properties also make it ideal for direct-write applications where a highly controlled source of energy with well-defined spatial qualities can be used to process materials in a specific location and time interval. By choosing the correct laser wavelength, fluence and optical beam delivery system, many types of materials can be deposited at room temperature under ambient conditions with feature sizes in the micron range. Various laser-based direct-write techniques have been used to deposit metals[2] and dielectrics[3] onto various substrates with varying degrees of success for each.

A promising new direct-write technique that allows the deposition of almost any kind of material onto any substrate type and shape is the MAPLE-DW process[4]. This technique combines aspects of both the MAPLE[5] and LIFT[6] processes into a simple but versatile direct-write technology. In the MAPLE process, large and fragile organic molecules to be deposited into thin film form are first dissolved in a dilute (usually frozen) matrix target. Then, a low fluence UV laser beam strikes the target to gently warm the solvent matrix to gently release the organic molecule while the now volatile solvent molecules are removed by vacuum pumping. This pulsed thermal process heats the surface to below the decomposition temperature of the organic molecules while the solvent matrix is heated to its evaporation point. The combined action of the evaporating matrix desorbs the large species intact and deposits them as uniform thin films.

LIFT is a simple pyrolytic direct-write technique where focused laser radiation vaporizes a thin film coating (<2000 Å) on one side of an optically transparent support. The vaporized material is transferred onto a substrate placed adjacent to this coating. Compared to MAPLE, LIFT requires a higher laser fluence because it must remove the thin film from its support by physical vapor deposition. For this reason and to maintain good lateral resolution, the thin film coating on the support is usually less than 1000 Å thick. Thicker depositions would require time-consuming iterative steps. Because the laser radiation tends to atomize the thin coating, LIFT is best suited for metals since multicomponent crystalline materials would not be able to be transferred intact. Other disadvantages of LIFT include poor spatial resolution, adhesion and morphology.

MAPLE-DW takes the experimental support of LIFT and combines it with the matrix desorption mechanism of MAPLE into a versatile direct-write process that takes place at room temperature. The support is transparent at the laser wavelength and consists of a coating of the materials of interest dispersed in a matrix. The matrix can consist of organic solvents, binders, dyes or other components, which aid in the transfer and particle bonding process. Ideally, when the laser beam strikes this coating and transfers it to the substrate, most of the matrix components should be removed, easily decomposed or evaporated after the transfer. An important benefit of MAPLE-DW is that unlike other approaches, this technique does not change the properties of the material of interest after the transfer.[7]

Another advantage of MAPLE-DW, which distinguishes it from other techniques, is that it can operate additively or subtractively. The presence of the laser beam allows *in-situ*, pre- or post-processing of the transferred material and substrate. For example, the laser can be used to pre-clean the substrate surface, micromachine vias or channels, trim circuit elements, or sinter the deposited material.

The MAPLE-DW process has been used in this work to successfully deposit metal lines, resistors and capacitor structures with good properties on various substrates.

3. Experimental Procedure

The experimental setup used in MAPLE-DW is very similar to that used in micromachining or the LIFT process. A UV laser operating at 355 nm with a 5 ns pulsewidth is focused onto a UV fused silica disk which acts as the optically transparent support. This disk is coated on one side with the material of interest and its corresponding matrix. The disk is placed with its coating side adjacent to the receiving substrate to within tens of microns gap separation. The entire disk and substrate is placed on a computer-controlled X-Y table which is synchronized to the output of the laser. The optical delivery system can generate UV focal spots from 10 to 300 micron diameter and fluences over 5 J/cm^2. The UV beam energies were monitored continuously during each deposition by an in-line beam-splitter and focal burn patterns were recorded on polyimide or UV photosensitive film. A secondary IR Nd:YAG laser operating in the free-running mode provides 1.06 μm pulses at 10-40 Hz with a 50 μs width for post-processing the transferred material. The table speed can be adjusted so that the IR focal spots overlap accordingly to give the required sintering dwell times.

Materials were transferred onto various substrates such as glass, alumina and polyimide. By optimizing the deposition parameters, deposited materials showed good morphology, linewidth and functional properties. Metal lines were transferred by MAPLE-DW between two photolithographically patterned Au electrode pads. An e-beam deposited gold line served as a reference on each sample. A standard 4—point probe DC measurement was used to characterize the resistivity of these lines. Resistor lines were transferred by direct-write between two Au electrode pads separated by 700 μm and its electrical properties characterized by both a 4-point probe measurement and an HP4291B impedance analyzer. Dielectrics were evaluated by transferring a (~0.7x0.8 mm) pad of material over a previously patterned interdigitated

capacitor structure (IDC). This structure allowed quick characterization of dielectric material properties and avoids the complication of depositing extra metal pad layers as would be found in a parallel-plate capacitor structure. The capacitance and loss tangent values of the capacitors were measured on an HP4284A LCR meter up to 1 MHz and on the impedance analyzer from 1 MHz to 1.8 GHz. Values measured at 1 MHz agreed within error on both systems and provide confidence in our measurement technique.

All samples were evaluated by optical and scanning electron microscopy (SEM). Both surface and fracture cross-sectional SEM's were performed on the different substrates.

4. Results and Discussion

Silver lines were transferred onto polyimide substrates and after a furnace anneal at 300 °C to react the metal precursor, the resistivities were measured to be 1.1 to 1.6X bulk Ag. A photograph of the line as well as profilometer scans across 6 different locations along a 7 mm-long segment are shown in Fig. 1. The lineshape definition is good with minimal debris as deposited. Only a single laser pass was used to deposit these 2.5 μm (average) thick lines and the 40-μm linewidth was comparable to the laser spot size. Silver lines were also deposited onto alumina and glass substrates with somewhat higher resistivities. A scotch tape test of the Ag line on glass left it intact which demonstrates the excellent adhesion of the transferred material.

Laser sintering was attempted on some of the higher resistivity silver lines with mixed results. At low levels of IR power absorption, only the surface silver layer showed signs of annealing or melting as shown in Fig. 2. When the IR laser power was increased, the silver line tended to "bead" or eventually delaminate from the substrate surface. The thermal diffusion depth for silver is over 10 μm for a 1 μs laser pulse so it is possible that sufficient porosity remains in the cross-section preventing efficient thermal

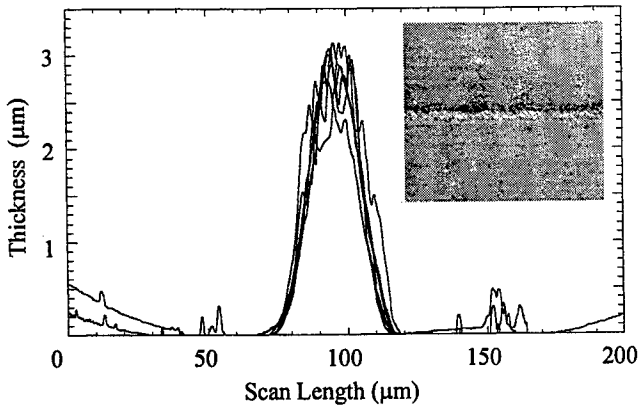


Fig. 1 Profilometer scans across a 7 mm-long Ag line segment deposited on polyimide. The inset shows an optical micrograph of the 40 μm wide line.

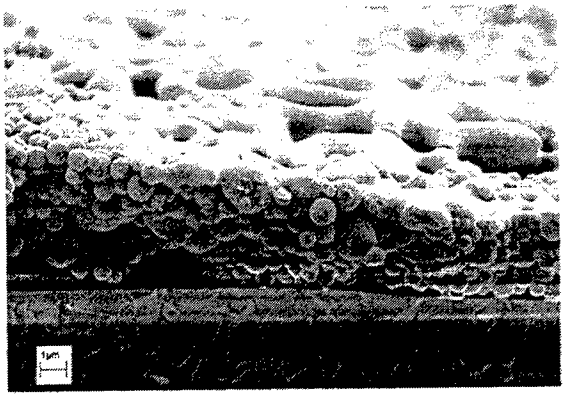


Fig. 2 SEM fracture cross-section of Ag line on alumina processed by a 1.06 μm laser.

conduction of the heat from the surface layer to the entire volume.

Polymer resistor lines were transferred between two Au pads on alumina substrates. By changing the formulations of the starting resistor material, nearly 4 orders of magnitude change in the sheet resistance was obtained in the transferred lines as shown in Fig. 3. The drop-off at higher frequencies is not unique to polymer resistors as it is also observed in cermet resistor material formulations[8]. The oscillations at the highest frequencies are due to resonance effects from the test leads and sample during the experiment. Note the good agreement between the measured sheet resistance values at 1 MHz and those actually specified for the starting material. This agreement demonstrates again that the MAPLE-DW process does not significantly alter the intrinsic properties of the material after transfer.

The dielectric material barium titanate (BTO) was transferred onto pre-fabricated IDC's on polyimide and alumina substrates. As shown in Fig. 4, an SEM cross-section of the transfer shows that a high packing density was achieved.

The measured capacitance and loss tangent of a BTO IDC from 1 MHz to 1.8 GHz are shown in Fig. 5. The measured dielectric constant ε_r of 70 and loss tangent of

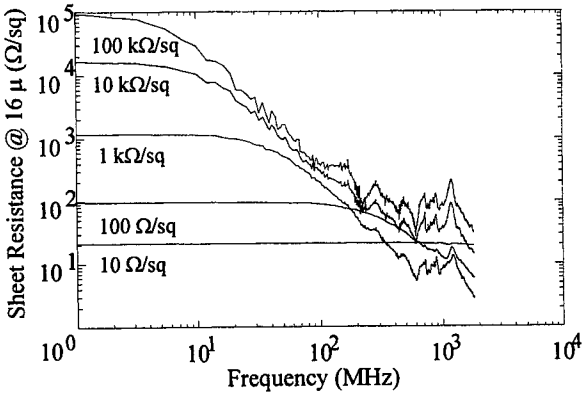


Fig. 3 Frequency behavior of sheet resistance of 5 different resistor lines made by MAPLE-DW.

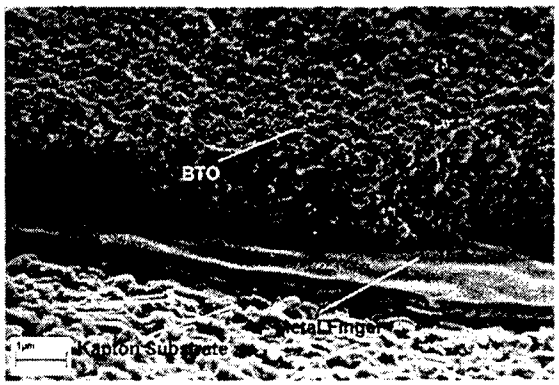


Fig.4 SEM fracture cross-section of BTO deposited on an interdigitated capacitor finger on polyimide.

4 % (after correcting for the substrate) at 1 MHz is significantly below the corresponding values for the powder starting material. Due to the high dependence of the dielectric constant on the porosity of the dielectric material[9], it is possible that the air volume fraction in the BTO transfer is still sufficient to dramatically lower the ε_r value.

5. Summary

In conclusion, we have demonstrated the versatility and strength of the MAPLE-DW technique as a rapid direct-write technology in depositing good-quality electronics materials under ambient environmental conditions. Silver lines with bulk-like conductivities have been deposited onto polyimide with a short furnace treatment as the only post-processing step. Resistor lines with sheet resistances of 4 decades have been obtained by only changing the composition of the starting material. Barium titanate compositions have been transferred as pads and their measured dielectric constants and loss show good promise as useful capacitor structures.

In addition, we have shown that MAPLE-DW can deposit different types of materials onto various substrates such as polyimide, metals, glass and alumina. The usefulness of this technique has been strongly demonstrated in this paper with high-quality material properties obtained directly with a simple transfer and furnace treatment step. No other pre- or post-processing procedures were used. Improvements in the materials formulations as well as a deeper understanding of the mechanism of the MAPLE-DW process should bring further success of this technology as a rapid prototyping tool.

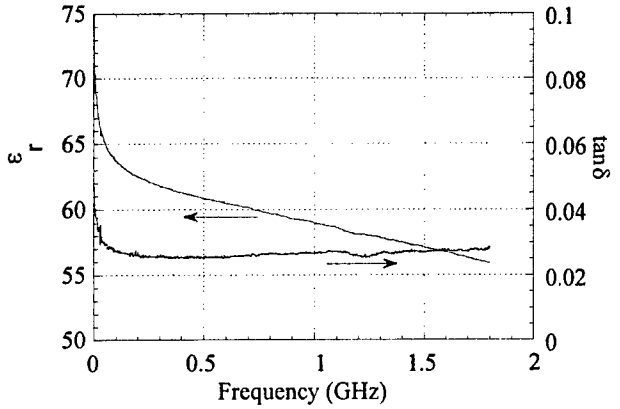


Fig.5 Frequency dependence of the dielectric constant and loss tangent of a BTO IDC deposited by MAPLE-DW on alumina.

6. Acknowledgements

We gratefully acknowledge support for this work by the DARPA-MICE program and the Office of Naval Research.

References

[1] J.M. Fitz-Gerald, D.B. Chrisey, A. Piqué, R.C.Y. Auyeung, R. Modi, H.D. Young, H.D. Wu, S. Lakeou and R. Chung: *Proc. Spring MRS, Symp. V, San Francisco, CA, 2000.*

[2] M.J. Renn, M. Essien, B.H. King and W.D. Miller: *ibid.*

[3] R. Pastel, P. Geiser, E. Nadgorny and A. Struthers: *ibid.*

[4] D.B. Chrisey, A. Piqué, R.C.Y. Auyeung, R.A. McGill, R. Chung, S. Lakeou, P. Wu, J. Fitz-Gerald, H.D. Wu and M. Duignan: Surface Engineering, "*Science and Tech. I*", ed. By A. Kumar, Y.-W. Chung, J.J. Moore and J.E. Smugeresky, (The Minerals, Metals & Materials Soc., 1999) pp.143.

[5] R.A. McGill, R. Chung, D.B. Chrisey, P.C. Dorsey, P. Matthews, A. Piqué, T.E. Mlsna, J.L. Stepnowski: *IEEE Trans. On Ultrasonics, Ferroelectrics and Frequency Control* **45**, (1998) 1370.

[6] J. Bohandy, B.F. Kim and F.J. Adrian: *J. Appl. Phys.*, **60**, (1986) 1538.

[7] J.M. Fitz-Gerald, A. Piqué, D.B. Chrisey, P.D. Rack, M. Zeleznik, R.C.Y. Auyeung and S. Lakeou: *Appl. Phys. Lett.*, **76**, (2000) 1386.

[8] B-S. Chiou, W.-Y. Hsu and J.-G. Duh: *IEEE Trans. on Components, Hybrids and Manufacturing Tech.*, **15**, (1992) 393.

[9] M.P. McNeal, S. -J. Jang and R.E. Newnham: *IEEE ISAF '96 Proc.*, 1996, pp. 837.

In Vivo Results of Corneal Surface Measurement with Optical Methods

Muhammad Muddassir GUALINI*, Hans STEINBICHLER**, Wajid Ali' KHAN***

*Pakistan Institute of Lasers and Optics, P.O. Box 1384, Islamabad, Pakistan,
E-mail: optica97@isb.comsats.net.pk

**Steinbichler Optotechnik GmbH, Am Bauhof, 4 – 83115 Neubeuren – Germany
E-mail: Steinbichler@steinbichler.de

***Al-Shifa Trust Eye Hospital, Rawalpindi, Pakistan
E-mail: wakhan@apollo.net.pk

We introduce some preliminary results of measurement on a simulated corneal surface. The possibility to devise a reliable mathematical model to simulate the corneal behavior in order to obtain target refraction (TR) is also discussed during and after Photo Therapeutic Keratectomy (PTK).

Keywords: Cornea, Excimer Laser, PTK, PRK, Shearography, Twymann-Green, FRAMESplus

1. Introduction

Excimer Laser Photo Refractive Keratectomy (ELPRK) has gained large popularity and acceptance nonetheless several limitations pointed out by the authors in previous works and also reported in literature [1, 2]. Patents have been registered to improve the technique by measuring the corneal geometry [3]. The introduction of innovative procedures, like LASIK and scanning, has improved the results. The present and future trend of ELPRK is in fact towards a more personalized surgery. Scanning heads and LASIK are constantly replacing classic PRK procedures. Today LASIK covers 70 % of the photo refractive procedures, 30 % is with the conventional PRK [4]. Therefore ELPRK will require more accurate devices capable to measure the vision parameters, like corneal curvature radii and diopters in order to maximize the number of patients obtaining TR.

T. J. Licznerski et al. announced using Twymann-Green interferometer (TGI) to evaluate in vivo the breakup characteristic of the human tear film[6]. J. Cambier and G. W. Rozakis patented an optical device that measures the corneal geometry in order to simulate excimer surgery. They introduced a mathematical model based on the diopters number D, and the relation D = 1/f, which is the physical definition of refractive power of a lens system with focal length f [3].

We firstly proposed adopting a combination of TGI and speckle interferometer [7,8] to accurately measure the geometry of the cornea surface along with the detection of the surface defects and/or anomalies in order to monitor and simulate the post operative evolution of PRK excimer laser procedures.

The present work reports some of our developments in the above outlined directions describing a device capable to measure with high accuracy all the corneal geometrical parameters as well as those directly limiting to obtain TR.

2. Modeling of the cornea

The impossibility to personalize the treatment accordingly to the real cornea conditions is one of the limits of current ELPRK procedures. ELPRK ablation is not as predictable as that with inorganic and organic materials, like metals or plastics. Corneal tissue has a nonlinear elastic behavior when the Intra Ocular Pressure (IOP) is varied [9]. The same behavior may also influence the reconstruction of the ablated corneal tissues. Corneal tissue elasticity changes from individuals due to many variables, being age one of the more important. The fact that properly dosed steroids help correcting results after ELPRK ablation may indirectly confirm the nonlinear elastic behavior. Sudden movements of the eyes during ELPRK ablation also sensibly affect TR. A more accurate, reliable and fast measurement device, useable in real time during the procedures, may improve the present limitations. Table 1 reports the latest results of TR at Al Shifa Trust Eye Hospital, Rawalpindi, Pakistan, the top line is the diopter range measured after six months from the ELPRK procedure, the bottom line the corresponding percentage of patients falling in the above range.

First International Symposium on Laser Precision Microfabrication, Isamu Miyamoto, Koji Sugioka,
Thomas W. Sigmon, Editors, Proceedings of SPIE Vol. 4088 (2000) © 2000 SPIE · 0277-786X/00/$15.00

Table 1 Eyes distribution versus corrective results.

Eyes	0.0 ± 0.5	±0.5 + ±1.0	±1.0÷±2.0	>±2.0
% over 2000	68.5%	25.6%	4.4%	1,5%

It appears that an accurate definition of the corneal geometry is a prerequisite to personalize the procedure increasing the flexibility of ELPRK procedures. This necessity has induced some authors to propose and patent optical methods that enable measuring the curvature radii of the cornea as well as other parameters like those that consider the "reactivity" of the specific patient's corneal tissue to the laser ablation. An explanation of Table 1 results is that corneal tissues are quite different not only from individuals but even in the same patient. Age, individual IOP, smoothness of the corneal surface and type of patient's activity have also to be considered beside the eventual misalignments of the optical axis, the values of the distance between the retina and cornea surface in order to correct at the TR conditions. The possibility of under correction or over correction remains as one of the limitation in ELPRK, no matter the type of procedure adopted. Moreover it has been demonstrated that biological debris produced during ELPRK ablation "fly" at supersonic speed, so intense is the stress applied to the corneal tissue by the laser pulses. Thus it is possible that intense stress may produce quite different results even in presence of slight variations of cornea characteristics.

We firstly suggested using a modified TGI with the option of speckle interferometry to detect the corneal geometry, its surface irregularities and behavior when stressed with a pressure tolerable by the patient determining the reaction time of the cornea tissues [1, 2]. The device high accuracy allows measuring the corneal geometry in a specified time interval after the application of the same stress conditions. For example the modified TGI can take a geometrical topographic measure of the corneal surface at the time $t_0 = 0$, when the stress is applied. Then a series of similar measures will be taken at regular time intervals, for example every one second with a 50 % duty cycle and a total period of two seconds. The time interval in which the cornea has returned at its original conditions can be defined as "reaction time" and gives an idea of the tissue elasticity when the same force is applied in the same position and under the same conditions to different eyes. The reaction times and the geometric measures determined experimentally maybe used in a mathematical model that considers time varying parameters. This model would be more close to the real cornea conditions than those presently available.

Assuming A, the cornea surface geometry before treatment. D, the desired corrected radius of curvature corresponding to the TR conditions. E the surface obtained after simulation. Surface E, is the final result of the simulation. It is obtained considering the cornea characteristics after simulating modifications of the surface A. Surfaces B represent the simulated surgical modifications induced on surface A. Surfaces C represent the measured geometry of a healed cornea. Simulation should enable to visualize TR conditions expressed by the equivalence C = D = E. The iterative process confronting surfaces D and E, after modifying A in B, can be made automatic and simulation carried out until the two surfaces, D and E, will be coincident. The real corrective data will be finally implemented in vivo. The same device will be used monitoring the corneal geometry modifications during the postoperative period and verify that effectively C = D = E. The postoperative measurements will also enable to quantify deviations between simulated and real surfaces, thus allowing to refine the model. Figure 1 and 2 describe the cornea in terms of A, B, C curves accordingly to the above definitions, for simplicity D and E are not reported. The curves are not in scale.

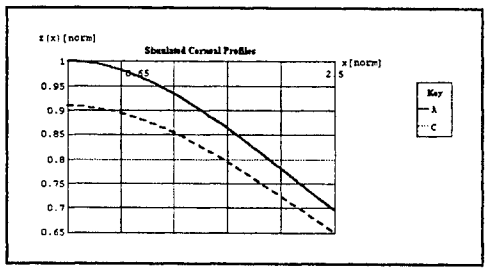


Fig. 1 Curves A before treatment, C after healing.

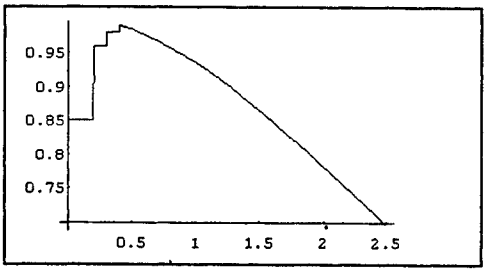


Fig. 2 Curve B immediately after MZ-PRK treatment.

Following the notation of von Bally[6] we can write for the curve A of figure 1:

$$x^2 + z^2 = (R_A)^2 \qquad (1)$$

while for the curve B we suggest the following set of equations:

$$z = a_z \qquad 0 \le x \le a_z$$

$$z = b_z \qquad a_z \le x \le b_z$$

$$z = c_z \qquad b_z \le x \le c_z$$

$$x^2 + z^2 = (R_B)^2 \qquad x \ge c_z, \qquad R_A \equiv R_B \qquad (2)$$

The radius C can be again described by an equation similar to (1) if the center is not translated but only shifted along the z-axis. This is the solution of the ideal correction. Again:

$$x^2 + z^2 = (R_C)^2 \qquad (3)$$

Position of the real curve C will depend on the different behavior of the corneal tissue on the x, y, z directions. We suggest here following a simple correlation between the curves B and C valid for the plane z, x but extendable to the space if necessary:

$$(x')^2 + (z')^2 = [k_x(t)]^{nx}.x^2 + [k_z(t)]^{nz}.z^2 \qquad (4)$$

where $[k_x(t)]^{nx}$ and $[k_z(t)]^{nz}$ express the time dependence of the non-linear deformation coefficients, being the non-linearity included in the unknown powers, nx and nz. One can solve (4) equating it to the fringes count for several couples of different deformations and different times so that $[k_x(t)]^{nx}$ and $[k_z(t)]^{nz}$ can be determined experimentally. Then the function can be approximated by a polynomial expansion.

3. Description of the Experimental Setup

Figure 3 shows the setup used for the preliminary tests. The laser beam is projected to the object plane with a suitable diameter obtained adjusting the beam expander. The beam is reflected from the surface and directed into the interferometer/speckle analyzer. A beam splitter divides the reflected beam in two components of almost the same intensity. Fringes are produced on the CCD Camera plane. Phase shift is introduced "sweeping" the position of mirror M_1, pzt mounted, while M_2 is fix. This setup enables to obtain interferometric measures of the divides the reflected beam in two components of almost the same intensity. Fringes are produced on the CCD Camera plane. Phase shift is introduced "sweeping" the position of mirror M_1, pzt mounted, while M_2 is fix. This setup enables to obtain interferometric measures of the object. Surface geometry without deforming it. The two components interfere on the CCD camera plane. Objective and diaphragm enhance the fringe contrast and reduce the environment light noise. The CCD output is connected with frame grabber board in the PC. The HV pzt driver is also an electronic board in the PC not visible in figure 3. The shutter on the laser output is essential to ensure working within the limits of the permitted exposure time [10].

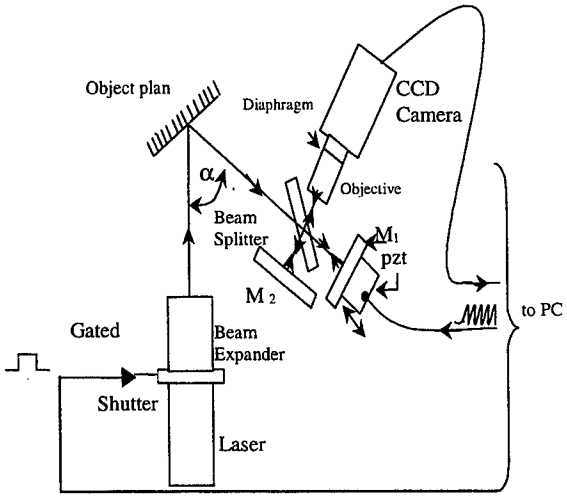


Fig. 3 The setup for measurement

4. Results on a simulated cornea

In order to simulate the cornea we have used a glass ball and the convex part of a teaspoon. Figure 4 shows the interference fringes obtained from the glass ball. Figure 5 shows fringes and speckle generated from the convex surface of a teaspoon.

In the case of the glass ball we have used a 5 mW HeNe laser and the angle $\alpha = 0$, so that the setup works as a pure Twymann-Green interferometer.

In the case of teaspoon we have used a 1 mW HeNe laser and an angle $\alpha \neq 0$.

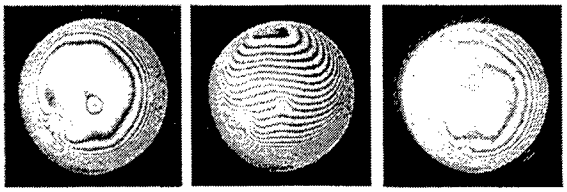


Fig. 4 Fringes from a glass ball.

5. Conclusions

We have introduced the use of a very accurate and safe laser interferometric and shearographic corneal

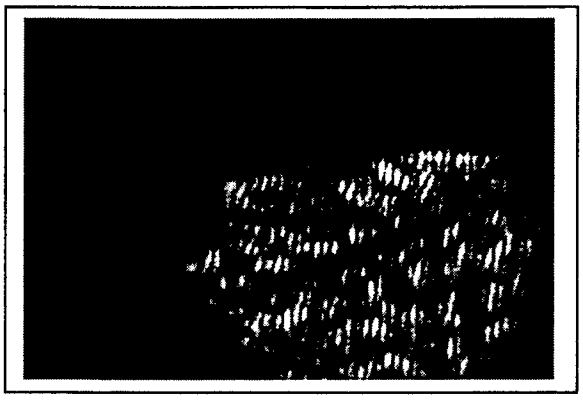


Fig. 5 Fringes and speckle from a teaspoon.

measurement device, which can measure the corneal geometry before, during and after ELPRK procedures. The device is combined with a mathematical model of the cornea that can simulate with proper accuracy its behavior during the post-op and forecast the expected final result customized for each patient. The development of such model, here only outlined in its general aspects, may have different complimentary approaches

6. Acknowledgements

The authors are particularly thankful to Mr. Mazhar Ishaque for drawings and type settings, to Miss Tanja Boheme for the great support in handling and coordinating e-mail, to Mr. Sixt and Engelsberger for the practical and experimental work. Finally to Dr. Ashraf Atta to have allowed the presentation of this work.

7. References

1. D.D. Garcia, C. van de Pol, S.A. Klein, B.B. Barsky, *Ophthalmic Technologies IX, SPIE Intenrational Symposium on Biomedical Optics, San Jose, California, January 23-29, 1999*
2. D.D. Garcia, B.B. Barsky, S.A. Klein, *Conference on Human Vision and Electronic Imaging", SPIE/IS&T Symposium on Electronic Imaging: Science and Technology, San Jose, California, January 24-30, 1998*
3. J. Cambier, G. W. Rozakis, *US Patent Number 5843970*
4. B.F. Boyd, *Highlights of Ophthalmology, International English Edition, N 2, Volume 27, 1999 Series*, pp 13 – 22
5. J. L. Calkins, *Sight Surveying Review, 42, 1972*, pp 133-144
6. T.J. Licznerski, H. T. Kasprazak, W. Kowalik, *Journal of Biomedical Optics, 4 (1), January 1999*, pp 176 – 182
7. M. M. S. Gualini, W. A. Khan, H. Steinbichler, *Europto'99, Munich, 1999*
8. M. M. S. Gualini, W. A. Khan, H. Steinbichler, *32nd ICALEO'99, San Diego, Ca, 1999*
9. G. von Bally, Ed., *"Holography in Medicine and Biology"*, Springer-Verlag, 1979

Removal Process of Metal Thin Films during Laser Rear Patterning

Tomokazu Sano and Isamu Miyamoto

Department of Manufacturing Science, Graduate School of Engineering, Osaka University
2-1 Yamada-Oka, Suita, 565-0871 Osaka, Japan
Email: sano@mapse.eng.osaka-u.ac.jp

In laser rear patterning, a thin film deposited on the supporting substrate is irradiated by a laser beam from the rear side of the thin film through the substrate to remove the irradiated area of the film. In this study, a KrF excimer laser with a pulse width of 30 ns and different values of fluences was focused onto metal such as a gold and a copper thin films, which were deposited on a fused silica substrate using the ion sputter deposition method. The intensities of the incident and the transmitted laser beams were measured simultaneously using photodiodes during the laser rear patterning. The results show that the film removal started after approximately 10 ns of laser irradiation under optimized deposition condition. During the laser rear patterning, it was found that the recoil force of the evaporation generated between the film and the substrate pressed the film. As a result, the molten part at the edge of the unirradiated part was peeled and ejected away by the momentum from the recoil force.

Keywords: laser rear patterning, metal thin film, material deposition, micro-deposition, removal process.

1. Introduction

Formation of micro-electrode and micro-electronic wiring are key techniques for production of high density, three dimensional, micro LSI chip. Techniques of filling conducting materials into micro holes with a few micro meter in diameter and deposition of conducting materials with a few micro meter in width are necessary for realization of the micro-electrode and micro-electrical wiring. Laser Rear Patterning (LRP) method has a potential to realize the above mentioned techniques. In LRP a thin film coated on a transparent supporting substrate, which is irradiated by laser through the substrate, is removed, transferred and deposited on the opposite substrate. LRP can be applied for both the removal patterning as well as widely used method that the laser is directly irradiated the thin film, and the additive patterning that removed material is transferred and deposited. LRP method has merits that the process can be done under atmospheric condition, room temperature and dry process. Although fundamental and applied studies have been done as Laser Induced Forward Transfer (LIFT)[1)-4)] and Laser Induced Back Ablation (LIBA)[5)6)], the removal process of thin film is not clarified yet. Removal mechanism of the thin film during laser front patterning, the thin film is irradiated by the laser and then removed, was analyzed at both the optimized and the excess fluences[7)8)]. In this study, removal mechanism of the thin film during LRP is investigated from the point of view that the dimension of the removed region and the deposited size. The transmitted laser during LRP was measured to investigate the delay time of the film removal from the laser irradiation. Deposition is carried out varying laser fluences, film thickness, and film to substrate distance.

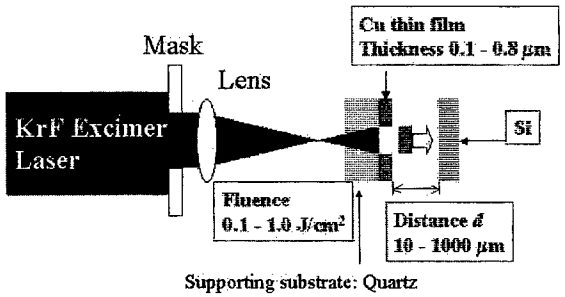


Fig. 1 Experimental setup for deposition of metal thin film using laser rear patterning method.

First International Symposium on Laser Precision Microfabrication, Isamu Miyamoto, Koji Sugioka, Thomas W. Sigmon, Editors, Proceedings of SPIE Vol. 4088 (2000) © 2000 SPIE · 0277-786X/00/$15.00

2. Experimental setup

KrF excimer laser with a pulse duration of 30 ns was irradiated from the rear side to remove the metal thin film. Cu thin film was deposited on a quartz glass using the ion sputter deposition method. The film thicknesses were 160 and 750 nm. Laser fluence was changed from 0.2 to 1.0 J/cm^2, and film-substrate distance was changed from 10 to 1000 μm. Si wafer was used as the substrates to be deposited.

Intensity of incident and transmitted beams were measured using highly sensitive PIN-Photodiodes as shown in Fig. 2.

3. Results and discussions

3.1 Measurement of intensity of incident and transmitted laser beams

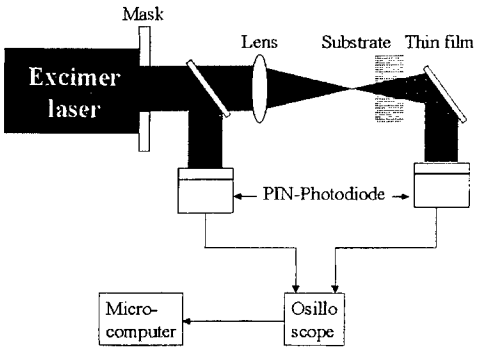


Fig. 2 Experimental setup for measurement of transmitted intensity during laser rear patterning.

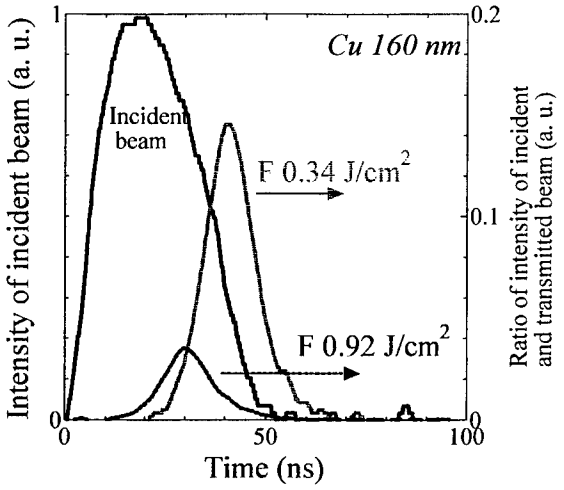


Fig. 3 Waveforms of the incident and the transmitted laser beams in case of Cu thin films with 160 nm in thickness.

Figure 3 shows the waveforms of the both incident and transmitted laser beam when Cu thin film with 160 μm in thickness was irradiated by the laser, of which fluence were 0.34 and 0.92 J/cm^2. The transmitted laser began to be detected at approximately 10 and 20 ns from the laser irradiation in cases of fluences of 0.92 and 0.34 J/cm^2, respectively. The reason why the transmitted laser in case of fluence of 0.92 J/cm^2 was detected earlier than that of 0.34 J/cm^2 is that the laser irradiated region reaches its melting and boiling point faster as the laser fluence is

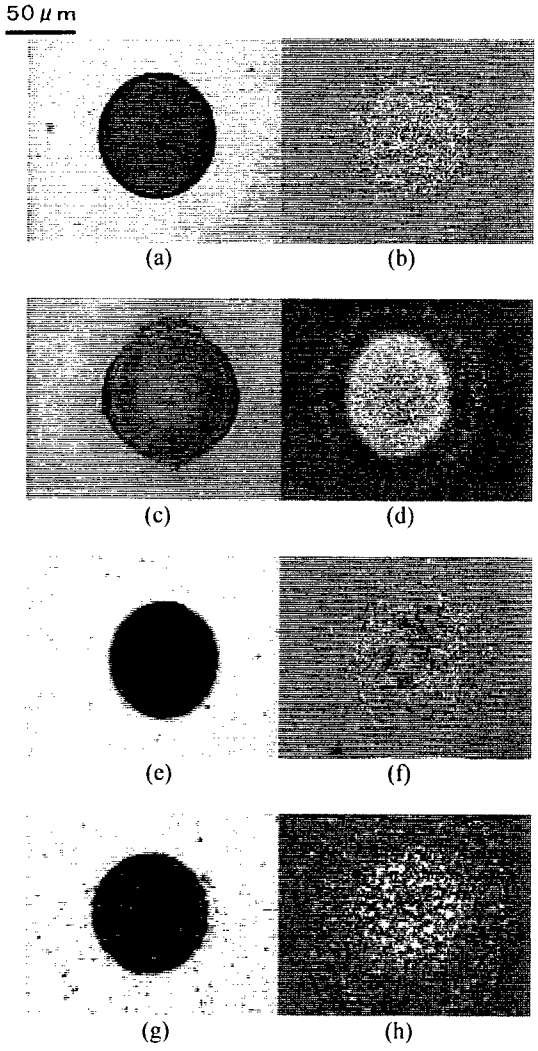


Fig. 4 Optical microscope images of the removed region of the films and the deposited materials deposited on the Si substrates. Film to substrate distance was 10 μm in each case. (a), (c), (e), (g); removed region, (b), (d), (f), (h); deposited material. (a), (b); film thickness 160 nm, fluence 0.34 J/cm^2. (c), (d); film thickness 160 nm, fluence 0.92 J/cm^2. (e), (f); film thickness 750 nm, fluence 0.34 J/cm^2. (g), (h); film thickness 750 nm, fluence 0.92 J/cm^2.

higher. On the other hand, in the front patterning the thin film circle is separated from the unirradiated region at approximately several hundreds of nanoseconds, and then the molten metal edge begins to move toward the center of the irradiated circle[7]. In case of the film thickness of 750 nm the intensity of the transmitted laser was 1/100 of that in this case. Fig. 4 shows the appearance of Cu deposited on the opposite Si substrates and the removed region of the film with a spot size of 140 μm. As shown in Fig. 4 (a) - (d), no particle and clear edge are seen in the removed region, and small grain size and high density deposition are achieved in case of film thickness of 160 nm. On the other hand, fragments which are not completely removed from the supporting substrate exist in the removed region in case of film thickness of 750 nm as shown in Fig. 4 (e) - (h).

3.2 Patterning dimension

As shown in Fig. 4(d), under optimized deposition condition a splattered ring is observed around the deposited circle, which consists of droplets of a size of several μm. The diameter of the splattered ring and the deposited circle are shown in Fig. 5 when Au thin film with 110 nm in thickness was irradiated by KrF excimer laser varying film to substrate distances and laser fluences with a spot size of 140 μm. The diameter of the removed region was 140 and 150 μm in case of the fluences of 0.16 and 0.37 J/cm^2, respectively. The diameter of the ring becomes larger as the fluence increases. Fig. 5 shows that the diameter of the splattered ring increases linearly in proportion to film - substrate distance at each fluence. On the other hand, the diameter of deposited circle was constant independent of the laser fluences. This means that the molten part detached at the edge of the unirradiated part flied away at an angle, which is dependent on the laser fluence. In addition, the same size of removed region as the spot size can be attained and the splattered ring becomes small as the laser fluence is low. Fig. 6 shows the appearance of the film removed by the irradiation of a KrF excimer laser at excess fluence using by front patterning method. The edge of the film is peeled from the substrate around the irradiated zone as shown in Fig. 6. The strong recoil force of vaporization presses down the molten metal to produce outward radial flow of the molten metal during laser front patterning at the excess fluences. On the other hand, no peeling and droplets can be seen in the film removed by using LRP at excess fluence as shown in Fig. 4(c).

3.3 Removal mechanism of thin film

Based on the above-mentioned results in the laser rear patterning, removal mechanism of the rear patterning under optimized deposition condition is shown in Fig. 7. During the laser pulse, the irradiated region is melted and

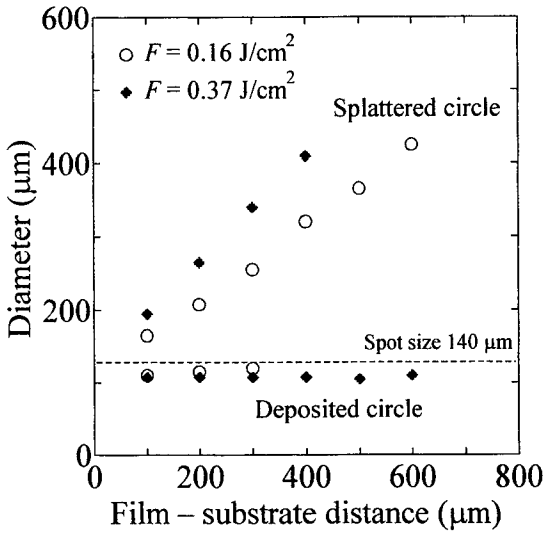


Fig. 5 Diameter of the splattered ring and the deposited circle varying film to substrate distances and laser fluences with a spot size of 140 μm.

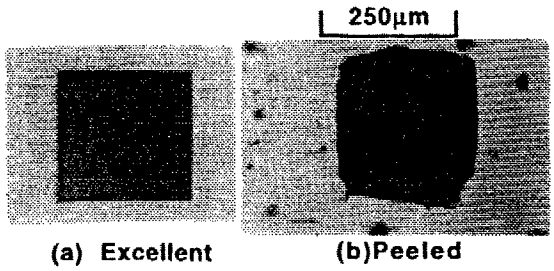


Fig. 6 Appearance of the Cu thin film removed by the irradiation of a KrF excimer laser at (a) optimized and (b) excess fluence using by front patterning.

evaporated, and then detached from the substrate by the recoil force due to evaporation. A part of melted region flows into the edge of the unirradiated region. Although the edge of the detached circle is driven toward the center by surface tension force, the film is broken into small clusters immediately after removal to make its surface energy minimum. The outer diameter of the circular disk consisting of molten clusters keeps constant as no external force exerts any more. The molten part at the edge of the unirradiated part flies away by the momentum at a given angle to produce. Eventually the diameter of the removed region in the film becomes larger than that of the laser irradiated region.

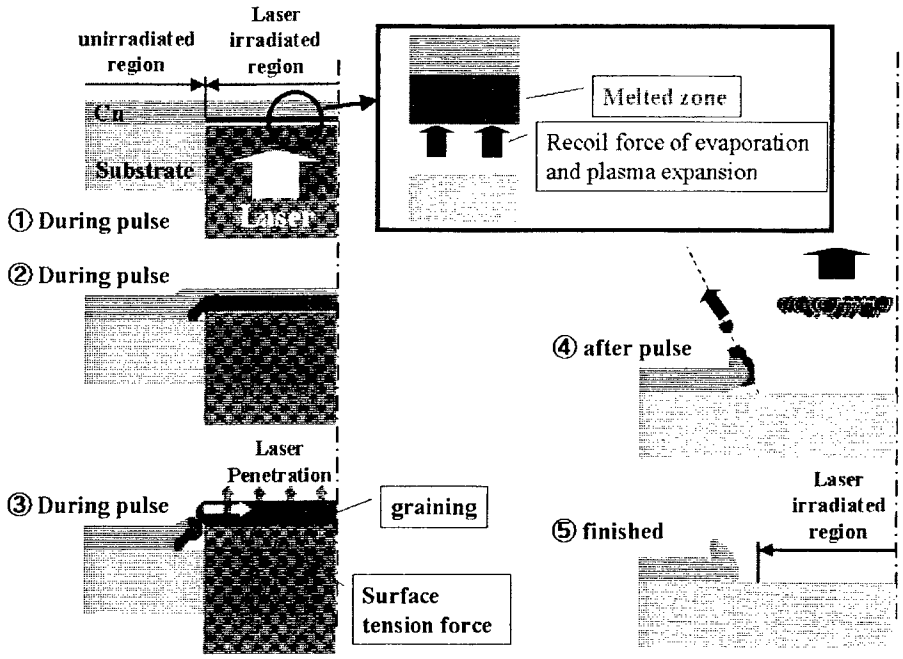


Fig. 7 Schematic illustration of removal process of thin film deposited on the supporting substrate under optimized deposition condition in the laser rear patterning.

4. Conclusion

The removal mechanism of metal thin film was analyzed in laser rear patterning with KrF excimer lasers. The obtained results are summarized as follows:

(1) High-density deposition with small grains is possible at optimized fluence by using LRP method.
(2) The difference of removal mechanism between laser rear and front patterning was clarified.

Acknowledgment

The authors wish to thank Mr. T. Nakayama, Mr. S. Asada and Mr. H. Yamada, Osaka University, for their assistance in performing the experiments, and Mr. Y. Tsukuda, Sanwa Kenma Co. Ltd., for his cooperation for preparing the thin film targets.

References

1) J. Bohandy, B.F. Kim, F.J. Adrian, A.N. Jette, J. Appl. Phys., 63 (4) 1158 (1988).
2) J. Bohandy, B.F. Kim, F.J. Adrian, J. Appl. Phys., 60 (4) 1538 (1986).
3) Z. Kantor, Z. Toth, T. Szorenyi, Appl. Surf. Sci., 86, 196 (1995).
4) Z. Kantor, Z. Toth, T. Szorenyi, Appl. Phys. A 54, 170 (1992).
5) A.B. Bullock, P.R. Bolton, J. Appl. Phys., 85 (1) 460 (1999).
6) A.B. Bullock, P.R. Bolton, J. Appl. Phys., 82 (4) 1828 (1997).
7) H. Hayashi, I. Miyamoto, Proc. of LIA, 80, 391 (1995).
8) T. Sano, I. Miyamoto, H. Hayashi, H. Ochi, Proc. of SPIE, 3933, 356 (2000).

Micro-cutting with pulsed fundamental mode Nd-YAG slab laser

T. Sidler, S.Favre, S. Benjamin, R.-P. Salathé
Institute of Applied Optics (IOA)
Swiss Federal Institute of Technology (EPFL-Switzerland).

Laser micro-cutting application performed with a zig-zag high power slab laser are presented. Most metallic, ceramic, glass and amorphous sheet materials of thickness up to 1mm can be processed with a minimum kerf width of 20 to 30 μm, depending on sheet thickness and material properties. With an advanced Nd-YAG zig-zag-slab laser, a pulse energy up to 300 mJ with a time duration of 200 μs can be obtained in a quasi gaussian fundamental mode beam (M^2 <1.5). The resulting laser beam, which has a very high brightness, is able to produce intensities up to 500 MW/cm^2 at a typical focal spot diameter of 20 to 30 μm. The mean output power of this laser (up to 15 W) permits cutting at speeds as high as 1mm/s (E_p =100 mJ, f_{rep} = 100 Hz, overlap 50%). Typical performances and applications for cutting samples with feature dimensions as small as 20 to 50 μm and small heat affected zones (< 3 μm) are presented.

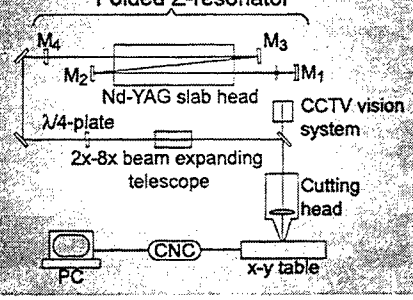
Institute of Applied Optics, Swiss Federal Institute of Technology - Lausanne

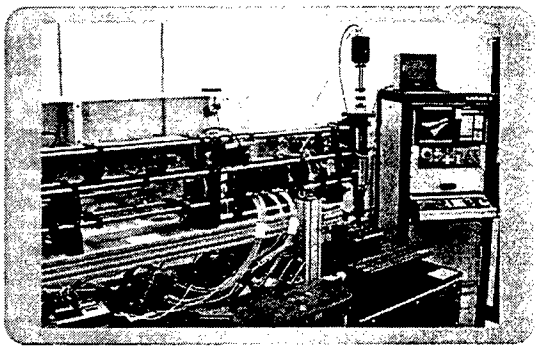
ÉCOLE POLYTECHNIQUE FÉDÉRALE DE LAUSANNE

Micro-cutting with pulsed fundamental mode Nd-YAG slab laser

T. Sidler, S. Favre, S. Benjamin, R.-P. Salathé

Set-up





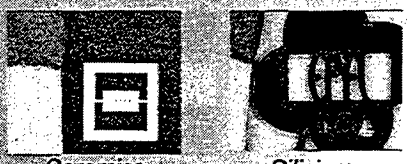
LASER DATA SHEET

Nd:YAG zig zag slab laser @ 1.064 µm
Gaussian beam: TEM_{00}, $M^2 < 1.3$
Pulse length: 100 µs to 5 ms
Pulse repetition: up to 300 Hz
Pulse energy: 10 to 500 mJ
Pulse power: up to 2 kW TEM_{00}
Focal lens for focalising on the sample: 100 mm
Focus diameter: $2w_0$= 12 - 60 µm
Intensity at focus: up to 500 MW/cm^2

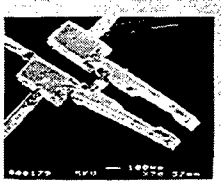
MATERIAL DATA SHEET

Most sheet materials such as stainless steel, aluminum, copper, silver, brass, glassy carbon, ceramic, glass, diamond, quartz, pyrex, silicon, GaAs wafer, etc...
Thickness from 10 µm to 1 mm depending on the material parameters.
Minimum kerf width up to 0.5 mm typically 30 µm
Heat affected zone 2-3 µm (Stainless Steel 0.5 mm)
Cutting speed typically 1.6 mm/s @ 100 Hz

Machining examples:



Ceramics *Silicium*



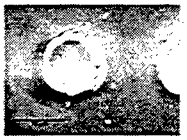
Stainless steel



Micro-gripper



Shape Memory Alloy

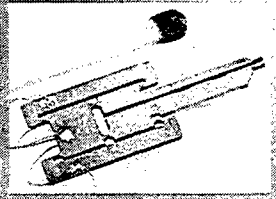


Input side

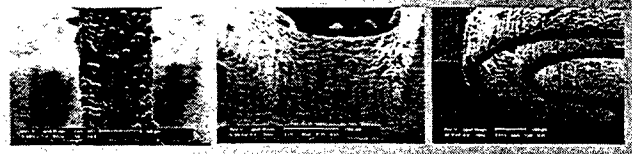


Output side

Glass



Piezo electric ceramics



NiTi detail of roughness

Author Index

Abeln, Tobias, 252, 256
Ahn, Min-young, 175
Akane, Toshimitsu, 70, 80
Andou, Satoshi, 191
Aoki, Naoko, 70, 80
Aoyagi, Yoshinobu, 70
Arai, Mikiya, 287
Asada, Shinsuke, 132
Ashkenasi, David, 17
Audouard, E., 48
Auyeung, Raymond C. Y., 393
Bachmann, Friedrich G., 220
Bado, Philippe, 140
Baets, Roel G., 327
Basting, Dirk, 118
Baubeau, E., 48
Bauer, Thorsten, 136
Bellouard, Yves, 160
Blom, Toon, 268
Bosse, L., 260
Campbell, Eleanor E. B., 17
Carey, Paul G., 73
Chen, Kevin P., 345
Chen, Z. Y., 307
Chiba, Teiichirou, 389
Chim, W. K., 232
Cho, Sung-Hak, 40
Chong, Tow Chong, 359
Chrisey, Douglas B., 393
Chung, Russell, 393
Clavel, Reymond, 160
Coosemans, Thierry, 327
Corkum, Paul B., 345
Courbon, M., 48
Dausinger, Friedrich, 252, 256
Delarbre, Erwin, 264
Du, Longlong, 168
Dubowski, Jan J., 55, 80
Ely, Kevin, 248
Enami, Tatsuo, 191
Endert, Heinrich, 201
Farson, Dave F., 248
Favre, Sébastian, 195
Fiebig, Michael, 118
Fitz-Gerald, J. M., 393
Fujikawa, Shuichi, 199
Fujioka, Tomoo, 284, 287
Fujishima, Susumu, 220
Fujita, Takeyoshi, 276
Fukumitsu, Kenshi, 216
Fukumoto, Ichirou, 84, 106
Fukushima, Tsukasa, 209
Fuqua, Peter D., 319
Furukawa, A., 140
Fushimi, Takashi, 284
Gedopt, Jan, 264
Gillner, Arnold, 260
Gotoh, Tamihiro, 351
Govorkov, Sergei V., 118
Gower, Malcolm C., 124
Grossmann, Sylvain, 268
Gualini, Muhammad Muddassir S., 272, 397
Hafez, Moustapha, 160, 268
Hammura, Kiyotaka, 70
Hanabusa, Mitsugu, 25
Hansen, William W., 319
Hartke, Kevin, 248
Hashidate, Yuji, 187
Hayakawa, Hirotoshi, 363
Hayashi, Ken-ichi, 44
Hayashi, Nobuya, 183
He, Yonghui, 240
Helvajian, Henry, 319
Herman, Peter R., 345
Hertel, Ingolf V., 17
Higashikawa, Kouji, 25
Higuchi, Sadao, 333
Hirao, Kazuyuki, 33
Hirose, Akio, 236
Hisada, Shigeyoshi, 276
Ho, Kai M., 98
Hoffmann, Patrik W., 337
Hong, M. H., 359, 371
Honma, Ryuichi, 295
Horisawa, Hideyuki, 280, 284
Horiuchi, Osamu, 341
Hoving, Willem, 268
Hu, B., 232
Huang, Huijie, 168
Ikeno, Junich, 341
Imai, Yoji, 311
Inmaru, Takahiro, 303
Inoue, Yoko, 199
Isaji, Kazuhide, 212
Ishii, Ken, 191
Itakura, Yasuo, 191, 205
Ito, Yoshiro, 94, 102
Itoh, Kazuyoshi, 44, 367
Janson, Siegfried W., 319
Jiang, Baocai, 168
Jiang, Jianfeng, 240
Jin, Guofan, 171
Jitsuno, Takahisa, 224, 355
Jonin, Christian, 48
Julliard, Karin, 268
Juodkazis, Saulius, 29, 51
Kamada, Kenji, 51
Kamata, Tatsuya, 276
Kamitani, Takayuki, 299
Karasaki, Hidehiko, 212

Kasai, Toshio, 341
Kato, Makoto, 212
Kawaguchi, Yoshizo, 355
Kawakami, Yuji, 228
Kawasa, Youici, 205
Khan, Wajid Ali', 397
Kimura, Seiichiro, 280
King, Kevin, 248
Kitamura, Naoyuki, 355
Kiyoku, Satoshi, 102
Kiyono, Satoshi, 385
Kobayashi, Kojiro F., 236
Kobayashi, Yuji, 187
Kojima, Tetsuo, 199, 209
Komura, Ryuusuke, 389
Konno, Susumu, 199
Korte, Frank, 136
Kramer, T., 260
Kubo, Hirokazu, 191
Kumagai, Hiroshi, 40
Kumagai, Toshiya, 311
Kurosaki, Yuichi, 102
Kuwahara, Gaku, 287
Kuzuu, Nobu, 355
Lakeou, Samuel, 393
Laporte, Pierre, 48
Le Harzic, R., 48
Lee, Cheon, 175
Lee, Hong-gyu, 175
Lee, Kyoung-cheol, 175
Liu, Liufa, 236
Liu, Wai Yip, 144
Lu, Dunwu, 168
Lu, Yong Feng, 232, 359, 371
Maeda, Mitsuo, 303, 333
Mai, Zhi Hong, 232
Malshe, Ajay P., 98
Manabe, Takaaki, 311
Marutani, Yoji, 299
Matsunga, Takashi, 191
Matsuo, Shigeki, 29, 51
Matsuzaki, Akiyoshi, 315
Mayer, Eric E., 118
Midorikawa, Katsumi, 40, 70, 80, 110, 359
Mikata, Hironari, 355
Misawa, Hiroaki, 29, 51
Miyamoto, Isamu, 1, 84, 106, 132, 244, 295, 401
Miyanagi, Naoki, 291
Miyoshi, Takashi, 385
Mizoguchi, Hakaru, 191, 205
Mizuta, Susumu, 311
Modi, R., 393
Molian, Pal, 98
Mori, Akira, 389
Mottin, Stephane, 48
Müller, Burkhard, 164
Muramoto, Junichi, 303
Murayama, Rina, 244
Naessens, Kris, 327
Nagatoshi, Hideaki, 212
Nakahara, Sumio, 276
Nakajima, Hiromasa, 284
Nakamura, Susumu, 94, 102
Nakata, Yoshiki, 303, 333
Nanri, Kenzo, 287
Naumov, Andrei, 345
Ng, Sandy, 345
Niino, Hiroyuki, 64, 311
Nikolaev, Sergey V., 179
Nishii, Jyunji, 29, 44, 367
Nishimae, Junichi, 209
Nishio, Satoru, 315
Nolte, Stefan, 136
Nomura, Shintaro, 70
Obara, Minoru, 40
Obata, Kotaro, 70
Ogura, Hiroshi, 187
Oguro, Isamu, 94, 102
Ohbu, Ayako, 191
Ohmura, Etsuji, 84, 106, 244
Ohta, Koji, 51
Ohta, Takeshi, 191
Oie, Tomonori, 216
Okada, Tatsuo, 303, 333
Okada, Toshiharu, 148
Okamoto, Yasuhiro, 291
Okoshi, Masayuki, 25
Okumura, Motoyoshi, 315
Olivetta, Lino, 268
Olowinsky, Alexander, 260
Ooie, Toshihiko, 1, 90, 307
Ootani, Masanori, 287
Osmanov, Rustem, 118
Ostendorf, Andreas, 136
Ozawa, Eiichi, 228
Pang, Lin, 171
Park, Seo-jeong, 295
Piqué, Alberto, 393
Radtke, Joachim, 252, 256
Ren, ZhongMin, 371
Rosenfeld, Arkadi, 17
Said, Ali A., 140
Sakakibara, J., 307
Salathé, René-Paul, 160, 195, 268
Sano, Tomokazu, 132, 401
Sasaki, Akira, 106
Sato, Hiroyasu, 315
Satoh, Saburoh, 183
Satoh, Yukio, 209
Sawaki, Daisuke, 341
Scaggs, Michael J., 118
Schwob, Hans-Peter, 268
Seto, Sachio, 287
Shakhno, Elena A., 179
Shihoyama, Kazuhiko, 140
Shimizu, Hiroki, 385
Shinozaki, Tatsuya, 90
Shirk, Michael D., 98
Sidler, Thomas C., 160, 195, 268
Sigmon, Thomas W., 73
Slobodchikov, Evgueni V., 118
Smith, Patrick M., 73

Song, W. D., 232, 371
Stamm, Uwe, 118
Steenson, David P., 144
Steer, Michael B., 144
Steinbichler, Hans, 272, 397
Stoian, Razvan, 17
Sucha, Gregg D., 201
Sugioka, Koji, 70, 80, 110, 359
Sugiyama, Tsutomu, 212
Sumitani, Akira, 191, 205
Sun, Hong-Bo, 29
Suzuki, Akiyoshi, 154
Suzuki, Toru, 191
Takahashi, Reiji, 220
Takeno, Shozui, 1
Taketani, Yoshiaki, 315
Tam, Andrew C., 380
Tamamura, Hisashi, 224
Tamura, Masataka, 280
Tanaka, Hirokazu, 191
Tanaka, Keiji, 351
Tanaka, Takao, 183
Tashiro, Yuko, 333
Terashima, Katsutomo, 191
Tetsuka, Masato, 287
Toet, D., 73
Tokumura, Keiu, 224, 355
Toma, Tadamasa, 44, 367
Tönshoff, Hans Kurt, 136
Toyoda, Koichi, 70, 80
Tsuchiya, Tetsuo, 311
Ueda, Kiyotaka, 333
Umeda, Hiroshi, 191
Uno, Yoshiyuki, 291
Utsumi, Takayuki, 106
Van Daele, Peter, 327
Van Hove, An, 327
Vanwassenhove, Luc, 327
Veiko, Vadim P., 9, 179
Verstuyft, Steven, 327
Wagner, Frank, 337
Wakabayashi, Osamu, 191, 205
Wang, Cai, 98
Wang, Jun, 64
Wang, Runwen, 168
Watanabe, Akio, 311
Watanabe, Mitsuru, 51
Watanabe, Takayuki, 191
Watanabe, Wataru, 44, 367
Weikert, Michael, 252, 256
Wickboldt, Paul, 73
Wiessner, Alexander O., 118
Wild, M., 260
Wu, H. D., 393
Wu, Minxian, 171
Xu, Yaohuan, 240
Yabe, Akira, 64, 311
Yajima, Hiroyoshi, 187
Yamabe, Chobei, 183
Yamada, Kazuhiro, 44, 367
Yamada, Osamu, 299
Yamaguchi, Iwao, 311
Yamaguchi, Shigeru, 284, 287
Yamasaki, Kazuhiko, 51
Yan, Yingbai, 171
Yan, Yonggen, 240
Yano, Tetsuo, 90, 307
Yasui, Koji, 199
Yasunaga, Nobuo, 284
Yoneda, Masafumi, 90, 307
Yoneda, Noriyuki, 276
Yoshida, Fumika, 205
Yoshida, Yoshikazu, 187
Young, H. D., 393
Yuan, Cailai, 168
Zhang, Jie, 345
Zhang, Tiejun, 187
Zhao, Jian Ping, 307
Zhao, Wansheng, 240
Zhao, Yongkai, 168
Zheng, Y. W., 371
Zhidkov, Alexei, 106